PAC

Proceedings of the

2003
Particle
Accelerator
Conference

Columbia River

Willamette River

PORTLAND, OREGON

BERKELEY LAB

APS

SLAC
STANFORD LINEAR ACCELERATOR CENTER

IEEE

Volume 2 of 5
pp. 743-1448

REPORT DOCUMENTATION PAGE

1. AGENCY USE ONLY (Leave Blank)	2. REPORT DATE	3. REPORT TYPE AND DATES COVERED
		Final

4. TITLE AND SUBTITLE

2003 Particle Accelerator Conference

Vol. 2

5. FUNDING NUMBERS

G

6. AUTHORS

variou

7. PERFORMING ORGANIZATION NAME(S) AND ADDRESS(ES)

IEEE

445 Hoes Lane, PO Box 1331

Piscataway, NJ 08855-1331

8. PERFORMING ORGANIZATION REPORT NUMBER

9. SPONSORING / MONITORING AGENCY NAME(S) AND ADDRESS(ES)

Office of Naval Research

Ballston Centre Tower One

800 North Quincy Street

Arlington, VA 22217-5660

10. SPONSORING / MONITORING AGENCY REPORT NUMBER

N00014-04-1-0417

11. SUPPLEMENTARY NOTES

12a. DISTRIBUTION / AVAILABILITY STATEMENT

DISTRIBUTION STATEMENT A
Approved for Public Release
Distribution Unlimited

12b. DISTRIBUTION CODE

13. ABSTRACT (Maximum 200 words)

The twentieth biennial Particle Accelerator Conference on Accelerator Science and Technology was held May 12 – 16, 2003 at the Hilton Hotel in Portland, Oregon. The Stanford Linear Accelerator Center and the Lawrence Berkeley National Laboratory organized PAC 2003, and it was held under the auspices of the Nuclear and Plasma Sciences Society of the Institute of Electrical and Electronics Engineers and the Division of Physics of Beams of the American Physical Society. The attendance was 1025 registrants from 21 countries. The Program Committee was co-chaired by Alan Jackson and Ed Lee. The program they arranged had opening and closing plenary sessions that covered the most important accomplishments, opportunities, and applications of accelerators. During the remainder of the conference there were parallel sessions with oral and poster presentations. In addition, there was an industrial exhibit during the first three days. The Proceedings present a total of 1154 papers from the invited, contributed orals, and poster sessions.

14. SUBJECT TERMS

Particle Accelerators and Colliders, Beam Dynamics, Magnets, RF Systems, Synchrotron radiation sources, Free Electron Lasers, Energy Recovery Linacs, Instabilities, Feedback Instrumentation, Pulsed Power, High Intensity Beams, Accelerator Applications, Advanced Accelerators.

15. NUMBER OF PAGES

3571

16. PRICE CODE

17. SECURITY CLASSIFICATION OF REPORT	18. SECURITY CLASSIFICATION OF THIS PAGE	19. SECURITY CLASSIFICATION OF ABSTRACT	20. LIMITATION OF ABSTRACT
Unclassified	**Unclassified**	**Unclassified**	

PAC 2003

PROCEEDINGS OF THE
2003 PARTICLE ACCELERATOR CONFERENCE

Portland, Oregon U.S.A.
May 12-16, 2003

Joe Chew, Peter Lucas, and Sara Webber, editors

Volume 2 of 5

SLAC **APS** ◈**IEEE**

20040311 167

ACKNOWLEDGEMENTS

Proceedings of the 2003 Particle Accelerator Conference

Volume 2

RHIC POWER SUPPLIES: LESSONS LEARNED FROM THE 1999 – 2001 RHIC RUNS*

D. Bruno[†], W. Eng, G. Ganetis, R.F. Lambiase, W.Louie, J. Sandberg, C. Schultheiss
Brookhaven National Laboratory, Brookhaven Science Associates, Upton, NY, 11973, USA

Abstract

The Relativistic Heavy Ion Collider (RHIC) was commissioned in 1999 and 2000. The two RHIC rings require a total of 933 power supplies (PSs) to supply currents to highly inductive superconducting magnets. These units function as 4 main PSs, 237 insertion region (IR) PSs, 24 sextupole PSs, 24 Gamma-T PSs, 8 snake PSs, 16 spin rotator PSs, and 620 correction PSs. PS reliability in this type of machine is of utmost importance because the IR PSs are nested within other IR PSs, and these are all nested within the main PSs. This means if any main or IR PS trips off due to a PS fault or quench indication, then all the IR and main PSs in that ring must follow. When this happens, the Quench Protection Assemblies (QPA's) for each unit disconnects the PSs from the circuit and absorb the stored energy in the magnets. Commissioning these power supplies and QPA's was and still is a learning experience. A summary of the major problems encountered during these first three RHIC runs will be presented along with solutions.

1 INTRODUCTION

The idea behind this paper is not to merely list detailed problems and solutions but to give an overview of the major problems and how they can be avoided the next time. Some detailed problems will be given but they will be used mostly as examples. Of course not all problems can be avoided completely but the more that are tackled up front then the less you have to deal with when the machine is running.

2 MANUFACTURING PROBLEMS

2.1 Some P.S. Manufacturer Problems

Dealing with manufacturers of the power supplies, at their facility, is where a lot of the problems you encounter can be taken care of up front.

- PSs, from the unipolar IR PS manufacturer, were very dependable when it came to the power components such as the transformers, chokes, and SCR's but the electronics they designed gave us no end of grief. We had problems with their voltage regulator card, firing card and DCCT electronics.
- The unipolar IR PS manufacturer also, had a problem with the way they energized the main contactor with a solid-state relay. This gave us problems because they did not place an MOV across the solid-state relay. A chattering main contactor would result.

- Some other problems encountered with the unipolar IR PS manufacturer were loose bus connections and mis-wiring to the isolation amplifier board.
- The bipolar PS manufacturer that was chosen needed to be shown how to design parts of the PSs. correctly. You should be worried about this manufacturer from the start but you may not have a choice because he may be the lowest bidder.
- The bipolar PS manufacturer was also very, very late with the PSs because of the small facility they had and limited experience with building these PSs.

2.2 Some P.S. Manufacturer Solutions

- For any manufacturer, closer monitoring at the facility would have helped solve many of these problems. Some of these problems could have been avoided if someone was up at the manufacturer watching a lot more of the manufacturing process and watching a lot more of the testing that was taking place.
- Choosing a manufacturer that is close also helps because it is easier to make more trips, even unscheduled ones.
- Also, with the unipolar IR PS manufacturer, if we had looked into the history of their electronics we would have seen they were not very dependable in this area. This could be difficult to do. Asking other people who have used their power supplies is a good way to gauge what kind of problems we might have had with their electronics. The other way to avoid this is to use manufacturers of firing cards and DCCT's (or whatever electronics it may be) that are known to be dependable and at the top of their field. You can also design some of the electronics yourself. This is helpful because all the cards are the same.
- Testing. It would have been great if the manufacturer would have been able to provide a load, which is as close as possible to the real load. This would bring out a lot problems that you wouldn't see until you get onto the real load. A burn in that lasts as long as 24 hours is a very good thing but sometimes not enough. Now the whole Power supply (PS) cannot be put into an environmental chamber but the electronics can and running those electronics with variations in temperature and humidity would have brought out a lot of problems for us much earlier.
- Always be suspicious of anything designed from scratch specifically for your PS Always check that standards are being met, such as the proper spacing for pins for a 208VAC connection.

- Use connections which are very reliable and don't fail if they are removed and replaced many times.

2.3 Some QPA Manufacturer Problems

- One of the biggest problems we had with the QPA's in the beginning were these QPA fan faults that were not real. The fans were working but the wrong type of switch was used. An AC switch was used instead of a DC switch, the wrong type of air vane was used and one problem we still have is that these switches are not sealed. Since we do not have the cleanest PS buildings we find that over time dust, dirt and moisture gets into the switches and they have to be removed and replaced because the contacts in the switch get dirty.
- Another problem we had with the QPA's were the transformers on the controller cards. These were mounted on the PC board. After the PC board was finished the manufacturer cleaned the boards off with water, which went into the transformers, and over time they started to fail. All of the transformers were replaced.
- These QPA's contain IGBT's. The IGBT's have IGBT driver cards, which the manufacturer designed. When there was an AC power dip one of the chips on this card would fail. The card was re-designed so this would not happen anymore.

2.4 Some QPA Manufacturer Solutions

Once again closer monitoring of the manufacturer could help catch more of these problems but not all. The transformers being contaminated by water someone may have seen if they were there more often. However, some of the design issues are usually left up to the manufacturer, such as, buying the right type of switch or designing an IGBT driver card correctly. It is difficult to catch all of these design problems when something as custom as this is being made. Looking at all aspects of the design in greater detail and asking a lot of questions about the design may have caught some more of these problems, if you have the time and the people. These problems cost the machine a lot of downtime and they have almost all been fixed. We are still looking at replacing the switches with sealed types. A burn in for an extended period of time might have also caught a lot of these problems.

3 SYSTEM INTEGRATION PROBLEMS

3.1 PLC/Node Card/Fiber Optic Interface Card

In order to test these power supplies locally the control system must be up and running and you need a laptop or a terminal nearby to send commands from. The commands are OFF, STANDBY, ON or RESET. These start from the Front End Computer (FEC) go to the PLC and then to a node card, which distributes the commands to as many as 12 different power supplies. The fiber optic interface card receives its signal from waveform generators, which reside in the FEC and then convert this signal to an analog signal to run the PSs up in current. There has been many times where one could not test the PSs. locally because the control system was down. There should be a way of just going up to a PS and plugging in one connector and controlling the whole PS from a laptop computer without any dependence on the control system. This would have saved a lot of time. If this did exist it would still be difficult to use in a p.s. setup that exists in RHIC because of something called the quench link. Since many of the PSs are nested, those nested PSs must all trip off if there is a p.s. fault or a magnet quench. Testing PSs individually still requires the quench detection system to be up to protect the magnets and the PSs. However, there are some PSs that are not nested and those could be tested locally without being as dependent on the control system.

3.2 Software Level Diagnostic Tools

In a nested p.s. system like this the more tools you have for determining what caused the quench link to drop the better off you are. Having these tools as early as possible also helps tremendously. We did not have all of these at the beginning and that made finding problems much more difficult and time consuming. Here are some of the tools, which we do use now:

- There is a page called a Quench Summary page, which tells you which building drops first when the main quench link drops. We did have this tool during the first run.
- There is a new tool called a Timing Resolver. After you have determined what building dropped the link first, the Timing Resolver will tell you what brought the link down first in the building you are looking at.
- There is something called a Post Mortem viewer. This saves all of the analog PSs setpoint, current, voltage and error signals for 3 seconds before a quench link trip and 1 second after this trip. Using this you can often determine which p.s. caused the link to drop in the building first. This tool also helps in troubleshooting the problem. This data is saved at 720Hz.
- There is a tool called snapshot, which is used for PSs on and off the main link. This gets triggered on any p.s. fault and saves the same four waveforms to look at for troubleshooting purposes. It saves the data for a longer period of time at 30Hz. There is not as much detail here as the 720Hz data but you have a much longer time span you are looking at.
- There is a tool called snapramp, which stores all of the ramps for all of the PSs. This allows you to see how the p.s. is performing while ramping. It also allows you to compare ramps from one p.s. to another p.s.
- There is a tool called BARHSOW, which also saves the ramps of the PSs, and this allows you to compare many different ramps of the same p.s.

- There is a tool called PSCOMPARE, which calculates the difference between whatever analog signals you select and they can also be compared against the wfg signal that is sent to the p.s.
- There is an Alarm Log as well which gives you the history of the p.s. faults
- There is something called QDPLOT which is associated with the quench detector and the magnet voltage taps and the p.s. current signals. This is used to determine if a magnet has quenched. This has been made more user friendly by sending information on which magnet has quenched to a Real Quench page that anyone can read.
- There is a page called PSALL that allows you to look at all of the RHIC PSs in both rings by building or p.s. type.
- The procedure for bringing the main quench link up, before the PSs are even turned on, is not simple and takes a long time when done manually. Only an expert was able to do this. Now programs have been written to do all of these steps automatically. They are still being improved upon.

4 TESTING

Testing at the manufacturers facility is very important and the more that is done the better. However, once we received the PSs it was even more important to run the PSs on the real load and in real building (environmental) conditions for at least two months. Just determining what time constants were needed for the unipolar nested IR PSs, and installing these time constants, took about 2 weeks. They were not optimized at the time and we are still going back and doing this today. Many problems were encountered because we were learning about all of the new p.s. problems and we were trying to integrate the PSs into the whole system, which was brand new. This system integration included not only p.s.' but also QPA's, the quench detection system (quench link), waveform generators, fiber optic interface cards, an MADC (analog readback) system, and a NODE CARD to PLC system for p.s. controls. These are the main ones but problems were found with each and every one of these systems, some of which we are still trying to correct 4 years later. Not all of them are big problems but they still need to be dealt with. Having people available from all of the different groups while this testing is going on is also a big help. Extended burn in times is a high priority test and even turning off and on the circuit breaker feeding the equipment while the equipment is running is a good idea to see how well the equipment survives. This would simulate power failures.

5 SUPPORT

During the construction phase there were a limited number of engineers and technicians. Some of these engineers and technicians stayed on during normal operations and they were the ones that would keep the power supplies running at first. This needed to change and it slowly is changing. At first only the engineers could fix the problems because they did not know what the problems were. After learning what the major problems were the technicians would be called in to fix the problems with or sometimes without the engineers. The next step was to write procedures and train the support people on shift 24 hours a day to make the repairs, if they were routine, and after consulting with the engineer. This has been a slow process but it is happening. During this last run a lot of progress has been made and the support people on shift have been making a lot of the more of the routine repairs after consulting with the engineer. Then again a lot of the major problems have been fixed so the workers on shift have not had as many problems to deal with. Many procedures have been written to assist with these repairs. A web page for the collider electrical ps. group has been developed so anyone can get to these procedures and any other documentation that deals with the PSs or QPAs. The web page for the Collider Electrical PS Group is **http://www.c-ad.bnl.gov/ceps/default.htm.**

6 DOCUMENTATION

Documentation of existing PSs, QPA's or whatever is being used in the system is very important not only to the engineer but almost more important to people who are not familiar with the equipment. If you are responsible for a piece of equipment and you go on vacation then someone else must know where the documentation is to fix it and the documentation must exist, in a readable format.

Documentation of each and every problem that creates machine downtime must also be done and this in itself can be a full time job. From this documentation many of our major shutdown lists get generated to fix the problems that cost the machine downtime. A philosophy of documenting, and understanding each and every fault must be followed so that all problems that exist can be accounted for and fixed. This will lead to an improvement in machine reliability

7 CONCLUSION

There are many things that can be done the second time around to reduce the number of problems we had when we commissioned and ran the RHIC PSs and QPA's but without the time and the people it would still be very difficult. That is why it is so important to choose the right manufacturer for the job, pay close attention to their design and do as much testing as you can at their facility.

BOOSTER MAIN MAGNET POWER SUPPLY IMPROVEMENTS FOR NASA SPACE RADIATION LABORATORY [#] AT BNL [*]

I. Marneris, K.A. Brown, J.W. Glenn, A. Mc Nerney, J. Morris, J. Sandberg, S. Savatteri.

Brookhaven National Laboratory, Upton, New York 11973 USA

Abstract

The NASA Space Radiation Laboratory (NSRL), constructed at Brookhaven National Laboratory, under contract from NASA, is a new experimental facility, taking advantage of heavy-ion beams from the Brookhaven Alternating Gradient Synchrotron (AGS) Booster accelerator, to study radiation effect on humans, for prolonged space missions beyond the protective terrestrial magnetosphere. This paper describes the modifications and operation of the Booster Main Magnet Power Supply (MMPS) for NSRL applications. The requirement is to run up to 1 sec flattops as high as 5000 Amps with 25 % duty cycle. The controls for the Main Magnet Power Supply were modified, including the Booster Main Magnet application program, to enable flattop operation with low ripple and spill control. An active filter (AF) consisting of a +/- 120 volts, +/-700 Amps power supply transformer coupled through a filter choke, in series with the Main Magnet voltage, was added to the system to enable further ripple reduction during the flattops. We will describe the spill servo system, designed to provide a uniform beam current, during the flattop. Results from system commissioning will be presented.

PARAMETERS

The Booster MMPS consists essentially of six pairs of thyristor controlled power supplies connected in series (the actual implementation is in 2 stations). Each pair is a 24 pulse controlled rectifier, rated at +/- 1000 volts dc, see Figure 1. For NSRL application only IAB and IIAB power supplies are used, because they are rated for 5000 Adc, while the rest of the units are rated for 2800 Adc. During the flattop only IAB unit will be on while IIAB is in bypass. The key parameters for the Booster MMPS are shown in Table 1.

Table 1: Booster MMPS ratings

Voltage dc max at 2800 amps dc max	+/- 6 kV
Voltage dc max at 5000 amps dc max	+/- 2 kV
Current dc max at +/-6000 V dc max	2800 A
Current dc max at +/-2000 V dc max	5000 A
Fundamental Ripple Frequency	1440 Hz
Magnet Resistance (R)	0.107 Ω
Magnet Inductance (L)	0.145 H
Nominal pulse rep. Rate for NSRL	4 sec
Nominal Flattop for NSRL	1 sec
3600 KVA Transformer primary current rms	150 A

Even though the units are operated as 24-pulse controlled rectifiers, the ripple requirement at flattop is very stringent. Note that running the power supply for NSRL application at 5000 A, with 1 sec flattop and a repetition rate of 4 sec, the 3600 KVA transformer's primary current was measured to be 145 A rms, which is very close to the rating of the transformer see Table 1. For that reason the Nominal pulse repetition Rate for NSRL was set to 4 sec with a Nominal Flattop of 1 sec, under the worst case flattop current of 5000 A.

ALGORITHM MODIFICATIONS

As noted in the previous paragraph, the Booster MMPS consists essentially of six pairs of thyristor controlled power supplies connected in series. There are bypass SCR's across every pair, except pair IAB. There is a Booster application program that calculates 6 voltage references and one current reference, based on a required magnetic field pulse. If the required magnet voltage is 2000 volts as it is the case for NSRL application, only pairs IAB and IIAB are used. The rest of the pairs are in bypass mode, meaning that the bypass SCR's are turned on automatically. During the 5000 A flattop however, the flattop voltage is 535 volts dc. With the original algorithm of the Booster application program, unit IIAB was firing at 0 volts during the flattop, and unit IAB was firing at 535 volts. As a result the ripple from unit IAB was added to the ripple from unit IIAB and this resulted in unnecessary voltage ripple during the flattop. Note that the most contribution to beam spill modulation, is due to the voltage ripple of the Booster MMPS during the flattop. The Booster application program, was as a result modified, to place unit IIAB in bypass mode during the flattop, since the total voltage needed 535 volts dc, was accommodated by unit IAB. At the end of the flattop however, unit IIAB had to be turned on to ramp down the current, using –1000 volts. For that reason the Booster application program was also modified, so that unit IIAB's voltage reference was becoming positive for 50 msec with an amplitude of 100 volts to commutate the bypass SCR off and then was going negative to –1000 volts.

ACTIVE FILTER DESIGN

As mentioned above, one of the most critical contributions to beam spill modulation, is due to the voltage ripple during the flattop of the Booster MMPS. The fundamental frequency at flattop is 1440 Hz.

However we have harmonics mostly at 60 HZ, some at 120 Hz, 180 Hz, 240 Hz, 300 Hz and 360 Hz, see Table 2. The damped passive filter at the output of the MMPS is a 40 db per decade filter with the 3-db point set to 400 Hz. As a result this filter attenuates frequency harmonics above 400 Hz without any attenuation at frequency harmonics below 400 Hz. The MMPS voltage ripple requirement by the spill, is an order of magnitude of 1 to 3 volts peak, for frequencies below 500 Hz. Therefore, in order to create a filter with the robustness required by the continuous and flexible operation of the Booster, it was decided to use a series transformer/choke as the coupling element to the MMPS circuit. Note that this design is already implemented as part of the AGS MMPS for the same reasons, with great success. The idea was to derive the ac component of the Booster MMPS voltage ripple during the flattop and inject it, 180 degrees out of phase as a voltage reference, into a voltage regulated power supply, connected to the series transformer/choke with the Booster magnets. As a result the coupled voltage through the transformer/choke would cancel out the actual Booster MMPS voltage ripple. A voltage regulated power supply rated at +/-120 Vdc, +/-700Adc, drives the series transformer/choke. The ac ripple during the flattop of the Booster MMPS, is fed into tuned filters with adjustable gains and phases, and the output of the tune filters drives the power supply. The tuned filters are tuned to correct 60 Hz, 120 Hz, 180 Hz, 240 Hz, 300 Hz, and 360 Hz. The power driver is a commercial, bipolar, 4-quadrant, switch mode power supply. The switching frequency is ~44 kHz, which results in a constant voltage full power bandwidth of 1.5 kHz. The input voltage is 480V three phase and can be disabled through a fuse disconnect switch. The back EMF from the Booster MMPS while the Booster MMPS is pulsing at +/- 6000 Vdc, is 20 Vdc peak-to-peak. The inductance of the transformer/choke was measured to be 25 mH and the resistance of it was measured to be 100 mΩ. Figure 1 is a block diagram of the overall system.
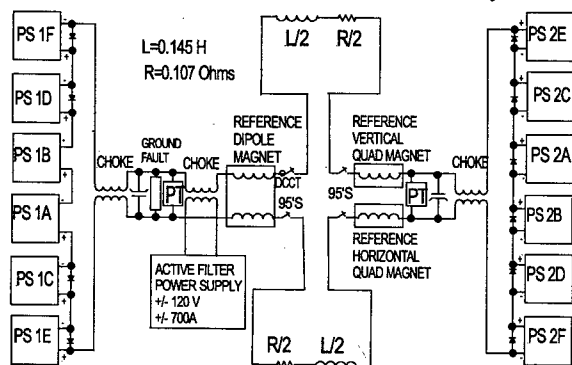
Figure 1: Booster MMPS block diagram

ACTIVE FILTER RESULTS

The active filter power supply system was fully commissioned with very encouraging results. We run a 3000 amps NSRL cycle for the Booster MMPS, with 0.5 sec flattop and a repetition rate of 5 sec. This cycle was being used to commission the NSRL extraction line. With

the active filter power supply off, we measured 55 volts peak to peak, magnet voltage ripple during the flattop. See oscilloscope Figure 2. Then we turned on the active filter power supply and independently adjusted the gain and phase of the tune filters feeding the active filter power supply for 60 Hz, 120 Hz, 180 Hz, 240 Hz, 300 Hz and 360 Hz. Oscilloscope Figure 3, shows the magnet voltage ripple during the flattop to be 27 volts peak to peak from 55 volts previously stated. Figure 3 also shows the active filter power supply voltage of 230 volts peak to peak, coupled through the transformer/choke into the main magnet voltage. The major component as can be seen is 60 Hz. Table 2, shows the magnet peak voltage ripple as a function of frequency, as measured by a spectrum analyzer with the active filter on and off, at the flattop current of 3000 A. Note that the MMPS 60 Hz harmonic was improved by a factor of 10. The rest of the MMPS harmonics were improved by a factor of 4 to 7 depending on the frequency component. Figure 4, shows a 1×10^{10} protons, 300 msec extracted beam as measured by an ion beam chamber, with the active filter power supply off. Figure 5 shows the 1×10^{10} protons 300 msec extracted beam as measured by the same ion beam chamber, with the active filter power supply on. Note that the 60 Hz ripple on the extracted beam was improved by a factor of 4.5.
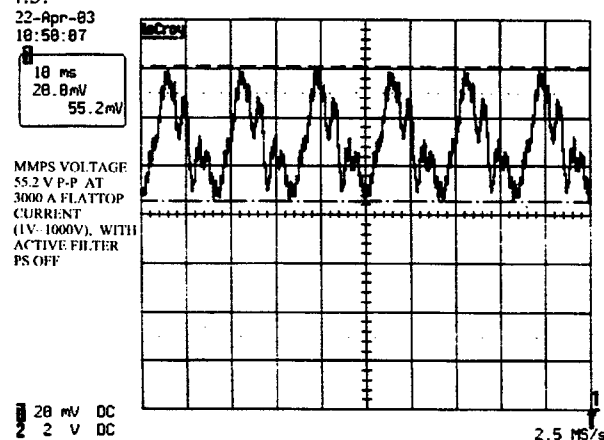
Figure 2: MMPS Flattop voltage, Active filter OFF
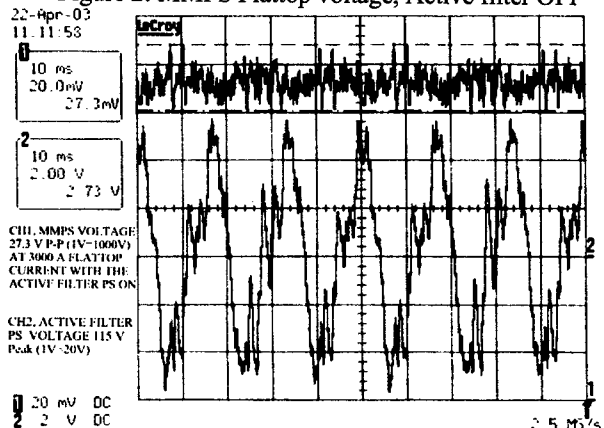
Figure 3: MMPS Flattop voltage and Active filter power supply voltage, Active filter ON

Table 2: MMPS Flattop voltages, Spill harmonics, Active filter ON and OFF (BLUE= Corrected frequencies)

Frequency (Hz)	MMPS Flattop Voltage Peak, At 3000A, Active filter OFF	MMPS Flattop Voltage Peak, At 3000 A, Active filter ON
60	16.38	1.56
120	7.0	0.96
180	3.06	0.48
240	3.78	0.54
300	2.4	0.54
358	0.84	0.12
378	1.95	0.48
420	2.4	1.2
720	0.84	1.32
1082	2.4	4.2
1440	4.44	6.3
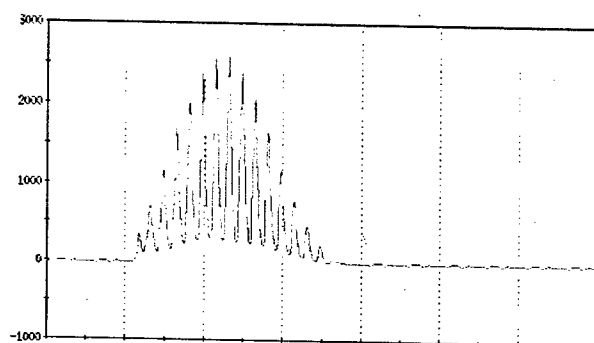
Figure 4: 1×10^{10} protons, 300 msec Beam spill, AF OFF
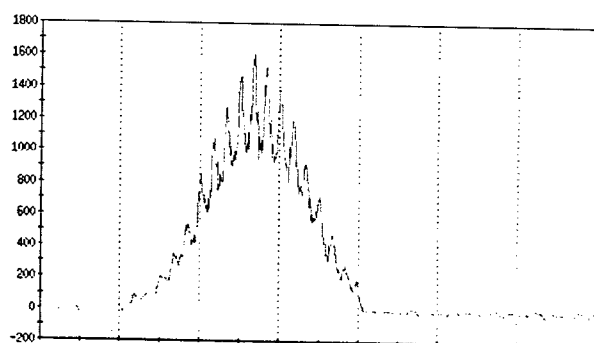
Figure 5: 1×10^{10} protons, 300 msec Beam spill, AF ON

SPILL SERVO

The spill servo is a feedback loop used to dynamically adjust the MMPS flattop current in order to ensure a uniform beam spill with constant spill length. Figure 6 is a block diagram of the system. The Booster spill servo is identical to the AGS spill servo. It has been built but not been fully commissioned yet. Since the Booster MM time constant is 1.35 seconds, it has a corresponding load breakpoint frequency of 0.12 Hz and thus can control very well the average spill rate and spill length. There is a 0 to 10 volts Booster Circulating Beam monitor (CBM) signal, coming to a sample and hold circuit in the spill servo. The CBM signal is sampled at the timing event called spill

start, which is usually 50 to 100 msec after the beginning of the flattop. The sample and hold, retains this value until another timing event comes in, called the end of flattop. This square wave signal is then multiplied by another 0 to 10 volts signal called spill rate. This signal through some amplifier gain, constitutes the actual spill reference of the spill servo loop. Once extracted beam is established, an ion chamber spill monitor intensity signal is used for measurement and for feedback. An error amplifier is then used to subtract the ion chamber spill monitor signal from the spill reference. The error signal is multiplied with another 0 to 10 volts signal, coming in the spill servo called the spill gain, which sets the gain of the loop remotely. This error signal is switched in only during the flattop and is being added to another signal coming in the spill servo, called the spill function. This signal is a 0 to − 10 volts square wave signal. The addition of these two signals goes through an integrator, which starts integrating at the beginning of the flattop and is being reset at the end of the flattop. The output of this integrator through some gain, is being added to the current error of the current loop of the Booster MMPS. Thus the MMPS flattop current is dynamically adjusted, in order to ensure a uniform beam spill during the flattop. Provisions are also made to learn what the spill error signal is through a data acquisition device and then play it back into the spill servo, without using the spill monitor feedback signal. This requirement, was set by NASA. Note that this provision does not exist in the AGS spill servo.
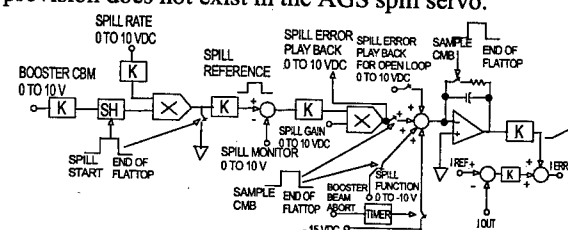
Figure 6: Booster MMPS Spill Servo

CONCLUSION

The algorithm modifications and the active filter have been fully commissioned. The 60 Hz ripple on the extracted beam was improved by a factor of 4.5. The 120 Hz, 180 Hz, 240 Hz, 300 Hz and 360 Hz components, were improved by a factor of 5 to 7 depending on the frequency. The spill servo has been built and is in the process of being fully commissioned.

ACKNOWLEDGMENTS

REFERENCES

[1] The active filter voltage ripple correction system of the Brookhaven AGS Main Magnet Power Supply. (WAR11) 1995 Particle Accelerator Conference.

LIGHT TRIGGERED THYRISTOR CROWBAR FOR KLYSTRON PROTECTION APPLICATION

J.-P. Jensen, W. Merz, DESY, Hamburg, Germany

Abstract

High power klystrons have to be protected in case of arcing or other failures. In most applications this is achieved by fast closing switches operating in parallel to the klystron path. These switches are known as crowbars. Most commonly used crowbar switches are sparkgaps, thyratrons and ignitrons. Recent progress in the development of high power semiconductors introduces the possibility to apply semiconductor closing switches as crowbars. The most promising approach is the application of the Light Triggered Thyristor (LTT). This especially is interesting for high power high voltage dc installations, like hvdc klystron power supplies with appropriate protection requirements. This paper describes a solution using series connected LTTs as a closing crowbar switch. Static and dynamic behaviour of the thyristors are introduced. The special requirements regarding the crowbar applications are pointed out. Results of a first prototype are presented to replace sparkgaps within an existing installation, where very high charge transfer capability has to be achieved.

INTRODUCTION

Despite recent attempts to introduce opening switches for klystron protection applications the closing switch approach is still the most commonly used. This is effected by the possibility to dump all the stored energy of the main circuit elements. This regards to lumped elements and parasitic elements respectively. Several high voltage switching technologies have been in use for years. Significant progress in high power semiconductor technology opens up new possibilities. The development of the Light Triggered Thyristor looks attractive for high voltage applications. These thyristors were developed for HVDC links in the power distribution industry. Improvements in their dynamic switching parameters made them suitable for high dI/dt requirements. Furthermore the optical gate control allows convenient series connections limited only by the quality of the applied optical fibre and its appropriate length.

LTT-CHARACTERISTICS

Light Triggered Thyristors are characterized as their electrically triggered counterparts. Except the triggering is achieved by a laser pulse applied to the integrated amplifying gate structure. The main electric parameters of LTTs for phase control applications are attractive in high voltage and high surge current capability. But they suffer from poor dI/dt values, which is required in crowbar applications. The break-through was made with the dedicated modification of the resistive area within the optical gate structure of the thyristor pellet [1]. This leads to application specific thyristors with hard switching behaviour. The result is a optimized thyristor combined with appropriate operating conditions. This method can be summarized as follows:

- Reduced voltage level to about half of the nominal value during dc operation, which results in significant lower off-state currents and minimizes the probability of charge carrier generation initiated by cosmic radiation.
- Reduced operating temperature leads to further reduction of the off-state current, which simplifies voltage balancing requirements in series connected thyristor assemblies.
- Modified gate resistor value gives the possibility of higher dI/dt and pulse currents.
- Increased optical power of the applied gate pulse leads to further improvement of pulse operation.

The general dependencies of the off-state current on voltage and temperature are given by the manufacturer [2]. The reduction of the off-state current for dc operation combined with the modification of the optical gate and reduced operating temperature are the most important steps toward the application of LTTs for klystron protection. The significant thyristor parameters are pointed out in the following table.

Table 1: Typical parameters of a LTT compared to its hard switching version.

	T1503N 75T (STANDARD)	T1503NH 75T S02 (HARD SWITCH)
V_{DD}, V_{DR} [V]	7500	7500
I_{TAV} [A]	1760	1760
I_{TSM} [kA]	40	40
I_D [mA]	500 @7500V/120°C	**0.8 @4000V/50°C**
di/dt $_{max}$ [A/µs]	1000	**5000**
$I_{peak-pulse}$ [A]	not specified	**5000**
$P_{optical\ gate}$ [mW]	40 @ 10µs	**100 @ 10µs**
t_{don} [µs]	5	3...4

Measured thyristors show I_D-values in the range between 100µA and 400µA instead of the promised 800µA. This gives an additional margin regarding static voltage balancing requirements. The improved dI/dt capability is attained by the appropriate integrated gate resistor value.

SPECIAL REQUIREMENTS FOR CROWBAR APPLICATIONS

Special requirements for crowbar switches used in klystron protection circuits can be summerized as follows.

- Continuous high voltage dc operation without self breakdown.
- High pulsed currents and high dI/dt during the starting phase of the capacitor discharge.
- High charge transfer capability due to large smoothing capacitors and the follow-through current of the power supply.
- Wide range of dc operating voltages to ensure protection during the power-on procedure of the power supply.
- Low trigger delay.

LTT CROWBAR PROTOTYPE

A first prototype has been build consisting of two LTT stacks with 7 thyristors each (figure 2). The thyristors are the special types T1503NH75TS02. The mechanical assembly of two stacks vertically within a movable construction has been chosen for simple replacement inside the high voltage room. The electronic unit with the laser diodes is located inside the bottom frame (figure 1).

Figure 2: Electrical configuration of the LTT crowbar

For static voltage sharing a simple 1 MOhm high voltage resistor in parallel to each thyristor is applied. This switch is designed for 50kV dc nominal operating voltage.

TEST RESULTS

The first tests have been carried out with a simplified test circuit (figure 3). In this configuration the dynamic behaviour during the starting phase of the capacitor discharge was studied. There is a significant influence of the commutation voltage on the achievable delaytime of the switch (figure 4). In this test set-up under nominal voltage conditions a delaytime of 3.5μs has been achieved (figure 5). Due to limitations of the main circuit parameters the maximum achievable dI/dt under no load condition was 3.5kA/μs.
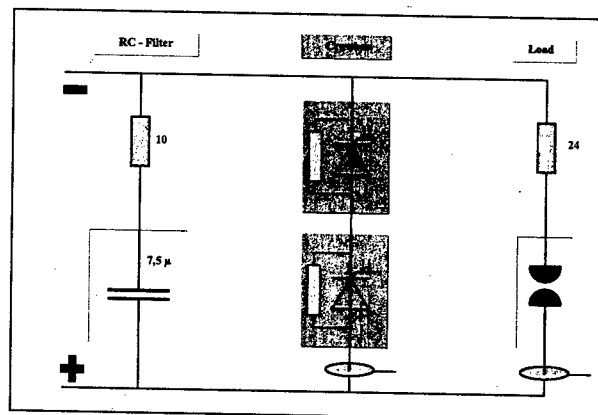
Figure 3: Test set-up
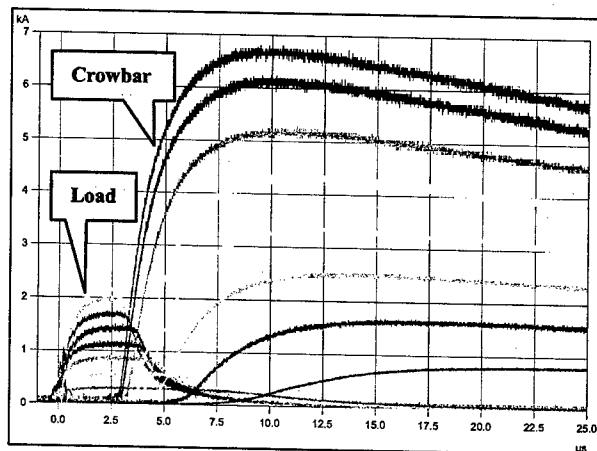
Figure 4: Crowbar operation at different operating voltages (Parameter U_{dc} = 10 / 20 / 30 / 40 / 50 / 60 / 70 / 76 kV)

Figure 1: LTT crowbar assembly consisting of two stacks mounted vertically.
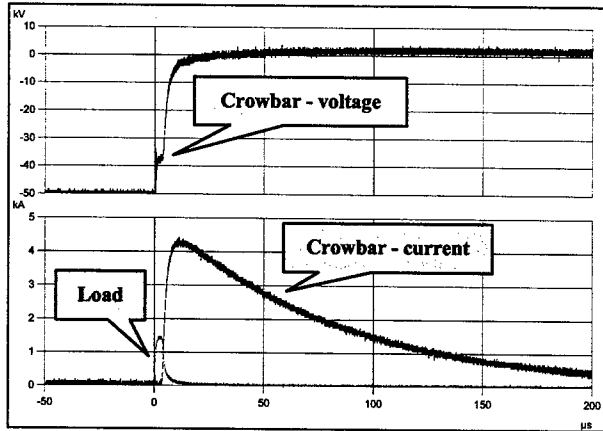
Figure 5: Crowbar operation at nominal voltage

DESY II - INSTALLATION

The new LTT crowbar is planned to operate for klystron protection in the existing DESYII-booster e^+/e^-. This installation is characterized by its large filter capacitor of 240μF at 50kV dc. The main components are shown in figure 8. The three sections (Power-Supply, RC-Filter and Klystron Hall) are linked with appropriate high voltage cables. The cable link between the capacitor bank and the crowbar has to be considered regarding dynamic behaviour of the circuit (figure 6).
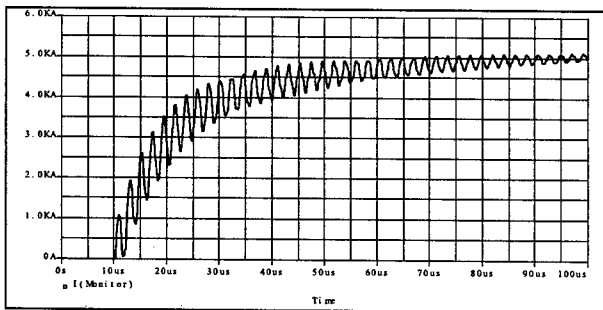
Figure 6: Simulation of the starting edge of the Crowbar current under noload discharge conditions.

Near the end of the discharge process of the capacitor the power-supply has loaded its smoothing choke. This stored energy must be dumped by the crowbar. It leads to

additional and very significant charge transfer with a relatively low but long current waveform (figure 7). In this application the total charge transfer is about 30 C, where 12 C is the part delivered by the capacitor bank.
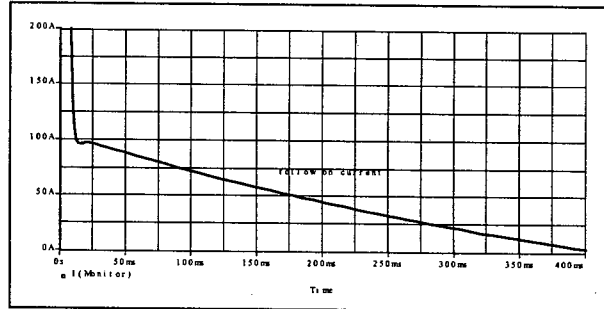
Figure 7: Simulation of the so-called follow through-current introduced by the power-supply smoothing choke.

The operation of the crowbar inside the DESY II – installation will be investigated in future tests.

CONCLUSION

Light Triggered Thyristors are strong candidates for high voltage crowbar applications, where high charge transfer is required. Their main advantages are simple insulation in series connected assamblies due to optical triggering and high charge transfer capability. Sufficient voltage margin leads to reliable HVDC operation. Special care has to be taken selecting the main circuit parameters to achieve optimized switching behaviour, namely the commutation voltage, dI/dt limits and sufficient damping in the main circuit.

REFERENCES

[1] J. Dorn, U. Kellner, F.-J. Niedernostheide, H.-J. Schulze, "State of the Art Light Triggered Thyristors with Integrated Protection Functions", Power Electronics Europe Issue2, P.29-35, 2002

[2] eupec GmbH, "Technical Information, Phase Control Thyristor, Application Notes" Rel. 2.1, Nov. 2000
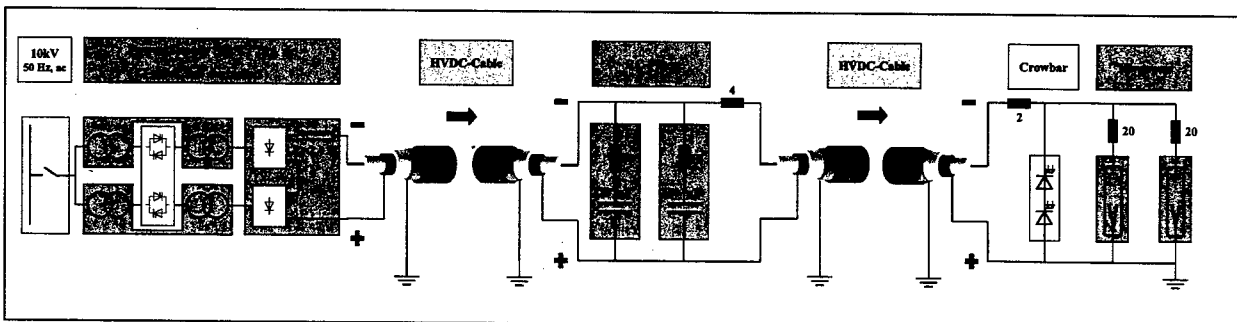
Figure 8: DESY II – Installation consisting of 3 sections (Power Supply, RC-Filter and Klystron Hall)

IMPROVING POWER SUPPLY PERFORMANCE FOR THE DUKE STORAGE RING *

Y. K. Wu[†], V. G. Popov, S. Hartman, I. Pinayev, S. F. Mikhailov, P. Morcombe,
O. Oakeley, P. Wallace, P. Wang, V. Litvinenko, FEL Lab, Duke University, NC 27708-0319, USA

Abstract

As part of the recent Duke storage ring hardware upgrade (2001–2002), a power supply improvement program was put in place to bring all major DC supplies to their specifications. In carrying out this program, power supplies have been modified, tuned, and thoroughly tested. In its actual operation configuration, each power supply was subject to extensive testing to determine its DC stability, reproducibility and linearity, AC ripple and noise, and ramping performance. As a result, all major DC supplies have been improved to meet most important performance specifications for 1 GeV operation.

1 INTRODUCTION

The Duke storage ring and its main light source, the OK4 free electron laser (FEL), were commissioned in 1994 [1] and 1996 respectively. Since 1998, the Duke FEL storage ring has been operated for FEL research in the UV and deep UV region for a variety of user applications in medicine, biophysics, solid state, and nuclear physics. However, prior to the 2001 upgrade, the Duke storage ring suffered from a number of hardware problems, resulting in frequent machine down-times and beam dropouts. A major contributor to these problems was the unreliable performance of the DC power supplies. All ring quadrupoles were powered individually by small DC supplies which did not meet specifications for a modern storage ring. The second problem was a quad coil overheating problem at high energy operation ($E > 750$ MeV). To address these problems, the following upgrades were carried out during an upgrade shutdown (2001-2002): (1) all arc quad coils were replaced with specially designed new coils with inline water cooling; (2) small arc quad supplies were replaced with higher performance supplies which fed families of arc quads in series; (3) straight section quad supplies were replaced by new supplies with better performance; (4) all major supplies were tested and tuned. In this paper, we first present the performance specifications for the main DC supplies. We then report power supply modifications carried out in order to achieve these specifications. Finally, we present the measured power supply performance including DC stability, reproducibly and linearity, AC ripple and noise, and ramping characteristics.

2 SPECIFICATIONS AND MODIFICATIONS

Three different types of DC power supplies are used to drive the main magnets in the Duke ring. Forty (40) ring dipoles are fed in series by a PEI supply in use since 1993 (PEI SR1074, 800V/700A). Two families of thirty-four (34) combined function quad-sextupoles in the arc are driven in series by four (4) new supplies (Bruker B-MN, 60V/833A) from Bruker Analytische Messtechnic GmbH in Germany. The end-of-arc and straight section quads are powered in series or individually by eighteen (18) new supplies (Walker HS-7040-4SS, 70V/40A and 50V/40A after modifications) from Walker Scientific, Inc. in US.

2.1 Performance Specifications

The specifications for these supplies are determined by beam stability requirements, in particular, the amount of tune variations allowed. The desirable maximum tune variation should not exceed that of the tune spread of the beam. The following beam parameters are assumed for nominal operation: (1) energy = 1 GeV; (2) horizontal and vertical chromaticities, $\xi_x = 1.3$, $\xi_y = 2.6$. The allowed tune variations are (RMS) $\nu_x = 0.75 \times 10^{-3}$ and $\nu_y = 1.5 \times 10^{-3}$ respectively. This translates to the following rather conservative power supply specifications:

- Dipole PS (PEI): $\frac{\Delta B}{B} \leq \pm 25$ ppm;
- Arc quads PS (Bruker): $\frac{\Delta K_1}{K_1} \leq \pm 25$ ppm;
- Straight section quad PS (Walker): $\frac{\Delta K_1}{K_1} \leq \pm 50$ ppm.

$d\nu_x, d\nu_y$ [10^{-3}]	Dipoles	Arc Quads	SS Quads	Total	Tune budget
DC, X	0.250	0.085	0.125	0.292	0.750
DC, Y	0.250	0.145	0.225	0.366	1.500
AC, X	0.250	0.170	0.400	0.820	0.750
AC, Y	0.250	0.290	0.700	1.240	1.500

Table 1: Allowed RMS tune variations for main supplies.

The allowed tune variations for various supplies are listed in Table 1. The tune drift (DC) caused by each supply is assumed to be uncorrelated. The total tune drift is calculated as the root of the quadratic sum of contributions from all supplies. For the AC performance, the tune jitter is assumed to be dominated by line-frequency related ripples. The total tune jitter is then calculated as the sum of all contributions. The Duke ring is operated with a wide energy range from 270 MeV to 1.2 GeV. Whenever possible, we strive to achieve the same level of power supply performance for all energies.

2.2 Power Supply Modifications

A number of modifications were made to the PEI, Bruker, and Walker supplies during the upgrade to achieve the desirable performance. The PEI dipole supply had been in operation since 1993. However, its ripple, noise, and

ramping performance were not satisfactory. The PEI performance was improved with the following modifications: (1) active damping was developed to suppress the resonance of the LC filter; (2) the firing circuit was adjusted for 60 Hz reduction; (3) the filter inductor was rearranged to suppress common-mode noise. In addition, the current regulator was modified to match the load impedance for overshoot reduction.
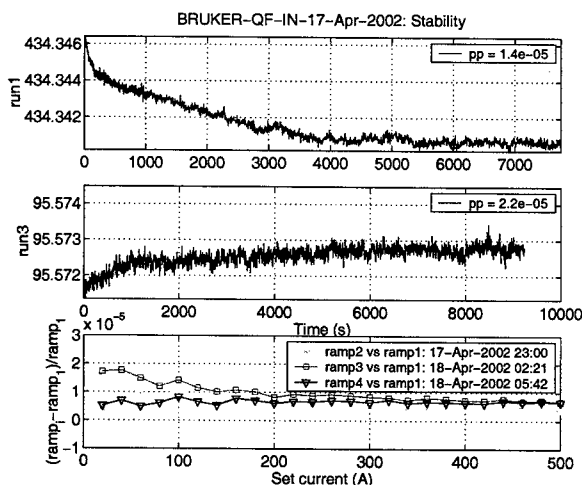
Figure 1: Stability and reproducibility for Bruker powering QF inner coils.

The new supplies had their share of problems. All of the five newly acquired Brukers were out of absolute calibration by about 1% and one had a large zero offset. These problems were corrected on site by a Bruker technician.

The most extensive modifications were made to the Walker supplies. First, the Walker transformers had to be reconfigured to match different loads. The load variation was the result of driving either two or four quads coils and of variations in output cable length. Second, the digital control (RS-232C) was found to be too slow for our ramping requirements and the internal ADC readback too inaccurate. All supplies were then retrofitted to provide differential analog control and readback. Third, the remote/local control did not work properly and had to be replaced. Fourth, the long-term (24-48 hours) stability was found inadequate because the current regulation shunt had a relatively large temperature coefficient. To overcome this problem, the shunt temperature was stabilized using a stand-alone water cooling system.

3 DC PERFORMANCE

DC measurements are performed to determine the stability, reproducibility, and linearity for each power supply. All DC measurements are completed in a single run using a test protocol which interleaves stability tests with slow-ramp tests. The stability tests cover several energies from injection to 1.2 GeV; the ramp tests takes the supply from its minimum to maximum operation current. The DC stability is calculated as the peak-to-peak (P-P) current varia-

tion. The linearity, more precisely the deviation from linearity, is computed as the difference between the readback and its linear fit. The reproducibility is calculated from the slow-ramp runs as the difference current for the same control setting.

A Danfysik current transducer was used for measuring DC currents for PEI and Brukers (Danfysik 860R, 2kA) and for Walkers (Danfysik 866, 600A). The Brukers were controlled digitally; the PEI and Walkers were controlled by 20-bit and 16-bit DACs, respectively. The output voltage from the transducer was recorded by a HP 3458A digital multimeter.
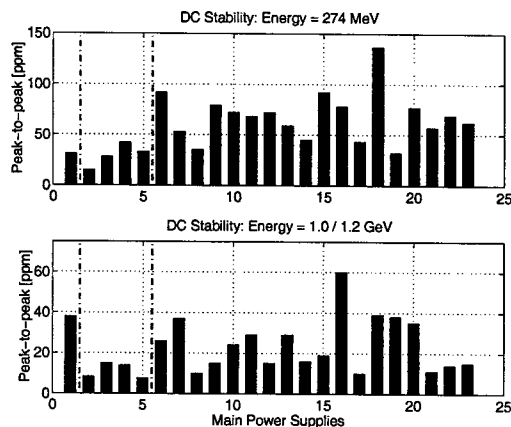
Figure 2: Main power supply DC stability. The first supply is PEI, followed by 4 Bruker and 18 Walker supplies. The test duration is typically 3 hours. The peak-to-peak variations are computed after dropping the first 10% of data.

Fig. 1 shows the DC performance of a Bruker supply powering the inner coils of the arc QF family. For all four Brukers, the P-P current variation (stability) is less than 50 ppm for energies from 270 MeV to 1.2 GeV. The reproducibility of all Brukers is less than 55 ppm for the entire energy range. The deviation from linearity is typically 100 to 150 ppm at 270 MeV settings and less than 50 ppm at 1 GeV. A relatively large deviation from the linear control is the result of using the 16-bit coarse DAC in the test. Due to the lack of integrated control of the internal coarse and fine DACs, only the coarse DAC was used for Bruker control.

The stability results for all major DC power supplies are shown in Fig.2 for two ring energies. With the exception of two Walkers, all supplies satisfy the stability and reproducibility specifications from injection (270 MeV) to full energy of 1.2 GeV. The linearity is a less critical performance requirement. All supplies are within a factor of three of the linearity specifications.

4 RIPPLE AND NOISE PERFORMANCE

AC ripple and noise measurements were performed at a number of DC current settings. The measurement system consists of a current transducer, a voltage amplifier with a built-in filter (1Hz - 3 kHz), and a LeCroy digital scope. The measured data were analyzed for line related ripples

(60 Hz, 120 Hz, etc.) and noise. To evaluate the overall AC performance of various supplies, a simple merit was chosen as the RMS variation of the current.

The overall ripple and noise performance for all major supplies is shown in Fig. 3. At the full energy (1.0-1.2 GeV), the AC performance of all supplies is within the specifications. At the injection energy, while all Walkers are still within the specifications, PEI and three Brukers are out of specifications. Since we have set a very conservative spec for the AC performance, it is expected that the amount of tune jitter at the injection energy is still quite acceptable.
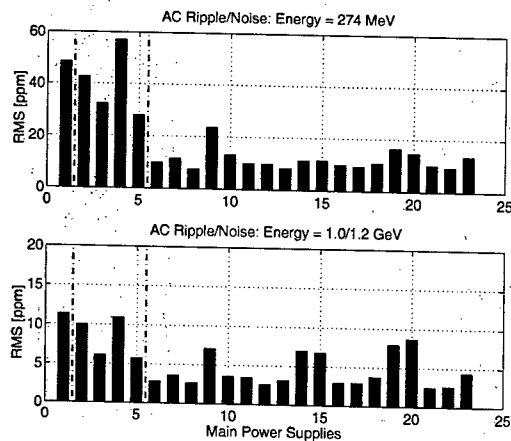
Figure 3: Main power supply AC ripple and noise performance. The first supply is PEI, followed by 4 Bruker and 18 Walker supplies.

5 RAMPING PERFORMANCE

Besides the DC and AC performance, the dynamic performance of the power supply is critical for reliable operation with energy ramping. Two important ramping parameters are the current overshoot and time constant for stepping control. These parameters determine the beam stability during ramping, the field reproducibility after ramping, and ultimately the total ramp time for reliable operation with energy ramping.

With digital control, the Brukers were found with satisfactory ramping performance after a simple adjustment of the internal slew rate. The Walker supplies were found to be relatively fast, with a time constants around 70 msec. However, significant overshoot were found at a 20% to 30% level. One test Walker supply was modified to demonstrate that the overshoot could be effectively suppressed with proper tuning. The rest of the Walkers remain to be tuned.

The reliability of energy ramping depends heavily on the performance of the dipole supply PEI. The PEI supply had been modified extensively in order to reduce the overshoot. Fig. 4 shows the measured step responses of the PEI output current before and after the modification. Before the modification, the current overshoot is about 50% of the step size. After the modification, the large overshoot is essentially eliminated and the time constant for stepping is 0.15

sec. This time constant is a good match with the ramping rate of the control system at 5 Hz [2].
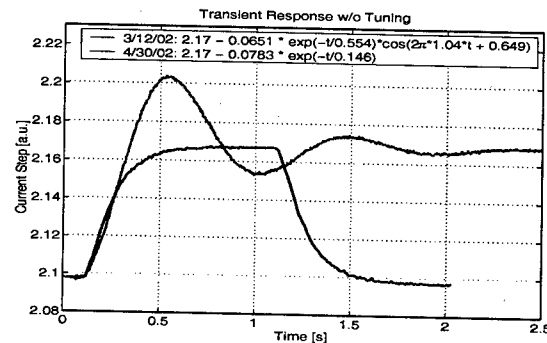
Figure 4: PEI dynamic response to stepping control voltages. A large overshoot was observed before tuning and was completely suppressed after tuning.

6 CONCLUSION

After modifications and tuning, all major supplies for dipoles and quadrupoles are found to have reasonable DC and AC performance at the high energy (1.0-1.2 GeV) in terms of stability, reproducibility, linearity, noise, and ripple. The AC noise performance of PEI and Brukers at the injection energy (270 MeV) needs further improvement. The dynamic performance of Walkers is not satisfactory; each Walker needs to be tuned to match its actual load in order to suppress the overshoot and achieve the same time constant. The overall performance of these DC supplies has been found to be rather adequate during past one-year operation. To sustain this level of performance, an active performance monitoring program [3] has been put in place to uncover emerging power supply problems.

With our power supply improvement program, we have learned several valuable lessons. First, very detailed and well thought-out specifications are critical in selecting an appropriate supply for a particular operation. This process will eliminate many unnecessary on-site modifications after delivery which can be time consuming and expensive. Second, one should expect that even a good supply will need some modifications and tuning in order to satisfy all performance requirements. Third, a thorough testing program with power supplies connected to their actual loads is essential to uncover problems for further modifications and to obtain actual performance of supplies under realistic operation conditions.

7 REFERENCES

[1] V. N. Litvinenko, Y. Wu, B. Burnham, et al., Proc. of PAC95, Dallas, Texas, p. 213 (1995).

[2] Y. K. Wu, S. Hartman, S. F. Mikhailov, "A Physics Based Control System for the Duke Storage Ring", these proceedings.

[3] J. Li, Y. K. Wu, S. Hartman, "Power Supply Performance Monitoring and Analyzing Using Operation Data", these proceedings.

COMPENSATION OF LOAD FLUCTUATION OF POWER SUPPLY SYSTEM FOR LARGE ACCELERATOR USING SMES

H. Sato, M. Muto, T. Shintomi, S. Igarashi, KEK

T. Ise, K. Furukawa, Osaka University

Abstract

In J-PARC 50GeV synchrotron, peak active power and the dissipation power of main magnets are estimated to be about 135MW and 37MW, respectively. Super Conducting Magnetic Energy Storage(SMES) is one of candidates to compensate these large load and line voltage fluctuation. Study on circuit configuration of the power supply with SMES will be discussed. Plan of experiment is also described.

INTRODUCTION

The J-PARC Project is under progress as the joint project by the Japan Atomic Energy Research Institute (JAERI) and the High Energy Accelerator Research Organization (KEK). The facility is located at the JAERI Tokai site and comprises a 600-MeV linac (200MeV in the phase I), a 3-GeV rapid-cycling synchrotron (RCS), and a 50-GeV synchrotron (MR). The 50-GeV synchrotron main ring comprises 96 bending magnets, 216 quadrupole magnets, 72 sextupole magnets and 186 steering magnets. The power supply system for the magnets of the 50-GeV synchrotron is made up of a large number of power supplies, one is for the bending magnets, 11 ones for the families of the quadrupole magnets, 3 ones for the families of the sextupole magnets and 186 ones for the steering magnets. These power supplies are operated with an excitation pattern of trapezoidal wave form as shown in Fig.1. The total amounts of active power of these power supplies become about +105MW~ -66.0MW in peak with only cable loss for 50-GeV operation[1].

As well known, conventional thyristor rectifiers with a high power and trapezoidal dc side output current usually generates a very large cyclic variation of reactive power and raises unallowable line voltage fluctuation. In order to overcome this problem, power converters using IGBT or IEGT are investigated for the power supply of the J-PARC project. By using power semiconductor devices of this type, it is possible to construct power supplies with the characteristics of unity power factor operation. The line voltage fluctuation estimated is about +2.5%~-2.5% for 50GeV operation, if the reactive power is compensated perfectly. However, this fluctuation is not acceptable for the power line. Then, some active power compensation device is necessary for 50GeV operation. At this present, adjustable speed flywheel generation system to flatten the very large power swing has been designed[1]. In the phase I, 50GeV synchrotron should be operated with on energy of 30GeV or 40GeV at highest with out flywheel. This paper shows the study on application of superconducting magnetic energy storage

(SMES) for this purpose. In the case of SMES, it is possible to connect the SMES magnet at the dc side of the synchrotron power supply and exchange energy between the accelerator magnet and the SMES magnet. Sveral circuit configurations are proposed and typical simulation result using is presented in this paper.

CIRCUIT CONFIGURATION OF POWER SUPPLY

The largest power supply for the synchrotron is for the bending magnets. Other power supplies for quadrupole magnets, sextupole magnets and steering magnets are small and do not affect line voltage fluctuation. Requirements for the power supply of the bending magnet is shown in TABLE1. Current pattern of the bending magnet is shown in Fig.1.

TABLE I

Requirements for Power Supply of Bending Magnet

Excitation dc current	202A ~ 3015A
Peak dc voltage	+25.2kV, -32.5kV
Active power (peak)	72.5MW, -54.4MW
Coil inductance	104mH/coil
Coil resistance	45mΩ/coil
Number of coils	96
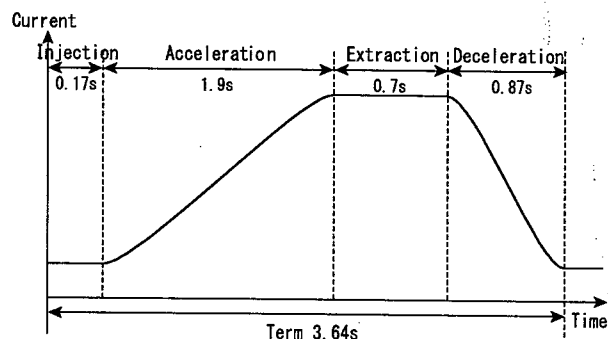
Fig.1. Typical excitation current pattern of the bending magnet for 50-GeV operation.

The power supply with SMES proposed in this paper is for the bending magnets.

Fig.2 shows various configuration of the power supply. Fig.2(a) shows the system using line commutated ac/dc converter. In this case, SMES should compensate both active and reactive power variation. As a result, the power

rating of the SMES becomes the largest. The configuration shown in Fig.2(b) shows the system using forced commutated ac/dc power converter using IGBT and IEGT. In this case, the magnet power supply can operate at unity power factor. As a result, SMES compensates only active power variation. But there is power exchange through two ac/dc power converters, resulting with high power supply cost and losses. The configuration shown in Fig.2(c) uses forced commutated ac/dc power converter and dc type SMES. In this case, power rating of the ac/dc converter for magnet power supply can be reduced, resulting with the reduced cost of the total system. The system shown in Fig.2(c) is the proposed system and studied hereinafter.

(a) Configuration using line commutated ac/dc converter

(b) Configuration using forced commutated ac/dc converter

(c) Configuration using forced commutated ac/dc converter and dc type SMES
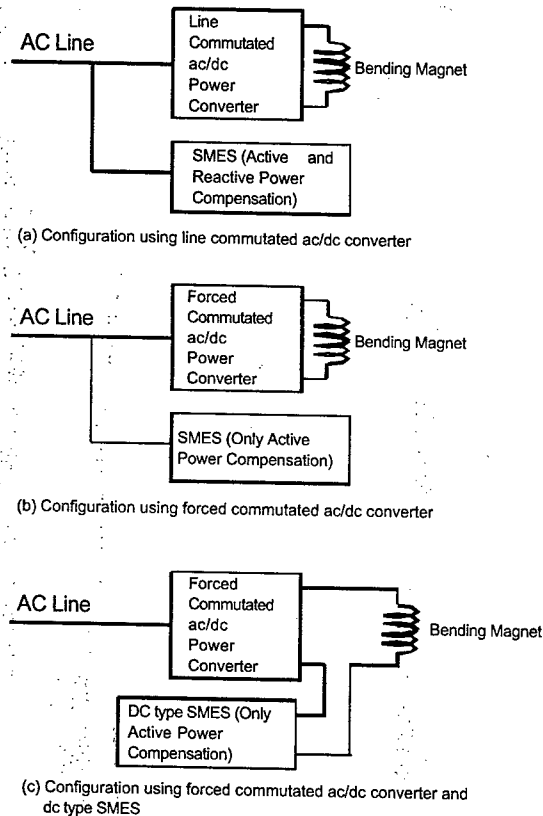
Fig.2. Various configuration of magnet power supply with SMES.

The power supply of the bending magnets is divided into six separated power units, because the electric power rate for the bending magnet is too large to construct a power supply as one unit. By this method, the power rating for one power unit is reduced to the possible level about 5 kV and 10MW. Fig.3 shows connection scheme between the power units and the bending magnets. As seen in the figure, the 96 bending magnets are divided into three groups and both upper and lower coil of the magnet are connected separately by series in each group, and connected with the power units in turn so as to make

one excitation loop. The simulation was done by the configuration of one power unit, which is 1/6 of the bending magnet power supply. Each of the power unit is composed of a current source ac/dc converter and SMES. The 40GeV operation can be carried out by the configuration without SMES, because of the acceptable voltage fluctuation in the case.
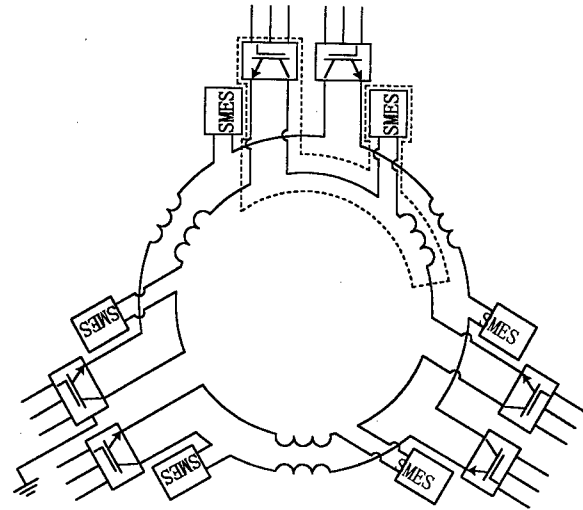
Fig.3. Connection of power supply of the bending magnets with SMES.

SIMULATION RESULTS

Fig.4 shows the simulation results for the 1/6 of the bending magnet power supply, using PSCAD/EMTDC software. The current of the bending magnet was controlled with the low tracking error. The reactive power was controlled at almost constant value, which is due to the capacitor of the ac side filter. The power variation of the ac/dc converter during the operation cycle was about 11 MW. The average current of the SMES coil is controlled to be constant except the initial transient. The charging and discharging energy of the SMES was about 5MJ.

Fig.5 shows the voltage and current waveform ac source. In this case, the phase difference between the voltage and the corresponding phase current is almost 180 degree, which shows low reactive power. The current waveform is almost sinusoidal.

The voltage fluctuation of ac line considering the total system was also calculated and the calculated results are shown in Fig.6. The calculated voltage fluctuation was acceptable for the system. Detailed simulation and the control system was presented in the reference[2].
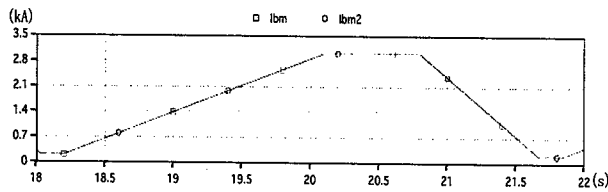
(a) Current of bending magnet (Reference and output are almost same)
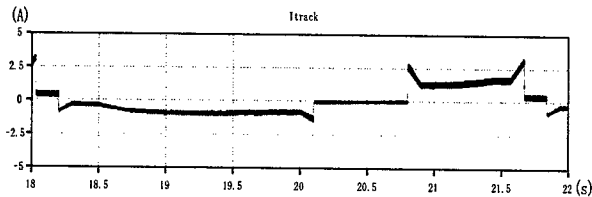
(b) Tracking error of bending magnet current
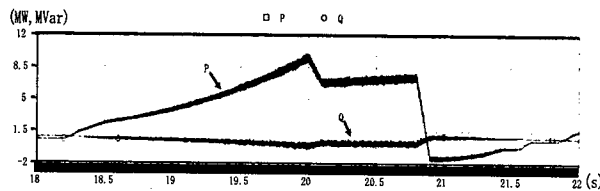
(c) Active (P) and reactive (Q) power of the ac/dc converter
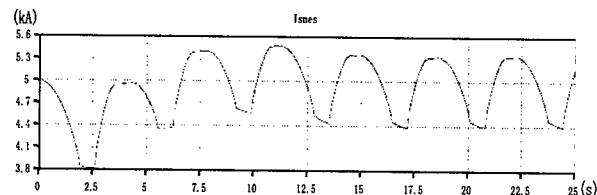
(d) Current of SMES coil

Fig.4. Simulation results of the proposed system.
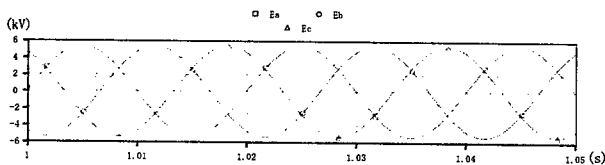
(a) AC source voltage
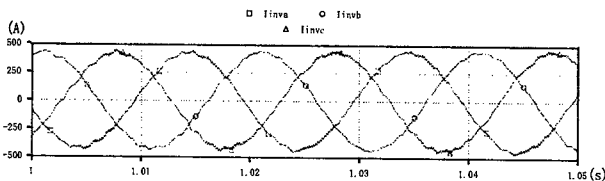
(b) AC source current

Fig.5. AC source side voltage and current waveforms.
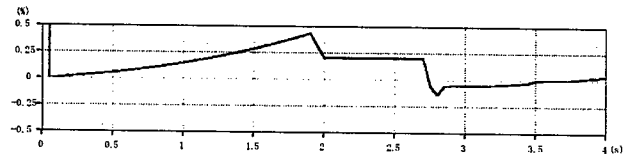
(a) 154kV line
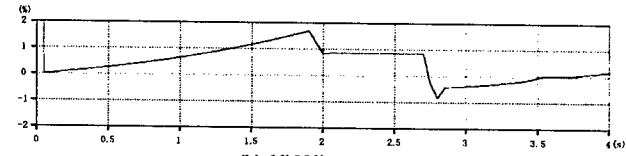
(b) 66kV line

Fig.6. Calculated line voltage fluctuation.

CONCLUSIONS

The power supply system using SMES for the J-PARC 50-GeV main ring was proposed and the fundamental characteristics of the configuration as shown in Fig.2(c) have been calculated. For the configuration of Figures2(a) and 2(b), the flywheel system gives the almost same effect, but Fig.2(c) system has advantages over the flywheel system, because of the dc side coupling between the energy storage device and the accelerator coil, resulting with the reduced ac/dc converter power rating. Then, the running cost of the electric power will be less than that of original design as 1/5. The proposed system can be applicable for the extension of the system from the initial 40-GeV operation without energy storage device.

Authors and colleagues are now considering to perform the SMES experiment at the KEK-12GeV PS extraction septum magnet power supply, of which total power in 1MW, with using the existing ESK[3] system under collaboration with KYUSHU Electric Power Company.

REFERENCES

[1] Accelerator Technical Design Report for High-Intensity Proton Accelerator Facility Project
(http://hadron.kek.jp/member/onishi/tdr/index.html).

[2] T.Ise, et.al., to be printed in IEEE Transaction on Applied Super conductivity

[3] T.Imayoshi, et.al., IEEE Transaction on Applied Super conductivity, 7(1997)844
KEPCO Research Laboratory's Catalogue, "SMES Field Test"

TEST RESULTS ON CAPACITOR COMMUTATION CHARGING TYPE OF RESONANT POWER SUPPLY FOR SYNCHROTRON RING MAGNETS

Dong Sai, Yao Chenggui, Zhang Yunxiang
National Synchrotron Radiation Laboratory, University of Science and Technology of China
Hefei, Anhui 230029, P.R.China, E-mail: sdong@ ustc.edu.cn

Abstract

A new dual resonant type current ramping power supply was built and tested. This paper describes experimental results on several different current waveforms: a triangular waveform with flat bottom, a trapezoidal wave with flat bottom and a waveform with reduced fall time. This paper also analyses the advantages of this type of power supply and the potential applications.

I INTRODUCTION

Conventionally, synchrotron ring magnet power supplies adopt resonant system with DC-bias[1,2,3,4,] or phase-controlled rectifiers[5,6,7]. The former, mostly used for fast-cycling synchrotrons, requires highly precise resonant frequency, and fixed cycle time. The advantage is that it eliminates the requirement of a large amount of reactive power. The latter approach, mostly used for slow-cycling synchrotrons, needs a large amount of reactive power compensation. But the load current waveforms and the cycle time can vary.

The dual resonant power supply [8,9,10] can produce flat top and flat bottom current pulse. But most of research work is on theoretical analysis and experimental project. So far no practical application was reported. In 1996, M. R. Pavan Kumar & J. M. S. Kim developed a circuit, namely, "HMSC"[11]. They consider that due to large reactive components used as energy storage device in the above-mentioned designs, these power supplies tend to have limited dynamic response. For the same reason, these designs also require high voltage power source.

In order to overcome these shortcomings, we propose a new type of resonant power supply. Its main advantages are:
the reactive power is eliminated; its reactive components reduced; and the circuit is simplified. The waveform of load current consists of rising and falling sections, a flat bottom and a flat top. The cycle time is adjustable, and it does not need high voltage power supplies. It is suitable for both fast and slow cycling synchrotrons.

Our research brings forth three main modifications:
- Insulated Grid Bipolar Transistors (IGBT) are used as the main switches,
- Electrolytic capacitors are used as energy store device.

- One DC regulator and one SCR are used to provide flat bottom current, and a large choke is eliminated.

Based on this idea, several different experiments of different load current waveforms with about 30A peak flat top value have been conducted. The results are promising. We believe that this type of power supply design can be applied to future accelerator projects.

II PRINCIPLE AND WORKING PROCESS DESCRIPTION

Figure1 is a diagram of the main circuit. The parts framed in dotted lines are optional depending on whether non-zero flat bottom or flat top is required.
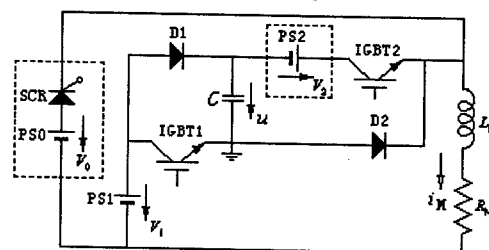
Figure 1: Fundamental Principle Diagram.
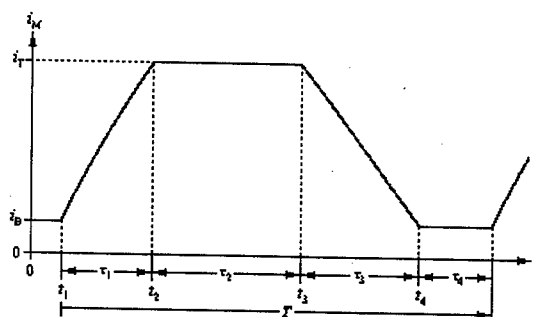
Figure 2: Load Current Wave Form.

Figure 2 is trapezoidal current waveform with nonzero flat bottom. Now we describe the principle and working process using this waveform as an example.

In Figure 1, L_M and R_M are the inductance and resistance of the load magnet respectively. PS0, PS1, PS2 are DC regulators. C is bank of capacitors for energy storage.

In a steady cycle, during the bottom period, the SCR has been on, and the voltage on the energy storage

capacitor C is charged to its full value of u=U. At $t=t_1$, IGBT1 and IGBT2 are turned on at the same time. The SCR turns off due to negative voltage across it. Capacitor C discharges resonantly through L_M, and the load current i_M rises. At $t=t_2$, i_M reaches the top current i_T. IGBT1 turns off and D1 starts conducting. DC power supplies PS1 and PS2 maintain load current $i_M=i_T$ through D1 and IGBT2. At $t=t_3$, IGBT2 turns off. This shuts off the current path and generates a high voltage across L_M. Diode D2 starts conducting. Capacitor C charges resonantly through L_M, PS1, D1 and D2. Load current i_M starts to fall. The energy stored in the load inductance flows back to capacitor C. At $t=t_4$, i_M falls to i_B. The SCR is turned on by an external signal, and the DC power supply PS0 maintains a flat load current $i_M=i_B$. D1 and D2 are off due to negative bias. This completes a full cycle, and the capacitor C is charged to U again.

When the system is turned on initially, the energy provided by the DC power supplies PS1 and PS2 exceeds that lost in the circuit. The voltage on capacitor C and the load current build up over many cycles. After this transitional period the provided energy by the DC power supplies equals that lost in the circuit and the system enters a steady state.

In some cases, it is desirable to reduce the fall time. We can achieve this easily by reconfiguring the capacitor bank. For example, if we want to reduce it to one nth, C is divided into n units. Each unit has a capacitance of C/n. These units are connected with $3(n-1)$ diodes as shown in Figure 3. This ensures that all capacitors are discharged in parallel (in rising period) and charged in series (in falling period). The fall time will be reduced approximately to one nth.
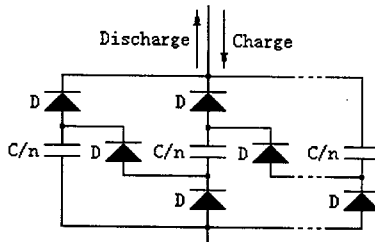
Figure 3:   Diagram of discharge /charge of n (C/n) s in series/parallel.

III   EXPERIMENTAL SET

Two single module unit IGBTs (200A/1200V), a SCR rated at 50A/500V and auxiliary circuits are installed in one IGBT/SCR driving-controller box. Other components in the main circuit are connected to the posts on the rear board.

Two 0~30V/0~30A DC voltage and current regulators are provided by the Magnet Field Measurement Group. One 0~12V/2A DC voltage and current regulator are provided by the Power Supply Group.

The electrolytic capacitors used as the energy storage capacitor (10000μF/100V, 5 in parallel) and two Diodes (50A/700V) are spare parts borrowed from the Power Supply Group.

The load inductor consists of six filter inductors connected in series. It has the following parameters: L_M=82mH, R_M =50mΩ.

Construction of an experimental set started at the beginning of April last year. By the beginning of July we had completed several experiments and recorded the waveforms of load current and capacitor voltage (see Fig. 4 to Fig. 8). The basic principle of the suggested design is fully verified.

IV   EXPERIMENT RESULTS
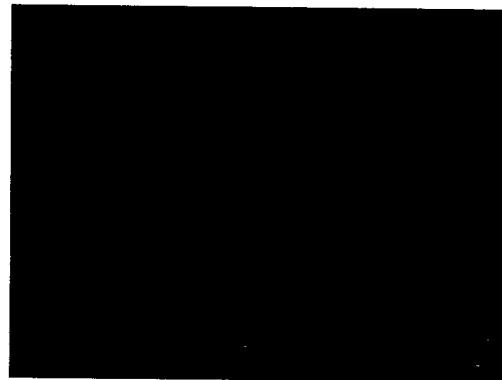
Figure 4: Trapezoidal waveform with 0.75V flat bottom.
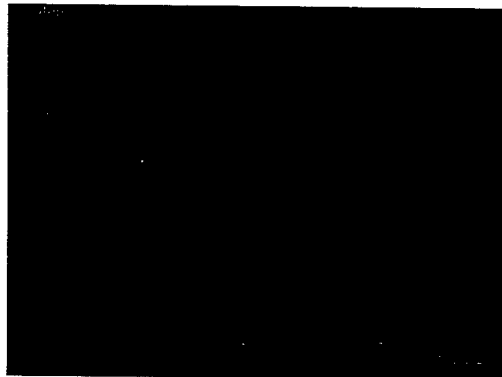
Figure 5: Triangular waveform with 0.75V flat bottom.
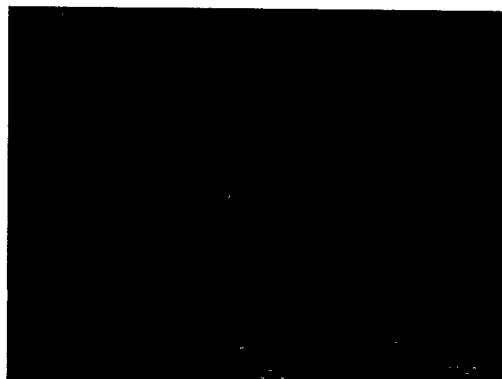
Figure 6: Trapezoidal waveform with 0V flat bottom.

Proceedings of the 2003 Particle Accelerator Conference
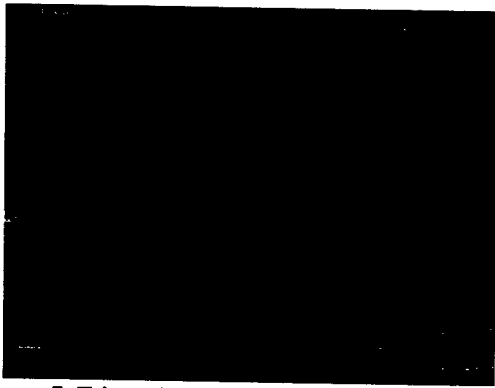
Figure 7: Triangular waveform with zero 0V bottom.
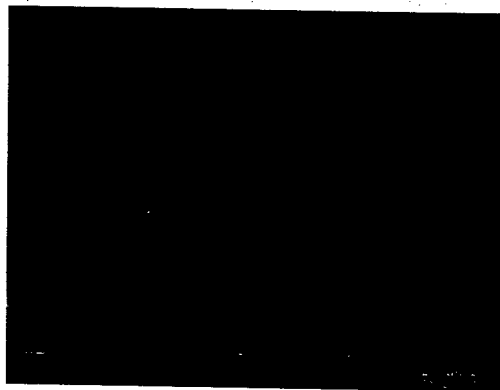
Figure 8: Triangular waveform with 0.75V flat bottom. The fall time is reduced using two capacitors in series/parallel configuration.

V SUMMARY

The flat bottom and top sections of the current waveform are directly provided by DC regulators. The rising and falling sections are generated by resonance of the energy storage capacitors, which are in series with DC regulators and the load inductance. Through properly set switch timings, transition between sections is optimized. The main characteristics are: energy store capacitor is charged automatically by the induced high voltage generated in the load inductor.

Using electrolytic capacitors as stored energy capacitors helps reduce cost and space. It is a viable alternative to other designs of slow cycling power supplies. It makes no strict demands on the capacitance value of the capacitor. So long as it is larger than a minimum value, the system can work properly. The larger the capacitance is, the lower the its charging voltage is, and the more linear the rising and falling sections of the load current are, and the lower the voltages across the IGBTs and diodes are, and also the lower the total power consumption is.

Utilizing IGBTs as the main switches, which can be turned off by external control, simplifies the design significantly. High power and current can be achieved by connecting IGBTs in series or parallel. The main

technical challenge here is to balance the current and voltage distribution.

Using one DC regulator and one SCR providing flat bottom of the load current helps to eliminate a large and expensive choke, and accordingly makes the design more flexible and less expensive.

The waveform of the load current and cycle time can be easily adjusted by changing the output voltage of the DC regulators and the timing of the switches. If the desired waveform is triangular with zero flat bottom, only one DC regulator is required.

VI REFERENCE

[1] H.Sasaki, "Magnets for Fast-Cycling Synchrotrons", KEK Preprint 91-216, March 1992.

[2] A. Young and B. E. shafer, "Electrical Characteristics of the SSC Low-Energy Booster Magnet System", Conference Record IEEE, Particle Accelerator Conference, pp.1285-1287, 1993.

[3] C. Jack, etc. "Energy Storage Inductor for the Low-Energy Booster Resonant Power Supply System", Conference Record IEEE, Particle Accelerator Conference, pp.1297-1299, 1993.

[4] J. M. S. Kim and K. W. Reiniger, "Frequency-Domain Analysis of Resonant-Type Ring Magnet Power Supplies", Conference Record IEEE, Particle Accelerator Conference, pp.1112-1114, 1993.

[5] H. Sato, etc. "Upgrade of the Main Ring Magnet Power Supply for the KEK 12 GeV Proton Synchrotron", Conference Record IEEE, Particle Accelerator Conference, pp.908-910, 1991.

[6] Masoud Fathizadeh, "Design and Simulation of High Accuracy Power Supplies for Injector Synchrotron Dipole Magnets", Conference Record IEEE, Particle Accelerator Conference, pp.917-919, 1991.

[7] Spring-8 Project. Part I, Facility Design 1990 [DRAFT], February 1991, pp.3-65 ~ 3-67.

[8] G. Karady, etc. "Resonant Power Supplies for a Large Synchrotron", IEEE Transactions on Nuclear Science, Vol. NS-32, pp.1480-1482, 1987.

[9] Ed Schneider "Test Results on Dual Resonant Power Supply with Flat Top and Flat Bottom Current", IEEE Transactions on Nuclear Science, Vol. NS-32, pp.1505-1507, 1987.

[10] W. F. Praeg, "Dual Resonant Power Supply with Flat-Bottom", IEEE Transactions on Nuclear Science, Vol. NS-30, No.4, pp.2873-2875, August 1983.

[11] M. R. Pavan Kumar & J. M. S. Kim, "A Hybrid Multi-level Switching Converter for Ring-Magnet Power Supplies", IEEE Transactions on Nuclear Science, Vol. 43, No. 3, pp.1876-1883, June 1996.

[12] W. F. Praeg and D. McGhee, "Ring Magnet Power Supply for a 500 MeV Synchrotron", Conference Record of the 1978 Industrial Applications Society, pp. 1118-1124.

760

HIGH RESOLUTION ANALOG / DIGITAL POWER SUPPLY CONTROLLER*

Evgeny Medvedko, Jeff Olsen, Greg Leyh, Stephen Smith, Robert Hettel, Clemens Wermelskirchen, Till Straumann, Stanford Linear Accelerator Center, Stanford, CA 94309, USA.

Abstract

Corrector magnets for the SPEAR-3 synchrotron radiation source require precision, high-speed control for use with beam-based orbit feedback. A new Controller Analog/Digital Interface card (CANDI) has been developed for these purposes. The CANDI has a 24-bit DAC for current control and three 24-bit Δ-Σ ADCs to monitor current and voltages. The ADCs can be read and the DAC updated at the 4 kHz rate needed for feedback control. A precision 16-bit DAC provides on-board calibration. Programmable multiplexers control internal signal routing for calibration, testing, and measurement. Feedback can be closed internally on current setpoint, externally on supply current, or beam position. Prototype and production tests are reported in this paper. Noise is better than 17 effective bits in a 10 mHz to 2 kHz bandwidth. Linearity and temperature stability are excellent.

OVERVIEW

Each magnet for orbit correction at SPEAR 3 will have a bipolar ±30 A supply, the MCOR [1]. One MCOR supply with CANDI daughter board occupies two slots in a 17-slot crate. One crate can support 8 MCORs. The CANDI board controls and monitors the supply's current and voltage, exchanges data with the interface board and the standard VME processor via the crate backplane. The processor plugs into the interface board, which adapts the VME processor to the MCOR crate.

CANDI BOARD DESCRIPTION

The 170 CANDI boards were fabricated and assembled. The CANDI board size is 6.5" x 3.95", about 0.062" thick. A shielding box covers the analog signal processing area. Figure 1 shows a module block diagram.

At the front of the CANDI card there is 4-digit LED display, showing the supply's current value and interlock status; the RS232 input, and the connector for re-programming the FPGA (Field Programmable Gate Array) boot PROM.

Two connectors go to the supply. One transmits the MCOR interlock signals. The other provides the current setpoint to the supply, it carries the output current to the magnet and monitor lines for the 65 Volt bulk supply, the output voltages, and the output current. The short buses connect the supply's signals with the output connector, plugging to the crate backplane. The supply's output signal is split in such a way that half load current goes through the supply's connector and half through the CANDI board connector.

The FPGA executes the processor's commands, reads status, writes and reads three ADCs and two DACs.
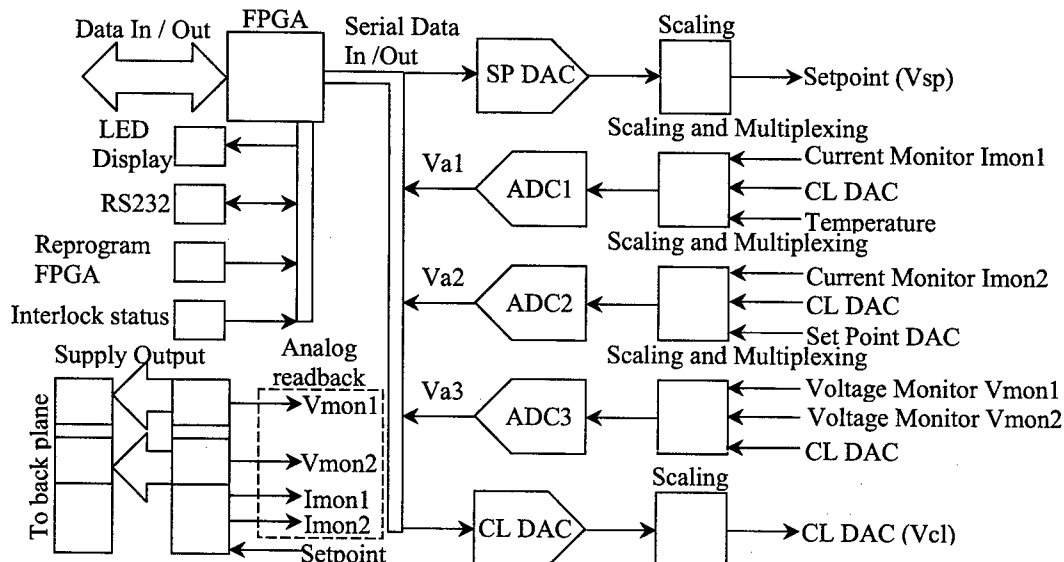
Figure 1. The CANDI block diagram.

The 24-bit resolution Set Point DAC (SP DAC), a Burr-Brown PCM1704, sets the MCOR control voltage from 0V to ±10 V to control the MCOR output current from 0 to ±30 A. Three 24-bit resolution Δ-Σ ADCs, a Burr-Brown ADS1251, digitize analog signals - the Imon1, Imon2, Vmon1 and Vmon2 [2]. A precision 16-bit DAC, a Maxim MAX542 [3] is dedicated to calibration of the ADCs (CL DAC).

The highest ADC output rate frequency is 20.8 MHz at an input clock frequency 8 MHz, the internal digital filter has notches at the output rate frequency and harmonics. The ADC has a fixed over-sampling ratio of 64.

Dual 4-channel multiplexers (MUX) are placed in the front of the signal processing chain. This provides for module calibration, and configuration of local, remote, or global feedback.

REQUIREMENTS

- Required data update frequency 4 kHz.

The analog setpoint and the readback requirements are shown below (Table 1 and Table 2).

Table 1. The current setpoint requirements.

Analog Setpoint	Requirements
Full scale voltage range	± 10 V
Bandwidth	DC - 2 kHz
Accuracy	± 10 mV
Stability (24 hours, ± 3.5 °C)	± 500 µV
Signal to Noise Ratio, integrated over 10 mHz - 2 kHz	105 dB or 17.2 ENOB

- The temperature coefficient limit is: 14.3 ppm/°C (± 500 µV / ± 3.5 °C, out of 10 V full scale).

Table 2. The current monitor readback requirements.

Analog Readback, Imon	Requirements
Full scale voltage range	± 10 V
Bandwidth	DC - 2 kHz
Accuracy	± 1 mV
Signal to Noise Ratio integrated over 1 Hz - 200 Hz	101 dB or 16.6 ENOB
Analog Readback, Vmon	
Full scale voltage range	70 V
Accuracy	± 10 mV
Signal to Noise Ratio, integrated over 1 Hz - 1 kHz	86 dB or 14 ENOB

The ENOB is the Effective Number of Bits, Signal to Noise Ratio = 6.02 dB * ENOB + 1.76 dB.

RESULTS

Accuracy

The following scheme was used to measure accuracy (Fig. 2). The SP DAC and the CL DAC are swept across a -10 V to +10V range in 2 V steps. The SP DAC output signal (Vsp) goes to the external Data Acquisition Unit (Vref) and to the ADC2 (Va21) via the multiplexer. After reading them, the multiplexer connects the ADC2 input to the CL DAC output (Vcl); the ADC1 and ADC3 are already connected to the CL DAC. One cycle of the measurements ends when ADC1 (Va1), ADC2 (Va22) and ADC3 (Va3) are read. A linear fit yields the relative gain and zero offset. Calibration results are saved for operational use.

Calibrated data and source signal differences are within the ± 300 µV peak-to-peak; the rms is 123 µV, better than required.
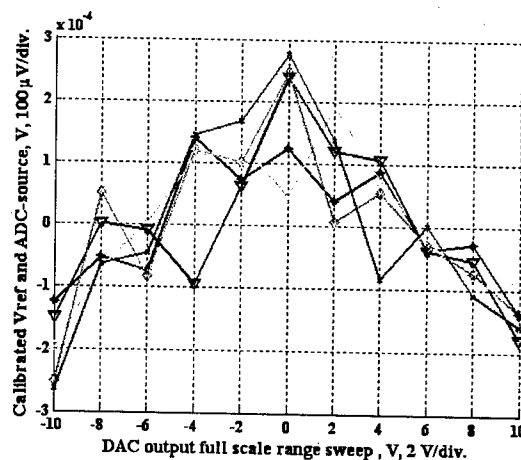
Figure 2. The setpoint and the readback accuracy.

The noise performance

The ENOB measurements were performed at 4 kHz data update frequency and 20 kHz ADC readback rate. The SP and CL DAC outputs were set to + full scale. In addition to the ADC 64 oversamplings, the FPGA averages 16 ADC samples. This is equivalent to increasing the ADC oversampling ratio a factor of 4. The set point and the read back ENOB spread is shown on the Table 3 below.

Table 3. The setpoint and readback ENOB.

Source signal to ADC #	ENOB	
	min	max
Setpoint: SP DAC to ADC2	17.3	17.7
Readback: CL DAC to ADC1 & 2	17.5	18.0
Readback: CL DAC to ADC3	17.0	17.9

The production module has no additional averages, the ADC output rate is 4 kHz, the readback ENOB is reduced another 1.25 bits.

Stability

Stability is tested by observing the setpoint output voltage for extended periods at fixed DAC setting near full scale. For example Figure 3 shows the setpoint output varying 1.1 mV over a 40 minute interval where ambient temperature drops 2.6 C. A temperature coefficient for the DAC of 44 ppm/°C at a 10 V full scale is estimated from this data.

Stability under local feedback was implemented using the internal ADC to compensate for DAC drift.
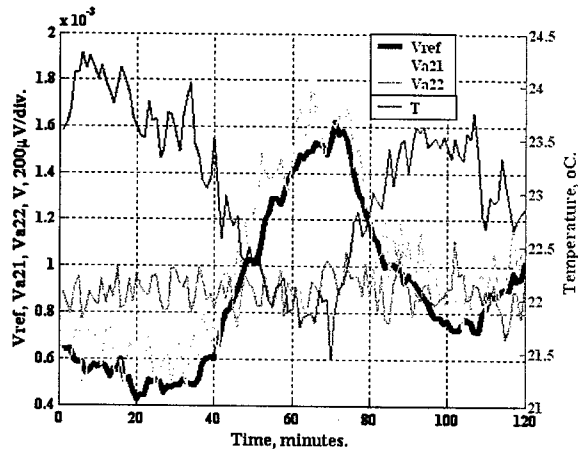
Figure 3. The Vref and Va21 follow the Vsp +10 V DC signal. The Va22 monitors the Vcl.

The test program was run for 50 hours. The average of every 100 points was taken, then averages were analyzed (Fig. 4).
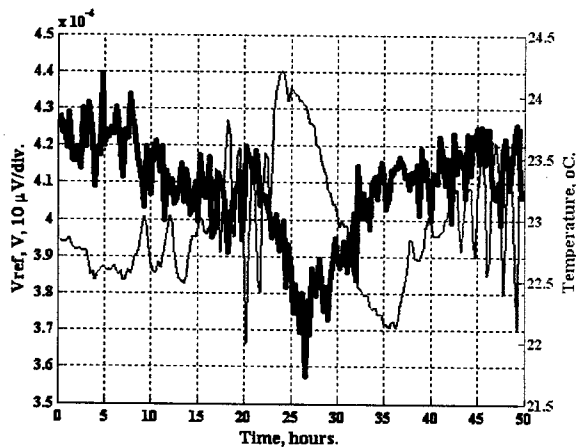
Figure 4. The Vref monitors the DC + 9 V signal of the SP DAC - ADC2 - SP DAC feedback loop.

- The deviation of the averaged data is less than ± 50 μV; not averaged result is ± 200 μV.

At the fast ramp after 23rd hour, Vref drifts to 43 μV (to the minimum), the temperature varies to 1.21 °C.

- Vref ramp drift is 3.6 ppm/°C.

The long slope from 0 to Vref minimum gives the Vref and temperature drifts: 82 μV and 1.7 °C respectively:

- Vref long term slope drift is 4.8 ppm/°C.

Probably, this drift is due to the External Reference 5.4 ppm/°C temperature coefficient at 9 V scale.

The same routine was performed with the CL DAC and ADCs. The Va3 (Vmon) and Va22 (Imon) deviation was ± 300 μV and ± 250 μV respectively. The feedback loop was closed through the ADC2. The feedback signal was bouncing within the CL DAC bit level, after few steps the CL DAC was tuned to the required value and then did not change it over 50 hours. So the feedback was not in use most of the time. The Va3 and Va22 averaged deviations

are 74 μV and 54 μV respectively. The maximum temperature drift was about 6 °C, the total drift - 1.2 ppm/°C and 0.9 ppm/°C for the ADC3 and the ADC2 respectively.

SUMMARY

The 170 CANDI corrector power supply controller boards were fabricated and assembled. Their performance was tested and exceeds requirements. Accuracy after the calibration is within ±300 μV at full scale.

Noise on the analog set point voltage varies from 17.7 to 17.3 ENOB. The current read back ranges from 18 to 17.5 ENOB. Stability over 50 hours is about ± 200 μV and 5 ppm/°C for the set point, and ±250 μV and 1 ppm/°C for the analog read back.

The whole system shall be assembled and commissioned on the SPEAR-3 light source.

REFERENCES

[1] G.E. Leyh, et. al. "A Multi-Channel Corrector Magnet Controller," PAC 95 and IUPAP, Dallas, Texas, 1-5 May 1995

[2] http://www.ti.com/ Burr - Brown Products from Texas Instruments.

[3] http://www.maxim-ic.com/index.cfm Maxim Integrated Products.

MODIFICATION OF THE CORRECTION BIPOLAR POWER SUPPLY OF THE STORAGE RING

Chen-Yao Liu, Justin Chiou, Yuan-Chen Chien, Chang-Hor Kuo
National Synchrotron Radiation Research Center 101Hsin-Ann Rd, Science-Based Industrial Park,
Hsinchu 30077, Taiwan, R.O.C.

Abstract

To satisfy performance 1.5GeV beam current requirement in storage ring, the correction power supplies' output current ripple have to be low enough from 0Hz to 10 kHz. To suppress the output current ripple noise from 0Hz to 10 kHz, the correction power supplies must be modified from the normal frequency response to higher bandwidth to make the beam current performance in storage ring better. The controller gain of the correction power supplies is changed to detect the high frequency dynamic current ripple. A control gain modification scheme is presented here and the correction power supply with control gain modified have been proven to exhibit excellent output current ripple reduction from 0Hz to 10kHz. Results and measured performance will be presented in this paper.

Figure 1: Model SRR-220-25-20-IV of the INVERPOWER power supply

INTRODUCTION

The correction power supplies are responsible to control the correction magnets to steer the beam current to stay within the desired trajectory in the storage ring. Hence, the output current performance of the correction power supply will greatly influence the stability of the beam current. To future improve the beam current stability, the correction power supply's output performance is measured and investigated. It is found that the correction power supply's control gain has major contribution on the stability of the beam current.

Three major factors are evaluated for the performance of the correction bipolar power supply: [1] 0~10kHz of the current ripple response [2] long term stability of output current [3] Output noise current level. After the internal control gain is modified inside the correction bipolar power supply, not only the output current performance is satisfied, but also the low and high frequency output current response is good for various correction magnet loads of the storage ring.

This makes the control gain more adaptable to different loads. Most of all, when changing different correction magnets load to the correction power supply, the output current ripple of the correction bipolar power supply is under the specified specification. Compared with the old correction bipolar power supply, correction power supply's adaptability to various load is achieved by adjusting the control gain of the correction bipolar power supply. The correction bipolar power supply of NSRRC mentioned in this paper is designed by INVERPOWER Corporation. The block diagrams of the model SRR-220-25-IV as shown in the following Figure 1.

MODIFICATION PRINCIPLE

The major principle to modify the controller gain of the correction bipolar power supply, is to make the control gain of the current feedback loop meet the requirement of the output current ripple response of the correction bipolar power supply and the magnet both under the spec. To reduce the current ripple response, the correction bipolar power supply and the correction magnet is combined and regarded as one single system in our modification scheme. The control gain adjusted is the total feedback gain of the whole system.

For the adjustable function of the current feedback loop circuit, the characteristic of the current ripple response is specially paid attention to. The DANFYSIK DDCT 866 current measurement system and the HP 35670A dynamic signal analyzer are applied to analyze the total quick response of the current ripple response. The current ripple response measurement is shown as Figure 2.
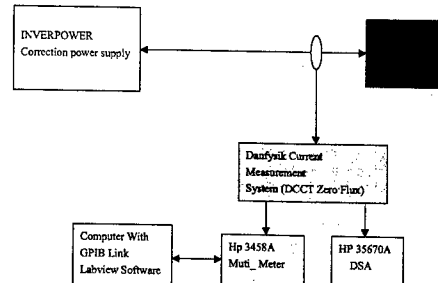
Figure 2: Block diagram of the current ripple response measurement system

Another important principle we certainly considered in the design is the stability of the feedback signal and the setting signal. A main circuit diagram of the control gain stage of the total correction bipolar power supply is shown as figure3.
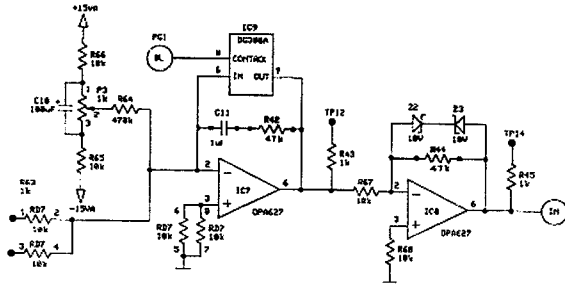
Figure 3: Main circuit diagram of the control gain stage of the correction bipolar power supply

For old requirement, the output current ripple variation has to be under 100ppm specification. For new control gain modification of the correction bipolar power supply, not only the adjusted correction power supply should meet the need of the old requirement, but also the current ripple from 0Hz to 10kHz is also controlled under 100ppm for the total ripple amount. To reach this purpose, the type and the structure of the controller was researched first for our designing the modified control gain step by step. Before we design the modified control gain. As shown and analyzed in Figure 3, the control stage of the correction bipolar power supply is of Proportional Integration Controller type (PI control), the error signal is first integrated and then amplified by a proportional gain stage. By adjusting the gains in both the integral and proportional stage. We can observe its effect on the output current ripple performance.
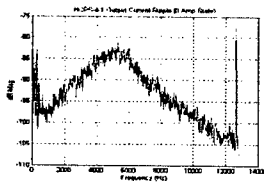
Figure 4: The current ripple increase from several hundred Hz to about 5kHz and then drops slowly as frequency increase.

Since the higher PI control gain of the correction bipolar power supply reacts with high speed, the fake signal produced by the parasitic noise in the circuit will make the feedback signal more sensitive. The resonance problem of the output signal will also contribute noise. To solve this problem, the control gain of the correction bipolar power supply is required to be low. The frequency response of the output current before gain adjustment is shown as Figure 4. It's observed that the current ripple

increase from several hundred Hz to about 5kHz and then drops slowly as frequency increase.

The reason for this peak is due to the high input impedance seen by the correction power supply. Figure 5 shows the frequency response of the impedance seen by the correction magnet power supply.
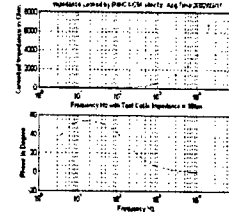
Figure 5: The frequency response of the impedance seen by the correction magnet power supply

The modification scheme is to lower the control gain to suppress high frequency output ripple but large enough to drive the correction magnet. The criteria to determine whether the control gain is too high is to observe the output current step response and check if there is overshoot occurs. The output current step response is shown in figure 6.

(a)   (b)
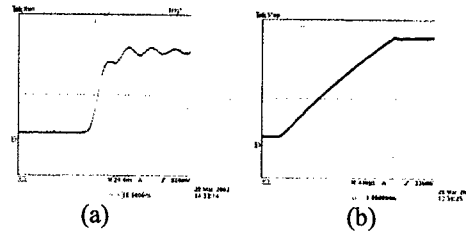
Figure 6: The setting signal (a) and current for step response of the correction bipolar power supply and magnet system (b)

TESTING AND RESULT

After obtaining the parameter values of the controller from our lab, we load these experimental data into the correction bipolar power supplies of the storage ring. After careful testing of every correction bipolar power supply of the storage ring, it is relatively workable, reasonable and of good performance in the storage ring.

The testing data is collected and integrated for the reference in the future. The important parameter of the control gain of the correction bipolar power supplies in the figure 3 are listed below:

PI Control Gain

Old Control Gain: R42=47k ohm & R44=47K ohm

New Control Gain: R42=22k ohm & R44=15K ohm

The measurement results are shown in Figure 7~8. It is shown that not only the current ripple of the high

frequency resonance is reduced, but the current ripples of 60Hz and 60Hz's harmonics are also reduced.
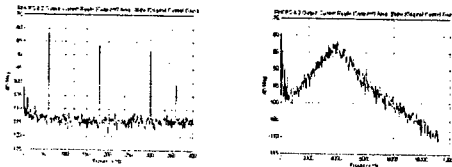
(Frequency: 0~400Hz)   (Frequency: 0~10kHz)

Figure 7: The output current ripple of the correction bipolar power supplies (old control gain at 0Amp.)
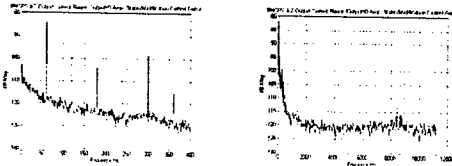
(Frequency: 0~400Hz)   (Frequency: 0~10kHz)

Figure 8: The output current ripple of the correction bipolar power supplies (new control gain at 0Amp.)

The output noise current level is observed to be reduced from original -110dB to be about -120dB.

Next, the output current is set to 10 Amp to observe it's output current ripple performance. The measurement result is shown as Figure 9~10:
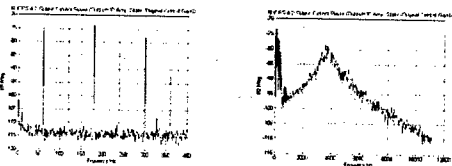
(Frequency: 0~400Hz)   (Frequency: 0~10kHz)

Figure 9: The output current ripple of the correction bipolar power supply (old control gain at 10Amp.)
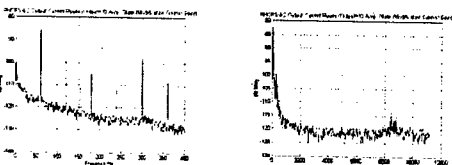
(Frequency: 0~400Hz)   (Frequency: 0~10kHz)

Figure 10: The output current ripple of the correction bipolar power supply (new control gain at 10Amp.)

Although the considerable achievements on reducing the current ripple, it has to be considered whether or not the long-term stability of the output current will be effected by changing the control gain, the long-terms time domain results are shown as Figure 11. It is shown that the output performance is not effected by the new controller parameter.
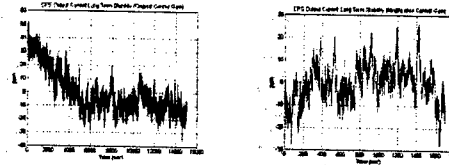
(Old control gain)   (New control gain)

Figure 11: The long-term stability output current (10Amp. Output) testing of the correction bipolar power supply

CONCLUSION

In the design and testing process, applying the technique of RC filter and π circuit to the output stage, the effect of this is limited since the high frequency current resonance problem is not solved. However, by adjusting the interior control gain of the correction bipolar power supplies, the output current ripple is greatly reduced. After modifying every correction bipolar power supply of the storage ring one by one and then putting all the correction bipolar power supplies back to the storage ring system, the performance of the beam current observed is found to be better. The beam current quality in NSRRC is greatly improved.

REFERENCE

[1] Benjamin C. Kuo, Automatic Control System, PRENTICE-HALL INTERNATION, INC. Fifth Edition, 1987.

[2] Join G.Kassakin, Martin F.Schlecht, George C, Verghes, Principles of Power Electronics, ADDISON -WESLEY Publishing Company, 1991.

[3] Bipolar Linear Correction DC Power Supplies Model SRR-220-25-20-IV Operation Maintenance Manual.

INCREASING OUTPUT CURRENT STABILITY OF POWER SUPPLY WITH COMPONENT REPLACEMENT

Kuo-Bin Liu, Chyi-Shyan Fann and Yuan-Chen Chien

Synchrotron Radiation Research Center

No.101 Hsin-ann Road, Hsinchu Science-based Industrial Park, Hsinchu 30077, Taiwan R.O.C.

Abstract

Quadrupole magnets of storage ring must be served with power supplies (quadrupole power supplies) with +/-100 ppm long-term output current stability in Synchrotron Radiation Research Center (SRRC). Using power supplies with lower long-term output current stability could save money but need another control loop to increase their performance that will increasing the complexity of circuitry of quadrupole power supply. Without adding another control loop, some components of quadrupole power supply are replaced by ones with more precious and insensitive to temperature variation; so that the same circuitry structure of quadrupole power supply is kept without increasing its complexity and could reach +/-25 ppm long-term output current stability.

1 INTRODUCTION

There are four families of quadrupole magnets at storage ring of SRRC, and each family of quadrupole magnets includes twelve quadrupole magnets. In original operation condition of SRRC, each family of quadrupole magnet is served with one SCR-type power supply that with +/-100 ppm long-term output current stability and these four power supplies were operated well in the operation period. After insertion devices were installed at the straight section of storage ring, there are there families of quadrupole magnets must be separate into six groups due to there are six sections in storage ring so that the quantity of power supplies should increase six times but with six times lower power.

The specification of these eighteen power supplies is +/-1000 ppm long-term output current stability instead of the original +/-100 ppm long-term output current stability because of the shortage of budget, so there must be some procedure to improve the stability of these eighteen power supplies to be ±100 ppm to meet the specification and let electron beam to be stored stably at storage ring.

Adding extra control loop formed by personal computer, HP 36601A DVM, Danfysik ULTRASTAB 866 DCCT[1], VISHAY 5 Ω burden resister[2] with 5ppm/°C temperature coefficient and computing algorithm could meet the +/-100 ppm long-term output current stability. These eighteen power supplies are controlled with AIAO and DIDO interface that is different to the original interface and this problem could be solved with installing IEEE-488 interface card into PC to communicate with main computer.

Due to communicating speed concern, finally, default AIAO and DIDO interface is the better way for Instrument & Control group to integrate and speed up their control environment so the added control loop with IEEE-488 based must be removed and +/-1000 ppm long-term output current stability should be improved to be +/-100 ppm by another method.

In this experiment, the method used to achieve higher long-term stability of output current of quadrupole power supply is to replace original devices of control circuitry of quadrupole power supply with lower temperature coefficient components.

There were several devices of control circuitry replaced and each one of them makes obvious contribution on long-term output current stability of quadrupole power supply, so measurement will be demonstrated for any replacement of device.

2 IMPROVEMENT OF STABILITY BY ADDING EXTRA CONTROL LOOP

The specification of long-term output current stability of these eighteen power supplies with AIAO & DIDO control interface is +/-1000 ppm and figure 1 shows the actual performance is about 600 ppm that is a little bit better than the specification.
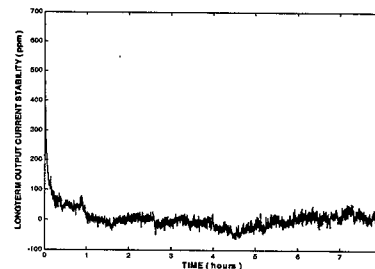
Figure 1: Original long-term output current stability

But from the stable operational point of view of storage ring, 600 ppm long-term output current stability is too high compared with +/-100 ppm requirement.

After adding extra control loop formed by personal computer, HP 36601A DVM, Danfysik ULTRASTAB 866 DCCT, VISHAY 5 Ω burden resister with 5ppm/°C temperature coefficient and computing algorithm, the improvement is obvious and figure 2 shows it's about 100

ppm that is good enough.
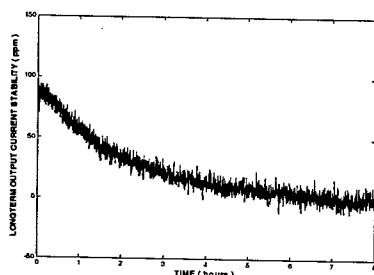
Figure 2 : Long-term stability of output current
after adding extra control loop

3 IMPROVEMENT OF STABILITY BY REPLACEING REFERENCE INPUT STAGE OP AMPLIFIER

Increasing over all control environment speed, Instrument & Control group requires more fast control interface for every subsystem, based on this requirement the control interface of quadrupole power supply is changed from IEEE-488 to AIAO and DIDO interface, and this change is just return the control interface of quadrupole power supply to default one.

With AIAO and DIDO control interface, current control and read-back are analog signals and there is a long distance between current control crate and quadrupole power supply so that ground loop between these two systems exists. Ground loop at times can be a source of noise, if the magnitude of noise is too large such that control circuit of power supply will be affected and the performance of power supply degrade. The effect of ground loop can be eliminated or at least minimized by isolating these two circuitry and isolation can be achieved by transformer, common mode choke, optical coupler, balanced circuitry, frequency selective grounding or isolation amplifier.

There are two current control reference input stages for quadrupole power supply, remote control state and local control state. In normal remote control state the only concern is the long-term output current stability of power supply. The circuitry used as remote current control analog input stage is an isolation amplifier BURR-BROWN ISO120BG[3]. The performance of isolation of BURR-BROWN ISO120BG is undoubted, but temperature coefficient of some parameters (include gain, input offset voltage, ...etc.) seems too large so that better long-term output current stability is impossible.

Instead of an isolation amplifier, the local reference input stage of quadrupole power supply is a differential amplifier composed of four resistors and an AD708[4] operation amplifier. As stated above, a differential amplifier is also able to eliminate or minimize the effect of ground loop. Furthermore, the temperature coefficient of AD708 is much lower than that of BURR-BROWN

ISO120BG and the differential amplifier could be used in the reference input stage of quadrupole power supply by changing some wiring. Long-term output current stability quadrupole power supply is improved as figure 3 after AD708 was introduced. Within 200ppm long-term output current stability is achieved and improvement is obvious compared with figure 1.
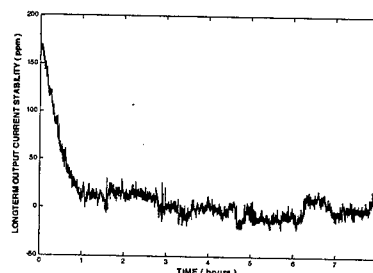
Figure 3 : Long-term output current stability after
modification of reference input stage

4 IMPROVEMENT OF STABILITY BY REPLACEING DIRECT CURRENT CURRENT TRANSDUCER

The original direct current current transducer(DCCT) is LEM LT 300 – S/SP 9[5], the accuracy of nominal analog output current is about 500 ppm and this parameter seems not good enough for power supply to get very good long-term output current stability because the temperature inside power supply should rise when power is delivered to magnet.

The temperature coefficient of secondary compensation current of Danfysik ULTRASTAB 866 DCCT is 1 ppm/ °C better than that of nominal analog output current of LEM LT 300 – S/SP 9, there is so much difference on temperature coefficient and the replacement of these two transducers is not difficult that make us believed this replacement could benefit long-term output current stability of quadrupole power supply. Figure 4 shows the result after Danfysik ULTRASTAB 866 DCCT is installed.
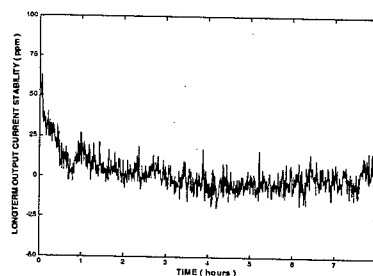
Figure 4 : Long-term output current stability after
replacement of DCCT

Long-term output current stability is improved obviously and under 75 ppm that is better than the

specification we need.

5 IMPROVEMENT OF STABILITY BY REPLACEING BURDEN RESISTER

No matter what DCCT we used for the feedback loop of quadrupole power supply, there still need a burden resistor to be a load for DCCT that output secondary compensation current in ratio to measured current to get a voltage value.

The original burden resister is a metal film 1% 10 ohm resister and it's temperature coefficient is unknown but it's a trial for this resister to be replaced with a VISHAY 5 ohm resister with 5ppm/°C temperature coefficient.

Long-term output current stability is under ±50 ppm as shown in figure 5 after VISHAY 5 ohm resister with 5ppm/°C temperature coefficient is installed and even more after about 10 minutes warm-up time ±25 ppm is achieved.
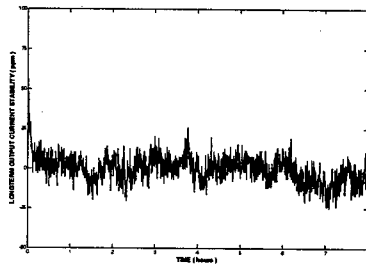
Figure 5 : Long-term output current stability after burden resistor is replaced

6 CONCLUSION

The long-term output current stability of quadrupole power supply used at SRRC is improved by utilizing lower temperature coefficient components to replace original ones that include reference input stage OP amplifier, direct current current transducer for current feedback and burden resister.

All experiments are proceed at full power output of maximum 250 amperes output current of quadrupole power supply, this should be the worst case because at this operational condition temperature inside quadrupole power supply should rise higher than other lower output current. There are obvious results show every replacement of component could contribute improvement on long-term output current stability and it's could be said performance of quadrupole power supply is less sensitive to temperature variation.

All of improvement procedures are just to replace some components and do not change the circuitry of quadrupole power supply that could simplify the maintenance work.

7 REFERENCES

[1] Manual of Danfysik ULTRASTAB 866 DCCT

[2] Data book of VISHAY resister

[3] Data book of BURR-BROWN, LINEAR PRODUCTS, 1995.

[4] Data book of ANALOG DEVICE, LINEAR DATABOOK, 1992.

[5] Manual of LEM current transducer

1400A, +/- 900V PEAK PULSE SWITCH MODE POWER SUPPLIES FOR SNS INJECTION KICKERS

S. Dewan (DPS), W. Eng (BNL), R. Holmes (IE), R. Lambiase (BNL), K. Rust (SNS),
J. Sandberg (BNL), J. Zeng (UOT)

Abstract

This paper describes simulation and experimental results for a 1400A, $\pm$ 900V peak rated, switch mode power supply for SNS Injection Kicker Magnets. For each magnet (13 mΩ, 160μH), the power supply must supply controlled pulses at 60 Hz repetition rate. The pulse current must rise from zero to maximum in less than 1 millisec in a controlled manner, flat top for up to 2 millisec, and should fall in a controlled manner to less than 4A within 500μs. The low current performance during fall time is the biggest challenge in this power supply. The simulation results show that to meet the controlled fall of the current and the current ripple requirements, voltage loop bandwidth of at least 10 kHz and switching frequency of at least 100 kHz are required. To achieve high power high frequency switching with IGBT switches, a series connected topology with three phase shifted (0°, 60° & 120°) converters each with 40 kHz switching frequency (IGBT at 20kHz), has been achieved. In this paper, the circuit topology, relevant system specifications and experimental results that meet the requirements of the power supply are described in detail. A unique six pulse SCR rectifier circuit with capacitor storage has been implemented to achieve minimum pulse width to meet required performance during current fall time below 50A due to the very narrow pulse width and non-linearity from IGBT turn-on/off times.

INTRODUCTION

This paper deals with the description, experimental and simulation results of the 1,400A, ±900V switch mode converter with six pulse SCR rectifier circuit and storage capacitors. In section 2, the basic converter topology including system parameters is described. The relevant specifications are outlined in section 3. The simulation results are outlined in section 4. In section 5, the experimental results show good agreement between experimental and simulation results both at low and high current values. Section 6 discusses the major conclusions of this research.

BASIC CONVERTER SYSTEM

Figure 1 shows the essential elements of the two-quadrant switch mode converter system. For the function of components with lighter lines, refer to reference 1 for details.

All the essential circuit parameters on Fig.1 are the same as reference 1. Additional components added to improve low current performance are shown in thicker lines in Fig.1. The function and parameter values of these additional components are as follows;

- DC storage capacitor Cs to provide essentially a DC source of approximately 60V with low ripple to keep minimum pulse width in the IGBT switching modules. The value of Cs is 1.64F.
- DC filter choke La (30μH) to reduce the 360 Hz ripple in the six pulse rectifier
- Six pulse SCR rectifier (SCRs, Q1 to Q6) that operates in the inverting region at delay angle α=135°.
- An isolating transformer LRT (460:58V) to isolate the load from the 3 phase input

SYSTEM SPECIFICATIONS

This section identifies the significant performance requirements/results for input and output of the pulse converter.

Input

Voltage RMS	460V, +10%, -5%
Current RMS	50A

Output

DC Voltage	0 to 900V, 0 to –900V
DC Current	0 to 1,400A max. Pulsed (400Arms equivalent)
Pulse Repetition Frequency	60Hz
Switching Frequency	108kHz
Large Signal Current Response	> 2kHz at 45° Shift at 1.4kA
Load Current Tracking	See Figure 2
Tracking Error	0.1%
Load Current Fall time	< 0.5msec. from 1.4kA to 4A
Current Stability In Flat Top	< 0.1% (1.4A)
Magnet Load	L= 160μH, R=0.013Ω

Note:
1. The linear rise plus the flat top of the current reference waveform varies from 2 to 3 ms and since fall varies from 280 μs to 1 ms, the worst case pulse width is 4 ms.
2. The fall time for the reference is 280 μs and the load current falls to less than 4A in less than 500 μs. Any overshoot on the current waveform shall settle in less than 300 μs.
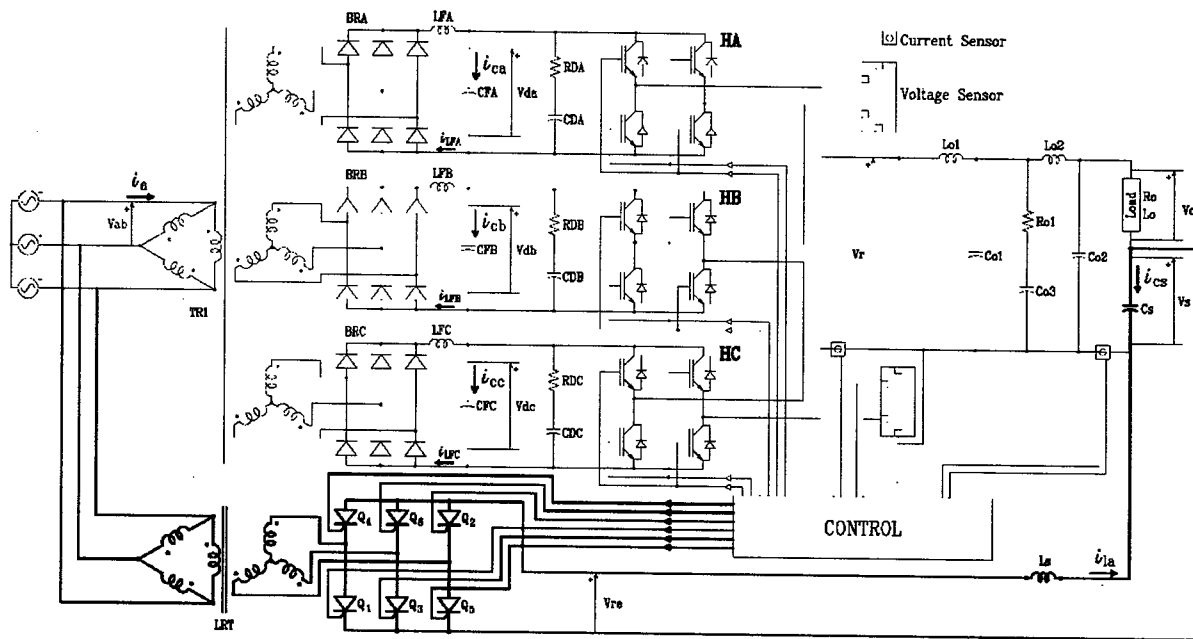
Figure 1 Basic 1,400A, ±900V Converter System with Energy Storage Capacitor CS and Six Pulse SCR Rectifier
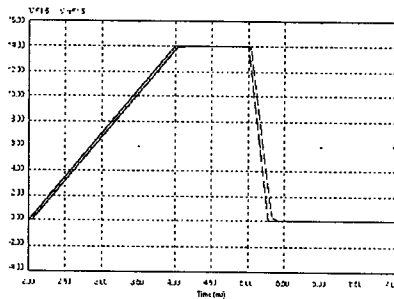
Fig.2 Output current (100A/V) and required output current feedback (100A/V), according to system specifications

SIMULATION RESULTS

This section provides the following simulation results (in addition to the simulation results in reference 1):

i.   Figure 3 shows output current i_o, and output voltage (v_o) for rated value of i_o
ii. Figure 4 shows energy storage capacitor current (i_{cs}) and output current io for rated value of io
iii. Figure 5 shows filter inductor (La) current (i_{la}) and six pulse rectifier voltage (v_{ro}) for rated value of io
iv. Figure 6 shows output current i_o, and output voltage (v_o) for i_o near zero for rated value of io

These results meet the required critical specification close to zero output current. These results show how a minimum DC voltage is introduced in the circuit that absorbs and acts as a DC battery source. A storage capacitor CS only absorbs AC current, DC current (i_{ra}) returns the active DC power to the ac source due to inverter region operation of the six pulse bridge (delay

angle α=135°). The steady state DC storage capacitor voltage (Vs) is 65V with 0.5V peak to peak ripple at pulsing frequency of 60 Hz.
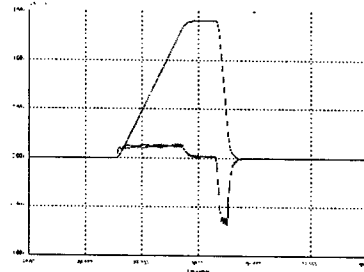
Figure 3 output current i_o (500A/div), and output voltage v_o(500V/div) for rated value of i_o
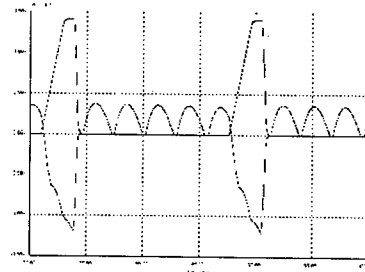
Figure 4 Energy storage capacitor current i_{cs} (500A/div) and output current i_o (500A/div) for rated value of i_o

771
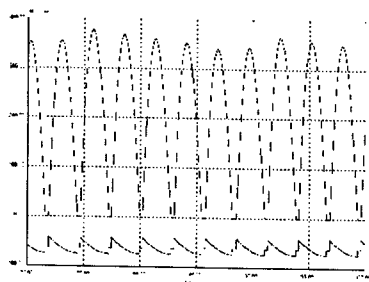
oltage

Figure 5 Filter inductor La current i_{la}(100A/div) and six pulse rectifier voltage v_{re}(100V/div) for rated value of i_o
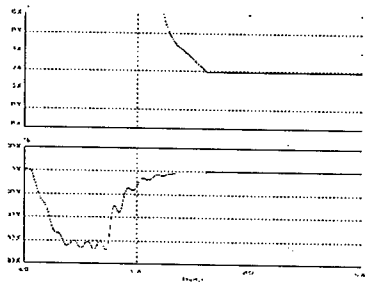
Figure 6 Output current i_o (5A/div), and output v v_o(200V/div) for i_o near zero for rated value of i_o

Figure 9 Output voltage of SCR rectifier v_{re} (25V/div) and filter inductor current i_{la} (250A/div)
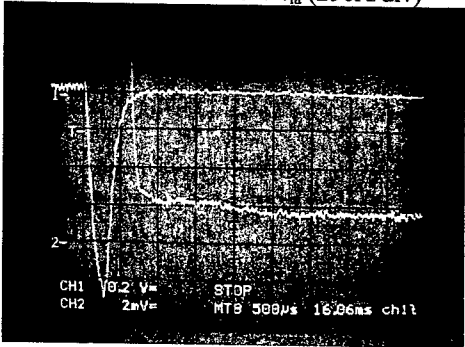
Figure 10 Output current i_o (4A/div), and output voltage v_o(100V/div) for i_o near zero for rated value of i_o

EXPERIMENTAL RESULTS

Experimental results shown in figures 7 to 10 are in close agreement with simulated results in figures 3 to 6.

Figure 7 Output voltage v_o (100V/div) and output current i_o (400A/div)

Figure 8 Capacitor current i_{cs} (240A/div) and output current i_o (140A/div)

CONCLUSIONS

This paper has discussed the features and results of a high power amplifier. The desired rise, flat top and fall time current results were achieved for pulse magnet current from 1,400A to 4A. The main problems are:

1). The peak to peak ripple current at flat top is about 4A (required is 1.4A)

2). The current tracking between two similar units should be better than 0.5%. A great deal of simulation work is needed to establish the most sensitive parameters that affect current tracking. Also means must be identified to correct for practical variations in load parameters.

Further modification to the converter circuit and controls to achieve desired ripple and tracking current performance will be presented in a subsequent paper. For any question, please contact

Shashi Dewan (dewandps@aol.com)
Bob Holmes (iepower@iepower.com)

REFERENCES

[1] S. Dewan, et.al " 1.12 MVA Peak Two Quadrant Pulse Switch Mode Power Supply for SNS Injection Bump Magnet," EPAC'02, Paris, June 2002, pp.2460-2462.

FLUKA SIMULATIONS OF THE LOSS OF THE STORED ELECTRON BEAM AT BESSY *

K. Ott [†], BESSY, Albert - Einstein - Str. 15, 12489 Berlin, Germany

Abstract

The synchrotron light source BESSY consists of a 50 MeV microtron, a full energy synchrotron and a 1.9 GeV storage ring. At synchrotron light sources the accidental loss of the stored beam can occur several times a year. This could mean a considerable risk for the users because of the bremsstrahlung flash coming through the open beamshutters. This is to our knowledge the first time, that this occurences are discussed in detail for synchrotron light sources. We used the particle interaction and transport code FLUKA for the calculations in different scenarios. We present here additional radiation safety measures based on the FLUKA results that decrease the possible personal dose from those beam losses below 1 mSv/year. Comparisons of the FLUKA results with semi - empiric formulas for radiation through lateral shielding are presented too.

INTRODUCTION

The storage ring BESSY II is in operation since 1998 and since 1999 used for a regular scientific program with synchrotron radiation. It has an extended double bend achromat lattice with a 16-fold symmetry. Up to 14 straight sections are suited for the installation for wigglers, undulators and wave length shifters (WLS). Two sections are used for the rf system and the injection septum. The full energy booster (1.9 GeV) operates in 10 Hz and is used asynchronously to fill the storage ring with bunch trains of 300 nsec. The short injection periods (< 2 min and 3 to 5 times a day) are crucial for the annual radiation dose outside the shielding wall.

The electron losses at the vacuum system causes γ - radiation, giant - resonance neutrons quasi - deuteron fission neutrons and neutrons from photo - pion production. (The maximum of the energy spectrum of both γ and neutron radiation is at about 1 MeV).

In every beam line angle at the closest transversal distance to the machine a stationary γ und neutron measurement system is installed outside the shielding wall in the experimental hall. The detectors are a ionisation chamber and a BF_3 counter and are sufficient to measure the pulsed γ and neutron radiation during injection without loss of information. The measurement period is dependent of the dose rate and can be reduced down to 1 sec automatically. The data are accumulated by a PC every minute.

The measurement system is in operation since 1998 and we found values between of 0.8 - 1.2 mSv/year at the sections 2 - 15 and 3.8 (1998) - 2.2 mSv/year (2002) at the

injection septum (section 1) with falling tendency because the machine test periods have been reduced. The values include the natural annual dose which is 0.6 mSv/a in Berlin.

The synchrotron radiation has a critcal energy of 2.5 keV (dipols), 2 keV (wigglers) and 1 keV (undulators), so it is completely absorbed in the vacuum system with 2 mm stainless steel. The critical energy at WLS beamlines rises up to 10 keV, so at these beamlines are located within hutches with a lead screening up to 5 mm.

At the ID beamlines the 8 m gas target of the straight section causes in forward direction 300 mSv/h gas bremsstrahlung at 10^{-7} Pa and 1.7 GeV in a cone with an angle of 0.6 mrad ($2/\gamma$). At ID beamlines with a mirror chamber this radiation is absorbed with 30 cm Pb in forward direction. ID beamlines without a mirror chamber are secured by a personal interlock system.

So from the considered contributions to the personal dose the limit of 1 mSv/a for non - radiation workers is hold in the experimental hall.

What we discuss now is the contribution of the accidental loss of the stored beam with opened beamshutters which occurs about 50 times a year at BESSY.

ACCIDENTAL BEAM LOSSES

At BESSY the electrons lose 170 keV per cycle within the convolution time of 840 nsec which is 10^{-4} of the nominal energy of the storage ring. Dependent of tune and chromaticity the storage ring accept electrons within max. 5 % of the nominal energy. That means that the electrons will be outside the dynamical aperture within 500 cycles or 0.4 msec if the rf system is switched off by a failure function or by an interlock circuit.

Beam losses are also caused by failures of power supplies or the control system. If the power supply circuit of the main ring dipoles is switched off, it lasts 700 msec (RL circuit) until the current is zero.

From

$$x(s_0) = \theta \cdot \frac{\beta(s_0)}{2 \tan \pi Q} \qquad (1)$$

and $Q_x = 17.8, Q_y = 6.7 \ \beta_x^{max} = 17m, \beta_y^{max} = 20m$ one gets the orbit change x where the distortion kick θ occurs. So in the horizontal and vertical direction a kick at a high β location of approximately 1 mrad is necessary for an orbit change of 10 mm, which is usual sufficient for a beam dump.

So if we compare this with the deflection angle of a BESSY dipole of 196 mrad, we can estimate, that a beam loss will occure within 3.6/32 msec if the power supply of the 32 main dipoles is switched off. (The dipoles are

located at places where the horizontal β_x function is maximal). This means too, that the primary particles cannot reach the experimental hall through a 0^0 insertion device beam line because at the time of the beam loss almost the complete magnetic field of the dipoles still deflects the electrons.

For beam losses caused by failures of the power supply or control system of other magnets (steerer, quadrupoles, sextupoles) we can estimate the time until the beam is lost < 1 msec with similar arguments.

In the average the electrons are lost by crossing the vacuum chamber at places where the β - function is large and / or the aperture is small around the ring.

If we consider the annual dose, we can assume that the annual electron losses are divided around the ring. But for a single event one cannot make this approximation. Because it is impossible to give a limit of electron losses at a given straight section or other place in an electron storage ring due to a single beam dump, we consider the situation conservativly and assume, that at a single event all electrons are lost at one place as a point source.

FLUKA SIMULATIONS

The consequences of a beam loss with open beam shutters has to be investigated with a Monte Carlo program [1] because the intensity of the resulting radiation field in the experimental hall has to be known as a function of the area. Semi - empirical formulas e.g for labyrinths are not applicable for these calculations.

At the BESSY beamline angles we have three openings for beam lines at 0^0 from insertion devices, 4^0 and 6.7^0 from the first dipol. The shielding wall in forward direction at the beamline angles consist of a 5 cm lead screen (beam height $\pm$ 20 cm) and 1 m heavy concrete.

There is also the possibility of using a 2^0 beamline of the second dipole, but this occurs up to now at only two sections. The beamline from the second dipole has to pass through the side shielding wall with a length of 8 m, so the risks of the accidental beam losses are far less because of collimating effect. We focus in the following on the situation in forward direction at the beamline angle.

Because of the correct inclusion of collimating and stray radiation effects, we use real beamline geometries with collimators and variabel cross sections at both dipole and insertion device beamlines. From the beam line types used at BESSY we used that with the largest aperture for the FLUKA calculations. The origin of the diagrams is located at the end of the straight section (at the beginning of dipole 1). The dipoles are not included, but can be localized as gaps between the machine beamline pieces.

Neutron doses caused by the accidental beam losses in forward direction are more than an order of magnitude lower than the γ doses and not considered in the following.

Scenarios

The most important scenario (see fig. 1) is the calculation of the electron - photon cascade in forward direction along the 0^0 beamline which passes through the first dipole too. We use here a 2.0 cm thick (radius 2.5 cm) target on which the electron beam ($10^{12} e^-$ of 1.7 GeV) hits at normal incident. Such a scenario can occure if the electron beam hits the vacuum chamber (d = 2 mm) of the first dipol at half of the deflection angle, a thin hindrance in the vacuum tube or a misaligned insertion device vacuum chamber in combination with a wrong four magnet bump.

This scenario is conservative because the target has approximately the thickness of the radiation length of iron (1.8 cm), that means two thirds of the energy can pass through the dipol as bremsstrahlung flash and the target is thin enough, so that it has no self absorption. These thickness was used also by Ferrari et al. [4] to maximize the bremsstrahlung in forward direction.

At the 0^0 beamline we use a steel box with a 15 cm thick piece of silicon to modelize the mirror chamber. The absorber for the bremsstrahlung is of lead (30 cm) within a lead wall (10 cm) to absorb stray radiation. On the left and right hand side of the bremsstrahlung absorber are two lead stripes (thickness 5 cm, length 30 cm, height 10 cm) perpendicular to the stray aborber and parallel to the beamline.
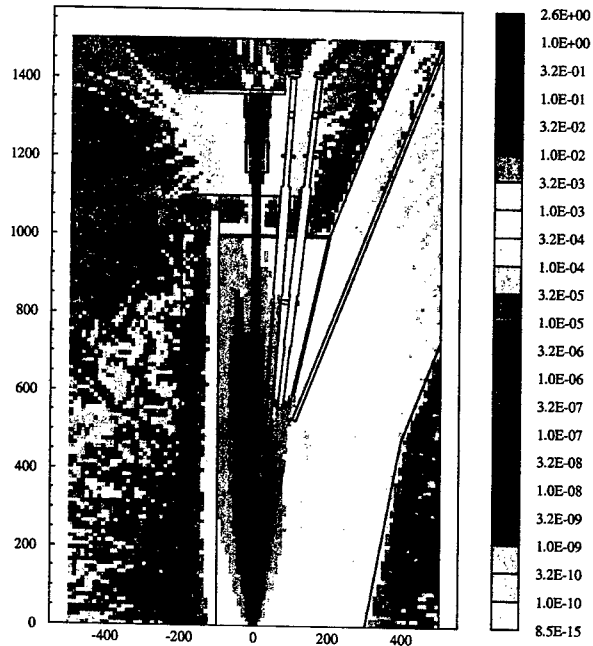
Figure 1: $\phi = 0^0 \gamma$ radiation, dose in Sv/ dump (10^{12} electrons)

The source term of the γ radiation for a target in forward direction was investigated by several authors [2], [3], [4] but their results differ at almost two orders of magnitude. One reason of this is that the detector or the binning geometry does not match with the small angle cone ($2/\gamma$) in

which the bremsstrahlung is emmitted. Therefore small detectors has to be used to investigate the geometrical spread of this type of radiation. But this decreases the statistics or increases the computing time. Another reason is that so called thick targets are used, whose self absorption in forward direction is considerable. In the case of thin unshielded targets the correct inclusion of the low energy part of the electron - photon cascade and the correct inclusion of β doses at close distances seems questionable.

To compare our calculations we use therefore the paper of Dinter et al [5], who investigated the dose behind beam absorber in forward direction. This geometry correspond with the situation at the 0^0 beamline behind the 30 cm lead bremsstrahlung absorber. With $E = 1.7$ GeV and 10^{12} electrons we get from [5] for dose behind this absorber 20 μSv/dump. This is close to our value of 8.5 μSv/dump. If we include our 2 cm iron target in the formula of Dinter et al. [5] (with good accuracy as copper, because no iron attenuation coefficient was given), we get 10.5 μ/dump which is in good agreement with our value.

As the next scenario (see fig. 2) we consider the electron beam hitting the vacuum chamber of stainless steel with $d = 2$ mm at an angle of $\phi = 2^0$ between dipole 1 and dipole 2. This results in effective thickness of 5.7 cm is sufficient for the electron - photon cascade to develop and it has no transverse self absorption. The dump doses > 300 μSv/dump are located in a transversal distance < 0.5m of the dipole beamlines in the experimental hall. At the end of the dipole beamlines is a beamstop located with 10 cm lead thickness. At these place the mirror chamber of the dipole beamline is located in the reality too.
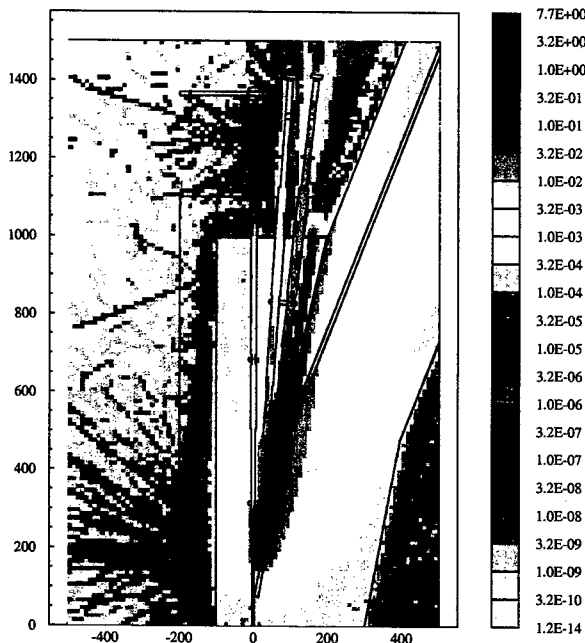
As last scenario we set the point source behind dipol 2. As scenario parameters we use again the hitting angle $\phi = 2^0$, target material iron, thickness d = 2 mm, $d_{eff} = 5.7$ cm or 3.3 radiation lengths.

The three openings of the beamlines are screened by a lead stripe with the length of 4 m, thickness 5 cm and height of 10 cm within the storage ring tunnel.

So from accidental beam losses downstream of dipole 2 the radiation field does not exceed 0.3 mSv/dump.

RESULTING SAFETY MEASURES

We decided, to divide the experimental hall in a large area where the annual personal dose is < 1 mSv/a and sixteen small control areas, which are accessible for BESSY staff only.

The borderlines of the 16 control areas are defined by the following criterions: a) The dose for a single beam dump has to be < 1 mSv/dump for the worst case scenario at the border of the control area. b) The annual dose of all beam dumps has to be lower than 1 mSv/section if the 50 dumps/year are divided to all 16 sections equally at the border of the control area.

From a) and b) results the maximum dump dose in the border of the control area as < 0.3 mSv/dump. According to this dose limit a fence was installed from the corner of the shielding wall to the lead screen. This lead screen against stray radiation was broadened to the left side. From the right edge of this lead screen the fence was installed 2 m parallel to the shielding wall. The enclosure of the area was completed by installing a door between the right dipol beamline and the shielding wall.

In the few cases where the 0^0 wiggler/undulator beamline has no mirror chamber (or the mirror chamber is far downstream) the complete beamline is surrounded by a fence. In the case of wave length shifter beamlines the complete beamline is enclosed in a hutch, so no further installations are necessary.

ACKNOWLEDGEMENTS

REFERENCES

[1] A. Fassò, A. Ferrari, P.R. Sala: "Electron - Photon Transport in FLUKA: status"; A. Fassò, A. Ferrari, J. Ranft, P.R. Sala: "FLUKA: Status and Prospective for Hadronic Applications", Proc. MonteCarlo 2000 Conf., Lisbon, Springer - Verlag Berlin (2001)

[2] W. P. Swanson, Tech. Rep. Ser. 188, IAEA Wien (1979)

[3] M. Sakano, H. Hirayama, S. Ban, Rad. Prot. Dos. 37, p165 (1991)

[4] A. Ferrari, M. Pellicioni, P.R. Sala, Nucl. Instr. Meth. B 82 p32 (1993)

[5] H. Dinter, J. Pang, K. Tesch, Rad. Prot. Dos. 28,3 p207 (1989)

Figure 2: $\phi = 2^0\gamma$ radiation, dose in Sv/dump (10^{12} electrons)

THE SHIELDING DESIGN OF THE METROLOGY LIGHT SOURCE *

K. Ott [†], BESSY, Albert - Einstein - Str. 15, 12489 Berlin, Germany

Abstract

MLS will consist of a 100 MeV microtron and a 600 MeV electron storage ring. The investigations of the radiation types occuring at those machines dependent of the electron energy, target and shielding materials, observating angles and geometric aspects are well established, often condensed in semi - empiric formulas and in good agreement with the results of Monte Carlo codes like FLUKA for lateral shielding. But as important as the pure physical aspects of radiation are for a shielding design the operating times and modes and the considerations of possible crash scenarios. We present here an approach of considering failure operating probabilities at electron storage rings based on years of radiation and operating observations of BESSY I and BESSY II for the shielding design of MLS. Comparisons of FLUKA calculations with the used semi - empiric formulas are presented too.

INTRODUCTION

The Physikalisch - Technische Bundesanstalt (PTB) needs a low energy storage ring as primary radiation normal for photon energies in a spectral range from ultraviolet to extreme ultraviolet to accomplish her tasks as a governmental metrologic institution. The optimal technical solution is to build a low energy compact storage ring with an electron energy from 200 MeV to 600 MeV close to BESSY II in Berlin - Adlershof. The concept was developed in cooperation with BESSY [1].

The preinjector will be a 100 MeV race track microtron, the acceleration to max. 600 MeV is resolved in the storage ring through ramping. Microtron and storage ring will be located in two different bunkers, so access to the microtron is possible during operation of the storage ring for i.e. attendance work. Access to the storage ring during operation of the microtron is not necessary.

The guidelines given by the EURATOM are now law in the most member states of the European Community and since 2001 in Germany. The most important change was the decrease of the personal dose limit for non radiation workers from 5 mSv/a to 1 mSv/a.

We decided to hold this limit within the experimental hall (surveillance area). The local dose limit for the general area (outside the buildung) are unchanged and 0.3 mSv/a for the indirect radiation, 1 mSv/a for direct radiation. The two bunkers are restricted area during operation because the dose rate limit respective to the german law of $\dot{H} >$ 3mSv/h can be exceeded.
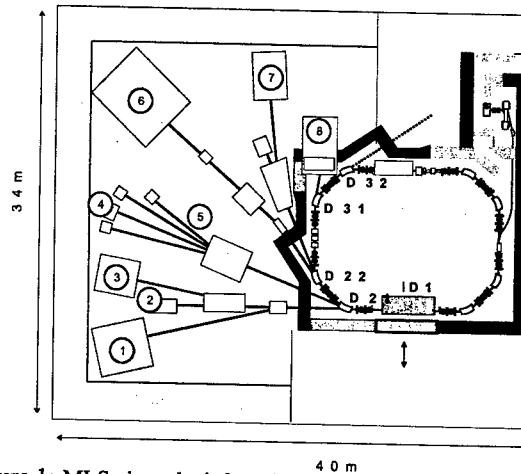
Figure 1: MLS view; the infrared experiment(8) is located on the roof; shielding black: heavy concrete, blue-green normal concrete

The roof of storage ring and micotron bunker is used for technical installations and so should be as accessible as the experimental hall with similar doses.

MACHINE PARAMETERS

The storage ring has a rectangular shape with four straight sections with pairwise different length. The two short straight sections are used for the rf and the injection septum, the two longer sections offer place for two undulators.

Microtron

Table 1: Microtron parameters	
Maximum energy:	100 MeV
Number of cycles:	19
ΔE / cycle:	5.3 MeV
Pulse current :	10 mA
Rf frequency :	2.9986 GHz
Pulse length :	100 nsec - 1 μsec
Max. rep. rate :	10 Hz
Energy spread :	0.1 MeV
Emitance :	0.1 mm mrad
Dipole field :	1.13 T

Such microtrons are used at the storage rings MAX I in Lund, Sweden and at ASTRID in Aarhus, Denmark. Both microtrons are identical and are offered now by Danfysik A/S commercially.

Storage ring

Table 2: Storage ring parameters

Injection energy :	100 MeV
Energy :	200 - 600 MeV
Current :	1 electron - 200 mA
Max. Current / bunch :	3.3 mA / bunch
Energy loss / cycle :	7.53 keV / cycle
Circumference :	48 m
Straight sections :	2 x 6 m, 2 x 2.25 m
Natural emitance :	85 nm rad
Number of dipoles :	8
Max. dipole field :	1.3 T

At 100 MeV the transversal damping times of the beta-tron oscillations during the injection are about 5 sec. Therefore a classical injection scheme would require an injection repetition rate of 0.2 Hz. M. Erikson developed at MAX I a different injection scheme using transversal stacking [2] which will be used at MLS too. With this injection method the repetiton rate is 10 Hz and the max. current of 200 mA is injected within 30 sec as optimal case as it is possible at MAX I. The 10 Hz injection scheme increases the electron losses considerable.

OPERATING OF MLS

For shielding design purposes, one has to distinguish between two cases of storage ring (synchrotron) operation:

a) The machine is used just to inject and produce synchrotron radiation (user mode).

b) The machine is used for machine tests, machine experiments and some phases of the commissioning (machine test mode).

The two modes differ considerable in electron losses and crash probabilities:

Table 3: Operating times,modes a: user, b: machine tests

Mode	a	b
Weeks of operating / year	40	12
Injections / day	5	10
Injections / year	1200	600
Operating of the microtron / injection [m]	<10	<20
Operating of the microtron / year [h]	200	200

ELECTRON LOSSES

The losses during acceleration in the microtron we estimate from respective numbers of the BESSY microtron as 70 %. These losses occure during the first cycles at lower energies, so we assume the energy of the losses as 15 MeV. The electrons leave the microtron after 19 cycles with the energy of 100 MeV. The electron losses during ramping are neglectable $< 10^{-4}$ in comparison with the losses during injection and are not considered further.

Electron losses occur in the transferline between microtron and storage ring with a percentage of approximately 10 % which we divide at one half in the microtron bunker and the other half in the storage ring bunker. The pulse length is 150 nsec and shorter than the revolution time of the electrons in the storage ring of 160 nsec so the injection is conducted as single turn injection. The storage ring is operated with the rf frequency of 500 MHz, and the microtron with 3 GHz. The electron losses due to the rebunching in the storage ring are typically 50 %. The main cause of electron losses in the storage ring is the inefficiency of the injection according to the transversal stacking. From the minimum injection time of 30 sec one can estimate that the total electron losses in the storage ring are 98.7 %. The electron losses in the storage ring are divided in the relation 4:6 between injection septum and four point sources.

FAILURE HANDLING

The electron losses presented in the previous section are the optimal case, the total losses the worst case. To prognosticate the annual dose, we have to estimate, how often per year the electron losses during injection are higher than the optimal case and how large the ammount of these increased losses is. We use an approach which has proved to be very successful for the prediction of annual doses at BESSY II [3].

We define P_U as the failure function probability for the user mode, P_M for the machine test mode and t_{max} is the operation time of the microtron with 200 h/a for user operation and machine tests respective. We get then expressions for the effective annual operating times of the machine component i (transferline 1 and 2, septum, point sources storage ring) for both normal and crash operation for user and machine test mode.

$$t_i^{normal} = t_{max} \cdot \prod_{k=1}^{i} (1 - P_{U/M}) \qquad (1)$$

$$t_i^{crash} = t_{max} \cdot P_{U/M} \cdot \prod_{k=1}^{i-1} (1 - P_{U/M}) \qquad (2)$$

The probabilites P_U and P_M we get from the comparison of the minimum injection time with the respective annual average injection times [2]. One of the reasons of the accuracy of this approach compared with the usual arbitrary estimates of the duration of crash szenarios is the fact, that electron storage rings are never operated optimized to minimum injection times. This is because injection times are usual short and the requirements of the users in respect of i.e. orbit accuracy and stability have priority.

PHYSICAL ASPECTS

The main contribution of the radiation doses at electron storage rings causes from the electron losses during the short injection periods. When electrons hit under small angles the vacuum system bremsstrahlung is produced. This bremsstrahlung causes electron positron pair production and therefore an electron photon cascade with a maximum energy at about 1 MeV [6]. The bremsstrahlung also causes with (γ,n) processes giant resonance neutrons and fast neutrons with quasi deuteron fission. The threshold energy for the photo - pion process is 150 MeV, so this process is neglectable for this consideration. The energy spectrum of the giant resonance neutrons is mainly determined by the material of the target (vacuum system) and in the case of steel (iron) it is similar to the Cf spectrum with a maximum at 1 MeV [5]. The cross - section for the quasi deuteron fission is an order of magnitude lower than that of the giant resonance neutron production. To calculate the effective cross - section for the production of the quasi - deuteron fission spectrum one has to fold the respective energy dependent cross section with the spectrum of the bremsstrahlung. Hence the spectrum of neutrons is strongly increased at energies around few MeV. Even we take into account the lower attenuation coefficients for the quasi deuteron fission neutrons and concrete, the contribution of them to the total neutron dose is lower than 5 % outside the shielding wall for this machine. So we can restrict our consideration of neutrons to giant resonance neutrons with good accuracy.

For calculation of the dose behind lateral shielding we used for the acceleration losses within the microtron the paper of Swanson [4]. For the electron - photon cascade of the accelerated electrons we used the paper of [6] for 90^0 ([7] for 0^0) observation angle because the authors investigated the behavior of an electron beam hitting a vacuum chamber which is the worst case in transversal direction. Other authors used so called optimal thick targets which used to be thick also in transversal direction which causes considerable self absorption. Because the lowest energy in [6] is 150 MeV we checked the applicability of the given semi - empirical formulas by [6] at 100 MeV which are based on EGS4 calculations with FLUKA [8]. As energy cuts we used 500 keV for charged particles and 10 keV for photons.

We investigated the source term H_A behind $75g/cm^2$ normal concrete in 1 m distance at the observating angle $\theta = 90^0$. As target we used an iron plate 2 mm thick, hitting angle $\phi = 2^0$, with an effective thickness of 5.7 cm. The radiation length is 1.7 cm, so the electron - photon cascade could develope.

$$H_A = H_{A1} \cdot \left(\frac{E}{E_0}\right)^\alpha \qquad (3)$$

with H_{A1} at 1 GeV, E in GeV, $E_0 = 1$ GeV.

From the fit we get $H_{A1} = 2.037 \cdot 10^{-17} Sv/e^-$ and $\alpha = 0.924$. At 100 MeV this is within a factor 1.3 of the extrapolation of [6] but we get a stronger energy dependence.
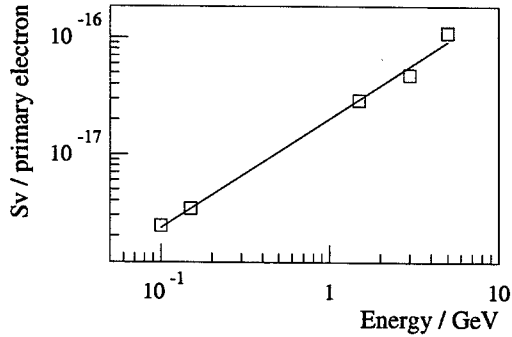
Figure 2: $90^0\gamma$ radiation, iron, $\phi = 2^0$, $d = 2$ mm, $d_{eff} = 5.7$ cm, source term H_A behind $75g/cm^2$ concrete, dose in Sv/primary electron

RESULTS

The outer wall of the storage ring is dimensioned 1 m normal concrete and at the beamline angles and the forward direction at quadrants 1 und 4 with 1 m heavy concrete and a 10 cm lead stripe (beam height $\pm$ 20 cm). The outer wall of the microtron is dimensioned 1 m heavy concrete. The roofs of both storage ring and microtron are 1 m thick. The roofs are of heavy concrete.

Table 4: Storage ring, point source transversal outside

$\gamma - \dot{H}_1$	5.30e − 04	Sv/h	$\gamma - \dot{H}_S$	2.14e − 06	Sv/h
$\gamma - H_U$	2.14e − 05	Sv/a	$\gamma - H_M$	1.07e − 05	Sv/a
$\gamma - \dot{H}_1^{tot}$	2.16e − 03	Sv/h	$\gamma - \dot{H}_S^{tot}$	8.74e − 06	Sv/h
$\gamma - H_U^{tot}$	9.74e − 05	Sv/a	$\gamma - H_M^{tot}$	6.63e − 05	Sv/a
$giant_n - \dot{H}_1$	2.86e − 02	Sv/h	$giant_n - \dot{H}_S$	1.10e − 05	Sv/h
$giant_n - H_U$	1.10e − 04	Sv/a	$giant_n - H_M$	5.51e − 05	Sv/a
$giant_n - \dot{H}_1^{tot}$	1.17e − 01	Sv/h	$giant_n - \dot{H}_S^{tot}$	4.48e − 05	Sv/h
$giant_n - H_U^{tot}$	4.99e − 04	Sv/a	$giant_n - H_M^{tot}$	3.40e − 04	Sv/a

The complete calculated annual local dose is 1.20 mSv/a transversal behind normal concrete and 0.4 mSv/a in forward direction at the beamline angles behind heavy concrete.

REFERENCES

[1] M. Abo-Bakr, G. Wüstefeld, R. Klein, G. Ulm; Proc. EPAC2000, Wien (2000)

[2] M. Erikson: Nucl. Instr. Meth. A261, p. 39 (1987); private communication (2003)

[3] K. Ott: The Shielding Design of BESSY II; Proc. PAC1999, New York (1999)

[4] W. P. Swanson: Tech. Rep. Ser. 188, IAEA Wien (1979)

[5] K. Tesch: Part. Acc. 9, p201 (1979)

[6] H. Dinter, J. Pang, K. Tesch, Rad. Prot. Dos. 22,1 p27 (1988)

[7] M. Sakano, H. Hirayama, S. Ban: Rad. Prot. Dos. 37, p165 (1991)

[8] A. Fassò, A. Ferrari, P.R. Sala: "Electron - Photon Transport in FLUKA: status"; A. Fassò, A. Ferrari, J. Ranft, P.R. Sala: "FLUKA: Status and Prospective for Hadronic Applications", Proc. MonteCarlo 2000 Conf., Lisbon, Springer - Verlag Berlin (2001)

FURTHER EXPERIENCE WITH SLC PERMANENT MAGNETIC (PM) MULTIPOLES

James Spencer, Stan Mao, SLAC MMG*, and Cherrill Spencer, SLAC, Menlo Park, CA 94025, USA

Abstract

PM multipoles have been used in the SLAC damping rings (DR) and their injection and extraction lines since 1985. Due to upgrades of the DR vacuum chambers for higher currents in 1993, there was an opportunity to check some of these magnets[1]. Nothing more was done until a program of real-time radiation measurements was begun in the electron ring to determine causes, levels and effects of integrated gamma and neutron doses on the strengths and harmonic contents for NLC purposes. We discuss results of the latest magnetic measurements, radiation measurement program, semiconductor dosimeters and a few unexpected but interesting conclusions.

INTRODUCTION

PM devices have many current and potential applications based on advantages in size, cost and simplicity e.g. they are self sustaining in the sense that they require no power, water cooling or control electronics for many applications. They do suffer from uncertainties related to environmental and damage effects. In the NLC, PM multipoles, solenoids, undulators and wigglers could have important uses if the limits of their stability to different kinds of high radiation environments could be established. We are revisiting this because future colliders imply beams with unprecedented energy densities, containment and damage problems. Further, the SLC DRs appear to be an ideal place to pursue such studies. As with most radiation measurements at such facilities, they are seldom real-time but only sweeps made after the beams go off for personnel entry and protection purposes. In contrast, we have been obtaining real-time measurements of the main radiation components around the ring i.e. the integrated dose of neutrons and gammas (n & γ).

Background

In 1985, it was difficult to justify using PM multipoles or any PM device in a storage ring. There were few radiation damage (RD) studies[2] and they weren't relevant. Further, there were few vendors and fewer reliable measurements of easy axis characteristics. However, because there was no alternative, 144 sextupoles were made and installed in the e$^\pm$ DRs for chromaticity correction as well as several quadrupoles for the injection and extraction lines[3]. In both cases, compactness was the essential ingredient. In 1993, 21 of the 144 sextupoles were replaced - mostly downstream of the injection kickers and in the electron ring either because their thermal stabilization temperatures of

80° C had been exceeded or because they showed serious mechanical deformation or high radiation levels (in some cases >1 R/hr on contact). These magnets were studied in various ways[1] and then stored. Several have been used for other purposes but not one PM magnet has ever caused loss of the beams or *had* to be replaced.

Current Situation

In 2002, one of the original sextupoles that had been in the ring for 17 years was removed, remeasured and replaced by one that had been stored in 1993 after it had also been remeasured. We then added two radiation detectors on the top and side of this magnet for remote monitoring. At the same time, we continued to monitor dose at other locations in the DR to understand the sources of damage. To our knowledge, no one has done real-time monitoring to ascertain the actual causes of beam loss and to correlate these with radiation damage to determine the actual or potential limits based on possible corrective measures. Likewise, no one has attempted to monitor all sources of radiation damage simultaneously i.e. n and γ in this case. Thus, the advantage of this work over others at this conference[4] is that it provides a more practical working test for NLC magnets in the SLC working environment so that it can be scaled to NLC and also provide guidance for the NLC design. In this respect, it is different but complementary and is, we believe, necessary because it uses real PM magnets with their range of load lines in a mixed, broad band radiation field that is impossible to simulate without artificial assumptions that make calculations practicable.

EXPECTED RADIATION DOSES

In electron and positron accelerators, damage depends on the materials, the location and the beam energy. At < 10 MeV or so, the damage comes predominantly from ionization and atomic excitation regardless of whether the beams are leptons or hadrons[4]. This is true when lepton energies $E^\pm < E_c$ – the critical energy for the material. In high energy lepton rings, radiative effects dominate. These come from synchrotron radiation, bremsstrahlung and bremsstrahlung produced photoneutrons via the (γ,n) giant resonances that typically occur above $E_\gamma > 10$ MeV for any element. Analogously, hadronic resonances occur for $E_\gamma > 200$ MeV. The main questions, of course, are what are the most damaging sources, where do they come from and how to eliminate them. Ref. [4] reviews the situation and shows that dose measurements alone do not determine RD. The difficulties of measuring neutrons makes it easy to ignore this source even though orders of magnitude more damaging per gray than electrons or photons.

---

*SLAC's Magnetic Measurements Group is headed by Zachary Wolf.

DOSIMETERS

One needs only to look at a neutron damage vs neutron energy plot[5] to appreciate the difficulty of such measurements and why the convention of referencing damage to 1 MeV equivalent energy has gained general acceptance. Nonetheless, the same inspection shows why it is highly desirable to obtain spectral data to determine the source and its correction. This is difficult and seldom done. Even in the case of PM studies, it is rarely done except in the form of a post-mortem activation analysis[1]. Similarly, thermal neutron studies have not been done even though B, Co, Nd and Sm have isotopes with large capture cross sections. Various techniques have been used - especially on the assumption that photons are the primary damage source. From this line of reasoning, one eliminates the need for neutron or electron beam loss measurements since the photons are "collimated" around the beam direction. Optical absorption dosimeters are then a common choice based on color changes that do not distinguish between γs or neutrons. While these can cover ranges up to 30 kGy(Si), their neutron responses are typically 50 % of their photon response[6] so they are not interesting for our use. Semiconductor devices are enjoying increased use since they are compact and easily read out and because there is a correlation between RD in semiconductor devices and the displacement damage in bulk silicon. Thus, devices such as bipolar transistors and PIN diodes whose operation depends on volume mechanisms can be expected to provide measures of neutron flux while ones such as MOSFETs that are governed by surface effects should be more sensitive to ionizing radiation e.g. gain degradation in either case. One expects the MOSFET to be the more sensitive[5] and less temperature dependent.
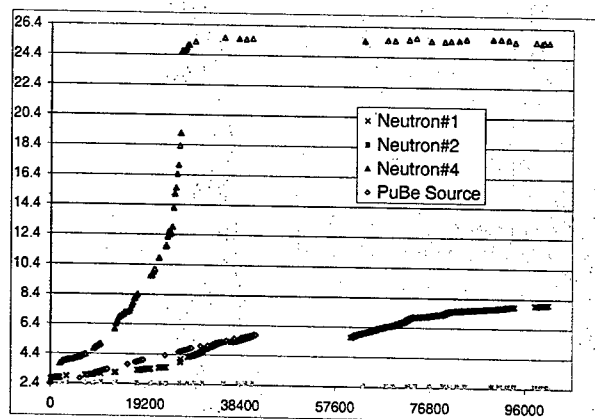
Figure 1: Some measurements of neutron dose in the SLC electron DR in terms of PIN voltage vs time in minutes.

One of many PIN diode[7] data samples at locations around the ring is shown in Fig. 1. Concurrent data for γ's was taken at these same locations with MOSFETs[7]. Fig. 2 shows the relative sensitivity of such detectors for the PuBe source of fast neutrons with $I_n/I_\gamma > 4$ located outside of the DR vault. Gaps in the data indicate beam turn-off or loss of readout hardware.

RADIATION MEASUREMENTS

The variations in Fig. 1 run from no observable damage at levels of 1 mGy up to saturation at $\sim$4 kGy or 25 Volts. The origin shows the values before beam turn-on with all detectors at 2.25 $\pm$ 0.02 V. The sensor varying linearly is the PuBe source. Detector N#4 was on top of a 1-in beam pipe downstream of the first dipole B560 after the extraction septum and in front of sextupole SF608. N#1 was at the exit crotch of the septum and N#2 was > 2 m above this area. There is a small rise during turn-on and tune-up with the abrupt rise to saturation on N#4 over $\sim$2 weeks indicating an average neutron dose rate of >10 Gy/hr.
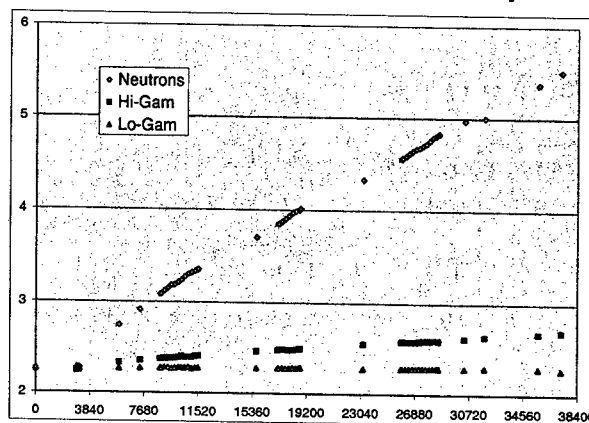
Figure 2: Simultaneous PIN & MOSFET measurements corresponding to the PuBe source data shown in Fig. 1.

High and low sensitivity γ sensors allow measurements up to $\sim$1 kGy and $\sim$30 kGy in Fig. 2. All sensors are nonlinear. The Hi Gam sensor is somewhat sensitive to neutrons and needs correction for optimal accuracy while the PIN sensor is more temperature sensitive. Both types need to have additional temperature readouts or corrections made. N#4 saturated well before Lo-Gam#4 and after Hi-Gam#4 indicating the sextupoles see significant, relative fast neutron flux.
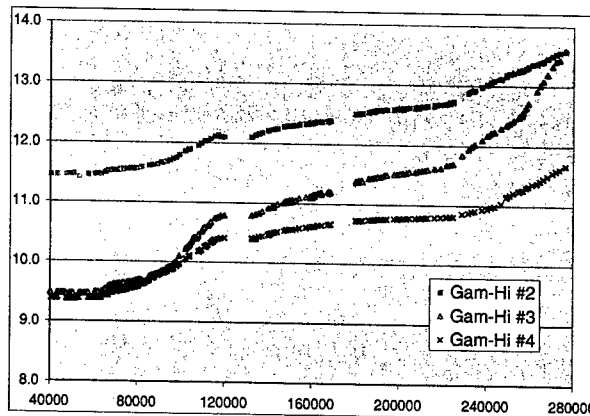
Figure 3: MOSFET data during the latest run cycle

Beam turn-on after unscheduled shutdowns often show significantly higher dose/damage rates in contrast to those that are well done as shown by the flat lines in Fig's. 3-4 where the first large gap defines the Christmas shutdown.

However, unscheduled outages that cause loss of beam and subsequent turn-on problems are not the worst cause of RD. From 1997-2001 there were 18 such failures per DR due to conventional magnet systems with a mean time to repair of ~14 hours. These are hardly visible. Of more interest, are the two regions with steep slopes that lasted for 2 and 3 weeks. In the first, there were vacuum and septa problems, thunder related power outages and a push to obtain luminosity. The second was due to a water leak with one DR quad spraying another. Because this did *not* turn beams off it took nearly 3 weeks to diagnose and caused far worse RD. The only sensor changes between Fig's. 1,2 and 3,4 were #3 & #4 on the side and top of the newly replaced SD708. The Gam-Hi sensors at 5 cm and 2 m above the beam pipe track quite closely in Fig. 3.

MAGNETIC MEASUREMENTS

Following 2, 8[1] and 17 years of operation in the SLC DRs we have observed, within ±0.25 %, a loss of sextupole strength of 0, 2.5 and 6.3 % respectively on single magnets selected at random. All harmonics through the first 16 were originally required to be < 1 % and typically < 0.5 %[3]. In those we remeasured, ignoring first order feeddown, we found no magnet with harmonics worse than ~1.7 %[1].

REFERENCES

[1] G. Gross, J. Spencer and SLAC's MMG, "Experience with the SLC Permanent Magnet Multipoles", EPAC'94, London, June 1994.

[2] R.D. Brown, E.D. Bush, Jr., and W.T. Hunter, LANL Rep. LA-9437-MS, July, 1982. R.W. Blackmore, *IEEE Trans. Nucl. Sci.*, NS32(1985)3669.

[3] J.E. Spencer, "Some Uses of REPMM's in Storage Rings and Colliders", PAC'85, Vancouver, May 1985.

[4] James Spencer, SLAC MMG and James Volk, "Permanent Magnets for Radiation Damage Studies", PAC'03, May 2003.

[5] ASTM Standards Doc. E722-94, November, 1994.

[6] Xiaotian S. Mao, James C. Liu and Gary Lum, "Photon and Neutron Responses of Optical Absorption Dosimeters Used at SLAC", 2001 IEEE Radiation Effects Data Workshop, Workshop Record 2001, 151.

[7] The monitor system was developed at the Center for Medical Radiation Physics at the University of Wollongong, Australia.
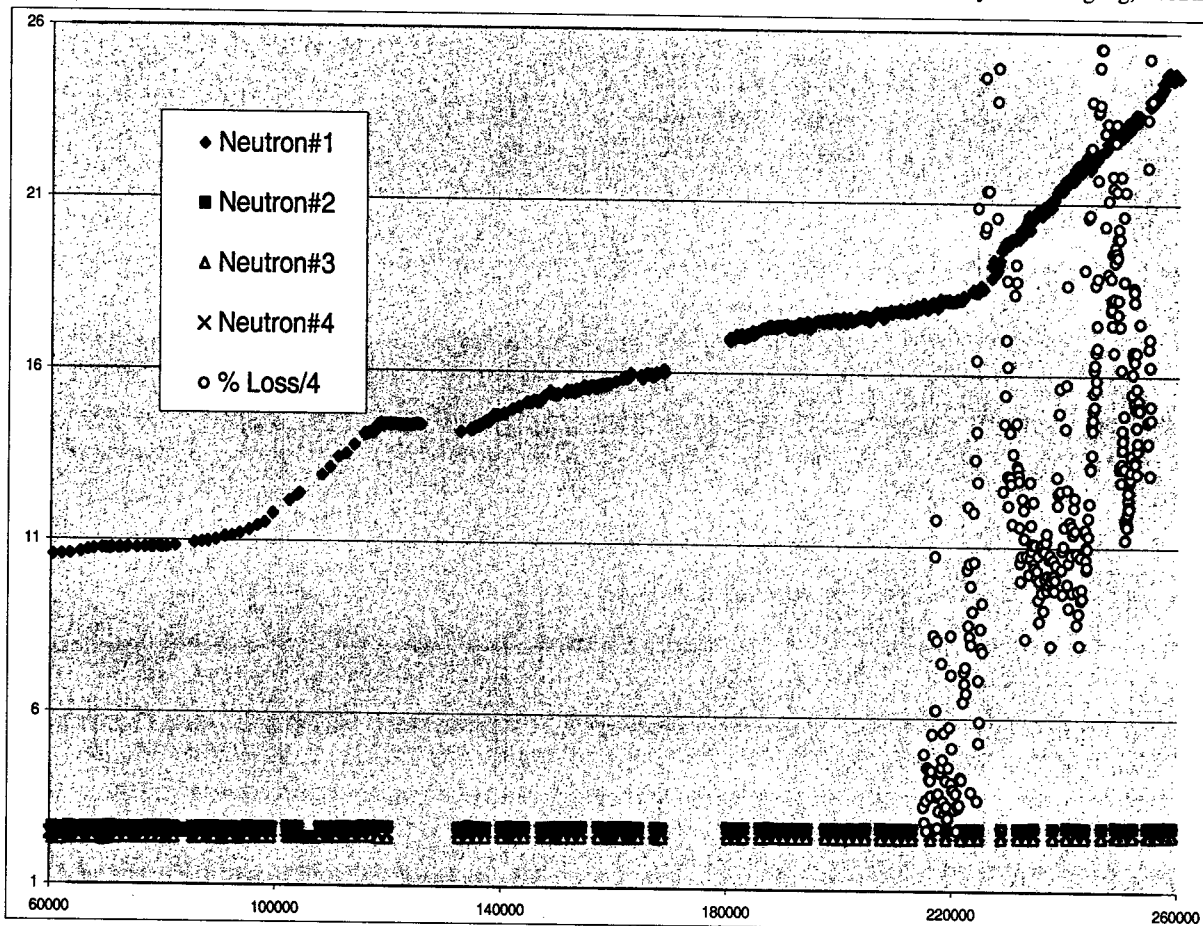
Figure 4: PIN data for Fig. 3 with correlated beam current loss (injected - extracted). Best efficiency was 90 %.

RADIATION MEASUREMENT
AROUND A 10-T SUPERCONDUCTING WIGGLER AT SPring-8

M. Shoji, K. Soutome, N. Kumagai, J. Tada, T. Magome, M. Oishi, T. Ohshima,
S. Sasaki, M. Takao, T. Takagi, K. Tsumaki, T. Yorita, and H. Yonehara,
JASRI/SPring-8, Sayo-gun, Hyogo 679-5198, Japan
Y. Asano, The Japan Atomic Energy Research Institute,
Sayo-gun, Hyogo 679-5148, Japan

Abstract

In August 2002, a 10-T superconducting wiggler was installed in the 8-GeV electron storage ring at SPring-8. High-energy (~3MeV) and intense synchrotron radiation was produced from the wiggler, and scattered photons were generated by the interaction of synchrotron radiation with photon absorber materials. The intense radiation environment in the storage ring tunnel damages accelerator components, such as cable insulators and coils for electromagnets. To suppress such damage, it is necessary to understand the dose distribution and the spectrum of scattered photons near the wiggler.

The dose distribution and the spectrum of scattered photons from the photon absorber was measured by thermoluminescent dosimeters (LiF TLD) with lead filters (0, 0.5, 1, 3, 6 mm in thickness). At the same time, alanine dosimeters and GafChromic film (made of polyethylene) were used to measure the dose of photons which exceeded the dynamic range of TLD dosimeters.

The results of an experimental data analysis showed that, as expected, photons of energies of several hundred keV were scattered over a wide range.

INTRODUCTION

SPring-8 is a synchrotron light source composed of an 8-GeV electron storage ring, a booster synchrotron, and a 1-GeV injector linac. The storage ring has 44 normal Chasman-Green cells, each of which has a 6.5-m straight section for insertion devices. The main parameters of the storage ring are listed in Table 1.

Table 1: Parameters of SPring-8 storage ring [1]

Electron energy		8 (GeV)
Beam current		100 (mA)
Circumference		1436 (m)
Number of cells	Normal cell	44
	Straight cell	4
SR from B-magnet	Power density	1.5 (W/mrad/mA)
	Critical energy	30 (keV)

We installed a 10-T superconducting wiggler (SCW) in one of the normal cells in August 2002. The main parameters of the SCW are described in Table 2. We tested its performance in September 2002[2]. A beam was successfully stored in the storage ring at SCW magnetic fields of up to 9.5 T. The stored current was limited to 0.1mA to maintain radiation safety. The storage ring is always operated at a beam current of 100mA for beamline users. If we use the SCW on 100-mA operation, the radiation level in the storage ring tunnel increases by high-energy photons scattered at the photon absorber. To reduce radiation damage to the accelerator components, we need quantitative data on the scattered photons from the SCW and we have to shield them from the intense radiation environment, effectively.

Table 2: Parameters of the SCW

Construction	Three pole magnet
Magnetic field	9.5 (T) (Max. 10.3 (T))
SR Power density	22 (W/mrad/mA peak)
Total power	1.0 (kW/1mA)
Critical energy	400 (keV)
Radiation angle	25 (mrad)

In this paper, we describe an investigation in dose distribution and the spectrum of high-energy scattered photons near the SCW. We then use the data to design the radiation shields for accelerator components.

EXPERIMENTS

Experimental setup

Figure 1 shows a schematic layout of the experimental setup. The SCW was installed close to the center of the straight section. The vacuum chamber of the photon absorber was placed downstream of the SCW. As shown in Fig. 1, two lead blocks (100-mm wide, 50-mm deep, and 200-mm high) were attached on both sides of the chamber (only on the outside of the storage ring circumference). They shaded the accelerator components, such as the vacuum gauge head, etc. The photon absorber was made of copper, and had a rectangular aperture with 52-mm horizontal and 32-mm vertical axes. SR with a larger angular spread than 10 mrad in the horizontal plane is influenced by the absorber walls. One TLD stand (2-m wide and 2.3-m high) was placed upstream of the absorber, at a distance of 1m. Another TLD stand (2.5-m wide and 2.3-m high) was placed downstream of the absorber, without touching the vacuum pipe of the beamline.
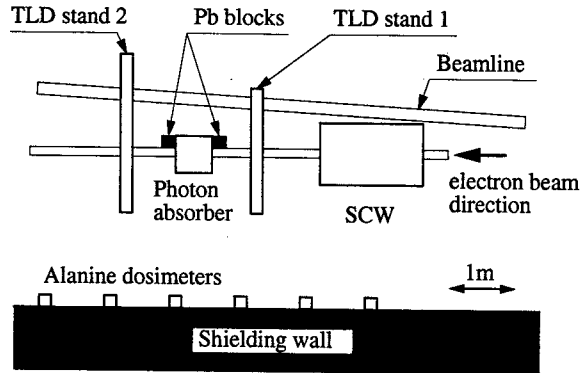
Figure 1:Schematic layout of the experimental setup. TLD dosimeters were attached on the TLD stands.

TLD dosimeters with lead filters were assembled on the holder made of paper. Eight TLD holders were attached on the upstream stand, and 7-holders were on the downstream stand. The arrangement of TLD holders on the upstream stand is shown in Fig. 2. The detection angle from the beam axis was from 45 to 50 degrees.
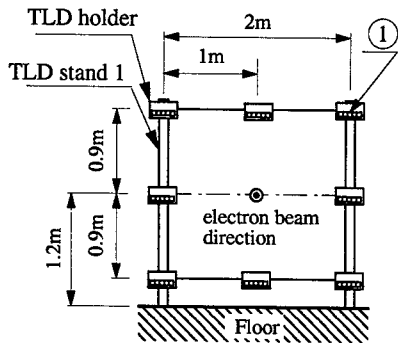
Figure 2:Arrangement of TLD holders.

On the shielding-wall, 1.2-m above the floor (the same height as the median plane of the electron orbit), twenty alanine dosimeters were mounted at intervals of 1m from just besides the SCW.

Measurements

We prepared two sets of TLD dosimeter assemblies. First, one set was mounted on the TLD-stands. Before dose measurement, we operated the storage ring at a very small current (0.1mA.10min) and fixed the electron orbit to hit the SR at the same place of the photon absorber. Dose measurement was carried out for one hour with the storage ring operated at a beam current of 1mA. The dose measured during the small current operation was about 2 percent of the dose measured at a 1-mA operation. Next, we dumped the stored beam, and changed the TLD assemblies for the other set. We then mounted twenty alanine dosimeters near the SCW to measure a dose that exceeds the dynamic range of a TLD dosimeter (more than 2 Gy). At the same time, we fitted a GafChromic

film around the vacuum chamber of the photon absorber to measure the dose distribution of the surface of the absorber.

All the dosimeters were irradiated for one hour at a beam current of 0.1mA. After irradiation, we analyzed them and got information on the dose of the scattered photons.

RESULT AND DISCUSSION

We found that the dose measured at the upper part of the median plane of the electron orbit is larger than the dose measured at the lower part. This result may be explained by the TLD assemblies being shaded with the accelerator components (such as Pb blocks, vacuum pumps, and girders of the vacuum chambers), which were installed near the photon absorber. We shall confine ourselves to analyzing the data which was obtained at the upper part of the median plane.
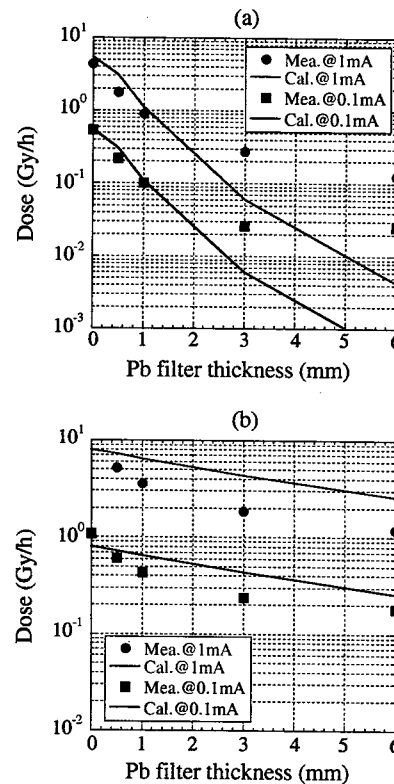
Figure 3: Dose measured and calculated on vertical plane of electron orbit. (a) is dose at upstream of the absorber, and (b) is at downstream. Dose is plotted as function of lead filter thickness.

Figure 3 shows a typical result of dose that was measured at the place pointed with 1 in Fig.2, and the result of dose calculation using STAC8 code. Data over 5 Gy was excluded because the TLD lost linearity with the dose sensitivity. The dose is in proportion to the stored beam current of the storage ring and the dose of the downstream is over an order of magnitude larger than the

783

dose of the upstream. They may be attributed to the angular dependence on the cross section of Compton scattering.

Scattered photon spectrum on the surface of the TLD was calculated by assuming the geometrical arrangement of the photon absorber and the TLD. From the calculation, we found that photons of energies mainly from 100 to 300 keV will be observed upstream the absorber and 100 to 1000 keV will be observed downstream. Using the spectra, we estimated the dose on the TLD. The calculated dose was drawn in Fig.3. The calculated dose agrees with the measured values except for a few points measured upstream using the thick filters. This discrepancy may be interpreted on the assumption that the TLD dosimeters placed upstream of the absorber were influenced by high-energy-photons such as secondary-scattered-photons from the SCW chamber. In order to support this explanation, it is necessary to calculate the dose taking account of the effect of secondary-scattered-photons.
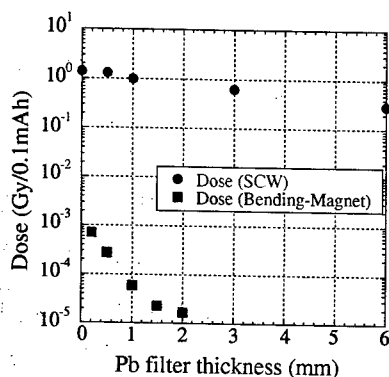
Figure 4:Comparison with dose from SCW and bending magnet.

We compared the dose of scattered photon from SCW with the dose from the bending magnet of the storage ring [3]. The result is shown in Fig. 4. Data was normalized by the stored current and the distance from the absorber. The difference between two slopes of the plots may be attributed to a difference in the critical energy of the incident photons. The total power of SR from SCW, that was absorbed by the photon absorber, is two orders of magnitude larger than the total power from the bending magnet at the same current operation. The order of magnitude between the dose from SCW and the dose from bending magnet cannot be interpreted from the difference in total power. The dose difference may be explained by the assumption that high-energy-scattered-photons from SCW escaped from the absorber chamber and increase the radiation level at the TLD dosimeters. To prove this assumption, it is necessary to carry out a detailed study on the energy of scattered photons from the bending magnet.

The measured values of alanine dosimeters were less than the search limit (less than 2 Gy). The reason for this

result is that all dosimeters were placed more than 3m from the photon absorber.
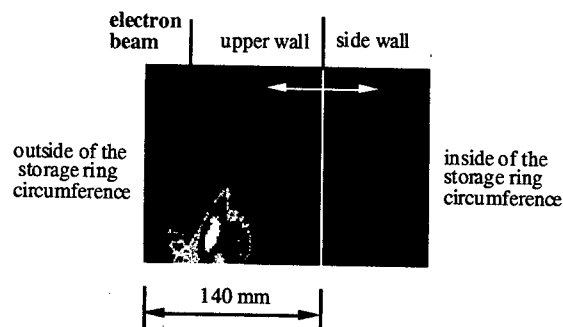
Figure 5:Dose distribution measured using GafChromic film on the photon absorber.

Figure 5 shows the dose distribution on the photon absorber. Maximum value of the dose is 1500 Gy. As shown in Fig. 5, GafChromic film that was put on the upper wall, was much exposed than the film put on the side wall. This fact is supported by several ways:

1. Thickness of the upper wall is a one-third of the side wall,

2. Dose distribution is influenced by the angular dependence on the cross section of Compton scattering,

3. SR from SCW is linearly polarized in a median plane of the electron orbit, and scattered photons have a maximum strength in a vertical direction of polarization. Further analysis is necessary.

CONCLUSION

The dose distribution and the energy spectrum of scattered photons from the photon absorber were measured near the SCW. The dose from the SCW is three orders of magnitude larger than the dose from the bending magnet. The dose distribution is predicted from the principle of Compton Scattering.

If we design the radiation shields for accelerator components it is necessary to investigate dose distribution and the energy spectrum of penetrated photons in future.

ACKNOWLEDGEMENTS

REFERENCES

[1] H. Ohkuma, et al., Proc. of the PAC 2001, Chicago, Illinois, June 18-22, 2001, p. 2824.

[2] K. Soutome, et al., "Generation of high-energy synchrotron radiation with a 10T superconducting wiggler installed in the Spring-8 storage ring", published at this conference.

[3] A. Imai, Master's Thesis to Kyoto university.

IMPROVEMENT OF RHIC WARM BEAM VACUUM FOR HIGH INTENSITY OPERATION*

P. He, H.C. Hseuh[†], R.C. Lee, M. Mapes, L.A. Smart, D. Weiss and S.Y. Zhang
Collider-Accelerator Department, BNL, Upton, NY 11973, USA

Abstract

With increasing ion beam intensity during recent RHIC operations, pressure rises of several decades were observed at a few warm vacuum sections. Improvement of the warm sections has been carried out in last year's shutdown. Extensive in-situ bakes, additional UHV pumping, electron detectors and beam tube solenoids have been implemented. Vacuum monitoring and interlock were enhanced to reduce premature beam aborts. The effectiveness of these measures in reducing the beam induced pressure bumps and in increasing the vacuum system reliability are discussed and summarized.

INTRODUCTION

RHIC has a circumference of 3.8 km and comprises two interweaving rings (named yellow ring and blue ring) that intersect with each other at six locations. The total length of warm sections is ~1.4 km, consisting of 24 insertion regions (single beam) at the ends of the long arcs, 12 final focusing regions between D0 and DX and six interaction regions (IP), as shown schematically in Fig. 1. The design vacuum of the warm sections is $<5 \times 10^{-10}$ Torr. The beam-gas lifetime, dominated by nuclear scattering with cross sections of $\sim 10^{-24}$ cm^2 for Au, is several hundred hours at the design vacuum level, much longer than the ten-hour intra-beam scattering lifetime [1]. Background noise to the detectors, due to beam-gas events in warm sections bracketing the experimental detectors establishes the requirements of RHIC beam vacuum systems [2].

Fig. 1 RHIC warm sections bracketing the interaction points showing the incoming and outgoing single beam lines and the common lines at IP and DX-D0.

The warm sections are pumped by ion pumps (IP) and titanium sublimation pumps (TSP), and monitored with cold cathode gauges (CCG) at intervals averaging 14m. The pumping speed at the neck of the pumps is ~500 l/s for active gases such as CO and H$_2$. Due to the small linear conductance of the beam tubes, the effective pumping speeds are in the order of tens l/s.m for H$_2$ and a few l/s.m for CO. Most of the warm sections are in-situ bakeable up to 250°C. The average pressures of the warm sections without beam have reached below the design

vacuum level, owing to the gradual bakeout of these sections over the last three years.

No notable changes in pressure were observed during the 2000 beam commissioning run. However, pressure spikes of several decades occurred during the high-intensity Au x Au, p x p and Au x d runs in the past three years. These rapid increases in pressure caused high detector background, sometimes exceeded the CCG set points for valve interlocks, and aborted the beams. The pressure rise was especially prominent during 110-bunch injection and became one of the major intensity-limiting factors for RHIC. Extensive bakeout of the warm sections and other improvement were carried out during 2002 summer shutdown to increase the intensity thresholds and to reduce the pressure rise. The effectiveness of these measures is summarized by comparing the beam and vacuum performance of 2003 Au x d and p x p runs with those of 2002 p x p and 2001 Au x Au runs. Further improvement of the vacuum systems planned for the 2003 shut down is also described.

VACUUM IMPROVEMENT

Pressure Rise vs In-Situ Bake

To reduce detector background, the common beam regions bracketing the four major experiments were in-situ baked before the 2001-2002 runs, and pressure of low 10^{-10} Torr and 10^{-11} Torr were achieved. Two types of pressure rise were observed [3, 4] during the 2001-2002 runs. The first type was the pressure rise at the beam injection, initially observed at intensity above a certain intensity threshold (I_{th}), which was very sensitive to bunch intensity and spacing, and tended to approach saturation at constant intensity. It seems that the electron cloud is responsible for this type of pressure rise [5]. It has limited the Au intensity for 55-bunch injection, and prevented the 110-bunch operation. The second type of pressure rise occurred at the transition, somewhat proportional to the total beam intensity, and not sensitive to the bunch intensity and spacing. This type of pressure rise has not limited the beam intensity. However, it has caused high detector background and hampers further luminosity improvement.

More warm sections were in-situ baked during the 2002 shutdown with the goal to reduce secondary electron yield (SEY) and molecular desorption yield, and the resulting pressure rise, and to increase I_{th}. The loosely bound surface contaminants have a much higher SEY and can be

removed through in-situ bake. The intensity thresholds of the 1st type of pressure rise can be obtained by analyzing the pressure rise patterns under various running conditions [3]. The effectiveness of the bakeout for increasing I_{th} is illustrated in Fig. 2 where the pressure rise at IP12 is compared with proton beam intensity before (2001-2002) and after (2003) bake. For the same increase in pressure, the intensity thresholds were about a factor of two higher after bake. The average I_{th} values for warm sections at IP12 for various running modes are summarized in Table 1. I_{th} for p and d are much higher than Au, even after factoring in the total charges. I_{th} increased by 50% or more after in-situ bake.
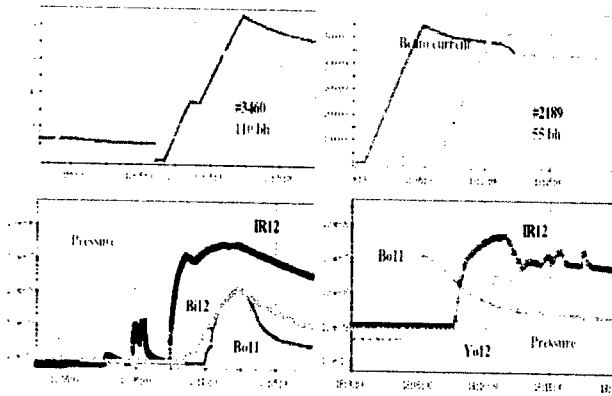
Fig. 2 Comparison of pressure rise with intensity at IP12 with 55- (2002, before bake, in 10^6 unit) and 110-bunch (2003, after bake, in 10^{11} unit) protons. The pressure rise is smaller while the intensity is ~50% higher after bake.

Table 1. I_{th} for different species and running modes at IP12

	IP	Single	comment
p – 55	7×10^{12}	4×10^{12}	2002 – not baked
p – 110	6×10^{12}	2×10^{12}	2002 – not baked
Au^{+79} – 55	7×10^{10}	2×10^{10}	2001 – not baked
Au^{+79} – 110	$\sim 6 \times 10^{10}$	1×10^{10}	2001 – not baked
Au^{+79} – 55	$> 12 \times 10^{10}$	4.5×10^{10}	2003 - baked
Au^{+79} – 110		3.5×10^{10}	2003 - baked
d -55	$> 12 \times 10^{10}$	$> 7 \times 10^{12}$	2003 - baked
d -110		7×10^{12}	2003 - baked
p -110	9×10^{12}	3.5×10^{12}	2003 - baked

Electron Detectors and Solenoids

Eleven custom electron detectors (ED) as shown in Fig. 3, were designed, fabricated and installed during the 2002 shut down. They were modeled after ED used at Argonne and CERN, but include an additional shield to reduce rf noise from the beam image current. The bias voltage of the grids can be varied to measure the energy spectrum of the electrons or ions. The transmission efficiency of the ED has been calibrated up to 1500 eV using an electron gun, and found to be around 10% [6].

Beam pipe solenoids were also installed on the 12cm beam pipes bracketing EDs, using 10 gage wire and alternating the winding direction every meter. The solenoid and the DC power supply provide up to 6000 Ampere turn per meter, equivalent to a 75 gauss axial field, which is sufficient to confine electrons of 300 eV

(which have peak SEY values) in spiral orbits of <1cm in radius. The solenoids have been energized during the machine studies in 2003. Significant reduction in both the electron signal and the pressure rise has been observed [5, 7].
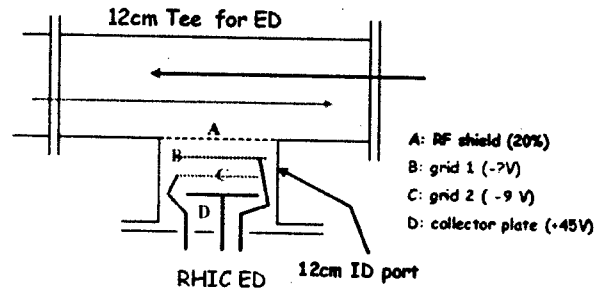
Fig. 3 RHIC electron detectors (ED) consist of an RF shield, two grids and a collector, and have an effective area of over 100cm^2.

Vacuum Monitoring and Interlock

During the 2001-2002 physics runs, the beam was aborted by the vacuum beam permit in a dozen cases. Among them, a few were caused by electrical noise that induced spikes in the vacuum gauge readings used for valve interlock through programmable logic controllers (PLC). These spikes would last a few seconds at most. Prior to the 2003 run, the PLC ladder logic software was modified to include a time delay for triggering the valve closures and beam aborts. No premature triggering has been recorded since. The time delay has also helped preserve beam stores during injection and transition, when pressure would rapidly rise and fall.

The monitoring and control of RHIC vacuum devices is through the use of RS485 serial communication. Up to 32 like devices are connected to a common PLC co-processor port. Due to the integral processing time of the co-processors, the vacuum readings are updated every 8 seconds for vacuum gauges, and about 30 seconds for devices like partial pressure analyzers and turbopump stations. To monitor and correlate the pressure rise with the beam intensity and other machine parameters, faster data logging was implemented during 2002 shutdown. The analog output signals from selected CCGs around the ring were fed into MADC modules, digitized and logged at a typical rate of 1 Hz. The enhanced data logging capability allows accurate comparison and correlation of the pressure rise with the signals from beam current monitors, ED and beam loss monitors.

FUTURE IMPROVEMENT

To meet the physics goals in RHIC for year 2004 and beyond, the total beam intensity has to be increased by a factor of two or more, either through increase in bunch intensity, number of bunches or both. The expected pressure rise during injection and transition will be excessive based on observation from the past years. The following remedies are being evaluated and/or implemented to reduce the pressure rise.

Bakeout of Outgoing Beam Lines

The major goal in the last few years was to lower the pressure at the incoming insertion beam lines and at the common beam lines around the detectors, thus reduce the detector background to the major experiments. However, during a few high intensity stores, excessive pressure rise was observed at the outgoing lines where most diagnostic equipments with high outgassing components were located. This high pressure has caused large amount of beam scattering and beam loss in the long arcs, which might have induced magnet quenches in the arcs. Therefore these outgoing sections will be in-situ baked to the maximum allowable temperature to reduce the static and dynamic pressure. Non-conventional bakeout methods will be developed for some of these sections.

Beam Tube Solenoids

Approximately 60m of beam tube solenoids were installed and operational for the 2003 run. Significant reduction in ED signals and pressure was observed when solenoids bracketing the ED were energized during machine studies. The present solenoid cables have PVC jackets and have to be removed prior to in-situ bakeout. Kapton insulated wire will be installed for additional solenoids for its radiation and temperature properties.

Collimators

The existing collimators, one in each ring, are not effective in removing the beam halos and had at times increased backgrounds to the detectors of nearby experiment. These two collimators will be relocated to IR12 region where no major experiment exists. Additional secondary collimators and second-secondary collimators will be installed downstream of the relocated primary collimators to stop secondary particles. By intercepting the beam halos and secondary particles at normal incidence, the molecular desorption rate is expected to be a few decades less than the estimate 10^7 desorbed molecules per ion at grazing angle [3]. The collimators will also be in-situ baked to reduce the magnitude of pressure rise during their operation.

NEG Coating and Lumped Pumps

Due to large pump spacing and the small linear conductance of the RHIC beam tubes, the effective pumping speed is in tens l/s.m range for H_2 and a few l/s.m for CO. To increase the effective pumping speed, additional lumped pumps or linearly distributed pumps are needed in the warm sections. Lumped pumps in the form of TSP will be effective in the insertion regions, perhaps midway between the existing IP and TSP. It will increase the effective pumping speed by a factor three or more. Linearly distributed pumps in the form of non-evaporable getter (NEG) coating [8] will be more effective in the interaction regions where little transverse space is available for lumped pumps and the linear conductance is smaller than that of insertion regions. The NEG coating will provide effective pumping speed of 10^2 l/s.m and will also reduce the SEY, and the electron and ion desorption rates. The coating of the existing 7cm Φ beryllium beam tubes is certainly challenging if not impossible. The addition of high Z material on the detector beam tubes has to be evaluated by the experimenters for its reduced transparency to the energetic particles. The periodic activation requirement of NEG coating has to be incorporated into vacuum system operation. A few NEG coated beam tubes will be installed at one warm section and evaluated during the upcoming run.

SUMMARY

Improvement of the RHIC vacuum system before 2003 physics runs has produced some positive effect on the beam intensity thresholds for the pressure rise as compared with those of the 2001 and 2002 runs. The magnitude of the pressure rise is also lower than that of the previous years. Solid evidence of electron cloud from the newly-installed electron detectors was seen during high intensity runs. The effect of the solenoids to suppress the electron activities has been observed. Further improvement is needed to allow increase in intensity. To that end, more warm sections will be in-situ baked and additional collimators will be installed to intercept the beam halo at normal incidence. Additional lumped pumps and NEG coating will also increase the effective pumping speed several-fold.

ACKNOWLEDGEMENTS

REFERENCES

[1] M.J. Rhoades-Brown and M. A. Harrison, RHIC Technical Note #106, BNL-47070, Dec. 1993.
[2] H.C. Hseuh, et al, Proc. PAC'99, New York, 557 (1999).
[3] H.C. Hseuh, L.A. Smart and S.Y. Zhang, Proc. EPAC'02, Paris, 2559 (2002).
[4] W. Fischer, et al, Proc. EPAC'02, Paris, 1485 (2002).
[5] S.Y. Zhang, et al, 'RHIC Pressure Rise and Electron Cloud', These Proceedings.
[6] P. He, et al, 'Calibration of RHIC Electron Detectors', These Proceedings.
[7] U. Iriso-Ariz, et al, 'Electron Detectors for Vacuum Pressure Rise Diagnostics at RHIC', These Proceedings.
[8] C. Benvenuti, Proc. PAC'01, Chicago, 602 (2001).

OUTGASSING AND SURFACE PROPERTIES OF TIN COATED SNS RING VACUUM CHAMBERS*

P. He, H.C. Hseuh, M. Mapes, R. Todd[†], Collider-Accelerator Dept, BNL, Upton, NY 11973, USA,
N. Hilleret, LHC, CERN, Geneva, Switzerland

Abstract

The stainless steel vacuum chambers of the 248m Spallation Neutron Source (SNS) accumulator ring are being coated with ~ 100 nm of titanium nitride (TiN) to reduce the secondary electron yield (SEY). The coating is produced by DC magnetron sputtering using a long cathode imbedded with permanent magnets. The outgassing rates of several SNS half-cell chambers, with and without TiN coating, and before and after *in-situ* bake, were measured. The SEY of the coated chamber coupons were also measured with primary electron energy of 50-3000 eV. By varying the coating parameters, films of different surface roughness were produced and analyzed by scanning electron microscopy. It was found that the outgassing rate varies as a function of surface roughness of the TiN layer, and chambers with a rougher surface have a lower SEY.

INTRODUCTION

The SNS ring, with a circumference of 248m, consists of 4 arc sections of 34m each and 4 straight sections of 28m each [1]. There are 32 half cell chambers in the arc sections. Each chamber, constructed of 316L stainless steel, is approximately 4m long and over 20cm in diameter. Prior to TiN coating, the chambers are degassed in a vacuum furnace at 450C for 48 hours. A coating of ~200 nm is subsequently laid down by DC magnetron sputtering using a long titanium cathode containing permanent magnets [2].

The operating pressure for the SNS storage ring is $<1\times10^{-8}$ Torr. The outgassing rate of stainless steel is well understood and confident estimates can be made for a wide variety of conditions. However, because of the required TiN coating to reduce the SEY, outgassing data for coated chambers is needed for vacuum simulations and to meet design requirements. The ring vacuum system will not be baked, so of particular interest is the outgassing data without *in-situ* bake.

OUTGASSING MEASUREMENTS

The outgassing rate of several SNS chambers was measured by means of the orifice method. The total surface area of each chamber is approximately 29,000 cm^2. A schematic of the outgassing test setup is shown in Figure 1. The orifice size was 3.2 mm in diameter and 2mm long. Outgassing measurements with *in-situ* bake were made with a 270 l/s sputter-ion pump (SIP)

supplemented with a titanium sublimation pump (TSP) with a speed of 1000 l/s for H_2 and base pressure of $<10^{-11}$ Torr. Inverted magnetron gauges, with a gauge correction factor of 2.4 for hydrogen [3] were placed on each side of the orifice, while a residual gas analyzer was placed on the pump side of the orifice to measure the gas composition. The entire system was baked at 250C for 48 hours. To measure the outgassing rate without an *in-situ* bake, a 150 l/s turbo-molecular pump with a base pressure of 10^{-9} Torr was employed in place of the SIP/TSP.
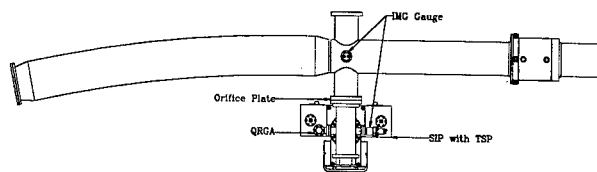
Figure 1. Schematic of outgassing measurement setup using orifice method.

A summary of the outgassing measurements is given in Table I. Outgassing rates for chambers without *in-situ* bake are given in N_2 equivalent. Log-log plots of the outgassing rates for the chambers are given in Fig. 2.

Table I. Outgassing data of chambers under a variety of conditions.

Cham #	Q(N_2 equiv.) (Torr-l/s cm^2)	Q (H_2) (Torr-l/s cm^2) *in-situ* bake	Hours under vacuum or post bake	Comments
2A	8.5E-12	2.5E-13	120	VD, no TiN
9A	3.7E-11	3.0E-12	120	no VD, no TiN
2A	1.2E-10		120	VD, HP
3A		2.1E-13	96	VD, HP
1C	7.1E-11		408	VD, HP, GDT
7A	2.5E-11		144	VD, LP
5B	9.6E-12		120	VD, LP, GDT
5B	2.4E-12		192	
5B		1.9E-13	72	
5B		1.6E-13	192	

(VD: vacuum degass, HP: coated at 4 mTorr, LP: coated at 1.5 mTorr, GDT:post glow discharge treatment)

H_2 Outgassing after 250C In-situ Bake

To determine the hydrogen outgassing rate, chambers were subjected to a 48 hour 250C bake to remove water vapor and other adsorbed gases. An outgassing rate of 3×10^{-12} Torr-l $s^{-1}cm^{-2}$ was measured for chamber 9A, which was uncoated and not subjected to vacuum degassing. This outgassing rate compares favorably with

some previous reports of 5×10^{-12} Torr-l $s^{-1}cm^{-2}$ for *not-vacuum degassed pipes* after a 300C bake [4, 5].
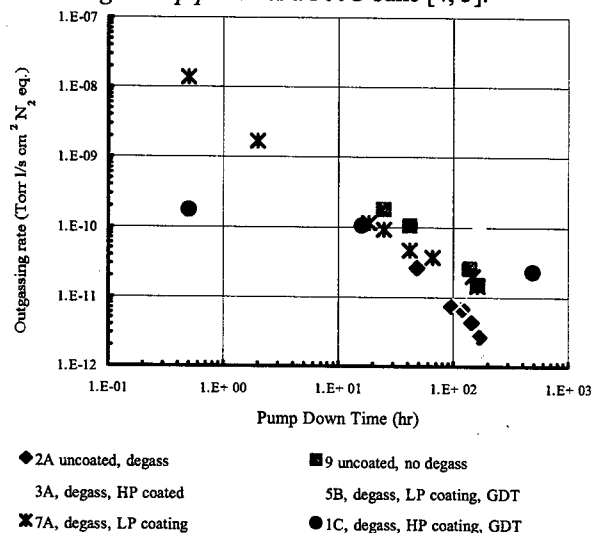
Figure 2. Outgassing rates for TiN coated and uncoated chambers without *in-situ* bake for a variety of coating conditions HP: ~4 mTorr, LP:~1.5 mTorr, GDT: glow discharge treatment.

Subsequent to a 450C vacuum degass, an outgassing rate of 2.5×10^{-13} Torr-l $s^{-1}cm^{-2}$ was measured 120 hours after bake for un-coated chamber 2A, an improvement of ~10x over chamber 9A. While diffusion theory would suggest a value as low as 4×10^{-15} Torr-l $s^{-1} cm^{-2}$ for our conditions [6], our measurements compare favorably with earlier measurements [4] of a lower limit of 1×10^{-13} Torr-l $s^{-1}cm^{-2}$ for 316LN tubes after 950C vacuum *fire* followed by a 300C *in-situ* bake. Deviation from the theoretical values shows possible evidence of "recombination limit outgassing" explained by Moore [6].

H_2 Outgassing with TiN Coating

Recent research by Saito [7] shows that TiN coating on stainless steel may act as a hydrogen permeation barrier and can reduce the hydrogen permeation rate by as much as 100x. The outgassing rates for chambers 3A and 5B coated at high and low pressure, respectively, were compared to that of the uncoated chamber 2A. Using linear interpolation, chamber 5B, coated at low pressure, attained an outgassing rate of 2×10^{-13} Torr-l.s$^{-1}cm^{-2}$ 120 hours after bake, for a reduction of ~30% and equilibrated at a value of 1.6×10^{-13} Torr-l.s$^{-1}cm^{-2}$. Chamber 3A showed an improvement of ~15%, but less than that of 5B, likely attributed to the reduced density of the TiN film.

These results may be evidence of a permeation barrier, but not the compelling evidence we were looking for. Implicit in Saito's findings were a minimum thickness of 1μm, as well stoichiometric films with few defects. Saito's substrates were electrolytically polished 304L stainless steel whereas the SNS chambers typically have a 2b matt finish, at best, and a TiN nominal thickness of 200nm. Any one of these variables can impact the results of measurements. The 30% reduction in outgassing on

chamber 5B is similar to the reported value of 50% reduction by Raiteri and Calcatelli [8] on smaller samples.

Outgassing without In-situ Bake

It is evident that even without an *in situ* bake, there is considerable improvement in the outgassing rate of the uncoated chamber subjected to a 450C vacuum degass (2A over that of 9A). TiN coatings sputtered at a pressure of 4 mTorr revealed a higher than expected outgassing rate (3A). At this pressure, with a mean free path of ~1 cm, the sputtered Ti was arriving at the chamber wall at a lower rate, and with less energy which produced a film with lower density and increased porosity. It was suspected that the film was very hydroscopic and RGA data showed that this gas load was almost entirely water vapor. The films produced at this pressure, were brown in color and less gold than what is typically associated with TiN. A correlation between the surface roughness of TiN films and color has been reported by Nah *et-al* [9]. They have determined that the more brownish TiN films are a result of increased grain size and reduced grain density.

The sputtering pressure was subsequently reduced to a level of ~1.5 mTorr, while still producing stable, uniform plasma. The resultant coating (7A) was more gold in color and found to have more acceptable outgassing rate which is a factor of ~8x lower at 100 hours than that of the high pressure coating (3A), but still ~ 4x higher than that of the uncoated chamber (2A). To improve the outgassing rate further, the surface was subjected to a glow discharge treatment (GDT) before and after TiN coating. The chamber wall was bombarded with argon ions for 5 minutes for an accumulated dose of 10^{17} ions/cm^2.
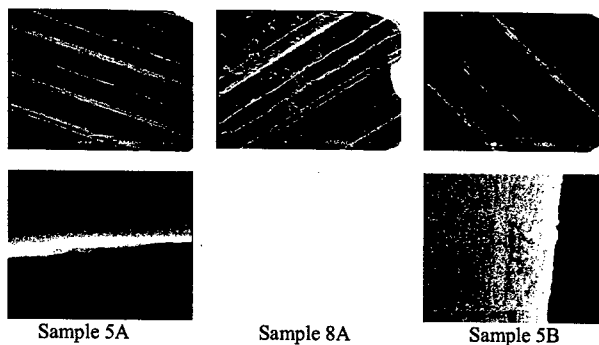
Fig. 3. SEM (top) and AES (bottom) images of TiN coated surface at high pressure (5A), low pressure (8A) and low pressure with GDT (5B).

Chamber 5B was subjected to GDT and found to have an improved outgassing rate over 7A by ~5x. More importantly, the outgassing rate is similar to that of an uncoated chamber (2A), indicating that the quantity of water adsorbed on the TiN surface is comparable to that of uncoated stainless steel. Evidence of this can also be seen in the SEM images of the coatings (Figure 3). Sample 5A (from a chamber with identical parameters to 3A), exhibits deep voids when compared to 8A (sample from a chamber with identical parameters to 7A), while sample 5B shows further smoothing and densification.

SEY MEASUREMENTS

SEY measurements were made on samples coated under a variety of conditions. All measurements were made *as received* to determine the initial SEY of the materials. Research by others have shown that significant reduction in SEY is accomplished by *in-situ* bakeout and ion or electron scrubbing. CERN has made extensive measurements on surfaces treated to an air bake, sputter cleaning, and oxidation treatments, and found them to be effective in lowering SEY [10]. Kirby *et al* has also shown that TiN has a significantly lower SEY over that of stainless steel (SS) after sputter cleaning [11].

A summary of the SEY results is given in Table II. Films produced with straight DC sputtering showed mixed SEY results and will not be discussed further. All production chambers are coated using MDC and most SEY measurements were made on coupons using this process. A summary of the SEY data is shown in Table II.

Table II. SEY data for coated and uncoated chamber coupons.

Sample #	SEY Max.	Coating Parameter	Coating Parameters Legend
SS	2.37	2b finish	LP- 1.5 mTorr
SSP	2.49	P	HP- 5 mTorr
3-Oct	2.25	DC/HP	GDT- Glow Discharge treatment
3-Jul	2	DC/HP	DC- Diode DC sputtering
19/1	1.89	MDC/HP	MDC- Magnetron DC sputtering
20/5	1.99	MDC/HP	P- Polished substrate
5A	1.66	MDC/HP	
2A	2.03	MDC/HP	
1C	2.4	MDC/HP/GDT	
8A	2.37	MDC/LP	
4B	2.8	MDC/LP/GDT	
5B	2.55	MDC/LP/GDT	

The effect of surface roughness on SEY has been reported [12] and demonstrated recently on copper by Baglin, *et-al* [13]. To measure the effect of substrate roughness, the SEY of both TiN coated and uncoated stainless steel (SS) coupons were measured. One coupon was polished, while the other retained its 2b finish. As expected, the polished coupons showed a slightly higher SEY in both cases.

If the substrate roughness had a bearing on the SEY, then the deposited film's roughness will have a corresponding effect. It was found that the film with the lowest SEY was generated at a high pressure with no post GDT, while the highest SEY was on a film produced at low pressure with GDT. Unfortunately the films produced at high pressure without GDT exhibited the highest outgassing rate. In hopes of reducing the outgassing rate, while retaining the lower SEY, a film was produced at high pressure with GDT. Much to our chagrin, this film exhibited a high SEY of 2.4 and high outgassing.

In the *as received* state, the SEY of films generated at HP without GDT were, on average, lower than both uncoated SS and LP coated films with or without GDT. Furthermore, TiN films produced at LP with or without GDT showed no significant reduction in SEY over uncoated SS. This lack of SEY reduction in the *as*

received state of TiN and SS, has also been observed by Baglin *et al* [13]. It is our conclusion that the surface roughness of our TiN films is the driving force in reducing the *as received* SEY, while the addition of *in-situ* methods such as bakeout, to remove water vapor and surface gases, as well as sputter cleaning, are required to lower the achievable SEY. Measurements with *in-situ* bakeout and/or sputter cleaning are still required to determine our films lowest SEY.

SUMMARY

The uncoated SNS chambers exhibit lower than expected outgassing rates. The benefits of a moderate vacuum degass at 450C are evident. The SNS chambers coated with TiN at low pressure with glow discharge treatment have an outgassing performance comparable to uncoated chambers. There is strong evidence that TiN films produced at high pressure, regardless of glow discharge treatment, result in high water adsorption into the porous film and cause unwanted outgassing characteristics. There is some indication that the TiN film may act as a permeation barrier to hydrogen diffusing from the bulk, but more conclusive evidence is required. Finally, the surface roughness of the deposited film(s) may have bearing on the SEY of the film.

ACKNOWLEDGEMENTS

REFERENCES

[1] H.C. Hseuh, C.J. Liaw and M. Mapes, Proc. PAC'99, New York, USA, p1345 (1999).
[2] P. He, *et-al*, Proc. PAC'01, Chicago, USA, p2159 (2001).
[3] N. Peakock, HPS Corporation, (private comm..).
[4] H.C. Hseuh, X. Cui, J.Vac.Sci.Technol. A7, 2418 (1989).
[5] H.C. Hseuh *et-al*, Outgassing rate of RHIC warm-bore beam pipe, (unpublished) BNL, 1996
[6] B. C. Moore, J.Vac. Sci.Technol. A13, 545 (1995).
[7] K. Saito, *et-al*, J.Vac.Sci.Technol. A13, 556 (1995).
[8] G. Raiteri and A. Calcatelli, Vacuum, 62, 7 (2001).
[9] J.W. Nah, *et-al*, J.Vac.Sci.Technol. A17, 463(1999).
[10] I. Bojko, N. Hilleret, C. Scheuerlein, J. Vac. Sci Technol., A18, 972 (2000).
[11] R. E. Kirby, F. K. King, 'Secondary Electron Emission Yields From PEP-II accelerator Materials', SLAC-PUB-8212, (2000).
[12] H. Bruining, Physics and Applications of Secondary Electron Emission, Pergamon, London, 1954.
[13] V. Baglin, et-al, Proc. EPAC'00, Vienna, Austria, p217 (2000).

PRESSURE DISTRIBUTION SIMULATION FOR SNS RING VACUUM SYSTEMS*

P. He[†], H.C. Hseuh and R. Todd

Collider-Accelerator Department, BNL, Upton, NY 11973, USA

Abstract

Brookhaven is responsible for the design and construction of the US Spallation Neutron Source (SNS) accumulator ring and beam transport lines. Ultrahigh vacuum of a few nano-Torr is required for the accumulator ring to minimize the residual gas ionization. To size the pumps and to optimize the pump locations, the pressure distribution in the vacuum systems has to be calculated based on chamber conductance, the static and dynamic outgassing of the chamber walls and the beam components. A computer program, based on finite differential approximation, was used to model the pressure in the accumulator ring, using the measured outgassing rates of chambers with and without TiN coating. The simulation results indicate that the designed vacuum will be achieved after prolonged pumping due to the high outgassing associated with the low secondary electron yield coatings.

INTRODUCTION

The SNS accumulation ring, with a circumference of 248m, consists of 4 arc sections of 34m each and 4 straight sections of 28m each for injection, collimators, extraction and RF & diagnostics [1]. The vacuum systems are conveniently divided into eight vacuum sectors isolatable with all-metal electro-pneumatic gate valves located at the interface of the arc sections and the straight sections. The ring schematic layout is shown in Fig.1 and a list of ring vacuum components and their parameters are given in Table 1.
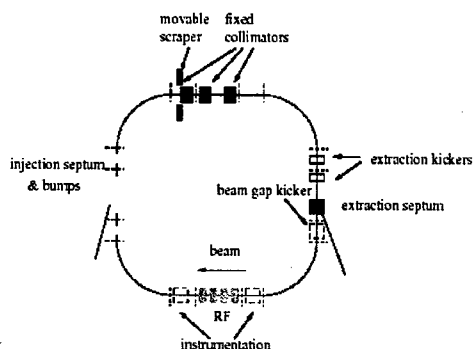
Figure 1. Schematic layout of the SNS accumulator ring. The four straight sections are designed for beam injection, collimation, extraction, and RF systems, respectively.

Table 1. Accumulator Ring Vacuum System Parameters

Description	# Unit	Length
Design Vacuum Level		$< 1 \times 10^{-8}$ Torr
Arc Half Cell Chamber	32	4 m
Arc Quarter Cell Chamber	4	2 m
Straight Region Doublet Chamber	8	> 3 m
Straight Region Special Chambers	16	0.5-4 m
Sputter Ion Pumps, 300 l/s	50	

Only UHV compatible metals and ceramics will be used in the construction of the ring vacuum system for their vacuum properties and radiation resistance. No organic materials are allowed. To minimize the RF impedance, the chambers will have tapered transitions wherever significant changes in cross sections occur. All the pump ports will be shielded with RF screens (thin mesh), which has little effect on the available pumping speed. Conflat type flanges and seals, for their cost and reliability, will be used to join the arc chambers. Quick-disconnect chain clamps, flanges and metal seals will be used at the straight sections where the expected beam loss will be higher, therefore minimizing the personnel radiation exposure during vacuum maintenance and repair. To reduce the secondary electron yield (SEY), the inner walls of the ring chambers are being coated with ~100nm titanium nitride (TiN).

Vacuum is obtained using lumped pumps (i.e. pumps appending the beam line at periodic intervals), thereby simplifying the mechanical design and improving serviceability (i.e. ALARA considerations). Often, vacuum systems of this design require special attention in determining the relationship of pump speed and spacing to avoid a condition of conductance limitation or unnecessary cost. An analysis of periodically pumped, longitudinal vacuum systems can be carried out using rudimentary vacuum formulas, assuming uniform outgassing, conductance and pump spacing, which can yield acceptable results for predicting general performance for many applications. One such analysis is given by Welch [2]. With the advent of vacuum simulation code, factors such as non-uniform outgassing, unequal pump spacing, and varying conductance, as is the case within regions of the SNS accumulator ring, can be more easily accommodated. The software used is a program called VACCALC, which solve the differential equations for the pressure piecewise [3]. This software

was used to estimate the pressure profile in the upgraded HERA interaction regions [4].

PRESSURE DISTRIBUTION COMPUTATION

In this section the pressure profile and average pressure of SNS ring arc and straight sections are calculated using VACCALC code. Varying the size, number and spacing of pumps for various outgassing rates will permit the design of a minimum cost accelerator vacuum system for predetermined vacuum performance requirements The real residual gas composition is not known precisely, however, for relative comparisons we assume the gas composition is $H_2(40\%)$, $H_2O(40\%)$, and $CO(20\%)$. The gas desorption loads from special beam components, such as stripping foil and the extraction kicker ferrite, limit the accuracy of the simulation to a factor of 2 or more.

Pressure Profile in Arc Section

Each ring arc section (Fig.2) has 8 halfcell chambers and one quartercell chamber. The vacuum chambers and the magnets are grouped symmetrical to the middle quadrupole, such that they are mirror images to each other. Five ion pumps will be installed in the Arc section for day-one operation. Pump ports are available at each halfcell chamber for future upgrade.
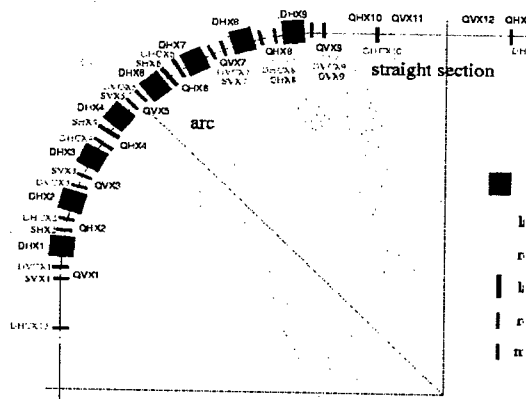
Figure 2. Schematic layout of arc sections.

The outgassing rate of stainless steel is well understood and confident estimates can be made for a wide variety of conditions. However, because of the required TiN coating to reduce SEY, outgassing data for coated chambers is needed for vacuum simulations and to meet design requirements. The ring vacuum system will not be baked, so of particular interest is the outgassing data without in-situ bake. The outgassing rate of several SNS chambers was measured by means of the orifice method and summarized below [5].

The purpose of TiN coating is to minimize the SEY from the chamber wall, thus avoid the so-called e-p instability caused by electron multi-pacting. TiN-coated coupons were sent to CERN for SEY measurements. The results [5] show that TiN films generated at higher sputtering pressures have an SEY ~ 50% lower than those films generated at a lower pressure. However, the outgassing rate of the higher pressure film is, on average, an order of magnitude higher than that of the low pressure film. Both the low SEY and high outgassing is a result of the increased surface roughness of the film. Because electron cloud effects will be more deleterious to accelerator operations than the increased pressure, chambers will be coated at higher pressure. The pressure profiles, with the specific outgassing rate of 1.2×10^{-10} $Torr.l/s.cm^2$ (with TiN coating) and 8.5×10^{-12} $Torr.l/s.cm^2$ (without TiN coating) are shown in Fig.3.

Table2. Outgassing for chambers under various conditions.

Description	Q	Hours
Chamber #2A(VD, no TiN)	8.5E-12	120
Chamber #2A(VD,HP, TiN)	1.2E-10	120
Chamber #5B(VD,LP, GDT, TiN)	9.6E-12	120

(VD: vacuum degass at 450°C, HP: TiN coated at 4 mTorr, LP: TiN coated at 1.5 mTorr, GDT:post glow discharge treatment)
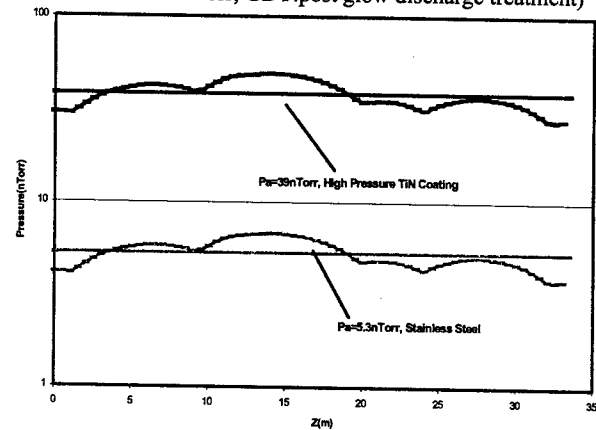
Figure 3. Pressure profiles in arc sections.

Pressure Profile in Injection Section

The SNS injection section has eight injection kickers, one injection septum, one dump septum, four injection bending magnets and two quad doublet assemblies. The layout is shown in Fig.4. The injection bending magnet No.2 has a thin carbon foil to strip the electrons off the H^- beam. This foil will be heated by the proton and the two accompanying electrons. Therefore an additional factor of 5 in gas desorption at B2 region is used in the simulation. Figure 5 shows the pressure profiles in the injection section.

LK: Injection Kicker, Long	B1: Injection Bending Magnet #1
SK: Injection Kicker, Short	B2: Injection Bending Magnet #2
QD:Quad Doublet Assembly	B3: Injection Bending Magnet #3
IS: Injection Septum	B4: Injection Bending Magnet #4
DS: Dump Septum	
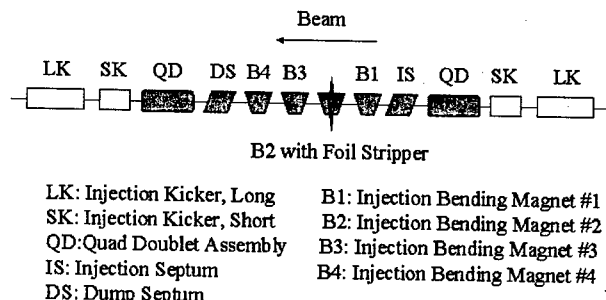
Figure 4. Schematic layout of injection section.
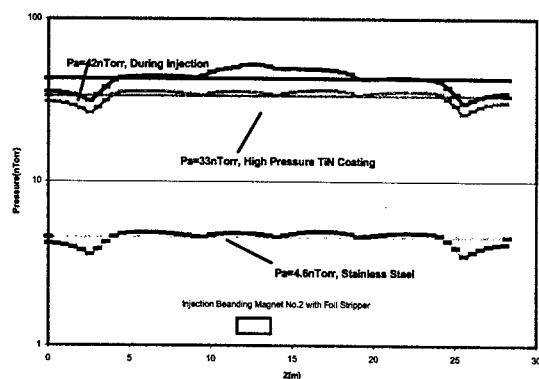
Figure 5. Pressure profiles in injection section.

Pressure Profile in Collimator Section

In the SNS accumulator ring, a straight section is dedicated to transverse collimation. The present ring lattice uses one primary and two secondary collimators (Fig.6) to mitigate beam halo caused by space charge and other collective effects. The collimator system is designed

QD:Quad Doublet Assembly   C2: Ring 2 Collimator
PC: Primary Collimator   C3: Ring 3 Collimator
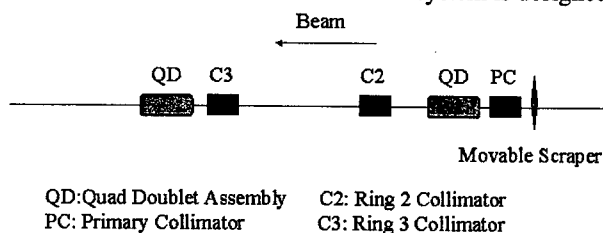
Figure 6. Layout of the collimation straight section
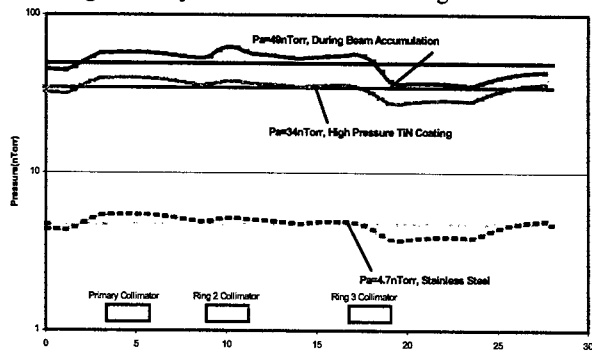
Figure 7. Pressure profiles in collimation section.

to handle the entire portion of the anticipated 2×10^{-3} fractional beam intensity. Therefore the simulation uses an additional factor of 5 for gas desorption and the result is shown in Figure 7.

Pressure Profile in Extraction Section

Figure 8 gives the extraction section layout. The extraction system of SNS ring has 14 kickers (separated into two groups) and the apertures of those kickers were adjusted with the betatron function to yield the overall SNS ring acceptance [6]. A total of 168 ferrite blocks will be installed inside the vacuum chamber. The specific desorption rate of ferrite is 3×10^{-11} Torr.l/s.cm^2 (before *in-situ* baking) and 2×10^{-12} Torr.l/s.cm^2 (after *in-situ* baking)

[7]. The pressure profiles are shown in Fig. 9 with and without in-situ baked ferrites.

QD:Quad Doublet Assembly   LamB: Ext. Septum(Lambertson)
EK1: Ext. Kicker 1   BK: Beam in Gap Kicker
EK2: Ext. Kicker 2
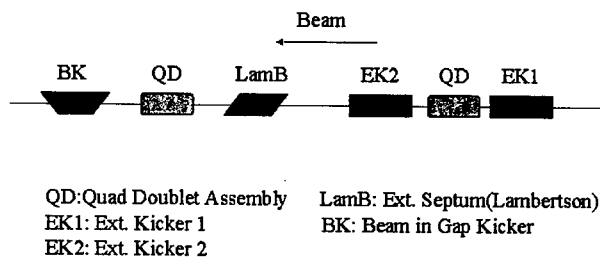
Figure 8. Schematic layout of extraction section.
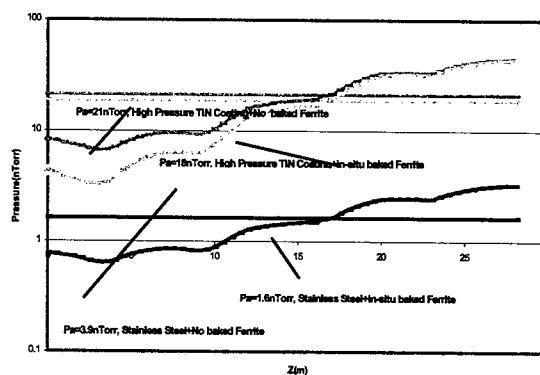
Figure 9. Pressure profiles in extraction section.

SUMMARY AND DISCUSSION

Pressure distribution simulation on the SNS ring vacuum system has been presented. Our simulation results show that the average pressure will be 3~4 times higher than the design value of $<1 \times 10^{-8}$ Torr due to higher outgassing rate with TiN coating done at higher sputtering pressure. The pressure will decrease with SNS beam conditioning based on CERN SPS beam scrubbing experience [8]. The pressure may also be reduced by adding titanium sublimation pumps and ion pumps at existing pump ports of vacuum chambers in future upgrade.

ACKNOWLEDGEMENTS

The authors would like to thank Dr. Bertolini of LLNL in providing the VACCALC simulation code.

REFERENCES

[1] H.C. Hseuh, C.J. Liaw and M. Mapes, Proc. PAC'99, New York, USA, p1345 (1999).
[2] K.M. Welch, Vacuum, 23, 271 (1973).
[3] M. Sullivan, Stanford Linear Accelerator Center (SLAC). Internal Note AP 94-6 (1994).
[4] M. Seidel *et-al*, Vacuum, 60, 267(2001).
[5] P.He, *et-al*, 'Outgassing and Surface Properties of TiN Coated SNS Ring Vacuum Chambers', this proceeding.
[6] N. Tsoupas, *et-al*, Proc. EPAC'00, Vienna, Austria, p2270 (2000).
[7] M. Mapes, Private communication.
[8] J.M. Jimenez, Private communication.

ELECTRON DETECTORS FOR VACUUM PRESSURE RISE DIAGNOSTICS AT RHIC*

U. Iriso-Ariz[†], A. Drees, W. Fischer, D. Gassner, O. Gould, J. Gullotta,
R. Lee, V. Ponnaiyan, D. Trbojevic, K. Zeno, S.Y. Zhang.
BNL, Upton, NY 11973, USA

Abstract

In the RHIC 2001 run, an unexpected vacuum pressure rise versus bunch increasing currents was observed in both gold and proton operations. This pressure increase due to molecular desorption is suspected to be induced mainly by electron multipacting, but other causes may coexist, such as ion desorption due to halo scraping. In order to get a reliable diagnostic of the phenomenon electron detectors have been installed along the RHIC ring. In this report we describe results measured by the electron detectors with energy filters during the RHIC 2002/2003 run.

1 INTRODUCTION

A pressure increase was observed during Au-Au FY2001 run at the Relativistic Heavy Ion Collider (RHIC) for high intensity beams. It is suspected to be due to molecular desorption, mainly substained by electron multipacting, but other causes may coexist, such as ion desorption or beam losses as seen in Ref. [1]. In order to have a reliable diagnostic for the phenomen, up to 16 electron detectors (ED) have been installed in the RHIC ring. Since the presence of ions is not rejected [1], ion collection will be possible through these detectors. A general description of the ED installed at RHIC follows:

- 4 Spallation Neutron Source (SNS) ED, and 1 Argonne National Laboratory (ANL) ED. Both of these ED are RF shielded very effectively and in a similar manner. No amplifiers were connected to them, and they all could be used to measure an electron energy (E_e) spectrum.

- 1 MicroChannel Plate (MCP) ED. Its low frequency cut off (f_{low}) is set to 0.3MHz, and it has a nominal gain (G) of 58dB. No E_e spectrum is available through this detector.

- 11 RHIC ED. Their design is based on the PSR model [2], and a general layout can be seen in Fig. 1. Most of these ED's are connected to the AC coupling amplifier *Sonoma* 310 (G=32 dB, bandwidth (BW) [10kHz-1GHz]). The final f_{low} ranges from 10kHz to 1MHz since it is a function of the Capacitor (C) used to protect the amplifier. An E_e spectrum is also possible through these detectors.

As a first measure to reduce the pressure (P) rises detected during RHIC 2001 run, most of the warm parts of the ring

were baked out before the FY2003 run. Despite the fact that the ring was filled several times with the same fill patterns as in 2001: 55 and 110 bunches, 216ns and 106ns bunch spacing, respectively. See Ref. [1] and [3] for more information. P rises were not as strong and generally reproduced around the entire ring, but only in certain locations. The bake out, together with the lower beam intensities achieved during this run, produced very low electron currents to the beam pipe wall. Therefore, only the EDs placed at very weak parts (in terms of vacuum stability) and with a high G were able to detect currents above the noise level. For technical reasons the MCP (58dB) was not fully utilized. Therefore, the RHIC ED has been the main ED providing electron cloud EC signals, and this note will report about the description of this detector.

2 THE RHIC DETECTOR LAYOUT

The general layout of the RHIC ED can be seen in Fig. 1. The top grid ('Grid 0' in Fig. 1) acts as an RF shield, and its transparency (T_0) is fixed to 23% in order to decrease the effect of the image currents without interfering the multipacting process. The middle grid (stated in Fig. 1 as 'Grid 1', with $T_1 = 80\%$) can be biased to different voltages through the remote controlled High Voltage supply (HV). It acts as an energy filter, allowing the E_e spectrum to be measured.
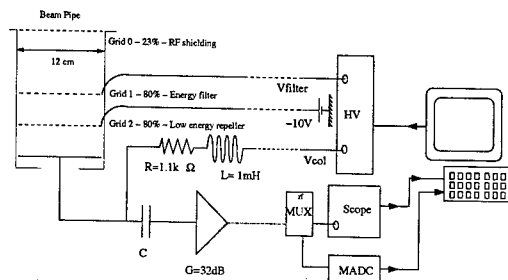
Figure 1: Layout of the RHIC ED. As stated in the text, C is not the same for all 11 detectors, but a typical value is 0.01 μF. The presence of C is needed to protect the amplifier.

The bottom grid (shown as 'Grid 2' in Fig. 1, with $T_2 = 80\%$) is held at -10V by a DC battery. It is used as a repel back the secondary electrons produced at the collector. The collector can be biased either positively or negatively through another output of the HV supply in order to check the presence of either electrons or ions, respectively

[1]. In order to be able to keep the collector at different voltages and polarities without damaging the amplifier, an

C circuit (Fig. 1) is used in a box placed as close as possible to the ED in the ring. The multiplexer (shown as 'MUX' in Fig. 1) allows for signal splitting and two data acquisition modes: 'fast' and 'slow'. The fast mode uses a scope to take a 20μ snapshot sampled at 1GHz which is done through the scope. This acquisition is triggered every AGS [1] cycle (approximately every 4s). The 'slow' mode uses a Multiplex Analog to Digital Converter (MADC) with a sampling rate of 720 Hz. This mode should be useful in linking the time evolution of P and $_{wall}$ for large time scales.

Signal differentiation

An AC coupled system differentiates the signals below the f_{low}, which is determined by C. The RHIC ED circuit has been evaluated using the commercial software $PSP\ CE$ [2], and its behavior has been tested for a given 'ideal' $_{wall}$. This $_{wall}$ has been taken from one of the existing computer EC simulation codes, in this case, $CSEC$ [5]. Figure 2 shows the signal differentiation when the EC starts. Although we are referring to an electron current which should always be negative (green light points in Fig. 2), the signal that will be seen in the scope (black line) is both positive and negative in order to keep the integral over one period null, i.e. one RHIC beam revolution, $_{rev} = 12\ 8\mu$. We can see that as the EC takes place, both the maximum and minimum parts of the signal increase in magnitude due to the electronics design. Using the MADC, we log the maximum and minimum values of the 720 samples taken per second and we can follow the slow evolution of EC at 1Hz. This will become the most reliable tool in evaluating the EC signal at large time scales (minutes).
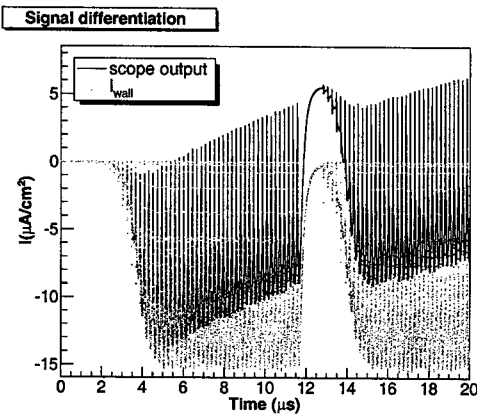
Figure 2: Theoretical $_{wall}$ calculated with $CSEC$ (green light dots). This signal is differentiated by the RHIC ED system, and has been evaluated with $PSP\ CE$ (black line).

---

[1]Alternating Gradient Source
[2]http://www.orcadpcb.com/pspice

Calibration

For a given scope voltage reading (V), we will be interested in the corresponding current into the wall ($_{wall}$). Given the surface area of the detector, S_{ed}=78 m^2, and taking into account that the effective transparency (T_{eff}) of the ED is calibrated as a function of the E_e (see [4]), $_{wall}$ in terms of $\mu\quad m^2$ can be calculated as:

$$_{wall} = \frac{V}{GS_{ed}T_{eff}} \qquad (1)$$

where $= 50\Omega$, and according to the specifications of the amplifier, G is significantly flat for the f we are interested in (80kHz to 20MHz). Therefore, the uncertainty in T_{eff} will be responsible for the error while computing the $_{wall}$ from the experimental data (V).

3 EXPERIMENTAL RESULTS

During this run, d circulated in the clockwise RHIC ring (blue ring), and the $^{79+}$ ions ran in the counterclockwise RHIC ring (yellow ring). The typical intensities have been $_{pb}$=6 10^{10} d per bunch ( ) in the blue ring, whereas in the yellow ring $_{pb}$=4 10^8 $^{79+}$ ions per bunch . These numbers are below the EC threshold in both cases. Together with the bake out, these facts produced some less severe P increases (see [3] for more details), and the possibilities of detecting electrons were significantly reduced. On the other hand, during the polarized proton ( ) run starting in March 26th 2003, the beam intensities were readily attainable above the EC threshold, and an $_{pb}$=10^{11} protons per bunch ( ) was easily achieved. We analyze the data collected for both the and run. Table 1 summarizes the experimental minimum beam parameters for which EC signals allow data collection using the ED.

Table 1: Experimental beam parameters producing EC signals at the RHIC ED. The beam bunch spacing is always 106ns, corresponding to the pattern for 110 bunches in the machine. Bunch length at injection is usually 15-20 ns, while when ramping it is about 10ns (head to tail). $_{wall}$ is estimated using T_{eff}=3.5% from [4].

		+79		
$_{pb}$		8 10^8	9 10^{10}	8$10^{10}$
process		ramp	injection	injection
$_{wall}(\mu$	$m^2)$	≈5	≈0.5	≈2
fill #		3107	3159	3460
P (torr)		5 10^{-6}	1 10^{-6}	4 10^{-6}

Fast mode observation

The Au case showed only one significat case of EC signal, and interested readers can see it in [3]. In the d case, no

clear snapshots of data have been logged with ED. However, in several cases, by smoothing the data it is possible to distinguish the EC signal from the noise level and image currents. The most critical region in the blue ring turned out to be the straight section 'bo2'. The RHIC ED there has the same characteristics as seen in Fig. 1, except that it is equipped with 2 amplifiers in series. Therefore its total nominal $G = 64dB$. Fig. 3 reports the case of fill #3159, where $I_{pb}=9\ 10^{10}\ dpb$. When 59 bunches where injected in the machine, the raw data does not show any clear EC signal (light green dotted lines). Numerically smoothing the data with a 10 MHz filter (black line), we can clearly see how the EC rises for the last bunches and disappears at the same time as the bunch train.

Figure 4: EC signal using MADC in bo2 sector while filling RHIC with 110 bunches. Injection was temporally interrupted after 45 bunches (t=200s) and resumed at t=320s. Note that P is plotted in logarithmic scale.

Figure 3: EC signal on the ED placed in the bo2 sector. The light dotted green line shows the raw data, whereas the black solid line shows the smoothed data using a numerical 10 MHz filter.

Slow mode observation

The ED placed in bo2 showed clear EC signals during the pp run using the 'smoothing' technique, and similar snapshots as in Fig. 3 are compared in [5]. Fill #3460 showed a general EC problem throughout RHIC. This clear case allowed us to carry out interesting studies using the 'slow' mode (MADC). Figure 4 shows the time evolution of P, and the V in the ED. The injection during this fill was temporally interrupted when 45 bunches were injected (t=250s, in Fig. 4). Injection resumed at t=320s and finished after 700 s. Correlation between the time evolution of P and V is visible, which shows that EC is the primary factor in the P rise. V is plotted in a linear scale, and it is worth mentioning that both magnitudes are ultimately a function of I_{beam}. Using Eq. 1, I_{wall} in this plot ranges from $0.2\mu A/cm^2$- $5\mu A/cm^2$.

4 CONCLUSIONS AND OUTLOOK

The EC could be observed with d, Au and p in the FY2003. P rises during the dAu run have in general been lower than expected due to the bake out performed during the 2002 shutdown and the technical difficulties in acieving high I_{pb}. However, under certain beam conditions, a substantial P rises were observed and several EC signals have been detected using the RHIC ED in the fast mode for both d and Au. The weak EC signal and the absence of an amplifier for the SNS and ANL ED did not allow the EC to be seen using these. In general, I_{wall} ranges [0.5-10] $\frac{\mu A}{cm^2}$. The RHIC ED has been very sensitive to of image currents, and signals below $\approx 0.5\ \frac{\mu A}{cm^2}$, corresponding generally to $P\quad 10^{-7}$ Torr were indistinguishable from the noise level. Only cases reported during the pp run allowed us to use the slow mode detection. The signal differentiation in the RHIC ED has been evaluated, and an estimation of the evolution of EC for large time scales (minutes) is possible. This fact allowed us to investigate the direct influence of I_{wall} on the P rise. A measure of the E_e spectrum, and a better estimation of the slow evolution of I_{wall} are in progress. A new DC amplifier is currently being designed and expected to be ready for use during the next run.

ACKNOWLEDGEMENTS

The authors would like to specially thank J-M. Laurent (CERN) for his helpful discussions and tips, S. Jao for his help in the calibration of the ED, and all the C-AD for their support. B. Brelsford and K. Zeno made the English in this paper readable.

REFERENCES

[1] W. Fischer et al. Vacuum pressure rise with intense ion beams in RHIC. Proceedings of EPAC'02, Paris, 2002.

[2] R. Macek et al. Recent experimental studies of the Electron Cloud at the Los Alamos PSR. KEK Workshop, Sept. 2001.

[3] S.Y. Zhang et al. RHIC pressure rise and electron cloud. In this proceedings.

[4] P. He et al. Calibration of RHIC Electron Detector. In these proceedings.

[5] U. Iriso-Ariz et al. Electron cloud and pressure rise simulations for RHIC. In these proceedings.

ELECTRON CLOUD AND PRESSURE RISE SIMULATIONS FOR RHIC*

U. Iriso-Ariz[†], M. Blaskiewicz, A. Drees, W. Fischer, S. Peggs, D. Trbojevic.
BNL, Upton, NY 11973, USA

Abstract

Beam induced electron multipacting may be among the main reasons for the vacuum pressure rise when circulating high intensity ion and proton beams in RHIC. Latest simulation results are benchmarked with recent experimental observations for RHIC, and compared to other general computer codes. The influence of the electron multipacting to the vacuum properties is also discussed.

1 INTRODUCTION

Pressure (P) rises were observed as bunch currents were increased during both gold (Au) and proton (p) operations at the Relativistic Heavy Ion Collider (RHIC). Preliminary indications from the RHIC 2001 run [1] suggest that an electron cloud (EC) may be the main cause of P rises that limit the beam intensity at RHIC. Ion desorption and beam loss may also be partially responsible. In the following, we benchmark the latest experimental observations with one of the existing computing codes, $CSEC$([2]). Preliminary results obtained from $ECLOUD$ [3] are also discussed. Following the results obtained by $CSEC$ and the experimental data, we give a reliable ranges for the main wall surface parameters contributing to the effect, which are necessary to determine the behaviour of the secondary electron emission, δ (Sec. 2). Observations have been made with the same fill pattern (106ns bunch spacing) and during the same process (injection, where bunches are typically 15ns head-to-tail long) as in the 2001 run. Due to the bake out carried out during the RHIC shutdown in 2002, the 55 bunch fills (with 216ns bunch spacing) did not show EC effects. Due to the high P rise observed in some cases, the number of injected bunches injected did not reach the target of 110. We also compare the simulation results with data when a solenoidal field is applied to suppress the effect. The experimental results are based on the electron detector in [4]. The direct output provided by this detector is a voltage, which can be converted to a current into the wall (I_{wall}) with a large uncertainty (factors ≈ 3 are possible [4]). Despite this large error, it has been decided to show the experimental observations in terms of I_{wall}, expressed in ($\frac{\mu A}{cm^2}$). Finally, and based in the experimental data, we discuss the influence of I_{wall} to the P for when the latter reaches a final steady state.

2 PARAMETRIZATION OF THE SECONDARY EMISSION YIELD

Following the notation in [5], for a normally incident electron with kinetic energy E, $\delta(E)$ is the total number of electrons leaving the surface due to all processes. The parametrization of $\delta(E)$ is one of the main concerns while simulating the EC effect, and there are still a lot of investigations currently being carried out [7]. $CSEC$ uses the following [2]:

$$\delta(E) = (R - R_{inf})\exp^{-E/E_r} + R_{inf} \tag{1}$$

$$+ SEY_{max}\frac{s(E/E_{max})}{s - 1 + (E/E_{max})^s},$$

where E_r, s, and R_{inf} are fitting parameters that have been fixed from [2] and [5] to 60eV, 1.813 and 0.2, respectively. E_{max} corresponds to the energy at which δ has its maximum value (δ_{max}). For stainless steel (RHIC), E_{max}=300eV [6]. The contributions to $\delta(E)$ can be divided into the reflected electrons (terms proportional to R and R_{inf}) and the 'true' secondaries (terms proportional to SEY_{max}). R stands to the electron backscattering probability at low E, whereas R_{inf} refers for the same probability for high E electrons. The angular distribution of the secondary electrons is also taken into account and can be seen in [2]. Figure 1 illustrates the global behaviour of δ and the individua contribution of the reflected electrons and the true secondaries, respectively.
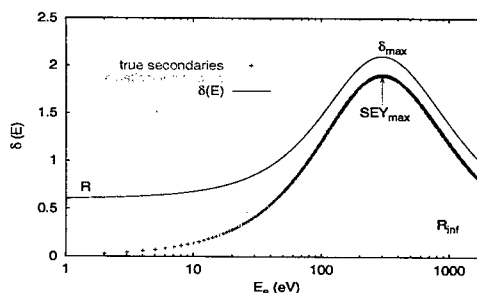
Figure 1: Separation between the processes influencing δ for R=0.6 and SEY_{max}=1.9.

EC is very sensitive to the SEY_{max} and R. By comparing $CSEC$ results with experimental observations, we give a reliable range for these SEY_{max} and R referring to the RHIC beam pipe wall. On the other hand, the freedom to change these specific parameters in the input file using the $ECLOUD$ code is reduced only to the value δ_{max} (Fig. 1). Note that δ_{max} is not the same as the SEY_{max} from $CSEC$. The way in which the reflected electrons are

evaluated in $ECLOUD$ is fixed. The parametrization used there has been updated following laboratory measurements. The latest version, which is the one used here, can be seen in [7].

3 SIMULATIONS COMPARED WITH EXPERIMENTAL DATA

Clear EC cases occurred during the RHIC FY2003 polarized proton (pp) run, where it was technically feasible to reach higher bunch intensities (I_{pb}) than during the dAu run. These cases occurred at the long straight section labeled 'bo2', where the vacuum chamber has cylindrical symmetry. The main machine characteristics, together with the beam parameters for fill #3460 can be seen at Table 1. Figure 2 shows a snapshot of the EC signal collected in the ED and the bunch intensity (I_{pb}) for fill #3460. I_{pb} ranges from $8\ 10^{10}$ to $5.5\ 10^{10}$ ppb during the bunch train. Note that the I_{pb} of the second group of less intense bunches (from bunch # 17 to 33) causes the EC signal to decrease. That may indicate a RHIC EC threshold of $I_{pb}=6\ 10^{10}$ protons per bunch (ppb) for the long straight sections.

Table 1: Machine and beam specifications used for the RHIC simulations based on fill #3460.

I_{pb}	$8\ 10^{10}\ ppb$
full bunch length	15 ns
bunch spacing	106.6 ns
# bunches (N_b)	110
revolution period (T_{rev})	12.8 μs
rms beam radius	2.4 mm
relativistic γ	25.8
beam pipe radius	6 cm
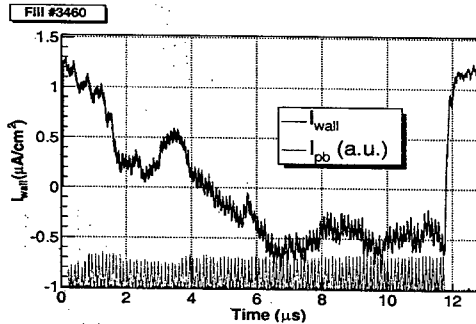
Figure 2: EC signal (black solid trace) and I_{pb} (red bars) for a RHIC revolution (12.8 μs during fill 3460). The signal goes from positive to negative values due to the electronic design of the ED.

In general, the computer code simulations assume equal intensity along the bunch train. Fill #3460 can be reproduced with the recently developed $CSEC$, which allows I_{pb} to be changed for different bunches. We tried to fix the wall surface parameters contributing to EC by sweeping SEY_{max} and R and comparing I_{wall} behaviour with

the experimental data. Due to the few EC cases found until now, the electron dose received can be neglected. It turned out that R<0.5 needs SEY_{max} >2.2 to multipact (far from the literature values for baked stainless steel surfaces, see [5] and [6]), whereas R=0.7 does not reproduce the observed decay time. Therefore, possible values for R are 0.6±0.1. Figure 3 shows the SEY_{max} sweep fixing R=0.6. In order to determine the proper values of SEY_{max} and R, we could fit the growth and decay times from both simulations and experimental data and compare the results. However, the experimental data comes from an AC coupled signal with a low frequency cut off, f_{low}=300kHz [4]. Therefore, the signal needs to be treated before fitting when slow dynamics (<300kHz) play a role, as they did for fill # 3460. This treatment is being developed, and the results of the first analysis indicate that R=0.6 and SEY_{max}=[1.8-2.0] match reasonably well with the estimated I_{wall} ($\approx$0.5-5$\frac{\mu A}{cm^2}$) and EC timing (saturation $\approx$ 6 μs). This combination is also found in scientific papers ([5] and [6]). The combination R=0.5 and SEY_{max} $\geq$2.1 is a possibility for the unbaked stainless steel vacuum chambers at RHIC. Note that these values are given for R_{inf}=0.2. Possible consequences of changes in this parameter are currently under study.
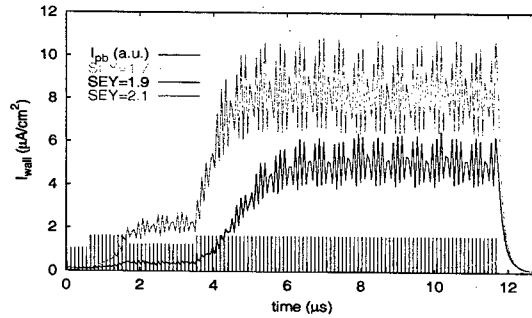
Figure 3: Sweep of possible values of SEY_{max} fixing R=0.6. The maximum value of the line density for these cases ranges from 0.1 nC/m (SEY_{max}=1.7) to 1nC/m (SEY_{max}=2.1).

Preliminary results using $ECLOUD$ with the latest parametrization for elastically reflected electrons using δ_{max}=1.9 produce a line density ρ at saturation on the order of $0.3nC/m$, which is in good agreement with $CSEC$ results for R=0.6 and SEY_{max}=1.8.

4 RESULTS OF APPLYING A SOLENOID FIELD

Figure 2 shows that less intense bunches produce a strong decrease in the ECE signal. Therefore, it was thought that a fill pattern with some missing gaps could avoid the EC build-up. To check this possibility, RHIC was filled with the 110 bunch fill pattern, but using some gaps in the bunch train, i.e. the same beam and machine parameters stated in Table 1 except for N_b=41 and I_{pb}=1.1

10^{11}. In this case, 16 'filled' bunches were followed by a gap of 425ns (corresponding to 4 missing bunches). During the third bunch train, only 9 bunches were injected because of the high P rise. So, the total number of bunches is N_b=16+16+9=41. Fig. 4 shows this pattern as well as the EC signal. The EC signal was quite evident and stable and a solenoid field (B) was applied. As can be seen in Fig. 4 (top), a very weak B (5.4 Gauss) already decreases the EC at RHIC by a factor of $\approx$4, and unfortunately sends the EC signal below the noise level. Observations with higher B did not show significant changes. Results from $CSEC$ simulations are shown on Fig.4 (bottom). According to Sec. 3, a good and reliable combination is SEY_{max}=1.8 and R=0.6. Simulation results for this case can be seen at Fig. 4 and confirm that B=5.4 Gauss is already a field strong enough to put the EC signal under the RHIC electron detector noise level. Further studies are currently carrying on to exactly determine the magnetic field supressing EC at RHIC.
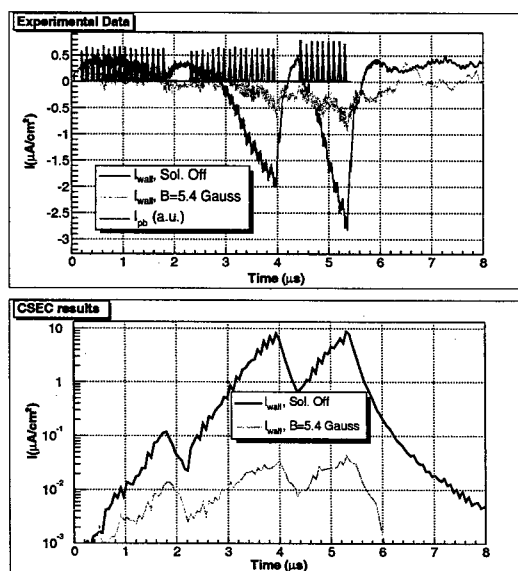
Figure 4: Experimental suppression of the EC using a solenoid (top). B=5.4 Gauss sends the EC signal to the noise level. The simulation results (bottom) show good agreement. Note a logarithmic scale is used for the simulation results to highlight the difference in the order of magnitude.

5 EVALUATION OF P

For I_{pb} and N_b fixed, the final I_{wall} is stabilized under certain conditions due to space charge effects. Observations show that the final P also reaches a certain equilibrium between the desorbed gas molecules in the wall and the gas pumped by the ion pumps. This P can be estimated directly proportional to I_{wall} ([1]) and depending on the the electron desorption coefficient (η_e) of the beam pipe wall. This becomes a critical parameter for this calculation. Although η_e changes significantly depending on

the gas species, temperature, surface material and the impinging electron E ([9]), we plan to use RHIC to give a global (regardless the gas species) estimate for η_e based on the experimental observations for both I_{wall} and P. Unfortunately, the amount of data is still not enough to give a reliable value for η_e and further studies are currently being carried out.

6 CONCLUSIONS

Observations at RHIC and simulation development are currently being carried and therefore the analysis is not definitive. However, preliminary results from simulations show good agreement with the latest experimental data (I_{wall} on the order of 0.5-10 $\frac{\mu A}{cm^2}$). Both $CSEC$, $ECLOUD$ and experimental results show a $\rho \approx 0.5$ nC/m. We determined a value for R=0.6 $\pm$ 0.1 for SEY_{max} (1.8-2.1) for baked stainless steel vacuum chambers used; and $SEY_{max} > 2.1$ for the unbaked case using $CSEC$ parametrization. However, variations on R_{inf} have not been considered, and these values may vary slightly. Weak solenoid fields ($\approx$ 10 Gauss) are strong enough to suppress the cloud for $I_{pb} \approx 10^{11}$ppb. We introduced also a preliminary plan to find a global value for η_e from the observations of P and I_{wall}.

ACKNOWLEDGEMENTS

REFERENCES

[1] W.Fischer et al. Vacuum pressure rise with intense ion beams in RHIC. EPAC'02, Paris, 2002.

[2] M. Blaskiewicz et al. Electron cloud instabilities in the PSR and SNS. PRST-AB 6, 014203. Jan. 2003.

[3] G. Rumolo and F. Zimmermann. Practical User Guide for ECloud. SL-Note-2002-016 AP. CERN, Geneva, May 2002.

[4] U. Iriso-Ariz et al. Electron detectors for vacuum pressure rise diagnostics at RHIC. In these proceedings.

[5] M. A. Furman and M. Pivi. Probabilistic model for the simulation of secondary electron emission. PRST-AB 5, 124404, Dec. 2002.

[6] C. Scheuerlein et al. The SEY of technical materials and its variation with surface treatments. Proceedings of EPAC'00, Vienna, June 2000.

[7] F. Zimmermann. Electron Cloud Progress, 13th LHC MAC. March 2003.

[8] S.Y. Zhang et al. RHIC pressure rise and electron cloud. In these proceedings.

[9] J. Gomez-Goni and A.G. Mathewson. Temperature dependence of the electron induced gas desorption yields on stainless steel, copper and aluminum. J. Vac. Sci. Technol. A 15 (6), Nov/Dec 1997.

DEVELOPMENT OF MOVABLE MASK WITH REDUCED-HOM DESIGN FOR KEKB

K. Shibata[#], Y. Suetsugu, T. Kageyama, KEK, Tsukuba, Japan

Abstract

At the high energy ring of the KEK B-factory (KEKB), it was found that some bellows near the movable masks were overheated due to the higher order mode (HOM) as increasing the beam current over 900 mA. To cope with this problem, a new mask was designed where the length of ramps beside the mask head was expanded from 30 mm to 400 mm. MAFIA T3 simulations showed that the loss factor for the new long mask was about a half of that for the previous short one. The power of the TE mode, on the other hand, which can easily couple with the bellows through the finger-type RF-shield, was expected to reduce to about 6 percent of that for the short one. During the summer shutdown in 2002, two long masks were installed as a test. In the following run the temperature rise of bellows near the long masks was about 20 percent of those near the short ones and the new design was found to be effective to reduce the HOM. The decrease in the temperature rise was larger than the reduction of the HOM power estimated from the loss factor. This result indicates that the overheating of the bellows is mainly due to the TE mode like HOM rather than the total HOM.

INTRODUCTION

The KEKB is a high-luminosity electron-positron synchrotron collider with asymmetric energies to produce copious B and anti-B mesons for the study on the CP violation [1]. It has two rings, one is the high energy ring for 8 GeV electrons (HER), and the other is the low energy ring for 3.5 GeV positrons (LER). The design beam current of HER and LER are 1.1 A and 2.6 A, respectively, and the luminosity goal is 1×10^{34} cm^{-2}s^{-1} [2]. To achieve such a high luminosity, there are various kinds of devices in the vacuum system of KEKB. A movable mask (or collimator) is one of them to cut off particles escaped from a bunched beam and to reduce background noise in the BELLE detector [3-5]. Sixteen movable masks (eight vertical and eight horizontal type masks) are now installed in each ring. The position of each mask head can be adjusted remotely balancing the background noise in the detector with the beam life time.

In 2002, overheating of bellows just near the vertical masks in HER was found at the beam current higher than 900 mA. This overheating was caused by the HOM which went inside of the bellows through slits between RF-shield fingers of bellows [6]. Some bellows were overheated up to about one hundred degrees and sometimes resulted in vacuum leaks. In order to solve this problem, the vertical movable mask was improved introducing a reduced-HOM design. Here the structure of new mask and the estimation of HOM power are

presented in detail.

REDUCED-HOM DESIGN

Structure

Figure 1 shows sketches of the previous short mask and the new long one (vertical type). A mask chamber is a bent chamber and the wall of the chamber has the function as a mask head. Since the cross section of the beam chamber is kept constant, there is no trapped mode at the mask head although the HOM is excited at the mask head where the beam passes off centre of the beam chamber [4]. The position of the mask head can be adjusted by moving the mask chamber with a stroke of ±10 mm around the nominal position. There are bellows with a finger-type RF-shield [6] at the both side of the mask chamber to absorb the motion of the mask chamber.

In order to reduce the power of the HOM generated at the mask head, the length of the ramps beside the mask head was expanded from 30 mm to 400 mm with the same height of 15 mm in the case of the improved long mask. The length of the ramp was limited to 400 mm by the space for installation.

Reduction of Loss factor

To estimate the effect of this new long mask, the loss factor of a vertical mask was calculated by using MAFIA T3 simulation code. The distance from the mask head to the beam and the bunch length were set for 10 mm and 6 mm, respectively. Figure 2 shows the loss factor, k, as a function of the ramp length of the mask head, l. The loss factor decreases rapidly with increasing the ramp length from 30 mm to 100 mm. After that the loss factor decreases gradually with the ramp length. When the ramp length is expanded from 30 mm to 400 mm, the loss
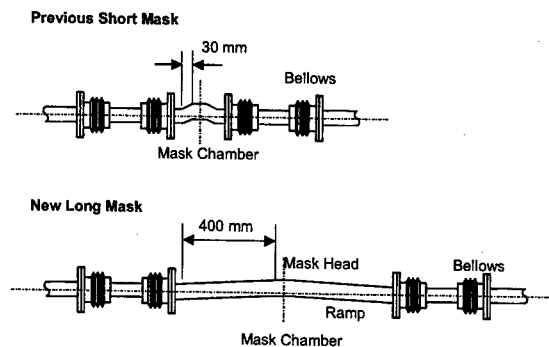
Figure 1: Previous short mask and new long mask. The length of the ramps was expanded from 30 mm to 400 mm.

[#]kyo.shibata@kek.jp
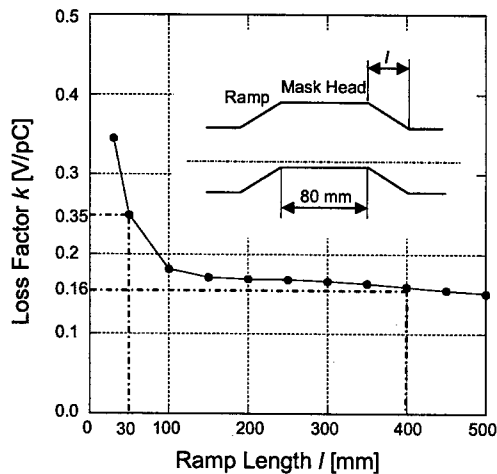
Figure 2: Loss factor, k, of the HER vertical mask as a function of the ramp length, l.

factor is reduced to about 46%. It is, therefore, expected that the temperature rise of the bellows near the mask should reduce to about a half at least. For 1000 mA beam with 1200 bunches, for an example, the power loss should reduce from 2.8 kW to 1.3 kW.

Reduction of TE mode

TE mode can easily couple with the bellows through the slits between RF-shield fingers. (The width and length of the slit are 0.5 mm and 20 mm, respectively [6].) It is,
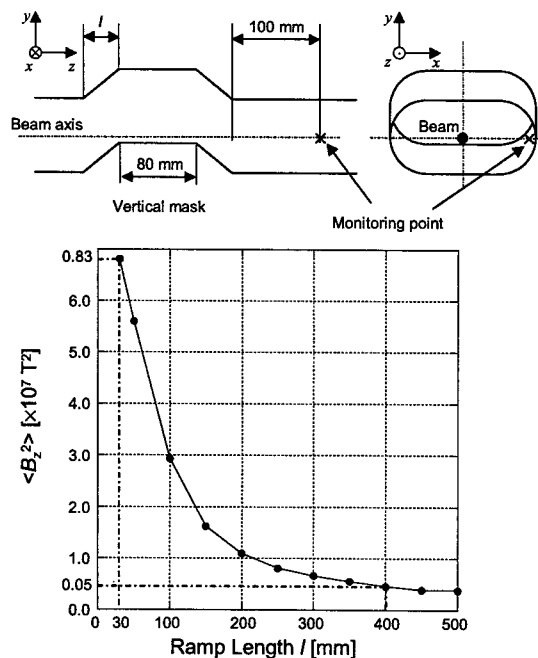
Figure 3: The averaged intensity, $<B_z^2>$, of the HER vertical mask as a function of the ramp length, l. The monitoring point is also indicated in the sketch above.

therefore, very important to consider the effect of the TE mode among various modes.

To estimate the power of the TE mode, the magnetic field component B_z, which is parallel to the beam axis, just near the inner wall of the beam duct was calculated. The monitoring point was 100 mm away from the edge of the ramp beside the mask head that is the nearest bellows position.

The results are shown in Fig. 3 as a function of the ramp length, where $<B_z^2>$ is the averaged intensity of B_z^2 for 5 ns after a bunch passed by the monitoring point (about a half of the present bunch spacing) excluding the beam induced field and it represents the power of the TE mode. The averaged intensity, $<B_z^2>$, decreases more drastically than the loss factor (Fig. 2). Comparing the case of 30 mm with 400 mm, $<B_z^2>$ reduces to about 6%. It is, therefore, expected that the temperature rise of the bellows near the masks could reduce to about 1/16.

RESULTS AND DISCUSSIONS

During the summer shutdown in 2002, two long masks were installed in HER as a test and the temperatures of bellows just near the vertical masks were measured. Figure 4 shows the behaviour of temperatures of bellows near new long masks and previous short ones against the beam current. Because of the resonance phenomenon, there are some differences between data. However, it is obvious that the temperature rises of the bellows near the new long masks are smaller than that of the previous ones. When the beam current was 950 mA, the temperature rise reduced to about 20% on average.

The ratios of the temperature rise of the bellows near the long mask to that near the short one are shown in Table 1, where ΔT, ΔT_k and ΔT_B represent the temperature rise obtained by the measurement, expected from k and $<B_z^2>$, respectively. There are some discrepancies between the expectations and the observations. The experimental result is between the expectations.

The expectation from the loss factor k is larger than the
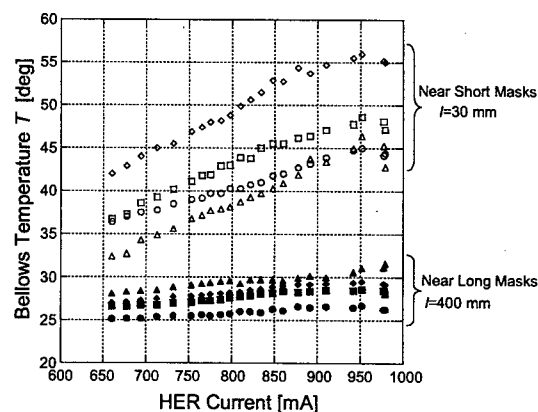
Figure 4: Behaviour of bellows temperature, T, against HER beam current.

Table 1: Reduction of the temperature rise obtained by the measurement and expected from k and B_z.

Expectation from k	$\dfrac{\Delta T_k (400 \text{ mm})}{\Delta T_k (30 \text{ mm})} = 0.46$
Experimental result	$\dfrac{\Delta T (400 \text{ mm})}{\Delta T (30 \text{ mm})} = 0.2$
Expectation from $<B_z^2>$ (full frequencies)	$\dfrac{\Delta T_B (400 \text{ mm})}{\Delta T_B (30 \text{ mm})} = 0.06$
Expectation from $<B_z^2>$ ($f > 2$ GHz)	$\dfrac{\Delta T_B (400 \text{ mm})}{\Delta T_B (30 \text{ mm})} = 0.2$

experimental result. This difference can be explained by that the effects of both the TE and TM modes were included in the expectation from k. Practically, only the TE mode can go through the RF-shield of bellows and contribute the heating of the bellows. According to the calculation by MAFIA, the reduction of the TE mode is larger than that of the TM mode with increasing the ramp length. The expectation from the loss factor must be underestimated.

On the other hand, the expectation from $<B_z^2>$, that represents the TE mode power, is less than the experimental result. One possible explanation for this difference is that heating of the bellows depends on frequency of the TE mode and all of the TE modes are not responsible for heating of the bellows.

Figure 5 shows the calculated spectrum of B_z for the short mask and the long mask. For the short mask there is a strong HOM around 1.5 GHz. However, the TE modes
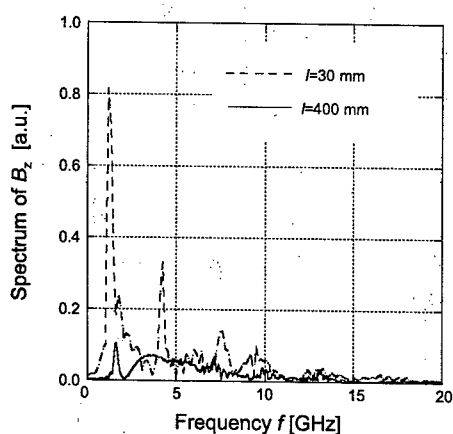
Fig. 5: Spectrum of B_z for the new long mask ($l = 400$ mm) and the previous short mask ($l = 30$ mm).

with low frequencies hardly go through the RF-shield of bellows, because the slits between RF-shield fingers are short compared to the wavelength. For example, taking into account only the TE modes with frequencies higher than 2 GHz, the expectation from $<B_z^2>$ gets close to the observed result (Table 1).

CONCLUSION

In order to suppress the heating of the bellows just near the vertical movable masks in HER, the movable mask with a reduced-HOM design was developed. The length of ramps beside the mask head were expanded from 30 mm to 400 mm. After installation of the new long masks, the temperature rise of the bellows just near the masks reduced to about 20%, and it was confirmed that this new long mask is very effective to reduce the temperature rise of the bellows. Furthermore, from MAFIA T3 simulation it was found that the TE modes with frequencies higher than 2 GHz mainly responsible for heating of the bellows.

During the winter shutdown in 2002-2003, more two long vertical masks were installed in HER. After installation of the new long masks the stored current was increased gradually, and at the beginning of May 2003 it was about 1.1 A for HER (design current [2]). The maximum peak luminosity exceeded the design value and reached 1.03×10^{34} cm^{-2}s^{-1}. Overheating of bellows near the new long masks has not been found. All the short masks in HER will be exchanged for the new long masks during the summer shutdown in 2003.

ACKNOWLEDGEMENTS

REFERENCES

[1] KEK Report 95-1, April (1995)
[2] KEK Report 95-7, August (1995)
[3] K. Kanazawa et al., "DEVELOPMENT OF THE MOVABLE MASK SYSTEM FOR KEKB", EPAC'00, Vienna, June 2000, p.2301
[4] Y. Suetsugu et at., "DEVELOPMENT OF THE MOVABLE MASK FREE FROM TARAPPED MODE FRO THE KEKB", PAC'01, Chicago, June 2001, p.2186
[5] K. Akai et al., Nucl. Instr. and Meth. A499 (2003) 191.
[6] Y. Suetsugu et al., Rev. Sci. Instrum. 67 (1996) 2796.

DEVELOPMENT OF WINGED HOM DAMPER
FOR MOVABLE MASK IN KEKB

Y. Suetsugu[#], T. Kageyama, Y. Takeuchi, K. Shibata, KEK, Tsukuba, Japan

Abstract

In a high luminosity lepton machine such as the KEK B-factory (KEKB), the vacuum components are likely to be annoyed by intense higher order modes (HOM) due to the high beam currents. A winged HOM damper equipped with SiC HOM absorbers was developed to absorb unnecessary HOM, especially TE mode like HOM with a power of several kW. Four dampers were installed in the KEKB ring near movable masks and relieved heating of bellows and pump elements effectively at the beam current up to 1.5 A.

INTRODUCTION

The KEK B-factory (KEKB) is an electron-positron collider with asymmetric energies consisting of two rings, that is, the High Energy Ring (HER) for 8.0 GeV electrons and the Low Energy Ring (LER) for 3.5 GeV positrons [1]. To realize the high luminosity, 10 nb^{-1} s^{-1}, the design currents are larger than those of conventional colliders and are 1.1 A and 2.6 A for HER and LER, respectively. The commissioning of KEKB started in December 1998 [2,3]. At the beginning of May 2003, the achieved stored beam currents were about 1.1 A and 1.5 A for HER and LER, respectively, with 1284 bunches. The KEKB is now able to serve the world-record peak luminosity of 10.3 nb^{-1} s^{-1} for the BELLE detector, which surpassed the design luminosity [4].

As increasing the stored beam current during the commissioning, the heating of vacuum components, such as bellows and pumps got apparent gradually due to the intense higher order modes (HOM) excited by the high currents [5]. The HOM in special problem is the TE mode like HOM since the RF shield of bellows (finger type) and the axial slots of pump port can shield well the TM mode like HOM [6,7]. To solve these problems, therefore, a new HOM damper specialized for the TE mode like HOM with a power of several kW was developed and installed. The developed dampers are working as expected now at the stored beam current of 1.5 A and will be also available for future high current operation.

TROUBLES DUE TO HOM

Heating of Bellows

A movable mask (or collimator) of KEKB is a device that captures spent electrons/positrons just near the beam orbit and reduces the background noise in the BELLE detector [8,9]. The mask head is protruded from the side wall of beam chamber and positioned just near the beam

[#] yusuke.suetsugu@kek.jp

orbit (a few mm). The intense HOM, especially TE mode like HOM, therefore, is excited there. A typical loss factor of a movable mask is about 0.6 V pC^{-1} (6 mm bunch length) and the beam current of 1.4 A with 1200 bunches, for an example, brings the energy loss of about 10 kW.

During operation, the bellows near the movable masks were apparently heated up compared to those far from masks [5]. The average temperature of some bellows at the beam current of 1.3 A was 57 °C while that of the other bellows far from the masks was less than 30 °C. The temperature showed a resonance phenomenon and depended on the bunch fill pattern, the bunch current and also the position of mask head.

Abnormal Vacuum Pressure Rise

Another example is the abnormal pressure rise near the movable masks again observed at the beam currents higher than 1.3 A in LER. The region that showed the abnormal pressure rise extended from about 30 meters downstream side to about 20 m upstream side of a block of movable masks (see Fig.4 later). It was also found that the main gas was hydrogen and the temperature of non-evaporable getter (NEG) pumps, the main pumps of the KEKB [5,6], was higher near movable masks than others. The pressure rise, therefore, was explained as the gas desorption from the NEG element heated by the HOM, again especially the TE model like HOM, excited at the movable masks. The element of NEG in the pump chamber is nearly insulated thermally and even a weak power (several tens W) can easily heat the NEG element over 100 °C.

DEVELOPMENT OF HOM DAMPER

Design

To solve the problems described above, a new beam chamber equipped with HOM absorbers (HOM damper) was developed specializing for TE mode like HOM. The damper has delta-type wings and two SiC rods (ϕ 55 mm × 400 mm) are installed inside the both wings as shown in Fig.1. The design is based on the grooved beam pipe scheme successfully applied to the KEKB ARES cavity system [10,11]. The SiC ceramics has the typical real and imaginary part of the relative dielectric constant of 21 and 5, respectively, at 1 GHz [12]. The SiC rod had been tested preliminarily up to the input power of about 4 kW using a 1256 MHz microwave. The test model was designed for the LER and the beam channel has a circular cross section with a diameter of 94 mm as other usual beam chamber [6]. The total length and width of the
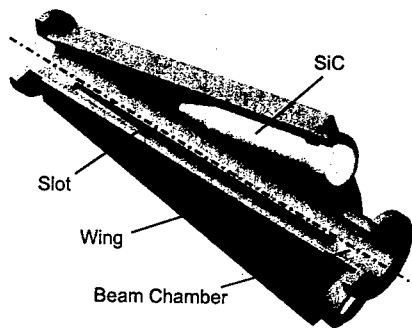
Figure 1: Structure of winged HOM damper.
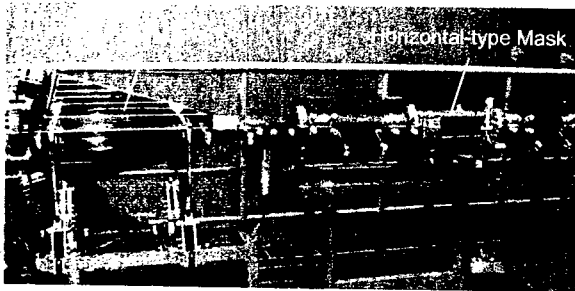
Figure 2: Winged HOM damper combined with horizontal–type movable mask.

winged damper are 1200 mm and 505 mm, respectively. The angle between the axis of SiC rod and the beam orbit is 15°. By making the axes of SiC rod and beam channel almost parallel, the HOM can be absorbed uniformly all over the SiC rod. The wing and the beam channel are connected with a long slot (20 mm wide × 707 mm long) and the TE modes with a polarization perpendicular to the wings can be absorbed efficiently. Whole view of a winged HOM damper together with an LER horizontal-type movable mask is presented in Fig.2.

RF Property

The calculation using the HFSS simulation code optimized the whole structure. The S_{21} (transmission) and S_{11} (reflection) parameter of a winged HOM damper for the TE_{11} mode in a circular wave guide is presented in Fig.3 for the frequencies from 2 GHz to 6 GHz. For that elementary mode, the absorption rate of the damper is more than 10 dB in average for the wide frequency range. The loss factor is estimated as less than 0.01 V pC^{-1} at the bunch length of 10 mm and much smaller than that of the other components such as a movable mask.

RESULTS

Effect of Installed HOM Damper

Two pairs of the winged dampers were installed into the LER in 2002 as a test putting a block of four movable masks (two horizontal-type and two vertical-type) between each pair. The schematic locations of the HOM dampers (Damper 1 – 4) and movable masks are shown in
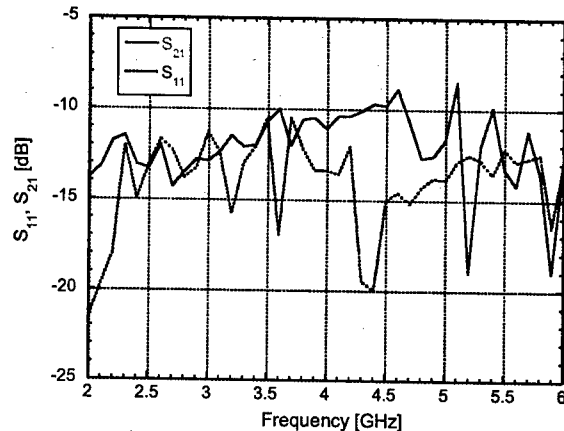
Figure 3: S parameters of winged HOM damper.

Fig.4. The distances between a pair of dampers and between two blocks are about 25 m and 50 m, respectively. Since the pump ports are at the bottom of beam chamber, the wings were placed vertically and near the horizontal mask as shown in Fig.2.

The powers absorbed by each HOM dampers at the beam current of 1.4 A are written down also in Fig.4 and the total power was about 11 kW. The total loss factor of four horizontal movable masks is about 2.4 V pC^{-1} and the corresponding energy loss is about 40 kW. Two pairs of HOM dampers, therefore, absorbed about 20 % of the power generated at four horizontal masks although the absorbed power in each HOM damper was somewhat scattered. Be careful that the power estimated from loss factor should include the whole HOM and the absorption rate for the TE mode like HOM will be higher. Measurements and identifications of modes in the beam chamber by carefully inserted antenna or experiments by rotating the winged HOM dampers may help the more accurate estimation.

After the installation, the temperatures of bellows just outside the paired dampers were measured. The temperature rises reduced to a half (from 33 °C to 16 °C) at the beam current of 1.3 A. The remained temperature rise of bellows should be due to the HOM that cannot be absorbed by the installed HOM dampers with vertical wings. The abnormal pressure rise near the mask was also disappeared outside of the HOM dampers even at 1.5 A.

Distribution of Absorbed Power

Although the effectiveness of the HOM damper was demonstrated, there was an interesting phenomenon on the distribution of the absorbed powers. As shown in Fig.4, the absorbed HOM power of the HOM dampers at downstream side of a block of masks (Damper 2 and 4, *D*-dampers here after) are larger than that at upstream side (Damper 1 and 3, *U*-dampers) by a factor 2. This tendency has been also recognized by the range showing abnormal pressure rise.

To investigate the imbalance of the absorbed power, the simulation was performed using MAFIA code. Figure 5
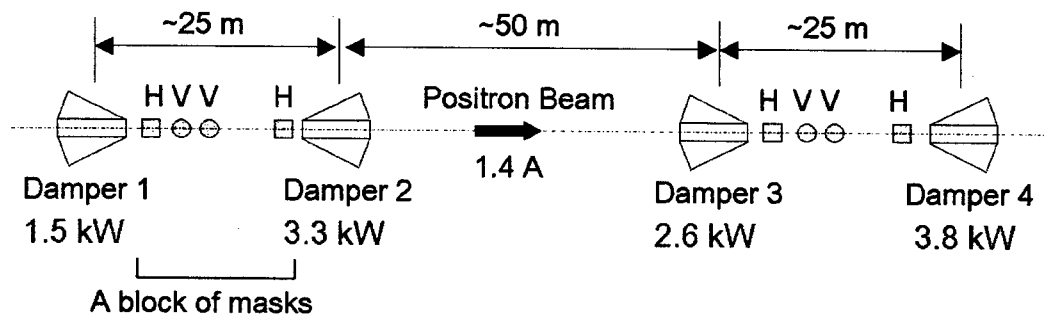
Figure 4: Locations of four HOM dampers (Damper 1-4) and movable masks in the ring, where "H" and "V" means the horizontal and vertical-type movable mask, respectively. The each absorbed power is that at 1.4 A.
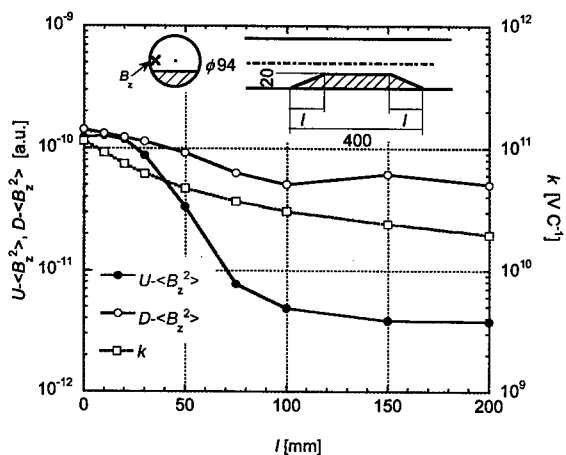
Figure 5: Intensity of axial magnetic field at downstream and upstream side, D-$<B_z^2>$ and U-$<B_z^2>$, and the loss factor, k, as a function of the ramp length, l [mm], of a trapezoidal HOM source as sketched in the figure.

shows the relative intensities of the axial component of magnetic filed at downstream and upstream side, D-$<B_z^2>$ [a.u.] and U-$<B_z^2>$ [a.u.], and the loss factor, k [V C^{-1}], as a function of the ramp length, l [mm], of a trapezoidal HOM source as sketched in the figure (10 mm bunch length). The trapezoidal HOM source is used considering the actual shape of a mask head [9]. The average intensity $<B_z^2>$ is the square of axial magnetic fields monitored at just near the side wall of beam duct (see the sketch in Fig.5) and averaged in the frequency range from 1 to 10 GHz. The distance between monitoring points and the source is 1 m. The $<B_z^2>$ can be regarded as a value in proportion to the intensity of TE mode like HOM.

As shown in the figure, the ratio of D-$<B_z^2>$ to U-$<B_z^2>$ is almost same if the ramp length is comparable to the bunch length. As increasing the ramp length, however, the ratio of D-$<B_z^2>$ to U-$<B_z^2>$ becomes larger. The higher TE mode like HOM intensity at downstream side of a trapezoidal HOM source may be explained by an interaction between the excited HOM at ramps and the passing bunched beam. Considering the actual size of

movable masks, l = 130 mm, the larger absorbed power at D-Dampers is reasonable qualitatively.

Quantitatively, however, there is still some discrepancy. The calculated ratio of D-$<B_z^2>$ to U-$<B_z^2>$ for the present mask size is larger than that of absorbed powers in D- and U- Dampers. One possible explanation of the observed small power imbalance between U- and D-Dampers is that the HOM excited other than the movable masks contributes the absorbed power. Further investigations should be required.

ACKNOWLEDGEMENTS

REFERENCES

[1] KEK Report 95-7, August (1995).

[2] H.Koiso et al., "PRESENT STATUS OF THE KEKB B-FACTORY", EPAC'02, Paris, June 2002, p.341.

[3] K.Akai et al., N.I.M.-P.R. 499 (2003) 191.

[4] http://www-kekb.kek.jp/

[5] K.Kanazawa et al., N.I.M.-P.R. A499 (2003) 66.

[6] H.Hisamatsu et al., Vacuum 47 (1996) 601.

[7] Y.Suetsugu, K.Ohshima and K.Kanazawa, Rev. Sci. Instrum. 67 (1996) 2796.

[8] K.Kanazawa et al., "DEVELOPMENT OF THE MOVABLE MASK SYSTEM FOR KEKB", EPAC'00, Vienna, June 2000, p.2301.

[9] Y.Suetsugu et al., "DEVELOPMENT OF THE MOVABLE MASK FREE FROM TRAPPED MODE FOR THE KEKB", PAC'01, Chicago, June 2001, p.2186.

[10] T.Kageyama et al., "Grooved Beam Pipe for Damping Dipole Modes in RF Cavities", Proc. 8th Symp. Acc. Sci. & Technol., Saitama, November 1991, p.116.

[11] T.Kageyama et al., KEK proceedings 99-24 (1999) 49.

[12] Y.Takeuchi et al., "THE SIC ABSORBER FOR THE KEKB ARES CAVITY", EPAC'96, Sitges, June 1996, p.2020.

CONCEPTUAL DESIGN OF VACUUM SYSTEM FOR SUPER KEKB

Y. Suetsugu[#], K.Shibata, K.Kanazawa, KEK, Tsukuba, Japan

Abstract

Conceptual design of the vacuum system for the upgrade of KEKB (Super KEKB) is presented. For its large storage current, the synchrotron radiation (SR) power is much higher than ever before. The beam chamber will have an ante-chamber structure to reduce the irradiated SR power density. To accommodate the intense higher order mode (HOM) arising from the short bunch length, the careful R&Ds are required for bellows, movable masks (collimators), HOM absorbers and so on. The first step of R&D has just begun using the KEKB.

INTRODUCTION

The luminosity goal of the Super KEKB is 100 nb^{-1} s^{-1}, ten times higher than that of KEKB. Main parameters related to the vacuum system of the Super KEKB are listed in Table 1 [1]. The most important feature is the high storage currents, 9.4 A and 4.1 A for the Low Energy Ring (LER) and the High Energy Ring (HER), respectively. The synchrotron radiation (SR) intensity, therefore, becomes much stronger than ever before. The major issues of the vacuum system consequently come from the intense SR. Another notable feature is the short bunch length, 3 mm, to relieve the hourglass effect at the collision point. That leads to severe impedance and heating problems for various vacuum components.

BASIC DESIGN

Structure of Beam Chamber

An ante-chamber scheme will be adopted for the beam chamber. A conceptual structure of the ante-chamber for the HER is shown in Fig.1 [2]. The ante-chamber consists of two channels, one is for the beam and another is for the SR. The SR hit the sidewall at far side of the ante-chamber. Since the irradiated point of SR at the side
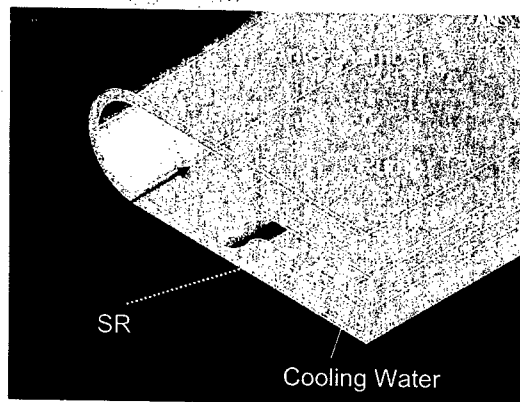
Figure 1: Typical structure of ante-chamber (HER).

Table 1: Vacuum related main parameters of Super KEKB. The parentheses are those for the KEKB.

	LER (e$^-$)	HER (e$^+$)
Goal Luminosity [nb^{-1} s^{-1}]	100	
Energy [GeV]	3.5	8.0
Beam Current [A]	9.4	4.1
Bunch Length [mm]	3	3
Bunch Number	5018	5018
Bending Radius [m]	16.31	104.46
Aperture [mm]	ϕ94	104×50
Total SR Power without Wigglers [MW]	7.64 (2.11)	14.21 (3.81)
Max. Line Power Density of SR* [kW m^{-1}] {present chamber}	53.50 (14.8)	21.64 (5.8)
Critical Energy of SR [keV]	5.84	10.88
Ave. Photon Density [photons m^{-1}s^{-1}] {C = 2200 m}	1.21E19	1.20E19
Ave. Gas Load [Pa m^{3}s^{-1}m^{-1}] {η=1E-6 molecules photon^{-1}}	4.56E-8 (1.35E-8)	4.52E-8 (1.31E-8)

* Using present single beam chamber.

wall goes far from the emitting point, the input SR power can be diluted. In the present ante-chamber design, the maximum power density at the side wall is 40 W mm^{-2} (LER), which is about 30 % of that expected for the existing chamber and almost same as that of the present one [3,4]. The photon stop scheme will not be realized due to the high concentrated power.

For the HER (e$^+$), the electron cloud instability [5] is aother major problem. The electrons, at least the seeds of the electron cloud, are mainly provided by the photoelectrons emitted from the inner surface irradiated by the SR. To avoid the problem, therefore, the ante-chamber scheme is also suitable for HER. Some additional measures will be prepared to suppress the photoelectron yield, such as the saw-tooth structure on the surface of sidewall [6]. Appling the external magnetic field by solenoids or permanent magnets are also considered, which has been working successfully in the KEKB [7].

Material of Beam Chamber

Copper should be the most suitable material for the beam chamber for its high thermal strength, the high electrical conductivity and the relatively low photoelectron yield [3]. Lots of experiences on the copper chamber have been accumulated in the KEKB, such as the welding method and the cleaning procedure. Aluminium may be another candidate. The manufacturing and welding is easier than copper, but the thermal properties is inferior to copper. Aluminium will be used only for special and complex chambers.

Pumping Scheme

The aimed pressure during the operation is on the order of 10^{-7} Pa. The low pressure is necessary to reduce the background noise in the particle detector rather than to ensure the sufficient beam life time. The linear pumping speed of about 0.1 m^3 s^{-1} m^{-1} is required assuming the photo-desorption rate, η, of 1×10^{-6} molecules photon^{-1} (Table 1). A distributed pumping scheme should be adopted and the pumps will be a combination of the strip type NEG pumps and the ion pumps as the present KEKB [3]. The pump ports are top or bottom of SR channel as shown in Fig.1 to reduce the impedance of beam channel and to evacuate effectively the desorbed gas.

Connection of Beam Chambers

The Helico-flex gasket has been working well in the KEKB as an RF-bridge between flanges [4]. For the Super KEKB, however, the impedance of that (~1 V nC^{-1}) will be a problem due to the short bunch length and its large quantity. The number of flange connections will be limited as much as possible. Instead, the welding in situ will be used to a large extent.

The heating of bellows chambers [8], usually installed between adjacent beam chambers, due to HOM will be a serious trouble. The heating has been actually observed already at the present KEKB [4]. The impedance of steps at the RF shield structure (~10 V nC^{-1}) will be also a problem for its large amount. Removing the bellows and connecting the adjacent chambers directly by welding in situ may be one countermeasure [2,9]. If the temperature of beam chamber is well controlled, the thermal stress would be tolerable. Remaining crucial problems, however, are how to absorb the errors of alignment or manufacturing, and how to fit the welding plane. For the Super KEKB, therefore, the bellows chamber with a new RF-shield structure, which will have higher thermal strength and lower impedance than before, is studied now as described below.

HOM Damper

In the Super KEKB, the current is so high and the bunch length is so short that intense HOM can be generated at various kinds of vacuum components. The intense HOM leads to excess heating or abnormal discharge of those. To avoid these troubles, the HOM absorbers will be indispensable in the Super KEKB. The R&D has started using KEKB as presented below. Reduced HOM design should be widely adopted for vacuum components at the same time.

Movable Masks

To protect the detector from damages by spent particles and to reduce the background noise, the movable mask (collimator) system will be equipped in the ring. The chamber-type movable masks, which has a trapped-mode free structure, have been installed to the KEKB and working almost well [10]. The major problems expected in the Super KEKB are grooves generated on the mask
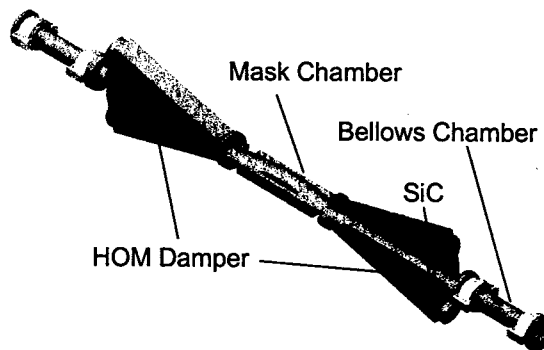
Figure 2: A set of movable masks combined with HOM dampers.

head and the excess heating of bellows just near the mask, which have been already experienced in the KEKB [4,7,10].

The grooves at the mask head are now understood as a result from the attack of abnormally steered beam. An effective way to avoid the generation of grooves is to use the light material as a mask head such as carbon or beryllium with a minimal length. The safe and rapid beam abort system using the beam orbit or the beam loss monitor will also help the damage of mask head.

Heating due to the HOM will be relieved combined with HOM damper described above. A schematic picture of a future movable mask is presented in Fig.2.

R&D PLANS

Ante-Chamber

A proto-type ante-chamber made of copper had been installed in the KEKB LER in 2001. Any severe problems have not been observed during the operation up to the stored current of 1.4 A. The number of electrons in the beam channel was found to decrease to about 1/7 of the case for usual single beam chamber without special coating inside [2]. The reduction of the electrons in the beam channel by the ante-chamber structure was verified. The external magnetic field was also found to be effective to reduce the electrons in the beam channel, that is, the electrons further decreased to 1/2 by applying the solenoid field of about 50-G.

The second trial model of the ante-chamber with almost the same design for the Super KEKB is now under manufacturing and will be installed in the KEKB LER in 2003. The SR hit the sidewall of the SR channel instead of photon stops. The saw-tooth structure is formed on the surface of sidewall. The thermal properties and the reduction of the electrons in the beam channel will be studied again.

HOM Damper

A winged HOM absorber chamber (HOM damper) was newly designed and the trial model was installed near the movable masks of the KEKB LER, where the heating of pump elements due to the HOM generated at mask heads has been observed [11]. The design is based on the HOM
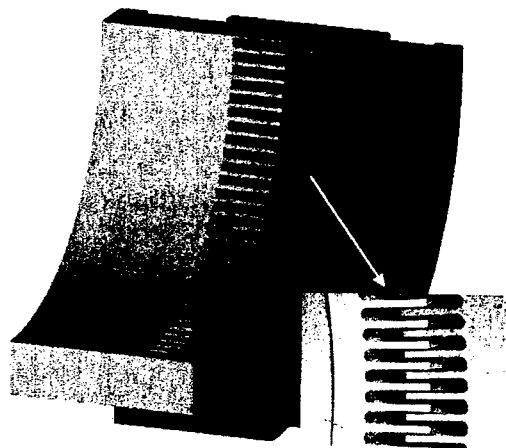
Figure 3: Comb-type RF-shield structure.

Figure 4: Loss factors for new and conventional RF-shield (1 mm step) as a function of bunch length.

absorber successfully applied for the KEKB ARES cavity system [12]. The long narrow slots in the beam direction (20 mm × 707 mm) connects the beam chamber and the HOM absorber. The damper can absorb effectively the TE modes. The loss factor is less than 0.01 V pC^{-1} (10 mm bunch length) and the impedance due to the HOM damper is sufficiently small. The chamber has two SiC rods and can absorb the HOM power up to 10 kW. In the autumn run 2002, two pairs of HOM damper is installed putting four movable masks inside of each pair. The absorbed power per one damper was about 3 kW. The pressure rise due to the heating of pump elements was disappeared and the heating of bellows near masks are also suppressed effectively. The study will be continued.

Bellows Chamber

Recently a new RF-shield structure for bellows chambers is proposed as shown in Fig.3 [13]. The RF-shield is not a finger-type as usual but the comb-type. At the initial design, a tooth has a width of 1 mm and a radial thickness of 10 mm. About 100 teeth surround the inner surface of LER beam chamber. Gap between each nested tooth is 0.5 mm. The thermal strength of the shield is much higher than before. The new RF-shield structure has a lower loss factor compared to the conventional one (1 mm step at inner wall) as indicated in Fig.4. The R&D of the RF-shied has just started and test bellows chambers will be installed in KEKB LER this summer. The RF-shield structure can be applied for that of gate valves.

REMAINING ISSUES

The following are the issues to be considered or studied in the future; (1) Design of the beam chambers at the interaction region. The design should take into account the aperture, the impedance, the SR mask and the effective pumping scheme. (2) Impedance estimation of various vacuum components, such as the tapers, the pumping slots and so on. (3) Radiation shielding. Lead shielding around the beam chamber may be necessary. (4) Alignment and supports of beam chambers. (5) Abort system. A rapid and safe beam abort system is required. (6) Alarm system. The flow rate of cooling waters and the temperatures of these components should be kept watching any time.
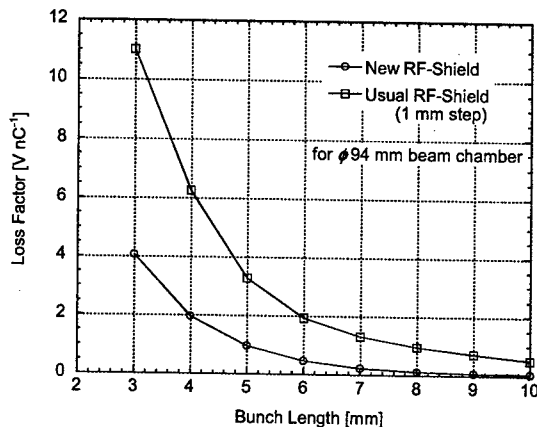
ACKNOWLEDGEMENTS

REFERENCES

[1] http://www-kekb.kek.jp/SuperKEKB/home.html.

[2] Y.Suetsugu, KEK proceedings 2002-17 (2002) 7.

[3] K.Kanazawa et al., Appl. Surface Sci. 169-170 (2001) 715.

[4] K.Kanazawa et al., N.I.M.-P.R. A 499 (2003) 66.

[5] For example, K.Ohmi and F.Zimmermann, P.R.L. 85 (2000) 3821.

[6] Y.Suetsugu et al., J.V.S.T. A 46 (2003) 186.

[7] K.Akai et al., N.I.M.-P.R. A 499 (2003) 191.

[8] Y.Suetsugu et al., Rev. Sci. Instrum, (1996) 2796.

[9] J.T.Seeman, "HIGH LUMINOSITY B-FACTORY", PAC'01, Chicago, June 2001, p.305.

[10] Y.Suetsugu et al., "DEVELOPMENT OF THE MOVABLE MASK FREE FROM TRAPPED MODE FOR THE KEKB", PAC'01, Chicago, June 2001, p.2186.

[11] Y.Suetsugu et al., "DEVELOPMENT OF WINGED HOM DAMPER FOR MOVABLE MASK INKEKB", in these proceedings.

[12] T.Kageyama et al., "THE ARES CAVITY FOR THE KEK B-FACTORY", EPAC'96, Sitges, November 1996, p.2008.

[13] Y.Suetsugu, KEKB Machine Advisory Committee, March 2003.

VACUUM SYSTEMS RENEWAL FOR THE PF-AR UPGRADE

Y. Tanimoto[#], T. Uchiyama, T. Nogami, Y. Hori
KEK, Tsukuba, Japan

Abstract

The Photon Factory Advanced Ring (PF-AR) at the High Energy Accelerator Research Organization (KEK) was upgraded to improve performance [1]. Vacuum systems were almost thoroughly redesigned and renewed to realize longer beam lifetime, higher stored current, and more reliable operation. Replacement of vacuum components was carried out in 2001. And the commissioning started in January 2002. After one-year operation, the beam lifetime grew 7 times longer than that of the former PF-AR.

INTRODUCTION

Originally constructed in 1984 as an 8GeV electron-positron booster injector for the TRISTAN main ring, the PF-AR became a 6.5GeV dedicated light source after the TRISTAN experiments ended in 1995. The PF-AR vacuum systems, however, were not satisfactory for a synchrotron light source, and therefore limited the beam lifetime to several hours and also the peak operating current to 40mA. In addition, frequent maintenance of pumps and cables were being required because of their breakdowns caused mainly by radiation.

In the PF-AR upgrading project, the vacuum systems were designed to meet the following requirements:

- Sufficiently low vacuum pressure ($<5\times10^{-7}$Pa) to realize the beam lifetime of more than 10 hours with a 6.5GeV-100mA single-bunch beam stored
- Thermal tolerance for a 6.5GeV-100mA beam load
- Adaptation for new devices, such as beam position monitors, steering magnets, insertion devices, and SR (Synchrotron Radiation) beam lines
- Unification of vacuum control system into the EPICS [2]

Table 1: Ring and Vacuum Systems Parameters

[ ] : objective

Beam Particle	Electron	Duct Material	OFHC Cu
Beam Energy	5.0-6.5 GeV	Flange Seal	Racetrack-shaped Al Helicoflex
Injection Energy	2.5-3.0 GeV		
Beam Current	55[100] mA Single Bunch	Vacuum Pumps	TSP × 185
			DIP × 56
Beam Lifetime	50[60] Amin		SIP × 33
Horizontal Emittance	260[160] nmrad		TMP × 9
		Total Effective Pumping Speed	60000 l/s (for N_2)
Circumference	377.3 m		
Magnetic Radius	23.7 m	VacuumGauges	CCG × 80
Bending Magnets	56	Gate Valves	18
Critical Energy	26 keV	Bellows	150
Radiated Power	666 kW @6.5GeV100mA	Thermometers	RTD × 190
		Vacuum Control System	EPICS-based I/F: CAMAC+PLC
Average Pressure	1E-5[5E-6] Pa/A		

These requirements involved drastic replacement of almost thorough vacuum components, for instance, beam ducts, vacuum pumps, vacuum gauges, thermometers, cooling water system, compressed air system, and their control system.

VACUUM PUMPS

The beam lifetime of the PF-AR is determined by ring average pressure because the main process of beam loss is bremsstrahlung. As the result of calculations of pressure distributions in arc sections, 168 TSPs (Titanium Sublimation Pumps; 300 l/s each) and 56 DIPs (Distributed Ion Pumps; 200 l/s each) were adopted as main pumps. And also 17 TSPs and 33 SIPs (Spatter Ion Pumps; 100-400 l/s each) were adopted in straight sections. Then the available pumping speed in the whole ring was estimated at 60000 l/s, and current-normalized pressure would be 5×10^{-6}Pa/A (CO equiv.) when the PSD (Photon-Stimulated Desorption) coefficient (η) reached 1×10^{-5} molecules/photon. In this case, the product of the beam current and the lifetime ($I\tau$) was expected to reach 60Amin (=100mA×10h).

Nine rough pump systems are placed along the ring, but during the accelerator operation they are separated from ring vacuum by valves.

BEAM DUCTS

From the viewpoint of thermal tolerance and radiation shield capability, OFHC copper was adopted as the material of main beam ducts. Thickness of the beam ducts is basically 6mm, which has almost the same shield capability as former 4mm thick Aluminum alloy ducts and 1mm thick lead sheets. The beam ducts are equipped with SR absorbers and cooling water channels to absorb the SR power load (4.5kW/m@6.5GeV-100mA in the bending region). Stainless steel bellows and flanges have less thermal conductivities, and are protected by the absorbers. Aluminum-oxide dispersion strengthened copper is also used for the photon absorbers at heavy load positions. Typical configuration of the beam ducts in the arc sections is shown in Figure 1. Each arc section consists of a series of these ducts.
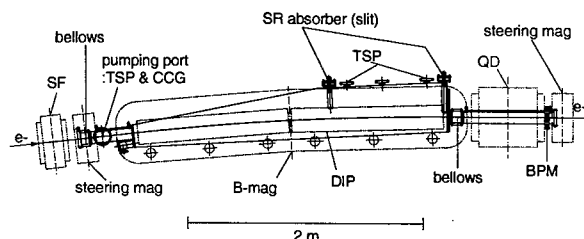
Figure 1: Typical Configuration of Beam Ducts

#yasunori.tanimoto@kek.jp

Outgassing process by thermal baking (150°C, 48hours) was performed on the beam ducts prior to the installation for the purpose of the reduction of an initial gas load and the verification of their vacuum properties.

Special implements were necessary to install the beam ducts into the bending magnets because they had to be inserted from outside of the existing bending magnets under spatial restrictions.

VACUUM GAUGES

About 80 CCGs (Cold Cathode Gauges) are used for the ring vacuum monitoring. Thermal cathode ionization gauges, the most suitable gauges for the pressure measurements in the upgraded vacuum systems, were not employed because of the possible radiation damage to their controllers and the restriction of the budget. On the other hand employing CCGs alleviates these difficulties, but ordinary CCGs have instabilities in the measurements of ultra high vacuum. Then we tested the magnetically improved CCGs that hold the Penning discharge even in the 10^{-8}Pa range, and acquired calibration data with a pre-calibrated B-A gauge (Figure 2a). Fabricating CCG controllers using the calibration data enabled the reliable measurements in the 10^{-8}Pa range (Figure 2b).
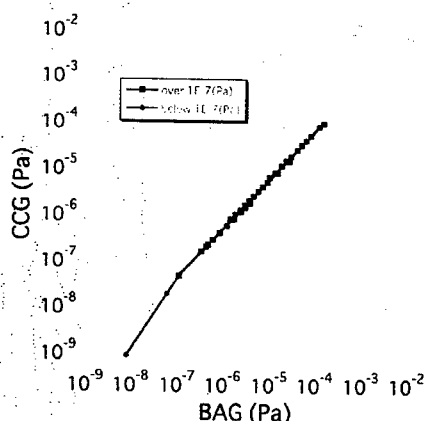
Figure 2a: CCG Calibration with Prototype Controller
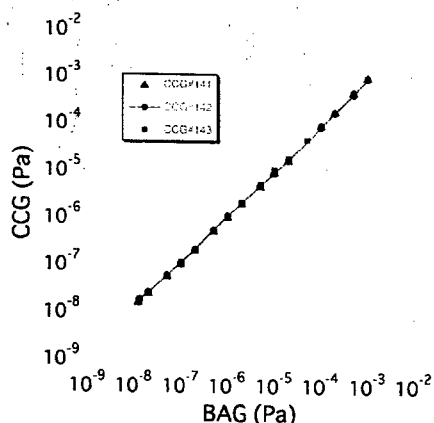
Figure 2b: CCG Calibration with Final Version Controller

VACUUM CONTROL SYSTEM

Vacuum control system was unified to the EPICS, which had already been adopted as the KEKB and the injector linac control system and was newly adopted as the PF-AR control system [3]. In the new vacuum control system, all of the vacuum devices except for the rough pumps can be controlled and monitored remotely on X terminals (Figure 3 as an example). Network connected CAMAC and PLC are used as the interfaces between the controllers of vacuum devices and the EPICS (Figure 4). PLC is also used for the vacuum interlock system.
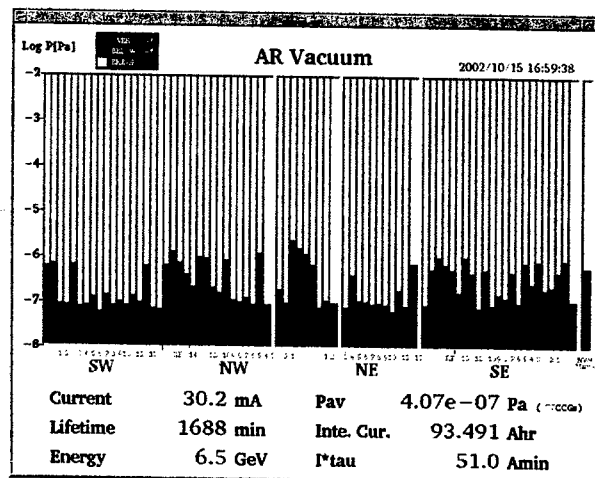
Figure 3: Ring Pressure Monitor Panel
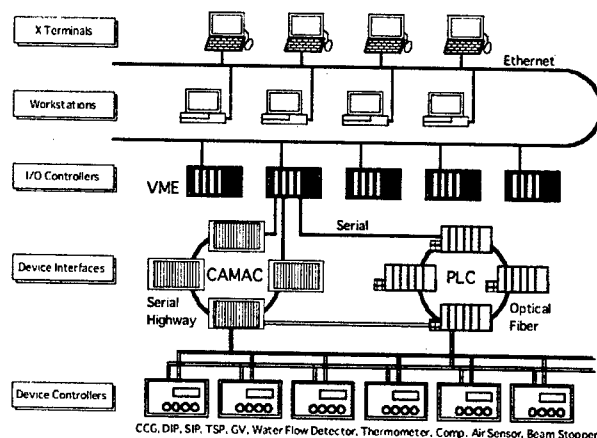
Figure 4: Diagram of Vacuum Control System

COMMISSIONING AND OPERATION

The commissioning of the upgraded PF-AR started in January 2002. Figure 5 shows the growth of the beam lifetime and the decrement of the ring average pressure. The beam lifetime as $I\tau$ has grown up to 50Amin, which is 7 times longer than that of the former PF-AR. Injection energy was raised from 2.5GeV to 3.0GeV in September 2002.
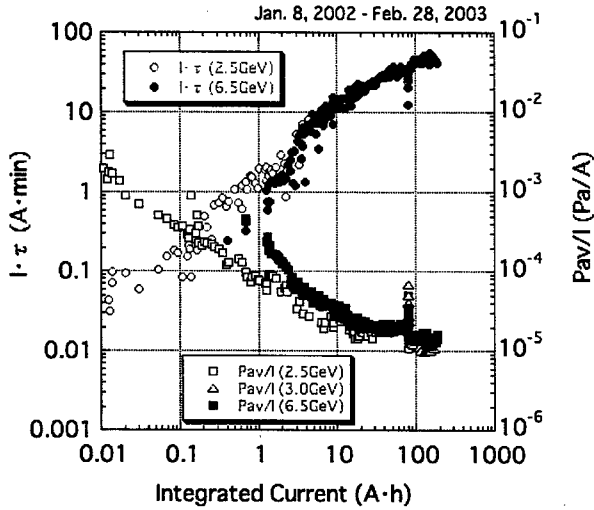
Figure 5:Progress of Ducts Self Cleaning and Growth of Beam Lifetime

Peak operating current has increased gradually, and currently reached 55mA. Operators inject the beam three times a day on schedule if neither a serious lifetime drop nor a sudden beam dump happens. Although the frequency of sudden lifetime drops is decreasing, this is one of the unsolved problems in the PF-AR operation.

While the growth of the beam lifetime seems ceasing, even longer lifetime is expected if lower pressure will be achieved. Because Figure 6, the relationship between the ring average pressure and the beam lifetime, indicates that the beam lifetime is currently being limited by the beam-gas scatterings (inversely proportional region), not by the Touschek effects (flat region).
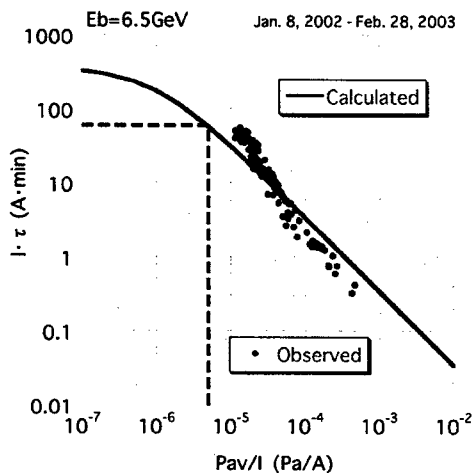
Figure 6: Relationship between Pressure and Lifetime

Figure 7a and 7b show the progress of the vacuum ducts self cleaning in the arc sections and the straight sections respectively. It is obvious that the pressures in the straight sections are dominant for the ring average pressure and seem still decreasing slowly. Reinforcement

of the pumping ability in the straight sections would be effective to lower the ring average pressure.
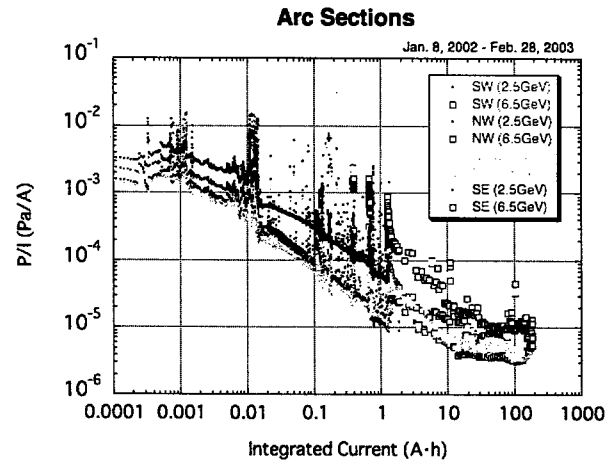
Figure 7a:Progress of Ducts Cleaning in Arc Sections.
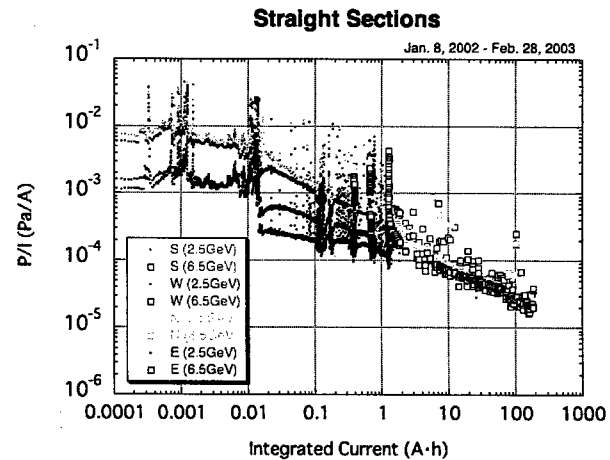
Figure 7b:Progress of Ducts Cleaning in Straight Sections

SUMMARY

The PF-AR vacuum systems had been upgraded and the commissioning and the operation started successfully. After one-year operation, the beam lifetime grew 7 times longer than that of the former PR-AR. Although the peak operating current is limited to 55mA, the required performances in vacuum systems have almost been achieved.

REFERENCES

[1] T. Miyajima, et al., "Present Status of Photon Factory Advanced Ring", these proceedings.

[2] http://lansce.lanl.gov/lansce8/epics/epics.htm.

[3] T. Obina, et al., "Improvement of Photon Factory Advanced Ring Control System", these proceedings.

RE-CIRCULATING LINAC VACUUM SYSTEM[*]

R.P. Wells, J. N. Corlett, A.A. Zholents, LBNL, Berkeley, California 94720, USA

Abstract

The vacuum system for a proposed 2.5 GeV, 10μA re-circulating linac synchrotron light source [1] is readily achievable with conventional vacuum hardware and established fabrication processes. Some of the difficult technical challenges associated with synchrotron light source storage rings are sidestepped by the relatively low beam current and short beam lifetime requirements of a re-circulating linac. This minimal lifetime requirement leads directly to relatively high limits on the background gas pressure through much of the facility. The 10μA average beam current produces very little synchrotron radiation induced gas desorption and thus the need for an "ante-chamber" in the vacuum chamber is eliminated. In the arc bend magnets, and the insertion devices, the vacuum chamber dimensions can be selected to balance the coherent synchrotron radiation and resistive wall wakefield effects, while maintaining the modest limits on the gas pressure and minimal outgassing.

INTRODUCTION

The baseline electron beam current is 10 μA (1nC/bunch at 10kHz) at an energy of 2.5GeV. However, to allow for potential upgrades to the design, the vacuum system is designed for 30 μA at 3.1 GeV. The bunch length is compressed from 20 ps at the cathode to 2 ps at the exit of the arc connecting the pre-accelerator to the re-circulating linac (Arc 0). The 2 ps bunch length is then held constant throughout the re-circulating sections. Note "Arc" as used throughout this section refers to entire circulation path at a given energy, straight sections as well as arcs at the ends of the straight sections. This present study considers the vacuum issues associated primarily with the bend sections of the lattice. The vacuum requirements of the electron gun, linac, undulators and beamlines will be addressed in future studies.

The design of vacuum systems for synchrotron radiation sources must consider several possible physical processes to establish the allowable background gas partial pressures and chamber dimensions including;

- Beam loss due to interaction with background gas by
  - o inelastic scattering of the beam by gas nuclei and
  - o large angle elastic scattering by gas nuclei.
- Energy loss, resulting in longitudinal emittance growth due to coherent synchrotron radiation (CSR)
- Transverse emittance growth due to resistive wall wakefields

To reduce the effects of CSR, the vacuum chamber aperture is reduced to shield against emission of longer wavelength radiation [2,3]. This has the effect of producing a higher cut-off frequency for the radiation propagating within the vacuum chamber and may be selected to narrow the frequency spectrum of coherent emission from a bunch. The coherent radiation emission process is then effectively suppressed. The CSR effect is present only in the bend magnets, and a larger aperture may be employed elsewhere.

The resistive wall wakefield generated by the electron beam traveling in a vacuum chamber of finite conductivity, is proportional to the chamber length and inversely proportional to both the square root of the chamber's electrical conductivity and the cube of the chamber's half-height. The resistive wall effect therefore has implications on the choice of vacuum chamber material, the minimum chamber height and the location tolerance of the chamber with respect to the beam axis.

The final chamber geometry, and most importantly the chamber inner height, will be determined by selecting an appropriate compromise between reducing CSR effects, resistive wall effects, and beam loss due to collisional scattering with background gas. An example of this compromise is the plot of the CSR energy loss and transverse resistive wall distortion as a function of chamber height shown in Figure 1. These affects are different for each beam pass due to the different beam energy and magnet bend radii, the optimal chamber height is therefore different for each arc. From an analysis of collective effects [2,3] a minimum vacuum chamber height of between 7 and 9 mm is indicated.
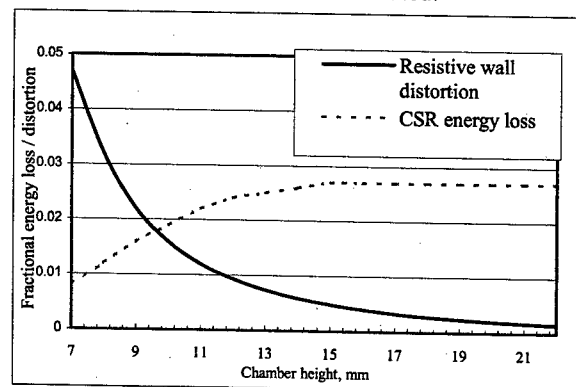
Figure 1. Comparison of energy loss due to CSR and beam distortion from resistive wall effects.

Since the actual combined collective effects is still under study, the selected beam chamber heights are preliminary estimates only.

BEAM LOSS

In storage ring type synchrotron light sources, beam-gas scattering may be one of the prime limitations on beam lifetime and hence allowable background gas pressures. The beam lifetime requirement for the re-circulating linac configuration is extremely modest due to the relatively small, 900 meter, total path length (or equivalently, ~3μs time of flight).

Charged particles passing through matter become deflected by the strong electric fields of the nucleus. This deflection constitutes a transverse acceleration of the particle and results in a loss of energy through Bremsstrahlung radiation. If the energy loss exceeds the energy acceptance of the accelerator, δ_{acc}, the particle is lost. Following the methodology of Wiedemann [4] and assuming a conservative energy acceptance fraction of δ_{acc} = 0.001, the Bremsstrahlung lifetime for residual gas pressures from 10^{-4} to 10^{-8} Torr is 0.8 − 8,000 seconds. While admittedly short by storage ring standards, this is well in excess of re-circulating linac requirements

An electron passing through background gas may also experience an elastic collision (Coulomb scattering) that causes an angular deflection large enough to give the particle a betatron oscillation amplitude larger than the limiting physical or dynamic aperture of the accelerator. For planning purposes, and to be consistent with the collective beam effects discussed above, a limiting physical rectangular aperture of 9mm high by 40mm wide was assumed. In accordance with good practice, we assume that the dynamic aperture will exceed the physical aperture throughout the accelerator.

For the present study, an average betatron function in the bend sections of 30 m was selected based on 150% of the MAD output for the lattice. A "worst-case" local betatron function of 90 m was selected based on the highest value found anywhere in the lattice. The beam lifetime and consequently the beam loss was calculated using the equation for a rectangular aperture from Turner [5]. Beam losses of less than 0.1% are expected at average pressures up to 2×10^{-6} Torr. Commensurate with the modest beam losses, the power deposition on the vacuum chamber due to scattering is relatively insignificant for residual gas pressures as high as 10^{-5} Torr.

VACUUM SYSTEM LAYOUT

The vacuum system must accommodate the magnet lattice as well as the various collective beam effects. With the exception of the first arc and the spreader regions, the lattice consists primarily of identical dipole, quadrupole and sextupole magnets. Pole gaps in the dipoles are 30 mm (full height) while the diametric clearance of the quadrupoles and sextupoles is greater than 60 mm. These magnets set the maximum external dimensions of the beam tube throughout the accelerator. Collective beam effects dictate the inner height of the vacuum chamber within bend magnets.

As with any vacuum system, the pressure is determined by the amount of gas introduced, the conductance of the gas to the pumps and the pump speed. The gas load is a product of thermal outgassing and photon induced desorption.

The amount and mixture of gas liberated from the vacuum wall is a function of the material selected and its preparation. For the purposes of this study, a vacuum baked (150°C–24 hrs.) aluminum beam tube and "conflat" type metal sealed fittings are assumed.

The proposed vacuum system consists of an extruded rectangular beam tube in the bend magnet locations transitioning to a circular tube in the straight sections. The internal height of the rectangular tube may vary with each arc as determined by collective effects described previously. The beam tube is connected periodically to a large diameter aluminum pipe that serves as a pumping manifold. A series of modular cryosorption pumps are distributed along the manifold to provide the primary pumping. A small number of turbomolecular pumps backed by oil-free roughing pumps will provide the initial system vacuum and cryopump regeneration.

The proposed system contains several variables that can be optimized based on the conditions within a given region of the accelerator. These variables include the width of the beam tube, spacing between manifold-beam tube connections, manifold diameter and cryopump spacing. While each portion of the accelerator section will behave differently, of primary concern are the bend magnets where gas production is the greatest and gas conductance is the least.

OUTGASSING

The equations derived by Mathewson, et.al. [6] were used to calculate outgassing rates due to synchrotron radiation. Gas is desorbed from the beam tube surface by thermal processes and by synchrotron radiation induced photoelectrons. The number of photoelectrons produced per meter of vacuum chamber range from zero in the injection arc to 6×10^{14} in the final arc. Calculated gas desorption rates, using species specific desorption efficiencies [7], η, are shown in Table 1.

Table 1. Desorption rates per meter of beam tube.

Gas	η	Arc 0	Arc 1	Arc 2	Arc 3	Arc 4
H_2	0.1	-	1.9 x 10-6	2.3 x 10-6	3.1 x 10-6	3.3 x 10-6
CO	0.03	-	5.8 x 10-7	6.8 x 10-7	9.2 x 10-7	1.0 x 10-6
CO_2	0.025	-	4.8 x 10-7	5.7 x 10-7	7.6 x 10-7	8.3 x 10-7
CH_4	0.008	-	1.5 x 10-7	1.8 x 10-7	2.4 x 10-7	2.7 x 10-7
Total			3.1 x 10-6	3.7 x 10-6	5.0 x 10-6	5.4 x 10-6

The power deposition on the vacuum tube wall from synchrotron radiation, estimated from emission of an electron beam in uniform circular motion [8], is 5.4×10^{-3} W/cm with a negligible peak flux is of 0.5 W/cm^2.

The quantity and composition of thermally desorbed gas is substantially altered by a moderate vacuum bake-out in aluminum systems. After baking the amount of

thermal outgassing is more than 6,000 times smaller than synchrotron radiation induced desorption.

GAS PRESSURE PROFILE

The most difficult pumping conditions are present in the arc sections due to the limited gas conductance and the synchrotron radiation induced gas load. The pumping of the straight sections is relatively straightforward in comparison and is not considered in this study. Given the assumption of a discretely pumped system, a rational configuration would include widely spaced pumps, a manifold sized to be consistent with the pump size and a limited number of beam tube penetrations. A system that meets the criteria consists of CTI-8 cryopumps centrally located on a 10 m span of 20 cm diameter manifold. Short, 30 cm long by 5 cm diameter tube and bellows assemblies connect the manifold to the beam tube. A representative section of the system is illustrated in Figure 2 and shown schematically in Figure 3.
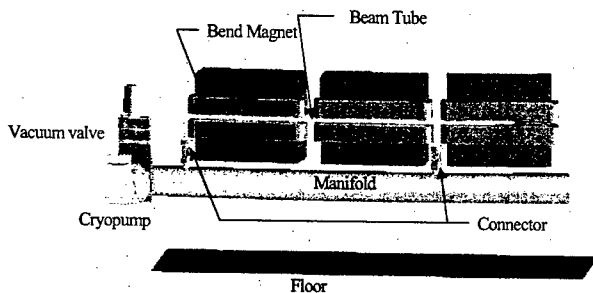
Figure 2. Section of Arc 4 vacuum system.

In addition to the outgassing rate, the pressure in the beam tube is a function of the gas conductance and pump speed. For ease of computation, gas evolved from the beam tube, connector tubing and manifold is treated as a single continuous distributed source along the length of the manifold. The conductance of the cylindrical tubing was calculated using Santeler's [9] correction to the common formula for a circular tube in molecular flow.
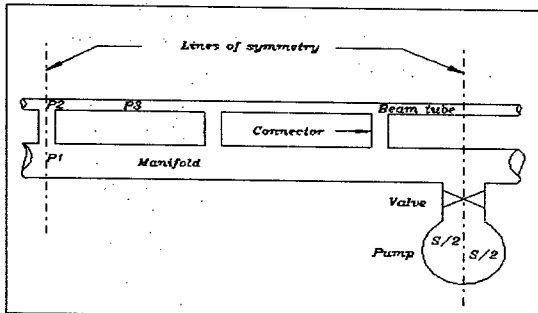
Figure 3. Schematic of a typical vacuum system section.

The pressure at the connecting tube entrance, P2, is determined by adding the pressure differential from gas flow through the connecting tube to the maximum pressure in the manifold, P1. The peak pressure in the beam tube, P3, is found by adding the maximum pressure increase along the beam tube, between connectors, to the pressure at the connector entrance, P2. The conductance of the beam tube is calculated using the equation from Roth [10] for a long rectangular tube of uniform cross section.

The plot shown in Figure 4 is an approximate pressure profile of the Arc 4 beam tube derived by applying the methodology used to find pressures P1-P3 to the other analogous positions along the beam tube and then applying a parabolic profile between them. By inspection, the average pressure along the path of the beam is 3×10^{-7} Torr. This residual gas pressure compares favorably with the pressure of $\sim 10^{-6}$ Torr required to limit beam losses from scattering to 0.1%.
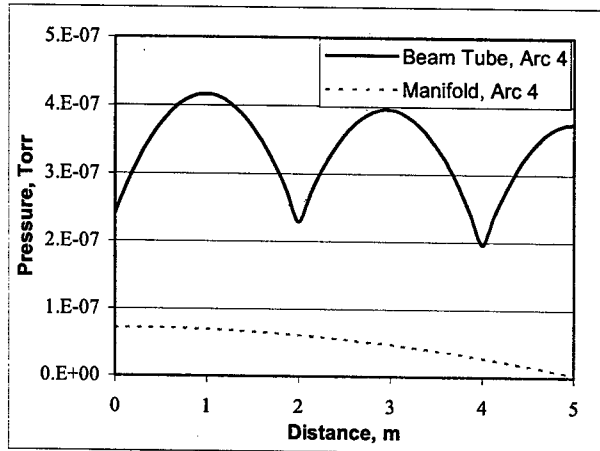
Figure 5. Pressure profile along a representative portion of the Arc 4 beam tube.

REFERENCES

[1] J.N. Corlett et al "A Recirculating Linac-Based Facility for Ultrafast X-ray Science", this conference

[2] S. De Santis et al "Collective effects analysis for the Berkeley femtosource", this conference

[3] A. Zholents et al, "Longitudinal phase-space control in the Berkeley Femtosecond X-ray light source", this conference.

[4] H. Wiedemann, Particle Accelerator Physics I, pp.378-380

[5] W.C. Turner, "Notes for a Course on Accelerator Vacuum Physics", CBP Tech. Note 188, June 11, 1999.

[6] A.G. Mathewson, G.H. Horikoshi, and H. Mizuno, "Some Notes on the Photoelectron Induced Gas Desorption Problems in the Photon Factor and Tristan", National Lab for High Energy Physics Report, Japan.

[7] M. Achard, "Electron and Ion Induced Gas Desorption from Stainless Steel, OFHC Copper, Titanium and Pure Aluminum", CERN-ISR-VA/76-34

[8] PEP-II Conceptual Design Report, June 1993, p305.

[9] D.J. Santeler, "New Concepts in Molecular Gas Flow", J.Vac. Sci. Tech. A, Vol.4, No.3, May/June 1986

[10] Roth, Vacuum Technology 2nd Ed., North-Holland, 1982 pp.84-87.

IMPROVEMENT OF THE STORAGE RING UHV SYSTEM OF NSRL

Y. Wang, W. Wei, F. Y. Zhao, J. P. Wang, D. M. Jing, L. Fan, C. Y. Guan,
Guanyuan Wu, National Synchrotron Radiation Laboratory, University of Science and Technology
of China, Hefei, Anhui 230029 P. R. CHINA

Abstract

NSRL storage-ring has been operated for fourteen years, The typical life time is 600 mins at 200mA and 800MeV. The new injection ceramic chamber, bend chamber, undulator and NEG pumps were installed, new vacuum measure and control system was debugged in 2002 summer, as part of NSRL phase II project to enhance the quality, stability and long-term reliability. The average pressure of storage ring is better than 2E-8 Pascal after 48 hour large current direct backout and 48 hour ion pumps operation, this better vacuum can benefit the phase II project's object, beam lifetime 600 mins at 300mA and 800MeV.

INTRODUCTION

The 800MeV Electron Storage Ring of the National Synchrotron Radiation Laboratory (NSRL) is a dedicated VUV and soft X-ray synchrotron radiation light source. The construction of NSRL facility began on November, 1983 and was completed in 1989. Its commissioning is to end in December 1991. The NSRL storage ring routinized to run for users in 1993. The typical beam lifetime of the NSRL stored beam was over 600 minutes at 200mA and 800 MeV. In the summer shutdown in1999, a 6 Tesla superconducting wiggler magnet has been setup, so that the radiation of shorter wavelengths near 1Å is already available for users, and a pure permanent magnets Transverse Optical Klystron (TOK) have been design and constructed for the Storage Ring FEL (free electron laser). It will be used for the coherent harmonic generation (CHG) experiment firstly. The experiments of spontaneous radiation have been carried out. The further more work will be continued. For these TOK chamber, wiggler vacuum system was install and some new chambers was modified to install the absorbers to protect the stainless steel beam ducts from wiggler magnet intense synchrotron radiation. Last summer the vacuum system of storage ring was shutdown to improve again in order to reach the Phase II project object of long-term reliability, stability and reliable operation [1].During this operation, the vacuum system had been exposed to air for 45 days, after the long exposure to air, the new equipments of ring vacuum system was assembled and the whole system was baked out by passing a large current through it. The average pressure without beam and RF power was 2·10-8 Pa, which is better than that before improvement. The operation and improvements for vacuum system of storage ring are presented here.

OPERATION

We started on the designing the UHV system of the NSRL in April 1983. The principal parameters for the storage ring vacuum system are shown in Table 1. The vacuum chambers of the ring were made of stainless steel pipes and plates (SUS304l, SUS316l). The whole system was baked out by passing a large current through it. The average pressure without beam and RF power was 5×10E-8 Pa. We welcomed the first synchrotron radiation light in April 1989.

NSRL Storage ring UHV system has been operating for fourteen years. The typical beam lifetime of the NSRL stored beam was over 600 minutes at 150mA and 800 MeV. The total accumulate beam dose is about 200A·hr every year.

Table 1: Main parameters of the NSRL ring

Beam Energy [MeV]	800
Beam Current [mA]	300
Circumference [m]	63.66
Bending radius [m]	2.222
Main ion pumps [l/sec]	11200
Auxiliary NEG pumps [l/sec]	2400
Power on chamber wall [Kw]	4.893
Average pressure [Pa]	2×10^{-8}
Dynamic pressure [Pa]	2×10^{-7}
Lifetime [hrs]	> 8
The total beam dose [A.hr]	> 400 (every year)

Based on operating results, we have determined the experimental relation of beam dose for NSRL to be [2]:

$$P/I=1.06\times10\text{-}6\cdot D\text{-}0.61 \ [\ Pa/mA \ ]$$

The storage ring vacuum system had been exposed to atmosphere eight times due to unexpected leaks and five times due to controlled venting with dry nitrogen at the end of last year. After vacuum system baked out and 75 A·hr of beam cleaning, The dynamic average pressure of general storage ring exposed to atmosphere had reached the design goals, and we got beam lifetime over 600 minutes at 150mA and 800 MeV. If only SIP pumps baked out, the same result could be got after 100 A·hr of beam cleaning or more.

We decided to make further improving performance of the vacuum system, so that much higher beam currents can be stored to reach the Phase II project goals of long-term reliability, stability and reliable operation.

VACUUM SYSTEM IMPROVEMENTS

In machine operation, we find the pressure rise high in the downstream of each bending chamber when the storage current over 150 mA. Based on the calculation, about 30% of the synchrotron radiation lights irradiate on the downstream of each bending chamber, which can cause PHD (photon stimulated disabsorb) gas disabsorb, and the pressure rising is due to the insufficient pumping speed of distribute ion pump. So the first improvement was to increase pumping speed in that area. Because of the space limits, the NEG pump with less volume and high pumping speed in high and ultra-high vacuum is the best choice. The GP100 MK4 NEG pumps made in SAES Getters Company of Italy were equipped in the downstream of every bending chamber. Each NEG pump has the pumping speed of is 240 l/s for H_2 and 85 l/s for CO, and was put in the downstream of every bending chamber to reduce dynamic pressure difference. The better vacuum can do help to store much higher beam currents and lengthen the beam's lifetime.

As a result of the operation of more than fourteen years, some welded bellows had been found to have gas leakage after the system had been baked for several times. So we use the oil pressured bellows instead of the welded bellows. The RF shields (Cu-Be) as the quadrate-round transition board between rectangle-cross chamber and circle-cross chamber have been used to reduce the impedance of bellows. The RF shield ought to keep good electrical contact and smooth mechanical movement. The vacuum impedance of new bellow chamber with RF shield is 3 times smaller than that of the old bellow chamber. [2] At the same time the new bellow chamber design makes it possible for us to setup NEG pumps in the downstream of bending chambers.

In order to research the relation between dynamic pressure of vacuum system and beam lifetime and stability, the vacuum measure, analyses and interlock system has been improved. The pressure distribution of storage ring differs very much and the vacuum system of our ring uses point pumping method, so it is difficult to find tiny leakage of the storage ring vacuum chamber. Now vacuum pressure monitor points by Bayard-Alpert type ionization gauge have been increased from 7 points to 21 points. Compared with the history note, small leakage is easily to find, because the distance from gauge to gauge is just 3 m length, and this method is much easier and more accurate than concluding leakage by the ion current of sputter ion pump. An Industrial PC is used as Input/Output Controller (IOC) and it connects the 7 Varian vacuum Multi-Gauge controllers with serial communication (RS485 mode). The pressure values are displayed in a PC with Linux, which is used as operator interface (OPI). The pressure values are archived in a database and some data analyses are also done, which is necessary to research the relation between dynamic pressure of vacuum system and beam lifetime and stability.

As a goal of our machine improvement we need lower emittance operation. So in injection equipment modification we use the thyratrons for pulse switch of kick power supply instead of the spark gap of the old one. The four ceramic chambers of kick in the same straight section for injection are set up instead of three kick chamber in the three straight section of the former injection scheme. Moreover, a new RF cavity and a new RF power supply are manufactured and installed, The cooling loop of the new cavity will be more reasonable and the frequency tuning capability will be larger than the old one. The RF power of the new transmitter will be larger than the old one. The RF cavity will provide higher RF voltage for a sufficient Touschek lifetime of electron beam, the new RF cavity is under test now. A 29-period gap-variable NdFeB permanent magnet undulator as an insertion device is being designed and installed in ring. Its wavelength range will be 100 to 2000 Å. The brilliance is about 2 or 3 orders higher than that of bending magnet generated radiation. The undulator chamber is a quadratic welded chamber, the beam channel cross section is 80×24mm and its length is 2750 mm. The straight degree and the plane degree of the undulator vacuum chamber is 1 mm. The photon beam ports of the two new bending chambers were changed to 0 degree to provide the radiation from the injected devices. The photon beam port of Infrared and Far Infrared Spectroscopy has to be rebuilt to provide a much larger vertical acceptance and much near to the light source point. The all metal valves with RF shields have been installed at each end of RF cavity, division point of phase II and phase III and that of phase IV and injection chamber, to make the future vacuum system maintains and components installation easier.

PRESSURE CHARACTERISTICS AT PRESENT

In the last summer shutdown, all the new vacuum equipment had been installed and the vacuum system improvement except the RF cavity had been finished. During the installation period the whole storage ring vacuum system had been exposed to air for 45 days. After the vacuum chamber were connect and evacuate and whole
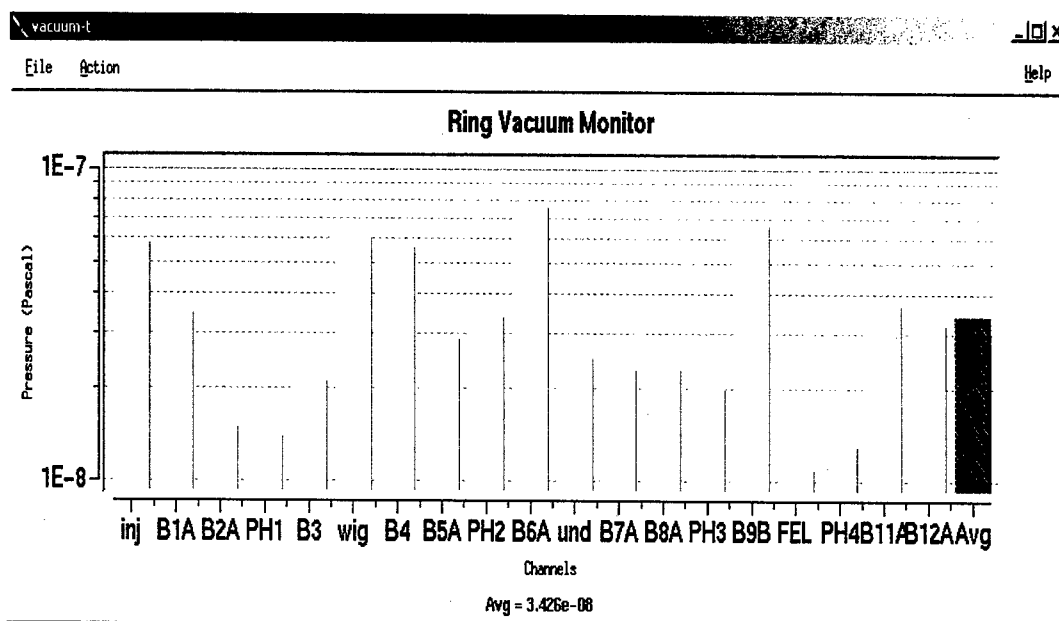
Fig.1: Display window of NSRL storage ring vacuum measure system

system was baked out in 200°C for 48 hrs by passing a large current through it, the lower static average ring pressure of 2×10-8Pa without beam had been get. Figure1 shows the distributed pressure in the beam orbit of the ring after improvement of the vacuum system. According to this picture the pressure distribution in the beam orbit is very small, due to the NEG pumps in the downstream of the bending chambers. So the improved vacuum system can provide the necessary vacuum environment for the high beam current, and its pumping speed with the NEG pumps is sufficient for the PHD disabsorb in the downstream of the bending chambers. The dynamic pressure has very important effects on the beam lifetime and it concern with the vacuum material's PHD character and cumulative irradiation dose. So the dynamic pressure of NSRL storage ring will be affected by the new equipment modulating and long-term stabile operation.

CONCLUSION

The improvement of NSRL storage ring vacuum system with RF shield oil pressured bellows chamber design has been proved to be successful by the low static vacuum pressure which is necessary to long-term reliability, stability and reliable operation. NEG pumps can pump the PHD gas effectively, and the four all metal gate valves with RF shields will benefit to the future maintain, new components installation and the system safety.

REFERENCES

[1] Zuping LIU, Xinyi ZHANG, NSRL PHASE II PROJECT Proc. 1st Asian PAC KEK JAPAN 1998
[2] Li Guihe. et al. The dynamic pressure and beam cleaning in HLS. Annual Report 1992-1993

ADSORPTION STUDY OF AL$_2$O$_3$ COATING ON THE PULSE SEPTUM MAGNET SURFACE

Hai-Ou Zhang,Yuan-Ji Pei[#], NSRL, HeFei, 230031,China

Abstract

The surface of pulse septum magnet in HLS was specially coated with Al$_2$O$_3$ powder by plasma spraying. It was found with such magnet in the injection vacuum chamber the pressure was relatively low. To investigate the mechanics 20 sheets of coating were made (120×80 × 20mm^2), adsorption capacity was tested. Pore constitution was studied by N$_2$ isotherm method. Results indicated ultimate pressure reduced obviously from 6.4× 10^{-5} Pa to 8.6×10^{-6} Pa. Coat adsorption capacity is about 3.68×10^{-4} Pa • l/cm^2. BET surface area is 201m^2/g, Coat is porous and pore is closed at one end. XPS results indicate there are hydroxyl, carboxyl etc on the surface, and they are most probably related with adsorption.

INTRODUCTION

HLS (HeFei Synchrotron Radiation Light Source) facility is a dedicated synchrotron radiation light source. It consists of a 200Mev LINAC and a 800Mev storage ring. The electron beam from transport line is injected into the storage ring by injection system which employs three kickers, a DC septum (D.S.) and a pulse septum (P.S.)[1].

D.S. magnet produce a deflection of 22.5° in the vertical direction and P.S. magnet produce a deflection of 6° in the horizontal direction for the coming beam. Electron beam goes into the vacuum chamber of the storage ring. Three kickers are fired and produce a localized bumped orbit close to the P.S. strip. The injection electron oscillate around the bumped orbit. In the following process, electron go inside the septum strip since the bumped orbit is contracted, so the injected beam run around the desired orbit.

It is important to develop a new material to reduce its outgassing rate so that the P.S. magnet could be directly mounted in the ultra-high vacuum chamber. Here a thin Al$_2$O$_3$ coating was sprayed on the surface of steel sheet and coil which composed the pulse septum magnet. With this coating in chamber pressure could reach less than 8×10^{-10}mbar after bakeout and pumped for 48 hour. Its electric insulation demonstrated good performance and magnet field undisturbed. Emittance of beam didn't get large. Injection efficiency increased[2][3].

In this paper some further study have been made to explore the mechanism of adsorption of Al$_2$O$_3$ coating.

EXPERIMENT AND TEST

Al$_2$O$_3$ coat was made. Its surface topography was observed. Its real surface area and adsorption capacity in vacuum chamber was tested. Adsorption species was investigated.

Coating Making

Al$_2$O$_3$ powder was sprayed on the steel sheet(120×80 ×0.6mm^3)by plasma spraying. Powder size is less than 0.065mm. Spraying parameters is listed in Table 1.

Table 1: Plasma Spray Parameters

Variable	Value
Ar flow rate	2000 l/h
H$_2$ flow rate	200 l/h
N$_2$ flow rate	250 l/h
Current	600A
Voltage	65V
Spray Distance	170mm
Spray angle	90°

Coating surface topography was observed by SEM (KYKY 1000B)(see in Fig.1)

30 μ m

Figure 1: Al$_2$O$_3$ coating topography(×1000)

Obviously coating consists of numerous flat granules with many pores and gaps. Al$_2$O$_3$ granule is heated in the plasma flame and nearly in fusing state. It strikes towards base steel sheet so heavily that it became flat. Because granules are different in size, moment, fusing level, so their area, shape, thickness etc. are not alike. If two adjacent granule don't solidify simultaneously, a gap would be formed. The pores arise because impurity and oxide burning, oxide film bursting [4].

XRD

XRD results showed that powder Al$_2$O$_3$ is α phase, Al$_2$O$_3$ coated is γ phase.

Specific Area and Pore Constitution

N$_2$ adsorption isotherm was tested to investigate the real surface area and pore constitution of coating and

[#]yjpei@ustc.edu.cn

powder. Tests were undertaken on ASAP 2000 system. Results are shown in Fig.2-5.
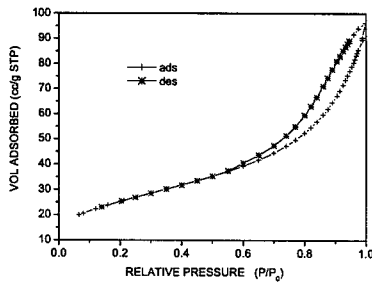
Figure 2: Al_2O_3 powder isotherm
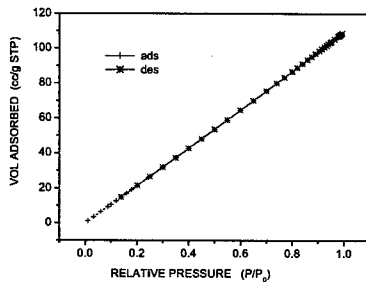
Figure 3: Al_2O_3 coating isotherm
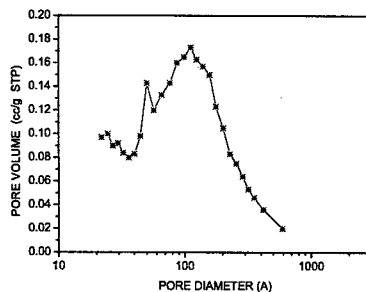
Figure 4: Al_2O_3 powder pore distribution
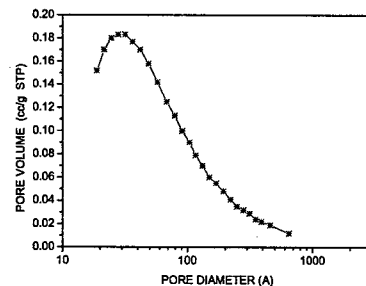
Figure 5: Al_2O_3 coating pore distribution

The specific surface area of powder Al_2O_3 is 91.1806m^2/g. It is clear in the isotherm curve that during adsorption process adsorbed volume increase slowly from p/p$_0$=0~0.65, but rises rapidly from p/p$_0$=0.65~1.0. No saturation appears up to P/P$_0$=1. During desorption process adsorbed volume decrease slower than counterpart during adsorption (see Fig.2). It is deduced that pore is of several shape: cone shaped or dual-cone shaped open at both-end, wedge-like open at four sides. Pores are existed among particles, formed by sloping face of particles. Multi-layer adsorption and capillary condensation occurs, interacting force between adsorbate

and adsorbent is relatively fierce. In the pore distribution curve more than one peak are appeared. The highest peak is at between 100~110A, the second is about at 60A (see Fig 4). Surface area of pores which is larger than 50A accounts for 49.98% of all.

The specific surface area of coating Al_2O_3 is 201m^2/g. Both adsorption amount and desorption amount are both linear with pressure. No hysterisis appears (see Fig.3). It is deduced that the pore is cylinder-like, cone-like or wedge-like closed at one end. Multi-layer adsorption and capillary condensation also occur. Only one peak appears between 20~30A in the pore size distribution curve (see Fig.5). Surface area of pores which is larger than 50A accounts for 25.84% of all[5][6].

It is clearly demonstrated that from powder Al_2O_3 to Al_2O_3 coated real surface enlarge, pore diameter shrank and pore shape was changed completely.

Adsorption Capacity

Adsorption capacity of coating was tested quantitatively and quantitatively. The test system scheme is shown in Fig.6. 20 sheets of steel coated with Al_2O_3 (~3,840cm^2) was put directly into a standard test dome. Orifice diameter $d = 2mm$, flow conductance $c = 0.34l/s$ (27℃,N$_2$). P$_1$, P$_2$ was measured by two B-A gauge (L-B Co.), which had been calibrated at an all-metal ultra-high vacuum calibration facility. One 200l/s SIP was used to obtain ultimate pressure, One 110l/s TMP unit was used to obtain backing pressure.
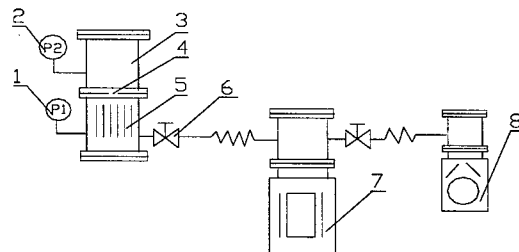
1,2 B-A gauge 3 test dome 4 orifice 5 coating sheet
6 gate valve 7 SIP 8 TMP unit
Figure 6: test system sketch

Total leakage is less than 5×10^{-9} mbar • l/s. Chamber was baked at 250℃ for 24hrs then cooled down to room temperature. P$_1$,P$_2$ was recorded. Gate valve was not shut off until ultimate pressure was reached.

Adsorption capacity

$$\Delta Q = C(P_1 - P_2) = C(P_{10} - P_{20})$$

$$G = \int_0^T \Delta Q dt$$

P_{10}, P_{20} ---- background pressure.

The results are shown in Fig6,7.
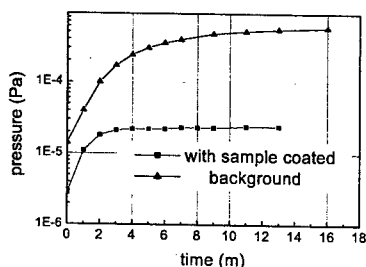
Figure 6: Pressure variation after gate valve shut off
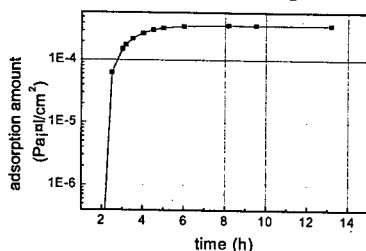
Figure 7: Al_2O_3 coating adsorption amount

With sample coated in the chamber ultimate pressure could reach 8.6×10^{-6}Pa, while background ultimate pressure is 6.4×10^{-5}Pa. Adsorption began to occur during cool-down process. In a few hours it attain saturation. Turn off the pump chamber could maintain certain pressure lower than background under the same condition. It means adsorption and desorption keep balance and coating has some absorbing capacity. It also imply the outgassing rate of coating is smaller than stainless steel.

XPS

XPS (X-Ray Photoelectron Spectroscopy) was used to investigate the adsorbate chemical state on surface. Excitation is Mg K α, $h\nu$ =1253.6eV, analyzer energy CAE=20eV, step=0.05eV. Specimen was heated up to 250 ℃ in the vacuum and re-adsorption in the air. The surface spectrum and C1s spectrum are scanned (see in Fig8, 9).
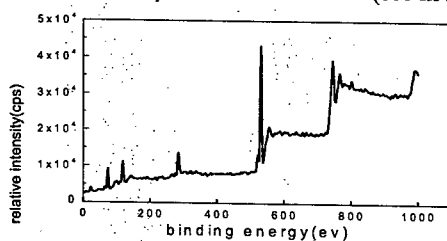
Figure.8: XPS of Al_2O_3 coating
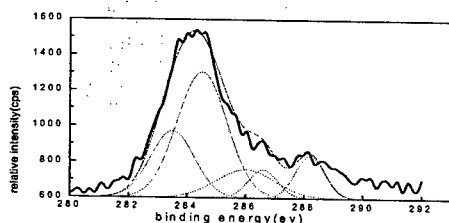
Figure.9: XPS of Al_2O_3 coating (C1s)

Content of elements is Al: 28.57%, O: 47.23%. 42.85% of O comes from Al_2O_3, the rest comes from adsorbate. There are several peaks at 283.5eV, 284.8eV 286Ev, 286.4eV and 288.1eV in C1s XPS spectrum. it is deduced kinds of chemical bonds existing on the surface as Al-O-C, C-H, –C–O, –C-OH, –C=O etc., which are most likely relate with the adsorption of CH_4, CO, CO_2, H_2O and other gases.

CONCLUSIONS

- The application of Al_2O_3 coating sprayed on the surface of magnet meterial brings some positive effects: difficulty of injection vacuum chamber design reducing, emittance of the beam no increasing, a good magnet performance, good vacuum condition and injection efficiency raising. The magnet has been successfully run for 10 years at NSRL.

- Due to particular forming process, Al_2O_3 coating have larger surface area than powder. It is beneficial to adsorption.

- The interaction between Al_2O_3 coating and gas is not only physical but also chemical adsorption.

- Further experiment and theory study on adsorption species is to be performed.

ACKNOWLEDGEMENTS

REFERENCES

[1] Y.J.Pei, X.Q.Wang et al., Design of the injection system for HESYRL, Inner Report, 1981.
[2] Y.J.Pei et al,. Vacuum 41 (1990) 1870.
[3] Y.J.Pei et al., Nucl. Instr..& Meth. A 398 (1997) 368.
[4] Z.Q.Jiang et al., Ordnance Meterial Science and Engineering, Vol.22, No.3 (1999) 56.
[5] Yan J.M., Adsorption and Coacervation, Science Publisher, BeiJing, 1979, p. 117.
[6] S.J.Gregy et al., Adsorption, Surface Area and Porisity, 2nd Edition, Acedemic Press, 1984, p. 130.

VACUUM COMMISSIONING FOR THE SWLS ABSORBER INSIDE A KICKER-CHAMBER AT TLS STORAGE RING

G. Y. Hsiung[#], S. N. Hsu, K. C. Kuan, C. S. Hwang, NSRRC, Hsinchu, Taiwan
J. R. Chen, NSRRC and NTHU, Hsinchu, Taiwan

Abstract

A 6T super-conducting wiggler, so called wavelength shifter, (SWLS) has been installed in the injection section of the 1.5 GeV Taiwan Light Source (TLS) electron storage ring. The intensive synchrotron radiation emitted from SWLS causes severe problems in the downstream kicker-chamber, such as radiation hitting on the ceramic parts, interfered non-uniform field and induced arcing from the absorber during kicker firing, etc.. A new absorber, designed to solve those problems, has been developed and installed in the kicker-chamber downstream the SWLS. The earlier stage of vacuum commissioning shows a high pressure-rise, stimulated by the photons, localized near the head of absorber that seriously constrains the beam lifetime. However, the pressure reduces by continuous beam cleaning. The injection efficiency of the electron beam is not degraded much. The temperature rise on the downstream chambers, behaves not so according to the beam current, is kept within allowable values.

INTRODUCTIONS

A 6T SWLS is installed in the 1.5 GeV TLS to obtain a higher flux and a critical energy of hard X-ray extend from 2.14 keV to 8.98 keV[1,2]. The irradiation from SWLS, 130 mrad photon span and 8.9 mm off-axis, hits the downstream taper, flange, kicker ceramic chamber, and drift chamber, etc.. An absorber is installed inside the 4th kicker ceramic chamber to prevent the non-cooled ceramic parts from irradiating the synchrotron light. The severe problem for the absorber inside the kicker chamber includes: (1) reducing the horizontal physical aperture that challenges the beam injection, (2) degrading the uniformity or kick-field, (3) causing the arcing and inducing serious problems of dramatic pressure rise and the micro-dust from the damaged film coated inside the ceramic chamber. Features of the absorber should be water-cooled, thin enough, higher thermal conductivity, electrical insulated from the chamber. The design and the commissioning result will be described in this paper.

DESIGN OF THE ABSORBER

Figure 1 illustrates the engineering drawing for the R1 straight section of TLS that contains SWLS and the 4 sets of kicker. There is not enough space between the SWLS and the 4th kicker for inserting an independent absorber. The parameters of SWLS at strength of 6 T and 5.3 T are shown in Table 1.
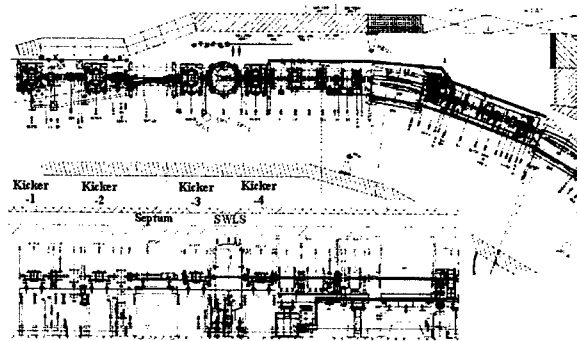
Figure 1: Engineering drawing for the R1 straight section of TLS, top view and side view.

Table 1: Comparison of the parameters of SWLS source at field strength of 6 T and 5.3 T

Field strength	6 T (260 A)	5.3 T (230 A)
Critical energy	8.98 keV	7.93 keV
Photon span	130 mrad	115 mrad
Total Power	2.56 kW	1.98 kW

Design

The absorber is made of OFHC copper sheet, 3 mm in width, 6 mm in height, and 460 mm in length, surrounded brazing with 1/4" stainless steel tube for cooling water. The flow rate is higher than 3 L/s. An extended Cu covers the tip of the SUS cooling tube to avoid the irradiation. The assembly is inserted from the downstream port of ceramic chamber, as shown in Fig. 2, where the RF bridge is installed to keep the same cross section.

(a) (b)
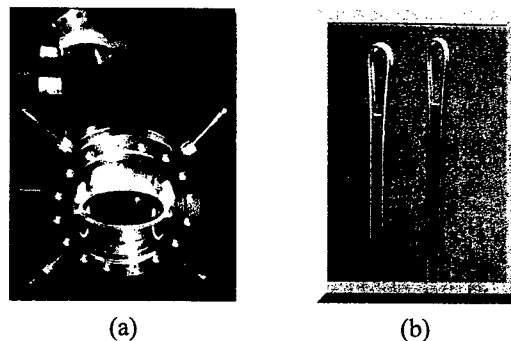
Figure 2: Photos of (a) the kicker chamber with the absorber, and (b) the cold head of the absorber.

[#]hsiung@srrc.gov.tw

Thermal analysis by ANSYS simulation

The curves of power distribution for SWLS at strength of 6 T and 5.3 T, located at 0.52 m from source, are shown in Fig. 3(a) and 3(b), respectively. Fig. 3(a) shows a maximum power density of 50 W/mm^2 at 0.04 m of horizontal position, the half width of ceramic chamber, in case of 6 T, and lower than 5 W/mm^2 in case of 5.3 T.
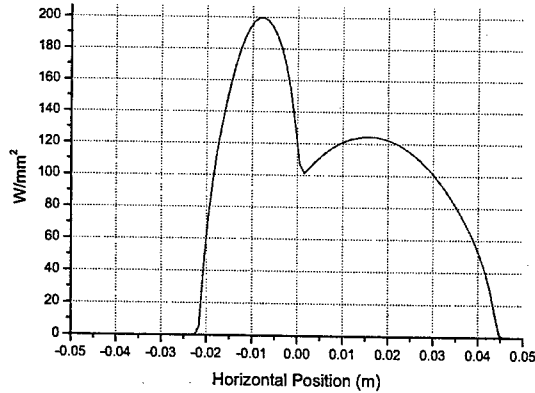
(a)
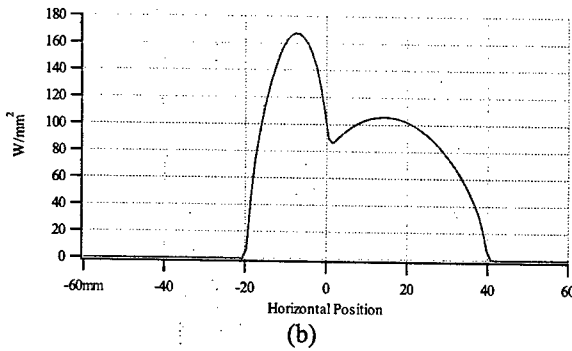
(b)

Figure 3: Power distribution for the SWLS at field strength of (a) 6 T, and (b) 5.3 T.

The thermal analysis by ANSYS for the absorber near the cold head without Cu cover, and with Cu cover and upstream absorber, are illustrated in Fig. 4(a), 4(b), respectively. The simulated results emphasize not only the necessity of covering the cold head with conductively cooled copper but also another upstream absorber to share the heat loads with the cold head. The upstream absorber is made by welding an Al absorber, 12 mm in height, on the inside wall of Al taper flange downstream the SWLS.

COMMISSIONING OF TLS

The absorber cannot protect the leading edge of kicker ceramic chamber from SWLS irradiated power density of 50 W/mm^2 in case of 6 T that causes the non-cooled ceramic spacer broken. The later commissioning of TLS is operated for SWLS at 5.3 T. Thus the photon span of SWLS light reduces from 130 mrad to 115 mrad. It is capable to shield the non-cooled ceramic chamber and

components from irradiation. Since there is not enough space for additional pumps and poor conductance near SWLS, the pressure rise of R1IG2 due to photon stimulated desorption out of the absorbers and SWLS beam duct is the highest in the storage ring. The averaged pressure, Pavg, is determined by R1IG2. The pressure rise per beam current, and the product of life time with beam current, as function of the beam dose are shown in Fig. 5(a) and 5(b), respectively.
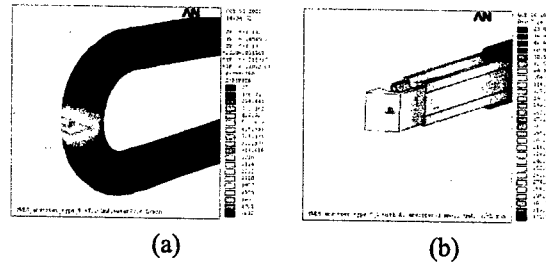
Figure 4: Thermal analysis by ANSYS for the absorber (a) without Cu cover, and (b) with both Cu cover and upstream absorber.

A beam lifetime, limited by nuclear scattering from residual gas, of longer than 10 hours at a beam current of 200 mA has been achieved after the beam self-cleaning at an accumulated beam dose of 50 Ah. The averaged pressure rise due to photon stimulated desorption reduced to a level below 5×10^{-12} Torr/mA. The dominant pressure rise is determined by R1IG2, located near SWLS, comprised of H_2, CH_4, and CO. Fig. 6 shows the mass spectrum by a quadrupole mass spectrometer near the SWLS section where the desorbed gas species are measured. The product of pressure rise, IG2 or Ravg, with lifetime is nearly constant of 2×10^{-7} Torr·h or 1×10^{-8} Torr·h. It illustrate a result of gas scattering dominant lifetime compared with the Touschek lifetime before beam dose of 50 Ah.

(a)

(b)
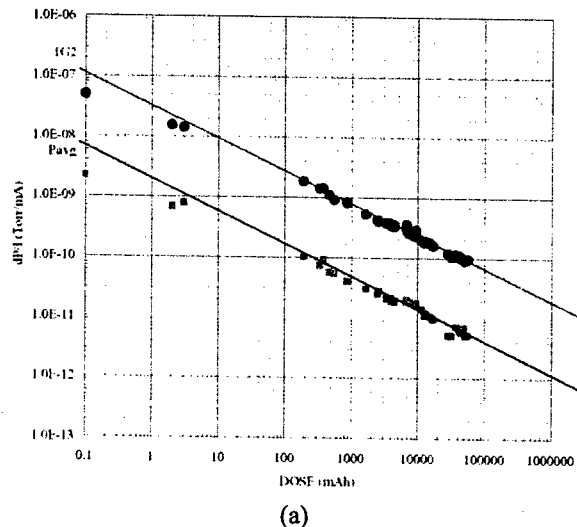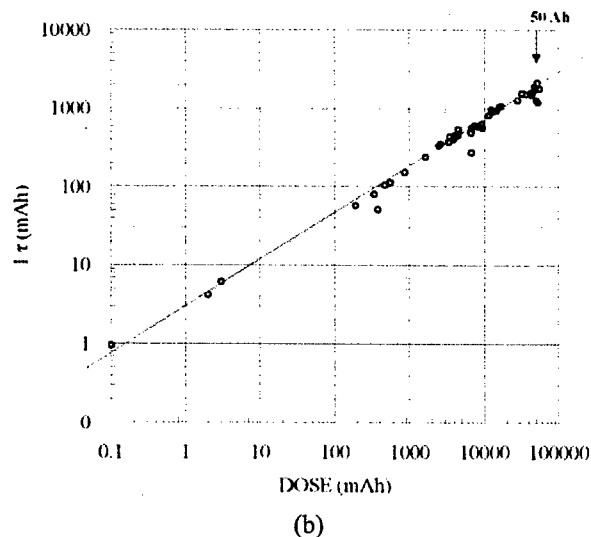
Fig. 5: Pressure rise per beam current, (a), and product of beam current and lifetime, (b), as function of beam dose. IG2 and Pavg represent the pressure rise near SWLS and the average pressure of the storage ring respectively.

The temperature rise near downstream taper of SWLS and near the 4th kicker ceramic chamber is monitored by the PT100 thermal sensor. Fig. 7(a) shows the beam current and pressure rise near injection section and SWLS, and 7(b) shows curves of temperature rise near SWLS and downstream kicker chamber. T1 ~ T4 represent the temperature near both sides of taper and flange downstream the SWLS, while T5, T6 and T7, T8 near upstream and downstream of kicker chamber respectively. The temperature near the SWLS and kicker chambers are < 13 °C, at 5.3 T of SWLS operation mode and 200 mA beam current.
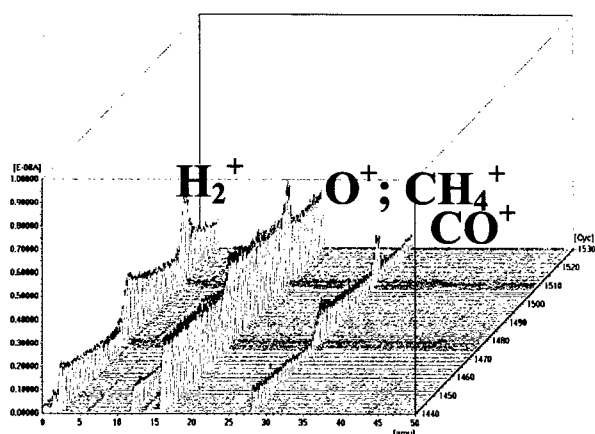
Fig. 6: RGA spectrum in mass range of 1 ~ 50 amu/e. The dominant residual gases include H_2, CO, and CH_4.

(a)

(b)
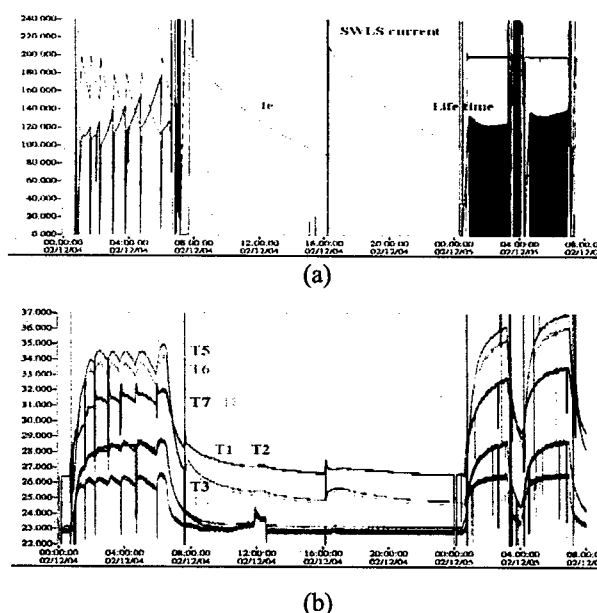
Fig. 7: (a)Beam current, pressure rise, lifetime; (b) Temperature near SWLS and 4th kicker chamber.

CONCLUSION

The commissioning result for the SWLS absorber inside the downstream kicker chamber is described. A lifetime of > 10 h at beam current of 200 mA was achieved after beam self-cleaning for accumulated beam dose of 50 Ah at SWLS field of 5.3 T. The dominant gas species are H_2, CH_4, and CO. The injection rate of > 200 mA / 3 min, after installing the SWLS, does not degrade. The cold head of the absorber is protected by an extended Cu cover and an Al upstream absorber. The temperature rise near the ceramic chamber is < 13 °C.

REFERENCES

[1] C. S. Hwang, C. H. Chang, C. T. Chen, J. R. Chen, Y. C. Chien, F. Z. Hsiao, G. Y. Hsiung, K. T. Hsu, C. C. Kuo, C. E. Wang, D. J. Wang, "Superconducting Insertion Devices for Synchrotron Hard X-ray at SRRC", EPAC 2002, Paris, France 2002, p. 2613.

[2] C. H. Chang, H. P. Chang, J. R. Chen, T. C. Fan, C. S. Hwang, G. Y. Hsiung, K. T. Hsu, C. C. Kuo, K. K. Lin, G. H. Luo, J. T. Sheu, D. J. Wang, and M. H. Wang, "Installation and Commissioning of 6-Tesla Superconducting Wavelength Shifter at Taiwan Light Source", XIV Russian Synchrotron Radiation Conference - SR-2002, July 2002, Novosibirsk, Russia.

INSERTION DEVICE VACUUM CHAMBER FOR THE LINAC COHERENT LIGHT SOURCE*

Soon-Hong Lee[#], Emil Trakhtenberg, and Patric Den Hartog
Advanced Photon Source, ANL IL 60439, USA

Abstract

The vacuum requirement for the undulator line of the Linac Coherent Light Source is extremely challenging: a low resistive wall impedance 3.42-m-long chamber that fits within a 6.3 mm undulator gap that has ultralow outgassing and a surface finish, less than 100 nm Ra. A prototype chamber will be fabricated from electropolished semiconductor-processing-grade stainless-steel seamless tubing. Since stainless-steel tubing has a high electric resistivity, which can increase the resistive wall wake, a thin layer of copper will be deposited to minimize this effect. A thin nickel plating will be deposited in advance for better adhesion. This process will be followed by electropolishing of the copper surface. The first approach for Cu coating of the vacuum chamber has been investigated. Roughness measurements and preliminary coating results with a one-meter-long tube will be presented.

1 INTRODUCTION

The Linac Coherent Light Source (LCLS) is a high-brightness x-ray free-electron laser (FEL) project that will be constructed at the Stanford Linear Accelerator Center (SLAC). In the LCLS project, the electron beam is accelerated through the 2 mile SLAC linac and will pass through a 121 meter array of 33 separate undulator segments. One of the most important contributions to performance in the LCLS is the control of the wakefield effects inside the undulator. The wakefield effects can be reduced by proper design of the vacuum chamber.

In the LCLS, the 6.3 mm undulator gap necessitates a narrow OD vacuum tube with inside radius of just 2.5 mm. The electron beam interaction with the narrow undulator vacuum tube can generate an energy gradient across the bunch that can potentially reduce the FEL gain. These wakefields are influenced by both beam pipe surface roughness and conductivity. The former are called the surface roughness wakefields, and the latter are called the resistive-wall wakefields. The resistive-wall wakefields can be reduced to a desired level by Cu coating on the interior of the stainless steel tubing or by using copper tubing [1-3]. In addition, wakefields due to surface roughness of the interior of tubing may interact with the beam in the vacuum chamber, which causes degradation of beam emittance.

In this report, techniques for minimizing the wakefield effects in the LCLS vacuum chamber design will be discussed. Specifically, technical issues such as the vacuum chamber material, surface roughness measurements, and Cu-coating process are addressed.

2 TECHNICAL ISSUES

The LCLS conceptual design report (CDR) recommends stainless steel (SS) 316L as the vacuum tube material [3]. In general, the vacuum properties of stainless steel (SS) are excellent, but it has a high electrical resistivity. The design requires minimizing the electric resistivity on the inside of the vacuum chamber surface, which the beam might closely approach, and minimizing the contribution of the resistive-wall wakefield to orbit distortion and emittance growth. To do that, the CDR recommends an application of a thin layer of oxygen-free electronic (OFE) copper (~10 μm thickness to cover the skin depth of 58 nm) followed by electropolishing of the copper-coated surface. A thin nickel substrate may be required as the undercoat before copper coating for better adhesion of the copper to the SS tube.

However, there are many technical challenges with respect to the Ni & Cu plating/coating process of a 3.42 m-long and 6 mm-narrow tube. In addition, the surface roughness of the chamber required by CDR must be less than 100 nm (4 μ inch Ra) after coating. To achieve this extremely smooth surface, the CDR recommends the coated surface of tubing to be electropolished. However, some special considerations must be taken, especially in soft metals like copper. Electropolishing can generally improve the surface roughness of a product by about 50%, based on the input surface Ra. For example, to achieve a surface finish of 4 μinch Ra, we might be able to finish the surface to at least an 8 μinch Ra by a mechanical method before electro-polishing. Also, the surface cannot be smeared in the mechanical polishing process, or the electropolishing may cause the surface finish to be made worse instead of better. Another option for the vacuum chamber is to use OFE annealed copper tube. In the CDR, OFE copper was considered as a vacuum chamber material as well. However, it mentions that this OFE copper material is marginal for repeated beam exposures at the same location and is not suitable for the scenario of continuous beam exposure. Herein, however, copper is still considered as one of materials for the LCLS vacuum chamber.

In this study, aluminum or ceramic materials may be some other possible options. Including all possible options, a comparison of vacuum chamber materials has been summarized in Table 1. There exist some technical challenges to complete the vacuum chamber design, such as Ni & Cu coatings and electropolishing of a long, narrow tube, etc.

Table 1: Comparison of possible approaches for the LCLS vacuum chambers.

Chamber	Advantages	Disadvantages
SS316L tube + Ni, Cu Coat + Electropolish	Low roughness, Vacuum quality	Coating, Electropolish, Mechanical tolerance
OFE Cu tubing + Electropolish	Conductivity, No coating, Cost reduction	Low melt temperature, Electropolish, Flange attachment
SS316L plate + Machining + Coating + Welding	Plating, Electropolish, Flexible design	Machining, Twists, Post-weld annealing Mechanical strength
Al Extrusion 6063-T5	No Coating, Cost reduction	Low melt temperature, Electropolishing

3 ANALYSIS OF VACUUM TUBE MATERIALS

To compare the surface roughness of chamber materials, sample specimens were prepared from SS and copper tubes. Surface roughness data were collected by using a KLA-Tencor alpha-step 500 profilometer and an atomic force microscope (AFM).

1″ long samples were cut from ¼″ OD x 0.036″ thickness SS 316L tubing and from 0.236″ OD x 0.020″ thickness OFE copper tubing by using a wire EDM process. The part was flushed with DI water during cutting. The EDM wire is made of brass and tungsten alloy. The finished samples were subsequently cleaned with Citrinox.

For the AFM measurements, we obtained the surface plots in noncontact mode and used the cantilever tips of a Veeco Metrology group (Model # 1650 for SS 316L and # 1895 for Cu). These tips have resonant frequencies of 260 and 280 kHz, respectively. The images were taken at scan rates between 50 ~ 100 μm/sec to accurately track the sample surface, and all images were flattened to reduce the effects of drift.

Sample measurement results

Typical AFM images of SS and Cu samples are shown in Figures 1-2 and Table 2 shows the summary of typical surface roughness measurement values. From these measurements, we found the sample from SS 316L tubing to have a very smooth surface. The tubes are available off the shelf with a maximum 5 μinch (130 nm) Ra surface. But, in the case of Cu tube samples, we had great difficulties imaging the sample despite several attempts, because it is too rough for the AFM cantilever tips we used for SS 316L. It was not easy to scan, particularly imaging areas larger than 20 x 20 μm with model # 1650 AFM tips. But, it was possible to scan the images with model # 1895 AFM tips.

As shown in Figures 1-2, both samples clearly exhibit striations, especially the Cu images, parallel to the longitudinal direction of the tube cut, and these features can be easily seen with a low-magnification light microscope.

Figure 3 shows a typical 2D surface roughness of a Cu tube by profilometer. We measured the roughness of the samples along both the longitudinal and azimuthal directions of the tube. Both SS 316L and Cu tubes exhibited roughness in the azimuthal direction that was much worse than that in the longitudinal direction.

(a) 20 x 20μm (24.64 nm Ra)   (b) 50 x 50μm (10.07 nm Ra)   (c) 100 x 100μm (16.15nm Ra)   (d) 3D - 100 x 100μm
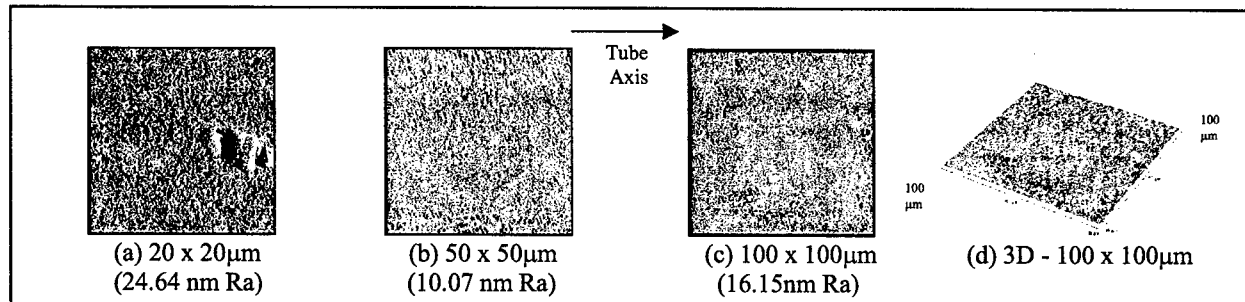
Figure 1: AFM images of the inner surface of stainless steel 316L tube.

(a) 20 x 20μm (297.98nm Ra)   (b) 50 x 50μm (317.49nm Ra)   (c) 75 x 75μm (207.98nm Ra)   (d) 3D - 75 x 75μm
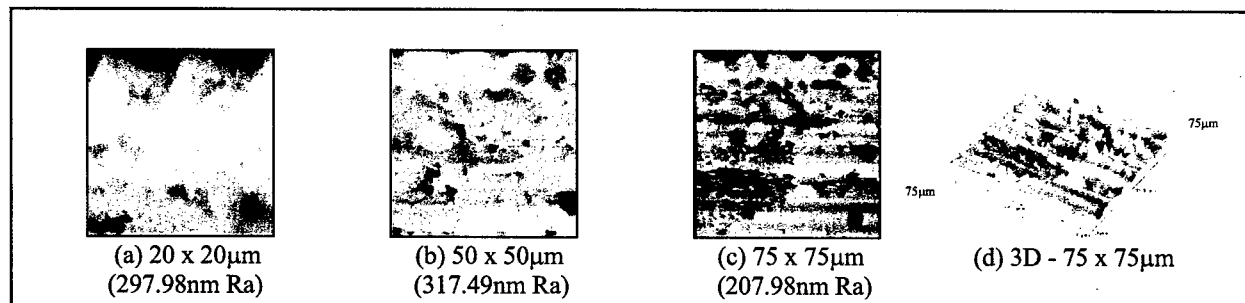
Figure 2: AFM images of the inner surface of OFE copper tube.
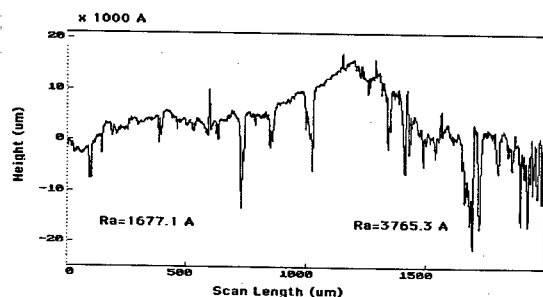
Figure 3: Typical surface roughness profile of a Cu tube along the longitudinal direction.

Table 2: Range of surface roughness measurement values for vacuum chamber materials.

Measurement Instrument	Tube Matl.	Ra (nm)	Rq (nm)
AFM (area)	SS316L	10.1~24.6	14.8~46.9
	OFE Cu	188.1 ~ 424.5	271.4~406.3
Profilometer	SS316L	48.30 ~ 313.4	-
	OFE Cu	71.45 ~ 412.5	-

4 COATING PROCESSES

Electroless plating metal deposition

This technique is defined as a chemical reduction reaction from an aqueous metal salt solution containing a reducing agent. After masking the outer surface of tubing, it is immersed into the plating bath. No external power supply is needed. In the narrow-long application, two problems are expected. First, it would be very difficult for an electrolytic reaction to occur on the inner surface of the narrow-long SS tubing. Second, deposition rates are generally much lower than electroplating rates, so it might not be easy to plate a 10 μm Cu layer. Also, non-uniform thickness is expected. This process requires further research.
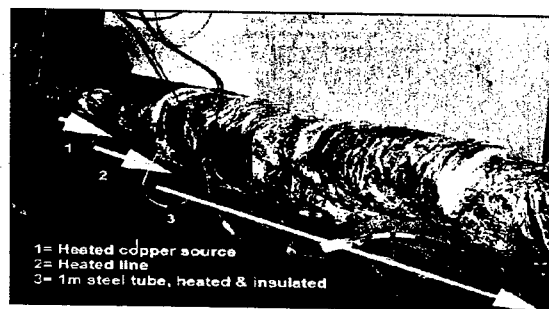
Figure 4: Equipment setup for copper coating by a CVD process inside a steel tube.

Chemical vapor depositions (CVD)

These vapor deposition techniques are based on homogeneous and/or heterogeneous chemical reactions. This process would be a strong candidate to complete the Ni and Cu coatings. As shown in Figure 4, copper coating has been tested with a one-meter-long tube at CVD Manufacturing, Inc. (Toronto, Canada). To deposit a layer of Cu film by CVD, two chemicals, such as copper

(II) hexafluoracetyacetonate [$Cu^{II}(hfac)_2$] and copper (II) acetylacetonate, were tested under the conditions listed in Table 3. It is easy to transport $Cu^{II}(hfac)_2$ at low temperature, however, the deposition rate is very low, and this material is also costly. After working on several tests with this material, we found it did not work well in our application. Using copper (II) acetylacetonate, a Cu film was also deposited under the conditions listed in Table 3, and the carrier gas (Ar + H_2) was passed through a bed of copper precursor to bring the vapor into the reaction chamber. The advantage of this material is that it is free from fluorine, and a high purity copper film can be achieved. It also deposits at a much higher rate than materials containing fluorine. A high deposition rate is essential for the long tube deposition. However, the vapor was stuck at some places inside the tubing, particularly at the joints (both tubing ends), because the temperature is lower at those points. Using the enhanced distribution of a uniform temperature, we can achieve more uniform thickness coverage inside the tube as shown in Figure 5.

Table 3: Deposition conditions for Cu CVD.

	$Cu^{II}(hfac)_2$	Cu^{II} acetylacetonate
Reactor Temp.	~ 70 (℃)	~ 190 (℃)
Deposition Temp.	275 - 330 (℃)	~ 400 (℃)
Vapor Pressure	1 - 10 Torr	
Conversion to Copper	Ineffective	Effective

(a) Inlet view   (b) 10x   (c) 60x
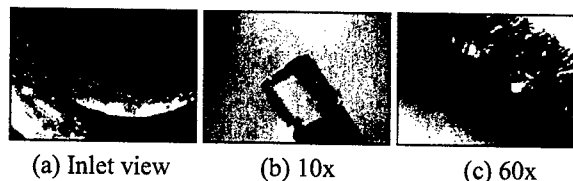
Figure 5: Tube section views of a copper-coated surface.

5 SUMMARY & FUTURE WORKS

The surface roughness of SS and Cu tubing has been measured. Copper coating has been tested with a one-meter-long tube. Uniform thickness coverage inside the tube was achieved by controlling the temperature distribution. Work is continuing to get a uniform Cu film with a 1-m-long SS 316L tube, by optimizing temperature and insulation. Eventually, a full 3.42-m-long tube will be tested. In addition, electropolishing of 3.42-m-long OFE copper tubes will be tested at Delstar Metal Finishing, Inc. (Houston, T□). We expect the finish should be approximately 1/2 of the as-drawn surface roughness and that electropolishing will aid in reducing the surface roughness and outgassing rate for Cu tubing.

REFERENCES

[1] □. Stupakov et. al., Physical Review Special Topics-Accelerators and Beams, Vol. 2, 060701 (1999).

[2] P. Emma, Proceedings of PAC 2001, Chicago, pp 241-244 (2001).

[3] LCLS Conceptual Design Report (2002), SLAC-R-593.

ADVANCED PHOTON SOURCE BOOSTER SYNCHROTRON SUBHARMONIC RF CAPTURE DESIGN*

Nicholas S. Sereno, Advanced Photon Source, ANL, Argonne, IL 60439, USA

Abstract

Recent efforts at the APS have focused on improving overall injector system reliability and availability for top-up mode storage ring operation. One proposal being considered is to implement direct injection of the beam from the linac into the booster synchrotron, thereby bypassing the particle accumulator ring (PAR). Efficient capture of the long linac macropulse (>~ 10 ns) can be accomplished by adding an additional rf system in the booster at an appropriate subharmonic of the 352-MHz rf system. The subharmonic system is used during injection up to approximately 3 GeV, then the 352-MHz system is turned on to accelerate the beam to 7 GeV. The particle tracking program elegant is used to simulate rf and magnet ramping, beam loading, and HOM effects at up to 10-nC beam charge. Issues addressed in this design are efficient beam capture and acceleration to 7 GeV while maintaining adjacent bunch purity. Tolerances on various rf system parameters are presented in order to maintain bunch purity to better than 1 part in 100,000.

REQUIREMENTS

Successful operation of the APS storage ring (SR) in top-up mode requires a reliable injector system that efficiently delivers beam at 7 GeV to the SR. One way to possibly improve injector reliability is to inject the linac beam directly into the booster and bypass the PAR. Direct injection into the booster imposes several requirements on the booster rf system. First, the rf must capture the complete linac beam or at least a large fraction of it. Second, bunch purity must be preserved. Third, the whole acceleration process from injection to extraction at 7 GeV must be as efficient (as measured by particle loss) as possible at up to 10 nC of extracted charge. Finally, the rf system parameters should be chosen to preserve the present linear ramp profile used in the booster (0.325 to 7 GeV in 225 ms). The last requirement minimizes the required recommissioning effort since the magnet family ramps are left unchanged.

These requirements can be achieved by adding a subharmonic rf system in the booster at the appropriate frequency and gap voltage. The subharmonic system in combination with the present booster 352-MHz rf system act together to accelerate the beam to 7 GeV while minimizing beam loss and preserving bunch purity. The central problem of this design is to determine the proper subharmonic and 352-MHz rf system parameters to satisfy these requirements. The acceleration and capture process is achieved by using the subharmonic system to capture the linac macropulse and turning on the 352-MHz

system at about 3 GeV to quickly capture and accelerate the beam to 7 GeV. The subharmonic system will also support future booster upgrades as well as a new, recently commissioned low-emittance booster lattice [1].

SUBHARMONIC FREQUENCY AND GAP VOLTAGE GENERAL CONSIDERATIONS

The thermionic gun macropulse length drives the choice of subharmonic frequency. The rf thermionic guns have nominal pulse lengths of 40 ns (gun 1) and 10 ns (gun 2). The subharmonic period sets the maximum macropulse length that can be captured in a stationary bucket. This maximum length is further reduced by a factor for nonstationary buckets [2]. For the booster, the beam is injected into an accelerating bucket so the achievable linac macropulse length that can be captured by the booster is approximately 30 - 50% less than the subharmonic period.

To capture the complete macropulse for both guns would require a $< (1/40$ ns$) = 25$ MHz subharmonic frequency. Due to the difficulty of building high-voltage, low-frequency rf cavities, this requirement can be relaxed so that at least the 10-ns pulse from gun 2 can be captured. Finally, the subharmonic frequency must be an integer subharmonic of 352 MHz (h = 432). Table 1 lists the subharmonic frequencies and numbers considered in this study. All four frequencies can completely capture the macropulse generated by gun 2. The exact choice of subharmonic frequency can be made based on rf considerations such as ease of construction and maximum gap voltage obtainable.

Table 1: Booster Subharmonic Capture Cavity Parameters

Frequency (MHz)	Subharmonic Number	Subharmonic Gap Voltage (kV)	Minimum Bunch Length (ns)
29.327	12	650	2.44
39.103	9	500	2.57
43.991	8	450	2.57
58.665	6	400	2.33

The subharmonic gap voltage required depends on the linac macropulse length and the bunch length required to efficiently capture and accelerate the beam by the 352-MHz rf system. The linac macropulse must be damped to < 2.84 ns before it can be captured and accelerated by the 352-MHz rf system. However, radiation damping is very small up to about 3 GeV where the damping time is 17.2 ms (at the injection energy of 0.325 GeV the damping time is 13.5 seconds). For energies less than approximately 3 GeV, adiabatic damping of the energy

spread is the dominant mechanism for reducing the bunch length since the bunch length is (nearly) proportional to the energy spread [2,3]. The proportionality is not exact since it is scaled by the synchrotron frequency, which changes as the synchronous phase and energy change.

The gap voltage needs to be large enough to provide an adequate overvoltage factor at 3.25 GeV to compensate for acceleration (36.4 keV/turn) radiation loss (296.7 keV/turn) as well as beam loading. This requires a subharmonic gap voltage of somewhere around 400 to 600 kV (depending on choice of frequency) to insure adequate overvoltage. The exact value of the gap voltage is explored via simulation described in the next section.

DETERMINATION OF SUBHARMONIC GAP VOLTAGE FROM TRACKING

Initial elegant [4] tracking simulations were performed to determine the gap voltage required for each frequency listed in Table 1 to capture and bunch the linac macropulse to < 2.84 ns. The initial linac macropulse length was varied depending on the subharmonic frequency, and the energy spread was taken to be ±1% (hard edge full width) at 0.325 GeV. These initial beam parameters resulted in ~ 0.5% particle losses at injection. The simulation used 35,000 particles to estimate the worst-case capture efficiency as well as bunch purity during capture and acceleration. Beam loading was simulated for the subharmonic cavity by using the standard resonator impedance model with $Q_o = 40,000$, $\beta = 1$, and $Rs = 5$ MΩ. Finally, elegant has the capability to simulate radiation damping and quantum excitation, and these effects were included in the simulations.

Table 1 shows the total gap voltage required for each subharmonic cavity frequency to achieve a 2.3- to 2.5-ns full width bunch length (defined as the difference in arrival time of the most downstream and most upstream particles in the bunch). The table clearly shows the tradeoffs involved in the choice of subharmonic frequency. One would like to use the lowest frequency possible to capture the longest possible linac pulse. A lower subharmonic frequency would require a much higher gap voltage to achieve the bunch length required for efficient 352-MHz capture. In general it is more difficult to design low-frequency cavities with high gap voltage (> 200 kV) because of voltage breakdown [5,6]. Next we explore a way to reduce the required total gap voltage yet still use a low-frequency cavity for capture of a long linac macropulse.

SIMULATIONS USING TWO SUBHARMONIC CAVITIES WITH DIFFERENT FREQUENCIES

Table 1 illustrates the tradeoff between subharmonic frequency and gap voltage. This is understood simply: the bunching required is inversely proportional to the time derivative of gap voltage, which is the product of the subharmonic frequency and peak gap voltage in the frequency domain [2]. One can increase the effective gap voltage time derivative by using a combination of low-frequency subharmonic cavity and high-frequency subharmonic cavity (both cavity frequencies need to be harmonically related to each other as well as to 352 MHz). This has the effect of reducing the total gap voltage required for a given desired final bunch length (~ 2.5 ns for efficient capture by the 352-MHz booster rf system).

The subharmonic frequencies chosen for this study were the twelfth subharmonic (29.327 MHz) previously described and the third subharmonic (117.310 MHz) of 352 MHz. The twelfth subharmonic was kept powered at a constant 200 kV throughout the ramp and the third subharmonic was ramped (linearly) to 250 kV in 10 ms to capture and bunch the beam when the beam energy reached approximately 2.40 GeV. After the beam was captured and compressed by the subharmonic cavities to <~ 2.5 ns (which occurred at a beam energy of approximately 3.16 GeV), the primary 352-MHz system was turned on and ramped to full power. The cavity mode parameters for the unloaded Q, shunt impedance, and coupling from the last section were used for the 3rd and twelfth subharmonic cavities. The design parameters $Q_o = 40,000$ and $Rs = 221$ MΩ were used for the quality factor and total shunt impedance of the four 352-MHz booster cavities. In all the simulations, elegant modeled tuning the 117- and 352-MHz cavities on resonance instantaneously at a given turn after injection when the bunch length was short enough for efficient capture.

Figure 1 shows the results of the simulation where 110,000 particles were used. The figure shows the beam captured and accelerated to 7 GeV by both subharmonic and 352-MHz systems without particle loss. The full-width bunch length plotted shows a transient at injection due to longitudinal phase-space mismatch where the initial momentum spread of the beam was ± 1%. Particle losses at injection were about 0.5% due to the mismatch. To reduce beam loss and enhance bunch purity, the 352-MHz system ramp profile was chosen to be a two-term, fourth-order polynomial (linear and quartic terms used), which guarantees a near linear ramp for approximately 50 ms after system turn-on. The full power level of the 352-MHz system is 10 MV.

The most critical point where particle loss can occur is when the 352-MHz system is turned on. Eight simulations were performed where the phase of the 352-MHz system was varied, which showed that particle loss starts to occur when the phase differs by more than ± 1 degree from nominal. The phase tolerance for the 117-MHz system at turn-on was found to be somewhat more relaxed at ± 5 degrees from nominal. A crucial design issue for the 352-MHz system is how to achieve ± 1-degree phase stability at system turn-on.

CONCLUSION

The studies presented here indicate that a subharmonic system optimized using both third and twelfth
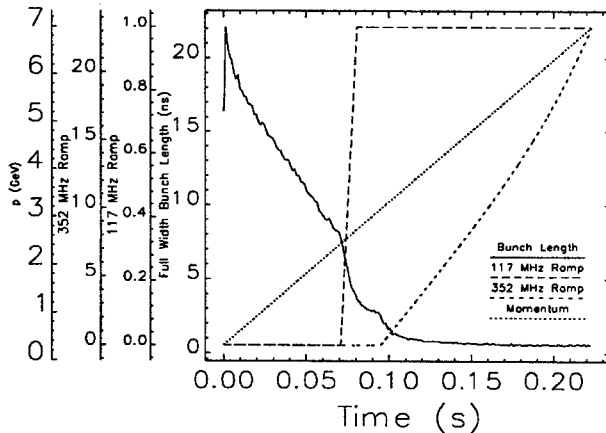
Figure 1: Full-width bunch length, 117- and 352-MHz ramps, and momentum as a function of time. Shown is the rapid bunching when both 117- and 352-MHz rf systems are powered. In this simulation no particles are lost when the ramped rf systems are powered. Not shown in the figure is the constant ramp profile (200 kV) of the twelfth subharmonic system. The 117-MHz and 352-MHz ramps are in arbitrary units. The peak gap voltage for 117- MHz and 352-MHz systems was 200 kV and 10 MV, respectively. Both 117-MHz and 352-MHz systems were tuned to resonance instantaneously when the ramp profile first becomes greater than zero.

subharmonic cavities (117.3 and 29.3 MHz) provides the minimum total gap voltage required to capture and accelerate a 15-ns linac macropulse at up to 10 nC with ± 1% energy spread. The simulations also show particle losses less than one part in 110,000 when including radiation damping, quantum excitation, and rf cavity beam loading. The only particle losses were found to be at injection due to phase-space mismatch. Optimization of the subharmonic capture idea requires knowledge of the gap voltage that can be achieved with an actual cavity. In general, the lower the cavity frequency the harder it is to engineer a cavity that can sustain a given gap voltage without breakdown. Phase and amplitude control of both subharmonic and 352-MHz systems also need to be carefully considered so that bunch purity is preserved and operational flexibility is maintained. Phase stability is particularly important for the high-power 352-MHz system, which preliminary simulation studies show needs 1-degree regulation at turn-on. Future optimization studies need to include amplitude stability tolerance studies for each ramped rf system at turn-on. In addition,

elegant has recently been modified to include realistic modeling of cavity tuning using a ramp profile.

The two-frequency, subharmonic capture system considered here has both advantages and disadvantages. On the one hand, up to a 20-ns pulse can be captured while requiring only a single 29-MHz cavity. This cavity would be very large and difficult to build and operate at up to 200-kV gap voltage. Operationally, a two-frequency subharmonic system would be more difficult to operate and manage spares. A good compromise and the focus of ongoing simulation studies is to use one or two sixth subharmonic cavities operating at 58.7 MHz and a total gap voltage of 400 kV. Using this frequency, most if not all of an 8- to 10-ns pulse can be captured. With two sixth subharmonic cavities, a degree of redundancy can be achieved; if one cavity becomes inoperable, the other can be used to fill the storage ring at the expense of bunch purity.

ACKNOWLEDGEMENTS

REFERENCES

[1] N. S. Sereno, M. Borland, "APS Booster Low Emittance Lattice Commissioning Results," these proceedings.

[2] H. Wiedemann, Particle Accelerator Physics: Basic Principles and Linear Beam Dynamics, Springer-Verlag, pp. 290-291, 1993.

[3] J. Murphy, Synchrotron Light Source Data Book, Version 4 NSLS/BNL, pp. 18, May 1996.

[4] M. Borland, elegant: A Flexible SDDS-Compliant Code for Accelerator Simulation, APS Light Source Note LS-287, September 2000.

[5] R. Kustom, 38.9 MHz Capacitively-Loaded Coaxial Cavity Design for the Booster, APS Light Source Note LS-26, June 1985.

[6] R. Kustom, Folded Coaxial Line Design for the 38.9 MHz Booster Cavity, APS Light Source Note LS-28, July 1985.

NEW INSERTION DEVICE VACUUM CHAMBERS AT THE ADVANCED PHOTON SOURCE *

Emil Trakhtenberg, Greg Wiemerslage, Patric DenHartog and Branislav Brajuskovic,
Advanced Photon Source, Argonne National laboratory, Argonne, Il 60439

Abstract

Six new types of insertion device vacuum chambers have been designed at the Advanced Photon Source (APS). One chamber has been designed for the APS canted undulator beamlines, two for the Canadian Light Source (CLS), and three for BESSY II. For the double canted undulators and CLS, a new extrusion shape with an oval aperture (not elliptical as usual) was developed and extruded. That required a thorough stress analysis and some compromise, which included a small increase of the vacuum chamber wall thickness. The details of the stress analyses and design of the chambers, along with lessons learned, are presented.

INTRODUCTION

The APS at Argonne National Laboratory developed a number of special vacuum chambers for the insertion devices (ID) [1]. Similar vacuum chambers designed and fabricated at Argonne National Laboratory are in use also at the Berlin Synchrotron Radiation Source (BESSY-II), Swiss Light Source (SLS), and European Synchrotron Radiation Facility (ESRF). This report is about a new type of ID VC designed and manufactured recently for the APS, Canadian Light Source (CLS) and BESSY-II.

NEW EXTRUSION SHAPE

All previous ID VC had an elliptical aperture. The deflection under atmospheric pressure for such a shape, even with 1 mm wall thickness, is below 100 μm per wall. Nevertheless, from the accelerator physics point of view, such a shape is not ideal. Each injected particle traces a rectangular area in x-y space because x and y motions are independent. The elliptical chamber reduces the aperture required for injection because some particles are lost at the corners of the ellipse. A rectangular aperture with small radiuses at the corners makes a better fit to the particle trajectories.

Of course, the deflection of the wall for a VC with a rectangular aperture is more than for an elliptical one. To keep the deflection reasonably small, we have found a compromise after a number of iterations: the horizontal aperture of the chamber was slightly decreased from ±20 mm to ±18 mm and the wall thickness was increased from the standard 1 mm to 1.25 mm while maintaining the same outside dimension of the ID VC as before: 10 mm. The new shape of the vacuum chamber is shown in Fig. 1.
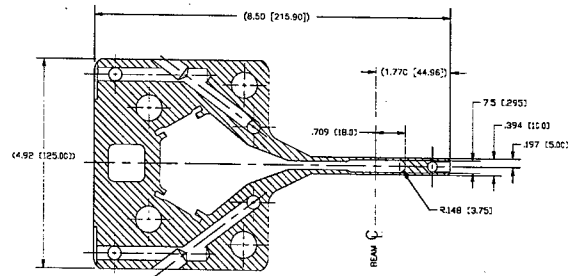
Fig 1: 7.5 mm vacuum chamber cross section.

Final results of the deflection calculation and stress analyses are shown in Fig. 2. The deflection at the location of the beam center is about 120 microns per side, and stresses are far away from the yield data.
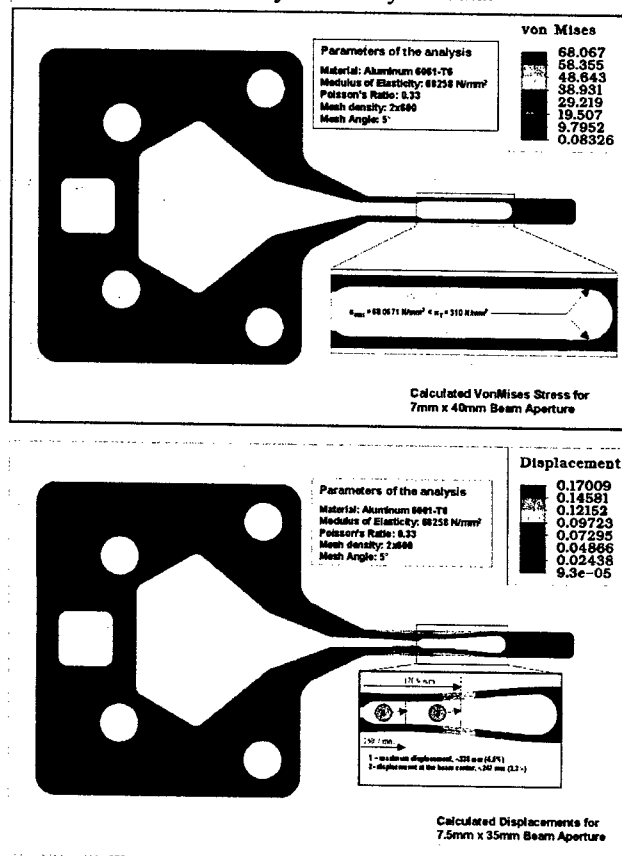
Figure 2: Stresses and deflection for 7.5 mm ID VC.

The extrusions of this new chamber were made, as usual, at Taber Metal, Russellville, Arkansas. Such a complicated extrusion shape, as always, is a puzzle, and this time it required 5 attempts. A uniform speed of the metal flow throughout the whole cross section must be achieved to yield a proper extrusion. Fig. 3 shows the extrusion cross sections after the second attempt and after the final attempt.
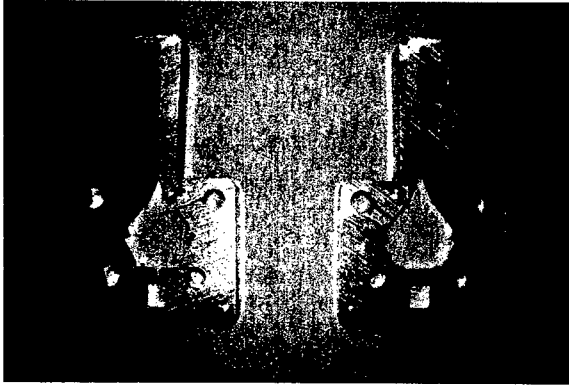
Figure 3: Extrusion cross section (left: second attempt, and right: final one).

DOUBLE-CANTED UNDULATOR VACUUM CHAMBERS

Three new sectors at the APS will be equipped with a new shape chamber, which will accommodate two undulators A and three dipole magnets [2]. From this straight section users can get two beams with a 1 mrad angular separation. The new VC will have the same length as usual (~5 m), but we added one additional set of beam position monitors (BPM) in the middle the of vacuum chamber to control the beam separation (Fig. 4).
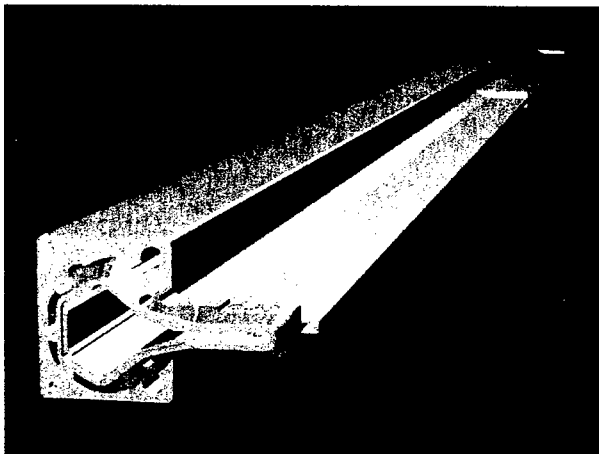
Figure 4: Double-canted undulator vacuum chamber.

End boxes for the 7.5 mm VC have almost the same design as in the previous APS ID VC [3]. The design of the RF-transition cone and its cooling was simplified. Such changes were implemented for the first time in the design of the ID VC for the SLS and proved to be

successful. During the design of this chamber, we have paid more attention to the smoothness of the RF-transition from the ID VC aperture to the standard accelerator vacuum chamber aperture (Fig. 5).
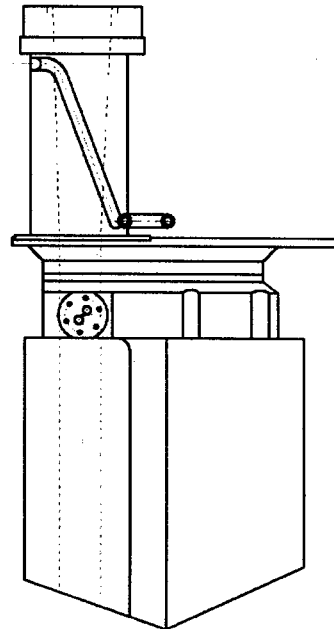
Figure 5: Smooth joint between vacuum chamber and end box.

Vacuum chambers for the same application will be used at the CLS with vertical apertures of 7.5 mm and 12 mm. The major difference in the design is that, for the CLS, two sets of BPMs were placed in the middle of the vacuum chamber. Also, the chamber length is shorter.

NEW VACUUM CHAMBERS FOR "BESSY-II"

Six new ID VCs are being manufactured now for BESSY-II: two standard ones, as APS has made previously and four short chambers with water cooling. The original 11 mm extrusion for BESSY-II had no provisions for the water cooling, so a gun-drilling procedure was used to place four cooling channels inside the body of the extrusion. One additional tube was welded to the flat plate and placed in a milled grove close to the VC aperture. Multiple screws and radiation-resistant thermal-conducting glue were used to enhance heat transfer. To avoid contamination of the chamber surface during the cleaning and certification, the glue applied only after final installation of the chamber in to the storage ring. One such chamber also has a laser channel welded to the downstream flange. The drawing of this chamber is shown in Fig.6.
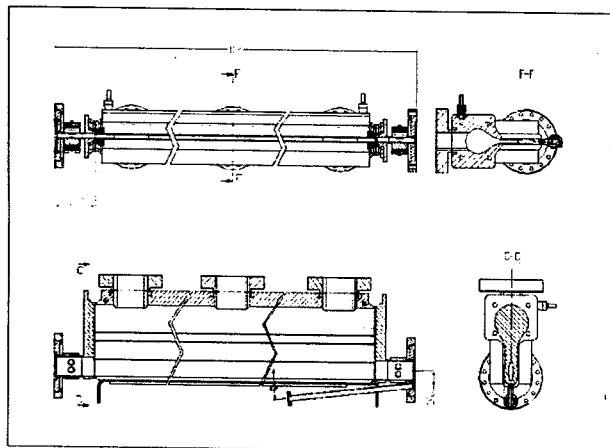
Figure 6: Vacuum chamber for BESSY-II with water cooling and laser channel.

REFERENCES

[1] P. Den Hartog, J. Gagliano, G. Goepner, J. Noonan, E. Trakhtenberg, G. Wimerslage, Proc. PAC-2001, Chicago, IL, July 2001, pp.607-609.

[2] Patrick Den Hartog, Glenn Decker, Lois Emery (ANL). "Dual Canted Undulators at the Advanced Phton Source, PAC-2003, Portland, Oregon, May 2003.

[3] E. Trakhtenberg, E.Gluskin, Shenglan Xu "The vacuum system for insertion devices at Advanced Photon Source", Rev. Sci. Instruments, Vol. 66 (2), pp.1809-1811, (1995).

DUAL CANTED UNDULATORS AT THE ADVANCED PHOTON SOURCE*

Patric K. Den Hartog[#], Glenn A. Decker, Louis J. Emery
Advanced Photon Source, Argonne National Laboratory, Argonne, IL 60439, USA

Abstract

At the Advanced Photon Source (APS), 34 straight sections are reserved for the installation of insertion devices for users. Each straight section allows space for up to two 2.4-meter-long devices. By sacrificing 0.4 m of undulator from each device and introducing a one milliradian chicane with three small electromagnets, two separate experimental programs can be conducted using the same straight section, thereby potentially doubling the scientific output with the same real estate. The design of the straight section and front end and plans for implementation and commissioning of this scheme at the APS during May 2003 are presented.

INTRODUCTION

The Advanced Photon source is a third-generation synchrotron radiation facility serving a wide variety of users. Since operations began in 1996, 30 of the available sectors have been allocated to various groups. Because of the increasing scarcity of unallocated beam line real estate, new ideas for enhancing productivity from the remaining straight sections have been considered. One of these ideas is the canted undulator (CU) straight section. In this configuration, a chicane is created with a trio of dipole magnets with an undulator in each leg (Figure 1). The result is an angular separation between the x-ray beams that can be exploited downstream to create two independent beam lines from a single straight section. The first application of the CU scheme at APS was implemented for an experimental program in polarization studies that uses both hard (>3 keV) and soft (0.5 – 3 keV) x-rays. A 270 μrad separation between the two x-ray beams was created with permanent magnet dipoles.
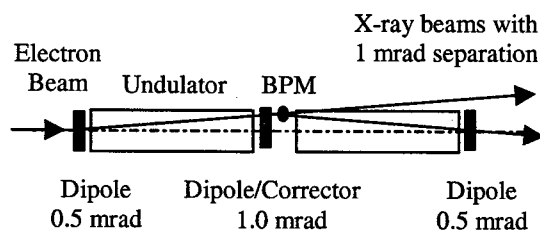
Figure 1. Schematic layout of a CU straight section showing the angular separation of the x-ray beams produced by the three dipoles. The dipoles are placed symmetric about the center of the straight section and the BPM is displaced 113 mm downstream.

Deflecting the soft x-ray beam outward using a pair of horizontally deflecting mirrors further increased the

separation between beam lines. This scheme was successfully implemented in 1999 [1]. For programs requiring two hard x-ray beams, however, additional angular separation of the x-ray beams by the dipoles is required as the deflecting mirrors lose their effectiveness at higher energies.

CU BEAM LINES

Protein crystallography experiments have grown in importance at many synchrotron facilities, occupying a growing proportion of the available beam lines. The unparalleled brilliance of third-generation facilities has made high throughput possible but in many cases the maximum usable x-ray flux is determined by sample lifetime. Typically the biology beam lines operate with only a single 2.4-m-long undulator in the 5-m-long straight section. Thus the research programs can benefit if more beam lines can be built within the available experimental floor space. The tradeoff is a somewhat reduced available length for undulators and a concurrent reduction in the x-ray flux and brilliance. Still, for some groups the gain in experiment throughput more than compensates the reduction in x-rays. Three new groups at APS are currently planning to use the CU arrangement.

CU COMPONENTS

The CU system consists of two shortened undulators, a special insertion device vacuum chamber, dipoles, and a corrector for the chicane and a specialized front end.

Undulators

The standard undulator used at the APS is a 2.4-m-long 3.3-cm-period hybrid planar magnetic structure mounted on a welded aluminum strongback [2]. To make room for the chicane dipoles, 5 periods were removed from each end. The strongback is normally supported by a gap-separation mechanism at the Airy points (.22315L from each end) to minimize the distortion of the magnetic structure by equalizing the droop of the overhanging ends and of the sag at the midpoint between the two supports. The reduction in magnetic attraction force at the ends causes an increase in the overall amplitude of the droop. Finite element calculations of the structure suggested that the deformation was within tolerances, which was confirmed by magnetic measurements [3].

ID Vacuum Chamber

APS has designed a number of small-aperture insertion device (ID) vacuum chambers based on aluminum extrusions [4]. Recently, a new extrusion was developed that changed the profile from an ellipse to an oval [5]. This new profile was used for the CU straight section. A

capacitive RF beam position monitor (BPM) was located at the center of the chamber, between the undulators, and displaced outboard horizontally 1.18 mm to match the electron beam trajectory.
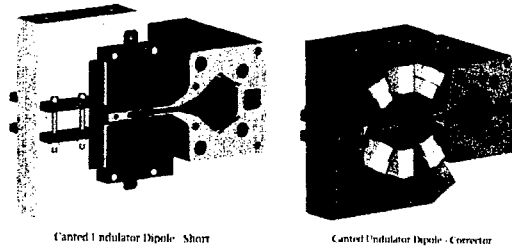
Figure 2. Short dipole (left) and corrector magnet.

Dipoles and Correctors

In order to provide maximum flexibility for operation of the storage ring, electromagnets were chosen for the dipoles. To maintain the symmetry of the chicane, the center dipole was designed to be twice as long as the end dipoles but with the same field. All three magnets are operated in series with a single power supply.

Although the IDs are designed and tuned to eliminate gap-dependent steering, some small residual remains (<30 Gauss-cm first integral and <61,000 Gauss-cm^2 second integral). In order to maintain the independence of the two beam lines, an x-y corrector was installed between the IDs that allows up to 30 μrad of steering correction. In this way, minor steering variations of the first undulator can be compensated with the APS feed-forward beam stabilization system [6] so as to eliminate any effect on the trajectory of the inboard beam by the first undulator. All of the steering magnets, including the x-y corrector, were designed to be installed over an existing ID vacuum chamber (Figure 2). The two undulators, three dipoles, and corrector were measured magnetically as a group on the APS 6 m bench. No gap dependence of the magnetic field was seen due to the proximity of the dipole magnets to the undulator magnetic structure. One possible failure mode occurs if the three dipole magnets responsible for the 1-mrad separation are de-energized, resulting in two co-linear x-ray beams, exceeding the front-end thermal design limits. For this reason, the power supply will be interlocked to the machine protection system and the stored beam will be dumped when $I_{mag} < 0.75\ I_{nominal}$ and $I_{SR} > 130$ mA.

Front End

A major challenge of the CU design was the thermal load on the front end [7]. The original front ends installed at the APS were designed to allow operation with a maximum x-ray power of 6.6 kW and maximum normal incidence power density of 0.6 kW/mm^2 [8]. Later versions of the front end were designed for 9 kW total power and 0.8 kW/mm^2 power density. Because of the desire to increase the stored beam current at APS in the

Table 1: Canted Undulator Front End Parameters

	PS1	PS2
Stored beam current (mA)	200	
Total power from two undulators (kW)	20.4	
Power density at normal incidence (kW/mrad^2)	281	
Temperature and equivalent stress for h=0.015 W/mm^2°C, T_0=20 °C)	**PS1**	**PS2**
Incident angle	0.91°	0.91°
Peak normal incidence power density (kW/mm^2)	0.79	0.64
Peak incident power density (W/mm^2)	12.7	10.4
T_{max} on Glidcop® strike surface (°C)	278	248
T_{max} on OFHC copper (°C)	180	163
T_{wall} of cooling channel (°C)	143	129
Maximum stress, σ_{eff} (MPa)	394	347
Temperature and equivalent stress for h=0.015 W/mm^2°C, T_0=20 °C)	**FM1**	**FM2**
Distance from center of straight section (m)	16.9	17.7
Inlet aperture (mm)	[64 x 26]	[46 x 17]
Exit aperture (mm)	[40 x 14]	[26 x 5]
Device active length (mm)	600	600
Vertical taper angle	0.57°	0.57°
Horizontal taper angle	1.15°	0.95°
Peak normal incidence power density (kW/mm^2)	1.10	1.02
Peak vertical incidence power density (W/mm^2)	11.0	10.1
Peak horizontal incidence power density (W/mm^2)	22.2	16.8
T_{max} on Glidcop® strike surface (°C)	218	198
Maximum stress, σ_{eff} (MPa)	397	333

future, it was decided to design for a maximum allowable stored beam of 200 mA. This placed a severe constraint on the design of the first mask and first photon shutter. Also, the horizontal displacement of the two beams required that the glancing incidence surface of the photon shutters be horizontal rather than vertical, which would have been desirable from the standpoint of reducing the incident power density. Shu et al. [8] developed a V-shaped shutter for the previous front end version 1.5 that could withstand 12 kW of total power, but this design was not practical for two separated beams. The requirement to absorb two separate x-ray beams led to a unique design for the photon shutters. The chosen design intercepts the beams on a horizontal Glidcop® strike plate in the closed position and functions as a vertical mask in the open position. Glidcop plate, chosen for its superior strength
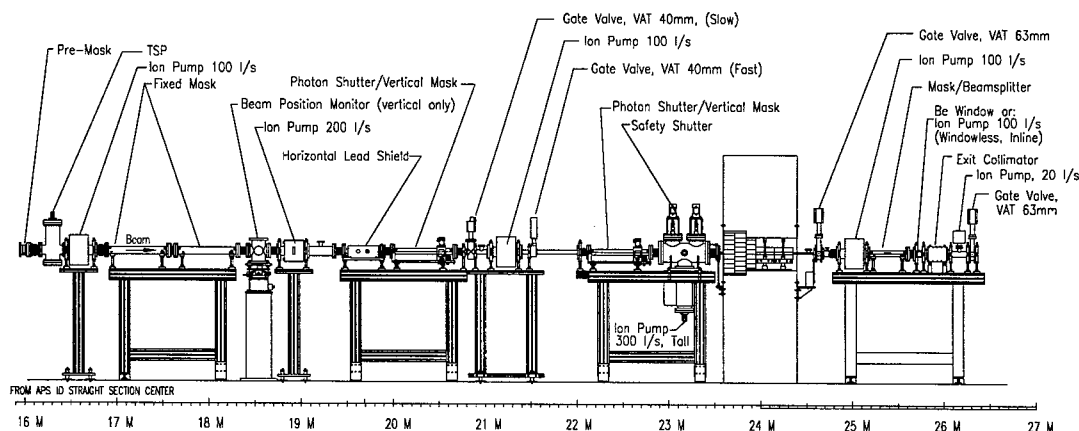
Figure 4. Layout of the components of the front end for the canted undulator beam lines.

compared to Glidcop bars or rounds, was brazed to the top internal surface of the Cu body. The lower OFHC Cu surface can only see a missteered beam in the open position at highly glancing angle (0.24°). The relatively small separation of the beams at the entrance of the front end also contributed to a difficult thermal engineering challenge. To enhance the film coefficient, h, all of the high-heat-load components have spring inserts in the cooling channels [9]. These inserts are much less prone to corrosion or erosion than the wire mesh that was used in earlier front-end components. Also, since the pressure drop due to the wire coils is much less than with the wire mesh, the saturation temperature rises. With a typical inlet pressure of 110 psig, the output pressure is > 75 psig and the minimum saturation temperature is 160°. Table 1 shows the thermal design limits for the system, the two photon shutters, PS1 and PS2, and the two fixed masks, FM1 and FM2. Design rules of $T_{max} < 300°$ C and $\sigma_{eff} <$ 450 MPa were used in order to limit the risk of fatigue failure due to thermal cycling. Figure 4 shows a layout of the front end for a CU beam line.

BEAM MISSTEERING LIMITS

The storage ring components are protected from an errant photon beam by a beam position limit detection (BPLD) system. When the 1-mrad dipoles are correctly powered, the two x-ray beams will move together under the influence of accidental closed orbit perturbations. For this reason, beam position monitors mounted on the extreme ends of the insertion device vacuum chamber trigger the machine protection system if the average trajectory through the two devices exceeds predefined limits, i.e., the beam is dumped within 500 microseconds when one of the BPMs at the ends of the straight section exceeds pre-calculated limits. The system is armed when one of the ID gaps is closed below 60 mm. For normal straight sections, the BPLD horizontal limits are calculated for an angle missteering of ± 0.9 mrad. For the CU, the limit will be 0.4 mrad, which is a significant reduction. For optimized steering through the front end,

we are aligning the beam line and the accelerator components in a consistent way and expect the beam to be well centered in the rf BPMs and the probability of false trips to be very low.

REFERENCES

[1] J. W. Freeland, J. C. Lang, G. Srajer et al., Rev. Sci. Instrum. **73** (3), 1408 (2002).

[2] E. R. Moog, I. Vasserman, M. Borland et al., in *Proc. 1997 Particle Accelerator Conference*, edited by M. Comyn, M.K. Craddock, M. Reiser et al. (IEEE, 1997), pp. 3224.

[3] M. Erdmann, B. Brajuskovic, and P. Den Hartog, in *Proc. of the 2003 Sync. Rad. Instrm. Conf. (to be published)*.

[4] P. Den Hartog, J. Gagliano, G. Goeppner et al., in *Proc. 2001 Particle Accelerator Conf.* (IEEE, 2001), pp. 607.

[5] E. Trakhtenberg, G. Wiemerslage, and P. Den Hartog, in *these proceedings* (2003).

[6] G. Decker and O. Singh, in *Proc. of the 8th Internat'l. Conf. on Accelerators and Large Experimental Physics Control Systems* (SLAC, 2002), pp. 249.

[7] Y. Jaski, E. Trakhtenberg, J. Collins et al., in *Proc. of the 2nd International Workshop on Mechanical Engineering Design of Synchrotron Radiation Equipment and Instrumentation*, edited by S. Sharma (ANL, Argonne, IL, 2003), pp. 390.

[8] D. Shu, M. Ramanathan, and T. M. Kuzay, Nucl. Instrum. Methods **A 467-468** (1), 762 (2001).

[9] J. Collins, C Conley, and J. Attig, in *Proc. of the 2nd International Workshop on Mechanical Engineering Design of Synchrotron Radiation Equipment and Instrumentation*, edited by S. Sharma (ANL, Argonne, IL, 2003), pp. 409.

LAYOUT OF A FEMTOSECOND X-RAY SOURCE AT BESSY II *

H.-J. Bäcker, J. Bahrdt, H. A. Dürr, V. Dürr, W. Eberhardt, A. Gaupp, E. Jaeschke, K. Holldack,
S. Khan, D. Krämer, H.-C. Mertins, W. B. Peatman, G. Reichardt, T. Quast, M. Scheer,
F. Senf, G. Wüstefeld (BESSY, 12489 Berlin, Germany)
I. Hertel, F. Noack, W. Sandner, I. Will, N. Zhavoronkov (MBI, 12489 Berlin, Germany)

Abstract

The generation of femtosecond x-ray pulses with circular polarization is planned at BESSY II. The paper describes the underlying principle ("femtoslicing"), its technical implementation, and the expected output, based on simulations and measurements.

INTRODUCTION

Probing structural changes and magnetic phenomena on a sub-picosecond time scale with x-rays is a new and exciting scientific field, initiated by the advent of femtosecond lasers and techniques to convert ultrashort visible pulses into x-rays. Compared to other approaches such as harmonic generation or plasma sources, the generation of ultrashort synchrotron radiation pulses described below offers a wider range of photon energies, better tunability in energy and polarization, and a larger brightness in the x-ray regime. This technique, now dubbed "femtoslicing", was proposed [1] and experimentally demonstrated [2] at the Advanced Light Source in Berkeley. The principle is to modulate the energy of electrons by the field of a femtosecond laser pulse co-propagating with an electron bunch in a wiggler ("modulator"). Off-energy electrons are then transversely displaced using a dispersive magnetic field to extract the short component of radiation emitted in a subsequent undulator ("radiator").

A user facility to produce x-ray pulses of 50 fs duration with linear and circular polarization is under construction at BESSY II in Berlin. Pilot experiments will concentrate on circular magnetic dichroism to probe element-specific spin and orbital properties of magnetic materials with unprecedented time resolution. Furthermore, the interaction of femtosecond laser pulses and electron bunches will provide a unique opportunity to gain experience in view of BESSY's soft-x-ray FEL project [3]. The energy-modulation process is the basis of FEL-seeding schemes such as high-gain harmonic generation [4] or sideband seeding [5]. Other hot topics are electron-laser synchronization and femtosecond diagnostics for electrons and photons.

TECHNICAL IMPLEMENTATION

All major hardware components described in this paragraph are underway and will be installed in a shutdown pe-

riod early in 2004. The layout of the femtosecond facility is based on the following considerations:

Minimum pulse duration: In order to preserve the temporal characteristics of the laser pulse in the electron distribution, the modulator and radiator should be placed in the same straight section. A scheme with two straight sections would not only use more space, but would require to operate the storage ring in a special isochronous mode.

Minimum background: As discussed in a previous paper [6], mirrors to create an image of the source for short-pulse separation may cause intolerably large background due to non-specular reflection. If, on the other hand, the energy-modulated electrons are displaced from the core bunch by a sufficiently large angle such that their respective radiation cones do not overlap, the short pulse can be separated just by an aperture. This angle should be at least 1 mrad which – assuming an energy modulation of 1% of the beam energy – implies a 100 mrad bending magnet between modulator and radiator.

Minimum impact on the storage ring: The previous considerations suggest to place two undulators and a dipole magnet of 100 mrad bending angle in a straight section of 5.4 m length, where the dipole must be part of a closed orbit bump. In the layout shown in figure 1, the bump is formed by three dipoles, all within the straight section. Other schemes involving the adjacent achromats would strongly break the symmetry of the storage ring and would make its circumference incompatible with the synchrotron.

The Laser System

The obvious choice for a laser with pulses of 30-50 fs duration is a Ti:sapphire system with chirped pulse amplification, operating at 800 nm wavelength. Analytical estimates and simulations suggest a pulse energy of 2-3 mJ, allowing for losses between laser and interaction region, moderate deviations from the diffraction limit ($M^2 < 1.5$), and for extracting a pulse of 0.1 mJ that is naturally synchronized with the short x-ray pulse for pump-probe applications. The repetition rate should be as high as possible, only limited by N/τ, where N is the number of electron bunches and τ is the decay time of the energy modulation (8 ms for BESSY II). The laser system will comprise an oscillator and two amplifier stages. In the first stage, liquid-nitrogen cooling of the Ti:sapphire crystal allows in principle to extend the repetition rate to the 10 kHz regime [7]. The second stage is required to produce multi-mJ pulses and will initially operate at 1 kHz [8].
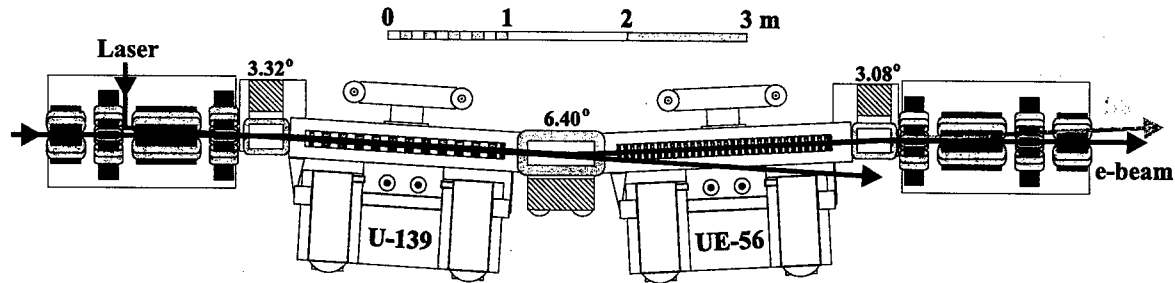
Figure 1: The magnetic system of the femtosecond facility, comprising two undulators (U-139 and UE-56) and three dipole magnets (yellow). Also shown are adjacent quadrupole (red) and sextupole (green) magnets.

Magnetic Components

For resonant laser-electron interaction, the modulator has to operate at the laser wavelength i.e. 800 nm. The U-139 is a planar wiggler with a period length of 139 mm and 10 full periods plus endpoles. The amplitudes of the first and third harmonic of the magnetic field are 1.4 T and 0.2 T, respectively.

In view of magnetic dichroism studies with variable polarization, the radiator (UE-56) is an apple-type elliptical undulator with a period length of 56 mm and 30 periods [9]. In March 2003, the original UE-56 double undulator was removed and its downstream part reinstalled on a new support structure.

Angular separation is provided by a 0.56 m long C-shaped dipole magnet with a bending angle of 112 mrad (6.4°). Together with two 0.28 m long dipoles, it forms a closed orbit bump. A moderate bending radius of 5 m (with a field of 1.13 T at 1.7 GeV) leaves ample margin to operate the storage ring at higher beam energy.

Vacuum System

The vacuum chambers will be replaced over a length of 9 m. The undulator chambers with a vertical aperture of 11 mm are fabricated by extrusion and subsequent machining of aluminium [10]. Other chambers with vertical apertures ranging from 11 mm to 35 mm are made of stainless steel. Carefully designed absorbers account for synchrotron radiation from the dipole magnets and the U-139 wiggler.

The laser beam enters through a window 2.3 m upstream of the U-139 center. Laser and wiggler radiation travel through a narrow pipe to a mirror chamber 3.9 m downstream of the U-139 center. Here, two mirrors extract the laser pulses as well as the near-visible part of the U-139 spectrum for diagnostics purposes. Synchrotron radiation from the UE-56 radiator exits at an angle of 3.08° with respect to the straight section axis.

Diagnostics

Beam position monitors at either end of both undulators help to keep the electron beam position fixed while the laser can be adjusted using remotely controlled mirrors. The laser-electron interaction requires spectral, transverse and

longitudinal overlap of laser pulses and spontaneous U-139 radiation. Once its x-ray part with 1-2 kW average power is removed by water-cooled mirrors, the U-139 radiation can be analyzed by the same instruments as the laser using e.g. a CCD camera, photo diodes, or a spectrometer.

Energy modulation can be detected and optimized by monitoring coherent infrared radiation a few meters downstream of the modulator. When the path length differences of energy-modulated electrons exceed the laser pulse length, they leave a hole in the longitudinal electron distribution, which is gradually filled by other electrons over $\sim 1/4$ of the ring circumference. This hole, being equivalent to a bunch of $\sim 20~\mu$m length, will emit coherent radiation at wavenumbers of 10-50 cm^{-1}. Here, BESSY can rely on its expertise from low-momentum-compaction studies [11].

Frontend and Beamlines

The orbit bump requires a 3.08° shift of the UE-56 frontend and two existing beamlines, one with a plane-grating monochromator (PGM), the other with a spherical-grating monochromator. The PGM beamline will be modified to improve the focus at the experiment, and a second branch will be added for femtosecond applications, where a coarser grating will be used to reduce pulse lengthening at the expense of energy resolution.

EXPERIMENTAL STUDIES

In order to verify the angular separation concept, the angular characteristics of radiation from the UE-56 undulator were studied experimentally and by simulation using the code WAVE [12]. An aperture 12 m downstream of the source with no optical elements inbetween was moved across the radiation distribution while monitoring the intensity at 708 eV behind the PGM monochromator with a GaAs photodiode. In order to cover a large angular range, the electron beam was moved by angular orbit bumps in 0.2 mrad steps. Previous results [6] were limited by noise at $3 \cdot 10^{-5}$ of the distribution maximum, while the noise floor of the measurement shown in figure 2 is at 10^{-7}. The data closely resemble the predicted distribution (solid line), a convolution of the calculated single-electron radi-

ation characteristics and the electron distribution, assuming a Gaussian core with tails from scattering processes. As a consequence of the angular bumps, radiation from the adjacent dipole magnets appeared below 10^{-6} (not shown in the figure). In the femtosecond facility, dipole radiation background will be avoided by an appropriate choice of the electron orbit.

EXPECTED PERFORMANCE

A simulation with 10^5 pseudo-electrons in the laser field, radiating according to their angle, energy and arrival time in the radiator, yields the broad distribution shown in figure 2 (dashed) from which the short pulse will be selected by an aperture. Its photon yield, signal-to-background ratio, spectrum and pulse duration can be estimated, depending in detail on many parameters – electron bunch and laser properties, background assumptions, settings of the undulator, monchromator and aperture. As an order of magnitude, 10^6 photons per second and 0.1% bandwidth can be expected to enter the beamline, if the laser repetition rate is 1 kHz. The measured angular distribution suggests a signal-to-background ratio better than 10. Thanks to the proximity of the radiator to the modulator, the pulse duration will be $\sim$ 50 fs (fwhm).

Since the modulator is in a dispersive region, the longitudinal offset of energy-modulated electrons does not just increase with distance from the modulator, but is, in fact, a complicated function of . As shown in figure 3, an electron with Δ / = 0.01 is almost isochronous in the next straight section (= 15 m) and crosses the nominal orbit at a large angle, allowing for angular separation of short x-ray pulses. One straight section further away (= 30 m), the angle of the electron trajectory is small, but the horizontal displacement is large. For femtosecond applications, the longitudinal deviation (0.33 ps) can be reduced by manipulating the momentum compaction of the ring. In addition, it is conceivable to tune the undulator in this straight section (U-125) to the second or third harmonic of the U-139 and test high-gain harmonic generation.

ACKNOWLEDGEMENTS

REFERENCES

[1] A. A. Zholents, M. S. Zoloterev, PRL 76 (1996), 912.

[2] R. W. Schoenlein et al., Science 287 (2000), 2237.

[3] M. Abo-Bakr et al., NIM A 483 (2002), 470.

[4] J. Wu, L.-H. Yu, PAC 2001, Chicago, 2716.

[5] W. Brefeld et al., NIM A 483 (2002), 62.

[6] S. Khan, H. A. Dürr, EPAC 2002, Paris, 700.

[7] S. Backus et al., Opt. Lett. 26 (2001), 465.
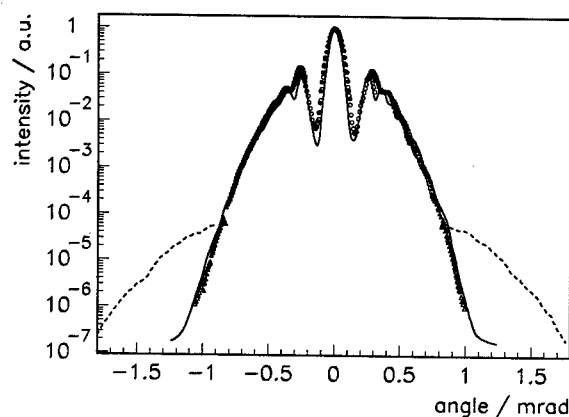
Figure 2: Measured (points) and calculated (solid line) angular distribution of UE-56 radiation at 708 eV. Also shown is the calculated short-pulse component (dashed lines).
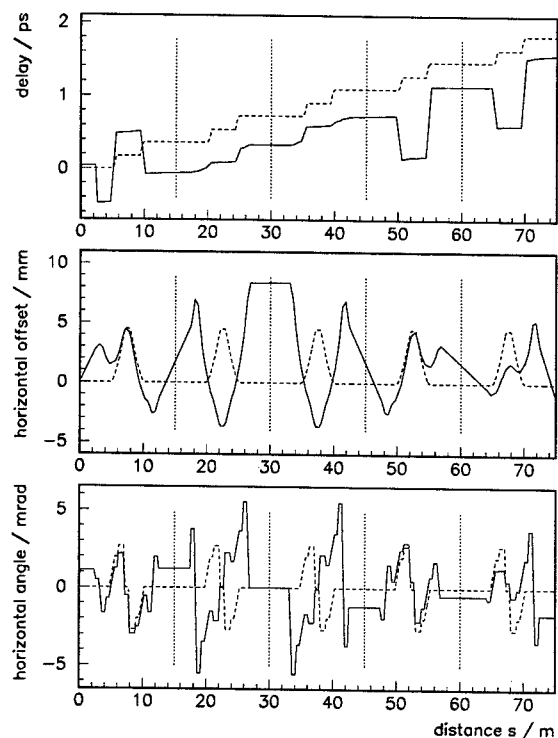
Figure 3: Calculated delay, horizontal offset and angle for an electron with energy deviation Δ / = 0.01 as function of distance from the modulator. For comparison, the dashed lines show the same functions for a modulator in a dispersion-free region. Each vertical line marks the center of a straight section.

[8] F. Noack, I. Will, M. Zhavaronkov, MBI Berlin, unpublished.

[9] J. Bahrdt et al., NIM 467-468 (2001), 21.

[10] E. Trakhtenberg et al., this conference.

[11] M. Abo-Bakr et al., PRL 88 (2002), 254801.

[12] M. Scheer, BESSY Berlin, unpublished.

COHERENT SYNCHROTRON RADIATION EXPERIMENTS AT BESSY II *

K. Holldack, P. Kuske, G. Wüstefeld (BESSY, Berlin, Germany)
and H.-W. Hübers (DLR, Berlin, Germany)

Abstract

Coherent synchrotron radiation (CSR) in the steady state and bursting mode is generated. The emitted radiation is analysed in the time and frequency domain. A step mode Fourier transform (FT) spectrometer is applied to analyse bursting CSR.

INTRODUCTION

Coherent synchrotron radiation in the sub-THz and THz range ($1THz \rightarrow \lambda = 0.3mm \rightarrow k = 30cm^{-1}$) has been detected at several electron storage rings [1]. The radiation is mostly emitted in irregular bursts, indicating a bunch instability. The BESSY II storage ring is presently the only place, were stable CSR can be produced [2]. The stable CSR is generated in a special mode of the ring optics, the 'low alpha' optics, where the momentum compaction factor α can be reduced by a factor of 100 and more to shorten the bunches. Our present understanding of the bursting and stable emission process is based on an interaction of the bunch with its own CSR wake field [3], [4], [5], [6]. At these short bunches the CSR impedance dominates the chamber impedance.

At currents below a threshold value, these wake fields lead to a static non-Gaussian, deformation of the bunches. The deformed bunches emit a CSR spectrum of much shorter wavelength than expected for purely Gaussian bunches. Increasing bunch current yields a larger bunch shape deformation and more CSR power and finally, above the current threshold, a bursting CSR emission. The stable CSR emission process is of large interest for application in THz spectroscopy. The application of this radiation for THz spectroscopy was recently shown in a dedicated experiment at BESSY [7]. As will be demonstrated in this note, in case of the bursting CSR emission good spectroscopic results can be achieved, if a FT spectrometer in the step mode is applied.

Moreover, the emitted bunch THz radiation opens new possibilities of beam diagnostics. For example, the power spectrum of the bunch can be measured by FT spectroscopy or unstable bunch oscillations can be detected in real time emitted CSR. This tool becomes the better, the shorter the bunches, were conventional methods such as strip line signal detection or streak camera measurements reach their limits.

In this note we present results from stable and bursting CSR emission. We firstly discuss the experimental set up, next we compare results from THz signals measured by

a spectrum analyser and FT spectra. The emitted power of stable and bursting bunches is compared and finally high quality FT spectra measured from strongly bursting bunches are shown.

EXPERIMENTAL SET UP
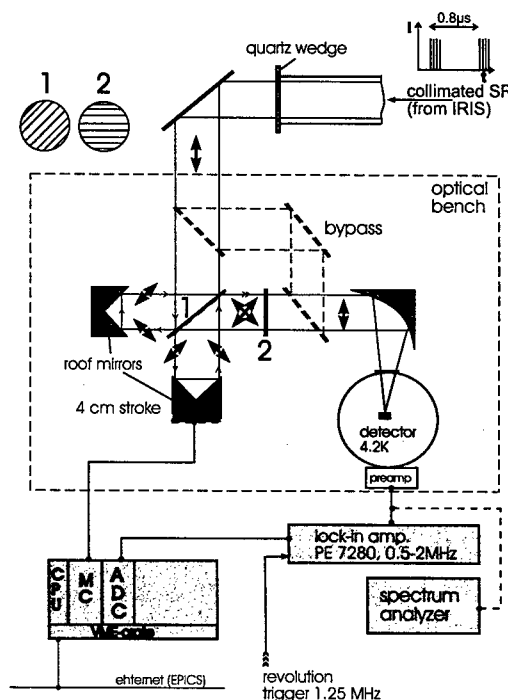
Figure 1: CSR detection system at the IRIS beam port.

Part of the CSR experiments were performed while the storage ring optics was tuned to the 'low alpha' optics with reduced bunch length. Starting from values which correspond to values of the regular user optics with $f_{s0} = 7.2kHz$, $\alpha_0 = 7.2 \cdot 10^{-4}$ and a zero current rms-bunch length of $\sigma_0 =4mm$, $f_s(\sim \alpha^2)$ can be lowered to less than 1 kHz. The 'zero current' bunch length is reduced in proportion with f_s, however, already at rather low currents (10-100 μA/bunch) there will be a bunch lengthening by potential well deformation.

The THz radiation is emitted in dipoles where the vacuum chamber has a full height of 35mm, and a cutoff wavelength of about 4 mm. The CSR experiments were performed at the BESSY infrared experimental place IRIS [8]. It has an acceptance of 60x40 mrad^2 and the photon beam is always kept in vacuum. The experimental set up is shown in Fig.1. The collimated THz-beam leaves the

vacuum section by a quartz window, then passes through a Martin-Puplett FT spectrometer into a liquid He cooled InSb-detector. The pre-amplified signal is fed through a lock-in amplifier and then via an ADC into the EPICS control system. The beam revolution frequency of 1.25 MHz is used as the reference for the lock-in amplifier. The InSb-detector is sufficiently fast to resolve the beam revolution time of 800 ns. Typically 200 out of 400 rf-buckets were filled to get a strong signal modulation avoiding any base line drifts and low frequency noise. Typical current values are 10 to 100 μA (5 to 50 $\cdot$ 10^7 electrons) per bunch. The equipment is sufficiently sensitive to measure the incoherent radiation spectrum down to current values of 1 μA per bunch.

TIME AND FREQUENCY CSR MEASUREMENTS
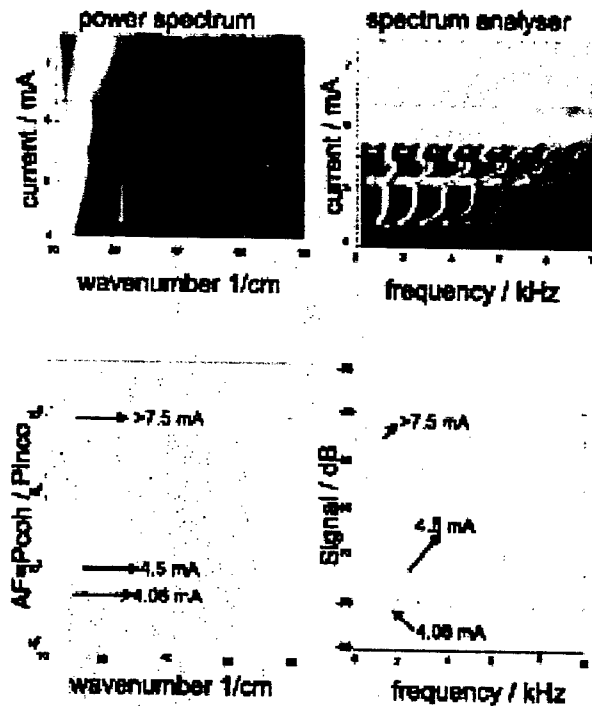
Figure 2: Current dependent scan of THz records from the FT spectrometer (left) and the spectrum analyser (right).

The temporal stability of the CSR signal can be well analysed by detecting sidebands of the revolution harmonics with a spectrum analyser. This is demonstrated with CSR signals analysed during the regular BESSY single bunch shift, where already CSR emission is visible at a low rate below 4 mA and with increasing power above 4 mA. In Fig. 2 a sequence of coherent THz-signals as a function of the bunch current is displayed, recorded during beam storage time with typical life times of few hours and varying from 7.5 to 4 mA. The left side shows the

THz-power spectrum from 2 cm^{-1} to 80 cm^{-1} (λ = 5 0.125mm)normalised by the incoherent spectrum of the same current.

To describe the enhanced CSR compared to the incoherent power the amplification factor, $_F$, is introduced. The radiated power $_\lambda$ at the wavelength λ is given by, $_\lambda$ = $_\lambda$ $_e(1 + f_\lambda$ $_e)$, where $_e$ is the number of electrons, $_\lambda$ the emitted power by one electron and f_λ is the form factor. f_λ is calculated from the square of the longitudinal FT of the charge density. From this relation we define F = $_\lambda$ $_{incoh}$ = f_λ. The incoherent power spectra $_{incoh}$ used for normalisation were recorded with a low current, multi bunch filling. Below 5 cm^{-1} $_F$ is declining, indicating that there might be still some coherent content in the 'incoherent' spectra (see Fig. 2 bottom, left).

The right part of the figure shows spectrum analyser (Rohde & Schwarz FSEK30) data of the temporal oscillation frequencies in the 0 to 10 kHz range. These signals are very sensitive to bursting emission. At 4 mA bunch current, CSR is emitted by a stable process, no sideband signal is detected with the spectrum analyser. The corresponding FIR spectra show intensities at around and below 10 cm^{-1}. The CSR spectrum contains up to 10000 times more intensity than the incoherent one. At 4.3 mA a periodic signal is detected with the spectrum analyser, with frequencies of about 1.3 kHz and higher harmonics. This is just at the threshold of the bursting process. With increasing current the spectral power spectrum gains intensity and is increasing at higher wave numbers. There are some pronounced transitions in the oscillation structure visible, immediately at 4.3, 5.2, 5.3 and 5.6 mA, followed by a broad range between 5.7 and 6.3 mA and finally above 6.4 mA a broad, nearly constant band of more than 10 kHz appears with some distinct lines (Fig. 2 right side). Sometimes these transitions are combined with sudden intensity changes (see Fig. 3), the full range of signal power was found to be increased by 45dB.

There are three cuts through the data to show better resolved details, at 4.06 mA just below the bursting threshold, at 4.5 mA when there is periodic bursting, and at 7.5 mA when the bursting shows an irregular temporal pattern with few distinct lines on it. The THz spectra at the first two cuts are quite similar, at 7.5 mA, within the bursting range, there is a broad line building up at around 40 cm^{-1}.

From single bunch streak camera measurements it is known, that the 4mA bunches are 50 % longer than the 'zero current' value and at 7.5 mA the bunches are around 85 % longer. This lengthening does not reduce the emission process as one would expect from Gaussian bunches, it still becomes more powerful. The spectrum analyser delivers a tool, to clearly distinguish between steady state and bursting CSR and to define the thresholds with better than 10 μA precision.

BURSTING CSR

The power of the detector signal was recorded as a function of the bunch current at different α settings. To have a well defined bunch current, this was performed in a single bunch measurent with a corresponding low signal in the steady state. The records started at currents below the bursting threshold. The bursting threshold is very well localised, as demonstrated in Fig.3, starting at very low current already. At small f_s-frequencies corresponding to small α-values the recorded CSR power grows continuously with increasing beam current. In this case, all power of the side bands (see Fig.2 for comparison) are still within the 300 Hz bandwidth of the detection system. If f_s 5 kHz the side bands could shift out of the accepted bandwidth range, leading to a strong modulations of the signal strength. The plots at f_s=7.2 kHz are measured with and without the two 7 Tesla wave length shifters (wls). The increased energy spread caused by the wls probably shifts the bursting threshold to larger values. In all 5 records the CSR stays stable only up to a power level of -85dB.

These data show, that the CSR power in the bursting case could be more than a factor 100 stronger (45dB), the upper limit was not yet tested. For further discussion of the bursting threshold see [6]. The power of the incoherent radiation into the acceptance of the IRIS beam line was estimated and scaled with the steady state radiation. An average value of 1 mW was found, whereas for the bursting emission 100 mW and more could be achieved.

The Martin-Puplett-FT spectrometer is operating in the step mode. At each position the spectrometer integrates the transmitted power for 200 ms. In case of bursting emission this leads to very reliable spectra, useful for spectroscopic applications. In Fig. 4 there are three successive runs demonstrating this. The life time of the beam was around 10 h and the synchrotron tune was $f_s = 1.85$kHz. The 44.45 mA (resp. 43.91mA, 43.28mA) multi bunch current, distributed in 200 buckets, is about 5 times above the

Figure 4: Interferogram and power spectra taken at strongly bursting CSR.

bursting threshold. In the range from 3 to 20 cm^{-1} the reproducibility is 2 % and better. The advantage for operating in the bursting range is the enhanced power output, such that strong absorbing or small samples can be probed in a range not accessible by other methods.

ACKNOWLEDGEMENTS

REFERENCES

[1] A.R. Hight-Walker, U. Arp, G.T. Fraser, T.B. Lucatorto, J. Wen, Proceedings of SPIE **3153**, 40 (1997).

Å. Andersson, M.S. Johnson, B. Nelander, Proceedings of SPIE **3775**, 77 (1999).

G.L. Carr, S.L. Kramer, J.B. Murphy, R.P.S.M. Lobo, D.B. Tanner, Nucl. Instr. and Meth. A **463**, 387 (2001).

J. M. Byrd, W. P. Leemans, A. Loftsdottir, B. Marcelis, M. C. Martin, W. R. McKinney, F. Sannibale, T. Scarvie, C. Steier, Phys. Rev. Lett. **89**, 224801 (2002).

[2] M. Abo-Bakr, J. Feikes, K. Holldack, H.-W. Hübers, G. Wüstefeld, Phys. Rev. Lett. **88**, 254801 (2002).

M. Abo-Bakr, J. Feikes, K. Holldack, P. Kuske, W. B. Peatman, U. Schade, H.-W. Hübers, G. Wüstefeld, Phys. Rev. Lett. **90**, 094801 (2003).

[3] K. Bane, S. Krinsky, J.B. Murphy, "Micro-Bunches Workshop", BNL, 1996, AIP Conf. Proc. **367**, 191 (1996).

[4] G. Stupakov, S. Heifets, Phys. Rev. ST AB **5**, 054402.

[5] M. Venturini, R. Warnock, Phys. Rev. Lett. **89**, 224802.

[6] Coherent emission of synchrotron radiation and longitudinal instabilities, M. Abo-Bakr et al., see PAC2003 proceedings.

[7] J. Singley et al., submitted to phys. Rev. Lett.

[8] U. Schade, A. Röseler, E.H Korte, F. Bartl, K.P Hofmann, T. Noll and W.B. Peatman., Rev. Sci. Instr. **73**(3), 1568 (2002).

Figure 3: Bursting intensities at different α settings of the machine optics.

LATTICE OPTIONS FOR A 5 GEV LIGHT SOURCE AT CORNELL*

I.V. Bazarov[†] and G.H. Hoffstaetter, Cornell University, Ithaca, NY 14850

Abstract

Cornell University has proposed an Energy Recovery Linac (ERL) based synchrotron-light facility [1] which can provide improved X-ray radiation due to the high beam quality which is available from a linac. To additionally utilize beam currents that are competitive with ring-based light sources, the linac has to operate with the novel technique of energy recovery. Cornell plans to address the outstanding issues of high-current injector, higher-order mode damping and extraction from superconducting RF environment, etc. in a downscaled prototype ERL prior to submitting a proposal for a full-scale machine. The flexibility of linacs allows for different modes of operating the ERL X-ray source, each of which requires specific manipulations of longitudinal phase-space that restrict the choice of the lattice. Here we discuss the different proposed modes of operating the ERL X-ray source and present options for corresponding lattices.

INTRODUCTION

Linac-based accelerators have the potential to deliver beam of exceptional quality in terms of both transverse and longitudinal emittance. While the former is determined primarily by the properties of the electron source, the latter typically is an interplay of initial bunch length, RF waveform and beam optics with nonzero time of flight terms (sometimes referred to as momentum compaction).

To match the natural bandwidth of X-rays in the central cone from an N-period undulator, the fractional rms energy spread of the electron beam has to be $\leq (5N)^{-1}$ (a factor of 2 here comes from the beam energy squared dependence of the emitted photon energy, and the additional factor is due to FWHM to rms conversion of the radiation bandwidth $\sim 1/N$). This way spectral brightness in the fundamental is guaranteed to increase proportionally with the number of undulator periods. When linac-based accelerators reduce the beam energy spread to values below those achievable with storage rings, efficient use of very long undulators becomes possible, improving monochromaticity of X-rays.

The much shorter bunch length than that from storage rings is thought to enable new areas of ultra-fast X-ray science. Herein, we address longitudinal phase-space manipulations feasible in an ERL and consider various options for lattices and regimes of operation of such a light source.

The electron beam is created in a source [2], in which the space charge forces create an effective randomization of phase-space positions, so that we here assume a Gaussian

beam in the longitudinal phase-space between the injector system and the linac. In the Cornell project, beam energy is planed to be 10 MeV at that region. The bunch length and energy spread are planed to be $\sigma_{z_0} = 0.64$ mm and $\sigma_{\delta_0} = 10^{-3}$. An energy recovering linac will accelerate this beam to 5 GeV. Magnetic lattice after the linac with adjustable time of flight terms, together with an off-crest acceleration of the beam, will then be used to reduce the bunch length to the desired amount. We herein compute limits on the achievable bunch length and provide analytical expressions that describe longitudinal dynamics in an ERL.

ANALYTICAL EXPRESSIONS

Significant insight into the beam's longitudinal phase-space after the linac and the bunch compressor can be obtained by investigating higher-order transfer maps. These describe the change of the phase-space variables, δ (fractional energy deviation from that of central ray) and z (difference of path lengths between a particle and that of central particle respectively) by a Taylor series. We will indicate phase-space coordinates between injector and linac by an index 0, after the linac by an index 1, and after the bunch compressor by an index 2. Retaining leading orders only, one writes:

$$\delta_1 \simeq \frac{E_0}{E_1}\delta_0 + \alpha_1 z_0 + \frac{\alpha_2}{2!}z_0^2 + \frac{\alpha_3}{3!}z_0^3 + \cdots. \quad (1)$$

The first term, δ_0, is due to the uncorrelated energy spread after the injector, normalized by the full beam energy, α_n is partial derivative at the location of the central ray: $a_n = \partial^n \delta_1/\partial z_0^n|_{z_0=0}$. Injected beam is accelerated from energy E_0 to E_1 according to $E_1 - E_0 = E_{\max}\cos(\varphi + k_{RF}z_0)$, i.e. coefficients α_n are:

$$\alpha_{2n-1} = (-1)^n \frac{E_{\max}}{E_1} k_{RF}^{2n-1} \sin\varphi,$$

$$\alpha_{2n} = (-1)^n \frac{E_{\max}}{E_1} k_{RF}^{2n} \cos\varphi,$$

here $E_{\max}$ is the maximum energy gain in the linac, φ is the off-crest phase, and $k_{RF} = 27$ m^{-1} is the wave number corresponding to the fundamental RF frequency. Note that we have transformed the particle position z into a time of flight term assuming that the velocity is c along the complete linac. Assuming a Gaussian beam between injector and linac with rms bunch length $\sigma_{z_0} = \sqrt{\langle z_0^2 \rangle}$ of the injected bunch and no initial energy-length correlation, the rms energy spread $\sigma_{\delta_1}^2 = \langle \Delta\delta_1^2 \rangle$, with $\Delta\delta_1 = \delta_1 - \langle \delta_1 \rangle$, and emittance $\epsilon_{z1}^2 = \langle z_1^2 \rangle\langle \Delta\delta_1^2 \rangle - \langle z_1\Delta\delta_1 \rangle^2$ after the linac become

$$\sigma_{\delta_1}^2 = \left(\frac{E_0}{E_1}\sigma_{\delta 0}\right)^2 + \alpha_1^2\sigma_{z0}^2 + \frac{\alpha_2^2 + 2\alpha_2\alpha_3}{2}\sigma_{z0}^4 + \cdots,$$

$$\epsilon_{z1}^2 = \left(\frac{E_0}{E_1}\sigma_{\delta 0}\right)^2\sigma_{z0}^2 + \frac{\alpha_2^2}{2}\sigma_{z0}^6 + \cdots .$$

The energy spread from the injector, $\frac{E_0}{E_1}\sigma_{\delta 0} \approx 2\times 10^{-6}$, is extremely small and will be neglected here, $\sigma_{z0} = 0.64$ mm corresponds to $\sigma = 0.017 = 1°$ of the 1.3 GHz RF phase or 2.1 ps. The off-crest RF-phase $\varphi \ll 1$. Thus, for all practical cases of interest, energy spread and emittance are estimated as

$$\sigma_\delta^2 \approx (\sigma\varphi)^2 + (\sigma^2/\sqrt{2})^2, \qquad (2)$$
$$\epsilon \approx \sigma^3/\sqrt{2},$$

here the bunch length and emittance without a subscript z are given in units of the RF phase, i.e $\sigma = k_{RF}\sigma_z$ and $\epsilon = k_{RF}\epsilon_z$.

Bunch compression

After an achromat, i.e. when only purely chromatic terms matter but transverse particle coordinates do not influence the time of flight, longitudinal phase-space transform using TRANSPORT notations is written as:

$$z_2 = z_1 + R_{56}\delta_1 + T_{566}\delta_1^2 + U_{5666}\delta_1^3 + \cdots , \qquad (3)$$
$$\delta_2 = \delta_1 .$$

Inserting δ_1 from equation (1) leads to the function $z_2(z_0,\delta_0)$. Ignoring the energy spread $\frac{E_0}{E_1}\sigma_{\delta 0}$ due to the injector leads to

$$z_2 = (1 + R_{56}\alpha_1)z_0 + (T_{566}\alpha_1^2 + R_{56}\frac{\alpha_2}{2})z_0^2$$
$$+ (U_{5666}\alpha_1^3 + T_{566}\alpha_1\alpha_2 + R_{56}\frac{\alpha_3}{6})z_0^3 + \cdots .$$

Since the initial coordinates z_0 and δ_0 are distributed by a Gaussian, the rms bunch length after the bunch compressor $\sigma_{z2}^2 = \langle z_2^2\rangle - \langle z_2\rangle^2$ evaluates to

$$\sigma_{z2}^2 \approx (1 + R_{56}\alpha_1)^2\sigma_{z0}^2 + 2(T_{566}\alpha_1^2 + R_{56}\frac{\alpha_2}{2})^2\sigma_{z0}^4$$
$$+6(1 + R_{56}\alpha_1)(U_{5666}\alpha_1^3 + T_{566}\alpha_1\alpha_2 + R_{56}\frac{\alpha_3}{6})\sigma_{z0}^4. \quad (4)$$

When the first and second order optics is chosen to minimize the bunch length, $R_{56} = -1/\alpha_1$ and $T_{566} = \alpha_2/(2\alpha_1^3)$, the final bunching is given by

$$\sigma_{z2}^2 = 15(U_{5666}\alpha_1^3 + \frac{3\alpha_2^2 - \alpha_1\alpha_3}{6\alpha_1^2})^2\sigma_{z0}^6 . \qquad (5)$$

After the third order bunch compression with $U_{5666} = (\alpha_1\alpha_3 - 3\alpha_2^2)/(6\alpha_1^5)$ the leading order term becomes

$$\sigma_{z2}^2 = 96(V_{56666}\alpha_1^4 - \frac{15\alpha_2^3 - 10\alpha_1\alpha_2\alpha_3 + \alpha_1^2\alpha_4}{24\alpha_1^3})^2\sigma_{z0}^8 . \qquad (6)$$

It is instructive to estimate various terms in expressions (4-6) in case of bunch compression to different order assuming typical ERL parameters, e.g. $\sigma = 1°$, $\varphi = 10°$.

The leading order in the initial energy spread $\sigma_{\delta 0}$ of the rms bunch length after the bunch compressor is neglected in equation (4) since it is very small. In case of linear bunch compression, $R_{56} = -1/\alpha_1$, it only amounts to $R_{56}\frac{E_0}{E_1}\sigma_{\delta 0} \approx 2\times 10^{-6}/(k_{RF}\varphi) = c\cdot 1.4$ fs. In case of an ideally linear compressor, i.e. $T_{566} = U_{5666} = 0$, equation (4) is estimated to $\sigma_{z2} \approx \sigma^2/(\sqrt{2}k_{RF}\varphi) = c\cdot 150$ fs. When the second order time of flight term is chosen for second order bunch compression, equation (5) leads to $\sigma_{z2} \approx \sqrt{15}\sigma^3/(2k_{RF}\varphi^2) = c\cdot 40$ fs. Expression (5) provides maximum compression for the parameters $R_{56} \approx k_{RF}^{-1}/\varphi = 21$ cm, $T_{566} \approx k_{RF}^{-1}/(2\varphi^3) = 3.4$ m. The third order bunch compression would be obtained for $U_{5666} \approx k_{RF}^{-1}/(2\varphi^5) = 113$ m. Assuming $V_{56666} = 0$, equation (6) then leads to $\sigma_{z2} \approx 15\sigma^4/(\sqrt{6}k_{RF}\varphi^3) = c\cdot 13$ fs.

Note that R_{56}, T_{566}, and U_{5666} should be of the same sign. Although achieving this is very hard in a conventional chicane bunch compressor [3], it can be done with relatively small effort in the arc of a flexible storage ring [4].

It is also straightforward to estimate tolerances for the RF phase φ from (4). If the optics were adjusted to third order bunch compression for a phase φ and the phase varied by $\Delta\varphi$, the bunch length would change by $(\frac{\Delta\sigma_{z2}}{\sigma_{z0}})^2 = (\frac{\Delta\varphi}{\varphi})^2[1 + 8(\frac{\sigma}{\varphi})^2 + 2\sigma^2] \approx (\frac{\Delta\varphi}{\varphi})^2$. Again, for the example at hand, assuming that tolerable bunch lengthening from RF phase errors is $\Delta\sigma_{z2} = c\cdot 50$ fs, the allowed phase jitter is estimated to be $0.2°$. Assuming state-of-the-art RF phase stability of $0.1°$, the bunch length would be stable up to 20 fs. Since a better stability seems unrealistic, this suggests that a bunch compression of higher order than 2 will not lead to further improvements.

Energy Recovery

Energy recovery requires that the accelerated bunch passes through the linac a second time with a phase shift of π with respect to the first pass. This puts constraints on the time of flight terms of the lattice. Ideally, the lattice should be isochronous (including higher orders), so that the RF waveform that the linac imposes in the longitudinal phase-space is cancelled when the bunch passes through the linac the second time.

For slight deviations from isochronicity, it is sufficient to analyze the energy distribution at the location of the beam dump, indicated by an index 3:

$$E_3 = E_0 + 2E_{max}\sin[\varphi + k_{RF}(z_0 + \frac{\Delta z}{2})]\sin k_{RF}\frac{\Delta z}{2},$$
$$z_3 = z_0 + \Delta z.$$
$$(7)$$

Here $\Delta z = z_2(z_0,\delta_0) - z_0$ is a position shift of a particle in the bunch that was initially at z_0, which it experiences due to nonzero time of flight terms of the recirculating arc.

If a lattice deviates significantly from the isochronous condition, the two RF waveforms will not cancel out and some parts of the bunch can have an energy deviation from the mean energy that is relatively large compared to the

ejection energy. This is especially severe for particles with less energy than the mean, since they can be over-focused and lost in the last section of linac. Such scenario can be avoided by proper control of the time of flight terms of the return arc.

An additional energy loss due to synchrotron radiation in the recirculating arc has to be included in equation (7), effectively lowering the injection energy E_0. In case when $k_{RF}z_0 \ll \varphi \ll 1$, the condition for successful energy recovery simplifies to $-E_{max}\varphi k_{RF}\Delta z \ll E_0$, e.g. for $E_{max} = 5$ GeV, $E_0 = 10$ MeV, and $\varphi = 10°$, the shift Δz of any electron's position in the bunch after the return arc should be less than 0.4 mm. Note that the sign is important here, since only particles with too little energy are lost in the linac.

LATTICE OPTIONS

Optics of the Return Arc

The requirements for the optics of the return arc include: adjustable time of flight terms, dispersion-free regions for insertion devices, and low aberrations for emittance preservation. Different approaches were considered such as a lattice composed of identical achromats with adjustable R_{56}, etc. We favor a lattice design with non-periodic Twiss parameters, where negative dispersion of several meters is generated at certain locations, as opposed to a more conventional lattice made of compact achromatic cells with intrinsically small dispersion. Our choice allows effective control of higher-order time of flight terms with only a few moderately strong sextupoles for the whole return arc. Such an approach has been used in the design of an ERL in the CESR tunnel [4]. Furthermore, it was discovered that the only important terms for clean transport of the transverse phase-space for a beam with ERL parameters are the purely chromatic ones, thus, a lattice with corrected second-order dispersion T_{166} and its derivative T_{266} has sufficiently low aberrations to enable transport of low emittance ERL beam for all practical cases with virtually no emittance growth due to nonlinearities in transverse phase-space. Therefore, a second-order achromat where both geometric and chromatic aberrations cancel to zero is thought to be an unnecessary sophistication, especially since its qualities are achieved at the expense of relatively inflexible higher-order time of flight terms [3].

Linac optics

Various linac configurations are under consideration for ERLs. These include single-pass straight-section RF structures, split linac arrangement, and multi-pass scenarios. Computer simulations of beam break-up instability [5], [6] suggest that a single-pass configuration is essential for a high-current ($\sim$ 100 mA) machine assuming state-of-the-art damping of higher-order modes in superconducting RF cavities, although for a lower current ERL a multi-pass scheme seems very attractive.

A single-pass straight-section linac is thought to have an advantage of containing a minimal number of bend sections and reducing the danger of coherent synchrotron radiation effects, i.e. the linac could be used to produce very short, high brightness electron bunches, which might be of use for certain applications (e.g. for SASE produced light). On the other hand, the split linac option allows better control of the transverse beam envelope due to smaller mismatch of the accelerated and decelerated beam energies in each of the linac sections. Furthermore, a split linac can allow advanced longitudinal phase-space manipulations, such as energy spread compression. It is clear from equation (2) that the minimum energy spread is achieved for on-crest running and scales as the bunch length squared. On the other hand, longer bunches are preferable since they produce less higher-order mode power. Also, longer bunches require less compression in the injector at low energies, leading to better transverse emittances.

As an illustration, consider a linac split in two parts separated by a transport line with adjustable time of flight terms. The first section is operated with nonzero phase φ, which generates a correlated energy spread. One then uses this spread to induce a positive quadratic term in $\delta(z)$. The second section runs with a phase of $-\varphi$ removing both the linear and quadratic correlation and leading to a small energy spread after the second linac section. The optimum condition for the transport line separating the two linac parts in this case is given by $R_{56} = 0$, $T_{566} = \alpha_2/\alpha_1^3 \approx k_{RF}^{-1}/\varphi^3$ and $U_{5666} = 0$. The remaining leading order in the energy spread for this case, and with $V_{56666} = 0$, becomes $\sigma_{\delta_1} \approx 5\sqrt{\frac{3}{2}\frac{\sigma^4}{\varphi^2}}$. E.g. for a bunch length of $\sigma = 1.5°$ and $\phi = 10°$, one obtains $\sigma_{\delta_1} = 9 \times 10^{-5}$. For longer bunches the remaining energy spread would quickly become worse. Also, the RF tolerances set a limit to the smallest energy spread achievable with this scheme. If there is a mismatch $\Delta\varphi$ between the phases of the two sections, the energy spread is limited to $\sigma |\Delta\varphi| /2$. Thus, to preserve the small energy spread in the given example, the phase mismatch $\Delta\varphi$ has to be $\Delta\varphi < 0.4°$.

REFERENCES

[1] S.M. Gruner, M. Tigner (eds.), *Phase I Energy Recovery Linac (ERL) Synchrotron Light Source at Cornell University*, Report CHESS-01-003 (2001)

[2] C.K. Sinclair, I.V. Bazarov, *High Brightness, High Current Injector Design for the Cornell ERL Prototype*, Proceedings of PAC'03.

[3] W. Decking, G.H. Hoffstaetter, T. Limberg, *Bunch Compressor for the TESLA Linear Collider*, Report TESLA-2000-40 (2000)

[4] G. Hoffstaetter, I. Bazarov, D. Sagan, R. Talman, *A Lattice for a 5 GeV ERL in the CESR Tunnel*, Proceedings of PAC'03.

[5] I.V. Bazarov, *2-pass Possibility for ERL*, Report ERL-02-4, available at http://www.lepp.cornell.edu/public/ERL/

[6] I.V. Bazarov, G.A. Krafft, L. Merminga, *Linac Optics for Energy Recovery Linac*, Proceedings of PAC'01.

LIFETIME REDUCTION DUE TO INSERTION DEVICES AT BESSY II*

J. Feikes, G. Wuestefeld, BESSY, Berlin, Germany

Abstract

After closing insertion devices at BESSYII to smallest gaps beside appearance of a vertical tune-shift due to the natural focussing of the IDs, it is observed that beam lifetime is considerably reduced, up to 30 %. The reduction neither depends on machine tune nor on the settings of the four BESSY II harmonic sextupole circuits. Here measurements and analytical results to explain and cure this effect are presented.

INTRODUCTION

The 3rd generation light source BESSY II actually has 12 insertion devices in user operation [1]. A few of them have an impact on the machine performance when they are turned on. An important issue is the observed reduction of beam lifetime due to the closing of the undulators to narrow gaps. Typical lifetime values at 250 mA stored current, the standard value at injection, are 5h - 8h with all gaps opened. This can go down by 30-40 % to 3h - 5h when the most harmful IDs are closed. Lifetime reduction leads to the need of shorter injection intervals and subsequent a loss of user beam time as data taking during injection is not possible. Investigating these lifetime reductions we revealed that one has to distinguish between two different phenomena:

– lifetime reduction effects strongly depending on the machine tune

– lifetime reduction effects not depending on tunes but on the optics distortion cause by the ID.

Both effects may occur at the same time. Here it is reported on activities to cure them.

TUNE DEPENDENT EFFECTS

TUNE SCANS

When the UE56 undulator went into user operation at BESSY II it was realized that beam lifetime changed according to gap position. As this was a tune dependent effect, systematic tune scans around the working points had been performed (see also [2]). One scan lasts about 8 hours and data like lifetime, beam loss monitor rates and source sizes at the pinhole monitors were taken at approximately 2000 different pairs of values for the two transversal tunes. As an example in Fig. 1 the product current x lifetime (normalized to the current value at start of the scan) is painted in a colour code vs. the horizontal and vertical frequency shift
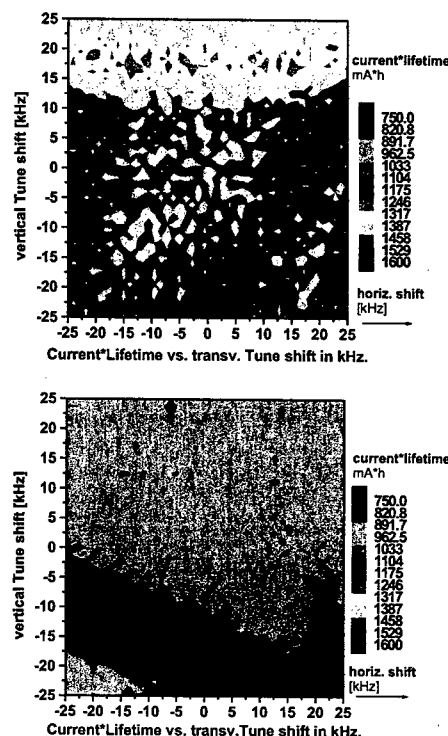
Figure 1: Tune scans with ID UE56 open (above) and closed to 16.6 mm (below). Parameter shown in colour code is current × lifetime in mA*h. Center points mark the actual working point at fx=1060kHz fz=925 kHz (17.848/6.74). BESSY II revolution frequency is 1249 kHz.

of the tune given in kHz. The beam revolution frequency is 1249 kHz, so the total axis range of 50 kHz corresponds to a fractional tune variation of 0.04. With all IDs opened only a vertical fourth order resonance at $fz \approx +20$ kHz corresponding to $4Qz=27$ is present. After closing the UE56 a squew octupole resonance appears (in the lower part of the diagram) with a lifetime degradation of up to 50 % relative to its value at open gaps. Initially the working point was located on that resonance but readjusted now vertically +20 kHz higher, about $\Delta Qz=0.016$ away from this resonance. The source of that fields driving this resonance could be identified [1]. and removed. The newly installed apple type IDs excite these resonances to a much less extent.

FEEDFORWARD

When all IDs are closed, their natural focussing induce a vertical tune shift of $\Delta f_z = +90$ kHz ($\Delta Q_z = 0.072$) much larger than the distance to the ID induced resonances. In order to fix the tune, a feedforward program for each ID was installed based on the SDDS toolkit [4] [1] The BESSY II optics consists of 16 double bend achromats and 16 straight sections [3]. Located outside the achromats there are 40 independent tunable quadrupole circuits each consisting of 2 quadrupoles. Standard tune correction is achieved with 32 of that circuits - the resting 8 circuits are used to define the horizontal betafunction in the straights. 16 circuits act focussing (F) and 16 are defocussing (D). Normally the tune is changed in a global way, which means that all F or D quadrupoles are changed by the same amount. Also the standard feedforward corrects in a global way adding the same increment to all F or D quadrupole power supplies with an amount depending on the value of the ID gap under consideration. Fig. 2 shows shifts of the vertical tune with feedforward "on" and "off" while ID gaps are changed. In this example a vertical tune shift of $\Delta f_z = +80$ kHz ($\Delta Q_z = 0.064$) without feedforward is reduced to +5 kHz, sufficiently small to avoid any resonance. The horizontal tune keeps constant within +/-2 kHz as well. Because the
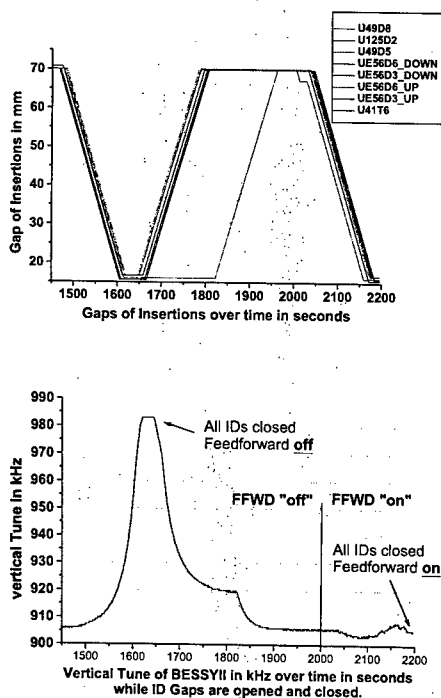
Figure 2: Upper picture: ID gaps in mm over time in seconds lower picture: corresponding value of vertical tune.

reference orbit keeps carefully centered in the quadrupoles

[1]Now most of the BESSYII feedfoward files operate under a new written program, based on a data bank system

routinely aligned by a beam based calibration, orbit stability is not affected despite the permanent changes in the quadrupole strengths due to ID movements.

DYNAMIC EFFECTS

OBSERVATIONS

Even with fixed tunes the strongest IDs (like the U125 producing a vertical tune shift of 28 kHz at its minimum gap of 15.7 mm) show considerable lifetime reductions. A tune scan does not reveal any resonance excitation, but the decrease of lifetime is independent of the working point. More observations:
– relative reduction of lifetime as function of gap runs parallel to the vertical tuneshift with gap
– optimum settings for harmonic sextupoles are independent of the value of the undulator gap
– a scraper measurements with gap open and closed does not give any hint on reduction of transversal aperture
– measurement of dynamic aperture using pinger magnets show that it is considerably reduced when ID gap is at closest value
– measurement of lifetime vs. cavity voltage shows that RF aperture is reduced from about 2.4 % (gap at 150 mm) to about 2.1 % (gap at 15.7 mm)
– only Touschek lifetime is reduced. Analysis of lifetime reductions with 100 mA beam current in 50 and 350 bunches and 0.25 -10 mA in a single bunch show that vacuum related lifetime contributions are not notably affected
– the effect depends on the transverse beam size (coupling).

OPTIC DISTORTIONS AND LIFETIME

Beside a tune shift the insertions generate also distortions of the optical functions. In order to compensate them, the strongest (U125) had a modified feedforward compensation ("local compensation") which beside the tune, also corrected the ID generated beta beat. This was achieved by powering that quadrupoles located in the same straight section as the ID with separate values from the others [2]. Reduction of beta beat was confirmed by direct beta function measurements (using the "golden rule"). But when closing the U125 gap to its narrowest value with this local feedforward, it was observed that life time degradation became worse, now 24 % instead of 16% (value with global feedforward active). As well as the origin of the effect this also had to be explained.

A tracking study (using MAD) of the complete nonlinear BESSY II optics predicts that the optical impact of the U125 reduces the dynamic aperture for off energy particles. Tracking results show that this does not only depend on the beat of the vertical beta functions, but even

[2]Simply compensating the natural tune shift of an undulator by the adjacent quadrupoles would strongly increase the beta beat in that straight. We used another method, adding about the same tune shift with the adjacent quadrupoles as that produced by the ID and then compensating the sum of both shifts in a global way. By this means beta beat keeps small everywhere.

stronger on the beat of the vertical beta phase. As an explanation for the life time reduction effect this is in accordance with all the observations stated above. As a consequence it was searched for a new feedforward scheme were not only the tune and the beta beat were corrected but also the vertical phase jump was kept localized. Fitting runs with MAD result in a feedforward pattern where all 40 available quadrupole circuits had to be used and each of them had a different but modest correcting strength (respecting the symmetry to the distortion). Fig 3 shows the relative change of each quadrupole strength due to the correction from the improved feedforward correction for narrowest gap of U125. The theoretically predicted distortion

No correction A   **Improved correction**

Local tune correction   **Global tune correction**

Figure 4: Vertical beta beat in % due to U125

Figure 3: Relative change of quadrupole strength due to action of the improved feedforward scheme.

of optical functions in four different feedforward schemes is shown in Fig 4 and Fig 5.The schemes are:

"no correction" - without feedforward

"improved correction"- scheme shown in Fig 3

"local tune correction" - correction of tune shift by only powering of adjacent quadrupoles

"global tune correction" - uniformly distributed correction.

We tried all these schemes at the U125. The predicted beta beats could be confirmed by direct beta function measurements.

Using the improved feedforward scheme life time reduction caused by the U125 could be improved from 16 % to 10% demonstrating that indeed phase beating is crucial in maintaining the dynamic aperture. Currently a very strong wiggler with a tune shift of Δf_z=+100 kHz and a accordingly strong impact on dynamic aperture started commissioning. In a first measurement at very low beam currents it was shown that an improved feedforward for this device also recovered considerably life time.

CONCLUSION

Effects **depending on tune** could be cured by:

– proper choice of working point

– fixing the working points using a feedforward.

– removing the resonance source inside the ID

no correction A   **improved correction**

local tune correction   **global tune correction**

Figure 5: Vertical phase beat in % due to U125

Not tune dependent effects could be traced down to be caused by a reduction of dynamic aperture for off-energy electrons. A cure was found which partially restored lifetime, using a special scheme of distributing the correcting quadrupoles strength used in the feedforward correction.

REFERENCES

[1] J. Bahrdt et al, "Elliptically polarizing insertion devices at BESSY II" Nucl. Instr. and Meth. in Phys. Res. A467-468 (2001) 21-29

[2] P. Kuske et al, Investigation of Non-Linear-Beam Dynamics with Apple II-Type Undulators at BESSY II, PAC2001, Chicago June 2001

[3] G. Wuestefeld et al, Optimization and Tracking Studies for the 1.7 GeV Light Source BESSY II, EPAC 94, London July 1994

[4] M. Borland, Application Programmer's Guide for SDDS Version 1.4, APS LS Note

A LATTICE FOR A 5 GeV ERL IN THE CESR TUNNEL*

G.H. Hoffstaetter[†], I.V. Bazarov, D. Sagan, R. Talman

Abstract

It has been proposed to build an Energy-Recovery Linac (ERL) based synchrotron-light facility at Cornell. Due to the high beam quality of a linac with photo injector, such a facility has the potential to provide better X-ray radiation than ring-based sources. To take advantage of the existing circular accelerator CESR for this 5 GeV ERL, it has been suggested that the linac should be split in sections that are at angles to each other and that half the CESR ring should be used as a return arc to connect the end of the last linac section to the beginning of the first. Here we specify the minimum optical requirements on such a layout and show a possible lattice for an ERL that uses CESR.

INTRODUCTION

Linear accelerators with a photo-emission electron source can produce transverse emittances and bunch lengths that are significantly smaller than those of storage rings. To build a light source that profits from this better beam, one has to accelerate to energies (several GeV) and use currents (several 100mA) that are typical for storage ring based light sources. This would require that klystrons deliver a power of order 1 GW to the beam. Without somehow recovering this energy after the beam has been used, such a linac would be practically unfeasible.

Energy recovery can be achieved when the high energy electrons are used to generate cavity fields which in turn accelerate new electrons to high energy. Since the high energy electron beam then delivers most of the RF power to the cavities, the required klystron power is very much reduced. However, to continuously transfer field energy from electrons to the RF cavities and back to new electrons, it is essential that the cavities are continuously filled with field energy and thus are operated in continuous wave (CW) mode. Therefore, cavities of an ERL should be super conducting (SC) since only SC cavities can achieve high fields in CW operation.

Since neither an electron source, nor an injector system, nor an ERL, has ever been built for the required large beam powers and small transverse and longitudinal emittances, the Wilson laboratory at Cornell University plans to build a prototype facility [1] that can verify the functionality of all essential devices and physical processes before endeavoring onto a large user facility.

While serving high-energy experiments, CESR has been used as the second generation synchrotron light source CHESS at 5 GeV. As a future light source for this labo-
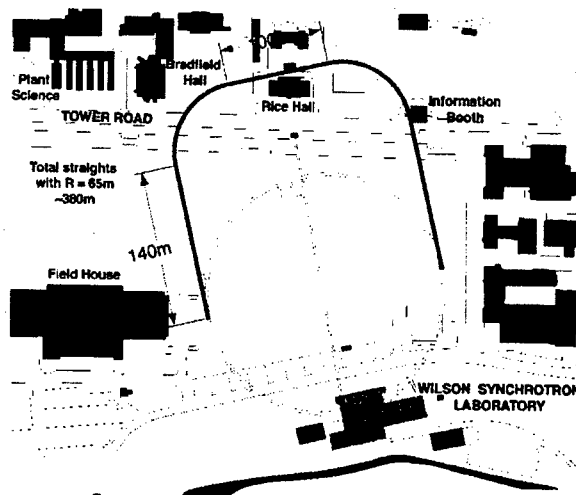
Figure 1: An ERL in an extended CESR tunnel

ratory, an ERL seems ideal. It can enlarge the wide range of applications of third generation light sources by producing beams similar to their CW beams, albeit with higher brilliance due to the much smaller horizontal emittance and possibly smaller energy spread. At the same time, it can serve more specialized experiments that require ultra small emittances for high spacial resolution or ultra short bunches for high temporal resolution [2]. After a successful prototype operation, it is therefore planed to build a large scale ERL light source at Cornell University. The current scheme has bunches of 77pC at the 1.3 GHz repetition rate of SC TESLA cavities with 20 MV/m, constituting a 100mA electron beam at 5 GeV. The normalized emittance should be 2μm and two operation modes should be possible: 2ps operation and short-bunch operation with less than 100fs.

AN ERL IN THE CESR TUNNEL

How the future light source at Cornell should be constructed is currently under investigation. Here we present an option that takes advantage of CESR, which will no longer be needed for high energy physics experiments after the CESR-c/CLEO-c project is phased down in about 5 years [3]. We have made a design that tries to reuse as much as possible of CESR. Whenever something could not be reused, we showed why not. While this study could have shown that the constraints of reusing the CESR tunnel are too tight, quite contrary it has turned out that the CESR tunnel could be extended for an ERL. This accelerator would reuse the tunnel, some components, and the in-

frastructure of CESR. The required extension of the tunnel is shown in Fig. 1. The three straight sections of the tunnel extension would house SC linacs of 140m, 100m, and 140m length. They are separated by arcs of 65m radius. A 10 MeV injector would send electrons from the South into the West straight section. These electrons would emerge from the third straight section with an energy of 5 GeV. The South half of the CESR tunnel would contain undulators and would return the electrons to the first linac section. There they enter the linac on the decelerating phase, thus each electron transfers its energy back to the cavities and emerges after the third straight section with 10 MeV into a dump.

The Site

In order to limit the cost of cooling, the accelerating gradient of the SC cavities should not exceed 20 MV/m. Thus, 250m of cavities would lead to 5 GeV of beam energy. However, much more space is required for the linac, since higher order mode (HOM) dampers and connecting tubes have to be places after each cavity and 2 quadrupoles have to be placed after each cryomodule of 8 cavities. Our analysis, which is based on 1.3 GHz cavities of the TESLA design, on four HOM couplers of the TTF type per cavity, and on one ferrite HOM damper of the CESR type per cavity, showed that for a beam tube radius of 39mm we could not obtain a fill factor larger than 67%. The total linac length would therefore have to be at least 373m. The tunnel extension shown in Fig. 1 has three straight sections with a total length of 380m. An extension of the CESR tunnel under the Cornell campus could infringe with existing and planed buildings and with infrastructure like power, water, or steam lines. A survey revealed that the top of the extended tunnel is nowhere closer to a steam line than 9.8m and nowhere closer to a foundation than 11.3m.

X-ray Needs

Before an ERL design could be made, it had to be determined how many undulators the X-ray users need and what types of undulator should be chosen. Together with the CHESS laboratory, it was decided that an initial design should contain two short undulators of 2m length, four with 5m length, and one 25m long undulator made of 5 modules. The beta functions should be 1m, 2.5m, and 12.5m in the center of these undulators respectively. The 1m beta function is designed for the production of micro beams, but a flexible lattice can produce larger beta functions easily. A facility with 7 undulators is relatively small, but considering that Cornell is a university and not a large national laboratory, this size might be favorable. Furthermore, it had to be decided how many undulators should be served with bunch length below 100fs. In this initial study only the 25m long undulator was required to have bunches with 100fs length. In short-bunch operation, the other undulators would have bunches of between 140fs and 600fs length.
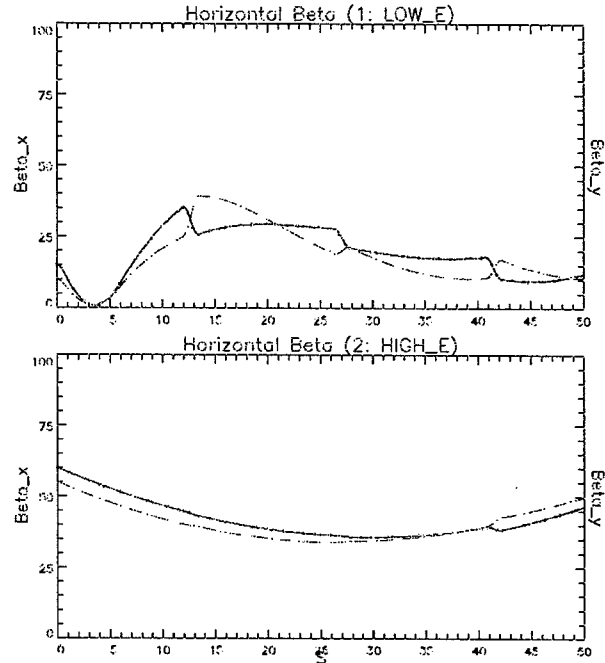
Figure 2: Beta functions at the start of the linac

Linac with Bends

While the necessity of segmenting the linac by bend sections initially seems unfortunate, it can have unexpected advantages for an ERL. The linac in an ERL contains one accelerating and one decelerating beam simultaneously, and these beams will have different paths in the bend sections. The two beams therefore have to be separated after the first bending magnet, then they have to be guided in two separate beam lines to be finally recombined in the last bending magnet. The advantage that such an arrangement can have over a 380m long linac is that the particle optics of the two different beams can be influenced separately in the two beam lines. While the two beams with initially very different energies (5 GeV vs. 10 MeV at injection) have to be guided by a common optical system for 380m in a single linac, in our design only 140m long sections are common to both beams. Consequently it is more difficult to find an acceptable optics for a straight linac, and in an initial design [2] a quadrupole triplet was needed after every cryomodule. In the design for the CESR extension that is shown in Fig. 2, only a quadrupole doublets of the TTF type are used. Only the first 50m are shown for the low energy (top) and the high energy (bottom) beam. Here, the second, third, and fourth cavity are operated 90° off crest, so that they only influence the longitudinal phase space but do not accelerate. This allows the beam to pass its focus at 4m without being over-focused by the RF field.

The threshold current of the beam breakup (BBU) instability has been calculated for this optics [5]. As in the analysis of a straight linac in [2], the HOM spectrum of TTF cavities was used and a BBU limit between 100 and
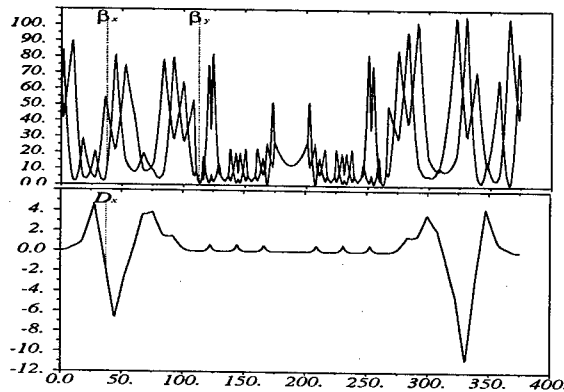
Figure 3: Beta functions and dispersion in the arc

200mA was computed.

Arc Optics

We studied whether a favorable optics can be found for the CESR South arc in spite of the constraints imposed by the existing tunnel. To reuse as much as possible from CESR, we maintained the bending magnets and quadrupoles in their current positions and only replaced the regions where the undulators would be installed. Each undulator has two matching quadrupoles at each side and is separated from the next undulator by a three-bend achromate. Finding an optics for the operation with 2ps bunch length turned out to be relatively simple. The matching constraint were: $\beta = 1$m, 2.5m, 2.5m, 12.5m, 2.5m, 2.5m, 1m in the seven successive undulators, and $\eta = 0$, $\eta' = 0$ in these seven places.

The optics for an rms bunch length of 100fs has to fulfill several additional requirements. The RF acceleration phase and the first and second order time of flight terms T_{56} and T_{566} of the first half of the arc have to be chosen to yield the desired bunch length in the central undulator [4]. For the second half of the return arc, T_{56} and T_{566} are determined by minimizing the energy spread after deceleration. The beta function and the dispersion for the return arc are shown in Fig. 3. Even though the magnet arrangement is symmetric around the center of the arc, the optics functions are not symmetric since the conditions for T_{56} and T_{566} are different for the two halves.

The second order time of flight term T_{566} is influenced by sextupoles and has to have the same sign as T_{56}. This is hard to achieve in the achromatic arrangements that have been proposed for this purpose. However, with the FODO like optics of the CESR arc this can be achieved with relatively weak sextupoles. This advantage is due to the large dispersion after the linac.

The nonlinear dynamics in sextupoles can increase the emittance. However, due to the weak sextupoles and the small transverse beam size, the dynamics is so weakly nonlinear that only the second order dispersion η_{166} and its slope η_{266} had to be eliminated in the center of the return arc. The second order conditions on T_{566}, η_{166} and η_{266}

were satisfied by three sextupoles on each side of the arc close to the three maxima of the dispersion in Fig. 3.

For short-bunch operation, coherent synchrotron radiation (CSR) can also increase the emittance. The emittance growth was computed with the code ELEGANT and is shown in Fig. 4. Since the beam dilution due to the nonlinear dispersion is included, the emittance is shown to decrease where the second order dispersion is corrected. In the central undulator, the emittance for 100fs bunch length has only increased by a factor of 1.8. To limit the emittance growth, it was found prohibitive to compress the bunch length to its minimum since this creates a spike in the longitudinal density and strongly enhances CSR. We therefore increased σ to obtain 100fs bunches without full compression.
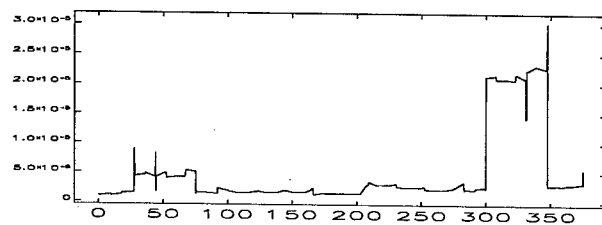
Figure 4: Effective emittance along the arc

CONCLUSION

The possibility of extending the CESR tunnel to include an ERL has been investigated. Geographically such an extension is possible. Furthermore, a suitable optics for the linac and for the return arc has been found that supports sub 100fs bunch lengths. The required dipole, quadrupole, and sextupole magnets are about as strong as the magnets of CESR.

REFERENCES

[1] G.H. Hoffstaetter et al., *The Cornell ERL Prototype Project*, proc. of PAC03.

[2] S.M. Gruner, M. Tigner (eds.), *Phase I Energy Recovery Linac (ERL) Synchrotron Light Source at Cornell University*, Report CHESS-01-003 at http://erl.chess.cornell.edu/papers/ERL_Study.pdf (2001)

[3] R. Talman, *Energy Recovery Linac in the Wilson Tunnel*, Report LEPP-ERL 02-06 (2002).

[4] I.V. Bazarov, G.H. Hoffstaetter, *Lattice options for a 5GeV Light Source at Cornell*, proc. of PAC03.

[5] I.V. Bazarov, *BI - a new BBU code*, User manual and source at *http://www.lns.cornell.edu/b38/bbucode/*

CHROMATICITY MEASUREMENTS IN THE ESRF BOOSTER

Y. Papaphilippou, G. Chazot, J.M. Koch, E. Plouviez, J.L. Revol, A. Ropert, ESRF, Grenoble, France

Abstract

In view of optimising the performance of the ESRF Booster, a series of experiments have been conducted in order to measure the chromaticity during the cycle for different sextupole settings. To this end, the betatron tunes were measured for different values of the RF frequency using the new tune-meter application. The experimental results were finally analysed and compared to theoretical data of the Booster model, showing good agreement.

THE ESRF BOOSTER

The ESRF Booster is a 300 m electron synchrotron which serves as the injector to the ESRF storage ring [1]. It accelerates electrons, coming from a 200 MeV linac, to a final energy of 6 GeV in 50ms and extracts them into the storage ring with a repetition rate of 1-10 Hz. The lattice is based on a FODO structure with a missing dipole, forming 39 cells with 12 straight sections and respecting a 3-fold symmetry. All magnets of the same family are independently powered by a resonant "white circuit", cycling at 10 Hz. The optics functions computed with MAD [2], along one super-period, for the nominal working point at injection $(11.8, 9.8)$, are pictured in Fig. 1 and a set of basic Booster parameters is displayed in Tab. 1.

Table 1: Main ESRF Booster parameters.

Parameter	Value
Circumference C	299.622 m
Extraction Energy E_{ext}	6 GeV
Repetition rate f_{rep}	1-10 Hz
Harmonic number h	352
Accelerating cycle t_{cycle}	50 ms
Working point (Q_x, Q_y)	$(11.8, 9.8)$
Momentum compaction factor α_c	$9.6\ 10^{-3}$
Emittances at 6GeV $(\epsilon_{x;ext}, \epsilon_{x;ext})$	(120,3) nm rad
Energy spread at 6GeV $(\delta E/E)_{ext}$	$1.1\ 10^{-3}$
Bunch length l_s	2.61 cm (87 ps)
Nominal current I_{nom} (long bunch)	5 mA

The chromaticity control is essential for the good performance of the Booster, especially at low energies. A new challenge under development is the cleaning of parasitic bunches inside the Booster [3]. This process, usually done in the storage ring, will enhance the bunch purity, improving the performance, especially of the "few-bunches" modes available for users at the ESRF, in the newly implemented "front-end" open operation procedure. For this purpose, the control of beam parameters such as the tune or the chromaticity are fundamental.

Two families of 21 horizontal and 30 vertical sextupoles are used to control the chromaticity in the Booster. A large
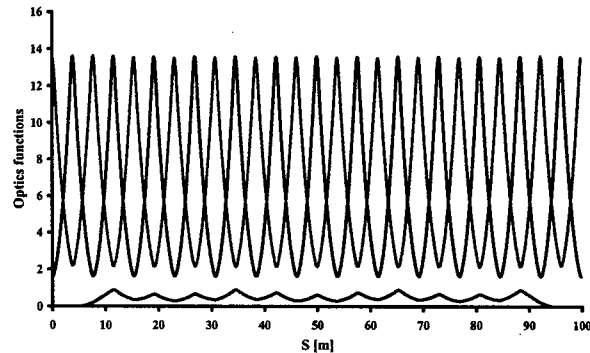
Figure 1: Horizontal (blue), vertical (red) β functions and dispersion (green) of the Booster for the nominal tunes.

amount of theoretical and experimental studies were performed a few years ago [4], including chromaticity measurements [5]. However, due to the poor performance of the tune meter, the accuracy of these measurements was not better than 10% as compared to theoretical calculations, especially for the horizontal plane. With a new tune monitor system installed, we aimed to improve these measurements with respect to precision and reproducibility. The method for measuring the chromaticity is straightforward: the RF frequency is varied and thus the momentum spread of the beam is changed. For small variations, the chromaticity should be a linear function of the tune shift, $\xi_{x,y} = -\alpha_c f_{RF} \frac{\Delta Q_{x,y}}{\Delta f_{RF}}$. Note that the momentum compaction factor α_c is normally a constant depending on the lattice. An independent measurement of this parameter can be done through the measurement of the sychnotron frequency for different accelerating voltages [4]. Taking into account the difficulty and the error introduced by this measurement, theoretical values were used, following previous experience.

TUNE MEASUREMENTS

One of the latest developments in the Booster, was the installation of a new tune monitor enabling the measurement of the tunes along the 50 ms acceleration cycle with a 1ms resolution, in both planes. The method consists of an FFT analysis of a BPM signal during the beam oscillation induced by a single turn kick given by a horizontal or vertical shaker . With a 1 MHz sampling rate and 1024 samples, a 1 KHz frequency and 1 ms time resolution can be achieved. At its actual state the system permits the acquisition of one measurement per plane, per accelerating cycle for a specific time during this cycle. Horizontal tune-shift measurements are presented in Fig. 2 for the whole magnet cycle of 100 ms, and different RF frequencies. The reproducibility of the measurement is excellent apart from the
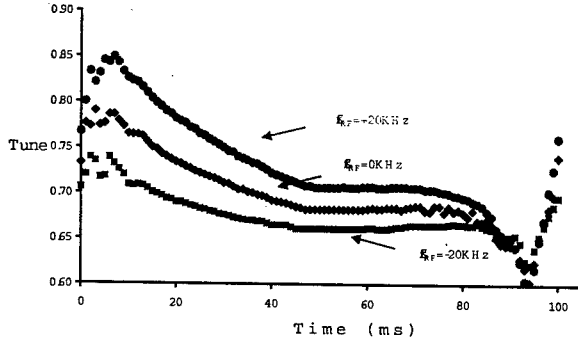
Figure 2: Horizontal tune measurements during one full Booster magnet cycle for different RF frequencies.

beginning and end of the cycle where the magnet settings are rapidly varying.

CHROMATICITY MEASUREMENTS

The total chromaticity in a sychnotron is a sum of three different terms. The first contribution comes from the natural chromaticity defined as the integral around the machine:

$$\xi_{x,y}^{\text{nat}} = \frac{1}{4\pi} \oint \beta_{x,y}(s) k_{x,y}(s) ds \ , \tag{1}$$

with $\beta_{x,y}$ the beta functions and $k_{x,y}$ the quadrupole normalised strengths. In addition, there is a contribution from the eddy currents induced on the metallic vacuum chamber of the dipoles, as a result of the field variation. It can be evaluated as:

$$\xi_{x,y}^{\text{eddy}}(t) = \pm \frac{1}{4\pi} \oint S^{\text{eddy}}(s,t) \eta_x(s) \beta_{x,y}(s) ds \ , \tag{2}$$

where S^{eddy} is the associated normalised sextupole strength produced by the eddy currents and $\eta_x(s)$ the horizontal dispersion (we imposed $\eta_y(s) = 0$). Finally, sextupoles with strengths $S_{h,v}$ used to control the chromaticity are producing an effect given by:

$$\xi_{x,y}^{\text{sext}}(t) = \frac{1}{4\pi} \oint [\pm S_h(s,t) \mp S_v(s,t)] \, \eta_x(s) \beta_{x,y}(s) ds. \tag{3}$$

The sextupole component due to dipole eddy currents in an elliptic vacuum chambers is given by [6]

$$S^{\text{eddy}}(t) = \frac{1}{B\rho} \frac{d^2 B_y}{dx^2} = \frac{1}{B\rho} \frac{\mu_0 \sigma_c d \dot{B}_y}{h} F(a,b) \ , \tag{4}$$

with μ_0 the free space permeability, σ_c the stainless steel conductivity and d the vacuum chamber thickness. The function depends on the vacuum chambers ellipticity a/b

$$F(a,b) = 1/2 \left[1 + \frac{b^2 \text{arcsinh}(\sqrt{a^2 - b^2}/b)}{a\sqrt{a^2 - b^2}} \right] \ , \tag{5}$$

and, for an almost circular vacuum chamber, as in the case of the Booster, it converges towards one. Taking into ac-
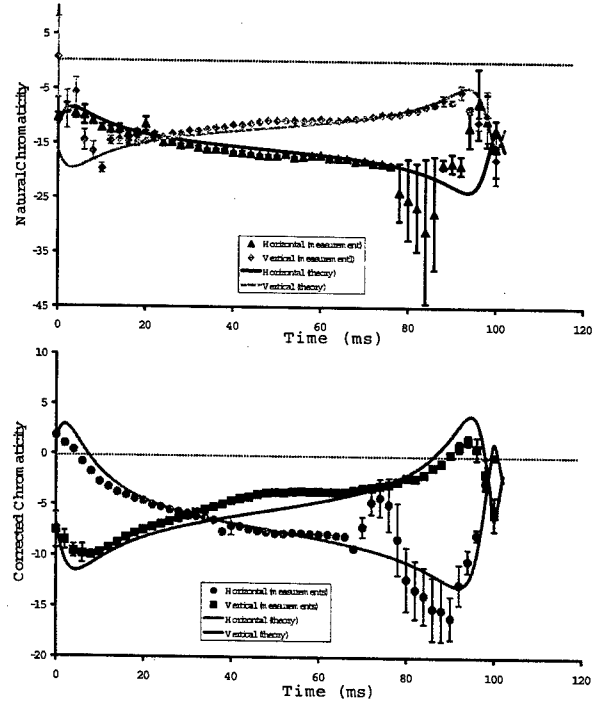
Figure 3: Booster chromaticity without [top] and with correction [bottom] from measurements (points) and theory (solid curves).

count that the dipole field has a sinusoidal behaviour

$$B_y(t) = \frac{B_{\max}}{1 + a_E} \left(a_E - \cos(\omega t) \right) \tag{6}$$

with ω the cycle frequency and the constant $a_E = \frac{E_{\max} + E_{\min}}{E_{\max} - E_{\min}}$ depending on the maximum and minimum energy, the sextupole strength due to the dipole eddy currents is

$$S^{\text{eddy}}(t) = \frac{\mu_0 \sigma_c t \omega}{h \rho} \frac{\sin(\omega t)}{a_E - \cos(\omega t)} F(a,b) \ . \tag{7}$$

Finally, the chromaticity sextupole strengths can be considered that they are scaled linearly with the total sextupole current using the simple formula

$$S_{h,v}(t) = \frac{6\mu_0 N I_{h,v}^{\text{sext}}(t)}{B\rho \, a_s^3} \ , \tag{8}$$

where $I_{h,v}^{\text{sext}}(t) = I_{h,v}^{\text{DC}} - I_{h,v}^{\text{AC}} \cos(\omega t + \phi_{x,y})$ with N the number of windings and a_s the sextupole aperture radius. Note that the beam rigidity $B\rho$ increases along the cycle.

A series of experiments have been performed in order to measure the chromaticity in the Booster with the following machine setup: a normal long bunch mode was used with optimised settings in the main power supplies with respect to beam losses. A reproducible 5mA current was accelerated with a 1Hz repetition rate. The chromaticity was measured, as described, from the slope between the tune-shift versus the momentum spread, for 5 different values of the RF frequency. The measurement error was estimated by the error in the slope coming from the linear data fit.
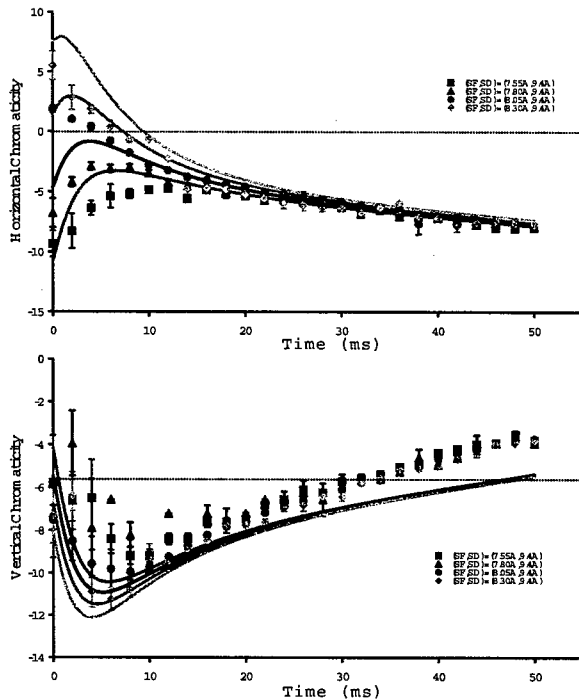
Figure 4: Horizontal [top] and vertical [bottom] Booster chromaticity for different settings of the horizontal sextupole DC current from measurements (points) and theory (solid curves).

Figure 5: Horizontal [top] and vertical [bottom] Booster chromaticity for different settings of the vertical sextupole DC current from measurements (points) and theory (solid curves).

In Fig. 3, the natural chromaticity behaviour is presented along the full magnet cycle (100 ms). Note that during the normal injection process to the storage ring the beam is extracted in the middle of this cycle, i.e. at 50 ms. The points represent the chromaticity measurements and the solid lines the theoretical values. In the top plot, the natural chromaticity is displayed, whereas in the bottom plot we present the chromaticity after correction with the chromaticity sextupoles. The agreement between the measurements and the theoretical evaluation is quite good, apart from the beginning of the cycle for the vertical (without correction) and the end of the cycle for the horizontal chromaticity. In all the cases, the discrepancy should be attributed to the strong values of the chromaticity at these areas: in that case, the FFT signal appears with strong synchrotron sidebands around its make peak which reduce the precision in the tune determination.

A series of measurement for different values of the horizontal and vertical DC current settings are presented in Figs. 4 and 5, respectively, for only the accelerating cycle of 50 ms. As before, the theoretical values are represented with solid lines. There is a fair agreement with the measurements apart from the beginning of the cycle, in most cases. As the agreement is very good when comparing the differences between the chromaticity and the applied currents, we suspect that the discrepancy should be due to the simplistic formula (8) used to compute the sextupole strength dependence with the current.

CONCLUSION

We have measured the ESRF Booster chromaticity along the cycle using the new tune monitor recently installed. The agreement between theory and experiment was very good (within a few percent) for the natural chromaticity and the nominal current settings in the sextupole power supplies. However, we found larger discrepancies when applied different power supplies DC settings, probably due to the simplistic form of the sextupole dependence to current in our theoretical evaluation and the occurrence of beam loss. In the future, we will perform more measurements varying also the AC currents in view of calibrating the sextupole settings. As the chromaticity control is essential for the bunch cleaning process, our perspectives include the use of a new application using up to 10 different harmonics for controlling the sextupole currents and finally writing a chromaticity control application, for the automatic setting of currents for a desired chromaticity along the cycle.

REFERENCES

[1] ESRF Foundation Phase Report, Chapter III, ESRF, February 1987; J. M. Filhol, EPAC'92, Berlin, 1992.

[2] H. Grote and C.H. Iselin, CERN SL 90–13 (AP).

[3] J.-L. Revol et al., these proceedings.

[4] G. Schmidt, PhD Thesis, ESRF (1996); G. Mülhaupt et al., EPAC'96, Sitges, 1996; J.P. Perrine et al, ibid.

[5] G. Schmidt, ESRF Machine Tech. Note, 1-96/INJ, 1996.

[6] G. Hemmie and J.Rossbach, DESY M-84-05, 1984; A. Chao, SSC-N-434, 1987.

OPERATION AND RECENT DEVELOPMENTS AT THE ESRF

P Berkvens, J.C. Biasci, J. Chavanne, P Duru, P. Elleaume, L Farvacque, T Günzel, L. Hardy,
J Jacob, R Kersevan, G Naylor, Y Papaphilipou, E. Plouviez, J.L. Revol, A. Ropert, K Scheidt,
ESRF, Grenoble, France

Abstract

The ESRF has been operating for more than 10 years. As a result of the maintenance policy a high level of beam availability as well as a long beam time between failures has been maintained. In addition, a continuous effort is made to develop the machine further. The operation status and the experience gained with the recent upgrades are reported. It concerns:

- The successful operation with 5 in-vacuum undulators operated at a 5-6 mm magnetic gap.
- The implementation of a new hybrid type filling pattern which combines groups of bunches at full current and single bunch.
- The successful qualification of a 5 metre-long, 8 mm vertical aperture insertion device (ID) aluminum chamber coated with non evaporable getter material.
- The evolution of the impedance with associated consequences on instability thresholds, following the installation of a number of low aperture insertion device chambers.
- The successful test of the SOLEIL superconducting cavity.
- The injection front end open in order to ensure a better thermal stability in the beamlines.

THE ESRF IN 2003

The European Synchrotron Radiation Facility (ESRF) located in Grenoble, France is a joint facility supported and chaired by 17 Countries. This third generation storage ring X-ray light source has been in routine operation for more than 10 years. The source delivers 5500 hours of beam to 43 beamlines simultaneously.

Particles	Electrons	
Energy	6.03	GeV
Circumference	844	m
Multibunch Current	200	mA
Lifetime (Uniform fill)	80	Hours
Horizontal emittance	4	nm.rad
Coupling	0.6	%
16 Bunch (Single) current	90 (16)	mA

Table 1: Main parameters

A large variety of insertion devices is installed in the 27 available straight sections:
- 64 in-air IDs (two or three 1.7 metre-long segments per straight section)
- 5 in-vacuum undulators (2 metre-long) [1]

The bending magnet radiation is now used by 15 beamlines.

OPERATION IN 2002

The figures of merit for 2002, namely the mean time between failure (MTBF) and availability, were maintained at the same level as in 2001. Out of the 5495 hours scheduled for beam delivery to the Users (USM), 5319 hours were delivered, which represents an availability of 96.8 %. The remaining hours are shared between the dead time for refills: 67 hours for 507 refills (i.e., 1.2 % of USM time) and the time lost due to failures: 110 hours (i.e. 2% of USM time). With 95 beam interruptions, the MTBF reached a record of 57.8 hours, which confirms the improvement of this figure of merit obtained in 2001 (see Fig 1). Another way to appreciate these figures is to bear in mind that there were 17 periods with more than 72 hours of delivery without a single failure, out of which 9 periods were greater than 120 hours! The efforts put by all groups on preventive maintenance and failure analysis has largely contributed to the continuous increase of the MTBF and availability during the last few years.

It is worth pointing out that these results, and in particular the low rate of failures, were maintained whilst a great deal of developments were under way: in particular, the successful tests of the Soleil superconducting cavity installed throughout 2002. These tests were performed without any change of the beam size, bunch length and with the same stability. Indeed, this was fully transparent to user operation.
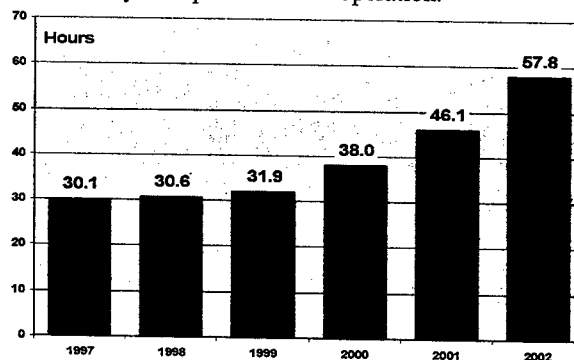
Fig. 1: Evolution of the Mean Time Between Failures.

Multibunch filling pattern, which represents 67 % of the total user time, was mostly delivered in uniform filling with a lifetime greater than 70 hours at 200 mA. Despite a slightly lower lifetime, the 2*1/3 fill is still used for time structure experiments. The rest is shared between the 16 bunch, single bunch and hybrid modes. The deterioration of the horizontal beam dynamics was clearly observed during last year, making the preparation of 20 mA single bunch and hybrid modes more difficult.

INJECTION WITH FRONT END OPEN

This year, the operation of the ESRF beamlines was dramatically changed by the implementation of the injection with front-ends open, allowing real continuous operation. Before, the shutters of all beamlines were closed for a few minutes during injection, resulting in large temperature variations on the optics which caused interruptions of data acquisition up to an hour after each injection. Leaving the shutters open during injection has dramatically improved the situation.

This mode of operation has to be compatible with the present ESRF radiation protection policy, which stipulates that all staff working at the ESRF are considered as non-exposed workers. This implies that the dose limits for the public, as defined in the Euratom/96-29 decree, do not exceed 1 mSv per year (or 2 µSv over 4 hours if taking into account working time). Radiation monitors interlock the beam in the linac if the dose exceeds the limit. The accidental steering of a single 1 µs electron beam pulse injected from the booster into a beamline with open front end would result in an integrated dose, largely exceeding the 2 µSv limit. No interlocked radiation monitor could therefore be fast enough to protect against such an accidental situation. A detailed study has demonstrated the impossibility of steering beam from the booster into a beamline if there is already a stored beam. A dedicated and redundant beam current monitor has been developed and integrated in the machine personnel safety system. Injection with FE open is only allowed if this current monitor measures a stored beam larger than 5 mA. During the first one and a half months of operation in this mode, uniform, 16 bunch, single bunch and 2x 1/3 filling modes were delivered. The evolution of the dose over 4 hours measured around all beamline optics hutches indicated that the injection losses, as well as the losses due to bunch cleaning in all filling modes, produce very low dose rates compatible with the limit. The measured dose is limited by the background level in the Experimental Hall (which varies between 80 and 100 nSv.h^{-1}), with a small contribution from scattered bremsstrahlung, which depends on the type of filling mode.

On the machine side, the implementation of the Injection FE Open as a standard mode of operation was rather straightforward. The main modifications concerned the logical unit of machine protection system and the implementation of a software counter indicating the remaining time before the next injection. The value of the counter can be used to synchronise the data acquisition. In order for the beamlines to fully benefit from Front Ends Open injection, it is essential to maintain the insertion device gap unchanged during injection. Since in-vacuum undulators (built with Sm_2Co_{17} magnets, more resistant than NdFeB) are the most sensitive to radiation damage when exposed to high energy electrons, their minimum gap is presently limited to 8 mm (instead of 6 mm) during injection [1]. For the corresponding beamlines, this generates a maximum 30 % heatload variation for a few minutes. In the long term, it is planned to reduce this gap

limit following a detailed quantitative study performed on ID6, the machine beamline.

User feedback was extremely positive despite the constraints imposed on the beamlines using in-vacuum devices. The strong reduction of thermal variation and the possibility to use the beam during injection result in an increase of beam availability for most beamlines. In multibunch modes with long lifetimes (50-90 hrs), the injection with front ends open twice a day is indeed close to ideal for the beamlines. However, it is less favourable in time structure modes where the reduced lifetime imposes more frequent injections. Moreover, the cleaning procedure renders the beam unavailable for a few minutes during each injection. Work has been initiated to improve this by performing the cleaning in the booster.

TEST OF A NEW HYBRID MODE

A new hybrid mode has been developed and was delivered for 8 hours during Machine Dedicated Time to Users who volunteered to test it. It consists of 24 groups of 8 bunches (1 mA each) with an additional single bunch of 4mA. The lifetime at 200 mA reached 26 hours; other beam parameters were close to the usual multibunch figures. Following the positive feedback received from Users, this mode will be proposed in replacement of the standard hybrid mode (9% of User time in 2002). The difficulties encountered with this new mode concern the cleaning of the parasitic bunches. Firstly, due to the low current per bunch, the detuning of the vertical betatron frequency induced by the machine impedance is small. Secondly, there is a strong quadrupolar detuning as a function of the total beam current induced by the low gap chamber resistivity and its asymmetry [2]. The precise definition of the cleaning frequency is obtained by injecting a few mA of multibunch beam. The excitation of the low populated bunches is performed at a higher order coupled bunch mode, using a stripline shaker to reduce the excitation of the main bunches through the narrow band resistive wall impedance.

INTENSITY RAMPING TO 250 mA

A beam current of 250 mA was stored in the machine for the first time in 2001. However, the radiation induced outside the shielding exceeded the authorised level and tests were temporarily interrupted. After a campaign of systematic shielding reinforcement, tests resumed in April 2003. Stable beam at 250 mA was stored in 1/3 and 2/3 filling modes. No abnormal pressure rise or temperature increase on critical components was observed. The lifetime reached 44 hours in 2/3 filling (to be compared to 60 hours at 200 mA). However, in uniform filling, the current was limited to 240 mA due to a transverse High Order Mode instability that still needs to be mastered. This is the first observation of an instability due to a transverse HOM at the ESRF! Further studies are planned to characterize and fully master the beam parameters at 250 mA.

PROGRESS WITH NEG COATED CHAMBERS

The installation of non-evaporable getter (NEG) coated vessels continued throughout the year. The main development was the production of a prototype followed by full tests of an 8 mm aperture 5 metre long aluminium vessel. The choice of aluminium instead of stainless steel was made to reduce both manufacturing costs and the excitation of the resistive wall instability. However, raw aluminium presents strong synchrotron radiation induced desorption compared to stainless steel. The conditioning of the prototype chamber (without NEG coating) installed in May 2002 was so slow and the bremsstrahlung produced was so high that the chamber was removed immediately after installation. When the same chamber coated with NEG was re-installed in October 2002 a rapid conditioning was observed (half the nominal multibunch lifetime was obtained after 20 minutes of beam at full current). The coating of the tiny 57 x 8 mm elliptical chamber was made at CERN. A NEG coating facility is being developed at the ESRF, which should allow the coating of 5 metre-long insertion device vessels.

EVOLUTION OF MACHINE IMPEDANCE AND INSTABILITY THRESHOLDS

The vertical and horizontal transverse impedance of most of the machine components have been determined using the electromagnetic field equation solver GdfidL. To explain the measured tune shifts, the impedance of each component is weighted by the local β-function. Due to the strong modulation of the optics, the β-functions play a key role in understanding the importance of the different machine elements in the impedance budget. The incoherent quadrupolar detuning is the second important effect which has to be taken into account to obtain the impedance in both planes. The resulting impedance budgets (without resistive wall part) show that in the vertical plane the RF-liners near the dipoles yield the largest contribution due to the β-value [3]. On the other hand the contribution of all tapers to the impedance is only 20% in the vertical plane, but amounts to 80% of the budget in the horizontal plane (scrapers not included). This effect could be confirmed qualitatively by the measured tune shifts and TMCI current thresholds. On the whole, values of about 5MΩ vertically and 1.8 MΩ horizontally have been computed at zero frequency.

Standard 5 metre-long stainless steel ID vessels (11 mm vertical beam stay clear) are currently being replaced by low gap (5 metre-long, 8 mm height) vacuum chambers (five NEG coated copper-coated stainless steel and one NEG coated aluminium) together with the installation of 5 in-vacuum undulators (2 meter long, 5.5 mm minimum gap). No evolution of the instability thresholds or of the quadrupolar detuning induced by the asymmetry of the chambers could be observed in multibunch mode. The reduction of the vertical aperture was compensated by the change in the resistivity of the material. This also confirms that both instability thresholds and detuning are largely governed by chambers in the achromat, due to the local high beta functions, compared to straight sections.

Vertical single bunch characteristics have not evolved, however, single bunch operation is now strongly affected in the horizontal plane. The incoherent detuning induced by the short range wake has significantly increased. The injection efficiency and saturation is directly affected by the beam blow-up occurring at high current. The horizontal transverse mode coupling instability threshold decreased from 4 mA in 1999 to 0.9 mA and the chromaticity used for operation had to be enlarged. The horizontal instability threshold now also depends on the tune and the horizontal emittance. For all these reasons, it is envisaged to reduce the maximum single current delivered to the Users to below 15 mA.

TEST OF THE SOLEIL SUPERCONDUCTING CAVITY

A cryo-module housing two superconducting 352 MHz strongly HOM-damped cavities has been developed within the framework of the SOLEIL project design study phase, in a collaboration agreement between CEA, CERN, ESRF and SOLEIL. In 2002 the prototype was installed on the ESRF storage ring and tested with beam at 4.5 K, with the cavities cooled by liquid helium poured from Dewars. Four such tests were carried out at the end of scheduled shutdowns at the ESRF. In passive operation at 300 K or 4 K, no instability was detected up to the maximum ESRF intensity of 200 mA. This demonstrated the validity of the concept of an effective damping of the Higher Order Modes (HOM). The superconducting (SC) module was tested successfully in the accelerating regime with 3 MV of accelerating voltage. A maximum power of 360 kW could then be transferred to 170 mA of beam.

In order to avoid disturbing the ESRF machine performance during user mode operation, the cavities were maintained detuned at room temperature in a passive regime. The heat generated by the beam was then evacuated by means of a helium gas flow, cooled by a heat exchanger. The test arrangement provoked only three beam trips over one year and was therefore almost transparent to normal ESRF operation.

With the successful prototype test, the concept of this almost HOM-free SC cavity has been validated [4]. The tests have also shown that this cavity constitutes a valuable option for a possible future upgrade at the ESRF.

REFERENCES

[1] J Chavanne, "In-vacuum undulators at the ESRF", this conference.

[2] R Nagaoka et al., "Incoherent transverse tune shifts due to resistive wall low gap chambers", EPAC 2002.

[3] T.F.Günzel, "Evaluation of the vertical impedance of the ESRF-machine" EPAC 2002, Paris.

[4] J Jacob et al., "Successful beam test of the SOLEIL SC HOM free cavity at the ESRF", this conference.

THE LATTICE DESIGN OF THE SUPER SOR LIGHT SOURCE

K. Harada, Y. Kobayashi, H. Takaki[#], H. R. Sakai[#], N. Nakamura[#], T. Koseki[+]
KEK-PF, 1-1 Oho, Tsukuba, Ibaraki, 305-0801, Japan
[#]ISSP-SRL, 5-1-5 Kashiwanoha, Kashiwa, Chiba, 277-8581, Japan
[+]Riken, 2-1, Hirosawa, Wako, Saitama, 351-0198, Japan

Abstract

The Super SOR light source is 1.8 GeV electron storage ring proposed for the third generation vacuum ultra violet (VUV) and soft X-ray light source, where is going to be constructed at Kashiwa campus of the University of Tokyo. The lattice design of the ring is going to be fixed due to the results of the particle tracking simulation for the chromaticity correction and the evaluations for the strength and the alignment error of the magnets.

INTRODUCTION

The Super SOR light source [1] is 1.8 GeV electron storage ring to be constructed at Kashiwa campus of the University of Tokyo. The main parameters of the ring are shown in Table 1, and the plan view in Figure 1. The circumference of the ring is about 280 m. The nominal emittance is 7.26 nm·rad at an energy of 1.8 GeV. The brilliances of the photons are over 10^{19} photons/sec/mm^2/mrad^2/0.1%b.w., as shown in Figure 2. The flux are over 10^{16} photons/sec/0.1%b.w..

In this paper, we present the lattice design of the Super SOR light source and the simulation results of the particle tracking for the chromaticity correction and the error correction.

Figure 2: The brilliances of the photons
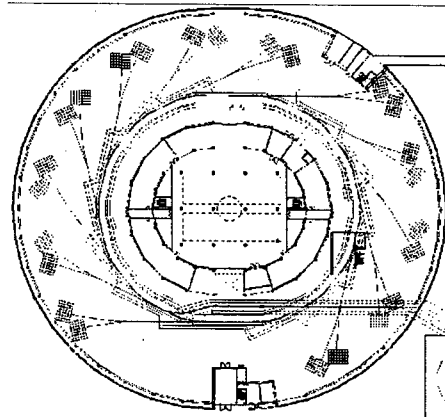
Figure 1: Plan view of the main ring

Table 1: Parameters of the ring

		normal	hybrid
Energy	GeV	1.8	
Circumference	m	280.55	
Emittance	nm rad	7.26	6.7
Energy Spread		6.68E-04	6.68E-04
Momentum Compaction		1.00E-03	1.00E-03
Betatron Tune			
horizontal		14.12	15.85
vertical		5.18	5.7
Chromaticity			
Horizontal		-43.277	-55.139
vertical		-19.442	-31.525
Magnetic Field of Bend.	T	1.12	
Critical Photon Energy	keV	2.42	
Energy Loss / turn	keV/rev	173.7	
Radiation Damping Time			
horizontal	msec	19.319	19.319
vertical	msec	19.4	19.4
longitudinal	msec	9.721	9.721
Revolution Frequency	MHz	1.0686	
RF Frequency	MHz	500.1	
Harmonic Number		468	
RF Voltage	MV	1.4	
Synchrotron Tune		0.00759	0.00759
Bunch Length	mm	3.935	3.935
RF Bucker Hight		0.0293	0.0293

DESIGN STRATEGY OF LATTICE

We have several conditions to design the lattice of main ring storage ring; the length of straight sections is over 6 m for the normal insertion device of 5 m and over 17 m for the longer one of 15 m, and number of the devices is over 10, and so on. Under the conditions, we designed so that the lattice of the ring has two long and twelve normal straight sections considering with the sections for the RF cavities and injection components. In addition, we have to consider the circumference of the ring because the area of the campus and the budget of the construction are limited. We adopted, therefore, the

857

structure of 14 double bend achromat (DBA) cells in the lattice configuration.

In the strategy of the normal cell, we compared the structure of two types; Type I is composed of B-QD-QF-QF-QD-B, and Type II of B-QF-QD-QF-B in the configuration of magnets of the cell. The large difference of two types appears in the shape of dispersion functions, as shown in Figs. 3. The function of Type I has the shape of Λ type and the flat region near the centre of cell. On the other hand, the shape of V type is formed in the function of Type II. The advantage of Type II is that small emittance is realized by the shorter length of cell. By adopting this Type, we can achieve the theoretical minimum emittance of DBA structure. However, it is hard to correct the chromaticity in this type because the dispersion function at sextupole magnets is quite small in spite of larger chromaticity. Thus, the dynamic aperture tends to narrow. Actually, it was very severe to ensure enough dynamic apertures in our simulations. In the case of Type I, though the length of cell tends to become longer, the chromaticity correction was easier than that in the case of Type II. We adopted, consequently, the structure of Type I. Including various boundary conditions for the ring components and the required conditions, we designed the lattice of the ring. The length of normal cell is about 18 m, and the circumference of the ring is about 280m. The nominal emittance at beam energy of 1.8 Gem is 7.26 nm·rad. Though the theoretical minimum emittance is 3.5 nm·rad, practical minimum emittance of the ring may be about 5 nm·rad. The betatron

tunes of one cell are $(\nu_{nx}, \nu_{ny})=(0.9743, 0.3653)$. To reduce the emittance, the horizontal tune ν_{nx} becomes close 1.0. The tunes of cell in the matching section for 17 m long straight section are $(\nu_{lx}, \nu_{ly})=(1.214, 0.3984)$, and finally tunes of the ring are $(\nu_x, \nu_y)=(14.12, 5.18)$.

The present optics of the ring is shown in Fig. 4. Because of two long straight sections, the optics has 2-fold symmetry.

NONLINEAR EFFECTS AND DYNAMIC APRTURES

We use four families of the sextupole magnets; two of them are for the chromaticity correction, and the others for the harmonic correction of avoidable nonlinearities produced by the chromaticity correctors. The latter magnets called harmonic sextupoles. The effects of them on the momentum dependent tune shift are shown in Figure 5. It is clear that the dynamic aperture may be limited by the resonance lines $\nu_x=14$ and $\nu_y=5$ without them. Using the harmonic sextupoles, however, the momentum dependent tune shift is drastically improved. The tunes of particles with large momentum deviation takes away from these resonance lines, As a result, the dynamic apertures is much expanded as shown in Figures 6.

(a) Type I (b) Type II

Figures 3: Two types of DBA cell
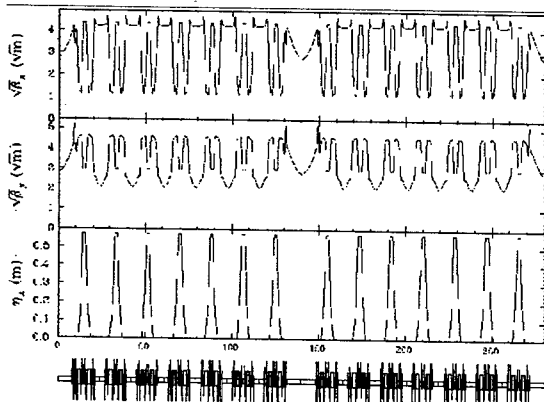
Figure 4: The optics of the normal mode
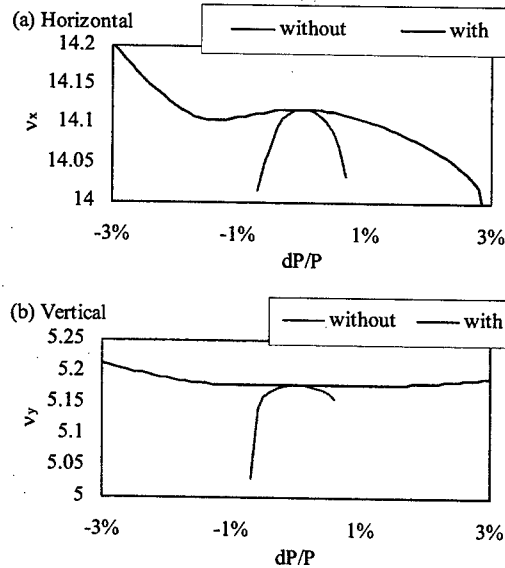
Figure 5: The effect of the harmonic sextupoles

HYBRID OPTICS

In order to suppress the effect of the higher order mode produced by the RF cavities and avoid various coupled bunch instabilities, we hope that the beta functions at a place of RF cavities are small as possible while the horizontal beat function at a place of injection section is large. Thus we prepared the hybrid optics where the

(a) Horizontal plane

(b) Vertical plane
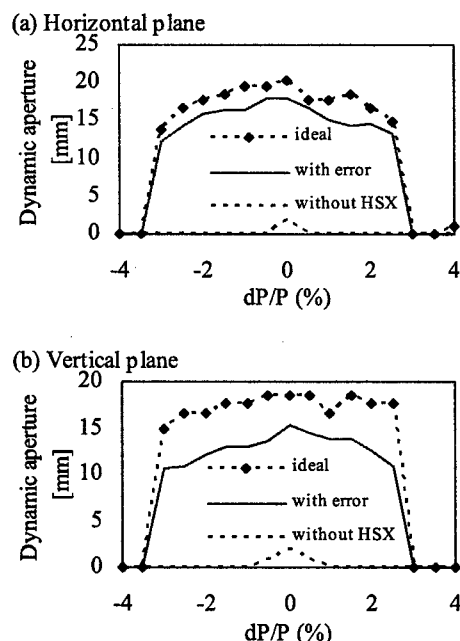
Figure 6: The dynamic apertures of the normal mode.
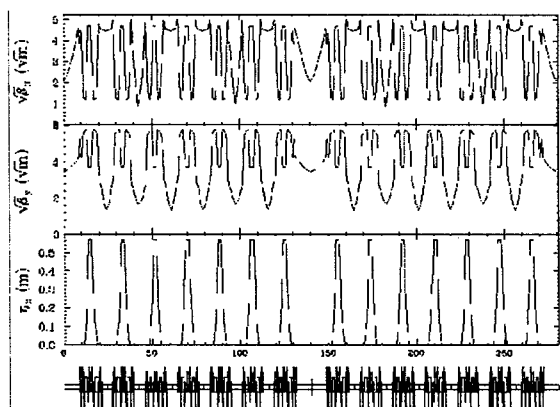
Figure 7: The optics of the hybrid mode.

normal cells with very small beta functions (low beta cells) are symmetrically arranged in the ring. The configuration of the low beta cell in the half part of the ring is the following,

$$(17m) - H - L - H - H - L - H -,$$

where H indicates the ordinary (high beta) normal cell and L the low beta cell, as shown in Fig. 7. For the low beta cell, the beta function at the centre of 6.2 m long straight section is about 1 m for both horizontal and vertical planes. Since we plan that the strength of all the quadrupoles and sextupoles can be independently changed, we have great flexibility in the adjustment of the optics and the chromaticity correction. However, the dynamic aperture of the hybrid mode has large asymmetry in the horizontal plane and especially small for the negative amplitude. In the next step, we are going to simulate the hybrid-optics increasing a number of families in the harmonic sextupoles to improve the dynamic aperture.

EFFECTS OF MAGNETIC ERRORS

We simulate the effect of the magnetic errors and the COD correction for the normal mode. The assumed magnetic errors are the alignment errors of $100\mu m$, the field error of 0.1% and the rotation error of $400\mu rad$ for the bending, quadrupole and sextupole magnets. The number of the beam position monitors is 140 and that of the steering magnets 112. We adopt the eigenvalue method for the COD correction and the number of the used eigenvalues is 50. We calculate ten random error seeds and take the average. The RMS and maximum values of the COD and dispersion function distortion ($\Delta\eta$) are shown in Table 2. The dynamic aperture after the COD correction is shown in Figure 6.

When the beam current is 400mA, the XY coupling 1%, the physical half aperture 25mm, and the vacuum pressure 1 nTorr, the estimated beam lifetime results in about 8 hours.

Table 2: The magnetic errors

		COD X max (mm)	$\Delta\eta_x$ max (mm)	COD X rms (mm)	$\Delta\eta_x$ rms (mm)
horizontal	before	11.282	301.22	5.509	129.78
	after	0.189	64.33	0.072	34.63
vertical	before	15.012	348.4	8.010	135.5
	after	0.252	160.2	0.083	71.3

SUMMARY

The lattice design of the Super SOR light source is presented. Because of the two 17 m long straight section, the optics has 2-fold symmetry. The effective use of the harmonic sextupoles, however, enables us to keep the large dynamic aperture and we achieve the beam lifetime of 8 hours with the beam current 400mA and the coupling 1%.

Besides the normal optics, we prepare the hybrid optics. The beta functions are about 1 m in the low beta cells and eight low beta cells are configured symmetrically in the ring. The further optimization of the harmonic sextupoles is needed to get the large dynamic aperture of the hybrid optics and this is the next step.

REFERENCES

[1] Design Report, Sep. 2002

PRESENT STATUS OF PHOTON FACTORY ADVANCED RING

T. Miyajima*, K. Ebihara, E. Ezura, H. Fukuma, K. Haga, K. Harada, Y. Hori, T.Ieiri,
S. Isagawa, T. Kasuga, T. Katoh, H. Kawata, M. Kikuchi, M. Kobayashi, Y. Kobayashi,
K. Kudo, Y. Minagawa, T. Mitsuhashi, S. Nagahashi, T. T. Nakamura, H. Nakanishi,
T. Nogami, T. Obina, Y. Ohsawa, Y. Onishi, M. Ono, T. Ozaki, Y. Sakamoto, S. Sakanaka,
M. Sato, M. Satoh, T. Shioya, M. Suetake, R. Sugahara, M. Tadano, T. Takahashi, S. Takasaki,
Y. Takeuchi, Y. Tanimoto, M. Tejima, K. Tsuchiya, T. Uchiyama, A. Ueda, K. Umemori,
N. Yamamoto, S. Yamamoto, S. Yoshimoto and M. Yoshioka
High Energy Accelerator Research Organization, Tsukuba 305-0801, Japan
T. Fujita
Hiroshima University, Higashihiroshima 739-8526, Japan

Abstract

The upgrade project of the pulse X-ray source PF-AR was successfully completed by the end of 2001. The initial beam current and the lifetime were largely improved. The injection energy was raised from 2.5GeV to 3.0GeV, the maximum beam current of 65mA was achieved. With a new global orbit feedback system, orbit drifts were largely improved.

INTRODUCTION

The AR that was originally constructed as a booster of the TRISTAN electron-positron collider has been parasitically used as an X-ray source [1-2]. It was converted into a ring dedicated to pulse X-ray research and renamed PF-AR(Photon Factory Advanced Ring for pulse X-rays) after completion of the TRISTAN project, however, its performance as a light source was not satisfactory: low reliability due to overage machine components, a short beam lifetime due to insufficient vacuum system performance, deficiency of closed-orbit controllability caused by the unreliable beam position monitor(BPM) system, etc. In order to improve these problems, the PF-AR upgrading project[3] was started in 1999. Old vacuum ducts made of Al alloy were exchanged for ones made of OFHC copper with improved BPM electrodes and the pumping system was largely reinforced. The power supplies for the steering magnets were all changed and the control system were completely renewed. New beamlines and in-vacuum type insertion devices were installed. The upgrading project were completed in the end of 2001, and commissioning of the upgraded ring was successfully done in the beginning of January, 2002 [4-5]. After fine tuning of the machine, users' operation started in April. The typical lifetime of 15 hrs at the energy of 6.5GeV and the beam current of 50mA in a single bunch was achieved, and the closed orbit controllability was largely improved.

The present layout of the PF-AR is shown in Fig. 1. Both the ring and the experimental halls are housed un-

derground. There are four SR beamlines from insertion devices (three in-vacuum-type undulators [6], one elliptically-polarized multipole wiggler [7]) and the other two from bending magnets. New north-west experimental hall, two beam lines(NW-2, NW12) and a new tapered undulator were constructed in the upgrade project.

OPERATION AND PERFORMANCE OF PF-AR

The PF-AR has been operated at beam energies of 6.5 and 5.0GeV, where the 5.0GeV operation is arranged for medical applications. The ring always stores a single-bunch beam of about 55mA, providing unique pulse X-rays for researches such as the time-resolved X-ray experi-
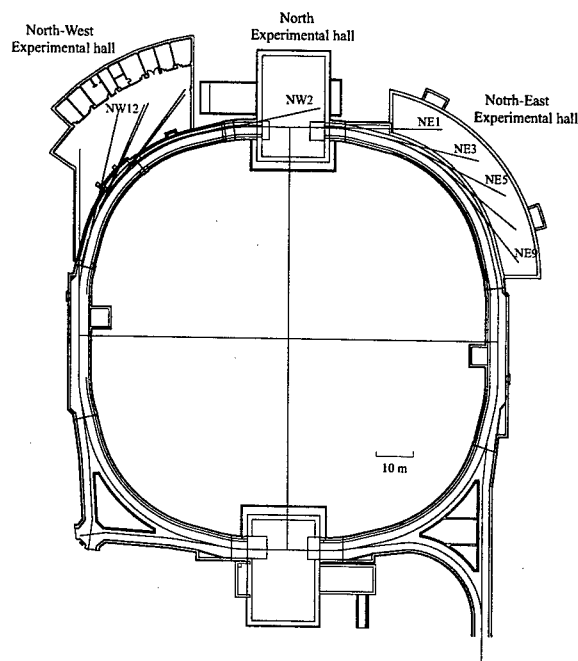
Figure 1: Layout of the PF-AR after the upgrade project.

* E-mail addres : tsukasa.miyajima@kek.jp

Table 1: Principal parameters of the PF-AR under the present optics.

Parameter	Value
Beam energy	5.0 - 6.5 GeV
Injection energy	3.0GeV (2.5GeV)
Circumference	377.26 m
Harmonic number	640
Horizontal betatron tune	10.15
Vertical betatron tune	10.21
rf frequency	508.58 MHz
Emittance (at 6.5GeV)	294nm·rad
Initial stored current	55mA (single bunch)

Figure 3: Typical one-day operation of the PF-AR after the upgrade project.

Figure 2: Optical functions in the PF-AR under 90-degree optics.
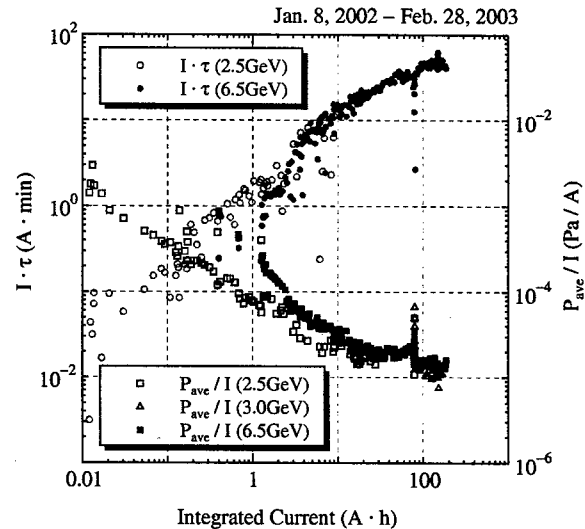
Figure 4: History of the vacuum conditioning after the upgrade project, where I and τ are the beam current and the beam lifetime, respectively.

ments. High beam energy and full-time single-bunch operation characterizes the PF-AR. The principal parameters of the ring are given in Table. 1

The PF-AR is made up of normal FODO-cells, four long straight sections and eight short straight sections. The ring is operated at 90-degree[1] optics for user operation, the emittance is 294nm·rad and the dynamic aperture is sufficiently large. Fig. 2 shows the optical functions of the PF-AR 90-degree optics.

Beam Lifetime

Before the PF-AR upgrade project, the beam lifetime was rather short; about 3 hours at a beam current of 40mA, to maintain an average current, injections more than ten times a day were necessary. After the upgrade project, the beam lifetime became longer (about 15 hours at a beam current of 50mA) and injections are reduced to 3 times a day. Fig. 3 shows the typical beam current and beam lifetime in one-day.

The history of the vacuum conditioning after the upgrade project are shown in Fig. 4, where I and τ are the beam

current and the beam lifetime, respectively. The value $I \cdot \tau$ have increased gradually with the integrated beam current.

3.0GeV Injection

Before the upgrade project, the injection energy was 2.5GeV. However, beam instabilities that limited the maximum stored beam current at about 47mA, were observed during the injection [8]. In order to improve the situation, the injection energy was raised from 2.5GeV to 3.0GeV. As a result of the 3.0GeV injection, a higher beam current over 65mA was achieved, however, instabilities still have been appeared during injection. Since 3.0GeV injection started from October, 2002 for user operation, the typical initial stored current is about 55mA.

---
[1]Phase advance per normal FODO cell.
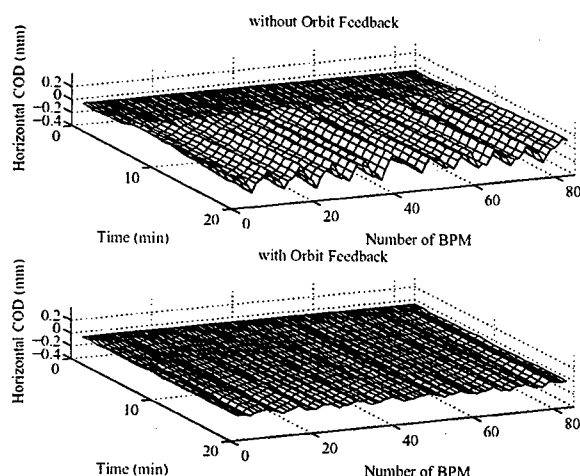
Figure 5: Horizontal orbit fluctuation with and without global orbit feedback. The fluctuation is reduced to 16μm from 85μm for orbit feedback.

Figure 6: Vertical orbit fluctuation with and without global orbit feedback. The fluctuation is reduced to 63μm from 29μm for orbit feedback.

Orbit Stabilization

A slow orbit drift is observed in proportion to decrease in the beam current in the user operation mode. The typical initial stored current is about 55mA as mentioned above, the current decreases down to 30mA in one operation shift of 8 hours. Thermal deformation of the magnet poles and the vacuum chambers generates the reproducing COD, and r.m.s values of the orbit drift in the horizontal and vertical planes are 85μm and 63μm, respectively.

To suppress this orbit drift, we have improved the global orbit feedback system and make COD correction every 20sec. With the new global orbit feedback system, the r.m.s value of the horizontal and vertical orbit drift are reduced to 16μm and 29μm, respectively. 3D plots of the horizontal and vertical orbit drift with and without global orbit feedback are shown in Fig. 5 and Fig. 6.

Low Emittance Optics

The PF-AR is currently operated at an emittance of 294nm·rad under 90-degrees optics in user operation. For the present lattice the emittance can be reduced to 160 nm·rad using 140-degree optics. In order to reduce the emittance for user operation, studies of low emittance optics have been started April, 2003. After adjusting the machine parameters, electrons could be stored at the low emittance optics. However the beam current was limited to 30mA. It seems that the current limit is caused by the beam instabilities that was observed in 2.5GeV injection. We will survey operating points free from beam instabilities and try to tune the acceleration to 6.5GeV.

SUMMARY

The PF-AR upgrade project was successfully completed. The beam lifetime became longer (about 15 hours at a beam

current of 50mA) and injections are reduced to 3 times a day. As a result of the 3.0GeV injection, a higher beam current over 60mA was achieved without beam instabilities. With the new global orbit feedback system, the orbit drift is suppressed. In order to reduce the beam emittance, we will survey operating points free from beam instabilities at the low emittance optics. We will also study beam stability for user operation. For example, sudden decrease of beam lifetime, stabilization of temperature in the ring tunnel and so on.

ACKNOWLEDGMENTS

REFERENCES

[1] Photon Factory Activity Report 1999, KEK.

[2] Photon Factory Activity Report 2000, KEK.

[3] "Design Report on Advanced Ring for Pulse X-rays (PF-AR)", KEK Report 97-2 (1997) [in Japanese].

[4] Photon Factory Activity Report 2001, KEK.

[5] T. Miyajima, Photon Factory News, Vol.20, No.1, 2002, p.17 [in Japanese].

[6] S. Yamamoto et al., ReV. Sci. Istrum. **63**, 400 (1992).

[7] S. Yamamoto et al., Phys. Rev. Lett. **62**, 2672 (1989).

[8] T. Fujita et al., in these proceedings.

A MODEL FOR PRODUCING STABLE, BROADBAND TERAHERTZ COHERENT SYNCHROTRON RADIATION IN STORAGE RINGS*

F. Sannibale[1], J. M. Byrd[1,2], A. Loftsdottir[1,2], M. C. Martin[1], M. Venturini[1],
[1]Lawrence Berkeley National Laboratory, One Cyclotron Road, Berkeley, California 94720
[2]Department of Physics, University of California, Davis, Davis, California 95616

Abstract

We present a model for producing stable broadband coherent synchrotron radiation (CSR) in the terahertz frequency region in an electron storage ring. The model includes distortion of bunch shape from the synchrotron radiation (SR), enhancing higher frequency coherent emission and limits to stable emission due to a microbunching instability excited by the SR. We use this model to optimize the performance of a source for CSR emission.

INTRODUCTION

Coherent synchrotron radiation (CSR) occurs when the synchrotron emission from a bunch of relativistic electrons is in phase. In this regime the radiation intensity is proportional to the square of the number of particles per bunch in contrast to the linear dependence of the conventional incoherent radiation. Considering that the number of particles per bunch is typically very large ($> 10^6$), the potential intensity gain for a CSR source is huge. Although CSR was predicted to occur in high energy storage rings over 50 years ago [1], it is only recently that steady state CSR has been observed for the first time in the BESSY-II storage ring [2, 3]. Coupled with the first successful application of such a source [4], there is the exciting possibility of using this radiation as an innovative and very powerful source in the far infrared/terahertz frequency range.

Attractive features of the BESSY-II radiation were a flux increase of about five orders of magnitude over the incoherent synchrotron spectrum, a broadband frequency range from about 3 cm^{-1} to 60 cm^{-1} and the stability of the source. However, several curious features of the radiation were also observed. First, the coherent emission spectrum extended to shorter wavelengths than expected from a Gaussian electron bunch of the measured length. Second, a significantly non-Gaussian longitudinal distribution of the electron bunch was observed. Third, a threshold current was observed above which the CSR was emitted in chaotic bursts. We have developed a model that accounts for the above-mentioned observations and provides a tool for predicting and optimizing the performance of a ring-based CSR source.

This paper presents the elements of the model and describes the design criteria for an optimized stable ring based CSR source. We consider only the case of a bending magnet.

CSR RADIATION AND SR WAKEFIELD

The synchrotron radiation (SR) power spectrum is given by [1, 5]:

$$\frac{dP}{d\lambda} = \frac{dp}{d\lambda}[N + N(N-1)g(\lambda)] \tag{1}$$

where λ is the wavelength of the radiation, p is the single particle emitted power, N is the number of particles per bunch and g is the so-called CSR form factor. This numerical quantity, whose value ranges between 0 and 1, is essentially the square of the Fourier transform of the normalized bunch distribution. In expression (1) both the incoherent and coherent terms are included. The first is simply the part proportional to N while the second is proportional to N^2 and to g. In order to have significant CSR emission at the wavelength of interest it must be $g(\lambda) > 1/N$. For short wavelengths, according to the definition of g, this implies having short bunches. For longer wavelengths g increases and approaches 1 but above the vacuum chamber cutoff wavelength the CSR emission is quickly inhibited. For the particular case of a Gaussian distribution, CSR occurs for $\sigma_z < \lambda/\pi$, where σ_z is the rms bunch length. In the general case, comparing at short wavelengths bunches with same rms length, non Gaussian distributions can present a g factor significantly larger than Gaussian ones. This implies that these 'distorted' bunches can have CSR emission at wavelengths remarkably shorter than in the purely Gaussian case. From the experimental results on references [2] and [3] it can be found that the BESSY-II CSR emission belongs to this category. In fact, streak camera measurements indicated bunch lengths ~ 1 mm while CSR was visible down to λ ~ 200 μm, in disagreement with the condition for Gaussian bunches and indicating the presence of distorted distributions.

Equilibrium longitudinal distributions in electron storage rings are usually Gaussian. The possible phenomena that can generate bunch distortions can be classified in two main categories. Non linear dynamics

effects and wakefield induced effects. RF and lattice nonlinearities belong to the first group, while CSR and vacuum chamber wakefields fall in the second one. For most of the storage rings, including BESSY-II, RF nonlinearities are very small and can be neglected. We have simulated the effects of lattice nonlinearities for the case of BESSY-II. The results showed a very small distortion effect that was clearly insufficient to explain the experimental data. In the wakefield category, the SR wakefield, which is always present, is the natural candidate for beginning this analysis and a reasonable approach consists in starting with the simplest model, the free space electron SR wakefield [6, 7, 8]:

$$W(\tau) = \frac{e}{2\pi\rho}\frac{dS(\tau)}{d\tau} = \frac{e}{2\pi\rho}\frac{d}{d\tau}\left(-Z_0\left(\frac{\rho}{3c}\right)^{1/3}\tau^{-1/3}\right) \quad (2)$$

where $Z_0 = 377$ ohms, ρ is the dipole magnet bending radius, c is the speed of light, e is the electron charge and τ is the distance from the wake inducing particle in time units. For $\tau < 0$ $W(\tau) = 0$, indicating that in the SR wakefield case particles in the head of the bunch cannot influence the ones in the tail. The free space assumption can be justified by the fact that for bunches much shorter than the vacuum chamber height, and an optimized CSR source must be designed to fulfill this requirement, the shielding effects are small.
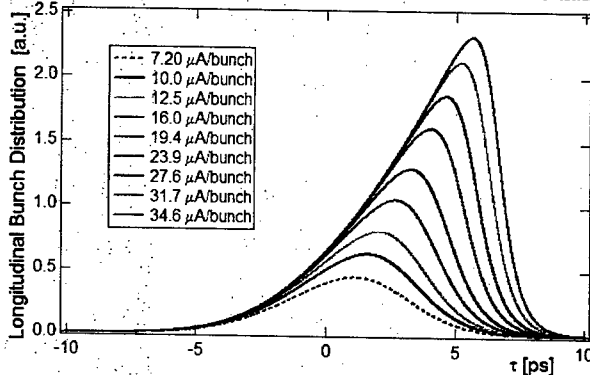
FIG. 1. Calculated equilibrium longitudinal distribution for different currents per bunch using the free space SR wakefield. BESSY-II case.

This free space SR case was already investigated in reference [8] where the Haissinski equation solution for the longitudinal current distribution $I(\tau)$ was numerically calculated:

$$I(\tau) = K e^{-\frac{(c\tau)^2}{2\sigma_z^2} - \frac{c^2}{\sigma_z^2 \dot{V}_{RF}}\int_0^\infty I(\tau-t)S(t)dt} \quad (3)$$

where σ_z is the natural bunch length, $\dot{V}_{RF}$ is the time derivative of the radio frequency (RF) voltage at the synchronous phase and K is a normalization constant.

Figure 1 shows, in the example of BESSY-II, the equilibrium longitudinal bunch profile calculated by this model for different currents per bunch. A strong distribution asymmetry (sharper leading edge) increasing with the bunch current and thus with the SR wake is clearly visible. The result demonstrates that the SR wakefield alone is able to produce non-Gaussian bunches that significantly enhance the CSR emission towards shorter wavelengths as shown in Figure 2.
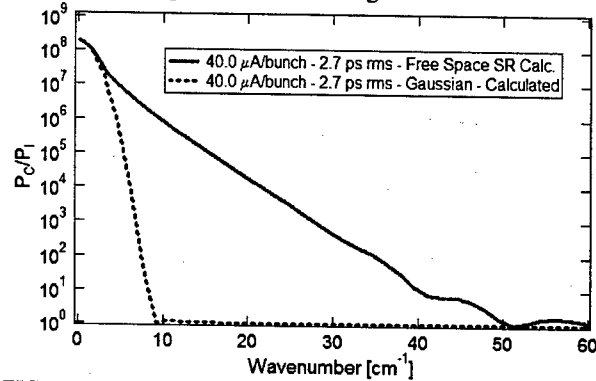
FIG. 2. Comparison between the CSR gain (ratio between coherent and incoherent SR power) for the two cases of Gaussian and SR wakefield distorted distribution for same current and bunch length. BESSY II parameters.

OPTIMIZING A STORAGE RING BASED CSR SOURCE

We want now to design a source exploiting this effect. In the design of such a source one of the fundamental requirements is the stability of the CSR emission. A SR driven single bunch instability has been theoretically predicted [9], simulated [10] and experimentally verified [11]. Above a current threshold the beam becomes unstable and transient longitudinal microstructures appears generating CSR bursts. In the following source optimization analysis, stability criteria are included. In the free space SR model, the number of particles per bunch at equilibrium is given by [8]:

$$N = A\frac{B^{1/3}f_{RF}V_{RF}\sigma_z^{7/3}}{E^{1/3}}F \quad (4)$$

where $A = 6.068\ 10^{-4}$ [MKS units], B is the dipole magnet magnetic field, f_{RF} is the storage ring RF frequency, V_{RF} the RF peak voltage, E is the beam energy, σ_z is the natural bunch length and F is a dimensionless quantity proportional to the integral of the bunch distribution. F and the bunch distribution are calculated by the free space SR model. The larger the current per bunch the stronger is

the distribution distortion and the larger is F. Using equation (1) for $Ng \gg 1$ and the expression for $dp/d\lambda$ when the wavelength is much larger than the critical wavelength (see for example [12]) we can write for a ring with N_b bunches:

$$\frac{dP}{d\lambda} = C \, N_b \frac{B^{1/3} f_{RF}^2 V_{RF}^2}{L \, E^{1/3}} \frac{\sigma_z^{14/3}}{\lambda^{7/3}} F^2 g(\lambda) \qquad (5)$$

where $C = 2.642 \; 10^{-21}$ [MKS units] and L is the storage ring length. In optimizing a CSR source we want to pursue the following tasks: increase as much as possible the band of wavelengths where the SR emission is coherent, maximize expression (5) and maintain the beam stability. The bandwidth of the CSR emission can be extended towards longer wavelengths by designing high cutoff frequency vacuum chambers. On the other side, as we said, the bandwidth can be extended towards shorter wavelengths by shortening the bunch and/or by increasing the bunch distortion. The second way is strongly preferred because it increases F and according to Eqn. (5) also the CSR power. On the other hand, Eqn. (5) shows that decreasing the bunch length dramatically decreases the power. The distortion is enhanced by increasing the number of particles per bunch but the maximum value that this quantity can assume is limited by the previously mentioned microbunching instability [9, 11]:

$$N \leq N_S = D \; \frac{B^{1/3} f_{RF} V_{RF}}{E^{1/3}} \frac{\sigma_z^3}{\lambda^{2/3}} \qquad (6)$$

where $D = 4.528 \; 10^{-3}$ [MKS units]. By combining equations (4) and (6) the following stability criterion can be derived:

$$F \leq F_{MAX} = \frac{1}{G} \left(\frac{\sigma_z}{\lambda} \right)^{2/3} \qquad (7)$$

where $G = 0.1340$ is a dimensionless constant. It must be remarked that the microbunching instability theory was derived for the case of a coasting beam. Anyway simulations and experimental results at the ALS [11] showed that the model works also for bunched beams and that the theory is able to predict the instability threshold when in Eqn. (7) $\lambda \sim 2\sigma_z$ is used obtaining $F_{MAX} \sim 4.7$. In the case that σ_z is greater than the vacuum chamber cutoff wavelength λ_{CO}, then $\lambda = \lambda_{CO}$ must be used in Eqn. (7). The maximum number of stable particles per bunch can be evaluated by using F_{MAX} in Eqn. (4). Once the bandwidth optimization is completed the quantities σ_z, F and $g(\lambda)$ in Eqn. (5) are frozen and cannot be modified anymore. All the remaining 'knobs' in Eqn. (5) can be freely changed, within the technological limits, for the

maximization of the CSR power. It must be remarked that the momentum compaction, which does not appear explicitly in Eqn. (5), is used in this scheme for keeping a constant σ_z when the other quantities are changing. Figure 3 shows an example of the impressive performances that a source designed with the presented criteria can achieve.
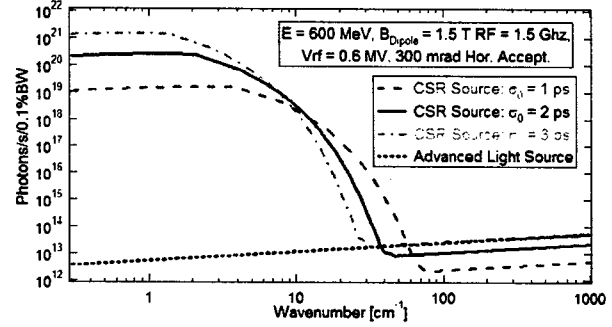
FIG. 3. Example of source optimized for the CSR production using the criteria described in this letter. The potential photon flux gain in the Far-IR THz region of the spectrum is huge if compared with an existing conventional source (ALS).

Such a source would have between 6 and 8 orders of magnitude greater average flux than other available sources in the THz and sub-THz frequency range.

ACKNOWLEDGEMENTS

REFERENCES

[1] J. S. Nodvick and D.S. Saxon, Phys. Rev. 96, 180 (1954)
[2] M. Abo-Bakr et al., Phys. Rev. Lett. 88, 254801 (2002).
[3] M. Abo-Bakr et al., Phys. Rev. Lett. 90, 094801 (2003).
[4] J. Singley et al.; submitted to Phys. Rev. Lett.
[5] G. Williams et al., Phys. Rev. Lett. 2, 261 (1989).
[6] J. B. Murphy, S. Krinsky, and R. L. Gluckstern, Part. Accel. 57, 9 (1997).
[7] Y. S. Derbenev, et al., DESY Report No. TESLA-FEL 95-05, 1995.
[8] K. Bane, S. Krinsky, and J. B. Murphy, in Micro Bunches Workshop, Upton, NY, 1995, edited by E. B. Blum, M. Deines, and J. B. Murphy, AIP Conf. Proc. 367 (AIP, Woodbury, NY, 1996), p. 191.
[9] S. Heifets and G. Stupakov, Phys. Rev. ST Accel. Beams 5, 054402 (2002).
[10] M. Venturini and R. Warnock, Phys. Rev. Lett. 89, 224802 (2002).
[11] J. M. Byrd, et al., Phys. Rev. Lett. 89, 224801 (2002).
[12] A. Hofmann, Synchrotron Radiation and Free Electron Lasers CAS, CERN 98-04.

COLLECTIVE EFFECTS ANALYSIS FOR THE BERKELEY FEMTOSOURCE[*]

J. Corlett, S. De Santis, A. Wolski, A. Zholents LBNL, Berkeley, CA 94720, USA

Abstract

We present an overview of collective effects in a proposed ultrafast x-ray facility, based on a recirculating linac. The facility requires a small vertical emittance of 0.4 mm-mrad and is designed to operate with a "flat bunch" with a large emittance ratio. Emittance control from the electron source at the RF photocatode to the photon production chain of undulators, including understanding and mitigation of collective effects, is critical to successful machine operation. Key aspects of accelerator physics involved in beam break-up, coherent synchrotron radiation, resistive wall impedance and other effects have been addressed and reported here.

INTRODUCTION

The proposed LUX femtosecond X-ray facility [1] is based on a 600 MeV superconducting recirculating linac. It accelerates up to 2.5 GeV a 2 ps electron beam, which is subsequently used to generate ultra-short X-ray pulses. It is vital to preserve a small vertical emittance throughout the machine since the X-ray pulse duration is a function of the vertical emittance.

In this paper we investigate the three main mechanisms that can lead to a degradation of machine performance by emittance or energy spread increase: wakefields in the main linac and the preinjector; resistive wall impedance in the vacuum chamber; and coherent synchrotron radiation.

WAKE FIELDS

The performance of LUX depends on preservation of low vertical emittance through the linac and the arcs. The short-range transverse wake fields from the linac cavities are a potential source of vertical emittance growth, and the effects need to be carefully evaluated. The size of the transverse kick from the wake fields increases with increasing offset of the bunch from the axis of the cavity, so there are possible implications for the alignment of the cavities and orbit control.

It is possible to arrive at a semi-analytical estimate of the effects of the wake fields of the linac, as presented in [2]. However, a more complete investigation including the nominal bunch distribution and tracking through the arcs requires a tracking code. For the present studies, we have used MERLIN [3], which allows simulation of required effects. We also present some estimates of the influence of long-range wake fields on emittance growth.

Short-range wake fields

The present design of the linac uses the TESLA 9-cell, 1.3-GHz superconducting cavities. An analytical expression for the wake fields is reported in [4], while the

lattice design used for the arc tracking can be found in [5]. For an exhaustive report of the technical details of the tracking, see [6].

To verify the wake field model in MERLIN, we first tracked a bunch with the nominal 2 ps bunch length, and (effectively) zero transverse emittance through four passes of the linac. In this case, the bunch was with a fixed vertical offset in each cavity, and the bunch was taken straight from the end of the linac on each pass and re-injected at the start of the linac: i.e. we modeled the effects of perfectly achromatic arcs with integer betatron phase advances. The results shown in Fig.1 are in very good agreement with our analytical model [2].
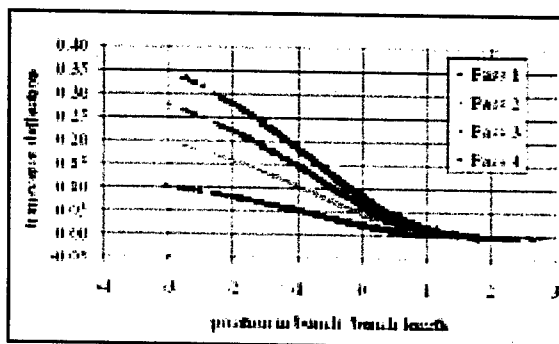
Figure 1. Transverse deflection of a 2 ps zero-emittance bunch, through four consecutive passes at constant vertical offset through the linac. Merlin tracking.

To estimate emittance growth from the wake fields in a linac with vertical cavity misalignments, we tracked a 10,000 macroparticle bunch with the nominal parameters specified in Table 1 from the entrance of the linac to the exit after the fourth pass. Vertical misalignments with a range of rms values (and a cut-off at 5 sigma) were applied to the cavities; the beam sees the same misalignments in the simulation on each pass. The cavity misalignments were the only imperfections applied to the machine; the arc optics and alignment were as designed. For large cavity misalignments, there is significant orbit distortion that is expected to lead to vertical emittance growth from coupling in the arc sextupoles.

Table 1: Bunch Parameters Used In Wakefield Simulations.

Initial bunch energy	120 MeV
Bunch charge	1 nC
Bunch length	2 ps
Energy spread	10^{-3}
Horizontal emittance (normalized)	20 μm
Vertical emittance (normalized)	0.4 μm

No distinction was made between cryostats; in reality, cavity offsets are expected to be correlated according to which cryostat they are in. Since we find that the wake field effects for any reasonable cavity misalignments are so small, our conclusions are not likely to be affected by the fact that we have neglected this effect.

Results of tracking with the sextupoles turned on are shown in Fig. 2; results with the sextupoles off are shown in Fig. 3. The emittance growth with wakefields off is due to the deflecting kick from the cavity fringe fields. It appears that the wake fields themselves make negligible contribution to the emittance growth. The wake field cancellation resulting from the phase advance across the arcs can easily reduce the head-tail displacement by more than an order of magnitude; in which case, we would expect to see an emittance growth of the order 5% (tracking with an extreme rms vertical cavity misalignment value of 2 mm. The actual misalignment is about 0.5 mm instead).
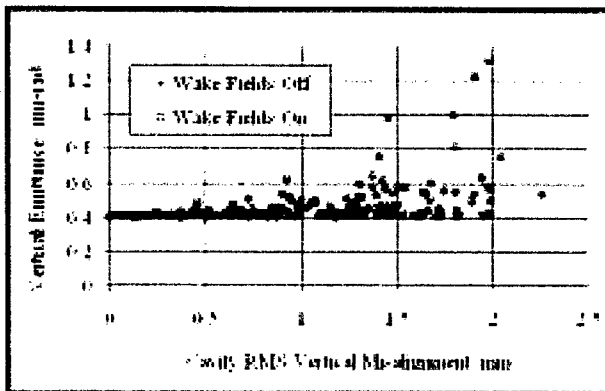
Figure 2: Results of tracking a nominal bunch from the first entrance of the linac through four passes (including the arcs) to the fourth exit from the linac. The arc sextupoles were turned on.
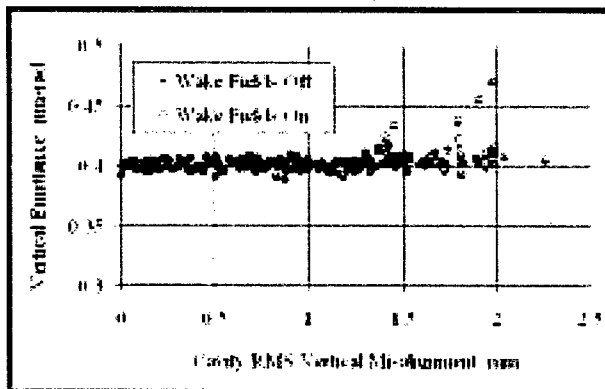
Figure 3: Results of tracking a nominal bunch from the first entrance of the linac through four passes (including the arcs) to the fourth exit from the linac. The arc sextupoles were turned off.

With the sextupoles turned on, any emittance growth from the wake fields is hidden by the very much larger emittance growth from the coupling. This should be easily fixed by proper orbit control and beam based alignment.

Long-Range Wake Fields

Since a bunch in LUX is recirculated four times through the main linac, we also investigate the influence of the transverse long-range wakefield on the bunch emittance. An estimate of the wakefield can be obtained by adding up the transverse wake from all the high-order modes of the 32 linac cavities. Figure 4 shows that the field amplitude decays by only a factor of 10 in the typical recirculation time of less than 1 μs. The long-range transverse wakefield is, in most cases, fairly constant over the bunch length and, therefore, its effect translates to a small additional displacement of the entire bunch (Fig.5), which does not affect the vertical emittance.
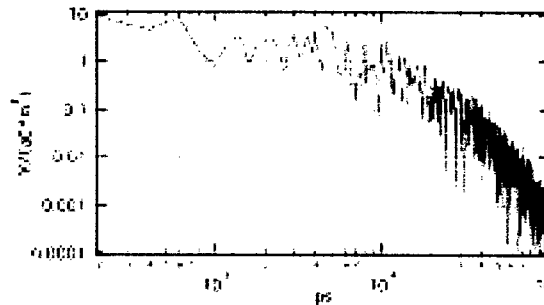
Figure 4: Long-range transverse wakefield with a 0.1% random detuning in the RF cavities HOMs.
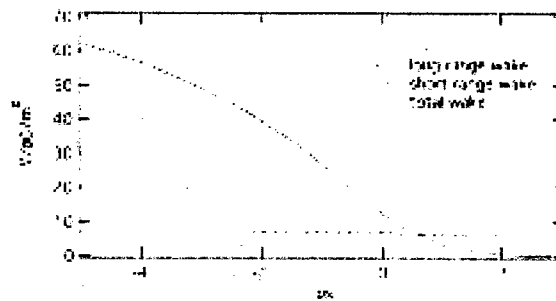
Figure 5: Total vertical displacement along a 2 ps bunch from short and long range transverse wakefields.

Resistive Wall Impedance

The resistive wall impedance also induces a vertical deflection along a bunch throughout the machine, which leads to a dilution of the vertical emittance. The resistive wall effects are worse at lower energies, for shorter bunches and for narrower apertures of the vacuum chamber. Figure 6 shows the oscillation of the bunch tail along the first arc for a beam pipe radius of 4.5 mm and an initial vertical offset of 100 μm. The tracking code results agree very well with a simple analytical model.
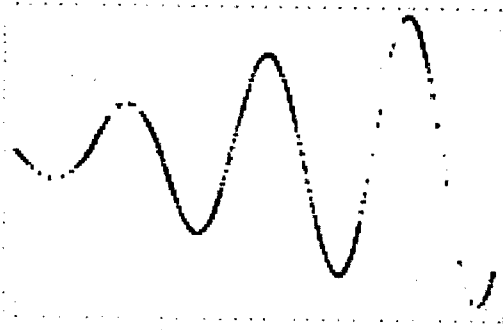
Figure 6. Vertical deflection of the bunch tail along an arc. Tracking (dots) and analytical model (solid line).

It can be seen that, even in this very conservative scenario, the resistive wall contribution is limited to less than 10% of the vertical beam size. This figure is expected to improve, as we expect to have an orbit control significantly better than 100 µm and larger beam pipes in most of the machine. The effects in the other arcs will be significantly smaller, because of the higher beam energy, so that we do not expect the resistive wall impedance to limit the performance of the light source.

COHERENT SYNCHROTRON RADIATION

Coherent synchrotron radiation (CSR) causes a variable energy loss along a bunch which, in turn, leads to emittance increase in the orbit plane. Since we have a relatively large horizontal emittance, the estimated small emittance growth does not seem to be harmful. Therefore, we are mainly concerned by the energy loss because of the resulting increase in the energy spread. CSR calculations are currently in progress.

Figures 7 and 8 show the tracking results [7] for a bunch with an assumed rectangular distribution in the horizontal emittance plane. It can be seen that, while CSR influences the bunch head and tail, the bunch core (90% of the particles) is relatively unaffected. Energy spread is controlled by careful design of the lattice [8].

Figure 8: Tracking (*elegant*) of the energy spread at the linac exit. Bunch core (green), head (blue) and tail (red).

CONCLUSIONS

We have investigated several fundamental aspects of the beam dynamics in LUX. We are mainly concerned with the preservation throughout the machine of the vertical emittance and the energy spread, which are vital for the generation of ultra-short X-ray pulses. Our results show that, while one must always pay attention to these aspects in the design phase, they do not present insurmountable problems towards obtaining the machine design parameters.

REFERENCES

[1] J. Corlett et al. A Recirculating Linac-Based Facility for Ultrafast X-Ray Science, these proceedings.

[2] S. De Santis and A. Zholents, Beam Break Up Analysis for the Berkeley Femtosource, EPAC 2002.

[3] N.J. Walkers MERLIN (a C++ class library for accelerator beamline simulation) can be found at http://www.desy.de/~njwalker/MerlinII/index.htm

[4] TESLA Technical Design Report, DESY 2001-011, March 2001.

[5] A. Zholents et al, Initial Lattice Studies for the Berkeley Femtosecond X-Ray Light Source, proceedings EPAC 2002, Paris, France, June 2002.

[6] A. Wolski, Tracking Studies of RF Cavity Transverse Wake Fields in the Berkeley Femtosecond Light Source, CBP Tech Note-265 (2002).

[7] M. Borland, Simple Method for Particle Tracking With Coherent Synchrotron Radiation, Phys. Rev. ST-AB, 4 2001.

[8] A. Zholents Longitudinal Phase Space Control in the Berkeley Femtosecond X-Ray Source LUX, these proceedings.

Figure 7: Tracking (*elegant*) of the horizontal emittance at the linac exit. Bunch core (green), head (blue) and tail (red).

NOISE REDUCTION EFFORTS FOR THE INFRARED BEAMLINE AT THE ADVANCED LIGHT SOURCE

Tom Scarvie, Nord Andresen, Ken Baptiste, John Byrd, Mike Chin, Mike Martin,
Wayne McKinney, Christoph Steier, LBNL, Berkeley, CA, 94720, USA

Abstract

The quality of infrared microscopy and spectroscopy data collected at synchrotron based sources is strongly dependent on noise. We have successfully identified and suppressed several noise sources affecting Beamline 1.4.3 at the Advanced Light Source (ALS), resulting in significant reductions to the noise in the users' FTIR spectra. In this paper, we present our methods of noise source analysis and the techniques used to reduce the noise and its negative effect on the infrared beam quality. These include analyzing and changing physical mounts to better isolate portions of the beamline optics from low-frequency environmental noise, and modifying the input signals to the main ALS RF system. We also discuss the relationship between electron beam energy oscillations at a point of dispersion and infrared beamline noise.

INTRODUCTION

Noise reduction for this beamline has been an ongoing project since it was commissioned in 1997. Transverse motions of the photon beam are transformed into intensity variations in the IR signal by an aperture or apertures in the beamline optics. There are two main sources of this photon beam motion: mechanical vibrations of beamline components and electron beam motion introduced by energy oscillations at a point of dispersion in the ring (the bending magnet IR source). The first noise type was previously lowered by mechanically isolating beamline components from environmental vibrations and the remaining noise damped with an active mirror feedback system [1-4]. Higher-frequency noise caused by electron beam motion was dramatically diminished when a quieter master oscillator was installed in the ALS RF system [5]. In order to further reduce noise in the FTIR spectra and bring the signal-to-noise levels closer to what is achieved using a standard Glowbar IR source, we revisited both of these noise types to further improve them.

DETAILS

Fourier transformed time domain signals from the first optical detector in the mirror feedback system and from the FTIR detector signal gave us baseline noise measurements. The spontaneous noise from 0-200Hz and 0-25kHz is shown in Fig. 1.
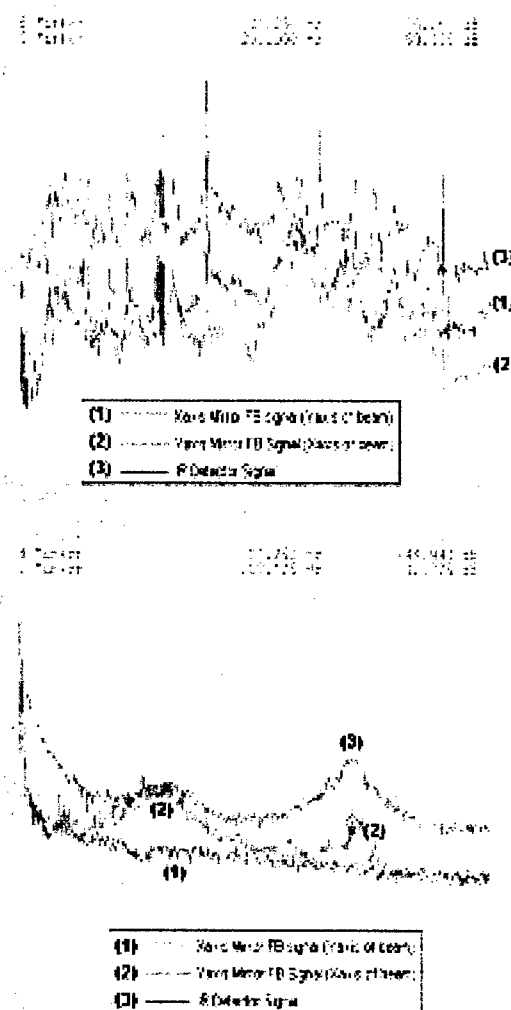
Figure 1. Spontaneous noise spectra at the Infrared Beamline 1.4.3, prior to any of the improvements discussed in this report.
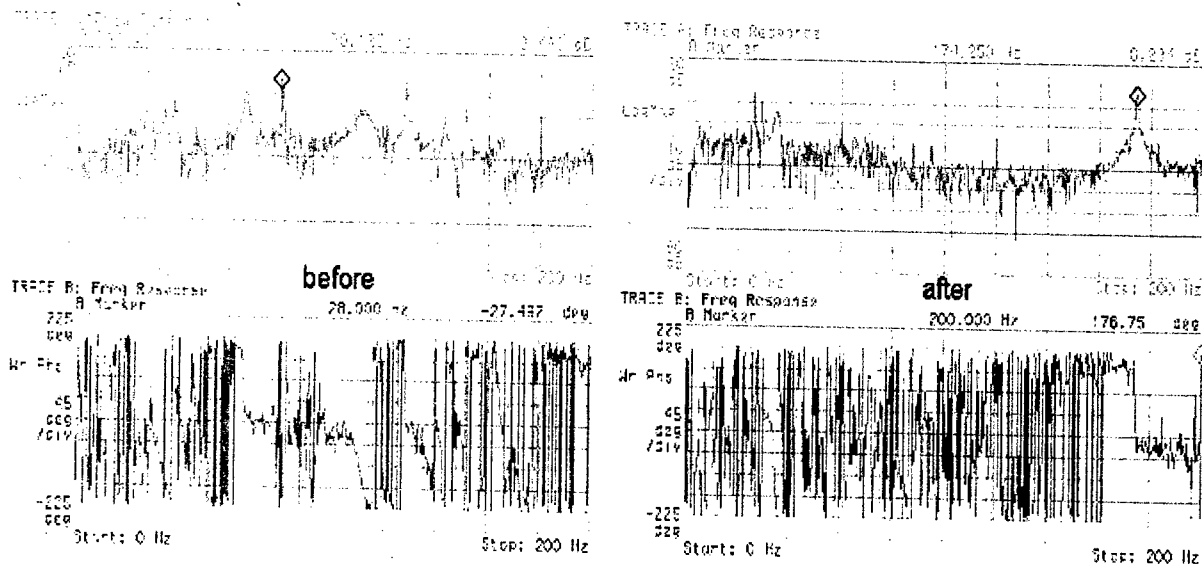
Figure 2. Transfer functions of the IR signal before and after the M2 mechanical modification. A distinct slope in the lower phase plot indicates a vibration correlated to the driving frequency and therefore a significant mechanical oscillation. Many of the mechanical vibration modes were reduced, especially those at 65 Hz, 110 Hz, 128 Hz. The peak that arose at 175 Hz is still under investigation.

Low frequency noise

In the low frequency range (0-200 Hz), previous mechanical isolation efforts identified the M1 and M2 beamline mirrors[6] as the main suspects for vibration induced noise. To further characterize this noise, a Wilcoxon Research Model F3 Electromagnetic Shaker was clamped to the mirror housing and transfer functions were taken by sweeping the driving frequency from 0 Hz to 200 Hz and recording the response of the signal from the first optical detector of the mirror feedback system and from the FTIR bench.

Upon seeing numerous correlated vibration peaks indicative of mechanical motion, it was discovered that a tensioning spring had been left out of the M2 mirror assembly.

The spring was installed and adding motor drive shafts for external adjustment further confined mirror motion. Transfer function measurements following these modifications showed a marked improvement in mirror stability and dropped noise levels in the lower frequencies of the FTIR signal, as seen in Fig. 2.

High frequency noise

At higher frequencies (500 Hz – 25kHz), mechanical vibrations are unlikely to be the cause of noise, so any introduced noise is most likely coming from transverse motion of the electron beam.

Fig. 1 shows that there are noticeable noise peaks centered at about 7.5 kHz and 18 kHz in the y-axis of the optical detector and in the overall IR signal, but none in the x-axis of the optical detector signal.

Due to the configuration of the beamline, x-axis beam motion is observed on the y-axis of the detector, and vice-versa, and so the traces correspond to what one would expect for horizontal beam oscillations. We know that the 7.5 kHz peak is due to synchrotron oscillations of the beam, because it slowly shifts as the beam current decays and also changes with beam energy. There is little that can be done to damp this oscillation. The 18 kHz peak, on the other hand, was also observed on the x-axis signal of a storage ring beam position monitor. This noise was found to be coming from a DAC output in the storage ring RF phase shifter system. The output of the DAC was filtered by the RF group and Fig. 3 (on the next page) shows the result – the 18 kHz noise is mostly gone.
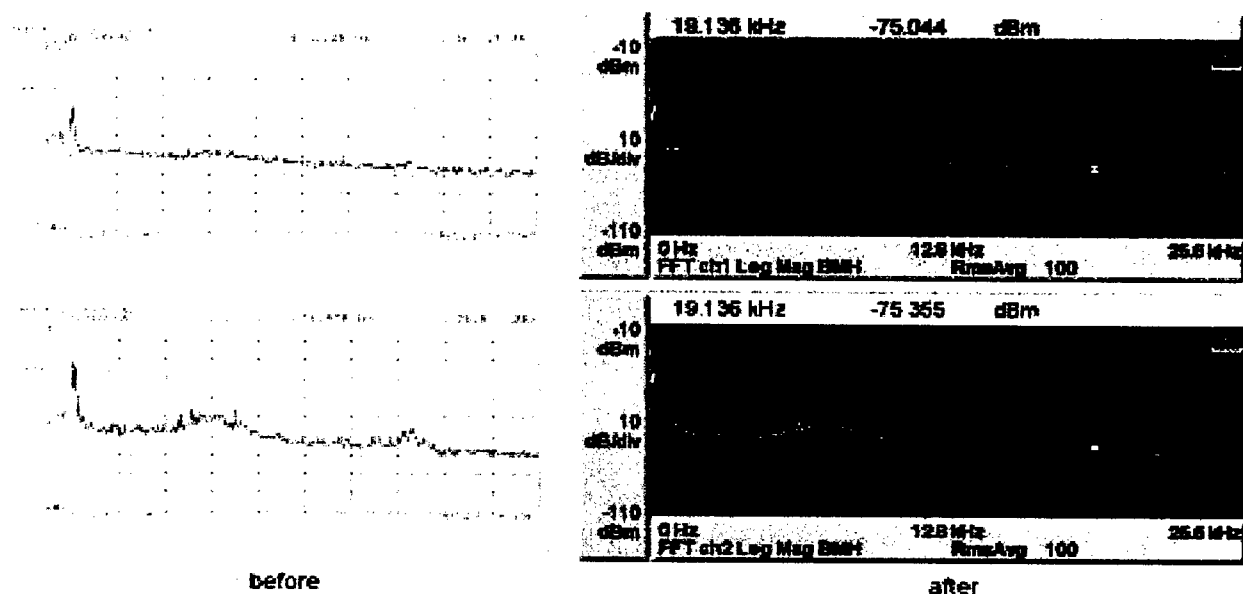
before   **after**

Figure 3. 0-25 kHz spontaneous noise on the first mirror feedback optical detector before and after RF phase shifter DAC filtering. The upper and lower plots represent vertical and horizontal electron beam motion, respectively. Different scopes were used, but the ranges are the same. Notice the substantial reduction in the 18 kHz peak in the bottom-right plot. The broad 7.5 KHz peak is due to synchrotron oscillations and is difficult to suppress.

CONCLUSION

Work on noise reduction efforts at BL 1.4.3 is ongoing. We are more thoroughly examining the beamline optics between the M2 mirror and sample stage to identify any particular aperture(s) where the photon beam motion is transformed to an amplitude modulation of the IR signal. The incoming infrared light also contains harmonics of 60 Hz power line noise, a problem noted by infrared beamlines at other synchrotron facilities. It is suspected that this noise is introduced by the RF system, but attempts at filtering it have been unsuccessful so far. With further noise improvements, we hope to bring the signal-to-noise ratio to a level competitive with other IR sources and increase the demand for synchrotron-based infrared science.

REFERENCES

1. J.M. Byrd, M.C. Martin, and W.R. McKinney, in 1999 Particle Accelerator Conference, eds. A. Luccio and W. MacKay, (New York, 1999), p. 495.

2. J.M. Byrd, in 1999 Particle Accelerator Conference, eds. A. Luccio and W. MacKay, (New York, 1999), p. 1806.

3. J.M. Byrd, M.Chin, M.C. Martin, W.R. McKinney, and R. Miller, SPIE Proceedings, 1999, Vol. 3775, pp.58-64. LBNL-44134

4. W.R. McKinney, M.C. Martin, J.M. Byrd, R. Miller, et al., SPIE Proceedings, 1999, Vol. 3775, p. 37.

5. J.M. Byrd, Proceedings of the 1999 Particle Accelerator Conference, New York, Editors: A. Luccio, W. MacKay, p. 1806, 1999. LBNL-43031

6. A schematic of Beamline 1.4 is available at http://www.als.lbl.gov/als/als_users_bl/1.4.3-Datassheet.pdf.

LONGITUDINAL PHASE SPACE CONTROL IN THE BERKELEY FEMTOSECOND X-RAY LIGHT SOURCE LUX*

A. Zholents LBNL, Berkeley, CA 94720, USA

Abstract

LUX, the proposed Berkeley femtosecond x-ray light source, is a ~2.5 GeV recirculating linear accelerator, where electrons reach their final energy in four passes through a 600 MeV superconducting linac after injection at ~ 120 MeV. An important consideration for this machine is the preservation of the electron beam longitudinal emittance through the various stages of acceleration including injection linac, bunch compression, and various passages through the linac and magnetic arcs. In this paper we analyze the longitudinal dynamics of electrons and define a strategy for the electron beam manipulation leading to a successful conservation of the longitudinal emittance. Particular attention is given to the management of the correlated energy spread induced by collective effects such as longitudinal wake fields and coherent synchrotron radiation (CSR).

INTRODUCTION

Here we report preliminary studies of the longitudinal dynamics of electrons in the recirculating linear accelerator LUX currently under design in Berkeley Laboratory [1]. In this machine the electron bunches are produced in an RF photocathode gun, accelerated in a superconducting injector linac, compressed in the bunch compressor and injected into the recirculating accelerator where they are accelerated to final energy in four passes through the superconducting linac. This scheme possesses rich opportunities for particle manipulation in the longitudinal phase space allowing simple optimization of electron beam parameters at top energy and along the acceleration cycle. One can launch the electron beam at different RF phases on each passage through the linac by adjusting the time that it takes for electron bunch to come back to the linac. This technique can be used to create (or compensate) an energy chirp along the electron bunch with individual features on each orbit turn. It is also possible to regulate the R_{56} time-off-flight parameters of different arcs and control the amount of bunch compression on every orbit turn of the recirculation.

During our study we exercised several different options and chose what we believe is an optimal one. The driving criterion for this choice was obtaining an electron bunch at top energy with small energy spread (less than 1 MeV) and with a pulse duration of 2-3 ps. In all studies significant effort was given to optimization of the injection chain, namely to acceleration in the injector linac, linearization of the electron beam footprint in the longitudinal phase space with a third harmonic cavity, creation of the correlated energy chirp along the electron bunch before bunch compression, and finally to the bunch compression. This system is briefly described in another report at this conference [2]. In this report we focus mainly on the electron beam acceleration in the recirculating accelerator.

RESULTS

Our present scheme assumes acceleration of a ~ 20 ps electron bunch to ~ 120 MeV and its compression to ~ 2.5 ps before injection into the recirculating accelerator. No further compression in the recicrculating accelerator is considered, since we found that it is difficult to deal with CSR effects in the magnetic arcs for a shorter bunch. We also tried gradual compression of the electron bunch in the recirculating accelerator along the acceleration and found it somewhat less attractive than acceleration of a short bunch right after injection. However the optimum is rather shallow as one can judge from Figure 1.
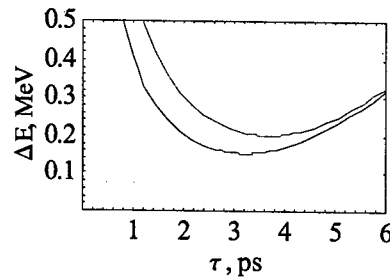
Figure 1. Energy spread at the end of the acceleration versus the bunch length: longitudinal emittance 6×10^{-7} eV-s (red curve) and 4×10^{-7} eV-s (blue curve).

This figure shows beam energy spread at the final energy as a function of the bunch length calculated for two values of the normalized longitudinal emittance: 6×10^{-7} eV-s and 4×10^{-7} eV-s. Since we consider a uniform rectangular distribution these numbers represent an entire phase space area. The emittance contribution dominates when the electron bunch is short while for a longer bunches electrons sample more non-linearity in the acceleration field and this leads to increased correlated energy spread in the bunch. Thus there appears a shallow minimum near 3 ps bunch length. We chose to have a slightly shorter bunch length to provide a better match to the x-ray beam line optics.

We include longitudinal wake field effects in the linac and CSR effects in the arcs in our analysis. In this study we did not consider wake fields related to the resistive wall effects. In order to account for the longitudinal wake field effects in the linac we use the wake function:

$$w(s)\left[\frac{V}{pC\,m}\right] = -38.1\left(1.165\exp\left(-\sqrt{\frac{s}{3.65\,mm}}\right) - 0.165\right) \quad (1)$$

given in [3] for a point charge steady state wake of a long linac. For a uniform stepped function charge distribution shown in Figure 2 we calculate energy loss of electrons as

872

a function of their position in the bunch using the following expression:

$$\frac{1}{Q}\frac{dE(s)}{dz}\left[\frac{eV}{pC\,m}\right] = -19.05\int_{-1}^{2s/l_b}\left(1.165\exp\left(-\sqrt{\frac{s-x(l_b/2)}{3.65\,mm}}\right)-0.165\right)dx \qquad (2)$$

where l_b is the bunch length. The right hand side of Eq. (2) can be fitted by a quadratic polynomial with high precision and for 2 ps bunch length we obtain:

$$\frac{1}{Q}\frac{dE(s)}{dz}\left[\frac{eV}{pC\,m}\right] = -15.25 - 13.72\left(\frac{2s}{l_b}\right) + 1.33\left(\frac{2s}{l_b}\right)^2 \qquad (3)$$

This formula was used in our calculations. The agreement between formulae (2) and (3) is demonstrated in Figure 3.
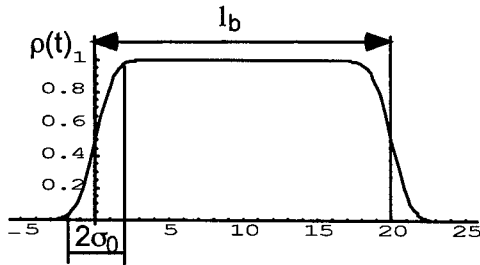
Figure 2. The longitudinal density of electrons.
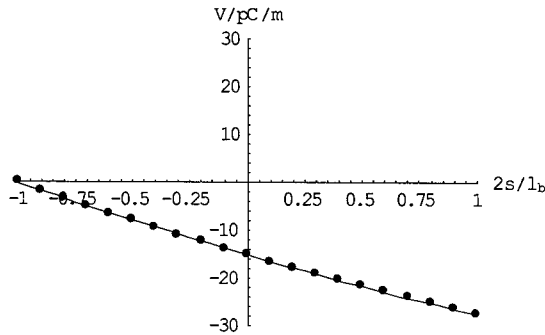
Figure 3. The longitudinal wake function for the linac. Dots show calculations using exact expression (2) and the solid line show calculations using fitting formula (3).

In order to account for CSR effects we used the CSR wake function from [4] and obtained the following energy loss per unit length of trajectory:

$$\frac{dE(s)}{dz} \cong -\frac{2}{3^{1/3}\sqrt{2\pi}}\frac{Ne^2}{\sigma_0\rho^{2/3}}\int_{-\infty}^{s}\left(e^{-\frac{s'^2}{2\sigma_0^2}} - e^{-\frac{(s'-l_b)^2}{2\sigma_0^2}}\right)\frac{ds'}{(s-s')^{1/3}}, \qquad (4)$$

where N is a number of particles per bunch, and e is the electron charge. Deriving (4), we assume a uniform longitudinal density distribution $\lambda(s) = N/l_b$ in interval $0 < s < l_b$ with smooth transitions at the edges with a characteristic length σ_0 as shown in Figure 2.

Integral (4) can be evaluated in analytical functions. Figure 4 shows the plot of $dE(s)/dz$. One can notice that $dE(s)/dz \sim 1/s^{1/3}$ over the entire length of the bunch excluding edges. For this functional dependence

one can consider partial compensation of the energy variation within the electron bunch induced by CSR by using off-crest acceleration in the linac.
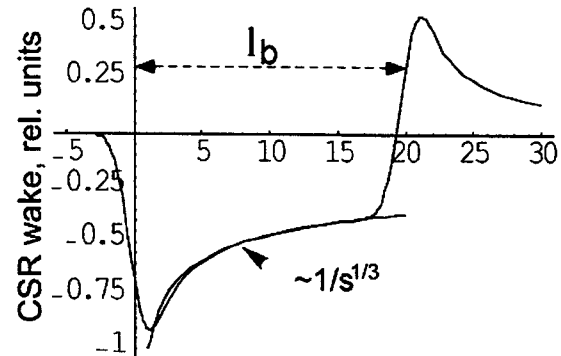
Figure 4. CSR induced energy loss $dE(s)/dz$ for an electron density distribution shown in Fig. 2.

Using $1/s^{1/3}$ dependence for CSR wake function one can calculate the average energy loss per electron due to CSR in the magnet of the length L_m for main core particles with the expression [4]:

$$\Delta E = \frac{L_m}{l_b}\int_0^{l_b}\frac{dE(s)}{dz}ds \cong \frac{3^{2/3}Ne^2}{\rho^{2/3}l_b^{4/3}}L_m. \qquad (5)$$

This is the so-called free space radiation. In practice, the electron bunch moves inside the vacuum chamber that acts as a waveguide for the radiation. Not all spectral components of the CSR propagate in the waveguide and therefore the actual radiated energy is less than in the free space environment. For an estimation of the shielding effect of vacuum chamber we follow recipe suggested in [5]:

$$\Delta E_{shielded}/\Delta E_{free\,space} \cong 4.2(n_{th}/n_c)^{5/6}\exp(-2n_{th}/n_c),$$

$$(n_{th} > n_c) \qquad (6)$$

Here $n_{th} = \sqrt{2/3}(\pi\rho/h)^{3/2}$ is the threshold harmonic number for a propagating radiation, h is the height of the vacuum pipe, $n_c = \rho/c_c$ is the characteristic harmonic number for a Gaussian longitudinal density distribution with the rms value of σ_c. The meaning of n_c is that the spectral component of the radiation with harmonic numbers beyond n_c is incoherent. We define $\sigma_c = l_b/3.22$. This gives us the closest approximation of spectra for the uniform stepped density distribution with the spectra for the Gaussian distribution. All our calculations were carried out for h=7mm and 1 nC bunch charge.

We apply this analysis beginning from the phase space distribution obtained after particle tracking through the bunch compressor and the first pass through the linac with CSR and longitudinal wake field effects, using Elegant [6].
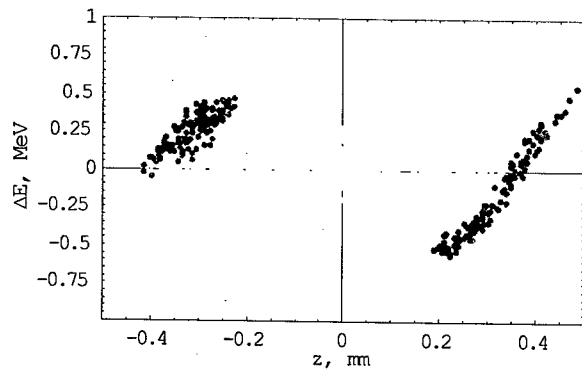
Figure 5. Longitudinal phase space at the end of the first pass through the linac.

This distribution is shown is shown in Figure 5. Red and blue color show approximately 10% of particles from the head and the tail of the bunch. The bulk of the particles are shown with yellow color. One can notice that most distortions are gained in the transition areas of particle density. The longitudinal phase space after the second and the third pass through the linac and at the final energy is shown in Figure 6. Noticeably not much energy spread is gained during the acceleration. We found that the RF phase of 8° for the first beam pass through the linac and RF phases of 5°, 3°, and 6° on subsequent passes are optimal to provide reasonable compensation for correlated energy variations along the bunch induced by the CSR and longitudinal wake field effects.

SUMMARY

The longitudinal dynamics of electrons during the acceleration in the proposed recirculating accelerator LUX has been analyzed. The preliminary results indicate that the machine has sufficient flexibility to be able to counteract and balance effects of coherent synchrotron radiation in the magnetic arcs and the longitudinal wake field effects in the linac. We conclude that the 1 nC electron bunches with bunch length of 2-3 ps can be accelerated to the final energy without excessive growth of the energy spread.

We acknowledge useful discussions with J. Corlett, S. Lidia, J. Staples and extremely helpful guidance regarding use of Elegant from P. Emma.

REFERENCES

[1] J.N. Corlett et al., *A recirculating linac based facility for ultrafast x-ray science*, this conference.
[2] S. Lidia, et al., *An injector for the proposed Berkeley ultrafast x-ray light source*, this conference.
[3] TESLA, Technical Design Report, March 20001, DESY–011, 2001.
[4] E.L. Saldin, E.A. Schneidmiller, and M.V. Yurkov, NIM A 398, (1997)373.
[5] R.Li, C.L. Bohn, J.J. Bisongnano, Particle Accelerator Conference, (1997)1644.
[6] M. Borland, Phys. Rev. Special Topics, Vol 4, 070701(2001).
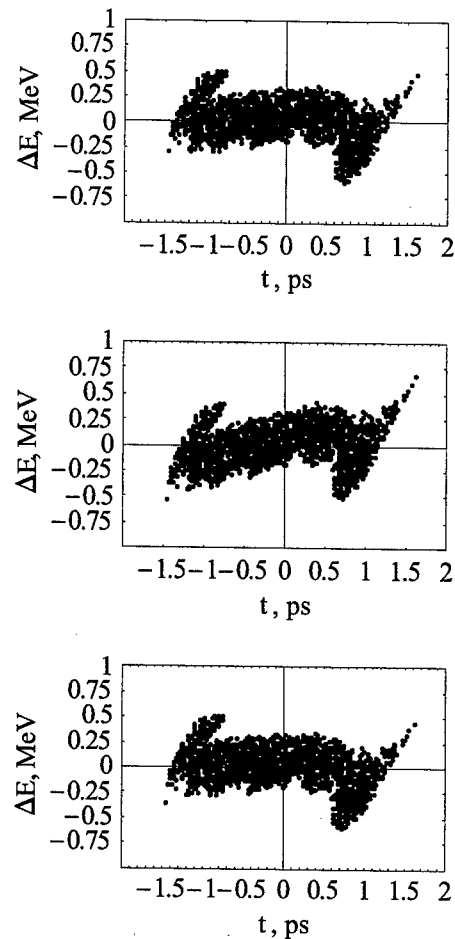
Figure 6. Longitudinal phase space at the end of the second pass through the linac (top plot), third pass through the linac (middle plot) and at the final energy (bottom plot).

NEWLY DEVELOPED INJECTION MODE OF PLS

M. G. Kim, J. Choi, J. Y. Huang and E. S. Park

Pohang Accelerator Laboratory, Pohang, Gyungbuk, 790-784 Korea

Abstract

At the Pohang Light Source, 2 GeV electron beam had been injected to the storage ring and increased to 2.5 GeV using an energy ramping system previously. This ramping process was regarded as a source of closed orbit distortions. The successful upgrade of injection power of the PLS linear accelerator has enabled to develop the full energy injection mode, where 2.5 GeV electron beam is injected and synchrotron radiation is provided to the photon beamlines without the ramping process. With the constraints of preserving the so called "golden orbit" and parameters something like betatron tunes, new optimized sets of magnetic fields are searched for, taking into account of possible septum magnetic field leakage. The observed results and improvements after the newly employed injection mode are reported.

INTRODUCTION

The Pohang Light Source (PLS) consists of a linear accelerator and a storage ring. The linear accelerator used to be a 2.0 GeV machine. But since the storage ring is capable of storing 2.5 GeV beam, energy ramping in the storage ring was used.

Obviously one of the primary requirements from users of third generation synchrotron light sources is the stringent transverse stability of the X-ray beam emitted from the bending magnets and insertion devices. However, a long-term drift of the closed orbit is routinely observed in PLS. Between each beam injection occurring in every 12 hours, the closed orbit is drifted up to 20-160 μm. Since the horizontal beam size is about 200 μm, this drift corresponds to 20-80 % of the beam size, which needs to be corrected to less than 10 %. Unfortunately, a part of this drift was found to come from the energy ramping procedure.

The storage ring has been operated at 2.5 GeV since 1999 by acceleration (energy ramping) procedure of the stored beam. We found that the acceleration procedure was one of the sources of long-term orbit drift. So we tried to inject 2.5 GeV full energy beam without using any acceleration procedure in the storage ring. This paper will describe problems caused by the acceleration process in the storage ring, and their cure by full energy injection.

ACCELERATION PROCESSES

Basically the ramping procedure simply consists of increasing the currents of the magnet power supplies (MPS) step by step. But the real procedure is not easy in order to keep the storage ring optics unchanged. The relation of the MPS current to the corresponding magnet current is not linear. In the normal operating region near 2.0 GeV, it is almost linear, but outside that region the discrepancy grows. Since the discrepancy is different for different magnets, even if all the MPS currents are increased by the same percentage, the real magnetic fields do not change correspondingly and thus the linear optics such as betatron tune is distorted. Even though the amount of distortion in each step is very small, if the ramping procedure continues this way, the betatron tune shifts keep growing and finally the beam blows up. Therefore we tried to keep the betatron tunes same in each step. For this purpose, all MPS should not change by the exactly same percentage, but each MPS current should be fine tuned with respect to the basic percentage was chosen to be 0.3 %. In a number of machine studies, we obtained data of appropriate MPS current setting values to keep the betatron tunes same in each step. In order to be sure of safe and stable ramping, we chose the conservative value 0.3 %.

Ramping/Degaussing

We accelerated the stored beam to 2.5 GeV with ramping/degaussing process from 1999 to 2001. There are several control steps in the process:

- 2.5 GeV stored beam dump down.
- Degaussing all magnets for 2.0 GeV beam injection.
- 2.0 GeV beam injection.
- Acceleration to 2.5 GeV.
- Set golden orbit for user service

After the injection, we found routinely long-term orbit drift above160 μm during user service. (See Fig. 1).
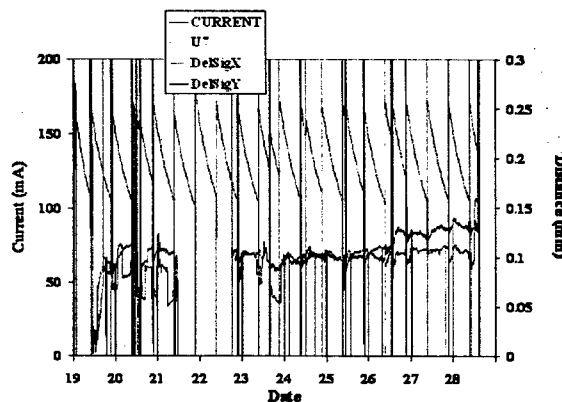
Fig. 1 RMS change during user service run with ramping/ degaussing process for 10 days.

In PLS, one user service run is normally 10 days. Therefore it is the primary job to keep the orbit stable for 10 days. But the ramping/degaussing procedure gave a perturbation to the orbit stability. Because of the degaussing, the magnet cooling system had sudden

chaotic effect of temperature fluctuation, which caused small perturbation to the beam orbit right after the injection/ramping procedure. Obviously, this perturbation vanishes after a long enough time, but it is preferable to eliminate the perturbation. And the ramping process had another problem; it gave a big load to control system and thus there were some control faults in each user service run.

To solve these problems, we separated the ramping control system from the main control system and used ramping/de-ramping process beginning from May 2001.
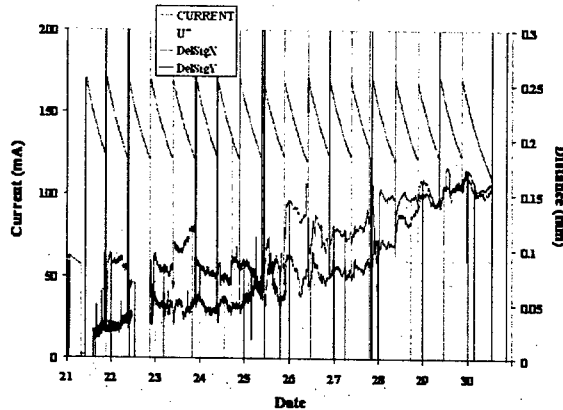
Fig. 2 RMS change during user service run with ramping/de-ramping process

Ramping/De-ramping

The new energy ramping system from 2.0 GeV to 2.5 GeV was installed and used for regular beam injections from May 2001 to Oct. 2002. De-ramping capability from 2.5 GeV to 2.0 GeV was added in the new system to reduce the thermal variation in the magnet cooling system. So we did not dump down the 2.5 GeV stored beam before the injection of 2.0 GeV beam. There are several control steps in the process:

- Deceleration of the stored beam to 2.0 GeV.
- Set injection orbit for 2.0 GeV beam injection.
- 2.0 GeV beam injection.
- Set intermediate orbit for acceleration.
- Acceleration to 2.5 GeV.
- Set golden orbit for user service.

Table 1: Control faults and injection time

Injection Mode	Fault number of control/run	Injection time (minute)
Ramping/old control system	4.0	20 ~ 15
Ramping/separated control system	1.2	15 ~10
Full energy injection	0.3	8 ~ 5

With the separated ramping control system, the number of control faults was reduced (See table 1).
But the orbit drift still existed (See Fig. 2). This is because the cooling temperature fluctuation still existed in ramping/de-ramping process. Furthermore the hysteresis of the magnets could not be eliminated in the process. So the orbit drift caused by cooling temperature fluctuation still remained as a problem to be solved.

FULL ENERGY INJECTION

We concluded that the injection process should be simplified and thus we tried the full energy injection of 2.5 GeV beam.

Linac Upgrade

The linear accelerator of PLS had been operated continuously by 11 modules, klystron-modulator system (MK) as an injector since December 1994. For 2.0 GeV operation, the required microwave output power from each MK system is approximately 45 MW average at a 10 Hz repetition rate. For the more stable operation, the 12th MK module was installed and has been operated since 1999. This has contributed to an improvement of the linac energy margin.

The MK12 module consists of two accelerating columns supplied with RF power by one klystron of 80 MW peak, an in-house made modulator of 200 MW peak, and one pulse compressor. The auxiliary systems such as vacuum and cooling water were established by extending the existing system. At commissioning, we obtained the maximum beam energy of about 147 MeV. One of the modulators has been running at 17 kV without RF power as it had to keep a spare modulator. This K&M system is kept at normal operational status throughout the whole year, except for the regularly scheduled maintenance periods.

Full energy of the linac has been raised continuously by various fine tunings like upgrade of IPA controller and cooling system. In November 2002, we achieved stable 2.5 GeV electron beam at the end of the linac for full energy injection.
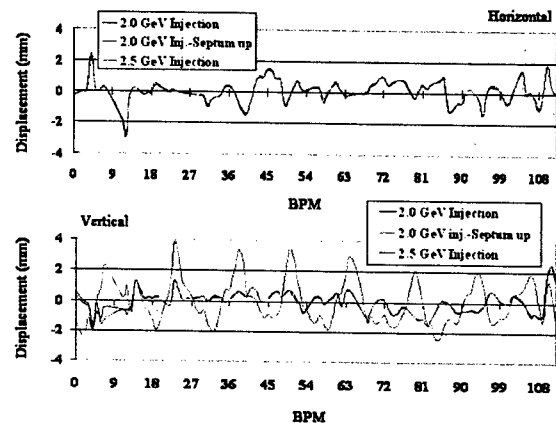
Fig. 3 Orbit correction due to the leakage filed of septum magnet.

876

Effect of the Leakage Field of Septum Magnet

In PLS, a Lambertson type septum magnet is used for injection from the linear accelerator to the storage ring. It bends the injected beam from the beam transfer line vertically and injects it horizontally to the storage ring. In the new 2.5 GeV injection circumstance, the septum magnet showed some leakage field, which can cause additional vertical orbit distortion (see Fig. 3). But it was found that the leakage filed is not strong enough and thus the orbit correction utility of PLS can correct the orbit without any problem. Hence the septum magnet leakage field is not any problem for keeping golden orbit for users.

Full Energy Injection

Since November 2002, full energy injection has been operated successfully. The most important outcome of this full energy injection mode is the improvement of the orbit stability. Fig. 4 shows the reduction of the orbit drift, especially in the horizontal plane (from 160 μm to 20 μm).
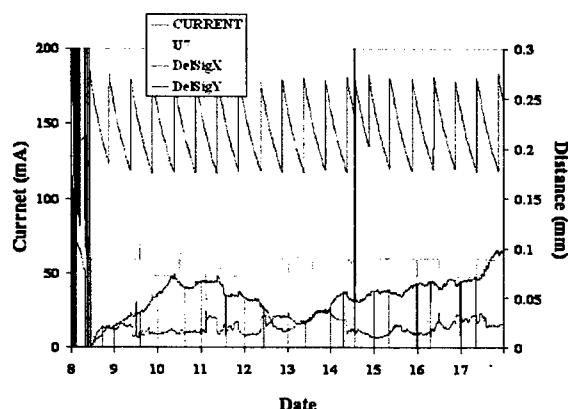
Fig. 4 RMS change with full injection mode during 10 days. Blue line shows stored beam current, sky blue line shows gap of insertion device, red line is horizontal RMS, green line is vertical RMS.

By reducing the orbit drift caused by energy ramping, we can focus more on other sources of orbit distortion such as gap variations of insertion device (see also Fig. 4) or effect of stored beam current (see Fig. 5). Fig. 5 shows

the orbit distortion at each injection. The variances of the orbit deviations from the orbit right after every injection suggest a strong dependency of the closed orbit distortions on the stored beam current as shown by the red and blue peaked lines, although it is not easy to thoroughly sort out all the errors involved in measuring the orbit distortions. In an operational point of view the figure shows that the 10% beam size stability requirement was approximately achieved by the newly developed full-energy injection mode.
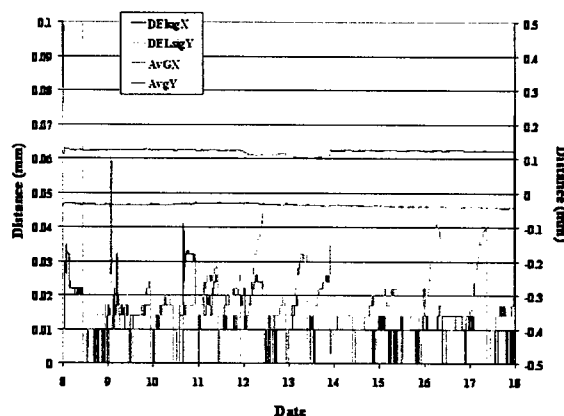
Fig. 5 RMS change in every injection about 12 hours

SUMMARY

By maximizing the capability of the PLS linear accelerator, it was possible to inject 2.5 GeV beam to the storage ring. This full energy injection improved the orbit stability. At the moment, PLS is using the full energy injection successfully.

REFERENCES

[1] K. Kim, K. Shim, J. Choi, M. Cho, W. Namkung and I. Ko, Jpn. J. Appl. Phys., Vol. 39, Oct. 2000, p.6094.

[2] 1998, 2000 and 2001 Pohang Accelerator Laboratory Annual Report.

[3] J. Huang, S. Park, W. Hwang, D. Kim and S. Nam, "Improved Closed Orbit Measurement System for PLS," PAC2001, Chicago, May 2001, p. 1384.

FIRST OPERATIONAL RESULTS OF THE 3RD HARMONIC SUPER CONDUCTING CAVITIES IN SLS AND ELETTRA

M. Pedrozzi, W. Gloor, PSI, Switzerland, A. Anghel, EPFL-CRPP, Switzerland
M. Svandrlik, G.Penco, P.Craievich, A.Fabris, C.Pasotti, Sincrotrone Trieste, Italy
E. Chiaveri, R. Losito, S. Marque, O. Aberle, CERN Switzerland, P. Marchand, Synchrotron
SOLEIL, France, P. Bosland, S. Chel, P.Brédy, G.Devanz, CEA/Saclay, France

Abstract

In both ELETTRA and the Swiss Light Source (SLS), a complementary 3rd harmonic (1.5 GHz) idle super-conducting RF system has been recently implemented and commissioned, in order to lengthen the bunches and therefore improve the Touschek dominated beam lifetime [1]. Here below we report on the commissioning results.

INTRODUCTION

The conceptual design and the fabrication of the cavity modules were realized within the framework of the SUPER-3HC collaboration including Sincrotrone Trieste, CEA/Saclay and PSI [2]. The system is based on a "scaling at 1.5 GHz" of the 350 MHz two-cell-cavity developed at Saclay for the SOLEIL project [3,4]. It consists of two Nb/Cu cells, connected by a tube on which stand the couplers for the damping of the Higher Order Modes [5] (Fig. 1).
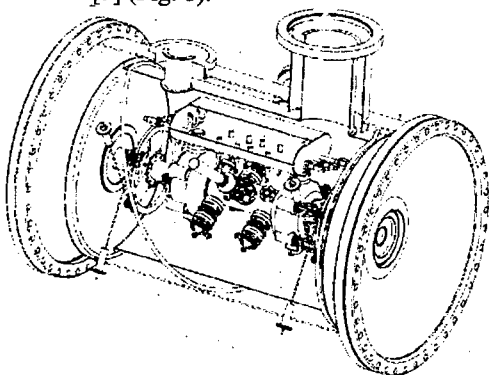
Figure 1: 3D view of the S3HC module, showing the liquid He tanks surrounding both cells and the six HOM couplers mounted on the central tube.

The maximum bunch lengthening (approximately a factor of 3) is achieved when the 3rd harmonic beam-induced voltage is about one third of the overall voltage produced by the main 500MHz RF system. The typical SLS operating conditions correspond to a main voltage of 2.4MV at 500 MHz and 800 kV (4 MV/m) at the third harmonic. Under these conditions one expects 2 - 3 times greater beam lifetime.

CRYOGENIC SYSTEM COMMISSIONING

ELETTRA and SLS chose a common approach for the cryogenic system that feeds liquid Helium into the cryo-module. This system, thoroughly described in [6], is based on the use of the HELIAL 1000 refrigerator-liquefier manufactured by the company AIR LIQUIDE.

Table 1 summarises the cryogenic load at full voltage, the required liquefier performance at 4.5 K in mixed mode (refrigeration + Liquefaction) and the maximum cryogenic power produced during the commissioning. As shown below, the cryo-source allows operation with a large safety margin that results in increased system reliability.

Table 1: Cryo-load with 4 MV/m gradient (Q_o=2 10^8) and cryogenic source performance

Components	Load	Comments
2 RF cells	22 W	Directly in LHe bath
2 L-HOM couplers	3 W	Cooled by conduction
4 T-HOM couplers	8.5 W	Cooled by conduction
2 Extrem. Tubes	0.2 W	With 2x0.05 g/s cold Ghe
Cryo-module static losses	5.1 W	With 0.071 g/s cold GHe in thermal shield (60K)
Cryo-lines	6.5 W	

Total power needed at 4.5 K: 45.3 W refrigeration
With tot GHe flow: 1.171g/s = 5.2 l/h of liquefaction

Specified power at 4.5K: 65 W (50% safety margin)
With specified liquefaction duty of 7.5 l/h

Max measured power at 4.5 K: 150 W of refrigeration
With measured Liquefaction duty of 9.5 l/h

After cooling of the S3HC cryo-module the measured static losses (without RF) were in very good agreement with the anticipate values

S3HC COMMISSIONING

SLS Warm Operation

At room temperature, although the cavity is detuned between two revolution frequency side bands (f_0=1MHz) and the induced voltage largely reduced, the beam can deposit a few 100W into the cavity. The cavity is then cooled circulating some warm GHe from the compressor directly into the cryo-module, or as a backup solution using some purified compressed air [6]. Under these conditions the SLS has been operated with stable beam up to 200 mA of stored current. At higher current an overheating of the module was observed, which led to the excitation of a Coupled Bunch Mode (CBM) instability generated by the fundamental mode of the warm third harmonic cavity. Better performance could eventually be achieved by improving the cavity gas cooling efficiency. At about the same current level a second CBM, related to the excitation of a HOM in the main RF system was also

observed. This instability could be eliminated with an improved tuning of the main RF system [7].

SLS Cold Operation

In the SLS, the S3HC "cold operation" started on October 1st, just after the first cavity cool down.

In cold operation and when excited sufficiently far from resonance ($\delta f \gg f_r/Q$), the induced RF voltage and the power losses are given by [1]:

$$V = I_b (R/Q) f_r/\delta f \quad \text{and} \quad P_b = V^2/(2R) \quad (1)$$

Here I_b, f_r and $\delta f = f_r - 3f_{RF}$ are respectively the beam current, the cavity resonant frequency and the detuning. R is the shunt impedance and $Q \sim 2.10^8$ the quality factor. The global R/Q of the cavity (2 cells) is 88.4Ohms.

In the parked position, when the cavity resonant frequency is set to 500kHz above the third harmonic ($f_r = 3f_{RF} + 500kHz$), the cavity is almost transparent to the beam and the induced voltage is negligible. Under these conditions, stable operation of the storage ring is presently limited to 200mA because of the CBM described above and correlated with an HOM of the main RF system. When the third harmonic RF voltage become larger the increased non-linearity of the global RF voltage generates additional Landau damping and the CBM instability no longer limits the operating current. This effects is re-enforced by the 20% empty RF buckets in the 1µs bunch train, used to suppress ion trapping. The transient beam loading due to the empty gap, results in a phase dispersion along the bunch train, which produces a broadening of the synchrotron frequency and therefore an increased Landau damping.
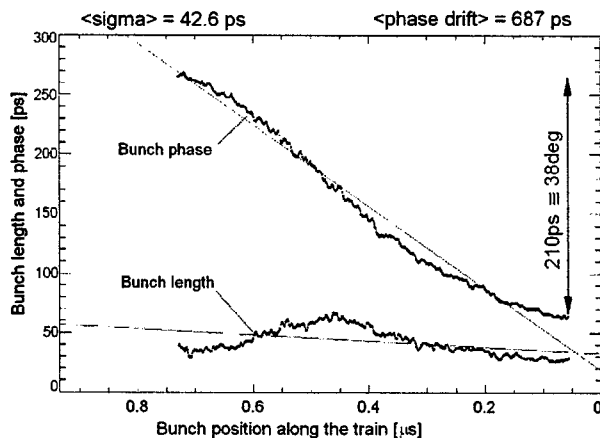
Figure 2: Streak camera measurement at 320mA. Bunch σ and phase in ps versus position in the bunch train.

Figure 2 shows a high resolution streak camera snap shot made at 320 mA for an average elongation factor of ~3. One can observe that the phase shift along the bunch train increases considerably and reaches 38deg. The bunch length also changes along the train from a maximum of 66ps to a minimum of 24ps for an average value of 42 ps (~13ps without harmonic system). A

detailed analysis of each single bunch shape nevertheless shows that the charge distribution within each bunch deviates only slightly from a Gaussian profile.

In Figure 3 the streak camera measurements, as well as the relative amplitude of the marginally excited CBM are plotted versus the elongation factor deduced from the measured average synchrotron frequency.
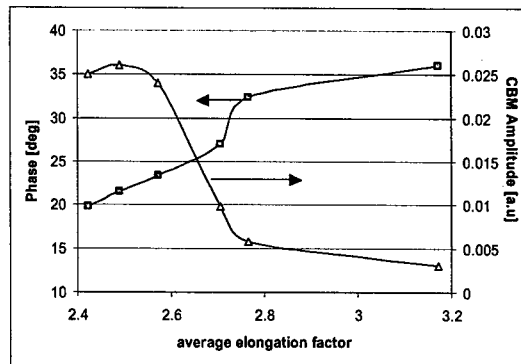
Figure 3: Phase drift and CBM amplitude at 320mA.

As expected, we can observe an increase of the phase drift versus bunch elongation that results in additional damping of the CBM.

A systematic beam lifetime measurement versus the induced voltage in the super-conducting cavity has been performed at 180mA, just below the CBM instability threshold, with a main RF voltage of 2.08MV (figure 4).
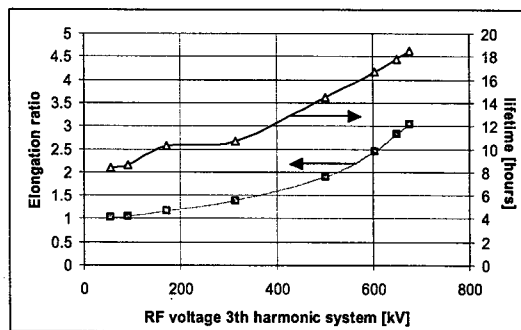
Figure 4: Average elongation ratio and lifetime versus S3HC voltage (180 mA – 2.08 MV operation).

The expected maximum elongation of a factor of 3 is reached for a voltage of ~690kV, with a corresponding lifetime improvement of a factor 2.2.

Stable operation at the design current of 400mA has also been demonstrated, with a lifetime of approximately 8 hours, a factor of two higher than the expected one without the third harmonic system.

ELETTRA Warm Operation

The ELETTRA system was assembled during the summer 2002 shutdown. The commissioning of the cryogenic system lasted longer than expected due to some faulty components. Warm operation was required until

December, the cavity being cooled by a purified air flux. When the warm cavity is parked between two revolution harmonics the power deposited in the cavity by the detuned fundamental mode is sufficient to warm up the cavity at 2.0 GeV, 300 mA. This results in an interaction between the parked fundamental mode and the beam spectrum lines such that the operation mode at 2.0 GeV could not be established. Thus an unforeseen operation at 2.4 GeV, 140 mA, where the warm cavity is still transparent to the beam was necessary until December.

ELETTRA Cold Operation

On the 9th of January 2003 the cavity could be finally cooled down. The cryogenic system performance is beyond its specification similar to the SLS system.

The cold cavity is almost invisible to the beam when parked, with a negligible induced voltage. It does not influence injection at 0.9 GeV and energy ramping to 2.0/2.4 GeV. ELETTRA is more sensitive to CBM instabilities at low energies compared to the SLS and therefore the safety margin on the damping factor of the HOM couplers of S3HC is much smaller. We therefore stress that no effects of the HOMs of the S3HC have been observed at ELETTRA, for 300 mA, 2.0 GeV.

Before installing the S3HC cavity the user's operation mode of ELETTRA at 300 mA and 2.0 GeV was with a controlled longitudinal CBM oscillation at a phase amplitude of about 20-25 degrees. The 500 MHz RF voltage at ELETTRA attains presently 1,68 MV thus the corresponding voltage at the third harmonic should be 560 kV, which in turn corresponds to a detuning of 72 kHz for 300 mA of stored beam. A 10% gap in the bunch train is used to avoid ion trapping.

When tuning the S3HC towards the 3rd harmonic frequency, at 300 mA and 2.0 GeV, longitudinal coupled bunch instabilities are suppressed at a detuning of ~100 kHz, where the total 3rd harmonic voltage is ~400 kV. At 90 kHz, 440 kV voltage, that is 80% of the nominal value, a bunch lengthening factor between 2.5 and 3.0 is achieved. The lifetime with these conditions is 12 hours, which is almost twice the theoretical value. Comparison with measured values with a detuned S3HC are not possible, since the beam becomes longitudinally unstable.
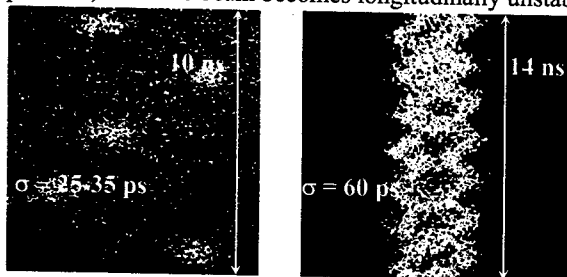
Figure 5: 250 mA, 2.0 GeV, streak camera images. On the left S3HC detuned, longitudinal oscillations present; on the right S3HC tuned, stable beam. Theoretical σ without S3HC is 18 ps.

At ELETTRA injection is performed once a day and the beam current decays in 24 hours from about 300 mA

down to 100 mA. To keep constant the effect of the S3HC a voltage feedback has been implemented which acts on the tuning system of each cell. The feedback is opened at about 160 mA because, for lower currents, the S3HC frequency approaches the +3fs sideband; an instability is then observed causing beam loss.

Tuning the cavity close to the nominal voltage is not straightforward. The voltage increase, even for small tuning steps, is large and eventually activates the cavity over-voltage interlock. So far the cavity has not been tuned for a total voltage larger than 450 kV.
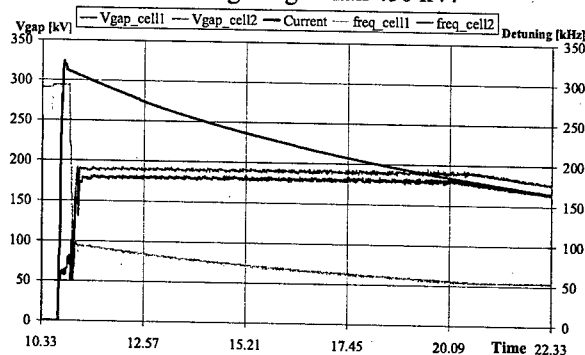
Figure 6: Voltage feedback operation; the measured voltage is 15% less than theory due to calibration errors.

Technological problems are still limiting cavity performance. A leak in the insulation vacuum of a cold helium gas line of the cryogenic plant caused an unstable behaviour of the system. Since mid March the tuning system of cell 1 is out of order; both problems will be sorted out during the next shutdown in June.

CONCLUSIONS

The third harmonic super-conducting system installed in the SLS storage ring significantly improved machine performance in terms of current and lifetime. The additional Landau damping generated by the harmonic system was demonstrated to be an efficient way to damp longitudinal coupled bunch instabilities. This effect allowed stable operation of the SLS at the design current of 400 mA. A lifetime improvement slightly higher than a factor of two has been measured up to 400mA.

Also at ELETTRA the results are quite satisfactory, despite technological problems that are still limiting complete system operation. The cavity has been active during operation for users, allowing for the first time to store a beam free of longitudinal coupled bunch instabilities at 2.0 GeV, 300 mA. At the same time a lifetime increase close to a factor two has been observed.

REFERENCES

[1] P. Marchand, et al PAC99, p. 989.
[2] M. Svandrlik et al, EPAC2000, p. 2052.
[3] P. Bosland et al, EPAC2000, p. 2046.
[4] P. Bosland et al, EPAC2002, p.2217.
[5] P. Bosland et al, presented at PAC2001.
[6] P. Marchand, EPAC2002, p. 2268
[7] P. Marchand et al, EPAC2002 , p.712

BEAM-PERFORMANCE IMPROVEMENT OF THE SPring-8 STORAGE RING

H. Ohkuma[#], S. Date, M. Masaki, T. Nakamura, T. Ohshima, K. Soutome, S. Takano, K. Tamura, M. Takao, H. Tanaka, and N. Kumagai, JASRI/SPring-8, 1-1-1, Kouto, Mikazuki, Sayo, Hyogo 679-5198, Japan

Abstract

The SPring-8 storage ring has improved its reliability and beam performance. At the beginning of year 2001, a project of beam orbit stabilization started aiming for the stability of sub-micron. By two years' activities, we have taken a remarkable progress on improvement of the orbit stability of the SPring-8 storage ring. Recently, optics of the ring was changed from the Double Bend Achromat type to new one with finite dispersion at the straight section for insertion devices. The horizontal emittance of 3 nm.rad was obtained which is close to the theoretical value. To increase time-averaged brilliance in several bunch operation, we have prepared a top-up operation in user time from September 2003. In this paper, the operational status and recent beam performance of the SPring-8 storage ring are presented.

OPERATION IN 2002

Operation Statistics

In 2002, the SPring-8 storage ring was operated on four- or five-week period for one operation-cycle. The total operation time of accelerator complex was 5542.9 hours. 70.3% (3896.7 hours) of the operation time was available to the users and 1.1% (60.8 hours) was injection time. 3.4% (190.5 hours) of the operation time was the down time due to failure. There was a major failure at June 2002 leading to a great deal of lost user time. Cooling water leak to vacuum vessel of in-vacuum undulator occurred, and the in-vacuum undulator was removed from the storage ring. And then, a dummy vacuum chamber was re-installed. As a result, user time of 134.5 hours was cancelled. The remaining 25.2% was dedicated for: (i) the machine and beamline study, (ii) the machine and beamline tuning, (iii) the commissioning of new photon beamlines.

Filling Modes

Three different filling modes were delivered to the user time; 35.0% in the multi-bunch mode operation, 47.2 in the several bunch mode such as 203-bunch mode (203 equally spaced bunches), 84 equally spaced 4-bunch trains, and the remaining 17.8% in the hybrid filling mode such as a 2/11-partially filled multi-bunch with 18-isolated bunches. For the hybrid filling mode, 1 or 1.5 mA is stored in each isolated bunch. A purity of isolated bunch better than 10^{-9} is routinely being obtained.

[#]ohkuma@spring8.or.jp

NEW OPTICS

We tried to reduce the emittance by breaking the achromatic condition imposed to Chasman Green cells[1][2][3]. This method is effective for the case where undulators with a moderate field are used as main insertion devices (IDs). The SPring-8 storage ring just meets this condition [4] and the calculation shows that about 20 % extra reduction is also obtained by closing gaps of all IDs to the minimum even after breaking the achromatic condition. In the summer shutdown, to realize the new optics we modified cabling of the quadrupoles in the dispersive arc to change the strengths of the quadrupoles keeping the phase matching condition over each long straight section. Since September 2002 we started the machine tuning of this new optics with the distributed dispersion. Figure 1 shows the new optical function. As a result, from the last operation-cycle of November 2002 this new optics was released to user operation. The achieved emittance is about 2.8nm·rad with all ID gaps closed. This agrees well with predicted value. The major beam parameters of the SPring-8 storage ring before and after introducing the new optics are listed in Table 1.
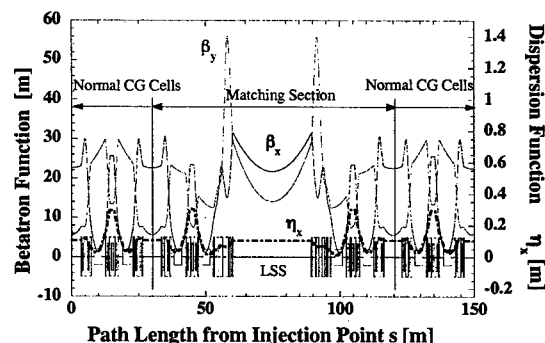
Figure 1: Optical function for new optics.

ORBIT STABILITY

A project of beam orbit stabilization has been started from February 2001. The first year was just for the survey of fluctuation sources and in the second year 2002 the suppression of the vibration sources was carried out as follows. (1) By observing the correlation between the vacuum chamber vibration and the beam fluctuation, the broad peak around 30Hz in the vertical beam spectrum is caused by the vibration of upstream chamber in a unit cell. When the vacuum chamber vibrates in quadrupole

magnetic field, eddy currents are induced on the vacuum chamber wall, which generate electro-magnetic fields and result in shaking the electron beam[5]. On the basis of measured data, we have done some improvements to reduce the chamber vibration. By this counter measures, the vertical beam fluctuations around 30Hz were reduced by one order in amplitude as shown in Fig.2. This improvement is also effective to suppress the horizontal beam fluctuations from 50 to 100 Hz and the amplitude in this frequency range was reduced by factor 3.
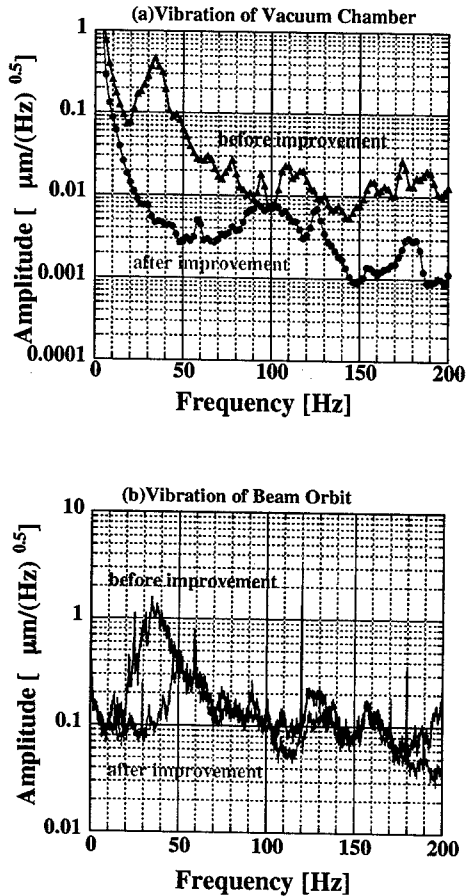
Figure 2: Vertical vibration of vacuum chamber and stored electron beam before and after improvements[6].

(2) To suppress the slow orbit drift, we increased the number of air-core type steering magnets with high resolution and low hysteresis from twelve to twenty-four in the summer shutdown of 2002. This increases the degree of freedom for the correction phase. In principle, this is effective to reduce the slow drift. To avoid the mixing between the circumference change and orbit distortion due to the increment in the steering number, we adopted the algorithm to subtract the contribution of the energy shift from the measured orbit. By using the new periodic correction system, horizontal and vertical orbit deviations were reduced by a factor two, down to about 5 mm in rms for one-day operation.

Table 1: Parameters of SPring-8 storage ring.

2003.05.08

		Old Optics	New Optics
Tunes (v_x / v_y)		40.15/18.35	40.15/18.35
Current[mA]:	single bunch	13	10
	multi bunch	100(120[S1])	100
Bunch length (FWHM)[psec]		32	34
Horizontal emittance[nm·rad]		6.3[S2]/6.6[S3]	3.1[S2]
Vertical emittance[pm·rad]		16.9[S3]	3.9[S4]/8.7[S3]
Coupling[%]		0.26[S3]	0.13[S4]/0.28[S3]
Operation chromaticities			
(ξ_x / ξ_y)		+7/+6	+8/+8
Momentum acceptance[%]		2.6	2.1
Energy spread (ΔE/E)		0.0011	0.0011
Lifetime[hr]:			
100mA (multi bunch)		~150[S5]	~97[S5]
1mA (single bunch)		~24	~9
Dispersion distortion[mm]:			
horizontal (rms)		4	9.3
vertical (rms)		1.1[S6]	1.1[S6]

Note: Lifetime before and after introducing the new optics can not be compared because of differences in operation chromaticityes.
[S1] maximum stored beam current at machine study
[S2] estimated with the beam size measured by a pulse bump and scraper[7]
[S3] estimated with the beam size measured by two dimensional interferometer[8]
[S4] estimated with the beam size measured by two photon correlation[9]
[S5] (12-1)*160 pulse train [normal beam-filling pattern for multi-bunch operation], Vrf=16MV, typical value at user time operation
[S6] with correction by 24 skew Q's

TOP-UP OPERATION

Since 1999 we have been investigating the realization of "top-up operation" in the SPring-8 storage ring. In the year 2002, we set a target to introduce top-up operation to user time from September 2003. To meet this time schedule, we are rushing to upgrade a machine control, beam monitors, and an interlock system for radiation safety, and to design and manufacture the new injection bump magnets and their power supplies.

There are two major problems as follows; (1)Demagnetization of undulator magnets due to frequent beam injections: This phenomenon is occurred by the loss of injected beams at a narrow vertical aperture of an in-vacuum undulator. In consideration with both the experimental and simulation results, we have designed the collimator system to cut the horizontal beam tail. This system will be installed in the beam transport-line from the booster synchrotron to storage ring. (2)Excitation of betatron oscillation of stored beam by beam injections: An off-axis beam injection was adopted to store the high current by repeating beam injections. The bump orbit for the injection is generated by 4 pulse bump magnets. The magnetic field pattern is a half-sine of which width is about 8 μs. As this bump orbit is not closed completely, the stored beam suffers error kicks in passing through 4 bump magnets and then the betatron oscillation is excited. We found that the oscillation was mainly excited by following two effects; (a) One is the effect of

nonlinearlity due to sextupoles within the bump orbit. We think that error kicks due to this effect can be compensated by one or two correction pulse magnets. (b) The other is cause by the existence of two types of bump magnet. These two have the different patterns of eddy current, which change the shape of the field overshoot. We think this comes from the eddy currents at the end plates of each magnet. To solve the problem, we have designed new magnets having end plates made by insulating material to reduce an eddy current effect.

LOW ENERGY OPERATION

In general, the emittance of stored beam is proportional to the square of its energy and can be reduced by lowering the beam energy. The bunch length is also reduced when we lower the energy. This reduction of emittance and bunch length will open up a new opportunity of using brighter synchrotron radiation with shorter pulse lengths in SPring-8. For this aim, we performed the ramping down of beam energy from a design value of 8GeV and the beam injection at 4GeV. In the ramping down experiments, we first stored a low-current beam of 5mA in a multi-bunch mode and then lowered the energy, step by step, down to 4GeV. At each step of beam energy we measured beam parameters, such as a horizontal beam size, bunch length, synchrotron frequency, etc., and compared with expected values obtained from a single-particle picture as shown in Fig.3. We found no significant difference between measured and expected values. Beam instabilities were not observed in the above-mentioned current and a filling mode. We also performed a beam injection at 4GeV. To improve the efficiency of beam injection and hence increase the stored current, further studies are planned such as optimization of the strength of harmonic sextupole magnets and correction of optics distortion.
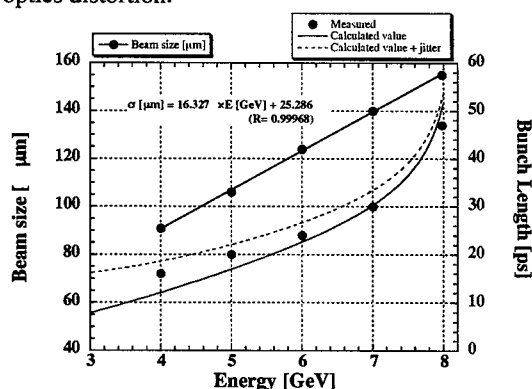
Figure 3: Horizontal beam size and bunch length as a function of beam energy.

ACCELERATOR DIAGNOSTICS BEAMLINES

The accelerator diagnostics beamline #1, which has a bending magnet light source, is in operation. The visible synchrotron light is used for longitudinal diagnostics of the stored electron beam, such as bunch length and single bunch impurity. Single bunch impurity is measured by a gated photon counting method that utilizes fast pockels cells for switching light pulses[10]. To improve the extinction ratio or isolation of the light shutter, the optical system was improved that two pockels cells are arranged in tandem. The sensitivity to satellite bunches of the order of 10^{-10} of the main bunch has been achieved.

A beam profile monitor based on a phase zone plate has been installed (Fig. 4)[11]. The synchrotron radiation from a dipole magnet source is imaged by a single-phase zone plate. Monochromatic X-ray is selected by a double crystal monochromator, which covers the energy range of 4 to 14 keV by Si (111) reflection. An X-ray zooming tube observes the X-ray image of the electron beam. Results from preliminary experiments show that the observed profile of the beam is affected by small bend in the monochromator Si crystals, which was predicted from extensive measurements of the rocking curves of the monochromator. The experiments will resume after improvement of the crystal holders of the monochromator.
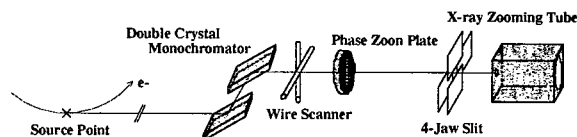
Figure 4: Optical system of X-ray imaging of the electron beam.

REFERENCES

[1] J. L. Laclare, et al., ESRF, ESRF/MaCH-LAT-93-08(1993).

[2] L. Farvacque, et al., Proc. of the 4th EPAC, London, June (1994) pp.612-614.

[3] A. Andersson, et al., Proc. of 4th EPAC, London, June (1994) pp.588-590.

[4] H. Tanaka, et al., NIM, A369 (1996) p.312.

[5] S. Matsui, et al., Jpn. J. Appl. Phys. 42 (2003) pp.L338-L341.

[6] M. Oishi and T. Yorita, *private communication*.

[7] K. Soutome, et al., SPring-8 Annual Report 1999, pp.136-138.

[8] M. Masaki and S. Takano, Journal of Synchrotron Radiation, *in press*.

[9] M. Yabashi, *private communication*.

[10] K. Tamura, the 12th Sympo. on Accel. Science and Technol., Wako, Saitama, Japan, 1999, pp.546-548.

[11] S. Takano, et al., Proc. of the 5th European Workshop on Beam Diagnostics Instrum. for Particle Accel., Grenoble, May (2001) pp.145-147.

MAGNET-RELATED FAILURE EXPERIENCES AT THE SPring-8 STORAGE RING

K. Tsumaki, N. Kumagai, S. Matsui, M. Ohishi, H. Yonehara, SPring-8/JASRI, Hyogo, Japan
T. Tateishi, Y. Torii, KOBELCO RESEARCH INSTITUTE, INC., Hyogo, Japan

Abstract

High operation rate is required for synchrotron radiation sources for their many users. Keeping high operation rate, we need to maintain the equipments continually and raise the reliability of each component. To raise the reliability, it is important to clarify the cause of failure of equipments. In this paper, we describe the major magnet-related failure experiences of the past six years for the SPring-8 storage ring: failure of flow switch, dissolution of copper in water, and radiation damage of equipments.

INTRODUCTION

The SPring-8 storage ring is the third generation synchrotron radiation source with 1436 m circumference and 6 nm emittance and has been operated since 1997[1]. Since radiation sources especially large facility like SPring-8 have many users, the high operation rate is required. To maintain the high operation rate, the high reliability of components of the storage ring is needed.

In the SPring-8 storage ring, actual operation rate for scheduled one since 1997 is 98.3 %. In 2001, total scheduled operation time is 5456.1 hours and the down time is 87.1 hours. Down time due to failures is only 1.6 %. In the failure time, about a half is due to beam line failures and the residual is due to injector and storage ring. The causes of the storage ring failures are due to RF, magnet, vacuum, and control. In this paper, magnet-related failure experiences are described.

In 1997, magnet-related failures were mainly power supply troubles. In 1998, failures of magnet flow switches occurred frequently. In the same year, strainers for cooling water was found to be covered with red substance, the main component of which was copper dissolved from the coil surface. In 2001, a rubber hose was broken due to radiation damage. Since then five rubber hose was broken. In 2002, cooling water leaked from the sextupole magnet coil. The causes of failures are changing with the operational years. We describe about the flow switch, coil and radiation damage in this paper.

FLOW SWITCH

Operation of cooling water system was started in May 1996. First failure of flow switch occurred in June 1998 for sextupole magnet and since September of that year, failures occurred frequently. We studied the cause of failure and concluded to change them for the other type of flow switch.

The number of flow switches and the parameters of cooling water are shown in Table 1 and the structure of a flow switch is shown in Fig. 1. When the water flows in a flow switch, the pressure difference between before and after orifice is generated and due to this pressure difference, a rod moves downward. If the flow rate reduces, the rod moves upward and a micro-switch becomes off state. There were two capabilities as the cause of failures. One was the hardening of rubber diaphragm and the other is the erosion of rod. The maker thought it was due to the hardening of a rubber diaphragm. We measured the hardness of the diaphragm. Results are shown in Table 2. There is only a small difference between used and unused diaphragms.

Table 1: The number of flow switches and parameters of cooling water.

	number	flow rate (l./min)	velocity (m/s)
bending	88	~20	1
quadrupole	464	10~18	2~4
sextupole	292	4~6	0.8~1.3
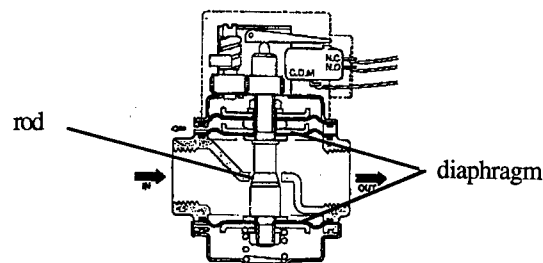
Figure 1: Structure of flow switch.

Table 2: Hardness of diaphragm rubber

	position	hardness
used	upper	81
	lower	82
unused	lower	79

Next we observed the rod. The rods for used and unused flow witches are shown in Fig. 2. The rod is seriously damaged by erosion. If the rod becomes thin by erosion, pressure loss becomes small. We measured the pressure loss for used and unused flow switches. Pressure losses for used and unused flow switches are 0.024 MPa and 0.054 MPa, respectively. We concluded the cause of failure is due to the erosion of rod and resultant reduction of pressure loss of water flow. We stopped the use of this

type of flow switch and employed float type flow switches.
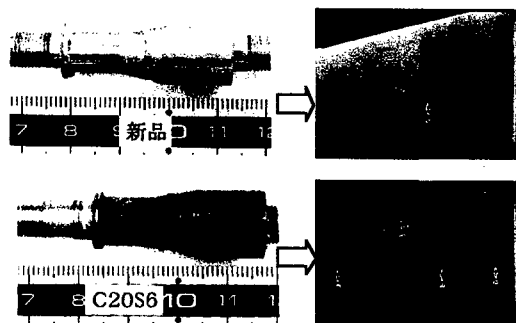
Figure 2: Rods of unused and used flow switch.

COIL

In 1998, it was found that the surface of strainers for cooling water was covered with red substances. We analyzed them and found they were copper oxides. We then investigated the water. Copper of 100~400 ppb was dissolved in the water. The cooling water system is for magnet and vacuum chamber. We investigated the copper pipes and magnet coils. The inner surface of hollow conductor was slightly eroded. We concluded the copper dissolved in the water was from magnet coils. The concentration of copper in water decreased with time and reached to the 10 ppb level. We thought that at first there was no copper oxide on the inner surface of coils but with time copper oxide covered the surface of inner surface of the coils and prevented copper to dissolve to the water.

In May 2002, water leaked from a sextupole magnet coil. We removed the coil and exchanged to the new one. The leakage was occurred at the point where two coils were connected by brazing. There was a small hole made by corrosion on the surface of brazing point. We cut the coil and found that the brazing was insufficient. We concluded that the slight corrosion at insufficient brazing point led to the leakage of water.

RADIATION DAMAGE

Damaged equipments

In January 2000, a new crane was installed for the magnet rearrangement to construct the 30 m long straight sections[2][3]. After two weeks beam time for users, we tried to operate the crane but it did not work. The electronic circuit of the crane was damaged. The crane was placed just above the crotch absorber. We thought the radiation from the crotch absorber damaged the electronic circuit of the crane.

In September 2001, cooling water leaked from the rubber hose for quadrupole magnet at injection cell. Usually magnet hoses face to the inside of the storage ring but at injection cell, the hoses face to the outside of the ring to avoid interference with a transport line from a synchrotron. For that reason the rubber hoses face the

absorber directly. We measured the radiation strength and the radiation level at the leaked hose is one or two order higher than the other cells. So we considered the injection cell was special. Rubber hose at injection cell was shielded by the lead. However in January 2003, water leaked from the other normal cell hose and during one month and a half since that time, water leakage occurred three times at normal cells. All leaked hoses were at Q7 and Q10 magnets, where they faced to the absorbers named AB3 and AB4. We exchanged the rubber hoses for all Q7 and Q10 magnets where radiation dose is higher than the other magnets.
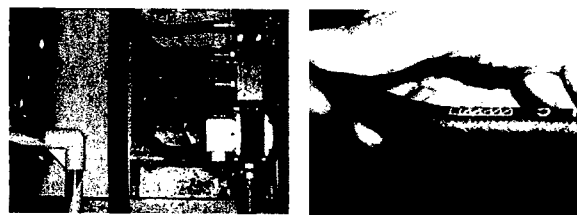
Figure 3: Water leakage from a rubber hose for a quadrupole magnet.

In 2001, damage of interlock wire became conspicuous as shown in Fig. 4 and Fig. 5. Cracked covers of the wires were mended in summer of 2002. As for the cover tube of connection point of interlock wire of heat switch, we left them untouched though the color is changed from brown to black.
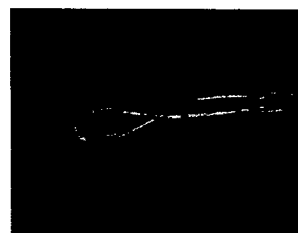
Figure 4: Cracked cover of interlock wire.
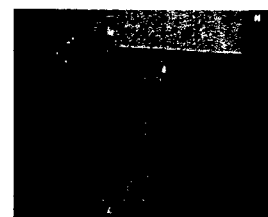
(a) Undamaged tube.   (b) Damaged tube.

Figure 5: Cover tube of connection point of interlock wire.

Measurement of radiation dose

Radiation sources are the absorbers (AB1~AB4) and crotch absorbers (CR1, CR2) as shown in Fig. 6. Radiations from bending magnets are scattered by these absorbers and damage the surrounding equipments.

885

We measured radiation dose around the absorbers and crotch absorbers: radiation around quadrupole magnet coils, rubber hose, absorbers, interlock wires, cover of connection point of interlock wire, cover of a bending magnet power cable. The dosimetry media (GAFCHROMIC film) was used for measurements.

AB4 (19.5%) CR2 (29.5%) AB3 (17.6%) CR1 (30%) AB2 (1%) AB1 (2.4%)

Q10 Q9 Q8 B2 Q7 Q6 Q5 Q4 B1 Q3 Q2 Q1
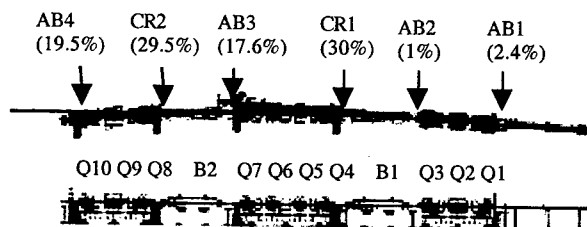
Figure 6: Magnet and absorber arrangement and radiation power distribution from the bending magnets. Total radiation power per cell is 21 kW.

Measurement Results

Magnet coil

Measurements were done for the quadrupole magnets of both ends of girders. One of the measurement results is shown in Fig. 7. Integrated current during irradiation was 0.1179 A*h. Integrated current at April 2003 is 1678 A. Therefore maximum integrated dose is 1.6×10^7 Gy. No radiation effect is observed for magnet coils until now, however, if there is any effect, it becomes serious. So we are planning to study the radiation effects for magnet coils.
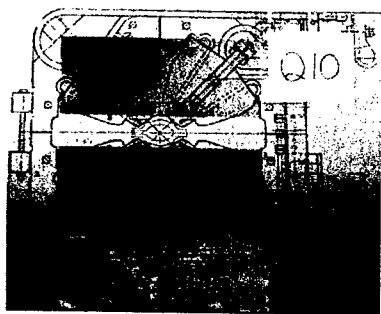
Figure 7: Measured results of radiation around the magnet coils.

Rubber hose

Radiation dose for the rubber hoses, from which the water leaked, was measured together with the rubber hoses for both ends of the girders. Radiation doses for Q7 and Q10 magnets are one or two orders higher than the other magnet. Maximum integrated dose is 4×10^5 Gy. There are eight rubber hoses for a magnet. Leakage occurred for the rubber hose at the same position. Rubber of leakage point was hardened by radiation.

Absorber

Radiation dose behind the absorber was measured as shown in Fig. 8. High energy x ray was transmitted through the chamber even though the lead plate was placed for shielding the radiation. Maximum integrated dose is 2×10^9 Gy. It is clear that the thickness of the plate should be increased.

Figure 8: Radiation distribution behind absorber 3.

Others

Radiation dose around the cover of interlock wires was measured but it was under the measurable level of GAFCHROMIC film. Radiation level around the thermal sensor wire was 4×10^5 Gy.

White powder appeared on the surface of the insulating cover of the bending magnet power cable owing to the radiation. But radiation dose was less than the measurable level.

SUMMARY

Six years have been passed since the operation of SPring-8 storage ring started. There were many failures in these six years. As for the magnet, following failures occurred.

Magnet flow switches began to give a false signal. The rods of flow switches were eroded and pressure loss of water in the flow switch became small even if the sufficient water flowed, which caused a false operation. We changed them for float type flow switch.

Water leaked from the brazing point of a sextupole magnet coil. The cause is that the surface of the coil at a brazing point was corroded and a small hole was made, where the brazing was not sufficient.

Water also leaked from the rubber hoses. Radiation scattered from the absorbers hit the rubber hoses of quadrupole magnet. Integrated radiation dose at the rubber hose was 4×10^5 Gy. We exchanged all the rubber hoses near the absorbers. We are planning to shield around the absorbers. Problems of the radiation damage become serious with the increment of integrated current and it is one of the important subjects for the operation of the storage ring.

REFERENCES

[1] H. Kamitsubo, and N. Kumagai, Proc. of the 1999 Particle Accelerator Conference, New York, U.S.A., May, p188.

[2] H. Tanaka et al., Nucl. Instr. and Meth. A486(2002)521.

[3] K.Tsumaki, et al., Proc. of the 7th Int. Workshop on Accelerator Alignment, November, 2002, SPring-8.

COMMISSIONING LOW EMITTANCE BEAM AT ALADDIN*

K.D. Jacobs[#], R.A. Bosch, D.E. Eisert, M.V. Fisher, M.A. Green, R.G. Keil, K.J. Kleman,
R.A. Legg, J.P. Stott, and W.S. Trzeciak, Synchrotron Radiation Center,
University of Wisconsin-Madison, 3731 Schneider Dr., Stoughton, WI 53589, USA

Abstract

The Aladdin storage ring is now routinely run in a low emittance configuration at 800 MeV. Vertical beam sizes and lifetime are comparable to the original lattice, while the horizontal beam size is reduced by a factor of three. Tools used to commission the new lattice include model based correction to obtain the design machine functions, and model independent correction to set the desired transverse coupling. Newly installed optical profile and position monitors, shunts to trim individual magnets, as well as implementation of a new control system scripting language, were important in achieving the desired results. Special attention was given to operation of the fourth harmonic bunch lengthening cavity used to improve the beam lifetime, and noise reduction in the RF system to improve photon beam quality on the infrared beamlines. In addition, compensation of undulators allows their strengths to be varied with minimum perturbation to the beam outside the regions of the undulators. Details of bringing the low emittance lattice to operational readiness are presented.

INTRODUCTION

The Aladdin storage ring at the Synchrotron Radiation Center (SRC) is operated at 800 MeV and 1 GeV as a VUV and soft x-ray source. A new lattice referred to as LF15 [1] has recently been commissioned for operation at 800 MeV, which reduces the horizontal emittance from 120 to 41 π nm·rad. The beam current is unchanged, remaining at 280 mA at the start of a fill. Combined with changes to the β functions, the horizontal beam sizes at the source points are reduced on average by a factor of three. Vertical beam sizes are unchanged. This increases the focused flux density available on most beamlines, and is especially useful for Users in fields such as spectromicroscopy. LF15 is now the usual operating mode for 800 MeV beam at SRC.

INSTRUMENTATION AND CONTROL UPGRADES

To bring LF15 to routine operational readiness, it was necessary to make several upgrades. These include improvements to the beam profile measuring system, implementing the ability to trim individual quadrupole magnet strengths in the ring, and a new scripting language for the accelerator control system.

In order to make more precise measurements of the

beam size, position, and rotation, the Optical Profile and Position Monitors (OPPMs) were replaced and expanded in number with improved versions. The new stations provide horizontal and vertical beam size, position, and beam rotation information at high data rates (10 Hz). Resolution of profile measurements is ~0.1 μm, with a minimum resolvable beam size of ~25 μm. These monitors have been important for determining beam reproducibility and stability, in particular with maintaining beam stability while scanning undulators, as detailed below.

The 48 quadrupoles in Aladdin are powered in families by 9 power supplies. In order to correct for small deviations in magnet strengths, shunts were installed on all quadrupoles to allow their strengths to be individually trimmed. The shunts are capable of reducing the current through each quad by 12%, up to a maximum of 25 A. Total currents in the quad families range from 60 to 296 A.

Finally, a new scripting language (Python [2]) was installed and interfaced with the existing accelerator control system. Its power and flexibility have facilitated both commissioning and routine operation of the low emittance lattice.

LATTICE OPTIMIZATION

The technique used for determination of the proper settings for the ring magnets depended on whether the deviation from the model lattice was due to a known effect (e.g., quadrupole strength errors), or of unknown origin (e.g., undetermined sources of x-y coupling.)

Model Based Correction

For the situation where the deviation from the ideal case was of known origin but unknown magnitude, corrections based on the lattice model where made. The code LOCO [3] was used to determine the appropriate settings for the 48 quadrupole shunts. Shunt currents ranged from 0.2 to 9.1% of the overall quadrupole current. When the LOCO calculated corrections were installed, the expected four-fold symmetry of the lattice was restored, and compensations for perturbations to the ring (specifically during undulator scanning) could be based on the ideal lattice.

Initial results with LOCO produced significantly better results correcting the ring β functions, than correcting the horizontal dispersion η_x around the ring. Inclusion of the "RFCAVITY" element in the MAD model used by LOCO, to guarantee the proper orbit circumference, improved the η correction.

We have also made a differential version of LOCO. This takes the measured change in the response matrix due to a change in the machine, and compares it to that expected based on the model. It is useful for dealing with incremental changes to a lattice, particularly when the measured lattice is far from the model.

Model Independent Correction

In the case where the source of lattice imperfections was not identified, a more general, model independent approach was taken [4]. The general concept is to measure the sensitivity of a set of parameters to the values of a set of input variables. This was used to set the desired vertical beam sizes, and minimize beam x-y rotations, while maintaining good lifetime. Sizes and rotations were measured at the OPPMs as a function of the settings of four skew quadrupoles. The optimum settings for the skew quads were then determined using Tikhonov regularization [5]. This was used to arrive at a balance between achieving the desired beam sizes and rotations, against the available strengths of the skew quads.

UNDULATOR COMPENSATION

SRC presently has three undulators in routine operation, each with maximum K values of 4.5 to 4.6. As a User scans the strength of an undulator, the vertical focusing strength of the undulator changes. To compensate for this change, eight quadrupoles in the vicinity of the undulator are simultaneously adjusted. Skew quadrupoles are also adjusted to address any x-y coupling issues. The goal is to maintain constant vertical beam size, and beamline throughput, to within 2% peak-to-peak outside the region of the undulator, over the full undulator scan range.

The strengths of the quadrupoles used in compensation are calculated using MAD [6]. The ideal LF15 lattice is used as a starting point. An undulator is then included, modeled as a series of dipoles, including the reduced strength periods at each end of the undulator. The matching capabilities of MAD are used to calculate quadrupole strengths for which the lattice functions outside the undulator straight section, and phase advance through the straight section, equal those without an undulator [7]. The quad strengths resulting from this calculation are automatically K^2 scaled by the control system as the undulator is scanned. Skew quadrupole strengths as a function of undulator strength are determined empirically by minimizing vertical beam size variations over an undulator scan. In addition to quad compensation for beam sizes, steering feed forward and feedback are used to maintain a constant beam position.

The effectiveness of this compensation is shown in Fig. 1. With the undulator scanned over its full range, up to K=4.6, the vertical beam sizes measured at the OPPMs had a total variation of <2%. Similar results were obtained when measuring the throughput on various beamlines over an undulator scan. Variations in β outside the region of the undulator were ~1%.
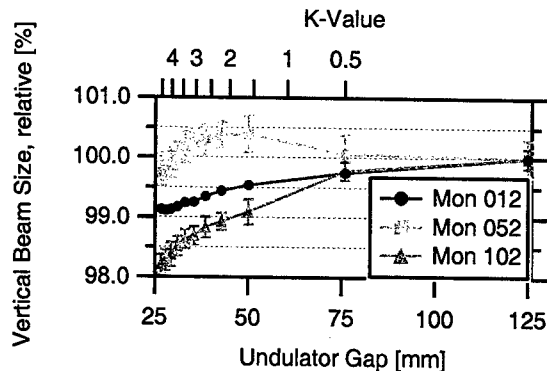
Figure 1: Variation in vertical beam size as an undulator is scanned over its full range. The beam size was measured by five OPPMs (three are shown), and is normalized to the size measured at full undulator gap (125 mm). The undulator period is 70.7 mm.

Further improvement in compensation can be made using LOCO. In particular, using the differential version of LOCO to compare the undulator in vs. undulator out cases has led to better tune correction by the eight compensating quadrupoles.

ADDITIONAL CONSIDERATIONS

Lifetime and Stability

With the decreased horizontal beam size, plus a shorter natural bunch length due to the decreased momentum compaction of the low emittance lattice, the lifetime in LF15 is primarily Touschek scattering dominated. The current·lifetime product can be restored to its nominal value of 900-1000 mA·hr by lengthening the bunch using the fourth harmonic (200 MHz) cavity. This also stabilizes the beam by suppressing coupled bunch modes. The cavity is run passively. Both the fourth harmonic cavity and the voltage on the main RF cavity are controlled as a function of beam current by a Python script, set up to optimize beam stability.

The Infrared Beamlines

The majority of beamlines at SRC average data over time scales of seconds to minutes. However, the IR beamlines make use of Fourier Transform spectroscopy, and is therefore sensitive to beam motions into the kilohertz range. Operation in LF15 initially proved problematical for the IR line, due to the fact that the synchrotron frequency of the lengthened bunch was reduced from ~10 kHz to ~3 kHz. Also, harmonics of the 60 Hz line frequency, present in the RF systems, produced noise on the beam at frequencies up to several kilohertz. This longitudinal noise appeared as source position noise at the IR line due to the finite dispersion at the source location, and as a current modulation [8].

A program of noise reduction was undertaken to stabilize the beam for IR operation. To reduce the 60 Hz harmonic noise several improvements were made,

including additional filtering and improved common mode noise rejection in both RF systems, a new low noise master oscillator, and conversion of the main RF amplifier tube filament from AC to DC. The results are shown in

a:

b:

c:

Figure 2: Spectra taken on the IR beamlines. For each plot 32 spectra are averaged, followed by another set of 32. The ratio of the two sets are shown as a function of wave number; a flat line at 100% would represent no noise. a) Before RF system improvements; b) After reducing 60 Hz harmonics; c) after implementing feedback to reduce coherent synchrotron oscillations.

Figs. 2a and 2b. After this noise reduction, the dominant contribution was due to coherent synchrotron oscillations. This was reduced by implementing phase feedback in the main RF system. Results are shown in Fig. 2c.

Higher Energy Operation

Running of LF15 is presently limited to 800 MeV. When scaled to 1 GeV, and taking magnet saturation into account, the limits of various magnets, power supplies, and cabling are exceeded. However, an intermediate solution, referred to as "MF15", has been found, having a horizontal emittance of $142\ \pi$ nm·rad. This is larger than the 800 MeV LF15 emittance E^2 scaled to 1 GeV $(64\ \pi$ nm·rad) but smaller than that of the 1 GeV lattice presently run $(187\ \pi$ nm·rad). MF15 has been tested, and showed the expected horizontal emittance reduction. Full implementation will require hardware upgrades (cabling), and is planned for the near future.

SUMMARY

We have successfully commissioned Aladdin in a low emittance configuration at 800 MeV. This is now the routine operating mode. In the process, we made use of new hardware and software, and lattice optimization techniques. Special attention was given to undulator compensation, and operation of the infrared beamlines. The result is a beam with increased flux density, good lifetime and unchanged vertical beam sizes. Future plans call for implementing a low emittance lattice at 1 GeV, and investigating at 800 MeV emittances lower than that of LF15. We also will study operation with smaller vertical beam sizes (subject to maintaining adequate lifetime), to take full advantage of low emittance.

REFERENCES

[1] J.J. Bisognano, et al., "Operation of Aladdin at Lowered Emittance," *Proc. of the 2001 Part. Accel. Conf.*, Chicago, IL, pp. 2671-2673.

[2] http://python.org; D. Eisert, et al., "A New Real-Time Operating System and Python Scripting on Aladdin," these proceedings.

[3] J. Safranek, *Nucl. Instr. Methods Phys. Res. A*, **388**, 27 (1997).

[4] J. Safranek and S. Krinsky, AIP Conference Proc. **315**, p. 163 (1994); P. Nghiem, M.-A. Tordeux, and M.-P. Level, *Nucl. Instr. Methods Phys. Res. A*, **480**, 339 (2002).

[5] Y.N. Tang and S. Krinsky, "Use of Regularization Method in the Determination of Ring Parameters and Orbit Correction," *Proc. of the 1993 Part. Accel. Conf.*, Washington, DC, pp. 492-494.

[6] H. Grote and F.C. Iselin, Report No. CERN/SL/90-13, 1990.

[7] R.A. Bosch, "Undulator Compensation in LF15," SRC Technical Note SRC-199 (2002).

[8] R.A. Bosch, et al., "Throughput and Noise of the Aladdin Infrared Beamline," these proceedings.

COUPLING CORRECTION STUDY AT NSRRC

C.C. Kuo[*], H.J. Tsai, H.P. Chang, M.H. Wang, G.H. Luo, K.T. Hsu, D.J. Wang
National Synchrotron Radiation Research Center
101 Hsin-Ann Road, Hsinchu Science-Based Industrial Park, Hsinchu, Taiwan
J. Safranek, G. Portmann, SSRL/SLAC, CA 94309, USA

Abstract

Emittance coupling between vertical and horizontal planes at TLS has been investigated. Using a set of skew quadrupoles, the coupling can be corrected to an acceptable value. The coupling sources are studied and possible errors are reduced.

INTRODUCTION

The equation of motion of the bunched beam is governed by the guiding fields, focusing quadrupole fields, nonlinear higher order fields such as the sextupole fields, and wake fields. It could be uncoupled or coupled motion either in the transverse planes and/or between transverse and longitudinal planes. In this study we are interested in the investigation of the error sources and the finding of the ways to controlling the coupling strength.

We have studied the error sources of the linear optics of the NSRRC 1.5 GeV storage ring TLS (Taiwan Light Source) and compared with the measured magnetic field data using LOCO code in the de-coupled case.[1] The results show that the major gradient field errors are from the sextupoles. Off-center orbits at the sextupole positions are attributed to be the case of the distortion of the linear optics in the NSRRC storage ring. Misplaced sextupole magnets might be the major contributions.

We also studied the coupled case using cross orbit response method and the results are useful for the routine operations at the NSRRC.[2] We also concluded that the major error sources are from the off-center orbit at the sextupole locations in the vertical plane. These are in good agreement with those using LOCO de-coupled case.

In this report, we describe the interesting results of the consistency between the simulated shifts of the sextupole center and the measured mechanical off-sets.

We also found that the rolls of the steering magnets are not negligible and a complete set of the rolls is mapped.

The MATLAB LOCO version is employed in this study of the linear optics in the coupled motion case.[3] The results with MATLAB LOCO are compared with the cross orbit response analyses.

THEORY

The vertical cross orbit response due to a horizontal orbit change through the coupling elements and the vertical dispersion functions due to the small effective "dipole fields" such as the steering magnets, off-center orbits in

the quadrupoles, skew quadrupoles and off-center orbits in the sextupoles in the dispersion region, are given as follows:

$$y_c(s) = \frac{1}{2\sin \pi v_y} \int_s^{s+c} g(s,z)G(z)dz, \tag{1}$$

$$\eta_y(s) = \frac{1}{2\sin \pi v_y} \int_s^{s+c} g(s,z)F(z)dz, \tag{2}$$

where

$$g(s,z) = \sqrt{\beta_y(s)} \sqrt{\beta_y(z)} \cos(\psi_y(s) - \psi_y(z) + \pi v_y)$$

$G(z) = \tilde{K}_1 x_c + K_2 x_c y_m - G_y$, $\tilde{K}_1, K_2, G_y$ are the skew quadrupole, sextupole strength and vertical dipole error, respectively. y_m is the orbit offset with respect to the sextupole magnetic center, and

$$F(z) = -G_y - K_1 y_c - \tilde{K}_1 \eta_x + K_2 y_c \eta_x .$$

Let **M** be a unified response matrix for a set of horizontal steering and installed (or virtual) skew quadrupoles (8 in total at the NSRRC) and **V** be the measured normalized vertical orbit and dispersion, the skew quadrupole array **K** in the ring can be obtained using singular value decomposition (SVD) for a linear equation **MK** = **-V** such that the betatron coupling and vertical dispersion can be minimized simultaneously. Once **K** is obtained, we can establish a virtual machine and compare it with the real machine in terms of the measurable parameters such as normal mode tunes, vertical dispersion, coupling ratio, etc.

On the other hand, MATLAB-LOCO was employed to this study. The MATLAB LOCO code links to the MATLAB-based AT accelerator modeling code. [4] The LOCO algorithm is well described in ref [3, 5, 6]. The response matrix, M, is the response of BPM shifts for a change of each steering strength,

$$\begin{pmatrix} \vec{x} \\ \vec{y} \end{pmatrix} = M_{meas,mod} \begin{pmatrix} \vec{\theta}_x \\ \vec{\theta}_y \end{pmatrix} \tag{3}$$

The quadrupole gradient errors are fitted to minimize the difference between the model and measured response matrices.

$$\chi^2 = \sum_{i,j} \frac{(M_{meas,ij} - M_{mod,ij})^2}{\sigma_i^2} \tag{4}$$

To calibrate the coupling strength, the off-diagonal sub-matrices are included in the fitting. The skew gradients, steering gain and tilt, BPM gain and coupling,

[*] cckuo@srrc.gov.tw

as well as quad gradients are included in the fit. The fitting can also include dispersion functions to minimize the vertical emittance and beam size. The fitted skew gradients in the above mentioned 8 locations are compared with those resulted from the other method.

EXPERIMENTAL RESULTS

In ref [2], we have reported some interesting results using cross orbit response matrix, for instance, the measured coupling strength $|G_{1,-1,3}|$=0.0119 and 0.0016 before and after correction, respectively; the consistency of the model and measured normal mode tunes as a function of the distance away from the linear coupling resonance line; the beam size as a function coupling ratio, etc. As examples, we display the normal mode tunes and coupling ratio κ, before and after correction, as a function of the proximity of the resonance line in Fig. 1.
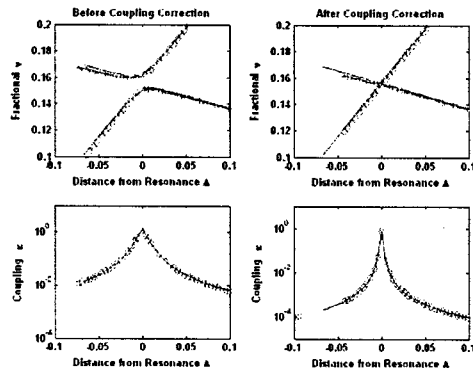
Figure 1: Extracted coupling ratio as a function tune difference from the resonance point

And we also show the turn-by-turn BPM data before and after coupling correction and corresponding Poincaré surface of the section in the resonant processing frame derived from (x, x') and (y, y') in Fig. 2 and 3, where

$$Q = \sqrt{2J_1\beta_x} \cos \phi_1, \quad P = \sqrt{2J_1\beta_x} \sin \phi_1.$$
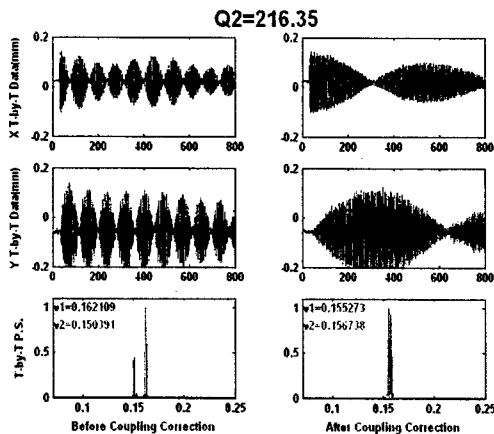
Figure 2: Measured turn-by-turn data after a horizontal kick and the corresponding tune spectra near the coupling resonance before and after corrections.
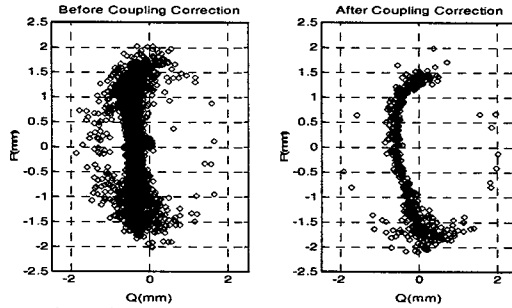
Figure 3: Poincaré surface of the section in the resonant processing frame derived from (x, x') and (y, y'), where $Q = \sqrt{2J_1\beta_x} \cos \phi_1$, $P = \sqrt{2J_1\beta_x} \sin \phi_1$. The overall coupling phase is 15° and 90° to have the upright cross section before and after correction, respectively.

To verify our previous conclusion that the coupling errors mainly stem from the off-center sextuples, we changed the sextupole strength and the corresponding fitted off-sets are examined. It is found that the fitted off-sets are similar as shown in Fig. 4. Two data sets obtained for six-month separation reveal that there are substantial changes in some sextupoles in the vertical plane. It is found that six sextupoles were adjusted by the Survey and Alignment Group with the movable girders in the vertical plane. Figure 5 is a comparison between fitted movement and measured mechanical shifts in these six sextupoles and the larger error bars in survey data is due to errors in the optical survey method, in which the resolution is about 0.1mm. Moreover, we changed one sextupole position in the vertical plan with high resolution mechanical readings and fitted data are also close to the measured movements as depicted in Fig. 6. It is shown that the coupling strength could be reduced by shifting the sextupole heights.
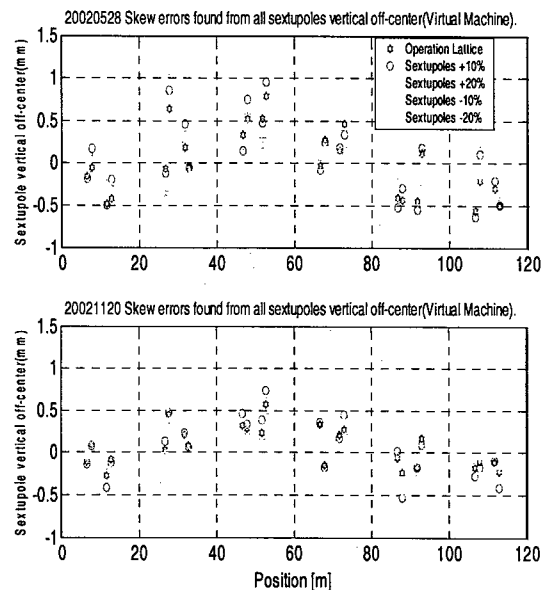
Figure 4: Fitted sextupole vertical position changes at different sextupole setting. Data taken on different date are compared.
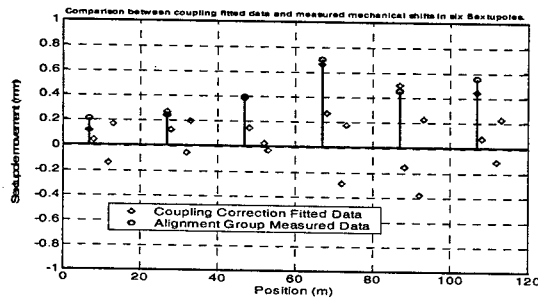
Figure 5: Girder movement data and fitted sextupole vertical position changes. The survey data is with resolution of 0.05 mm.
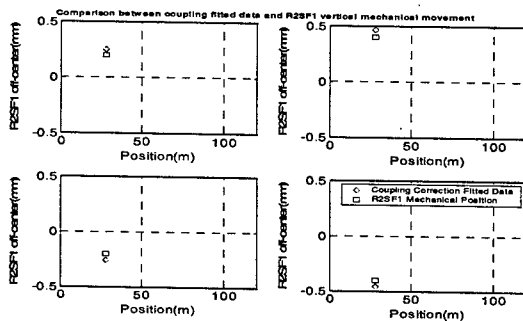
Figure 6: A comparison between the girder movement in one sextupole and coupling fitted data.

By employing the MATLAB-LOCO code, we can obtain not only gains and couplings (tilts) of the steering magnets and BPMs but also the quadrupole and skew quad strengths so that the linear optics can be adjusted to restore the model optics, and the linear coupling as well as dispersions can be corrected. Figure 7 shows the gains and tilts of the horizontal and vertical steering magnets from LOCO and using cross orbit response method. The skew quad strengths are also shown, both from the cross orbit response analysis and LOCO code, in Fig 8. Both results are in good agreement with each other.
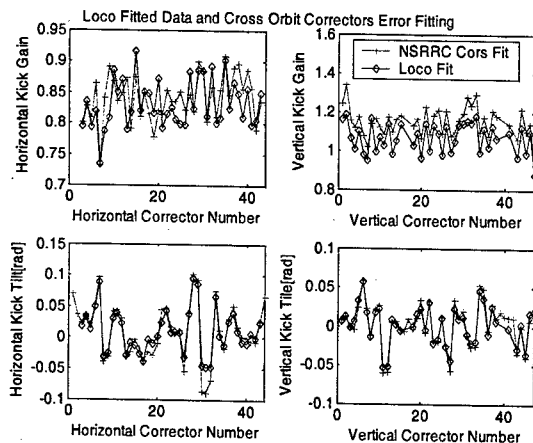
Figure 7: A comparison between the LOCO and cross orbit response analyses results for the gain and tilt of the steering magnets.
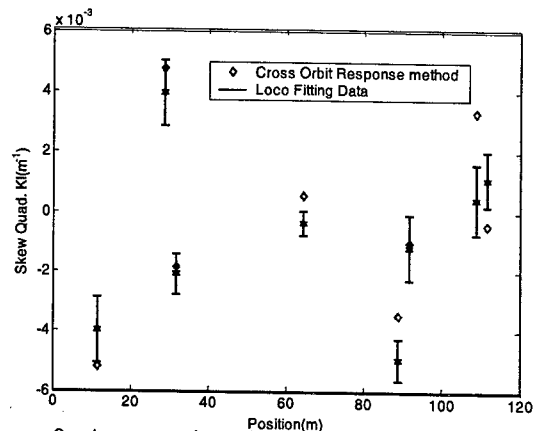
Figure 8: A comparison between the LOCO and cross orbit response analyses results for the correction skew quad strengths.

CONCLUSION

Using cross orbit response method and SVD correction algorithm as well as MATLAB-LOCO, we can characterize the betatron coupling behavior and conduct corrections using a set of independent skew quadrupoles in the 1.5 GeV storage ring at the NSRRC. As a result, both coupling strength and vertical dispersion can be well corrected. A virtual machine can be established and it is found that the vertical alignment errors of the sextupoles are the major coupling error sources.

ACKNOWLEDGEMENT

REFERENCE

[1] C.C. Kuo, J. Safranek, H.P. Chang, K.T. Hsu," Experimental Calibration of SRRC Lattice Optics", PAC97, p 841.

[2] C.C. Kuo, H.P. Chang, K.T. Hsu, H.J. Tsai, "Vertical Beam Size Control at SRRC", EPAC'02, p1148-1150.

[3] J. Safranek, G. Portmann, A. Terebilo, "MATLAB -Based LOCO", EPAC'02 , p1184-1186.

[4] A. Terebilo, "Accelerator Modeling with MATLAB Accelerator Toolbox", PAC'01, p3202-3205.

[5] J. Safranek,"Experimental Determination of Storage Ring Optics Using Orbit Reponse Measurements', Nucl. Inst. & Meth. A 388, 27 (1997).

[6] A. Terebilo, G. Portman, J. Safranek, "Linear Optic Correction Algorithm in MATLAB", this proceedings.

STUDIES OF BEAM LIFETIME AT ANKA

E.Huttel, I.Birkel, A.-S.Müller, F.Perez, M.Pont,
Institute for Synchrotron Radiation – ANKA
Forschungszentrum Karlsruhe, P.O. Box 3640, D-76021 Karlsruhe, Germany

Abstract

Beam lifetime studies have been performed at the 2.5 GeV electron storage ring ANKA. Measurements under different condition allow to differentiate between Touschek, elastic and inelastic beam lifetimes. The measurements are compared with theoretical predictions.

INTRODUCTION

ANKA is a Synchrotron Radiation facility with a nominal energy of 2.5 GeV, a horizontal emittance of 90 nmrad and currents up to 200 mA. The desired user mode is one injection per day. Thus long lifetimes are important. Presently typical lifetimes are larger than 30 h for a current of 100 mA.

The beam lifetime is determined by scattering of the electrons at the nucleus and the shell of the atoms of the residual gas (gas lifetime) and the scattering of electrons within a bunch (Touschek lifetime). For low RF voltages also the quantum lifetime becomes important.

THEORETICAL FORMULAE

The lifetime of the electrons in an storage ring is determined by the inelastic (i) and the elastic scattering (e) at the nuclei (N) and at the electrons (e) of the residual gas, and the Touschek scattering (τ_T). The expressions for the different contributions are given by [1]:

$$\frac{1}{\tau_{total}} = \frac{1}{\tau_e^N} + \frac{1}{\tau_i^N} + \frac{1}{\tau_e^e} + \frac{1}{\tau_i^e} + \frac{1}{\tau_T} \quad [1]$$

$$\frac{1}{\tau_e^N} = \frac{2\pi\, r_e^2}{\gamma^2} Z^2\, c\, n_G\, n\, \frac{\langle\beta\rangle \beta_a}{a^2} \quad [2]$$

$$\frac{1}{\tau_i^N} = \frac{4 r_e^2 Z^2}{137} c\, n_G\, n\, \frac{4}{3}\left(\ln\frac{183}{Z^{1/3}}\right)\left(\ln\frac{1}{\Delta p/p} - \frac{5}{8}\right) \quad [3]$$

$$\frac{1}{\tau_e^e} = \frac{2\pi r_e^2 Z}{\gamma} c\, n_G\, n\, \frac{1}{\Delta p/p} \quad [4]$$

$$\frac{1}{\tau_i^e} = \frac{4 r_e^2 Z}{137} c\, n_G\, n\, \frac{4}{3}\left(\ln\frac{2.5\gamma}{\Delta p/p} - 1.4\right)\left(\ln\frac{1}{\Delta p/p} - \frac{5}{8}\right) \quad [5]$$

$$\frac{1}{\tau_T} = \frac{r_e^2 c\, n_e D(\varsigma)}{8\pi\, \gamma^2 (\sigma_x \sigma_y \sigma_z)(\Delta p/p)^3} \quad [6]$$

with, $D \sim \sqrt{\varsigma}\left(-\ln(1.78\varsigma - 1.5)\right)$ and $\varsigma = \left(\frac{\Delta p/p\, \beta_x}{\gamma\, \sigma_x}\right)^2$ [7]

The symbols used in the above formulae and their typical values are given in Table 1.

Table 1: Symbols used in this text and their typical values

γ	Lorentz factor	4892 for 2.5 GeV
r_e	Classical electron radius	$2.8\ 10^{-15}$ m
c	Velocity of light	$3\ 10^8$ m/s
Z	atomic number of residual gas	7
n_G	Residual gas density	$2.47\ 10^{20}$ for 1 Pa
n	Residual gas (CO), atoms per molecule	2
n_e	electrons per bunch	$5\ 10^9$
$\Delta p/p$	Energy acceptance	0.01
a_s	Vertical half aperture	8 mm
βs	Beta function at aperture	9.5 m
σ_x	Rms horizontal beam size, avg	0.67 mm
σ_y	Rms vertical beam size, avg	0.12 mm
σ_z	Rms bunch length	12 mm

For the residual gas a Z=7 is assumed, which is in accordance with a real gas composition made of H_2 (not contributing, due to the low Z) and CO as measured with a mass spectrometer in the storage ring.

The contribution from the elastic scattering with the electrons of the residual gas is negligible and will not be considered any further.

MEASUREMENTS AND RESULTS

Lifetime versus current

Both the gas lifetime and Touschek lifetime depend on the current. The Synchrotron Radiation induces gas desorption which is proportional to the current and the Touschek lifetime depends linearly on the bunch current. Fig. 1 shows this dependence as a function of total current for 1.7 and for 2.7 % betatron coupling between the horizontal and the vertical plane.

ANKA is run most of the time with a 2.7 % coupling in order to increase the lifetime.

The measurements were performed with a total RF voltage of 1360 kV. The beam current was distributed in 25 bunches. Extrapolating the measurements to zero current, where the Touschek contribution should be negligible, the data indicates a limit to the lifetime of 42 h due to gas lifetime. This lifetime is now shorter than before the vacuum chamber was contaminated with Kr [2].
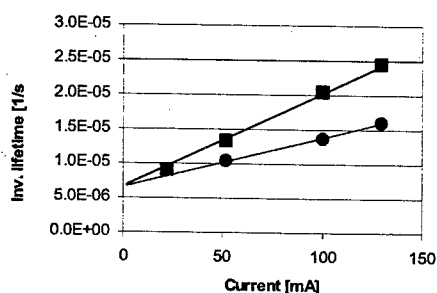
Figure 1: Inverse lifetime as a function of current for 1.7 % (square) and 2.7 % (circles) coupling.

Longitudinal quantum lifetime

If the RF Voltage is reduced to a level below 1000 kV the quantum lifetime becomes dominant. This is shown in Fig.2.
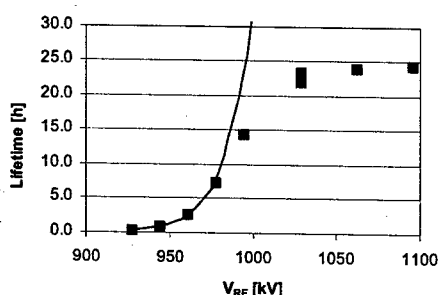
Figure 2: Lifetime as a function of the RF Voltage, squares correspond to measured data, line is the calculated quantum lifetime at low voltage points

The drop of the lifetime is very sharp and depends on the exact energy, RF voltage and momentum compaction factor. Since the exact energy and momentum compaction factor were determined using resonant depolarisation [3], a calibration factor for the RF voltage could be determined to be 0.93.

Elastic gas scattering lifetime

Measurements of lifetime as a function of the position of a vertical scraper can be used to determine the elastic component of the gas lifetime. At ANKA a scraper is positioned at the end of a long straight section. It has two blades, which can be operated from top and bottom independently. The present measurements were done at 2.5 GeV for beam currents of 50 and 90 mA. The measurements when moving the top blade for a current of 50 mA are shown in Figure 3.

It turned out that the bottom blade could be moved further in than the top one for the same effect on the beam. This is due to an offset of the center of the scraper compared to the center of the electron beam.

Equation 2 for the Coulomb scatering can be written as:

$$\frac{1}{\tau_e^N} = C \frac{1}{a^2} \qquad [8]$$

where C is a constant that depends on residual gas pressure, beam energy and betatron functions.

The measured data have been fitted to equation 8 assuming an additional scraper independent contribution from Bremstrahlung and Touschek scattering.
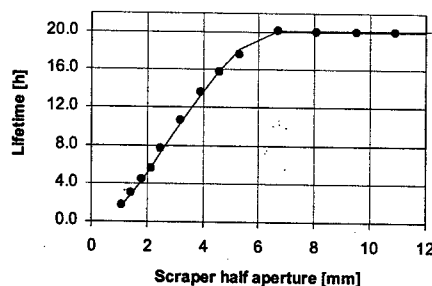
Figure 3: Lifetime as a function of the scraper position

The fit gave the following values for the measurements with 50 mA,

$$\tau_e^N [h] = 1.5 \, a^2 \qquad for \ a \leq 6 \ mm$$

$$\tau_{others} = 32 \, h$$

The 6 mm limit is smaller than the half aperture of 8 mm in the wiggler vacuum chamber, which is assumed to be the limiting aperture. In addition, the fit gave a +/-0.6 mm offset for the top and the bottom blade respectively. Theoretical predictions indicate a pressure of 1.4×10^{-9} mbar (CO) to obtain the factor 1.5. The average pressure measured at the gauges was 1.2×10^{-9} mbar (for 90% H_2 +10 % CO).

Measurements were also performed at injection, i.e. 0.5 GeV. The measured data were also fitted to equation 8 with the following results from the fitting:

$$\tau_e^N [h] = 0.2 \, a^2 \qquad for \ a \leq 6.5 \ mm$$

$$\tau_{others} = 8 \, h$$

Once again the 6.5 mm limit, which is in good agreement with the results at 2.5 GeV is smaller than the expected limiting aperture. The factor 0.2 agrees with the theoretical calculation when using a pressure of 4.10^{-10} mbar, in good agreement with the measured one.

Touschek lifetime

In order to determine the Touschek contribution the lifetime has been measured as a function of bunch current for different RF voltages and tune settings. To this purpose 150 mA have been distributed over 25, 50, 75 and 100 bunches. Since the total current is the same for all the measurements the gas pressure and thus the gas lifetime should be the same. Its contribution to the lifetime has been considered constant and has been determined by a linear extrapolation to zero bunch current. The measurements were performed at 2.5 GeV and care was taken to ensure that the beam was longitudinally stable.

894

The Touschek lifetime is expected to be inversely proportional to the bunch current,

$$\frac{1}{\tau} = \frac{1}{\tau_T} + \frac{1}{\tau_{others}} = c_T i_B + \frac{1}{\tau_{others}} \qquad [9]$$

Figure 4 shows the measured inverse lifetime as a function of the bunch current, for an RF voltage of 1360 kV and for two different couplings.
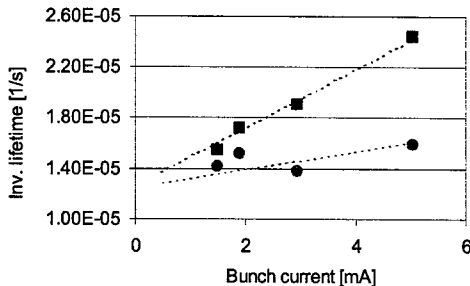
Figure 4: Inverse lifetime as a function of the bunch current, for 1.7 % (squares) , 2.7 % (circles) coupling

From Figure 4 the fitted Touschek is 60 h for 1.7 % coupling and almost 200 h. for the 2.7 % coupling for a current of 2 mA/bunch.

The increased coupling increases the vertical beam size by a factor 1.5 as observed on the synchrotron light monitor. If only the different beam size was responsible for the difference in Touscheck lifetime observed, then we would expect that the results for the 2.7 % coupling were a factor 1.5 larger than the results for the 1.7 % coupling situation. The Touscheck lifetime increases but by a factor 3.

Values of $c_T(V_{RF})$ and τ_{others} were determined by fitting equation 9 to measurements at different RF voltages. The value of τ_{others} have been assumed to be independent of the RF voltage, since the inelastic gas scattering shows only a weak dependence on it. Touschek lifetimes calculated from the fit for a current of 2mA/bunch as a function of the RF Voltage together with the theoretical predictions are given in Figure 5.
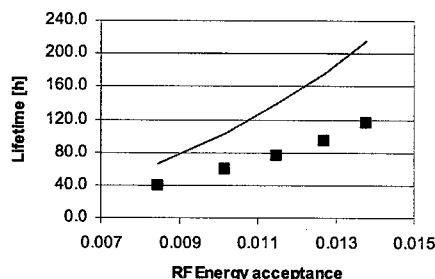
Figure 5: Touschek lifetime as a function of the RF energy acceptance for 2 mA/bunch and 1.7 % coupling

The differences point to an energy acceptance not limited by the RF voltage but by the dynamic aperture of the storage ring. Further studies are in progress in order to understand these results.

Lifetime versus Dose

The gas lifetime of the electron beam in a storage ring increases with the accumulated dose by which the vacuum system is cleaned. The increase of the lifetime for ANKA is shown in Figure 6.
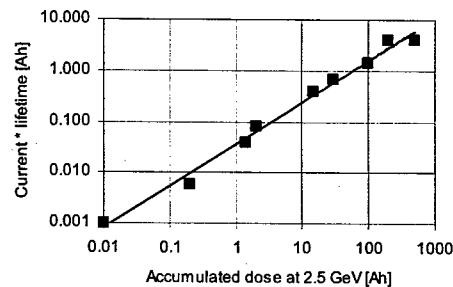
Figure 6: Lifetime times current as a function of the accumulated dose

SUMMARY

Beam lifetimes at the ANKA electron storage ring have been measured and the different components have been identified. Table 2 lists the different contributions for a 50 mA current [2 mA/bunch] with a RF energy acceptance of 1 % and a coupling of 1.7 %.

Table 2: The different contributions to the lifetime for a 50 mA current [2 mA/bunch] and a RF energy acceptance of 1 %

Lifetime	Measured [h]	Theory [h]
Elastic	54	62
Inelastic	68	40
Touschek	60	103
Total	20	20

REFERENCES

[1] H.Wiedemann in Particle Accelerator Physics, Springer-Verlag, 1993
see also J.Le Duff, Nucl. Instr. Meth. A239 (1985) p. 83
[2] F.Perez, E.Huttel, M.Pont and R.Rossmanith, EPAC'02, Paris, June 2002, p. 730
[3] A.-S.Müller, I.Birkel, E.Huttel, F.Perez, M.Pont and R.Rossmanith, these Proceedings

REFINED TRACKING PROCEDURE FOR THE SOLEIL ENERGY ACCEPTANCE CALCULATION

M. Belgroune, P. Brunelle, A. Nadji, and L. Nadolski, Synchrotron SOLEIL, L'Orme des Merisiers Bât. A, Saint-Aubin BP 48 – 91192 Gif-sur-Yvette cedex (FRANCE)

Abstract

In third generation light sources like SOLEIL, the inevitable strong sextupoles lead to significant non-linearities affecting the transverse beam dynamics. We already emphasized the large contribution of transverse and longitudinal non-linearities to the SOLEIL energy acceptance: energy dependence of Twiss parameters, non-linear off-momentum closed orbit and non-linear synchrotron motion. In order to face other effects as non-linear betatron motion, synchrotron oscillation, coupling, and diffusion processes, a refined tracking was performed using a 6D tracking code. This work confirms the strong effect of the non-linear synchrotron motion and suggests to choose the working point so as to avoid any crossing of the linear coupling resonance for off-momentum particles. The use of the Frequency Map Analysis (FMA) helps to understand the different kinds of particle losses.

1 INTRODUCTION

To account for the higher order effects in energy deviation (δ), a module for automatic calculation of energy acceptance (ε_{acc}) and Touschek beam lifetime (τ_T) had been introduced earlier in the BETA code [1]. We showed that when particles are Touschek scattered with large δ in dispersive sections, the non-linear chromatic closed orbit as well as the variation of the optics with energy have to be taken into account. This algorithm is very helpful during a design phase because ε_{acc} variation along the storage ring is obtained within 2 minutes, which allows us to test a large number of cases.

Nonetheless, in order to approach a more realistic modelling, we have to face other effects such as:
- non-linear betatron motion, i.e. deviation from phase space ellipses (non-linearity is worst inside the achromat),
- non-linear synchrotron motion, i.e. effects of higher order chromaticities and momentum compaction factor (already partly implemented in BETA [2]),
- coupling from horizontal to vertical plane (small vertical gaps limitations),
- synchrotron radiation: behaviour of the particles during the damping process (diffusion, resonance crossing).

The best way to take into account all these effects is to perform a 6D tracking, i.e. with synchrotron oscillation and radiation turned on. ε_{acc} calculation problem is then reduced to the very simple question: is the particle with starting coordinates $(0, 0, 0, 0, \pm\delta, 0)$ stable or not after a sufficient number of turns?

We present here the results of our calculations, using the 6D tracking code TRACYII [3]. In order to better understand these results and to know how the particles get lost we used the FMA [4] which has the advantage of providing a good understanding of the inner complex structure of the dynamic aperture. The results are presented so as to highlight two important effects: a full betatron coupling which can be reached for given δ and the effect of non-linear synchrotron motion.

2 TOUSCHEK TRACKING

The particle energy is changed from -6% to +6% (RF energy acceptance) by steps of 0.1%. For each δ, particles are tracked over 500 turns. The calculations take into account the vacuum chamber limitation and particularly a limiting 5mm vertical aperture in the short straight section. By including some quadrupole rotation errors we generate some coupling in order to check whether the lost occurs in the horizontal (x) or the vertical (z) plane. The synchrotron oscillation period is roughly 140 turns and the damping times are 5600 and 2800 turns respectively in the transverse and longitudinal planes. This means that an integration over 500 turns will be mainly relevant for studying the variation of the working point with energy in the tune space (resonance crossing).

Two working points have been studied :
- *Optics 1*: $\nu_x = 18.30$ $\nu_z = 10.27$
  - can reach $3\nu_x = 55$ at large amplitude
  - close to $\nu_x - \nu_z = 8$ ($\Delta\nu = 0.03$)
  - tunes crossing at given δ (Figure 1)
- *Optics 2*: $\nu_x = 18.20$ $\nu_z = 10.30$
  - far from third order resonances
  - far from $\nu_x - \nu_z = 8$ ($\Delta\nu = 0.1$)
  - no tunes crossing (Figure 1)
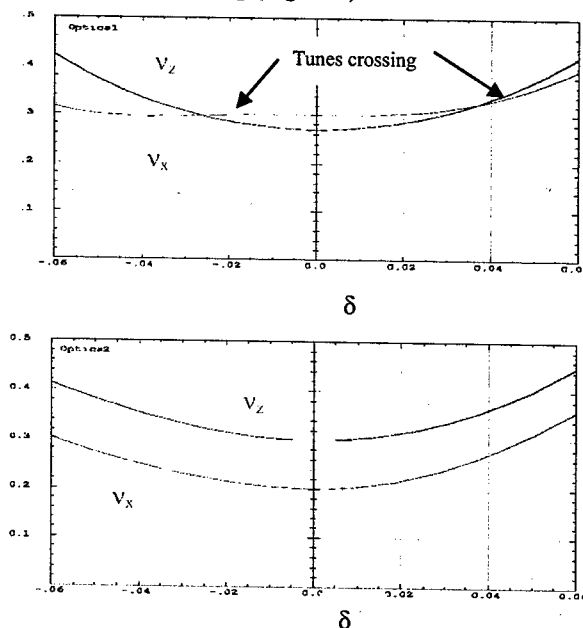
Figure 1: Zero amplitude tune shifts with energy.

3 IMPACT OF TUNES CROSSING AT GIVEN ENERGY DEVIATION

A 4D tracking taking into account coupling errors and including the vacuum chamber dimensions has been performed for the two optics in order to test the influence of tunes crossing (full coupling) at given δ. Figures 2 and 3 show ε_{acc} along one super-period of SOLEIL respectively for the optics 1 and 2. We define the local energy acceptance ε_{acc} (s) as the maximum momentum deviation that keeps the particle having zero initial amplitude stable.

Figure 4 : Highly diffusive vertical motion.

The lowest value in the positive side is constant and equal to 4.5%. This clear-cut is the signature of non-linear resonances.

The FMA has been used in order to investigate the dynamics of the two optics. We combined the particle tracking code DESPOT [5] with the FMA. Particles are tracked with different initial conditions over 1026 turns. If the particle survives then the tunes and diffusion rate [6] are calculated. Coupling errors and vacuum chamber limitation (half horizontal aperture of 25mm (septum position) and half vertical aperture of 7mm) are considered but not synchrotron radiation and damping.

The optics 1 presents much information. The dynamics is dominated by the coupling resonance v_x-v_z = 8. Figures 5 and 6 exhibit frequency maps and dynamic apertures (given in reference to the centre of the machine and calculated in the long straight section where β_x =10m and β_z = 8m) respectively for particles having +4% and +5% energy deviation. The very dangerous node formed by 3rd order unallowed resonances ($3v_x$ = 55, v_x+$2v_z$ = 39, $3v_z$ = 31) and the coupling resonance splits the stability domain and creates empty areas. At 4% the dynamic aperture is particularly affected. This agrees with the result of figure1 where the crossing point is not far from +4%.

Figure 2 : Local energy acceptance for Optics 1.
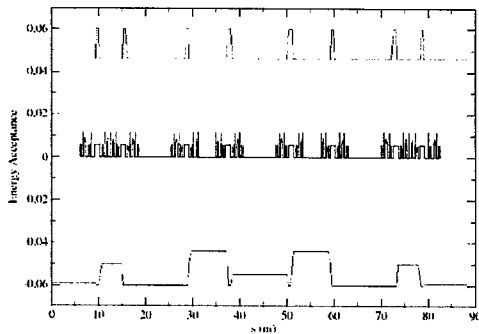
Figure 3 : Local energy acceptance for Optics 2.

For optics 1, the negative ε_{acc} is very low at certain locations of the lattice and the positive one, except in the bending magnet, reach an upper limit of about +3.5%. Most of the particles are lost in the vertical plane. An illustration of this kind of loss process is given in figure 4. This is possible when some particles cross a region in tune space where their motion is resonantly excited to large vertical amplitudes. We have seen in figure 1 that at δ=+3.5% the particles cross the linear coupling resonance. This might be a contribution to the particle diffusion in the vertical plane. The situation for optics 2 is different. Negative ε_{acc} is between -4.2% (particles are lost in the horizontal plane essentially in the achromat and short sections where the horizontal dispersion is the highest) and -6% (RF limit).

Figure 5 : Optics1 : Frequency map and dynamic aperture (for δ = +4%).
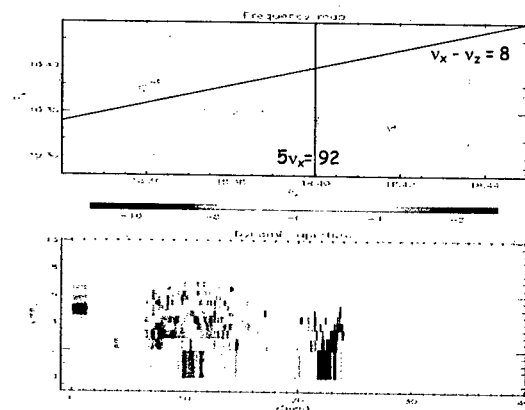
Figure 6 : Optics1 : Frequency map and dynamic aperture
for $\delta = +5\%$.

The optics 2 which has been optimized in order to avoid
the off-momentum tunes crossing does not present similar
problems. As a comparison, figures 7 and 8 show the
results for +4% and +5% energy deviations.
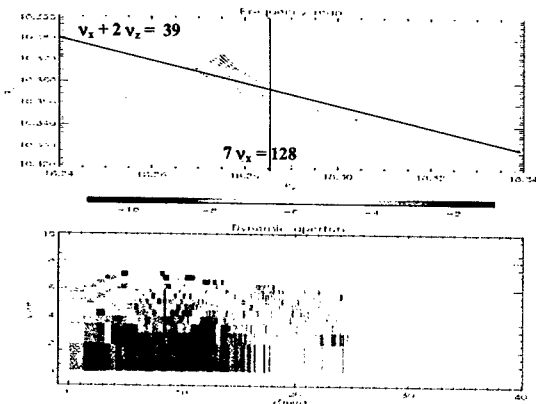
Figure 7 : Optics2 : Frequency map and dynamic aperture
for $\delta = +4\%$.
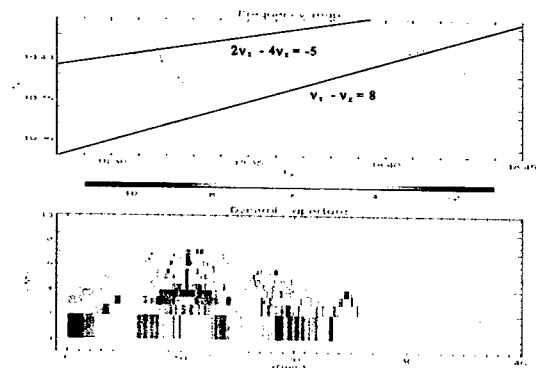
Figure 8 : Optics2 : Frequency map and dynamic aperture
for $\delta = +5\%$.

4 IMPACT OF NON-LINEAR SYNCHROTRON MOTION

A 6D tracking has been performed using TRACYII. As
already shown [2], due to the high value of the second
order momentum compaction factor, the RF-bucket is
asymmetric in energy. For optics 2, a particle with a
positive δ of 4.5% (stable during a 4D tracking, see figure
3) for example can be lost because the corresponding
energy deviation after one half synchrotron period is –8%,
which leads to loss.

Figure 9 shows the results for the ε_{acc} in the case of
optics 2. When comparing with the 4D tracking, one can
note that the negative side is almost unchanged while the
positive side has been shifted down to 4% even in the
bending magnets where ε_{acc} was of 6%. Using this full 6D
tracking, including the vacuum chamber with vertical
apertures of 10mm in medium straight sections and 5 mm
in short straight sections, the calculated Touschek beam
lifetime is about 36h at 2.75GeV, using the natural bunch
length of 12ps (500mA in 416bunches) and a 1%
coupling. The corresponding value using a 4D tracking
(non-linear synchrotron motion not taken into account)
was 55h for the same conditions.
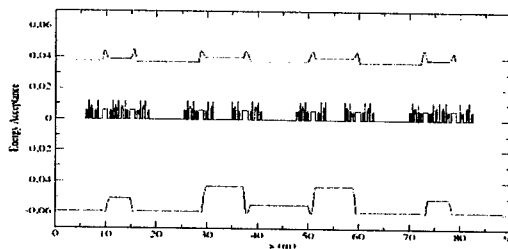
Figure 9 : 6D tracking local energy acceptance
for Optics 2.

5 CONCLUSION

The use of the Frequency Map Analysis has shown that it
is important to avoid a crossing between tunes inside the
energy deviations range of interest. The strong effect of
the non-linear synchrotron motion has also been shown.
The 6D computation of the Touschek beam lifetime
becomes then a reliable criteria to tolerance magnetic
errors, vacuum chamber dimensions and septum position.

REFERENCES

[1] A. Nadji et al., PAC97, Vancouver, June (1997)
[2] A. Nadji et al., PAC99, New-York, Mai (1999).
[3] TRACYII: we enhanced the Pascal to C version
    (M.Böge) for our calculation.
[4] J. Laskar, Icarus 88, 266-291 (1990)
[5] E. Forest et al., DESPOT (1991), unpublished
[6] C. Steier et al., EPAC2000, Vienne, June (2000)

898

FIELD ERROR COMPENSATION AND THERMAL BEAM LOAD IN A SUPERCONDUCTIVE UNDULATOR

S. Chouhan, R. Rossmanith, S. Strohmer, Institute for Synchrotron Radiation, Research Center Karlsruhe, Germany

D. Doelling, A. Geisler, A. Hobl, S. Kubsky, ACCEL Instruments, Bergisch Gladbach, Germany

Abstract

During the last few years prototypes of superconductive undulators have been built and tested [1,2]. Measurements of the magnetic field showed that both the first and the second field integral are, as expected, not fully compensated and that a small but not negligible phase error exists. In order to compensate for these errors, electric shimming techniques are applied. Integral shimming is already part of the two 14 mm undulators under construction. The electric phase- shimming is still under investigation. At the end of this paper the thermal beam load for a small-gap superconductive undulator is estimated defining the layout of the cooling system.

STATUS OF THE SUPERCONDUCTIVE UNDULATOR PRODUCTION

Fig.1: the 14 mm test undulator (one half of the undulator) .Shown is the side close to the beam.

After early attempts [3,4] to build a superconductive undulator in Stanford and Brookhaven, ANKA and ACCEL together developed a new concept described in [5]. Four superconductive undulators based on these new concept have been built or are in the process of being built: a 3.8 mm period length, 100 period long undulator has been tested with beam, a 14 mm ten period long undulator prototype has been built and the magnet field was measured. The construction of a 14 mm period length, 50 period undulator to be installed at the University of Singapore/ Singapore Synchrotron Light Source has just been completed and is now waiting to be tested. A 14 mm/ 100 period long undulator equipped with a cryostat suitable for operation in a storage ring with a minimum gap of 5 mm is under construction.

The field data of the 10 period undulator were analysed in detail [2] and the following arguments are based on these findings.

Fig. 2 Calculated trajectory (A) without the correction coils shown in fig. 3, (B) corrected trajectory with the superconductive coils shown in fig. 3.

CORRECTION OF THE FIRST AND SECOND FIELD INTEGRAL WITH SUPERCONDUCTING CORRECTION COILS

The 10 period superconductive undulator as seen from the beam is shown in fig. 1. The field measurements are discussed in detail in [2].

The calculated beam trajectory from these data is shown in fig. 2. In order to compensate the trajectory, superconductive coils parallel to the beam are installed as shown in fig. 3 (green wires).

ELECTRIC PHASE SHIMMING

As in the case of a permanent magnet undulator, there may be need for phase shimming. The measured phase error of the undulator (fig. 1) is shown in fig. 4.

The proposed shimming is done with superconductive wires. The arrangement of the phase shimming wires is shown schematically in fig. 5. The shimming wires are thin wires parallel to the existing wires. The wires can be powered separately.

The changes in the field are shown in the lower part of fig. 5. Using this wire arrangement, the field is only

affected in one half period. The form of the field change is similar to the form of field change at phase shimming with permanent magnet undulators.
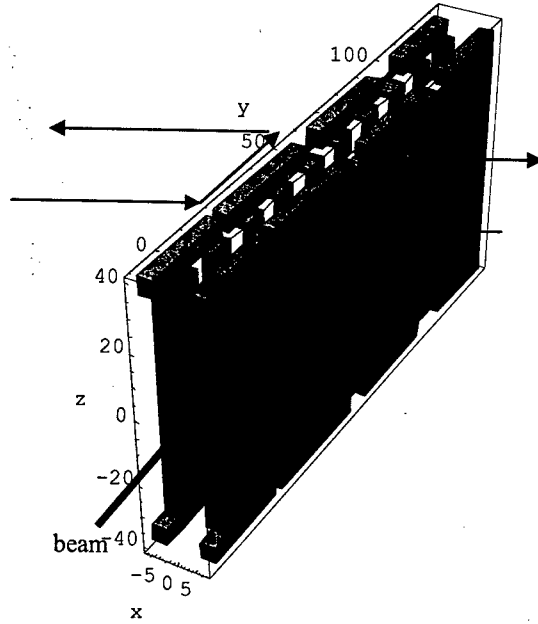
Fig. 3 Model of the superconductive undulator with the iron and the superconductive wires. The additional correction coils are parallel to the beam.
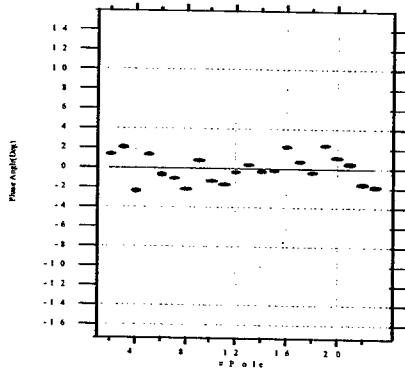
Fig. 4 Measured phase error of the undulator prototype shown in fig. 1
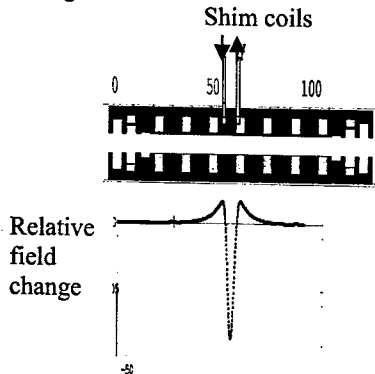
Fig. 5 Principal idea of local phase shimming

RESISTIVE WALL HEATING BY THE BEAM

The indirectly cooled superconductive undulator is heated by the beam (resistive wall effects). In the following the magnitude of this effect is estimated.

The parasitic heating of a surface by unit length P/L caused by the beam is [6]:

$$P/L = \frac{I_{av}^2}{M.f_0.L} \frac{c^2}{\pi} \int_0^\infty S^2(\omega) R_{wall}(\omega) d\omega \qquad (1)$$

where I_{av} is the average current, M are the number of bunches, f_0 is the revolution frequency, L is the circumference of the accelerator, R_{wall} is the wall resistance and S is the bunch spectrum:

$$S = \frac{1}{c} \exp\left[-\frac{\sigma_z^2 \omega^2}{2c^2}\right] \qquad (2)$$

Integrating equation (1) and using the relation

$$R_{wall} = \frac{L}{2\pi r} \sqrt{\frac{\omega \mu_0 \rho}{2}} \qquad (3)$$

where $\mu_0 = 4\pi 10^{-7}$ Vs/Am, r is the shortest distance between beam and surface and ρ is the resistivity of the surface material in Ohm.m. Combining these formulas yields

$$P/L = 1.225 \frac{1}{4\pi^2 r} \left(\frac{c}{\sigma_z}\right)^{1.5} \sqrt{\frac{\mu_0 \rho}{2}} \frac{I_{av}^2}{M.f_0} \qquad (4)$$

In equation (4) for a given geometry the only unknown parameter is ρ. At low temperatures ρ for a given material depends on various parameters:

a.) The temperature. In the following it is assumed that the surface is copper. The values of ρ depend on the quality of the material [7]. Copper used for coating has a resistivity of $1.7.10^{-8}$ Ohm.m at room temperature and a resistivity of $2.8.10^{-10}$ Ohm.m. The resistivity at low temperatures is reduced by a factor called RRR (Residual Resistance Ratio) and this factor is close to 61. This high RRR factor is one of the advantages when operating magnets with a cold bore. The heat load is reduced dramatically, but at the same time the transport of heat at low temperatures also becomes very limited.

b.) The magnetic field. The resistivity depends on the magnetic field. This dependency is described by the Kohler law [8]:

$$\rho(B,T) = \tag{5}$$
$$= \rho(B = 0,T)\left(1 + 10^{(1.055 \cdot \log(|B| \cdot RRR) - 2.69)}\right)$$

c.) The anomalous resistivity effect. Equation (3) is not strictly valid for higher frequencies [9]. The deviations vary with the structure of the surface and are difficult to predict using theoretical methods. Measurements are necessary to evaluate the magnitude of this effect.

In the following the magnitude of the effects are estimated for ANKA. Starting point is a ρ of 2.8. 10^{-10} Ohm.m according to a.). This value has to be corrected for the magnetic field. according to b.). The maximum assumed undulator absolute field (ANKA-undulator: 1.5 T at a gap of 5 mm) has to be averaged over a full period. The averaged field is only about 60 % of the maximum field. This leads to a final ρ of 3.5 10^{-10} Ohm.m for a maximum field of 1.5 T.

Based on these assumptions the deposited power for the ANKA undulator according to equation (1) is about 200 mW/m for a gap of 5 mm, a beam current of 200 mA and a bunchlength of 1 cm.

It has to be noted that a reduction in bunch length limits the use of superconductive undulators. A bunch length reduction by a factor of 3 brings the heat load for an ANKA-type undulator above 1 W (assuming otherwise unchanged parameters). This would require a different cooling system and could mean that the idea of using only cryo-coolers is no longer acceptable.

The anomalous effect c.) is not well documented but, extrapolating from measurements, the heat load might increase by up to 20% depending on the type of surface treatment. As a result the copper-coated shield must be carefully prepared in order to minimise the unwanted heat load.

Summarizing this chapter, the superconductive undulator is almost ideal for low gap operation as long as the bunch lengths are not excessively short at average currents of about 200 mA. The high electrical conductivity at low temperatures prevents the build-up of excessive heat load. Also excessive pumping for the small gaps is not necessary since the gap temperature is close to 4 K.

THE PROPOSED MEASUREMENT OF THE HEAT-LOAD AT ANKA

In order to obtain experimental data on the heat load, it is intended to conduct a beam test at ANKA . The test equipment is shown schematically in fig. 6.
The superconductive undulator (red blocks in the center of the drawing) will be installed in one of the four straight sections of ANKA. The period length is 14 mm,

the undulator is 100 periods long. The undulator will be equipped with corrections for compensating the first and the second integral (see fig. 3) but not with phase shimming coils.

The vessel surrounded by the undulator is cooled to 4 K by cryo-coolers schematically shown in the center of the cryostat. The outer vessel is cooled to 60 K.

The gap of the undulator can be varied in steps. At injection at 500 MeV and during ramping, the undulator gap is fully opened to 25 mm. In this position the undulator cannot be powered. The gaps at which it can be powered are 5mm, 8 mm, 12 mm and 16 mm.

In order to protect the undulator, a scraper in front of the undulator is opened and closed to the same gap width as the undulator. A horizontal scraper pair, not shown in this diagram, protects the undulator from synchrotron radiation.

The flanges of the undulator are equipped with valves making it possible to remove the undulator from the beamline and replace it by a normal beampipe even when the undulator coils are still cold. The measurement of the temperature of the cryocooler system makes it possible to measure the beam-induced heat.

The beam pipe vacuum is separated from the insulation vacuum. This parts in the storage ring vacuum have only metalic surfaces.
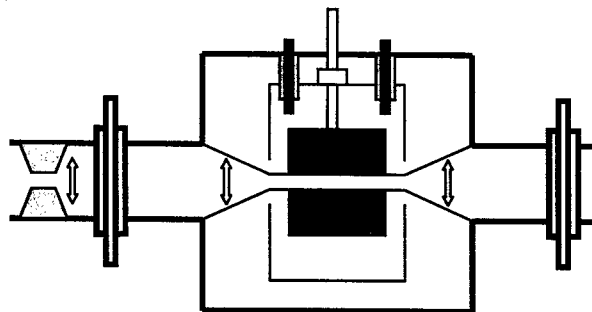
Fig. 6 The planned test at ANKA

REFERENCES

[1] T. Hezel et al., PAC 99, New York, http://www.jacow.org/
[2] R. Rossmanith et al, EPAC 2002, Paris, http://www.jacow.org/
[3] L. R. Elias, et al., Phys. Rev. Lett. 36 (1976) 717
[4] I. Ben-Zvi et al., Nucl. Instr. Meth. A 297 (1990) 301
[5] T. Hezel et al., J. Synchrotron Radiation 5 (1998) 448
[6] W. Chou and F. Ruggiero, LHC Project Note 2 (SL/AP), Geneva 9/8/1995
[7] F. Caspers, M. Morvillo, F. Ruggiero, J. Tan, LHC Project Report 307, August 1999
[8] M. Kohler, Ann. Physik, Ser. 532, 211, 1938
[9] F. Caspers et al., EPAC 2000, Vienna, http://www.jacow.org/

THE SAGA SYNCHROTRON LIGHT SOURCE IN 2003

T. Tomimasu*, S. Koda,Y. Iwasaki, Saga Light Source, Tosu, 841-0002, Japan
H. Ohgaki, Institute of Advanced Energy, Kyoto University, Kyoto, 611-0011, Japan
H. Toyokawa and M. Yasumoto, PRI, AIST, Tsukuba, 305-8568, Japan
Y. Yamatsu, T. Kitsuka, Y. Hashiguchi, Y. Ochiai,
Saga Prefectural Government, Saga, 840-8570, Japan

Abstract

The Saga third-generation synchrotron light source (Saga-LS) is being constructed and is operated before the fall of 2004 in Tosu, Saga Prefecture in the northern part of Kyushu-island. The Saga SLS consists of a 262-MeV electron linac injector and an eight-hold symmetry 1.4-GeV storage ring with eight double-bend (DB) cell and eight 2.93-m long straight sections. The DB cell structure with a distributed dispersion system was chosen to produce a compact design. The circumference is 75.6 m and the emittance is 15 nm·rad at 1.4 GeV. Six insertion devices including a 7.5-T wiggler can be installed. The critical energies of synchrotron light from the bending magnet and the 7.5-T wiggler are 1.9 keV and 9.8 keV, respectively. The 262-MeV linac beam is used for injection and a 40-MeV linac beam branched off from the first accelerator tube (AT-1) is used for two-color infrared (IR) free electron laser (FEL) generation. We are planning to supply high brilliant photon beams covering wavelength range from 34 keV to 0.063 eV by using the Saga 1.4-GeV storage ring with six insertion devices including the 7.5-T wiggler and the IR- FEL facility.

1 INTRODUCTION

The Saga-LS consists of the 262-MeV linac injector and the 1.4-GeV storage ring with eight DB cells and eight 2.93-m long straight sections. The DB cell structure with a distributed dispersion system was chosen to produce a compact design. The circumference is 75.6 m and the emittance is 15 nm·rad at 1.4 GeV. Six insertion devices including a 7.5-T wiggler can be installed. The 262-MeV linac beam is used for injection and a 40-MeV beam from the AT-1 is used for two-color IR-FEL generation. The Saga-LS project is operated by the Saga Prefectural Government.

The building has been constructed in fall of 2002 in Tosu, Saga Prefecture. Tosu is 25 km north-east of Saga and 25 km south of Fukuoka. The ring magnets, vacuum chambers made of aluminum alloy except for the long straight sections and four tempearature controlled cooling water systems for the linac accelerator tubes, the ring cavity, klystrons, magnets and wave guides are already ordered in 2002 and the other parts are ordered in 2003. The installation of the Saga SLS starts in fall of 2003. The commissioning will start in October 2004.

2 THE SAGA 1.4-GEV STORAGE RING

The layout of the Saga 1.4-GeV storage ring, the 262-MeV linac injector and the two-color IR-FEL facility [1] is shown in Figure 1. The C-shaped dipoles, symmetric closed yoke type quadrupoles and sextupoles are used. The symmetric closed yoke consists of an upper and a lower half bolted vertically with each other for setting their vacuum chambers. The C-shaped dipole cores are fabricated from A94068-100 steel laminations 1.0mm thick. The magnet cores of quadrupoles and sextupoles are from A94068-50 steel laminations 0.5mm thick. The laminations are compressed and glued with a packing factor no less than 97 %. The main coils are made of water-cooled hollow copper conductor insulated with fiberglass and vacuum impregnated with epoxy. Trim coils and power supplies for a 1~2% field adjustment are prepared for the dipoles and quadrupoles. Steering coils are built in sextupole magnets. The magnet control system is discussed elsewhere [2]. For magnet support and precise alignment, the spherical rod end bearings are used.

The lattice has been designed by relaxing the constraint of zero-dispersion in the long straight section as MAX-II [3]. For various dispersions, the rms electron beam sizes are calculated from the electron beam emittance ε_x, the horizontal and vertical beta functions, (β_x and β_y) and the relative momentum spread $\Delta p/p$, assuming 1 % coupling ratio in the vertical direction. The horizontal beam size is minimized for a dispersion $\eta_x = (\varepsilon_x\beta_x)^{1/2}/(\Delta p/p)$. The minimum value is close to $2^{1/2} \eta_x (\Delta p/p)$. The beam emittance is also minimized by distributing dispersion. Figure 2 shows the circumference of medium-scale storage rings and their emittances at a 1.4-GeV operation energy. The solid line shows the present lowest emittance of available medium-scale storage rings. It well demonstrates that the Saga storage ring is of compact and lowest-emittance type. Table 1 shows main parameters of the Saga ring magnets and stored beam.

Eight 2.93-m long straight sections are used for six insertion devices (IDs), a septum magnet, four kickers, various type beam monitors and an RF cavity. The available lengths for IDs are 2.5 m × 5 and 1.6 m × 1. In total, twenty beam ports are constructed and more than twenty beam lines can be installed. All vacuum chambers are made of aluminium alloy except for eight long straight

*Corresponding author, e-mail: tomimasu@saga-ls.jp, tel: 81-942-83-5017, fax: 81-942-83-5196
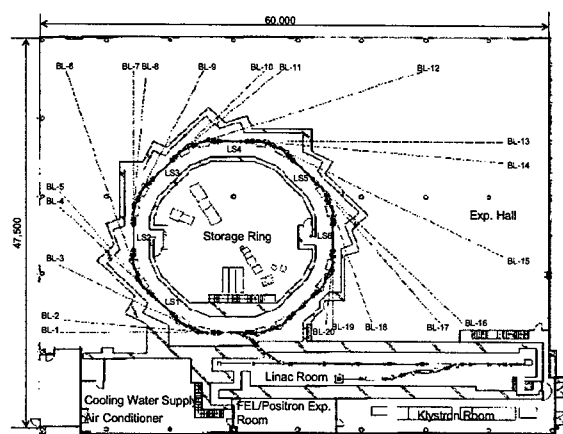
Figure 1: Layout of the 1.4-GeV Saga storage ring, the 262-MeV linac injector and the two-color IR-FEL facility.

Figure 2: Circumferences of medium-scale storage rings and their emittances at 1.4 GeV.

sections. The chamber at the quadrupoles and sextupoles is 100 mm wide and 40 mm high because the damping time is of the order of 1 second due to the 262-MeV injection. The calculated dynamic aperture [4] for a stored beam is the same as the physical aperture of the vacuum chamber.

A 500-MHz RF damped cavity with SiC beam-duct [5] is used for stable storage of high-current beam and the expected RF voltage is 500 kV for a 90-kW RF power.

At the present, we are planning to install a 7.5-T superconducting wiggler, two permanent magnet undulators, and five beam lines for soft X-ray scanning and X-ray imaging microscopes [6], for XAFS [7] and crystallography.

The wiggler is to shift the synchrotron radiation spectrum to the hard X-ray region (ε_c = 9.8 keV) and a permanent magnet undulator (λ_u = 5 cm, K=1.2, N=49, photon energy 200 eV) provides high intensity photons of 4.8×10^{15} [photons/s $\cdot$ (0.1mrad)$^{-2}$ $\cdot$ (1%bw)$^{-1}$], since the rms irradiation angle of the undurator photons is 0.052 mrad.

The wiggler is three-pole planar type like the 5-T wiggler of Electrotechnical Laboratory TERAS Ring [8] and the 7-T wiggler of the Louisiana State University, Center of for Advanced Micro-structure and Devices [9]. Betatron-tune shift induced by the 7.5-T wiggler can be corrected by reducing the exciting current applied to QF1-QD1 doublets installed on each side of the wiggler to 95~85 %, at most, of the exciting current applied to the other QF1-QD1 doublets. The insertion effect of the 7.5-T wiggler for the beam parameters is also shown in Table 1 as key parenthesis.

Figure 3 shows the magnetic lattice of one full cell. The separation between the bending magnets is 1300 mm. Small magnets installed at the down stream of QF2 magnets are for steering. Vacuum chambers are also shown in Fig.3. Total pumping speeds of sputter ion pumps and titanium getter pumps are 8800-l/s and 48000-l/s, respectively.
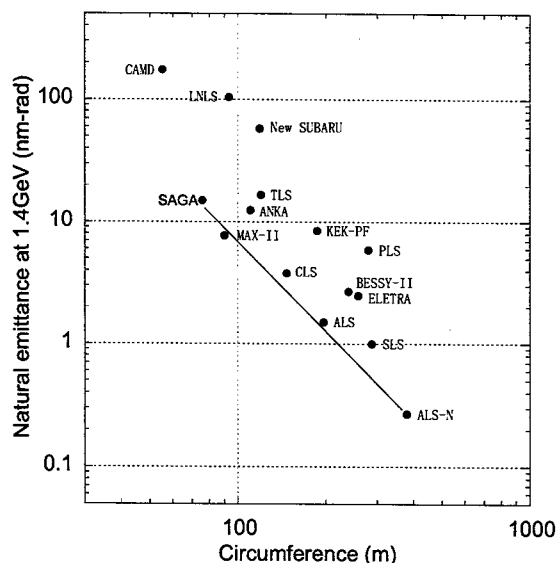
Table 1. Main parameters of the Saga storage ring magnets and stored beam.

Electron beam energy	0.2~1.4 GeV	
Beam current & life	300 mA & 5 hs at 1.4 GeV	
Circumference	75.6 m	
Lattice	DB(A) × 8 (eight fold symmetry)	
Straight sections	2.93 m × 8	
Emittance (nm-rad)	15	[35 (7.5-T wiggler)]
Tunes (v_x, v_y)	6.796, 1.825	[6.796, 1.825]
Momentum compaction	0.008074	
Energy spread	0.000672	[0.00079]
Radiation loss (keV)	106	[123]
RF frequency (MHz)	499.8	
RF power & field	90 kW & 500 kV	
Harmonic number	126	
Bunch length σ(mm)	8.8	[10.35]
Beam sizes at straight section (coupling = 0.01) at η=0.62		
σ$_x$ (μm)	580	[680]
σ$_y$ (μm)	34	[52]
Injection energy (MeV)	262	
Dipoles & number	11.25° edge focusing & 16	
Radius & field	3.2 m & 1.459 T	
Number of quadrupoles	40 (16QF1, 16QD1, 8QF2)	
Length (m)	0.2(QF1), 0.2(QD1), 0.3(QF2)	
Max. gradient(T/m)	27(QF1), 27(QD1), 25(Qf2)	
Number of sextupoles	32 (16SF, 16SD)	
Length (m)	0.10(SF), 0.14(SD)	
Max. gradient(T/m^2)	150	

903
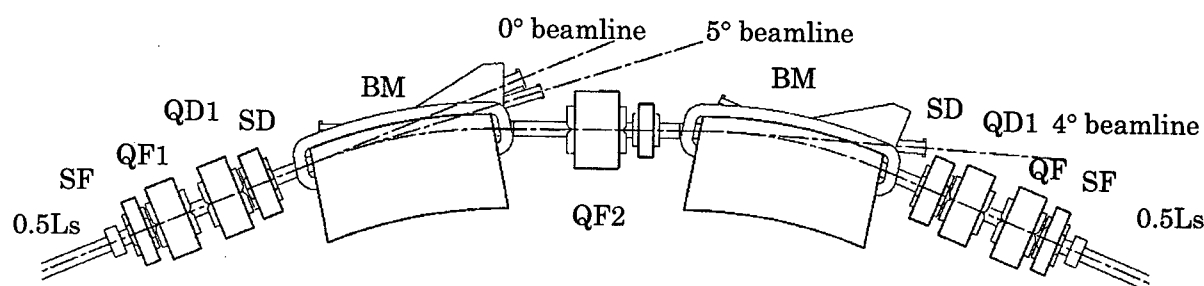
Figure 3: Magnetic lattice of one full cell (9447.23mm)

3 THE 262-MEV LINAC FOR ELECTRON INJECTION AND FEL OSCILLATION

The 262-MeV linac injector is operated in two modes; 1-μs and 9-μs macro-pulse operations. The 262-MeV electron beam with macropulse length of 1μs is for the storage ring injection and the 25~40-MeV electron beam with macropulse length of 9 μs is for two-color FEL oscillation. The linac consists of a 120-keV thermionic triode gun, a 714-MHz prebuncher, a 2856-MHz standing-wave type buncher, and six Electrotechnical Laboratory type accelerating tubes. The accelerating tubes with a length of 2.93 m are of linearly narrowed iris type to prevent beam blow up effect [10].

An electron gun with a dispenser cathode and a grid pulser emits 0.6-ns pulses of 2.3 A at 22.3125 or 89.25-MHz. These pulses are compressed to 60 A × 10 ps by the prebuncher and the buncher. The RF source for prebuncher is a 714-MHz semiconductor type RF source. A 2856-MHz klystron (Toshiba E3729, 36 MW) is for the buncher and the first two accelerating tubes.

At the injection mode, a 2856-MHz klystron (Toshiba E3712, 88 MW) is used for the following four accelerating tubes. At the FEL mode, the 9-μs macropulse electron beam is accelerated up to 40-MeV at the end of the AT-1.

The electron beam consists of a train of several ps, 0.6-nC microbunches repeating at 22.3125 or 89.25-MHz like the Free Electron Laser Research Institute (FELI) linac [10]. The 1-μs macropulse operation mode at the 262-MeV is for electron injection and an electron charge of 12-nC (0.6-nC × 20 pulses) is injected to the storage ring per second. The beam energy is ramped from 262-MeV to 1.4 GeV after beam storage in a minute, since all magnets are made of laminations of 1mm or 0.5mm thick steel. The RF frequencies of the linac accelerator tube and the ring cavity are selected to be 2856 and 499.8-MHz to achieve time overlap on the macropulse of the IR-FEL and the SR so as to do pump-probe experiments [12].

Before installation of the 7.5-T wiggler in the fall of 2005, we expect that the stored beam current and its lifetime will be 300-mA at 1.4-GeV and 5 hours, respectively.

REFERENCES

[1] T. Tomimasu et al., Proc. of APAC01, Beijing (2001) p.340.

[2] H. Ohgaki et al., this Proceedings.

[3] A. Andersson, M. Eriksson, L.-J. Lindgren, P. Rojsel, and S. Werin, Nucl. Instru. Meth. A343 (1994) 644.

[4] Y. Iwasaki et al., this Proceedings.

[5] T. Koseki, M. Izawa, and Y. Kaimiya, Tech. Report of ISSP No.2980 (May 1995) pp.1-8.

[6] M. Yasumoto et al., Proc. of APAC01, Beijing(2001) p.349.

[7] Y. Kondo, S. Koda, and Kamada, REPORTS OF THE FACULTY OF SCIENCE AND ENGINEERING SAGA UNIVERSITY, 31(2), (December 2002) pp. 21-27(in Japanese).

[8] S. Sugiyama et al., J. Syn. Rad. (1998). 5, 437.

[9] V. M. Borovikov et al., ibid. p. 440.

[10] T. Tomimasu, IEEE Trans. NS-28(3),(1981)3523.

[11] T. Tomimasu, E. Oshita, Y. Kanazawa, and A. Zako, Nucl. Instr. Meth. A429 (1999) 141.

[12] M.Yasumoto et al., Jpn. J. Appl. Phys. 41(2002) Suppl. 41-1, pp. 44-48.

TEMPORAL CHARACTERISTICS OF A SASE FEL[*]

Y. Li[#], Z. Huang, J. Lewellen, S. V. Milton, V. Sajaev, K.-J. Kim, ANL, Argonne, IL 60439, USA

Abstract

We have performed a single-shot, time-resolved measurement of the output field of a SASE FEL using the frequency-resolved optical gating (FROG) technique. The measurement reveals the phase and the amplitude of the SASE output as functions of time and frequency, hence enables us to perform a full characterization of the SASE FEL output. We examined both the single-shot field evolution as well as the statistics over multiple shots on the phase and intensity evolution.

INTRODUCTION

In a SASE FEL, a favorable instability occurs due to the interaction of an electron beam and the electromagnetic wave it produces as the beam propagates down an undulator. Provided the interaction is strong enough, the radiation power grows exponentially with the undulator distance until it reaches saturation [1,2]. Due to the mirrorless operation, such single-pass, SASE FELs are proposed for the next generation of high-brightness, coherent X-ray sources [3,4]. Recent experiments have demonstrated saturation of such SASE FELs [5-7] and their capability of achieving shorter and tunable wavelengths by direct amplification [6] as well as by harmonic generation [7,8].

We report the first single-shot time-resolved characterization of SASE pulses using the frequency-resolved optical gating (FROG) technique [9]. The measurement revealed the phase and intensity evolution of the FEL and their statistics over multiple shots. In this paper we will concentrate on the phase evolution [10].

EXPERIMENT

The measurements were conducted at the low-energy undulator test line at the Advanced Photon Source [5,10]. Table 1 is a summary of the main parameters for the two experiments. Briefly, a high-brightness electron bunch generated from an rf photocathode gun is compressed through a magnetic chicane, accelerated to 217 MeV in energy, and sent into an undulator line. A full diagnostic system for the FEL output and the electron bunch are installed at each undulator, enabling us to verify the gain of the FEL [5,11]. A mirror at each station can direct the SASE light toward diagnostics located outside of the tunnel, where the FROG device resides.

Table 1: Experimental Parameters

Experiment	A	B
Peak current	850 A	530 A
Effective bunch length (σ_z)	0.5 ps	0.13 ps
Energy chirp (σ_δ/σ_z)	28 m^{-1}	65 m^{-1}
rms normalized emittance	9 π μm	6 π μm
Undulator period (λ_u)	3.3 cm	
Undulator length (each)	2.4 m	
Undulator parameter (K)	3.1	
Beam energy (γmc^2)	217 MeV	
Nominal wavelength (λ)	530 nm	
Repetition rate	6 Hz	
Gain length (L_G)	0.68 m	0.87 m
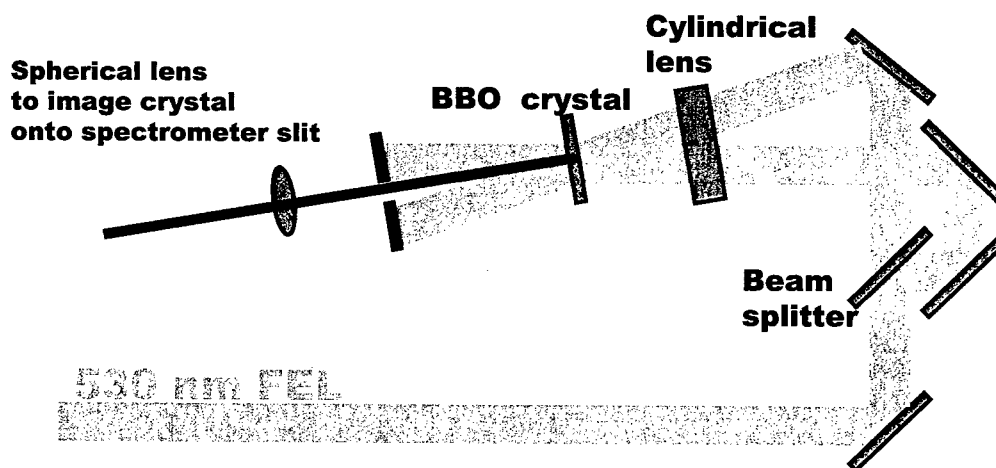
Figure 1: Setup of the second harmonic frequency-resolved optical gating device.

Negative energy chirp of the electron bunch σ_δ/σ_z in data set A is determined by energy spread on a spectrometer using a modified linac zero-phasing technique. Here σ_δ is the relative correlated energy spread, and σ_z is the rms bunch length. Exponential gain was verified by measuring the FEL output as a function of the distance along the undulators.

A single-shot FROG device using the second harmonic gating geometry [9] records single-shot spectrograms (see Fig. 1 for the device setup). In this configuration, the

signal is $I_{FROG}(\omega,\tau) \propto \left| \int_{-\infty}^{\infty} E(t-\tau)E(t)\exp(-i\omega t)dt \right|^2$, where

E is the field of the optical pulse and contains both amplitude and phase information.

Example traces of the FROG measurement along with the retrieved pulse shape and phase in the time and frequency domains are given in Fig. 2.

In general, the traces measured by the FROG have large fluctuations. Figure 2 shows cases with single (a) and multiple (b) intensity spikes. The asymmetry in the frequency axis in the trace is an indication of overall energy chirp. While the phases for each spike are very complicated, there are clearly phase discontinuities at the edge of some spikes.

To interpret the observation in Fig. 2, we recall that the temporal characteristics of a SASE pulse, due to the noisy startup, are those of chaotic light. Under the one-dimensional, cold-beam approximation with the electron energy chirp considered, the electric field in the exponential growth regime is a sum of N_c wave packets [12-15]:

$$E(t,z) = E_o(z) \sum_{j=1}^{N_c} \exp\left[i[\omega_j + \Phi''_\gamma(t-t_j - \frac{z}{v_p})](t-t_j - \frac{z}{c}) \right] \quad (1)$$

$$\times \exp\left[-\frac{1}{4\sigma_t^2}(t-t_j - \frac{z}{v_g})^2(1-\frac{i}{\sqrt{3}}) \right],$$

where N_e is the total number of electrons in the bunch, $\omega_j = \omega_0 + 2\Phi''_\gamma(t_j-t_0)$, $v_p = c/(1+\lambda_0/\lambda_u)$, $\Phi''_\gamma = \omega_0 c\sigma_\delta/\sigma_z$ with ω_0 being the instantaneous resonant frequency at t_0, $E_0(z)$ contains the exponential growth factor, t_j is the arrival time of the jth electron, v_g is the group velocity of each wave packet with an rms coherent length $\sigma_t \approx (N_u/\rho)^{1/2}/2\omega_r$, N_u is the number of undulator periods, and ρ is the FEL scaling parameter [2]. Clearly, an intrinsic chirp exists within a coherent spike as indicated by the quadratic phase term of $(t-t_j-z/v_g)^2/4\sqrt{3}\,\sigma_t^2$ in Eq. (1), and an overall frequency chirp exists from spike to spike through Φ''_γ. Collecting all coefficients of quadratic terms in Eq. (1) and taking into account the dispersion in the collecting optics, the chirp observed by the FROG is

$$\phi'' = \frac{d^2\phi}{dt^2} = -2\,\text{Im}(\Gamma) = 2\frac{\Omega\Theta + \Phi''_m}{\Omega^2 + \Phi''^2_m}, \quad (2)$$

where $\Omega = 4\sigma_t^2 + \Phi''_m\Theta$, $\Theta = 1/3^{1/2} + 4\,\sigma_t^2\,\Phi''_\gamma$, and Φ''_m is the dispersion in the collecting optics of 1.9-cm fused silica.

The experimentally measured chirp $|\phi''|$ for both data sets are given in Fig. 3 (a) and (b) as a function of the coherence length (approximated as the spike length) for

(a) Shot A070

(b) Shot A707
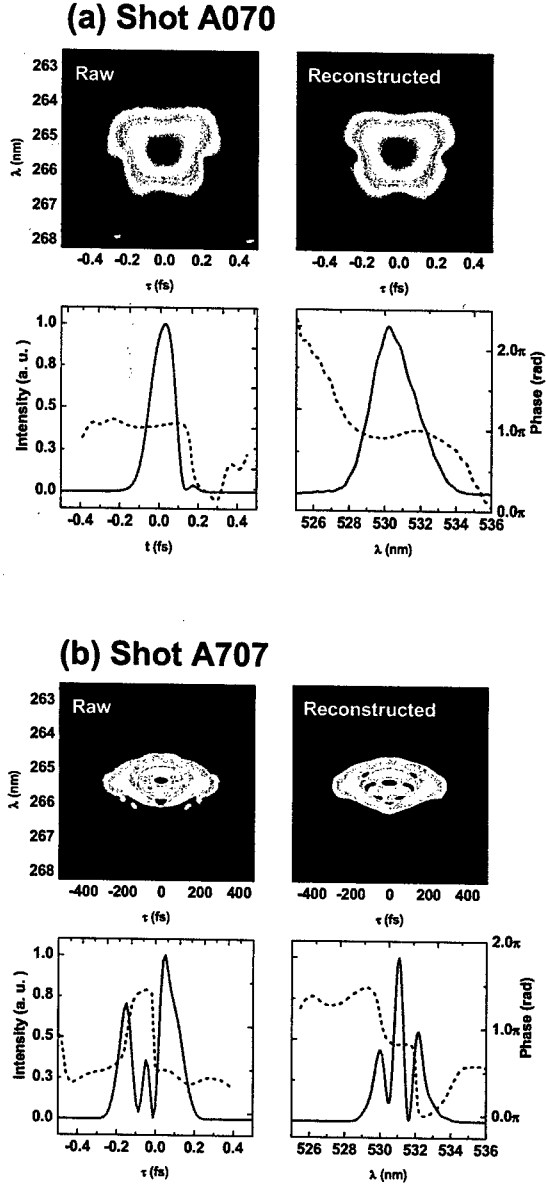
Figure 2: Two sample FROG traces with retrievals, showing the raw and reconstructed traces, as well as the intensity (solid lines) and phase (dashed lines) in the time and frequency domains.

individual spikes. Due to the intrinsic jitter and complicated behavior of each spike, the data are rather scattered. Even so, one can clearly identify a sharp dip at around $\sigma_t=75$ and 50 fs for data sets A and B, respectively, that corresponds to $\Theta \approx 0$ in Eq. (2). By slightly adjusting the electron beam energy chirp in Eq. (2), we are able to fit the position of the dips at -28/m and -75/m for data sets A and B, respectively (see curves in Fig. 2). Simulation shows that, the chirp can be due to the uncompensated chirp from the bunch compressor, as well
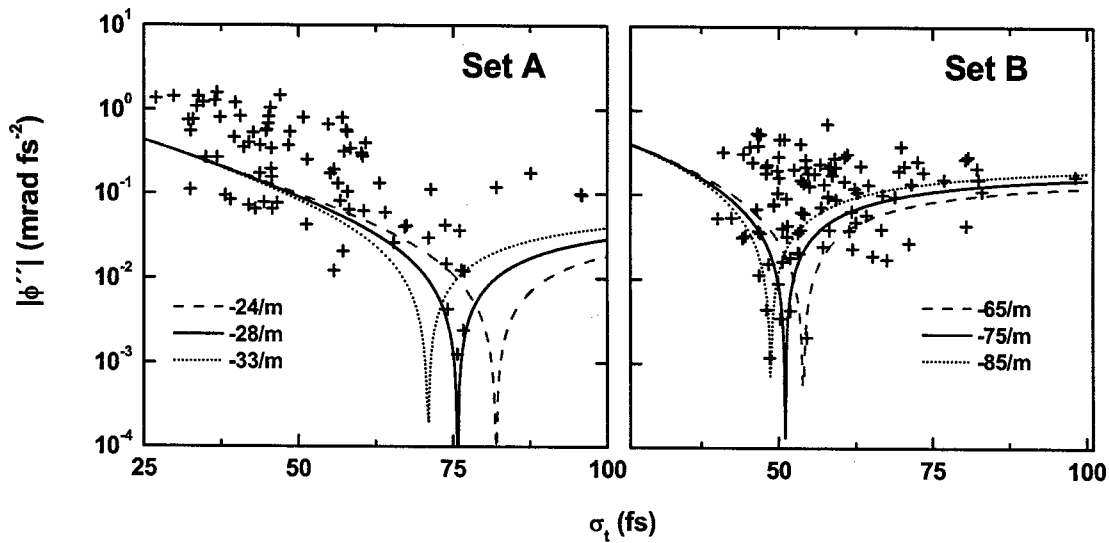
Figure 3: The experimentally measured FEL pulse chirp as a function of the coherence length for experiments A and B. The symbols are the experimental data and the curves are fittings using Eq. (2) with different electron beam chirps.

as the effect of the longitudinal wake field, if not intentionally imposed.

The results in Fig. 3 unambiguously reveal the positive intrinsic SASE chirp. They also verify that the electron beam energy chirp directly maps into the FEL output, a key process for compressing and slicing the pulse from future X-ray FELs. Figure 3 also serves as an independent measurement of the electron bunch energy chirp.

The FROG traces also provide rich information on the statistics of the SASE output, especially the temporal information on these pulses. As the FROG traces provide the information in the frequency domain simultaneously, a correlation analysis between the time and the frequency domain is now possible. A more detailed analysis of the statistics is underway.

SUMMARY

In conclusion, we observed a positive intrinsic chirp in the SASE FEL spikes, and we confirmed that the energy chirp in the electron bunch does map to the SASE output. These observations have very important applications for future X-ray FEL sources in pulse engineering and manipulation.

The authors are grateful for help by O. Markarov and R. Dejus for performing the gain length measurement and processing the data. We also thank L. Teng for insightful discussions.

REFERENCES

[1]   A. M. Kondratenko, E. L. Saldin, Sov. Phys. Dokl. **24** (12), 986 (1979).

[2]   R. Bonifacio, C. Pellegrini, L. M. Narducci, Opt. Commun. **50**, 373 (1984).

[3]   M. Cornacchia et al., "Linac Coherent Light Source (LCLS) Design Study Report," Report SLAC-R-521 (Stanford Linear Accelerator Center, Stanford, CA), revised 1998.

[4]   R. Brinkmann, G. Materlik, J. Rossbach, A. Wagner, Eds., "Conceptual Design of a 500 GeV e^+e Linear Collider with Integrated X-Ray Laser Facility," DESY Report DESY97-048 (Deutsches Elektronen-Synchrotron, Hamburg), 1997.

[5]   S. V. Milton et al., Science **292**, 1953 (2001).

[6]   V. Ayvazyan et al., Phys. Rev. Lett. **88**, 104802-1 (2002).

[7]   A. Tremaine et al., Phys. Rev. Lett. **88**, 204801-1 (2002).

[8]   S. G. Biedron et al., Nucl. Instrum. Methods Phys. Res. A **483**, 94 (2002).

[9]   R. Trebino et al., Rev. Sci. Instrum. **68**, 3277 (1997).

[10] Y. Li et al., Phys. Rev. Lett. **89**, 234801 (2002).

[11] E. Gluskin et al., Nucl. Instrum. Methods Phys. Res. A **429**, 358 (1999).

[12] R. Bonifacio et al., Phys. Rev. Lett. 74, **70** (1994).

[13] K.-J. Kim, "Towards X-ray free electron lasers," AIP Conference Proc. 413, R. Bonifacio and W. A. Barletta, Eds. (American Insitute of Physics, New York), p. 3 (1997).

[14] C. B. Schroeder et al., Nucl. Instrum. Methods Phys. Res. A **483**, 89 (2002).

[15] S. Krinsky and Z. Huang, Phys. Rev. ST-AB, in press.

BEAM-BASED UNDULATOR FIELD CHARACTERIZATION AND CORRECTION AT DUV-FEL

H. Loos*, T. Shaftan,
BNL, Upton, NY 11973, USA

Abstract

We present the results of the commissioning of the 10 m long NISUS undulator of the Deep Ultra Violet Free Electron Laser (DUV-FEL) project. The magnet and diagnostics geometry is discussed and tolerances on the beam trajectory straightness are shown. The beam-based alignment algorithm and its application to correct the NISUS field errors are described.

DUV-FEL PROJECT

Up to date the Deep Ultra Violet Free Electron Laser (DUV-FEL) project is fully commissioned at the NSLS (BNL) [7]. The magnetic system of the FEL includes the 10 m long permanent magnet hybrid undulator NISUS [5] with 3.89 cm period length and 0.31 T peak field at 2.08 cm gap. The NISUS undulator consists of 16 sections with 32 poles in each. The six poles in the middle of every section are alternatingly canted with a cant angle of 0.108 rad. Additional magnetic fields can be superimposed onto the static magnetic undulator fields by means of a so-called 4-wire structure in every section consisting of 4 independently powered wires, which allows for any combination of vertical and horizontal dipole as well as normal and skew quadrupole fields. These coils are integrated within the vacuum chamber for the electron beam. Additional horizontal correction is provided by so-called pancake coils, which have a rather uniform dipole field within the gap.
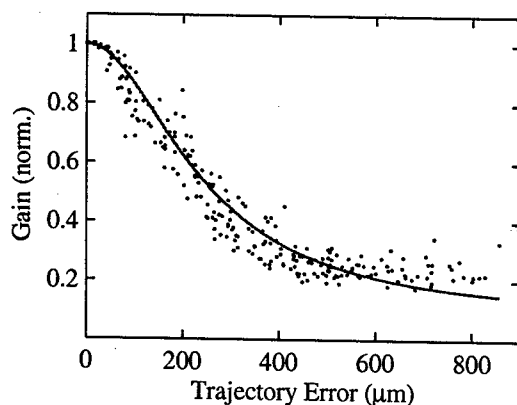
Along NISUS are 16 retractable YAG monitors [8] each with a periscope and image relay to an attached CCD camera. Two additional monitors 1 m and 6 cm in front of the wiggler are included to record the initial conditions of the electron beam with respect to the undulator. A HeNe laser beam, aligned to apertures before and after the undulator, provides a reference position for each monitor. The monitors are calibrated individually and have a resolution of approximately 10 μm (rms). An automated procedure in the MATLAB/EPICS control system records electron and laser beam images to obtain beam centroid and size at every monitor location. From these data the beam emittance, Twiss parameters, and launching condition at the wiggler entrance can be determined and corrected with upstream magnets [9].

To determine the tolerances on trajectory straightness we used the GENESIS 1.3 code [10], assuming the actual NISUS design. Gain length values were calculated for the beam parameters used in the HGHG experiment of 266 nm wavelength, 350 A peak current, 3 μm emittance and $2 \cdot 10^{-4}$ relative energy spread. For the error model used in the simulation we assumed that every section of NISUS has an error field value which is distributed uniformly over the section length. Correlated trajectory deviations which correspond to betatron oscillations were inhibited by imposing appropriate constraints on the field errors. The relative efficiency reduction, i.e. gain length increase, is shown in Fig. 1. A 10% relative increase of the gain length is induced by a field error of 1 mT (rms) or a trajectory error of 100 μm.

UNDULATOR FIELD MODEL

The fixed and variable electromagnetic focusing in NISUS can be regarded as uniform along the wiggler, since the resulting betatron wavelength is much longer than the section length. The electron beam trajectory for the horizontal plane $x(z)$ and similar for the vertical is then determined by the differential equation

$$x'' + k^2 x = \frac{B(z)}{B\rho} , \qquad (1)$$

where $B_y(z)$ is the error magnetic field and k the betatron wavenumber. The solution of this differential equation,

$$
\begin{aligned}
x(z) = \ & x_0 \cos(k\,z) + \frac{x_0'}{k} \sin(k\,z) \\
& + \int_0^z dz' \frac{B(z')}{k\,B\rho} \sin\left(k(z - z')\right) , \qquad (2)
\end{aligned}
$$

Figure 1: Gain reduction in NISUS for SASE at 266 nm due to rms trajectory deviation from field errors simulated with GENESIS 1.3. An empirical fit is shown in red.

* loos@bnl.gov
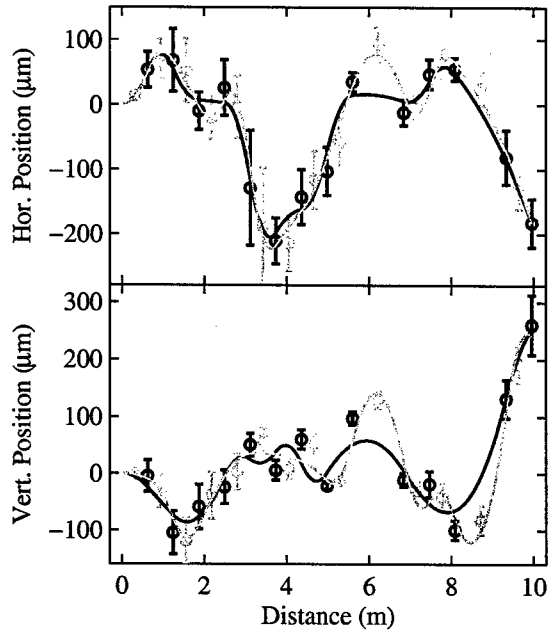
Figure 2: Horizontal and vertical beam position in NISUS with betatron oscillation removed. The green midpoints are obtained by quadratic interpolation. The solid curves represent the trajectories according to the field errors (Fig. 3) obtained from the linearly (blue) and quadratically (green) interpolated data.

Figure 3: Correction currents for the trim coils required to compensate the calculated field errors from the linear (blue) and quadratic (green) model.

EXPERIMENTAL RESULTS

To determine the uncorrelated field errors, the pancake and 4-wire system was initially set to uniform values, which provide equal focusing strength and a magnetic axis at the reference laser position. Any remaining betatron oscillation from missteering at the undulator entrance was obtained by a fit to the data and subtracted to retrieve the trajectory corresponding to the inhomogeneous solution of Eq. (3). Figure 2 shows he uncorrelated trajectory deviation and the midpoints from quadratic interpolation (the midpoints in the linear case are not shown). The best fit of the field error distribution to the given beam positions are presented in Fig. 3 for both the linear and quadratic interpolation of the midpoints. The magnetic field is already scaled to corresponding trim corrector currents using $_{PC} = 58\,\mu$T/A for the pancake correctors and $_{4W} = 57\,\mu$T/A for the 4-wire trim coils. The two methods give very similar results. However, some of the calculated field errors are already dominated by the accuracy of the trajectory measurement, thus limiting the achievable precision of the correction discussed below.

contains two homogeneous terms, which correspond to non-zero initial conditions, and an inhomogeneous term caused by the field errors. The explicit solution of Eq. (2) depends on the field error model and can be integrated for uniform error fields B_i of length $_i$ centered within each section at location $\bar{z}_i$. For any trajectory propagating close enough to the undulator axis with small amplitude of betatron oscillation the focusing strength k in Eq. (1) can be neglected. The solution of this differential equation then gives at the monitor locations between consecutive sections for the inhomogeneous term

$$x_n^{\text{inh}} = \frac{1}{B\rho} \sum_{i=1}^{n} B_i \; _i(z_n - \bar{z}_i) \qquad (3)$$

This linear set of equations $x_n^{\text{inh}} = \;_{ni} B_i$ can in principal be used to obtain the average field errors for each section from the measured beam positions. However, inspecting   reveals that it is badly conditioned and can not simply be inverted. Since there is no constraint for the trajectory angle at each monitor position, the trajectory obtained from the calculated field errors can have a large oscillation with a period of twice the section length. To avoid the oscillations, the trajectory angle can be constrained by introducing virtual monitors located between the real ones and interpolating the trajectory there with either a linear or a quadratic function.

Correcting the obtained field errors with corresponding changes in the trim coils and measuring the resulting trajectory, an iterative procedure was established to remove the field errors. The initial and final trajectory after three iterations can be seen in Fig. 4. The original trajectory deviation in respect to the betatron oscillation of 90 μm for both the horizonal and vertical direction was reduced to 38 μm and 29 μm, respectively. The remaining deviation is comparable to the one of the reference laser, as shown in Fig. 5.

The displayed reference laser position is a single measurement in reference to the average over multiple scans, thus showing the reproducibility of the monitor positions and the jitter of the laser beam centroid. The iterative method converges within the precision of the trajectory measurement.
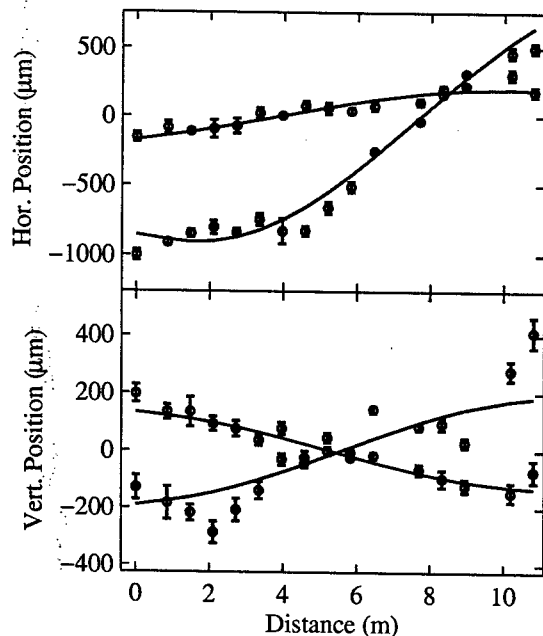
Figure 4: Initial (blue) and final (green) trajectory after three iterations of the correction algorithm.
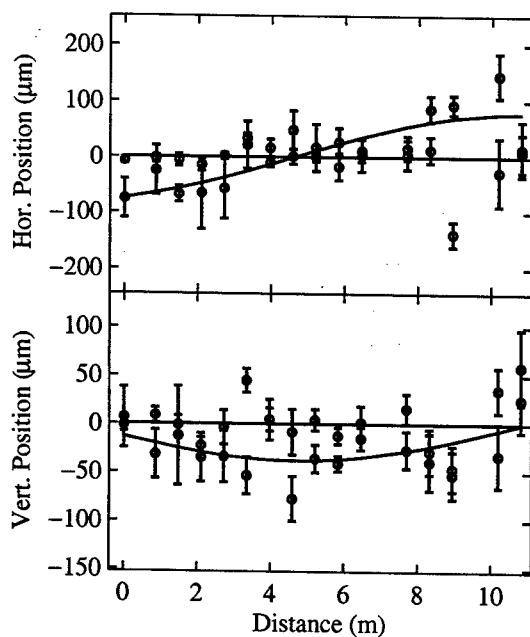
Figure 5: Final (blue) trajectory and reference laser position (green).

SUMMARY

The applicability of the BBA method presented here is demonstrated for the NISUS undulator. It is shown that for a complex undulator geometry including static and electromagnetic focusing a beam-based method works efficiently, providing electron beam parameters sufficient for a successful FEL performance.

ACKNOWLEDGEMENTS

REFERENCES

[1] Ya. S. Derbenev, A. M. Kontratenko, E. L. Saldin, Nucl. Instr. and Meth. A, 193 (1982) 415

[2] L. H. Yu, S. Krinsky, R. L. Gluckstern, Phys. Rev. Lett. 64 (1990) 3011

[3] L. H. Yu, S. Krinsky, R. L. Gluckstern, J. B. J. van Zeijts, Phys. Rev. A 45 (1992) 1163

[4] P. Tenenbaum, T. O. Raubenheimer, Phys. Rev. ST Accel. Beams 3 (2000) 052801

[5] D.C. Quimby et al., Nucl. Instr. and Meth. A 285 (1989) 281

[6] G. Rakowsky et al., PAC 1999, New York, March 1999, p. 2698

[7] T. Shaftan et al., First SASE and Seeded FEL Lasing of the NSLS DUV-FEL at 266 & 400 nm, FEL 2002, Argonne, IL, September 2002

[8] A. Doyuran et al., Diagnostics System for the NISUS Wiggler and FEL Observations at the BNL Source Development Lab, EPAC 2002, Paris, June 2002, p. 802

[9] H. Loos et al., Beam-based trajectory alignment in the NISUS wiggler, EPAC 2002, Paris, June 2002, p. 837

[10] S. Reiche, Nucl. Instrum. Meth. A 429 (1999) 243

ELECTRON BUNCH SHAPE MEASUREMENTS AT THE TTF-FEL

K. Honkavaara, S. Schreiber*, Ch. Gerth, Ph. Piot, DESY, 22603 Hamburg, Germany

Abstract

The TESLA Test Facility linac has been operated in the first half of 2002 with two bunch compressors to drive the TTF-FEL free electron laser. During this running period, SASE radiation with a wavelength around 100 nm has been routinely delivered to experiments. The longitudinal shape of the electron bunches is a crucial property of the electron beam: a peak current in the order of 1 kA is required to drive the SASE process with the given undulator design, transverse emittance, and energy spread. We report on measurements of the bunch length and shape for different operating conditions of the two bunch compressors.

INTRODUCTION

To drive the TTF-FEL free electron laser at DESY, excellent beam properties in the transverse and longitudinal planes are essential: a small transverse emittance in the order of a μm, a high peak current in the kA range, and a small uncorrelated energy spread below 0.1 %.[1] Optimized TTF beam parameters for the FEL runs are discussed in Ref. [2]. The saturation has been achieved in the VUV wavelength region (80 to 100 nm)[3], and SASE radiation has been routinely delivered to the experiments during several running periods in 2001 and 2002.

A sketch of the TTF linac is shown in Fig. 1. The electron source is a laser-driven RF gun with a Cs_2Te cathode. The RF gun section is followed by a booster, a standard TESLA 9-cell superconducting accelerating cavity operated at 11.5 MV/m. After the booster the beam energy is 16.5 MeV. The beam is accelerated by two 12 m long TESLA accelerating modules containing eight 9-cell superconducting accelerating structures each. After a collimation section, the beam is injected into the undulator modules with an energy of up to 300 MeV. Two magnetic chicane bunch compressors are installed: BC1 is downstream of the booster cavity, BC2 between the accelerating modules.

At the end of the last FEL run beginning of 2002, both bunch compressors have been used to shape the longitudinal charge distribution of the electron bunch. In the following, measurements of the longitudinal bunch shape using a streak camera for different settings of the two compressors are presented.

EXPERIMENTAL SET-UP

To measure the bunch distribution, we use synchrotron radiation emitted by the horizontally deflecting spectrometer dipole after the undulator (see Fig. 1). The optical

* siegfried.schreiber@desy.de

part of the synchrotron radiation is guided by four flat aluminum mirrors to a streak camera situated outside of the accelerator tunnel. An achromat lens is used to focus the light onto the entrance slit of the camera. In order to reduce chromatic effects, a narrow-band wavelength filter is being used. [4] The data presented here are obtained using a filter of 500 ± 40 nm.

The streak camera (Hamamatsu FESCA-200 C6138) has an intrinsic resolution of 208 fs (FWHM) measured with a fs probe laser.[5] Only some data have been taken with the fastest streak speed of 20 ps/10.29 mm. Most of the the data presented here are obtained with the second fastest streak speed of 50 ps/10.29 mm. For this speed, the resolution is 200 fs (sigma) only. In the case of long uncompressed bunches, the streak speed of of 100 ps/10.29 mm was more suitable. The entrance slit is adjusted to be as small as required to obtain the best resolution. In most of the measurements the slit is between 20 μm and 40 μm, the latter has a better photon yield. For these slit sizes the intrinsic camera resolution is not significantly changed. The gain of the streak camera multi-channel plate has been adjusted in a way to maximize the signal but to avoid saturation effects.

A bunch signal with a jitter of about 50 ps served as a trigger for the streak.[6]

DATA ANALYSIS

For a given machine setting, several streak images have been recorded. The images are projected onto the time axis. In order to reduce the noise due to photon statistics, several single profiles (typically from five to ten) are overlayed. Due to the trigger jitter, the recorded images are not in the same time position. The shifting of the profiles for overlaying along the time axis is performed manually taking the leading edge of the profile as a reference. The average of the overlayed profiles is calculated. Since the bunch charge was stable during the measurement, a charge scaling of the profiles was not necessary. An example of nine overlayed profiles with the average profile superimposed is shown in Fig. 2.

All profiles shown in the following are averaged profiles, and scaled according to their peak intensity. The profiles have not been corrected for the resolution of the camera.

EXPERIMENTS AND RESULTS

The longitudinal electron bunch profile has been measured with different settings of the bunch compressors. Table 1 summarizes some design parameters. In all the measurements presented here, the beam was passing through BC2 with a deflecting angle of 18°. Nominally, the first
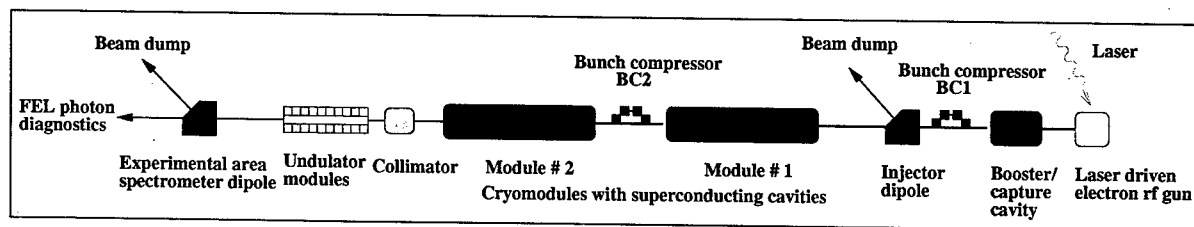
Figure 1: Schematic overview of the TTF-FEL linac phase 1 (not to scale). Beam direction is from right to left, the total length is 100 m.
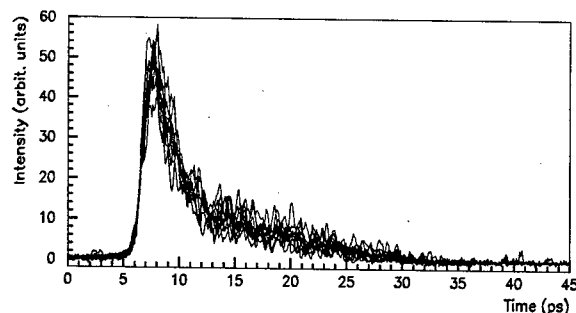
Figure 2: Several measurements of the same longitudinal beam profile. The average of the profiles is superimposed.

accelerating module (module 1) RF is dephased by 12° to obtain maximum compression. BC1 is either bypassed or used with two different deflecting angles: 24° and 30°. When BC1 is bypassed, the booster cavity RF is operated with a phase 10° off-crest corresponding to a minimum in energy spread. The RF phase of the RF-gun has always been nominal 40° from zero crossing. The second module is operated with on-crest acceleration.

Table 1: Some design parameters of the bunch compressors.

parameter	BC1	BC2
defl. angle (°)	22.5	18
R56 (mm)	88	180
max. disp. (mm)	-15	-346
compression ratio	2	4

For all settings, the general shape of the bunch is dominated by a sharp leading peak and a long tail. The smallest measured width of the peak is 600 ± 100 fs (sigma) and containes about 1/3 of the charge, yielding in a peak current of 1 kA.[2]

Figure 3 shows the effect of the booster phase and module 1 phase on the bunch shape. The beam passes through both compressors, BC1 is operated with a deflecting angle of 30°, BC2 with 18°. The bunch charge is about 1 nC.

In the upper plot, the module 1 phase is on-crest. The profiles are for the case of the booster at minimum energy spread (+10°, red), and at compression (+22°, blue). The compression effect of BC1 is only visible in the tails and in
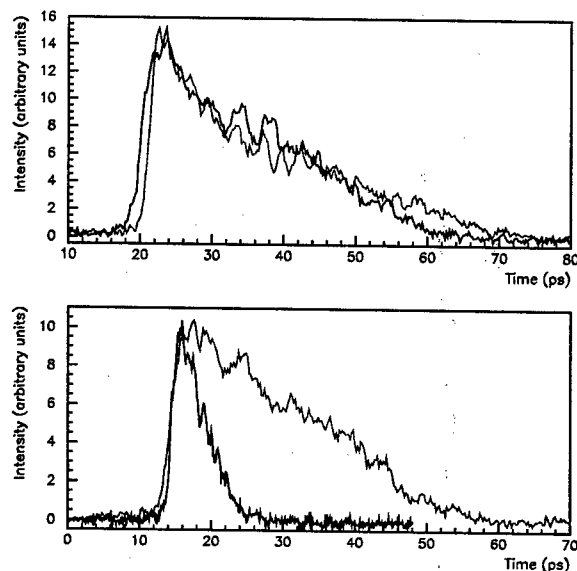
Figure 3: Average bunch profiles with both BC1 and BC2 in use (1 nC). *Upper:* Module 1 on-crest. Booster cavity phase corresponding to minimum energy spread, 10° off-crest (red), booster cavity phase at 22° off-crest (blue). *Lower:* Booster phase 22°, module 1 phase on-crest (0°) (red), module 1 phase in full compression (12°) (blue).

the calculated rms over the whole distribution.

The lower plot shows the effect of the module 1 phase: the module is on-crest as before (red), and with a phase of +12° corresponding to maximum compression (blue).

The compressing effect of BC2 is very clear (Fig. 3, lower plot). A similar behavior has been observed bypassing BC1 [4], as well as in our earlier measurements with a lower resolution camera[7], where the peak could not have been resolved.

The effect of the booster cavity phase is small (Fig. 3, upper plot). The aim of using BC1 is not to fully compress the bunch, but rather to *shape* the leading peak. We expect the precompression with BC1 to shorten the bunch before acceleration with module 1, and thus to reduce the curvature in the longitudinal phase space due to the RF. The reduced curvature leads – after compression with BC2 – to a larger and more gaussian peak and a shorter tail.

Figure 4 compares three bunch shapes, while the machine was lasing with SASE close to saturation. In one

case, BC1 has been bypassed (red), in the other cases, BC1 has been set to compression (24° deflection), and tuned to keep the machine lasing. The booster phase is 25° (green) and 26.5° (blue). For all cases, the bunch charge was between 2.5 and 3 nC.

From the comparison it is clearly visible, that the pre-bunching with BC1 effectively widens the sharp peak and shortens the tail. The effect of this tailoring of the lasing bunch slice on the measured internal mode structure of the FEL radiation has been reported in [8].
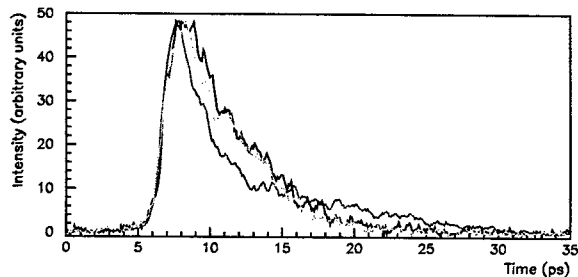
Figure 4: Average bunch profiles for settings, where the FEL was lasing. (a) BC1 is bypassed (red), (b) BC1 set to compression (24° deflection), booster phase at 25° (green) (c) and 26.5° (blue). Charge for all cases between 2.5 and 3 nC.

DISCUSSION AND CONCLUSION

We have measured longitudinal bunch shapes with different settings of the bunch compressors. The data show clearly a shape with a dominant leading peak of a cuurent of 1 kA and a long tail. The first bunch compressor BC1 is used as a pre-buncher to tailor the leading peak of the bunch profile. This peak shows up after compression with the second chicane BC2. It is actually the part or slice of the bunch which contributes to the SASE lasing process.

In this sense, TTF1 was able to influence the mode structure of the SASE FEL radiation by carefully adjusting phases and compression of BC1.

ACKNOWLEDGEMENT

We like to thank E. Janata from HMI, Berlin for the synchronization unit of the streak camera trigger and L. Plucinski, DESY for his help in setting up the synchrotron radiation beam line.

REFERENCES

[1] J. Andruszkow et al., "First Observation of Self-Amplified Spontaneous Emission in Free-Electron Laser at 109 nm Wavelength", Phys. Rev. Lett. 85 (2000) 3825-3829.

[2] S. Schreiber et al., "Performance of the TTF Photoinjector for FEL Operation", Proc. of the workshop "The physics and applications of high brightness electron beams", Chia Laguna, Sardinia, July 1-6, 2002

[3] V. Ayvazyan et al, "Generation of GW radiation pulses from a VUV Free-Electron Laser operating in the femtosecond regime", Phys. Rev. Lett., 88 (2002) 104802.

[4] Ch. Gerth et al, "Bunch Length and Phase Stability Measurements at the TESLA Test Facility", FEL2002, Argonne, Ill., USA, Sept 9-13, 2002, to be published

[5] Hamamatsu C6138 FESCA-200, Test report, September 2000.

[6] The synchronization of the trigger has been provided by E. Janata, HMI, Berlin

[7] K. Honkavaara, Ph. Piot, S. Schreiber, D. Sertore, "Bunch Length Measurements at the TESLA Test Facility using a Streak Camera", Proc. of the 2001 Partical Accelerator Conference, Chicago, Ill., USA, June 18-22, 2001, p. 2341.

[8] V. Ayvazyan et al, "Study of the statistical properties of the radiation from a VUV SASE FEL operating in the femtosecond regime", FEL2002, Argonne, Ill., USA, Sept 9-13, 2002, to be published.

START TO END SIMULATIONS FOR THE SPARX PROPOSAL

M. Biagini, M. Boscolo, M. Ferrario, V. Fusco, S. Guiducci, B. Spataro, C. Vaccarezza, M. Zobov
INFN-LNF, Frascati, ITALY
L. Serafini, INFN-Mi, Milan, ITALY
R. Bartolini, G. Dattoli, L. Giannessi, L. Mezi, M. Quattromini, C. Ronsivalle,
ENEA-Frascati, ITALY
E. Chiadroni, University of Rome II, Rome, ITALY
P. Emma, SLAC, Stanford, USA
J. B. Rosenzweig, UCLA, Los Angeles, USA

Abstract

We report in this paper the results of start to end simulations concerning the SPARX option based on an S-band normal conducting linac. One of the most critical systems is the bunch compressor. The effects on beam dynamics of a magnetic chicane system and a rectilinear RF compressor integrated in a high brightness photoinjector, are analyzed and compared in this paper.

INTRODUCTION

The SPARX proposal is devoted to the realization in Italy of a large scale ultra-brilliant and coherent X-ray source [1]. Two spectral complementary regions around 13.5 nm and 1.5 nm, are considered for the radiation source. A preliminary set of the required beam parameters are reported in table 1. Two basic schemes have been considered for the Linac, as shown in figure 1: the first one, the Hybrid Scheme, consists in an advanced high brightness photoinjector, with a RF compression stage [2], followed by a first linac (Linac 1) that drives the beam up to 0.5 GeV with the correlated energy spread required to compress the beam in the next magnetic chicane. The second linac (Linac 2) drives the beam up to 2.5 GeV while damping the correlated energy spread, taking profit of the effective contribution of the longitudinal wake fields provided by the S-band accelerating structures.

Table 1 – Beam Parameters

Beam Energy	2.5	GeV
Peak current	2	KA
Emittance (projected)	2	μm
Emittance (slice)	1	μm
Energy spread	0.1	%

In the Fully Magnetic Scheme the first compression stage is provided by a magnetic chicane after the Linac 1 at 350 MeV. An intermediate linac section, Linac 2, drives the beam up to 1 GeV. The next magnetic chicane compresses the beam up to the project requirements. The final Linac 3 brings the beam up to 2.5 GeV, while compensating the final energy spread of the beam.
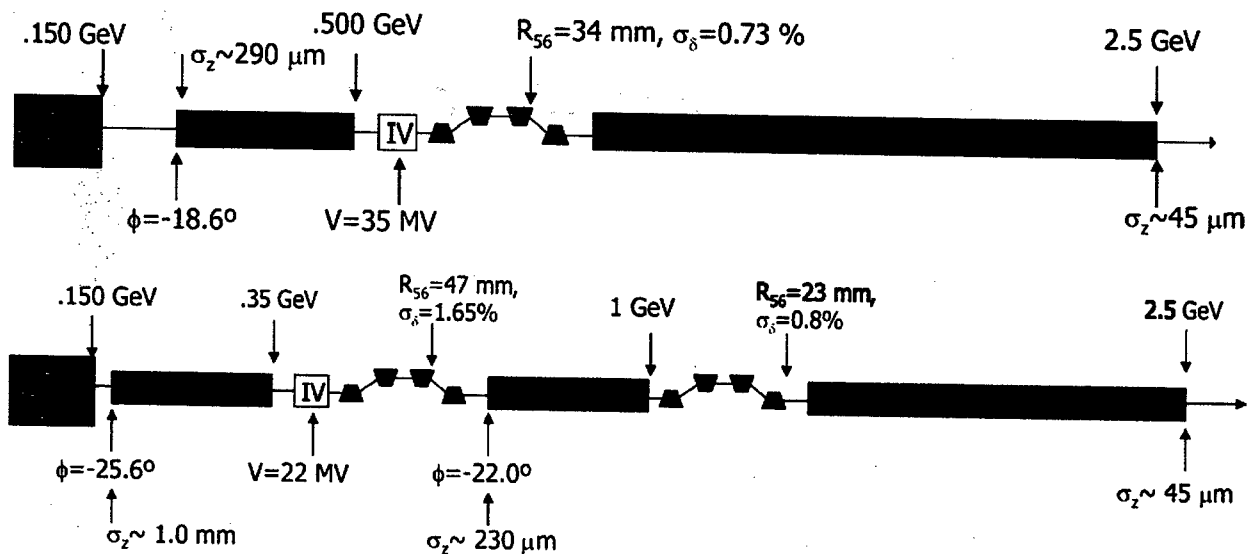
Figure 1: Schematic layout of the two SPARX linac designs: upper plot the Hybrid scheme, lower plot the Fully Magnetic scheme

HYBRID SCHEME

The PhotoInjector design considers a 1 nC bunch, 10 ps long (flat top) with a 1.2 mm radius, generated inside a 1.6-cell S-band RF gun of the same type of the BNL-SLAC-UCLA one, operating at 140 MV/m peak field equipped with an emittance compensating solenoid (B=3090 G). Three standard SLAC 3-m TW structures each one embedded in a solenoid boost the beam up to 150 MeV. Applying the RF compression method, together with the proper setting of the accelerating phase and solenoid strength it is possible to increase the peak current while preserving the beam transverse emittance [2]. We have obtained, (Parmela [3] simulation), a bunch average current of 300 A with a normalised rms emittance below 1 μm, as shown in figure 2, using the parameter setting listed in table 2.
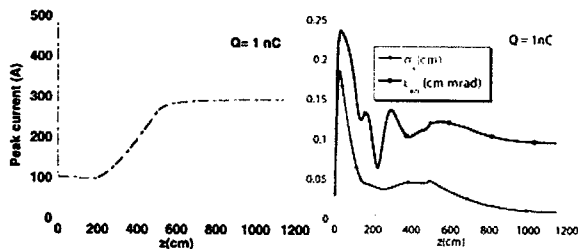
Figure 2: Parmela simulations of the peak current (left), rms norm.emittance and rms beam envelope (right), along the PhotoInjector structure.

Table 2

TW section	I	II	III
Gradient [MV/m]	15	25	25
Phase [Deg]	-86	-37	0
Solenoid field [G]	1120	1280	0

The Linac consists in a first accelerating section, Linac I, where 7 standard SLAC 3-m structures bring the beam up to an energy of .5 GeV. The accelerating phase is -18.6°, and the resulting energy spread is about 0.7%. A fourth harmonic cavity (11.424 GHz), follows, 60 cm long, in order to linearise the beam energy correlation. A magnetic chicane with $R_{56} = 34$ mm, about 15 m long, compresses the beam from 290 μm to 45 μm. A second accelerating section, Linac II , with 34 SLAC structures, in which the beam travels on crest, brings the beam energy up to 2.5 GeV and remove the energy spread .

FULLY MAGNETIC SCHEME

The PhotoInjector system consists of a 1.6 cell RF gun operated at S-band and high peak field on the cathode, (120 MV/m), generating a 6 MeV beam. The gun solenoid field is B=2730 G, and the injection phase is 33°. The beam is then focused and matched into 2

accelerating sections of the SLAC type, as described in [4]. Our simulations using PARMELA indicate that we can generate in this way a beam at 155 MeV with a rms correlated energy spread of 0.2%, and a rms norm. emittance of 0.6 μm (at 1.0 nC bunch charge and I = 90 A peak current). The slice energy spread and the slice norm. emittance, calculated over a 130 μm slice length, are well below 0.04% and 0.5 μm respectively, all over the bunch.

In the first accelerating section, Linac I, four standard SLAC 3-m structures bring the beam energy up to .35 GeV. The accelerating phase is -25.6°, and the resulting energy spread is about 0.17%. A fourth harmonic cavity follows in order to linearise the beam energy correlation. A magnetic chicane, about 3m long, with $R_{56} = 47$ mm compresses the beam from 1 mm to 230 μm. A second accelerating section, Linac II , with ten SLAC structures, operating at 22° off crest, accelerates the beam up to 1 GeV with energy spread 0.8%. The second chicane, $R_{56} = 23$ mm, 15 m long, compresses the beam up to 45 μm. In the third linac section, Linac III, twenty seven structures, accelerating the beam on crest, bring the beam energy up to 2.5 GeV and compensate the energy spread

TIMING JITTER ANALYSIS

One of the relevant aspects in the SPARX project is the sensitivity of the compression system to the laser pulse temporal jitter [5]. The performances of the two proposed schemes have been analysed and compared adding a 1° phase error at the RF gun injection stage.

The two channels have been optimized, with the code Litrack [6], to obtain the minimum sensitivity of the compressed beam properties to the phase error. For the hybrid scheme the optimized on has been performed on the channel downstream the RF compression stage, looking for the best combination of the relative phase of the first linac section, the X-band cavity voltage and the R_{56} value of the magnetic chicane. The same has been done for the purely magnetic channel regarding the parameters of the first two linac sections, the X-band and the two magnetic chicanes. The results are reported in table 3 and in figures 3 and 4. It's worth to notice that with the optimized Hybrid scheme in all of the three cases the final peak current is higher than 2 kA, and with the Purely Magnetic scheme, we have two cases with 2 kA and one with the peak current 10% lower.

Table 3

	Hybrid	F. Magnetic
$\Delta\phi$ (ps)	I_{peak}(kA)	I_{peak}(kA)
0	2.0	2.0
+1	1.9	1.8
-1	2.4	2.3
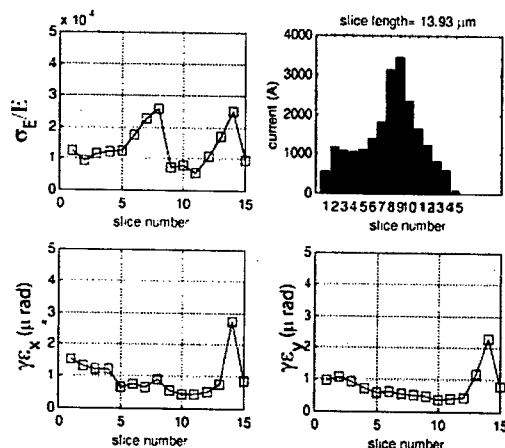
Figure 3: Slice analysis of the beam properties at the exit of the linac, for the hybrid reference case.
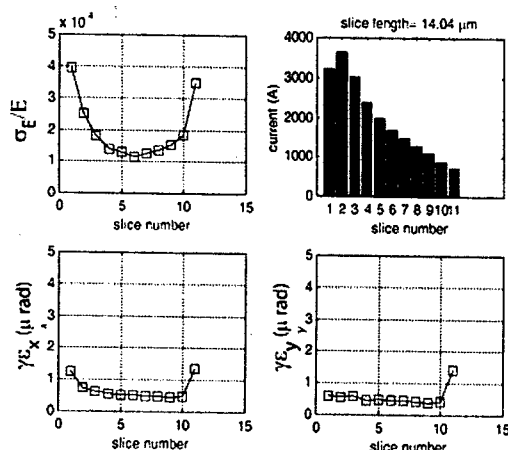
Figure 4: Slice analysis of the beam properties at the exit of the linac, for the fully magnetic reference case.

THE FEL SASE SOURCE

The beam quality has been tested by simulating the FEL process at the wavelength of 1.5 nm with the beam parameters obtained at the end of the last compression stage. The simulations have been done with the time dependent version of PERSEO [7]. The beam has been longitudinally "sliced" in five regions where the average parameters (emittance, energy, energy spread, current) have been calculated. The parameters of the slice with the higher current have been selected for the simulation. In table 4 a list of the "best slice" beam parameters for each case are shown. In table 5 the saturation length in presence of $\pm 1°$ of phase jitter are reported for both schemes. The hybrid scheme with a phase jitter of $+1°$ shows overcompression effects, resulting in more than 2 μm x-emittance. The magnetic saturation length is in this case of about 36 m.

Table 4

Case	I_{peak} (A)	ε_{nx}(m-rad)	ε_{ny}(m-rad)	γ	σ_E/E
Hybrid Reference	2790	0.83E-06	0.49E-06	4977	1.82E-04
Hybrid +1°	2230	0.95E-06	0.51E-06	4982	5.53E-04
Hybrid -1°	3330	2.13E-06	0.66E-06	4977	5.64E-04
Magnetic Reference	3237	0.84E-06	0.56E-06	5038	3.49E-04
Magnetic -1°	2748	0.84E-06	0.62E-06	5038	2.80E-04
Magnetic +1°	3744	1.10E-06	0.56E-06	5038	4.60E-04

Table 5

Case	Sat. L (m) (Steady State)	Sat. L (m) (Time Dependent)
Hybrid Reference	18.7	19.5
Hybrid +1°	23.3	23.6
Hybrid -1°	36.5	36.7
Magnetic Reference	18.5	19.0
Magnetic -1°	19.6	20.5
Magnetic +1°	19.9	20.2

CONCLUSIONS

We have analysed the effects of a phase jitter ($\pm 1°$) on the SPARX beam quality considering two different concept for compression schemes,. The parameters have been set to obtain an equivalent compression factor between the two schemes. The slice parameters in terms of emittances, energy spread are comparable. The purely magnetic compression provides a more linearised longitudinal phase space which could in principle allow a further compression. We expect to obtain similar results also in the hybrid scheme with the IV harmonic cavity located upstream the RF compressor. The beam quality have been tested with time dependent PERSEO simulations showing a slightly lower sensitivity to phase jitter for pure magnetic compression. The low number of macroparticles considered in the ELEGANT simulations doesn't allow a correct representation of collective effects arising from the CSR coupling. A further effort in this direction is required to complete the analysis.

REFERENCES

[1] D. Alesini, et al. "Conceptual Design of a High-Brightness Linac for Soft X-ray SASE-FEL Source", to be published on Nucl. Instr. and Meth. A

[2] M. Boscolo et al., proc EPAC02, p 1762, Paris 02

[3] J. Billen, "PARMELA", LA-|UR-96-1835, 1996.

[4] M. Biagini et al., "Beam Dynamics studies for the SPARC project", these conference

[5] P.J. Emma, proc. EPAC-02, p. 49 Paris 02.

[6] P.J. Emma , private communication

[7] L. Giannessi, http://www.perseo.enea.it

CRYSTAL UNDULATOR AS A NOVEL COMPACT SOURCE OF RADIATION

S. Bellucci, S. Bini, G. Giannini, *INFN-LNF Frascati, Italy*; V.M. Biryukov, G.I. Britvich, Yu.A. Chesnokov, V.I. Kotov, V.A. Maisheev, V.A. Pikalov, *IHEP Protvino, Russia*; V. Guidi, C. Malagù, G. Martinelli, M. Stefancich, D. Vincenzi, *Univ. Ferrara, INFM-INFN Italy*; Yu.M. Ivanov, A.A. Petrunin, V.V. Skorobogatov, *PNPI, St. Petersburg, Russia*; F. Tombolini; *Univ. Roma Tre, Italy*

Abstract

A crystalline undulator (CU) with periodically deformed crystallographic planes is capable of deflecting charged particles with the same strength as an equivalent magnetic field of 1000 T and could provide quite a short period L in the sub-millimeter range. We present an idea for creation of a CU and report its first realization. One face of a silicon crystal was given periodic micro-scratches (grooves), with a period of 1 mm, by means of a diamond blade. The X-ray tests of the crystal deformation have shown that a sinusoidal-like shape of crystalline planes goes through the bulk of the crystal. This opens up the possibility for experiments with high-energy particles channeled in CU, a novel compact source of radiation. The first experiment on photon emission in CU has been started at LNF with 800 MeV positrons aiming to produce 50 keV undulator photons.

undulator radiation has much higher spectral density and the background radiation is not essential.
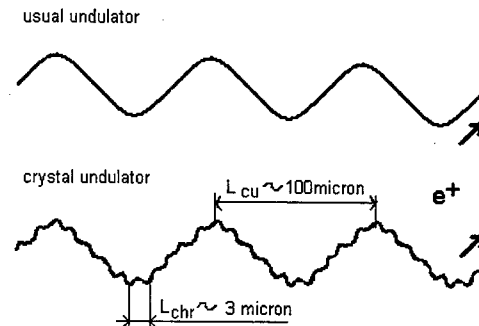
Fig.1 Peculiarities of a crystalline undulator.

INTRODUCTION

The energy of a photon, E, emitted in an undulator is in proportion to the square of the particle Lorentz factor γ and in inverse proportion to the undulator period L: $E=h\gamma^2 c/L$. Typically, at the modern accelerators the period of undulator in the synchrotron light sources is a few centimeters [1].

With a strong worldwide attention to novel sources of radiation, there has been broad interest [2-12] to compact crystalline undulators. A CU with periodically deformed crystallographic planes bends the charged particles as an equivalent electromagnetic field in the order of 1000 T and could provide a period L in sub-millimeter range. This way, a hundred-fold gain in the energy of emitted photons is reached, as compared to a usual undulator.

PECULIARITIES OF CRYSTALLINE UNDULATOR

Particle trajectories in a deformed crystal are more complicated than in a usual undulator (Fig. 1). Undulator radiation is accompanied by a harder component (channeling radiation). This component is harder than undulator radiation because of the smaller period of oscillations $L_{chr} \sim 3$ micron (for typical energies of a few GeV, where undulators are used). On the other hand it is lower in intensity because the amplitude of oscillations is also small $A_{chr} \sim 1$ Å. At the condition $A_{cu} \gg A_{chr}$ the

METHOD OF CU CREATION

Different ideas have been proposed for creation of CU [2-15], but they are still pending realization. We have recently [2] demonstrated by means of X-rays that microscratches on the crystal surface make sufficient stresses for creation of a CU by making a series of scratches with a period of 1 mm. Now we have optimized this process and were able to produce an undulator with a period in sub-millimeter range and with a good amplitude. A series of undulators was manufactured with the following parameters: length along the beam 1 to 5 mm, thickness across the beam 0.3 to 0.5 mm, 10 periods of oscillation with step from 0.1 to 0.5 mm, amplitude on the order of 50 A. The undulators were tested with X-rays as described in ref. [2].
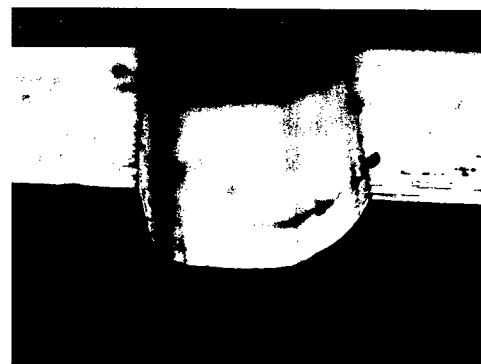
Fig.2 Example of a microgroove on crystal surface.

The X-ray (17.4 keV) beam was collimated to 2 mm height and 40 μm width before incidence on the sample surface. The sample could be translated with accuracy of 1 μm and 1" by use of a standard theodolite. A NaI counter with wide-acceptance window detected the diffracted radiation. The count rate of diffracted quanta is maximal under Bragg condition, achieved by rotation of the sample. Fig.3 shows the measured angles as functions of the beam incidence position at the crystal surface. On the same absolute scale, the position of grooves is shown as well. The periodic angular deformations of the crystal planes reach an order of 40-50 μrad. The plane deformation amplitude is in the order of 20 Å as obtained by analysis of the angle-versus-position function of Fig. 3, measured on the opposite (unscratched) face of the crystal. This means that a sinusoidal-like shape of crystalline planes goes through the bulk of the crystal.
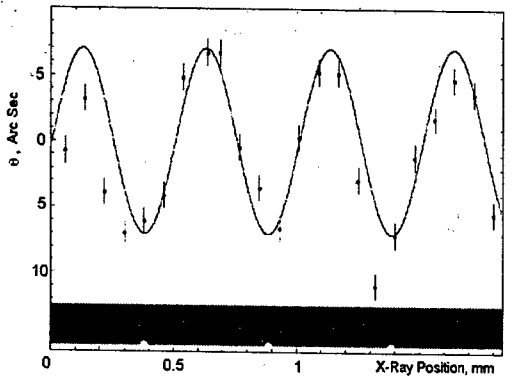
Fig. 3 X-ray test of one of the undulators.

SCHEME OF A PHOTON EMISSION EXPERIMENT

Our collaboration has two appropriate sites for an accelerator experiment on generation of photons in a crystalline undulator. These are LNF with the positron beam energy 500-800 MeV, and IHEP where one can arrange positron beams with energy above 2 GeV. In order to improve background condition, one needs to place the CU into vacuum. A goniometer provides an angling of crystal within ±20 mrad with a step size of about 0.050 mrad. Right after the vacuum box, a cleaning magnet is positioned. The vacuum system is ended by a tube as long as 3 m, 200 mm in diameter, which has at the end a Mylar window 0.1-0.2 mm thick.

As a detector of photons, we use a crystal of NaI (Tl) with a diameter of 1 cm ×10 cm. To calibrate the γ-detector, we use radioactive sources [241]Am with E_γ=59 keV, and ^{60}Co with E_γ=1.15 MeV. Aim of the experiment is the observation of undulator photons emitted with expected energy in a CU, measurement of its spectrum, experimental comparison to the case of a usual straight crystal, and finally demonstration that the crystalline

undulator works. First experimental results are expected soon, subject to the schedule of our accelerators.

EXPECTED PHOTON SPECTRUM

The calculations of radiation intensity were carried out for the (011) plane of the silicon single crystal. It is obvious that only positrons under channeling conditions can emit the low frequency radiation in the periodic above-considered structure. Thus, the channeling radiation will take place for similar crystal structures. In general, radiation is characterized by dimensionless parameter [14] $\rho = 2\,\gamma^2\,<v_p^{\,2}>/c^2$, where $<v_p^{\,2}>$ is the mean squared transversal velocity of the particle. For CU, $<v_p^{\,2}>\approx<v_u^{\,2}>+<v_c^{\,2}>$ if the curvature of trajectory is not large. Here $<v_u^{\,2}>$ and $<v_c^{\,2}>$ are mean squared transversal velocities for undulator and channeling motion, correspondingly.

When $\rho \leq 1$, the total radiation spectrum is a simple additive combination of the strictly undulator and channeling ones. The total spectrum will be the sum of contributions from mainly two basic frequencies of the both processes. When $\rho \gg 1$ one can expect that the spectrum will be similar to photon spectrum of synchrotron radiation.

For ρ slightly more than 1, the radiation spectrum is complicated and consists of some peaks. The last case is more difficult for consideration. Besides, in CU, the dechanneling process and radiation of the above-barrier positrons is expected, and it is necessary to take into account their influence on photon spectrum. For calculations of the photon spectrum from 800 MeV positron beam we chose the period and amplitude of deformation of the silicon single crystal equal to 0.01 cm and 80 Å, respectively; we expect to obtain these values in nearest future.
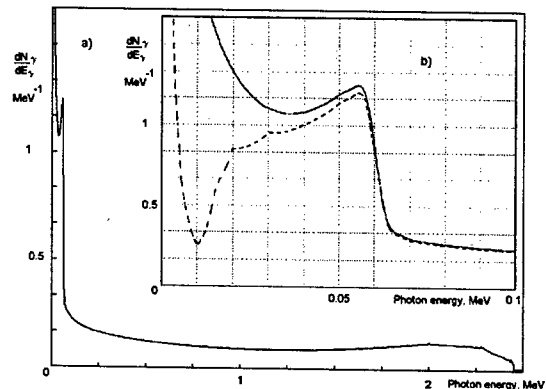
Fig.4 Expected photon spectrum for 800 MeV positrons in range (0 – 2.5) MeV (a) and (0 – 0.1) MeV (b). The dashed curve is for photon absorption in the body of undulator taken into account. Normalized on one positron incident within channeling angle.

When ρ is about or below 1, one can calculate the expected photon spectra for LNF experiment.

Fig. 4 shows the calculated spectrum of photons radiated in CU for 800-MeV positrons. The maximum of the distribution corresponds to $\approx$ 55 keV. Our calculations take into account the following factors:

1) channeling radiation and dechanneling process;

2) finite length of the crystalline undulator, 0.1 cm;

3) radiation of the above-barrier positrons;

4) absorption of gamma-quanta in the undulator bulk (calculated in assumption that absorption in undulator is similar to that in amorphous silicon media [15]).

The channeling radiation is computed in accordance with the paper [16] and these results are in a good agreement with experimental data [17]. Our calculations allow one to make the following conclusions concerning the photon spectrum.

(a) Clear peak of the photon number one can observe in the range 30-60 keV. The sum of the photons within this peak is equal to approximately 20 % of all the photon spectrum (or 0.05 photons per positron). The major part of the photons owe to channeling radiation. These photons are distributed in the wide range (up to 2.5 MeV) and their spectral density (per MeV) is 5 times less than in the range where the undulator photons are.

(b) The influence of the finite length of the single crystal and the dechanneling process are crucial for the density and the form of the undulator photons' spectrum: the density decreased 1.5-2 times and the maximum of the distribution shifted from 61 keV to 55 keV.

(c) The contribution of radiation of the above-barrier positrons is negligible, thereby a sophisticated collimation of the positron beam is not required.

(d) The strong absorption process at energies < 30 KeV allows to obtain more monochromatic undulator photons.

Positrons energies at IHEP accelerator (beamline 4) are 2–15 GeV. In this case, $\rho \approx$ 1. Our calculations were carried out for the (011) plane of a silicon single crystal. The thickness of the crystal undulator, amplitude and period of the deformations were 0.3 cm, 40 Å and 0.015 cm, respectively. The calculated number of photons in the range (100–600) keV is 0.15 per one positron passing through the crystalline undulator.

At positron beam energies higher than 3 GeV and selected parameters of the crystal undulator the values of $\rho > 1$ are achieved and can run up to 100 (for energies 10–15 GeV). For a usual undulator this case was solved analytically [14]. However, for CU (where there are two practically independent frequencies of particle motion) finding an analogous solution is an important actual problem. More detailed information concerning the calculations will be published elsewhere.

CONCLUSIONS

Our studies on the creation and characterisation of the periodically deformed crystalline structures, and calculations of the expected photon spectra allow us to draw the conclusion that crystalline undulator will be able to produce intense X-rays of 10 to 1000 keV. Crystalline undulator would allow to generate photons with the energy on the order of 1 MeV at the synchrotron light sources where one has at the moment only 10 keV, and for this reason crystal undulators have great prospects for application.

REFERENCES

[1] Beam Line, V. 32, N 1, 2002

[2] S. Bellucci et al., Phys. Rev. Lett. 90 (2003) 034801

[3] V.V. Kaplin, S.V. Plotnikov, and S.A. Vorobiev, Zh. Tekh. Fiz. 50, 1079-1081 (1980).

[4] V.V. Kaplin, S.V. Plotnikov, and S.A. Vorobiev, in: Abstracts of the 10-th Conference on the Application of Charged Particle Beams for Studying the Composition and Properties of Materials, Moscow, 1979, p.28.

[5] V.G. Baryshevsky, I.Ya. Dubovskaya, and A.O. Grubich, Phys. Lett., 77A, 61-64 (1980)

[6] H. Ikezi, Y. Lin, and T. Ohkawa, Phys. Rev., B30, 1567-1568 (1984).

[7] S.A. Bogacz and J.B. Ketersom, J. Appl. Phys. 60, 177-188 (1986).

[8] G.B.Dedkov, Phys.Stat.Sol.(b)184, 535-542 (1994).

[9] A.V. Korol, A.V. Solovev, and W. Greiner, Intern. Journal of Mod. Phys., 8, 49-100 (1999).

[10] U. Mikkelsen and E. Uggerhoj, Nucl. Instr. and Meth., B160, 435 (2000).

[11] R.O. Avakian, et al. NIM B173, 112 (2001)

[12] R.O. Avakian, et al., NIM A 492, 11 (2002).

[13] V.M. Biryukov, Yu.A. Chesnokov, and V.I. Kotov, Crystal Channeling and Its Application at High-Energy Accelerators (Springer: Berlin, 1997)

[14] V.N. Baier, V.M. Katkov, V.M. Strakhovenko, Electromagnetic processes at high energies in oriented single crystals. World Scientific, 1998

[15] J.H. Hubbell, Natl. Stand. Ref. Data ser. NSRDS-NBS 29 (1969)

[16] V.A. Maisheev. Nucl.Instr.Meth. B254, 42, (1996)

[17] J. Bak, et. al. Nucl. Phys.B254;491, (1985).

PHOTOINJECTOR RF CAVITY DESIGN FOR HIGH POWER CW FEL*

S.S. Kurennoy, D.L. Schrage, R.L. Wood, L.M. Young, LANL, Los Alamos, NM 87545, USA
T. Schultheiss, V. Christina, J. Rathke, Advanced Energy Systems, Medford, NY 11763, USA

Abstract

The project is under way to develop a key enabling technology for high-power CW FEL: an RF photoinjector capable of producing continuous average current greater than 100 mA. The specific aim is a π-mode, normal-conducting RF photoinjector, 3 nC of bunch charge, 100 mA of current (at 33.3-MHz bunch repetition rate) and emittance less than 10 mm-mrad. This level of performance will enable robust 100-kW-class FEL operation with electron beam energy <100 MeV, thereby reducing the size and cost of the FEL. This design is scalable to the MW power level by increasing the electron bunch repetition rate to a higher value. The major challenges are emittance control and high heat flux within the CW 700-MHz RF cavities. Results of RF cavity design and cooling schemes are presented, including both high-velocity water and liquid-nitrogen cooling options.

INTRODUCTION

For a MW-class FEL, a high-current emittance-compensated photoinjector is a key element. This paper presents results on the RF cavity design and cooling schemes for a demo 700-MHz RF photoinjector (PI) accelerating 100 mA of the electron beam (3 nC per bunch at 33.3-MHz repetition rate) to above 5 MeV [1]. Further accelerating and focusing provides the transverse rms emittance below 10 mm-mrad at the wiggler. The beam energy spread should be below 1% to allow the bunch compression down to 20 ps before the wiggler. The PI is designed to be scalable to higher beam currents, up to 1 A, by increasing the bunch repetition rate. To keep the beam emittances low, high electric-field gradients, especially near the photocathode, are needed, plus an external magnetic field to compensate space charge. However, the wall power losses increase as cavity fields squared, for a given cavity shape, leading to serious challenges for cavity cooling and increasing the RF power required. Therefore, an optimal design must be a trade-off between the requirements of beam dynamics, RF power, and feasibility of the cavity thermal management.

RF CAVITY

We consider a $(n+1/2)$-cell, π-mode RF structure, with cell-to-cell coupling of 0.03-0.05. A few options for the cell coupling have been studied [2], including magnetic coupling via slots and more conventional on-axis electric coupling through apertures. It was found that using slots provides effective structures with high shunt impedance, but leads to very high power-loss densities near the slots.

As the result, the on-axis coupled cavity structure was chosen [2]. This structure has an additional advantage: its septa (cell-separating walls) are easier to cool than those with coupling slots. An emittance-compensating external solenoid, as well as a bucking coil that cancels its magnetic field near the cathode, have designs similar to those for the 1.3-GHz AFEL [3]. Superfish-Poisson codes [4] have been used for 2D and the CST MicroWave Studio (MWS) [5] for 3D electromagnetic calculations. Beam dynamics has been simulated with Parmela [6] to select field configurations minimizing the emittance for a given cavity shape. We found that a long structure, n=6 or 7, is needed to achieve the beam energy of 5 MeV while keeping the heat flux manageable. However, fields in such a long cavity would be unstable, with a rather small mode separation. Our solution was to split the structure. The resulting two-stage configuration consists of a 2.5-cell cavity with the accelerating gradient E_0=7 MV/m (the PI proper) that brings the electron beam energy to 2.7 MeV, followed immediately by a conventional 4-cell booster with E_0=4.5 MV/m, where the beam is accelerated to 5.5 MeV. Results of Parmela simulations presented in Fig. 1 confirm that this design satisfies all beam requirements.
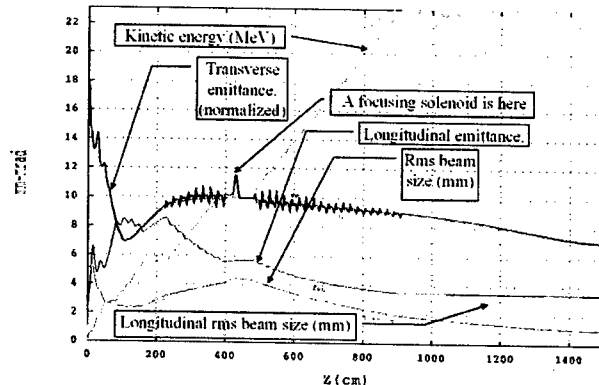
Figure 1: Results of Parmela simulations for the split PI.

The wall power density in the 4-cell booster, due to its lower gradient, is below 35 W/cm², so that its cooling will not present problems. The most challenging part of the PI is the 2.5-cell RF cavity. Its schematic, including cooling channels and RF tapered ridge-loaded waveguides, is shown in Fig. 2. With aperture radii of 65 mm and septum thickness of 20 mm, the cell coupling in the 2.5-cell structure is near 0.03, so that the π-mode at 700 MHz is well separated from its nearest neighbors. The cavity design is a result of a few iterations made with Superfish (SF) and the MWS eigensolver, followed by a thermal analysis. SF runs were used to adjust the cavity radii to achieve a flat field distribution, which gives minimal emittances at the wiggler. MWS eigenmode computations included 3D effects, like frequency shifts due to vacuum

ports, RF couplers, or slug tuners. Time-domain simulations with MWS have been used to design and optimize the RF waveguide-cavity couplers [7].
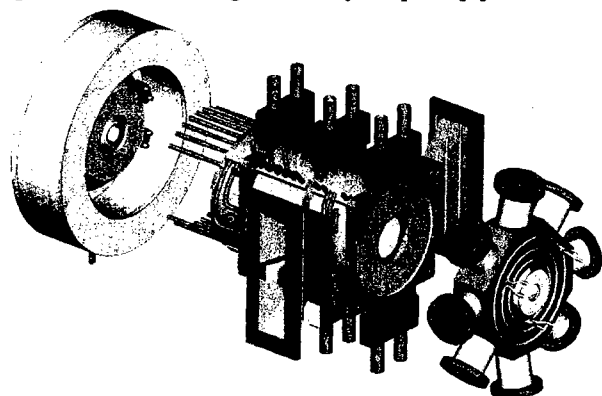
Figure 2: 2.5-cell RF cavity (center) with emittance-compensating magnets (left) and vacuum plenum (right).

The electric field of the π-mode in the PI 2.5-cell RF cavity is shown in Fig. 3 produced by MWS. The field magnitude corresponds to the MWS solver normalization of eigenmodes (the mode field energy is 1 J), so it should be scaled (by a factor of 2.38) to provide the required gradient of 7 MV/m. One can see how the field alternates its direction from one cell to the next one. The vacuum plenum (shown in front in Fig. 3) is not excited since its resonance frequency is much lower, at about 650 MHz. Its downstream wall will also house the laser window.
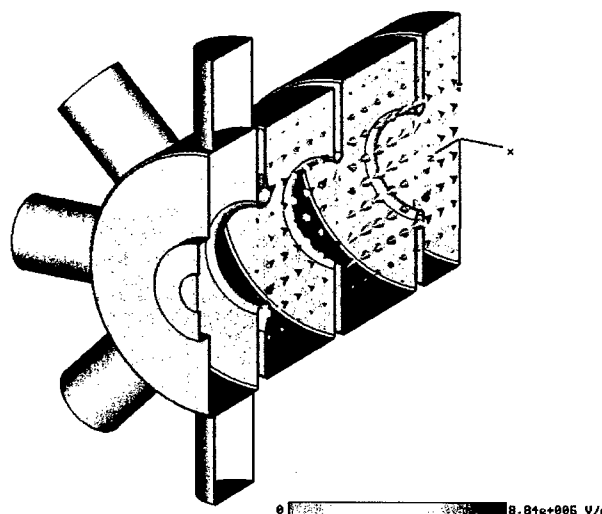
Figure 3: Electric field of π-mode in 2.5-cell PI RF cavity.

Wall power densities have been calculated using both codes, SF and MWS. The surface current distribution inside the cavity is illustrated in Fig. 4. The same field scaling as in Fig. 3 is assumed. The highest power density is on the cell septa and particularly on the 1st half-cell end wall (xy-plane), where it reaches slightly above 100 W/cm^2 for the nominal gradient E_0=7 MV/m (Tab. 1). The power density increases even higher, above 200 W/cm^2, near the RF couplers connected to the 3rd cell (cf. Fig. 2),

see [7] for details. However, these hot spots are small and can be cooled efficiently using special cooling channels placed near the coupler iris in the thick cavity wall.
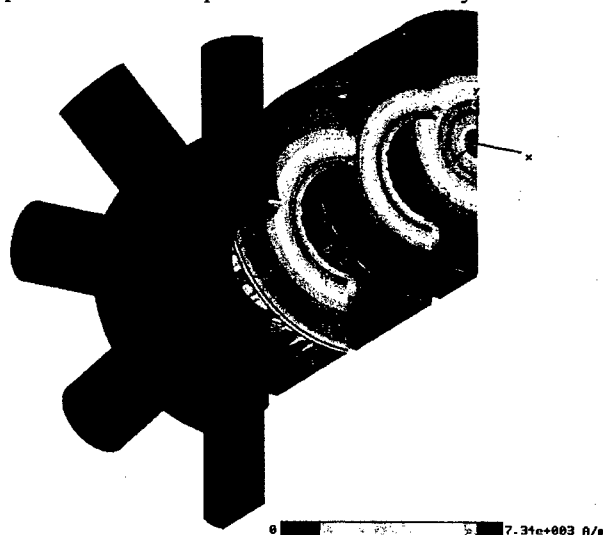
Figure 4: Surface current distribution for the π-mode.

THERMAL MANAGEMENT

The required high field operation of this cavity results in high RF losses on the surface. While cooling with liquid nitrogen (LN$_2$) as opposed to water would lower the wall loads significantly (Tab. 1), the cost of a high-pressure liquid nitrogen system was prohibitive for the demonstration photoinjector. A high-pressure system ensures that boiling does not occur at these high heating rates. A forced flow / boiling cooling system, though cheaper, was considered too risky. Therefore, a water-cooled design was pursued. This design, with some tuning to adjust the frequency (e.g., with slug tuners in the 2nd cell of the 2.5-cell cavity), would also work with high-pressure liquid nitrogen if desired.

Table 1: RF losses at LN$_2$ and room temperature

	LN2 Cooled	Water Cooled
Cathode Field (MV/m)	9.92	9.92
Temperature (K)	77	293 (20C)
Total Power (kW)	306.	786.
Maximum Power Density (W/cm²)	41.0	105.
Structure Q (includes cathode losses)	81800.	31800.
NC Resistivity (mW-cm)	.261	1.72
Q_T/Q_{RT} (SUPERFISH)	2.57	1.0
Segment Average Power Density (W/cm²)		
Cell 1 (cathode)	.309	.794
Cell 1 end wall (outside cathode)	31.2	80.2
Cell 1 Outer Wall	31.8	81.6
Cell 1 Septum 1 wall	32.5	83.5
Cell 1 Output Bore	4.09	10.5
Cell 2 LE Septum wall	32.3	83.0
Cell 2 Outer Wall	31.6	81.3
Cell 2 HE Septum wall	32.5	83.4
Cell 2 HE Bore	4.20	10.8
Cell 3 Septum wall	28.0	71.9
Cell 3 Outer Wall	29.6	76.2
Cell 3 HE Septum wall	38.6	99.1
Cell 3 HE Nose upper	36.0	92.5
Cell 3 HE Nose lower	23.0	59.2
Cell 3 HE Bore	9.42	24.4

About eight hundred kilowatts of RF power are deposited on the walls of the 2.5-cell cavity. This requires intricate cooling channels and a relatively large flow of cooling water. Cooling tubes for the cylindrical walls and cooling plenums for the septa can be seen in Fig. 2. Flow requirements that are based on RF heat loads at surface temperature are given in Tab. 2.

Table 2: Flow requirements for 2.5-cell RF cavity

Total RF ohmic loss*	823 kW
Max surface heat flux*	112 W/cm^2
Water inlet temperature	20 C
Coolant channel dimensions	.100"x.175" (2.5x4.5 mm)
Flow rate	36 l/s at 5 m/s
RF surface temperature	52 C
Coolant channel surface temp.	46 C
Pressure drop	15.8 psi within channel, 50 psi overall
Mean coolant outlet temp.	26 C

* At RF surface temp, OFE Cu surface

An axisymmetric model of the cavity was developed using the finite element code ANSYS. RF loads were mapped on the surface of the model from Superfish output and modified based on the surface temperature. The resulting steady-state temperature distribution is shown in Fig. 5. The left cell is the half cell with the photocathode on the far left wall. The septa separating the cavity cells have simple shapes to allow for simple coolant channel design. The fourth cell (far right) is the non-resonant vacuum pumping cell. The RF losses are relatively small on this cell, so only limited cooling is required.

Water cooling
Inlet temperature 20 C
Applied model bulk temperature 24.5 C
From 2-D model RF losses 823 kW
(local temperature distribution)

Cooling of non-resonant cell designed such that thermal expansion nearly matches adjacent cell
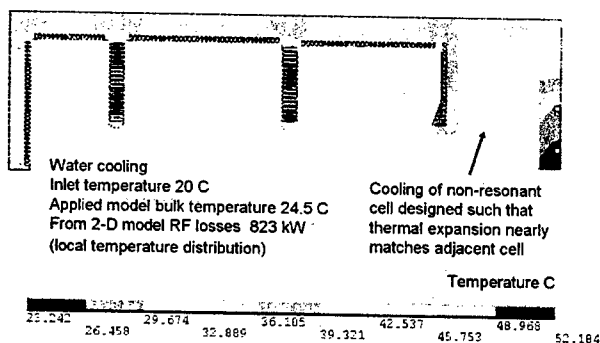
Temperature C

Figure 5: Steady-state temperature distribution.

The significant stresses generally occur between the heated RF surface and the cooling channels. GlidCop®, a dispersion strengthened copper, is used in the high stress regions throughout this cavity. It has a yield strength of 39 ksi and provides significant margin for this design. The steady-state temperature distribution is subsequently mapped onto a structural finite element model using the same nodes and element connectivity as the thermal model. The resulting steady-state von Mises stress distribution is shown in Fig. 6.

The PI is designed to be a fully hydrogen furnace brazed structure. The core of the structure will be fabricated from Glidcop® AL-15 with some external elements made from OFE copper and stainless steel. The double-ridged waveguide tapers are also made from Glidcop®. The majority of the complex machining required for the cooling channels will be done in the Glidcop® structures. They will then be copper plated to facilitate assembly by brazing. Final cuts on the inside diameter of the cells will be done to establish the desired field profile and frequency prior to stack brazing the cavity assembly.

Local stress in corner 9811 psi

von Mises stress, psi
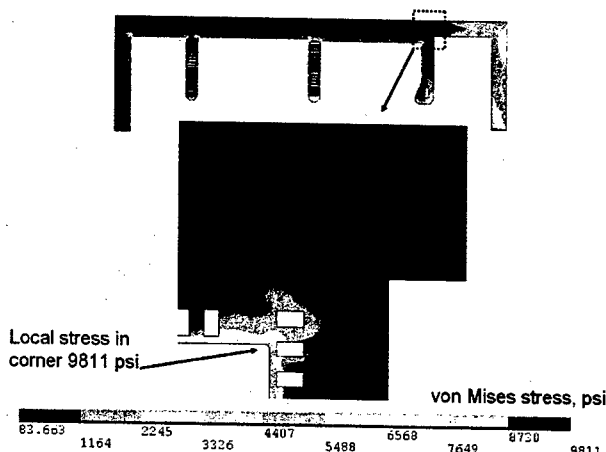
Figure 6: Steady-state thermal stress distribution.

CONCLUSIONS

The presented design allows us to surpass the required beam parameters while addressing the key issue for a high-current normal conducting CW RF photoinjector, namely, an effective structure cooling. It provides a path forward to a very high power amplifier FEL.

We plan to construct the full-power prototype, install it in the existing facilities at LANL, and to perform RF and thermal testing without beam in early 2005. Once the RF/thermal management with high heat flux has been demonstrated, the system will be upgraded to operate with electron beam, by adding a real photocathode and drive laser, a second RF power source, and a short beam line with a beam dump and appropriate diagnostics.

REFERENCES

[1] D.C. Nguyen, et al. "Development of a CW, High-Average-Current 700 MHz Photoinjector at Los Alamos", FEL 2002, Argonne, IL, 2002.

[2] S.S. Kurennoy, et al. "CW RF Cavity Design for High-Average-Current Photoinjector for High Power FEL", ibid.

[3] R.L. Sheffield, et al. NIM, A318 (1992) 282.

[4] J.H. Billen, L.M. Young. Report LA-UR-96-1834, Los Alamos, 1996 (rev. 2002).

[5] MicroWave Studio, v.4.2. CST GmbH, www.cst.de.

[6] L.M. Young, J.H. Billen. Report LA-UR-96-1835, Los Alamos, 1996 (rev. 2002).

[7] S.S. Kurennoy, L.M. Young. "RF Coupler for High-Power CW FEL Photoinjector", these proceedings.

SIMULATION STUDIES OF A XUV/SOFT X-RAY HARMONIC-CASCADE FEL FOR THE PROPOSED LBNL RECIRCULATING LINCAC *

W.M. Fawley[†], W.A. Barletta, J.N. Corlett, and A. Zholents, LBNL, Berkeley, CA 94720, USA

Abstract

Presently there is significant interest at LBNL in designing and building a facility for ultrafast (i.e. femtosecond time scale) x-ray science based upon a superconducting, recirculating RF linac (see [1] for more details). In addition to producing synchrotron radiation pulses in the 1-15 keV energy range, we are also considering adding one or more free-electron laser (FEL) beamlines using a harmonic cascade approach to produce coherent XUV & soft X-ray emission beginning with a strong input seed at ~ 200 nm wavelength obtained from a "conventional" laser. Each cascade is composed of a radiator together with a modulator section, separated by a magnetic chicane. The chicane temporally delays the electron beam pulse in order that a "virgin" pulse region (with undegraded energy spread) be brought into synchronism with the radiation pulse, which together then undergo FEL action in the modulator. We present various results obtained with the GINGER simulation code examining final output sensitivity to initial electron beam parameters. We also discuss the effects of external laser noise and shot noise upon this particular cascade approach which can limit the final output coherence.

INTRODUCTION

In the past decade, there has been an increasingly strong interest in developing intense sources of tunable, coherent radiation at extreme ultraviolet and soft x-ray wavelengths. While much of this effort has been concentrated on free-electron lasers (FELs) based upon the principle of self-amplified spontaneous emission (SASE), there is an alternative "harmonic cascade" FEL approach [2][3] which begins with a temporally and transversely coherent input signal from a "conventional" laser in the ultraviolet region (e.g. $\lambda_{in} \sim 240$ nm). This input is then effectively frequency-upshifted via resonant electron-radiation interaction in a series of FEL undulators to produce a short wavelength (e.g. $\lambda_f \sim 4$ nm) final signal with excellent transverse and temporal coherence. This approach relies upon the higher harmonic longitudinal microbunching which naturally accompanies strong microbunching at the fundamental wavelength of FEL resonance $\lambda_s = \lambda_w \times (1 + a_w^2)/2\gamma^2$. Here λ_w is the undulator wavelength, γ is the electron beam Lorentz factor, and a_w is the normalized RMS undulator strength parameter.

Recently, Yu et al. [4] have reported successful results from a one stage, High Gain Harmonic Generation (HGHG) experiment at BNL in which a seed laser was used

to produce strong microbunching modulation at 800 nm followed by both strong coherent emission and accompanying FEL gain to saturation at the third harmonic wavelength of 266 nm. At LBNL we are interested in augmenting the proposed LUX (Linac-based Ultrafast X-ray) facility by a multi-stage, harmonic cascade FEL which would operate from UV to soft x-ray (i.e. 1.2 keV) photon energies. Each cascade stage would consist of a "modulator" undulator plus achromatic bend/dispersive section, which strongly microbunches a short portion (e.g. 200 fs) of the electron beam, followed by a "radiator" undulator whose resonant wavelength is tuned to an integral harmonic of the preceding modulator resonance.

By exploiting the ps- or better timing synchronization possible with the recirculating linac configuration of LUX, we will adapt the "fresh beam" idea of Ben-Zvi et al.[5] by placing a delay chicane following each radiator undulator. This ensures that a "virgin" e-beam section, lying closer to the pulse head with electrons whose instantaneous energy spread has not been increased by FEL interaction in the upstream modulators, will be brought into temporal synchronism with the radiation pulse. Importantly, both this delay and the use of high radiation power in the modulators (a GW-class seed laser for the first and 100+ MW-class coherent spontaneous emission (CSE) for the subsequent modulators) produces sufficient microbunching in the low gain regime, thus permitting quite short undulator lengths (typically $\leq 1.5 L_{gain}$). This design philosophy[6] is different from that studied by Saldin et al. [7] who had to limit the amount of induced energy spread in each modulator which thus required the use of high gain radiators. High input power to each modulator also helps alleviate the problem of noise growth accumulating from stage to stage which otherwise can degrade the output longitudinal coherence at short wavelengths.

BASIC CASCADE PERFORMANCE

Here we describe a present design of a FEL harmonic cascade system for LUX. We use reasonably conservative electron beam parameters: 2.5 GeV energy with a uniform $\sigma_E = \pm 200$ keV, 500 A current (1 nC in 2 ps), and 2π mm-mrad normalized emittance. The external laser seed has 1 GW power and is presumed to be fully tunable over the wavelength range $190 - 250$ nm. Using time-steady (i.e. monochromatic) simulations with the GINGER code[8], we designed and partially optimized a 4-stage harmonic cascade reaching from 240-nm down to 1-nm wavelength. The undulator and dispersive section parameters are displayed in Table I. The FEL parameter ρ strongly decreases after the 48-nm stage while the effective nor-

Table 1. Undulator Parameters for a Sample 4-Stage Harmonic Cascade for LUX

λ_s (nm)	λ_w (mm)	a_w	B_w (T)	FEL ρ	L_w (m) rad.	L_w (m) mod.	τ_{slip} (fs) rad.	τ_{slip} (fs) mod.	P_{out} (MW) rad.	P_{out} (MW) mod.	$\langle b_1 \rangle$ rad.	$\langle b_1 \rangle$ mod.	R_{56} (μm)
240	120	9.69	1.22	2.3×10^{-3}	—	3.6	—	24.0	—	1000	—	0.21	11.3
48	75	5.43	1.10	2.4×10^{-3}	4.0	6.0	8.5	12.8	345	395	0.36	0.22	4.9
12	40	3.65	1.38	1.2×10^{-3}	6.0	5.0	6.0	5.0	113	121	0.16	0.19	2.8
4	30	2.32	1.17	7.6×10^{-4}	5.0	4.0	2.2	1.8	139	142	0.27	0.18	0.4
1	25	0.96	0.58	4.1×10^{-4}	8.0	—	1.1	—	11	—	0.07	—	—
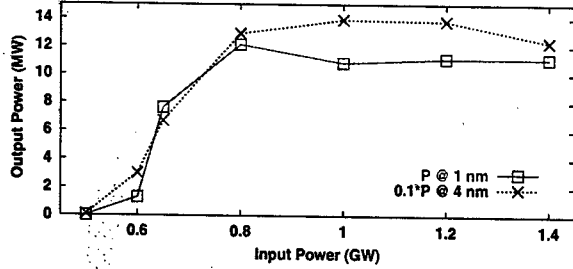
Figure 1: Sensitivity of output power from 4-nm and 1-nm radiator stages to external laser input power at 240 nm.
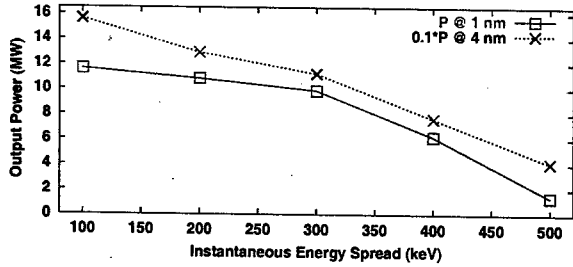
Figure 2: Output power sensitivity to energy spread.
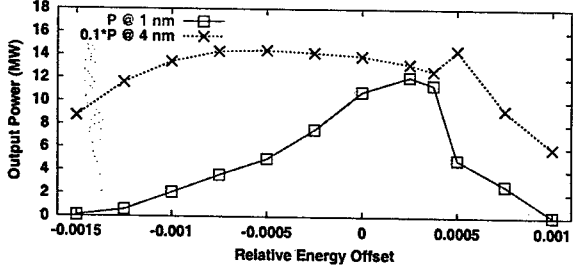
Figure 3: Output power sensitivity to energy offset.

malized energy spread corresponding to transverse emittance increases from 7.5×10^{-5} in the 48-nm radiator to 7.5×10^{-4} in the 1-nm radiator. This last increase strongly exceeds ρ with the consequence of reduced radiation emission due to longitudinal debunching.

The two columns listed under $\langle b_1 \rangle$ refer to the average/output microbunching parameter at the fundamental wavelength for each radiator/modulator, respectively. Our basic philosophy was to make each modulator sufficiently long that $\langle b_1 \rangle$ approached 0.2 at which point the next few higher harmonics typically have $\langle b_M \rangle$ between 0.002 and 0.02. Each dispersive section immediately downstream raises the microbunching approximately 10-fold for the de-

sired harmonic resonant in the following radiator. Figures 1 through 3 show the sensitivity of output power from the 4- and 1-nm radiators to various input parameters. By operating in the low gain regime and by optimizing the dispersion sections's strengths to a particular input power, P_{out} appears relatively insensitive to P_{in}. This insensitivity also applies in part to input noise fluctuations in amplitude (see the next section).

NOISE GROWTH

It has long been known that up-conversion to harmonic M of a signal containing phase noise will in general increase the noise level of the output *power* by a factor M^2; when considering output field amplitude or phase, the relevant scaling is M^1. Previous studies of FEL harmonic cascades [6][7] have shown that similar scaling can apply in the *high-gain* limit for amplitude noise (*i.e.* a time-varying $\tilde{E}$ in Eq.1) although the latter reference has pointed out that the scaling is much weaker than M^2 in the high power, low-gain limit, where $\partial \log \langle b \rangle / \partial \log I \ll 1$.

With the exception of temporal slippage effects, it appears virtually impossible to escape the power law dependency upon M. Slippage results in a given electron slice interacting with a temporal radiation region $\tau_{slip} = (L_w/\lambda_w) \times \lambda_s/c$ which helps filter out the highest temporal frequency components from $d\phi/dt$. Here ϕ refers to the slowly varying phase in the eikonal approximation:

$$E(\vec{x}, t) \equiv \tilde{E}(\vec{x}, t) \times \exp\left[i\left(k_0 z - \omega_0 t + \phi(\vec{x}, t)\right)\right] \quad (1)$$

Figure 4 shows the evolution of the phase noise level in a series of GINGER runs for which the initial 240-nm input laser signal had either broad-band electric field phase or amplitude noise at a level equivalent to 22 mrad rms per 240-nm wavelength superimposed upon a constant base signal. The output phase noise level (after removal of $\langle d\phi/dt \rangle$ which corresponds to a simple frequency offset) is plotted at the end of each radiator stage. For the 48-nm stage (*i.e.* $M = 5$), we show a second point which corresponds to the phase noise level near the beginning of the radiator; the decrease in noise level between the beginning and end of the 48-nm radiator illustrates the filtering effects of slippage.

At least three conclusions can be drawn from this figure (and close inspection of the actual $d\phi/dt$ curves):
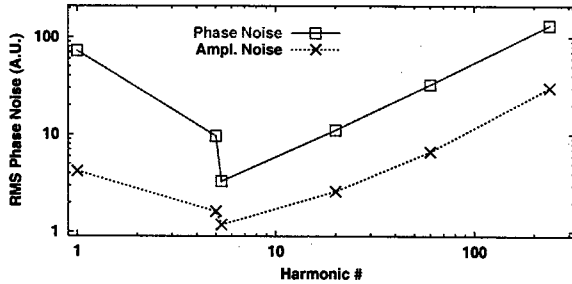
Figure 4: Residual rms phase noise $d\phi/dt$ following removal of the mean value at various harmonic stages for a LUX cascade initiated with pure phase/amplitude noise on the external seed laser.

(1) For the first two stages, slippage acts as a low-pass filter and suppresses overall noise growth.

(2) Eventually, phase noise components with small frequency offsets from ω_0 (*i.e.* with longitudinal scale lengths $\geq c\tau_{slip} \gg \lambda_0$) dominate and together with their M^1 growth scaling. The slope on the log-log plot in Fig. 4 for $M \geq 10$ is ≈ 1.0 as expected.

(3) For our low-gain, high input power design, broad-band noise distributed purely in amplitude is much less important than that distributed purely in phase. In the initial cascade stages, amplitude noise partially converts to phase noise which then becomes dominant and with the expected power law scaling in the later stages.

We also examined the evolution of shot noise in the harmonic cascade. Due to the "fresh-beam" design and to slippage effects in the first two stages, the noise level remains small and is only of order 10 kW in the final 1-nm stage, less than one-thousandth the coherent output signal. Consequently, despite the 240× increase in harmonic number, noise growth in this design may not significantly degrade output coherence down to wavelengths as short as 1 nm.

SHORT PULSE EVOLUTION

Some user applications may require output radiation pulse durations much shorter than the nominal ≈ 200 fs adopted in our sample design. For a *high gain* FEL cascade initiated with a Gaussian temporal profile, Saldin *et al.* [7] have predicted that the rms radiation pulse duration will tend to shrink by a factor $\sqrt{M}$ from one stage to the next. However, as shown in Fig. 1, our high power, low gain design is less sensitive to input power variations and one expects less shrinkage. Moreover, in the extreme limit where the radiation pulse duration is quite short, one expects that slippage effects will place a lower limit on the output pulse duration from each stage. To study these phenomena, we initiated a LUX cascade with a Gaussian pulse with $\sigma_t = 5$ fs (11.2-fs FWHM) and examined the downstream $P(t)$. The GINGER simulations were done in full time-dependent mode and included shot noise effects. In
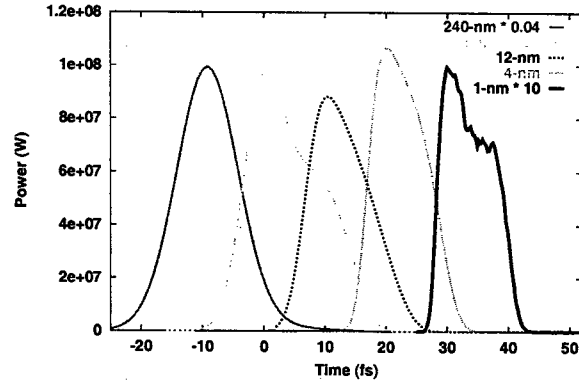
Figure 5: Predicted $P(t)$ profiles at different stages for a LUX cascade initiated with a Gaussian profile pulse with a 5-fs RMS duration. Each curve has been scaled by the indicated factor to fit on the plot.

order to obtain sufficient energy modulation in the first stage, the peak input power was increased to 2.5 GW from the nominal time-steady value of 1.0 GW. Figure 5 shows the output power profiles from each radiator stage. The FWHM temporal duration first increases to ≈ 15 fs at 48 nm, presumably because $\tau_{slip} = 24$ fs, but then shrinks back to a nearly constant ≈ 11 fs in the next 3 stages, in strong contrast to the scaling observed in [7]. Since the slippage is less than 3 fs in the 4- and 1-nm stages, the lack of additional pulse shrinkage must be due to high power effects. Some noise modulation appears on the 1-nm output $P(t)$ but it remains nearly completely temporally coherent.

SUMMARY

Our preliminary simulation results show that a XUV/soft x-ray FEL built upon the principle of a harmonic cascade will greatly enhance the proposed LBL LUX facility by providing coherent radiation in the ≤ 1 keV energy range. Future studies, which will include additional realistic effects such as undulator errors, electron beam transport optics, *etc.*, can help further determine the reality of the promise of a multi-stage harmonic cascade for LUX.

REFERENCES

[1] J.N. Corlett *et al.* , "A Recirculating Linac-Based Facility for Ultrafast X-ray Science", this conference.

[2] L.H. Yu, *Phys. Rev. A*, **44**, 5178 (1991).

[3] R. Bonifacio *et al.*, *Nucl. Inst. Meth. A*, **296**, 787 (1990).

[4] L.H. Yu *et al.* , "First Ultraviolet High Gain Harmonic-Generation Free Electron Laser", BNL-71203-2003-JA, submitted to *Phys. Rev. Let.* (2003).

[5] I. Ben-Zvi, K. M. Yang, and L. H. Yu, *Nucl. Inst. Meth. A*, **318**, 726 (1992).

[6] L.H. Yu and J. Wu, *Nucl. Inst. Meth. A*, **483**, 493 (2002).

[7] E.L. Saldin, E.A. Schneidmiller, and M.V. Yurkov, *Opt. Comm.*, **202**, 169 (2002).

[8] W.M. Fawley, *A User Manual for GINGER and Its Post-Processor XPLOTGIN*, LBNL-49625 (2002).

LIMITATIONS OF ELECTRON BEAM CONDITIONING FOR FREE-ELECTRON LASERS

P. Emma and G. Stupakov
Stanford Linear Accelerator Center,
Stanford University, Stanford, CA 94309

INTRODUCTION

The most demanding requirement for future FELs in the x-ray regime [2, 3] is the generation of a sufficiently small transverse electron emittance. To mitigate this problem, ideas have been proposed to 'condition' an electron beam by increasing each particle's energy in proportion to the square of its betatron amplitude [1, 4]. This conditioning enhances FEL gain by reducing the axial velocity spread within the electron bunch. We present a new conditioning scheme using solenoid magnets, which looks promising. But a strong head-tail focusing variation arises, as in [1]. We quantify the resulting 'projected' (bunch-length integrated) emittance growth, relating it directly to the FEL parameters. We then present a general symplectic beam conditioner and show the unavoidable relation between conditioning and projected transverse emittance growth.

FEL BEAM CONDITIONING

Electron beam conditioning, as proposed in [1], increases each particle's energy in proportion to the square of its betatron amplitude. A particle with high energy travels a shorter path in an undulator (increased mean axial velocity), while a large betatron amplitude delays a particle by lengthening its path through the undulator [5]. The conditioning correlation establishes a cancellation of these two effects, resulting in a reduction of the axial velocity spread, enhancing the FEL gain. The energy conditioning requirement, for natural undulator focusing, can be written as [1]

$$\delta_u = \delta_n + \frac{1}{4\gamma_u} \frac{\epsilon_N}{\beta_u} \frac{\lambda_u}{\lambda_r} r^2, \qquad (1)$$

where $\delta_n (\ll \delta_u)$ is the non-conditioned component of the particle's relative energy deviation, γ_u is the electron energy in the undulator (in units of rest mass), $\epsilon_N (= \gamma_u \epsilon)$ is the normalized rms transverse emittance (equal in x and y), $\beta_u (= \beta_x = \beta_y)$ is the constant beta-function in the undulator, λ_u is the undulator period, λ_r is the FEL radiation wavelength, and r is the invariant normalized 4D betatron amplitude of the particle,

$$r^2 \equiv \frac{x^2 + (\beta_u x')^2 + y^2 + (\beta_u y')^2}{\beta_u \epsilon}. \qquad (2)$$

The betatron amplitude, r, is expressed in terms of a particle's transverse positions, x and y, and angles, x' and y', with natural focusing where $\alpha_x = \alpha_y = 0$. A conditioner beamline is designed to imprint this $\delta_u \sim r^2$ correlation within the electron bunch, with coefficient given in Eq. (1).

In a general case, the conditioning might be performed at low energy where the bunch is still relatively long. For short wavelength FELs, the bunch is compressed and accelerated after the injector. Both effects scale the conditioning, but in the absence of mixing, do not alter its correlation. Acceleration from γ_0 to γ_u ('energy' in undulator) reduces the conditioned relative energy spread, while compression from an initial bunch-length, σ_{z_0}, to a shorter final bunch-length, σ_{z_f}, amplifies the conditioning. The relative energy deviation, δ, at the location of the conditioner, before acceleration and compression, must then be scaled by the acceleration and compression factors:

$$\delta = \frac{\sigma_{z_f}}{\sigma_{z_0}} \frac{\gamma_u}{\gamma_0} \left(\delta_n + \frac{1}{4\gamma_u} \frac{\epsilon_N}{\beta_u} \frac{\lambda_u}{\lambda_r} r^2 \right). \qquad (3)$$

A ONE-PHASE SOLENOID CONDITIONER

As an example conditioner, and to show the limitations of conditioners, we describe here a simplified system composed of a solenoid magnet and RF accelerating sections. The conditioner is composed of a solenoid magnet sandwiched between two RF accelerating sections operated at opposing zero-crossing phases. (A similar idea was proposed at the end of reference [4].) The first RF section 'chirps' the energy along the bunch, and the final section removes the chirp. The conditioning is generated in the solenoid by the delay of particles with large amplitudes in x and y. The solenoid strength is set to produce a +I linear transfer matrix in 6D with the relation $|k|L = n\pi$ $(n = 1, 2, 3, ...)$, where $k \equiv \frac{1}{2}B_z/(B\rho)$, L is the solenoid length, B_z is its axial magnetic field, and $(B\rho)$ is the standard magnetic rigidity $(= p_0/e)$. The particle coordinates within the bunch at the entrance to the system are $(x_0, x_0', y_0, y_0', z_0, \delta_0)$, where $\delta_0 \equiv \Delta p/p_0$, and we assume these variables are initially uncorrelated and have zero mean. For simplicity, we use a cylindrically symmetric beam with initial Twiss parameters: $\beta_x = \beta_y = \beta$, and $\alpha_x = \alpha_y = 0$. The Twiss parameters are unchanged, to 1st-order, across the solenoid and across each 'thin' RF section. The electrons are assumed to be ultra-relativistic.

The first RF section changes the relative energy deviation of a particle to: $\delta_1 = \delta_0 + h_1 z_0$, where h_1 is the linear RF-induced slope $(h \equiv d\delta/dz)$. For simplicity, the RF sections are treated as thin elements which do not alter the transverse coordinates. After the solenoid, the coordinates are unchanged to 1st-order, but a chromatic 2nd-order aberration is added to the angles with $\Delta x' =$

$2T_{216}x_0(\delta_0 + h_1 z_0)$ and $\Delta y' = 2T_{436}y_0(\delta_0 + h_1 z_0)$. All other 2nd-order transverse aberrations are small in comparison for the case: $|k|\beta \gg 1$, $|k|L = n\pi$ [6].

The energy is not changed in the solenoid, but the particle is delayed by the helical trajectory according to $z_1 = z_0 + T_{511}x_0^2 + T_{533}y_0^2$ (bunch head at $z > 0$). Similarly, all other 2nd-order longitudinal aberrations are small for the case $|k|\beta \gg 1$. The 2nd-order coefficients of a solenoid with $|k|L = n\pi$ are related to each other by: $T_{511} = T_{533} = -T_{216} = -T_{436} = -k^2 L/2$ [6], which, as shown in section , is an unavoidable connection for symplectic systems. The final RF section, h_2, changes the energy according to $\delta = \delta_1 + h_2 z_1 \approx (h_1 + h_2)z_0 - \frac{1}{2}k^2 L h_2(x_0^2 + y_0^2)$. The second chirp is chosen equal and opposite to the first, $h_1 = -h_2 \equiv h$, and the final coordinate map across the conditioner, to second order and for $|\delta_0| \ll |hz_0|$, becomes

$$
\begin{aligned}
x &= x_0, \qquad x' = x_0' + k^2 L h z_0 x_0, \\
z &= z_0 - \frac{1}{2}k^2 L(x_0^2 + y_0^2), \\
\delta &= \delta_0 + \frac{1}{2}k^2 L h(x_0^2 + y_0^2),
\end{aligned} \tag{4}
$$

with similar relations in y and y'. The final energy deviation, δ, is clearly conditioned (for $h > 0$) in both planes but in only one betatron phase (i.e., x_0, but not x_0'). This system provides spatial (but not angular) conditioning described by

$$
\delta = \delta_0 + \frac{1}{2}k^2 L h \beta \epsilon_0 r^2, \qquad r^2 \equiv \frac{x_0^2 + y_0^2}{\beta \epsilon_0}. \tag{5}
$$

Two solenoids can also be used, separated by a $\pi/2$-transformer to condition both betatron phases, but here we simplify the description by considering only a one-phase conditioner.

The bunch-length coordinate, z, in Eqs. (4) also includes a non-linear distortion due to the solenoid delay of large amplitude particles. This can easily be removed, without changing the energy conditioning, by adding a four-dipole chicane with $R_{56} = 1/h > 0$, after the final RF section.

ENERGY CONDITIONING AND TRANSVERSE EMITTANCE GROWTH

The conditioning coefficient in Eq. (3) can be equated to that in Eq. (5) producing the conditioning requirement for the solenoid system

$$
k^2 L h \beta \sigma_{z_0} = \frac{1}{2}\frac{\lambda_u}{\lambda_r}\frac{\sigma_{z_f}}{\beta_u} \equiv a, \tag{6}
$$

where the solenoid-conditioner parameters are on the left side and the FEL parameters are on the right, and here we define the dimensionless conditioning coefficient, a. In the typical case of a short wavelength FEL, the conditioning parameter a is large, $a \gg 1$, (see table below).

The chirp parameter, h, is related it to the rms relative energy spread in the solenoids by: $\sigma_{\delta_1} \approx |h|\sigma_{z_0}$, showing

Table 1: FEL parameters for LCLS [2] and VISA [7].

parameter	sym	LCLS	VISA	unit
und. energy/mc^2	γ_u	28000	140	
undulator period	λ_u	3	1.8	cm
rad. wavelength	λ_r	1.5	8500	Å
und. $\beta_{x,y}$	β_u	72	0.6	m
und. bunch length	σ_{z_f}	24	100	μm
conditioning coef	a	33	1.8	

the transverse aberrations in Eqs. (4) as chromatic ($\delta_1 \approx h z_0$), which we now quantify as an projected transverse emittance growth. The rms emittance after the solenoid is

$$
\epsilon_x^2 = \langle(x - \overline{x})^2\rangle\langle(x' - \overline{x'})^2\rangle - \langle(x - \overline{x})(x' - \overline{x'})\rangle^2. \tag{7}
$$

The mean values, $\overline{x} = \langle x\rangle$, and $\overline{x'} = \langle x'\rangle$ are zero since the initial coordinates are uncorrelated and have zero mean. The correlation $\langle xx'\rangle$ is zero for the same reasons, so the x-emittance after the solenoid is:

$$
\epsilon_x^2 = \langle x^2\rangle\langle x'^2\rangle \approx \epsilon_{x0}^2[1 + (k^2 L h \beta \sigma_{z_0})^2], \tag{8}
$$

where $\epsilon_{x0} = \langle x_0^2\rangle/\beta = \langle x_0'^2\rangle\beta$, and $\sigma_{z_0}^2 = \langle z_0^2\rangle$, with a similar form in y. The relative emittance growth after the solenoid is

$$
\frac{\epsilon_x}{\epsilon_{x0}} \approx k^2 L h \beta \sigma_{z_0} = a \gg 1, \tag{9}
$$

which is identical to the conditioning relation in Eq. (6), providing a direct connection between transverse emittance growth and FEL conditioning requirements.

For parameters of the LCLS [2] shown in Table 1 (using a beta function for natural focusing, to be consistent with Eq. 1), the relative emittance growth is extremely large at $\epsilon_x/\epsilon_{x0} \approx 33$. The parameters for the VISA FEL [7] are also included showing that conditioning may still be possible at longer wavelengths. This growth is actually an increase of the 'projected' transverse emittance integrated over the bunch length. The second line of Eq. (4) shows that the bunch head ($z_0 > 0$) is de-focused (equating: $k^2 L h z_0 = 1/f$), while the bunch tail ($z_0 < 0$) is focused.

With a chirped energy spread, the chromatic effects of the solenoid are equivalent to the effects of an RF-quadrupole (RFQ). It is interesting to compare this result with that of reference [1], where a completely different conditioner beamline, employing transverse RF cavities, produced an undesirable RFQ effect. In fact, as shown in the next section, FEL beam conditioning in a symplectic beamline always produces an undesirable RFQ-effect, which is extremely large for short wavelength FELs, as given in Eq. (9).

A GENERAL CONDITIONER

We will now show that the transverse emittance growth associated with conditioning is not related to the specific design outlined in the previous section, but is a general feature of any conditioner, and is due to the symplecticity of the map between the entrance to and exit from the

conditioner. To simplify consideration, we assume that the conditioner does not introduce coupling between the vertical and horizontal planes, and consider only the horizontal plane with the initial values of coordinates (x_0, x_0') at the entrance, and the final values (x, x') at the exit. Consideration of the vertical coordinates y, y' can be carried out analogously to x, x'. We will also assume that the initial and final values of the longitudinal coordinate are the same: $z = z_0$. Instead of using the variables x_0, x_0' and x, x', it is convenient and more general to introduce new variables u_0, v_0, and u, v, such that

$$\begin{pmatrix} u_0 \\ v_0 \end{pmatrix} = Q_0 \begin{pmatrix} x_0 \\ x_0' \end{pmatrix}, \quad \begin{pmatrix} u \\ v \end{pmatrix} = Q \begin{pmatrix} x \\ x' \end{pmatrix}, \quad (10)$$

where the matrices Q_0 and Q are

$$Q_0 = \frac{1}{\sqrt{\beta_0}} \begin{pmatrix} 1 & 0 \\ \alpha_0 & \beta_0 \end{pmatrix}, \quad Q = \frac{1}{\sqrt{\beta}} \begin{pmatrix} 1 & 0 \\ \alpha & \beta \end{pmatrix}, \quad (11)$$

with β_0, α_0 and β, α the Twiss parameters at the entrance and exit of the conditioner, respectively. Being symplectic linear transformations, Q and Q_0 conserve the symplecticity of the map from (u_0, v_0) to (u, v). Note, that in linear approximation this map has a form

$$\begin{pmatrix} u \\ v \end{pmatrix} = \begin{pmatrix} \cos\psi & \sin\psi \\ -\sin\psi & \cos\psi \end{pmatrix} \begin{pmatrix} u_0 \\ v_0 \end{pmatrix}, \quad (12)$$

with ψ the betatron phase advance across the conditioner. Also note that the contribution of the x-coordinate $x_0^2/(\beta\epsilon_0)$ to the parameter r in Eq. (5) is equal to u_0^2/ϵ_0, and the conditioning requirement Eq. (5) can be written as

$$\delta = \delta_0 + \frac{1}{2} b u_0^2, \quad (13)$$

where $b = a/\sigma_{z_0}$, and the conditioning constant a is given by Eq. (6).

To derive a general symplectic map which in linear approximation reduces to the linear map Eq. (12) and also includes the conditioning given by Eq. (13), we will use a method of generating functions [8]. We choose a generating function which depends on initial coordinates u_0 and z_0 and final momenta v and δ, $F(u_0, z_0, v, \delta)$. The map is defined by the relations

$$v_0 = \frac{\partial F}{\partial u_0}, \quad \delta_0 = \frac{\partial F}{\partial z_0}, \quad u = \frac{\partial F}{\partial v}, \quad z = \frac{\partial F}{\partial \delta}. \quad (14)$$

In paraxial approximation all coordinates and momenta are considered small and we can expand F in a Taylor series. The linear terms in this expansion vanish because zero initial coordinates and momenta map to zero final ones. The expansion begins from the second order terms $F \approx F_2 + F_3 + \dots$, where F_2 is a quadratic, and F_3 is a cubic function of the coordinates and momenta. The function F_2 should generate the linear map Eq. (12) for u and v with a unit transformation for z and δ—a direct calculation shows that

$$F_2 = \frac{1}{2}(u_0^2 + v^2) \tan\psi + u_0 v \sec\psi + \delta z_0. \quad (15)$$

The function F_3 generates 2$^{\text{nd}}$-order abberations in the system, out of which we choose only a term responsible for the conditioning:

$$F_3 = -\frac{1}{2} b z_0 u_0^2. \quad (16)$$

Indeed, using the second of Eqs. (14) with Eqs. (15) and (16) we find $\delta_0 = \delta - \frac{1}{2} b u_0^2$, in agreement with Eq. (13). At the same time the first and the third of Eqs. (14) yield $v_0 = u_0 \tan\psi + v \sec\psi - b z_0 u_0$, $u = v \tan\psi + u_0 \sec\psi$. These equations can be easily solved for u and v:

$$\begin{aligned} u &= u_0 \cos\psi + v_0 \sin\psi + b z_0 u_0 \sin\psi, \\ v &= -u_0 \sin\psi + v_0 \cos\psi + b z_0 u_0 \cos\psi. \end{aligned} \quad (17)$$

We emphasize here that the same term in the symplectic map Eq. (16) that is responsible for the conditioning of the beam also introduces in Eq. (17) the transverse deflection that varies along the bunch. This also means that adding a system that 'fixes' this deflection downstream of the conditioner would inevitably remove the conditioning itself.

To calculate the emittance increase of the beam due to the conditioning we use Eq. (7) for the emittance, with $\bar{u} = \bar{v} = 0$, we find $\epsilon_x^2 = \langle u^2 \rangle \langle v^2 \rangle - \langle uv \rangle^2$. Substituting the map, Eqs. (17), into this yields

$$\epsilon_x^2 = \epsilon_{x0}^2 (1 + b^2 \sigma_{z_0}^2) = \epsilon_{x0}^2 (1 + a^2), \quad (18)$$

in agreement with Eq. (8), but now in a general case with arbitrary phase advance, ψ, and non-zero initial alpha function, α_0. For the specific conditioner described above, we have $\psi = 2n\pi$, $\beta_0 = \beta$, $\alpha_0 = \alpha = 0$, and Eqs. (17) reproduce the first two of Eqs. (4).

CONCLUSIONS

We have demonstrated for a general one-phase conditioner that a strong head-tail focusing variation always accompanies the energy conditioning correlation, and that this focusing variation is set solely by the FEL parameters, and not the conditioner. A two-phase conditioner is more complicated, but does not qualitatively change the arguments presented here.

REFERENCES

[1] A. Sessler et al., Phys. Rev. Lett., 68, 309 (1992).

[2] LCLS CDR, SLAC Report No. SLAC-R-593, 2002.

[3] TESLA TDR, DESY Report No. DESY-2001-011, 2001.

[4] N. A. Vinokurov, Nucl. Inst. and Meth. A 375 (1996) 264.

[5] S. Reiche, Nucl. Inst. and Meth. A 445 (2000) 90.

[6] F. C. Iselin, The MAD Program Ver. 8.13, Physical Methods Manual (1994), p. 29.

[7] A. Tremaine et al., in Proc. of the PAC'01, Chicago, IL (IEEE, Piscataway, NJ, 2001), p. 2760.

[8] H. Goldstein, Classical Mechanics, (Addison-Wesley, London, 1980).

THROUGHPUT AND NOISE OF THE ALADDIN INFRARED BEAMLINE*

R. A. Bosch,[#] R. L. Julian, R. W. C. Hansen, M. A. Green, K. J. Kleman and K. D. Jacobs,
Synchrotron Radiation Center, University of Wisconsin-Madison,
3731 Schneider Dr., Stoughton, WI 53589, USA

Abstract

The infrared beamline at the Aladdin electron storage ring utilizes edge radiation for spectromicroscopy. For wavelengths of 0.8–16 μm, computations indicate that ~20% of the collected radiation is transported through the microscope. Transverse oscillations of the electron beam cause oscillations in microscope throughput that account for about one-third of the beamline's zero-burst noise.

1 BEAMLINE THROUGHPUT

The Aladdin infrared (IR) microspectroscopy beamline [1] transmits and detects radiation at wavelengths of 0.8–16 μm. The lower end of this range is determined by transmission of a KBr beam splitter substrate, while the upper end results from the detector response. To study its performance with our low-emittance electron beam [2], we model our beamline with the SRW code [3]. We neglect flat mirrors and treat focusing mirrors as ideal thin lenses, as shown in Fig. 1. The source is edge radiation from a 200 mA, 800 MeV electron beam traversing a straight section of length $L = 3$ m, terminated by 1.28 T bending magnets. The bending magnet fringe field length is 108 mm, while the entrance aperture is at distance $R = 1.5$ m from the edge-radiation source at the downstream end of the straight section. For our beamline, a 1-μm source translation causes a 3.1-μm translation and 6.6-μrad deflection of the photon beam at the microscope entrance.

In transmission mode, the microscope is expected to admit and focus an annulus of collimated radiation with outer diameter of 7 mm and inner diameter of 3.5 mm. In our model, we assume that all radiation admitted by the microscope is transmitted through it.

The SRW code computes emittance effects for an electron beam that undergoes no focusing. Since the Aladdin 3-m straight section contains two quadrupole magnets near its midpoint, an approximate description is necessary. One approach is to consider an electron beam with constant size $(\sigma_x, \sigma_y) = (200$ μm, 100 μm$)$. This method approximately describes the low-emittance beam size throughout the straight section, while neglecting its divergence, which is smaller than the IR-radiation opening angle. Another approach is to specify the lattice functions at the downstream end of the straight section to model the beam size and divergence downstream of the quadrupoles, while misrepresenting the upstream half of the straight section. We obtained similar results with both approaches, and show modeling of a constant beam size.

Figure 2 displays flux computations at wavelengths λ of 1 and 10 μm. At the entrance aperture, a flux of 2–3×10^{13} photons/s-0.1% bandwidth is obtained for wavelengths of 0.8–16 μm. Wavelengths exceeding ~1 μm form an asymmetric hollow ring with radius of $\sim [\lambda R(R+L)/L]^{1/2}$. At the microscope entrance, the collimated photon beam forms an asymmetric hollow ring with radius of $\sim (\lambda D)^{1/2}$, where $D = 6$ m is the length of the collimated photon beam. These radii equal the diffraction-limited sizes of near-field edge radiation and a collimated photon beam.

In contrast, SRW modeling of a source of ordinary synchrotron radiation (located 1.5 m from the entrance aperture) shows radiation bands at the top and bottom of the entrance aperture, and a 30 mm × 20 mm rectangle of collimated radiation at the microscope. While radiation from an edge-radiation source is transported to the microscope quite effectively at wavelengths of 0.8–16 μm, the beamline greatly overfills the microscope when used with ordinary synchrotron radiation.

At a representative wavelength of 3 μm, edge radiation provides 77% more flux into the entrance aperture than synchrotron radiation. When best aligned for λ = 3 μm, the microscope admits 20% of the edge radiation incident upon the entrance aperture, but only 5% of the ordinary synchrotron radiation. For our beamline, edge radiation is computed to increase the 3-μm flux through the microscope by a factor of seven.

By computing the flux distribution for several wavelengths, the distribution of power in the wavelength range of 0.8–16 μm was computed at the microscope entrance plane. Figure 3(a) shows the power admitted by the microscope versus photon beam position (i.e., optical axis position with respect to the microscope). In the wavelength range of 0.8–16 μm, the power collected by the entrance aperture is 5.7 mW. When best aligned, the microscope admits 18% of this collected power. In
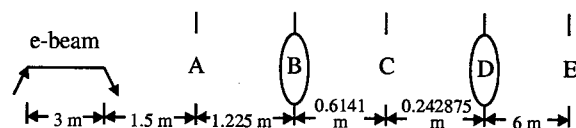
Figure 1. The IR source is a 3-m straight section of the electron storage ring. Beamline components are:
A. Entrance aperture, 30.5 mm hor. × 22.3 mm vert.
B. Focusing lens, focal length = 459 mm, diameter = 76.2 mm.
C. Diamond window, diameter = 10 mm.
D. Collimating lens, focal length = 305 mm, diameter = 50.8 mm.
E. Entrance of the IR microscope.

contrast, the microscope admits only ~5% of the collected power in this wavelength range from a source of ordinary synchrotron radiation.

For a given photon beam position, dividing the slope in Fig. 3(a) by the admitted power gives the relative sensitivity to a horizontal change in photon-beam position. For photon-beam positions of −0.7, −1.4, or −3.6 mm, the slope is zero, giving "optimal" horizontal alignment in which the admitted power is insensitive to a small horizontal motion of the photon beam.
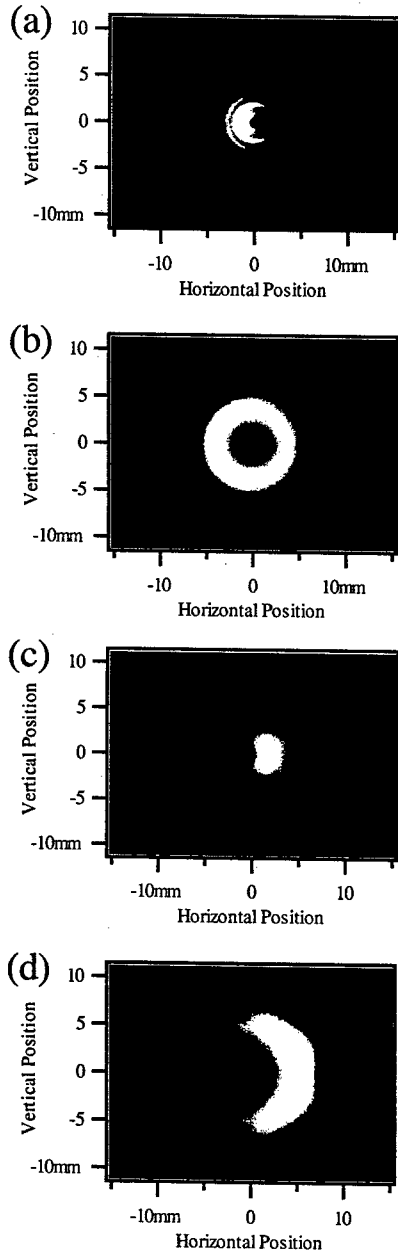
Figure 2. Infrared edge radiation modeled by SRW.

(a) $\lambda = 1$ µm at the entrance aperture.

(b) $\lambda = 10$ µm at the entrance aperture.

(c) $\lambda = 1$ µm at the entrance of the microscope.

(d) $\lambda = 10$ µm at the entrance of the microscope.

When the microscope is operated in reflection mode, it is expected to admit radiation in the upper half of the annulus admitted by transmission mode. For an optimal horizontal photon beam position of −3.6 mm, Fig. 3(b) shows the computed power in transmission and reflection modes. With optimal vertical alignment for transmission mode, the reflection-mode sensitivity to a vertical photon beam motion is 0.013%/µm. When using a single alignment for both modes, one mode is computed to have a vertical sensitivity of 0.01–0.02%/µm.

Experimentally, we maximized the zero-burst signal (which measures power through the microscope) by translating the electron beam from its standard position by −540 um horizontally and −190 µm vertically. The associated change in photon beam position is −1.7 mm horizontal and −0.6 mm vertical. The zero burst increased 15%, while the flux increased by > 8% for wavelengths of 0.8–16 µm. Figure 4 shows the zero-burst signal as the electron beam was translated. The difference between Figs. 3 and 4 may result from the wavelength dependence of optical elements and detector, uncertainty in the photon beam position, lens aberrations, and additional apertures.

2 IR BEAMLINE NOISE

The Aladdin IR beamline is adversely affected by motion of the electron beam at audio frequencies [4]. The
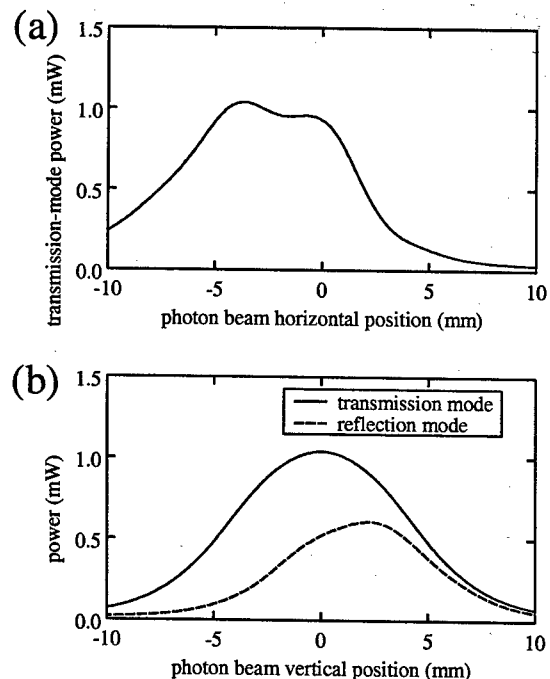
Figure 3. Computation of power admitted by the microscope for wavelengths of 0.8–16 µm.

(a) Transmission-mode power versus horizontal photon beam position, where the vertical photon beam position equals zero.

(b) Transmission-mode and reflection-mode power versus vertical photon beam position, where the horizontal photon beam position equals −3.6 mm.

zero-burst signal variation is in the range of 0.15–0.25% rms. A portion of this variation may be caused by transverse motion of the electron beam.

The transverse electron motion is dominated by a 60-Hz oscillation in which the horizontal and vertical positions vary by ~1 µm rms; the oscillation of the beam's direction of propagation is unknown. The motion is comparable in horizontal and vertical directions, in non-equivalent bending magnets, and with high- and low-emittance beams. This suggests that a large portion of the 60-Hz oscillation is caused by the electromagnetic field of ripple current penetrating the vacuum chamber [5].

For the standard electron beam position, the horizontal sensitivity to photon beam motion from Fig. 4 is ~0.01%/µm and the vertical sensitivity is ~0.02%/µm. Electron-beam oscillations of ~1 µm rms are expected to cause photon-beam oscillations of ~3.1 µm rms, causing a zero-burst variation of ~0.06% rms, about one-third of its measured value. Translating the electron beam to maximize the zero-burst signal (giving optimal alignment) reduced the zero-burst variation by 23%.

A subsequent realignment of the microscope and interferometer increased the zero-burst signal in transmission mode by 20% while achieving a reflection-mode signal equal to one-half of that in transmission mode. With this alignment, the transmission mode signal was 20% below the maximum achievable. According to Fig. 4(b), the transmission-mode sensitivity to a vertical photon beam translation is ~0.03%/µm when the zero

burst is 20% below maximum. The expected zero-burst variation caused by transverse motion of the electron beam is ~0.09% rms, about 50% larger than before the realignment. Consistent with this expectation, the realignment increased the zero-burst variation by 21% in transmission mode. This zero-burst variation is 60% larger than that observed when the electron beam was translated to achieve optimal transmission-mode alignment, suggesting that about one-third of the zero-burst noise arises from transverse electron-beam motion. Oscillations of the electron-beam size and longitudinal bunch positions, as well as detector background, may also contribute to the zero-burst noise.

At frequencies >> 100 Hz, beam motion is primarily driven by radiofrequency (RF) system noise [5]. For these frequencies, the noise spectrum of a detector on the IR beamline is similar to that of the electron beam's longitudinal phase, peaking at the 3–4 kHz frequencies of Robinson modes [6]. We have recently installed a crystal master oscillator from Wenzel Associates and improved the common-mode rejection and high frequency filtering of the RF system. This has reduced RF noise by 20–30 dB. Noise at frequencies around 3 kHz has been reduced an additional 20 dB by feedback that damps oscillations of the bunch centroids [6]. These reductions of RF noise greatly improve the IR beamline performance, but have only a small effect on the zero-burst signal variation. This indicates the limitation in using the zero-burst signal variation to characterize the beamline's performance.

3 SUMMARY

For wavelengths of 0.8–16 µm, SRW computations indicate that ~20% of the collected edge radiation is transported through the microscope. Experiments and modeling suggest that about one-third of the IR zero-burst noise in transmission mode is caused by 60-Hz transverse oscillations of the electron beam. Since a single microscope alignment is used for both transmission and reflection modes, this noise was not reduced by realignment. Modifications to the RF system have reduced noise in the 1–6 kHz range by 20–40 dB, greatly improving IR beamline performance.

Figure 4. Zero-burst voltage in transmission mode as the photon beam is scanned (a) horizontally and (b) vertically through the position of maximum zero burst. For the standard electron beam position, the photon beam is at (0, 0).

REFERENCES

[1] T. E. May, R. A. Bosch and R. L. Julian, in *Proc. 1999 PAC* (IEEE, Piscataway, NJ, 1999), p. 2394.

[2] J. J. Bisognano, R. A. Bosch, D. E. Eisert, M. A. Green, K. J. Kleman and W. S. Trzeciak, in *Proc. 2001 PAC* (IEEE, Piscataway, NJ, 2001), p. 2671.

[3] O. Chubar and P. Elleaume, in *Proc. Sixth European PAC* (IOP, Bristol, 1998), p. 1177.

[4] R. A. Bosch and R. L. Julian, Rev. Sci. Instrum. **73**, 1420 (2002).

[5] R. Biscardi, G. Ramirez, G. P. Williams and C. Zimba, Rev. Sci. Instrum. **66**, 1856 (1995).

[6] R. A. Bosch, K. J. Kleman and J. J. Bisognano, "Robinson modes at Aladdin," these proceedings.

PERIODIC ION CHANNEL LASER*

R. A. Bosch,[#] Synchrotron Radiation Center, University of Wisconsin-Madison,
3731 Schneider Dr., Stoughton, WI 53589, USA

Abstract

Radially polarized radiation is amplified by a free electron laser (FEL) in which the undulator is an ion channel with periodic density. To ensure stable beam propagation, the undulator period is much shorter than the betatron wavelength. The gain at a given distance from the axis equals that of a planar magnetostatic undulator with the same quiver velocity. When an ultrarelativistic electron beam propagates in a periodic ion density of 10^{11}–10^{17} cm^{-3}, a short-wavelength FEL may be obtained.

1 INTRODUCTION

When a round electron beam propagates in an ion channel whose density varies periodically [1], the electrons undergo forced radial oscillations in addition to damped betatron oscillations [2]. A periodic ion channel undulator may be created by ionizing a periodic gas density [1] or by using a modulated ion beam [2, 3], and may have application as an FEL [4].

A periodic ion channel FEL is similar to a non-periodic ion channel laser [5, 6] in that no magnetic field is required, while benefiting from forced transverse oscillations similar to those in a magnetostatic undulator FEL with ion channel guiding [7, 8, 9]. In contrast to an ion ripple laser where oblique propagation through a periodic ion density causes a periodic beam deflection [10], we consider propagation in the direction of the periodic density gradient. In this case, lasing results from periodic focusing rather than a periodic beam deflection.

We calculate amplification of a radially polarized wave by a periodic ion channel FEL for a cold beam in the low-gain-per-pass limit. To ensure stable beam propagation, we consider the case where the undulator period is much shorter than the betatron wavelength [2,11].

2 RADIAL MOTION

To model "force" bunching [6], radiation is included in the transverse dynamics. We consider an undulator, in which an electron's velocity deviates by less than the angle $1/\beta\gamma$ from the axis, where γ is the beam's relativistic factor and $\beta > 0$ is the beam velocity divided by the speed of light c. In an undulator, the electron motion is non-relativistic in the frame of reference moving with the beam as it enters the undulator, so we calculate the dynamics in this frame, which is related to the laboratory frame by $\gamma_\parallel$ and $\beta_\parallel$.

Consider a periodic ion channel undulator with entrance at $z_{lab} = 0$, whose density is given in the laboratory frame (i.e., the frame where ions are stationary) for $z_{lab} > 0$ by

$$n_{i-lab}(r, z_{lab}) = n_{0-lab}(r) + n_{1-lab}(r)\cos(k_{w-lab}z_{lab}), \quad (1)$$

where z_{lab} and r are axial and radial coordinates, while $k_{w-lab} > 0$ is the undulator wave number equaling 2π divided by the undulator period λ_{w-lab}. When the undulator period greatly exceeds the beam radius, the ions' electric field in the laboratory is mostly radial [1], given by Gauss's law in SI units as $(-e/2\pi r\varepsilon_0)\int_0^r n_{i-lab}(r', z_{lab})2\pi r'dr'$, where $e < 0$ is the electron charge and ε_0 is the permittivity of free space. In the frame moving with the beam's axial velocity as it enters the undulator, the radial electric field from the ion channel is increased by the factor $\gamma_\parallel$ [12], giving [2]

$$E_w(r, z, t) = (-e/2\pi r\varepsilon_0)$$
$$\times \left[\int_0^r n_0(r')2\pi r'dr' + \int_0^r n_1(r')2\pi r'dr'\cos(k_w z + \omega_w t)\right]. \quad (2)$$

Here, z is the axial coordinate, $n_0(r) = \gamma_\parallel n_{0-lab}(r)$, $n_1(r) = \gamma_\parallel n_{1-lab}(r)$, $k_w = \gamma_\parallel k_{w-lab}$ and $\omega_w = \gamma_\parallel \beta_\parallel c k_{w-lab}$. The magnetic field in the e-beam frame is in the azimuthal (ϕ) direction, with ϕ-component $B_w = -\beta_\parallel E_w/c$. The axial electric field in the beam frame equals that in the laboratory; it is therefore negligible for $\gamma_\parallel \gg 1$.

For a radially polarized wave traveling forward, the radial electric field in the low-gain-per-pass limit is

$$E_r(r, z, t) = E_0(r)\cos(k_r z - \omega_r t + \phi_r) \quad (3)$$

The azimuthal magnetic field B_r equals E_r/c, with wave number $k_r > 0$, phase ϕ_r, and frequency $\omega_r = ck_r > 0$.

The radial electron motion consists of forced oscillations from the undulator and radiation E-fields, in addition to damped betatron oscillations from mismatched injection [2]. For brevity, we will suppress the dependence of functions upon r in our notation. In the case where the undulator period is short compared to the betatron wavelength [$\omega_w \gg \omega_\beta = (n_0 e^2/\varepsilon_0 m)^{1/2}$, where m is the electron mass], we consider a small injection mismatch so that betatron oscillations are negligible. The radial velocity of an electron at radius r with constant axial velocity $\ll c$ is the sum of an undulation with quiver velocity [2]

$$v_w(z, t) = -\hat{a}_w c\sin(k_w z + \omega_w t), \quad (4)$$

and a forced oscillation from the radiation

$$v_r(z, t) = a_r c\sin(k_r z - \omega_r t + \phi_r). \quad (5)$$

Here, $\hat{a}_w$ obeys

$$\hat{a}_w = \frac{e^2\langle n_1\rangle r}{2\varepsilon_0 m\omega_w c} = \frac{e^2\langle n_{1-lab}\rangle r}{2\varepsilon_0 m\beta_\parallel c^2 k_{w-lab}} \quad (6)$$

with $\langle n_1\rangle \equiv (1/\pi r^2)\int_0^r n_1(r')2\pi r'dr'$ (and similarly for $< n_{1-lab}>$), while $a_r = -eE_0/mc\omega_r$. Since $k_w = \omega_w/\beta_\parallel c$ in eq. (4), the undulation wavelength in the laboratory is independent of the electron's axial velocity.

Any axial velocity function may be approximated to arbitrary accuracy by constant-velocity segments, so that eqs. (4)–(6) also apply when the axial velocity is not constant. Since $v_w = 0$ at the undulator entrance, a matched beam has $\beta = \beta_\parallel$ and $\gamma = \gamma_\parallel$. Our assumption of nonrelativistic electron velocities in the beam frame requires $\hat{a}_w \ll 1$.

3 AXIAL MOTION

To describe "inertial" bunching, radiation is included in the axial dynamics [6]. An electron whose initial axial position z is 0 and radius is r obeys, to lowest order in the radiation field

$$\frac{d^2 z}{dt^2} = \frac{e}{m} v_w B_w + \frac{e}{m} v_w B_r + \frac{e}{m} v_r B_w, \qquad (7)$$

where radius $= r$ on the right hand side (RHS). The solution with initial conditions $z(0) = dz/dt(0) = 0$ is the sum of three functions describing radiation-independent axial motion, inertial bunching, and force bunching. The radiation-independent motion obeys $d^2 z_0/dt^2 = (e/m)v_w B_w$ where $z \approx v_0 t$ on the RHS of the equation, with v_0 equaling the average axial velocity in the undulator. The solution with initial conditions $z_0(0) = dz_0/dt(0) = 0$ is

$$z_0(t) = \frac{e^2 \beta \hat{a}_w r}{2m\varepsilon_0 \hat{\omega}_w^2} \left[\begin{array}{c} \langle n_0 \rangle (\sin \hat{\omega}_w t - \hat{\omega}_w t) \\ + \frac{\langle n_1 \rangle}{8} (\sin 2\hat{\omega}_w t - 2\hat{\omega}_w t) \end{array} \right], \qquad (8)$$

where $\hat{\omega}_w \equiv \omega_w (1 + v_0/\beta c)$ is the undulator frequency experienced by an electron with axial velocity v_0. Equation (8) gives the average axial velocity as

$$v_0 \approx -\frac{\hat{a}_w^2 \beta c}{4} \left(1 + \frac{4\langle n_0 \rangle}{\langle n_1 \rangle} \right) \qquad (9)$$

The inertial bunching term [6] results from the axial radiation force on an electron, obeying $d^2 z_i/dt^2 = (e/m)v_w B_r$ where $z \approx z_0(t)$ on the RHS. For $\hat{a}_w \ll 1$, approximating $z_0(t) \approx v_0 t$ on the RHS for the fundamental FEL mode gives the solution with initial conditions $z_i(0) = dz_i/dt(0) = 0$:

$$z_i(t) = \frac{e\hat{a}_w E_0}{2m} \left[\begin{array}{c} \frac{\sin(\omega_+ t - \phi_r) + \sin \phi_r - \omega_+ t \cos \phi_r}{\omega_+^2} \\ + \frac{\sin(\omega_- t + \phi_r) - \sin \phi_r - \omega_- t \cos \phi_r}{\omega_-^2} \end{array} \right] \qquad (10)$$

where $\omega_+ \equiv \hat{\omega}_w + \hat{\omega}_r$ and $\omega_- \equiv \hat{\omega}_w - \hat{\omega}_r$, in which $\hat{\omega}_r \equiv \omega_r (1 - v_0/c)$ is the radiation frequency experienced by an electron with axial velocity v_0. Since the undulation wavelength in the laboratory is independent of the electron's axial velocity, the inertial bunching is also called "axial" bunching [6].

The force bunching term [6] results from the transverse radiation force on an electron, obeying $d^2 z_f/dt^2 = (e/m)v_r B_w$ where $z \approx z_0(t)$ on the RHS. For $\hat{a}_w \ll 1$, approximating $z_0(t) \approx v_0 t$ on the RHS for the fundamental FEL mode gives the solution with initial conditions $z_f(0) = dz_f/dt(0) = 0$:

$$z_f(t) = \frac{\beta e^2 a_r r}{4m\varepsilon_0} \left[\begin{array}{c} \frac{2\langle n_0 \rangle [\sin(\hat{\omega}_r t - \phi_r) + \sin \phi_r - \hat{\omega}_r t \cos \phi_r]}{\hat{\omega}_r^2} \\ + \frac{\langle n_1 \rangle [\sin(\omega_+ t - \phi_r) + \sin \phi_r - \omega_+ t \cos \phi_r]}{\omega_+^2} \\ - \frac{\langle n_1 \rangle [\sin(\omega_- t + \phi_r) - \sin \phi_r - \omega_- t \cos \phi_r]}{\omega_-^2} \end{array} \right] \qquad (11)$$

For effective amplification of radiation, $\omega_- \ll \omega_+$, so that

$$z_i(t) = \frac{z_f(t)\omega_r}{\beta\omega_w} = \frac{e\hat{a}_w E_0}{2m} \left[\frac{\sin(\omega_- t + \phi_r) - \sin \phi_r - \omega_- t \cos \phi_r}{\omega_-^2} \right]. \qquad (12)$$

Because the undulator field is periodic, the inertial bunching and force bunching are nearly equal for an ultrarelativistic e-beam when $\omega_- \ll \omega_+$.

4 GAIN

The change in an electron's energy from interaction with the radiation obeys

$$\frac{d\varepsilon}{dt} = ev_r E_r + ev_w E_r \qquad (13)$$

where v_r, v_w and E_r are evaluated at radius r and the axial position $z(t)$ calculated in the previous section. The change in an average electron's energy is given by averaging over the phase of the radiation ϕ_r. To order E_0^2, the first term on the RHS does not contribute to this average, so that for $\hat{a}_w^2 (1 + 8 < n_0 > / < n_1 >) \ll 8$

$$\langle d\varepsilon/dt \rangle_{\phi_r} = \langle ev_w E_r \rangle_{\phi_r} \approx$$

$$\langle z \cos \phi_r \rangle_{\phi_r} \left[\frac{-e\hat{a}_w c E_0}{2} (k_+ \cos \omega_- t + k_- \cos \omega_+ t) \right] \qquad (14)$$

$$+ \langle z \sin \phi_r \rangle_{\phi_r} \left[\frac{e\hat{a}_w c E_0}{2} (k_+ \sin \omega_- t - k_- \sin \omega_+ t) \right]$$

where $k_+ \equiv k_w + k_r$ and $k_- \equiv k_w - k_r$. Equation (12) gives

$$\langle z \cos \phi_r \rangle_{\phi_r} = \frac{(1 + \beta\omega_w/\omega_r)e\hat{a}_w E_0}{4m\omega_-^2} (\sin \omega_- t - \omega_- t)$$

$$\langle z \sin \phi_r \rangle_{\phi_r} = \frac{(1 + \beta\omega_w/\omega_r)e\hat{a}_w E_0}{4m\omega_-^2} (\cos \omega_- t - 1) \qquad (15)$$

where for $\beta \approx 1$, $1 + \beta\omega_w/\omega_r = 2/(1 + v_0/c)$.

Let $\Delta\varepsilon \equiv \int_0^T \langle d\varepsilon/dt \rangle_{\phi_r} dt$ be the average energy change per electron from interacting with radiation. Here, T is the undulator transit time, obeying $\hat{\omega}_w T = 2\pi N$ with integer or half-integer N equaling the number of undulator periods. For $\omega_- \ll \omega_+$ and $\gamma \gg 1$, eqs. (14) and (15) give

$$\Delta\varepsilon = \frac{-e^2 E_0^2 \hat{a}_w^2 c k_+ T^3}{4m(1 + v_0/c)} \left(\frac{2 - 2\cos \omega_- T - \omega_- T \sin \omega_- T}{\omega_-^3 T^3} \right). \qquad (16)$$

In the beam frame, the number of electrons passing through the undulator within a transverse area A_0 during a time t_0 is $n_e A_0 \beta c t_0$, so that the energy transferred to the forward wave is $-n_e A_0 \beta c t_0 \Delta\varepsilon$, where n_e is the electron density. The time-averaged Poynting vector of the radiation is $<S> = \varepsilon_0 c E_0^2/2$, with energy density $<S>/c$. Since the relative velocity between the forward wave and

undulator is $(1+\beta)c$, the electromagnetic energy passing through the undulator is $(<S>/c)(1+\beta)ct_oA_o$. The radiation energy gain per pass at radius r therefore obeys

$$gain = \frac{-n_eA_o\beta ct_o\Delta\varepsilon}{\langle S\rangle(1+\beta)t_oA_o} = \left(\frac{-2\beta}{1+\beta}\right)\frac{n_e\Delta\varepsilon}{\varepsilon_oE_o^2} . \quad (17)$$

Equations (16) and (17) give for $\gamma \gg 1$

$$gain = \frac{n_ee^2k_+c\hat{a}_w^2T^3}{4m\varepsilon_o(1+v_o/c)}\left(\frac{2-2\cos\omega\_T - \omega\_T\sin\omega\_T}{\omega\_^3T^3}\right). \quad (18)$$

In the laboratory frame, the maximum transverse velocity divided by c is obtained from the radial and axial velocities in the beam frame when $|v_w|$ is largest:

$$\beta_{\perp-lab} = \frac{a_w}{\gamma} \approx \frac{\hat{a}_w}{\gamma[1-(\hat{a}_w^2/2)(1+2\langle n_0\rangle/\langle n_1\rangle)]} \quad (19)$$

where a_w is the wiggler parameter. The gain at radius r is given to lowest order in the wiggler parameter a_w as

$$\frac{n_{e-lab}e^2\omega_{w-lab}a_w^2L_{lab}^3}{2m\varepsilon_oc^3\gamma^3}\left[\frac{2-2\cos\omega\_T-\omega\_T\sin\omega\_T}{(\omega\_T)^3}\right] \quad (20)$$

where n_{e-lab} is the e-beam density, $\omega_{w-lab} = \beta ck_{w-lab}$ is the angular frequency of electron undulations, and L_{lab} is the undulator length measured in the laboratory frame. Here,

$$\omega\_T = [k_{w-lab}(1+v_o/c)-k_{r-lab}(1-v_o/c)/2\gamma^2]cT_{lab} \quad (21)$$

where $T_{lab} = L_{lab}/\beta c$ is the undulator transit time and k_{r-lab} is the radiation wave number in the laboratory. For optimal amplification, $\omega\_T = 2.61$ [4], so that for $N \gg 1$, $\gamma \gg 1$ and $a_w \ll 1$, maximum gain occurs for

$$k_{r-lab} \approx \frac{2\gamma^2k_{w-lab}}{1+\frac{a_w^2}{2}\left(1+\frac{4\langle n_{0-lab}\rangle}{\langle n_{1-lab}\rangle}\right)} . \quad (22)$$

When $n_{1-lab}(r)$ and $n_{0-lab}(r)$ are proportional to $1/r$ and $n_{e-lab}(r)$ is independent of r, the electron quiver velocity, gain, and wavelength at which maximum gain occurs are independent of r, giving ideal undulator performance. For an ultrarelativistic beam, the gain equals that of a planar magnetostatic undulator with the same quiver velocity [13], while the wavelength experiencing maximum gain is modified because $<n_{0-lab}> \neq 0$ in eq. (22).

5 APPLICATION

To maximize FEL gain while minimizing the ion density, a strong undulator with $a_w \approx 1$ at the beam radius and a strongly modulated ion channel with $n_{1-lab}(r) \approx n_{0-lab}(r)$ may be utilized. To ensure stable propagation, we consider an undulator period much shorter than the betatron wavelength [2, 11]. The ion density required for $a_w \approx 1$ is given by eq. (6). For a relativistic e-beam, a periodic ion density $<n_{1-lab}>$ of 3.5×10^{11} cm^{-3} is required for a beam radius r_b of 1 cm and $\lambda_{w-lab} = 10$ cm, while $<n_{1-lab}> = 3.5\times10^{13}$ cm^{-3} is required for $r_b = 1$ mm and $\lambda_{w-lab} = 1$ cm. A periodic density of $<n_{1-lab}> = 3.5\times10^{15}$ cm^{-3} is required for $r_b = 100$ μm and $\lambda_{w-lab} = 1$ mm, while $<n_{1-lab}> = 3.5\times10^{17}$ cm^{-3} is required for $r_b = 10$ μm and $\lambda_{w-lab} = 100$ μm. In all cases, the undulator period is much shorter than the betatron wavelength for $\gamma \gg 3$.

One method of obtaining a periodic ion channel is to create a periodic plasma channel by ionizing a periodic gas density [1]. When an e-beam propagates in the channel, the plasma electrons are expelled, provided that the electron beam density exceeds the peak ion density. For a strongly modulated ion channel, this requires a beam current exceeding $(17 \text{ kA})(k_{w-lab}r_b)\beta^2a_w$. For the above examples, the beam current must exceed 11 kA. The parameters for $r_b = 1$ cm are comparable to those of a magnetostatic X-band FEL with ion channel guiding [7], suggesting that a periodic plasma channel FEL may be operated in the ion-focusing regime.

When a strongly modulated ion beam is used as a channel, the electron beam density may be smaller than that of the ions, since ejection of plasma electrons is not required. Transporting ions out of the FEL within an ion bounce period may limit the ion hose instability [3].

6 SUMMARY

A cold electron beam propagating in a periodic ion channel amplifies radially polarized radiation. When the undulator period is much shorter than the betatron wavelength, the gain at a given distance from the axis equals that of a planar magnetostatic undulator with the same quiver velocity. Our analysis suggests that an X-band FEL may operate in the ion-focusing regime when an electron beam expels plasma electrons from plasma with periodic density. When an ultrarelativistic electron beam propagates in a periodic ion channel with density of 10^{11}–10^{17} cm^{-3}, a short-wavelength FEL may be obtained.

REFERENCES

[1] J. D. Miller and R. M. Gilgenbach, Phys. Fluids 30, 3165 (1987).

[2] R. A. Bosch and R. M. Gilgenbach, Phys. Fluids 31, 634 (1988); Phys. Fluids 31, 3127 (1988).

[3] Yu. Ya. Golub' and N. E. Rozanov, Tech. Phys. 40, 346 (1995); Tech. Phys. 40, 1053 (1995).

[4] T. C. Marshall, Free-Electron Lasers (Macmillan, New York, 1985).

[5] D. H. Whittum, A. M. Sessler and J. M. Dawson, Phys. Rev. Lett. 64, 2511 (1990).

[6] K. R. Chen, J. M. Dawson, A. T. Lin and T. Katsouleas, Phys. Fluids B 3, 1270 (1991).

[7] K. Takayama et. al., J. Appl. Phys. 77, 5467 (1995).

[8] P. Jha and P. Kumar, IEEE Trans. Plasma Sci. 24, 1359 (1996).

[9] M. Esmaeilzadeh, H. Mehdian and J. E. Willett, Phys. Rev. E 65, 016501 (2001).

[10] K. R. Chen and J. M. Dawson, Phys. Rev. A 45, 4077 (1992).

[11] R. Pakter and F. B. Rizzato, Phys. Rev. Lett. 87, 044801 (2001).

[12] J. D. Jackson, Classical Electrodynamics, 2nd ed. (Wiley, New York, 1975).

[13] R. A. Bosch, these proceedings.

BEAM-FRAME CALCULATION OF FREE-ELECTRON LASER GAIN*

R. A. Bosch,[#] Synchrotron Radiation Center, University of Wisconsin-Madison,
3731 Schneider Dr., Stoughton, WI 53589, USA

Abstract

The amplification of radiation is calculated in the beam frame for a free electron laser (FEL) with a planar or helical undulator. The effect of the radiation force upon the transverse electron trajectory is included; this effect accounts for one-half of the gain in the undulator regime. Our calculated gain agrees with conventional formulas.

1 INTRODUCTION

In some FEL derivations, the effect of the radiation force upon the transverse electron motion ("force bunching" [1]) is neglected. When force bunching is neglected, using a standard method for calculating the axial velocity yields conventional gain formulas [1], while an alternative method yields one-half of the conventional gain [2]. Thus, it is inconsistent to assume that force bunching is negligible in an FEL [2].

We calculate FEL gain in the low-gain-per-pass undulator regime, performing our analysis in the frame of reference moving with the electron beam. In this frame, force bunching is easily included. We show that force bunching accounts for one-half of the bunching and gain in the undulator regime. For planar and helical undulators, our calculated gain agrees with conventional expressions, in which the helical gain is twice as large as the planar gain for a given wiggler parameter [3].

2 TRANSVERSE MOTION

For amplification of a weak radiation field by an ultrarelativistic beam, we include radiation in the transverse dynamics to model "force" bunching [1]. We first consider a planar undulator, in which an electron's velocity deviates by less than the angle $1/\beta\gamma$ from the z-axis, where $\gamma \gg 1$ is the relativistic factor for the beam and $\beta \approx 1$ is the velocity divided by the speed of light c. In an undulator, the electron motion is non-relativistic in the frame of reference moving with the beam as it enters the undulator, so we calculate the dynamics in this frame using SI units. The relativistic factor and velocity describing this frame are denoted $\gamma_\parallel$ and $\beta_\parallel c$.

The undulator field appears in this frame as linearly polarized radiation traveling in the negative-z direction, with electric field in the x-direction

$$E_{wx}(z,t) = E_{wo}\cos(k_w z + \omega_w t) \qquad (1)$$

The undulator magnetic field B_{wy} equals $-E_{wx}/c$, where $\omega_w = \beta_\parallel c k_w \approx c k_w > 0$. The undulator entrance obeys $k_w z + \omega_w t = 0$.

The radiation field is also linearly polarized, traveling

in the z-direction, with

$$E_{rx}(z,t) = E_{ro}\cos(k_r z - \omega_r t + \phi_r) \qquad (2)$$

and magnetic field $B_{ry} = E_{rx}/c$, where $\omega_r = ck_r > 0$.

Consider an electron with constant axial velocity v_z. The forced transverse oscillation from the undulator obeys

$$d^2 x/dt^2 = (e/m)(1 + v_z/c)E_{wx}(z(t),t) \qquad (3)$$

where $e < 0$ is the electron charge and m is its mass. The undulation velocity is therefore

$$v_{wx}(z,t) = -\hat{a}_w c \sin(k_w z + \omega_w t), \qquad (4)$$

where

$$\hat{a}_w = -eE_{wo}/m\omega_w c \qquad (5)$$

Similarly, the forced transverse oscillation velocity from the radiation is

$$v_{rx}(z,t) = a_r c \sin(k_r z - \omega_r t + \phi_r), \qquad (6)$$

where

$$a_r = -eE_{ro}/m\omega_r c \qquad (7)$$

Any axial velocity function may be approximated to arbitrary accuracy by constant-velocity segments, so that eqs. (4)–(7) also apply when the axial velocity is not constant. Since $v_{wx} = 0$ at the undulator entrance, a matched beam flows parallel to the axis with $\gamma_\parallel = \gamma$. Our assumption of non-relativistic velocities requires $\hat{a}_w \ll 1$.

3 AXIAL MOTION

To describe "inertial" bunching, we include radiation in the axial dynamics [1]. An electron whose initial axial position z is 0 obeys, to lowest order in the radiation field

$$\frac{d^2 z}{dt^2} = \frac{e}{m}v_{wx}B_{wy} + \frac{e}{m}v_{wx}B_{ry} + \frac{e}{m}v_{rx}B_{wy} \cdot \qquad (8)$$

The solution with $z(0) = dz/dt(0) = 0$ is the sum of three functions describing radiation-independent axial motion, inertial bunching, and force bunching. The radiation-independent motion obeys $d^2 z_0/dt^2 = (e/m)v_{wx}B_{wy}$ where $z \approx v_0 t$ on the right hand side (RHS) of the equation, with v_0 equaling the average axial velocity in the undulator. The solution with $z_0(0) = dz_0/dt(0) = 0$ is

$$z_0(t) = \frac{-e\hat{a}_w E_{wo}}{8m\hat{\omega}_w^2}(\sin 2\hat{\omega}_w t - 2\hat{\omega}_w t), \qquad (9)$$

where $\hat{\omega}_w = \omega_w(1 + v_0/c)$ is the undulator frequency experienced by an electron with axial velocity v_0. For $\hat{a}_w \ll 1$, equation (9) gives the average axial velocity as

$$v_0 = -\hat{a}_w^2 c/4 \qquad (10)$$

Inertial bunching [1] results from the axial radiation force on an electron, obeying $d^2 z_i/dt^2 = (e/m)v_{wx}B_{ry}$ where $z \approx z_0(t)$ on the RHS of the equation. For $\hat{a}_w \ll 1$, approximating $z_0(t) \approx v_0 t$ on the RHS for the fundamental FEL mode gives the solution with $z_i(0) = dz_i/dt(0) = 0$

$$z_i(t) = \frac{e\hat{a}_w E_{ro}}{2m}\left[\frac{\sin(\omega_+ t - \phi_r) + \sin\phi_r - \omega_+ t\cos\phi_r}{\omega_+^2} + \frac{\sin(\omega_- t + \phi_r) - \sin\phi_r - \omega_- t\cos\phi_r}{\omega_-^2}\right] \quad (11)$$

where $\omega_+ \equiv \hat{\omega}_w + \hat{\omega}_r$ and $\omega_- \equiv \hat{\omega}_w - \hat{\omega}_r$, in which $\hat{\omega}_r \equiv \omega_r(1 - v_o/c)$ is the radiation frequency experienced by an electron with axial velocity v_o. Since the undulation wavelength in the laboratory is independent of the electron's axial velocity, the inertial bunching is also called "axial" bunching [1].

Force bunching [1] results from the transverse radiation force on an electron, obeying $d^2 z_f/dt^2 = (e/m)v_{rx}B_{wy}$ where $z \approx z_o(t)$ on the RHS of the equation. For $\hat{a}_w \ll 1$, approximating $z_o(t) \approx v_o t$ on the RHS for the fundamental FEL mode gives the solution with $z_f(0) = dz_f/dt(0) = 0$

$$z_f(t) = \frac{-ea_r E_{wo}}{2m}\left\{\frac{\sin(\omega_+ t - \phi_r) + \sin\phi_r - \omega_+ t\cos\phi_r}{\omega_+^2} - \frac{\sin(\omega_- t + \phi_r) - \sin\phi_r - \omega_- t\cos\phi_r}{\omega_-^2}\right\} \quad (12)$$

For effective amplification of radiation, $\omega_- \ll \omega_+$, so that

$$z_i(t) = \frac{\omega_r}{\omega_w}z_f(t) = \frac{-a_r \hat{a}_w c\omega_r}{2}\left[\frac{\sin(\omega_- t + \phi_r) - \sin\phi_r - \omega_- t\cos\phi_r}{\omega_-^2}\right] \quad (13)$$

In the periodic undulator field, inertial bunching and force bunching are nearly equal when $\omega_- \ll \omega_+$.

4 GAIN

The change in an electron's energy from interaction with the radiation obeys

$$\frac{d\varepsilon}{dt} = ev_{rx}E_{rx} + ev_{wx}E_{rx} \quad (14)$$

where v_{rx}, v_{wx} and E_{rx} are evaluated at the axial position $z(t)$ calculated in the previous section. The change in an average electron's energy is given by averaging over the phase of the radiation ϕ_r. To order E_{ro}^2, the first term on the RHS does not contribute to this average, so that for $\hat{a}_w^2 \ll 8$

$$\langle d\varepsilon/dt\rangle_{\phi_r} = \langle ev_{wx}E_{rx}\rangle_{\phi_r} \approx$$

$$\langle z\cos\phi_r\rangle_{\phi_r}\left[\frac{-e\hat{a}_w cE_{ro}}{2}(k_+\cos\omega_- t + k_-\cos\omega_+ t)\right] \quad (15)$$

$$+ \langle z\sin\phi_r\rangle_{\phi_r}\left[\frac{e\hat{a}_w cE_{ro}}{2}(k_+\sin\omega_- t - k_-\sin\omega_+ t)\right]$$

where $k_+ \equiv k_w + k_r$ and $k_- \equiv k_w - k_r$. Equation (13) gives

$$\langle z\cos\phi_r\rangle_{\phi_r} = \left(1 + \frac{\omega_w}{\omega_r}\right)\frac{e\hat{a}_w E_{ro}}{4m\omega_-^2}(\sin\omega_- t - \omega_- t)$$

$$\langle z\sin\phi_r\rangle_{\phi_r} = \left(1 + \frac{\omega_w}{\omega_r}\right)\frac{e\hat{a}_w E_{ro}}{4m\omega_-^2}(\cos\omega_- t - 1) \quad (16)$$

where $1 + \omega_w/\omega_r \approx 2/(1 - \hat{a}_w^2/4)$ for $\omega_- \ll \omega_+$.

Let $\Delta\varepsilon \equiv \int_0^T \langle d\varepsilon/dt\rangle_{\phi_r} dt$ be the average energy change per electron from interacting with radiation. Here, T is the undulator transit time, obeying $\hat{\omega}_w T = 2\pi N$ with integer or half-integer N equaling the number of undulator periods. Then, for $\omega_- \ll \omega_+$, eqs. (15) and (16) give

$$\Delta\varepsilon = -\frac{e^2 E_{ro}^2 \hat{a}_w^2 ck_+ T^3}{4m(1 - \hat{a}_w^2/4)}\left(\frac{2 - 2\cos\omega_- T - \omega_- T\sin\omega_- T}{\omega_-^3 T^3}\right). \quad (17)$$

In the beam frame, the number of electrons passing through the undulator within a transverse area A_o during a time t_o is $n_e A_o \beta ct_o$, so that the energy transferred to the forward wave is $-n_e A_o \beta ct_o\Delta\varepsilon$, where n_e is the electron density. The time-averaged Poynting vector of the radiation is $<S> = \varepsilon_o c E_{ro}^2/2$, with energy density $<S>/c$. Since the relative velocity between the forward wave and undulator is $(1+\beta)c \approx 2c$, the electromagnetic energy passing through the undulator is $(<S>/c)(1+\beta)ct_o A_o$. The radiation energy gain per pass therefore obeys

$$\text{gain} = \frac{-n_e A_o \beta ct_o\Delta\varepsilon}{\langle S\rangle(1+\beta)t_o A_o} = \left(\frac{-2\beta}{1+\beta}\right)\frac{n_e\Delta\varepsilon}{\varepsilon_o E_{ro}^2}. \quad (18)$$

Equations (17) and (18) give for $\beta \approx 1$

$$\text{gain} = \frac{n_e e^2 k_+ c\hat{a}_w^2 T^3}{4m\varepsilon_o(1 - \hat{a}_w^2/4)}\left(\frac{2 - 2\cos\omega_- T - \omega_- T\sin\omega_- T}{\omega_-^3 T^3}\right). \quad (19)$$

In the laboratory frame, the maximum transverse velocity divided by c is obtained from the transverse and axial velocities in the beam frame when $|v_{wx}|$ is largest:

$$\beta_{\perp\text{-}lab} = a_w/\gamma \approx \hat{a}_w/[\gamma(1 - \hat{a}_w^2/2)], \quad (20)$$

where a_w is the wiggler parameter. The gain is given in the laboratory to lowest order in a_w:

$$\frac{n_{e\text{-}lab}e^2\omega_{w\text{-}lab}a_w^2 L_{lab}^3}{2m\varepsilon_o c^3\gamma^3}\left[\frac{2 - 2\cos\omega_- T - \omega_- T\sin\omega_- T}{(\omega_- T)^3}\right] \quad (21)$$

where $n_{e\text{-}lab}$ is the e-beam density, $\omega_{w\text{-}lab} = ck_{w\text{-}lab}$ is the angular undulation frequency, and L_{lab} is the undulator length, all measured in the laboratory frame. Here,

$$\omega_- T = [k_{w\text{-}lab}(1 - a_w^2/4) - k_{r\text{-}lab}(1 + a_w^2/4)/2\gamma^2]cT_{lab} \quad (22)$$

where $T_{lab} = L_{lab}/c$ is the undulator transit time and $k_{r\text{-}lab}$ is the radiation wave number in the laboratory. For optimal amplification, $\omega_- T = 2.61$, so that for $N \gg 1$, $\gamma \gg 1$ and $a_w \ll 1$, maximum gain occurs for

$$k_{r\text{-}lab} \approx 2\gamma^2 k_{w\text{-}lab}/(1 + a_w^2/2). \quad (23)$$

For $a_w \ll 1$, the gain is twice as large as that resulting from inertial bunching alone.

5 HELICAL UNDULATOR

Consider a helical undulator in the frame of reference moving with a matched beam's axial velocity at the undulator entrance. Equations (1)–(7) are supplemented by equations describing radiation with y-polarization and motion in the y-direction. The additional undulator electric field is

$$E_{wy}(z,t) = E_{wo}\cos(k_w z + \omega_w t + \pi/2), \quad (24)$$

with additional magnetic undulator field $B_{wx} = E_{wy}/c$.

$$E_{ry}(z,t) = E_{ro}\cos(k_r z - \omega_r t + \phi_r - \pi/2) \quad (25)$$

describes the additional radiation whose magnetic field is $B_{rx} = -E_{ry}/c$. The undulation velocity in the y-direction is

$$v_{wy}(z,t) = -\hat{a}_w c \cos(k_w z + \omega_w t), \tag{26}$$

while the forced transverse oscillation velocity from the radiation in the y-direction is

$$v_{ry}(z,t) = -a_r c \cos(k_r z - \omega_r t + \phi_r), \tag{27}$$

Since $v_{wy} \neq 0$ at the helical undulator entrance (where $k_w z + \omega_w t = 0$), a matched beam has $\gamma_\parallel < \gamma$.

The axial motion of an electron whose initial axial position z is 0 obeys, to lowest order in the radiation field

$$\frac{d^2 z}{dt^2} = \frac{e}{m}\left(v_{wx}B_{wy} - v_{wy}B_{wx}\right) + \frac{e}{m}\left(v_{wx}B_{ry} - v_{wy}B_{rx}\right)$$
$$+ \frac{e}{m}\left(v_{rx}B_{wy} - v_{ry}B_{wx}\right) \tag{28}$$

The solution with initial conditions $z(0) = dz/dt(0) = 0$ is the sum of three functions describing radiation-independent axial motion, inertial bunching, and force bunching. The radiation-independent motion obeys $d^2 z_0/dt^2 = (e/m)(v_{wx}B_{wy} - v_{wy}B_{wx})$ where $z \approx v_0 t$ on the RHS, with v_0 equaling the average axial velocity in the undulator. The solution with $z_0(0) = dz_0/dt(0) = 0$ is

$$z_0(t) = 0, \tag{29}$$

indicating that the average axial velocity v_0 is zero.

The inertial bunching term obeys $d^2 z_i/dt^2 = (e/m)(v_{wx}B_{ry} - v_{wy}B_{rx})$ where $z \approx 0$ on the RHS. The solution with $z_i(0) = dz_i/dt(0) = 0$ is

$$z_i(t) = \frac{e\hat{a}_w E_{ro}}{m\omega_-^2}\left[\sin(\omega_- t + \phi_r) - \sin\phi_r - \omega_- t \cos\phi_r\right] \tag{30}$$

where $\omega_- \equiv \omega_w - \omega_r$.

The force bunching term obeys $d^2 z_f/dt^2 = (e/m)(v_{rx}B_{wy} - v_{ry}B_{wx})$ where $z \approx 0$ on the RHS. The solution with $z_f(0) = dz_f/dt(0) = 0$ is

$$z_f(t) = \frac{ea_r E_{wo}}{m\omega_-^2}\left[\sin(\omega_- t + \phi_r) - \sin\phi_r - \omega_- t \cos\phi_r\right]. \tag{31}$$

Thus,

$$z_i(t) = \frac{\omega_r}{\omega_w}z_f(t) = -a_r\hat{a}_w c\omega_r\left[\frac{\sin(\omega_- t + \phi_r) - \sin\phi_r - \omega_- t \cos\phi_r}{\omega_-^2}\right]. \tag{32}$$

Since $\omega_w/\omega_r = 1$ for $\omega_- \ll \omega_+ \equiv \omega_w + \omega_r$, force bunching accounts for one-half of the bunching.

To order E_{ro}^2,

$$\langle d\varepsilon/dt\rangle_{\phi_r} = \langle ev_{wx}E_{rx} + ev_{wy}E_{ry}\rangle_{\phi_r}$$
$$= -e\hat{a}_w cE_{ro}k_+\left(\cos\omega_- t\langle z\cos\phi_r\rangle_{\phi_r} - \sin\omega_- t\langle z\sin\phi_r\rangle_{\phi_r}\right) \tag{33}$$

where $k_+ \equiv k_w + k_r$ and

$$\langle z\cos\phi_r\rangle_{\phi_r} = \left(1 + \frac{\omega_w}{\omega_r}\right)\frac{e\hat{a}_w E_{ro}}{2m\omega_-^2}(\sin\omega_- t - \omega_- t)$$
$$\langle z\sin\phi_r\rangle_{\phi_r} = \left(1 + \frac{\omega_w}{\omega_r}\right)\frac{e\hat{a}_w E_{ro}}{2m\omega_-^2}(\cos\omega_- t - 1) \tag{34}$$

The average energy change per electron when $\omega_- \ll \omega_+$ is

$$\Delta\varepsilon = -\frac{e^2 E_{ro}^2 \hat{a}_w^2 ck_+ T^3}{m}\left(\frac{2 - 2\cos\omega_- T - \omega_- T\sin\omega_- T}{\omega_-^3 T^3}\right). \tag{35}$$

For a helical FEL, the time-averaged Poynting vector of the radiation is $<S> = \varepsilon_0 cE_{ro}^2$, with energy density $<S>/c$. Since the relative velocity between the forward wave and undulator is $(1+\beta)c$, the electromagnetic energy passing through the undulator is $(<S>/c)(1+\beta)ct_0 A_0$. The radiation energy gain per pass therefore obeys

$$\text{gain} = \frac{-n_e A_0\beta ct_0\Delta\varepsilon}{\langle S\rangle(1+\beta)t_0 A_0} = \left(\frac{-\beta}{1+\beta}\right)\frac{n_e\Delta\varepsilon}{\varepsilon_0 E_{ro}^2}. \tag{36}$$

Equations (35) and (36) give for $\beta \approx 1$

$$\text{gain} = \frac{n_e e^2 k_+ c\hat{a}_w^2 T^3}{2m\varepsilon_0}\left(\frac{2 - 2\cos\omega_- T - \omega_- T\sin\omega_- T}{\omega_-^3 T^3}\right). \tag{37}$$

In the laboratory frame, the transverse velocity divided by c obeys

$$\beta_{\perp-lab} = a_w/\gamma = \hat{a}_w/\gamma_\parallel \tag{38}$$

where a_w is the wiggler parameter and γ is the relativistic factor for the beam. Using the relation $1/\gamma_\parallel^2 = (1+a_w^2)/\gamma^2$ we obtain the gain to lowest order in a_w

$$\frac{n_{e-lab}e^2\omega_{w-lab}a_w^2 L_{lab}^3}{m\varepsilon_0 c^3\gamma^3}\left[\frac{2 - 2\cos\omega_- T - \omega_- T\sin\omega_- T}{(\omega_- T)^3}\right] \tag{39}$$

where

$$\omega_- T = [k_{w-lab} - k_{r-lab}(1 + a_w^2)/2\gamma^2]cT_{lab} \tag{40}$$

Maximum gain occurs for

$$k_{r-lab} \approx 2\gamma^2 k_{w-lab}/(1 + a_w^2) . \tag{41}$$

The gain is twice as large as that from inertial bunching alone, and twice as large as that of a planar FEL with the same wiggler parameter. Our gain expression agrees with the conventional expression for a helical FEL [1].

6 SUMMARY

For planar and helical FELs, we have calculated the gain in the beam frame in the low-gain-per-pass undulator limit. Inertial and force bunching give equal contributions to the gain in the undulator regime. For planar and helical undulators, our calculated gain agrees with conventional expressions in which the helical gain is twice as large as the planar gain for a given wiggler parameter.

REFERENCES

[1] K. R. Chen, J. M. Dawson, A. T. Lin and T. Katsouleas, Phys. Fluids B **3**, 1270 (1991).

[2] B. W. J. McNeil and W. J. Firth, IEEE J. Quantum Electron. **QE-21**, 1034 (1985); Comments and author's reply in: P. Luchini, IEEE J. Quantum Electron. **QE-23**, 130–131 (1987)

[3] R. Coisson, IEEE J. Quantum Electron. **QE-17**, 1409 (1981).

SUB-PICOSECOND, HIGH FLUX, THOMSON X-RAY SOURCES AT JEFFERSON LAB'S HIGH POWER FEL*

James R. Boyce[#], David R. Douglas, Hiroyuki Toyokawa, Thomas Jefferson National Accelerator Facility, Newport News, VA 23606, USA
Winthrop J. Brown, Fred Hartemann, LLNL, Livermore, CA 94550, USA

Abstract

With the advent of high average power FELs, the idea of using such a device to produce x-rays via the Thomson scattering process is appealing, if sufficient flux and/or brightness can be generated. Such x-rays are produced simultaneously with FEL light, offering unprecedented opportunities for pump-probe studies. We discuss non-invasive modifications to the Jefferson Lab's FEL that would meet the criteria of high flux, sub-picosecond, x-ray source. One allows proof-of-principle experiments, is relatively inexpensive, but is not conducive as a "User-facility." Another is a User facility configuration but requires FEL facility modifications. For all sources, we present Thomson scattering flux calculations and potential applications.

INTRODUCTION

Atomic vibrations in crystals occur on femtosecond time scales. In order to image motion in that temporal regime, one needs a stroboscopic source of x-rays capable of generating crystallographic images in the same time frame. This requires pulses of x-rays of high brightness and shorter than a few hundred femtoseconds. Electron beam technology in the form of synchrotrons provides x-rays of high enough brightness for "snapshots" of frozen protein crystal structures - for example - but because the x-rays are nanoseconds in length, these sources cannot make the "molecular movies" required for understanding the molecular dynamics of such crystals. Progress in electron beam generation and control systems over the past 15 years has yielded several possible means of shortening x-ray pulses by three or four orders of magnitude, but these sources have yet to be bright enough. [1-4] Simultaneously generating both high brightness AND short pulses is a technological challenge.

The advent of high power Laser technology, has led to exploring the feasibility of using Thomson scattering off of very short, high energy, electron bunches to produce the desired x-ray sources. [5] Significant 300 femtosecond Thomson x-ray fluxes from the 2 kilo-Watt IR FEL at Jefferson Lab, predicted by Krafft [6] and measured by Boyce [7], demonstrate the feasibility of such approaches to generating pulses of x-rays with both high flux and femtosecond pulse length.

The Jefferson Lab FEL is currently being upgraded to a 10 kW IR and 1 kW UV capabilities. In this paper we present concepts and supporting calculations for expected Thomson scattering x-ray beams resulting from such increase in lasing power with the upgrade FEL configuration.

JLAB FEL FACILITY

Jefferson Lab's high average power (10 kW) FEL facility, described elsewhere [8], is in commissioning. When complete, it will have the capability of producing 10 kW of IR light and 1 kW of UV. It is based on the first Jefferson Lab's FEL which used superconducting rf (srf) and energy recovery technology to produced 2 kW of IR.

Figure 1 shows the layout of the upgrade FEL facility with a proposed additional electron beam transport loop. There are three locations in the electron beam line where significant Thomson x-rays can be generated: inside the optical cavity – specifically inside the wiggler – and in the last leg of the chicane prior to the wiggler. A third location, C, requires additional electron beamline.

In the wiggler, the IR in the optical cavity is automatically focused onto the electron beam, producing Thomson x-rays. The Rayleigh range of the cavity, however, limits the IR beam spot size to a value that is about twice the size of the electron beam spot size. Thus only a fraction of the available IR beam actually intercepts the electrons.
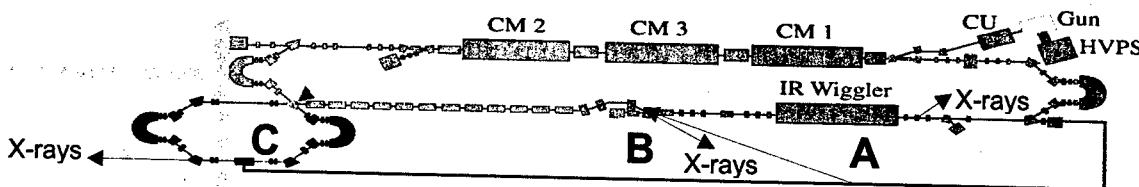
Figure 1: The Jefferson Lab Upgrade FEL layout (modified) with three site locations for Thomson x-ray sources. A) is intra-cavity production by the IR in the cavity automatically focused onto the electron beam. B) requires extracted IR brought to focus onto the electron beam in the chicane. C) has extracted IR brought to the loop and allows both beams to be focused to the smallest rms size.

The second location, B, for Thomson scattering is in the last section of the electron beam line chicane around the first optical cavity mirror system. This location requires extracted IR transported back to this location and focused onto the electron bunch. Extracted power is about 10% of the IR power in the optical cavity, but it can be focused to match the electron beam spot size, thus fully utilizing the available IR. The limitation of this location is the minimum spot size of the electron beam, a limitation set by electron beam transport requirements for energy recovery. (Full IR power requires transporting the electron beam back through the cryomodules (CM1, CM2, and CM3) for energy recovery.

The third location, C, requires an additional beam line (achromatic) loop. By turning off the magnet that normally directs the electrons down the straight-a-way, the electrons can enter the loop, travel clockwise around a pi-bend, focused down to a minimum spot size of about 75 microns rms, then back around another pi-bend and into a straight section and into the straight-a-way. Thomson x-rays are produced by transporting extracted IR to this region and focusing it down to the same size as the electrons. The IR can then be transported to user labs for experiments there. Part or all of this IR could be used as the pump of a pump-probe system.

X-RAY PRODUCTION

In order to adequately evaluate and compare the merits of each location, we need to calculate the anticipated x-ray source strengths for each case. The theory of photon scattering off electrons is well known. [See, for example, Refs. 9 and 10]. Careful treatment here also requires inclusion of the Rayleigh range of the IR in the optical cavity and the wiggler characteristics, which, in our case, has adjustable field strengths.

One assumption we have made is that both the electron and IR beams are Gaussian distributions. This simplifies the calculations while maintaining the ability to compare source strengths of each site.

The number of x-rays, N_x, produced by an IR bunch colliding with an electron bunch is:

$$N_x = \frac{N_e N_{IR}}{4\pi\sigma^2}\sigma_T \qquad (1)$$

where N_e and N_{IR}, are the number of electrons and IR photons respectively, σ is the bunch rms size, and σ_T is the Thomson cross section of the electron.

Table 1 is a comparison of the Jefferson Lab FEL Thomson x-ray sources using equation (1). It included values for the IR DEMO – the first FEL.

Table 1: Jefferson Lab FEL Thomson X-ray Sources

FEL → Parameter	IR DEMO Wiggler	IR Upgrade A. Wiggler	B. Chicane	C. Loop
E_e: e⁻ beam energy (MeV)	37	80	80	80
γ (E_e/m_0c^2)	72.41	156.56	156.56	156.56
Charge per bunch (pC)	60	130	130	130
N_e	3.7E+08	8.1E+08	8.1E+08	8.1E+08
frequency (MHz)	75	75	75	75
IR Power (kW)	10	100	10	10
IR wavelength (µm)	5	10	10	10
N_{IR}	3.4E+15	6.7E+16	6.7E+15	6.7E+15
e⁻ bunch $\sigma_x = \sigma_y$ (µm)	500	250	200	75
IR bunch $\sigma_x = \sigma_y$ (µm)	800	500	200	75
E x-ray max (keV)	5.20	12.15	12.15	12.15
X-rays per bunch	17	2306	721	5125
N_x (x-rays/sec)	1.2E+09	1.7E+11	5.4E+10	3.8E+11

Another feature of these sources is the tunability of the x-rays. Figure 2 emphasizes this point. These curves are calculated for the "A" source location and show the peak brightness for four settings of the wiggler strength parameter K_w.
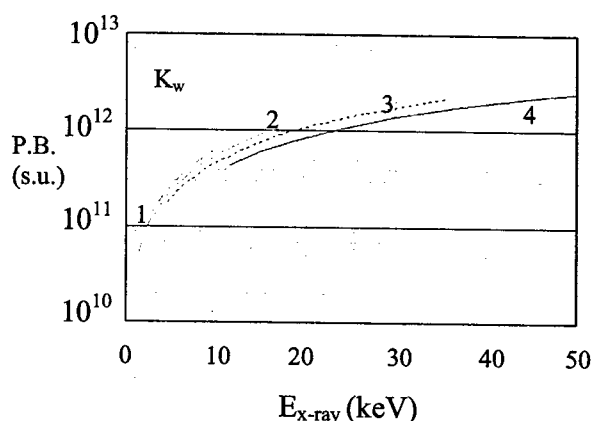
Figure 2: Peak brightness curves for Thomson x-rays generated in the wiggler of the Upgrade FEL, in standard units (s.u.): x-rays/sec/mm2/mrad2/(0.1% bandwidth). Input to these calculations include electron beam energy from 75 MeV to 125 MeV, intra-cavity IR power of 65 kW, and bunch frequency of 75 MHz.

CONCLUSIONS

Jefferson Lab's new 10 kW FEL is shown to be a source of high flux, sub-picosecond, x-rays. Three configurations have been examined and compared. The intra-cavity location requires the least amount of modification to the existing beam line, but the resulting

User Station, located inside the accelerator ring, would be inconvenient for experimenters. The location with the highest flux, and thus brightness, requires a loop addition to the electron beam line, and a modification to the FEL facility. Once built, however, such a facility is ideal for a User Laboratory outside the main accelerator vault.

ACKNOWLEDGEMENTS

REFERENCES

[1] *LCLS Design Study Report*, SLAC-R-21, UC-414, April 1998.

[2] *TESLA Test Facility Linac – Design Report*, D. A. Edwards, ed., TESLA 95-01, DESY Print March 1995.

[3] V. N. Litvinenko, *et al.*, *Physical Review Letters*, **78**, 4569 (1997).

[4] R. W. Schoenlein, *et al.*, *Science*, **287**, 2237 (2000).

[5] K.-J. Kim, S. Chattopadhyay, C.V. Shank, *Nuclear Instruments and Methods in Physics Research A* **341**, 351, (1994).

[6] G. A. Krafft, *Proc. of the 1997 IEEE Particle Accelerator Conference*, IEEE Cat. No. 97CH36167, 739 (1997).

[7] J.R. Boyce, et al., *Proc. Of the 2002 Conference on the Application of Accelerators in Research and Industry*, November, 2002, (In press).

[8] G. Neil, et al., "Status of the Jefferson Lab IR/UV High Average Power Light Source", FEL 2002, Chicago, IL 8-13 Sept. 2002.

[9] J.D. Jackson, *Classical Electrodynamics*, © 1962 John Wiuley & Sons, Inc., New York, NY.

[10] K-J Kim, "Section 2: Synchrotron Radiation," *X-ray Data Booklet*, LBNL/PUB-490 Rev. 2. January 2001. Also found at http://www.xdb.lbl.gov

IMAGE CHARGE UNDULATOR: THEORETICAL MODEL AND TECHNICAL ISSUES *

Yuhong Zhang, Yaroslav Derbenev, James R. Boyce, Rui Li

Jefferson Lab, Newport News, VA 23606, USA

Abstract

A relativistic electron beam undergoes undulating motion due to its image charge wakefields while passing close to a conducting grating surface. A new device, an image charge undulator, has been proposed recently [1] to utilize this mechanism for generating coherent hard radiation. We demonstrate the physics principle of this device by a 2D model of a uniform sheet beam. The transverse image charge wakefields, synchrotron radiation frequency and coherent radiation gain length are presented. We discuss a proof-of-principle experiment that takes into consideration such technical issues as grating fabrication, flat beams and beam alignment.

1 INTRODUCTION

A relativistic electron beam passing near a metal surface generates an electric polarization (image charges) of the surface, which applies a Lorentz force (image charge wakefields) back on the beam. These wakefields become wiggler type fields when the metal surface is a grating. The electron beam undergoes undulating motion due to these wakefields and emits/amplifies radiation just as in a conventional magnetic undulator. To enhance wakefields and also to stabilize the electron beam, we close the single grating by a second identical surface shown in Fig. 1. Such an asymmetric periodic structure is named an image charge undulator (ICU).
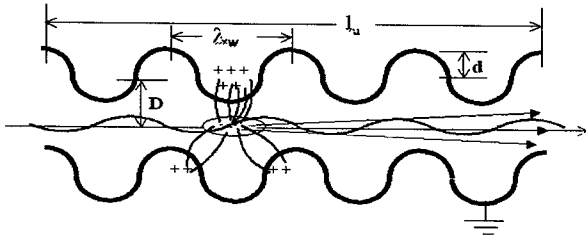
Figure 1. Schematic drawing of image charge undulator.

Let us consider a uniform sheet beam (surface charge density σ_0) in an infinitely long planar undulator as shown in Fig. 1. In this case, the alternating component of magnetic field vanishes, while the alternating electric field coincides with electrostatic solution for a charged sheet of the same density. The transverse image charge wakefields (defined as the total field minus the field of the source charges) have the following general form

$$E_x(x,z) = \sum_{n=1}^{\infty} E_{xn}(x) \sin(nk_w z + \varphi_{xz}) \qquad (1)$$

to reflect periodicity in the longitudinal direction, where φ_{xn} are phases, $k_w = 2\pi/\lambda_w$, and λ_w is the period of the

structure. Due to the linearity of Maxwell equations,

$$E_{xn}(x) \sim E_0 \qquad (2)$$

for all n, where $E_0 = 2\pi\sigma_0$ is the static electric field of a uniform sheet charge in free space. This relation implies that the image charge wakefields are always proportional to the surface charge density of the sheet beam, i.e., total charge and dimensions of a flat bunch.

Normally, higher harmonic terms in Eq. (1) decay very fast so the wakefields are dominated by the first several nonzero terms. Keeping only the first term in Eq. (1), we obtain from the electron equation of motion that

$$v_x(z) \approx \frac{cK}{\gamma}\cos k_w z, \qquad K = \frac{eE_{x1}(0)}{mc^2 k_w} \qquad (3)$$

where γ is the Lorentz factor, and $E_{x1}(x) \approx E_{x1}(0)$ because x is very small for high energy electrons. This result shows that electrons indeed undergo undulating motion and therefore emit/amplify radiation in a way similar to a conventional magnetic undulator. According to the synchrotron radiation theory, the resonance frequency of this planar undulator is

$$\lambda = \lambda_w(1 + \frac{1}{2}K^2)/2\gamma^2 \qquad (4)$$

2 A SIMPLE 2D MODEL

The 2D model of ICU shown in Fig. 2 can be viewed as a 2D waveguide (vertical size $2D$) attached by two sets of identical 2D rectangular cavities (width L and depth d). Cavities are uniformly distributed along the z-axis. The period of this ICU is $2L$. Both waveguide and cavities are made of perfectly conducting material. A uniform sheet beam (of zero thickness) passes through the *center* of the ICU. In Ref. 1, we have shown analytically the transverse image charge wakefield *at the center of the ICU* is

$$E_x(0,z) = E_0 \sum_{n=0}^{\infty} N_{x2n+1} \sin(2n+1)k_w z \qquad (5)$$

The dimensionless coefficients N_{x2n+1} depend only on the ICU geometry (i.e., ratios d/L and D/L), not on parameters of the flat beam, and are given as follows

$$N_{x2n+1} = -\frac{\tilde{a}_n \tanh(2n+1)\pi\frac{d}{L}}{\left(n+\frac{1}{2}\right)\pi \sinh(2n+1)\pi\frac{D}{L}} \qquad (6)$$

$\tilde{a}_n$ in Eq. (6) can be solved from linear equations

$$\tilde{a}_n = 1 + \sum_{m=0}^{\infty}\left[\tilde{\Gamma}_{nm} - \tilde{\Lambda}_{nm}\right]\tilde{a}_m \qquad (7)$$

where

$$\tilde{\Gamma}_{nm} = -\frac{2n+1}{2m+1}\tanh(2m+1)\pi\frac{d}{L}\int d\rho \frac{\tilde{I}_{sn}(\rho)\tilde{I}_{cn}(\rho)}{i \tanh 2\pi\frac{D}{L}}\sum_{\alpha} e^{i2\alpha\pi} \qquad (8)$$

$$\tilde{\Lambda}_{nm} = -\frac{2n+1}{2m+1}\tanh(2m+1)\pi\frac{d}{L}\int d\rho\frac{\tilde{I}_{sn}(\rho)\tilde{I}_{cn}(\rho)}{i\sinh 2\pi\frac{D}{L}}\sum_{\alpha}e^{i(2\alpha+1)\pi} \quad (9)$$

are elements of coupling matrices between two eigen modes of cavities on the same or opposite sides of the waveguide, and

$$\tilde{I}_{cn}(\rho) = \frac{1}{\pi}\frac{i\rho[1+e^{-i\rho}]}{(2n+1)^2-\rho^2}, \quad \tilde{I}_{sn}(\rho) = \frac{1}{\pi}\frac{[1+e^{+i\rho}]}{(2n+1)^2-\rho^2} \quad (10)$$

Further, one can use the following relation

$$\sum_{\alpha=-N}^{N}e^{i2\alpha\pi\rho} = \frac{\sin N\pi\rho}{\sin\pi\rho}\xrightarrow{N\to+\infty}\sum_{l=-\infty}^{+\infty}\delta(\rho-l) \quad (11)$$

to simplify Eq. (8) and (9).

It should be noted that we have used here a slightly simplified notation from Ref. 1, and have used a tilde on all new variables to denote this difference.
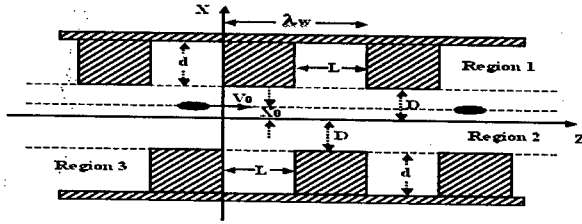
Figure 2. 2D Image charge undulator made of 2D waveguide and 2D rectangular cavity.

3 ASYMPTOTIC BEHAVIOR

Calculating matrix elements $\tilde{\Gamma}_{nm}$ and $\tilde{\Lambda}_{nm}$, and then solving linear equations (7) to find $\tilde{a}_n$ normally require numerical computations. However, it is useful for gaining physics insight to develop an asymptotic formula for N_{x2n+1}. Considering the fact that $\tilde{a}_n$ are slowly varying numbers in order of one, then

$$N_{x2n+1} \sim -\frac{\tanh(2n+1)\pi\frac{d}{L}}{\left(n+\frac{1}{2}\right)\pi\sinh(2n+1)\pi\frac{D}{L}} \quad (12)$$

In particular, for the first nonzero term, $n=0$,

$$N_{x1} \sim -\frac{2}{\pi}\tanh\pi\frac{d}{L}/\sinh\pi\frac{D}{L} \quad (13)$$

This leads to

$$N_{x1} \to -2\frac{d}{L}/\sinh\pi\frac{D}{L} \to 0, \quad when \quad d \ll L \quad (14)$$

$$N_{x1} \to -\frac{2}{\pi}/\sinh\pi\frac{D}{L}, \quad when \quad d \gg L \quad (15)$$

and

$$N_{x1} \sim -\frac{2}{\pi^2}\frac{L}{D}\tanh\pi\frac{d}{L} \to -\infty, \quad when \quad D \ll L \quad (16)$$

$$N_{x1} \sim -\frac{4}{\pi}e^{-\pi\frac{D}{L}}\tanh\pi\frac{d}{L} \to 0, \quad when \quad D \gg L \quad (17)$$

Both Eq. (14) and (17) are well expected since the transverse wakefields vanish when either the cavity depth reduces to zero so the structure becomes symmetric or two gratings are placed too far away. On the other hand, the transverse wakefields reach plateau values as shown in Eq. (15) when the cavity depth is much larger than the undulator period. The wakefields are dominated by the

image charges of the nearest metal surface, and since the image charges on the other surface are much farther they can be neglected. Eq. (16) displays a direct inversely proportional relationship between the wakefields and vertical size of the waveguide, i.e., one can increase wakefields by reducing the distance between two gratings.

4 A NUMERICAL EXAMPLE

We now present numerical calculations of undulating motion for a flat electron beam of 250 MeV energy in an ICU of 50 μm period using the analytical formulas in section 2. The flat bunch is 100 μm long, 100 μm wide and 4 μm thick, and contains $6\cdot10^{10}$ electrons (total charge is about 10 nC). Since the longitudinal bunch size is twice the ICU period, the assumption of infinitely long sheet beam in the 2D model is only an approximation. We should expect certain deviations from the theoretical model. Other ICU dimensions, i.e., grating tooth depth d and separation of two gratings $2D$, are parameters of numerical calculations, and their values typically are equal or close to the grating period λ_w. Matrices $\tilde{\Gamma}_{nm}$ and $\tilde{\Lambda}_{nm}$ in Eq. (7) are truncated to 100 by 100, and we use the Gaussian elimination method to solve Eq. (7).
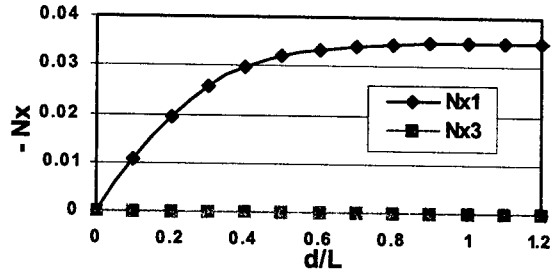
Figure 3. The first two ICU geometry dependent factors as functions of d/L, when D/L=1.
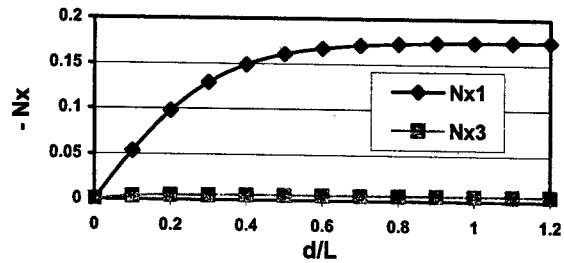
Figure 4. The first two ICU geometry dependent factors as functions of d/L, when D/L=0.5.

The geometric factors $N_{x\,2n+1}$, as well as the wakefields, are sensitive functions of ratios D/L and d/L, as shown in Figs. (3-5). The wakefields quickly reach plateau values when d is larger than L, while on the other hand, they can go very high when the two gratings are very close. These behaviors confirm the asymptotical formulas of the previous section. The separation of two gratings is limited by flat beam emittance and alignment, and at the present

time, $D \approx 0.5L \approx 12.5$ µm is a challenging but still reachable value.
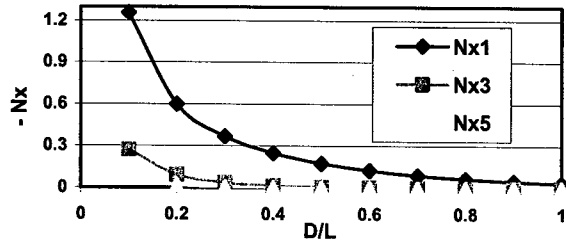
Figure 5. The first three ICU wakefield numerical factors as functions of D/L, when d/L=1.

To provide a direct and quantitative comparison between an ICU and a conventional magnetic undulator, we define an *equivalent* magnetic field derived from the Lorentz force formula

$$B_{eqv} = E_{x1}(0)/c \qquad (18)$$

This magnetic field would produce the same strength Lorentz force as the image charge wakefields. It is plotted in Fig. 6 as a function of D/L while d/L=1. The values are very significant, and can be as high as 35 T for D=12.5 µm, a value unreachable by conventional undulators or wigglers of current technologies.
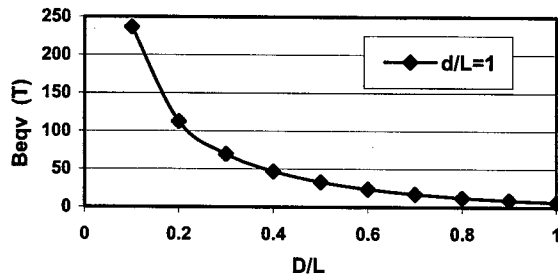
Figure 6. Equivalent magnetic field as a function of D/L, when d/L=1

Fig. 7 shows the undulator parameter K, ranged from 0.03 to 1.2. The gain length [2] of a FEL process is plotted in Fig. 8. Its range is from 0.3 to 3.4 cm depending on the separation between two gratings. This points to a very promising large radiation gain and even possible saturation in an ICU of less than 1 m in length.
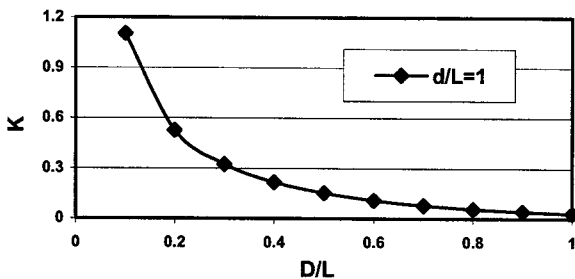
Figure 7. Undulator parameter K as a function of D/L, when d/L=1.
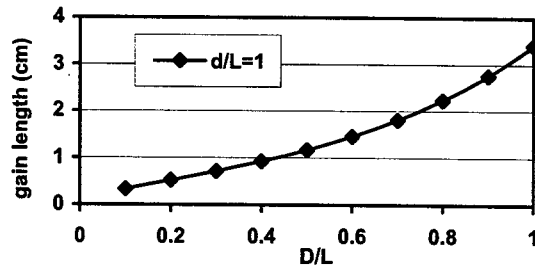
Figure 8. Gain length as a function of D/L, when d/L=1.

5 PROPOSED PROOF-OF-PRINCIPLE EXPERIMENT

The concept of ICU can be experimentally verified in a straightforward manner. First produce a flat beam with the required characteristics, then send the beam between properly machined and positioned flat plates, and finally monitor the resulting radiation downstream.

Flat beams of a very small x-emittance (0.01 µm, norm, or less) can be obtained from electron guns with the cathode immersed in a solenoid field. After acceleration to the energy range of tens of MeV, the electron beam can be ejected from the solenoid and transformed to a flat area, applying the vortex-plane beam adapters [3]. The y-emittance then becomes correspondingly large since the geometrical mean of the two emittances is equal to the beam normalized emittance at the cathode. See also [4].

The flat beam is then sent through a beam line cross fitted with standard, remotely controlled, linear motors with alignment guides all in the vacuum. Metallic plates, machined with the desired periodic surface ridges, can be mounted on the motors. (Commercially available machining techniques can cut grating ridges down to as small as 10 µm.) The plates face each other. Temperature stabilization can be added to back sides of the plates and the e-beam can be pulsed to control induced heating.

Initially, the separation between plates is large so the electron beam can be tuned without striking either plate. When the beam is aligned, the plates are moved towards each other in pre-determined steps. Photon radiation can be monitored downstream as a function of plate separation.

6 CONCLUSIONS

A new device, image charge undulator, has been theoretically examined as a potential source for hard radiation with an uncomplicated device. A straightforward experiment is proposed to verify these studies.

7 REFERENCES

[1] Y. Zhang, Ya. Derbenev and R. Li, Proceedings of FEL 2003, NIM, in *press*.

[2] E. L. Saldin, et al., The Physics of Free Electron Lasers, Springer-Verlag (2000)

[3] A. Burov, et al., Phys. Rev. E66: 016503, (2002)

[4] Y. Sun, et al., Proceedings of PAC 2003, (2003)

DESIGN AND STATUS OF THE VISA II EXPERIMENT

G. Andonian*, R. Agustsson, A. Murokh, C. Pellegrini, S. Reiche,
J.B. Rosenzweig, G. Travish, UCLA, Los Angeles, CA 90095, USA
M. Babzien, I. Ben-Zvi, V. Yakimenko, BNL, Upton, NY 11973, USA
L. Palumbo, C. Vicario, Univ. of Rome, "La Sapienza", Italy

Abstract

VISA II is the follow-up project to the successful Visible to Infrared SASE Amplifier (VISA) experiment at the Accelerator Test Facility (ATF) in Brookhaven National Lab (BNL). This paper will report the motivation for and status of the two main experiments associated with the VISA II program. One goal of VISA II is to perform an experimental study of the physics of a chirped beam SASE FEL at the upgraded facilities of the ATF. This requires a linearization of the transport line to preserve energy chirping of the electron beam at injection. The other planned project is a strong bunch compression experiment, where the electron bunch is compressed in the chicane, and the dispersive beamline transport, allowing studies of deep saturation.

INTRODUCTION

The development of a source of high brightness x-rays is an important instrument for studying structural dynamics at the atomic level. The fundamental time scale for atomic motion is on the order of tens of femtoseconds [1]. A single pass self amplified spontaneous emission (SASE) free electron laser (FEL) has the capability to bring about such short pulse x-ray lasers [2]. One way to achieve such high frequency resolution, is to chirp the radiation pulse, then compress the pulse using diffraction gratings. This would reduce the pulse length to the order of tens of femtoseconds [3]. Radiation pulse chirping can be obtained by injecting a chirped electron bunch into the undulator. Theoretical studies have shown that the coherence time is independent of chirp [4], but have yet to be verified experimentally. Another method to drive an x-ray FEL is to inject a short compressed pulse into the undulator.

EXPERIMENTAL OVERVIEW

Summary of VISA I Results

The succesful VISA I experiment was designed to investigate physical properties of SASE-FEL as it relates to future LCLS operation. Saturation was achieved at 840 nm with a SASE power gain length of 17.9 cm and total gain of 10^8. A novel bunch compression mechanism was developed during the VISA I experiment. This scheme utilized second order momentum error effects in the dispersive line. The proper choice of linac phase detuning and

___
* gerard@physics.ucla.edu

quadrupole settings yielded strong longitudinal bunch compression, and as a result, much higher current [5].

Another achievement of the VISA I experiment, was the development and deployment of a start-to-end (cathode to undulator) computational model. The computational effort involved employing UCLA-PARMELA for gun and linac calculations (emittance, charge, energy, energy spread), ELEGANT for transport lattice calculations (bunch length, beam size, emittance growth after dispersive line), and GENESIS 1.3 for undulator studies (gain length, saturation, angular wavelength, and spectra). This computational undertaking, compared with the detailed experimental data, yielded new levels of insight into the dynamics of SASE FEL processes. The same numerical tools will continue to be used for VISA II.
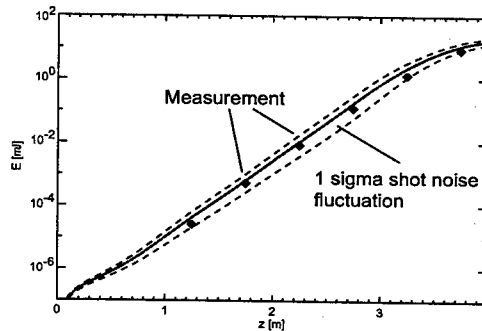
Figure 1: VISA I saturation curve. Measured data is consistent with theoretical calculations.

Experiment Setup

VISA II will encompass a number of hardware changes to investigate the different regimes mentioned above. The undulator and diagnostics will remain unchanged.

Chicane: The chicane compressor consists of four dipole magnets with a nominal field of 0.2 T. The dipoles have a bend radius of 1.2 m and a length of 41 cm. The effective magnetic length is 44.6 cm, with a path length of 41.89 cm. Once the chicane is installed, the electron bunch is expected to compress from 300 μm to less than 30 μm [6]. The current of the bunch is projected to increase from 60 A (VISA I uncompressed running conditions) to 1 kA. Simulations also show that coherent synchrotron radiation

(CSR) may amplify during compression and in the process microbunch the electron beam. Emittance degradation of 4-10 mm mrad is anticipated [7].

The initial experiment to be performed at VISA II is running the FEL with a short compressed beam (current of 1 kA, charge of 200 pC). According to GENESIS 1.3 simulations, the short compressed bunch should produce extremely high gain. Saturation is expected by the 3rd meter of the 4 meter long undulator (Fig.2). With additional compression, the slippage can be so severe that the gain may not be purely exponential.
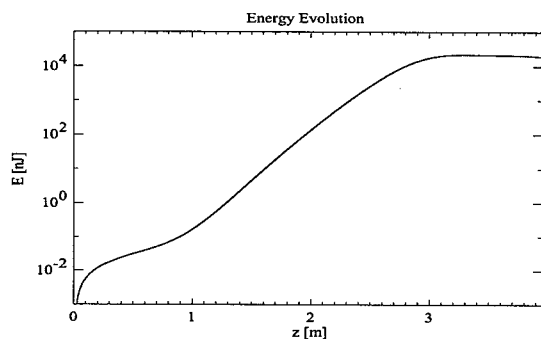
Figure 2: GENESIS 1.3 simulation of the energy evolution within the undulator. Saturation is reached at approximately 3 m, well before the undulator end.

Linearization of Transport: In order to maintain a chirped electron bunch from the linac to the undulator, the transport to beamline 3 must be linearized. Linearization requires a stronger control of the dispersion along the dog leg. The addition of sextupoles will allow VISA II to run in two distinct modes. By diminishing the T_{566}, the linear phase space chirp is maintained, as is illustrated by the ELEGANT simulations in Fig.3. The sextupoles are 5 cm long and have a calculated gradient of 22.0 T/(m^{2}A) [8].

Undulator: The VISA undulator is 4 m long and divided into 4 sections. There are a total of 220, 1.8 cm long periods. The on-axis peak field is about 0.75 T. The undulator has a superimposed quadrupole focusing channel (FODO lattice) throughout the length of the undulator. The electron beam walk-off tolerance inside the undulator is approximately 80 μm [9]. The quadrupoles were aligned so that the beam trajectory would meet this tolerance . Undulator alignment is conducted via a CCD based optical monitoring system [10].

There are eight intra-undulator diagnostics located 50 cm apart. Each port has a double-sided silicon mirror which leases the ability to measure both SASE radiation properties, by reflecting FEL light into the diagnostics, as well as electron beam position and envelope outline, by generating optical transition radiation (OTR) for the beam imaging diagnostics [11].
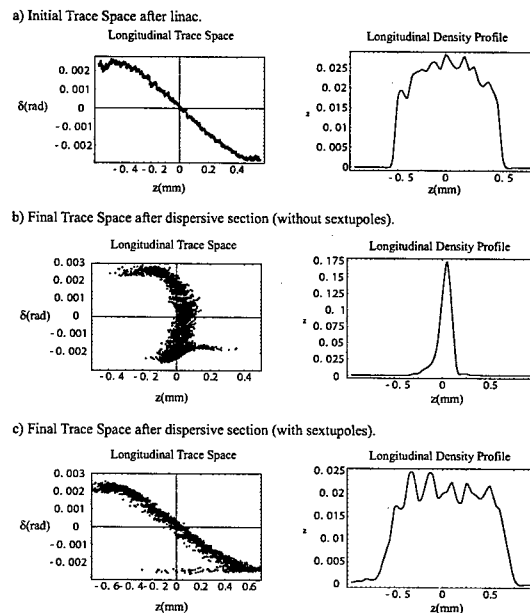
Figure 3: ELEGANT simulations of electron beam linear chirp preservation through dispersive line. VISA II can be run in two distinct modes: the compressed case, due to the natural R_{56} of the dog leg, and the energy chirped case, where the sextupoles are turned on.

CHIRPED PULSE MEASUREMENTS

Conditioning

By accelerating the electron beam at an off-crest RF phase, a linear chirp (energy spread - longitudinal position correlation) may be imparted onto the beam. Once sextupoles are utilized the T_{566} component of the transfer matrix can be minimized, allowing control of the linear chirp throughout the beamline. The input linear chirped phase space will be preserved and injected into the undulator. This will allow control of the frequency distribution of the generated radiation pulse. The natural negative R_{56}, discovered from the original VISA runs, stretches the pulse slightly. However, altered compressor settings can make the R_{56} positive. Experimental and computational analyses will determine various modes of operation, balancing compression, linearity, and degree of chirping. The initial measurement for VISA will be to run with the largest possible chirp obtainable, without degrading the FEL gain. Preliminary calculations show that this chirp is on the order of 4-5 %. In addition, the beam may be partially precompressed in the chicane, without removing its chirp, to raise the current in a chirped beam expertiment.

Simulation Results

Numerical studies have been conducted on the spectral response of a driving initially chirped electron beam. Simulations show that total energy at saturation is not affected

by chirping up to 4 % (no gain degradation), even for the case of the 60A (uncompressed) beam. It is necessary to exceed 2 % chirp to overcome the intrinsic frequency width of the FEL amplification in order to achieve a measureable correlation between frequency and time.
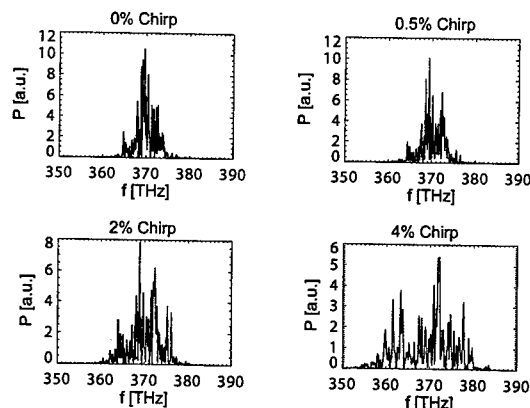
Figure 4: GENESIS 1.3 simulations of chirped pulse radiation spectrum (frequency domain) for varying degrees of chirping.

Proposed Measurements

The goals of the chirped beam experiment are to determine the gain length as a function of degree of chirping, and to measure the spectral correlation of the output beam. Theoretical studies show that the effects of the electron beam chirp on FEL is small if the resonant radiation frequency change within a cooperation length is small [4]. These results must be verified experimentally. FEL properties to be measured include saturation power, intenstiy fluctuations, and spectral and angular properties of the chirped radiation.

The wavelength chirping of SASE radiation can be used to make pulses on the order of 100 fs. Using a monochromator and double diffraction grating the radiated output can be compressed. This encompasses a few experimental complications. Creating short pulses on the order of 10 fs from pulses already on the order of 10 ps, is an experimental challenge. Measuring such short pulses requires reliance on nonlinear effects in materials.

The proposed scheme to measure this output is named Frequency Resolved Optical Grating (FROG) [12]. The signal is split and recombined to overlap at different times in a nonlinear, frequency doubling, crystal. The doubled output light has a time dispersed axis and is sent to a spectrometer which disperses frequency in the other dimension. Standard algortihms are used to reconstruct amplitude and phase informatin of the input radiation. A simplified FROG device (Grenouille), using a thick nonlinear crystal and a Fresnel biprism, yields a simplified single-shot, ultrashort-pulse intensity-and-phase reconstruction device [13]. The measurement of the epxected pulses will be simplified in operation by the use of Grenouille.

EXPERIMENTAL STATUS

The VISA II program is in its initial stage. The Particle Beam Physics Lab (PBPL) of UCLA has developed and is presently installing a chicane compressor for the ATF at BNL. The chicane magnets, vacuum vessel, and coherent synchrotron radiation (CSR) diagnostics have been developed at UCLA. The hardware installation of the chicane is nearing completion. The improvements to the diagnostics on the dispersive line and the mathcing line are underway. The addition of sextupoles will take place in the early summer of 2003, coincident with the chicane dipole installation.

Initial runs for VISA II are dedicated to bringing the beam up to successful operating conditions. The upgraded facilities of the ATF require revising the original run settings; technicalities must be addressed to reestablish high gain lasing conditions. Preparatory runs have yielded successful characterization of beam envelope evolution, and emittance measurements, utilizing the quadrupole scanning technique, are imminent. Optical methods have been used to measure the undulator alignment, however, they have been indeterminate as to whether undulator alignment is adequate. Undulator electron beam trajectory measurements are forthcoming and will be used to confirm alignment before any attempts to re-align are undertaken.

ACKNOWLEDGEMENT

REFERENCES

[1] G.K. Shenoy, J. Stoehr (eds.), LCLS - The First Experiments, Stanford (2000)

[2] C. Schroeder et al., J. Opt. Soc. Am. B 19 (8), 1782-1789 (2002).

[3] C. Pellegrini, Nucl. Inst. & Meth. Phys. Res. A 445, 124-127 (2000)

[4] S. Krinsky and Z. Huang, Phys. Rev. STAB 6, 050702 (2003)

[5] A. Murokh et al., Phys. Rev. E 67 (2003)

[6] R. Agustsson, M.S. Thesis, UCLA (2003)

[7] R. Agustsson, private communications.

[8] J. England, private communications.

[9] P. Emma and H.D. Nuhn, FEL Proc. 1998, II, 35

[10] A. Tremaine, A. Murokh, and X. Wang, BNL Rep. No. 68170 (2001)

[11] A. Murokh, Ph.D. thesis, UCLA, 2002

[12] R. Trebino et al., Rev. Sci. Inst. 68, 3277-3295 (1997).

[13] P. O'Shea et al., Opt. Lett., 26, 932-4 (2001).

THE FEL PROGRAM AT THE PEGASUS INJECTOR

S. Reiche, G. Andonian, P. Frigola, J.B. Rosenzweig, S. Telfer, and G. Travish
UCLA Department of Physics & Astronomy, Los Angeles, CA 90095-1547, USA

Abstract

The PEGASUS photo injector at UCLA can produce a photo-electron beam with a normalized emittance of 2 mm·mrad at an energy of 12-15 MeV, capable of driving a Free-Electron Laser in the mid IR regime. The FEL program, associated with the PEGASUS injector and presented here, is based on a Self-Amplifying Spontaneous Emission (SASE) FEL. The studies focus on increasing the efficiency of an FEL by novel undulator design and compensation of diffraction effects, using waveguides of millimeter size. In this presentation we also discuss the possibility of the PEGASUS FEL as a THz user facility.

INTRODUCTION

The PEGASUS Photo injector [1] is a novel standing-wave S-band structure for generating photo electrons and to accelerate them to 12 – 17 MeV. The high-brightness beam is suitable to drive a Self-Amplifying Spontaneous Radiation Free-Electron Laser (SASE FEL) [2] down to a wavelength of 10 μm without further acceleration.

The injector can also deliver the required beam to drive a Thomson backscattering source [3]: The mechanism is closely related to undulator radiation which is the basic radiation process of a Free-Electron Laser. Although the Thomson backscattering process does not amplify its own radiation as a SASE FEL does, the resonant wavelength lies in the X-ray regime, making this radiation source attractive to the scientific community.

We present here the possible applications for the PEGASUS injector, oriented towards light sources, spanning a range of THz radiation to X-rays. Other application are reported elsewhere [4].

INFRARED FREE-ELECTRON LASER

The FEL program is initiated with an existing undulator, previously used to demonstrate the first SASE FEL amplification of more than 5 orders of magnitude [5]. The 2 m long undulator consists of 98 periods with a period length of 2.05 cm. The configuration is planar and additional magnets supply equal focusing in both plane. The β-function is 22 cm.

With the expected beam parameters of the PEGASUS injector (Tab. 1, [6]) the SASE FEL resonates at 13 μm. Because the electron beam size is 170 μm and only one order of magnitude larger than the radiation wavelength, the diffraction during the FEL amplification is strong and lengthens the saturation length to 3 m.

Table 1: Electron beam parameters of the PEGASUS Injector

Energy	12 – 18 MeV
Energy Spread	0.15%
Emittance	4 mm·mrad
Charge	1 nC
Bunch Length	1 mm
Repetition Rate	1 – 5 Hz

Although we do not expect saturation, the radiation can be used to calibrate the IR diagnostics and to compare the measured performances with the predicted ones, based on start-end simulations with the codes PARMELA [7] and Genesis 1.3 [8].

The degradation due to diffraction can be overcome by embedding an IR waveguide within the undulator. The waveguide is a glass or silicon tube with a metal and dielectric layer deposited on the surface. Using silver and silver-iodide leyers of a few hundred nanometer each, the transmission is optimized for the wavelength region of interest. Measurements have shown losses of less than 2 dB over 2 m [9] and these hollow glass waveguides have already been successfully used for transportation of IR light [10].

The saturation length is reduced to 2 m with a 1 mm bore diameter of the hollow glass waveguide. Fig. 1 shows the performances for different bore diameters. The case for 5 mm differs only by a few percent from the free space case, excluding any waveguide. A 1mm diameter gives enough matching tolerance for the electron beam to the undulator focusing structure to avoid particle losses. The performance is insensitive to beam offsets or larger emittances. Although the waveguide is overmoded, the FEL eigenmode consists predominately of the fundamental TE mode of the empty waveguide.

THZ FREE-ELECTRON LASER

THz radiation sources are of particular interest to the science community [11] for various solid state, cluster and molecular studies. A tunable source such as a Free-Electron Laser is highly desirable. The undulator parameters are modified to increase the radiation wavelength without changing the energy of the driving electron beam. In order to radiate at 100 μm, which corresponds to a frequency of 3 THz, the period is increased to 5 cm and the undulator parameter to 1.5 at a beam energy of 15 MeV. A helical
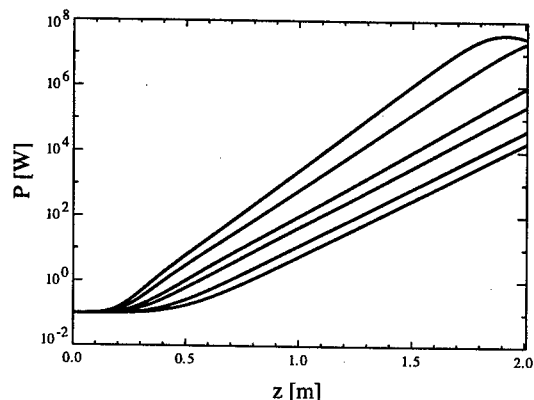
Figure 1: FEL performance of the PEGASUS IR waveguide FEL. The corresponding bore diameters are from the top: 0.8 mm, 1 mm, 1.5 mm, 2 mm, 3.5 mm, and 5 mm.

undulator has the advantage of increasing the output power and reducing the saturation length as compared to a planar undulator. The latter helps to reduce the impact of diffraction, which is even stronger than in the case of the IR FEL. In the gain guiding mode of the linear regime of the FEL the equilibrium radiation size is 2 mm. The impact of the strong diffraction yields an FEL performance very similar to the IR FEL, except for the wavelength. Three meters are required to reach saturation. Fig. 2 shows the radiation and current profile at saturation, which occurs at 3.5 m and the total energy of the radiation pulse is 120 μJ.

Although we have not studied the problem in detail yet, it is expected that an embedded waveguide will improve the performance of the FEL as is the case for the IR FEL. The aspect ratio between wavelength and bore diameter is smaller and the waveguide is less overmoded. This reduces the coupling to higher waveguide modes because the phase velocity is different and, thus, they are less synchronized to the electron beam.
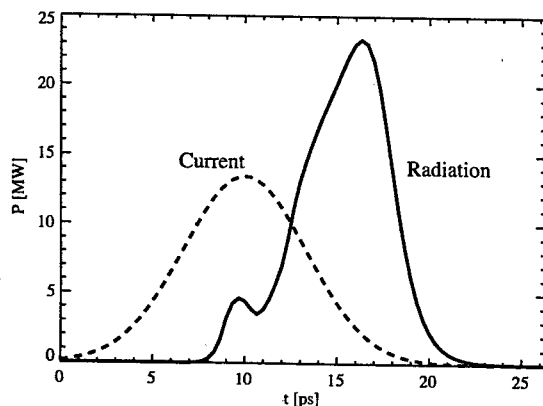
Figure 2: Radiation and current profile (solid and dashed line, respectively) at saturation for a THz SASE FEL.

THOMSON BACKSCATTERING X-RAY SOURCE

Thomson Backscattering is an alternative to multi-GeV electron beams and long undulators for a tunable X-ray radiation source. The necessary electron beam energy is between 10-50 MeV for a wavelength of 800 nm of the scattering laser. Despite the fact that the process lacks the collective instability of the FEL and emits on the spontaneous radiation level, the reduced size of the driving linear accelerator and the existence of TW drive laser makes this radiation source attractive. The obtained pulse length are comparable to those of an Free-Electron Laser such as LCLS [12] or TESLA FEL [13].

With the high-brightness electron source of the PEGASUS injector, a Thomson backscattering source becomes feasible. A schematic of the beam line and the drive laser is shown in Fig. 3. There are two different method of operation. With an incident angle of 90 degrees the pulse length of the X-ray pulse is determined by the shorter length of the electron or laser pulse: for a reasonable focused $50 - 100$ fs Ti:S laser it is around 100-200 fs. However the overlap of the laser pulse with the electron beam is minimal, resulting in a rather low photon flux of about $2 \ 1 \cdot 10^5$ photons per pulse, based on the parameter given in Tab. 2.

A head-on collision maximizes the overlap between the electron beam and the laser pulse. The flux is three order of magnitude higher ($1 \ 0 \cdot 10^8$) but the X-ray pulse is stretched to 3 ps. In this case the wavelength is 2.2 Å – twice as short as for the 90 degree incident case.

We are considering a set-up which allows the operation of both 90 and 180 degree incident angle. The required instrumentation for X-ray transport and diagnostic has to be further studied.
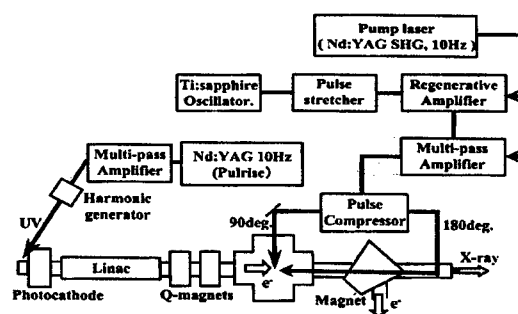
Figure 3: Schematic layout of a Thomson backscattering X-ray source at the PEGASUS injector.

CONCLUSION

With the compact design of a high-brightness photo electron beam source the applications of Free-Electron Lasers and the related Thomson backscattering process become feasible and attractive. In particular the small scale of the

Table 2: Expected performance of the Thomson Backscattering X-ray source at the PEGASUS injector.

Incident Angle	90°	180°
Wavelength	4.4 Å	2.2 Å
Pulse Length	250 fs	3 ps
Photon Flux	$2.1 \cdot 10^5$/pulse	$1.0 \cdot 10^8$/pulse
Opening Angle	33 mrad	33 mrad

required space is appealing as a tunable radiation source "on location" for a wide class of science experiments instead of the remote location of light sources such as APS, ESRF or Spring 8 [14].

The prospect of a light source for the PEGASUS lab can be enhanced with the combination of the Thomson backscattering experiment with the THz SASE FEL, both attractive to the science community. The backscattering process does not degrade the beam quality of the electron beam and, thus, allows for a downstream operation of the THz FEL. A delay line of the X-ray pulse is required for pump-probe experiments with the THz pulse. It is desirable to use a variable-gap undulator for the THz FEL, so that an independent tuning of the X-ray and THz wavelength is possible.

REFERENCES

[1] X. Ding et al., Proc. of the Particle Accelerator Conference, New York, 1999

[2] R. Bonifacio, C. Pellegrini, and L.M. Narducci, Opt. Comm. **50** (1984) 373; A.M. Kondradenko and E.L. Saldin, Part. Accel. **10** (1980) 207

[3] K.-J. Kim, S. Chattopadhyay, C.V. Shank, Nucl. Instr. & Meth. **A341** (1994) 351

[4] G. Andonian et al., Presented at this conference

[5] M. Hogan et al., Phys. Rev. Lett. **81** (1998) 4867

[6] J.B. Rosenzweig et al., Proc. of the Particle Accelerator Conference, New York, 1999

[7] L.M. Young and J.H. Billen, *PARMELA*, LA-UR-96-1835 (2000)

[8] S. Reiche, Nucl. Inst. & Meth. **A 429** (1999) 243

[9] Y. Matsuura et al., Appl. Opt. **34** (1995) 6842

[10] H.S. Pratisto et al., Clinical beam delivery of the Vanderbilt FEL: Design and performance of a hollow waveguide-based handheld probe for neurosurgery, in: *Specialty Fiber for Medical Application*, J. Harrington, A. Katzir (eds), SPIE, Bellingham, (1999)

[11] Proc. of the 27th International Conference on Infrared and Millimeter Waves, R. J. Temkin, Ed. (2002)

[12] *Linac Coherent Light Source (LCLS)*, SLAC-R-521, UC-414 (1998)

[13] *TESLA – Technical Design Report*, DESY 2001-011, ECFA 2001-209, TESLA Report 2001-23, TESLA-FEL 2001-05, Deutsches Elektronen Synchrotron, Hamburg, Germany (2001)

[14] V. Litvinenko, *Storage Ring-based Light Sources*, Proc. of the 17th Advanced Beam Dynamics Workshop on Future Light Sources, Argonne, USA, 1999

A NUMERICAL MODEL OF ELECTRON BEAM SHOT NOISE

B. W. J. McNeil, G. R. M. Robb, Department of Physics, University of Strathclyde, Glasgow, UK
M. W. Poole, ASTeC, Daresbury Laboratory, Warrington WA4 4AD, UK

Abstract

A numerical method of simulating electron beam shot noise in free electron lasers is presented. The method uses a quasi-uniform phase space distribution of appropriately charge weighted macroparticles. The statistical properties of the macroparticles are derived directly from the temporal Poisson statistical properties of the real electron distribution. Unlike previous methods, our method does not rely upon any averaging over a resonant radiation period timescale and so more correctly describes the underlying physics. The method also allows shot noise to be modelled self-consistently in un-averaged FEL models which are able to describe sub-wavelength phenomena such as Coherent Spontaneous Emission.

INTRODUCTION

Any computer code that attempts to model Self Amplified Spontaneous Emission in a FEL, or any other electron beam source, should have a valid numerical model of the electron beam shot-noise. In order to model shot-noise, a macroparticle distribution should simulate the statistical properties of the real electron distribution. Many, if not most simulation codes use the algorithm of [1] as the basis of their macroparticle loading algorithm to describe shot-noise. However, this algorithm, although effective, has been derived directly from the statistical properties of an averaged quantity, b, the bunching parameter [2]. This averaging occurs over a resonant radiation period. There has not been, to the authors' knowledge, a contiguous derivation from the statistical properties of the individual electrons in an electron beam to the algorithm of [1]. A noise model derived directly from the properties of the individual electrons would also allow the introduction of shot-noise into FEL models that have not been averaged over a radiation period in a consistent way. Although the method of [1] has been used in unaveraged models such as [3] it cannot be considered consistent to use methods developed from averaged equations in an unaveraged model. The work presented here derives such a macroparticle model directly from a Poisson statistical electron distribution [4].

THE MODEL

The arrival of electrons at the beginning of an interaction region, $z = 0$, is assumed to be a Poisson process. We first discretise time into small intervals of uniform duration Δt so that $t_n = n\Delta t$ where $n = 0, \pm 1, \pm 2, \ldots$ In the notation hereafter subscript n always refers to these discrete times. It will be seen that the time interval Δt is the mean interval between macroparticles introduced to model the real electron distribution. Furthermore, Δt is small with respect to any radiation period to be subsequently modelled i.e. $\Delta t \ll 2\pi/\omega_{max}$.

Consider the arrival of electrons over one such time interval $t_n \leq t < t_{n+1}$. The mean rate of the Poisson process is the rate of electron arrival $\nu_n = I(t_n)/e$ which is assumed constant over the interval Δt. The electron arrival times obey Poisson statistics and the number of electrons, N_n, arriving within the interval Δt is a statistical variable determined by the Poisson distribution:

$$P(N_n) = \frac{\bar{N}_n^{N_n} e^{-\bar{N}_n}}{N_n!} \qquad (1)$$

where $\bar{N}_n = \nu_n \Delta t$, is the expectation for the number of electrons in the interval Δt. It can been shown [5] that the ordered arrival times of the electrons have identical statistical properties to those with unordered arrival times each of which have been distributed within the interval Δt with an identical uniform probability density $p_n = \nu_n/\bar{N}_n = 1/\Delta t$. The statistics of variables distributed with uniform probability density over a finite interval are well known [7], from which we obtain the mean and variance of each of the unordered electron arrival times $t_j, j = 1..N_n$ to be

$$\begin{aligned} \mu_n &= t_n + \Delta t/2 \quad \text{and} \\ \sigma_n^2 &= \Delta t^2/12 \end{aligned} \qquad (2)$$

respectively.

For a total of N_n electrons the mean arrival time is given by

$$\bar{t}_n = \frac{1}{N_n} \sum_{j=1}^{N_n} t_j$$

with expectation and variance of $\bar{t}_n$ easily shown to be

$$\begin{aligned} E(\bar{t}_n) &= \bar{\mu}_n = \mu_n; \quad \text{and} \\ V(\bar{t}_n) &= \bar{\sigma}_n^2 = \frac{\sigma_n^2}{N_n} = \frac{\Delta t^2}{12 N_n} \end{aligned} \qquad (3)$$

respectively.

The distribution of the N_n electrons within the interval $t_n \leq \Delta t \leq t_{n+1}$ may now be modelled by replacing the distribution with a single macroparticle whose statistical properties of charge and temporal distribution equal those of the N_n electrons. This is the physical basis of the model presented here.

The statistical properties of the macroparticle charge are given simply by the Poisson distribution (1). When loading the macroparticles in a numerical simulation code each would be assigned a charge weight of $\quad_n = N_n e$ where e is the charge of an electron and N_n, the macroparticle electron number, would be generated by a Poisson random deviate generator of mean $\bar{N}_n$.

The statistical properties of the macroparticle arrival time may be found by firstly placing the macroparticle at the mean electron distribution arrival time $\bar{\mu}_n$. This mean arrival time then has added to it an independent random variable $\quad$ with uniform probability distribution over the interval $[-\ t/2,\ t/2]$. The interval t is chosen so that the variance in the macroparticle arrival time is equal to that of the real electron distribution (3). Similarly to relation (2) the variance for the macroparticle arrival time is $t^2/12$. Equating this macroparticle variance to that of the real electron distribution (3) the following relation for t is obtained

$$t = \frac{\Delta t}{\sqrt{N_n}} \approx \frac{\Delta t}{\sqrt{\bar{N}_n}} \tag{4}$$

where the latter approximation may be used when $\bar{N}_n \gg 1$.

An electron pulse defined by a mean current $I(z,t)$ may be modelled to include the effects of shot-noise by assigning macroparticles, with charge and arrival time as described above, over many such consecutive time intervals defined by t_n. The macroparticle arrival times describing the complete electron pulse may then be written as

$$t_j = \bar{t}_j + \ _j, \quad j = 1..N_m \tag{5}$$

where N_m is the total number of macroparticles and the $j = 1$ macroparticle arrives in the nth time interval so that $\bar{t}_j = t_n + (j - 1/2)\Delta t$. For consistency, the Poisson variate N_n, the electron number for the jth macroparticle, is now written N_j.

It is important to note that the electron distribution and its statistics have been modelled by the macroparticles without reference to any external lengths or timescales such as a resonant radiation frequency or its harmonics. In this sense this analysis is self-consistent.

BUNCHING STATISTICS IN 1-D

The following scaled form of the 1-D wave equation describing the FEL interaction may be derived:

$$\left(\frac{}{\bar{z}} + \frac{}{\bar{z}_1}\right) \ (\bar{z}, \bar{z}_1) = \frac{1}{\bar{n}_{p\parallel}} \sum_{j=1}^{N} \exp\left(-\frac{\bar{z}_1}{2}\right) \ (\bar{z}_1 - \bar{z}_{1j}). \tag{6}$$

Details of the scaling may be found in [6]. The right hand side of the wave equation is written in terms of the real electron distribution, where N is the total number of electrons in the electron pulse and at the beginning of the interaction region, $z = 0$, so that $\bar{z}_1 = -2\ \omega t$ where $\quad$ is the FEL scaling parameter [2]. Note that the total number of electrons in the electron pulse, N, is itself a Poisson variate of mean $\bar{N}$, the expectation value of the total electron number given by

$$\bar{N} = \int_{-\infty}^{\infty} \frac{I(t)}{e} \ t. \tag{7}$$

The Dirac delta function transforms to real units as

$$(\bar{z}_1 - \bar{z}_{1j}) = \frac{(\omega t - \omega t_j)}{2}. \tag{8}$$

and the electron distribution may be replaced by a macroparticle distribution as described in the previous section to give the right hand side of the wave equation (6) in terms of the macroparticle distribution

$$\frac{2\pi}{N_{m\lambda}} \sum_{j=1}^{N_m} \frac{N_j}{\bar{N}_{\text{pk}}} e^{i\omega t} \ (\omega t - \omega t_j) \tag{9}$$

where $N_{m\lambda} = 2\pi/\omega\Delta t$ is the number of macroparticles within one radiation period and $\bar{N}_{\text{pk}} = I_{\text{pk}}\Delta t/e$ is the expectation of the macroparticle electron number at the peak of the electron pulse current, I_{pk}.

When averaged over a radiation period the right hand side of the wave equation yields a quantity known as the 'bunching parameter' [2]. If the macroparticle model is valid then the statistics of the bunching parameter must be the same for the macroparticle distribution as for a real electron distribution, and we now test for this.

Averaging (9) by integrating over one radiation period centred at time t yields an expression for the localised macroparticle bunching parameter:

$$b(t) = \frac{1}{N_{m\lambda}} \sum_{j=1}^{N_{m\lambda}} \frac{N_j}{\bar{N}_{\text{pk}}} e^{i\omega\tau_j} e^{i\omega\bar{t}_j}. \tag{10}$$

The delta function has extracted those macroparticles within the interval (we retain j as the index for simplicity) and we have used relation (5).

The expectation of the bunching parameter (10) is then given as

$$E(b) = \frac{1}{N_{m\lambda}} \sum_{j=1}^{N_{m\lambda}} E_{N_j} \left(\frac{N_j}{\bar{N}_{\text{pk}}} E_{N_j|\tau_j} \left(e^{i\omega\tau_j}\right)\right) e^{i\omega\bar{t}_j} \tag{11}$$

where $E_{N_j}(...)$ signifies the expectation value with respect to the macroparticle electron number N_j and $E_{N_j|\tau_j}(...)$ signifies the expectation value with respect to the randomness of the macroparticle arrival time $\quad_j$ for a given value N_j. The latter expectation is obtained by averaging in

951

τ_j over the interval $[-\delta t/2, \delta t/2]$ from which using relation (4) the following result is obtained:

$$E_{\tau_j|N_j}\left(e^{i\omega\tau_j}\right) = \frac{\sqrt{N_j N_{m\lambda}}}{\pi}\sin\left(\frac{\pi}{\sqrt{N_j N_{m\lambda}}}\right). \quad (12)$$

Substituting for (12) into (11), using the result that for a Poisson distribution $E_{N_j}(N_j) = \bar{N}_j$ and assuming the usually easily satisfied condition $\sqrt{N_j N_{m\lambda}} \gg 1$ so that

$$\sin\left(\frac{\pi}{\sqrt{N_j N_{m\lambda}}}\right) \approx \frac{\pi}{\sqrt{N_j N_{m\lambda}}},$$

the expression for the expectation of the bunching is

$$E(b) = \frac{1}{N_{m\lambda}}\sum_{j=1}^{N_{m\lambda}}\frac{\bar{N}_j}{\bar{N}_{\text{pk}}}e^{i\omega\bar{t}_j}. \quad (13)$$

A similar but more lengthy analysis for the expectation of $|b|^2$ may also be carried out to obtain

$$E\left(|b|^2\right) = \frac{1}{N_{m\lambda}^2 \bar{N}_{\text{pk}}^2}\sum_{j=1}^{N_{m\lambda}}\bar{N}_j + |E(b)|^2 \quad (14)$$

from which an expression for the variance of the bunching, $V(b) = E(|b|^2) - |E(b)|^2$, is obtained.

It can be seen from (13) for the expression for $E(b)$ that if the current is not uniform over the radiation period, i.e. $\bar{N}_j \neq$ constant $\forall j$, then $E(b)$ will be non zero. Such non-zero bunching is caused by a current gradient and is the source of Coherent Spontaneous Emission [6].

In the limit of a uniform current beam we may set $\bar{N}_j = \bar{N}_{\text{pk}} \forall j$, $E(b) = 0$ and there is no CSE. In this case $\bar{N}_{m\lambda}\bar{N}_{\text{pk}} = \bar{N}_\lambda$, the expectation of the total number of electrons in the radiation period, and we obtain from (14) the result that $E(|b|^2) = 1/\bar{N}_\lambda$, which for the single radiation period under consideration here, is in agreement with previous analysis of averaged Poisson statistical models [4].

HIGHER DIMENSIONS

In the above analysis, electron beam properties such as energy and transverse momentum spread were neglected. In order to describe these effects and include the effects of shot-noise, the above model must be extended to a multi-dimensional electron phase space.

Phase space is first discretised into elemental 'volumes' by discretising along each phase space ordinate in a method similar to that carried out for time in the previous section. The populating by electrons of each phase space 'volume element' at $z = 0$ is then assumed to be a Poisson process with each element being populated at a local Poisson rate given by

$$\nu(\alpha, t) = \frac{I(t)}{e}(\alpha) \quad (15)$$

where α is a generalised phase space coordinate (e.g. $\alpha = (\mathbf{r}_\perp, \mathbf{p})$, the transverse coordinate and the momentum respectively) and (α) is a normalised distribution function. Note that, in general, the distribution function itself may have a temporal dependence via α.

The same algorithm as was used for allocating the temporal noise of the previous section is now used for each phase space coordinate of the macroparticles. The macroparticles are placed at the 'centre' of each phase space volume element and have added to each of their phase space coordinates an independent random variable of uniform probability distribution. This random variable is equivalent to the τ_j of the previous section and, for a generalised ordinate k, will have a range

$$\left[-\frac{\Delta_k}{2\sqrt{\bar{N}_j}}, \frac{\Delta_k}{2\sqrt{\bar{N}_j}}\right] \quad (16)$$

where Δ_k is the discretisation interval and from (15)

$$\bar{N}_j = \nu(\alpha, t)\Delta V_\alpha \Delta t = \frac{I(t)}{e}(\alpha)\Delta V_\alpha \Delta t \quad (17)$$

where $\Delta V_\alpha = \prod_k (\Delta_k)$ is the elemental phase space volume. Each macroparticle will also have assigned to it a Poisson random variate electron number of mean $\bar{N}_j$.

CONCLUSIONS

The derivation of the shot-noise model presented here is perhaps more physically intuitive, and therefore appealing, than those used in current FEL simulation codes: The macroparticle properties of arrival time *and* charge are derived directly from the intrinsic Poisson statistical properties of the individual electron arrival times at the beginning of the interaction region. The model is therefore independent of any external factors such as a resonant radiation period. The algorithm has been tested successfully in a numerical code and these results will be presented in a forthcoming publication.

REFERENCES

[1] C. Penman and B.W.J. McNeil, Opt. Commun. **90**, 82, (1992)

[2] R. Bonifacio, C. Pelligrini and L.M. Narducci, Opt. Commun. **50**, 373, (1984)

[3] B.W.J. McNeil and G.R.M. Robb, Phys. Rev. E **65**, 046503, (2002); **66**, 059902(E), (2002)

[4] B.W.J. McNeil and G.R.M. Robb, J. Phys. D **30**, 567, (1997); **31**, 371(E), (1998)

[5] W.B. Davenport *Probability and Random Processes* (London: McGraw-Hill, 1970)

[6] B.W.J. McNeil, G.R.M. Robb and D.A. Jaroszynski, Opt. Commun. **165**, 65, (1999)

[7] John E. Freund *Mathematical Statistics* (2nd Edition), (London: Prentice/Hall, 1972)

AN IMPROVED 1-D MODEL FOR ULTRA HIGH POWER RADIATION PULSE PROPAGATION IN THE HELICAL WIGGLER FREE ELECTRON LASER

B. W. J. McNeil, G. R. M. Robb, Department of Physics, University of Strathclyde, Glasgow, UK
M. W. Poole, ASTeC, Daresbury Laboratory, Warrington WA4 4AD, UK

Abstract

A one dimensional model of a helical wiggler Free Electron Laser is presented that does not average the Maxwell-Lorentz equations describing the interaction between electrons, wiggler and radiation fields. Furthermore, no relativistic approximations in the equations governing electron motion are made and transverse motion of the electrons is self-consistently driven by both the wiggler and radiation fields. Numerical solutions of the resultant equations allow for the modelling of radiation pulses with peak powers orders of magnitude greater than the steady state saturation value and with pulse widths significantly less than one radiation period. Preliminary numerical modelling of such pulses was investigated by simulating injection of a suitable high power seed pulse into an FEL amplifier. These studies suggest a possible new regime of operation where sub-period radiation pulses may extract energy from the electrons in a periodic burst mode.

INTRODUCTION

In the non-linear regime of operation Free Electron Lasers can produce very high intensity spikes of radiation. One example of where such spikes arise is in FEL superradiance where a self-similar spike may grow and propagate through the electron pulse [1]. However, it is as yet unknown either analytically or through numerical simulation whether or how such spikes saturate and the self-similar solution breaks down. In this paper we present a model that should allow such investigation at least in the 1-D limit. We minimize any assumptions. In particular, none are made with respect to the relative strengths of the wiggler and radiation fields, and by not performing any average over a wiggler period, sub-period radiation evolution is included. Furthermore, no assumptions are made regarding the efficiency of energy exchange between electrons and radiation. While not answering the question regarding spike saturation our preliminary results nevertheless demonstrate some potentially interesting phenomena.

THE MODEL

The physics of the FEL in the 1-D limit may be described by the coupled Maxwell/Lorentz equations:

$$\left(\frac{\partial^2}{\partial z^2} - \frac{1}{c^2}\frac{\partial^2}{\partial t^2} \right) \mathbf{E}(z,t) = \mu_0 \frac{\partial \mathbf{J}_\perp(z,t)}{\partial t} \quad (1)$$

$$\frac{d\mathbf{p}_j}{dt} = -e\left(\mathbf{E}(z_j,t) + \frac{\mathbf{p}_j}{\gamma_j m} \times \mathbf{B}(z_j,t) \right) \quad (2)$$

where $j = 1..N$, the total number of electrons, and the transverse current density may be written

$$\mathbf{J}_\perp(z,t) = -\frac{e}{m}\sum_{j=1}^{N} \frac{\mathbf{p}_{\perp j}}{\gamma_j} \delta\left(\mathbf{r} - \mathbf{r}_j(t)\right). \quad (3)$$

The wiggler and radiation electric field are assumed to be

$$\mathbf{B}_w(z) = \frac{B_w}{\sqrt{2}}\left(\hat{\mathbf{e}}\, e^{-ik_w z} + c.c. \right) \quad (4)$$

$$\mathbf{E}(z,t) = \frac{1}{\sqrt{2}}\left(\hat{\mathbf{e}}\, \mathcal{E}(z,t)e^{i(kz-\omega t)} + c.c. \right), \quad (5)$$

where $\hat{\mathbf{e}} = (\hat{\mathbf{x}} + i\hat{\mathbf{y}})/\sqrt{2}$. The magnetic component of the radiation field $\mathbf{B}(z,t)$ required in the Lorentz equation (2) was calculated from the Maxwell equation $\nabla \times \mathbf{E} = -\partial\mathbf{B}/\partial t$. In performing this calculation for $\mathbf{B}$ the independent variables (z,t) are transformed to their scaled form $(\bar{z}, \bar{z}_1)$ [2] which will be used in the final scaled equations. Then under the assumption that:

$$\left| \left(\frac{\partial}{\partial \bar{z}} + \frac{\partial}{\partial \bar{z}_1} \right) E_{x,y} \right| \ll \left| \frac{\bar{\beta}_z}{1-\bar{\beta}_z}\frac{\partial}{\partial \bar{z}_1}E_{x,y} \right|, \quad (6)$$

where $c\bar{\beta}_z$ is the initial mean scaled z component of the electron velocity, the cartesian components of the radiation magnetic field $B_{x,y} \approx \mp E_{y,x}/c$ yielding

$$\mathbf{B}(z,t) = \frac{-i}{\sqrt{2}c}\left(\hat{\mathbf{e}}\, \mathcal{E}(z,t)e^{i(kz-\omega t)} - c.c. \right). \quad (7)$$

By introducing the notation $p_\perp = p_x - ip_y$ (so that $\mathbf{p}_j \cdot \hat{\mathbf{e}}^* = p_\perp/\sqrt{2}$), taking the scalar product of the wave equation (1) with $\hat{\mathbf{e}}^*$, integrating over the common electron/radiation transverse area σ and making the assumption (6), the second order wave equation (1) reduces to:

$$\left(\frac{\partial}{\partial \bar{z}} + \frac{\partial}{\partial \bar{z}_1} \right) \mathcal{E}(z,t) = \frac{e}{2\sigma\epsilon_0 mc}\frac{\bar{\beta}_z}{1-\bar{\beta}_z} \quad \times$$

$$\sum_{j=1}^{N} e^{-i\left(\frac{\bar{z}_1 - \bar{z}}{2\rho}\right)} \frac{p_{\perp j}}{\gamma_j \beta_{zj}} \delta(\bar{z}_1 - \bar{z}_{1j}(\bar{z})) \qquad (8)$$

Substituting the fields (4,5,7) into the Lorentz equation (2), taking the scalar product with $\hat{e}^*$ and changing the independent variable from t to $\bar{z}$, the following equation for the perpendicular momentum is obtained

$$\frac{dp_{\perp j}}{d\bar{z}} = \frac{e}{2_w} \left(iB_w e^{-i\frac{\bar{z}}{2\rho}} - \frac{1 - \beta_{zj}}{\beta_{zj}} \frac{\mathcal{E}}{c} e^{i\left(\frac{\bar{z}_{1j} - \bar{z}}{2\rho}\right)} \right).$$
$$(9)$$

Similarly, the z component of the Lorentz equation (2) yields

$$\frac{d\beta_{zj}}{d\bar{z}} = -\frac{e}{4m^2c^3 {}_w \gamma_j^2} \times$$

$$\left[\left(\frac{1 - \beta_{zj}}{\beta_{zj}} \right) \left(p_{\perp j}^* \mathcal{E} e^{i\left(\frac{\bar{z}_{1j} - \bar{z}}{2\rho}\right)} + c.c. \right) - \right.$$

$$\left. icB_w \left(p_{\perp j} e^{i\frac{\bar{z}}{2\rho}} - c.c. \right) \right] \qquad (10)$$

We now introduce the following notation:

$$\epsilon_j = \frac{1 - \beta_{zj}}{\beta_{zj}}, \quad \epsilon = \frac{1 - \bar{\beta}_z}{\bar{\beta}_z}, \quad = \left(\frac{2 \gamma_r}{w} \right)^2,$$

$$\bar{p}_\perp = \frac{p_\perp}{mc}, \quad = \frac{e\mathcal{E}}{mc_{p\sqrt{\gamma_r}}} \qquad (11)$$

which allow the previous equations describing the FEL interaction to be written as:

$$\frac{d\bar{z}_{1j}}{d\bar{z}} = 1 - _j \qquad (12)$$

$$\frac{d_j}{d\bar{z}} = \frac{_w}{4} \frac{_j(\epsilon_j + 2)}{1 + |\bar{p}_{\perp j}|^2} \left[-i \left(\bar{p}_{\perp j} e^{i\frac{\bar{z}}{2\rho}} - c.c. \right) + \right.$$

$$\left. \epsilon_j \left(\bar{p}_{\perp j}^* \, e^{i\left(\frac{\bar{z}_{1j} - \bar{z}}{2\rho}\right)} + c.c. \right) \right] \qquad (13)$$

$$\frac{d\bar{p}_{\perp j}}{d\bar{z}} = \frac{_w}{2} \left[ie^{-i\frac{\bar{z}}{2\rho}} - \epsilon_j \, e^{i\left(\frac{\bar{z}_{1j} - \bar{z}}{2\rho}\right)} \right] \qquad (14)$$

$$\left(\frac{\partial}{\partial \bar{z}} + \frac{\partial}{\partial \bar{z}_1} \right) (\bar{z}, \bar{z}_1) = \frac{\sqrt{}}{2} \frac{1}{_{p\|}} e^{-i\left(\frac{\bar{z}_1 - \bar{z}}{2\rho}\right)} \times$$

$$\sum_{j=1}^{N} \frac{\bar{p}_{\perp j} \sqrt{\epsilon_j(\epsilon_j + 2)}}{\sqrt{1 + |\bar{p}_{\perp j}|^2}} \, \delta(\bar{z}_1 - \bar{z}_{1j}(\bar{z})). \quad (15)$$

Note that in the previous notation of [2] $_j = 1 - 2 p_j$. These are the working equations used for the following numerical simulations. In deriving these equations, and within the 1-D assumptions, the only approximations that have been made are the neglect of space charge effects and that of (6), equivalent to that made for the planar undulator case as described in more detail in [3]. Hence, very short high power pulse effects may be described where electrons may exchange a significant fraction of their energy in a short timescale. In the limit $(\epsilon, \,) \ll 1$, and assuming a moderate, slowly varying radiation envelope $(\bar{z}, \bar{z}_1) \gg 1$, the working equations may be expanded to first order in $(\epsilon, \,)$ and a little analysis simplifies them to those of [2].
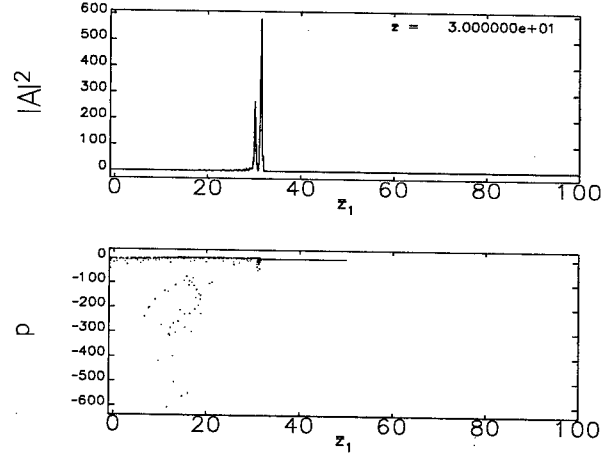
Figure 1: The scaled radiation power $|\,|^2$ and electron phase space $(\bar{z}_{1j}, p_j)$ for a scaled distance through the interaction region of $\bar{z} = 30$.

AN NUMERICAL EXAMPLE

We now present a numerical solution of the equations (12..15) for the case of high power, short pulse injection into a FEL amplifier and compare this with the solution from an averaged model such as [1]. The electron pulse has a rectangular charge profile over the limits $0 \quad \bar{z}_1 \quad _e$ for $_e = 50$ and propagates a scaled length $\bar{z} = 50$ through the wiggler interaction region. The macroparticles are distributed uniformly over the electron pulse interval with initial conditions $p_{\perp j} = -_w$ and $_j = 1 \, \forall j$. Other parameters are $= 1/4$, $\gamma_r = 100$, $_w = 2$. This value of means that at fixed $\bar{z}$ one radiation period corresponds to an interval $\Delta \bar{z}_1 = 1$. A uniform power radiation pulse of two period duration is injected at $\bar{z} = 0$ with scaled field defined by $_0(\bar{z}_1) = 10$ over interval $0 \quad \bar{z}_1 \quad 2$, and zero elsewhere. This corresponds to a power of the order of 10^2 greater than the steady-state scaled power of $|\,|^2_{sat} \approx 1.4$ [1]. The equations (12..15) are solved using the streamline method of Finite Elements as in [3] with third order elements of scaled length in $\bar{z}_1$ of $_{el} = 0.1$, so that there are 10 elements per radiation period. The electron/radiation interaction was artificially switched off ahead of the injected radiation pulse i.e. for $\bar{z}_1 \quad \bar{z} + 2$. This suppressed any radiation evolution and allowed the radiation pulse to propagate into 'fresh' electrons. Although perhaps not strictly physically valid it does allow for a tentative preliminary investigation of the propagation characteristics of short high power pulses and is also similar to radiation pulse evolution over a large number of passes in a FEL oscillator.

In figure 1 we plot the scaled radiation power and the electron phase-space at an intermediate distance $\bar{z} = 30$ through the interaction region. It can be seen that the radiation pulse centre initially at $\bar{z}_1 = 1$ at $\bar{z} = 0$ has propagated through the electron pulse to $\bar{z}_1 \approx \bar{z} = 30$ and with a peak scaled power amplified to $\approx 6\times$ that at the begin-
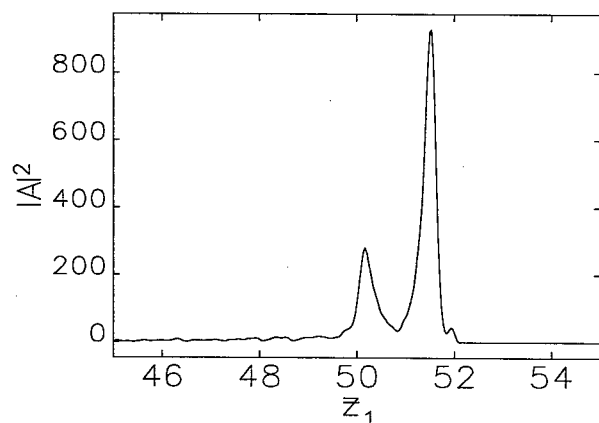
Figure 2: The scaled radiation power $|A|^2$ as a function of scaled pulse position $\bar{z}_1$ for a scaled distance through the interaction region of $\bar{z} = 50$.

Figure 3: The scaled radiation power $|A|^2$ of the averaged model as a function of scaled pulse position $\bar{z}_1$ for a scaled distance through the interaction region of $\bar{z} = 50$.

ning of the interaction. The radiation pulse shape has been transformed from the rectangular shape to that suggesting a superradiant type spike [1]. The electrons react strongly in their interaction with the radiation spike and some may lose a large fraction of their initial energy to it. The electrons centred around $\bar{z}_1 \approx 15$ with large negative p have experienced a rapid deceleration to a mean of ≈ 0.2 of their original energy and rapidly propagate to negative values of $\bar{z}_1$ and out of the main body of the electron pulse. This deceleration and ejection of electrons from the pulse is a periodic feature of the radiation spike/electron interaction and occurs at the wiggler period. Figure 2 shows the scaled radiation power in a narrow window about the radiation spike at the end of the interaction $\bar{z} = 50$. The peak power is now a factor ≈ 10 greater than that at the beginning of the interaction and the pulse width (FWHM) is seen to be ≈ 0.25 of a radiation period. This very short pulse will clearly have different interaction dynamics with the electrons than that usually associated with the FEL interaction with a SVEA field where the transfer of energy from electron to radiation is considered a 'slow' process with one complete radiation wavelength passing over a resonant electron in one wiggler period. For very short radiation pulses the greatest rate of energy transfer between electrons and radiation will clearly be at the radiation spike. If this spike has duration less than a radiation period then it may only extract energy from the electrons during a fractional interval of the wiggler period when $\dot{\gamma} \propto \mathbf{v}_\perp \cdot \mathbf{E} < 0$. This may tentatively explain why, when radiation pulse lengths become shorter than the radiation period, the electrons are seen to loose energy in 'bursts' at the wiggler period as seen in figure 1.

We also include a simulation using an averaged model in the Compton limit [1]. We attempted to model the very short pulses generated with the above parameters by sampling the electron pulse at a sub-wavelength interval. We used 10 sample points per ponderomotive period and averaged about each sample point over a ponderomotive period.
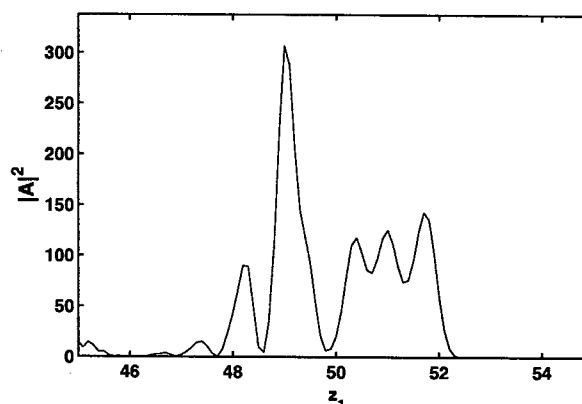
Each interval of $\Delta \bar{z}_1 = 4\pi\rho$ was therefore modelled by 10 overlapping but mutually non-interacting ponderomotive potentials. This averaged model result for the equivalent of the unaveraged model's figure 2 is shown in figure 3. It can be seen that, whereas for the unaveraged case of figure 2 where the original rectangular pulse has been amplified ($50 < \bar{z}_1 < 52$), for the averaged case of figure 3 the original rectangular pulse ($50 < \bar{z}_1 < 52$) appears to have been modulated with the growth of a less intense pulse appearing in its wake ($48 < \bar{z}_1 < 50$). This method of sampling at sub-period intervals appears to allow modelling of sub-period phenomena. However such a model is not physically valid as made clear in the comparison between figures 2 and 3.

CONCLUSIONS

A model has been derived that should allow the analysis and numerical modelling of high power radiation spikes in a FEL. It will be apparent that the numerical simulations presented here are of a preliminary nature and that much work remains to be carried out. Nevertheless, some interesting results have come to light, particularly the burst mode of interaction between the electrons and a sub-period radiation spike.

REFERENCES

[1] R. Bonifacio, N. Piovella and B. W. J. McNeil, Phys. Rev. A, **44**, R3441, (1991) (and refs. therein.)

[2] B.W.J. McNeil, G.R.M. Robb and D.A. Jaroszynski, Opt. Commun. **165**, 65, (1999)

[3] B.W.J. McNeil and G.R.M. Robb, Phys. Rev. E **65**, 046503, (2002); **66**, 059902(E), (2002)

DESIGN STUDY FOR THE RF PHOTOINJECTOR FOR THE MIT-BATES X-RAY LASER*

M. Farkhondeh, W. S. Graves, R. Milner, C. Tschalaer, J. B. van der Laan, F. Wang, A. Zolfaghari, T. Zwart, MIT-Bates Linear Accelerator Center, Middleton MA 01949

Abstract

A multiple cell 1.3 GHz room-temperature photoinjector is under design for the MIT Bates x-ray laser project. The design features include tunable intercavity phase shifts allowing separate phasing of the cells for velocity bunching of the beam in the following drift, and optimization of cell shape for high shunt impedance and low wall power density. Beam dynamics are studied for charges ranging from 0.1 to 1 nC using a model, non-ideal laser profile shape. It is shown that collective effects at the high end of the range cause loss of beam brightness.

INTRODUCTION

MIT is studying the possibility of building an x-ray laser user facility [1] based on a seeded free electron laser. The facility would have up to 30 beamlines and be driven by a superconducting linac based on TESLA structures [2] producing a ~4 GeV electron beam. The range of wavelengths produced will be from 100 to 0.3 nm.

The current design foresees using a room-temperature copper RF photoinjector operating at repetition rates up to 10 kHz, and a cesium telluride cathode. Initial design of the RF structure using SUPERFISH is presented in the section below. Following that section, simulations of beam dynamics with the PARMELA code are presented.

These simulations differ from many others in that we do not assume the nearly ideal drive laser distribution having sub-ps rise and fall times and a flat top. The flattop distribution is ideal because it produces linear space charge forces that do not cause emittance growth or fast timescale modulation of the transverse and longitudinal electron beam properties. When the flattop distribution is used, the injector performance can be optimized by matching the beam onto the invariant envelope [3], which relies on linear space charge forces to perform emittance correction. The drawback to this approach is that the flattop distribution has been difficult to produce in practice, leading to photoinjector performance that falls short of simulation predictions. This is due to local in time modulations of the electron beam properties due to modulation of the initial charge distribution. Fig. 1 shows our model laser profile consisting of a distribution with both fast and slow modulation. The details of the modulation are less important than finding an operating mode for the injector that does not depend on the detailed distribution to meet its performance goals.
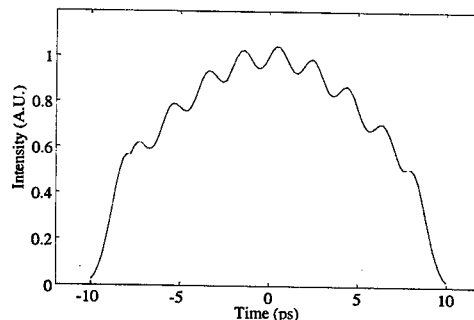
Figure 1: Model laser profile showing 2 ps rise time, and both slow and fast modulations. The fast modulation is +/- 5% amplitude with 2 ps period.
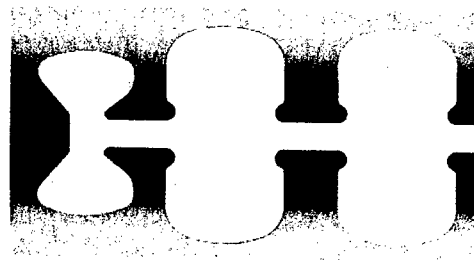
Figure 2: SUPERFISH model of 2 1/2 cell injector with short gap in 1/2 cell

RF STRUCTURE DESIGN

The shape of the 1.3 GHz RF structure is shown in Fig. 2. The cells are uncoupled, and each is independently powered to optimize its separate phasing and peak field. Cell shapes are designed to provide high shunt impedance and low peak wall power density. This is a high repetition rate injector, operating at up to 10 kHz. The important RF design parameters are summarized in Table 1.

Table 1: RF parameters.

Quantity	½ cell	Full cell
Peak gradient	80 MV/m	60 MV/m
Peak power	1.4 MW	2.7 MW
Max wall power density	41 W/cm^2	34 W/cm^2
Q	16140	27870
Rs*Q	151 Ohm	262 Ohm
r/Q	242 Ohm	224 Ohm

0.1 nC   0.5 nC   1 nC
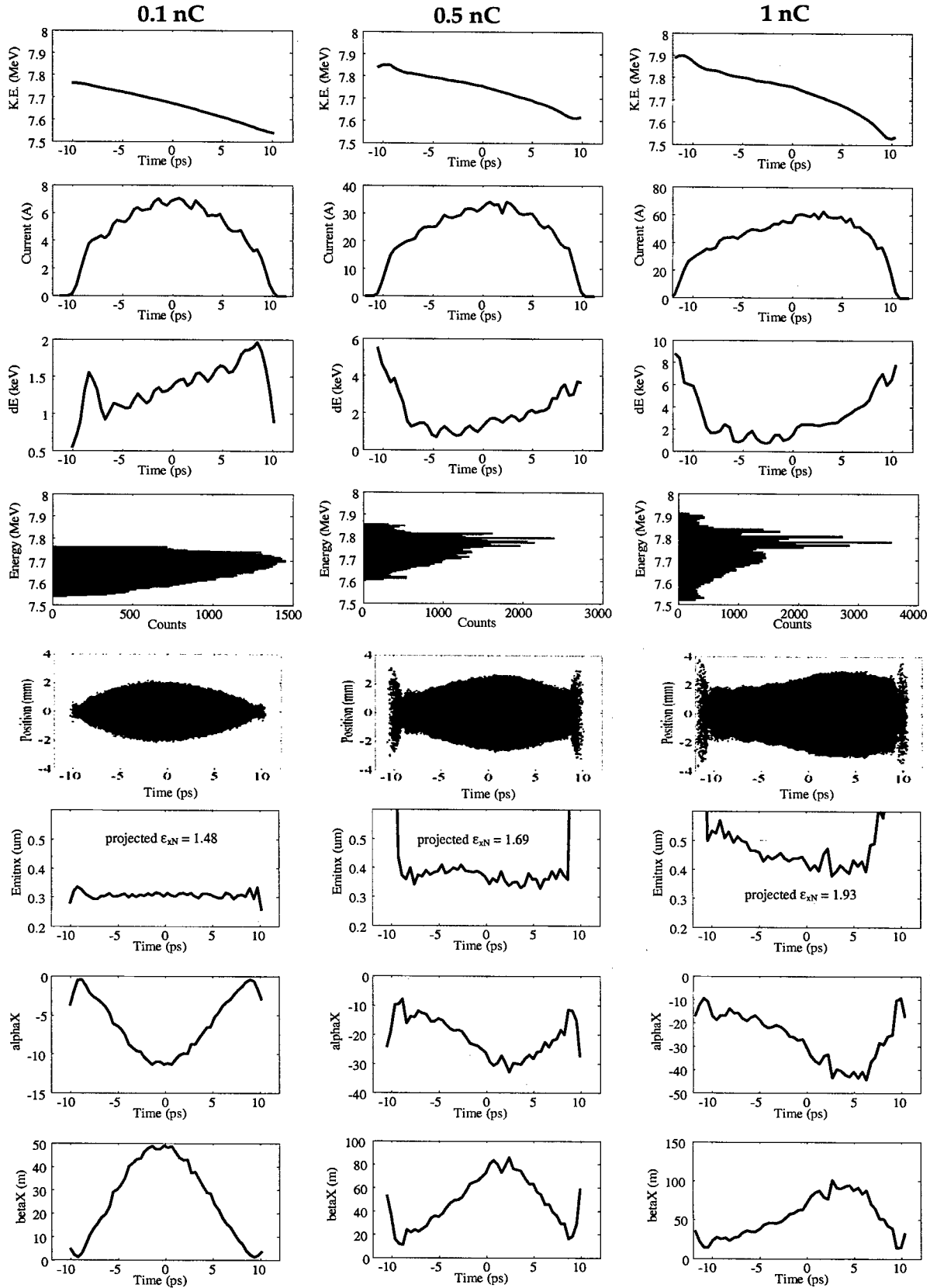
Figure 3: Left, middle, and right columns show electron beam properties vs timeslice for 0.1, 0.5, and 1.0 nC respectively. The slice beam properties evidently deteriorate due to space charge interaction as the charge is increased. Rows 1-4 show longitudinal beam properties, and rows 5-8 show transverse properties.

The power values in Table 1 assume 1% duty factor. The average current is low, approximately 1 μA, so that the structure is not significantly loaded by the beam. The re-entrant cavity design has better RF properties compared with the pillbox design in common use for RF photoinjectors. There has been some concern that the shapes create nonlinear radial fields that could cause emittance growth. In our studies, for beam sizes of ~2 mm, the fields are quite linear and no emittance growth is detected.

BEAM DYNAMICS

The initial beam distribution for each column of fig. 3 is shown in fig. 2. The charge was varied, but the initial pulse length and time profile held constant. The solenoid setting for each charge was adjusted to produce nearly optimum beam properties at the end of a 3 m drift following the injector exit. Each of the figures is of the beam properties at the end of this drift. The PARMELA input file was carefully constructed to vary the space charge mesh and time step to track the (nonrelativistic) birth of the beam from the cathode. Each run used 50k simulation particles with 100 longitudinal mesh points. The transverse distribution was uniform with a hard edge at 0.75 mm radius. Peak cathode gradient was 80 MV/m. The cells were phased for near on-crest acceleration. MATLAB code is used to generate the initial 6D distribution [4], including initial RMS normalized thermal emittance of 0.3 μm.

The linear correlation in energy and time (row 1 of fig. 3) was created by delaying the launch phase to give the bunch head a higher energy. This creates a distribution at the gun exit with symmetry in the Twiss parameters at the head and tail of the bunch (rows 7 and 8). Examining the plots in each column of fig. 3, the evolution of the slice bunch properties from non-space charge dominated case of 0.1 nC (left column) through the space charge influenced case of 1 nC (right column) is apparent. The energy/time plots in row 1 evolve from the highly linear correlation for 0.1 nC to a distorted, stair-stepped distribution for 1 nC. The steps are caused by the 5% fast modulation on the laser profile. Row 2 shows the current profiles. The original laser profile is reproduced accurately in the low charge case, but space charge has smoothed the 1 nC profile, resulting also in higher slice energy spread (row 3). The transverse beam properties are also strongly affected by the time modulations. The symmetric distributions shown in the low charge case of rows 5, 7, and 8 are due to time-varying RF forces. This distortion is repeatable and correctable [5] at high energy. The non-symmetric distortion for the high charge case is only partially correctable. In addition, while the 0.1 nC bunch preserves the 0.3 μm initial thermal emittance in each slice (row 6), the high charge case does not. This instantaneous emittance growth cannot be reversed through solenoid emittance correction. The projected

normalized emittance printed on these plots also illustrates the large twist in phase space that occurs at high charge. This is the twist that emittance corrections schemes are designed to remove, however the asymmetries in the head and tail of the bunch complicate its application for this beam distribution.

The 6D beam brightness can be defined as

$$B = \frac{Q}{\varepsilon_{6D}}$$

where Q is the charge and ε_{6D} is the 6D normalized emittance defined as

$$\varepsilon_{6D} = \gamma^2 \sqrt{\det(\text{cov}([x \; x' \; y \; y' \; t \; E]))}$$

in units of $\mu m^2 \cdot ps \cdot MeV$. The 6D emittances for 0.1, 0.5, and 1 nC are 0.0054, 0.13, and 0.41 μm^2 ps MeV respectively, showing the much more compact phase space volume of the low charge case. The corresponding brightness figures are 18.5, 3.9, and 2.4 nC/($\mu m^2 \cdot ps \cdot MeV$) showing that the low charge case has a higher phase space density by nearly an order of magnitude despite an order of magnitude less charge. The key point is that by running the injector at low charge, the phase space is preserved even in the presence of an imperfect initial distribution. The parameters that are important for the FEL are emittance, energy spread, and peak current. The injector should be designed to produce best emittance and energy spread, while the peak current is generated by compression at high energy.

CONCLUSIONS

The RF design for an efficient 2 ½ cell photoinjector operating at kHz repetition rates has been presented. Beam dynamics studies that include a less than ideal laser distribution point toward operation of the photoinjector in a non-space charge dominated regime to preserve the initial low thermal electron beam emittance in the presence of time modulations.

ACKNOWLEDGEMENTS

REFERENCES

[1] http://mitbates.mit.edu/xfel.

[2] TESLA Technical Design Report, http://tesla.desy.de/new_pages/TDR_CD/start.html.

[3] L. Serafini and J.B. Rosenzweig, Phys. Rev E 55, 7565 (1997)

[4] C. Limborg, private communication

[5] P. Emma and W.S. Graves, "Emittance reassembly using harmonic RF and sextupole pairs", unpublished

X-RAY LASER SEEDING FOR SHORT PULSES AND NARROW BANDWIDTH

W. S. Graves, M. Farkhondeh, F. X. Kaertner, R. Milner, C. Tschalaer, J. B. van der Laan, F. Wang, A. Zolfaghari, T. Zwart, MIT-Bates Linear Accelerator Center, Middleton MA 01949

W.M. Fawley LBNL, Berkeley CA 94720,

D.E. Moncton, ANL, Argonne IL 60439

Abstract

The performance of an x-ray free electron laser can be substantially enhanced if a coherent seed source is used to provide sufficient initial power that it dominates the spontaneous emission in the early part of the undulator. The FEL output then becomes an amplified reproduction of the input seed having, under certain conditions, the same pulse length and bandwidth. For studies of molecular and atomic time dynamics the pulse length may be very short, reaching below 1 fs with a transform limited bandwidth of a few tenths of a percent. For spectroscopy and diffraction experiments the beam may alternatively be made monochromatic at the level of one part in 10^5 or better, with a pulse length of tens of femtoseconds. Simulation studies of seeded FEL performance at 0.3 nm using the code GINGER are presented.

INTRODUCTION

The first generation of x-ray lasers based on single-pass free electron laser amplifiers have been approved for construction [1,2], and will operate on the principle of self amplification of spontaneous emission (SASE) wherein the electron beam amplifies its own initial spontaneous emission. SASE radiation has the advantage of being self-starting, that is, it does not amplify an initial radiation seed pulse. However, the output (right column of Fig. 1) has a spiky structure in time and frequency. It is not longitudinally transform limited, and suffers from large shot-to-shot fluctuations in power and wavelength.

Longitudinal coherence may be achieved if a coherent seed radiation pulse is introduced. If the seed power dominates the spontaneous emission, then the coherence and timing properties of the seed will be accurately amplified by the FEL. While conventional lasers are attractive as seed sources in the IR, visible, and UV wavelength ranges, strong absorption in materials of shorter wavelength light has until recently prevented emergence of a candidate seed in the x-ray regime.

High harmonic generation of seed power

Two technologies have recently demonstrated experimental results that show promise for future generation of fully coherent x-ray FEL output. The first of these is the generation of high harmonics of a

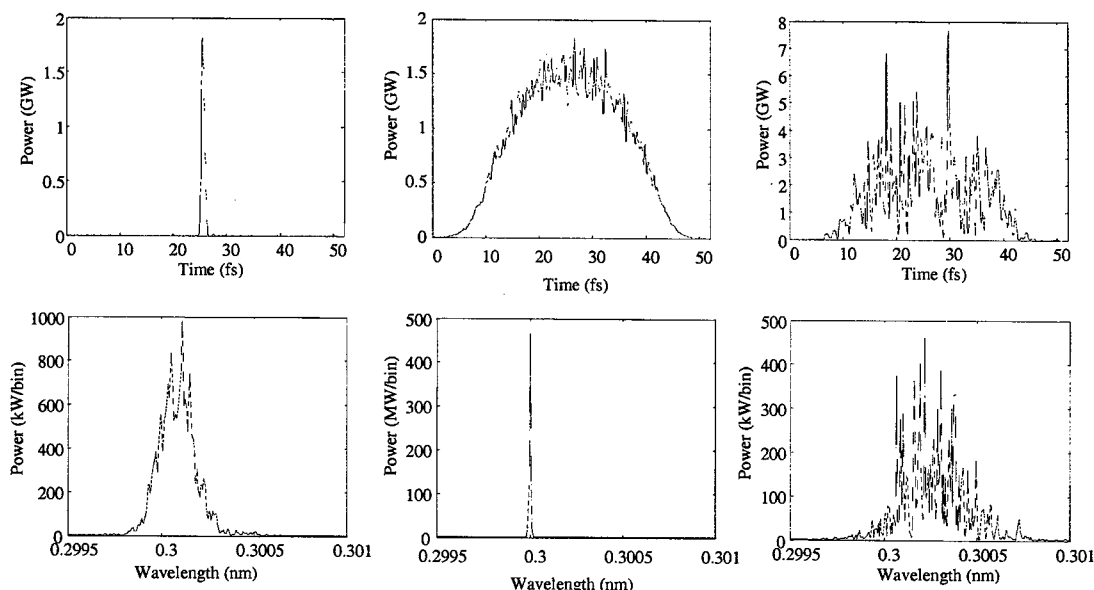Figure 1: Time dependent GINGER simulations for 3 different initial conditions of 0.3 nm FEL. Top row shows FEL pulse time profile for, from left to right, seeding from a short pulse, seeding from a temporally coherent long pulse, and SASE. The bottom row shows the spectrum associated with each time profile above it. Short pulse FWHM is 0.75 fs from a 50 fs ebeam pulse. Narrow bandwidth seed produced 10^{-5} relative linewidth.

conventional laser in a noble gas jet [3]. Very broad bandwidth Ti:Sapphire lasers operating near 800 nm now generate few fs, few cycle output pulses with very high peak fields. The pulse is focused into a gas jet where the high electric field briefly ionizes the atoms before passing and allowing the electron to re-collide with the nucleus creating a short burst of bremsstrahlung at many high harmonics of the 800 nm. Harmonics as short as 3 nm have been achieved, but the best power is in the wavelength range of 10 – 30 nm. This process is known as high harmonic generation (HHG). Power in a particular harmonic may be optimized by pulse shaping of the drive laser. The pulse energy produced by HHG has been limited to a few nJ, which will improve as the technique develops. Even this low energy, in a sufficiently short pulse, is adequate to seed the FEL process.

High gain harmonic generation FEL

Although HHG radiation is much shorter wavelength than other laser-based sources, it is still an order of
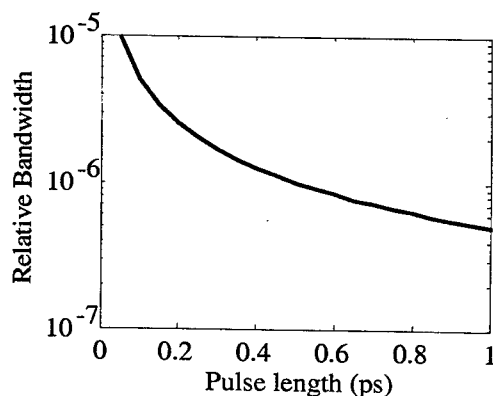
Figure 2: Transform limited bandwidth for different pulse lengths at 0.3 nm wavelength. Energy resolution of meV is possible without the need for monochromaters.
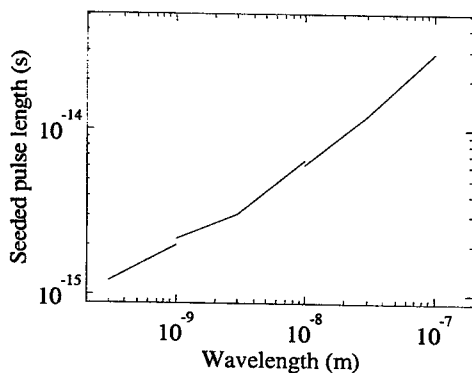
Figure 3: Minimum pulse lengths possible for different wavelengths. The FEL has sufficient gain bandwidth to support pulse lengths less than 1 fs at 0.3 nm wavelength.

magnitude or two longer than required for x-ray seeding. This problem has been addressed by the second important technology demonstration, which is an FEL technique that produces coherent short wavelength output from a long wavelength seed.

When an electron beam is bunched in an undulator, the bunching spectrum contains harmonics of the fundamental frequency. We can take advantage of these harmonics to lase at shorter wavelengths than the input seed using the method of high-gain harmonic-generation (HGHG) [4]. In this method an electron beam is resonant in a first undulator with a long wavelength seed, then the microbunching of the beam is optimized to produce harmonic radiation in a second undulator tuned to that harmonic. The primary role of the first undulator is to produce energy modulation in the electron beam rather than radiation. This energy modulation is converted to temporal bunching optimized for a particular harmonic in a dispersion section consisting of a magnetic chicane. The coherently bunched electron beam radiates at the harmonic frequency in the second undulator, and the pulse energy grows exponentially until saturation is reached.

The description above is of a single-stage HGHG system. This technique has been successfully demonstrated in the IR [5] and UV [6] at BNL. The recent experiments in the UV seeded the electron beam with 800 nm light and lased at the 266 nm 3rd harmonic. The radiation output reached saturation in a substantially shorter distance than possible with SASE, and showed the expected improvements in bandwith, coherence, and stability compared with SASE. A single-stage device can typically lase at the $2^{nd} - 5^{th}$ harmonic. To achieve shorter wavelengths, multiple stages are required, a technique referred to as cascaded HGHG. Soft x-ray FELs proposed at BESSY [7], Lawrence Berkeley Lab [8], and MIT [9] all plan to use HGHG to produce coherent output.

SEEDING STUDIES

As a guide for numerical studies of seeded FEL output, semi-analytical estimates of the best achievable bandwidth and shortest pulse lengths are shown in figures 2 and 3. The separate curves in fig. 3 use the numerical FEL performance parameterization of Xie [10], and are optimized as a function of wavelength. Figure 2 is a simple analytical estimate of transform limited bandwidth at 0.3 nm.

Time dependent runs of the GINGER FEL code [11] have been performed to numerically verify the estimated performance. These runs do not model the entire HGHG process from long wavelength seed to final FEL output, but rather assume a particular input seed power and pulse length at the entrance of the final radiator section and study the FEL gain and pulse properties. A simulation model of the entire cascaded FEL process is under development and will be reported in the future.

The electron beam properties for these runs were 0.8 μm RMS normalized emittance, 10^{-4} relative energy spread, and 2 kA peak current, consistent with the

Figure 4: Top plot shows theoretical pulse length achievable for chirped pulse amplification using FEL. Bottom plot shows peak power.

proposed MIT source [12]. The FWHM of the electron beam was approximately 50 fs for a total charge of just 100 pC. Figure 1 shows the spectrum and pulse length for both seeded and SASE FEL output at 0.3 nm. The left column of the figure shows a simulation output of the FEL when seeded with a short input pulse. The seed parameters for this case are FW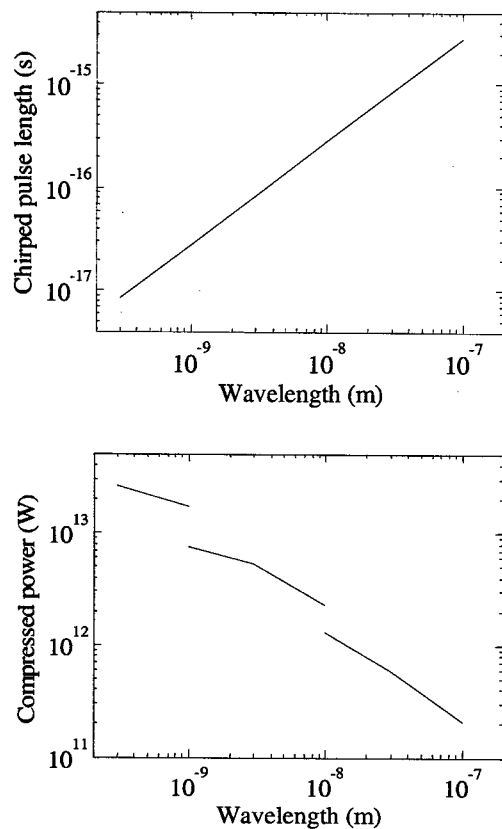HM of 0.5 fs and 10 MW peak power for total pulse energy of 5 nJ. The output pulse length was 0.75 fs FWHM with a nearly transform limited bandwidth indicating good coherence and limited pulse stretching due to slippage of the electron beam relative to the radiation. Saturation length is 20 m to produce peak power of 2 GW and total pulse energy of 1.5 μJ, much shorter than the 59 m required for SASE saturation at the same power. Note that although the peak power is the same as SASE, the total pulse energy is lower because of the short pulse length.

The middle column of figure 1 shows a GINGER simulation of a bandwidth seeded FEL at 0.3 nm. In this case the seed pulse energy was still 5 nJ but the pulse length was 50 fs to overlap the full electron beam. The FWHM of the output spectrum is 10^{-5} in good agreement with the analytical estimate. The bandwidth seeded FEL produces the same peak power and pulse energy as the SASE output, but the bandwidth is nearly two orders of

magnitude narrower, producing a much brighter beam with all photons in the same mode.

CHIRPED PULSE AMPLIFICATION

In the absence of a time/frequency correlation (chirp), the minimum pulse length achievable is determined by the gain bandwidth of the FEL. By imposing a chirp on the input seed laser pulse, and a matching time/energy correlation on the overlapping electron beam it is possible to produce a high power output pulse with the same chirp as the input. This output x-ray pulse may then be compressed with a grating or asymmetrically cut crystal to compress in the same manner as chirped pulse amplifiers are used for conventional lasers in the visible and IR. Figure 4 shows the minimum pulse length and maximum peak power versus wavelength for a pulse having a 6% chirp (3% electron beam chirp), and assuming that it can be fully compressed. The maximum amount of compression possible is determined by the ratio of chirp amplitude to FEL bandwidth. In practice, effects such as slippage, phase distortions in the FEL gain process, and nonlinearities in the x-ray compressors will limit the maximum compression to a smaller value. However it may be possible to generate sub-fs pulses with peak powers approaching 1 TW.

REFERENCES

[1] LCLS Conceptual Design Report, SLAC-R-593, http://www-ssrl.slac.stanford.edu/lcls/cdr.

[2] TESLA Technical Design Report, DESY 2001-011, http://tesla.desy.de/new_pages/TDR_CD/start.html.

[3] M. Schnurer et al, "Coherent 0.5 keV x-ray emission from Helium driven by a sub-10-fs laser", Phys. Rev. Lett. 80, p 3236 (1998).

[4] L.H. Yu, "Generation of intense uv radiation by subharmonically seeded single-pass free-electron lasers", Phys. Rev. A 44, p. 5178 (1991)

[5] L.H. Yu et al, "High-gain harmonic-generation free-electron laser", Science 289, p 932 (2000).

[6] L.H. Yu et al, "First ultraviolet high-gain harmonic-generation free electron laser", submitted to Phys. Rev. Lett.

[7] M. Abo-Baker et al, "The BESSY soft x-ray single-pass FEL design", proceedings of the 2002 FEL conference, to appear in Nuc. Instr. Meth. A.

[8] W.M. Fawley et al, "Simulation studies of an XUV/Soft x-ray harmonic-cascade FEL for the proposed LBNL recirculating linac", this conference.

[9] D.E. Moncton et al, "X-ray laser user facility at Bates Laboratory", http://mitbates.mit.edu/xfel

[10] M. Xie, "Design optimization for an x-ray free electron laser driven by the SLAC linac", proceedings of 1995 Particle Accel. Conf, p. 183 (1995)

[11] W.M. Fawley, GINGER User's Manual, LBNL-49625

[12] T. Zwart et al, "The MIT Bates x-ray laser project", this conference.

ON THE REALISTIC GAIN ESTIMATION OF THE CSR MICROBUNCHING INSTABILITY IN BUNCH COMPRESSORS

Yujong Kim*, DESY, D-22603 Hamburg, Germany

T. Shintake and H. Kitamura, RIKEN, SPring-8, Hyogo 679-5148, Japan

D. Son and Y. Kim, The Center for High Energy Physics, Taegu 702-701, Korea

Abstract

For a realistic gain estimation of the CSR microbunching instability, we describe limitations of the current gain estimation methods in detail and several smearing effects which we do not consider yet.

INTRODUCTION

Unlike the normal CSR which may dilute the projected transverse emittances in a bunch compressor (BC), CSR may also be generated for a wavelength much shorter than the bunch length if the bunch has a periodic modulation in its current or energy profile before the bunch compressor [1]-[4]. In this case, the initial amplitude of the modulation can be amplified by CSR in the BC, and the slice emittances and the slice energy spread can be increased by the amplified microbunching [2], [5]. This is called the CSR microbunching instability in bunch compressors [2]-[5]. Since the slice emittances and the slice energy spread should be small enough for SASE FEL's, the CSR microbunching instability which dilutes the slice parameters is an important issue and is still under deep study [2]-[6]. The gain of the CSR microbunching instability is defined as the ratio of the final amplitude of the modulation after compression with respect to the initial amplitude of the modulation before compression [4]. Although new gain-increasing effects such as the short range wakefield in the linac and the longitudinal space charge force were recently reported, the estimated gain is still somewhat over-estimated [5], [6]. In this paper, we describe limitations of the current gain estimation methods in detail and the several smearing effects which we do not consider yet.

GAIN OF CSR INSTABILITY

According to Ref. [4], the gain G of the CSR microbunching instability due to the charge density or current modulation is given by

$$G = \left| \frac{b(k_f; f)}{b_0(k_0; 0)} \right| \approx \left| \exp\left[-\frac{1}{2}\left(\frac{k_0 R_{56} \sigma_{\delta u}}{1 + h R_{56}} \right)^2 \right] \right.$$

$$\left. + A \bar{I}_f \left\{ \frac{\sqrt{\pi} \mathrm{erf}(\bar{\sigma}_x)}{2\bar{\sigma}_x} \exp\left[-\frac{1}{2}\left(\frac{k_0 R_{56} \sigma_{\delta u}}{1 + h R_{56}} \right)^2 \right] + \mathcal{F}_1 \right\} \right.$$

---

*E-Mail: Yujong.Kim@DESY.de, URL: http://TESLA.DESY.de

$$\left. + A^2 \frac{(I_{pk} k_0^{4/3} R_{56} L_b)^2}{(\gamma I_A \rho_0^{2/3})^2} \mathcal{F}_0 \mathcal{F}_2 \right|, \qquad (1)$$

$$k_0 = \frac{2\pi}{\lambda} = (1 + h R_{56}) k_f, \quad A = 1.63i - 0.94,$$

$$\bar{I}_f = \frac{I_{pk} k_0^{4/3} R_{56} L_b}{\gamma I_A \rho_0^{2/3}}, \quad \bar{\sigma}_x = k_0 L_b \frac{\sqrt{\beta_0 \epsilon_{nx}/\gamma}}{\rho_0},$$

where λ is the initial modulation wavelength before the BC, R_{56} is the momentum compaction factor of the BC, $h = d\delta/dz$ is the chirping constant where δ is the relative energy deviation dE/E, $\sigma_{\delta u}$ is the uncorrelated relative rms energy spread, ϵ_{nx} is the normalized horizontal rms emittance, I_{pk} is the peak current after compression, and γ is the Lorentz factor. Others are defined in Ref [4].

In order to estimate the gain of a single chicane which can generate a high peak current, we have applied Eq. (1) to a model chicane used at the CSR workshop [7]. In the case of a cold beam with $\epsilon_{nx} = 0$ and $\sigma_{\delta u} = 0$, its gain is high as shown in the red line of Fig. 1(left). But the gain can be damped at small λ if $\sigma_{\delta u}$ is increased to 2.0×10^{-6} as shown in the green line of Fig. 1(left) [8]. For the case $\epsilon_{nx} = 1.0 \, \mu\mathrm{m}$ and $\sigma_{\delta u} = 2.0 \times 10^{-6}$, the gain is significantly reduced as shown in the blue line of Fig. 1(left) [4].

Recently, it was found that the signs of R_{56} and h for the gain estimation were different with those for the CSR calculation [4]. After correcting the wrong signs of R_{56} and h, the gain becomes smaller than 7 as shown in the magenta line of Fig. 1(left) [4]. If $\sigma_{\delta u}$ is 9.5×10^{-6} which is close to the uncorrelated energy spread due to the intrabeam scattering in the linac $\sigma_{\delta u, IBS}$, the gain is about 5 as shown in Fig. 1(right) [9]. For the case $\sigma_{\delta u} = 5.0 \times 10^{-5}$, the gain is around 1 although I_{pk} is 6.0 kA. If $\sigma_{\delta u}$ is increased up to 1.0×10^{-4} which is close to the allowable maximum value for the SASE FEL saturation, the gain becomes smaller than 1. In the case of a single chicane, a nonzero $\sigma_{\delta u}$ and ϵ_{nx} can effectively suppress the CSR microbunching instability although the peak current is high enough [4], [8], [9]. Note that we have some margin in $\sigma_{\delta u}$ but the margin of ϵ_{nx} is small in suppressing the CSR microbunching instability [2].

LIMITATION AND SMEARING EFFECT

Originally, the microbunching instability due to CSR in the bunch compressor was found by ELEGANT during the
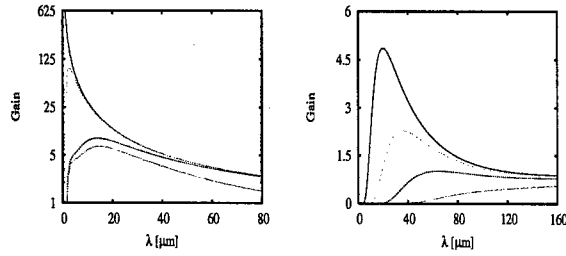

Figure 1: Gain of a model chicane as a function of the modulation wavelength λ. Here all used parameters are summarized in Table 1 where four numbers in a column are the parameters of red, green, blue, and magenta lines, respectively. More details can be found in Ref. [7].

Table 1: Parameters of model chicane used in Fig. 1.

Parameter	Unit	Fig. 1(left)	Fig. 1(right)
energy E	GeV	5.0	
I_{pk}	kA	6.0	
R_{56}	mm	-25, -25, -25, +25	+25, +25, +25, +25
h	m^{-1}	+36, +36, +36, -36	-36, -36, -36, -36
ϵ_{nx}	μm	0.0, 0.0, 1.0, 1.0	1.0, 1.0, 1.0, 1.0
$\sigma_{\delta u}$	10^{-6}	0.0, 2.0, 2.0, 2.0	9.5, 25, 50, 100

Figure 2: ELEGANT results of SCSS BC at the Phase-II stage with 5×10^4 macroparticles (upper row) and 2×10^6 macroparticles (lower row): (left column) population frequency versus the relative energy deviation after the BC (right column) longitudinal phase space after the BC. Here all initial conditions except the macroparticle number are the same for two cases. The main parameters are summarized in Table 2, and others are summarized in Ref. [1].

start-to-end simulation for the LCLS project [2]-[3]. Now ELEGANT as well as the analytical formulas are used in estimating the total gain of the CSR microbunching instability for the entire FEL driver linac. However a special attention is needed when we estimate the gain by the tracking code. If an initial distribution is generated by a random number generator, and the number of simulated macroparticles in a bunch is too low, the modulation can be amplified by a factor $\sqrt{N_b/N_m}$ where N_b is the actual number of electrons, and N_m is the number of simulated macroparticles in the bunch [8]. Although we use a quiet-start method based on Halton sequences to reduce the numerical noise in ELEGANT simulation, a modulation in the energy profile is artificially generated as shown in the upper two plots of Fig. 2. Here the bin number for the CSR calculation is 600 for the two cases [3]. TraFiC^4 also has a similar noise.

When the bunch length is compressed in the BC, the initial uncorrelated energy spread before the bunch compressor $\sigma_{\delta u,i}$ is increased by the compression factor $C = (1 + hR_{56})^{-1}$ due to the conservation of the longitudinal emittance. Generally, CSR induces a correlated energy spread along the bunch length during compression. However an uncorrelated energy spread may also be generated by quantum diffusion due to incoherent synchrotron radiation (ISR) and CSR. According to an ELEGANT simulation with consideration of ISR and CSR, the uncorrelated energy spread after the bunch compressor $\sigma_{\delta u,f}$ is much higher than $C \times \sigma_{\delta u,i}$ as shown in Fig. 3 and summarized in Table 2. In the case of the SCSS BC at the Phase-II stage,

Table 2: Parameters of SCSS bunch compressor.

Parameter	Unit	Phase-I	Phase-II
E	MeV	230	218
single bunch charge Q	nC	1.0	1.0
I_{pk}	kA	0.5	2.0
compression factor C	·	4	8
ϵ_{nx}	μm	1.5	1.5
$\sigma_{\delta u,IBS}$	10^{-6}	9.5	9.7
$\sigma_{\delta u,i}$	10^{-5}	5.4	5.7
$\sigma_{\delta u,f}$	10^{-5}	25	58.4
$\sigma_{\delta u,SR}$	10^{-5}	3.4	12.8

the uncorrelated energy spread growth due to ISR and CSR $\sigma_{\delta u,SR} = \sigma_{\delta u,f} - C \times \sigma_{\delta u,i}$ is about 12.8×10^{-5}. In this paper, we used the sixth order polynomial fitting to remove the correlation, and the estimated $\sigma_{\delta u,f}$ is not changed significantly though we increase the fitting order up to ten. Note that only the $\sigma_{\delta u}$ growth due to compression is considered in the analytic gain estimation formula as shown in Eq. (1). If the peak current is not small, the uncorrelated energy spread growth due to ISR and CSR should be also considered in estimating the gain of the CSR instability with the analytic gain estimation formulas.

For the LCLS start-to-end simulation, PARMELA is used to consider the space charge (SC) force before the first bunch compressor. Then ELEGANT is used from the first bunch compressor without consideration of the SC force.

Figure 3: ELEGANT results with 2×10^6 macroparticles: change of the uncorrelated energy deviation dE_u in the SCSS BC Phase-I (left) and Phase-II (right). Here red and green dots are dE_u before and after the BC, respectively.

However according to the recent ASTRA trackings up to the TTF-2 second bunch compressor (BC3) without consideration of CSR, if the bunch length is compressed, the effects of the nonlinear space charge force is not ignorable though the beam energy is high [10]. Before the first bunch compressor, we consider the SC force, and the est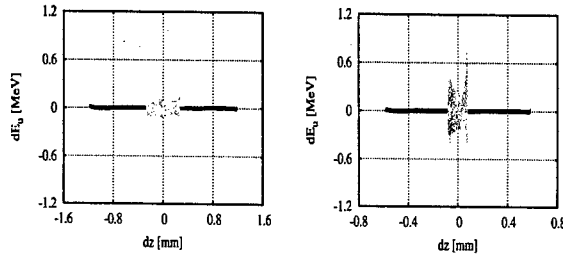imated uncorrelated rms energy deviation due to the SC force $(dE_{u,SC})_{rms}$ is about 3.1 keV for $Q = 1.0$ nC as shown in Fig. 4(upper left) and summarized in Table 3. If we ignore the SC force from the first bunch compressor, $\sigma_{\delta u,SC}$ is not increased although the bunch length is compressed as shown in Fig. 4(upper right). Note that the uncorrelated energy spread growth due to compression by a factor $C = 8$ is already subtracted in Fig. 4, and $\sigma_{\delta u,SC}$ and $(dE_{u,SC})_{rms}$ are only due to the SC force. When the SC force is considered after the bunch compressor, $\sigma_{\delta u,SC}$ is increased about 2.5 times as shown in Fig. 4(lower left). Although the beam energy is increased up to about 441 MeV where the second bunch compressor (BC3) will be located, $(dE_{u,SC})_{rms}$ is still around 7.7 keV as shown in Fig. 4(lower right). In this case, $\sigma_{\delta u,SC}$ is decreased due to the increased beam energy or acceleration. Since the smearing effect due to the nonlinear space charge force in the linac is not considered in analytic formulas as well as in ELEGANT, their estimated gains are somewhat over-estimated in the linac. In the case of new gain-increasing effects such as the short range wakefield in the linac and the longitudinal SC force, it is also assumed that there is no uncorrelated energy spread growth in the linac [5], [6].

SUMMARY

In the case of a single chicane, the gain of the CSR microbunching instability is small for a beam with nonzero ϵ_{nx} and $\sigma_{\delta u}$. Although a modulation is amplified in the bunch compressor, it may be small or smeared out in the linac by various uncorrelated energy spread sources such as ISR and CSR in the BC and the intrabeam scattering and nonlinear space charge force in the linac. We expect that the total gain of the CSR microbunching instability for the entire FEL driver linac will not be high.
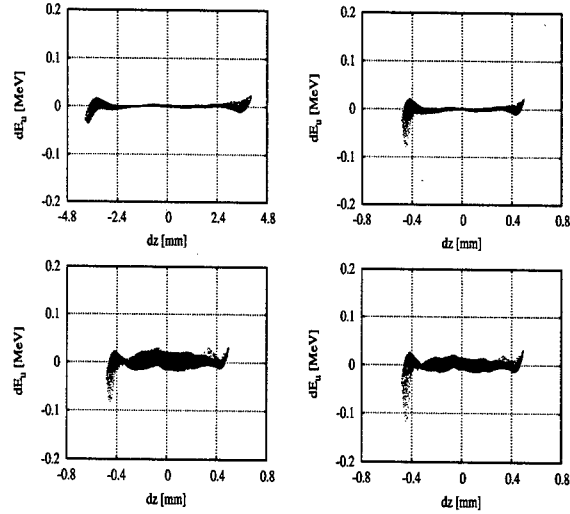
Figure 4: ASTRA trackings from the cathode with 5×10^5 macroparticles for dE_u estimation around the TTF-2 first bunch compressor (BC2) located at 20.88 m [10]: (upper left) before BC2 with the SC force, (upper right) before ACC2, with the SC force before BC2 then without the SC force from BC2 to ACC2, (lower left) before ACC2 with the SC force, (lower right) before BC3 with the SC force. The main parameters are summarized in Table 3 where four numbers in a column are the parameters of (upper left), (upper right), (lower left), and (lower right), respectively.

Table 3: Parameters of TTF-2 used in Fig. 4.

Parameter	Unit	Value
E	MeV	122, 122, 122, 441
bunch length σ_z	mm	1.9, 0.23, 0.23, 0.23
beam size σ_r	mm	0.2, 0.3, 0.3, 0.3
ϵ_{nx}	μm	1.87, 1.91, 1.98, 2.14
longitudinal position	m	20.8, 38.0, 38.0, 63.6
space charge force	·	on, on until 20.8 m then off, on, on
$(dE_{u,SC})_{rms}$	keV	3.1, 3.2, 8.0, 7.7
$\sigma_{\delta u,SC}$	10^{-5}	2.5, 2.6, 6.4, 1.8

REFERENCES

[1] Y. Kim et al., in Proc. LINAC2002, Gyeongju, Korea, 2002.

[2] LCLS Conceptual Design Report, SLAC-R-593, 2002.

[3] M. Borland, in Proc. LINAC2002, Gyeongju, Korea, 2002.

[4] Z. Huang et al., in Proc. FEL2002, Argonne, USA, 2002.

[5] Z. Huang et al., in these proceedings.

[6] E. L. Saldin et al., DESY TESLA-FEL 2003-02, 2003.

[7] http://www.desy.de/csr/

[8] E. L. Saldin et al., NIM A **490** (2002) 1.

[9] Z. Huang, SLAC Report No. LCLS-TN-02-8, 2002.

[10] The TTF FEL team, DESY TESLA-FEL 2002-01, 2002.

TOLERANCES OF TTF-2 FIRST BUNCH COMPRESSOR

K. Flöttmann and Yujong Kim*, DESY, D-22603 Hamburg, Germany
T. Shintake and H. Kitamura, RIKEN, SPring-8, Hyogo 679-5148, Japan
P. Emma, Stanford Linear Accelerator Center, Menlo Park, CA 94025, USA
D. Son and Y. Kim, The Center for High Energy Physics, Taegu 702-701, Korea

Abstract

In bunch compressors for SASE-FEL facilities, the projected transverse emittance can be diluted by magnetic multipole component errors in dipoles and dipole misalignments as well as by coherent synchrotron radiation (CSR). In this paper, we describe the multipole field tolerances and the misalignment tolerances of the first bunch compressor (BC2) for the TESLA Test Facility Phase-2 (TTF-2).

INTRODUCTION

In SASE-FEL and linear collider projects such as TTF-2, TESLA X-ray FEL, and TESLA linear collider, a high quality beam with small transverse emittance and high peak current should be supplied in order to achieve a saturation and a high brightness of SASE sources and a high luminosity of colliding beams. Generally, CSR is the main source of the transverse emittance growth in a bunch compressor (BC). However we can control the emittance growth due to CSR by several methods [1]. Since bending magnets may have magnetic multipole components as well as the dipole component, the transverse beam emittance can be diluted in a high dispersion region such as the magnetic chicane. Besides the multipole components, the transverse emittance can be diluted by the dipole field strength error and magnet misalignment errors. To control the emittance growth in the BC, bending magnets should be fabricated and aligned within their tolerances. We have used ELEGANT code to consider CSR induced emittance growth in investigating the multipole field, misalignment, and rotational tolerances of the TTF-2 first bunch compressor (BC2) [2].

TOLERANCES INVESTIGATION

Multipole Component Tolerances with CSR

The vertical magnetic field of a bending magnet in the horizontal middle plane can be expanded in a series of multipoles, which is given by

$$
\begin{aligned}
B_y(x,0) &= \sum_{n=0}^{\infty} B_n \frac{x^n}{n!} = (B_0\rho) \sum_{n=0}^{\infty} K_n \frac{x^n}{n!}, \\
&= \sum_{n=0}^{\infty} b_n \frac{(x+iy)^n}{a^n}\bigg|_{y=0}, \\
&= B_0 + (B_0\rho)K_1 x + \frac{1}{2!}(B_0\rho)K_2 x^2 + \dots,
\end{aligned}
$$

*E-Mail: Yujong.Kim@DESY.de, URL: http://TESLA.DESY.de

$$
= b_0 + b_1 \frac{x}{a} + b_2 \frac{x^2}{a^2} + b_3 \frac{x^3}{a^3} + \dots, \tag{1}
$$

where x and y are the horizontal and vertical coordinates whose origin is the center of the bending magnet, a is the reference radius of expansion, and ρ is the bending radius [3]. Here $B_0 = b_0 = B_y(x,y)|_{x=0,y=0}$ is the magnetic field at the origin, and it is also given by $p_0/\rho q$ where p_0 is the momentum of the reference particle, and q is the particle charge. The momentum-normalized multipole component K_n is given by

$$
K_n = \frac{B_n}{B_0\rho} = \frac{1}{B_0\rho} \frac{\partial^n B_y}{\partial x^n}\bigg|_{x=y=0} = \frac{1}{B_0\rho} \frac{n!}{a^n} b_n. \tag{2}
$$

If we choose that a is the half gap height between the magnet poles and estimate the field error at a horizontal middle point with $x = a$ and $y = 0$, $B_y(x = a, 0)$ is given by

$$
B_y(a, 0) = b_0 + b_1 + b_2 + b_3 + b_4 + \dots. \tag{3}
$$

At the estimation point $(a, 0)$, the quadrupole, sextupole, octupole, and decapole component errors with respect to the dipole component b_0 are defined as

$$
\frac{QM}{BM}\bigg|_{x=a,y=0} = \frac{b_1}{b_0} = \rho K_1 a, \tag{4}
$$

$$
\frac{SM}{BM}\bigg|_{x=a,y=0} = \frac{b_2}{b_0} = \frac{1}{2!}\rho K_2 a^2, \tag{5}
$$

$$
\frac{OM}{BM}\bigg|_{x=a,y=0} = \frac{b_3}{b_0} = \frac{1}{3!}\rho K_3 a^3, \tag{6}
$$

$$
\frac{DM}{BM}\bigg|_{x=a,y=0} = \frac{b_4}{b_0} = \frac{1}{4!}\rho K_4 a^4. \tag{7}
$$

We have swept K_n for each dipole with ELEGANT including CSR wakefields while monitoring the projected transverse normalized emittance growth at the end of the bunch compressor. From Eqs. (4), (5), (6), and (7), the tolerance of the multipole strength error can be determined by a K_n which gives 2% emittance growth [2].

Misalignment Tolerances

With the help of the method described in the previous section, we can determine the multipole component tolerances. For the misalignment tolerance investigation, we have assumed that all dipoles have multipole component errors about 60% of the tightest tolerances. Under those

Table 1: Parameters of TTF-2 BC2.

Parameter	Unit	Value
initial beam energy E	MeV	121
initial projected energy spread σ_δ	%	1.0
initial uncorrelated energy spread $\sigma_{\delta u}$	10^{-5}	5.0
initial horizontal emittance $\epsilon_{nx,i}$	μm	1.32
initial vertical emittance $\epsilon_{ny,i}$	μm	1.32
final horizontal emittance $\epsilon_{nx,f}$	μm	2.18
final vertical emittance $\epsilon_{ny,f}$	μm	1.34
bunch charge Q	nC	1.0
initial rms bunch length $\sigma_{z,i}$	mm	2.1
final rms bunch length $\sigma_{z,f}$	mm	0.3
momentum compaction factor R_{56}	mm	180.6
bending angle θ	deg.	18.0
maximum horizontal dispersion η_x	mm	346.1
maximum horizontal beam size σ_x	mm	3.47
bending radius ρ	m	1.62
pole width	mm	200
vacuum chamber width	mm	135
dipole geometric length	mm	500
half gap height between poles a	mm	12.5

Figure 1: Beamline of TTF-2 BC2.

artificial multipole component errors, we have tracked an electron bunch in the bunch compressor. By increasing the horizontal misalignment error Δx, vertical misalignment error Δy, or the rotational misalignment error $\Delta \phi$ while monitoring the projected transverse emittance growth, we can determine the misalignment tolerances. If we can use the real measured multipole component errors instead of our assumed 60% magnitude, the misalignment tolerances will be estimated more precisely.

TOLERANCES OF TTF-2 BC2

BC2 Beamline for Tolerance Investigation

We have investigated the tolerances of TTF-2 BC2 for its nominal operation conditions. Since the 3rd harmonic cavity will be turned on for the nonlinearity compensation in the longitudinal phase space during the nominal operation, the beam is decelerated from 136 MeV to 121 MeV [1], [4]. The main parameters of BC2 used in this investigation are summarized in Table 1. Here all energy spreads are the rms relative values, and all emittances are the projected transverse normalized rms values. For the tolerance investigations, we have used an optimized BC2 lattice shown in Fig. 1, where β-functions are asymmetric around the chicane, and α-functions are close to zero at the fourth dipole magnet (DM4). This asymmetric lattice helps in reducing the CSR induced projected horizontal emittance growth in the bunch compressor [1]. Although we have optimized the chicane beamline, ϵ_{nx} is increased to 2.18 μm at the end of the bunch compressor. However ϵ_{ny} is not significantly increased because the vertical CSR force is weak enough under the condition that the vertical dispersion η_y is zero.
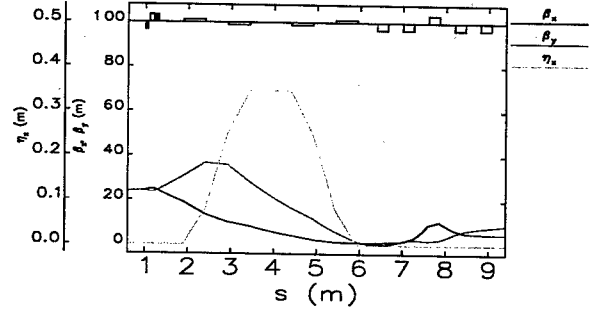
Quadrupole components in a bending magnets dilute the horizontal emittance because the horizontal dispersion is changed. Without consideration of CSR, the analytical formula of the quadrupole component tolerance is given by

$$\left| \frac{b_1}{b_0} \right| < \frac{1}{|\theta|} \frac{a}{\eta_x \sigma_\delta} \sqrt{\frac{2\epsilon_{x0}}{\beta_x} \left(\frac{\Delta \epsilon_x}{\epsilon_{x0}} \right)}, \qquad (8)$$

where ϵ_{x0} is the initial projected horizontal emittance and $\Delta \epsilon_x$ is the projected horizontal emittance growth [5]. From Fig. 1 and Eq. (8), we can expect that the quadrupole component tolerances of the second and third dipoles (DM2 and DM3) will be tighter than those of the first and fourth dipoles (DM1 and DM4) because η_x is highest at DM2 and DM3. And the quadrupole component tolerance of DM1 will be tighter than that of the DM4 because β_x is higher at DM1 although the horizontal dispersion is the same at DM1 and DM4.

Sextupole components in bending magnets dilute the transverse emittance due to chromaticity and second order dispersion. Without consideration of CSR, the analytical formula of the sextupole component tolerance for the horizontal emittance growth is given by

$$\left| \frac{b_2}{b_0} \right| < \frac{1}{|\theta|} \frac{a^2}{\eta_x^2 \sigma_\delta^2} \sqrt{\frac{\epsilon_{x0}}{\beta_x} \left(\frac{\Delta \epsilon_x}{\epsilon_{x0}} \right)}. \qquad (9)$$

From Fig. 1 and Eq. (9), we can expect that the behavior of the sextupole component tolerance will be similar to that of the quadrupole component tolerance.

When a dipole magnet has a rotational error $\Delta \phi$, the horizontal magnetic field in the horizontal middle plane can be given by $|B_y(x,0) \sin \Delta \phi|$ which generates a nonzero vertical dispersion η_y and a vertical emittance growth in the chicane. Without consideration of CSR, the analytical formula of the rotational error tolerance is given by

$$\Delta \phi < \frac{1}{|\theta|} \frac{1}{\sigma_\delta} \sqrt{\frac{2\epsilon_{y0}}{\beta_y} \left(\frac{\Delta \epsilon_y}{\epsilon_{y0}} \right)}, \qquad (10)$$

where ϵ_{y0} is the initial projected vertical emittance and $\Delta \epsilon_y$ is the projected vertical emittance growth [5]. Under CSR wakefields, the vertical CSR force becomes strong because
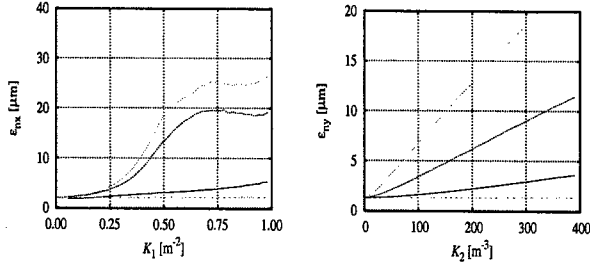
Figure 2: ELEGANT simulation results at the TTF-2 BC2: (left) quadrupole component error versus ϵ_{nx}, (right) sextupole component error versus ϵ_{ny}. Here red, green, blue, and magenta lines mean the projected transverse emittances at DM1, DM2, DM3, and DM4, respectively.

η_y is not zero. Hence the projected vertical emittance is significantly increased when a dipole in the bunch compressor has a rotational error. From Fig. 1 and Eq. (10), we can expect that DM1 has the tightest rotational error tolerance because β_y is highest at DM1.

Estimated Tolerances

From Fig. 2, we have determined K_1 and K_2 which give 2% projected transverse emittance growth ($\Delta\epsilon_{nx} = 0.0436~\mu m$, $\Delta\epsilon_{ny} = 0.0264~\mu m$). Hence the quadrupole and sextupole component tolerances are determined from Eqs. (4) and (5). Other multipole component tolerances can be obtained by the same method and are summarized in Table 2 where left and right values in a column mean the tolerances for the horizontal and vertical planes, respectively, and smaller bold-faced numbers mean the tightest tolerances of them.

Under artificial multipole component errors which are 60% of the tightest tolerances, we have investigated the misalignment tolerances by tracking with consideration of CSR. From Fig. 3, we have determined misalignment tolerances Δx, Δy, Δ , and $\Delta\phi$ which give 2% projected transverse emittance growth ($\Delta\epsilon_{nx} = 0.0421~\mu m$, $\Delta\epsilon_{ny} = 0.0278~\mu m$). Their tolerances are summarized at the bottom of Table 2. Here transverse misalignment tolerances are tight at DM2 and DM3 because the multipole component tolerances are tight at those dipoles, and the longitudinal misalignment tolerance is large at DM4 because α_x is close to zero at DM4.

To determine the tolerance of the magnet power supply ripple Δ / , we have linked all four dipoles and applied the same error to them simultaneously. We should keep the magnetic power supply ripple smaller than 0.12% to control the emittance growth within 2%.

SUMMARY

We have investigated the magnetic multipole component tolerances and misalignment tolerances of dipole magnets for the TTF-2 first bunch compressor including the effect of

Table 2: Tolerances of TTF-2 BC2 for $a = 12.5$ mm.

		Unit	DM1	DM2	DM3	DM4
Δ	0	%	0.26	0.8	0.8	1.8
	1 0	%	0.38, 0.55	0.18, 0.71	0.06, 1.94	0.57, ∞
	2 0	%	1.01, 0.25	0.04, 0.03	0.14, 0.06	5.70, 2.03
	3 0	%	16.9, 6.33	0.39, 0.18	0.14, 0.36	70.3, 60.6
	4 0	%	128, 52.7	0.25, 0.12	0.85, 0.24	∞, 250
Δ		deg.	0.07	0.18	1.65	3.21
Δ		mm	11.2	1.8	5.6	12
Δ		mm	2.9	1.4	1.4	12
Δ		mm	1.6	5	6	12
Δ		%	0.12			

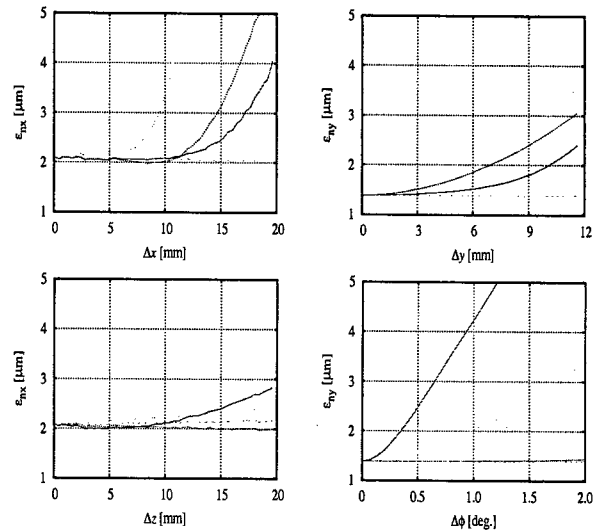Figure 3: ELEGANT simulation results at the TTF-2 BC2: (upper left) horizontal misalignment error versus ϵ_{nx}, (upper right) vertical misalignment error versus ϵ_{ny}, (lower left) longitudinal misalignment error versus ϵ_{nx}, (lower right) rotational misalignment error versus ϵ_{ny}. Here color lines have the same meanings of Fig. 2.

CSR. The second and third dipoles have the tightest multipole component tolerances because they are located at the highest horizontal dispersion. The first dipole has the tightest rotational error tolerance due to the combined actions of the vertical CSR force under nonzero η_y and the highest β_y. We expect that those tolerances can be achievable by the current magnet fabrication and alignment technologies.

REFERENCES

[1] Y. Kim et al., in Proc. LINAC2002, Gyeongju, Korea, 2002.

[2] M. Borland, Phys. Rev. ST Accel. Beams 4, 074201 (2001).

[3] Karl L. Brown, SLAC Report No. SLAC-R-75, 1982.

[4] K. Flöttmann et al., in Proc. EPAC2002, Paris, France, 2002.

[5] P. Emma, DESY Report No. TESLA 95-17, 1995.

COHERENT HARMONIC GENERATION EXPERIMENT ON HEFEI SYNCHROTRON RADIATION SOURCE*

J. Y. Liu, C. Z. Diao, D. H. He, Q. K. Jia, G. Li, H. L. Xu, P. F. Zhang, S. C. Zhang
University of Science and Technology of China, Hefei, Anhui 230026,P. R. China

Abstract

An experiment facility for coherent harmonic generation in ultraviolet spectral range has been built on the storage ring at University of Science and Technology of China. In this paper, the facility, the measurement of the spontaneous radiation spectrum of the optical klystron and preparations for coherent harmonic generation experiment are described.

INTRODUCTION

Hefei synchrotron radiation source at University of Science and Technology of China (USTC) consists of an 800MeV storage ring and a 200MeV injector Linac [1]. The optical klystron (OK) for coherent harmonic generation (CHG) experiment is located in the forth of the four dispersion free long straight sections of the storage ring (Fig. 1).

Although both the injector Linac and the storage ring can be used for FEL experiments, due to limited resources we started with CHG experiment on the storage ring, to gain experience for future Linac based FEL studies using high gain harmonic generation (HGHG) scheme [2]. Concerning the energy of the Linac for FEL experiment, it may be extended to 400MeV in the existing tunnel and klystron gallery for half energy injection into the storage ring, and it is also possible to increase its energy up to 800MeV for full energy injection by replacing klystrons with more powerful ones. Of cause, these will also benefit short wavelength FEL studies. In addition, the nuclear physics experiment hall is available for FEL experiments.

At present, our group collaborates with Shanghai Institute of Nuclear Studies and Institute of High Energy Physics on Shanghai Linac based HGHG type deep

ultraviolet FEL (SDUV-FEL). The experience gained from the CHG experiment at USTC will also benefit SDUV-FEL project.
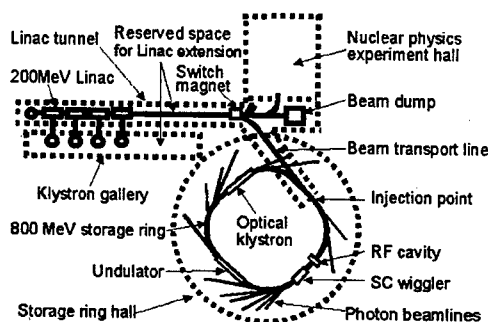

Fig. 1 Layout of Hefei synchrotron radiation source

CHG FACILITY

Figure 2 shows the schematic layout of the CHG experiment facility (bold lines). It consists of an OK, a seed laser and a CHG experiment station, connected by evacuated pipes. The OK is comprised of two undulators separated by a dispersive section. Seed laser light is reflected by mirror 1, focused by two lenses (a telescope) onto the center of the first undulator (modulator), and interacts with the electron beam, causing energy-modulation of electrons. This energy modulation is converted into spatial bunching while traversing through the dispersive section. In the second undulator (radiator) the micro-bunched electron beam emits coherent harmonic radiation. To protect the CHG experiment station from strong bremsstrahlung, coming out of the long straight section where the OK is located, Mirror 2 and mirror 3 are placed on the path of the output radiation beam, forming a parallel displacement. Radiation shielding is mounted on a support behind

mirror 2. Both mirror 2 and mirror 3 reflect the desired output harmonic radiation and transmit other harmonics and the seed laser. The connecting pipes are evacuated to prevent air disturbance and absorption, and they are isolated from the ultra-high vacuum environment of the storage ring by upper-stream and down-stream quarts glass windows.
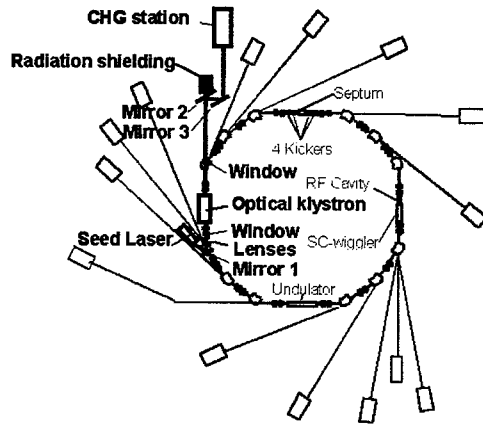

Fig. 2 Layout of CHG Facility

At the beginning, a symmetrical permanent magnet OK was constructed, and a homemade Nd:YAG laser of 1.06μm was chosen as the seed. Output of the third harmonic was desired. The OK is made of NdFeB blocks. The period length and period number of each undulator is 72mm×12. The dispersive section has only one period of 216mm. The magnet gaps of the three sections can be adjusted independently from 40mm to 140mm. The minimum gap is for CHG experiment due to beam lifetime requirement, while the maximum gap is for synchrotron radiation operation of the storage ring. In CHG experiment, the gap of the dispersive section must be adjusted to optimize the output, and the operation energy of the storage ring must be 163MeV, which is lower than the injection energy of the storage ring. Electrons must be decelerated after injection. This was tested successfully, when the gaps of the OK sections were at 140mm. But it was very difficulty to store sufficient beam current at 163 MeV when the gaps of the modulator and the radiator were set at 40mm. This led us to consider upgrade of the CHG facility to run the storage ring above 200 MeV. Meanwhile, we started R&D of SDUV-FEL, which is based on a 300 MeV

Linac. Obviously, it is better to take 200~300 MeV as the operation energy of the storage ring for the upgrade program of the CHG experiment facility.

In the upgrade, the wavelength of the seed is changed to 532 nm, and the NdFeB blocks of the modulator are replaced with the ones of the recent built undulator, which has been installed in the third long straight section. The period length of the modulator increases from 72mm to 92 mm, resulting in an unsymmetrical OK. The modulator resonates at the wavelength of the seed, but the radiator resonates at its harmonics. The varying range of electron energy and the corresponding varying range of modulator strength and radiator strength are listed in table 1.

Table 1 Electron energy and undulator strength

Output harmonics	3	2
Electron energy (MeV)	240~400	200~325
Modulator strength K_m	1.77~3.5	1.25~2.7
Radiator strength K_r	0.4~2.0	0.5~2.0

Table 2 Sample parameters

Electron beam (Single bunch mode)	Energy (MeV)	251
	Energy spread	0.016%
	Beam current (mA)	10
	Beam size (mm,mrad) σ_x, σ_y, σ_z, $\sigma_x{'}$, $\sigma_y{'}$	0.518,0.051,11.3, 0.024,0.015
Seed laser	Wavelength (nm)	532
	Power (MW)	30
	Radius (mm)	0.5
Optical klystron	K_m	1.9
	K_r	1.26
	Dispersive section parameter N_d	90
Output radiation	Wavelength (nm)	266
	Power (KW)	54
	Spectral ratio	1.9×10^9

As a sample, a set of parameters of the facility after upgrade, the calculated output power and spectral ratio are listed in table 2 [3]. The spectral ratio for a harmonic is defined as the ratio between coherent intensity and incoherent intensity in an infinitesimal solid angle aperture on the axis and infinitesimal bandwidth at that harmonic [4].

969

SPONTANEOUS RADIATION

Because the spectral ratio is proportional to the square of modulation rate of spontaneous radiation spectrum of an OK, deep modulation is desired [5]. The spontaneous radiation of the symmetrical OK was measured. At the beginning, the measured modulation rate was only 0.23. After re-alignment and adding an aperture of small diameter the modulation rate reached 0.4. For further improvement, numerical simulation was carried out, and results show that when the vertical orbit offset of the electron beam in the storage ring is 2mm and 1mm the modulation rate is 0.43 and 0.74 respectively. When orbit correction was carried out, the measured modulation rate reached 0.75 (Fig. 3).
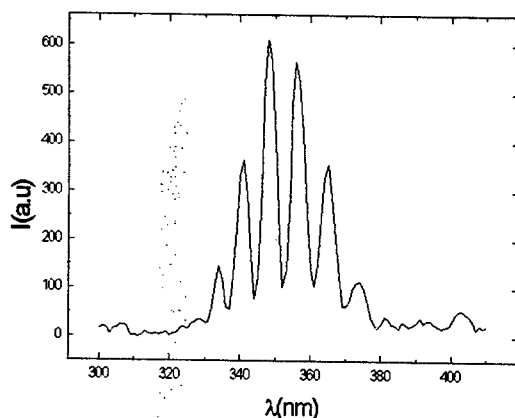

. Fig. 3   Modulated spontaneous radiation spectrum of the optical klystron

CHG MEASUREMENT SYSTEM

The main interest is to measure the spectral ratio. Figure 4 shows the layout of the measurement system. The difficult is the repetition rate of the spontaneous radiation pulses is much higher than that of the seed. In single bunch operation mode of the storage ring the former is 4.343 MHz. Due to the damping time of the electron beam in the storage ring and the performance of the seed laser, the latter is 1~10 Hz. To select and measure any coherent radiation pulse or incoherent radiation pulse from the radiation pulse train, a high on-off ratio ICCD is used as an optical shutter. The synchronization system is also shown in Fig. 4. An aperture of small diameter is placed before the spectrometer to eliminate off-axis radiation. The

measured ratio is integral ratio. The spectral ratio can be calculated, according to the actual solid angle aperture and bandwidth of the measurement system.
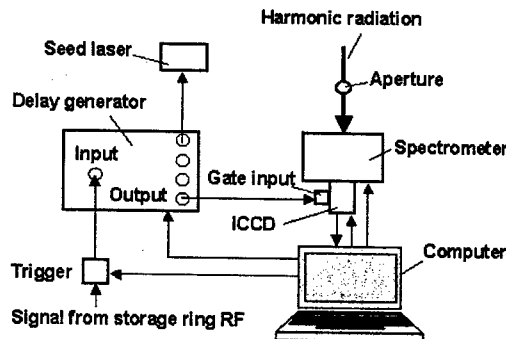

Fig.4 Measuring and synchronizing system

REFERENCES

[1] D. He, Construction and Commissioning of Hefei Synchrotron Radiation Source, Particle Accelerators, Vol.33, pp21-26, Gordon and Breach Science Publishers, Inc., (1990)

[2] L. H. Yu, et al, "High-gain harmonic generation free electron laser", Science, 289 (2000)

[3] Q. K. Jia, The Upgrade Program of CHG FEL, Presentation at the Conference on Accelerator Physics, Chengdu, China, (2002)

[4] R. Prazeres, et al, Coherent Harmonic Generation in the Vacuum Ultraviolet Spectral Range on the Storage Ring ACO, NIM in Physics Research A272, 68-72, (1988)

[5] R. Coïsson and F. De Martini, Physics of Quantum Electronics, Vol. 9, 939 (1982)

NUMERICAL STUDY OF COHERENT HARMONIC GENERATION IN THE VUV ON THE NIJI-IV FEL

H.Ogawa[#], K. Yamada, N. Sei, M. Yasumoto, T. Mikado,

National Institute of Advanced Industrial Science and Technology, 1-1-1 Umezono, Tsukuba, Ibaraki 305-8568, Japan

Abstract

Generation of the VUV radiation has been numerically performed based on coherent harmonic generation (CHG) scheme at NIJI-IV with an external laser. The CHG process in an optical klystron was simulated using the code GENESIS1.3 incorporating with its extended code. After performing the optimization of the parameter for the optical klystron, the dependence of the input laser power and the effect of the energy spread on the output radiation power are discussed.

INTRODUCTION

Coherent harmonic generation (CHG) is an attractive method as a source of tunable coherent radiation in the VUV. Considering advantage of operation without an optical cavity in CHG, we are preparing to produce the harmonics in the storage ring NIJI-IV FEL [1] by using either an external laser focused into an optical klystron [2,3] or the FEL oscillator itself. In this study we focus on the investigation of the harmonic generation by an external laser (3rd harmonic of Nd:YAG laser) with Monte Calro simulation.

The layout of the CHG in the transverse optical klystron, which consists of three sections, is illustrated in Fig. 1. In the first section, the energy exchange between the electron beam and the optical wave, supplied by an external pulsed laser, induces the energy modulation of the electron. In the second section, the energy modulation is transformed into an electron density modulation. The amplitude of the magnetic filed in the dispersive section is optimized so as to obtain the maximum radiation intensity at the end of the optical klystron. Consequently, in the last section, the coherent harmonic radiation is emitted from the second undulator. In this work, this CHG process is simulated in the case of a 6.3-m optical klystron ETLOK-II [1].
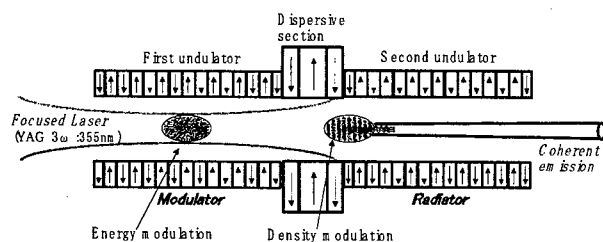
PROCEDURE OF SIMULATION

The electron beam is interacted with the third harmonic at 355nm of an external Nd:YAG laser which is focused into the center of the first undulator as shown in Fig.1. The electron beam dynamics in the first undulator is simulated along the undulator axis by using the code GENESIS 1.3 [4] which allows for the treatment of three-dimensional electron dynamics and non-axi-symmetric radiation field. The initial parameters for the electron beam at the entrance of the optical klystron are listed in Table 1. The external laser beam field is taken to be a fundamental Hermite-Gauss mode, and the magnetic field parameter of the undulator is chosen so that the wavelength of the external laser is resonated with the fundamental radiation of the undulator. As a result, the 6D phase space distribution $(x,y,p_x,p_y,\gamma,\theta)$ of the electron beam at the exit of the first undulator is obtained by GENESIS 1.3.

Table 1: Simulation parameters for the NIJI-IV FEL system.

Electron beam	
Energy	310 MeV
Relative energy spread	3.3×10^{-4}
Bunch length	17.4mm
Beam size σ_x	~0.8mm
σ_y	~0.3mm
Emittance ε_x	6.0×10^{-8}m rad
ε_y	8.4×10^{-9}m rad
Optical Klystron	
Magnetic period	
Undulator section	72mm
Dispersive section	216mm
Number of period	42×2
Total length	6.288m
K-value	2.29
Input laser (Nd:YAG)	
Wavelength	355nm
Energy	300mJ/pulse
Peak power	60MW
Repetition rate	10Hz

Figure 1: Schematic view of the setup for Coherent Harmonic Generation (CHG).

[#]ogawa.h@aist.go.jp

In the dispersive section, the phase shift is induced by the different transit time depending on the difference of the electron energy. We took the phase energy relation [5]

$$\Psi_j = \frac{\omega_{s1}}{\omega_{s2}}\left[\theta_j + \frac{d\theta}{d\gamma}(\gamma_j - \gamma_0)\right] \quad (1)$$

between the ponderomotive phase of the electron θ_j and Ψ_j at the entrance and the end of the dispersive section for jth electron, respectively. Here $\gamma_j - \gamma_0$ is the energy deviation from the mean energy of the electron beam in terms of the Lorentz factor, and the ratio ω_{s1}/ω_{s2} gives the harmonic number of the input laser. The factor $d\theta/d\gamma$ is a function of length and field strength of the dispersive section. Inserting the phase distribution at the end of the first undulator calculated by GENESIS 1.3 into Eq.(1), the 6D phase space distribution $(x, y, p_x, p_y, \gamma, \Psi)$ at the exit of dispersive section is determined.

Thus, the obtained parameters $x, y, p_x, p_y, \gamma, \Psi$ are written into a file as an input to GENESIS 1.3 for calculation in the second undulator. The coherent emission from the bunched electrons is again simulated along the second undulator axis using GENESIS 1.3, and then we get the harmonic radiation distribution at the exit of the optical klystron.

SIMULATION RESULTS

Optimization of the optical beam waist

First of all, the dependence of the third harmonic intensity on the radius of the optical beam waist w_0 was investigated. The number of emitted photons corresponding to the three different input laser powers P_{in}=30, 60 and 90 MW is plotted in Fig.2. In this simulation, the factor $d\theta/d\gamma$ in Eq.(1) was chosen so as to obtain the maximum harmonic intensity for the corresponding P_{in} and harmonic number. For example $d\theta/d\gamma = 0.3$ is the optimum value for the third harmonic at $P_{in} = 60$ MW.

As shown in Fig.2, the output intensities grow with increasing the waist size w_0 up to $w_0 \sim 1.0$ mm since the overlap of the electron beam with the optical wave increases. On the other hand, above $w_0 \sim 1.4$ mm, the intensities decrease due to diminishing electric field of pumping laser. It is interesting to note that the waist size w_0, which gives the maximum harmonic intensity, increases with increasing P_{in}. This optimum w_0 shift can be understood as the inhomogeneous transverse profile of electron bunching. For the low P_{in}, electric field of laser is insufficient to produce the electron density modulation, so the waist size w_0 must be reduced. On the contrary, for the high P_{in}, overbunching of the electron density occurs in the center of the beam, thus reducing the efficiency of the harmonic generation. To avoid the overbunching, the w_0 should be larger value, giving constant radial profile of the electron bunching.
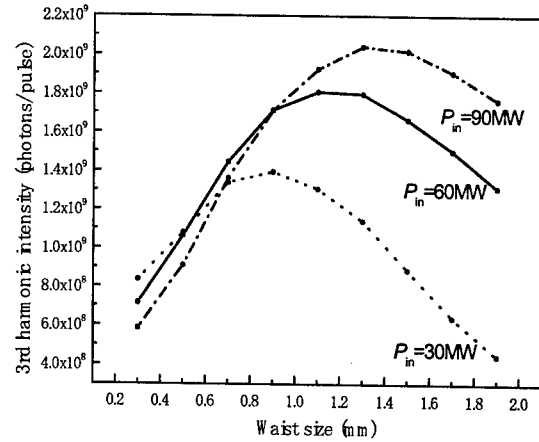

Figure 2: Dependence of the third harmonic intensity on the radius of the optical beam waist at the input laser power P_{in}=30, 60 and 90 MW with the electron average current 1 mA.

Power Dependence

Figure 3 shows the calculated photon intensities on the third and fifth harmonics of a pumped laser at 355 nm as a function of the laser peak power P_{in}. The calculation has been also performed taking into account an optimization of $d\theta/d\gamma$ parameter for each P_{in}, while w_0 is fixed at 1.1mm. The number of photons increases proportional to P_{in} in low laser power region, and is saturated above ~ 60 MW owing to the overbunching effect, giving a limit of the harmonic intensity. In the case of our laser power, P_{in} = 60MW, the number of photons were calculated as $\sim 2 \times 10^9$ and $\sim 3 \times 10^8$ photons/pulse for the third and fifth harmonics, respectively, at the electron average current 1mA in one bunch ring operation.
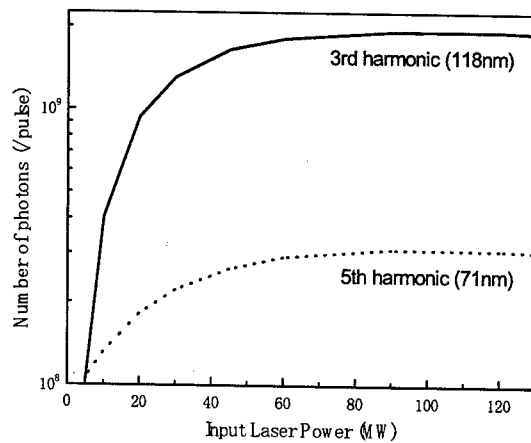

Figure 3: Calculation results of number of photons on the third and fifth harmonics as a function of the input laser power with the electron average current 1 mA.
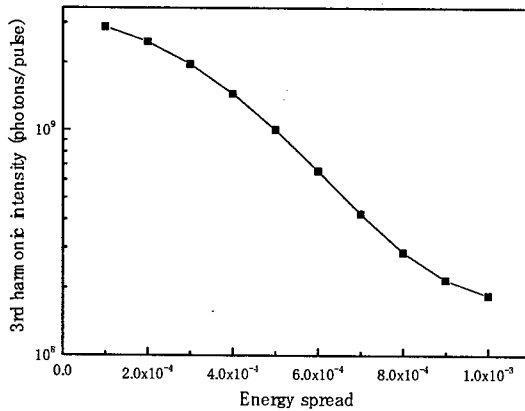
Effects of the Energy Spread

Figure 4: Effects of the relative energy spread on the output intensity.

Figure 4 shows the calculation result of dependence of the third harmonic intensity on the relative energy spread at the entrance of the first undulator. The efficiency of harmonic generation is critically dependent on the energy spread value.

The phenomenon which increases the energy spread, called turbulent anomalous bunch lengthening, appears above a certain current threshold. The anomalous bunch lengthening has been observed in NIJI-IV above an average current of 2-3 mA [6,7]. The obtained third harmonic intensity, which was simulated taking into account the effect of increasing energy spread with the beam current, is shown in Fig.5 by dash-dotted line. The photon intensity is saturated at $\sim5\times10^{10}$ photons/pulse due to the energy spread at higher beam current beyond the threshold current.

Recently we have replaced ring vacuum chambers in NIJI-IV with new low-impedance-type ones over 75 % of the ring circumference in order to suppress the microwave instability. [7]. After the replacement, the longitudinal broad-band impedance was reduced and the anomalous bunch lengthening doesn't appear below 15.3 mA which means energy spread of the beam is stable below ~15mA in the present experimental setup. As shown in Fig.5 by solid line, the third harmonic intensity grows proportional to the square of the average beam current in one bunch ring operation. Consequently, the number of photons on

the third harmonic can be expected to obtain $\sim4\times10^{11}$ photons/pulse and increase by a factor of 8 for the new vacuum-chamber system compared to the old one.
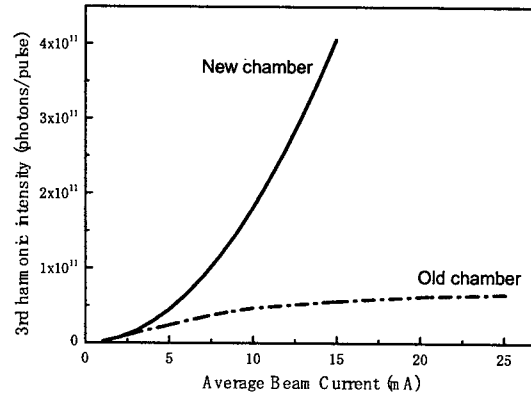

Figure 5: Expected number of photons for the new and old vacuum-chamber system as a function of the average beam current in one bunch ring operation.

ACKNOWLEGMENTS

REFERENCES

[1] T. Yamazaki *et al.*, Nucl. Instr. and Meth. A331 (1993) 27.

[2] K. Yamada *et al.*, Nucl. Instr. and Meth. A407 (1998) 193.

[3] H. Xu *et al.*, Proc. of PAC01, Chicago, 2001, p.2836.

[4] S. Reiche, Nucl. Instr. and Meth. A429 (1999) 243.

[5] L.H. Yu, Phys. Rev. A44 (1991) 44.

[6] K. Yamada *et al.*, Nucl. Instr. and Meth. A475 (2001) 205.

[7] K. Yamada *et al.*, Proc. 24th Free Electron Lasers Conf., Argonne, 2002, to be published

MEASURED PERFORMANCE OF THE FREE ELECTRON LASERS AND ELECTRON BEAM IN THE COMPACT STORAGE RING NIJI-IV

N Sei[#], K. Yamada, H. Ogawa, M. Yasumoto, T. Mikado, H. Toyokawa,

National Institute of Advanced Industrial Science and Technology, 1-1-1 Umezono, Tsukuba, Ibaraki 305-8568, Japan

Abstract

The temporal performance of the free electron lasers and the electron-beam qualities have been measured with the compact storage ring NIJI-IV at the electron-beam energy of 310 MeV. It was found that the pulse width and spectral width kept decreasing after the peak of the FEL macropulse intensity. It was confirmed that the bunch length and the energy spread increased due to the FEL oscillations. The ratio of the FEL gain to the cavity loss estimated from the beam qualities on and off FEL oscillations was almost in accord with the ratio evaluated directly with the measured data of the FEL gain and the cavity loss.

INTRODUCTION

A study of broad-band free electron lasers (FELs) has been developed with the compact storage ring NIJI-IV at the AIST. Although the circumference of the NIJI-IV is 29.6 m, it has two 7.25 m straight sections. A 6.3 m optical klystron ETLOK-II has been installed in one of the straight sections, and a 14.8 m optical cavity has been set on the extended part of this long straight section. The FEL oscillations have been achieved with the ETLOK-II at a wavelength region between 211 and 595 nm [1]. At present, we are aiming at the FEL oscillations in the VUV region. Moreover, a new optical klystron ETLOK-III for infrared FELs will be installed at the other straight section. FEL oscillations will be realized with using the higher harmonics from the ETLOK-III in a wavelength region between 1 and 12μm [2].

In order to advance the enhancement of the FEL wavelength region, we have renewed old vacuum chambers to low-impedance ones in the NIJI-IV. Because it was confirmed that the microwave instability was suppressed below the beam current of 15 mA, the longitudinal broad-band impedance became below 2 Ω [3]. The peak electron density in an electron bunch was expected to become 1.4 times or more before the improvement.

It is necessary for the enhancement of the FEL wavelength region to estimate the FEL gain accurately. Then, we checked the evaluation of the FEL gain based on the one-dimension theory of the storage ring FEL by investigating the NIJI-IV electron beam qualities before the improvement of the vacuum chambers [4]. The increase of the beam sizes was measured on the FEL

oscillations, and the enhancement of the energy spread due to the FEL oscillations was estimated from the increase of the beam sizes. The increase of the bunch length due to the bunch heating was also measured with a dual streak camera. In this article, we report the measured performance of the FEL and the electron beam qualities on and off the FEL oscillations in detail.

NIJI-IV ELECTRON BEAM

The electron beam qualities on the FEL oscillations at the wavelength of 300 nm were measured. The electron beam energy in the NIJI-IV was about 310 MeV. The electron bunch vibrated longitudinally by the amplitude of 3-9 μm and the period of 100 Hz. We ascertained that the power supply of the main magnets had line noise with the same period, but we could not remove it completely. The bunch length gently increased up to the beam current of 2-3 mA because of the potential well distortion. As Fig. 1 shows, the bunch length increased rapidly above 2-3 mA. The energy widening was also observed above the threshold beam current, so that the microwave instability would cause the increase of the bunch length and energy spread. The electron bunch had the complex shape in the higher current region where the microwave instability was remarkable. However, we regarded one standard deviation of a Gaussian fitting to the bunch shape as the bunch length. Because the bunch length is proportional to the
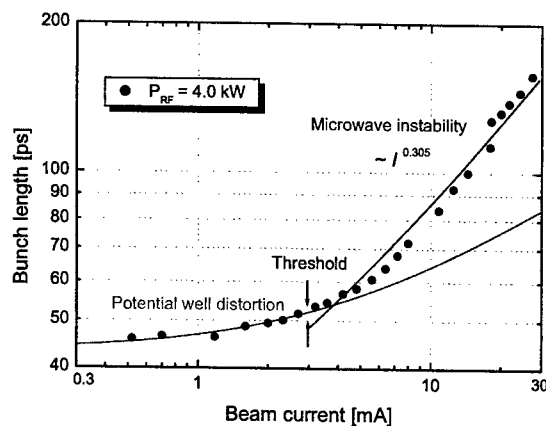

Fig. 1: Dependence of the bunch length on the beam current.

[#]Sei.n@aist.go.jp

energy spread, the bunch length $\sigma_l(I)$ at the beam current of I is described by

$$\sigma_l(I) \cong \sigma_{lp}(I)\left[\frac{\sigma_\gamma(I)}{\sigma_{\gamma 0}}\right]^{1+\delta} , (1)$$

where $\sigma_{lp}(I)$ is bunch length included an effect of the potential well distortion, $\sigma_\gamma(I)$ is energy spread and $\sigma_{\gamma 0}$ is natural energy spread [4]. The exponent δ_γ is ideally zero. Experimental value for the exponent δ_γ which was estimated by the fitting curve was about –0.06, and it was near an ideal value zero.

The beam sizes at the dispersive section of the ETLOK-II were measured. Because the betatron functions changed considerably in the long ETLOK-II, the beam sizes averaged through the ETLOK-II are needed to estimate the gain of the NIJI-IV FEL system. The ratio of the averaged beam size to the local beam size at the dispersive section was 1.01 in horizontal direction and 1.40 in vertical direction. The horizontal beam size was almost constant in the observed beam current, and it was about 0.85mm. The vertical beam size gently increased due to the multiple Touschek effect as the beam current increased. It was about 0.27 mm at the beam current of 30 mA.

The peak-electron density in a bunch, ρ_p, can be calculated with the bunch length and the beam sizes. The increase rate of ρ_p became small above ~10 mA due to the beam instabilities. The obtained maximum ρ_p was about 1.0×10^{17} m^{-3}. The FEL gain at relative beam energy γ is proportional to the peak-electron density. The FEL gain for the fundamental wavelength of an optical klystron, G_0, is described by the one-dimension theory as following equations [5]:

$$G_0 = 1.12 \times 10^{-13} \lambda_u^2 N_u^2 \left(N_u + N_d\right)K^2 , (2)$$
$$\left[J_1(\xi) - J_0(\xi)\right]^2 f\rho_p F_f \gamma^{-3}$$

$$\xi = K^2 \left(4 + 2K^2\right)^{-1} , (3)$$

where λ_u, N_u, f and F_f are period of the undulator sections, period number of the one undulator section, modulation factor and filling factor, respectively. A factor N_d is the interference order due to the dispersive section, and it was set to be 68, which was optimum value for the FEL gain in the beam-current region of 20-30 mA. The maximum FEL gain estimated with these equations was about 4.6% for the wavelength of 300 nm.

FEL AND ELECTRON BEAM

We observed the temporal and spectral structure of the FEL micropulse. It is known that the cavity-mirror loss except the optimum wavelength increases as the exposure of the optical klystron radiation increases [6]. Although the FEL gain on the FEL oscillations depends on the cavity detuning length strictly, it is approximately equal to the loss of the optical cavity. Therefore, the cavity loss can be evaluated by the threshold beam current for the FEL oscillation. In the case of the small cavity detuning length, the FEL micropulse composes the macropulse and
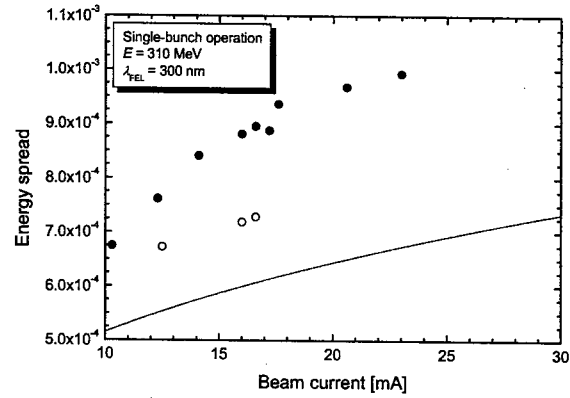

Fig. 2: Energy spread estimated from the horizontal beam size on the FEL oscillations (solid circle) and RF detuning of 2000 Hz (open circle).

the macropulse period depends on the detuning length. When the exposure was comparatively little and the cavity loss was about 1%, the macropulse period was 3.5-5 ms. When the cavity loss became about 2%, the macropulse period decreased down to 2.5-3.5 ms. We observed that the pulse width of the FEL micropulse was minimized in the macropulse mode when the FEL intensity did not become the maximum but decreased. We also observed that the spectral width decreased more than 1ms after the peak of the FEL intensity. These features of the FEL micropulse in the macropulse mode can be explained with simple one-dimension finite difference equations based on the bunch heating theory. The results obtained from the simulations were reported in another paper [7].

We measured the electron-beam qualities on the FEL oscillations at the cavity loss of 2%. According to the bunch heating theory, the interaction between the FEL and electron beam enhances the energy spread. Then we observed the beam sizes at the BM3 where the dispersion function was about 0.31. The horizontal beam size on the FEL oscillations increased as much as 1.1-1.2 times compared with that off the FEL oscillations. The FEL oscillation did not cause an effective change in the vertical beam size. The energy spread estimated with the machine functions on the FEL oscillations is plotted in Fig. 2. This figure shows that the energy spread with RF detuning of 2000 Hz also was enhanced by the bunch heating.

The bunch length on the FEL oscillation was observed to increase due to the bunch heating. The increase rate of the bunch length and energy spread is shown in Fig. 3. The increase rate of the bunch length had a peak at around 10 mA, and it decreased in the higher beam current. The reason was in the bunch shape. The bunch shape off the FEL oscillation was peaky at around 10 mA, and it became like a bell over 20 mA. Because the microwave instability was suppressed by the enhancement of the energy spread on the FEL oscillation, the bunch shape became close to Gaussian. Then, the standard deviation of
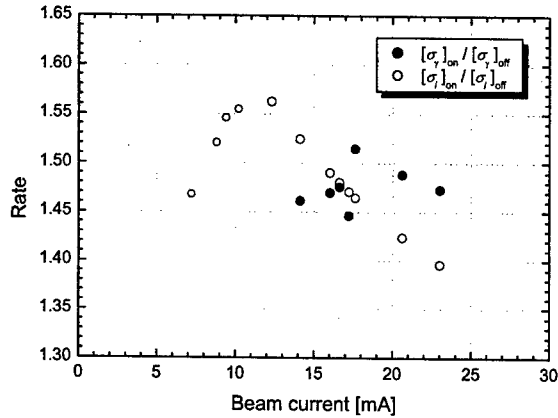
975

Fig. 3: Increase rate of the bunch length and energy spread due to the bunch heating.
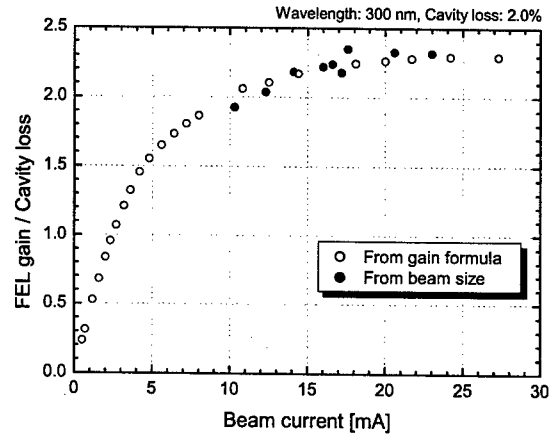

Fig. 4: Ratio of the FEL gain to the cavity loss estimated from the beam qualities on and off the FEL oscillations (solid circle) and the measured data of the FEL gain and the cavity loss (open circle).

the bunch length was increased easily at around 10 mA, and it was not easy to increase in the higher current region. In the case of the energy spread, the increase rate was almost constant over 12 mA. The reason is that the FEL gain is also constant in the beam-current region.

Considering the observed bunch length and energy spread on and off the FEL oscillations, we can obtain a ratio of the FEL gain to the cavity loss. Because the FEL gain is given by eqs. (2) and (3), the ratio R_G is given by the following description [4]:

$$R_G \equiv \frac{[G_0]_{off}}{[G_0]_{on}} = \frac{[\sigma_l]_{on}}{[\sigma_l]_{off}} \frac{[f_\gamma]_{off}}{[f_\gamma]_{on}} \; , (4)$$

where suffixes "on" and "off" represent the state of the FEL oscillation. The R_G evaluated from the data in the FEL experiments is plotted in the Fig. 4. We knew the FEL gain from eq. (2) and the cavity loss from the threshold beam current of the FEL oscillation, so that we could evaluate R_G directly without using eq. (4). Because the optical cavity slowly shifted from the best tuning in the low beam-current region where time passed from the start of the FEL experiment, the ratio calculated with eq. (4) tended to be undervalued. However, it is noted that the ratio calculated with eq. (4) was almost in accord with the ratio evaluated directly. This fact suggests that the evaluation of the energy spread was correct.

CONCLUSIONS

We have measured the NIJI-IV electron-beam qualities and the temporal feature of the FEL micropulse. We noted that the pulse width and spectral width kept decreasing after the peak of the FEL macropulse intensity. The bunch length and energy spread were observed to increase due to the bunch heating while the FEL oscillated. The increase

rate of the bunch length gently decreased over ~10 mA because the bunch shape off the FEL oscillation changed due to the microwave instability. The increase rate of the energy spread was almost constant. The ratio of the FEL gain to the cavity loss estimated from the beam qualities on and off the FEL oscillations was almost in accord with the ratio evaluated directly with the measured data of the FEL gain and the cavity loss. Then we can conclude that the FEL gain estimation based on the well-known one-dimension theory is applicable to the NIJI-IV FEL system.

We have replaced the vacuum chambers in the NIJI-IV so as to suppress the microwave instability. The longitudinal broad-band impedance have been confirmed to be below 2Ω. We will investigate the new electron-beam qualities and the feature of the FEL micropulse in the VUV region.

REFERENCES

[1] N. Sei *et al.*: Proc. of APAC01, Beijing, 2001, to be published.

[2] N. Sei *et al.*: Jpn. J. Appl. Phys. **41** (2002), 1595.

[3] K. Yamada *et al.*: Proc. 24th Free Electron Lasers Conf., Argonne, 2002, to be published.

[4] N. Sei *et al.*, submitted to Jpn. J. Appl. Phys.

[5] M. Billardon *et al.*:IEEE J. Quantum Electron. **21** (1985) 805.

[6] K. Yamada *et al.*: Nucl. Instrum. & Methords **A393** (1997) 44.

[7] N. Sei *et al.*, submitted to J. Appl. Phys.

HIGH-POWER ELECTRON BEAM INJECTORS FOR 100 KW FREE-ELECTRON LASERS[†]

A. Todd, H. Bluem, V. Christina, M. Cole, J. Rathke, T. Schultheiss,
Advanced Energy Systems, P.O. Box 7455, Princeton, New Jersey 08543-7455, USA

I. Campisi, E. Daly, D. Douglas, G. Neil, J. Preble, R. Rimmer, C. Rode, J. Sekutowicz, T. Whitlatch,
M. Wiseman, Thomas Jefferson National Accelerator Facility, Newport News, VA 23606, USA

P. Colestock, J. P. Kelley, S. Kurennoy, D. Nguyen, S. Russell, D. Schrage, R. Wood, L. Young,
Los Alamos National Laboratory, Los Alamos, NM 87545, USA

Abstract

A key technology issue on the path to high-power FEL operation is the demonstration of reliable, high-brightness, high-power injector operation. We describe two ongoing programs to produce 100 mA injectors as drivers for 100 kW free-electron lasers. In one approach, in collaboration with the Thomas Jefferson National Accelerator Facility, we are fabricating a 750 MHz superconducting RF cryomodule that will be integrated with a room-temperature DC photocathode gun [1] and tested at the Laboratory. In the other approach, in collaboration with Los Alamos National Laboratory, a high-current 700 MHz, normal-conducting, RF photo-injector [2,3] is being designed and will undergo thermal management testing at the Laboratory. We describe the design, the projected performance and the status of both injectors.

INTRODUCTION

High-power free-electron lasers (FEL) have been proposed for both commercial and defence applications. Commercial FEL material processing applications [4] have been proven using conventional lasers and patented, but their market insertion has been impeded by the lack of suitable, economic light sources. 100 kW IR and 10 kW UV FEL devices producing radiation for a lifecycle cost of less than one cent per delivered kJ in the IR and a few cents per kJ in the UV have tremendous market potential. However, in order to achieve these radiation cost targets, high-current, low emittance electron beam injectors must be developed to drive the energy-recovery-linacs (ERL) [5] that can deliver the required wall-plug electrical efficiency needed to approach these radiation costs [6].

Advanced Energy Systems (AES) has been collaborating with Los Alamos National Laboratory and the Thomas Jefferson National Accelerator Facility (JLAB) on the development of two distinct 100 mA high-brightness electron injector systems. The Los Alamos device is a normal-conducting, water-cooled 700 MHz RF

photo-injector while the JLAB device closely couples a DC gun and a 750 MHz superconducting RF (SRF) accelerator that utilizes single-cell cavities to handle the high RF input power. The injectors described below, given performance requirements of > 100 mA, < 1% energy spread, < 10 microns transverse and < 100-200 keV-psec longitudinal rms normalized emittance will be capable of driving 100 kW and higher power IR FEL devices.

DC GUN AND SRF INJECTOR

The JLAB 10 kW IR FEL will utilize a DC gun and CEBAF "quarter cavity" linac to deliver 10 mA to the recirculating arc. For the 100 mA injector needed to drive a 100 kW FEL, the electron beam power approaches one megawatt and it is desirable to utilize single cell cavities. To provide high-order mode (HOM) and beam breakup (BBU) instability headroom, the frequency has been reduced to the 750 MHz subharmonic of the present FEL.
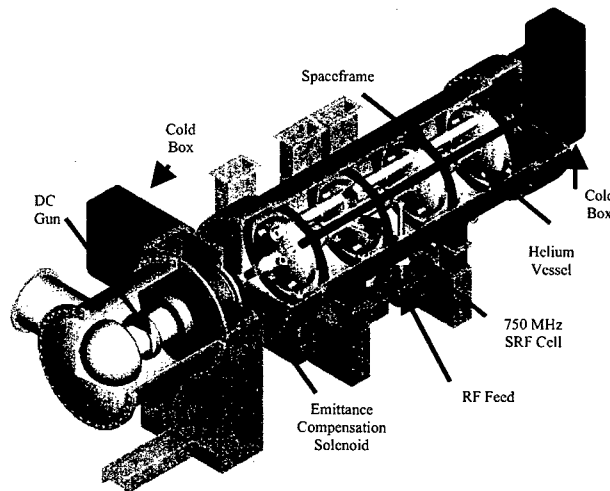

Figure 1: Isometric diagram of the 750 MHz DC gun and single-cell 100 mA SRF injector.

AES has completed the physics design of the three cell 750 MHz, 7 MeV SRF injector linac, utilizing transverse emittance compensation [7], that is shown in Fig. 1. The fourth upstream cell location is presently used for helium inventory and does not contain an accelerating cell. With a 500 kV DC gun, a pulse repetition frequency (PRF) of

750 MHz and 133 pC bunches, our analysis shows that this injector delivers a 7 MeV, 100 mA beam with a transverse normalized rms emittance of 1.2 microns, a longitudinal emittance of 44 keV-psec and an energy spread of 0.5%. As noted, this will meet the beam requirements at the wiggler for a 100 kW IR FEL.
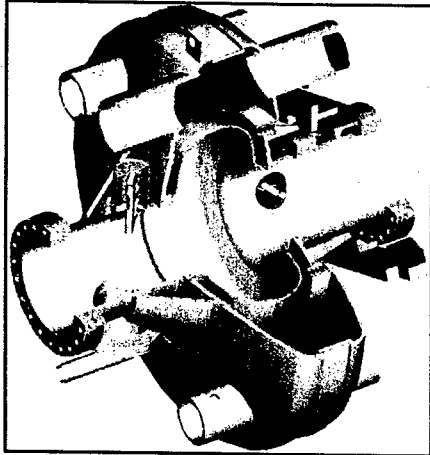

Figure 2: SRF injector cell

The key engineering issues with the injector are the achievement of 500 kV from the upgraded JLAB DC gun [8] and the impact of the high RF power level in the SRF accelerator. The present JLAB DC gun on the 10 kW FEL is undergoing conditioning to the 500 kV level. We have performed RF, thermal and stress analysis on the SRF cells that indicates the device should be capable of CW 100 mA operation and removing the expected HOM power load. A single cell cavity is illustrated in Fig.2.

Figure 3: SRF injector cold model undergoing testing

This injector is now in the midst of the fabrication cycle and all components are scheduled for delivery to JLAB by late 2003. Cold modelling to finalize the RF coupler and HOM outcoupler details is in progress at AES as shown in Fig. 3. The device is "100 mA-capable" with the exception of the three SNS-style RF power couplers [9]. 500 kW replacement couplers are presently being developed in a parallel program, but because the funding for the RF and DC power supplies needed to drive the device at 100 mA CW has not been authorized at this time, initial testing will be at full bunch charge but lower PRF in the JLAB injector test stand. Reduced PRF 1 nC

single bunch performance measurements are also planned to examine the viability of extrapolating this technology to even higher power levels. Should the device meet the specified performance goals, it has been proposed that it be installed on the existing JLAB FEL as shown in Fig. 4 as the front end of a 100 kW upgrade to that device.
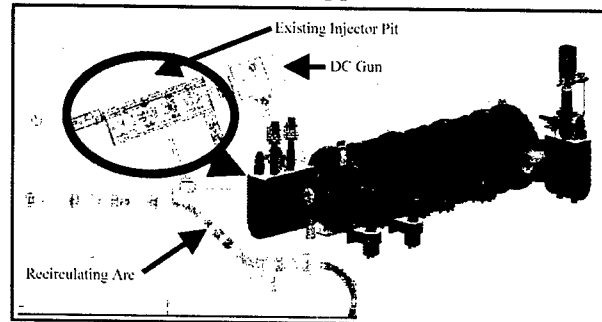

Figure 4: Injector accelerator cold mass in proposed installed position at the JLAB IR FEL.

RF PHOTO-INJECTOR

The Los Alamos 100 mA injector concept begins with a 2.5 cell water-cooled, RF photo-injector with a focusing and bucking solenoid. This is followed by a 4 cell normal-conducting booster linear accelerator. The accelerating field in the gun is held to 7 MV/m and reduced in the booster to control resistive power losses. The solenoid magnetic and gun accelerating fields are shown on Fig. 5. The end cavity on the right is a non-resonant vacuum pumping cavity.
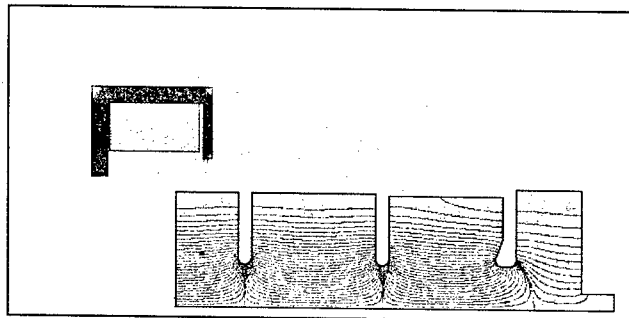

Figure 5: Focussing and bucking solenoids with their magnetic fields and the electric fields in the accelerator for the normal-conducting injector.

The physics and conceptual engineering design of this injector has been performed by Los Alamos. With a bunch charge of 3 nC, the design achieves a transverse rms normalized emittance of 7 microns, a longitudinal emittance of 200 keV-psec and an energy spread of less than 1%. The energy at the end of the gun is 2.7 MeV rising to 5.5 MeV after the booster. At a PRF of 33.3 MHz, the injector delivers 100 mA, which value increases to greater than 1 A at a PRF of 350 MHz.

The key issue for this normal-conducting copper injector, which is illustrated in Fig. 6, is the thermal management of the resistive losses at the high accelerating gradient needed to generate high-brightness
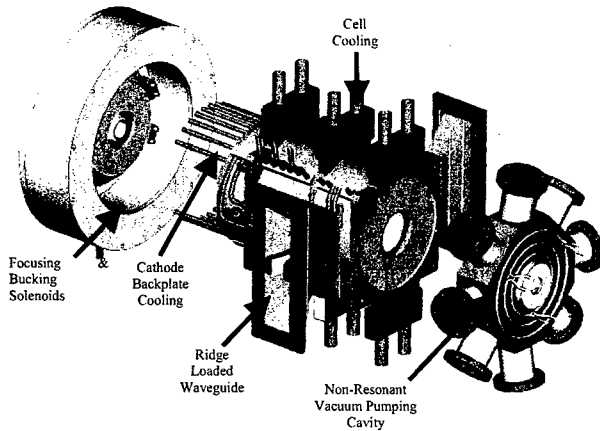
Figure 6: Schematic diagram of the 700 MHz, 100 mA photo-injector.

in the electron beam. AES has performed the critical thermal and stress analysis of the device which demonstrates that adequate cooling can be provided at flow rates that do not cause erosion or excessive vibration while maintaining the desired temperature stability. Fig. 7 shows the steady-state thermal distribution where it can be seen that the temperature variation is constrained to less than 30 C throughout the gun. The corresponding stress analysis indicates sufficient margin for the Glidcop gun material as shown in Fig. 8.
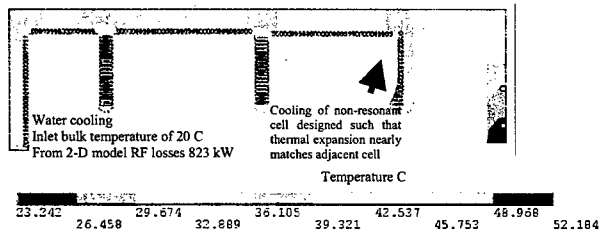

Figure 7: Steady-state thermal distribution in the 2.5 cell photo-injector gun.
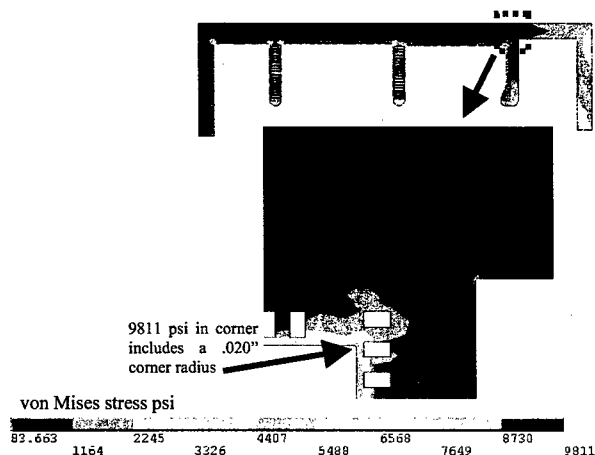

Figure 8: Steady-state thermal stress in the 2.5 cell photo-injector gun showing the peak stress.

This injector has completed the preliminary engineering design phase and long lead item procurement is in

process. As with the previous SRF injector concept, it is presently not possible to perform a full power beam test. Consequently, the plan is for AES to deliver the fabricated gun to Los Alamos in May 2004 for thermal management testing. This will demonstrate that the gun can satisfy the engineering operating requirements. The confirmation of the projected physics performance of the injector can then be completed under a follow-on program.

CONCLUSIONS

The projected performance and fabrication status of two 100 mA high-brightness electron beam injector concepts were described. The physics designs of both devices, which are intended to drive 100+ kW IR FEL's, meet the requisite performance specifications. The DC Gun and SRF injector device is in fabrication, with component delivery to JLAB scheduled for late 2003. The RF photo-injector device has completed preliminary design, with gun delivery to Los Alamos scheduled for mid 2004. The testing of both injectors is presently planned for 2004. Because of equipment limitations at both Laboratory sites, neither device can be beam tested at full current at this time. The JLAB test will be at full charge and reduced current while the Los Alamos test will demonstrate CW thermal management without beam. Both injectors are designed to deliver the specified 100 mA performance under follow-on programs. In particular, the JLAB injector will be used as the front end of a 100 kW upgrade to the existing FEL if the required performance is demonstrated and the upgrade program is funded.

REFERENCES

[1] C. K. Sinclair, *Nucl. Instr. Meth.* **A318** (1992) 410-414.
[2] J. S. Fraser et al., "Photocathodes in Accelerator Applications," *Proceedings of the 1987 Particle Accelerator Conference*, IEEE 87CB2387-9 (1987) 1319.
[3] S. Kurennoy et al., "Photocathode RF Cavity Design for High-Power CW FEL," these *Proceedings*.
[4] http://www.jlab.org/FEL/LPC/applications.html.
[5] G. R. Neil and the Jefferson Laboratory IR FEL team, "Sustained Kilowatt Lasing in a Free-Electron Laser with Same Cell Energy Recovery," *Phys. Rev. Lett.* **84**, (2000) 662-665.
[6] M. J. Kelley, "Materials Processing Research and Development Opportunities with the New Generation of FEL's," SPIE Proc. **3888** (2000) 598-605.
[7] B.E. Carlsten, "Photoelectric Injector Design Code," *Proceedings of the 1989 IEEE Particle Accelerator Conference*, IEEE 89CB2669-0 (1989) 313.
[8] S. V. Benson et al., "A 10 kW IRFEL Design for Jefferson Lab," *Proceedings of the 2001 IEEE Particle Accelerator Conference*, IEEE 01CH37268 (2001) 249.
[9] I. E. Campisi et al., "The Fundamental Power Coupler for the Spallation Neutron Source (SNS) Superconducting Cavities," *Proceedings of the 2001 IEEE Particle Accelerator Conference*, IEEE 01CH37268 (2001) 1140.

THE MIT BATES X-RAY LASER PROJECT

T. Zwart, M. Farkhondeh, W. S. Graves, F. Kaertner, R. Milner, D.E. Moncton, C. Tschalaer,
J. B. van der Laan, F. Wang, A. Zolfaghari, MIT Bates, Middleton MA 01949, USA

Abstract

MIT and the Bates Linear Accelerator Center are exploring the construction of an x-ray free electron laser user facility. It will be based on a superconducting linac of 4-8 GeV energy, and produce XUV light in the 0.3-100nm range at kilohertz repetition rates. The facility will be a full user facility incorporating up to 30 beamlines. Conventional lasers that produce the electron beam, seed the FEL and execute pump-probe experiments are carefully integrated. The current design of the facility is discussed.

INTRODUCTION

Recent advances in accelerator, laser and undulator technology [1] [2] have created the possibility of constructing a national user facility based on an intense free-electron laser at extreme ultraviolet and x-ray wavelengths. MIT is exploring the construction of such a facility at its Bates Laboratory site. The facility would produce x-ray beams with peak brilliance some ten orders of magnitude greater than are available from today's synchrotron sources, and pulse durations from 100 femtoseconds to less than 1 femtosecond. The wavelengths produced will range from 0.3 nm to 100 nm in the fundamental, with substantial power in the x-ray 3rd harmonic at 0.1 nm. The possibility of future upgrades to even shorter wavelengths will be preserved in the design. Based on a superconducting linac (with energy above 4 GeV) incorporating a number of extraction points, the complex will include the potential for 30 undulators and x-ray beamlines.

EXPERIMENTAL PROGRAM

The characteristics of the proposed x-ray laser source will enable a class of experiments that are beyond the reach of today's technology. For the first time, this source will combine short pulses, high power and coherence in the range between 100-0.1 nm. The science that is foreseen spans many disciplines including atomic and fundamental physics, condensed matter physics and materials sciences, femtochemistry, structural biology and various fields of engineering. The x-ray laser proposal [3] includes eight contributions from scientists at MIT, Brandeis, Yale, Argonne, and the Stanford Synchrotron radiation Laboratory. In some instances the techniques of the proposed experiments will require fundamentally new approaches and may have more similarity with experiments performed using table top lasers than those using synchrotron sources.
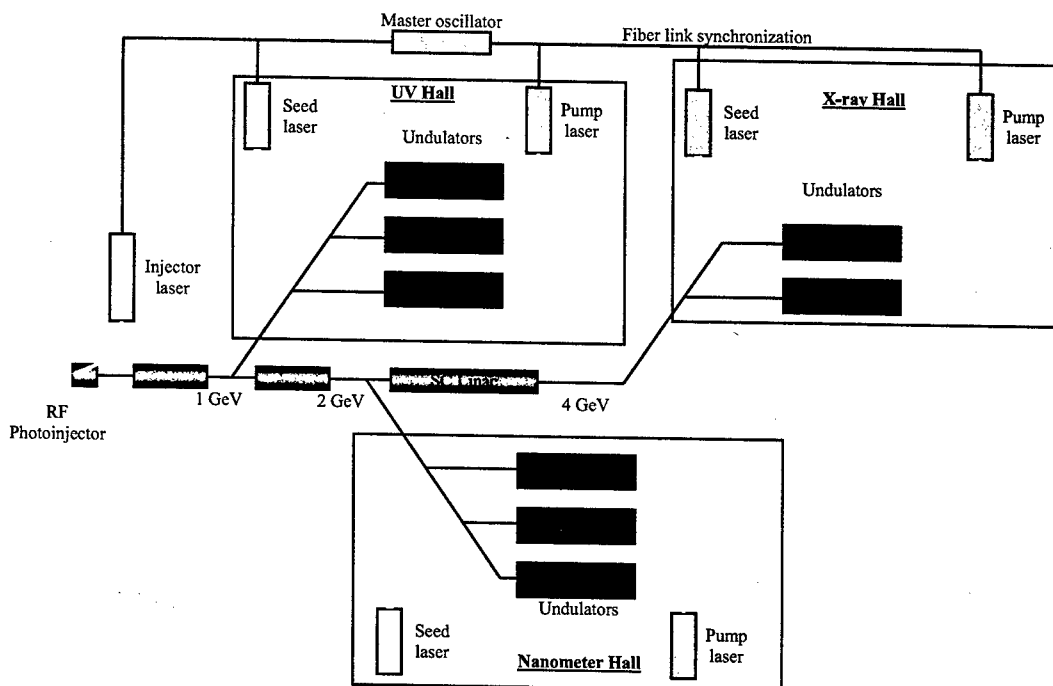

Figure 1: Layout of the MIT x-ray laser facility.

PRELIMINARY FACILITY DESIGN

While detailed design of the x-ray laser user facility will require additional resources, considerations of initial facility parameters and how best to integrate the various systems have already begun. Figure 1 shows a schematic layout of the facility and table 1 lists many of the accelerator parameters.

Table 1: Facility Parameters

Injector:	
Structure	1.3 GHz Copper 2 ½ Cell Independent Phasing
Repetition rate	1-10 kHz
Duty factor	2 %
Bunch charge	100-500 pC
Transverse emittance	0.5-2 um
Linac:	1.3 GHz TESLA structure
Gradient	20 MV/m
Active length	200 m
Total length	300 m
Linac duty factor	10%-CW
2K Dynamic heat load	<10 kW
RF coupling (Q_{ext})	$2 \cdot 10^7$
RF power/cavity	15 kW
Total Facility Power	<15 MW
Electron beam switches	1-10 kHz RF separators or Fast Ferrite Magnets TBD
Undulators:	
Undulator Beamlines	10-30
Undulator Periods	15-50 mm
Saturation Lengths	5-50 m
Rep. Rate/Undulator	~1 kHz
Total facility length	500 m

A room temperature RF photoinjector produces moderate charge, bright electron bunches at multi-kilohertz repletion rates. These bunches are accelerated in a superconducting 1.3 GHz TESLA-style linac [4] to energies up to ~4 GeV. The distortion of ~20 ps bunches in longitudinal phase space is linearized with a 3rd harmonic 3.9 GHz RF structure and compressed to sub-picosecond lengths at two bunch compressors located in the early stages of the accelerator. Three extraction points serviced by either RF separators or fast ferrite deflecting magnets deliver the bunches to the three experimental halls (VUV, nanometer and x-ray). In the baseline concept, each extraction point feeds 3-6 undulator lines, with each undulator receiving kHz repetition rates, and each capable of supporting multiple x-ray beamlines. As can be seen in the figure, conventional laser systems are tightly integrated into the design.

LASER PERFORMANCE

Advanced laser technology will be used throughout the proposed facility. Laser systems will provide an extremely stable base clock for the RF master oscillators and all other facility timing systems. Picosecond, UV lasers operating at kHz rates are now available which will meet the requirements of the RF photoinjector. Conventional laser systems will also be present in all experimental halls for use as either pumps or probes in conjunction with the FEL x-ray beams and to generate seed pulses.

In order to produce beams of the highest quality, various methods of seeding the electron beam with high harmonics of laboratory lasers are currently under investigation, as is lasing by self-amplification of spontaneous emission (SASE). A number of these methods will be exploited to produce radiation sources to match experimental needs. The spectral and timing characteristics of both SASE and seeded beams have been modeled using the GINGER FEL simulation code and are reported in reference [5]. Seeding opens the possibility of creating diffraction limited FEL beams which can be tailored either for short pulse length (τ~1 fs) or narrow bandwidth ($\Delta E/E < 10^{-5}$). Table 2 shows how the parameters of the proposed MIT x-ray laser compare with existing synchrotron sources and several other proposed FEL facilities. The peak brilliance is ten orders of magnitude greater than is available at today's 3rd generation synchrotron sources, and is comparable to the peak brilliance expected at other propsed FEL facilities. While the peak brilliance is one of the strong suits of the proposed machine, it's time averaged flux is still comparable to the synchrotron sources.

EFFICIENT UPGRADE PATHS

The proposed facility allows several efficient paths for later upgrades. The use of a high duty factor, possibly CW, superconducting linac will support additional beamlines, to a maximum of 30 in the present concept. The development of shorter period (λ~10mm) high field (B~1T) undulators could be used with the 4 GeV beam to reach x-ray wavelengths shorter than 0.3 nm in the fundamental. The development of substantially brighter injectors, with transverse emittance < 1 um, will reduce saturation lengths and thus undulator costs. Finally, the 1.2 km Bates site allows for the extension of the linac to higher energies which would also extend the reach of the facility to shorter wavelengths. This energy upgrade would be possible while the proposed machine was operational, a vital consideration for a user facility.

Table 2: FEL Beam Properties

	APS	MIT Bates			BESSY	LCLS	TESLA	Cornell
	Und. A	SASE FEL	Min bandwidth seeded FEL	Min pulse length seeded FEL	FEL	FEL	FEL	ERL
X-rays per pulse (0.1% max BW)	1.E+08	3.E+11	3.E+11	6.E+09	1.E+13	2.E+12	2.E+12	1.E+07
Peak power (GW)	3.E-06	4.0	4.0	4.0	7.0	8.0	20.0	7.E-05
Peak brilliance (p/s/0.1%/mm2)	3.E+22	1.E+33	3.E+35	7.E+33	5.E+32	1.E+34	3.E+34	3.E+25
Peak flux (p/s/0.1%)	1.E+18	6.E+24	6.E+24	1.E+23	5.E+25	7.E+24	1.E+25	4.E+19
Peak trans. coh. flux (p/s/0.1%)	4.E+14	6.E+24	6.E+24	1.E+23	5.E+25	7.E+24	1.E+25	2.E+17
Avg. flux (p/s/0.1%)	7.E+14	3.E+14	3.E+14	6.E+12	8.E+16	2.E+14	5.E+15	2.E+16
Average brilliance (p/s/0.1%/mm2)	4.E+19	5.E+22	1.E+25	3.E+23	1.E+24	4.E+23	1.E+25	1.E+22
Average coherent flux (p/s/0.1%)	2.E+11	3.E+14	3.E+14	6.E+12	8.E+16	2.E+14	5.E+15	8.E+13
Trans. coh. fract. (%)	0.03	100	100	100	100	100	100	0.5
Degeneracy parameter	0.03	4.E+09	3.E+11	6.E+09	8.E+11	4.E+09	1.E+08	100
Pulse length (fs)	73000	50	50	1	200	230	200	300
Photon beamlines	34	10-30	10-30	10-30	3	1	5	~20
Wavelength (nm)	0.015 - .4	0.3 - 100	0.3 - 100	0.3 - 100	1.2 - 60	0.15 - 1.5	0.1 - 1.5	0.03 - .5
Pulse frequency (Hz)	7.E+06	1000	1000	1000	8000	120	2300	1.30E+09

CONCLUSIONS

The proposed MIT x-ray laser user facility seeks to capitalize on the recent advances in accelerator FEL technology. Use of the latest low emittance RF photoinjectors, TESLA SRF linac structures, and hybrid permanent magnet undulators will allow the facilty to serve multiple users with 100-0.3 nm beams of unprecedented brilliance and coherence. The careful integration of conventional laser systems in the design from the outset will allow the facility to exploit both the ultrafast or narrow bandwidth x-ray beams that will be available with the successful implementation of seeding.

The MIT team and its collaborators have produced a three year design study proposal that is now before the National Science Foundation. An accelerator review committee is being assembled and will convene in Fall 2003. A series of workshops on the science that would be possible with such a facility will also begin in Fall 2003 on the MIT campus. A major goal of the proposed study is to prepare the facility design to sufficient maturity such that construction of the x-ray laser could begin in 2007.

REFERENCES

[1] S.V.Milton et al., "Exponential gain and saturation of a self-amplified spontaneous emission free-electron laser," Science **292**, 2037 (2001).

[2] V. Ayvazyan et al. "Generation of GW radiation pulses from a VUV free-electron laser operating in the femtosecond regime," Phys. Rev. Lett. **88**, 104802 (2002).

[3] http://mitbates.mit.edu/xfel

[4] TESLA Technical Design Report, http://tesla.desy.de/ ew_pages/TDR_CD/start.html

[5] W.S. Graves, "Simulations of an x-ray FEL seeded with attosecond pulses," these proceedings.

THE MUCOOL TEST AREA LINAC EXPERIMENTAL FACILITY AT FERMILAB

D. Errede, University of Illinois, Urbana-Champaign, IL USA

R. Alber, A. Bross, M. Foley, S. Geer, C. Johnstone, N. Mokhov, B. Norris, M. Popovic, I. Rakhno, K. Vaziri, FNAL, Batavia, IL 60510, USA

E. Black, Illinois Institute of Technology, Chicago, IL USA,

M. A. C. Cummings, Northern Illinois University, Dekalb, IL USA

Abstract

The initial phase of civil construction has begun on a new Linac Experimental Facility at Fermilab with beneficial occupancy anticipated in fall, 2003. This facility is being designed for multipurpose use by establishing direct and independent control over incident beam parameters; for example, pulse duration from 1 – 50 μsec, and beam transverse sizes from 1 – 15 cm (95% of beam). The facility will be capable of accepting up to the full Fermilab Linac beam intensity (1.6 x 10^{13} protons/pulse @ 15 Hz) making it one of the few areas where a primary beam is available for high intensity experiments. The purpose of the facility initially is to test the basic techniques and components proposed for muon ionization cooling in a proton beam judged equivalent in impact to a muon beam for a Neutrino Factory or Muon Collider. As such, the facility will provide the advanced cyogenic capability and safety systems required to perform R&D on liquid hydrogen targets. However, parallel future experiments are invited and, as a general facility, many areas of physics including radiation, medical, nuclear, atomic and beam diagnostics and control will be supported.

INTRODUCTION

A new test beam facility is under construction currently at Fermilab. The Mucool Test Area (MTA) consists of an experimental hall and a support building housing the cryogenic facilities. The MTA has megawatt power capability. It uses the fully diverted Linac 15 kW proton beam. Construction is expected to be completed in Fall of 2003 and the facility made available to the Mucool experiment for muon ionization cooling channel component testing. Thereafter others users are invited to make use of the test beam facility, to be one of the only full intensity linac test beams available in the world.

FACILITY DESCRIPTION AND USE

The MTA is a test beam facility located southwest of the Fermilab Linac. The experimental hall (Figure 1) was designed to have the capacity to perform tests on the liquid hydrogen absorbers of the Mucool (muon ionization cooling) experiment. This includes all safety requirements associated with the handling of liquid hydrogen and liquid helium. Filling tests and flow tests of different types of hydrogen absorbers are scheduled in the MTA initially. Others include high power tests from both heat sources and the high intensity beam available from the Linac beam. Linac beam parameters are listed in Table 1[1]. Beam design parameters requested by the
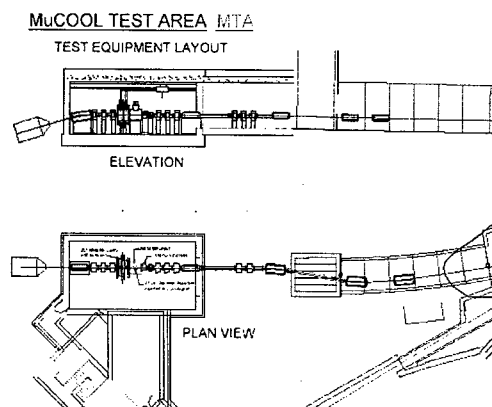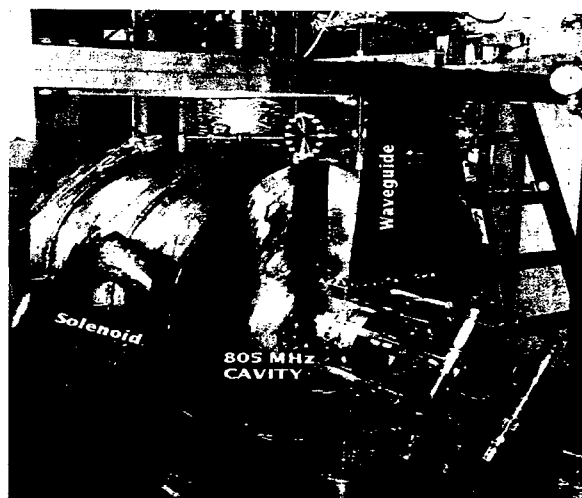

Figure 1: Plan and elevation layout of MTA.

Figure 2: Solenoid and 805 MHz RF cavity

Table 1: General Linac beam parameters

Parameter	Value	Unit
Kinetic Energy	401.5	MeV
Energy Spread	1	MeV
Peak Current	52	mA
RF Structure	201.24	MHz
Bunch Length	0.208	ns
Pulse Length	50	μs
Max Particles/Bunch	1.6	10^9
Max Particles/Pulse	1.6	10^{13}
Max Beam Power	15.7	kW
Beam Emittance(95%)	8	mm-mrad
σmax (rms)	9	mm

Table 2: Beam parameters proposed for Mucool Test Area

Parameter	Minimum	Maximum	Unit
Beam Size $\pm 3\sigma$	1	30	cm
Beam Divergence $\pm 3\sigma$	± 0.5	± 14	mr
#pulses/sec	0	15	Hz
#protons/pulse	1.6	16	10^{12}
Pulse duration	5.0	50	μs

the initial users of this new test beam facility are listed in Table 2[1].

In order to simulate the effects of a large precooled muon beam depositing energy into the hydrogen absorber the proton beam must be adjustable just prior to the devices. For instance the beam must be able to cover the entire face of the absorber for which present designs vary from 11 to 18 cm in radius. A triplet of large-aperture quadrupole magnets before the experiment increases the beam size. Downstream of the experiment a similar set of quadrupoles focuses the beam down into an absorber designed to stop the full Linac beam, which requires more than nineteen feet dirt equivalent of shielding. A primary collimator scrapes the beam to within 3σ upstream of the shielding wall. A secondary collimator is recommended downstream of the shielding to prevent unnecessary activation of other equipment in the experimental hall.

The Mucool experiment also includes an 805 (201) MHz NCRF copper cavity to be tested in the magnetic field of a superconducting solenoid (see Figure 2 and 3) which can be run in "solenoid mode" at 5 Tesla or "gradient mode" at 2.5 Tesla. At 2.5 Tesla the two coils' fields are opposing. The MTA is equipped with a 1500 kVA power transformer to handles the needs of the facility (not including the RF).

The experimental hall is 840 sq-ft and the service building is 1225 sq-ft. There is a sloped access from the equipment lift area (elevation 745'-6") to the experimental hall (elevation 736'-6").

Figure 3: Mucool/MICE SFOFO lattice cell

Other constraints on the facility include the radiation environment of the experimental hall and hands-on maintenance issues associated with highly-irradiated components. With respect to hands-on maintenance issues associated with the hydrogen absorber, a surface contact dose of 40mr/hr has been suggested as the limiting activation of exposed surface areas, such as the cryostat surface. From a MARS simulation[3] performed on the experimental hall, hall components, and the full-

beam absorber, this residual activation limit was reached after approximately 100 days of Linac beam. Table 3 presents residual activation results for 30 days of beam and 1 day of cooling for 10^{13} protons per pulse at 15 Hz for various elements of a typical Mucool experiment and MTA configuration[3]. As a result, an operational limit of 10^{21} protons/year was established for the facility.

Table 3: Peak dose (mSV/hr) on contact after 30 days irradiation and 1 day of cooling for 10^{13} ppp at 15 Hz (1mSV = 100 mrem)

Averaged over pump and heat exchanger cryostat	0.11
SC solenoid inside vessel (downstream end)	160
SC solenoid inner coils (downstream end)	54
SC solenoid outside vessel (downstream end)	10
Downstream beamline magnets, inner radius	100
Downstream beamline magnets, outer radius	3
Beam dump core	90000

This yearly limit was then applied in the design of the full-beam absorber to meet ground and surface water, and occupational limits associated with the facility. Since users and employees at Fermilab are limited to 100 mr/week and 1500 mr/year and, further, radiation exposure at or above 5 mr/hr constitutes a defined radiation area with full radiological controls, proper design of the full-beam absorber became important to ensure sufficient access to the facility. (Staying well below this limit allows workers to remain the experimental hall for a typical 40 hour work week.) The final beam absorber design was fully simulated in MARS and these results were applied in a Concentration Model[4] and ANSYS analysis[5] for a full radioisotope and thermal assessment of the beam absorber.

SCHEDULE

Approval of the Mucool Test Area project came on January 6, 2003. Construction of the MTA began in February 2003. The project is on schedule and beneficial occupancy is expected in September 2003.

CONCLUSIONS

The Mucool Test Area is presently under construction at Fermilab. Beneficial occupancy is expected fall of 2003 for the testing of components of the Mucool experiment. The MTA is to be one of the only test facilities in the world that uses a full intensity Linac beam (15 kW, 1.6 x 10^{13} ppp @ 15 Hz). After the Mucool component testing is complete others users are invited to make use of the test beam facility for many areas of physics including radiation, medical, nuclear, atomic and beam diagnostics and control.

ACKNOWLEDGEMENTS

REFERENCES

[1] C. Johnstone and D. Kaplan, "Linac Test Facility Beam Properties," MUCOOL NOTE 201, April 4, 2001

[2] E. Black, "Mucool Test Area (MTA) experiment program lay out," February 20, 2003

[3] N. Mokhov, "The MARS Code System User's Guide", Fermilab-FN-628 (1995);
N. Mokhov, O.E.~Krivosheev, "MARS Code Status", Proc. Monte Carlo 2000 Conf., p. 943, Lisbon, October 23-26, 2000; Fermilab-Conf-00/181 (2000); http://www-ap.fnal.gov/MARS/.
N. Mokhov and C. Johnstone, private communication, May, 2003

[4] K. Vaziri, P. Kesich, I. Rakhno and C. Johnstone, "Surface and Groundwater Assessment of the Mucool Beam Absorber," internal FNAL note, April, 2003

[5] A. Lee, "The Temperature Study of the Beam Absorber used in the Muon Cooling Experiment," internal FNAL note, March 28, 2003

CREATING MICROBEAMS AND NANOBEAMS BY CHANNELING IN MICRO- AND NANO-STRUCTURES

V.M. Biryukov, Y.A. Chesnokov, IHEP, Protvino, Russia; S. Bellucci, INFN, Frascati, Italy; V. Guidi, INFN, Ferrara, Italy; W. Scandale, CERN, Geneva, Switzerland

Abstract

A particle beam of very small cross-section is useful in many accelerator applications including biological and medical ones. We show the capability of channeling technique using a micron-sized structure on a surface of a single crystal, or using a nanotube, to produce beam of a cross-section down to 1 square micrometer (or nanometer). The channeled beam can be deflected and well separated in angle and space from the primary and scattered particles. According to our Monte Carlo simulations of channeling and experience with crystal channeling at IHEP (Protvino), emittances down to 0.1-0.001 nanometer-radian, and flux up to 1 million ions per square micron per second, can be achieved for protons and ions in the range 0.1-3 GeV/u. We discuss the experimental techniques to achieve suitable structures for particle beam channeling.

INTRODUCTION

Bent crystals have efficiently channeled particle beams [1] in the energy range from 3 MeV [2] to 900 GeV [3]. Today, crystals are largely used for extraction of 70-GeV protons at IHEP with efficiency reaching 85% at intensities well over 10^{12} particles/s, steered by silicon crystal as short as 2 mm [4]. A bent crystal (5 mm *Si*) is installed into the Yellow ring of the Relativistic Heavy Ion Collider where it channels *Au* ions and polarized protons of 100-250 GeV/u as a part of the collimation system [5].

Carbon nanotubes are cylindrical molecules made of carbon atoms. Nanotubes can be manufactured of different diameters - from a fraction of a nm to a few microns, of different lengths - from a micron up to a few millimeters, of different materials - usually carbon but also others [6]. This makes nanotubes a very interesting object for channeling research.

The purpose of the present paper is to look at how the channeling technique could be used to make beams of very small emittance. As a potential application we consider a microbeam facility being developed at BNL [7] where a variety of beams from Fe^{+26} to protons of 0.1-3 GeV/u is needed with the beam size of ~10 μm at a target. A traditional approach to creation of a microbeam would be a ~20-μm-thin wire placed in a circulating beam and a set of micro-collimators cutting out a small part of the scattered-beam phase space [7]. Here the weak points can be a low flux of scattered particles in the direction of extraction line; primary and secondary particles scattered off the collimators may contaminate the microbeam.

If a channeling structure is used instead of wire, it can trap the incident particles and deliver them into a single required direction (i.e. the extraction line) instead of scattering them all the ways around. That may give a large gain in the microbeam flux. The rest of the system may be unchanged: the same set of collimators etc. Further benefit is a low divergence of the channeled beam as set by channeling acceptance; that would reduce the need in collimation down the line, and may reduce the emittance of microbeam. Finally, the channeled beam would have well-defined sharp edges and contain solely primary particles. The open point is how to make a channeling structure as small as about the size of wire, ~0.02 mm, or smaller. Below we suggest two approaches, with crystals and with nanotubes.

CRYSTAL MICRO-BEAM

The first suggestion is to use a micron-sized structure on a surface of a single crystal; such structures are a well-developed technique [8]. The easy way to do it is to take a crystal plate, mask a strip 10μm (or 1μm) wide on the surface, and etch the surface to the depth of 10 (or 1) μm. That leaves a strip of 10 by 10μm (or 1 by 1μm) on the surface; this strip can channel particles, thus forming a microbeam. In order to separate in the angle and space the beam channeled of the strip from the particles nearby (in the crystal bulk and outside), we suggest having a strip shorter than the substrate plate (Fig.1), and bending the whole structure. That makes a perfect separation downstream.
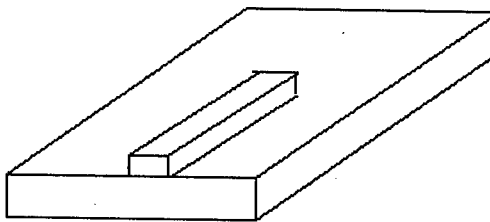
Fig.1 Crystal with a micron-sized strip on the surface.

While the size of the microbeam source is set by the strip size, the divergence in the direction of bending is set by the channeling angle, $(2Ec/pv)^{1/2}$, where Ec is the critical transverse energy for channeled particles and pv is the particle's momentum times velocity per unit charge. E.g., in slightly bent Si(100) with Ec≈5 eV, the 0.1-3 GeV protons have divergence of 0.05-0.2 mrad. For fully stripped ions of Fe+26 in the range of 0.1-1 GeV/u, the divergence is 0.08-0.15 mrad. One can pick crystal channels with bigger or smaller angular acceptance.

With 1-μm source, this gives a microbeam emittance of (0.025-0.1) π nm·radian for protons of 0.1-3 GeV, and (0.04-0.08) π nm·radian for Fe+26 ions of 0.1-1 GeV/u, in horizontal plane. For comparison, the horizontal emittance expected [7] from the traditional approach is 23π nm·radian at any energy. If realized, the channeling approach would give an improvement by a factor of ≈200-1000 for protons and 300-600 for ions. It can be improved even further by collimation downstream.

In the direction orthogonal to bending, microbeam divergence equals that of the circulating beam. However, the vertical size of microbeam is set by the strip, down to ~1 μm, while in traditional approach it has to be cut by micro-collimation. Therefore, an improvement ≈100 in vertical emittance can be expected from channeling approach due to small size of the source.
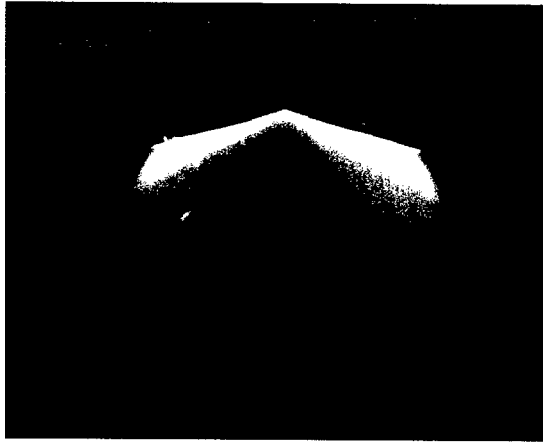
Fig.2 An example of micron-sized structure machined on a Si surface at Ferrara.

Figure 2 shows an example of a micron-sized structure (5-micron pyramid) machined on the surface of Silicon crystal at the Semiconductor group of Ferrara University.

NANO-BEAM

While crystal channeling is a well-established technique, nanotube channeling is just emerging as a beam instrument [9-13]. Here, beam can be trapped in a single nanotube cylinder of ≈1 nm diameter or in a rope consisting of many nanotubes. The depth E_c of the potential well in a carbon nanotube is ~15-60 eV for channeled particles, depending on nanotube configuration [11]. The critical angle for channeling $\theta_c=(2E_c/pv)^{1/2}$ is factor of ~1.5-3 greater than with Si crystal. Provided that nanotubes can efficiently channel and deflect particle beams, they offer an interesting opportunity to make clean beams of potentially very small size, down to 1 square nanometer if needed.

We have developed a Monte Carlo code and done simulations of particle channeling in bent single-wall nanotubes, aimed at finding how useful nanotubes are for channeling of positively-charged particle beams, what kind of nanotubes are efficient for this job, and how nanotubes compare with crystals in this regard [12].
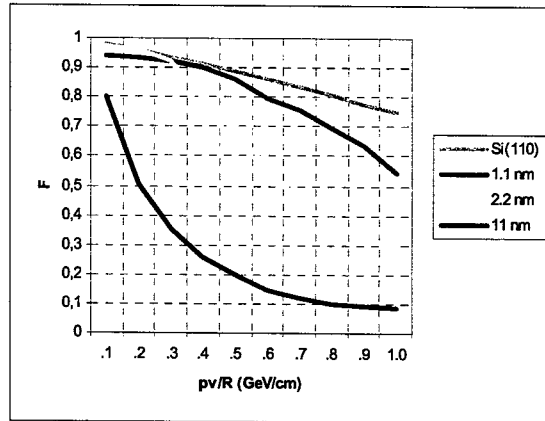
Fig.3 Channeling efficiency vs nanotube curvature *pv/R* **for tubes of different diameter and for Si(110) crystal.**

Figure 3 shows how the number of 1 GeV protons channeled through 50-μm-long nanotube depends on nanotube curvature *pv/R* for tubes of different diameters. For comparison, also shown is the same function for Si(110) crystal. The channel length of 50 μm, with bending of 1 GeV/cm, gives the 1 GeV particles a deflection of 5 mrad - sufficient for many accelerator applications like extraction [1,3-5]. Nanotube as narrow as 1 nm is comparable to silicon crystal in beam bending.

For the simulations of nanotube channeling of Fe[+26] ions and protons of 0.1-3 GeV/u, we use the tubes of 1.1-nm diameter, typical for easily manufactured carbon nanotubes. We take the curvature radius of 2 cm; then the beam energy range to be studied does nearly correspond to the *pv/R* range studied in Fig.3. We choose the nanotube bending angle of 5 mrad. Figure 4 shows two examples of the angular distribution of protons downstream of the bent nanotube, shown in the direction of bending. Similarly to pictures of bent crystal channeling, there is clear separation of channeled and nonchanneled peaks, with few particles lost (dechanneled along the tube) between themOverall, the transmission of particles by the tube is reasonably good on both ends of the energy range. The intermediate energies fall between the two cases shown.
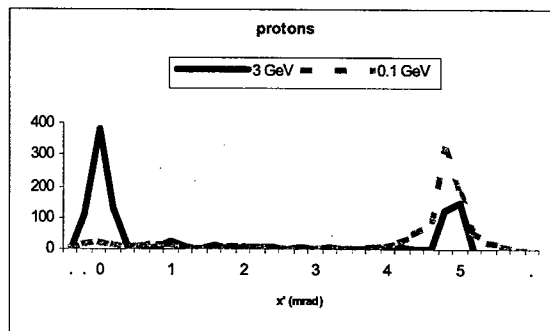
Fig.4 Angular distribution of protons downstream of a bent nanotube, shown for two energies.

The case of Fe[+26] ions is shown in Figure 5, again for both ends of the energy range of interest, 0.1 to 1.0 GeV

per nucleon. Similar picture can be seen, as with protons. Overall, for the similar ratio of beam momentum per unit charge, the angular distributions of Fe ions and protons are similar. The transmission efficiency is reasonably good for all particle species. The same nanotube deflector could be used in each case, throughout the range of energies and particle species.

For 0.1-1 GeV/u ions of Fe^{+26}, the divergence of the channeled beam in a nanotube of arbitrary helicity like *(11,9)* is 0.24-0.77 mrad. The size of the source could be quite small. A typical nano-rope (consisting of 100-1000 nanotubes) would be a source that gives an emittance of the nano-beam of the order of 0.001π nm·radian both horizontally and vertically, factor of 10000 down from the figure potentially achievable with a "traditional amorphous" source.
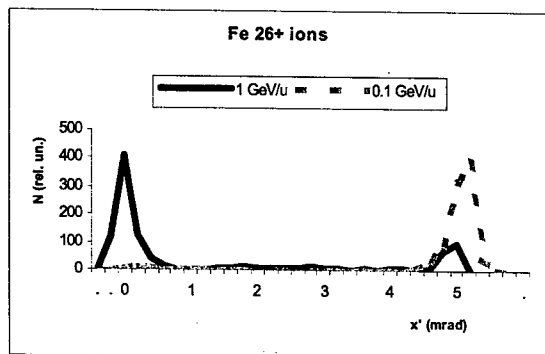
Fig.5 Angular distribution of Fe^{+26} ions downstream of a bent nanotube, shown for two energies.

INTENSITY OF MICROBEAM

With small emittance, microbeam intensity is also small. However, the applications like a microbeam facility [7] require quite small intensities, down to 1-1000 particles/s. With some 10^9-10^{11} particles stored in the AGS ring, this gives enough room for constructing beams of very small emittances discussed above.

Let us take the example of AGS to estimate the achievable intensity of channeled microbeam. The beam circulating in the AGS ring has the size about ±5 mm before the extraction septum. The beam store is typically 10^9 ions or 10^{11} protons. An area of 1 μm^2 would be hit by ~10 ions (or 1000 protons) in the time of a single turn in the ring (~1 μs at 1 GeV per nucleon); the hit rate is then ~10^7 ions/s per 1 μm^2.

The divergence of particles incident at crystal in periphery of the circulating beam, after crossing a stripping foil, is expected to be several times bigger than channeling acceptance. For particles trapped by a crystal or nanotube, the transmission factor would be 10 to 100% (e.g., Figs. 4-5) if channeled particles are bent a few mrad.

Microbeam intensity of 10^5-10^7 ions/s appears even far greater than needed (though it is easily reduced by moving the crystal away from the core of the beam or misaligning it). One can put the question differently: how much a crystal can survive? The IHEP experience shows that crystals can channel up to ~$3\cdot10^{12}$ particles/s per cross-section of 0.5×5 mm^2 without cooling measures. This corresponds to $10^6/(s\cdot\mu m^2)=1/(s\cdot nm^2)$. So, a micro-crystal structure can channel much more particles than needed, and even a nano-rope could do the job.

A lifetime of ~$5\cdot10^{20}$ proton irradiation per cm^2 as measured [14] for channeling crystal, corresponds to $5\cdot10^{12}/\mu m^2$; this means over 100 years of operation of 1-μm^2 crystal with channeling of ~1000 protons/s, or one year for $(20\text{-nm})^2$ nano-rope operating at 100 protons/s.

REFERENCES

[1] V.M. Biryukov, Yu.A. Chesnokov and V.I. Kotov, *"Crystal Channeling and its Application at High Energy Accelerators"* (Springer, Berlin, 1997). See also http://crystalbeam.narod.ru

[2] M.B.H. Breese, *Nucl. Instr. and Meth. B* **132**, 540 (1997)

[3] R.A.Carrigan, Jr., et al. *Phys. Rev. ST AB* **1**, 022801 (1998). R.A.Carrigan, Jr., et al. *Phys. Rev. ST AB* **5**, 043501 (2002)

[4] A.G. Afonin, et al. *Phys. Rev. Lett.* **87**, 094802 (2001)

[5] R.P. Fliller III, et al., EPAC 2002 Proceedings (Paris), p.200; these Proceedings.

[6] T.W. Ebbesen, *Phys. Today*, **49**, 26 (1996). Z.Y. Wu, et al., *Appl. Phys. Lett.* **80**, 2973 (2002)

[7] K.A. Brown, et al., EPAC 2002 Proceedings (Paris), p.554; these Proceedings.

[8] P. Kleimann, J. Linnros, R. Juhasz. *Appl. Phys. Lett.* **79**, 1727 (2001)

[9] V.V.Klimov and V.S.Letokhov, *Phys. Lett. A* **222**, 424 (1996)

[10] L.G.Gevorgian, K.A.Ispirian, R.K.Ispirian. *JETP Lett.* **66**, 322 (1997)

[11] N.K. Zhevago and V.I. Glebov, *Phys. Lett. A* **250**, 360 (1998)

[12] V.M. Biryukov and S. Bellucci, *Phys. Lett. B* **542**, 111 (2002)

[13] S. Bellucci, et al., *Nucl. Instr. and Meth. B* **202**, (2003); [ArXiv:physics/0208081]

[14] Baurichter et al., *Nucl. Instrum. Meth. B* **164-165**, 27 (2000)

A NEUTRON SOURCE FACILITY FOR NEUTRON CROSS-SECTION MEASUREMENTS ON RADIOACTIVE TARGETS AT RIA*

L. Ahle, L. Bernstein, B. Rusnak, R. Berio, LLNL, Livermore, CA 94551, USA

Abstract

The stockpile stewardship program is interested in neutron cross-section measurements on nuclei that are a few nucleons away from stability. Since neutron targets do not exist, radioactive targets are the only way to directly perform these measurements. This requires a facility that can provide high production rates for these short-lived nuclei as well as a source of neutrons. The Rare Isotope Accelerator (RIA) promises theses high production rates. Thus, adding a co-located neutron source facility to the RIA project baseline would allow these neutron cross-section measurements to be made. A conceptual design for such a neutron source has been developed, which would use two accelerators, a Dynamitron and a linac, to create the neutrons through a variety of reactions (d-d, d-t, deuteron break-up, p-Li). This range of reactions is needed in order to provide the desired energy range from 10's of keV to 20 MeV. The facility would also have hot cells to perform chemistry on the radioactive material both before and after neutron irradiation. The present status of this design and direction of future work will be discussed.

SBSS AND RIA

The Science Based Stockpile Stewardship program (SBSS) insures the reliability and safety of the US nuclear weapon stockpile without testing. It relies on state of the art simulation capabilities whose inputs include nuclear cross sections with an emphasis on neutron reaction cross sections. Nuclear cross sections play their most important role when interpreting measurements of isotope production to determine neutron and charged particle fluxes in brief intense neutron flux environments. While many of the cross sections of interest for stable nuclei and a few unstable nuclei have been measured, most of the cross sections involving unstable nuclei are determined from theory alone. In addition to the measurements of nuclei used as flux monitors, neutron cross section measurements on prompt fission fragments near mass number 95 and 143 and the actinides thorium, uranium, neptunium, and plutonium also play important roles in SBSS.

The Rare Isotope Accelerator (RIA) promises the ability to make a wide variety of isotopes throughout the chart of the nuclides [1]. Of most interest to the nuclear physics community are those far from stability that cannot be produced by any other facility. But RIA also promises never before achieved production rates of near stability

nuclei. Both of these capabilities offer opportunities to make cross section measurements that were not possible before. For nuclei with a half-life of one day or more, targets can be made and irradiated with neutrons. SBSS is therefore interested RIA and developing the necessary infrastructure to allow the desired nuclear cross section measurements to occur.

NEUTRON CROSS SECTION MEASUREMENTS AT RIA

The first step in performing neutron cross-section measurements is the production and collection of the wanted isotopes. RIA promises a production rate of 10^{11}-10^{12} pps for near stability isotopes. Figure 1 plots the minimum require production rate versus half-life for producing 10 and 100 micrograms of material. This plots assumes an atomic number of 100 for the isotope in question. The figure illustrates at RIA it will be possible to collect 10 micrograms of material for an isotope with a half-life of 1 day. Presently, possible methods for collecting these isotopes at RIA are being studied.
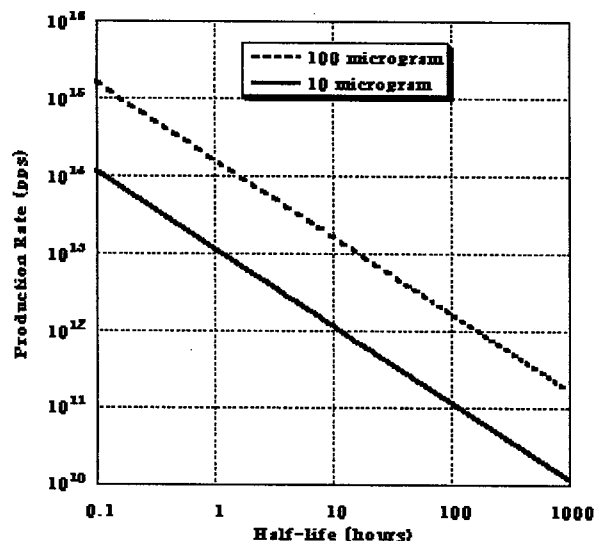
Figure 1: A plot of required production rate versus half-life for producing 10 and 100 micrograms of an isotope with mass number of 100.

A 10-microgram sample of an isotope with a mass number 100 and a half-life of one day corresponds to around 15 Curies of activity. Thus, a radiochemistry facility must be located at RIA capable of handling 100's of Curies of activity and processing the material into a target suitable for neutron irradiation. Hot cells capable of handling 1 kCi of hard gamma activity are not

uncommon and techniques have been developed for handling such material. The chemistry facility may also need to handling the target after irradiation and separate out the desire products for measurements.

In most cases, 10 micrograms of material should be sufficient to perform neutron cross-section measurements. The exact minimum amount will depend on the details of the nucleus, the desired output channel, and the method of measurement. It also depends on the neutron flux. Presently it is assumed delivering 10^{10}-10^{11} neutrons per cm^2 per second on target will be possible. The achievable neutron flux will also be a function of the desired neutron energy. For SBSS, cross-section data from 50 keV up to 20 MeV are of interest, with different reaction being important at different energies. But given the half-life of the material it will be important to have the neutron source on the RIA site. Figure 2 is a conceptual layout of such a neutron source facility. It has locations for doing radiochemistry on either side and three experimental halls for doing experiments. At the heart of the facility are two accelerators designed to accelerate protons and deuterons at high currents. The details of these accelerators and reasons why are discussed below.
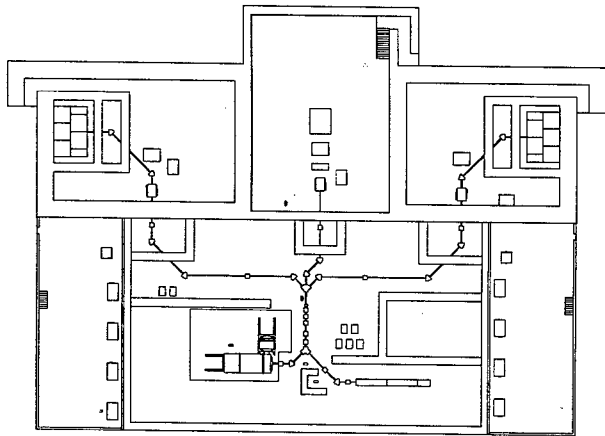
Figure 2: A drawing of a possible design for a neutron production facility at RIA. The experimental areas are up top, with a low energy neutron area in the middle. The two rooms on either side at the bottom are areas for radiochemistry. See text for other details.

NEUTRON PRODUCING REACTIONS

There are two approaches for producing neutrons across the entire energy range of interest. A facility that produces a white source of neutrons is one, but a white source will put limitations on how the experiments are carried out since one must use methods that can distinguish between neutron energy. Also, white neutron sources of reasonable fluxes at high energies require large facilities. The other option is a tunable, "monoenergetic" neutron source. No neutron source is perfectly monoenergetic but certain reactions can be used to produce a neutron spectrum with a reasonably small energy spread. Unfortunately, no one single reaction is

suitable for producing neutrons across the entire energy range. Table 1 lists several reactions that could be used to make neutrons and the energy range in which it works the best. Notice that all these reactions involve either beams of protons or deuterons.

Table 1: List of reactions for making neutrons

Reaction	Q value	Best Neutron Energy
$^7Li(p,n)^7Be$	-1.64 MeV	0.1-0.4 MeV
$^3H(p,n)^3He$	-0.76 MeV	0.1-3 MeV
$^2H(^2H,n)^3He$	3.27 MeV	4-10 MeV
$^3H(^2H,n)^4He$	17.59 MeV	13-16 MeV
$X(^2H,pn)X$	-2.25 MeV	>6 MeV

For neutrons below about 200 keV, it is hard to make an intense beam of monoenergetic neutrons. First, a significant fraction of the beam energy is lost in a short distance (2.1 MeV protons stop in 180 microns of lithium), which causes the width of the neutron energy distribution to be large compared to 100 keV. Minimizing the energy spread will mean a thin target, which reduces the neutron flux. This can be recovered only somewhat by increasing the beam current before beam power issues on target become important. Another way to overcome these difficulties is to use moderators to shape the neutron energy spectrum to one that is desirable [2]. It will still be broad after this shaping, but it should be possible to gain some information about neutron cross-sections at these energies. If the beam is pulsed, then time of flight techniques can be used in the experiment to determine neutron energy [3]. While this becomes problematic for higher energy neutrons, this technique may still be viable at lower energy ranges, as only modest distances would be needed to distinguish neutrons of different energies.

Both the $^7Li(p,n)^7Be$ and the $^3H(p,n)^3He$ reactions work well for producing neutrons in the several hundred keV range. The lithium reaction has the practical advantage of not needing a tritium target, but unfortunately ^7Be has an excited state at 429 keV that results in a bimodal neutron distribution from these reactions. The $^3H(p,n)^3He$ reaction does not have this problem and could be used to make neutrons up to a few MeV.

Somewhere between 3 and 4 MeV, it becomes practical to use the $^2H(^2H,n)^3He$ reaction. This reaction has a positive Q value which gives the neutron about 3 MeV more energy than the incoming deuteron beam. The neutron is emitted isotropically at the lower beam energies, though there is forward focusing due to kinematics as the beam energy increase. Once the deuteron beam energy rises above 2.2 MeV, deuteron breakup can occur. Initially this will be a much smaller contribution to the neutron flux than the fusion reaction, but when the deuteron beam energy reaches 9 MeV, the yield from deuteron breakup will equal the yield from the fusion reaction [4]. Fortunately, there is a significantly large gap in neutron energies. The fusion reaction at this energy produces a sharp peak of neutrons around 12 MeV while the breakup reaction produces a neutron spectrum

with a peak at 4 MeV and with a FWHM of 1 MeV. Depending on the reaction of interest this still may be a useable spectrum, especially if the threshold for the reaction lies between the two neutron distributions. Even though this type of bimodal distribution persists even at higher deuteron beam energies, but this reaction has been used to produce neutrons at energies up to 16 MeV [5] and it should be possible to go higher.

For neutrons above 14 MeV, the $^3H(^2H,n)^4He$ reaction become a possible production reaction. The production cross-section peaks near 5 barns at a deuteron beam energy of 120 kV, which is why this reaction has been used in the past for producing 14 MeV neutrons [6]. The cross-section falls quickly to 0.2 barns at a beam energy of 1 MeV. By contrast the cross-section for the $^2H(^2H,n)^3He$ reaction peaks around 0.1 barns near a deuteron beam energy of 1.6 MeV falling slowly with increasing energy so that at 10 MeV the cross-section is still about 0.08 barns. The disadvantages of using the $^3H(^2H,n)^4He$ reaction are the need for a tritium target and the lack of focusing due to kinematics compared to using $^2H(^2H,n)^3He$.

It is also possible to consider using the deuteron breakup reaction to produce neutrons. As mentioned earlier, the neutron energy distribution from this reaction will be much broader then the other reactions mentioned above. One would use a much heavier target than the deuteron, because the coulomb field would be much higher and neutrons from fusion and transfer reactions would be much less a factor.

THE ACCELERATORS

As noted above, all the reactions involve a beam of either deuterons or protons at low energies. Since, the neutron flux is directly proportional to beam intensity, maximizing beam current is desirable. Thus, at the heart of this neutron source facility must be one or more low energy, high current accelerators for light ions. There are several options for the choice of accelerator all with advantages and disadvantages. Due to the combination of high current and energy variability, it was found that not one machine adequately met all the criteria. Thus, the present design includes two, a 3 MeV dynamitron and a 30 MeV linac.

A dynamitron has been used before as a neutron source [7] and is presently a commercially available system [8]. A dynamitron rectifies an RF power system to create a DC acceleration potential up to much as 5 MV depending on the system. A dynamitron also offers high average beam currents, up to tens of milliamps, depending on the voltage. Thus, the dynamitron becomes an attractive system for producing low energy neutrons. In addition to providing a DC neutron source, it has also been used as a pulse neutron source [9], which will be necessary if an experiment needs to use time of flight to distinguish neutron energy.

In order to reach higher neutron energies, a higher energy beam is needed. Though there are several options, the current approach being evaluated is a linac. The linac would start with a 1-2 MeV RFQ followed by multiple, short, independently-driven DTL modules each capable of adding another ~1 MeV of acceleration per unit. As the modules would be short, the velocity acceptance of each section is broad, allowing transport, acceleration, bunching, and longitudinal focusing over a variety of beam energies. This configuration allows the linac to be more energy variable than a conventional RF linac designed for high efficiency, and thereby facilitates a tunable neutron source. The linac should be able to provide several hundred microamps of average beam current and would be designed for a species with a charge to mass ratio of one-half, allowing operation with molecular hydrogen, deuterium, alphas, and similar species.

SUMMARY

The Science Based Stockpile Stewardship Program is interested in neutron cross sections on many unstable nuclei. The Rare Isotope Accelerator promises the capability of producing unstable isotopes in sufficient quantities allowing neutron cross-section measurements. Thus, the stockpile stewardship community is very interested in RIA and insuring the correct infrastructure is present to allow direct neutron measurements. These include the ability to collect the appropriate isotope, process the material into to a target at a radiochemistry facility, and irradiate the target with neutrons at a separate but co-located neutron source. This neutron source must be able to deliver high neutron fluxes on target for neutron beam energies from around 50 keV to 20 MeV. It will do this with two, high current, low energy, light ion accelerators providing beams appropriate for several different nuclear reactions. The final specifications of these pieces are still being developed and we are working with the rest of the RIA community to develop these ideas.

REFERENCES

[1] http://srfsrv.jlab.org/isol/ISOLTaskForceReport.pdf .

[2] H. Beer and F. Kappeler, Physical Review C 21 (1980) 534.

[3] K. Wishak et al., Nuclear Instruments and Methods A 292 (1990) 595.

[4] S. Cabral, G. Borker, H. Klein, and W. Mannhart, Nuclear Science and Engineering 106 (1990) 308.

[5] H. J. Breide et al., Nuclear Instruments and Methods, 169 (1980) 349.

[6] R. Booth et al., Nuclear Instruments and Methods 145 (1977) 25.

[7] J. Walker, D. Weaver, and J. Owen, IEEE Transactions on Nuclear Science 26 (1979) 1475.

[8] http://www.iba-tg.com.

[9] S. Matsuyama et al., Nuclear Instruments and Methods A 348 (1994) 34.

DETERMINATION OF LOW LEVEL RF CONTROL REQUIREMENTS FOR SUPERCONDUCTING CAVITIES FROM MICROPHONICS MEASUREMENTS *

J. R. Delayen, L. H. Harwood[#]

Thomas Jefferson National Accelerator Facility, Newport News, VA 23606

Abstract

In lightly beam loaded superconducting accelerators the rf power requirements are dictated by the maximum amount of microphonics that the system must be able to control and by the energy content of the cavity. In previous machines, such as heavy-ion boosters, the energy content of the cavities was relatively small and one could afford to specify a large control window and still use low power (~100 W) rf sources. In newer accelerators that are being contemplated —such as the CEBAF 12 GeV upgrade or RIA— the energy content of the cavity is quite large requiring rf sources in excess of 10 kW. Conservatism in the control window specification would be quite costly; on the other hand loss of lock could have adverse effect on machine availability or beam property or even, in some cases, result in activation. We present a model to estimate the requirements to be placed on the rf control system based on the properties of the cavities, the frequency tuning system, and the characteristics of the accelerator.

OVERVIEW

Linacs based on superconducting RF (SRF) technology present novel optimization challenges to system designers. This is particularly true when the cavities are lightly beam loaded. In these cases the required RF power is not determined by the beam but rather by how much is required for phase and amplitude control in cavities whose resonant frequency deviates from the rf system's frequency. The amount of allowed detuning (deviation from the rf frequency) is strongly coupled to the expectations on the system's stability. A simple solution to the problem is to increase the available rf power; this has the negative effect of increasing the system cost. We describe below a methodology for projecting system performance utilizing a straightforward parameterization of the system parameters. This methodology then permits evaluation of trade-offs between system cost and system performance.

BASIC REQUIREMENTS

The generator power P_g required to operated a cavity in the presence of beam loading and detuning is given by

$$P_g = \frac{P_c}{4\beta}\left\{(1+\beta+b)^2 + \left\lceil(1+\beta)\tan\psi - b\tan\phi\right\rceil^2\right\}$$

where $P_c = V_c^2/R_{sh}$ is the power dissipated in the cavity walls at voltage V_c; β is the usual coupling coefficient; $b = R_{sh}I\cos\phi/V_c$ is the ratio of power absorbed by the beam and the power dissipated in the cavity walls; ϕ is the phase of the beam with respect to the rf; $\tan\psi = -2(1+\beta)\delta\omega/\Delta\omega_0$ is the ratio of the frequency detuning and half the loaded bandwidth. Given the operational parameters of the cavity (voltage, beam current and phase), there is an optimal coupling coefficient β that minimizes the generator power P_g required to accommodate the frequency detuning $\delta\omega$. At this optimal coupling, the generator power increases roughly linearly with the maximum amount of detuning that needs to be accommodated.

If the actual detuning exceeds what was assumed, the available power will not be sufficient to maintain control of the phase and amplitude of the cavity's field. When this occurs, the system is said to "lose lock" and the amplitude and phase of the cavity field will deviate from their set values resulting in a change in the energy gain provided by the cavity to the beam. If the shortfall is brief and/or is small, then the problems caused by the acceleration error may be minor. If the shortfall persists, the problems could be sufficiently large that other systems cannot correct for them. This may also result in beam impingement in some part of the accelerator which, in some circumstances, may not be acceptable.

MODEL FOR THE AMOUNT OF TIME CAVITIES ARE OUT OF LOCK

Basic parameters

Everything else being constant, there is a one-to-one relationship between the available rf power from the generator and the amount of detuning that can be accommodated. We will refer to this as the "detuning budget", v_{budget}.

Most SRF cavities have a resonance control system, typically called a "tuner", to mechanically adjust the cavity so that its average resonant frequency, v_{cavity}, matches the rf frequency, v_0. The control algorithms for the tuners usually do not activate the tuner until the cavity's frequency deviates from the rf frequency for more than some value, v_{tuner}. There is no physical reason that v_{tuner} must be smaller than v_{budget}. However, as we will

show later, the system performance is rather unsatisfactory if v_{tuner} is even comparable to v_{budget}

A description is needed for the time distribution of v_{cavity}. Figure 1 shows frequency-vs-time data taken on an SNS cavity at JLab [1]. A simple characterization of the data would be that of a high frequency "noise" superimposed on a slow drift.
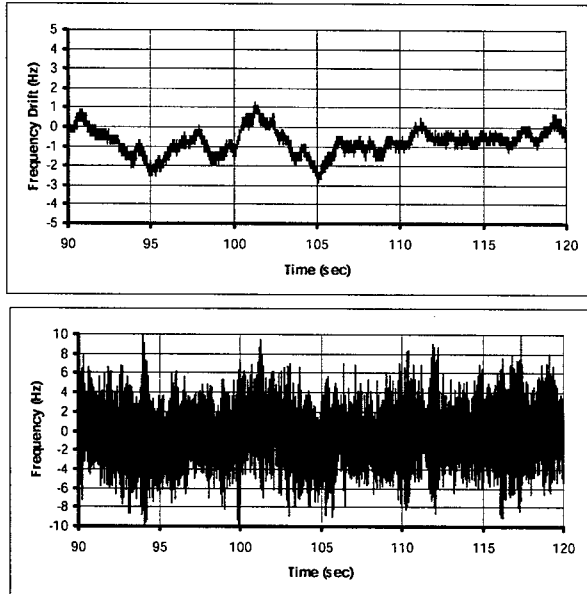
Figure 1:Frequency vs time measured for an SNS 805 MHz cavity at JLab during a 30 second period. The upper graph shows data using a 1 Hz low-pass filter; the data in the lower graph did not have the filter.

A natural approach would be to separate the distribution of frequency excursions into two classes, i.e. slow and fast. The slow events are those in which v_{cavity} changes slowly enough for the tuner control to respond; the fast ones are those where the tuner is unable to respond and need to be accommodated by the rf control system. In other words, we will use one description for the "noise" and another for the centroid of the "noise".

- "Noise": A probability density analysis of the data in Figure 1 yields a curve that is well characterized by a Gaussian. This data is consistent with the character of data for the 338 SRF cavities installed in CEBAF. In general, the width of the distribution, will depend on the specific cavity and cavity environment. The probability density associated with Fig.1 is shown in Fig. 2.
- Slower events: the centroid of the Gaussian may not be static. Various options are available.
- ◊ One is to be very optimistic and assume that the centroid stays at center of the tuner range.
- ◊ Another is to assume that the centroid has equal probability to be anywhere between v_0-v_{tuner} and v_0+v_{tuner}.
- ◊ A third is that the centroid undergoes a random walk from the origin. In this model the location of

the centroid from its starting point since the last tuner operation would evolve as $t^{1/2}$, and the probability density for the centroid location would be quadratic inside the tuner window.

◊ And, finally, things could conspire to leave the centroid at the edge of the tuner window.

There are, of course, many other options, but the ones listed here likely span the range of credibility. The overall picture is illustrated in Figure 3.
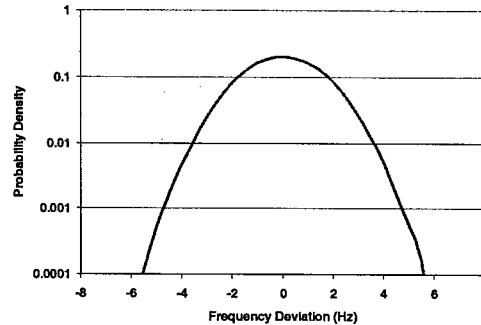
Figure 2: Probability density of the microphonics-induced frequency deviations. This was obtained from 400000 measurements of the instantaneous cavity frequency over an 800 sec time span.
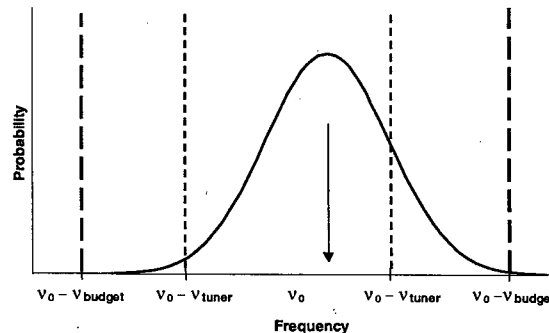
Figure 3: Illustration of segmentation of frequency spectrum and "noise" spectrum (as represented by a Gaussian).

With choices for σ, v_{cavity}, v_{tuner}, and v_{budget} we can calculate the fraction of the time the system would be outside the v_0-v_{budget} to v_0+v_{budget} band. After calculating these probabilities for all/some values of v_{cavity} between v_0-v_{tuner} and v_0-v_{tuner}. Next we select a model for the centroid drift and apply the appropriate weightings for that model to the probabilities we have calculated for each value of v_{cavity}. The result is the time averaged probability that the system will be "out of lock" within the assumptions of the model and for those values of the parameters.

Results of the model

Perhaps a more useful approach here is to generalize the problem by recasting it with dimensionless parameters rather than the previously described physical ones. First

we note that it is not the absolute frequencies that are important, but rather their difference from ν_0; we therefore shift the frequency axis by subtracting ν_0 from all frequencies. Now the only quantities that enter the calculation are: σ, ν'_{cavity} ($=\nu_{cavity}-\nu_0$), ν_{tuner}, and ν_{budget}. We now shift to dimensionless parameters by dividing all of the quantities in the previous sentence by ν_{budget}. The results are shown in Figure 4.
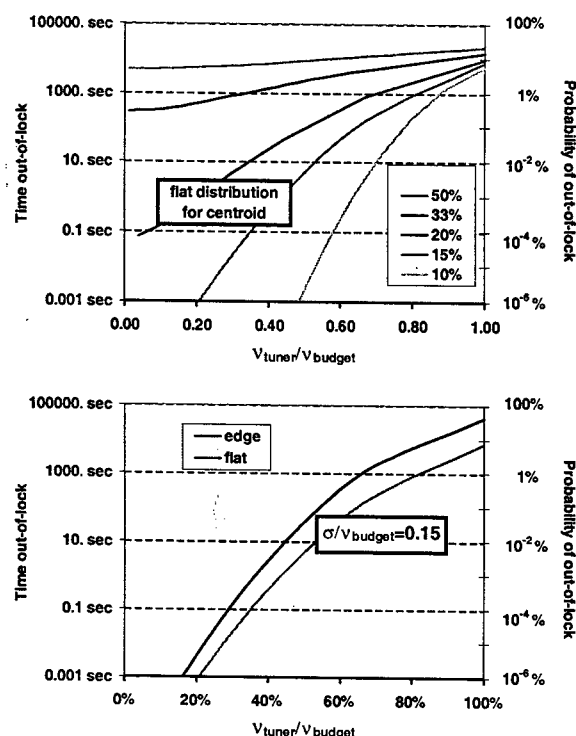
Figure 4: Probability of a cavity being out-of-lock and corresponding time per day of being out of lock. The upper graph shows the results for the flat distribution of and various values of σ/ν_{budget}. The lower graph shows the results for σ/ν_{budget} with both the flat distribution and with the centroid sitting at ν_{budget}.

As can be seen, the probability of a cavity being out of lock is strongly dependent on both σ/ν_{budget} and ν_{tuner}/ν_{budget} ratios. One can also see that it is much less dependent on the choice for the distribution of the centroid.

Limitations of the model

The choice of a Gaussian to represent the "noise" distribution is an oversimplification of reality. In the data taken at Jefferson Lab, the "out of lock" time was best described by a Gaussian (whose characteristics could be determined from data taken over a fairly brief period of the order of 15 min.) with a few rare events superimposed on it. Thus, in practice if one chooses to use the Gaussian model, then it is imperative to acquire data over a long period, i.e. at least a day and preferably longer, when determining the σ to use. And alternative would be to use

the σ from a short duration measurement and then assume that there will be some events that lead to additional "out of lock" time. It is also possible that there could be a strong source of mechanical noise that at a mechanical resonance of the cavity which could drastically distort the probability distribution away from a Gaussian.

Extension beyond a single cavity

The data shown in Figure 4 is for a single cavity and few systems have a single cavity. Predicting the net effects when there are several/many cavities becomes even more situationally dependent. For example, all the cavities could be acting completely independently; in this case one would simply multiply the probability for a single cavity by the number of cavities. On the other hand, they could all be affected by a single source of noise, e.g. the cryogenics system. Then the probability for the ensemble is close to that of a single cavity.

MITIGATIONS

As was mentioned earlier, the effect of going out of lock is that the cavity's gradient and phase wander. Should this occur, the quality of the beam will degrade. It is possible that the quality will degrade sufficiently and cause beam loss somewhere in the accelerator. Mitigating the degradation could be imperative.

It is possible for a feedback system that monitors the linac energy gain to compensate for some of the out-of-lock events; this is most tractable if there is only a small number of cavities that are out-of-lock. If, on the other hand, several cavities are out-of-lock, then it is quite unlikely that it would be possible to compensate for it.

Another option would be to temporarily provide extra rf power or, at least, reduce the total rf power load. The former option might be possible if there is something, e.g. a modulating anode in a klystron that is throttling the power below the maximum. The latter could be achieved by temporarily reducing the beam current or cavity voltage, thereby making available a larger portion of the rf power for control.

SUMMARY

We have presented a methodology for predicting the amount of time an rf system will be out-of-lock which is consistent with measurements on real cavities. In addition, we have presented potential mitigations for those times when the cavities are out-of-lock. We believe both are valuable when planning the rf system for anticipated accelerators where the cost of rf power is a significant constraint.

REFERENCE

[1] Jean Delayen, Ed Daly, Kirk Davis, Steve Smee, "Frequency Measurements on the Prototype SNS Medium-β Cryomodule Under Pulsed and CW Operation," JLab Tech Note 02-049.

AN AXIAL INJECTION SYSTEM FOR THE ORIC

G. D. Alton, Y. Zhang and B. A. Tatum

Oak Ridge National Laboratory, P.O. Box 2008, Oak Ridge, TN 37831-6368, USA

Abstract

An axial injection system has been designed for injection of high intensity beams of H^-, D^-, and He^{++} into the Oak Ridge Isochronous Cyclotron (ORIC). The device consists of two high-voltage platforms, two external ion sources, a double-drift-tube beam bunching system, a spiral inflector and integrated beam analysis diagnostics and focusing elements. With the axial injection system, it is expected that more than 100 μA of high quality, primary light ion beams will be extracted from the ORIC using either the existing septum extraction system for He^{++} beams or a foil stripping extraction system for extracting either H^+ or D^+ beams. In addition, beam scattering and the consequent internal activation problems, endemic with the present short lifetime internal Penning discharge source along with the down times attributable to its maintenance will be dramatically reduced.

1 INTRODUCTION

The ORIC is the driver accelerator for producing radioactive isotopes for the Holifield Radioactive Ion Beam Facility (HRIBF) [1]. Extracted beam intensities from the ORIC are limited by the internal cold-cathode Penning discharge source due to beam scattering from residual gas in the vacuum system that also leads to serious activation of internal components. The internal source also has a very short lifetime, particularly, for generation of He^{++} beams because of the brute force method used for producing these ions. Consequently, source maintenance accounts for a major part of the ORIC down time. The maximum deliverable beam-on-target intensities from the ORIC range between 10 and 20 μA; however, in practice, the beams are further limited to <10 μA by the power handling capabilities of ISOL targets. An axial injection system with two external ion sources (a multi-cusp, filter-field source for H^- and D^- generation and an ECR ion source for He^{++} generation) have been conceptually designed as a potential upgrade for the ORIC. The injection system consists of two 60-kV platforms, a double-drift beam bunching system and a spiral inflector [2]. When implemented, the axial injection system will be capable of injecting >100 μA beams of H^-, D^-, or He^{++} into the ORIC.

A top view of the injection system is shown schematically in Fig. 1. Since the injection system must transport space-charge-dominated, high-intensity beams, the injection energy will be as high as practically achievable (limited by the voltage holding capability spiral inflector). Where possible, all beam manipulation devices will be magnetic in order to avoid serious space-charge blow-up effects. The beam bunching system consists of a beam chopper and buncher designed to efficiently inject beam into the cyclotron while reducing stray beam scattering and the consequent activation problems. Since the magnetic field inside the cyclotron yoke increases from nearly zero at the entrance to the yoke to more than one Tesla at the central field region of the cyclotron, the action of the field on injected particles behaves like a strong magnetic mirror, which would reflect most of the injected beams without the action of a strong beam-focusing lens during injection. To solve this problem, a magnetic solenoid was designed for installation inside the yoke to compensate for the strong mirror effect to ensure high-efficiency injection into the ORIC.
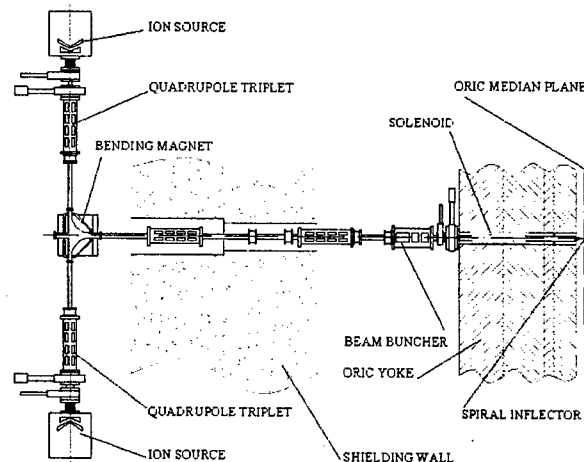
Fig. 1. Layout of the injection system for the ORIC.

2 SPIRAL INFLECTOR

An electrostatic mirror [3] is the simplest device for axial injection of beams into a cyclotron. However, for the present injection system, a spiral inflector has higher beam transmission efficiency - up to 100% - compared to a typical efficiency of ~65% for an electrostatic mirror. Although a mirror is smaller in dimension, it requires a very high voltage for operation. For example, an electrostatic mirror must operate at a voltage of more than 25 kV in order to inject 50-keV proton beams into the gyration plane of a cyclotron, while only ~10 kV is required for a properly designed spiral inflector. This reduction will reduce sparking and reliability problems associated with high-voltage breakdown and shorting.

In a spiral inflector, the central beam trajectory is generally used as the first-step in the design. A spiral inflector consists of a pair of coaxial, spirally twisted electrostatic deflection plates submerged in a strong magnetic field. Consequently, the beam trajectories are

more complicated due to the actions of both fields on particles during transit through the device. In order to simplify the problem for computing the position coordinates of beam trajectories, the fringe fields at the entrance and exit of the spiral are usually ignored and the transverse electric field within a spiral inflector through which the beam passes is assumed to be uniformly distributed so that the central trajectory of the beam can be expressed analytically. Fig. 2 shows the two meshed electrodes of a spiral inflector simulated with the 3D finite element code ANSYS [4]. Unfortunately, fringe fields at the entrance to an inflector and the twisted electrode structure of the inflection system have significant affects on the electric-field distribution and consequently, the trajectories of injected beams within the device deviate considerably from those derived by analytical means [2].

Fig. 2. Meshed electrodes of a spiral inflector.

It is a common practice to design a spiral inflector with a large gap size, nearly twice the dimension of the beam envelope [5], to deflect the beam into the central field region of the cyclotron and to tolerate shifts in beam trajectories inside the inflector. However, the large gap scenario is not desirable for injection of high-energy beams that require a higher operating electrode voltage for the spiral inflector. The problem cannot be solved simply by increasing the bending path length, since shifts in beam trajectories within a spiral inflector also increase with increasing bending path length. Efforts have been made to reduce the trajectory shift problem by using a smaller bending radius and by modifying the shape of the electrodes at the entrance to the inflector [6]. However, the approach cannot eliminate the problem, and it compromises the maximum voltage that can be used for operating the inflector.

In numerical electric field analyses and beam trajectory simulation studies, ploys are sought that reduce or even eliminate completely, beam shift problems while permitting operation of the inflector at electrode voltages commensurate with efficient injection into the central region of the cyclotron. By rotating the electrodes at entrance to the inflector or reshaping the inflector appropriately, the beam-path shift problem can be significantly reduced. Another practically tractable approach, that completely eliminates the path shift problem, can be affected by re-centering the inflector electrodes according to the actual central beam trajectory [2]. By use of powerful numerical tools, a high

transmission efficiency, small electrode gap spiral inflector with zero path shift has been designed that can operate at an electrode voltage of approximately 12 kV for injection of 50-keV proton beams into the ORIC (~40% lower than that of conventional large gap spiral inflectors.) Fig. 3 shows the zero path shift device with a vertical bending radius of A = 4.06 cm.
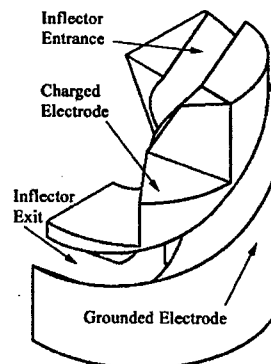
Fig. 3. The spiral inflector for the ORIC [7].

3 THE BEAM BUNCHING SYSTEM

An ideal beam-bunching system should use a saw-tooth waveform. However, a high-power, high-frequency saw-tooth wave generator is expensive and quite difficult to realize in practice. Typically, beam bunchers utilize sinusoidal waveform generators with a few higher order harmonics. The ORIC injection system uses a double-drift tube design. Among the advantages of this type of beam bunching system, include simplicity in structure, ease of control and operation, and low cost. One of the drawbacks of the design is that the tube length depends on beam velocity. With this buncher, ~65% of the injection beam will be captured (e.g., approximately 130 µA of beam will be captured from an ion source capable of generating 200 µA DC beams of H^-, D^- and He^{++}) and therefore, the intensities of the bunched beams will be high enough for injection into the ORIC. However, higher injection efficiency (>70%) can be achieved with a multiple-harmonic bunching system that is insensitive to variations in beam velocity [8].
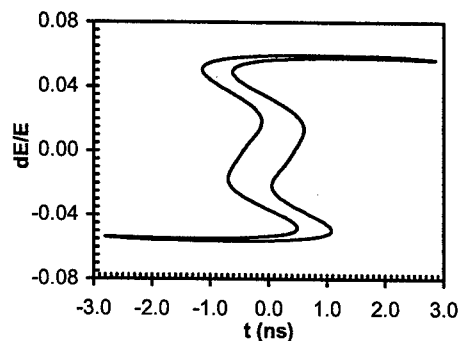
Fig. 4. Simulated longitudinal beam envelope for 50-keV bunched proton beam at entrance to the spiral inflector.

The buncher must be mounted as close as possible to the entrance to the magnet yoke to reduce beam pulse widths as required for efficient injection of beams into the RF field of ORIC. Only a vacuum valve and a Faraday cup follow the buncher before entrance to the magnetic yoke. Fig. 4 displays simulations of the longitudinal phase of the beam bunching system for a 50-keV proton beam. The optimized drift lengths of the first and second buncher are, respectively, 8.03 cm and 3.96 cm with no grid installed (a little less than $\beta \cdot \lambda / 2$ because of the transit time factor). A beam chopper is needed to remove the long tails produced by the beam-bunching system. Their removal will reduce beam scattering and consequently, activation of components in the cyclotron. In order to be compatible with the operating frequency range of the ORIC, the bunching system must be tunable between 14 and 19 MHz.

4 IN-YOKE SOLENOID

The distance from the entrance to the magnetic yoke to the median plane of the ORIC is ~1.5 m. Over this distance, the axial magnetic field inside the yoke increases from nearly zero to more than one Tesla, the action of which is equivalent to a magnetic mirror that reflects injected beams. When designing an axial injection system, careful attention must be given to solving this problem. In beam optics studies, the axial magnetic field was treated as a series of equivalent solenoids, as illustrated in Fig. 5. A focusing element inside the yoke is necessary to compensate for the strong magnetic mirror effect that otherwise would lead to loss of >75% of injected beams. The installation of a solenoid inside the ORIC magnet yoke is quite challenging because of the small-bore diameter in the yoke (~12 cm). A special solenoid with an outer diameter of 12 cm and inner diameter of 6 cm was designed to mount inside the yoke for matching the injected beam as indicated in Fig. 1.
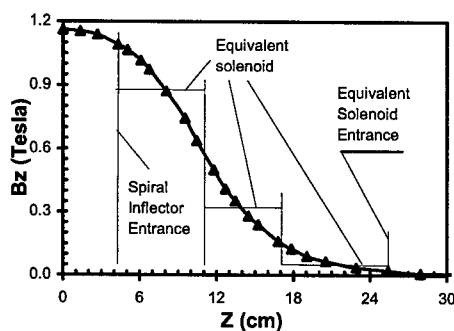
Fig. 5 Axial magnetic field in the yoke treated optically as a series of equivalent solenoids.

From beam optical studies with the in-yoke solenoid, no significant beam emittance deterioration occurs in the axial injection system at beam intensity levels up to 200 μA. When the axial injection system is well matched, the beam transport efficiency is expected to be nearly 100% for bunched beams, injected into the cyclotron *dees*. Fig. 6 shows simulated beam envelopes at the entrance and

exit to the spiral inflector. As noted, they are well confined in the spiral inflector and coupled to the ORIC *dees*.
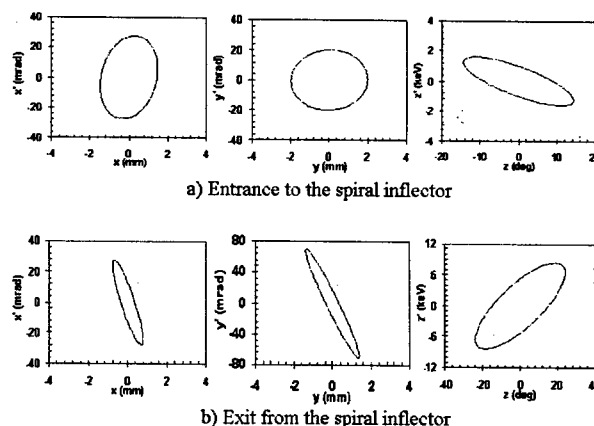
Fig. 6. Simulated beam envelopes for a 50-keV proton beam at entrance to and exit from the spiral inflector

5 CONCLUSIONS

According to computational studies, ~65% of the DC beams extracted from the external ion sources will be injected into and accelerated by the cyclotron with the proposed axial injection system. It is expected that more than 100 μA of high quality, primary light-ion beams will be extracted from the ORIC using either the existing septum extraction system for He^{++} beams and a foil stripping extraction system for extracting either H^+ or D^+ beams. In combination with an appropriately designed raster scan system for use in dispersing the beam-on-target power density, the new injection system will make possible the production and post acceleration of RIBs with intensities of 10 to 20 times those presently available at the HRIBF.

REFERENCES

1. http://www.phy.ornl.gov/hribf/
2. Y. Zhang, G. D. Alton, "*Electric field distribution in a spiral inflector for cyclotron injection applications,*" to be published in this proceedings.
3. A. J. Cox, et al., Nucl. Instrum. Methods 18 (1962) 25.
4. *ANSYS,* ANSYS Inc., Canonsburg, PA.
5. P. Belicev and D. V. Altiparmakov, Nucl. Instrum. Methods Phys. Res. A456 (2001) 177.
6. D. Toprek, D. Reistad, B. Lundstrom and D. Wessan, Nucl. Instrum. Methods In Phys. Res. A486 (2002) 539.
7. Y. Zhang, G. D. Alton and B. A. Tatum, "*The design of a spiral inflector*", to be published.
8. R. Zierl, W. Czech, P. Kienle, *et. al.*, Nucl. Instrum. Methods 164 (1979) 219.

INITIAL PERFORMANCE OF A 6 GHZ "VOLUME" ECR ION SOURCE

Y. Liu, G. D. Alton, H. Bilheux, J. M. Cole, F. W. Meyer, G. D. Mills, C. A. Reed, C. L. Williams

Oak Ridge National Laboratory, P.O. Box 2008, Oak Ridge, TN 37831-6368, USA

Abstract

An all-permanent-magnet, 6-GHz "volume-type" ECR ion source has been constructed and evaluated. This source employs a novel magnetic field configuration with an extended central flat region to form a large, on-axis, ECR volume. It can also be converted to a traditional minimum-B source where the ECR zones are surfaces. Comparisons are made of the performance of the source when operated in both "volume" and "surface" modes. According to the preliminary results, the "volume" mode is superior in terms of ion beam intensities and charge-state distributions.

1 INTRODUCTION

In electron-cyclotron-resonance (ECR) ion sources with traditional minimum-B magnetic-field profiles, ECR zones are thin annular, ellipsoidal-shaped surfaces when powered by narrow bandwidth, single frequency microwave radiation. These ECR surfaces constitute a small percentage of the plasma volume and consequently, the efficiency of RF power coupling as well as the performance of the sources are limited by the sizes of their ECR surfaces. It has been suggested that the performances of ECR ion sources can be improved by increasing the physical sizes of the ECR zones in relation to the sizes of their plasma volumes [1-4]. This can be done by flattening the central magnetic field such that a large ECR volume on the axis can be formed [1] or by injecting multiple-discrete or broadband microwave radiation into conventional minimum-B ECR ion sources [2-5].

Multi-frequency heating has proven to be an effective way to enhance the performances of ECR ion sources and is being used in many ECR ion sources [4,5]. The volume ECR technique employs a novel magnetic field configuration with an extended central flat region that is tuned to be in resonance with single-frequency microwave radiation [1], resulting in a significantly larger ECR volume. Thus, more RF power can be coupled into the plasma, heating electrons over a much larger volume than possible in conventional ECR ion sources. All other parameters being equal, the volume-type ECR sources should result in higher charge-state distributions, and higher beam intensities.

Heinen et al., have successfully demonstrated that volume-type ECR ion sources can out perform conventional minimum-B sources in terms of charge-state distributions and intensities within a particular charge state [6,7]. An all-permanent-magnet, 6-GHz "volume-type" ECR ion source that incorporates the flat-field concept has been constructed at the Holifield Radioactive Ion Beam Facility, Oak Ridge National Laboratory. The source is designed to be convertible from the flat-B configuration to a traditional minimum-B configuration and vice versa, so that comparisons can be made of the performance of the source in "volume" ECR and "surface" ECR modes under similar operation conditions. Initial results of charge-state spectra and intensity distributions of the source are presented. The performances of the source are compared in terms of the charge-state distributions and intensities within a particular charge-state for the "volume" and minimum-B configurations.

2 SOURCE DESCRIPTION

A schematic representation of the source is shown in Fig. 1. The axial mirror field is produced by two, 50-mm thick, annular NdFeB permanent magnets radially magnetized in opposite directions. With specially designed and positioned iron cylinders, magnetic field profiles can be formed with flat central region for volume ECR operation and parabolic central region for conventional minimum-B operation. The corresponding axial magnetic field profiles are shown in Fig. 2. A 12-pole multicusp radial magnetic field is used for the volume ECR configuration in order to increase the ECR volume in the radial direction. In combination with the axial mirror field, a magnetic-field strength of 5 kG, approximately equal to that of the axial mirror field, is generated at the inner wall of the plasma chamber. The multicusp field can also be changed to a $N = 6$ field distribution when the source is configured as a conventional minimum-B source. The plasma chamber is made of Al and is 15.6 cm in length and 5.4 cm in diameter. The source is designed to operate at a central frequency of 6 GHz and features the ability to tune the central flat magnetic-field region by mechanical means to the resonance condition within the limits of 5.6 to 6.6 GHz. Microwave radiation is coupled into the plasma chamber via a tapered rectangular-to-circular transition, starting from a rectangular WR137 waveguide and ending with a circular diameter that matches the dimension of the plasma chamber. Design details of the source can be found in [8]. The RF power supply consists of an RF signal generator and a klystron power amplifier (KPA). The RF frequency can be varied between 5.85 to 6.40 GHz with output power up to 3 kW. The ion source is

mounted on a high voltage platform and a three-electrode extraction has been designed for the source [9].
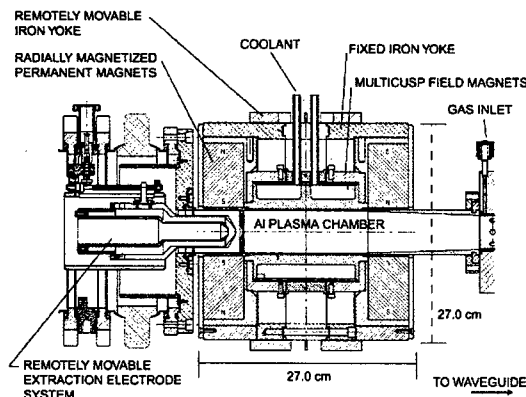
Fig. 1. Schematic view of the flat-*B* ECR ion source.
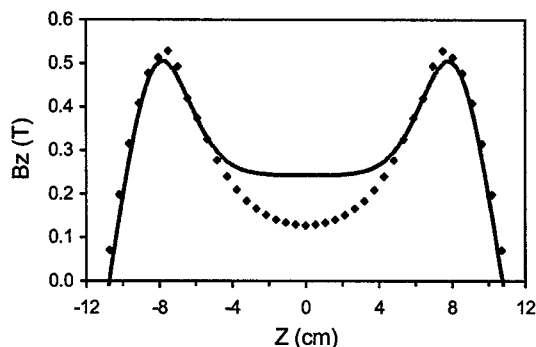
Fig. 2. Axial magnetic field profiles for the "volume" (solid) and minimum-*B* (dotted) configurations.

3 FIRST RESULTS

Initial testing of the source was conducted first for the "volume" ECR configuration, and then for the conventional minimum-*B* configuration, using *Ar* as the operating gas. Ions were extracted from the source at a voltage of 20 kV and mass analyzed with a 45° dipole magnet. Ion beam intensities were measured with Faraday cups before and after the mass analyzing magnet. The primary focus of our effort has been to commission this new source and characterize the source performance for various operating parameters including gas pressure, power and polarization of the microwave radiation, plasma electrode position and extraction gap for each configuration [10]. Operation of the source was reproducible. In general, the total beam currents and intensities of low-charge-state ions increased, while the production of high-charge-state ions (>6+) decreased, with increasing *Ar* pressure inside the plasma chamber. Our studies focused on source performance for high-charge-state ions. During the initial test phase, gas mixing was not studied and most of the data were obtained with the source operated with *Ar* gas. Fig. 3

shows an *Ar* charge-state distribution obtained with the "volume" ECR configuration without gas mixing.
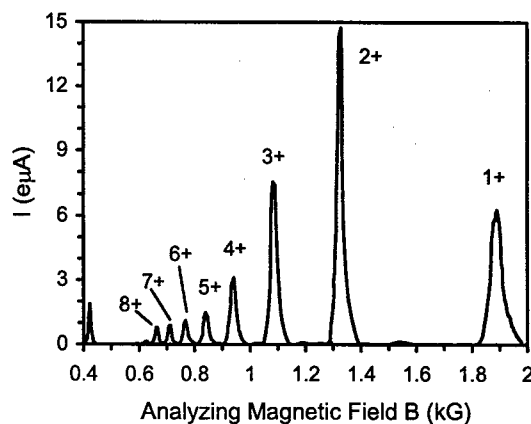
Fig. 3. *Ar* charge-state-distribution observed with the flat-*B* configuration. The source was optimized for Ar^{8+} without gas mixing at RF power of 800W.

The performances of the source in each configuration were evaluated and compared, based on the observed charge-state distributions and intensities within a given charge state, *X*-ray spectra, and high-charge-state production for *Ar* ion beams. A comparison of the best performances for *Ar* obtained with the flat-*B* and conventional minimum-*B* configurations is displayed in Fig. 4. The data were obtained under similar operating conditions for each configuration, optimized for high-charge states using *Ar* as the operating gas without gas mixing. It is clear that the "volume" ECR configuration produced higher charge states and higher intensities for each charge state than the conventional minimum-*B* configuration. In general, the flat-*B* configuration required more RF power applied to the source due to the much larger ECR zones in this configuration. It was also observed in *X*-ray measurements that much higher *X*-ray intensities and energies were generated with the flat-*B* configuration, suggesting the presence of more hot electrons in the "volume" ECR source [10].
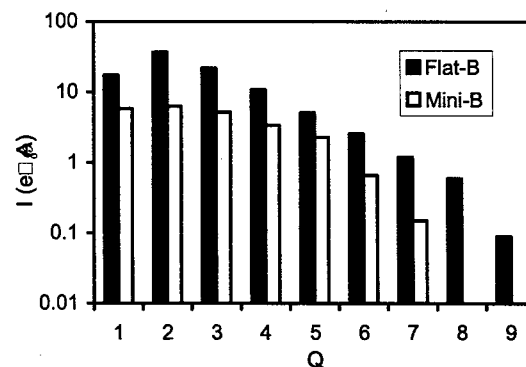
Fig. 4. A comparison of *Ar* charge states obtained with flat-*B* and conventional minimum-*B* ECR configurations.

4 SOURCE IMPROVEMENTS

The first performances of the source for high-charge-state production with both "volume" and conventional minimum-B configurations were poor. The total extracted currents were low, typically 200 to 300 eμA from the flat-B configuration, when the source was tuned for high-charge-state ions. The charge-state distributions were mostly peaked at Ar^{2+} and Ar^{9+} and Ar^{7+} were the highest charge states observed with intensities >0.1 eμA from both flat-B and minimum-B configurations, respectively. To improve its performance, several modifications were made to the source and tested with the minimum-B configuration. The vacuum inside the source was improved and the source operating parameters for high-charge-state ions were refined and optimized. The location of the plasma aperture was studied. It was found that the optimal aperture position was 3 cm behind the apex of the mirror magnetic field, closer to the plasma region. The optimal plasma aperture position led to several times higher total ion currents and better high-charge-state distributions. A major modification was to add a small iron plug on the axis in the RF injection region and changing the on-axis RF coupling system to an off-axis system. The RF radiation was originally coupled into the plasma chamber using an on-axis, tapered transition between the rectangular WR137 waveguide and the circular plasma chamber. The new RF coupling system consists of a transition from the on-axis WR137 waveguide to an off-axis WRD580 double ridge waveguide that ends abruptly at the location of the plasma chamber. This modification has three effects: (1) the on-axis iron plug increased the magnetic-field strength in the injection side; (2) the addition of the iron plug plus off-axis coupling eliminated a confined parasitic ECR zone in the RF injection region; (3) the plasma chamber became a cavity structure, instead of a traveling wave structure for the microwave radiation. The gas mixing technique was also studied and O_2 gas was used for ion cooling.

The performance of the source in the conventional minimum-B configuration was significantly enhanced with all the improvements using the new RF injection system. The total extracted Ar ion beam currents were increased by an order of magnitude when the source was tuned for high-charge-states. The charge-state distribution was peaked at Ar^{8+} and the highest charge state was moved to Ar^{11+}. The intensities of Ar^{7+} and higher charge-state ions were increased by more than 2 orders of magnitude. Fig. 5 shows a comparison of the Ar charge-state distributions before and after the improvements. Evaluation of these improvements for the flat-B configuration is being conducted and similar enhancement is expected.
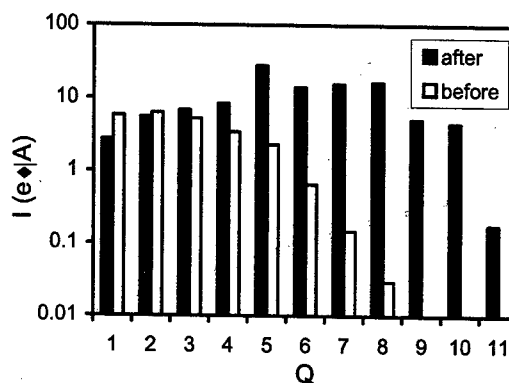
Fig. 5. Comparison of charge-state distributions for Ar ion beams extracted from the conventional minimum-B configuration before and after improvements made to the source.

5 CONCLUSION

Although much work remains to bring the source to levels competitive with existing sources, the initial comparative studies on the performance of the source clearly show that the flat-B configuration surpasses its conventional minimum-B counterpart in terms of charge-state distributions and ion-beam intensities in each Ar charge state. Since the initial studies, the performance of the source in the conventional minimum-B configuration has been significantly enhanced with various improvements and modifications made to the source and the use of a new off-axis RF coupling system. Similar enhancement in performance is expected for the flat-B configuration.

6 REFERENCES

1. G. D. Alton, and D. N. Smithe, *Rev. Sci. Instrum.* **65** (1994) 775.
2. C.M. Lyneis, Proc. of the 8th Int. Conf. On ECR Ion Sources and their Applications, East Lansing, Michigan (1987) 42.
3. G. D. Alton, *Nucl. Instr. and Meth. A* **382** (1996) 276.
4. Z. Q. Xie, and C. M. Lyneis, Proc. of the 12th Int. Workshop on ECR Ion Sources (Wakoshi, Japan, April 25-27, 1995), eds. M. Sekiguchi and T. Nakagawa, INS-J-182 (1995) 24.
5. G. D. Alton, F. W. Meyer, Y. Liu, J. R. Beene, and D. Tucker, *Rev. Sci. Instrum.* **69** (1998) 2305.
6. A. Heinen, et al., *Rev. Sci. Instrum.* **69** (1998) 729.
7. L. Mueller, et al., Proc. of 15th Int. Workshop on ECR Ion Sources (University of Jyvaskyla, Finland, June 12-14, 2002).
8. Y. Liu, G. D. Alton, G. D. Mills, C. A. Reed, and D. L. Haynes, *Rev. Sci. Instrum.* **69** (1998) 1311.
9. H. Zaim and G.D. Alton, *Computation Design Studies for an Ion Extraction System for the Oak Ridge National Laboratory ECR Ion Source*, Proceedings of the 2001 Particle Accelerator Conference, Chicago, 2001.
10. H. Bilheux, Ph.D. thesis.

ELECTRIC FIELD DISTRIBUTION IN A SPIRAL INFLECTOR FOR CYCLOTRON INJECTION APPLICATIONS

Y. Zhang and G. D. Alton

Oak Ridge National Laboratory, P.O. Box 2008, Oak Ridge, TN 37831-6368, USA

Abstract

The results of numerical studies of the electric field distributions in a spiral inflector, designed for axial injection system of H^-, D^- and He^{++} beams into the Oak Ridge Isochronous Cyclotron (ORIC), are presented in this report. Discrepancies are found between the electric fields obtained from numerical computations and those derived from theoretical field distributions within the inflector. Fringe fields at the entrance to the inflector, in combination with the field discrepancies, lead to significant deviations in particle trajectories from those derived from analytical expressions for fields within such devices. A method is described for shaping the electrode surfaces of the spiral inflector that is effective in compensating for fringe fields at the entrance to the inflector and a simple solution is introduced that eliminates the seemingly unavoidable shift in the central beam path. As a consequence of these studies, we arrive at a design for a spiral inflector that operates at a low voltage with greatly improved optical properties in which the paths of injected particles are precisely known.

1 INTRODUCTION

In order to deliver higher intensity, H^+, D^+ and He^{++} beams for ISOL target production of radioactive species for post acceleration at the Holifield Radioactive Ion Beam Facility (HRIBF), an axial injection system for the ORIC has been proposed [1]. The injection system utilizes a spiral inflector to inject beams from an external ion source system into the gyration plane of the cyclotron [2]. For this application, the energy of the injected beam must be as high as practical in order to reduce space charge effects associated with the high-intensity beams required to meet future radioactive ion beam intensity needs at the HRIBF. However, maximum injection energies are limited by the voltage-holding capability of the device.

A spiral inflector must bend beams through 90 degrees into an orbit that, after first turn acceleration by the cyclotron *dees*, misses the device. Therefore, the physical size of the device must be small. Belmont and Pabot invented the first spiral inflector at Grenoble [3] to fit within the limited space available in the central region of their cyclotron. The device demonstrated a high injection efficiency (up to 100%), superior to that of an electrostatic mirror. Since this development, these devices have been widely used in axial injection systems [4-6]. However, it is well known that beam trajectories within a spiral inflector do not follow the theoretical path and are shifted by the action of fringe fields at the entrance to and exit from the inflector [7,8]. By modifying the electrodes

at the entrance to the inflector, these shifts can be reduced but cannot be completely eliminated by this method. It is a common practice to design a spiral inflector with an electrode gap size nearly twice that of the beam dimension to guide the injected beam through the spiral electrode system. This design requires that higher voltages be applied to the device. The inflector, described in this paper, eliminates path shifts and operates at much lower voltages than prior art devices.

The results of numerical electric field studies for the inflector with the 3D finite-element code ANSYS [9] show that, aside from fringe-field effects at the entrance and exit of these devices, electric-field distributions inside inflectors do not agree with those derived from theoretical treatments of the problem due to the nature of the twisted electrode structures. These effects lead to significant deviations of particle trajectories through these devices that affect the accuracy of injection into the gyration planes of cyclotrons. By reshaping the electrodes at the entrance and exit of the spiral inflector, discrepancies of the electric fields within the inflector can be reduced and completely eliminated by re-centering the inflector electrode system.

2 DESIGN OF THE SPIRAL ELECTRODES

A spiral inflector with an electric bending radius, $A = 4.06$ cm, and magnetic gyration radius, $R = 2.77$ cm and $K = 1.13$ (K is defined in Refs. [2-6].) has been designed for injection of 50-keV proton beams into the ORIC. The central beam trajectory in the spiral inflector, derived analytically, serves as the starting point for the design [2]. Fig. 1 schematically represents the spiral inflector electrodes. Since the structure is twisted, electric-field distributions inside the inflector will deviate from those of the symmetrical structure resulting in combined forces from all the adjacent surfaces that alter the trajectories of particles through the system, as seen in Fig. 2.

Since the spiral inflector has an entrance to and exit from a gap between the twisted electrode pair, fringe fields exist at the entrance and exit of the inflector. Fig. 3 displays the computed and theoretical electric-field distributions at the mid-point of the spiral inflector. Although the fringe fields at the exit of the inflector are modified by the RF field of the cyclotron *dees*, the major component of the field accelerates beams toward the *dees*, and therefore, does not appreciably affect the trajectories of particles since they have already passed through the inflector. However, the same is not true for particles at entrance to the device, the field pushes the trajectories away from the desired path. The maximum shift of the

central beam inside the original spiral inflector is approximately 1 mm, as simulated with a code especially written for calculating this effect [2].
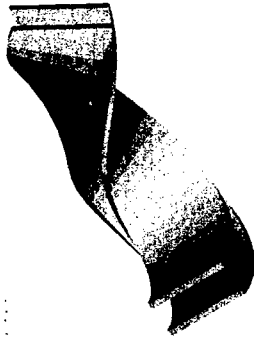
Fig. 1. Computed electrodes of a spiral inflector.

(a) Symmetry electrodes   (b) Twist electrodes
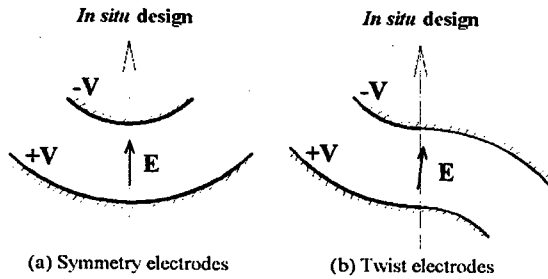
Fig. 2. Actual direction of electric fields (solid arrow) and those of the *in situ* design (dashed arrow) in (a) symmetric electrode system and in (b) a twisted electrode system.
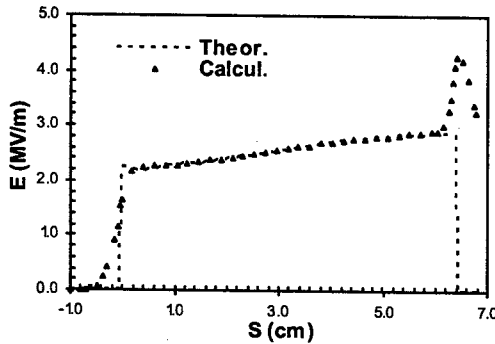
Fig. 3. Calculated and theoretical-field distributions of the original spiral inflector, fields at exit of the inflector are influenced by the cyclotron *RF* field.

By shortening the inflector electrodes at entrance to compensate for the fringe field, the shift in beam path can be reduced (e.g., shortening by 1.1 mm reduces the central ray shift to ~0.4 mm). Fig. 4 shows the electric-field distribution at the mid-plane of the spiral inflector with the electrodes shortened by 1.1 mm. However, the method cannot eliminate the beam path shift completely because electric field discrepancies inside the twisted electrode structure are unaffected by this operation. In fact, after shortening the electrodes, the position of the electric field curvature is changed, as noted in Fig. 4. The direction of the fringe field is rotated by ~3.5°, although not obvious in the figure.
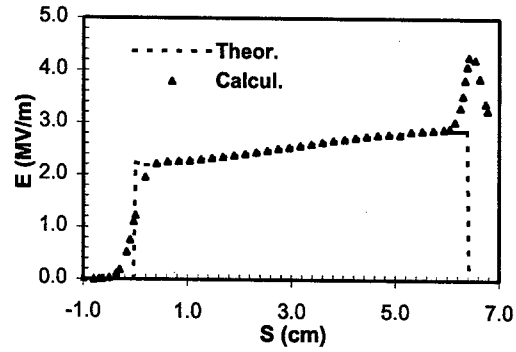
Fig. 4. Calculated and theoretical field distributions of the spiral inflector with the entrance electrodes shortened by 1.1 mm.

3 ROTATION OF THE ELECTRODES

Discrepancies between the calculated and theoretical electric-field distribution inside the spiral inflector can be seen by comparison of the three field components. Significant differences only occur for the perpendicular field components (x and y components). Fig. 5 shows the calculated and theoretical x and y components of the field inside the inflector. The calculated fields have magnitudes quite close to those of the theoretical forms but have slightly different peak locations. However, these seemingly very small differences lead to significant shifts in positions of beam trajectories in the device due to the twisted nature of the electrodes, and therefore, have significant influences on the accuracy to which beams can be injected into the central region of a cyclotron.
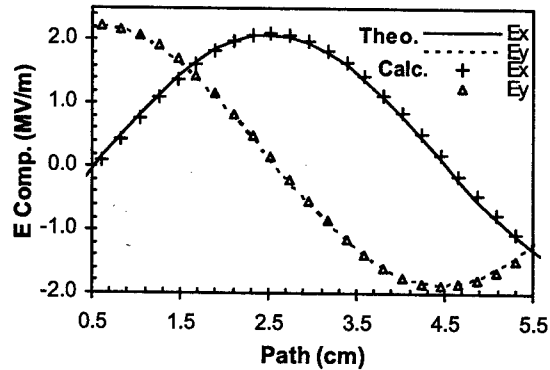
Fig. 5. Computed and theoretical perpendicular electric field components, Ex and Ey inside the spiral inflector.

By rotating the inflector electrodes horizontally, the field discrepancies within the twisted electrode structure can be reduced. The following term is used to determine the rotation of the electrodes [2],

$$\delta\phi = F \cdot [2Kb - \frac{(2Kb)^2}{K \cdot \pi}] \qquad (1)$$

where, F is constant and; b is the particle deflection angle from the axis of the magnetic field (0 to $\pi/2$). (For definitions of other parameters, see Ref. [2].)

1002

Fig. 6 shows the perpendicular electric-field components of the theoretical distributions in the spiral inflector and those computed with the inflector electrodes rotated for $F = 0.027$. As noted, the discrepancies in electric-field distributions are reduced. After the shortening of the electrodes, the shift in the central beam path inside the inflector is reduced from 1 mm to ~0.7 mm.
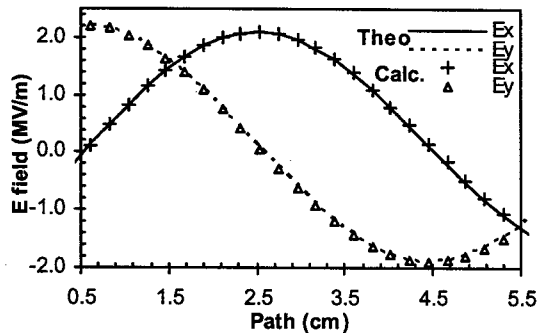
Fig. 6. Calculated and theoretical perpendicular electric-field components, Ex and Ey inside the spiral inflector with electrodes rotated at $F = 0.027$.

Rotation of the inflector electrodes can also be used to partially compensate for fringe fields at the entrance to the spiral inflector and thereby, reduce shifts in the beam path [2]. Shortening the electrodes at the entrance to the inflector reduces the effective length of the electric bend and therefore, the voltage across the inflector electrodes must be increased accordingly. However, rotating the entrance electrodes of the inflector does not affect the operational voltage of the device. Fig. 7 shows top views of the spiral electrodes of the design before and after rotating the electrodes at entrance by 15°. The beam path shift is reduced to approximately 0.6 mm after rotation.

(a) Original spiral inflector   (b) Entrance electrodes rotate 15°
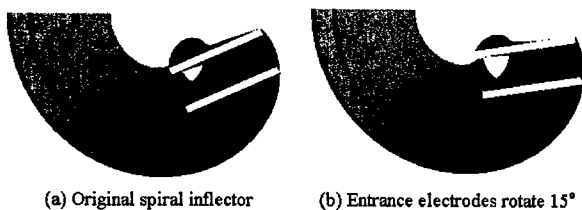
Fig. 7. Top view of the spiral inflector electrodes: (a) the original design; (b) entrance electrodes rotated by 15°.

4 RE-CENTERING THE INFLECTOR

Fringe fields effects at the entrance to the spiral inflector and discrepancies of the electric-field distributions inside the device displace the injected beam away from the intended path. In principle, the shift in path can be completely eliminated by shortening the entrance electrodes and by rotation of the electrodes appropriately. However, such iterations require many time consuming, tedious numerical computations because of the complicated electrode structure and the large effects on beam trajectories caused by small changes. Nevertheless, a spiral inflector with zero shift of the central trajectory is

pursued that can operate at relatively low voltages for injection of 50 keV p and 59 keV d beams into the ORIC. A conventional large-gap spiral inflector is not commensurate with the available space and energies of beams required for an axial injector for the ORIC because of the high voltages required for operation and the incumbent high voltage breakdown and shorting problems that accompany this design.

A simple solution has been found that can be used to completely eliminate beam path shifts inside an inflector. The technique involves the re-centering of the spiral inflector according to the actual (or precisely calculated) central beam path. This re-centering technique is performed in two steps: (1) by calculating the central beam path in the original inflector, and then (2) by re-centering the inflector electrodes according to the shift in the calculated central trajectory. By use of these simple procedures, the shift in central trajectory can be reduced to less than 0.1 mm and the gap size and operational voltage can be reduced by ~40%.

5 CONCLUSIONS

Numerical electric-field analysis provides a powerful tool for the design of spiral inflector systems. Fringe-field effects at the entrance and field variations within the inflector cause deviations of the central trajectory from the desired path. By re-shaping the inflector to compensate for fringe-field effects and re-centering the electrodes of the inflector according to the actual beam trajectory, beam path shifts can be completely eliminated. A low voltage, high transmission efficiency, spiral inflector design for accurately injecting intense beams into the central magnetic field regions of cyclotrons can be realized.

ACKNOWLEDGEMENT

REFERENCES

1. G. D. Alton, Y. Zhang and B. A. Tatum, "*An axial injection system for the ORIC*", to be published on these proceedings.
2. Y. Zhang, G. D. Alton and B. A. Tatum, "*The design of a spiral inflector*", to be published.
3. J. L. Belmont, J. L. Pabot, IEEE Trans. Nucl. Sci. NS-13 (1966) 191.
4. P. Mandrillon, "*Injection into Cyclotron*", CERN 96-12.
5. P. Heikkinen, "*Cyclotrons*", CERN 94-01.
6. D. Toprek, Nucl. Instrum. Methods Phys. Res. A440 (2000) 285.
7. P. Belicev and D. V. Altiparmakov, Nucl. Instrum. Methods Phys. Res. A456 (2001) 177.
8. D. Toprek, D. Reistad, B. Lundstrom and D. Wessan, Nucl. Instrum. Methods Phys. Res. A486 (2002) 539.
9. *ANSYS,* ANSYS Inc. Canonsburg, PA.

AN RFQ INJECTION SYSTEM FOR THE HRIBF

Y. Zhang and P. E. Mueller

Oak Ridge National Laboratory, P.O. Box 2008, Oak Ridge, TN 37831-6368, USA

Abstract

At the Holifield Radioactive Ion Beam Facility (HRIBF) at Oak Ridge National Laboratory (ORNL), molecular ions extracted from a positive ion source and subsequently broken up in a charge-exchange cell produce Radioactive Ion Beams (RIBs) with several hundred eV energy spread, preventing effective magnetic isobar separation. In order to perform magnetic isobar separation prior to charge exchange, a multi-harmonic buncher and a 12-MHz RFQ (Radio-Frequency Quadrupole) is proposed to supplement the present 300-kV injection system for the 25-MV tandem electrostatic accelerator. The RFQ will be mounted on a variable high voltage platform to accelerate ions with masses from 10 to 150 amu.

1 INTRODUCTION

The HRIBF [1] has been successfully conducting a research program of nuclear structure physics [2], nuclear reaction physics [3], and nuclear astrophysics [4] for several years. It is one of the first-generation Isotope Separation on Line (ISOL) RIB facilities. At the HRIBF, the target/ion source is mounted on a 300-kV rated platform. A light-ion beam from the Oak Ridge Isochronous Cyclotron (ORIC) bombards the target producing radioactive nuclei that are extracted from the ion source as 20-keV singly charged positive ions and subsequently accelerated to 40 keV. Negative ions are required for injection into the 25-MV tandem electrostatic accelerator. Therefore, after first-stage magnetic mass separation, the 40-keV singly charged positive-ion beam is injected into a recirculating jet cesium vapor charge-exchange cell. The energy spread of the resulting negative-ion beam is several tens of eV for an injected positive atomic beam and several hundreds of eV for an injected positive molecular beam, the increase being due to the three-body kinematics of molecular breakup. The negative-ion beam is finally accelerated to a nominal energy of 200 keV and sent through a second stage magnetic isobar separator with an intrinsic mass resolution of 20,000 prior to injection into the tandem accelerator.

Unfortunately, the actual mass resolution of the isobar separator is significantly degraded by the energy spread due to positive atomic beams and essentially eliminated by the energy spread due to positive molecular beams. This is a serious problem, particularly in the case of the high isobar contamination of RIBs that are produced from fission products. Various element specific isobar separation techniques are available [5], but magnetic isobar separation is applicable to a wide range of RIBs. A multi-harmonic buncher and a 12-MHz RFQ is proposed here to supplement the existing high voltage platform system. Charge exchange would be performed after isobar separation and before injection into the RFQ, which, in turn, would inject into the tandem accelerator.

A negative-ion beam cooler is also being studied at ORNL to reduce both the longitudinal and transverse emittance of RIBs [6]. If successful, the cooler could be used with the 300-kV platform system when negative-ion sources are used and charge exchange is not required.

2 LAYOUT OF INJECTION SYSTEM

Fig. 1 shows the present injection system for the HRIBF. Fig. 2 shows the proposed injection system for the HRIBF consisting of a multi-harmonic buncher and a 12 MHz RFQ. In the new system, the RIB is transmitted to the isobar separator at 60 keV instead of 200 keV. The charge-exchange cell has been moved downstream of the isobar separator. The RFQ is mounted on a ±100-kV platform to accelerate ions with masses from 10 to 150 amu. Due to severe space restrictions, both the diameter and the length of the RFQ are limited to approximately one meter. Consequently, there is no adiabatic bunching section, which would result in an RFQ more than three meters long. A multi-harmonic buncher that is designed to capture more than 80% of the injected DC beam can be located at ground potential within the available space.
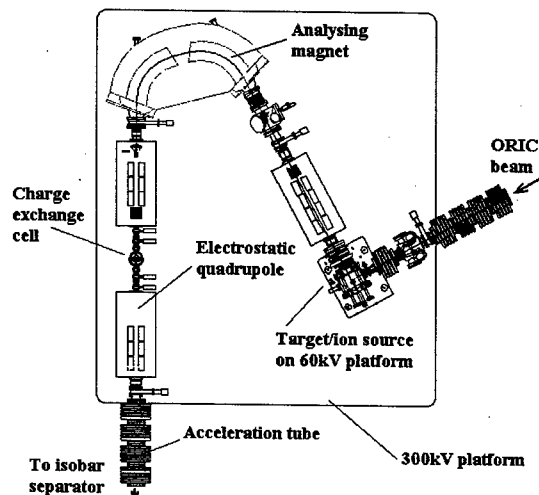
Fig. 1. Present injection system for the HRIBF.
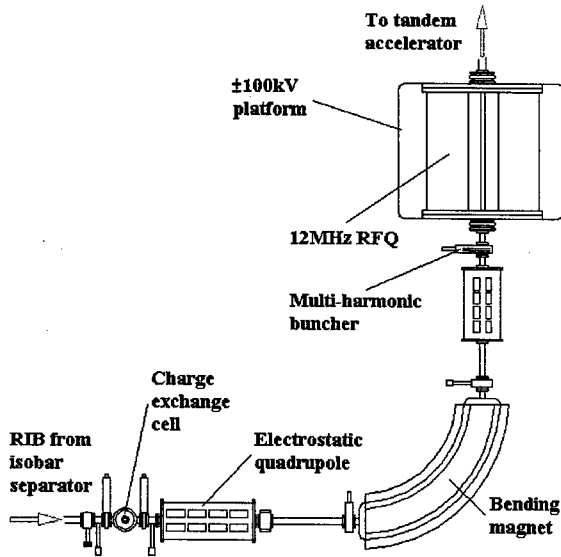
Fig. 2. Proposed RFQ injection system for the HRIBF.

In the RFQ injection system, the target/ion source is at 60 kV, and the first-stage mass separator and charge-exchange cell are now at ground potential. This will enhance operation and maintenance of the proposed injection system. Fig. 3 shows the beam envelopes from the image slit of the isobar separator to the entrance of the RFQ, calculated with the TRACE3D code [7].
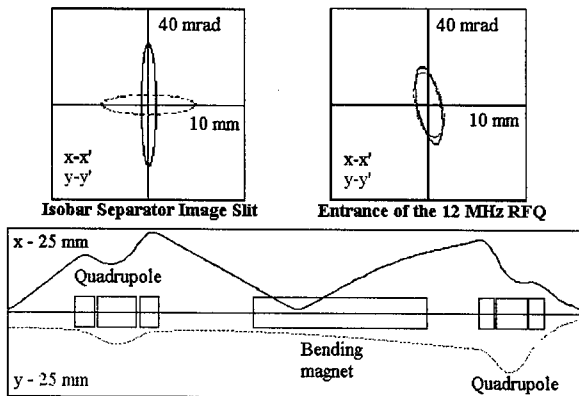
Fig. 3. Beam envelopes of the RFQ injection system from the isobar separator image slit to the entrance of the RFQ.

3 MULTI-HARMONIC BUNCHER

The multi-harmonic buncher will have 12, 24, 36, and 48 MHz modes with relative voltage amplitudes of 1.0, 0.44, 0.23, and 0.12, respectively. Since the beam may have several hundred eV energy spread after charge exchange, the buncher should be as close as possible to the RFQ to minimize time dispersion. Mounting the buncher on the ±100-kV platform along with the RFQ would minimize the distance between the two at the expense of requiring more RF power at high voltage. Table 1 lists features of a buncher located at ground

potential for different ion masses. Since the time spreads of the bunched beams are less than the acceptance of the RFQ, this buncher design is satisfactory.

Table 1. Features of the multi-harmonic buncher.

Ion mass	Equivalent drift length (cm)	Bunching voltage (kV)	Full width (ns)
10	222.2	0.695	12.0
20	97.9	1.11	8.7
40	50.8	1.55	7.4
80	32.2	1.81	7.7
150	25.0	1.82	10.1

The longitudinal phase space for a 20-amu bunched beam and the longitudinal acceptance separatrix of the 12-MHz RFQ are shown in Fig. 4. The buncher can capture 84% of the DC beam for injection into the RFQ in principle. However, there is a 15% beam loss due to the buncher grids [8] that reduces the overall efficiency to approximately 70%. This is less than that of an RFQ with an adiabatic bunching section, but still acceptable.
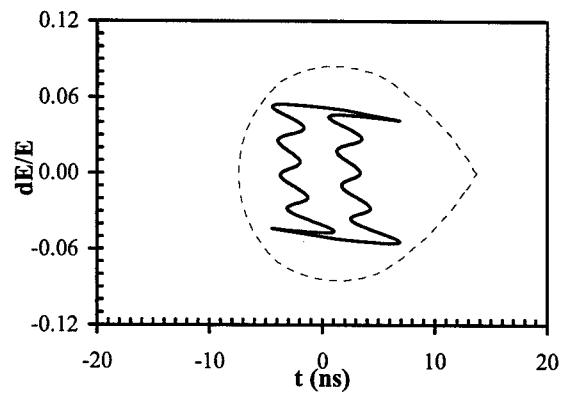
Fig. 4. Longitudinal phase space of a 20-amu bunched beam and the acceptance separatrix of the 12-MHz RFQ.

4 HEAVY ION RFQ

A 12-MHz heavy-ion RFQ with overall length of one meter has been designed using the code PARMTEQ [9]. Fig. 5 shows the various beam profiles at the exit of the RFQ with an injected 1-keV/amu 150-amu singly charged negative beam. The normalized transverse acceptance of the RFQ is 0.6 π·mm·mrad. The maximum required RF input power is approximately 15 kW as with the Atlas 12 MHz RFQ [10]. Because the RFQ has a narrow velocity acceptance, it must be mounted on a ±100-kV platform in order to accelerate RIBs from 10 to 150 amu. The injection parameters for different ion masses are listed in Table 2.

Various existing and proposed RFQs utilize split-coaxial [11,12], ring-connected [13], split ring [14] or four-rod spiral [15] structures to achieve low resonate frequencies. Since the proposed HRIBF RFQ has 94 cm electrodes, a split-coaxial structure would exceed the one-

1005

meter tank diameter restriction. However, a four-vane spiral structure with its larger end capacitances should reduce the tank diameter sufficiently. Fig. 6 shows the electrode structure of the RFQ. Some design parameters for the HRIBF RFQ are given in Table 3. Further mechanical, thermal, and RF efficiency studies need to be conducted.
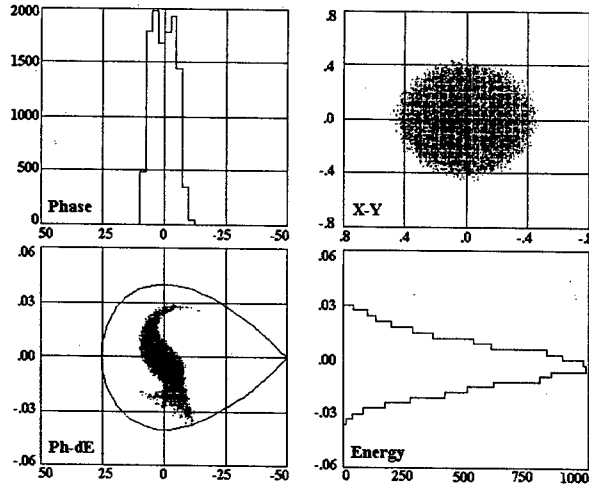
Fig. 5. PARMTEQ simulation of beam profiles at exit of the 12-MHz RFQ (Units: energy in MeV, phase in degree, x-y in cm). Ion mass: 150 amu; Charge: -1; Injection energy: 150 keV; Output energy: 774 keV; Normalized transverse acceptance: 0.6 π·mm·mrad.

Table 2. Injection parameters for different ion masses.

Mass	E_{IN} keV	$U_{PLATFORM}$ kV	U_{RFQ} kV	E_{OUT} keV
10	60	-50	6.67	102
20	60	-40	13.3	143
40	60	-20	26.7	226
60	60	0	40.0	310
80	60	20	53.3	393
100	60	40	66.7	476
120	60	60	80.0	559
140	60	80	93.3	642
150	60	90	100	684
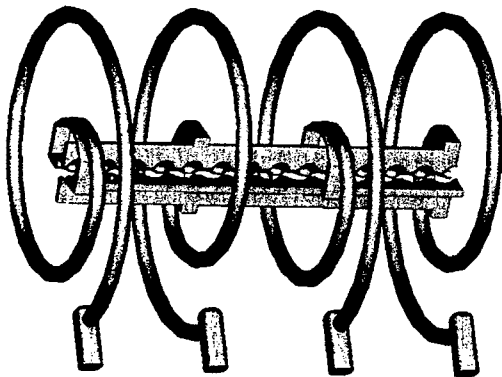
Fig. 6. Electrode structure of a four-vane spiral RFQ.

Table 3. Design parameters for the HRIBF RFQ.

Resonate frequency	12 MHz
Injection energy	1 keV/amu
Output energy	5 keV/amu
Inter vane voltage	100 kV
Vane length	94.2 cm
Number of cells	33
a	0.8 cm
m	1.5
ϕ_S	-25°

5 CONCLUSIONS

A multi-harmonic buncher and 12-MHz heavy ion RFQ injection system can allow magnetic isobar separation prior to charge exchange of positive atomic and molecular RIBs at the HRIBF. Isobar contamination of RIBs will be significantly reduced with the proposed injection system. Operation and maintenance of the target/ion source and other devices presently mounted on the 300-kV platform will be simplified.

ACKNOWLEDGEMENT

REFERENCES

1. http://www.phy.ornl.gov/hribf.
2. D.C. Radford, et al., Phys. Rev. Lett. 88 (2002) 222501-1.
3. J. Gomez del Campo, et al., Phys. Rev. Lett. 86 (2001) 43.
4. D. W. Bardayan et al., Phys. Rev. Lett. 83 (1999) 45.
5. P. Van Duppen, A. Andreyev, et al., Nucl. Instrum. Methods B 134 (1998) 267-270.
6. Y. Liu, J. F. Liang, G. D. Alton, et al., Proc. PAC 2001, pp. 3885-3887, Chicago, USA, June 2001.
7. TRACE3D, Los Alamos Accelerator Code Group, LANL.
8. F. J. Lynch, R. N. Lewis, et al., Nucl. Instrum. Methods 159 (1979) 245-263.
9. RFQ Design Codes, Los Alamos Accelerator Code Group, LANL.
10. M. P. Kelly, P. N. Ostroumov, et al., Proc. PAC 2001, pp. 506-508, Chicago, USA, June 2001.
11. R. A. Kaye, K. W. Shepard, et al., AIP Conf. Proc. 473 (1998) pp. 528-535.
12. S. Arai, Y. Arakaki, et al., Proc. LINAC 96, WE203 (http://linac96.web.cern.ch/Linac96/) August 1996.
13. V. A. Andreev, A. A. Kolomiets, et al., Proc. PAC 1997, pp. 1090-1092, Vancouver, Canada.
14. R. Laxdal, R. Baartman, et al., Proc. LINAC 98, pp. 786-788, Chicago, USA, August 1998.
15. A. Schempp, Nucl. Instrum. Methods A 278 (1989) 169.

MICROWAVE RADIATION STIMULATED BY ATOM OR ION BEAMS

V.Grishin*, Institute Nuclear Physics of Lomonosov Moscow State University
119992 Moscow, Russia

Abstract

Perspectives of high-frequency stimulated emission source applying accelerated beams of charged atoms which ones are widely used at present are analyzed. Radiation mechanism based on high-frequency intratomic electronic transitions due to anomalous Doppler's effect on slow waves is considered, while the low-frequency oscillations of atoms are neglected. Several slow surface wave systems with dielectric layers are estimated. In aggregate process has a complex nature since photon radiation is accompanied by excitation of atoms with following emission of more high-frequency photons. Requires to parameters of such systems and atomic beams for observation of stimulated emission needed for diverse applications are established.

INTRODUCTION

In the present work one of new possibilities of generation (specially created or as an attendant effect) high-frequency radiation with the help of fast beams of atoms or ions is considered. Fluxes of atoms, in which electrons remain in ground states, as well as system with excited atoms, can be unstable and be sources of high-frequency coherent electromagnetic radiation.

From an electrodynamical point of view an atomic flux is a flow of electron oscillators which ones due to anomalous Doppler's effect even in non-excited state can be a source of induced radiation. Here radiation of photons is supported by transferring of the particle kinematic energy. Besides the effect is accompanied by an inverse change of interior states of oscillators. Said is concerning to beams of both neutral atoms and positive and negatively ionized ones (if to neglect the interaction of latter with rather low frequency oscillations where the ions figure only as unstructured massive charges; therefore further specially is not stipulated charge states of atoms).

This mechanism, marked on a heuristic level still in [1,2], discovers broad application in systems with electronic beams (see, for example, [3]). Now analysis of atomic systems acquires also practical interest in connection with wide possibilities for deriving fast atomic and ion beams on modern accelerators.

One of the key moments is the estimation of excitation requirements of the mentioned above radiation of high-frequency collective instability in originally undisturbed flow of atoms. The anomalous Doppler effect can be

watched in systems with slow (in comparison with an atom beam) electromagnetic waves. One of them can be the gaseous medium. This case is parsed (apparently for the first time) in work [4] (author and T. Novikova). It was indicated that in similar system the effect of stimulated radiation can be watched, at least in infrared range of radiation. By analogy with a known case of Cerenkov instability of a charged beam in plasma [6], the marked effect of induced radiation of atoms can be described as manifestation of atomic two-stream instability (including, as well as in a plasma physics, case of a motionless gas).

However practical observation of effect will be enough difficult. In particular, the processes of a dissipation are an actual hindrance to development of induced high-frequency excitation, that defines rather small lifetime of exited states of atoms in a beam and gas. Therefore it is necessary to utilize here a dense gas and intensive beams rather accelerated.

Therefore it is expediently to analyze other varieties of systems with atomic beams, for example, systems with different dielectric elements. In particular, the system is of interest, in which walls of the drift chamber are plated with a dielectric layer possessing high coefficients of a refraction and transparence in the region of presupposed radiation frequencies. In such a scheme the excitation of slow surface waves (like as Smith-Purcell's waves) is possible, which ones can actively interact with slipping beams of particles. Let's remind that Cerenkov free electron lasers which ones have the similar scheme was experimentally tested, at least, in far infrared region[5].

ANALYTIC APPROACH. ESTIMATIONS

Consider a conventional boundary problem being analog to practical systems. The monochromatic atomic beam is injected with velocity $v_e = \beta_e c$ where c is the light velocity, along the axis z in half-infinite space ($z \geq 0$) of a travelling chamber near to its lateral wall plated with a dielectric layer. In an initial point of the chamber, a triggering signal is put in as an electromagnetic wave propagating along axis z:

$$(\mathbf{E}, \mathbf{B}) = (\mathbf{E}, \mathbf{B})_0 \, exp(i(kz - \omega t)).$$

Here ω and k are frequency and wave vector of a signal. Allowing fast damping of a amplitude wave across the chamber, it is possible to neglect curvature of a wall and be restricted to considering of a flat one-dimensional problem. Then the excited slow wave has configuration: $\mathbf{E} = (E_x, 0, E_z)$, and $\mathbf{B} = (0, B_y, 0)$.

* grishin@depni.sinp.msu.ru

Here axes (x, y) are directed across and along a wall of the chamber; the system is homogeneous along the axis y.

Evolution of a signal during its propagation together with a beam along system will be featured by the dispersion equation [6]:

$$\kappa_1 \tan (\kappa_1 a) = -\epsilon_1 \kappa_2 / \epsilon_2 \qquad (1)$$

where $\kappa_1 = \sqrt{\epsilon_1 \omega^2 / c^2 - k^2}$, $\kappa_2 = \sqrt{k^2 - \epsilon_2 \omega^2 / c^2}$, ϵ_1 is a permittivity of dielectric layer with thickness at a, and ϵ_2 is permittivity of atomic medium. The latter generally consists from atomic gas filling the chamber near wall volume (a sub-index p), and atomic beam (sub-index b). Therefore [7]

$$\epsilon_2 = 1 + \frac{\omega_p^2}{2 \Omega_p (\Omega_p - \omega - i\Gamma_p)}$$
$$+ \frac{\omega_b^2 \omega_l^2}{2 \Omega_b (\Omega_b + \omega_l + i\Gamma_b) \omega^2}, \qquad (2)$$

where

$$\omega_{p,b}^2 = (4\pi e^2 N_{p,b} f_{p,b})/m. \qquad (3)$$

Here e and m are charge and mass of electron, $N_{p,b}$ is atom density of gas and beam, $f_{p,b}$ and $\Omega_{p,b}$ are oscillator force and frequencies of electron transitions in the nearest exited atom states (other transitions are neglected), $\Gamma_{p,b}$ are values opposites to times of life in exited states, $\omega_l = \omega - k v_e$.

In virtue of said above, the terms in which atoms, if they are not neutral and act as massive unstructured charges, are omitted in the ratio (2). Further it is necessary to say that frequencies of excited waves are close to resonant ones. It is important also that atomic beam is lowly relativistic. Due to this the difference between longitudinal and cross components of beam dielectric tensor can be neglected.

Let's address at first to a case when it is possible to neglect the influence of gas in the vacuum chamber. Dispersion properties of a waves in "cold" system (without beam) are defined by the equation (1) at $\omega_b^2 \to 0$ and $\epsilon_2 \to 1$.

The influence of a beam is strongest near to frequency $\omega \simeq k v_e - \Omega_b$ (slow beam wave is "working" here; stable fast wave $\omega \simeq k v_e + \Omega_b$ is not taken into account in the equation (1)). The interaction of a beam with environment gets resonant character if values of frequencies and wave vectors simultaneously coincide with one of own values of these parameters ω_0 and k_0 for waves in cold system:

$$\omega_0 = k_0 v_{ph} ; \quad \omega_0 = k_0 v_e - \Omega_b \qquad (4)$$

where v_{ph} is phase velocity of a wave in cold system. Obviously, the resonant conditions (4) are consistent, if $v_e > v_{ph}$. Then the frequency generated is $\omega_0 = \Omega_b/(v_e - v_{ph})$.

Believing now condition (4) executed, we write down $k = k_0 + \delta k$. Considering $| \delta k | \ll k_0$ also we obtain from (1) and (2) the equation:

$$\delta k (\delta k - i\eta) = -Q, \qquad (5)$$

where $\eta = \Gamma_b/v_e$, $Q = (\pi^2 \omega_b^2 \Omega_b)/(4 a^3 c^3 k_0^4)$. Here we use in virtue of $k_0 a \gg 1$ that the solution of the cold dispersion relation gives $\kappa_1 a \sim \pi/2$.

Estimation for increment of assumed spatial amplifications of the initial signal follows from here:

$$Im \, \delta \, k = \left(-\sqrt{4 Q + \eta^2} + \eta \right)/2 \qquad (6)$$

Amplification (i.e. stimulated radiation) takes place if $Im \delta k < 0$ [8]. We see the equation (6) gives no threshold condition for development of a stimulated radiation.

Swift development of a stimulated process can be observed only in the case of using a very intensive atomic beam when

$$\omega_b^2 \geq \frac{\Gamma_b^2 c^3 a^3 k_0^4}{\pi^2 v_e^2 \Omega_b} \qquad (7)$$

Practically, for low current beams we have $4 Q < \eta^2$, and $Im(\delta) k \sim Q v_e/\Gamma_b$. So we should not neglect a signal absorption in the dielectric layer. Therefore we must make a change $\epsilon_1 \to \epsilon_1 + i \delta \epsilon_1$. Then the first multiplier undergoes a modification

$$\delta k \to \delta k - i \zeta$$

where

$$\zeta = \frac{\epsilon_1 v_{ph}^2/c^2 - 1}{\epsilon_1^2 a} \delta \epsilon_1 \simeq \frac{\pi^2 \beta_e}{4 k_0^2 a^3} \frac{\delta \epsilon_1}{\epsilon_1}$$

In this case an amplification appears if threshold condition is carried through: $Q > \zeta \eta$, and the increment value is

$$Im\delta k = \left(-\sqrt{4 Q + (\zeta - \eta)^2} + \zeta + \eta \right)/2$$

For transparent media there is the condition $\zeta \ll 1$, and a signal absorption reveals very weakly. For high current beams a stimulated radiation can take place also in a low transparent dielectric.

Judging by (5) and (8), reasonably acceptable minimal values of density beam corresponds to intratomic transitions in infra-red radiation with $\Omega_p < 10^{15} \div 10^{14} c^{-1}$, i.e. with length of a radiated wave $\lambda > 1.5 \div 15$ mkm. However only long-lived transitions with $\Gamma_{p,b} \simeq 10^7 c^{-1}$ can participate in stimulated process. At last, the atomic beams should be enough accelerated with $\beta \geq 0.1$, that corresponds to energy of particles about ≥ 5 MeV / nucleon.

Therefore beams of the accelerated negative ions of light atoms can be real objects for observation of the phenomena examined there (for example, H^-, widely used nowadays in experiments [9]). So, at $\Omega_b = 10^{14} c^{-1}.\beta_e = 0.1 - 0.3$, development length of instability makes tens centimeters for slipping beams with density at several $10^{19} atom/cm^2$.

However here it is necessary to make one rather important addition. The beam, sliding along a wall of the chamber, will inevitable form a gas cloud. Density of gas can reach the rather large values, and the thickness of a cloud

will surpass considerably a wave length of radiation generated. To estimate influence of gas it is necessary to address again to the relation (1) and to use the relation (2). Atomic gas, marked in (2) by sub-index p, changes a spatial distribution of electromagnetic waves, and can make damping of their amplitude. So the wave spatial distribution in cold system ($\omega_b^2 \rightarrow 0$)is described by function $exp(-\kappa_2 x)$ where only the real part of second number in ϵ_2 is present.

We see that the wave spatial cross-decreasing can be weakened for a sufficiently dense atomic medium. Moreover if $Re\,\epsilon_2\,\omega_0^2\,/\,c^2 > k_2^2$, the wave character is changed principally: the wave cross structure becomes oscillatory. In this case a wave generated is deeply penetrating in beam zone. In result the increment of agitation rises considerably (see [10] too). Besides the beam boundary can be displaced from a chamber wall, that is realized in practical schemes.

But this conclusion is correct only in certain frequency strip. Really, $Re\,\epsilon_2$ obtains a maximum if $\omega_0 \rightarrow \Omega_p + \Gamma_p$, and $Re\,\epsilon_2 \rightarrow 1$ as $\sim 1/\Delta$ where detuning $\Delta = |\Omega_p - \omega_0|$. In the same time the imaginary part (responsible for signal damping) $Im\,\epsilon_2 \rightarrow 0$ as $\sim 1/\Delta^2$. Therefore since, as a rule for gas atoms, $\Omega_p \gg \Gamma_p$ in frequency strip with $\Omega_p \gg \Delta \gg \Gamma_p$ gas damping is not important.

CONCLUSION

Present work is aimed at to attract attention on very interest and non-ordinary phenomenon — on high frequency radiation by fast flux of heavy particles with complex structure. Ones of objects for possible application of heavy particle fluxes are different plasma traps. Radiation provoked by particle flux can signal about state of gas and plasma densities, pollution of chamber wall and so on.

Of cause it is necessary to analyze (for estimation of information obtained) the influence of various accompanying processes - excitation, ionization and the dispersion of atoms of a beam and gas. Nevertheless we may assume that these processes have an effect only for subsequent stages, because an effective cross-section of atomic collisions already for slightly relativistic particles does not exceed about $10^{-19}\,cm^2$.

Therefore the doubtless interest represents the investigation of further dynamics of considered above processes, which (after fast excitation of beam during of radiation on slow wave) can result in additional radiation of photons (on fast wave !).

REFERENCES

[1] V.L.Ginsburg // USSR, 1947, N_0 56, p. 145.

[2] V.L.Ginsburg, Teoreticheskaia phyzika i astrophyzika. Moscow, Nauka, 1981.

[3] M.V.Neslin, Dynamika puchkov v plazme. Moscow, Energoisdat, 1982.

[4] V.Grishin, T. Novikova// Proceeding of PAC'01, New York. 2001. P.

[5] Felch K., Busby K.O., Laymon R.W. et al.// Appl. Phys. Lett. 1981. V.38. P.601.

[6] A.F.Aleksandrov, L.S.Bogdankevich, A.A.Rukhadze Osnovy elektrodinamiki plasmy. Moscow, Vysshaia shkola, 1978.

[7] A.S.Davydov, Quantovaia mechanika. Moscow, Gosud.Izd.Fiz.Mat.Lit., 1963.

[8] A.I.Akhieser, I.A.Akhiese, P.B.Polovin. Elektrodinamika plazmy. Moscow, Nauka, 1974.

[9] H.Massey, Negative ions. New York, Cambrige, 1976. [10] V.K.Grishin, C.M.Cricket //Proceeding of 9-th Inter.Conf."Beams-92", Washing,1993, v.3,p.1776

EFFECTIVE SOURCE OF SHARP FOCUSED ELECTROMAGNETIC RADIATION OF ELECTRONS WITH MODERATE RELATIVISTIC ENERGY

V. Grishin[†], S. Likhachev, Institute of Nuclear Physics of Lomonosov Moscow State University, Moscow, Russia

Abstract

The new circulation scheme of intense bremsstrahlung source with a sharp directed flow of X-ray and gamma-photons is proposed. In traditional sources the summary output, due to notable self-absorption of generated photon in target, makes no more than 1/3 from all radiative electron losses. Besides because of strong electron scattering in the target material, the photon radiation happens in an angle, which is much more than an inverse electron relativistic factor. In a circulating source the thin target placed in a magnetic field is used, and electrons are radiating, multiple crossing the target. Thereof all flow of generated photons is kept, and the total radiation output essentially raises. The new configuration of magnetic fields improving the electron focusing and simultaneously reducing angular divergence of radiation is considered. Moreover the scheme permits to produce here a lateral drift that displaces circulating particles and to"cleans" a target space. Computer modeling with using of the software package GEANT confirms high efficiency of proposed scheme. So the yield of hard photons in 5-degrees cone rises at order in comparison with traditional devices. Accordingly, the portion of widely dispersed radiation is reduced.

INTRODUCTION

Hard X-ray and gamma-radiation of relativistic electrons are actively employed in different fundamental researches and manifold industrial applications, and it is very important to increase efficiency of their generation. In present work the new scheme of bremsstrahlung radiation source (BRS), one of most spread sources of hard radiation, is proposed.

The traditional BRS have a series of essential defects owing to which the small part of possibilities included in the mechanism of bremsstrahlung radiation (BR) can be utilized only. In the main, it is explained by a certain contradiction of the requirements declared to traditional BRS. In the latter electrons with given energy are directly dropped on the bremsstrahlung target made. The generation of bremsstrahlung photons grows in accordance with thickness of the target. However the photon absorption increases in a material of the target in the same time. An optimum target thickness is equal approximately to 0.3-0.5 part of electron range in the target material when the BR yield reaches a maximum. In total, the noticeable part of initial energy of radiating electrons is "unexpended", and the optimum summary output of BR energy makes no more than 1/3 from all radiative losses of electrons in the target

In reality even this limit is not reached. Due to a strong dispersion of electrons in the target the radiation of photons happens in a cone, a polar angle of which is much more than an electrodynamic limit $1/\gamma_e$ where γ_e is the relativistic factor of an electron. At the same time scattering angle of electrons is $\theta_e \approx \sqrt{t}/\gamma_e$ where t is the target thickness. Therefore the angle of a radiation cone forecasted theoretically can de observed only at rather small thickness about 10 microns (for a tungsten target) that is much less than the optimum value. In the total, the radiating electrons spend no more than third of initial energy.

The marked BRS inconsistencies and defects can be removed in circuital scheme proposed below. In this scheme the thin target immerged in a magnetic field is used, and electrons hitting the target are returning back. In results the electrons are multiple crossing the target and gradually losing all initial energy. In the thin target the soft photons are absorbed rather weakly. Therefore all generated photons are radiated, sharply raising an aggregate photon output.

Notice that the scheme of circuital BRS was offered for the first time in work [2], which reflected different features of such sources. Then similar schemes were considered in other works [3-6] and partly in [7]. Mark that only in the works carried out with author's participation, an attention is paid to an estimate of device efficiency. In the present work the more effective scheme of BRS with a magnetic field with planar symmetry is considered. It is shown by a method of computer simulation that in this case BRS have noticeably higher overall yield and much best angular characteristics of radiation. Thank to applicaion of a special magnet system the circuital source efficiency is essentially risen, and sharp direction property of BR is restored.

SOURCE LAYOUT. MAGNET SYSTEM PROPERTIES

The experimental setup proposed is represented in Fig. 1. Here in a vacuum chamber VC a target T is installed. The target is immersed in a magnetic field. The electron beam EB is injecting through a special channel EI in a operation volume. Electrons circling in the magnet field are hitting the target several times. Then they are been removed

---

[†] grishin@depni.sinp.msu.ru

through a channel EO. BR generated by electrons is been taken out through a photon channel BRO.
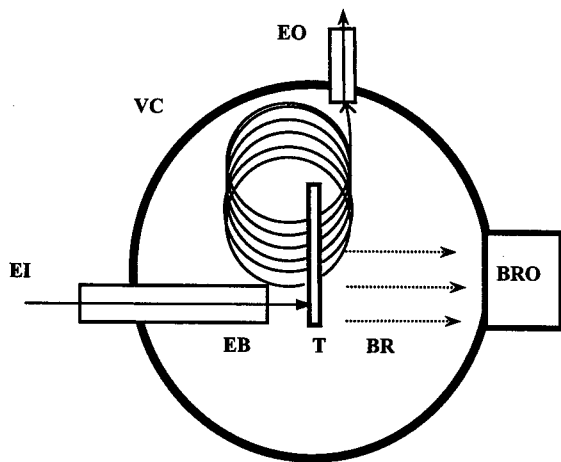
Figure 1. The scheme of experimental setup.

A magnetic field must carry out some functions. The first one is ensuring a stable circulation of electrons with their properly focused back fall on the target. The second one is a necessity to shift the rotating particles along the target. For this the special configuration of magnetic field is considered. At first approximation a suitable field configuration can be creating by means of magnetic poles of a rather simple form. These are two parallelepipeds placed over and below the target and stretched along it. The poles are slightly shifted across target plane. In this case the fields dispersed on poles ridges are ensuring spatial focusing of circling particles. Due to a displacement of poles, mean magnitudes of fields are not equal "before and after" the target, and the latter provides a lateral drift of particles. By results of our previous works [3], the similar magnetic configurations provides reliable focusing of particles.

However for sharp directed radiation obtaining, a system proposed must provide homogeneity of focusing for particles of various energies during a radiation cycle. Therefore a more fine magnet system must be applied if we want to reduce the radiation divergence. The latter requires circling electrons return on the target along trajectories which are close to be parallel to preceding ones (in this case the divergence angle of electrons is not "accumulated"). The problem is being resolved in system with special profile of magnet poles optimized for reaching full homogeneity of radiant particle focusing.

MODELING AND RESULTS. BACKGROUND FACTOR

In the present work, the method of computer modeling with use of the software package GEANT (CERN) is applied [8]. The software library GEANT represents extensive one of the programs for modeling atomic and nuclear experiments.

As a result package GEANT allows to carry out a full-scale numerical experiment (in area examined by us) at reasonable expenses of computing resources. Computer testing has been performed for new and traditional schemes with initial energies of radiant electrons at 5, 20 and 50 MeV. Tungsten target thickness was equal to 0.1 and 0.4 part of electron ranges in first and second schemes accordingly.

Testing has confirmed the high efficiency of circuital schemes which ones are surpass at several times over traditional bremsstrahlung devices in generation of the full BR flux.

But the main attention was paid to optimization of magnet system to obtain best focusing of circling electron and to deduce a radiation divergence. Finally we received very perspective and in certain aspects non-expected results. So some data describing characteristics of radiation generated in cone with polar angle at 5 ° are presented in fig. 2, fig.3, and fig. 4.

Statistic of data illustrated corresponds to number of incident electrons at several hundreds of thousands. We see distributions of photon number yield along an energetic scale for different energies of incident electron in proposed and traditional schemes.
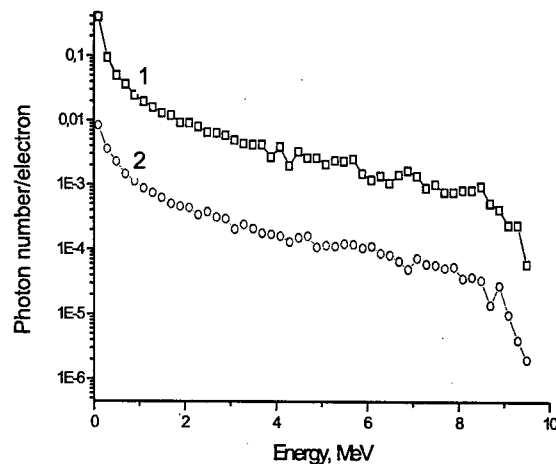
Figure 2. Dependence of specific yield of photon number, irradiated in cone with polar angle at5 °, per one incident electron with energy at 5 MeV on photon energy for circuital (curve 1) and traditional schemes (curve 2).

Their comparison indicates that a circuital scheme "right" organized permits to restore BR sharp direction. Of cause the greatest effect is observed in sources with low initial energy electrons. However computer estimates indicate we obtain almost on the order a gain at electron energy of 50 MeV.

Modeling data permit to make the other important conclusion. Introduce a term "background factor" (BF) which is equal to the relation of photon numbers radiated in 5 ° - cone and in the rest space.

CONCLUSION

Thus computer testing confirms very high efficiency of proposed circuital scheme with new magnet system which allows to increase appreciably a total output and to improve considerably angular characteristics of BR radiation.
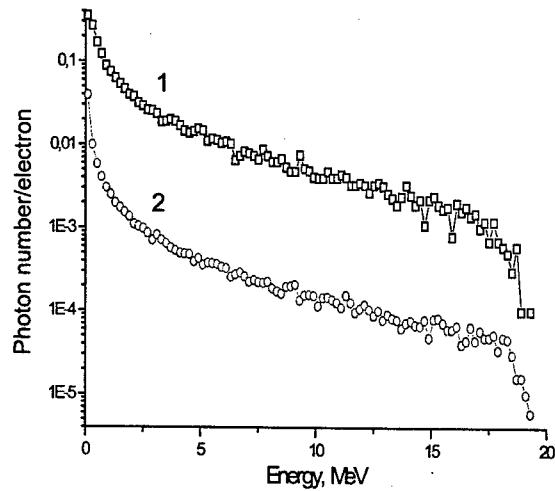
Figure 3. Dependence of photon number yield, irradiated in cone with polar angle at 5 ^{0}, per one incident electron with energy at 20 MeV on photon energy for circuital (curve 1) and traditional schemes (curve 2).

REFERENCES

[1]. M.J. Berger and S.M. Seltzer// Phys. Rev. **C2** (1970) 621.

[2] Grishin V.K., Ishkhanov B.S., Shvedunov V.K. // Moscow University Physics Bulletin, 1996, v. 51, №. 1., p. 69. Allerton Press. Inc.

[3]. V.K. Grishin, B.S. Ishkhanov, S.P. Likhachev, D.A. Rodionov // IEEE, Proceeding of international PAC'97, 1997, p. 3866.

[4]. B.Bogdanovich, V.Kudinov, A.Nesterovich, Yu.Pomasan, E.Tsygankov, V.Janenko, Proceeding of "PAC'97"(Vancouver, 1997), 1998 IEEE, P.276

[5]. M.Yu.Andreyashkin, V.V.Kaplin, S.R.Uglov, V.N. Zabaev, M.A.Piestrup, Appl. Phys. Lett., Vol. 72, No. 11, 1998

[6] V.V.Kaplin, L.W.Lombardo, A.A.Mihalchuk et al.//Nucl.Instr.and Meth. in Phys.Res.1998. B 145.P.244-252

[7] V.K. Grishin, B.S. Ishkhanov, S.P. Likhachev // Proceeding of international Conference EPAC2002 (Paris, 3-7 June). P.2789.

[8]. Brun R., Bruyant., Maire M. et al. GEANT3 (User manual). GERN, Geneva, Switzerland, 1990

Figure 4. Dependence of photon number yield, irradiated in cone with polar angle at5 ^{0}, per one incident electron with energy at 50 MeV on photon energy for circuital (curve 1) and traditional schemes (curve 2).

This factor allows to estimate "usefulness" and "efficiency" of device usage. So, for traditional and circuital devices with of electron energy 10 MeV we have, accordingly, BR = 0.5 and BR = 0.6 at the registration of photons of all energies, and BR = 0.55 and BR = 1.43 for photons with energy being higher 2 MeV.

So the efficiency of the circuital device at hard photon radiation appears not only higher, but also at three times smaller "background pollution ".

EFFECTS OF PROPAGATION FOR HIGH POWER CW ELECTRON BEAM IN AIR

S. Korenev, STERIS Corporation, Libertyville, IL 60048, USA
I. Korenev, Northern Illinois University, DeKalb, IL 60115, USA

Abstract

The question of effects at during of propagation for high power scanning electron beam in air presents the scientific and applied interest. The high power (80 kW) CW electron accelerator Rhodotron with kinetic energy of electrons 5 MeV was used in the experiments. The experimental results for propagation of scanning electron beams in air are presented and discussed. The physical model for explanation of these results is suggested.

INTRODUCTION

The propagation for scanning relativistic electron beam in air observes effects of variation of current density and cross section of beam, erosion of beam front [1,2,3]. These effects can not be explain by standard physical models and it presents the motivation of this research.

The results of experimental research for propagation of high power parallel scanning relativistic CW electron beam in air are presented in this report.

EXPERIMENT

The CW electron accelerator "Rhodotron" from IBA [4] was used in the experiments with next main parameters:

- kinetic energy of electrons............... 5 MeV;
- power of electron beam (max) .... 80 kW;
- diameter of beam after foil window... ... 8 cm;
- repetition of scanning beam..............60-100 Hz;
- frequency of CW mode.....................108 MHz.

The scanning mode for electron beam is given on Figure 1.

The current transformers (Rogowski Coils) and Faraday Cups with current shunts were used for measurements of beam current.

The sensor for measurements of conductivity of air plasma is presented on Fig. 2. The principle of work for this sensor is next. The scanning electron beam across thin Ti foil and absorbed in the these foil with small factor. The capacitor C charges as a results of absorption of electron beam. When electron beam moves to other side from sensor, the capacitor C discharge on the resistor R. The air plasma forms by scanning electron beam is switch for this C-R circuit.

The standard Cellulose TriAcetate (CTA) films dosimeters (FTR-125) were used for measurements of dose distribution in cross section. The CTA films with width 100 cm were fixed with step 20 cm after foil

window of electron accelerator. The distance between first CTA film and foil window of accelerator was 10 cm.
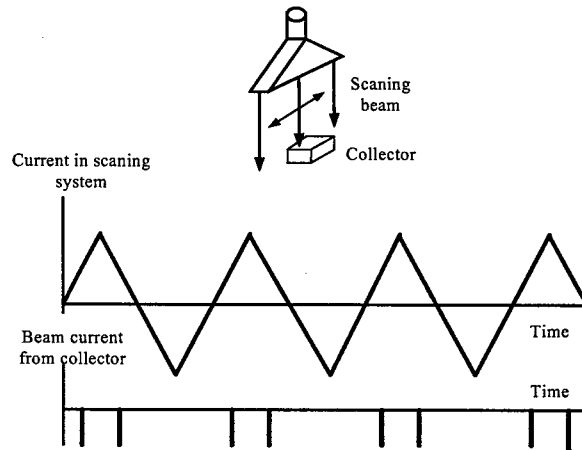
Figure 1: Scanning mode of beam
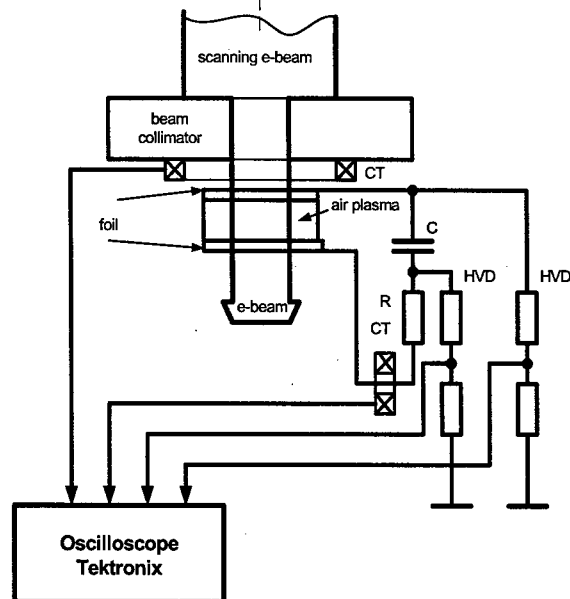
Figure2: Measurements of plasma conductivity.

EXPERIMANTAL RESULTS

The cross section distributions of absorbed doses in air are shown on Figure 3. This distribution has place for electron beam in cross section.

0809 testing
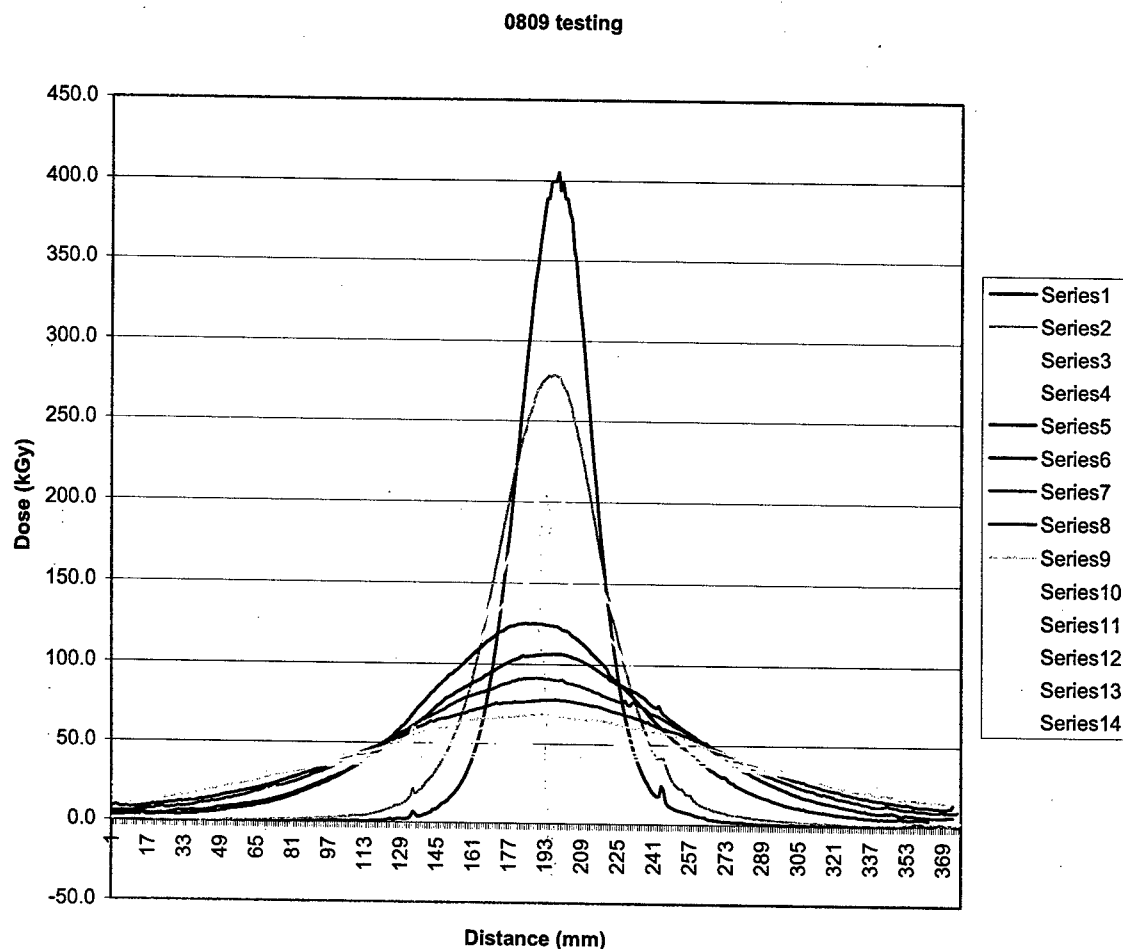
Figure 3: The dose distribution in CTA film dosimeters in cross section of electron beam in air.

The measurements of conductivity of air plasma are given high resistance air plasma. For current 1 mA the resistance between 1x1 cmxcm Ti foil and gap 1 cm is 280 kOhm and resistance is 110 Kohn for beam current 16 mA.

DISCUSSION

At during of the propagation of CW relativistic electron beam in air we can consider the next main physical processes:

* the ionization of air molecules by electrons of beam and forming air plasma;
* the heating of air and air plasma;
* the chemical reactions with produce of ozone.

The mechanism of forming of air plasma can be explain using of perpendicular component of beam velocity for ionisation of air molecules by electron beam. In this case we have low velocity and the cross section of ionisation

by electrons increases. As a result of it, we form high resistance air plasma. The scattering of primary electron beam on the components of this air plasma leads to

increasing of beam dimensions in cross section. The effects of neutralization of space charge of electron can be neglected for small value of beam current (the max current is 16 mA) .

CONCLUSION

As results of conducted research we can make next conclusions:

1. The beam current density is decreasing in cross section along propagation of electron beam in air.
2. The air plasma forming by scanning electron beam has high resistance.

REFERENCES

[1] S.Korenev, K. Khodataev, N. Rubin, Preprint JINR No R10- 417, JINR, Dubna,1982.
[2] S.Korenev, Proc. XII International Conference on Photonic, Electronic and Atomic Collisions. Santa Fe, USA, 2001, p. 234
[3] J. Pottie,. Nuclear Instruments and Methods in Physics Research B40/41, (1989), 943.

THE CONCEPT OF BEAM LINES FROM RHODOTRON FOR RADIATION TECHNOLOGIES

S. Korenev, STERIS Corporation, Libertyville, IL 60048, USA

Abstract

Among of main requirements to electron beam for industrial radiation technologies the variation of absorbed doses in irradiated product and kinetic energy of electrons is very important for increasing of efficiency of processes. The CW electron accelerator Rhodotron has technical opportunities for design of multi-lines system for radiation lines in industrial scale. The variant of multi-lines system on the basis of Rhodotron is considered in the report. The variation of current beam and time characteristics with multistage kinetic energy allows realizing this concept.

INTRODUCTION

The radiation technologies have different requirements on the dependence of radiation process [1]. The variation of absorbed doses can be realize using many different methods including the speed of conveyer (time of irradiation), beam current, kinetic energy. For using of multi-line's system with few beams, the variant of lines with different kinetic energy was considered for Rhodotron. Rhodotron is described in paper [2]. The main problem for same throughput of irradiated product is variation of absorbed doses for same thickness of product.

The concept of beam lines from Rhodotron is considered in this paper.

MAIN CONCEPT

The main concept of new beam lines consists in the variation of pulse duration of beam current for lines with fix kinetic energy:

1. the using of one Rhodotron accelerator with system of distributions of beam- lines (see Fig.1);
2. the using of time diagram for distribution of electron beams (see Fig.2).
3. the suing of effects of Rhodotron for receiving of beams with step distribution of kinetic energy for electrons (see Fig.3,4).

The main goal of this concept consists .in the receiving of simple system for irradiation of product with different thickness and different absorbed dose. It is very important question for radiation technologies. The question of multi-lines system discussed on the basis of separated electron accelerators with different kinetic energy. The multi-line system on the basis of accelerators is complex system and difficult engineering task.
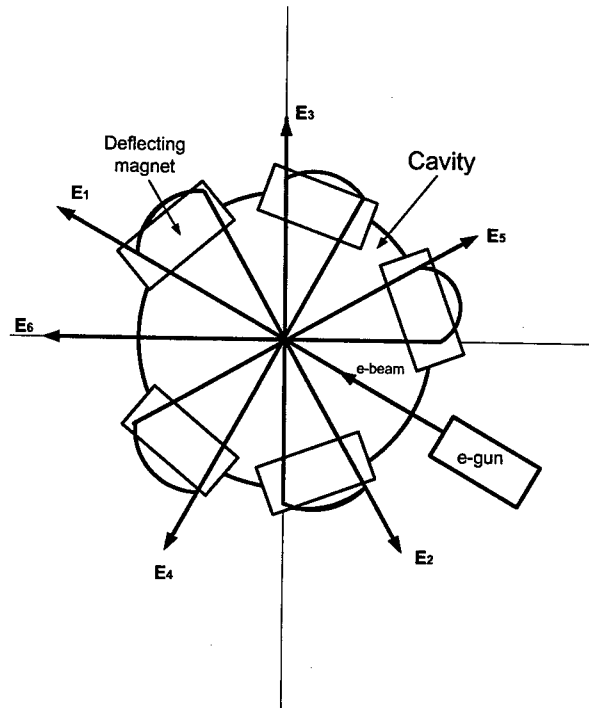
Figure 1: The main principle of multi-beams lines.
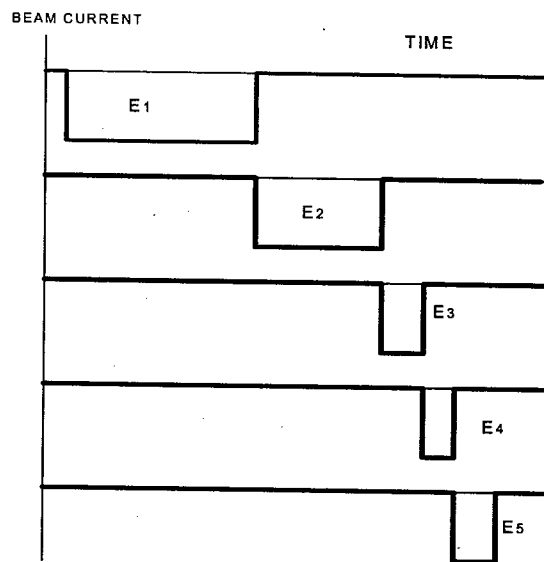
Figure 2: Time diagram of multi-line mode for Rhodotron
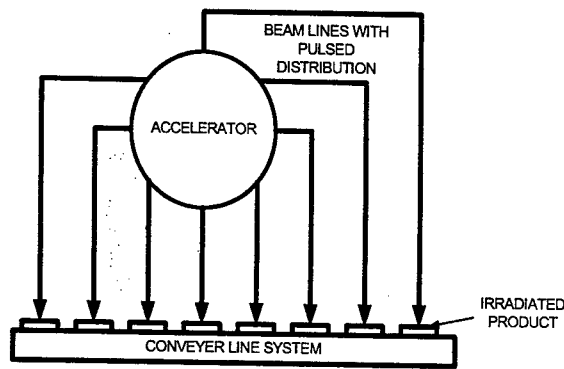
Figure 3: Multi-lines system.
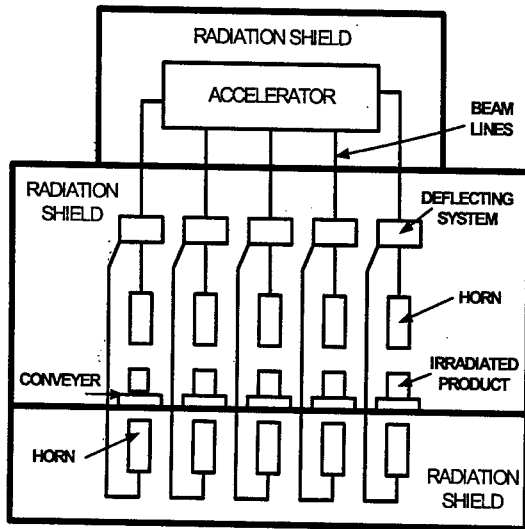
Figure 4: Structure of multi-lines with
2 sides of irradiation.

The absorbed doses D in irradiated product can be calculated using standard formula:

$$D = \frac{E}{m} = \frac{E_k \cdot I \cdot t}{\rho \cdot S \cdot d_{opt}} , \qquad (1)$$

where: E is absorbed energy, m is mass of irradiated product, E_k is kinetic energy (accelerating voltage), I is beam current, ρ r is density of irradiated product , s is square of irradiated product and d_{opt} is optimal thickness of irradiated product.

The variation of kinetic energy allows the determination of optimal thickness for irradiated product. This type of accelerator allows to create the beam lines with step distribution of kinetic energy 1-2 MeV. The different thickness of irradiated product leads to increasing of efficiency of radiation process.

The variation of time of irradiation by regulation of pulse beam from Rhodotron allows to regulation of absorbed doses. The value of beam current for all lines is same.

The time diagram of supply of magnet system is same with pointed on Fig.2.

The using 2 sides of irradiation allows to increase the thickness of irradiated product. It is very critical for high density of materials.

The low level of absorbed doses about few kGy for many radiation technologies lead for simple variation of time beam in the beam –line. It is simple in the operation in comparison with speed of v conveyer. The other opportunity of variation of time irradiation is regulation by speed of conveyer line, but it is more technically difficult in comparison with regulation of time diagram for supply of magnet system for accelerator.

The consideration of magnet system shows the realization of suggested concept.

The simulation of magnetic field in the magnets of Rhodotron also shows the realistic approach. The development of current power supply with pulsed modes made big progress at last time with using of fast switches and it can be used for design of prototype of this system.

The question of beam dynamics at the process of study and primary consideration of non-stability of electron beam in cavity allows to hope on the small factor of non-stability of electron beam. The question of influence of space charge in the complex dynamics of beam in cavity is open. The effects of influence of secondary electrons in cavity need to consider more detail.

CONCLUSION

In conclusion we can point, that considered concept of beam multi-lines on the basis of electron accelerator Rhodotron is attempt for increasing efficiency of accelerator and radiation processes. The considered concept can be modified on dependence of radiation process. The suggested concept of multi-lines system on the basis of Rhodotron permits to autoimmunization of full system

Also I want to say thank you to many scientists for discussion of this topic, especially to John Masefield, Andrey Mishin, Vadim Dudnikoiv, Nikolay Mokhov.

REFERENCES

[1] R. Wood, A. Pikaev, "Applied radiation Chemistry: Radiation Processing", W-I Publication, New York, 1994.

[2] J. Pottie, Nuclear Instruments and Methods in Physics Research B40/41, (1989), 943

MECHANICAL ANALYSIS OF THE PROTOTYPE UNDULATOR FOR THE LINAC COHERENT LIGHT SOURCE

B. Brajuskovic, P. Den Hartog, E. Trakhtenberg, ANL/APS, Argonne, USA

Abstract

The Linac Coherent Light Source (LCLS) will require undulators with unprecedented mechanical precision in order to achieve the magnetic field requirements. Distortion of the undulator strongback due to the thermal effects and magnetic and gravitational forces could seriously degrade the performance. To minimize the distortion, a C-type, fixed-gap undulator with titanium strongback will be used. An analysis of the design of the structure and a comparison of the predicted results with the mechanical requirements and with magnetic measurements is presented.

INTRODUCTION

The LCLS undulator will consists of 33 individual undulator segments. Each segment will be a permanent–magnet device, 3.42 m long, with 226 poles per jaw. Undulator segments will have a fixed gap of 6.3 mm. The electron beam trajectory has to be straight to within a few microns over a distance of ~10 m, thus limiting trajectory walk-off from a straight line to ≤ 2 µm per segment [1].

Challenges in the mechanical design of the undulator segments are threefold. The material selected for the strongback has to be nonmagnetic but provide minimal deformation, the shape has to be optimized to provide maximum freedom of access for magnetic tuning, and the design should allow accurate assembly to provide the required geometry. This paper discusses the selection of the material and the effect of the selected shape on the strongback's deformation. The issues related to the assembly and alignment are discussed elsewhere [1, 2].

ANALYSIS OF THE UNDULATOR SEGMENT DEFORMATION

The mechanical structure of LCLS undulator segments is shown in Figure 1. It consists of a strongback (1), magnetic structure (2), and upstream and downstream supports (3). The structure deforms due to attractive (magnetic) forces between the halves of magnetic structure, the weight of the halves and the strongback itself, and the changes in ambient temperature. Residual stresses introduced during the machining can also contribute to the deformation.

The attractive force and the weight of the magnetic structure are given in Table 1. Temperature changes influence deformation in two ways: ambient temperature can be uniform but different than the reference (zero strain) temperature, and a temperature gradient can develop within the strongback due to the spatial gradient of ambient temperature. The residual stresses due to the machining cannot be properly quantified, and their effect on the deformation is discussed only qualitatively.
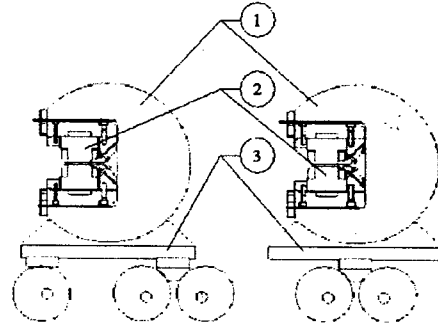
Figure 1: Undulator segment – schematic view

In the initial stages of the design, two possible cross-sectional shapes, "C" and "O", were considered. A C shape introduces asymmetry and is disadvantageous when deformation is considered, but the advantages of having open access to the magnetic structure and the vacuum chamber decided in favor of a C-shaped strongback.

Table 1: Undulator Segment Parameters

Parameter	Value
Attractive force (per jaw)	58.3 kN
Magnetic structure weight (per jaw)	123.4 kg
Vertical sag due to the weight	0.002 mm
Pole gap tolerance	±0.006 mm
Pole transverse displacement	± 0.2 mm
Pole displacement in Z-direction	±0.10 mm
Zero-strain ambient temperature	293.15 K

The Selection of Strongback Material

The choice for the strongback material is limited since it has to be nonmagnetic. Brass, bronze, aluminum and titanium-based alloys and austenitic stainless steels are nonmagnetic and were considered. Brass and bronze were eliminated due to their poor strength-to-weight ratio. Material properties [3] of the remaining three classes of material were compared using the following criteria:

- Young's Modulus, E
- Coefficient of thermal expansion, α
- Specific stiffness, $M_1 = E/\rho$
- Thermal performance index, $M_2 = \lambda/\alpha$

Young's modulus was used to evaluate the material performance under the magnetomechanical loads other than the weight of the strongback. The coefficient of thermal expansion was used to compare the effect of temperature changes on geometry. Specific stiffness and thermal performance index [4] were used to compare the influence of the weight and temperature gradients within the material, respectively. Normalized criteria for different materials are shown in Figure 2. Aluminum 6061-T6 properties were used for normalization. Austenitic stainless steels have the best overall mechanical and the

worst thermal properties. Titanium alloy Ti-6Al-4V has good strength-to-weight ratio, good torsion strength and moderate Young's modulus. It expands the least but has the lowest M_2 values. Aluminum alloys have the best strength-to-weight ratio but lowest torsion strength and Young modulus. They have excellent thermal performance index but expand the most.

a) Mechanical properties

b) Thermal properties
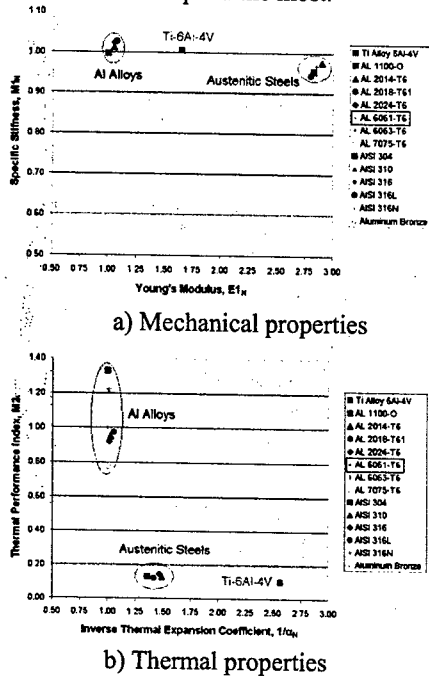
Figure 2: Normalized material properties.

The Finite Element Method Analysis

Comparison of material properties was inconclusive, and FEM analysis was performed. Deformation due to the gravity and attractive forces was computed for different materials. Also, the effect of temperature changes was computed for uniform changes in ambient temperature of ±2K and for a 2K ambient temperature gradient along the strongback. Model loads and restraints are shown in Figure 3. The magnetic structure was not included in the model due to the minor influence on the stiffness of the structure. However, its weight was taken into account as two uniformly distributed loads of 1.2 kN each, acting in the same direction. Attractive forces were represented as uniformly distributed forces of 58.3 kN acting in opposite directions. One support had no translational degrees of freedom, while the other could translate in the Z direction only. The zero strain temperature was 293.15K.
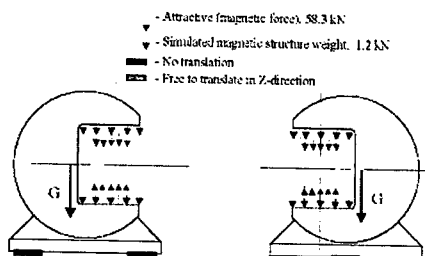
Figure 3: FEM loads and restraints

FEM Analysis Results

The weight-caused displacements computed for different materials are shown in Figures 4 - 6.
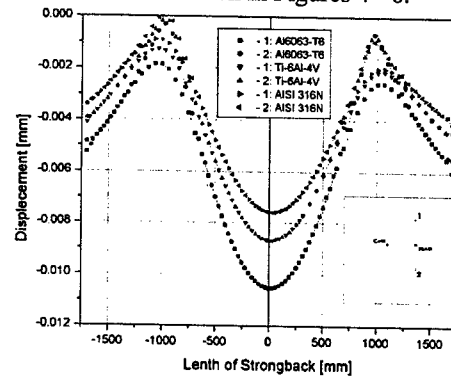
Figure 4: Gravitational Y-displacement in the beam plane.

The aluminum strongback deforms the most. Maximum Y displacement (12.5 μm) appears in the center of the strongback at the outer end of the upper jaw. The Y displacement decreases towards the center of the profile, and, in the plane of the beam, the maximum is 10.6 μm (Figure 5). Similar behavior is observed for titanium alloy and AISI 316N steel, but the computed values are lower, 8.8 μm for titanium alloy and 5 μm for stainless steel.
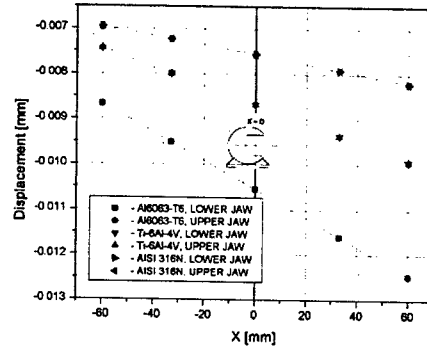
Figure 5: Gravitational Y displacement in the central cross section.

Calculated displacements indicate that jaws displace in opposite directions (so-called rolling of the profile, Figure 6). The upper jaw displaces outwards and lower one inwards. Rolling is the most obvious for the aluminum strongback and the least visible for the stainless-steel one.
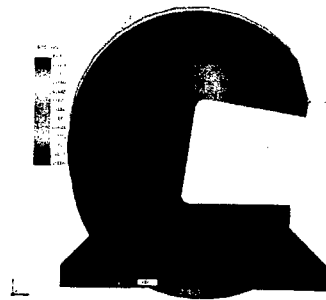
Figure 6: Rolling of the profile.

Displacements due to the gravity and attractive forces are shown in Figures 7 and 8. The tendencies remain the same, but the influence of the attractive forces is visible in the increase in displacement of the upper jaw and decrease in displacement of the lower. Again, the aluminum strongback deforms the most and the Y displacement of the upper jaw in the beam plane is 22.5 μm (112% increase). For the titanium strongback, the computed increase is 88% (16 μm), and for steel 71% (12 μm). The rolling of the profile is also more pronounced.
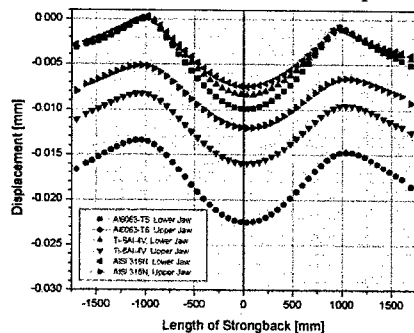
Figure 7: Y displacement in the beam plane due to gravity and attractive forces.
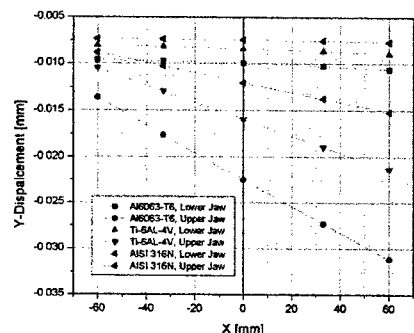
Figure 8: Y displacement in the central cross section due to gravity and attractive forces.

Differences in deformation of the lower and upper jaw affect the gap width along the entire section. The gap reduction is shown in Figure 9.
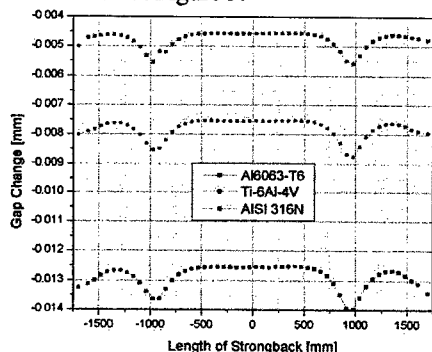
Figure 9: Gap change due to gravity and attractive forces.

Analysis of the influence of temperature gradients shows that ambient heating or cooling affects deformation more than temperature gradients within the material. The largest displacement in this case is in the Z direction. Again, aluminum displaces the most, the overall Z displacement is 0.16 mm (Figure 10), stainless steel displaces 0.11 mm and titanium displaces 0.06 mm. It is interesting to note that heating-related expansion reduces the displacement in the Y direction and the gap change.
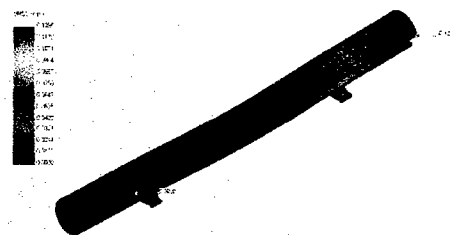
Figure 10: Z Displacement in the aluminum strongback due to the 2K increase in ambient temperature.

CONCLUSIONS

Results of FEM analysis show that both titanium alloy Ti-6Al-4V and AISI 316N stainless steel strongbacks surpass aluminum one in both mechanically and thermally related deformation. Easier machining [5], lower magnetic permeability, and absence of need for stress relieving provide titanium alloy with the advantage over austenitic stainless steels despite larger deformation and somewhat higher price of the entire device.

Computed deformation levels were somewhat higher than specified except for thermal expansion. Regardless of that, the results of magnetic measurements [6] performed on the prototype made of titanium alloy were satisfactory, which confirms the initial design assumption that the success of the device depends more on the ability to adjust and magnetically fine tune than on manufacturing precision.

REFERENCES

[1] J. Arthur et al, Linac Coherent Light Source Conceptual Design Report, SLAC-R-593, April 2002, p. 8.1-8.99.

[2] E. Trakhtenberg, V. Tcheskidov, M. Erdmann, I. Vasserman, N. Vinokurov, O. Makarov, P. Den Hartog, "First Prototype Undulator for the LCLS Project – Mechanical Design and Prototype Lessons," MEDSI 2002, Argonne, September 2002, p. 339.

[3] http://www.matweb.com/

[4] D. Cebon and M.F. Ashby, "Materials Selection for Precision Instruments," Meas. Sci. Technol. 5 (2002) 297.

[5] "Guide to Machining Carpenter Stainless Steels and Specialty Metals," Carpenter Technology Corporation, 1993, USA.

[6] I.B. Vasserman, S. Sasaki, R.J. Dejus, O.A. Makarov, E.R. Moog, E.M. Trakhtenberg, N.A. Vinokurov, "Magnetic Measurements and Tuning of the LCLS Prototype Undulator," FEL 2002, Argonne, September 2002, to be published.

DEVELOPMENT OF A SHORT-PERIOD SUPERCONDUCTING UNDULATOR AT APS*

S.H. Kim[†], R.J. Dejus, C. Doose, R.L. Kustom, E.R. Moog, M. Petra and K.M. Thompson

Advanced Photon Source, Argonne National Laboratory

9700 S. Cass Ave., Argonne, IL 60439, USA

Abstract

A planar superconducting undulator (SCU) with a period of 15 mm is under development at the Advanced Photon Source (APS). The intended users require a photon energy that can be tuned from 19 to 28 keV for inelastic x-ray scattering studies. The SCU design consists of two low-carbon-steel cores that are positioned above and below the beam chamber. There are 20 turns of NbTi/Cu superconducting (SC) wire within a coil cross section of 4.3 x 4.0 (w x h) mm^2. At a pole gap of 8 mm, the necessary average current density in the coil will be about 1 kA/mm^2 to achieve a peak field of 0.8 T on the beam axis. The design and fabrication progress of a 12-period prototype SCU are presented, and some challenging requirements are discussed.

INTRODUCTION

Demands for undulators with shorter periods and/or higher peak fields than those available from permanent magnet (PM) undulators are emerging for the storage-ring-based synchrotron radiation facilities and for future free-electron lasers. Superconducting undulators (SCUs) with high current densities in the coils have the potential to overcome these limitations. In the past, there has been considerable progress in developing short-period SCUs at Brookhaven National Laboratory and ANKA/ACCEL [1, 2]; here we report on recent developments at APS.

The goal of the SCU program at APS is to develop, fabricate and install an undulator tunable over a photon energy range from 19 to 28 keV in the first harmonic. Further extensions to this energy range can be achieved by using the third harmonic of the radiation, which would require a high field quality in the SCU. The intended users at the 7-GeV APS storage ring (SR) require this tuning range for inelastic x-ray scattering studies in condensed-matter physics. The possibility of shorter period SCUs (~ 12 mm) with acceptable pole gaps will also be investigated. This is of interest for future programs in applied materials research and geological studies. The lowest reachable energy of the first harmonic depends on the highest magnetic field achieved. Using a 15-mm period at 0.8 T, 19 keV can be achieved, and at 1.0 T, 16 keV. Figure 1 compares the on-axis brilliances calculated for the PM Undulator A (33-mm period), which is the mainstream undulator at the APS and the 15 mm SCU described here. This paper reports on the progress of a 12-period prototype SCU.
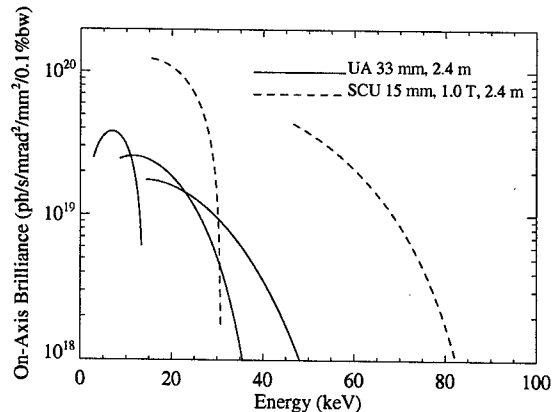
Figure 1: On-axis brilliances calculated for the permanent magnet Undulator A with 33-mm period (harmonics 1, 3, 5) and a SCU with 15-mm period (harmonics 1, 3) for the APS storage ring (7.0 GeV, 100 mA, 2.5 nm-rad). The on-axis brilliance is six times higher for the SCU at 25 keV, an energy of interest for selected experiments.

SCU DESIGN

Figure 2 depicts a 3-D model of one period of the SCU with a period length of 15 mm. It consists of two low-carbon-steel cores with SC coils. The two halves of the core are placed symmetrically with respect to the SCU midplane. The flat sides of the cores adjacent to the midplane are the top and bottom undulator poles. The beam chamber with an elliptical cross section will be inserted in between the poles providing a gap of 8 mm. The design concept assumes that the cooling of the device is "pool boiling" by immersing both the SCU and the beam chamber in liquid helium. The core has grooves for 20 turn coils with cross sections of 4.3 x 4.0 (w x h) mm^2.

Plotted in Fig. 3 are the vertical peak field B_0 in the SCU midplane (*top*) and the maximum field B(coil) in the SC coil (*bottom*) as a function of the average current density in the coil. Also plotted in the same figure are the critical current densities measured for three selected NbTi/Cu SC wires as a function of applied magnetic field (*bottom*) at 4.2K. The rectangular wire Jc(#2), which has a Cu/SC ratio of 1.25 and dimension of 1.05 x 0.8 mm^2, has been chosen for the fabrication of this prototype. By choosing a rectangular wire instead of a round wire, a packing factor over 90% can be achieved and better control of the wire positioning in the grooves can be made. To achieve a peak field of 0.8 T for the rectangular wire, we find that the required current density of 1 kA/mm^2 will be less than 70% of the critical current density at a B(coil)
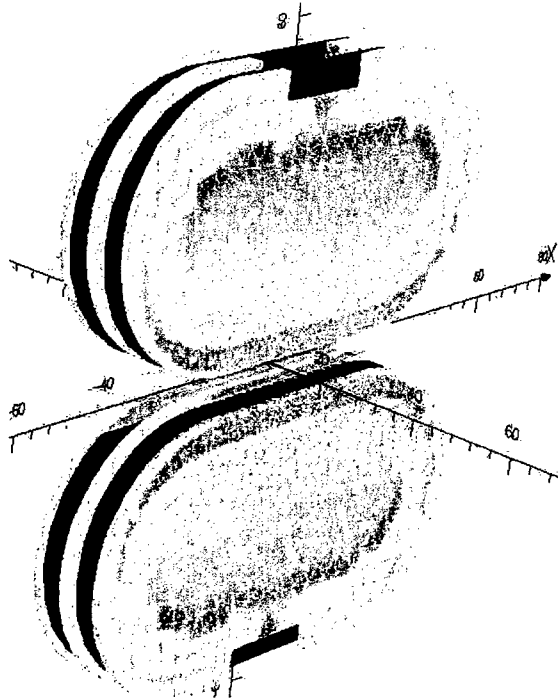
Figure 2: One 15-mm-period, 3-D model of the SCU was used for the magnetic field calculations. Two steel cores (*gray*) are positioned to form a central gap of 8 mm to accept the beam chamber. The core has grooves 4.3 x 4.0 (w x h) mm² for 20 turns of SC coil windings (*black*).
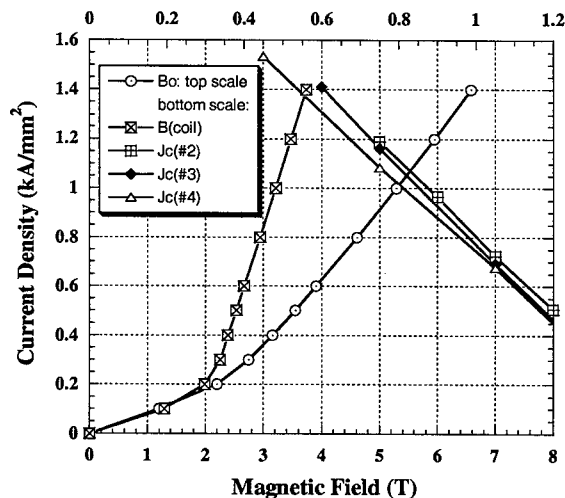
Figure 3: The vertical peak field B_0 (*top scale*) and the maximum field in the coil B(coil) (*bottom*) for a period of 15 mm and gap of 8 mm are plotted as a function of the average current density. The critical current densities under applied magnetic field (*bottom*) at 4.2K are plotted for three SC wires, Jc(#2): rectangular cross section (1.05 x 0.8) used for this work, Jc(#3): dia = 0.896 and Jc(#4): dia = 0.753; all in mm units.
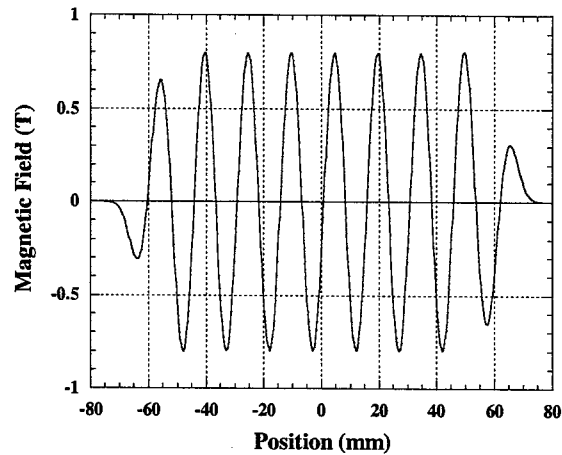
Figure 4: The vertical magnetic field was calculated at a current density of 1 kA/mm² along the beam trajectory in a short-section undulator. The end fields were adjusted by reducing the number of turns from the nominal 20 to 17, 10 and 3 turns for the three end coils.

of 3.2 T. This relative low ratio of the current density will however not guarantee that the coil will be cryogenically stable because of the high value of the current density and the low Cu/SC ratio. The required current with 20 turns of the wire will be 860 A.

Figure 4 shows the calculated vertical field along the beam axis of the SCU. The calculation has not yet been fine-tuned, but it demonstrates that the end fields may be adjusted by reducing the number of coil windings from the nominal 20 to 17, 10 and 3 turns for the three end coils. The end fields will also depend on the wire positions within the coil grooves. Small correction coils may be required at both ends to adjust for proper field integrals through the device. However, one way to avoid the correction coils may be to reduce the thickness of the end poles to match the permeability variation with the nominal poles.

Current Status

One core for a 12-period device was machined from "1006~1008 low-carbon" steel. The cross section of the core is approximately 76 mm x 40 mm. Figure 5, (*a*) and (*b*), shows the bottom and top sides of the core, respectively. The transverse width of the poles is approximately 50 mm, and the core has coil grooves with a cross section of 4.3 x 4.0 (w x h) mm². The choice of the groove dimensions make the pole thickness 3.2 mm. The flat bottom side of the core shows the coil grooves with windings for the first two periods. The top side has additional grooves for the transitions of the SC wire to the adjacent periods. The coil is designed to be first wound in one direction into every other groove for the full length. The alternate coil grooves are then similarly wound in the opposite direction.

(a)

(b)
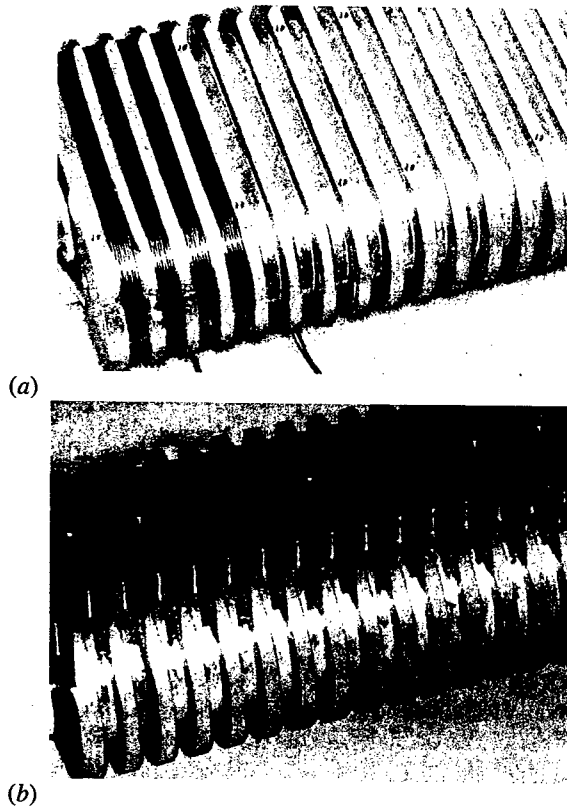
Figure 5: One core for the 12-period prototype was machined from "1006~1008 low-carbon" steel. The cross section of the core is approximately 76 mm x 40 mm. (a): Bottom flat side of the core shows coil grooves and windings for two periods. (b): Top side shows additional cross-over slots connecting every other coil groove for the SC wire transition to the next period after complete winding of the 20 turns in one groove.

DISCUSSION

The coil cross section for the present prototype was not designed to achieve the highest peak field B_o. Rather it was adjusted to use a readily available SC wire. Increasing the total current by increasing the coil cross section, but keeping the current density constant, at 1 kA/mm^2 for example, increases the peak field B_o by only a small fraction for the prototype SCU. Also, a reduced pole thickness will result in the field quality being more sensitive to wire position errors. And overall increasing the total current would also reduce the cryogenic stability

of the device. Thus, the chosen design is expected to be a good prototype for further studies.

One of the challenging requirements for the SCU is the high current density in the coil. This demands a low Cu/SC ratio and a high packing factor of the coil. Because of the high current density and the low Cu/SC ratio, the minimum quench propagation length is estimated to be less than 2 mm. Moreover, the minimum quench energy is not expected to be larger than 1 mJ. This is a typical value for SC dipoles used in high-energy accelerators. Commonly, this small amount of the energy can be released by small wire displacements in the coil during energizing. The first excitation of the coil will therefore be done by slowly cycling the current to higher values. Future studies will involve the stability of the coils and magnetic measurement of the field quality to identify the sources of the field errors.

The peak field is limited by the average critical current density for the selected SC wire (0.98 T at 1.4 kA/mm^2 under ideal conditions--no energy release due to the conductor displacements, no eddy current and hysteresis losses due to operating current ripples, and no direct heating of the coils by effects of the electron beams, etc.; see Fig. 3). Thus, to achieve a 1.0-T, 8-mm-gap SCU, one may need to cool below the lambda point for stable operations.

REFERENCES

[1] I. Ben-Zvi, et al., "Performance of a superconducting, high field subcentimeter undulator," Nucl. Instrum. Methods A318 (1992) 781.

[2] R. Rossmanith, et al., "Superconductive 14 mm period undulators for single pass accelerators (FELs) and storage rings," Proc. 8th EPAC, p. 2628 (2002).

A MAGNETIC FIELD MODEL FOR WIGGLERS AND UNDULATORS *

D. Sagan, J. A. Crittenden, D. Rubin, Cornell University, Ithaca, NY, USA
E. Forest, 1–1 Oho, Tskuba, Ibaraki, Japan

Abstract

Recent interest in applications of wiggler magnets in storage rings has motivated efforts to incorporate their effects in calculations of beam dynamics. This paper presents an analytic model of wiggler fields that can be used with symplectic integration to evaluate such effects. Coefficients needed by the model are generated by fitting to the results of a finite–element field calculation. The model has been used successfully in the CESR–c project, which imposes tolerances of a few parts in 10^4 on the modeling of 2-Tesla superconducting wigglers. In contrast to models based on Fourier transforms, the model presented here uses a relatively small number of terms, leading to correspondingly fast integration times. Fringe fields are included and no assumption about the periodicity of the field is made.

INTRODUCTION

A prerequisite for the study of particle dynamics is the ability to calculate transfer maps for each element in a storage ring. This is difficult for wigglers (wiggler here can mean either wiggler or undulator) since analytic formulas do not exist except in the most simplified cases. Wigglers can have strong nonlinear components[1, 2], which can be a major limitation on the dynamic aperture, and impose stringent conditions on any analytic approximations.

Symplectic integration is an excellent technique for doing tracking and for constructing transfer maps[3]. In order to do symplectic integration through a wiggler, however, one needs to know the field as well as the gradient and higher derivatives. This generally precludes simply using data from a measurement or a calculation since the discrete nature of the data will make the higher derivatives inaccurate. What is needed is a model functional form that fits the data and can be easily and quickly differentiated. Such a model is presented below. This model has the advantage that end fields are easily incorporated into the model.

FIELD MODEL

Planar symmetry is assumed and the model functional form for the magnetic field of a wiggler $\mathbf{B}_{\text{fit}}(x, y, s)$ is written as a sum of N terms

$$\mathbf{B}_{\text{fit}} = \sum_{n=1}^{N} \mathbf{B}_n(x, y, s; C_n, k_{xn}, k_{sn}, \phi_{sn}, f_n) . \quad (1)$$

Each term $\mathbf{B}_n$ is parameterized by 5 quantities C, k_x, k_s, ϕ_s, and f. The index $f_n = \{1, 2, \text{or } 3\}$ is used to designate

which of 3 forms a $\mathbf{B}_n$ term can take. The first form is

$$B_x = -C \frac{k_x}{k_y} \sin(k_x x) \sinh(k_y y) \cos(k_s s + \phi_s)$$
$$B_y = \quad C \quad \cos(k_x x) \cosh(k_y y) \cos(k_s s + \phi_s)$$
$$B_s = -C \frac{k_s}{k_y} \cos(k_x x) \sinh(k_y y) \sin(k_s s + \phi_s)$$
$$\text{with } k_y^2 = k_x^2 + k_s^2 . \quad (2)$$

The second form is

$$B_x = \quad C \frac{k_x}{k_y} \sinh(k_x x) \sinh(k_y y) \cos(k_s s + \phi_s)$$
$$B_y = \quad C \quad \cosh(k_x x) \cosh(k_y y) \cos(k_s s + \phi_s)$$
$$B_s = -C \frac{k_s}{k_y} \cosh(k_x x) \sinh(k_y y) \sin(k_s s + \phi_s)$$
$$\text{with } k_y^2 = k_s^2 - k_x^2 , \quad (3)$$

and the third form is

$$B_x = \quad C \frac{k_x}{k_y} \sinh(k_x x) \sin(k_y y) \cos(k_s s + \phi_s)$$
$$B_y = \quad C \quad \cosh(k_x x) \cos(k_y y) \cos(k_s s + \phi_s)$$
$$B_s = -C \frac{k_s}{k_y} \cosh(k_x x) \sin(k_y y) \sin(k_s s + \phi_s)$$
$$\text{with } k_y^2 = k_x^2 - k_s^2 . \quad (4)$$

k_y is considered to be a function of k_x and k_s and the relationship between them ensures that Maxwell's equations are satisfied.

Given a calculation or measurement of the field at a set of points $\mathbf{B}_{\text{data}}$, the problem is to find a set of N terms such that $\mathbf{B}_{\text{fit}}$ and $\mathbf{B}_{\text{data}}$ agree to some given precision set by how accurately one needs to be able to track through a wiggler. This is a standard problem in nonlinear optimization. The solution is to minimize a merit function M

$$M = \sum_{\text{data pts}} |\mathbf{B}_{\text{fit}} - \mathbf{B}_{\text{data}}|^2 + w_c \sum_{n=1}^{N} |C_n| . \quad (5)$$

The second term in M is to help preclude solutions with degenerate terms that tend to cancel one another. The weight w_c should be set just large enough to prevent this but not so large as to unduly distort the fit.

The minimization of M can be done by any number of well known algorithms[4, 5]. The fitting process is simplified since the three forms can be combined into one continuous function via

$$\mathbf{B}_n = \begin{cases} \text{Form \#1} & 0 < k_{xn} \\ \text{Form \#2} & -|k_{sn}| \leq k_{xn} \leq 0 \\ \text{Form \#3} & k_{xn} < -|k_{sn}| \end{cases} \quad (6)$$
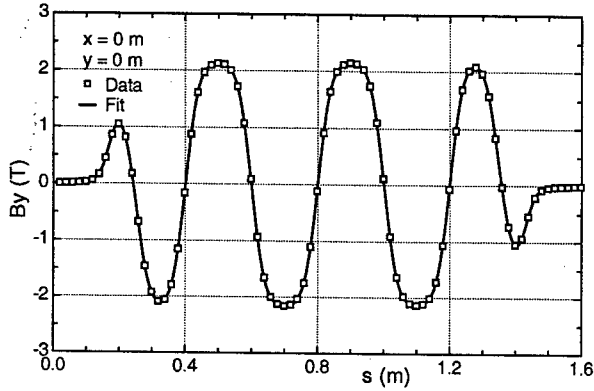
Figure 1: B_y as a function of s at $x = y = 0$. The data points are from a finite element modeling program. The curve is calculated from an 82 term fit.

Figure 2: B_y as a function of x at $y = 0$ and $s = 0.9$m. The data points are from a finite element modeling program. The curve is calculated from an 82 term fit.

Once B_{fit} is calculated, symplectic integration is performed using the Hamiltonian $H(x, p_x, y, p_y, z, \delta; s)$ in the paraxial approximation

$$H = \frac{(p_x - a_x)^2}{2(1 + \delta)} + \frac{(p_y - a_y)^2}{2(1 + \delta)} - a_s, \qquad (7)$$

where $p_{x,y} = P_{x,y}/P_0$ is the normalized transverse momentum, $\delta = \Delta E/P_0 c$ is the relative energy deviation, z is the longitudinal position relative to the reference particle, and $a(x, y, s) = qA/P_0 c$ is the normalized vector potential. To save on computational speed, the gauge with $a_x = 0$ is used in the calculations. With this choice of gauge, formulas for $a(x, y, s)$ from Eqs. (2), (3), and (4) are readily derived.

The symplectic integration procedure is given by Wu et al.[6] with the modification that Wu's prescription uses the $a_s = 0$ gauge. This procedure has been integrated into the PTC (Polymorphic Tracking Code) subroutine library of Étienne Forest[7] which in turn has been integrated into the Cornell BMAD particle simulation software library[8].

A 2nd order symplectic integrator[3] is used for the calculations. 4th order and 6th order integrators were also tried but, it was found, that after adjusting the number of integration steps to achieve a given accuracy, the 2nd order integrator was fastest. This is not surprising given the large higher-order nonlinearities inherent in a wiggler field.

CESR–C WIGGLER

The wiggler magnets being installed in the Cornell CESR–c storage ring[9] have been modeled using the above procedure. Using the finite element modeling program OPERA–3D, a table of field versus position was generated. The validity of the field calculations was experimentally confirmed by measurements of tune as a function of beam position in a wiggler[10]. The spacing between points in the table was 4 mm horizontally, 2 mm vertically, and 2 mm longitudinally. The extent of the table was ±48 mm horizontally, ±26 mm vertically and 1.6 m longitudinally. Table data and fit curves of B_y as a function of s
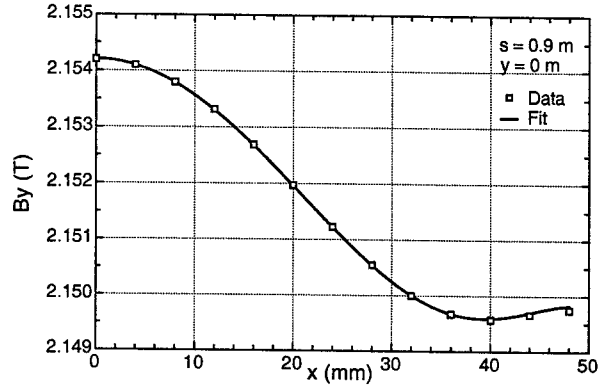
and x for the CESR–c 8–pole wiggler are shown in Figs. 1 and 2. 82 terms were used for the fit. The peak field is about 2 T and the RMS of the difference $|\mathbf{B}_{\text{data}} - \mathbf{B}_{\text{fit}}|$ was 9 G which gives an RMS to peak field ratio of 0.05%. The gradual roll-off of B_y as a function of x shows the advantage of allowing the k_{xn} to vary continuously instead of using a Fourier series. With a Fourier series the k_{xn} would be quantized which would necessitate the use of more terms in the fit and slow any symplectic integration.

Figs. 3 and 4 show tracking simulation results for the the CESR–c 8–pole wiggler. Fig. 3 shows p_x at the end of the wiggler as a function of x at the start with a starting condition of $y = 20$ mm. Fig. 4a shows p_y at the end as a function of y at the start with x_{start} set at 30 mm. The solid lines in Figs. 3 and 4a are the results of using a Runge–Kutta (RK) integrator with adaptive step size control[4] and with the field values obtained from interpolating the table from OPERA–3D. The dashed lines are from symplectic integration (SI) using the fitted field and 250 integration steps. The dash–dotted lines are from a 7th order Taylor map (TM) which is generated using symplectic integration with 250 integration steps.

RK tracking, since it is derived directly from the equations of motion and the magnetic field table, is the gold standard with which to compare other tracking results. Fig. 4b shows the difference between the SI and RK tracking as well as the difference between the TM and RK tracking. Additionally, for comparison, a line is shown whose slope represents a tune shift of $\Delta Q = 0.001$ assuming a β of 10 m. The SI tracking agrees well with the RK, better than 4 μrad in Fig. 3 and 8 μrad in Fig. 4. Slope differences of the curves are also small, representing tune shifts of less than 0.001 (at $\beta = 10$ m) everywhere in the figures. The advantage of the SI tracking is that it preserves the Poincaré invariants, such as phase space density, while the RK does not. This is an important consideration in long term tracking where RK can give unphysical results.

The TM also show excellent agreement with the RK tracking except in Fig. 3 when the magnitude of x is larger
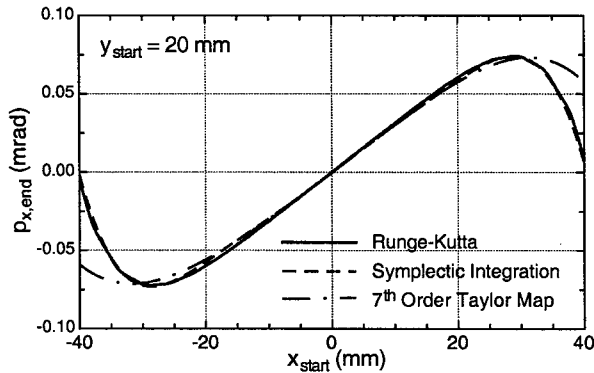
Figure 3: p_x at the end of the wiggler as a function of x at the start using three different tracking methods. At the start $p_x = p_y = \delta = 0$ and $y = 20\,\text{mm}$.

than 30 mm or so. In the domain where the TM agrees with the RK, the TM can be used for such purposes as lattice design and other analyses that are not sensitive to non-symplectic errors. The advantage of the TM is that it is fast. In the present instance the TM was over a factor of 30 faster than the other two methods. (This does not include the time to calculate the TM to begin with, but that only has to be done once). To overcome the non–symplecticity of the TM it can be partially inverted to form a symplectic generating function[3]. Preliminary investigations comparing the long term tracking results from SI and from a generating function show good agreement.

CONCLUSION

The wiggler model presented here is useful because it can accurately model a wiggler including end fields. This leads to efficient symplectic mapping which is needed in long term tracking, and avoids the non-physical violation of conserved quantities inherent when tracking is dependent upon interpolation of a field table. For applications where symplecticity is not a concern, a Taylor map, generated using the fit with symplectic integration can greatly reduce computation time.

For long periodic wigglers, the number of terms needed to fit the field may become large. In this case, a simple solution would be to divide the wiggler into 3 sections: the periodic center section and two end sections. Each section can be fitted separately. Since the center section is periodic, the number of terms needed to fit it is independent of its length. For the end sections it might be possible to cut down on the number of fit terms by making use of three additional forms that have an exponential s–dependence. These forms can be derived from Eqs. (2), (3), and (4) using the substitution $k_s \rightarrow -\,k_s$.

If pole misalignments need to be simulated, then planar symmetry cannot be assumed. In this case, Eqs. (2), (3), and (4) can be modified, at some small increase in complexity, by using $k_x x + \phi_x$ in place of $k_x x$, and $k_y y + \phi_y$ in place of $k_y y$. With this, any arbitrary magnetic field profile
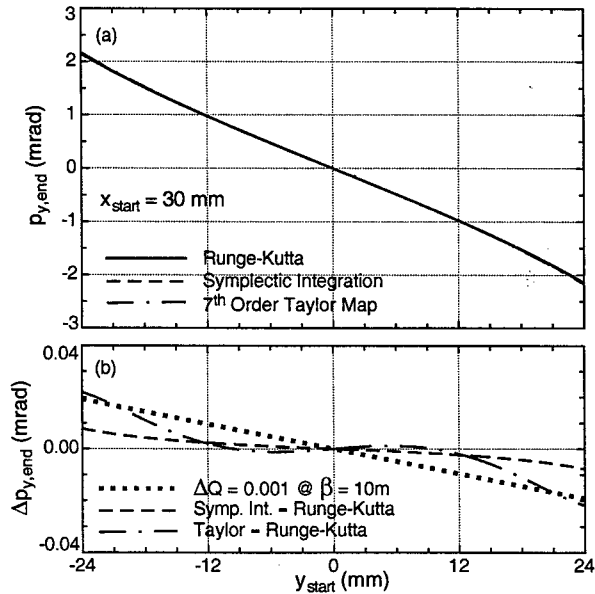
Figure 4: a) p_y at the end of the wiggler as a function of y at the start using three different tracking methods. At the start $p_x = p_y = \delta = 0$ and $x = 30\,\text{mm}$. b) Difference between RK tracking and the two other methods. Also shown is a line that represents a tune shift of $\Delta Q = 0.001$.

can be modeled.

REFERENCES

[1] P. Kuske, R. Görgen, and J. Kuszynski, "Investigation of Non–Linear Beam Dynamics with Apple II–Type Undulators at Bessy II," Proc. 2001 Part. Acc. Conf., pg. 1656 (2001).

[2] C. Milardi, D. Alesini, G. Benedetti, et al., "Effects of Non-linear Terms in the Wiggler Magnets at DAΦNE," Proc. 2001 Part. Acc. Conf., pg. 1720 (2001).

[3] E. Forest, *Beam Dynamics: A New Attitude and Framework*, Harwood Academic Publishers, Amsterdam (1998).

[4] W. Press, B. Flannery, S. Teukolsky, and W. Wetterling, *Numerical Recipes in Fortran, the Art of Scientific Computing*, Second Edition, Cambridge University Press, New York, 1992.

[5] F. James, *MINUIT, Function Minimization and Error Analysis*, CERN program library writeup D506

[6] Y. Wu, E. Forest, D. S. Robin, H. Nishimura, A. Wolski, and V. N. Litvinenko, "Symplectic Models for General Insertion Devices," Proc. 2001 Part. Acc. Conf., pg. 398 (2001).

[7] See: <http://bc1.lbl.gov/CBP_pages/educational/ TPSA_DA/Introduction.html>.

[8] D. Sagan, and D. Rubin, "CESR Lattice Design," Proc. 2001 Part. Acc. Conf., pg. 3517 (2001)

[9] J.A. Crittenden, A. Mikhailichenko, and A. Temnykh, "Design Considerations for the CESR-c Wiggler Magnets," these proceedings.

[10] A. Temnykh, J. A. Crittenden, D. Rice and D. Rubin, "Beam-based Characterization of a New 7-Pole Superconducting Wiggler at CESR," these proceedings.

VIBRATING WIRE AND FLIPPING COIL MAGNETIC MEASUREMENT OF A CESR-C 7-POLE WIGGLER MAGNET *

A. Temnykh [†]

Laboratory of Nuclear Studies

Cornell University, Ithaca NY 14953, USA

Abstract

To increase radiation damping at $1.8 GeV$ beam energy 12 super-conducting wiggler magnets will be installed in the Cornell Electron Storage Ring (CESR). The first 7-pole wiggler has been manufactured, tested and installed in the ring.

This paper describes the wiggler magnetic measurement using flipping coil and vibrating wire techniques. The field integrals along *straight* lines were measured with flipping coil, vibrating wire technique was used to measure both, straight line field integrals and field integrals along *wiggling* lines reproducing beam trajectories.

INTRODUCTION

Magnets with alternating magnetic fields (wigglers and undulators) are used in storage rings to increase radiation damping or as synchrotron radiation sources. Although radiation damping improves the beam stability, nonlinear beam dynamics effects caused by the wiggler's magnetic field may significantly compromise machine performance. Thus, the measurement of the magnetic field characteristics of wigglers and undulators is a subject of a great importance.

The methods traditionally used for wiggler magnetic measurements such as field integrating with long flipping coil, field mapping with a Hall probe or with a small searching coil provide information about field integrals along *straight* lines. However, because beam trajectory is *wiggling*, the particles passing the wiggler see a quite different field. So, it is particularly important to measure field integrals along lines representing the *wiggling* beam trajectory.

In the described magnetic measurement of a CESR-c 7-pole wiggler flipping coil [1] and a modified vibrating wire [2],[3] techniques were used. The latter was employed to measure magnetic field integrals along lines representing wiggling beam trajectory.

The vibrating wire technique uses a section of wire stretched through the testing region as a magnetic field probe. Lorentz forces between DC current flowing through the wire and the wiggler magnetic field cause the wire wiggling resembling the beam trajectory. Applying AC current with frequencies matching vibrating mode resonances and measuring amplitude and phase of the excited standing waves, one can obtain magnetic field characteristics along
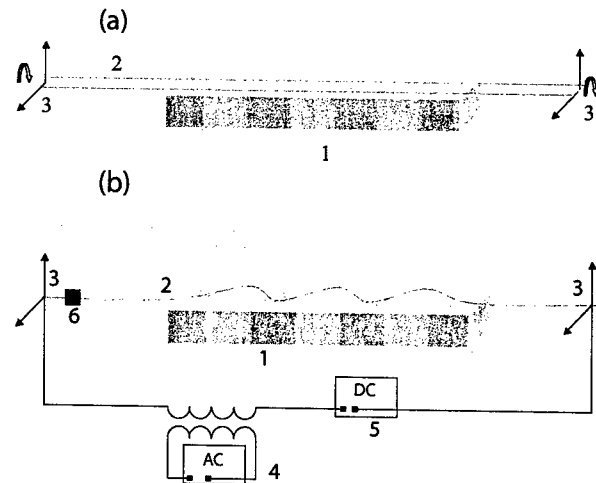
Figure 1: Schematic view of long flipping coil (a) and vibrating wire (b) measurement setup. Shown are: 1 - bottom halfe of tested 7-pole wiggler; 3 - stages for horizontal and vertical positioning of the coil or vibrating wire ends . On plot (a): 2 - 3/8in wide, 3m long coil consisting of 3 turns of $0.15mm$ copper wire. On plot (b): 2 - 4.648m section of $0.15mm$ copper wire; 4 - AC current generator; 5 - DC current power supply; 6 - horizontal and vertical wire motion sensors.

the wire, i.e., along the path reproducing the beam trajectory.

The paper describes the wiggler magnetic field measurement with flipping coil technique as well as with straight and "wiggling" vibrating wire and compares the results with model calculation. The "wiggling" vibrating wire measurement reveals all effects associated with the beam trajectory wiggling.

SETUP

A description of the tested 7-pole CESR-c wiggler is given in reference [4]. The measurements were done at several wiggler magnetic field levels between 1.7T and 2.1T.

The flipping coil measurement setup is schematically shown in Figure 1a. A 3/8in wide, $\sim$ 3m long coil consisted of three turns of 0.15mm copper wire stretched through the wiggler. The coil ends were mounted on rotating stages providing the coil flipping. These stages, in turn, were mounted on moving stages for precise positioning in horizontal and vertical plane. The voltage induced in the

coil was measured by digital integrating multi-meter "HP 3465".

The vibrating wire setup is depicted in Figure 1b. It consisted of $4.648m$ section of 0.15mm copper wire stretched through the wiggler with ends mounted on 2D movable stage assemblies. For wire motion sensing two "Π" shaped opto-electronic LED-phototransistor assemblies H21A1 (Newark Electronics) were used. DC current power supply with $1A$ of maximum current was connected to the wire ends in series with a transformer. An AC current component in wire was excited by wave form generator "HP33120A" connected to the other transformer's input. A DAQCard-6024E and program based on "Lab-View" software provided all needed control and signal analysis.

FLIPPING COIL MEASUREMENT

Results of vertical and horizontal magnetic fields integral measurements as a function of horizontal coil position, $I_{y,x}(x)$, for various field levels are presented in Figure 2 and Table1. The vertical field integral reveals a large quadratic component (normal sextupole) which depends on the wiggler field level. This dependence can be explained by well known specifics of symmetric (odd number of poles) magnetic structure. In this design, the central pole is compensated by two opposite polarity end poles. But because the magnetic field environment is different in the middle and at the ends, the compensation can be done only in a very limited range of field. The asymmetric structure with even number of poles is free of this problem. The horizontal field integral, Figure 2b, has skew quadrupole component significant for beam dynamics. It is practically constant for all fields. The origin of this component is nor clear.

a_n, b_n	Wiggler field		
$\frac{Gm}{cm^n}$	$1.7T$	$1.9T$	$2.1T$
a_1	1.02	1.37	1.53
b_1	−0.24	−0.21	−0.19
b_2	0.18	−0.02	−0.28
b_3	0.007	0.007	0.004

Table 1: Shown are coefficients of polynomial the fit: $I_{y,x}(x) = \sum(b_n, a_n) \cdot x^n$.

VIBRATING WIRE MEASUREMENT

Theory

From formulas in [2] one can find that for the setup shown in Figure 1 the fundamental standing wave amplitude in horizontal and vertical plane, $A^1_{x,y}$, excited by AC current flowing through the wire with fundamental resonance frequency will be:

$$A^1_{x,y} \propto I_0 \int_{-l_w/2}^{l_w/2} B_{y,x}(z)cos(\pi z/L)dz \qquad (1)$$
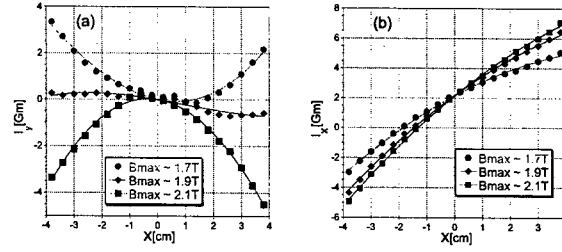
Figure 2: Vertical (a) and horizontal (b) field integrals measured with flipping coil as function of horizontal coil position.

Here I_0 is the AC current amplitude, indices x, y indicate the horizontal and vertical planes, l_w and L are for wiggler and wire lengths. If $L \gg l_w$, variation of $cos(\pi z/L)$ can be neglected and expression (1) can be rewritten as:

$$A^1_{x,y} \propto I_0 \int_{-l_w/2}^{l_w/2} B_{y,x}(z)dz = I_0 \cdot I_{y,x} \qquad (2)$$

i.e., the standing wave amplitude is proportional to magnetic field integral multiplied by the driving AC current. Thus, the field integral can be obtained by measuring standing wave amplitude normalized by driving current, the integral sign can be determined from phase between driving AC current and the wire motion. For zero DC current (straight wire) it will be straight line integral similar to a flipping coil measurement, for non-zero DC current it will be an integral along the path imitating a beam trajectory.

"Straight" wire measurement ($I_{dc} = 0$)

The "straight" wire, $I_{dc} = 0$, measurement results at $2.1T$ wiggler field are given in Figure 3 in comparison with the flipping coil measurements. Shown are fundamental horizontal and vertical standing wave amplitudes (solid marks, left scale) with a sign given by the phase between driving current and the wire motion measured as a function of horizontal wire position. Flipping coil measurements (right scale) are indicated by open marks. There is a good agreement between these two data sets. Left and right scales comparison suggests that $1r.u.$ in vibrating wire measurements corresponds to $\sim 7.7Gm$ of field integral.

"Wiggling" wire measurement

The Lorentz forces between DC current flowing through the wire and wiggler magnetic field cause the wire wiggling which reproduces the beam trajectory. Optical measurement indicated that at $2.1T$ wiggler field, $0.5A$ of DC current flowing through the wire resulted in $\sim 3.7mm$ peak-to-peak wire wiggling which is similar to the beam trajectory wiggling at $1.8GeV$ beam energy.

Figure 4 presents the vertical field integral as a function of horizontal position measured with the "wiggling" wire in comparison with a) straight wire measurement and b)
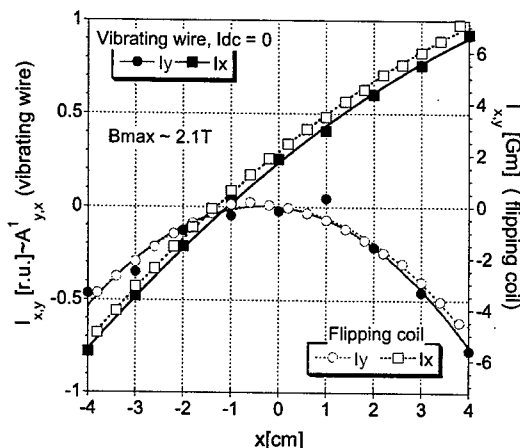
Figure 3: Vertical and horizontal field integrals measured with a straight vibrating wire, $Idc = 0$, as a function of horizontal position (left scale) in comparison with flipping coil measurement (right scale) at 2.1T wiggler field.
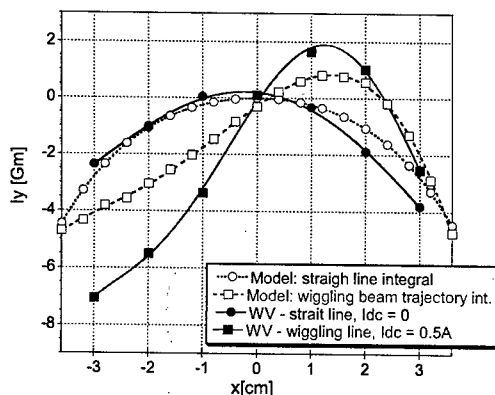
Figure 4: Vertical field integral as a function of horizontal position measured with a straight, $I_{dc} = 0$, and wiggling, $I_{dc} = 0.5A$, wire. Model calculation is indicated by open marks.

with the "wiggling" and straight field integrals calculated from the model. For the wire measurement the calibration obtained in the previous experiment was used. One can see that the measured effect of the path wiggling analogous to that calculated from the model, but has a bigger amplitude. This inconsistency could be due either to factors missing in the model or because of inaccuracy of the vibrating wire measurement calibration. Note that the variation between the straight and wiggling line vertical field integrals is mostly due to vertical field non-uniformity across the wiggler poles [5].

The beam vertical focusing effect in wigglers is another result of the trajectory wiggling. This effect can be seen from horizontal field integral measured with wiggling wire as a function of the wire vertical position, see Figure 5. While the straight wire data, $I_{dc} = 0$, indi-
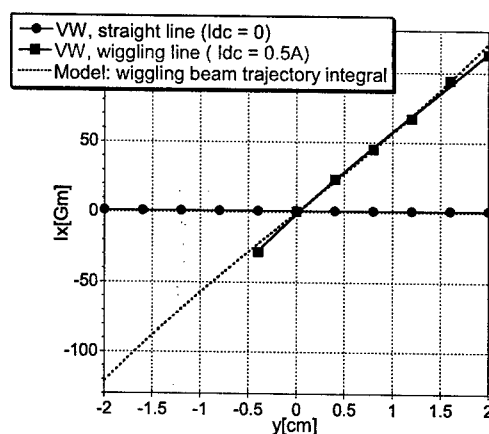
Figure 5: Horizontal field integral as a function of vertical position measured with a straight, $I_{dc} = 0$, and wiggling $I_{dc} = 0.5A$, wire. Dashed line shows a model calculation.

cated zero horizontal field integral for all y, integral measured with a wiggling wire, $I_{dc} = 0.5A$, has linear dependence $dI_x/dy(measured) \sim 62.3Gm/cm$ which is consisted with the model calculation $dI_x/dy(model) \sim 60.3Gm/cm$.

CONCLUSION

Two complementary magnetic measurement techniques were employed for CESRc super-conducting wiggler magnetic measurement. A long flipping coil technique was used to measure vertical and horizontal field integrals along straight lines, the relatively new vibrating wire technique was applied for field integral measurements along a path representing wiggling beam trajectory. The latter revealed all effects caused by the beam trajectory wiggling predicted by model.

ACKNOWLEDGEMENTS

I would like to thank James Crittenden for providing a model calculation and help in the paper preparation.

REFERENCES

[1] This measurement technique was first developed by the ID group at ESRF. See *Developpment de Banc de measures magnetiques pour undulateurs et wigglers*, D. Frachon Thesis, April 1992.

[2] A. Temnykh, *Vibrating wire field-measuring technique*, Nuc. Inst., A 399 (1997) 185-194

[3] A. Temnykh, *Some Aspects of the Use of Vibrating Wire Technique for a Wiggler Magnetic Field Measurement*, CBN 01-17, Cornell 2001.

[4] J.A. Crittenden at al., *Design Considerations for the CESRc Wiggler Magnets*, to be published in PAC2003 proceedings.

[5] J. Safranek et al., *Nonlinear Dynamics in SPEAR Wigglers*, EPAC' 2000, p.295

STATUS OF THE DIAMOND INSERTION DEVICES

J. A. Clarke, N. Bliss, D. G. Clarke, F. E. Hannon, C. Hill, A. A. Muir and D. J. Scott, Daresbury Laboratory, Warrington, UK.

V. Francis, Rutherford Appleton Laboratory, Didcot, UK.

Abstract

Seven insertion devices must be provided for the first DIAMOND beamlines on Day 1 of operations. A variety of devices have been selected, including four short period in-vacuum undulators, one 5m conventional planar undulator, one 5m helical undulator and a 3.5T superconducting wiggler. Construction of several of these devices will soon commence. This paper will detail the magnetic solutions that have been adopted and also the mechanical designs, highlighting the key features that have been included.

INTRODUCTION

The DIAMOND Light Source is now in the construction phase of the project with significant progress being made over all of the major areas [1]. Funding for the first phase of the project makes provision for seven operational insertion device based beamlines. The selection of the insertion devices for these beamlines occurred approximately 12 months ago [2] and since then the designs have been developed so that now we are about to procure the first major items for these IDs. Table 1 summarises the main parameters for the first DIAMOND IDs. Note that the K value quoted for the helical undulator is for the circular polarization mode.

Table 1. Summary of the parameters for the first DIAMOND IDs.

Name	Period (mm)	K_{Max}	Length (m)
MPW60	60	19.6	1.0
U33	33	1.63	4.9
U23 IVa	23	1.49	2.0
U23 IVb	23	1.49	2.0
U21 IV	21	1.24	2.0
U27 IV	27	2.02	2.0
HU64	64	3.44	2 x 2.2

IN-VACUUM UNDULATORS

Since DIAMOND will make use of a significant number of in-vacuum undulators, with four initially but probably more than ten when the ring is fully populated, it was decided to design and build these in-house. This then ensures there is a common design philosophy and in-house expertise available to maintain the magnets during the operational phase of the project. Although four undulators are required before operations begins it was further decided to build a single device first to ratify the

design and assembly process and then to build the other three approximately 15 months later.

Mechanical Design

The mechanical design of the in-vacuum undulators is very closely based upon the ESRF design [3] although some fundamental changes have also been made. In particular, the ability to taper the magnet arrays has been added and also the rf finger taper sections at each end of the device will be water cooled. The array tapering system is based upon the rotation of offset cams at one end of the magnet array support beam (outside of the vacuum) with a pivot at the other end.

The nominal minimum beam stay clear in the central 2m of the 5m ID straights is set by lifetime considerations to be 7mm. This value has been used to design the in-vacuum undulators to meet the needs of the users. However, mechanically the magnets are designed to reach an absolute minimum gap of 4mm so that if smaller gaps can be tolerated by the machine the users will be able to benefit. The maximum magnet gap has been selected to be 30mm.

There are already serious proposals for a second undulator to be installed in the same straight as an in-vacuum undulator to serve a side station (see Figure 1). Although the in-vacuum undulator magnet blocks fill a length of ~2.0m it is physically ~2.6m because of the room needed for the rf tapers, bellows, flanges etc. Allowing some space for steering magnets to apply an angular offset (1mrad) between the radiation from the two undulators leaves a length of ~0.8m for a second (out of vacuum) undulator. It is planned to install the corrector magnets and the in-vacuum undulator with a horizontal angular offset from Day 1 to enable easier introduction of the second undulator in the future.
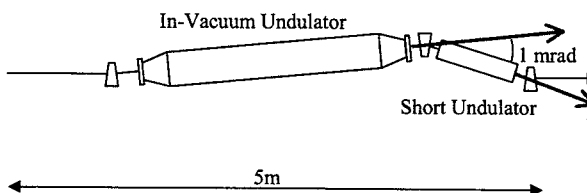
Figure 1. Sketch of proposed layout of DIAMOND straight.

Magnet Design

The choice of magnet material for in-vacuum undulators is an interesting issue [4]. Since the magnets have to be baked to ~140 °C irreversible losses will occur with NdFeB magnets but not with SmCo magnets. Despite these magnetization losses the NdFeB magnets

will still give a larger on axis field than the intrinsically weaker SmCo. Also, since the in-vacuum undulators are often the limiting vertical aperture in a storage ring they can experience high radiation doses. There is evidence that NdFeB magnets are more susceptible to radiation damage than SmCo [5, 6] and also that the Sm_2Co_{17} grade is more resistant than $SmCo_5$. For the reasons outlined above we decided to base our magnet designs on Sm_2Co_{17} with an assumed remanent field of 1.03 T.

The magnet design is a conventional symmetric pure permanent magnet four block per period structure with block height and width of 16 and 41mm respectively. The end design is shown schematically in figure 2. The length of the last block has been optimised to minimise the 1st field integral over the full range of operating gaps. Figure 3 shows how the integral varies for different block lengths. The chosen length of 2.7mm gives a theoretical maximum integral without block errors of less than $0.5\mu Tm$ which corresponds to an angular deviation of $0.05\mu rad$ for the 3GeV electron beam.
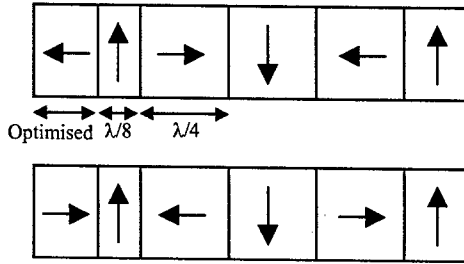
Figure 2. End structure adopted for the in-vacuum undulator.
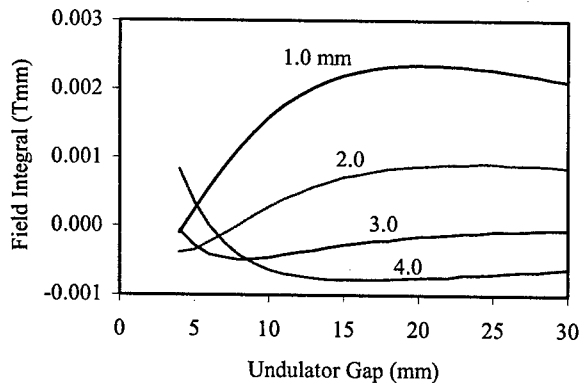
Figure 3. First field integral as a function of undulator gap for different end block lengths.

HELICAL UNDULATOR

For the same reasons outlined for the in-vacuum undulator it was decided to design and build the out of vacuum permanent magnet undulators in-house as well. A common support structure philosophy was also adopted whereby all out of vacuum undulators will use the same structure design as far as possible. It is relatively easy to alter the length of the support structures for different length modules as necessary.

It was also decided that the helical undulator, which was originally planned to be 5m long built of two modules, should actually be two separate modules acting independently with an electromagnetic phasing unit placed in-between. This gives more flexibility to the beamline operation in the use of the polarization as well as easing the need for a complex interlock system to prevent one module striking another. Overall, a few periods have to be sacrificed to make space for the phasing unit but the loss in flux is not critical.

Also, the ability to taper the magnet beams has been included in the support structure design by implementing a four motor system (two per beam) for the gap changing mechanism.

The helical design adopted is the APPLE-2 configuration [7] which requires a longitudinal phasing movement of one magnet array on each support beam. However, it is possible that future designs might adopt a three array per beam system and so the phase change mechanism has been designed to cope with this. The forces generated by the undulator can be very large, particularly in the axial direction when the diagonally opposite arrays are moved in opposite directions to generate arbitrary inclination linear polarization. The phase change mechanism is designed to cope with forces up to 40kN. The forces on each array were calculated as a function of the magnet block size (Figure 4). A block size of 40 x 40 x 16mm was chosen as a compromise between magnet field strength and quality and the forces generated. A view of the HU64 mechanical support structure is given in Figure 5.
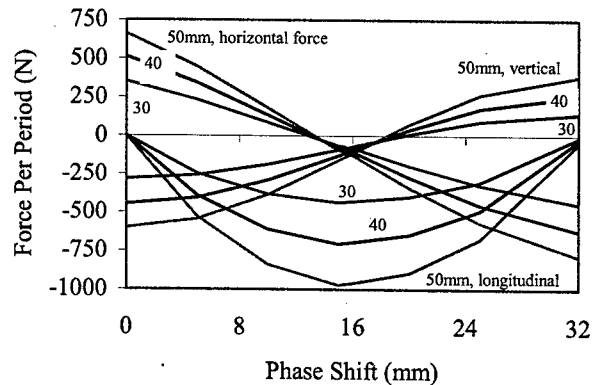
Figure 4. Force per period on the HU64 undulator operating in the arbitrary linear polarization mode at a 15mm gap as a function of transverse dimension for square magnet blocks.
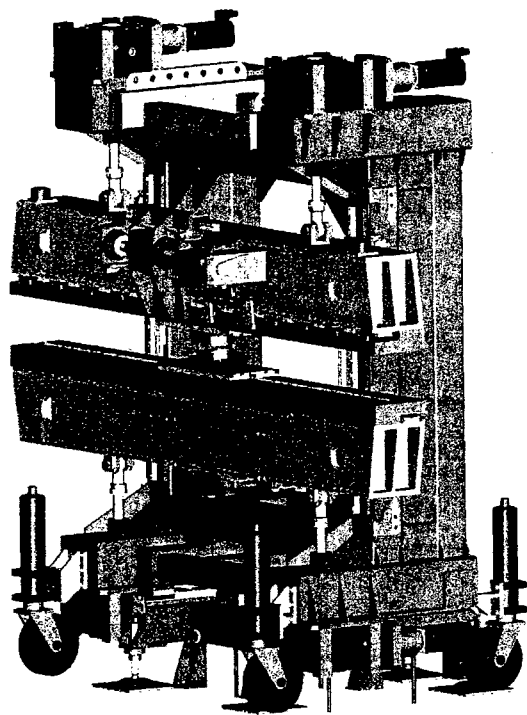
Figure 5. View of the helical undulator support structure. Only a few magnet blocks are shown mounted on the beams.

PLANAR UNDULATOR

Mechanically the 4.9m long planar U33 will be very similar to the helical undulator described above, though without the phase changing mechanism of course. It will consist of two modules mounted very closely together to form one continuous undulator. The exact space between the magnets at this junction has yet to be selected.

Magnetically it is a relatively straightforward pure permanent magnet planar undulator with four blocks per period. The end structure is expected to be similar to that described for the in-vacuum undulator.

SUPERCONDUCTING MULTIPOLE WIGGLER

The superconducting multipole wiggler is the only Day 1 device that will not be built in-house. Instead a specification will be written for a turn key system that is expected to include the magnet with cryogenics, power supplies, control system etc.

As yet the exact requirements for this magnet have not been agreed with the beamline users. This is because a 3.5T MPW can produce a considerable amount of power (~21kW/m in DIAMOND) and the beamline designers have to be satisfied that such high power levels can be coped with. The magnet length is likely to be set between 1 and 2m.

REFERENCES

[1] R.P. Walker, "Progress with the DIAMOND Light Source Project", these proceedings.

[2] J.A. Clarke, F.E. Hannon and D.J. Scott, "The Initial Insertion Devices for the DIAMOND Light Source", EPAC 2002, p2607.

[3] J. Chavanne, C. Penel and P. Van Vaerenbergh, "Construction of APPLE II and In Vacuum Undulators at ESRF", PAC 2001, p2459.

[4] J. Chavanne et al, "Magnetic Design Considerations for In-Vacuum Undulators at ESRF", EPAC 2002, p2604.

[5] Y. Ito et al, "Magnetic Flux Loss in Rare-Earth Magnets Irradiated with 200 MeV Protons", NIM B 183 (2001) p323.

[6] T. Ikeda and S. Okuda, "Magnetic Flux Loss of the Permanent Magnets used for the Wigglers of FELs by the Irradiation with High-Energy Electrons or X-Rays", NIM A 407 (1998) p439.

[7] S. Sasaki, "Analyses for a Planar Variably Polarizing Undulator", NIM A 347 (1994) p83.

DESIGN AND EVALUATION OF A SHORT PERIOD Nb₃Sn SUPERCONDUCTING UNDULATOR PROTOTYPE*

S. Prestemon, D. R. Dietderich, S. A. Gourlay, P. Heimann, S. Marks, G. L. Sabbi, R. M. Scanlan, R. Schlueter, Lawrence Berkeley National Laboratory, Berkeley, CA, 94720, USA
B. Wang, B. Wahrer, Wang NMR, Livermore, CA, 94550, USA

Abstract

The design of a class of short period superconducting undulators is presented. We begin with a parameter-based analysis that provides insight into potential device performance as a function of the properties of superconducting materials. We present data on candidate low-temperature superconducting materials and the motivation to consider low-copper fraction, high Jc materials. Measured data on recent Nb₃Sn conductors is provided, together with wire and cable design issues that are tailored for undulator applications. Key design concerns are then addressed, in particular the quench protection system limitations and the system performance. Progress on the construction and testing of a prototype 30mm period device is described.

INTRODUCTION

The development of short-period superconducting undulators (SCU's) is critical to extend the capabilities of existing synchrotron rings and to leverage their future upgrades, and is a key component of a number of future synchrotron radiation sources, such as the proposed LUX at LBNL [1]. For a fixed period, increasing the field compared to conventional devices results in an extended photon energy range (on the higher end) and improved harmonic overlap.

Due to the important role of superconducting undulators in plans for existing and future light sources, an R&D effort has been initiated at LBNL to investigate the potential performance characteristics for a class of such devices, and to evaluate the performance of a Nb₃Sn-based design by constructing and testing a prototype.

We begin by presenting computed optimal designs and attainable fields as a function of conductor performance and coilpack parameters.

A review of the design of a Nb₃Sn 6-period prototype that is being constructed jointly by LBNL and Wang NMR and tested at LBNL is then provided. The motivation to use low Cu:SC ratio material is presented, together with a discussion of options for superconductors, in particular Nb₃Sn strands and cable designs. A winding method is described that is flexible with respect to period size and conductor geometry. The impact of choosing a low Cu:SC ratio conductor on the quench protection is discussed, along with a passive protection design.
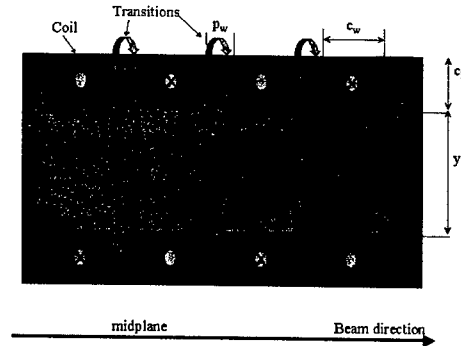
Figure 1 Superconducting undulator upper-halfplane.

Table 1 Parameters and variables used for undulator design optimization.

λ	Undulator period
h	Magnetic half gap (gap = $2h$)
p_w	Pole width (beam direction)
c_w	Coil width (beam direction)
c_h	Coil thickness
y_h	Yoke thickness
r_{pc}	$= p_w / c_w$
J_{av}	Engineering, or overall, current density
J_{sc}	Superconductor current density
J_{cu}	Copper current density (e.g. during a quench)
B_0	Peak field on the axis
B_{max}	Peak field on the conductor
K	$= eB \dfrac{\lambda}{2\pi mc} = 0.934\lambda[cm]B[T]$

OPTIMAL DESIGNS

We consider planar undulators with soft iron poles and yoke, as shown in Figure 1. A list of parameters and variables is provided for reference in Table 1.

For design optimization, we consider a design variable set $\{h, \lambda\}$ and the design parameters $\{r_{pc}, c_h, y_h\}$. For a given average current density J_{av} the figure of merit $f_m = B_{max} / B_0$ can be minimized with respect to the design parameters. An "optimal load line" $B_0(J_{av})$ for each design variable set, i.e. magnetic gap and period, can then be determined.

Peak performance for an actual device is derived from J_c data and the superconductor cross section, which is used to relate J_{av} to J_{sc}. The peak attainable field is defined by the intersection of the "optimal load lines" with the J_c curve, i.e. when $J_{sc} = J_c(B_{max})$.

Data for "optimal load lines" has been calculated for design variables in the range $15 < \lambda[\text{mm}] < 30$ and $4 < gap[\text{mm}] < 16$, using a parametric 2D TOSCA script. As an example, performance curves obtained for a Nb$_3$Sn superconductor with $J_c(5T, 4.2K) = 8060$ A/mm^2 and with a $J_{av}/J_{sc} = 0.27$ (aggressive performance yet realistic, i.e. manufacturable – see parameters for the prototype in Table 2) are provided in Figure 2.

The optimization methodology outlined above is applicable to all types of superconductor. A thorough comparison of the theoretical performance of SCU's using different superconductors is beyond the scope of this paper, as it involves detailed comparison of stability and protection characteristics associated with the choice of the Cu:SC ratio, analysis of the attainable insulation thickness and packing factor in each case, and an understanding of the cryogenic operating conditions and cooling method.

UNDULATOR PROTOTYPE

A 6-period prototype Nb$_3$Sn undulator is currently being fabricated that will test key design issues that arise when operating in the type of regime discussed above (see table 2). Issues that are being addressed include selection of a suitable state-of-the-art conductor, determining a coil winding method that is applicable for a variety of undulator designs and conductor geometries, and quench protection for designs with extremely high Cu current densities (~ 6000 A/mm^2). Increasing the allowable copper current density will allow for the full benefits of advanced superconductors to be realized (see figure 3).

Superconductor selection

Superconductors for SCU's must support very high current densities in order for these devices to exceed the performance characteristics of pure permanent magnet and hybrid magnet devices. Due to the relatively low peak field on the conductor (typically ~4-6 T), extremely high superconductor current densities are possible. In the case of a quench the current is carried by the Cu stabilizer, and the protection system and conductor Cu fraction must be correctly matched.

The importance of increasing J_{cu} is shown in Figure 3. Traditional magnet designs keep J_{cu} to ~ 2000 A/mm^2 or less. Under such conditions the use of advanced superconductors, such as APC NbTi or Nb$_3$Sn, will result in a higher Cu fraction (which increases the conductor stability and facilitates protection), but will not translate into a significant increase in attainable axial field (see figure 3, line A).
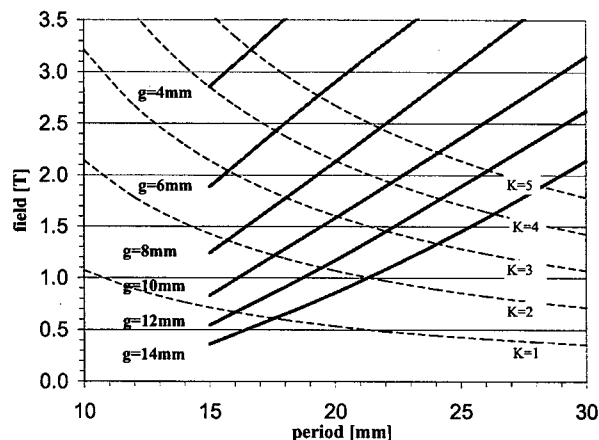
Figure 2. Performance curves for Nb$_3$Sn superconducting undulators (see text for assumptions)
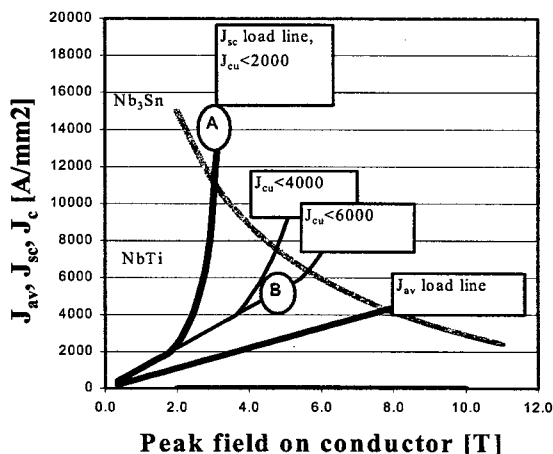
Figure 3 Effect of a copper current density limitation on the attainable performance of a device. The model corresponds to a linear B(J) load line and assumes Cu:SC=1 at low current. Once the J_{cu} limit is attained, the copper cross section is "increased " to keep J_{cu} constant.

High copper current density can be achieved by using a high J_c superconductor with a low Cu:SC ratio, traits found in recent Nb3Sn conductors. We have investigated both internal-Sn mono-element conductors [2] and Oxford jelly-roll strands [3]. J_c measurements were performed at LBNL. The internal-Sn strands were unstable below 10 T, perhaps due to flux jumps occurring under high transport current conditions. The jelly-roll strand (see cable parameters in table 2), was stable throughout the field range of interest (5-6 T), and yielded $J_c(5.9T, 4.2K) = 6115$ A/mm^2. A six-strand Rutherford cable was then fabricated at LBNL and is being used in the undulator prototype.

Coil winding method

The coilpack design keeps all turn-to-turn, layer-to-layer, and coil-to-coil transitions on the far side, away from the beamline (see figure 4). The reaction and potting fixtures are designed to force the coilpack flat on the straight sections. Only the potting fixture plate on the beam side needs to be removed during operation. In the flat coil section on the beam side the net Lorentz force is directed toward the yoke, i.e. away from the beam.

The coil-to-coil transitions incorporate "buttons" (see figure 4) so as to minimize hard-way bends in the conductor in the case of a cable or tape. The winding approach is applicable for any period size.
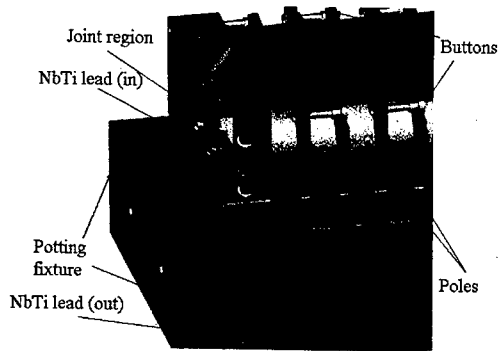
Figure 4 Model of the LBL 6-period Nb$_3$Sn prototype.

Quench protection

The jelly-roll strand is 52% Cu, resulting in $J_{cu} \approx 5650$ A/mm^2 during a quench at peak field. A simple thermal model [4] equating Joule heating and the heat capacity of the Cu yields

$$\int_{4.2}^{T_m} \gamma C_p(T)/\rho(T)\,dT = \int_0^\infty J^2(t)\,dt = J_0^2 t_d$$

where t_d is a characteristic heating time. For $T_m = 300$K we obtain $t_d \sim 40$ms. A passive protection system incorporating diodes eliminates the uncertainty of triggering an active system with such a short time constant. Diodes in a parallel circuit across the upper and lower undulator sections will begin to conduct as soon as they see a voltage larger than ~5V. Most of the supply current will be diverted through them, and the coil current will decay rapidly. Since the inductance $L = 2E/I^2$ is low (see table 2), little voltage is needed to energize the coils and a single diode can be used for each undulator half.

Calculations show that a single coil can absorb half of the stored energy of the system (mutual inductance between the upper and lower halves will trigger a quench in the opposing coil) without exceeding ~350 K. By incorporating diodes, however, the design insures that most of the energy is diverted elsewhere.

Voltage taps are being installed at each period to provide experimental verification of the quench behavior.

The protection system design is scalable to full length devices.

Table 2 Nb$_3$Sn prototype undulator design parameters and anticipated performance.

Coil Geometry	
λ [mm]	30
p_w [mm]	4.8
c_w [mm]	10.2
c_h [mm]	5.4
y_h [mm]	28
Average turn length [mm]	21.9
Turns/layer	5
Number of layers	5
Conductor	
Strand diameter [mm]	0.48
Number of strands in cable	6
Cable width (bare) [mm]	1.75
Cable height (bare) [mm]	0.90
Insulation thickness [mm]	0.065
Cu:SC	1.08:1
RRR	21
Cabling packing factor	0.72
Overall SC fraction	0.24
$J_c(5.9T, 4.2K)$ [A/mm^2]	6115
Anticipated performance (h=5 mm)	
B_0 [T]	3.2
B_{max} [T]	5.9
I_{max} [A]	3200
E (stored energy/period) [J]	2000

CONCLUSION

Superconducting undulators have the potential to significantly enhance the operation of existing and future light sources. In order to make full use of the most advanced superconductors, the protection system must be capable of handling values of J_{cu} well beyond those typically used in superconducting magnet design. A prototype Nb3Sn undulator design is currently being fabricated to verify the passive protection method presented in this paper.

REFERENCES

[1] J. N. Corlett et al, "Initial feasibility study of a dedicated synchrotron radiation light source for ultrafast X-ray science", LBNL-48171, Oct., 2001.

[2] B. A. Zeitlin et al, "Progress on a high current density low-cost Nb$_3$Sn conductor scalable to modern NbTi production", Advances in Cryogenic Engineering (Materials), vol. 48B, pp978-985, 2002

[3] J. A. Parrell et al, "High Field Nb$_3$Sn Conductor Development at Oxford Superconducting Technology", to be published.

[4] Martin N. Wilson, "Superconducting Magnets", Clarendon Press, Oxford, 1989, p. 201

HARMONIC CONTENTS OF AND DETAILED STUDY ON A HIGH-GAIN HARMONIC GENERATION FREE ELECTRON LASER*

Juhao Wu[†]

SLAC, Stanford University, Stanford, CA 94309

Abstract

In this paper, we calculate the third harmonic of a High Gain Harmonic Generation (HGHG) Free Electron Laser (FEL) at saturation. In the HGHG FEL scheme, there is an external dispersion section, which provides an efficient microbunching. Study on the emittance effect in such an external dispersion section suggests a new optimization for the HGHG FEL. We finally discuss how to reduce the incoherent undulator radiation which is a noise with respect to the seed laser.

INTRODUCTION

High-Gain Harmonic Generation (HGHG) Free-Electron Laser [1] is perceived as a candidate for a coherent light source in the Deep UV to X-ray regime [2, 3]. So far, our main interest is on the fundamental radiation [2]. However, at the end of the amplifier, the HGHG FEL is in deep saturation regime, hence harmonic contents are significant. These harmonic contents [4, 5] are the natural extension to shorter wavelengths. We hence upgrade the TDA simulation code [6] to calculate the harmonics.

To enhance the microbunching process, in the HGHG scheme, an external dispersion section is adopted. Such a dispersion section enhances microbunching more efficiently than the undulator does. Besides this, emittance effect is less stringent in the external dispersion section than in the undulator. This then provides a new optimization scheme.

When it passes through the undulator together with the seed laser, the electron beam will produce undulator radiation, which is a noise with respect to the seed laser. We suggest an approach to reduce such noise effect.

TDA-HARMONICS SIMULATION CODE

Numerical simulation of Self-Amplified Spontaneous Emission (SASE) FEL is normally performed using time-dependent computer codes [7], which require large CPU time and memory. Time-independent simulation code such as TDA [6] relaxes this, though people normally think it will be less accurate. Previous studies proved that TDA is still a very useful code as long as we use it properly [8]. For HGHG FEL, the input seed laser well dominates the shot noise, so TDA is sufficient. We therefore upgraded the

TDA code to include harmonics. We test our code against published results [5, 9, 10].

Equations of motion

We keep the same notation as those in TDA. We here present the dynamics equations for a planar undulator. Similar to TDA, TDA-Harmonics (TDA-H) uses the following two equations for the longitudinal motion: one for the Lorentz factor γ and the other for the electron phase $\theta = (k_s + k_w)z - \omega_s t$. They are

$$\frac{d\gamma}{dz} = \frac{k_s a_w}{\gamma} \sum_{f=1}^{\infty} f \, \mathrm{Re}\{G_f\}, \tag{1}$$

and

$$\frac{d\theta}{dz} = k_w - \frac{k_s}{2\gamma^2}\left[1 + a_w^2 + \gamma^2\beta_{\perp 0}^2 - 2a_w \sum_{f=1}^{\infty} \mathrm{Im}\{G_f\}\right]; \tag{2}$$

where,

$$\begin{aligned}
G_f \equiv \ & (-i)^{f-1}\exp(if\theta) \times \left(\frac{i\beta_{x0}\gamma}{\sqrt{2}a_w}K_f^{\perp}a_s^f\exp(i\phi_s^f)\right.\\
& + \ iK_f^{(1)}a_s^f\exp(i\phi_s^f)\\
& + \left.\frac{a_w}{\sqrt{2}\gamma k_w}K_f^{(2)}\frac{\partial}{\partial x}(a_s^f\exp(i\phi_s^f))\right).
\end{aligned} \tag{3}$$

Here, the radiation field is characterized by the wavenumber $k_s = 2\pi/\lambda_s = \omega_s/c$, the dimensionless vector potential rms value $a_s = eA_s/(mc)$ and the phase ϕ_s. The wiggler field is specified by the wavenumber k_w and vector potential $a_w = eB_w/(mck_w)$. In these equations, $\beta_{\perp 0} = \sqrt{\beta_{x0}^2 + \beta_{y0}^2}$ is the transverse drift speed and β_{x0} and β_{y0} are the smooth motions of the guiding center. In addition, f is the harmonic number, and the K functions are defined the same as Eqs. (34) and (A7) in Ref. [11], i.e.,

$$\begin{aligned}
K_f^{(m)}(\xi,\sigma) \equiv \ & (-1)^f \sum_{-\infty}^{+\infty} J_n(f\xi)\\
& \times [(-1)^m J_{2n+f-m}(f\sigma) - J_{2n+f+m}(f\sigma)]
\end{aligned} \tag{4}$$

and

$$K_f^{\perp}(\xi,\sigma) \equiv 2(-1)^f \sum_{-\infty}^{+\infty} J_n(f\xi)J_{2n+f}(f\sigma), \tag{5}$$

where,

$$\xi \equiv \frac{a_w^2 k_s}{4\gamma^2 k_w},\qquad(6)$$

and

$$\sigma \equiv \sqrt{2}a_w\beta_{x0}k_s/(\gamma k_w).\qquad(7)$$

Notice, our a_w, the same as that in TDA is the rms value, while a_w in Ref. [11] is the peak value.

The two dynamic equations (1) and (2) should be compared with Eqs. (1.a) and (1.b) in Ref. [6]. The equations of the transverse motions are not changed formally.

Wave equation

There are f equations, each stands for a harmonic field. They are

$$\left[\frac{\partial}{\partial z}+\frac{1}{2ifk_s}\nabla_\perp^2\right]a_s^f\exp(i\phi_s^f)$$
$$=if\frac{eZ_0}{mc^2}\frac{1}{2fk_s}\frac{I}{N}\sum_{j=1}^N\delta(y-y_{0j})\frac{a_w}{\gamma_j}\exp(-if\theta_j)$$
$$\times\left\{\frac{\beta_{x0j}\gamma_j}{\sqrt{2}a_w}K_f^\perp\delta(x-x_{0j})+K_f^{(1)}\delta(x-x_{0j})\right.$$
$$+\frac{iK_f^{(2)}}{2}\left[\delta\left(x-x_{0j}-\frac{a_w}{\sqrt{2}\gamma_j k_w}\right)\right.$$
$$\left.\left.-\delta\left(x-x_{0j}+\frac{a_w}{\sqrt{2}\gamma_j k_w}\right)\right]\right\}.\qquad(8)$$

The power balance equation could be derived straightforward and it could be used as a self-check for the numerical simulation results.

Initial conditions

We specify the electron distribution function on the 6-dimensional phase space $F(\gamma,\phi,p_x,x,p_y,y)$ at the entrance of the wiggler at $z=0$. For the initial radiation field, we assume a Gaussian TEM$_{00}$ mode at $z=0$ for each harmonic as well as for the fundamental radiation as what was done in TDA.

Preliminary results

We compare TDA-H with TDA and other available results. Good agreements are found. Summary is in Table 1, where we compare with the experiments and make prediction for the LCLS project at SLAC as well.

Now, let us study the harmonic content in an x-ray HGHG FEL. In our scheme [2], there is a 33.5 m long amplifier, which is resonant at 1.5 Å. In the amplifier, the HGHG FEL is in the deep saturation regime, hence substantial harmonic contents are expected. We use TDA-H to calculate the 3rd harmonic content. The result shows that there is about 30 MW radiation at the third harmonic, i.e. at 0.5 Å. The evolution of the radiation power in the amplifier is illustrated in Fig. 1. Different from the SASE

		TDA-H	TDA	Ref.
LCLS	Fund.	14 GW	14 GW	8 GW
1.5 Å	3rd	28 MW		15 MW
LCLS	Fund.	9 GW	9 GW	7 GW
4.5 Å	3rd	35 MW		40 MW
LETUL	Fund.	76 MW	78 MW	70 MW
SASE	3rd	520 kW		600 kW
ATF	Fund.	33 MW	35 MW	30 MW
HGHG	3rd	630 kW		350 kW

Table 1: Comparison of the results from TDA-H with those from TDA[6] and other references. For ATF HGHG experiment, we use Ref. [9]; for the others. we refer to Ref. [5].

FEL, the electron beam in HGHG FEL is already highly microbunched when it enters the final amplifier. Hence, the harmonic contents have quite large initial power. This is explicitly shown in Fig. 1, though, initially, there is not much growth for the harmonics. Basically the electron beam and the harmonic exchange energy back and forth, but not much net growth in the harmonic power. Later, when the fundamental radiation is exponentially amplified, the bunching at the harmonics is also enhanced substantially. This is the nonlinear region for the harmonics [5].
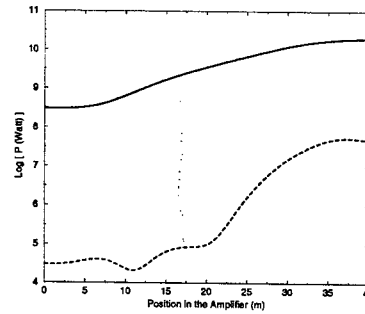
Figure 1: The evolution of the radiation power in the amplifier. The vertical axis stands for the logarithm of the radiation power to the base of 10. The solid line is for the fundamental radiation at 1.5 Å; and the dashed line for the 3rd harmonic at 0.5 Å.

EMITTANCE EFFECTS

In the SASE FEL, the microbunching is produced purely in the undulator. The path length difference induced by the energy spread and that by the emittance are both second-order effect. Hence, the emittance is an important effect, which will lead to microbunch diffusion. In the HGHG FEL, there is an external dispersion section, where the path length difference produced by the energy modulation is a first order effect, hence the emittance is not important[12].

We called this the Natural Emittance Effect Reduction (NEER) mechanism.

In an undulator, the effective energy spread due to the emittance is

$$\left.\frac{\sigma_\gamma}{\gamma}\right|_{eff,\epsilon}^{undul} = \frac{k_s\,k_\beta}{2\,k_w}\,\epsilon, \qquad (9)$$

where k_β is the betatron wavenumber.

In an idealized dispersion section, the emittance acts like an effective energy spread of

$$\left.\frac{\sigma_\gamma}{\gamma}\right|_{eff,\epsilon}^{disp} = \frac{48\,R^2\,\epsilon}{L_s^2\,\beta} \approx \frac{k_s\,k_\beta\,L_s\,\epsilon}{\gamma\,\left.\frac{d\psi}{d\gamma}\right|_{disp}}, \qquad (10)$$

where k_s is the wavenumber in the radiator, and $L_s = 4L_1$ is the total length of the dispersion section, which is assumed to consist of 4 pieces of dipole, each is L_1 long.

The ratio of these two effects is then

$$\eta \equiv \left(\left.\frac{\sigma_\gamma}{\gamma}\right|_{eff,\epsilon}^{disp}\right) \Big/ \left(\left.\frac{\sigma_\gamma}{\gamma}\right|_{eff,\epsilon}^{undul}\right) = \frac{2L_s k_w}{\gamma\,\left.\frac{d\psi}{d\gamma}\right|_{disp}}. \qquad (11)$$

This ratio is generally small due to the huge γ. A detailed study [13] on our cascading HGHG approach [2] shows that the effective energy spread due to the emittance in the dispersion section is far smaller than that in the undulators. Hence, by reducing the undulator length, the emittance effect is greatly reduced. This NEER mechanism suggests a new operation mode [13], i.e., we could use an electron bunch with a higher current, though an unavoidably higher emittance, in the Harmonic Generation stages.

INCOHERENT/COHERENT SYNCHROTRON RADIATION EFFECT

Saldin et al. [14] pointed out that the undulator radiation is the noise with respect to the seed laser. The Noise-To-Signal (NTS) ratio is increased by a factor of N_h^2, where N_h is the harmonic number. Hence, for the cascading HGHG approach [13], the worst problem comes at the first stage. To overcome this, in the modulator of the first stage, we increase the input seed power to 1 GW. Then the final NTS ratio is about 14% in the 1.5 Å HGHG FEL. The first sideband locates at $1/(2\,N_h\,N_u)$ [13], where N_u is the number of undulator period. Hence, as long as this sideband is outside the signal bandwidth, it would not be a concern. In the radiator, together with the HGHG FEL, there will be a SASE FEL. In order to reduce the SASE FEL, we increase the energy modulation $\Delta\gamma$ produced in the modulator, and reduce the dispersion strength $\frac{d\psi}{d\gamma}$ in the dispersion section accordingly to keep $\Delta\gamma\frac{d\psi}{d\gamma}$ constant. Recall that the bunching factor

$$b_n \equiv \exp\left[-\frac{1}{2}\sigma_\gamma^2\left(\frac{d\psi}{d\gamma}\right)^2\right] J_n\left[\Delta\gamma\left(\frac{d\psi}{d\gamma}\right)\right]. \qquad (12)$$

Hence, by doing so, b_n is increased! Now recall that the start-up coherent emission (CE) power $P^{Coh} \propto |b_n|^2$ [13].

Hence the start-up CE power is in fact increased! However, since the energy modulation is an effective energy spread, the power e-folding length increases to be $L_{G\,r} = 0.9$ m, while $L_{G\,r} = 0.6$ m for the case without energy modulation [2]. Because of the larger energy spread, the saturation power is reduced. At about $L_{Rad.} = 4$ m, the system reached saturation. In such a radiator the SASE FEL is only about 2 kW. Recall that the HGHG FEL has a power of 10 GW, and now $N_h = 450/1.5 = 300$. The final NTS ratio is about 2%. The contribution from the other undulators is smaller because N_h is reduced along the device. Hence, the undulator radiation is not serious.

The dispersion section between two adjacent undulators is essentially a bunch-compression chicane. As an estimate, we assume an ideal dispersion section, i.e., a three-dipole chicane with no drift space among the dipoles, so that the length of the first and third magnets both to be L_1, the middle magnet length to be $2L_1$. The momentum compaction is $R_{56} = 4L_1\left(\frac{1}{\cos\psi} - \frac{\psi}{\sin\psi}\right)$, where ψ is the bending angle. Now we hope to get a path difference of $\lambda_r/4$ for a relative energy modulation of $\Delta\delta$, i.e. $\lambda_r/4 = R_{56}\Delta\delta$. If we assume the magnetic field to be $B = 0.5$ Tesla, and $L_1 = 8$ cm, then the bending angle is only $\psi \approx 0.3°$. Simulation by Elegant[15] shows that the CSR effect is essentially zero.

ACKNOWLEDGMENTS

REFERENCES

[1] L.H. Yu, Phys. Rev. A **44**, 5178 (1991); L.H. Yu, et al., Sciences **289**, 932 (2000).

[2] J. Wu, L.H. Yu, Nucl. Instr. Meth. A **475**, 104 (2001); L.H. Yu, Proc. of IFCA, Argonne, (1999).

[3] G. Dattoli, et al., J. Appl. Phys. **86**, 5331 (1999); S.G. Biedron, et al., Nucl. Instr. Meth. A **475**, 401 (2001).

[4] W.B. Colson, IEEE J. Quant. Elect. QE-**17**, 1417 (1981); J.B. Murphy, et al. Opt. Com. **53**, 197 (1985).

[5] Z. Huang, K.J. Kim, Phys. Rev. E **62**, 7295 (2000).

[6] T.M. Tran, J.S. Wurtele, Comput. Phys. Commun. **54**, 263 (1989).

[7] W. Fawley, et al., Bull. Am. Phys. Soc. **38**, 1327 (1993); H.P. Freund, Phys. Rev. E **52**, 5401 (1995); E.L. Saldin, et al., Nucl. Instr. Meth. A **429**, 233 (1999).

[8] L.H. Yu, Phys. Rev. E **58**, 4991 (1998); V. Kumar, et al., ibid., **65**, 016503 (2001).

[9] S.G. Biedron, et al., Nucl. Instr. Meth. A **475**, 118 (2001).

[10] A. Doyuran, et al., Phys. Rev. Lett. **86**, 5902 (2001).

[11] M.J. Schmitt, C.J. Elliott, Phys. Rev. A **41**, 3853 (1990).

[12] I. Boscolo, V. Stagno, Nucl. Instr. Meth. A **188**, 483 (1982).

[13] J. Wu, Ph.D. Dissertation, SUNY-Stony Brook (2002); L.H. Yu, J. Wu, Nucl. Instr. Meth. A **483**, 493 (2002).

[14] E.L. Saldin, et al., Opt. Com. **202**, 169 (2002).

[15] M. Borland, Phys. Rev. ST-AB, **4**, 070701 (2001).

CALCULATION OF THE COHERENT SYNCHROTRON RADIATION IMPEDANCE FROM A WIGGLER*

Juhao Wu[†], T.O. Raubenheimer and G.V. Stupakov

SLAC, Stanford University, Stanford, CA 94309

Abstract

Most studies of coherent synchrotron radiation (CSR) have considered only the radiation from independent dipole magnets. However, in the damping rings of future linear colliders and many high luminosity factories, a large fraction of the radiation power will be emitted in damping wigglers. In this paper, the longitudinal wakefield and impedance due to CSR in a wiggler are derived in the limit of a large wiggler parameter K. After an appropriate scaling, the results can be expressed in terms of universal functions, which are independent of K. Analytical asymptotic results are obtained for the wakefield in the limit of large and small distances, and for the impedance in the limit of small and high frequencies.

INTRODUCTION

Many modern advanced accelerator projects call for short bunches with low emittance and high peak current where coherent synchrotron radiation (CSR) effects may play an important role. CSR is emitted at wavelengths longer than or comparable to the bunch length whenever the beam is deflected [1]. The stringent beam requirements needed for short wavelength Self-Amplified Spontaneous Emission (SASE) free-electron lasers have led to intensive theoretical and experimental studies [2] over the past few years where the focus has been on the magnetic bunch compressors required to obtain the high peak currents. In addition to these single-pass cases, it is also possible that CSR might cause a microwavelike beam instability in storage rings. A theory of such an instability in a storage ring has been recently proposed in Ref. [3] with experimental evidence published in [4].

The previous study of the CSR induced instability assumed that the impedance is generated by the synchrotron radiation of the beam in the storage ring bending magnets [3]. In some cases (e.g. the Next Linear Collider (NLC) damping ring [5]), a ring will include magnetic wigglers which introduce an additional contribution to the radiation impedance. The analysis of the microwave instability in such a ring requires knowledge of the impedance of the synchrotron radiation in the wiggler. Although there have been earlier studies of the coherent radiation from a wiggler or undulator [6, 7], the results of these papers cannot be used directly for the stability analysis.

In this paper, we derive the CSR wake and impedance for a wiggler. We focus our attention on the limit of a large wiggler parameter K because this is the most interesting

case for practical applications. It also turns out that, in this limit, the results can be expressed in terms of universal functions of a single variable after an appropriate normalization.

ENERGY LOSS AND LONGITUDINAL WAKE IN WIGGLER

The longitudinal wake is directly related to the rate of energy loss $d\mathcal{E}/dt$ of an electron in the beam propagating in a wiggler. For a planar wiggler, a general expression for $d\mathcal{E}/dt$ as a function of the position s of the electron in the bunch and the coordinate z in the wiggler was derived in Ref. [7]. We reproduce here the results of that work using the authors' notation:

$$\frac{d\mathcal{E}}{c\,dt} = e^2 k_w \int_{-\infty}^{s} d\,s'\, D(\hat{s} - \hat{s}', K, \hat{z}) \frac{d\lambda(s')}{ds'}, \quad (1)$$

where $\lambda(s)$ is the bunch linear density,

$$D(\hat{s}, K, \hat{z}) = \frac{1}{\hat{s}} - 2 \times$$

$$\frac{\Delta - K^2\, B(\Delta, \hat{z})\, [\sin\Delta\cos\hat{z} + (1-\cos\Delta)\,\sin\hat{z}]}{\Delta^2 + K^2\, B^2(\Delta, \hat{z})}, \quad (2)$$

$$B(\Delta, \hat{z}) = (1 - \cos\Delta - \Delta\sin\Delta)\cos\hat{z}$$
$$+ (\Delta\cos\Delta - \sin\Delta)\sin\hat{z}, \quad (3)$$

and Δ is the solution of the transcendental equation

$$\hat{s} = \frac{\Delta}{2}\left(1 + \frac{K^2}{2}\right) + \frac{K^2}{4\Delta}\{[2(1-\cos\Delta) - \Delta\sin\Delta]$$
$$\times (\cos\Delta\cos 2\hat{z} + \sin\Delta\sin 2\hat{z}) - 2(1-\cos\Delta)\}. \quad (4)$$

In the above equations, we use the following dimensionless variables: $\hat{s} = \gamma^2 k_w s$ and $\hat{z} = k_w z$. The parameter Δ is equal to $k_w (z - z_r)$, where z and z_r are the projected coordinates on the wiggler axis of the current position of the test particle and the retarded position of the source particle, respectively. The internal coordinate s is defined so that the bunch head corresponds to a larger value of s than the tail. The wiggler parameter K is approximately $K \approx 93.4\, B_w \lambda_w$, with B_w the peak magnetic field of the wiggler in units of Tesla and λ_w the period in meters. In addition, γ is the Lorentz factor, e is the electron charge, c is the speed of light in vacuum, and $k_w = 2\pi/\lambda_w$ is the wiggler wave number. Note that the function D is a periodic function of $\hat{z}$ with a period equal to π. Also note that, despite assuming $K \gg 1$, we still assume a small-angle orbit approximation, i.e., $K/\gamma \ll 1$.

We introduce the longitudinal wake $W(s)$ of the bunch as the rate of the energy change averaged over the z coordinate:

$$W(s) = -\frac{1}{e^2}\frac{d\bar{\mathcal{E}}}{c\,dt} = -k_w \int_{-\infty}^{s} ds'\, G(s - s')\frac{d\lambda(s')}{ds'}, \quad (5)$$

where
$$G(s) = \frac{1}{\pi} \int_0^\pi d\hat{z}\, D(\hat{s}, K, \hat{z}), \qquad (6)$$

and we dropped K from the list of arguments of the function G. The positive values of W correspond to the energy loss and the negative values imply the energy gain. The usual longitudinal wake $w(s)$ corresponding to the interaction of two particles is then defined as

$$w(s) = -k_w \frac{d\,G(s)}{d\,s}, \qquad (7)$$

so that
$$W(s) = \int_{-\infty}^s ds'\, w(s - s')\lambda(s'). \qquad (8)$$

Note that the wake Eq. (7) is localized in front of the particle and vanishes behind it; $w = 0$ for $s < 0$.

In the limit of large K, we can neglect unity in the first bracket of Eq. (4), assuming that $K^2/2 \gg 1$. Such an approximation is valid, if we are not interested in the very short distances of order of $(K\, k_w\, \gamma^2)^{-1}$ (0.5Å for the NLC damping ring wiggler [5]). We also introduce a new variable $\zeta \equiv \hat{s}/K^2$ which eliminates the parameter K from Eq. (4):
$$\zeta(\Delta, \hat{z}) = \frac{\Delta}{4} + \frac{1}{4\Delta}\{[2(1 - \cos\Delta) - \Delta\sin\Delta]$$
$$\times (\cos\Delta\cos 2\hat{z} + \sin\Delta\sin 2\hat{z}) - 2(1 - \cos\Delta)\}. \qquad (9)$$

In this limit, the expression for D, Eq. (2), can also be simplified:
$$D(\zeta, \hat{z}) = 2\,\frac{\sin\Delta\cos\hat{z} + (1 - \cos\Delta)\sin\hat{z}}{B(\Delta, \hat{z})}, \qquad (10)$$

as long as Δ is not too small, $\Delta \gg 1/K$. Again, the parameter K is eliminated from this equation.

WAKEFIELD

Using Eq. (6) and (10) we find

$$G(\zeta) = \frac{2}{\pi} \int_0^\pi d\hat{z}\, \frac{\sin\Delta\cos\hat{z} + (1 - \cos\Delta)\sin\hat{z}}{B(\Delta, \hat{z})}, \qquad (11)$$

where $\Delta = \Delta(\zeta, \hat{z})$ is implicitly determined by Eq. (9). The integrand in this equation has singularities at points $\hat{z} = \hat{z}_s$ where $B(\Delta(\zeta, \hat{z}_s), \hat{z}_s) = 0$. It could be checked that in the vicinity of a singular point $B(\Delta(\zeta, \hat{z})) \propto (\hat{z} - \hat{z}_s)^{1/3}$, and the singularity is integrable.

We plot the function $G(\zeta)$ calculated by numerical integration in Fig. 1. A characteristic feature of the function G is the presence of cusp points, at which the function reaches local maxima and minima. Approximately, they are

$$G(\zeta) = \begin{cases} -\frac{4\,(2\,n-1)\,\pi}{4 + [(2\,n-1)\,\pi]^2}; & \text{at } \zeta \approx \frac{(2n-1)\,\pi}{4} - \frac{1}{(2n-1)\,\pi} \\ 0; & \text{at } \zeta = \frac{n\,\pi}{2} \end{cases} \qquad (12)$$

with $n = 1, 2, \cdots$. These are the "$\times$" points in Fig. 1, showing very good agreement with the numerical result. The longitudinal wake given in Eq. (7) will reach infinity when approaching the maxima and minima from one side, and negative infinity on the other side.

In the limit $\zeta \ll 1$, it follows from Eq. (9) that $\Delta \ll 1$ as well. Equation (9) can then be solved using a Taylor

expansion of the right-hand side: $\Delta = \left(24\,\zeta/\cos^2\hat{z}\right)^{1/3}$. Expanding the integrand in Eq. (11), keeping only the first nonvanishing term in Δ yields

$$G(\zeta) = -\frac{1}{\pi} \frac{2}{(3\,\zeta)^{1/3}} \int_0^\pi d\hat{z}\, \cos^{2/3}\hat{z}$$
$$= -\frac{4\, 3^{2/3}\, \Gamma\left(\frac{11}{6}\right)}{5\,\sqrt{\pi}\,\Gamma\left(\frac{4}{3}\right)} \zeta^{-1/3} \approx -0.99\,\zeta^{-1/3}. \qquad (13)$$

The above result can also be obtained if one considers a wiggler as a sequence of bending magnets with the bending radius $R = \gamma/k_w K |\cos\hat{z}|$, since in this limit the formation length of the radiation is much shorter than the wiggler period, and one can use a local approximation of the bending magnet for the wake. In the limit $\zeta \gg 1$, the parameter Δ
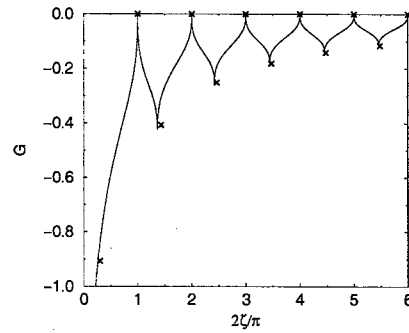
Figure 1: The solid curve represents the $G(\zeta)$ defined in Eq. (11) as a function of the normalized coordinate $2\zeta/\pi$. The ($\times$) signs are the approximation given in Eq. (12).

is also large, and Eq. (9) can be further simplified:

$$\zeta = \frac{\Delta}{4} - \frac{\sin\Delta\,\cos(\Delta - 2\hat{z})}{4}. \qquad (14)$$

In Eq. (3), we keep only the largest term $B(\Delta, \hat{z}) = -\Delta\sin(\Delta - \hat{z})$. For D, one now finds, $D(\zeta, \hat{z}) \equiv F(\zeta, \hat{z})/\zeta$, with
$$F(\zeta, \hat{z}) \equiv \frac{\sin\hat{z}}{2\sin(\hat{z} - \Delta(\zeta, \hat{z}))} - \frac{1}{2}, \qquad (15)$$

where the function $\Delta(\zeta, \hat{z})$ is implicitly determined by Eq. (14). Averaging over one wiggler period, we find $G(\zeta) \equiv \bar{F}(\zeta)/\zeta$, with

$$\bar{F}(\zeta) \equiv \frac{1}{\pi} \int_0^\pi d\hat{z}\, F(\zeta, \hat{z}) = \frac{1}{2\pi}\left(-\pi + \int_0^\pi d\hat{z}\, \frac{\sin\hat{z}}{\sin(\hat{z} - \Delta)}\right). \qquad (16)$$

It is easy to check that the function $\bar{F}$ is periodic, $\bar{F}(\zeta + \pi/2) = \bar{F}(\zeta)$, and $\bar{F}(0) = 0$, $\bar{F}(\pi/4) = -1$ in agreement with Eq. (12). The average value $\bar{F}(\zeta)$ is equal to $-1/2$. Since $\bar{F}$ is periodic in ζ with a period of $\pi/2$, using Eq. (16), we can obtain a Fourier series representation for $\bar{F}(\zeta)$. The corresponding long-range wake is then

$$G(\zeta) = -\frac{1}{2\zeta} +$$
$$\frac{1}{2\zeta}\sum_{n=0}^\infty \left[J_n\left(\frac{2n+1}{2}\right) - J_{n+1}\left(\frac{2n+1}{2}\right)\right]^2 \cos(4(2n+1)\zeta). \qquad (17)$$
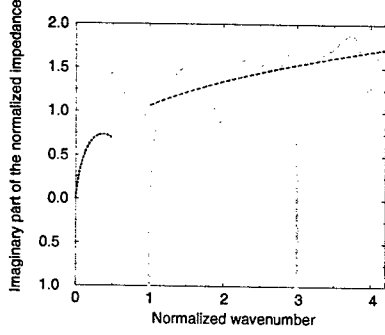
Figure 2: The imaginary part of the normalized impedance $Z(k)/k_w$ as a function of the normalized wave number k/k_0. Solid line: numerical solution from Eq. (18); dotted line: analytical low-frequency asymptotic behavior from Eq. (19); and dashed line: analytical high-frequency asymptotic behavior from Eq. (20).
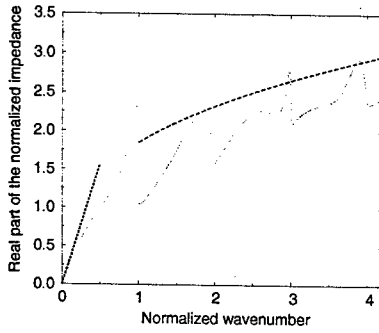
Figure 3: The real part of the normalized impedance $Z(k)/k_w$ as a function of the normalized wave number k/k_0. Solid line: numerical solution from Eq. (18); dotted line: analytical low-frequency asymptotic behavior from Eq. (19); and dashed line: analytical high-frequency asymptotic behavior from Eq. (20).

IMPEDANCE

The impedance $Z(k)$ is defined as the Fourier transform of the wake,

$$Z(k)=\int_0^\infty ds\, w(s)e^{-iks}=\frac{-ikK^2}{\gamma^2}\int_0^\infty d\zeta\, G(\zeta)e^{-4i(k/k_0)\zeta}, \quad (18)$$

where $k_0 \equiv 4\gamma^2 k_w/K^2$ is the wiggler fundamental radiation wave number.

We evaluated the integral in Eq. (18) using numerically calculated values of the function $G(\zeta)$ in the interval $[\zeta_{min}, \zeta_{max}]$, where $\zeta_{min} \approx 10^{-3}$ and $\zeta_{max} \approx 50$. The contribution to the integral outside of this interval was calculated using asymptotic representations Eqs. (13) and (17). The resulting imaginary and real parts of the impedance are shown in Figs. 2 and 3, respectively.

Simple analytical formulas for the impedance can be obtained in the limit of low and high frequencies. The low-frequency impedance corresponds to the first term in Eq. (17) for function G which does not oscillate with ζ: $G(\zeta) = -1/(2\zeta)$. Using the definition in Eq. (18), we

then obtain the low-frequency asymptotic behavior of the impedance as

$$Z(k) = -i\, 2\, k_w \frac{k}{k_0}\left[\gamma_E + \log\left(\frac{4k}{k_0}\right) + i\frac{\pi}{2}\right]$$

$$\approx \pi\, k_w \frac{k}{k_0}\left[1 - \frac{2i}{\pi}\log\left(\frac{k}{k_0}\right)\right], \quad (19)$$

where, $\gamma_E \approx 0.5772$ is the Euler gamma constant. Since we have an analytical expression for the short-range $G(\zeta)$ in Eq. (13), we get the asymptotic high-frequency impedance as

$$Z(k) = -i\frac{6\,\Gamma\left[\frac{11}{6}\right]}{5\sqrt{\pi}\,\Gamma\left[\frac{4}{3}\right]}A\left(\frac{Kk_w}{\gamma}\right)^{2/3}k^{1/3}$$

$$\approx -0.71\, i\, A\left(\frac{Kk_w}{\gamma}\right)^{2/3}k^{1/3}, \quad (20)$$

with $A = 3^{-1/3}\Gamma(2/3)(\sqrt{3}\,i - 1) \approx 1.63\,i - 0.94$ [3]. The asymptotic low- and high-frequency impedance are plotted in Figs. 2 and 3 for comparison with the numerical solution.

DISCUSSION AND CONCLUSION

In this paper, we derived the wakefield and the impedance for wigglers with $K^2/2 \gg 1$ due to the synchrotron radiation. Analytical asymptotic results are obtained for the wakes in the limit of small and large distances and for the impedance in the limit of small and high frequencies. The results obtained in this paper are used for the beam instability study due to the synchrotron radiation in wigglers [8].

REFERENCES

[1] R.L. Warnock and P. Morton, Part. Accel. **25**, 113 (1990); K.-Y. Ng, *ibid.* **25**, 153 (1990).

[2] J.B. Murphy, S. Krinsky, and R.L. Gluckstern, Part. Accel. **57**, 9 (1997); Ya.S. Derbenev *et al.*, DESY Report No. DESY-TESLA-FEL-95-05, 1995; B.E. Carlsten and T.O. Raubenheimer, Phys. Rev. E **51**, 1453 (1995); E.L. Saldin *et al.* Nucl. Instrum. Methods Phys. Res., Sect. A **398**, 373 (1997); R. Li, *ibid.*, **429**, 310 (1999); J.-M. Wang, Phys. Rev. E, **58**, 984 (1998); H. Braun *et al.*, Phys. Rev. Lett. **84**, 658 (2000).

[3] G. Stupakov and S. Heifets, Phys. Rev. ST Accel. Beams **5**, 054402 (2002).

[4] J.M. Byrd *et al.*, Phys. Rev. Lett. **89**, 224801 (2002).

[5] A. Wolski, URL: http://awolski.lbl.gov/nlcdrlattice/default.htm.

[6] Y.-H. Chin, Lawrence Berkeley National Laboratory Report No. LBL-29981, ESG-118, 1990.

[7] E.L. Saldin, E.A. Schneidmiller, and M.V. Yurkov, Nucl. Instrum. Methods Phys. Res., Sect. A **417**, 158 (1998).

[8] J. Wu, G.V. Stupakov, T.O. Raubenheimer, and Z. Huang, SLAC Report No. SLAC-PUB-9629, 2003, "Impact of the Wiggler Coherent Synchrotron Radiation Impedance on the Beam Instability", these proceedings.

DESIGN OF A REVOLVING HELICAL STAGGERED UNDULATOR

C. H. Chang[#], C. S. Hwang, Ch. Wang , T. C. Fan and G. H. Luo, NSRRC, Taiwan

Abstract

This investigation proposes a revolving helical staggered undulator with 10-mm and 15-mm period lengths for free electron laser operation. The helical staggered structure with a 10-mm period length is designed to produce vertical and horizontal field strength of 0.625 T at a phase shift of 90 degrees, by driving a longitudinal solenoid field of 0.7 T with a 3-mm gap. Three-dimensional magnetic field analysis was performed using RADIA computer code. An optimized magnetic structure was studied over various operating field ranges. A revolving helical undulator is equipped with two helical magnetic arrays to switch the helicity of radiation and broad radiation spectrum. Accordingly, the design of a helical staggered undulator is outlined.

INTRODUCTION

Several insertion devices can generate circular polarized light, including the APPLE II type undulator and the crossed undulator. In a planar undulator, the APPLE II provides the highest circular polarization rate, which depends on the gap and the phase position [1]. Hence, an APPLE II undulator has been used in the storage ring at various laboratories. However, for free electron laser (FEL) operation, the undulator must satisfy strict mechanical tolerances and magnetic field quality requirements. In most cases, the undulator is constructed with a fixed gap to prevent the severe complications associated with gap movement and phase shift.

A shorter period undulator with higher fields can extend the spectral range. For FEL applications, a shorter periodic length corresponds to a smaller overall undulator length. Typically, an aperture needs only to be large enough for single-pass beams. It made possible to lead a helical undulator with a small gap width. In addition, a helical undulator always generates a higher magnetic field than a planar undulator. Hence, a helical staggered undulator, which can be operated simply and stably, is being developed at the National Synchrotron Radiation Research Center (NSRRC) in Taiwan.

In this work, a helical staggered undulator with a 10-mm period length is designed to create strong vertical and horizontal magnetic fields. In principle, the magnetic field strengths must be equal, and the phases of the magnetic fields must be 90° apart to produce circularly polarized light. The helical staggered undulator is comprised of two planar staggered arrays shifted by a quarter of a period length parallel to the longitudinal axis to generate By $\sin 2\pi z$ and Bx $\cos 2\pi z$ magnetic fields along the longitudinal z axis [2]. Figure 1 presents the

proposed helical undulator design. Table 1 lists the main parameters.

Table 1: Main parameters of helical staggered undulator

Undulator type		Helical/Revolving	
Period length	mm	10	15
Fixed gap width	mm	3	3
K value		0.8	1.58
Peak on-axis field	T	0.86	1.13
Horizontal field strength	T	0.62	0.8
Vertical field strength	T	0.62	0.8
Polarization mode		circular	circular

Fig. 1 Schematic view of the helical staggered array

MAGNETIC DESIGN

In designing an undulator for a given energy, the

$$E_f[eV] = \frac{950\ E_e^2[GeV\ ]}{\lambda_u\ (1 + K^2/2 + \theta^2\gamma^2)}$$

wavelength of the emitted radiation is given by

Where $K = 0.934\ B\ (T)\ \lambda u\ (cm)$,

$$B = \sqrt{B_x^2 + B_y^2}$$

For circular polarized light, $Bx=By$, Note that a helical magnetic field has $\sqrt{2}$ times the peak magnetic field strength of the identical horizontal and vertical field as compare to a planar undulator. The periodic magnetic circuit must be optimized by a reasonable gap to maximize the magnetic field strength. Wake field effects

and magnet radiation damage determine the gap limit on the vacuum chamber aperture and the undulator gap [3]. An undulator must be used in vacuum to widen the aperture as much as possible. The permanent magnet is not employed in the staggered undulator without concerning the magnet degradation in the small gap. Accordingly, the helical staggered undulator enables the horizontal and vertical gaps to be as narrow as possible.

The original planar "staggered-array wiggler" was built at Stanford University [4]. A staggered-array undulator consists of a superconducting solenoid coil and two rows of vanadium permendure pole stacks and stainless steel half-blocks. The solenoid field is deflected vertically into each vanadium permendure face, to generate an alternating vertical field. Two planar staggered undulators, shifted a quarter of a periodic length, are separated by a fixed gap width to generate a helical field. In the helical undulator, the pole region is completely symmetrical at a declination angle of 45° to the axis, increasing the available space in both the vertical and the horizontal directions.

Figure 1 presents the configuration of the magnetic structure with 10-mm period length. The alternating sinusoidal field is derived from the helical staggered magnetic array by changing the current in the superconducting solenoid coil. The pole blocks are constructed from vanadium permendur. Magnetic field calculations have been made using RADIA 3D computer code [5]. Three-dimensional field analysis optimized the periodic magnet structure. Figure 2 plots the variation of the peak fields as a function of the magnetic gap at a current density of 30 A/mm^2.
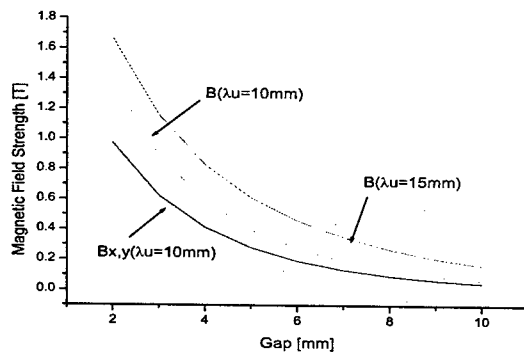
Fig. 2 The variation of the peak fields as a function of the magnetic gap at a current density of 30 A/mm^2.

The horizontal staggered magnetic array was in the quarter-period shift position. The 3-mm wide sharp pole must accommodate a minimum magnetic gap width. The width of the pole is chosen to yield the strongest magnetic field in the mid-plane. Varying the current density between 0 and 50 A/mm^2 yields a maximum field of 0.625 T due to saturation of the vanadium permendur pole. A peak vertical and horizontal magnetic field of 0.625 T was achieved by driving a longitudinal solenoid field of 0.7 T in a 3-mm wide gap. Figure 3 presents the

horizontal and vertical fields in one period length, derived from solenoid field with vanadium permendur pole.
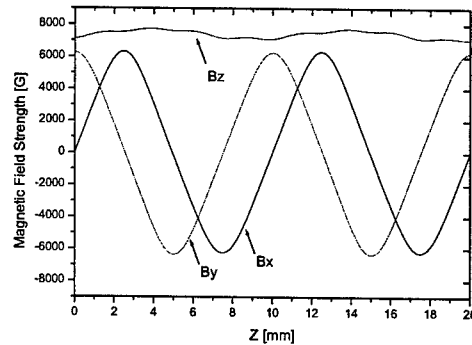
Fig. 3 The horizontal and vertical fields in a 10-mm period length, derived from solenoid field

The region of uniform field is also sensitive to the width of the narrow gap. The small width of pole is constrained by the width of gap. Therefore, the homogenous field is constrained in a narrow region around the beam axis. The magnetic field is less uniform nearer the axis because the ferromagnetic pole pieces from the conjunctive magnetic array. The integrated multipole errors are not very critical in an electron single pass undulator. Figure 4 plots the vertical field distributions along the horizontal axis at y=0 mm and the vertical axis at x=0 mm.
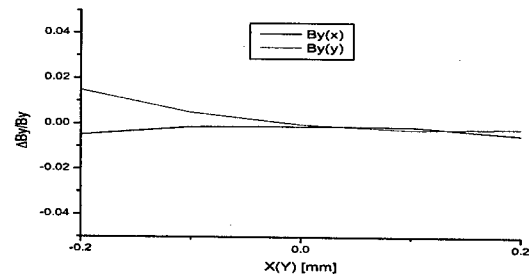
Fig. 4 The vertical field distributions along the horizontal axis at y=0 mm and the vertical axis at x=0 mm.

An anti-symmetric magnetic array configuration was designed under stringent magnetic field requirements to increase the effective magnetic pole. The end pole field is analyzed using three-dimensional calculations. The magnetic pole is magnetically saturated, and the helical fields are thereafter insensitive to the strong longitudinal field strength. The trim coils in the end coil region can be partially adjusted to compensate for the homogeneity of the helical field at both ends. The effective poles were optimized to reduce the vertical and horizontal fields integral using various solenoid currents. Figure 5 plots the calculated vertical, horizontal and longitudinal field distributions in a helical staggered with 10-mm period length undulator.
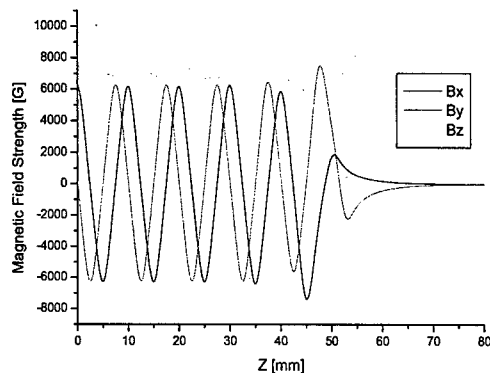
Fig. 5 The calculated vertical, horizontal and longitudinal field distributions at the end pole region.

Fig. 6 The configuration of revolving multi-magnetic arrays.

REVOLVING HELICAL STAGGERED ARRAYS

The phase of two planar staggered arrays must be longitudinally movable to reverse the helicity of radiation. However, the phase shift of magnetic arrays in vacuo requires a complicated mechanical design and may be disrupt the electron beam in FEL. The challenging requirement on the magnetic and mechanical designs is to maintain the overlap between the electron beam and the photon beam over the entire length of the undulator. In this study, the revolving undulator with multi-staggered arrays in a single device is proposed. Figure 6 outlines the proposed configuration. One magnetic array creates left circularly polarized light and another creates right circularly polarized light. The back-beam may be interchanged. Right or left circularly polarized light can be selected by rotating the cylindrical strongback frame. The electron beams pass through an offset center so a single device is used to generate both right and left circularly polarized light.

Ordinarily, the high magnetic field is limited in the short period undulator. Accordingly, the short period undulator generates a narrow or discontinuous photon spectrum between the high harmonics. Here, several period lengths can be served with a single device for compensating the discrete photon spectrum. Such multi-magnetic arrays provide various periodic lengths to broaden the photon spectrum. A cylindrical diameter of 200 mm can support four different magnetic structures as indicated in Fig. 6.

The helical staggered undulator, with perfectly identical horizontal and vertical fields generates ideally circularly polarized radiation at the fundamental harmonic. Circularly polarized spectra can be generated using a helical undulator with 10-mm and 15-mm period lengths at fundamental harmonics. The photon energy from a 50 MeV linear accelerator is produced in the 0.7-2.4 eV range.
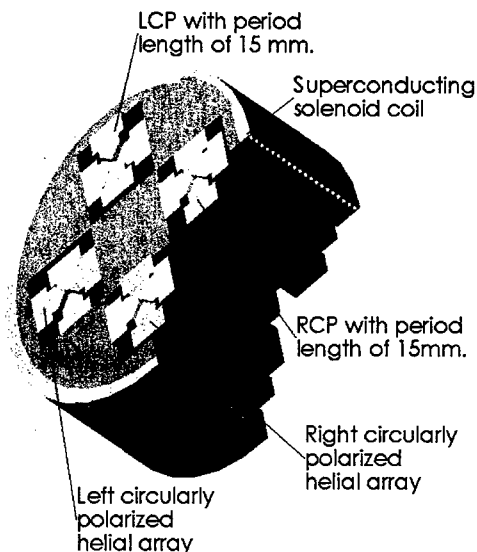
CONCLUSIONS

Decreasing the periodic length of the helical staggered undulator significantly increases the number of periods. This device with 10-mm period length generates both sinusoidal and helical on-axis magnetic fields of 0.625 T in a gap width of 3 mm. Such an undulator can produce perfectly circularly polarized radiation whose direction of circular polarization can be changed by multi-magnetic arrays on a single support. Moreover, the multi-magnetic arrays concept is applied to broaden the photon energy. This proposed revolving helical undulator provides the advantages of ease of fabrication and low cost in a particular gap width. The helical staggered undulator is mostly effective undulator in terms of mechanical tolerance, magnetic field error and cost.

REFERENCES

[1]   S. Sasaki, Nucl. Inctru. And Meth., A347(1994), 83.
[2]   J. Pfluger, "Undulator for SASE FELs", Nucl. Instr. and Meth., A445, 366-372 (2000)
[3]   H. Onuki, Nucl. Instru. Methods, A246, p94 (1986)
[4]   Y. C. Huang, etc., Nucl. Instr. and Meth., A341, 431-435 (1994)
[5]   O. chubar, P. Elleaume, J. chavanne, "A 3-Magnetostatics Computer Code for Insertion Devices" J. Synchrotron Rad. (1998), 5, 481-484

OPERATIONAL EXPERIENCE OF THE INSERTION DEVICES AND EXPECTATION OF THE FUTURE SUPERCONDUCTING WIGGLERS AT NSRRC

H.P. Chang, C.H. Chang, Jenny Chen, K.T. Hsu, C.S. Hwang, C.C. Kuo, C.H. Kuo, G.H. Luo

National Synchrotron Radiation Research Center

No. 101, Hsin-ann Road, Hsinchu Science-Based Industrial Park, Hsinchu 30077, Taiwan

Abstract

Since 1995, we have continuously installed five insertion devices (IDs) in the 1.5 GeV storage ring TLS at NSRRC. They include three undulators (U5, U9 and EPU5.6), one 1.8 Tesla wiggler (W20) and one 6 Tesla superconducting wavelength shifter (SWLS). All these five IDs are located in the long straight sections. The real time orbit correction and betatron tune compensation routine have been successfully operated. With these IDs, the machine emittance reduces substantially. We plan to install four more superconducting multi-pole wigglers (SMPWs), one in the long straight and three in the archromat sections. These devices therefore can offer more beam time for the hard X-ray community. The impacts of these IDs on the beam dynamics effects are reported in this paper.

INTRODUCTION

The TLS has six long straight sections, each 6 meters long for the installation of insertion devices, injection elements and RF cavities. Each of IDs, W20, U5, U9 and EPU5.6 occupies one long straight. With the limited space, we squeeze SWLS in the injection section and also plan to install one SMPW besides the RF cavities in this year. Three SMPWs will be put near second bending magnet of the triple bend achromat section [1]. SWLS and SMPWs will serve more X-ray beam time for the increasing X-ray community. Table 1 describes the insertion devices in the TLS storage ring. Figure 1 shows the photon flux vs. the photon energy of bending magnets and IDs at TLS. Two Taiwan beamlines, SP8-BM and SP8-U3.2, at Spring 8 are also depicted.
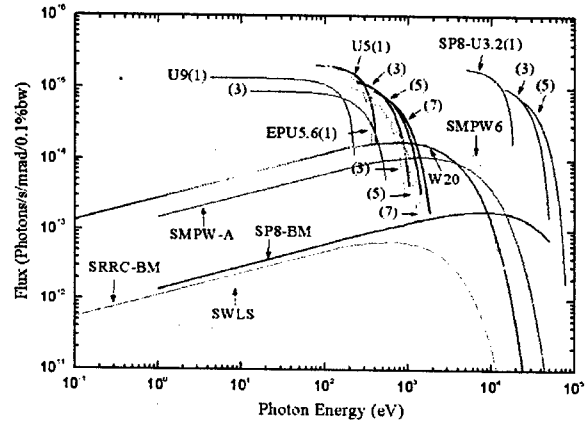
Figure 1: The photon flux vs. photon energy of bending magnets and IDs at TLS. Two Taiwan beamlines, SP8-BM and SP8-U3.2, at Spring 8 are also depicted.

Table 1: Insertion Devices in the TLS storage ring of NSRRC.

Insertion Device		SWLS	EPU5.6	U5	SMPW6	W20	U9	SMPW-A
Location Section		S1/Injection	S2	S3	S4/RF	S5	S6	Arc 2,4,6
Type		Supercon.	Pure	Hybrid	Supercon.	Hybrid	Hybrid	Supercon.
Magnet Length (M)		0.835	3.9	3.9	1.404	3.0	4.5	0.85
Period Length λ (cm)		25	5.6	5	6	20	9	6
(Min.) Gap (mm)		55	18	18	18	22	18	18.5
Number of Periods		1.5	66	76	16	13	48	7.5
Maximum By (Bx) Field (Tesla)		6	0.67 (0.45)	0.64	3.2	1.8	1.25	3.5
Photon Energy (eV) [Used Range]	Min.	4000	80	60	5000	800	5	5000
	Max.	38000	1400	1500	14000	15000	100	14000
Defection Parameter Ky (Kx)		190.5	3.52(2.37)	2.99	17.9	33	10.46	19.6
Vertical Tune Shift Δv (Horizontal Tune Shift)		0.0504 (-0.014)	0.011 (-0.012)	0.008	0.036	0.036	0.033	0.05
Installation Date		Apr.2002	Sep.1999	Mar.1997	Dec.2003	Dec.1994	Apr.1999	2005

INJECTION AND ORBIT STABILITY

With the insertion devices in the beam line, we need to study the beam dynamics effects, such as the lattice optics perturbations, the emittance change, the impact on the dynamic aperture, the orbit stability, lifetime, size reduction of the beam duck and increase of the vacuum reading, etc. It is also important to know if the injection can be seriously jeopardized with any setting of the ID's gap and phase at this 1.5 GeV low energy storage ring.

More cares should be taken in the construction of these IDs and it is necessary to meet the specifications to ensure the minimum impact on the beam dynamics.

It is concluded that for W20 wiggler and SWLS the magnetic field strength are almost set at its maximum operational values even during injection. Therefore it is less complicated to operate such devices in terms of the field scan. However, during the commissioning period, the orbit drift, tune shift and path-length while field is ramped should be carefully compensated for and a correction table thus was established.

Undulator, U5 and U9, EPU5.6, are allowed to be capable of field scan during users shifts. To this end, in addition to a fast global orbit feedback system, we need to apply look-up tables to reduce the orbit fluctuation and tune shift when the gap or phase of these IDs are changed.

Emittance and Dynamic Aperture

The integration of the six IDs in the dispersion-free long straight sections will bring the natural emittance from 25.6 nm-rad of the bare lattice to 21.0 nm-rad. Adding three more superconducting multipole wigglers in the achromats, however, will increase the emittance to 32.0 nm-rad due to large dispersion in these SMPWs locations. The synchrotron loss is increased from 128 keV/turn of the bare lattice without insertion devices to 202 keV/turn with all 9 IDs. The required RF power at 400 mA stored beam should be enough after installing a superconducting RF cavity in the near future. Initial stored current of present routine operation is 200 mA.

Simulation of the dynamic aperture with these IDs has been carried out and including all field errors in all magnets (measured or specified), we obtain an acceptable reduction of the dynamic aperture from PATPET as shown in Fig. 2. Similar results are also from other codes such as MAD.
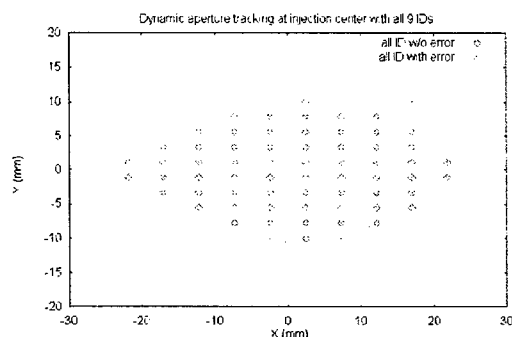
Figure 2: Dynamic aperture simulated from PATPET with field errors and all insertion devices.

Gap and Tune Scan

The EPU5.6 is an elliptical polarization ID and is more complicated than the other IDs, U5 and U9. For U5, U9, and EPU5.6, linear effects such as tune shift and orbit change by the non-zero first- and second- integral field strengths are studied in detail in references [2,3].

Horizontal closed orbit distortion (COD) of those IDs at TLS is about 0.2 to 0.3 mm without correction. It shows the main vertical field errors are almost in the same level. The orbit distortion in vertical plan of an ID may indicate the ID's horizontal field error and the vertical beta-function variation caused by the ID. The observed peak values are 0.2 mm for U5, 0.3 mm for U9, and 1.5 mm for EPU5.6.

In establishing a follow-gap look-up table for orbit correction of each ID, we found that the rms closed orbit distortion can be reduced within a few microns if only one ID gap varies at one time.

The corrector strengths beside the EPU5.6 in the look-up table are both functions of the gap and phase. However it was found that the orbit distortion by varying the phase of EPU5.6 is so small that the phase parameter has been ignored.

The peak of real-time orbit distortion is large than 10 microns when this look-up table method was applied for ID's field scan. In addition, with the help of a fast digital orbit feedback system, the peak of orbit variation thus can be maintained within a few microns (see Fig. 3).
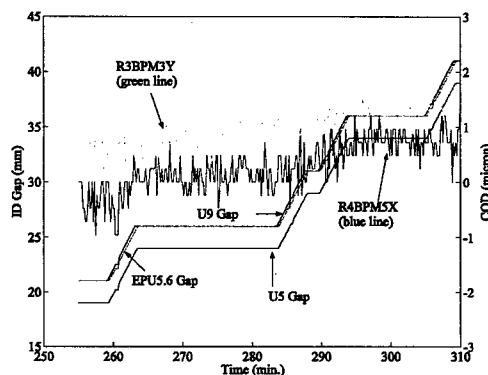
Figure 3: With the follow-gap look-up table and global orbit feedback system, the orbit drift of the field scan of U5, U9 and EPU5.6 can be reduced from a few hundred microns to a few microns. When the gaps of U5, U9 and EPU5.6 are scanned from 19, 21, and 21 mm to 39, 41, and 41 mm, the closed orbit distortions indicated by the R4BPM5X (blue) and R3BPM3Y (green), those are used in the faster orbit feedback system, are within 2 microns in both horizontal and vertical planes.

As shown in Table 1, with the EPU5.6's gap fixed at 20 mm, the observed horizontal tune shift is –0.012 when its phase is tuned from 0 to 180 degree (the encoder is from 0 to 28 mm). There is no horizontal tune shift effect for U5 and U9. The range of total vertical tune shift of these tuneable undulators is about 0.052, which may cross some resonance lines if no tune compensation is followed when ID's gaps are changed. We found the tune shift crossing some of the 5th order resonance lines caused the photon beam instability. The photocurrent drops, when the tune crosses 5Vy = 21 and Vx+4Vy = 24 resonance lines.

We added a follow-gap tune compensation mechanism in the look-up correction table of U9 to avoid the resonance problem. The tune compensation mechanism may use two Q1 and Q2 families or two Q1 and Q2 pairs beside the U9. The Q1 and Q2 families are finally adopted

since the optics perturbation is less than the local quadrupole pairs.

Commissioning of the 6 Tesla SWLS

In April 2002, a 6 Tesla, 3-pole cryogenic-free SWLS was installed between two injection kickers in the injection straight section [4,5]. In May, we started charging the SWLS and tests with beam. First stored beam with SWLS at 6 Tesla was observed on May 21. Injection with SWLS fully charged was of no any difficulty. Compensation of the orbit excursion and tune shift while increasing the magnetic field was conducted and as a result there are no major impacts on the beam dynamics effects. It is found that the measured tune shifts, path-length compensation (RF increase by 1.7 kHz at 6 Tesla), etc., are in consistent with the model predicted values (see Fig. 4). Vacuum cleaning with synchrotron light is needed to obtain an acceptable lifetime and beam stability. In August 2002, we found there was a crack in the ceramic chamber of the downstream kicker magnet because of the insufficient shielding against the powerful synchrotron radiation from the high field SWLS. The shielding was reinforced and replaced in October. In reality, the routine operations of SWLS are now at 5.3 Tesla such that the system is cryogenic-free. This field strength is acceptable for the hard X-ray users. As of April 2003, the beam current lifetime at 200 mA of the stable beam is about 8 hours. The commissioning of the associated photon beam line is currently underway.
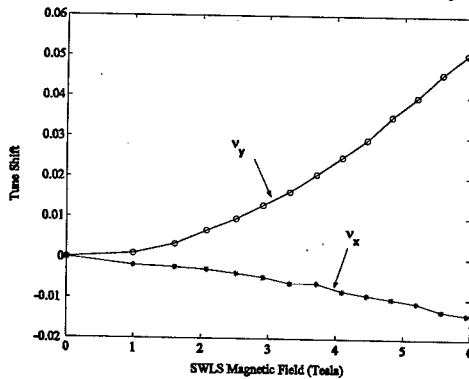
Figure 4: The measured tune shifts of SWLS.

Top-up Injection Mode

Top-up injection scheme is an attractive operation mode demonstrated by the APS and SLS, and NSRRC plans to adopt this operation mode in the near future. Major benefits with top-up mode are less thermal gradient in the accelerator components and photon beam line mirrors, more reduction of the insertion magnetic gap, and allowing smaller emittance lattice operations, etc. Lifetime issue will be of less concern after all. We have proved that the top-up injection is executable with the field scans of insertion devices while keeping the orbit locked with the orbit feedback system (see Figure 5). Major concern of the top-up mode is the injection loss budget, i.e., the control of the radiation dosage level with the heavy-metal shutter opened in the photon beam lines.

Studies of the injector reliability and injection efficiency are ongoing.
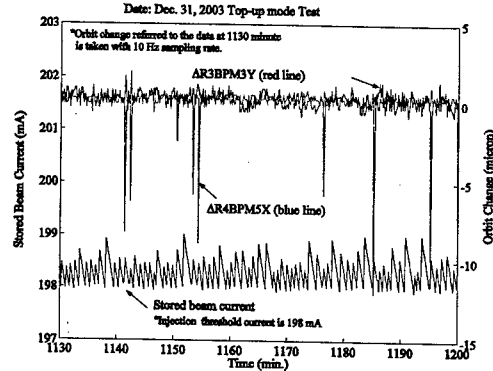
Figure 5: Top-up mode test with SWLS.

A photon beam stability indicator in one of the diagnosis beam line LSGM branch is used to study the beam stability during gap and phase scans. $\Delta I/I$ is a number of photocurrent change ratio of a wire in 256 seconds [6]. Beam current decay ratio is subtracted off. Cases with and without turning on SWLS are shown in Table 2.

Table 2: Beam quality of the lattice with and w/o SWLS for top-up mode operation.

ID Gap (Unit: mm)		$\Delta I/I$ % (LSGM)	
Status	U5/U9/EPU5.6	w/o SWLS	SWLS
Fixed Gaps	20/20/20	0.064	0.071
U5 Scan	(20−40)/20/20	0.075	0.076
U9 Scan	20/(20−40)/20	0.162	0.165
EPU5.6 Scan	20/20/(20−40)	0.653	2.207

CONCLUSION

Five insertion devices have been successfully installed in the 1.5 GeV storage ring TLS at NSRRC and provide versatile light sources for the users. Routine operations with top-up injection mode, in which ID field can be scanned during injection, have been successfully tested. The beam orbit is kept within micron level and photon beam stability is excellent during ID field scan. Four superconducting multipole wigglers are planned to put into the TLS and the beam dynamics effects are studied.

REFERENCES

[1]. C.S. Hwang, et al., EPAC02, p.2643.
[2]. Peace Chang, et al., EPAC96, p. 694.
[3]. Peace Chang, et al., PAC97, p. 3533.
[4]. G.H. Luo, et al., EPAC2K, p.651.
[5]. G.H. Luo, et al., SSRC'02, Russian, July 16-22, 2002.
[6]. C.K. Kuan, et al., "The Photon Stability Measured by a Precision Io Monitor System in the TLS", these proceedings.

MAGNETIC FIELD MEASUREMENT ON SUPERCONDUCTING MULTIPOLE WIGGLER WITH NARROW DUCT

T.C. Fan, F.Y. Lin, M.H. Huang, C.H. Chang, C.S. Hwang, NSRRC, Taiwan

Abstract

The first superconducting multipole wiggler with period length of 6.0 cm (SMPW6) of the National Synchrotron Radiation Research Center (NSRRC) is currently under construction. SMPW6 will be tested and installed at the RF cavity section of storage ring by the autumn of 2003. For quality control, the magnetic field is checked at three main phases according to the assembly process. To operate the field measurement in a narrow duct and at different temperature of duct at different phases, three small-gap measurement systems were specially designed. Not only the centerline field can be measured point-by-point but also the multi-pole field can be mapped. All the measurement systems have been carefully tested. The consideration of the measurement systems and preliminary measurement are shown in this paper.

INTRODUCTION

For a medium energy synchrotron radiation facility like NSRRC, the demand of x-ray has been increasing. After all the straight sections for insertion devices of storage ring have been occupied, NSRRC explores any possibilities to provide hard x-ray to users. NSRRC has made a superconducting wavelength shifter (SWLS), with operation field of 6T, and tested it in even the injection section [1]. Next, in the residual space of the superconducting RF (SRF) cavity straight-sections, a superconducting multipole wiggler (SMPW6) will be installed (see Fig. 1)[2]. At this residual space of only 140.56 cm for SMPW6, 28 effective poles (32 total poles) with the periodic length of 6.0 cm will be created and a 3.2 T field will be excited. The SMPW6 is a cooperative project with Wang NMR Inc., US. To control the quality carefully, the magnetic field is to be checked at three main phases according to the assembly process.

The SMPW6 is designed to operate in liquid helium. To reduce the heat load of the 4.2 K cold mass, a thermal-shielding elliptic beam-duct of 1 mm thick with 77K interception, and a vacuum barrier of 1 mm thick as thermal barrier are employed. As a result, the 12 mm cold beam gap and a cold iron pole separation of 18 mm are required. For final acceptance test, an extensive field measurement is affordable if operating at room temperature. Thus an additional flat warm duct is provided. The allowed vertical inner space is only 5.9 mm. Because of the variant measurement conditions at different phases, in terms of limited space and space temperature, three small-gap measurement systems were specially designed. Other than centerline field, the multi-pole field can be mapped as well.
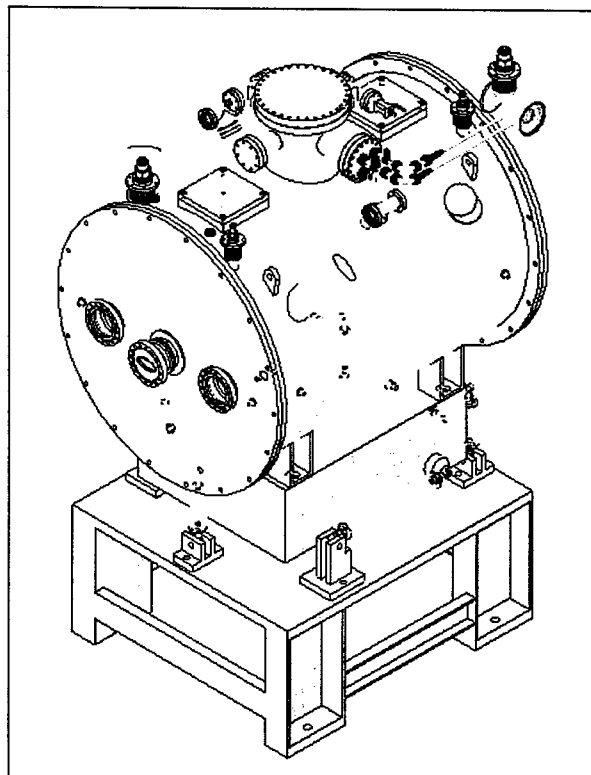
Figure 1: Schematic drawing of SMPW6.

At the first phase, a 5-pole prototype is tested at NSRRC. The newly built cryogenic plant will not be functional until the end of 2003 (actually the SWLS is cryogen-free and conduction-cooled by a 1.5-Watt GM-type cryo-cooler.). Therefore, the magnet is tested in a test tank cooled by a cryo-cooler. To operate under small heat-load budget, a measurement system featuring small-diameter pipe was proposed to provide a convenient room-temperature measurement. At this phase, the measurement is called project A.

While going to the second phase, all the magnetic poles have been fabricated and assembled. Before the magnet was enclosed into the cryostat, all the problems related to the magnet itself have to be clarified. The magnet is immersed in a dewar and a Hall probe capable of operating at liquid helium can be scanned in an easy rail. The measurement at this stage is named Project B.

At final phase, the magnet is assembled into a cryostat as a whole and an acceptance test begins. An extensive measurement is essential to characterize the magnetic performance for beam dynamics and spectrum output. A wide flat duct at room temperature is preferred. However wide duct corresponds to a big heat load. Project C covers the final measurement.

MEASUREMENT SYSTEMS

Two categories of measurement system, namely Hall probe and stretched wire, are adopted in SMPW6 certification. The former presents different transportation method at each of three phases.

Project A

A tailored stage equipped a narrow cylinder tube (referred to as endo-chamber) provides low heat-leak as well as room-temperature space for measurement sensors. The magnet is mounted in a test chamber, then vacuumed barrier and cooled to 4.5K. A flat epi-chamber connected to 70K interception to further reduce the heat load. Utilizing the endo-chamber, one can shuttle the Hall probe by a long strike x-y stage or rotate the long loop of stretched wire to measure the point field or integral field. Fig. 2 shows a cartoon of Project A.

With the mounted bellow and small x-y stage, one can level the endo-chamber and move it horizontally to scan the field. As the bellow will absorb the tremendous atmosphere pressure, the small x-y stage must be fastened well and the distortion of endo-chamber is to be cautious. The sag of endo-chamber owing to gravity needs suitable pads to compensate.
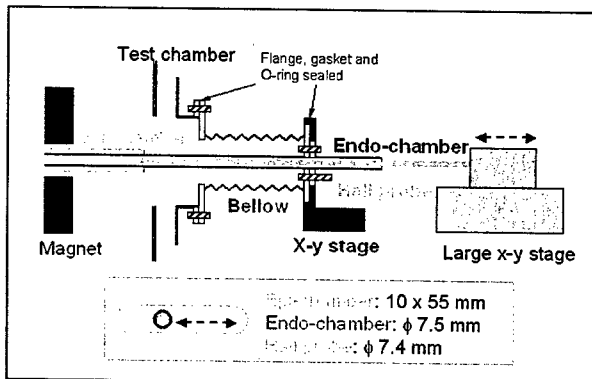
Figure 2: A cartoon of the measurement system Project A. Endo-chamber can move horizontally within the epi-chamber with the help of bellow. Large x-y stage can shuttle the Hall probe along the endo-chamber to map the field.

Project B

The easiest way to map the field of the superconducting magnet is to immerse the magnet in liquid helium of dewar and then move a crogenic Hall probe *vertically* to measure the field point-by-point. To confine the probe without transverse position error, a precise rail structure guiding the probe is equipped. A stepping motor and screw bolt provide a precise longitudinal movement. In project B, a Lake Shore probe MCA-3160-WN, featuring wide operating temperature range (1.5K to 350K), is used. To travel into a high dewar, a 60" stem is chosen. A set of 3 parallel rails provide the hall probe the field mapping along x=-20, 0 and =20 mm, so as to check the roll-off and quadrupole component. To reduce the boiling-off of the liquid helium, a transfer rail set made of FRP and radiation shielding on top of the magnet are equipped. The vertical configuration avoids the sag of horizontal hall stem. Due to low temperature, the rail bending and reduction of tolerance of space between probe head and rail have to be taken care. Fig. 3 shows the project B system under assembling and testing.
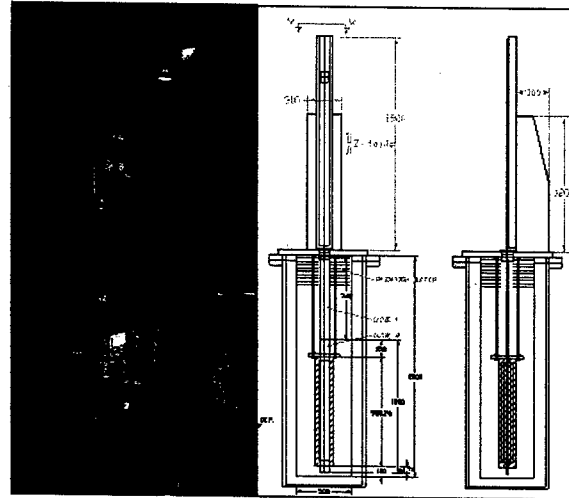
Figure 3: The measurement system Project B under assembly (left photo) and merged into dewar and core magnet (right drawing).

The preliminary measured field in vertical dewar was shown in Fig. 4 and 5. The measured field on-axis shows that the second field integral is quite good without any correction.
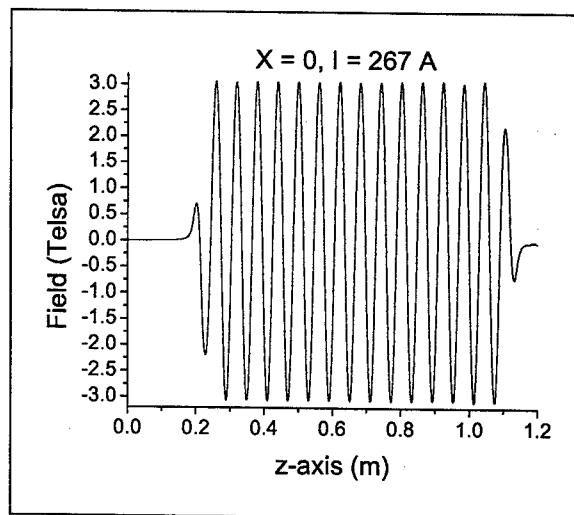
Figure 4: Magnetic field measured in Project B.
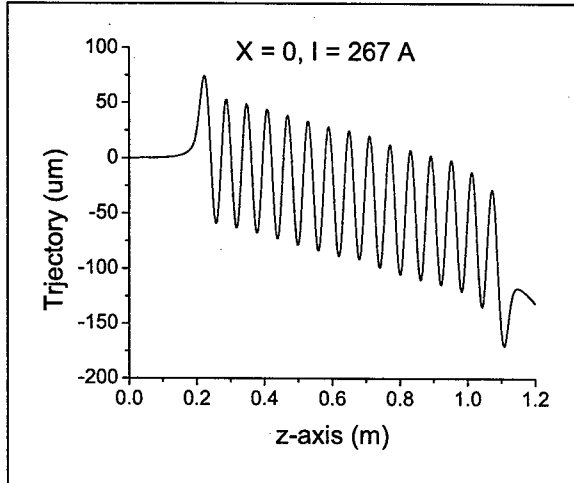
Figure 5: The centerline trajectory calculated from the second integral field of Project B.

Project C

The magnetic field measurement system is operated at room temperature at the final phase. A flat warm duct with a space of 50 mm width while 5.9 mm high is required. In such a narrow vertical space, the position of the Hall probe on the end of a thin stem is not predicable, due to the sag and the friction with the duct. Instead, a Hall probe is assembled on a taut strip of FRP tensioned by a strong bow of I-beam. The I-beam is rested on an x-y stage to map the periodical field profile point-by-point. The bow beam with I shape can facilitate the weight balance and alignment. With the help of a strong back, the moving track of the x-y stage achieves the lowest deformation. The FRP strip instead of metal one can support the on-the-fly measurement without worry of eddy current. Fig. 6 and 7 show the configuration of the Hall probe system in Project C.
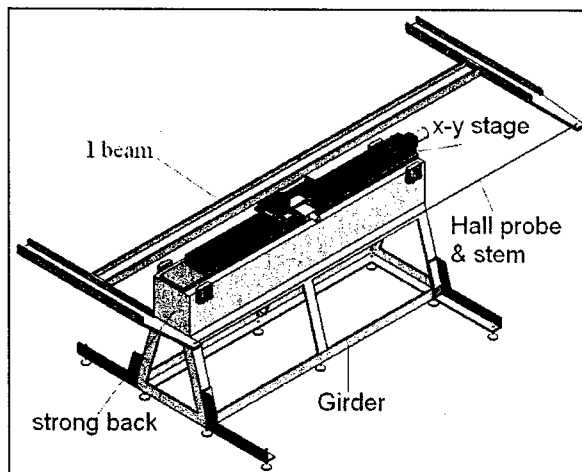
Figure 6: A cartoon of the I-beam hall probe measurement system used in Project C.

On the other hand, to fulfill the extensive measurement, the horizontal space is wide. Wide duct means big heat leak. Cryo-cooler cannot afford such

heat load and a large consumption of liquid helium is expected. Meanwhile a big temperature gradient occurred during test. A small air injection system and a Senstron YM12-4 probe with well-defined temperature coefficient are used to control the temperature range and calculate the correction value. Moreover, the water vapor will quickly condense and freeze on the inner surface of duct and shrink the space. Frequent clearance of ice is necessary during the measurement. In addition, the drift due to the bending of signal line during stage movement is well calibrated. The final reproducibility is within ± 2 Gauss.

Figure 7: I-beam system under testing.

The stretched-wire technique is also used to measure the mulipole components of 1st and 2nd integral field directly with horizontal range of ±20 mm (see Fig. 8).
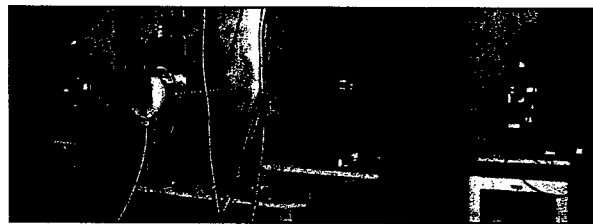
Figure 8: A stretched wire measurement system under test for Project C.

CONCLUSION

The strategy of the measurement system for SMPW6 at different phases was reported. A solution of small-gap measurement on low- temperature magnet appeared feasible. From the preliminary measurement, the SMPW6 has good magnetic performance in terms of beam dynamics.

REFERENCES

[1] C. S. Hwang, et al., IEEE Trans. Appl. Supercond., vol. 12, no. 1, 686 (2002).
[2] C. S. Hwang, et al., will be published in IEEE Trans. Appl. Supercond. (2003).

COMMISSIONING OF TWO NEW INSERTION DEVICES AT ELETTRA

D. Zangrando, L.Tosi, B. Diviacco, S. Di Mitri, C. Knapic

Sincrotrone Trieste, Trieste, Italy

Abstract

Two new insertion devices have recently been installed in the ELETTRA storage ring: a 3.5 Tesla superconducting multipole wiggler and a Figure-8 permanent magnet undulator. The first is the radiation source for a future X-ray diffraction beamline, while the second is designed to generate photons in the 5-11 eV range for inelastic UV scattering experiments. The impact of these devices on the electron beam dynamics was already studied at the design stage [1]. In this paper initial commissioning results are presented and discussed, including the measured effects on the closed orbit and tune.

SUPERCONDUCTING WIGGLER

The superconducting multipole wiggler (SCW) fabricated at Budker Institute of Nuclear Physics, BINP (Novosibirk, Russia) was successfully tested in presence of Sincrotrone Trieste personnel in August 2002. After being disassembled and delivered to ELETTRA, it was reassembled and tested again to confirm the performance measured at Novosibirsk. In November 2002 it was installed (see fig. 1) and the commissioning started.

The main parameters of the wiggler are listed in table 1. It is equipped with a special cold copper liner (20 K) to reduce the heat flux generated by the electron beam; more details about this device can be found in [2].

Table 1: Main parameters of wiggler.

Maximum field on beam axis (T)	3.5
Pole gap (mm)	16.5
Period length (mm)	64
Internal liner gap (mm)	10.7
Critical photon energy at 2 GeV (keV)	9.3
Total radiated power at 2 GeV, 100 mA (kW)	4.6
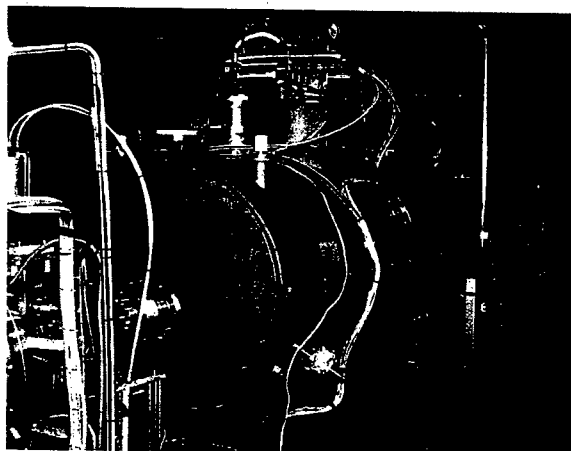
Figure 1: The SCW installed in the storage ring.

The magnet can be operated both in power mode (with the power supplies connected) and in persistent mode (power supplies disconnected). The minimum tested ramping up time from 0 to 3.5 T is about 300 seconds. The ramping down time with (without) field integral control is about 460 (300) seconds.

The liquid Helium (LHe) consumption measured at 3.5 T was 0.9 (0.5) l/h in power (persistent) mode. With the electron beam the LHe consumption increases by a large factor: at 2 (2.4) GeV with 300 (140) mA we measured a LHe consumption of 5 (1) l/h. In order to overcome this anomalous consumption, which is believed to be due to the beam interaction with the liner slots [3], the liner itself will be removed next November and replaced with a modified version.

The SCW as initially installed in the storage ring had a vertical misalignment of about 2 mm, caused by an extra force of about 7000 kN on the magnet vessel created after pumping the insulating chamber, which had not been taken into account at the design stage. The closed orbit distortion at 2 GeV before and after the realignment is shown in fig. 2. The horizontal distortion will be further reduced by recalibrating the current table [2]. With the SCW set in persistent mode at 3.5 T we measured a maximum horizontal beam (angle) position variation of 20 μm (1 μrad) and 2 μm and 5 μrad in the vertical plane in an hour of operation. These values also include the machine's thermal drift.
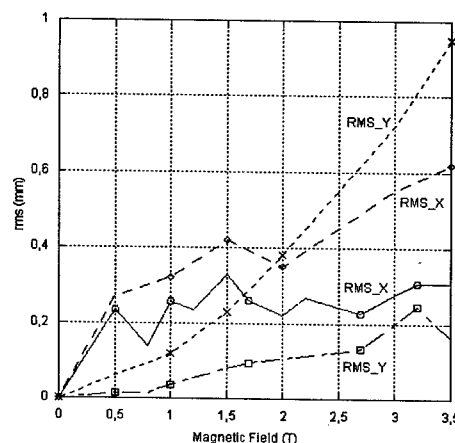
Figure 2: Closed orbit distortion (RMS) as a function of the magnetic field (dotted line are measured with a vertical misalignment of 2 mm).
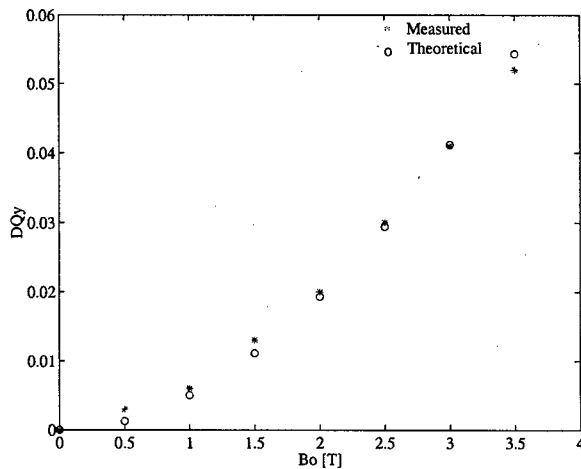
Figure 3: Measured and theoretical vertical tune shift as a function of magnetic field at 2 GeV.

Figure 3 shows the good agreement between the theoretical and measured vertical tune shifts as a function of the magnetic field at 2.0 GeV. In the horizontal plane the tune shift is only 0.003 at 3.5 T, as expected.

Dynamic aperture and lifetime variation could not be measured at this stage, but will be measured before the replacement of the liner.

FIGURE-8 UNDULATOR

Linear effects

A twin Figure-8 undulator has recently been constructed and installed in the storage ring. Details on its design and characteristics can be found in [4,5]. Following assembly, the magnetic field properties were measured and found in good agreement with the design parameters. Table 2 shows the measured peak field intensity, optical phase error and residual normal and skew quadrupole for three representative gaps (average values of the two undulator modules). The small phase error implies that the spectral intensity will be close to the theoretical limit, and the low quadrupole content shows that no significant perturbation to the linear beam dynamics will be introduced.

The most important parameter governing the interaction with the electron beam is therefore the field roll-off, which determines the undulator focussing potential. The measured transverse field variation was found to be in excellent agreement with that predicted by 3D field calculations, as can be seen in figure 4.

Table 2: Main measured magnetic field parameters.

Gap (mm)	Bxo (T)	Byo (T)	σ_Φ (°)	Q_N (G)	Q_S (G)
19	0.14	0.75	1.5	-11	26
30	0.13	0.56	1.5	3	11
50	0.12	0.33	1.7	0	-23
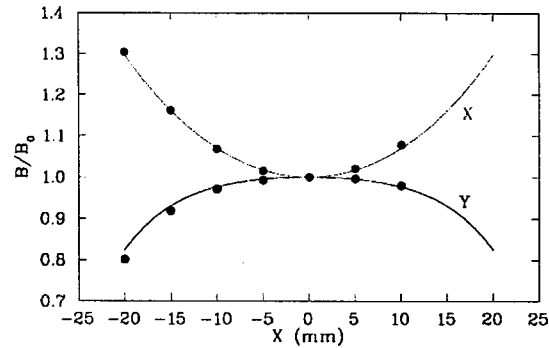
Figure 4: Measured (dots) and computed (solid line) transverse field distributions at minimum gap.

Based on the above results, we expect the undulator to behave as an ideal device. This is demonstrated in figure 5, where the measured tune shift is compared with that predicted from the ideal magnetic field. The effect is fairly small, and of the same order of that of the other conventional undulators in operation at ELETTRA.
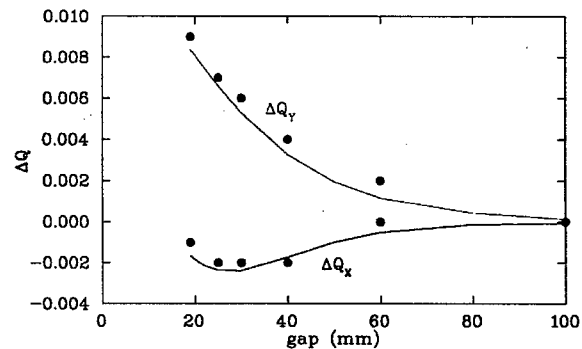
Figure 5: Measured (dots) and computed (lines) tune shifts as a function of the gap for one undulator segment at 2 GeV (black=horizontal plane, red=vertical).

Non linear effects

Due to the temporary absence of scrapers in the machine, it was not possible to confirm the dynamic aperture studies which had been carried out prior to the construction of the devices [1]. In order to study non-linear effects, phase space measurements have been performed at 2.0 GeV with the Figure-8 undulator set to minimum gap. Turn by turn data was acquired with the transverse multibunch feedback system [6] which uses only one beam position monitor. While the horizontal motion was excited using the injection kickers, the vertical one was induced with the vertical kicker of the system in antidamping mode. The method used to extract the conjugate momenta from the data is the one proposed in ref. [7], in which a Hilbert transformation is performed on the beam positions. This transformation introduces a 90° phase rotation in the data, allowing the representation of the motion in the two conjugate variables:

$$x = (\beta \cdot J)^{1/2} \cos(\phi) \quad \text{and} \quad p_x = (\beta \cdot J)^{1/2} \sin(\phi).$$

A characteristic of non-linearities is the decoherence of particles within a bunch which results in the damping of the centre of mass motion with a rate proportional to the strength of the non-linearities [8]. In phase space this is reflected as a collapse of the bunch centre of mass towards the origin [9]. Fig. 6 and 7 show comparisons of the vertical phase spaces when the device is open and when it is closed for two different values of the vertical tune (8.20 and 8.25). As the tune satisfies a resonance condition, branches which spiral towards the centre appear. In both measurements it can be clearly seen that the collapse in the phase spaces occurs more rapidly in the case in which the undulator is closed. Fig. 8 shows the comparison of the horizontal phase spaces for a horizontal tune of 14.250. Whereas the branches are clearly seen when the device is closed, those when it is open are hidden by the longer time required to collapse and the number of turns. The number of turns required to collapse with the device closed have been found to be 0.67 (horizontally) and 0.5 (vertically) times of those when it is open.

Figure 8: Comparison of the horizontal phase spaces with the undulator open (top) and closed (bottom) with Q_x=14.25.

Theoretical computations of the amplitude dependent tune shift coefficients as well as the chromaticities with the distorted optics due to the undulator revealed a too small variation to explain the difference in the collapse rate. Thus, the intrinsic non-linearities of the device may be the cause.

Figure 6: Comparison of the vertical phase spaces with the undulator open (top) and closed (bottom) with $Q_y = 8.20$.
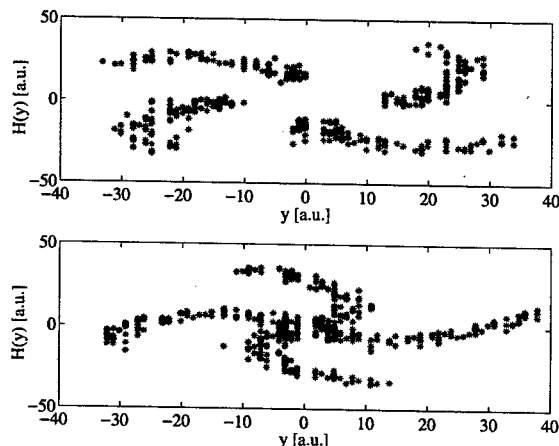
Figure 7: As figure 6 but with $Q_y = 8.25$.

REFERENCES

[1] L.Tosi and R. P. Walker, "Dynamic Aperture Simulations for a Figure-8 Undulator and a Superconducting Wiggler", Sincrotrone Trieste Internal Note ST/M-TN-00/09, 2000.

[2] A.Batrakov et al., "A Superconducting 3.5 T Multipole Wiggler for the ELETTRA Storage Ring", Proc. EPAC 2002, pag. 2634.

[3] N.Mezentsev, private communication.

[4] B.Diviacco et al., "New Insertion Devices for ELETTRA", Proc. PAC 2001, pag. 2468.

[5] Diviacco et al., "Design of a Figure-8 Undulator foe ELETTRA", Proc. EPAC 2002, pag. 2610.

[6] Bulfone et al., "Operation of the Digital Multibunch Feedback Systems at Elettra", this conference.

[7] R.T.Burgess, "The Hilbert Transform in tracking, mapping and multiturn measurements", SL-Note-99-046 AP, CERN, 1999.

[8] L.Tosi, V. Smaluk, E. Karantzoulis, "Landau damping via the harmonic sextupole", to be published on Phys. Rev. Special Topics – Accelerator and Beams.

[9] S. Di Mitri, "Dinamica Trasversa di Singola Particella in Presenza di Non-linearita' Sestupolari nell'Acceleratore Circolare DAFNE", to be published.

CAMD LOW BETA CONFIGURATION FOR THE 7 TESLA WIGGLER

M.Fedurin[#], B.Craft[##], G.Vignola, CAMD LSU, Baton Rouge, LA 70806, USA

Abstract

The photon beam from 7 Tesla wavelength shifter wiggler is available since April, 2002 for Protein Crystallography beamline of CAMD storage ring, operating at 1.3GeV. To improve the property of the photon beam from the wiggler, a low beta function configuration in the wiggler straight section has been developed. Different electron beam optics configurations for wiggler operations are described. Response matrix analysis and tune derivatives tools were applied for low beta configuration studies.

7 TESLA WIGGLER COMMISSIONING

The CAMD storage ring magnetic lattice is a 4 period Chasman-Green type: the optical functions are shown in Figure 1. The electron beam is accumulated from a Linac at 180 MeV and then accelerated at 1.3 GeV, which is the normal operating energy, even tough the ring can reach 1.5 GeV. The 7 Tesla wiggler [1] was installed in a zero dispersion straight in September 1998. A magnetic field of 6.5 Tesla was achieved at that time, but at an operating energy of 1.5 GeV. The wiggler field was ramped from zero to the required level of 7 TESLA at top energy. The focusing effect of the wiggler was compensated with 2 families of q-pole (QF & QD) by keeping the betatron tunes constant. Later on, the currents of the 4 q-poles in the wiggler straight section (QFW & QDW) were shunted to measure the wiggler perturbation on the optics and to correct the betatron tunes. Due to the current limitation in the shunts, the optics perturbation was fully compensated up to 5 Tesla. The field level of 7 Tesla was empirically reached in winter 2002, by using the 4 families of q-poles to correct the tunes.

Table 1: Wiggler normalized gradients, in vertical and horizontal planes, at various magnetic field.

Magnetic field (Tesla)	Wiggler focusing	
	Ky (m-2)	Kx (m-2)
2	0.0071	0.0087
3	0.0104	0.0211
4	0.0316	0.0211
5	0.064	0.0146
6	0.110	-0.0035
7	0.169	-0.030

Figure 1 Standard optical functions for half ring. Solid and dashed lines are the horizontal and vertical beta functions respectively, while the points represent the dispersion function. All the scales are in meters.

This achievement allowed to evaluate the wiggler normalized gradients (Ky and Kx) by using tune response matrix analysis. Ky and Kx are listed in Table 1, while the perturbed optical functions are shown in Figure 2.
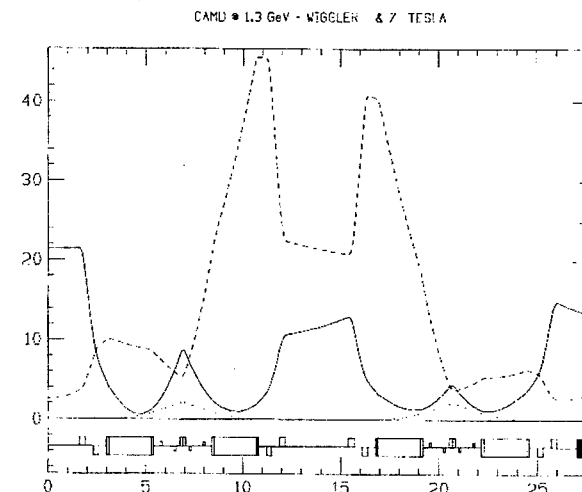
Figure 2 Optical functions for half ring with the focusing effect of the wiggler uncorrected. Black spot in the right is the wiggler location.

[#]fedurin@lsu.edu
[##]Deceased
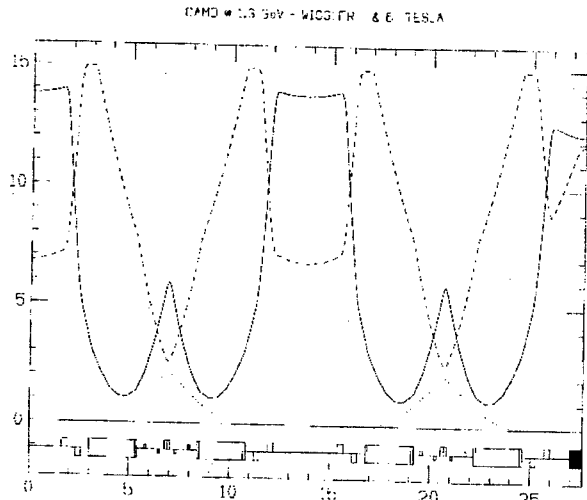
Figure 3 Shunted configuration. Vertical beta function increases in the wiggler straight

Figure 5. Low beta configuration with non zero η-function. No wiggler field in this plot

OPTICS MATCHING

There are 3 ways to compensate the optical functions perturbed by the wiggler, by keeping the same betatron tunes:

- The currents of QFW and QDW, in the wiggler straight section, are shunted (decreased) [2]: the vertical beta function increase in the wiggler straight section (see Figure 3);
- Low beta configuration in the wiggler straight section (see Figure 4). In this case it is necessary to substantially increase the currents of QFW & QDW.
- Low beta configuration in the wiggler straight section with non-zero dispersion in the straights (see Figure 5).

In order to satisfy the wiggler synchrotron light users request all these solutions were implemented and commissioned. We summarize in the following the main results of the commissioning.

LOW BETA STUDIES

The wiggler commissioning was based on the adoption of an experimental model of CAMD storage ring, which reproduces pretty well the variation of the betatron tunes as function of the q-pole strengths, and on the use of the response matrix analysis technique [2] in the vertical plane. In CAMD the vertical trims are integrated in the defocusing (QD) and achromatic(QA) quadrupoles, while the BPM (20) are located near each quadrupole around the ring. Figure 6 and Figure 7 show the BPM signal versus trims kick for the 4-fold Chasman-Green standard lattice as given by the model and as measured. Let us point out that what is important, when one compares Figure 6 and Figure 7 is the relative shape of the BPM signal and not the absolute value.

The BPM are organized in families with the same amplitude as predicted by the model. To make the wiggler commissioning easier we measured also the tune response matrix and built the "beta-knob". This means varying four variables (the strength of QF, QD, QFW, QDW) and keeping the vertical and horizontal betatron

Figure 4. Low beta with zero η-function
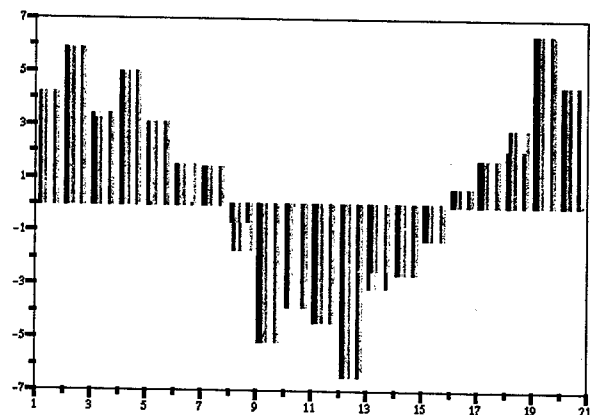
Figure 6 Theoretical response matrix for the standard lattice. 20 PUE reading organized in coloured 8 trims families

1054
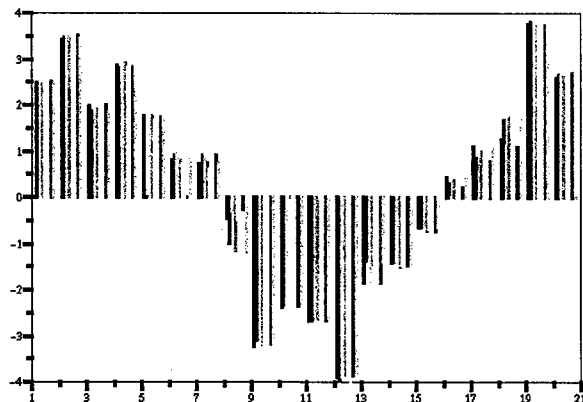
Figure 7 Measured response matrix for the standard lattice

tunes constant. Under the condition of constant tunes we have 2 free variables that we use to find the best match between theoretical and experimental response matrix.

Low beta with zero dispersion function.

This configuration was commissioned up to 7 Tesla, with good shape of beta functions. The beam lifetime was 20 hrs at 6 Tesla and dropped to 6 hrs at 7 Tesla.

Due to the poor beam lifetime at 7 Tesla we decided to investigate the next solution with non zero dispersion.

Low beta with non zero dispersion function.

The configuration with dispersion in "dispersion free" straight sections was implemented (Figure 5). In this configuration the beam equilibrium emittance is a factor 2 lower than the emittance in the standard configuration, therefore the beam emittance grow due to the wiggler is compensated by this emittance reduction.

Figure 8 show the theoretical response matrix while in Figure 9 and Figure 10 the measured response matrix are plotted.

This configuration, with the wiggler field at 7 Tesla, is routinely in operation with a beam lifetime of 30 hrs at 70 mA of stored current.
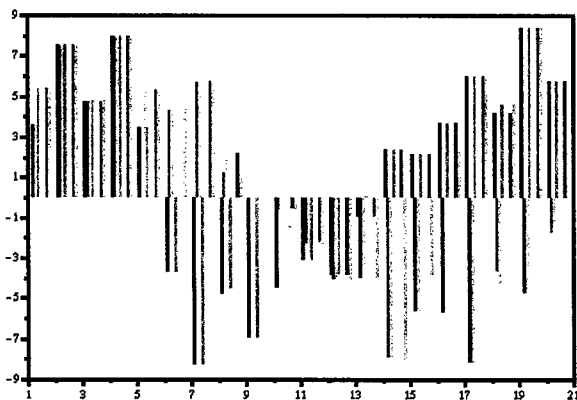
Figure 8. Theoretical response matrix of non zero dispersion function low beta configuration.
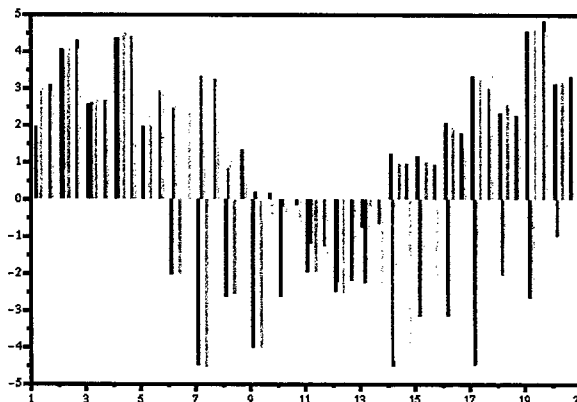
Figure 9. Measured response matrix of non zero dispersion function low beta configuration without wiggler.

This configuration still need a refinement of the wiggler model which takes in account the dispersive part and a measurement of the beam emittance.

CONCLUSION

A low-beta optics configuration has been designed and implemented at CAMD to routinely operate a 7 Tesla wiggler at 1.3 GeV.

The commissioning has been carried out by the technique of vertical response matrix analysis together with tunes measurement ("beta-knob")

REFERENCES

[1] Borovikov V.M. and all "Superconducting 7 Tesla Wiggler for LSU CAMD", Journal of Synchrotron Radiation, Vol.5, Part3, pp440-442(1998)

[2] B.Craft "A novel SC Wiggler for PX" http://ssils.ssrc.ac.cn/symposium/Insertion_Devices.ht ml (2001)
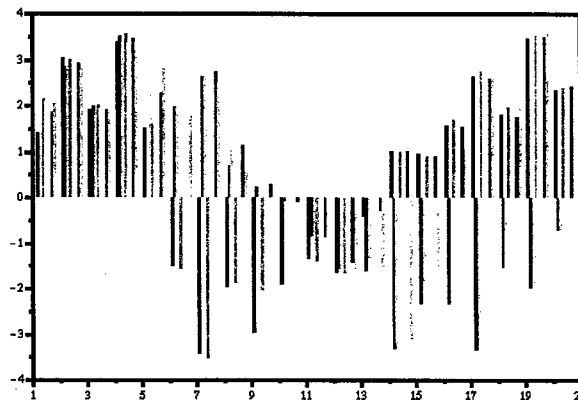
Figure 10 Measured response matrix of non zero dispersion function low beta configuration with the wiggler at 7 Tesla.

PERIOD LENGTH OPTIMIZATION FOR THE LNLS UNDULATOR

X.R. Resende*, LNLS, Campinas, SP 13083-970, Brazil

Abstract

The aim of the present work is to find the optimum magnetic period length for the LNLS elliptically polarizing undulator (EPU). An objective function for the radiation which takes into consideration both intensity and polarization over the energy range desired by LNLS users is proposed and used in the optimization calculation. Results of such calculation are presented and discussed after a review of EPUs and their radiation characteristics.

ELLIPTICALLY POLARIZING UNDULATORS

APPLE-II Undulator

Planar undulators can only produce on-axis vertical fields that accelerate electrons that in turn radiate light with fixed linear polarization. If a variably and/or elliptically-polarized radiation is sought then the simple design of two parallel Halbach cassettes has to be abandoned. Many designs have been proposed in order to realize elliptical fields. A particularly optimized undulator that presents horizontal field with high amplitude was proposed by S.Sasaki[1]. Sasaki devised an EPU, named APPLE-II in the literature, which is composed of four parallel Halbach cassettes, one in each of the four quadrants in the transverse $x - z$ plane. Sasaki's undulator can be thought of as a combina-
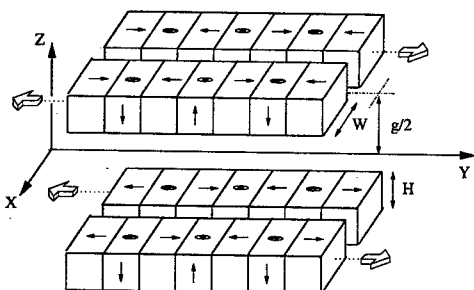
Figure 1: APPLE-2 undulator with its four Halbach cassettes. Diagonally opposed cassettes are fixed relative to each other but move longitudinally with respect to the other two cassettes. In the picture, the undulator is shown in the phase $\phi = \pi/2$

tion of two other undulators, each made of two diagonally-opposed cassettes. These two undulators create on-axis fields with the same profile, both the horizontal and vertical components. But while the vertical field components from the undulators are in phase, the horizontal field components

are 180-degree out of phase. In this way, by shifting longitudinally the undulators with respect to each other, it is possible to create elliptical magnetic fields[1]:

$$B_x = B_x^{max}(g/\lambda) \cos \phi \sin qy = B_{x0} \sin qy, \quad (1)$$
$$B_z = B_z^{max}(g/\lambda) \sin \phi \cos qy = B_{z0} \cos qy,$$

where $\phi = \pi \delta l/\lambda$ and $q = 2\pi/\lambda$. The shift between cassettes δl is relative to an undulator configuration in which the vertical field is zero. By symmetry the longitudinal component B_y vanishes for a period undulator. The maximum amplitudes B_x^{max} and B_z^{max} of the field components depend on undulator parameters: gap g between upper and lower cassettes, period length λ, transverse dimensions and remanent field of the permanent magnets (PMs). The plot in Fig.[2] shows this dependence on the magnetic gap. Note from the plot that, since the ratio B_x^{max}/B_z^{max} varies with g/λ, whenever the gap is changed in order to tune the energy peaks of radiation, the relative cassette phase ϕ has to be adjusted as well, if a specific field ellipticity is to be kept.
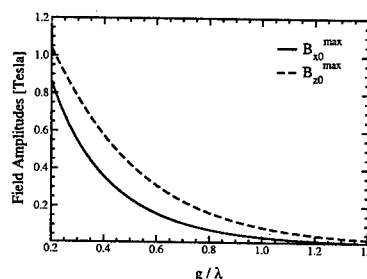
Figure 2: Vertical and Horizontal maximum field amplitudes as a function of the gap for an APPLE-II undulator with $\lambda = 50$ mm. Permanent magnets have transversal dimensions W = 40 mm, H = 40 mm and remanent magnetization $B_r = 1.2$ T. Separation between front and back cassettes is 1 mm.

UNDULATOR RADIATION OF A ZERO EMITTANCE E-BEAM

As electrons traverse the undulator they experience the magnetic field of Eq.[1] and, for an arbitrary EPU phase ϕ, they start moving in a helical trajectory. The equations of motion can be expanded in the parameter $1/\gamma$ and solved analytically up to second order. Such calculated trajectory can then be used to evaluate the radiation characteristics of the EPU[2]. In the Radiation Regime, the photon flux

expression is given by

$$\frac{dN}{dt} = n_0\gamma^2 N_p^2 \sum_{k=1,3,\ldots} \left(\frac{kK}{1+K^2/2}\right)^2 g_k^2(\omega)|\mathbf{F}_k|^2. \quad (2)$$

This flux is proportional to both the number of undulator periods N_p and the e-beam energy γ squared. This holds true because the approximative assumption of small solid angle Ω_0 for the observation window was used ($\Omega_0\gamma^2 \ll \pi$). In the expression for the flux, $n_0 = (I/e)\alpha_f(\Delta\omega/\omega)\Omega_0$ is a quantity with dimension of particle flux that is proportional do the electron flux, fine-structure constant, frequency integration window and solid angle of the observation window. The complex vector $\mathbf{F}_k = \sin\phi_0(J_n - J_p)(i\mathbf{x}) + \cos\phi_0(J_n + J_p)\mathbf{z}$ contains contributions from both horizontal and vertical oscillating electrical field components. $J_n = J_{(k-1)/2}(u)$ and $J_p = J_{(k+1)/2}(u)$ are integer-order bessel functions of the first kind evaluated at $u = kK^2\cos 2\phi_0/(4+2K^2)$, where K is the undulator parameter. For an arbitrary EPU phase, $\cos^2\phi_0 \equiv B_{x0}^2/(B_{x0}^2+B_{z0}^2)$ is neither zero nor one and the two contributions for $\mathbf{F}_k$ lead to elliptically polarized radiation on axis. When the EPU cassette phase is set in a way that the amplitudes B_{x0} and B_{z0} of horizontal and vertical field components are equal, the argument u of the bessel functions vanishes and only the first harmonic $k = 1$ contributes to the radiation. All higher harmonics are absent when the EPU operates with circularly polarized light.

The complex vector $\mathbf{F}_k$ can be expanded in any vector basis. In particular, using the basis $\sqrt{2}\mathbf{e}_+ = \mathbf{x} + i\mathbf{z}$ and $\mathbf{e}_- = \mathbf{e}_+^*$, it is possible to decompose the expression $|\mathbf{F}_k|^2$ in Eq.[2] into right-handed and left-handed circularly polarized radiation contributions, dN^+/dt and dN^-/dt respectively. For magnetic dichroism experiments, where pure circularly polarized light is needed, a figure of merit can be defined as the normalized different between left and right circularly polarized radiation components: $p_k \equiv (dN^+/dt - dN^-/dt)/(dN^+/dt + dN^-/dt)$. This expression can be explicitly evaluated from $\mathbf{F}_k$:

$$p_k = \frac{\sin 2\phi_0(J_n^2 - J_p^2)}{\sin^2\phi_0(J_n - J_p)^2 + \cos^2\phi_0(J_n + J_p)^2} \quad (3)$$

OBJECTIVE FUNCTION

There are two polarization cases of radiation that users may be interested in: horizontal and circular. These two cases can be realized with the EPU that is going to be built at LNLS by setting its phase ϕ appropriately. Energy ranges which can be covered with radiation harmonics depend on the choice of period length λ. For each energy and polarization state there is a unique λ that maximizes photon flux. Moreover, users of the undulator radiation are interested in a broad energy range, from absorption lines of elements Carbon (286 eV), Nitrogen (400 eV) and Oxygen (525 eV) (linear light polarization) to L-edge transitions in metals like Manganese ($\sim$ 640 eV), Iron ($\sim$ 710
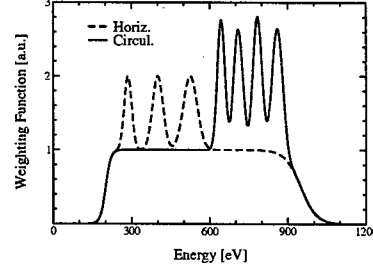
Figure 3: Weighting functions for horizontally (dash lines) and for circularly (solid lines) polarized light cases.

eV), Cobalt ($\sim$ 780 eV) and Nickel ($\sim$ 860 eV), for circular magnetic dichroism experiments. As a consequence, the choice of period length is not obvious and a compromise between radiation output for different energies has to be achieved. The most generic method that can take into account this compromise is one in which a weighting number is assigned to each energy-polarization state. An objective function then is defined as the summation of the radiation flux at each energy multiplied by its corresponding weighting number. The optimized period length comes out of maximizing this function.

$$F(\lambda) = \int d\epsilon \left\{ W_H(\epsilon)\frac{dN_H}{dt} + W_C(\epsilon)\frac{dN_C}{dt} \right\} \quad (4)$$

It is important to realize that the condition of 100% circularly polarized light for higher energies can not be attained since the first order harmonic is the only term that exists. In order to cover the L-edge transition lines of metals the ideal unit polarization ratio has to be abandoned and elliptically polarized light from the third and fifth harmonics has to be used instead. This consideration implies that, for the case of circular radiation, the quantity that enters the objective function has to deal with the compromise between polarization ratio and photon flux. For such quantity the product of the flux and the polarization ratio can be chosen, as it appears in Eq.[4]. The weighting functions picked for both polarization cases are plotted in Fig.[3].

OPTIMIZATION OF OBJECTIVE FUNCTION

The algorithm for evaluating the integral in Eq.[4] consists in calculating maximum flux for each of the two polarization cases, over all energies, for λ values. The calculation for the horizontal case is simple: for a given λ and energy ϵ, check for which harmonic bands this energy lies within its limits, calculate the photon flux for those bands, pick the one with higher value and add its contribution to the integral over energy. The case of elliptically polarized radiation is more elaborate because for each λ and photon energy the optimum EPU cassette phase that maximizes the figure if merit has to be calculated. Given λ and ϵ, the optimum phase is calculated for each harmonic. The figure of

merit for each band is evaluated and the biggest one is chosen and used in Eq.[4]. Table[1] lists all parameters used in

Table 1: Parameters used in the calculation for the period length optimization

EPU	PM width	$W = 40$ mm
	PM height	$H = 40$ mm
	Min. gap	$g_{min} = 23$ mm
	Length	$L = 2900$ mm
	PM magnetization	$B_r = 1.2$ Tesla
E-beam	Energy	$E = 1.37$ GeV
	Emittance	$\epsilon = 0$
Observation Window	Opening angle	$\theta = 0.2$ mrad

the optimization just described and Fig.[4] shows the result of the optimization calculation. The contributions from the horizontal and circular cases to the objective function are plotted separately, as well as the objective function itself. The optimum period length for the undulator turned out to be 48 mm. Fig.[5] shows the flux for the horizontally po-
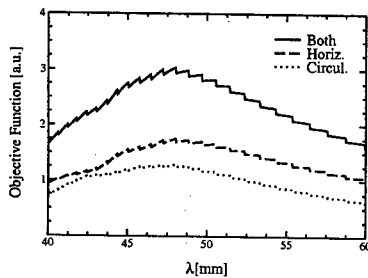
Figure 4: Weighting functions for horizontally (dashed lines) and for circularly (solid lines) polarized light cases.

larized radiation case with optimum λ. Three bands corresponding to the first, third and fifth harmonics can be identifies in the plot. Since the vertical magnetic field for the minimum undulator gap is such that $K > 2$, there are no gaps between the bands. In Fig.[6] the on-axis radiation
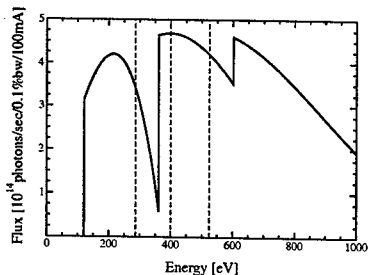
Figure 5: The three vertical dash lines correspond to transition energies of Carbon (286 eV), Nitrogen (400 eV) and Oxygen (525 eV).

flux and polarization ratio are plotted as functions of photon energy for the elliptical case. For energies covered by the first harmonic it is apparent from the plot that the polarization ratio is one and therefore the radiation is 100%
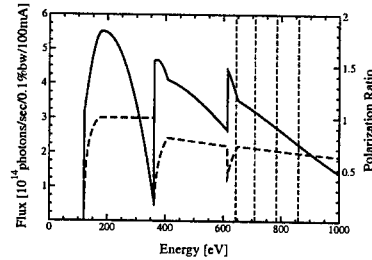
Figure 6: The solid curve is the radiation flux and the dash curve is the polarization ratio. Vertical lines correspond, in energy order respectively, to transitions in metals: Mn, Fe, Co, Ni.

circularly polarized. This is shown in the plot for energies above 183 eV. Energies below this value can not be attained with perfectly circular polarization because the maximum K value with minimum gap is not high enough. As for the third and fifth harmonic bands, the undulator phase that maximizes the figure of merit does not correspond to a circular polarization state and it is energy-dependent over the whole energy interval of the bands.

FINAL REMARKS AND ACKNOWLEDGEMENTS

We have optimized the undulator period length by maximizing an objective function that takes into account the energy range and the polarization states of radiation that are relevant for the beamline users. The optimum value was 48mm. It was assumed that the solid angle related to the observation window is much smaller than the opening angle of the radiation. This assumption overestimates the photon flux, specially for higher harmonics and higher energies. A proper convolution integral of the radiation over the observation window has to be implemented for a more accurate calculation of the photon flux. On the same footing the beam emittance of the storage ring should be considered. The lower energy limits of the harmonic bands are expressed in terms of the maximum field amplitudes for minimum undulator gap. In this work the field amplitudes were calculated assuming a unit permeability for the permanent magnet blocks. For typical NdFeB magnets this permeability is slight above one. Demagnetization effects can lead to somewhat smaller field amplitudes and consequently they can change the lower limits of the harmonic bands. Finally I would like to thank Pedro F. Tavares, G. Tosin and A.R.B. de Castro for fruitful discussions on the subject of e-beam dynamics and radiation characteristics of undulators.

REFERENCES

[1] S. Sasaki, "Analyses for a Planar Variably-polarizing Undulator", Nucl. Instr. and Meth. A **347**, 83 (1994).

[2] H. Wiedemann, "Particle Accelerator Physics", Vol. I, 2nd ed., Springer-Verlag, (1999).

STUDIES ON SEXTUPOLE COMPONENTS GENERATED BY EDDY CURRENTS IN THE RAPID CYCLING MEDICAL SYNCHROTRON *

J. Cardona, Dan T. Abell, S. Peggs, BNL, Upton, NY , USA

Abstract

The Rapid Cycling Medical Synchrotron is a second generation medical accelerator that it has been designed with a repetition frequency of 30 Hz. This repetition frequency is far above the typical repetition frequency used in medical accelerators. An elliptical beam pipe has been chosen for the RCMS design in order to win as much physical aperture as possible while keeping the magnet dimensions as small as possible. Rapid Cycling induces Eddy current in the magnets. Eddy currents and elliptical beam pipes generate sextupole components that might be neccesary to consider. In this paper, the effects of these sextupoles components are evaluated, first by looking at the phase space of a bunch of particles that has been tracked for 62530 turns, and also by evaluating the dynamical aperture of the accelerator. The effect of the sextupoles component in the tuneshift is also evaluated.

First results obtained with Marylie show that the width of a phase space ellipse of a bunch of particles is slightly affected by the sextupoles due to the Eddy currents.

INTRODUCTION

The RCMS is a second generation proton therapy synchrotron offering more flexible performance in a simpler lighter and more robust implementation (see for example [1] or [2]).

The RCMS will reduce the typical treatment time and at the same time will reduce the risk of dumping a large amount of radiation into the patient. All of the above is possible thanks to the 4 design choices of the RCMS: strong focusing, rapid cycling, fast extraction, and 7 MeV energy injection.

One of the challenging aspects of the RCMS is its fast repetition frequency of 30 Hz. Due to the elliptical shape of the beam pipe chosen for the RCMS, the induced Eddy currents at that repetition frequency might induce significant sextupole components in the beam.

The effect of the induced sextupoles in the tunes and the dynamical aperture are studied in this paper. The ultimate goal of these studies is to determine whether the RCMS would require sextupole correctors or not.

MAGNETIC MULTIPOLES COMPONENTS GENERATED BY EDDY CURRENTS

Eddy currents in the vacuum chamber induce magnetic multipole components in the beam. When the chamber is between iron poles such multipole components are [3]:

$$b_n + ia_n = \frac{\mu_0 \sigma h \dot{B}_0}{2\pi n! B_0} \left(\frac{\pi}{2g}\right)^{n+1} \int_{v.c.} x\left(\alpha_n + \beta_n\right) ds, \quad (1)$$

where σ, h, and g are the conductivity, thickness and diameter of the beam pipe respectively, and $\dot{B}_0$ and B_0 are the rate of variation of the magnetic field and the magnetic field itself.

The coefficients α_n and β_n can be found analytically and for the case of the lower non linear component (sextupoles) those coefficients are given by:

$$\alpha_2 = -2 \frac{\tanh(-\frac{\pi z_c^*}{2g})}{\left(\cosh(-\frac{\pi z_c}{2g})\right)^2},$$

$$\hfill (2)$$

$$\beta_2 = 2 \frac{\coth(-\frac{\pi z_c^*}{2g})}{\left(\sinh(-\frac{\pi z_c}{2g})\right)^2},$$

where $z_c = x_c + i y_c$ is an arbitrary position in the vacuum chamber walls. The sextupoles components can now be found from Eq. 1 by numerical integration. Values of the b_2 have been estimated in reference [3] for different beam pipe shapes and sizes. The corresponding values for the elliptical beam pipe of the RCMS can be quickly estimated from the tabulated values in reference [3] since b_2 scale either proportional or inversely proportional with most of the parameters involved in the calculation. Using the RCMS parameters:

$$
\begin{aligned}
a &= 3 cm \\
b &= 1.5 cm, \\
h &= 0.64 mm, \\
\sigma^{-1} &= 1.25 \mu\Omega m, \\
\dot{B}/B &= 188.49/s,
\end{aligned}
$$

the sextupole strength induced in the body of the main dipole of the synchrotron ring is 0.687 $\frac{T}{m^2}$ or equivalently an integrated sextupole strength of 0.522 $\frac{T}{m}$.

MARYLIE SIMULATIONS

In order to evaluate the effect of the sextupole component in the beam, particularly dynamic aperture and

tune footprints, particles were tracked with the software Marylie [4]. Marylie uses a "map" that translate the initial phase space coordinates into the corresponding phase space coordinates at the end of the ring. Simulation of the particles going through many turns are done by successively applying the mentioned maps.

Maps used by Marylie are built with the so called Lie transformations (see for example [5], [6]). The importance of the use of Lie transformations in the construction of maps for tracking particles resides in the concept of symplecticity. Physical systems that are described by Hamiltonian flows must comply with the symplecticity condition. Since orbits of charged particle are well described by Hamiltonian flows the maps derived from such Hamiltonian must be symplectic. This is guarantee if Lie transformations are used to construct such maps. If the conventional Taylor expansions are used to construct the maps instead, such maps could not be symplectic and unphysical effects can appear when tracking simulations are done with those maps with a large number of turns.

Lattice Preparation and Main Dipole Splitting

The original design of the lattice was done in the simulation program MAD [7]. Most of the elements and commands used in MAD have their equivalent in Marylie. However, neither MAD neither Marylie has built in elements that allow to put sextupole components in the dipoles. In order to circumvent this problem, it was neccesary to divide the main dipoles and place thin multipoles at the divisions to simulate the effect of the sextupoles. The main body of the divided magnet consist then of sector bends with multipoles located at every common point between the sector bends (see Fig. 1). Since the main dipoles of the ring are combined function magnets (dipole and quadrupole at the same time) the thin multipoles are also used to introduce the required quadrupole components. The number of divisions in the dipole is determined by how
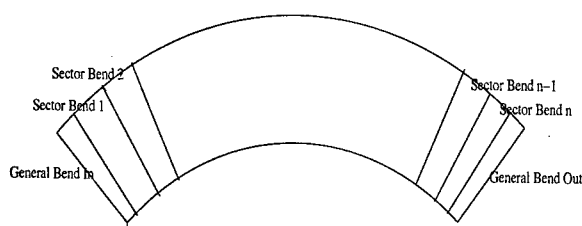
Figure 1: The main dipoles are divided in n sector bends and the multipolar elements are inserted between them. The edges of the magnet are carefully modeled with general bending magnets that allow individual pole phase rotation of the faces of the magnet. Fringe fields in the edge are also added.

much the resultant map change when the number of divisions changes. Allowing a change of 0.01% the number of division needed turn out to be 1984. Since the magnets has been designed with pole phase rotations special care has to

be taken at the edge of the magnets. The edges are built with maps that represent magnets with pole phase rotation and maps that represent fringe fields in sector bends.

Once the dipoles have been appropriately divided and the whole lattice has been written in terms of Marylie elements it is neccesary to make some comparisons with MAD outputs like tunes and lattice functions.

Comparison between the tunes given by Marylie and MAD lead to small differences that start to be evident in the second significant figure. Since the tunes are one of the most determinant parameters in tracking simulations the quadrupole components of the dipole magnets were slightly re-tuned until it was possible to achieve an agreement between the MAD and Marylie tunes of at least 6 significant figures. The beta functions produced by the two simulations programs were also compared and differences below 1% were found.

Effect of the Sextupole Components on the Dynamic Aperture of the RCMS Ring

Before doing the tracking simulations neccesary to determine the dynamic aperture of the ring it is convenient to determine the effect of the sextupole in the phase space ellipses. Extensive tracking simulations were done in Marylie for this purpose. In particular, the final distribution of particles on an initial 4D 2-torus distribution for different sextupole strengths was studied (see Fig. 2). Fig. 2 shows some growth and distorsion of the the phase space ellipses when the strength of the sextupole is increased. The vertical phase space ellipses (no shown) also show some thickness growth but is smaller than for the horizontal case. Similarly, studies done with negative sextupole strengths showed that the thickness growth of the ellipses were smaller than for positive sextupole strengths. Having
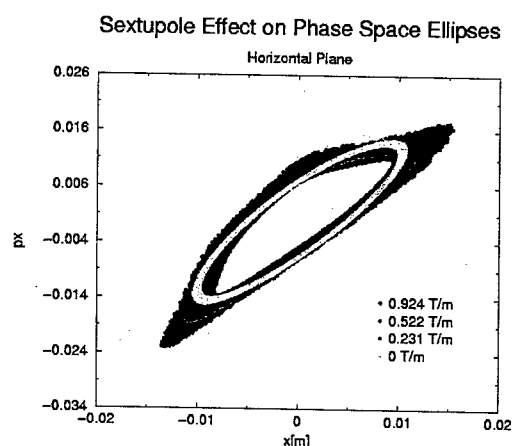
Figure 2: Horizontal phase space ellipses at one location of the ring after tracking for 62530 turns with different sextupole strengths. The nominal sextupole strength of 0.522 T/m is represented by the red ellipse

evaluated the effect of the sextupoles in the phase space

Table 1: The radius for which particles start to get lost in the tracking simulations is found as function of the sextupole strength. The chromaticities Qx' and Qy' are also calculated in each run.

Sext. Str. [T/m]	Qx'	Qy'	r [mm]
-0.924	91.56	-9.20	10.2
-0.522	64.70	11.05	10.9
-0.231	45.32	25.66	14.1
0	29.90	37.28	10.9
0.231	14.49	48.90	10.8
0.522	-4.89	63.51	11.2
0.924	-31.76	83.75	8.7

Figure 3: Horizontal tune distribution of the particles after tracking for 62530 turns.

ellipses the dynamic apertures of the ring can now be evaluated. This can be done by finding the biggest ellipse allowed in the ring before particle start to get lost. This is a process that involved tracking of particles several times in the ring, every time with a different size particle distribution.

The process was repeated for all the sextupoles strengths studied before (positive and negative) with results that are summarized on Table 1. The maximum radius of the RCMS beam is expected to be about 3 mm at one sigma. Even in the worst case when the sextupole strength is +0.924 (which is almost double the nominal strength), the maximum transverse radius allowed for the particles before they start to get lost (r = 8.7mm) is just enough to keep most of the particles inside the beam pipe during the acceleration cycle of the RCMS.

Footprints

Non linear components in the ring can introduce some dependence of the particles tune with the amplitude of oscillation. In the RCMS it is important to know if the tune spread caused by the eddy currents and other non linear effects can excite unwanted resonances in the ring.

In order to calculate such tune spread, a uniform distribution of particles in the x- y space were tracked for 62530 turns with the Marylie software. The tunes of each individual particle were determined using the orbit information provided by the 62530 simulated turns. The particles are then sorted out according to their horizontal and vertical actions J_x and J_y given place to Fig. 3 and an equivalent figure in the vertical plane (no shown). These graphs are done with the nominal sextupole strength of 0.522 T/m and a bigger strength of 0.924 T/m. The biggest tune spread in the horizontal plane is about 8.15^{-4} and 2.55^{-4} in the vertical plane, both of them for the extreme situation of a sextupole strenght of 0.924 T/m. These tune spreads are no large enough to move the nominal tune into the strongest resonances of one half at one third and hence the operation of the machine is stable within the sextupole range considered in this study.
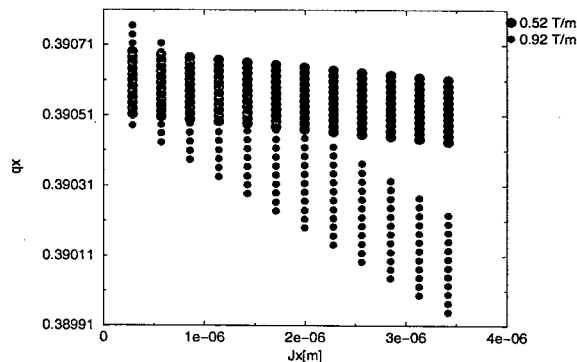
CONCLUSIONS

The sextupole component induced by the eddy currents in the beam pipe has a visible effect in the phase space distribution of the particles but the dynamic aperture is not sensitive to this sextupole component in the range of sextupole strenghts used in this study. Even in the very extreme case in which the sextupole component is almost double the nominal strenght the dynamic aperture although reduced is big enough to hold most of the particles of the beam.

It was also shown through Marylie simulations that the tune spread of the particles due to their different amplitudes is not significant and hence it doesn't represent any risk for the stable operation of the machine. The addition of sextupoles correctors to the RCMS design doesn't seem neccesary according to the results that has been presented in this paper.

REFERENCES

[1] S. Peggs (Editor), *Pre-conceptual Design of a Rapid Cycling Medical Synchrotron*, C-A/AP/6 , BNL, 1999.

[2] S. Peggs, J. Cardona, M. Brennan, J. Kewisch, G. McIntyre, N. Tsoupas, M. Schillo, A. Todd, B. Ludewigt, N. Lockyer, *RCMS - A Second Generation Medical Synchrotron*, PAC, Chicago, 2001.

[3] S. Y. Lee, "A multipole expansion for the field of vaccum chamber eddy currents", Nuclear Instruments and Methods in Physics Research A300.,1991, pg 151-158.

[4] A. Dragt et al, "Marylie 3.0 Uaer's Manual: A Program for Charged Particle Beam Transport Based on Lie Algebraic Methods",University of Maryland, College Park, Maryland, 1999.

[5] A. Dragt and D. Abell, "Symplectic Maps and Computation of Orbits in Particle Accelerators", Fields Institute Communications, Vol 10 , 1996, pg 59-85.

[6] A. Dragt, "Lie Methods for Nonlinear Dynamics with Applications to Accelerator Physics", University of Maryland, College Park, Maryland, 1999.

[7] H. Grote, F. C. Iselin, "The MAD Program", Ver. 8.19, Ed. European Organization for Nuclear Research, 1996.

STATUS OF THE INTEGRATED RFQ-DRIFTTUBE-COMBINATION FOR THE MEDICINE-SYNCHROTRON IN HEIDELBERG*

A. Bechtold, U. Ratzinger, A. Schempp, IAP, J. W. Goethe-Universitaet, Frankfurt, Germany

B. Schlitt, GSI, Darmstadt, Germany

Abstract

Design and construction of the RFQ including an integrated rebunching section as a part of the LINAC system is our contribution to the medicine project in Heidelberg. The building of the machine has been finished, first rf-measurements at low power have been done. The concept of assembling, especially the alignment of the electrodes, and the results of the rf-measurements will be presented.

1 INTRODUCTION

A common solution for matching the longitudinal properties of a beam after an RFQ to the acceptance of a following drift tube structure is a separate buncher cavity in a suitable distance. We have developed a new concept: A drift tube is mounted directly to the last RFQ stem at the high energy end forming a boosting or bunching unit, depending on the HF-phase it is operated with [1] (fig. 1). The advantages of an integrated solution like this are a very compact and easy to use machine, which saves building and operating costs, no extra power supply and control-unit is needed. The loss of flexibility for example in adjusting phase and amplitude independently, which might be of interest in physical laboratories is unimportant in a clinical surrounding. Once the machine is switched on, it should operate with high reliability, without the need to do further adjustments.
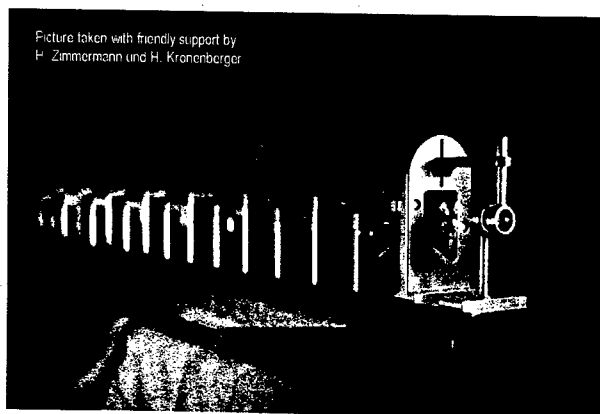
Figure 1: The adjusted RFQ-Drifttube-Combination right before its installation into the tank.

The 217 MHz RFQ will be a part of the accelerator complex, which is generally divided into two parts: a linac-section for pre-acceleration of $^{12}C^{4+}$ up to 7 MeV/u and the following synchrotron ring-structure for acceleration of stripped $^{12}C^{6+}$ to final energies between 50 and 430 MeV/u. The linac consists of an IH-type drift tube structure [2] following the RFQ. The main parameters of the RFQ are listed in Table 1. The Ions are coming from two separate ECR sources, to switch between two different ion species very fast.

2 RFQ DESIGN

At the generation of the RFQ structure the simulation program PARMPRO uses the well known two term potential:

$$V(r,\varphi,z) = A_{0,1}\left(\frac{r}{a}\right)^2 \cos(2\varphi) + A_{1,0}\, I_0(kr)\cos(kz),$$

where k is the wave number of the modulation, I_0 is the modified Bessel function of order 0. $A_{0,1}$ and $A_{1,0}$ are functions of k, a and m and are scaling with the electrode voltage U. Fig. 2 shows the ideal electrode shape in a transverse intersection for modulation $m = 2$, based on the two term potential.
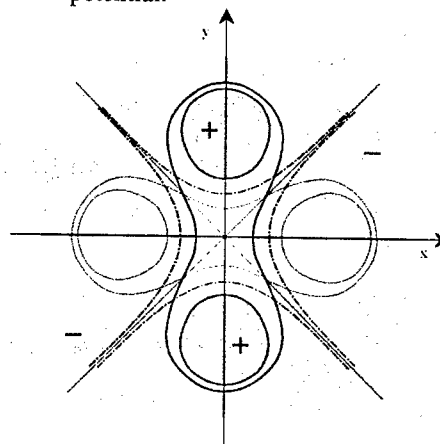
Figure 2: transverse intersection of the ideal electrode shape for modulation $m = 2$, based on the two term potential. Intersections in three different planes at the beginning, in the middle (ideal hyperbolic shape) and at the end of the cell are printed.

Each curve of the surface of ideal electrodes, which reaches closer to the beam axis is closing behind the other ones. As it is impossible to manufacture an electrode like this, one has to find an approximate solution.

Two types of electrodes are widely in use with the 4-rod-RFQ: The so called mini-vane type and the original rods. In the case of the rods, the modulation is done by changing the diameter periodically, which fits very well to the geometry shown in fig. 3, while the mini-vanes are milled and the transverse diameter is kept constant throughout the whole cell. Indeed simulations with Los Alamos PARMTEQ indicate a slightly better transmission of about 1 % with rod type electrodes in some cases. On the other hand one has much more freedom to vary the modulation or the aperture along the structure with the mini-vane electrodes without causing to many trouble in view of the alignment. However mini-vanes do have a higher capacity, which leads to a higher power consumption of the whole structure.

The medicine-RFQ has been manufactured by the use of mini-vane type electrodes, the main parameters of the RFQ are listed in table 1.

Table 1: Main RFQ parameters.

Ion species	$^{12}C^{4+}$, protons
Length of the electrodes	1,28 m
Length of tank	1,40 m
Tank diameter	250 mm
# of RFQ cells	219
# of matching in cells	8
Min. aperture	2.63 mm
Max. modulation	1.867
Max. focusing strength B	4.84
Input energy	8 keV/u
Input emittance	$\varepsilon_{x,y}=150 \pi$ mm mrad
Electrode voltage	70 kV
Exp. Power consumption	165 kW
Current	max. 2 mA H^+
Output energy	400 keV/u
max. beam angle at the exit	± 20 mrad (in both planes)
Phase width at IH entrance	$\Delta\varphi \leq \pm 15°$

3 ALIGNMENT

As the beam axis should be congruent with the tank axis, the first step of alignment was to determine the position of the ground plate mounted inside of the tank relative to the tank axis defined by the centers of the two end-flanges (fig. 3) [3]. Stems and electrodes where adjusted afterwards with respect to these measurements outside of the tank (fig. 4). The adjustment has been done by silver plated shims vertically and by shifting the electrode horizontally to equalize manufacturing tolerances with an accuracy of less than 30 μm.

Figure 3: A line of special flange inserts as a connecting surface for the ground plate on the left. Determination of the exact position of the ground plate inside of the tank in the middle. And the tank axis defined as the two centres of the whole circles of the two end-flanges.
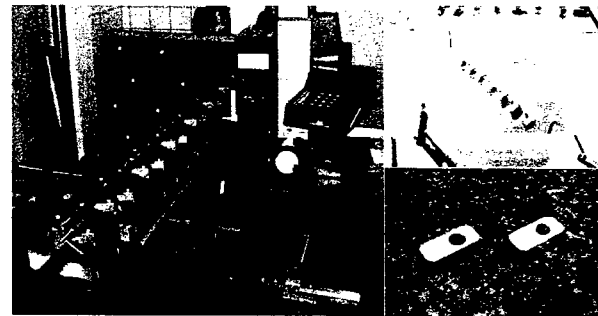
Figure 4: Adjustment of the electrodes outside of the tank on the left. Electrolytic process of silver plating and plated distant plates on the right.

4 MEASUREMENT OF BASIC RF-PROPERTIES

After the installation of the RFQ-structure into the cavity, first measurements of basic rf-properties have been done. First of all the resonance frequency was measured to f_0 = 193 MHz, which is about 10 % below the desired frequency of 217 MHz. This is a very comfortable result as it gives enough space to equalize inhomogeneities of the voltage distribution along the electrodes of about 20 % [1]. A first fine tuning has already been done by movable short circuit plates between stems near the end stems of the structure.

The quality factor was measured with the 3 dB method to Q = 2500. Together with R_p = 30 kΩ, which is the shunt impedance divided by the length of the structure measured with a perturbation capacity of 1 pF, and an electrode voltage of U_{el} = 70 kV the expected power consumption of the RFQ-Drifttube-Combination will be 165 kW.

5 VOLTAGE VARIATION OF THE INTEGRATED BUNCHER

One of the main aspects of the RFQ-Drifttube-Combination is the variation of the bunching voltage by adjusting the height in which the second drifttube is connected to the last oversized RFQ-stem, as one can see in fig. 5.
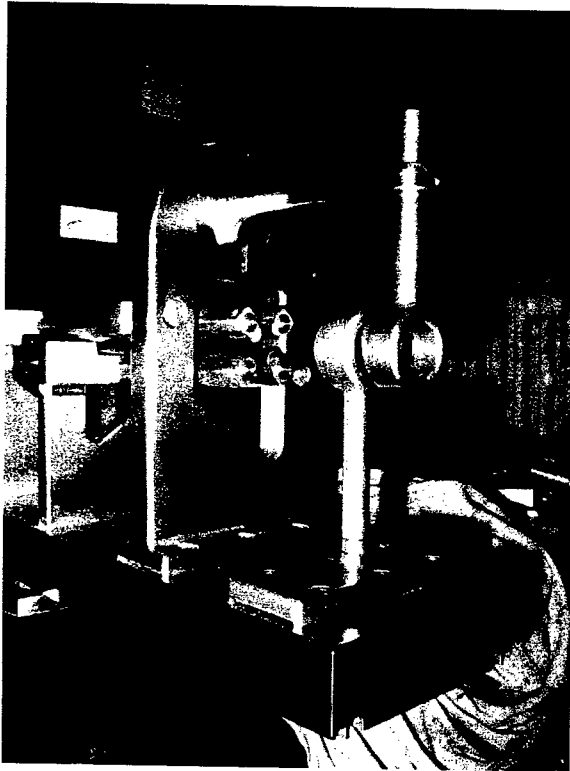
Figure 5: The integrated buncher unit.

In our case the measurements have been done with a bead made of copper, 5 mm in diameter. Because of the very limited geometrical conditions inside of the tank, the ball was speared on a small wooden stick, not as usual where it is fixed on a nylon string. The special measuring device inside of the tank for supporting the stick (fig. 6) was made of PVC and is not effecting the measurement very much, because almost all of the electric fields are concentrated between the electrodes. The results of these measurements are shown in fig. 7. The calculated total cap voltage of ca. 86 kV [4] has to be corrected by the transit time factor of the exact drifttube geometry and will be in the end about 20 % higher, which is no problem.
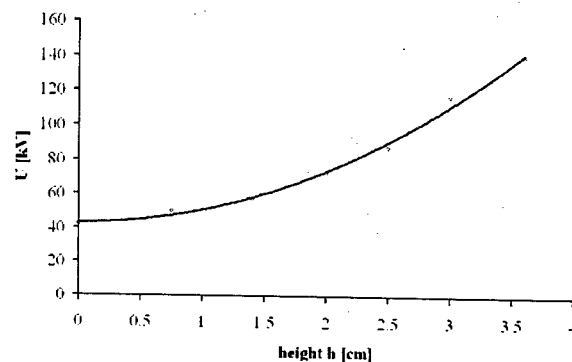
Figure 7: Measured total bunching voltage as a function of the height in which the drifttube is attached to the last RFQ-stem.

To determine the range in which the voltage is adjustable, we just had to measure the ratio between the voltage of the electrodes and the drifttubes. This has been done by the bead perturbation method where a peace of matter with an $\varepsilon > 1$ is moved along an interesting path always parallel to the electric field components while watching the phase shift caused by its presence. Because $\Delta\varphi \sim E^2$, which is true for little perturbations, the phase shift at a certain point gives information about the strength of the electric field.

6 CONCLUSIONS

The rf-measurements on the now aligned and installed medicine RFQ are promising as they are very close to the desired specifications of the machine. Next step will be the conditioning of the structure at higher power levels. A final adjustment of the bunching unit will be done in the course of a beam test in the near future.

REFERENCES

[1] A. Bechtold, A. Schempp, U. Ratzinger, B.Schlitt, "Design and Construction of an RFQ-Drifttube-Combination for a Medicine Synchrotron", Proc. EPAC2002, 2715.

[2] B. Schlitt, U. Ratzinger, "Design of a Carbon Injector for a Medical Accelerator Complex", Proc. EPAC98, 2377.

[3] A. Bechtold, A. Schempp, U. Ratzinger, B. Schlitt, "The RFQ-Drifttube-Combination for the Medicine Synchrotron in Heidelberg", Proc. LINAC2002.

[4] A. Bechtold, A. Schempp, U. Ratzinger, B. Schlitt, " Design Studies of an RFQ-Injector for a Medicine-Synchrotron ", Proc. PAC2001, 2485.

Figure 6: A special electrode top for the transition of the bead on the left and the whole measuring device on the right.

POTENTIAL ALTERNATE BEAM SOURCE FOR PROTON THERAPY

W. P. Jones, D.L. Friesel, and S.Y. Lee

Indiana University Cyclotron Facility, Bloomington, IN 47408, USA

Abstract

Studies have been carried out to determine the suitability of the IUCF Cooler Injector Synchrotron (CIS) as a potential replacement or supplement to the Indiana University Cyclotron as a source of proton beams for the Midwest Proton Radiotherapy Institute (MPRI). The primary modification to the synchrotron would be the development of a slow extraction system. An achromatic beam line connecting CIS and the MPRI beam trunk line has been designed and could use magnets from the recently decommissioned Cooler ring at IUCF. In addition to providing redundancy, this project would increase the proton energy to 240 MeV and could provide higher resolution beams to the radiation effects target stations.

MPRI FACILITY DESCRIPTION

A complete description of the present status of the MPRI project will be given later this week by D.L. Friesel [1]. 206.5 MeV proton beams for the treatment facility will be accelerated by the Indiana University Cyclotron. The first treatments will be carried out using a fixed horizontal beam line. Over the course of the next two years, two additional treatment rooms will be commissioned and brought into operation. Each of these treatment rooms will contain an IBA 360° - rotating gantry. This paper will consider the possibility of using the IUCF Cooler Injector Synchrotron (CIS) [2] as a source of protons for the MPRI treatment rooms.

DESCRIPTION OF CIS

A complete description of CIS has been published by D.L. Friesel et al. [2]. Figure 1 shows the configuration of CIS, which has four superperiods. Each superperiod is composed of a drift space, a dipole magnet with 90° bending angle and 12° edge angle at both ends. Four trim quadrupoles are used in order to have flexibility in adjusting betatron tunes. Including the injection chicane dipoles the horizontal betatron tune is 1.48 In its current configuration CIS has accelerated protons to 240 MeV and extraction is accomplished via a fast rise time horizontal kicker which jumps the beam across the septum of a vertical extraction Lambertson magnet in the following straight section.
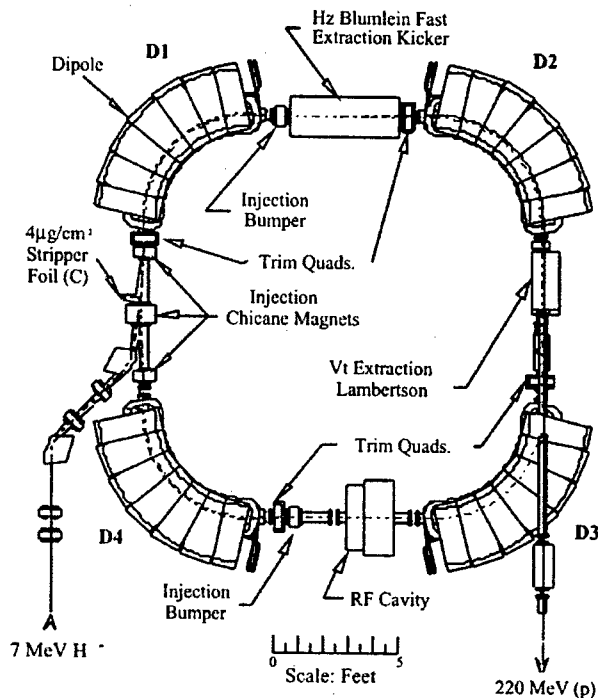
Figure 1. Current Layout of Cooler Injector Synchrotron (CIS)

DEVELOPMENT OF A SLOW EXTRACTION SYSTEM

In order to use CIS as a source of proton beam for a proton radiotherapy facility it will be necessary to develop a slow extraction system. Kang et al. [3] have studied slow extraction using the half integer resonance. The half integer resonance extraction method was chosen because the horizontal tune 1.48 of CIS is close to 1.50. The quadrupole magnets can be used to drive the half integer resonance. The fast extraction kicker magnet would be removed from CIS and in its place an electrostatic deflection system with a thin wire septum would be installed. Extraction efficiency can be increased by optimizing the location of the trim quadrupoles and by locating the wire septum as close to the dipole magnet as possible. This system could be implemented fairly quickly because it does not involve rearrangement of the basic CIS ring. There are concerns about the overall extraction efficiency that can be achieved with this

method because of the relatively low value of horizontal beta in the straight sections (~1m).

A second method would involve modification of the CIS ring elongating two of the straight sections is based on a study by Al Harbi and Lee[4]. The stretched CIS would have a horizontal betatron tune near 1.70 at its operating point. This is close to the third order integer resonance and the trim quadrupoles can be used to adjust the tune to allow the use of third order resonance to move the beam across the deflection system's thin wire septum. Because of the additional length in two of the straight sections, it would be possible to keep the fast kicker magnet and maintain the flexibility of having both fast extraction and slow extraction systems available. Because of the necessity of significant modifications to CIS for this system, the time scale for this would be considerably longer.

DESIGN OF THE CIS – MPRI TRANSFER BEAM LINE

A beam transfer line has been designed using magnets which can be recycled from the recently decommissioned IUCF Cooler. This design, which would use 12 of the Cooler quadrupoles and 3 of the Cooler 30° dipole magnets, had as its goals matching the beam phase shape at the entrance to the Kicker-Lambertson system for Treatment Room 2, having high transmission from CIS to the MPRI Trunk Line, and being achromatic in the Trunk Line. Fig. 2 shows the horizontal and vertical beam envelops along with the quadrupole apertures at their locations along the length of the transfer line. The transfer beam line is achromatic after the third dipole magnet.

The dipole and quadrupole magnets which would be used in the transfer line are all laminated magnets and would be able to be reset very quickly as new energies are requested by the Treatment Room. While the rest of the magnets in the MPRI Beam Trunk Line are solid core magnets, they are either relatively small quadrupole or steerer magnets and can their strengths can be varied fairly rapidly. If the speed of their variation became an issue, the quadrupole magnets in the Trunk Line could be replaced by additional laminated magnets from the Cooler. Figure 3 shows the proposed layout of the Beam Transfer Line connecting CIS with the MPRI Trunk Line.

ADVANTAGES AND DISADVANTAGES OF USING CIS FOR MPRI

A major advantage of CIS relative to the IUCF cyclotron for MPRI is the higher energy of the proton beam (240 MeV rather than 206.5 MeV). Another advantage would occur when a beam scanning system is implemented in the Treatment Rooms in that it would be simpler to control the dose delivered at each treatment depth with a active system controlling the energy for each layer of dose rather than using a passive range shifting system such as a propeller or ridge filter.

Disadvantages to using CIS rather than the cyclotron include the fact that beam from CIS cannot be brought to Treatment Room 1 with the system currently under consideration and a much more complex system would be required to reach Treatment Room 1. With the current design, the cyclotron could still be used to provide beam to Treatment Room 1.

The beam delivered to the Radiation Effects Research Program (RERP) target stations (at the exit from the MPRI Trunk Line) would be improved in that the range of energies available would be increased and the beam quality at low energies would be better because they would not be degraded from a high fixed energy but rather extracted from CIS at the energy desired by the experiment.

REFERENCES

[1] D.L. Friesel et al. Paper FOAA003 this conference.
[2] D.L. Friesel and S.Y. Lee, "CIS, A Low Energy Accelerator for the IUCF Cooler, IEEE95CH35843, 336 (1995).
[3] X. Kang et al., Proceedings of the 1998 European Particle Accelerator Conference, p. 1283.
[4] Nader Al Harbi and S.Y. Lee, Design of a compact medical synchrotron, Review of Scientific Instruments 74, 2540 (2003).

Figure 2. Vertical and Horizontal Beam Envelopes in CIS to MPRI Transfer Line
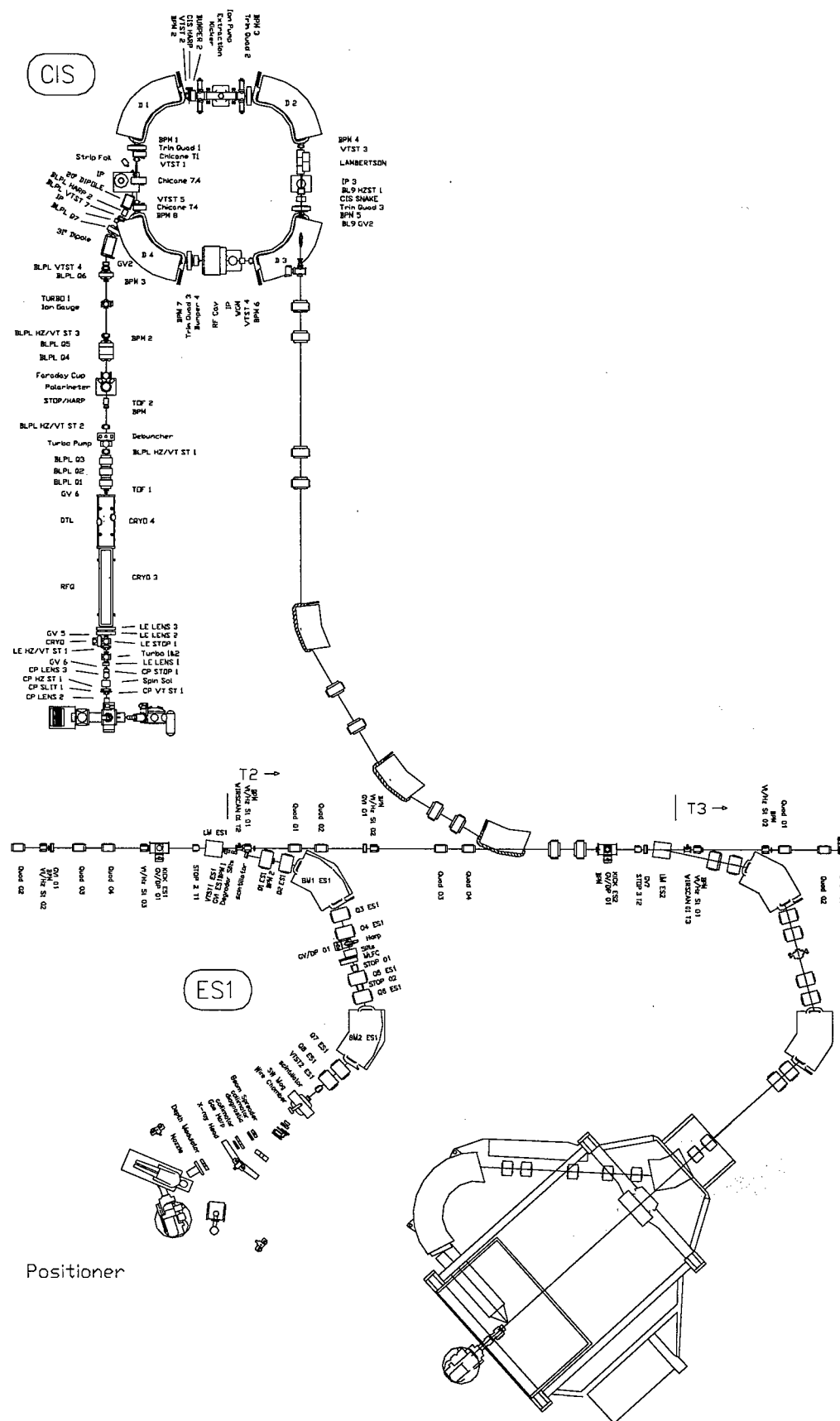
Figure 3. Layout of CIS to MPRI Beam Delivery System Transfer Lines.

PROTON THERAPY TREATMENT ROOM CONTROLS USING A LINUX CONTROL SYSTEM

J.Katuin

Indiana University Cyclotron Facility, Bloomington, IN 47408, USA

Abstract

The Indiana University Cyclotron Facility (IUCF) is in the process of completing the building of the Midwest Proton Radiotherapy Institute (MPRI). The design of MRPI's proton therapy system required the development of several control systems responsible for delivery of proton beam to a patient and patient positioning. One such control system is the Treatment Room Controller. This system allows for management of the other control systems, and is the primary user interface to the proton therapy system. This control system was developed with a Linux operating system, the KDE/QT widget sets for the user interface, and the KDevelop IDE. The control software uses the unixODBC API to provide an interface to a MySQL database for record and verify functions and for history functions. The control system also uses the Comedi driver library so that a National Instruments PCI DAQ card can be used to interface to various treatment room devices.

MPRI PROTON THERAPY SYSTEM CONTROLS DESCRIPTION

The MPRI Proton Therapy System (PTS), as shown in Fig. 1, is designed to provide proton therapy using two primary control lines, the Beam Delivery Line and the Patient Handling line. Both lines contain sub-systems with their respective control systems that together provide proton therapy to a patient. Such systems are grouped into two categories, Beam Delivery, and Patient Handling [11].

The Beam Delivery Group is responsible for proton beam delivery, dose monitoring, and radiation safety. This group is composed of the Beam Delivery System (BDS), the Dose Deliver System (DDS), the Kicker Enable System (KES), and the MPRI Interlock and Radiation System (MIRS).

The Patient Handling Group is responsible for patient positioning and position verification of a target. This
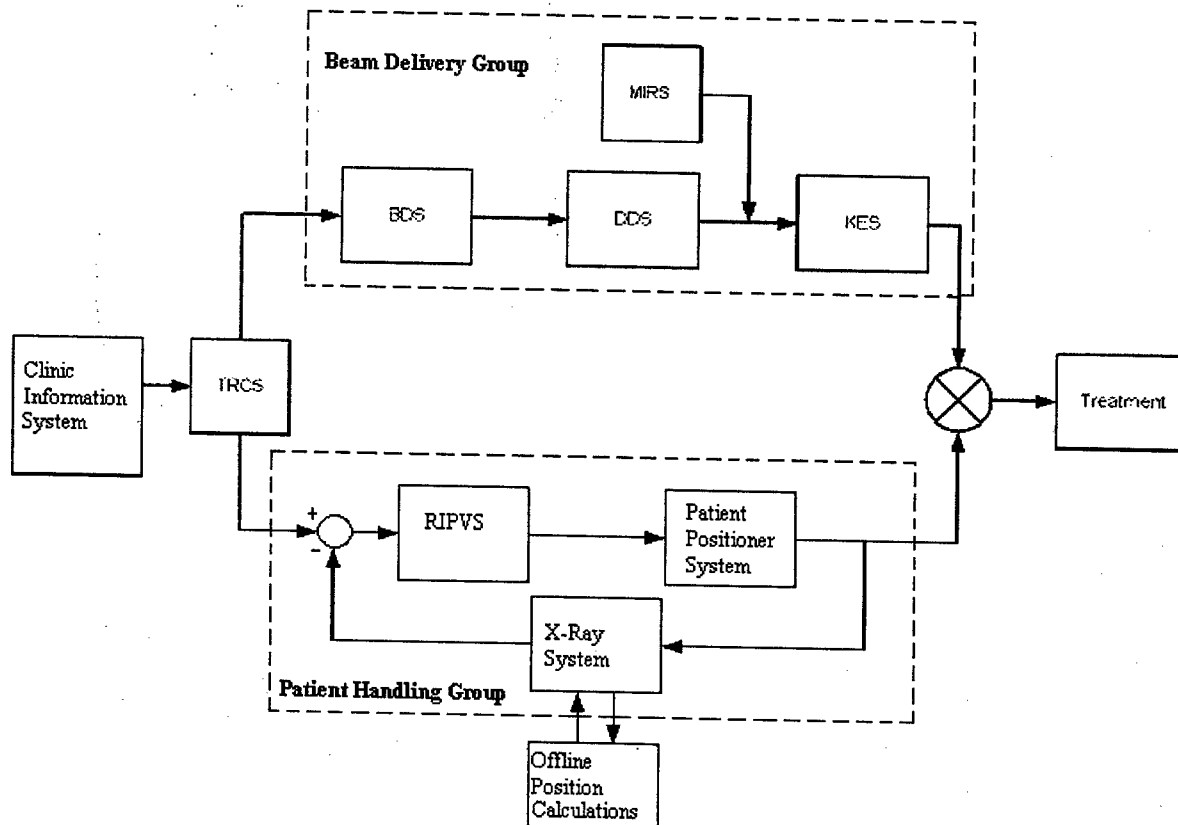
Figure 1: The Proton Therapy System.

group is composed of the Patient Positioning System (PPS), the Robot Interface and Position Verification System (RIPVS), and the X-Ray System.

The Treatment Room Control System (TRCS), an Intel Pentium based computer system, provides clinic personnel with the primary user interface for the PTS system for implementing and managing the treatment process. The TRCS accomplishes this by providing the interface with the Clinic Information System for treatment requirements and results.

When a treatment process is initiated, the TRCS retrieves the Treatment Planning Package from the Clinic Information System. This package contains treatment specific parameters, instructions, and files used for treatment by the various systems in the PTS. The TRCS downloads the elements of the package to the respective systems, and then verifies the information for correctness. Upon completion of a fraction the treatment events are sent back to the Clinic Information System in the form of a History Package, including x-ray images, log files, and corrections.

The TRCS also inspects the installation of treatment specific devices such as apertures, boluses, and ridge filters that are associated with a patient using bar code identification and limit switches. The TRCS will also display nozzle position by providing a signal from a potentiometer mounted to the nozzle assembly. The TRCS will monitor energy setup by analyzing hall probe data from a switching magnet located in the Beam Delivery System. This monitoring will allow for an independent check on the energy setup in the BDS.

OPERATING SYSTEM AND SOFTWARE DESIGN

Operating System

A requirement of the control system design was to use a Linux operating system so that during the development

phase of the project there could be an X-windows mechanism for monitoring other PTS control systems that had X-server capabilities. Also, a Linux operating system provides flexibility during the development of the TRCS by allowing remote logins, free development tools, and a relatively stable multitasking environment for applications. The Linux operating system needed to conform to an accepted standard. The intent was to ensure that the kernel release would allow for simple implementation of open source components such as the unixODBC and Comedi drivers. Consequently, SuSe 8.1 [1] was chosen for the operating system since it follows the United Linux Standard [2].

Software Design

The software requirement for the TRCS was to provide a GUI application called the "Treatment Room Manager" (TRM). The architecture of this software, as shown in Fig. 2, was to be divided into 5 groups, Patient Data Group, which handled patient/treatment information in the form of Treatment Package and History Package, Treatment Management, which handles direct therapy treatment commands from the Radiotherapy Technologist (RTT), the Maintenance Group, which allows for testing and configuration of the system, the Communications Group, which manages the communications and treatment requests to and from the other PTS systems using TCP/IP sockets, and the DAQ Group, which handles the analog and digital input/output signals, as well as control logic.

The application GUI uses the KDE and QT widget sets [3][4]. Consequently, the user interface was designed with several user interface screens. TRM uses an Explorer Layout, as shown in Fig.3. Access to such screens is controlled through user specific privileges.
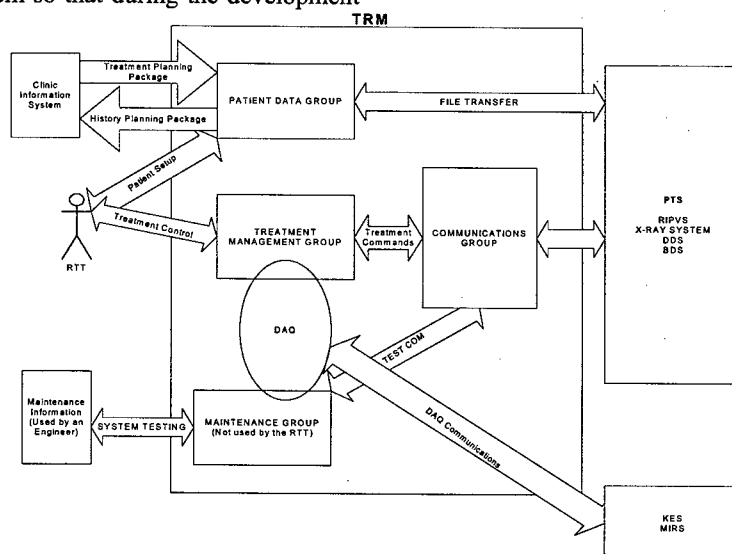
Figure 2: Software Architecture.
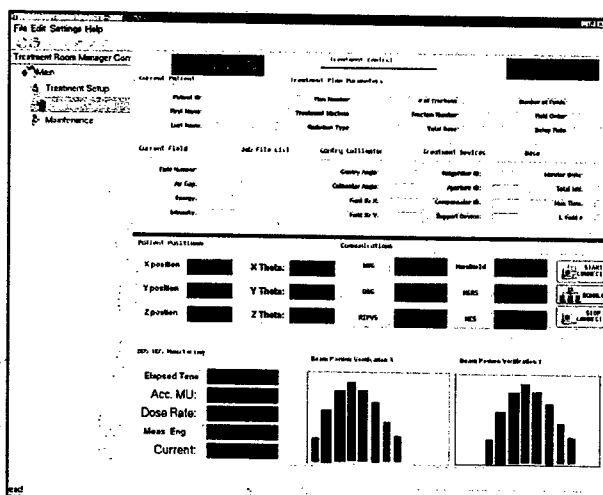
Figure 3: TRM GUI screen for the Treatment Management.

Since the application is written in C++, the QT and KDE widget were easily implemented. Also, the QT and KDE widget sets provide a signal/slot mechanism, which allows for simple inter-process and event driven communications [5].

KDevelop 2.1[6] was chosen as the development environment because it provides open source application-building tools that allow for rapid development of X-windows programs. Since the TRM application uses QT widgets for each screen, basic screen layout was accomplished using QT Designer [7], and then the widgets were added to the TRM project for compilation.

Database Interface

Early in the development of the TRM the actual database server was undefined, so a more general solution to the database interface was sought. Consequently, unixODBC [9] was chosen so that the code would require little to no changes regardless of the database server platform. Currently, the TRM interfaces to a MySQL Server in the MPRI Clinic Information System. Although the unixODBC web site provides some basic code examples, it lacks information on all of the API calls available to the unixODBC driver. However, this driver is compatible to Microsoft's ODBC references found at Microsoft's MSDN web site under Data Access[10]. Consequently most ODBC API calls described by Microsoft are applicable to the unixODBC.

Data Acquisition and Control

Data Acquisition and control for reading the magnet hall probe, nozzle potentiometer, and various limit switches was accomplished using a National Instruments PCI-6025E card. This card was chosen for the number of digital I/O channels, and analog channels. National Instruments recommends the use of the open source Comedi driver [8]. This driver package provides libraries for both real-time and non real-time Linux releases and can be used with a wide range of DAQ card manufactures.

The TRCS required both sets of libraries for the control application. The non real-time library (Comedilib [8]) was used for TRM because the DAQ and control requirements are non-critical, and the TRM is a user space application. A time critical feature was specified as a health signal to the KES, which oscillated at a fixed frequency of 10 hertz. If KES does not receive the signal then beam delivery into the treatment room will stop.

A kernel module was written using the real time library (Kcomedilib [8]). This module received a software health signal from TRM through a Char driver file [12], which allows user space/kernel space application communication. The TRM processes that need verification of operation were summed in intervals that were acceptable to the kernel module, which in turn allowed the kernel module to continue outputting a signal to the KES. The significance of this arrangement was that both drivers could communicate with a single NI card, and that the timing output of the kernel module was a consistent 10 hertz. If the TRM is disabled for any reason then the health signal will stop.

CONCLUSIONS

The TRCS has been designed using Linux and open source resources and standard hardware to meet the clinic requirements of MPRI's PTS. The tools are available at a minimal to no cost to developers of such a system. The development environment available with KDevelop and the KDE and QT widget sets allow for relatively fast application development. The unixODBC driver provides a means by which a programmer can create database applications that are server platform independent. The Comedi driver package provides a means of programming DAQ cards in a Linux environment, including kernel level applications. Support for this work is provided by the State of Indiana, Indiana University, the DOE (Grant No. DE-FG-02000ER62966) and the NIH (Grant No. CO6 RR17407).

REFERENCES

[1] http://www.suse.com
[2] http://www.unitedlinux.com
[3] http://www.kde.org
[4] http://www.trolltech.com
[5] http://www.trolltech.com/products/qt/whitepaper
[6] http://www.kdevelop.org
[7] http://www.trolltech.com/products/qt/designer.html
[8] http://www.comedi.org
[9] http://www.unixODBC.org
[10] http://msdn.microsoft.com/library/
[11] http://www.ni.com/linux/daq_comedi.htm
[11] J. Katuin & A.N. Schreuder, Proc. CAARI 2002, Denton, TX (2002) to be Published.
[12] Rubini & Corbet, "Linux Device Drivers, 2nd Edition", O'Reilly, June 2001

DEVELOPMENT OF HIGH FIELD DIPOLE AND HIGH CURRENT PULSE POWER SUPPLY FOR COMPACT PROTON SYNCHROTRON

K. Endo and K. Egawa, KEK & SKD, Tsukuba, Japan
Z. Fang, NIRS & KEK, Chiba, Japan
M.Mizobata and A. Teramoto, Mitsubishi Electric Corp., Kobe, Japan

Abstract

A small dipole magnet of 3 T is developed with its pulse power supply feeding 200 kA at maximum for the table-top proton synchrotron which is now under development for the radiotherapy. The experimental field distribution is consistent with the 3D dynamic field simulation results satisfying the required beam aperture. The dipole field was measured at an interval of 2 msec with 15 tiny search coils aligned accurately to the radial direction in the pole gap. The dipole is excited by the discharge current of the capacitor bank of 53 kJ with the rise time of 5 msec. Transverse beam behavior is also simulated using a time dependent beam optics code under the influence of the RF acceleration field to estimate the required beam apertures. Performances of the dipole and power supply will be treated in detail in conjunction with the numerical simulations.

INTRODUCTION

In order to make the proton synchrotron of 200 MeV for the radiation therapy small enough for installation and daily clinical treatment in the hospital environment, the development of the high field compact dipole magnet with performance of the accelerator grade is indispensable [1, 2]. The pioneering work has been initiated at BINP using a compact electron synchrotron model ring which was followed by the development of a small 5 T dipole magnet with a small beam aperture [3, 4]. Another requirement to the compact ring is to reduce the overall longitudinal dimension of the RF cavity with the average accelerating gradient of ~40 kV/m [5]. Its RF frequency range is well wide and the accelerating voltage is very large to accomplish the acceleration within duration while the ohmic heat dissipation can allow the temperature rise of the dipole coil. The RF issues are treated by the paper of this conference [6].

According to the size of the horizontal beam aperture, the cross-sectional dimensions of the dipole become large. If they are limited by the ring size, the iron core saturation becomes large when attaining a high magnetic field. There is a room for a trade off between the maximum field strength and the beam aperture. The present optics design has a preference to the beam aperture so as to obtain the sufficient beam intensity extracted for the medical treatment. The peak field of the dipole is suppressed to 3 T at 200 MeV, however, the dipole core saturates considerably.

The pulse power supply was also manufactured. It depends on the charge/discharge of the energy storage capacitor and the discharge current steps up through the pulse transformer to attain the peak current of 200 kA corresponding to the dipole field of 3 T. The power supply and the dipole magnet compose a resonant circuit of which rise time is used for the acceleration [7].

RING PARAMETERS

Main machine parameters are tabulated in Table 1 and the present ring layout is shown in Fig.1. Each design has the different dispersion and the horizontal/vertical tunes depending on the cell structure. The present design adopts the triplet cell structure to decrease the dispersion at the dipole magnet.

Table 1: Parameters for a 200 MeV proton synchrotron.

	BINP	BINP-Frascati	KEK	unit
Max. energy	200.0	200.0	200.0	MeV
Inj. energy	1.0	12.0	2.0	MeV
Circumference	4.7	6.4	11.9	m
Av. diameter	1.5	2.0	3.6	m
Bending radius	0.43	0.54	0.72	m
Max. dipole field	5.0	4.0	3.0	T
Period	4	4	4	
Tune, Q_x/Q_y	1.4/0.45	1.42/0.54	2.25/1.25	
Max. dispersion	0.4	0.63	0.5	m
Cell structure	FODB	BODO	FODOFB	
Frequency range	4.16~36.1	7.4~26.5	1.86~16.2	MHz
Acc. voltage	11.5	12.4	13.0	kV
Acc. time	2.5	3.5	5.0	msec
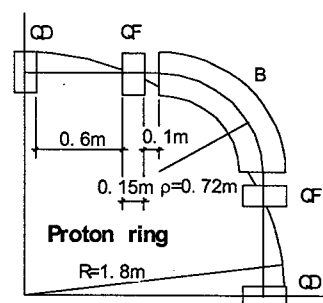
Figure 1: Layout of the compact proton synchrotron.

DIPOLE MAGNET

The ring consists of 4 dipole magnets. One of them was manufactured as a model according to the design (Fig.2) by the time dependent 3D field simulation (Fig.3). Both ends of the pole extending 5 cm from the core edges are tapered to attain a uniform effective dipole length as

shown in Fig.4 and the completed dipole magnet is given in Fig.5.
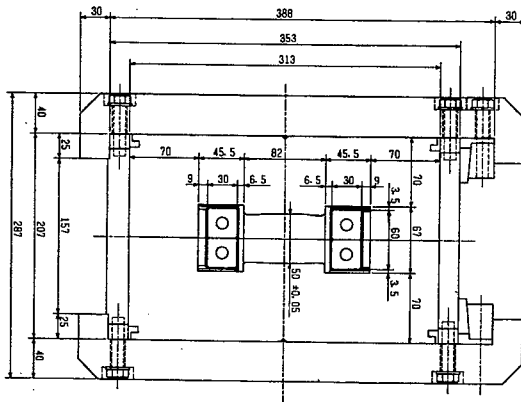
Figure 2: Cross-sectional dimensions of the dipole.
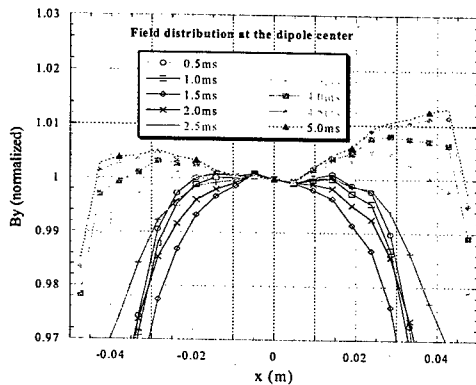
Figure 3: Field distribution at the dipole center without correction windings at every 0.5 msec.
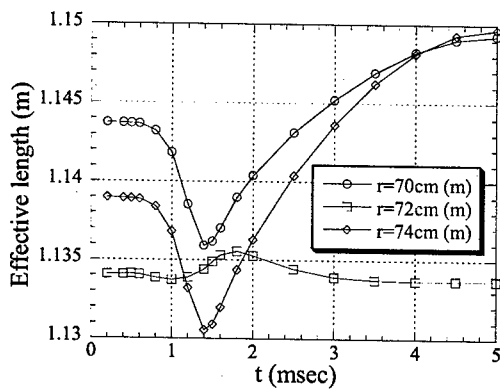
Figure 4: Numerically obtained effective length as a function of time. The squares correspond to the central orbit.

The field distribution is measured by using 15 search coils precisely aligned to the radial direction in the probe holder which are moved manually at every 0.9 or 0.45 deg. step on the girder. Induced voltage is saved at every 2 μsec and integrated to convert it to the field data in the personal computer. The normalized distribution at the center of the dipole is given in Fig.6 which reproduces the

numerically obtained distribution of Fig.3. The effective magnet length along the central orbit is given in Fig.7. At low field the effective length is longer by about 20 mm than the simulation. The time base differs somewhat in Fig.6 and Fig.7 where the maximum field is 2.94 T at 5.56 msec.
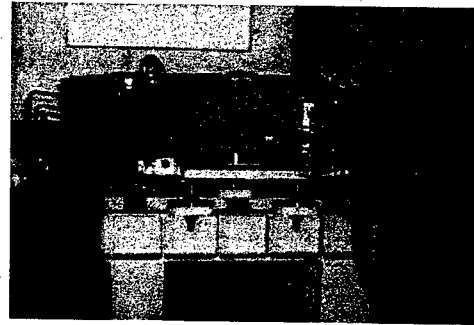
Figure 5: Completed dipole magnet.
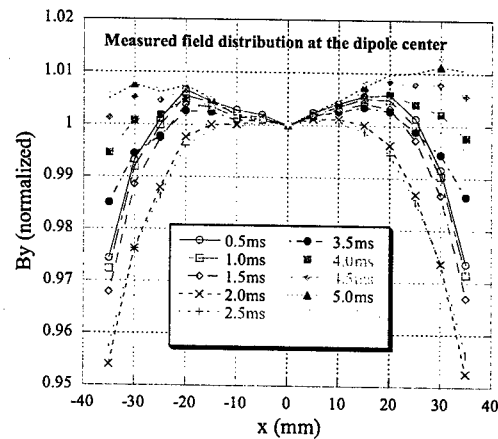
Figure 6: Measured field distributions.
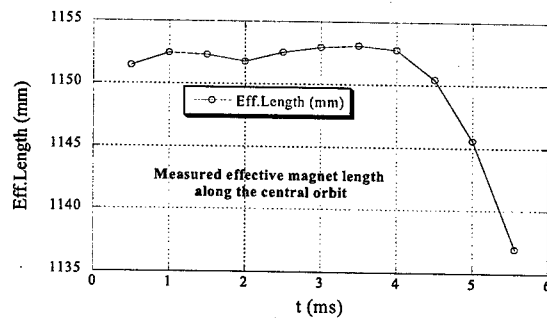
Figure 7: Measured effective magnet length.

The effective magnet length is obtained by integrating numerically the measured field map of the gap medium plane. As the search coil moves on the circular arc both inside and outside of the dipole, the outside integration on the tangential line (Fig.8) was made of the interpolated field, which is calculated by the method of the iso-parametric transformation in conjunction with the generalized matrix inversion.

PULSE POWER SUPPLY

By the thermal restraint, the current pulse width should be short. Assuming the sinusoidal excitation with a peak current I_p and a pulse rate η repetitions/sec, the effective current is $I_{eff} = 0.5 I_p \sqrt{\eta / f}$ for the rise and fall time equivalent to f Hz. This case is $I_{eff} = 14.1 \sqrt{\eta}$ [kA]. In practice, the current differs from the sinusoidal pattern due to the saturation of the dipole magnet and the repetition rate is 5 or less depending on the heat dissipation. To avoid the skin effect the coil is made of the strand Cu cable impregnated with the epoxy resin of which heat conductivity is considerably small.
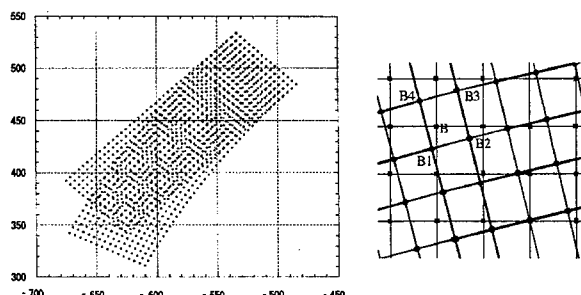
Figure 8: Interpolation of the magnetic field. (Left) Blue spots: the measured field points, and red spots: interpolated if surrounded by 4 blue points. (Right) A red point field is interpolated from 4 black point data in a green rectangle.

As the discharge current of the capacitor bank is utilized to excite the dipole, the precise current control is difficult. However, the precise tracking of the quad current must be established by sensing the dipole current or field which is the reference signal to the quad power supplies. This kind of control is easy because the current of these quad power supplies is about one tenth of the dipole current.

The power supply shown in Fig.9 has the capacitor bank (2.5 mF, 6.5 kV) to excite one dipole.

Before manufacturing the pulse power supply, the charge, discharge and residual energy recovery circuits are simulated using PSpice code for all dipoles serially connected. The current pulse width is adjusted to 10 msec (50 Hz equivalent) by changing the circuit parameters such as the pulse transformer winding ratio, capacitor, charging voltage and etc. The measured current pulse and the central dipole field are plotted in Fig.10 when the energy recovery circuit is working.
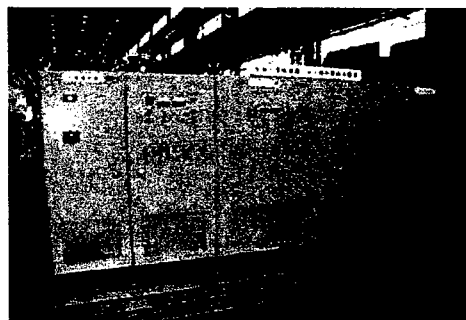
Figure 9: Completed pulse power supply for a dipole magnet. From left to right; charge, control, capacitor bank and discharge blocks.
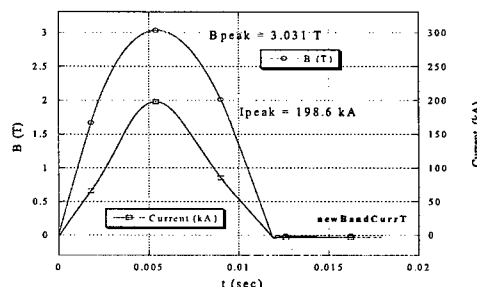
Figure 10: Measured time-dependent excitation curve.

REFERENCES

[1] K. Endo et al, "Table-Top Proton Synchrotron Ring for Medical Applications," Proc. EPAC2000, Wien, pp.2515-7.

[2] K. Endo et al, "Compact Proton and Carbon Ion Synchrotron for Radiation Therapy," Proc. EPAC2002, Paris, 2733-5.

[3] I.I. Averbukh et al, "Project of Small-Dimensional 200 MeV Proton Synchrotron," EPAC88, Rome, 1988, pp.413-6.

[4] L. Picardi et al, "Preliminary Design of a Very Compact Protosynchrotron for Proton Therapy," EPAC94, 1994, pp.2607-9.

[5] Z. Fang et al, "A Broadband and High Gradient RF Cavity for a Compact Proton Synchrotron," Proc. EPAC2002, Paris, pp.2145-7.

[6] Z. Fang et al, "RF Cavities and Power Amplifier for the Compact Proton Synchrotron," this conference.

[7] K. Endo et al, "Resonant Pulse Power Supply for Compact Proton and/or Heavy Ion Synchrotron," Proc. APAC2001, Beijing, pp.636-8.

RF CAVITIES AND POWER AMPLIFIER FOR THE COMPACT PROTON SYNCHROTRON

Z. Fang, K. Endo, K. Egawa, KEK, Tsukuba, Japan
T. Hirashima, Denki Kogyo Co., Aikou-gun, Japan
I. I. Averboukh, BINP, Novosibirsk, Russia

Abstract

A project to build a compact proton synchrotron is now underway [1-4]. Protons will be accelerated from 2 MeV to 200 MeV within 5 ms with an operation repetition rate of 10 Hz, in the synchrotron ring with a circumference of 11.9 m. The acceleration system is required to be of a wide bandwidth, with the frequency sweeping from 1.64 MHz to 14.26 MHz, and of a high gradient, with the maximum acceleration voltage of 20 kV. The acceleration section, consisting of a 2-cell rf cavity loaded with 4 high-permeability magnetic alloy cores in each cell, has been designed. A push-pull power amplifier with two 35 kW tetrode tubes will be used to drive the 2 cavities in parallel. Calculations and test results on the cavity characteristics will be presented and discussed, including the cavity impedance and equivalent circuit. The simulation results of the amplifier system using the ICAP code will also be given. The prototype of the rf system is being developed, and a high power test will be performed soon.

1 INTRODUCTION

For the compact design of the proton synchrotron [1-4] the acceleration system is required to be of a wide bandwidth and high gradient [5]. A 2-cell rf cavity loaded with 4 high-permeability magnetic alloy cores in each cell has been designed as shown in Fig. 1. The core dimension is 397 mm and 170 mm in outer and inner diameters, and 25 mm in length. The length of each cell is 200 mm, and the total length of the acceleration section is 500 mm. A push-pull power amplifier with two tetrode tubes 4CX35,000C will be used to drive the 2 cavities in parallel.
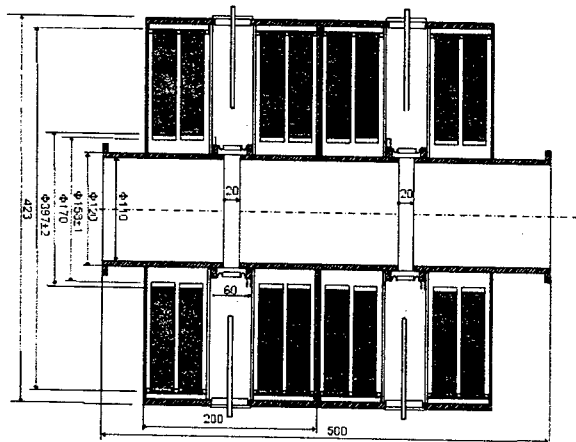
Figure 1: Structure of the rf cavity.

The rf frequency and required gap voltage as functions of acceleration time are shown in Fig. 2.
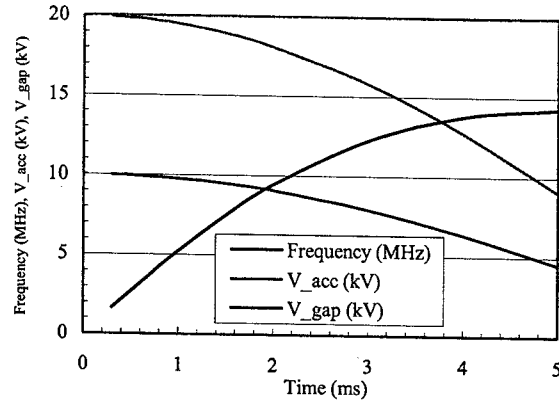
Figure 2: RF frequency and required gap voltage as functions of acceleration time.

2 RF CAVITY

2.1 Test of Cavity Model and Core Permeability

We made a test model with one quarter of the rf cavity, filling with 2 cores only in one side of the gap, and measured the cavity impedance. In this model, the equivalent circuit is a parallel circuit of lumped elements of cores and a gap capacitor C_g. The cavity impedance is:

$$Z_{cav} = \cfrac{1}{\cfrac{1}{j\omega(u'-ju'')L_0} + j\omega C_g}$$

where $u = u' - ju''$ is the complex permeability of cores, and $L_0 = \frac{u_0}{2\pi} h \ln\frac{b}{a} = 2\times10^{-7} \times h \ln\frac{b}{a}$, where a and b are the inner and outer diameters of cores, and h is the core length.

The measured value of core permeability is:

$$u' = 3000\times(\frac{f}{0.5})^{-1} \quad \text{and} \quad u'' = 6000\times(\frac{f}{0.5})^{-0.8}$$

where f is in MHz.

The calculation results of impedance for different gap capacitance and test results of the cavity model are shown in Fig. 3. It is shown that the test results agree with the calculation results very well. And in this model the gap capacitance is about 28 pF.
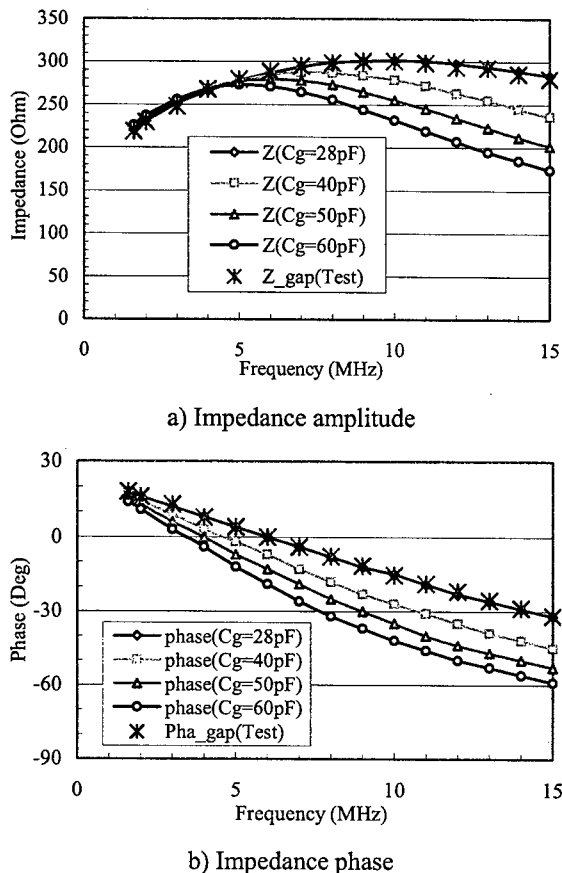
a) Impedance amplitude

b) Impedance phase

Figure 3: Calculation results of impedance for different gap capacitance and test results of the cavity model.

2.2 Equivalent Circuit of RF Cavity

Since the cavity wall is connected to the ground, for the rf cavity (see Fig. 1) which is driven by a push-pull amplifier, the equivalent circuit is shown in Fig. 4. In Fig. 4, R_{1a}, L_{1a}, and C_{1a} are the core resistance and inductance, and the distributed capacitance at one side of gap for the first cell. R_{1b}, L_{1b}, and C_{1b} are the ones at the other side of gap. C_{g1} is the distributed capacitance at gap area. Similar parameters are used for the second cell.
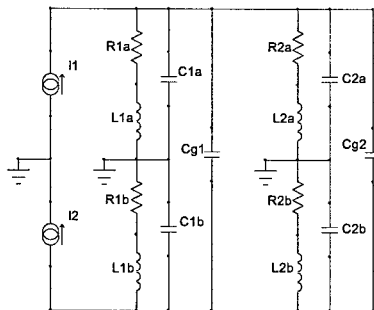
Figure 4: Equivalent circuit of rf cavity.

From the equivalent circuit, each cell of the rf cavity can be separated into two cavities same as the model

cavity we made. That is, the total rf system consists of 4 units with 2 cores in each unit. The impedance of each unit given in Fig. 3 shows a good performance of frequency response, and the impedance is used to calculate the necessary rf driving current and power. For our case, the impedance of each unit is about 220 Ohm at 1.64 MHz, and the required maximum rf voltage is 5 kV, so an rf current of 23 A is necessary for each cell. And for one tube, the maximum rf current should be about 46 A, namely, the maximum plate current should be larger than 92A.

3 POWER AMPLIFIER

3.1 Simulation of RF system

In the rf system, two tetrode tubes 4CX35,000C is used to form a push-pull amplifier to drive the two cells of rf cavity. Each side of the cavity gaps is directly connected to the anodes of the two tubes through the DC blocking capacitors. The rf system has been simulated by using ICAP code, as shown in Fig. 5. The input and output capacitances of the tube are 440 pF and 51 pF, respectively. The anode and screen voltage are set as 10 kV and 2 kV, respectively. Due to the wide bandwidth, two rf driving sources are used for the two tubes respectively, and the phase difference between the two rf driving voltages is 180 degrees. The anode power supply is designed to be of maximum DC current of 100 A.
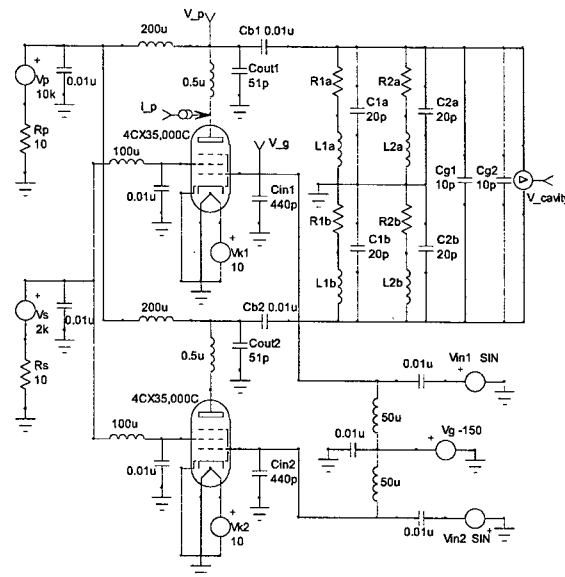
Figure 5: Simulation of rf system by using ICAP code.

Fig. 6 shows the simulation results at different acceleration time. It is shown that we can get the required voltage at gap by applying a driving rf voltage, which is nearly proportional to the ratio of the required gap voltage

to the impedance of one quarter of the rf cavities, which is shown in the black curve in Fig. 6. Fig. 7 shows one example of simulation results at 1.64MHz. From the simulation results, the rf system will work well to satisfy the rf requirements of the proton synchrotron.
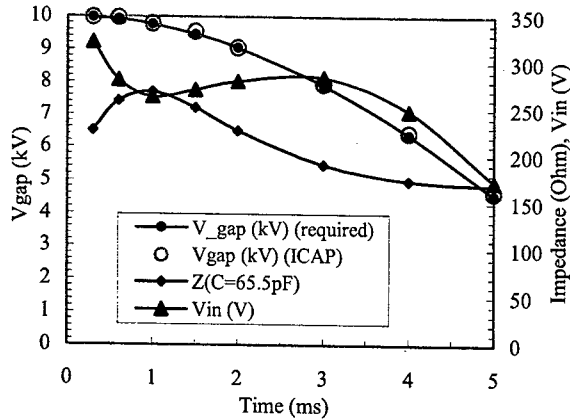
Figure 6: Simulation results of the rf system at different acceleration time.
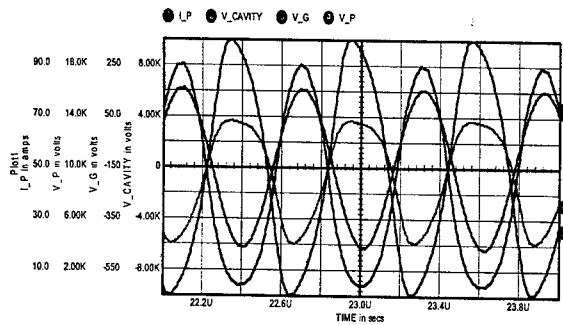
Figure 7: Example of simulation results at 1.64MHz. (I_P, plate current; V_CAVITY, cavity voltage; V_G, grid voltage; V_P, plate voltage)

3.2 Improvement of Cavity Frequency Response

From the simulation results, its also shown that the frequency response of cavity can be improved by inserting a small inductance about several μH between the amplifier tube and cavity, as shown in Fig. 8.
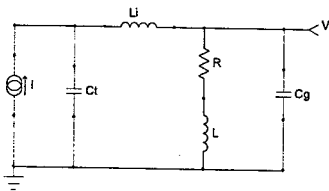
Figure 8: Equivalent circuit with an inductor inserted between the amplifier tube and cavity.

The amplitude ratio of cavity voltage to rf current is:

$$\frac{|V|}{|I|} = \sqrt{\frac{R^2 + \omega^2 L^2}{\left[1 - \omega^2 LC - \omega^2 C_i L_i (1 - \omega^2 LC_g)\right]^2 + \left[\omega R(C - \omega^2 C_g C_i L_i)\right]^2}}$$

where $C = C_i + C_g$.

If $L_i = 0$, then

$$\frac{|V|}{|I|} = \sqrt{\frac{R^2 + \omega^2 L^2}{\left[1 - \omega^2 LC\right]^2 + \left[\omega RC\right]^2}}$$

From the above formula, we can get the same conclusion that the cavity frequency response can be improved by inserting a small inductor (L_i). And the optimized value can be determined in the test process of rf system.

3 SUMMARY

The rf cavity has been designed to be of a wide broadband and high gradient, and a test model with one quarter of the rf cavity has been made. The test results agree with the calculation results very well. The power amplifier system with two tetrode tubes 4CX35,000C has been simulated by using ICAP code. The prototype of the rf system is being developed, and a high power test will be performed soon.

4 REFERENCES

[1] K. Endo et al, "Table-Top Proton Synchrotron Ring for Medical Applications", EPAC2000, 2515-2517, Vienna.

[2] K. Endo et al, "Compact Proton and Heavy Ion Synchrotron for Cancer Therapy and Bio-Science", Proceedings of the 13th Symposium on Accelerator Science and Technology, 426-428, Osaka, Oct. 2001.

[3] K. Endo et al, "Compact Proton and Carbon Ion Synchrotrons for Radiation Therapy", EPAC2002, 2733-2735, Paris.

[4] K. Endo et al, "Development of High Field Dipole and High Current Pulse Power Supply for Compact Proton Synchrotron", this conference.

[5] Z. Fang et al, "A Broadband and High Gradient RF Cavity for a Compact Proton Synchrotron", EPAC2002, 2145-2147, Paris.

APPLICATION OF STATISTICAL PROCESS CONTROL (SPC) IN THE MANUFACTURING OF MEDICAL ACCELERATORS.

S. M. Hanna*, Siemens Medical Solutions USA, Inc., Oncology Care Systems Group

Concord, CA 94520, USA

Abstract

Most radiation therapy machines are based on microwave linear accelerators. Manufacturing reliable accelerators and hence, reliable radiation therapy machines requires accurate, efficient, and well-controlled processes throughout the steps of electron accelerator manufacturing. Statistical Process Control (SPC) techniques are utilized at Siemens – Oncology Care Systems (OCS) to meet these requirements. SPC is routinely used to monitor different accelerator manufacturing processes. Analysis of the resulting data is used to initiate actions to preserve consistent and high-quality performance. This results in processes that are stable and predictable at both higher effective capacity and lower cost. In addition, it is expected that high-energy physics projects such as the Next Linear Collider (NLC) should benefit from these techniques. Quality control techniques similar to those used by Siemens are essential to the fabrication of the large number of cavities and accelerator sections in an industrial environment.

QUALITY ASSURANCE IN THE MANUFACTURING OF MEDICAL DEVICES

Consistent high-quality and defect-free production is a clear requirement in medical devices. To achieve this requirement, medical device manufacturers usually employ Quality Management Systems (QMS) to maintain quality. Additionally, QMS help medical device manufacturers meet various regulatory quality standards such as the ISO 9001 (as a generic quality system standard) and the ISO 13485 (as a quality system standard for medical devices). In recent years, Statistical Quality Control (SQC) and its subset the Statistical Process Control (SPC), [1-3] have proven effective in improving and maintaining the quality of the medical device industry and supporting the FDA's good manufacturing practices.

STATISTICAL QUALITY CONTROL

Statistical Quality Control (SQC) is a scientific method to analyze manufacturing data. Based on this analysis, measures are taken to maintain the quality of the manufactured product. One of the techniques that are used to monitor manufacturing processes and provide feedback is Statistical Process Control (SPC). The feedback is used

to maintain and improve the capability of the process and to ensure product conformance. SPC is used to control the process by signaling when adjustments may be necessary. Some techniques associated with SPC include frequency histograms and control charts. A control chart is the tool used to monitor the variation in a process and ensure that the process is in a state of control. This allows the operator to monitor the trends occurring in the process. The control chart reflects the specification limits, namely, the Upper Specification Limit (USL) and the Lower Specification Limit (LSL). In addition, it has upper and lower control limits that lie within the specification limits. The Upper Control Limit (UCL) and the Lower Control Limit (LCL) are determined by evaluating the dispersion (variability) in process, see Fig. 1. In a well-controlled process, these limits can be chosen to be equal to $\mu \pm 3\sigma$ respectively, where σ is the process standard deviation and μ is the process mean. These statistical limits are normally called the "3 sigma control limits". In a normal (Gaussian) distribution, 99.73% of the values measured lie in interval of width 6σ.
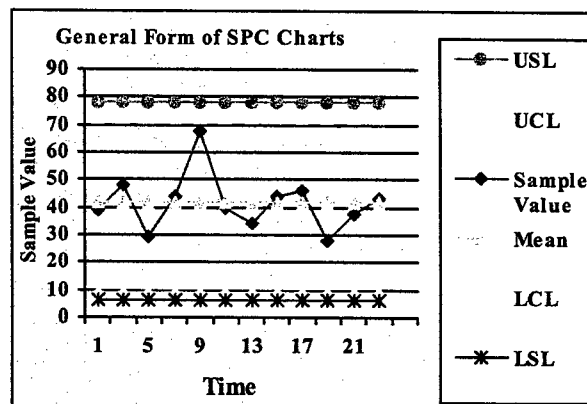
Figure 1: Typical SPC chart.

APPLICATIONS OF SPC IN THE MANUFACTURING OF SIEMENS MEDICAL ACCELERATORS

At Siemens Medical Solutions USA, Inc., Oncology Care Systems Group, we have been implementing various Computer–Aided Processes (CAP) in several critical areas of the accelerator manufacturing. The CAP approach provides accurate and efficient techniques to characterize accelerator structures [4-6]. These techniques are implemented at different phases of development and of

*E-mail: samy.hanna@siemens.com.

manufacturing of the accelerators. These CAP techniques lend themselves to the use of SPC. The data is analyzed and displayed graphically a control chart, from which one can analyze variations in the process. Based on these control charts, the processing engineer can decide on the stability of the process as well as causes of deviations. The role of SPC is depicted in Fig. 2, below.
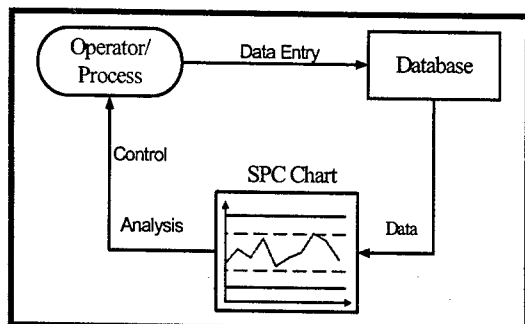
Fig. 2 Role of SPC in controlling different accelerator manufacturing process.

Each manufacturing process is characterized by a set of measurable parameters. These parameters, tables, and plots are transmitted to a database where they are stored on the network. The flow of data and documents used in accelerator manufacturing process at Siemens-OCS is shown schematically in Fig. 3, below.
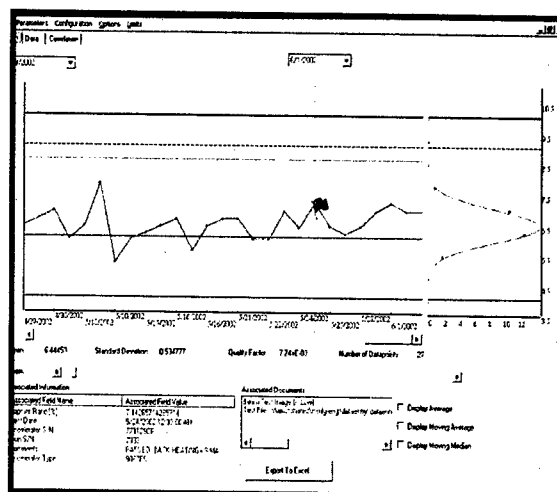
Figure 4: SPC chart of a parameter characterizing a linear accelerator at Siemens-OCS.

Our operators are trained to recognize trends occurring in the process by observing the SPC charts such as the one shown in Fig. 4. They are also trained to correct the conditions before the process approaches one of its limits. By being alert to these trends and acting accordingly and promptly, consistent process output is achieved. Ultimately, higher yield would result as the process is guarded from approaching its limits and fewer parts are out of their engineering specifications.
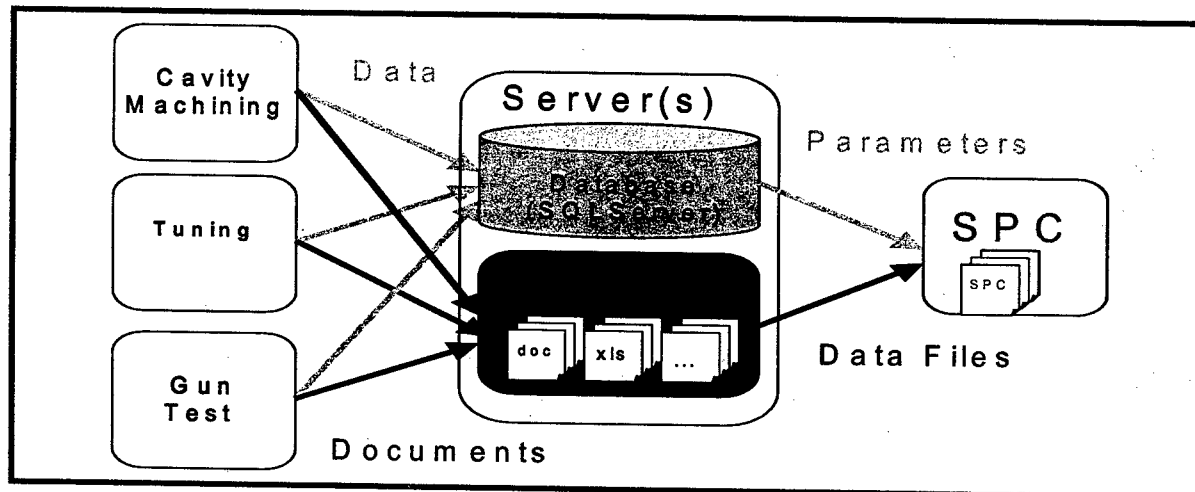
Figure 3 Flow of data and documentation to the database and the SPC system.

We are also using the approach depicted in Fig. 3 to archive data records resulting from each manufacturing process. On the resulting SPC chart one can use the curser to select a data point. A summary of related parameters are instantly displayed. If further information is needed, the full record (a table or a plot) can be retrieved from the server on the network. The example displayed in Fig. 4, shows some of data retrieval capability of our approach.

As shown in Fig. 4, the overall performance of the process over long periods of time is displayed as a frequency histogram and a fitting distribution. Our process engineers use these resulting distributions to verify the effect of the measures taken to tighten the process limits and hence improve consistency even further.

SPC AS A FEEDBACK TOOL FOR ENGINEERING DESIGN

In designing a linear accelerator, many constraints are to be considered and satisfied. Some of these constraints have competing, or even conflicting, Therefore, trade-offs are usually needed. Our processing engineers use SPC tools to analyze the ultimate limits of different manufacturing processes. Results of these analyses and supporting data are then shared with the accelerator design engineers. This feedback on the process capabilities can provide the design engineer with information needed to tighten some tolerances related to the manufacturing process. This would allow the relief of other competing design constraints and still meet manufacturing requirements. Ultimately, a better design that is efficiently manufactured is achieved. Fig. 5 depicts the role of SPC in the design cycle.
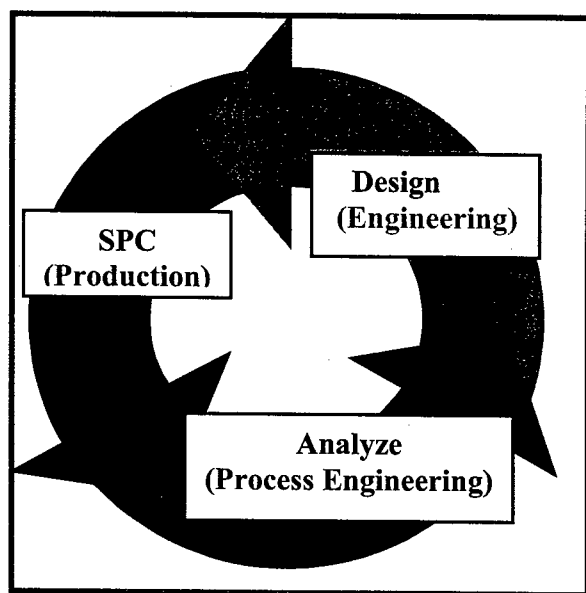
Fig. 5 Role of SPC in the design cycle.

APPLICATIONS OF SPC IN PARTNERSHIPS WITH SUPPLIERS

A strengthening factor in the partnerships with our suppliers is providing feedback information on the quality of their supplied components in a timely manner. Our SPC tools have been effective in compiling data measured by our suppliers as well as our processes and analyzing them. Reports resulting from these analyses and the associated data are shared with the relevant suppliers.

REFERENCES

[1] D. Raheja, " Assurance Technologies: Principles and Practices ", McGraw Hill, Inc., 1991.

[2] J. Heizer and B. Render, "Operations Management", 6th Ed., Prentice Hall, 2001

[3] R. T. Amsden, H. E. Butler, and D. M. Amsden, " SPC Simplified: practical Steps to Quality", Productivity, Inc. , 1998.

[4] S. M. Hanna, "Development of Characterization Techniques for X-Band Accelerator Structures," Proc. Of the 2000 European Particle Accelerator Conference, Vienna, Austria, pp 2521-2523, 2000.

[5] S .M. Hanna, et al., "Automated System for Conditioning A Linear Accelerator", US Patent No. 6483263, Issued November 2002.

[6] S .M. Hanna, et al., "Computer-Aided Tuning of Charged Particle Accelerators ", US Patent No. 6498444B1, Issued December 2002.

RADIATION-ACOUSTIC MONITORING OF THERAPEUTIC BEAM

A.I. Kalinichenko, V.T. Lazurik, G.F. Popov, V.V. Tovstiak,
Kharkov National University, P.O. Box 60, 61052 Kharkov, Ukraine

Abstract

A method of dose field control in patient's body during radiation treatment is proposed. It is based on detection of thermoacoustic pulse to be generated by pulsed radiation beam *in vivo* and on reconstruction of dose field characteristics by stress amplitude. A possible scheme of realization of the proposed method is considered. Typical variants of dose fields and corresponding solutions of radiation thermoacoustic equation are discussed. The values of stress pulses and accuracy of dose field location are estimated for electron, X-ray and proton beams.

1 INTRODUCTION

One of lines of advanced medicine is the use of directed beams of ionizing radiation – electrons, X-ray, protons. So, radiosurgery has become an important method of treatment of small lesions such as benign or malignant primary tumors and isolated metastases. For the most effective application of radiation beam without healthy tissue overirradiation one should control characteristics of irradiation zone in the patient's body directly during the treatment, i.e. to determine form, location and dose distribution in this zone. At present, dose field parameters are determined by preliminary calculation that demands thorough initial data preparation, considerable expense of computer time and aware experts in the physics of radiation– matter interaction. This approach does not guarantee coincidence the real dose field with the calculated one because of dispersion of the beam and the target characteristics, personnel's mistakes, etc.

In the paper, a new method of radiation- acoustic monitoring of therapeutic beam is proposed. This method is based on detection of thermoacoustic pulse generated by pulsed radiation beam *in vivo* and recovery on its basis dose field characteristics.

2 METHOD DESCRIPTION

A short-pulsed radiation beam causes "instant" heating of a target material and generation in it a thermoelastic stress pulse which is initially directly proportional to absorbed energy density and diverges from generation zone with longitudinal sound velocity s. Time of pulse arrival to i-th acoustic detector permits determining distance $l_i = t_i s$ from zone of energy release to detector.

The heat energy density $\varepsilon(\vec{r},t)$ to be coincide with absorbed dose determines unambiguously amplitude of generated thermoelastic pulse $\sigma(l,t)$ connected with it by an integral relation of the convolution type. In some particular cases one can express the absorbed dose $\varepsilon(\vec{r},t)$ per thermoelastic pulse amplitude $\sigma(l,t)$ and distance l

[1,2]. Indications of several wideband acoustic detectors connected to patient's body permit determining position, form and value of dose field.

A possible scheme of radiation- acoustic monitoring of therapeutic beam in patient's body is shown in Fig. 1. (The case of intracranial irradiation).

Cylinder or converging therapeutic beam (1) goes out a pulsed accelerator (2) passes through filter- transformer (3) of beam characteristics. Thermoacoustic dosimeters of external monitoring (4-6) are positioned on the path of the beam. Passing through the dosimeter the beam generates the thermoacoustic pulse containing information concerning particle distribution, duration and diameter of the beam. Joint data at least of two dosimeters permit determining axis direction and angle of convergence of the beam. Coming in detectors (7-9) the acoustic pulses transform into the voltage ones which go to **SYGNAL PROCESSING SYSTEM (SPS)**. Also, accelerator sync pulse and signals from internal monitoring detectors (10-13) detecting thermoacoustic pulse from dose field in patient's body come there with corresponding delays. SPS determines position, form and value of dose field. The number of detectors is chosen assuming necessary accuracy of measurements. Dose field data come in **CONTROLLED COMPUTER** that yields directive on change of relative position of radiation source and target.

3 THEORETICAL JUSTIFICATION

3.1 Radiation-Acoustic Equation and Solutions

The thermoacoustic displacement potential $\Psi(\vec{r},t)$ is found from the wave equation [2]:

$$\frac{\partial^2 \Psi(\vec{r},t)}{\partial t^2} - s^2 \Delta \Psi(\vec{r},t) = -\frac{\Gamma}{\rho}\varepsilon(\vec{r},t), \qquad (1)$$

Here Γ and ρ are the Gruneisen's parameter and density. The solution of Eq. (1) for unbounded medium is:

$$\Psi(\vec{r}_0,t) = -\frac{\Gamma}{4\pi\rho s^2} \iiint \frac{\varepsilon\left(\vec{r}, t - \frac{|\vec{r}_0 - \vec{r}|}{s}\right)}{|\vec{r}_0 - \vec{r}|} dxdydz, \qquad (2)$$

where $\vec{r}_0$ is the position vector of the observation point. The range of integration is $|\vec{r}_0 - \vec{r}| \le st$. For quasi-liquid medium, we have the following expression for nonzero (diagonal) elements of the stress tensor:
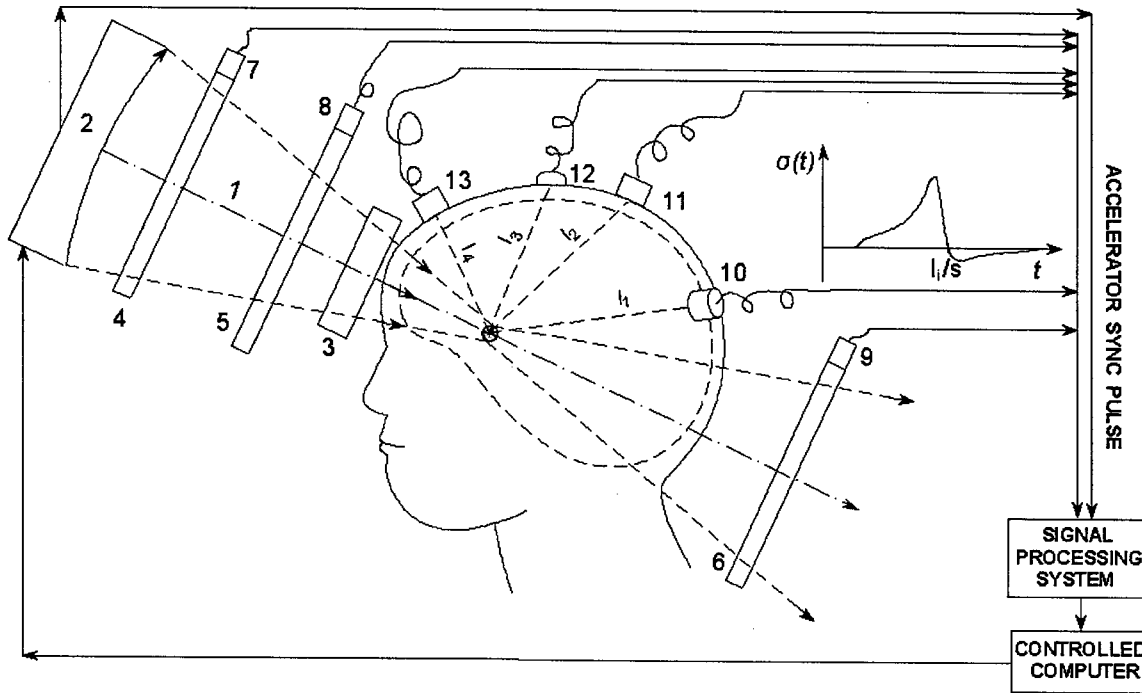
Figure 1: Scheme of radiation- acoustic monitoring of therapeutic beam in patient's body-

$$\sigma(\vec{r}_0,t) = \rho\frac{\partial^2\Psi}{\partial t^2} + \Gamma\varepsilon =$$

$$= -\frac{\Gamma}{4\pi s^2}\frac{\partial^2}{\partial t^2}\iiint\frac{\varepsilon\left(\vec{r},t-\dfrac{|\vec{r}_0-\vec{r}|}{s}\right)}{|\vec{r}_0-\vec{r}|}dxdydz, \ (r_0 >> D/2). \ (3)$$

For some special dose fields, Eq. (3) permits a simpler analytical representation. It simplifies reconstruction of the dose field $\varepsilon(\vec{r},t)$ by thermoacoustic response of the target. The simplest pulse form produces one-dimensional instant radiation heating of the target material: $\varepsilon(\vec{r},t) \equiv \varepsilon(x)\theta(t)$. In this case the thermoacoustic pulse propagating in positive direction of x-axis has the form

$$\sigma(x,t) = \frac{\Gamma}{2}\varepsilon(x-st), \qquad (4)$$

i.e. the acoustic response $\sigma(x,t)$ is directly proportional to dose field $\varepsilon(x-st)$ in the target, and its time delay determines distance from generation zone to observation point. In case of near-surface irradiation the total pulse consists of superposition of direct and reflected pulses.

The thermoacoustic responses of cylinder or spherical dose fields have more complex forms. The corresponding expressions for stress amplitudes as well as the inverse problem solutions were found and analyzed in [1,2].

3.2 Dose Field Characterization

Therapeutic beam characteristics, i.e. sort and energy of its particles, diameter D, duration T, are chosen depending on location and form of irradiated lesion. These characteristics determine a type of a dose field behaving as the thermal loading in the thermoacoustic equation.

Consider some specific features of dose fields generating by electron and X-ray and proton beams.

A small dose spot formation on considerable depth of tissue by pencil or focused electron beam is problematic. Electron beam can be used for surface and near-surface irradiation. Existing program packages permit finding the dose field of arbitrary electron beam [3]. These codes allow justifying results of radiation-acoustic dosimetry. In the case of $X<<D$, and flat surface of the target, the quasi-one-dimensional acoustic response (4) is realized. Here X is the maximum penetration depth.

A pencil beam of monoenergetic photons attenuates in matter exponentially. Supposing axisymmetric Gaussian distribution of photons with initial radius R we have the following expression for dose field of a pulsed converging photon beam in (semi)infinite medium:

$$\varepsilon_\gamma(x,r,t) = \frac{N_\gamma E_\gamma \mu_{en}(E_\gamma)\varphi(t)e^{-\mu(E_\gamma)x - \dfrac{r^2}{R^2\left(1-\dfrac{x}{f}\right)^2 + \Delta r^2}}}{\pi\left[R^2\left(1-\dfrac{x}{f}\right)^2 + \Delta r^2\right]}, \ (5)$$

where N_γ is the total number of photons, $\mu(E_\gamma)$ and $\mu_{en}(E_\gamma)$ are the extinction coefficient and the energy absorption coefficient depending on gamma quantum energy. E_γ, f is the focal distance and Δr is the focal spot radius. The function $\varphi(t)$ determines the time dependence of absorbed dose. The following one-parameter approximation $\varphi(t) = 0.5(1+\text{erf}(2t/T))$ is mostly acceptable for electron and proton beams. The instant heating approximation $\varphi(t) = \theta(t)$ is realized under

condition $T << R/s$. Here $\theta(t)$ is the Heavyside's unitary function. In this case the dose field recovery is possible by indications of a few detectors.

The extreme case $f \to \infty$ corresponds to a pencil (nonconvergent) beam. Besides, if the condition $\mu(E_\gamma)x << 1$ is satisfied everywhere in the target then the dose field depends on the only spatial variable r. In this case the solving of the inverse problem is facilitated and one can reconstruct the dose field $\varepsilon(r)$ by indications of the only detector [1,2].

For ionization loss of nonrelativistic proton with energy E from 10 MeV to 200 MeV, one can use the approximate expression $dE/dx \approx -B/E$ where $B \approx 2 \cdot 10^3 \rho$, MeV^{2}cm^{2}g^{-1}. Within the framework of this approximation, the expression for the dose field of a focused proton beam is

$$\varepsilon_p(x,r,t) = \frac{NB\theta(E^2-2Bx)}{\sqrt{E^2-2B(x-\Delta x)}} \frac{\varphi(t)e^{\frac{r^2}{R^2\left(1-\frac{x}{f}\right)^2+\Delta r^2}}}{\pi\left[R^2\left(1-\frac{x}{f}\right)^2+\Delta r^2\right]}, (6)$$

where N is the number of protons in the beam pulse, $\Delta x \approx 1.3$ cm is the fitting parameter of the model. Limit $f \to \infty$ corresponds to the case of the pencil beam.

Brought dose field characteristics are the initial information for simulating thermoacoustic response of a target. This simulation helps solve the basic problem: to reconstruct *in vivo* or in phantom position, form and value of dose field by thermoacoustic response of the target.

3.3 Numerical Estimations

Consider the thermoacoustic responses of biological tissue on pulsed electron, X-ray and proton irradiation.

The estimation of absorbed dose of relativistic electron beam is $\varepsilon_e \approx \frac{N_e}{\pi R^2}\chi_{ion}\rho$, where $\chi_{ion} \approx 2$ MeV·cm^2/g is the linear energy loss of relativistic electron , N_e – is the number of electrons in the pulse. Assuming $N_e = 10^{10}$, $R = 1$ cm, $\rho = 1$ g/cm^3, we have $\varepsilon_e = 1$ Gy. The stress pulse value σ in case of one-dimensional dose field can be estimated by (4). Assuming $\Gamma = 0.2$ we have $\sigma \approx 100$ Pa.

For bremsstrahlung beam generating by electron beam, the estimation of absorbed dose is the following $\varepsilon_\gamma \approx \frac{k_{e\gamma}E_eN_e\mu_{en}}{\pi R^2}$. Here $k_{e\gamma}$ is the conversion coefficient of electron to gamma energy. Assuming $E_e = 8$ MeV, $E_\gamma = 0.4$ MeV, $k_{e\gamma} = 0.1$ [4], $N_e = 10^{10}$, $\mu_{en} \approx 0.03$ cm^{-1}, $R = 1$ cm we have $\varepsilon_\gamma \approx 0.03$ Gy. One can estimate the stress pulse value from instant cylinder photon beam by equation $\sigma(l) \approx 0.32 \cdot \Gamma\varepsilon(R/l)^{1/2}\left(1+s^2T^2/4R^2\right)^{-3/4}$. Assuming $T = 0$, $\Gamma = 0.2$, $R = 0.5$ cm, $l = 5$ cm we have $\sigma \approx 0.5$ Pa that is approximately in ten times exceeds threshold of sensitivity of wideband acoustic detector with passband

from 0 to 0.5 MHz at room temperature [2]. The use of high-intensive and focused electron beams permits obtaining X-ray beams that in 100 to 1000 times exceed the above. On the other hand, they are not harmful because produce dose $\varepsilon \leq 1$ Gy to be small compared with really used therapeutic doses.

The proton energy loss increases considerably at the end of its range (so-called the Bragg's peak). The absorbed dose estimation by (6) in the Bragg's peak for the proton beam with $N = 10^{10}$ and $R = 1$ cm results the value $\varepsilon_p \approx 20$ Gy. Given the focusing and the Bragg's peak effect the absorbed dose in focus can exceed considerably the external one. So one can use expression $\sigma(l) \approx 0.21 \cdot \Gamma\varepsilon(R/l)\left(1+s^2T^2/4R^2\right)^{-1}$ to be valid in the wave zone of the spherically symmetric Gaussian dose field. Assuming $T = 0$, $\Gamma = 0.2$, $R = 0.5$ cm, $l = 5$ cm we have $\sigma \approx 80$ Pa

The accuracy of positioning of flat, cylinder and spherical dose fields is approximately equal to $\Delta r \approx \sqrt{R^2+(sT/2)^2}$ if one can neglect sound absorption and dispersion.

4 CONCLUSION

On the basis of authors' experience in thermoacoustic dosimetry of unmoved and scanning pulsed radiation beams [1,2], the method and possible scheme of radiation-acoustic monitoring of therapeutic beam in patient's body was considered.

Parallel indications of several wideband acoustic detectors connected to patient's body or to phantom permit determining position, form and value of dose field during irradiation. The estimations have shown that really used therapeutic doses are much more then those necessary for reliable thermoacoustic dosimetry. It validates realizability and safety of the proposed method. Sound absorption and dispersion as long irradiation time and presence of reflected pulse impair the accuracy of determination of above characteristics.

5 REFERENCES

[1] A.I. Kalinichenko, G.F. Popov "Non-disturbing thermoacoustic dosimetry of electron and bremsstrahlung beams," Radiation Physics and Chemistry V.63, pp.755-758, 2002.

[2] A.I. Kalinichenko, V.T. Lazurik, I.I. Zalyubovsky "Introduction to Radiation Acoustics," In a series "The Physics and Technology of Particle and Photon Beams," Vol.9, Harwood Academic Publishers, 2001.

[3] V.T. Lazurik, V.M. Lazurik, G.F. Popov, Yu.V. Rogov The Software ModeRTL for Simulation of Radiation Processes in Electron Beam Technologies. Abstract book of the ICAP-2002 Conference. p.49, East Lansing, MI, USA. (The paper in a press).

CLOSING IN ON THE DESIGN OF THE BESSY-FEL*

D. Krämer for the BESSY FEL Design Group[#], BESSY, Berlin, Germany

Abstract

The SASE-FEL at LEUTL (APS) [1], the demonstration of SASE laser saturation at wavelengths below 100 nm at TTF (DESY) [2] and the operation of the HGHG-FEL at BNL [3] has stimulated proposals on future 4th generation light source user facilities in the VUV to soft X-ray spectral range and hard X-rays worldwide, refs. [4-10].

The BESSY Soft X-Ray FEL is planned to be built next to the 3rd generation BESSY II light source, covering the spectral range 62 nm to 1.24 nm. A superconducting 2.25 GeV linac will supply three independent FEL-lines with a highly flexible electron-bunch pattern; the use of APPLE II type undulators will deliver variable photon-beam polarization. These SASE-FELs will permit unprecedented spectral-, spatial- and temporal resolution for user experiments.

A Status of the design work is presented in the paper.

INTRODUCTION

The scientific case for the BESSY-FEL was published in 2001 [11]. The technical features of the Soft X-Ray FEL will guarantee a tremendous improvement compared to present day synchrotron radiation and conventional laser facilities.

The laser-like coherent radiation with extremely short pulses will extend existing research techniques to ultra-short time resolution for investigations of the electronic structure of matter. The intrinsic pulse duration determined by the electron pulse will be shortened to less than 20 fs. This opens the field for unprecedented studies on the structural and electron dynamics of systems.

The flexible time structure provides various possibilities to synchronize the FEL with external laser sources to perform unique pump-probe experiments. The pulse peak power of a few GW will enable the study of non-linear properties of matter, while non-linear processes involving core electrons localized at individual atomic centers, are adding a totally new quality to experiments.

THE SOFT X-RAY FEL

General Layout

The general layout of the FEL facility is shown in fig. 1. Bunches of electrons are generated in a normal conducting 1.3 GHz RF-photoinjector at a normalized emittance of 1.3 πmm·mrad at a charge of up to 1 nC with a typical pulse length of $\sigma_{l,rms}$ = 2000 µm. Repetition frequency of the injector is 1000 Hz. The bunches are compressed in two stages (BC1 and BC2). In BC1 the bunch is shortened by a factor of 10 at an energy of 200 MeV while in BC2 the 715 MeV beam is compressed by a factor of 4 resulting in a final bunch length of 50 µm rms. The peak current thus is about 5 kA. A superconducting CW linac based on the TESLA design accelerates the beam to suitable energies which are 1.875 GeV for the "Low-Energy-" and "Medium-Energy FEL" while the "High Energy FEL" operates at variable energies of 1.5 to 2.25 GeV.
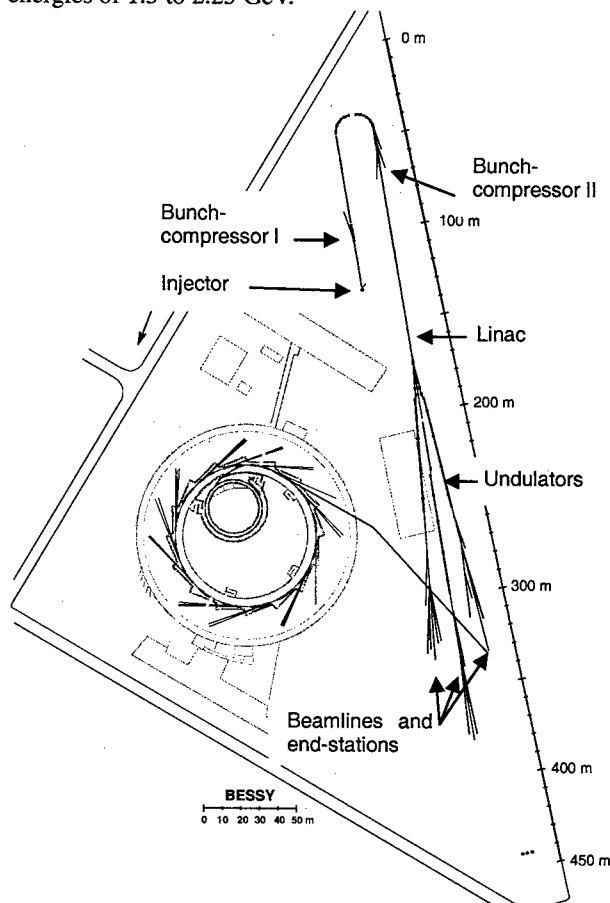
Fig. 1: Overview on the FEL adjacent to the present 3rd generation SR-source BESSY II operational since 1998.

[#] M. Abo-Bakr, W. Anders, R. Bakker[$], J. Bahrdt, K. Bürkmann, O. Dressler, H. Dürr, V. Dürr, W. Eberhardt, S. Eisebitt, J. Feikes, R. Follath, A. Gaupp, M. v. Hartrott, K. Holldack, E. Jaeschke, Th. Kamps, S. Khan, J. Knobloch, D. Krämer, B. Kuske, P. Kuske, F. Marhauser, M. Martin, A. Meseck, G. Mishra[$], R.Müller, M. Neeb, K. Ott, D. Pflückhahn, H. Prange, T. Quast, I. Will*, G. Wüstefeld.

[$]DAVV, Indore, *Max-Born-Institut, [$]now Sincrotrone Trieste

To cover the photon energy ranges of 20 to 300, 250 to 550 and 500 to 1000 eV, undulators of length up to 60 m will be installed. Eight beamlines of up to 80 m distance between undulator exit and target station were designed. Four beamlines are optimized for short pulse techniques as XPS, UPS and PEEM, while others are for high resolution experiments as HR-PES, XRMS and RIXS.

To save space for future activities a 85 m zone towards the site boundary is presently not used, made possible by folding the linac with a 180° bend in-between BC1 and BC2.

Start to End Simulations

The code ASTRA [12] is used to evaluate the beam emittance in the injector region up to BC1. Simulation of coherent synchrotron radiation in the bunch compressors, in the 180° bend and for single particle wakes in the linac structures were carried out with ELEGANT [13] to derive realistic beam parameters at the entrance to the undulators. To study the SASE-process time-dependent, the code GENESIS [14] was utilized. Figure 2 gives typical results for the most demanding case: the 1 keV beam at the HE-FEL; plotted are output power along the undulator, pulse duration, radial beam-size and photon-beam spectrum.
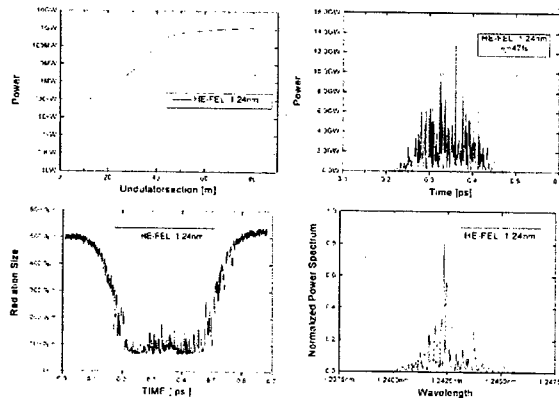
Figure 2: Results from Start to End simulations. Top graphs, left hand: output power along the undulator, right hand: photon pulse duration. Lower graphs, left hand: radial size of the photon beam at saturation, right hand: photon beam spectrum. All calculations apply for a 1 keV (1.24 nm) photon-beam.

Starting with a normalized beam emittance of 1.3 π mm·mrad at the gun exit, insignificant dilution of phase space occurs up to the end of the linac. As the FELs photon-energies span wide ranges, the active lengths of the undulators have to be adjusted according to the saturation-length. Thus the undulators are segmented to a typical length of 3.5 m by independent gap drive. More than 50% of the segments have to be opened in the case of the long wavelength limit at the 'Low Energy FEL', e.g. at 20 eV.

Table 1 gives a summary of major undulator- and photon-beam parameters for the three FEL lines.

Table 1: Summary of undulator- and FEL performance parameters for the three FEL lines. Values are listed according to their operation range e.g. for rms beam size σ and divergence σ'.

Parameter	LE-FEL	ME-FEL	HE-FEL
Photon energy (eV)	20 - 300	270 - 550	500 - 1000
U-period (mm)	66	36.5	27.5
K-value	4.3 - 0.82	1.5 - 0.80	0.82
No. of periods	312 - 728	864 - 1344	1560 - 1820
Output power (GW)	10 - 2	5 - 1	2.5
Peak brilliance (s·mm^2·mrad^2·0.1% bw)	$3.8 \cdot 10^{29}$ - $0.4 \cdot 10^{29}$	$1.5 \cdot 10^{31}$ - $0.3 \cdot 10^{31}$	$2.5 \cdot 10^{31}$
Pulse duration (fs)	40 - 50	~ 40	~ 40
σ$_{rms}$ (μm)	110 - 230	~ 80	~ 80
σ'$_{rms}$ (μrad)	12 - 105	~ 13	~ 12

Detailed studies on tolerances have been performed using GENESIS in time-independent mode. The influence of rms-beam wander caused by different sources on the saturation power is displayed in figure 3. As expected, beam wander should not exceed 20% of the electron beam radial size in order not to decrease saturation power.
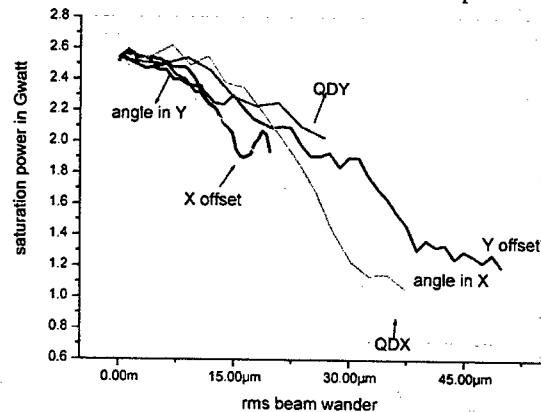
Figure 3: Influence of beam wander on saturation power caused by horizontal and vertical quadrupole misalignment (QDX, QDY), electron beam position offset (X offset, Y offset) and angle error (angle in X, angle in Y) at the undulator entrance. Calculations apply for the HE-FEL.

The n.c. Photoinjector

Generation of electron beams at a charge of up to 1 nC at a normalized emittance of approximately 2π mm·mrad has been demonstrated within the PITZ collaboration [15].

Based on this n.c. photoinjector a high power gun-cavity is developed to operate at a repetition frequency of 1 kHz in short bunch mode. 100 kW of input power are

needed to generate a gradient of 40 MV/m at the cathode surface, essential to achieve small beam emittance. The cavity, see fig. 4, will be tested at the PITZ facility.
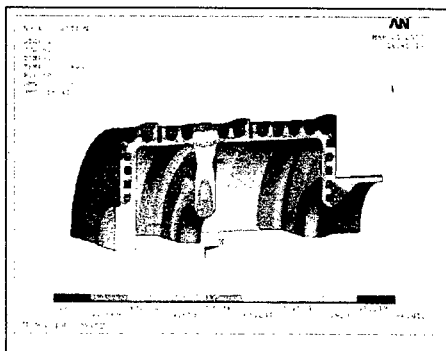
Figure 4: Temperature distribution in ¼ of the gun-cavity when operating at an input power of 100 kW.

The s.c. Photoinjector

In order to fully exploit the capabilities of the CW linac generating a free selectable bunch pattern, a super conducting photoinjector is required as a phase II upgrade for the BESSY Soft X-Ray FEL

A collaboration of FZR Rossendorf, MBI and BESSY presently started to work on an improved s.c. gun, based on recent work [16].

The s.c. Linac Modules

For the linac superconducting modules of the TESLA type [17] will be used. The modules of 12 m length are equipped with eight 9-cell cavities, delivering an energy of 125 MeV to the beam at a gradient of 15 MV/m.
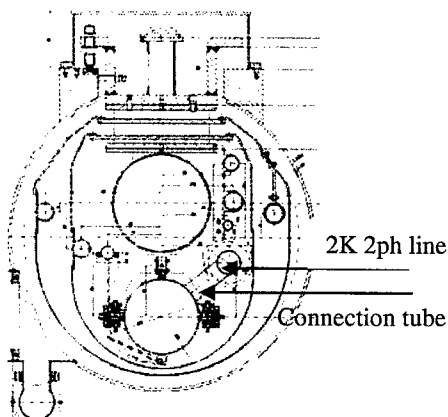
Fig. 5: Cross section of the TESLA cryo-module. The 2-phase-LHe line and the connection to the LHe-bath cryostat will be modified for CW operation.

There will be 18 modules grouped into three sections to accelerate the beam to 1.875 and 2.25 GeV respectively.

Detailed studies on the CW operation mode show that minor modification have to be introduced to the original design as a consequence of the 40 times larger cooling requirement at 2K, see fig. 5. The dimensions of the connection tubes from the cavity-LHe tank to the 2-phase-2K-He-return line and the return line itself have to be increased.

In preparation of qualifying s.c. linac components for CW operation mode, a horizontal bi-cavity test stand is set up. The stand [18] enables detailed studies on operation and RF control of the cavities at high loaded Q, controlling of micro phonics and test of fast piezo-tuners. Also couplers and tuners will be tested under realistic conditions.

ACKNOWLEDGEMENTS

REFERENCES

[1] S.V. Milton et al., Phys. Rev. Lett. 85 (2000) 988.

[2] J. Andruszkow et al., Phys. Rev. Lett 85 (2000) 3825.

[3] J. Wu, L.H. Yu, Proc. PAC 2001, Chicago, p. 2799.

[4] FERMI@ELETTRA,
http:/www.elettra.trieste.it/projects/lightsrc/linac-fel/.

[5] L. Palumbo, Proc. EPAC 2002, Paris, p. 825.

[6] S. Werin, X. Workshop on Europ. Synchrotron Light Sources, Böttstein, Switzerland (2000).

[7] M.W. Poole et al., Proc. EPAC 2002, Paris, p. 733.

[8] D.E. Moncton, X-ray Laser User Facility at Bates Laboratory, April 2003,
http://mitbates.mit.edu/index2.stm.

[9] Linac Coherent Light Source, Conceptual Design Report, SLAC-R-593, April 2002.

[10] TESLA XFEL, Technical Design Report, DESY 2002-167, October 2002.

[11] Visions of Science, The BESSY SASE-FEL in Berlin Adlershof, BESSY 2001, http://www.bessy. de /publications/01.felscientific/files/sc.pdf.

[12] K. Flöttman, ASTRA, A Space Charge Tracking Algorithm, http://desy.de/~mpyflo.

[13] M. Borland, http://www.aps.anl.gov/asd/oag/ oaghome.shtml.

[14] S. Reiche, Proc. FEL 1998, Williamsburg.

[15] F. Stephan, Proc. EPAC 2002, Paris.

[16] D. Janssen et al., Nucl. Instr. and Meth. in print.

[17] C. Pagani et al., TESLA Report 2001-36, DESY Hamburg.

[18] W. Anders, J. Knobloch, Proc. FEL 2002, Chicago.

ANALYSIS OF THE HOM DAMPING WITH MODULATED BEAM IN THE FIRST PROTOTYPE OF SUPERSTRUCTURE

P. Castro*, A. Gössel, S. Schreiber, J. Sekutowicz, M. Wendt, DESY, 22603 Hamburg, Germany,
N. Baboi†, SLAC, CA 94025, USA, G. Devanz, CEA-Saclay, France

Abstract

Superstructures, groups of weakly coupled cavities fed through a single power coupler, are currently investigated as a more cost effective alternative to the 9-cell TESLA cavities. Two Nb prototypes of the superstructure have been built, consisting of two 7-cell cavities, and installed in the TESLA Test Facility at DESY. The HOM damping of these superstructures has been investigated with a modulated beam using the method described in [1]. A charge modulation imposed on the 54 MHz bunch train excites HOM at frequencies $n \cdot f_b \pm f_{mod}$, where n is an integer, $f_b = 54$ MHz is the bunch frequency and f_{mod} is the charge modulation frequency between 0.5 and 27 MHz. The effects of the excited HOMs on the beam transverse position are observed at a downstream BPM, followed by a direct analysis of the modes at the HOM couplers.

INTRODUCTION

An alternative layout of the TESLA Linear Collider [2], based on weakly coupled multi-cell superconducting structures (so-called superstructures) reduces cost due to a simplification of the 1.3 GHz RF system. The concept of superstructures is discussed in more detail elsewhere [3, 4]. Two 2x7-cell superstructures have been installed in the TESLA Test Facility (TTF) linac downstream of the injector. The goal of this test is to proof experimentally the expected performance of superstructures in terms of energy stability, Higher Order Mode (HOM) damping, frequency and field adjustment methods. An overview of the test results is given in [5]. The investigations of the HOMs of the superstructures with modulated beam are presented here. A HOM study on superstructures has been accomplished in combination with two other methods described in [5, 6]

MEASUREMENT PRINCIPLE

The principle of the experiment [1] is to excite HOMs resonantly by modulating the bunch charge of a long train of bunches which travels through the cavities with a transverse offset. The charge modulation generates side-bands around the bunch harmonics $n \cdot f_b$, with n an integer and f_b the bunch frequency. A HOM with a frequency f_{HOM} that coincides with one of the side-band frequencies $n \cdot f_b \pm f_{mod}$ will resonate (see Fig. 1). Once excited, the HOM deflects the next bunches in the train. Thus, the transverse position

---

* pedro.castro@desy.de
† On leave from NILPRP, PO Box MG-36, 76900, Bucharest, Romania

of the bunches observed with a BPM located downstream of the module is modulated with the frequency f_{mod}. Varying slowly the modulation frequency between zero and $f_b/2$ all modes with high impedance can be found. This method has been previously applied in 1998 [7] and in 2001 [8] on 9-cell TESLA cavities in the TTF linac.
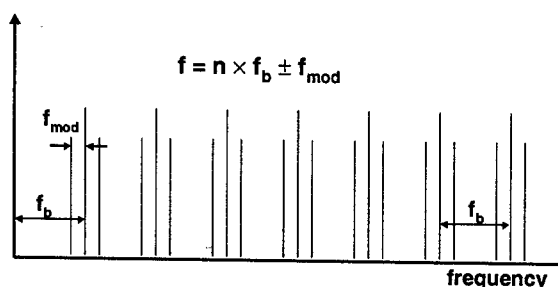
Figure 1: Spectrum of the modulated charge in the bunch train.

EXPERIMENTAL SETUP

The TTF injector is based on a laser driven RF gun [9]. Short UV laser pulses illuminate a CsKTe photocathode and produce a train of electron bunches with high peak current. For this experiment, the laser system [10] was modified to deliver 54 MHz pulse trains with a modulated charge up to 80% in the frequency range between 100 kHz and 27 MHz. The bunch train has a duration of 400 μs with an average beam current of about 2 mA.

The beam position inside the superstructures has been horizontally and vertically displaced using dipole correctors located upstream (see Fig. 2). When a HOM is excited, it kicks the beam and the induced bunch-to-bunch oscillations are detected using a re-entrant cavity Beam Position Monitor (BPM) and a stripline BPM located downstream. The difference signal between opposite antennas/electrodes is filtered at the appropriate frequency using a spectrum analyser in zero span mode. During the first 200 μs of charge modulation, the BPM difference signal is dominated by the charge variation itself. For the last 200 μs, the beam current is constant and the amplitude of the signal corresponds to an oscillation in the beam position along the bunch train caused by the deflecting HOM. An example can be seen in Fig. 3 for the modulation frequency $f_{mod} = 16.981$ MHz.

The determination of the HOM frequency has been done by picking up the signal at the three HOM couplers at-
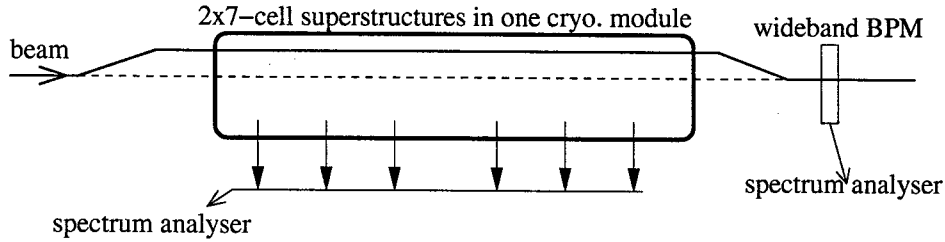
Figure 2: Schematic layout of the experimental setup.
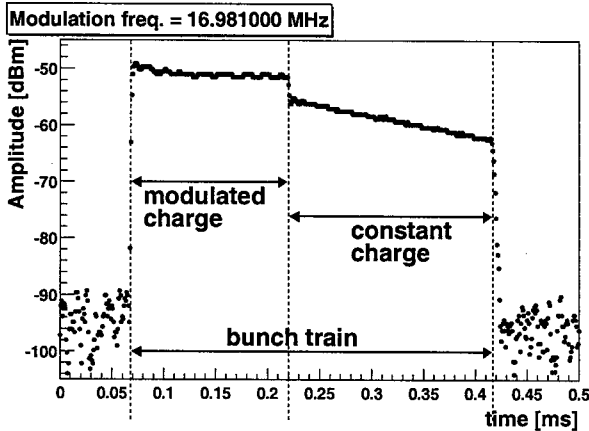
Figure 3: BPM difference signal filtered with a spectrum analyser.

tached to each superstructure. The spectrum analyser is used again in zero span mode and scanned through the signals of the HOM couplers. All frequencies $n \cdot f_b \pm f_{\text{mod}}$ situated in (or close to) the frequency ranges of the first five dipole passbands are scanned. Thus, the mode frequency is identified and the Q value of the resonance is determined from the decay-time of the signal. An example of the signals obtained is given in Fig. 4.
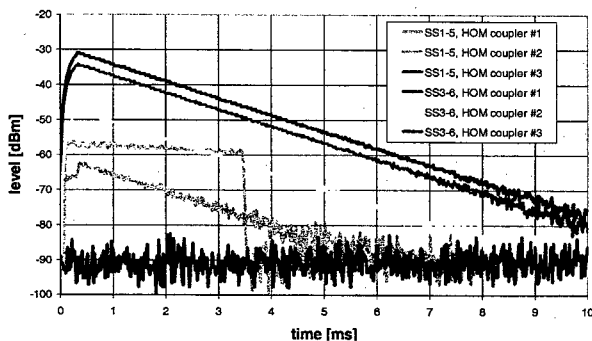
Figure 4: An example of the signals from the HOM couplers of the first superstructure SS1-5 and of the second superstructure SS3-6 at 3076 MHz.

RESULTS

A scan over all frequencies between 0.5 MHz and 27 MHz has been done in both horizontal and vertical planes, in order to cover modes of any polarization. The results are shown in Fig. 5. The amplitude of the oscillations induced by the excited HOM(s) after 200 μs of charge modulation is plotted as a function of the modulation frequency. The beam offset and charge are slightly different in the two scans, and therefore the amplitudes of the resonances can not be compared directly, but with an appropriate factor.
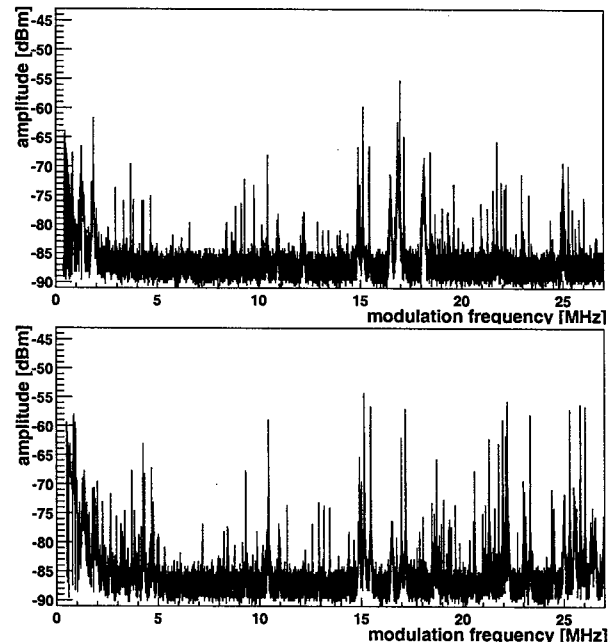
Figure 5: Beam oscillation amplitude after 200 μs charge modulation as function of the modulation frequency. Upper plot: horizontal scan. Lower plot: vertical scan.

About 90 modes have been excited and detected using this method. The mode frequency has been obtained from the HOM signals. The Q value is obtained from the decay time of the HOM signal. The results are compared with the measurements made with the network analyser [5]. An example of this analysis is shown in Fig. 6 for the range of modulation frequency between 26.0 MHz and 26.4 MHz. Not all HOMs are detected with this method. Modes with a

decay time shorter than 4 μs could not be observed with this technique, but are in general not dangerous for the beam.
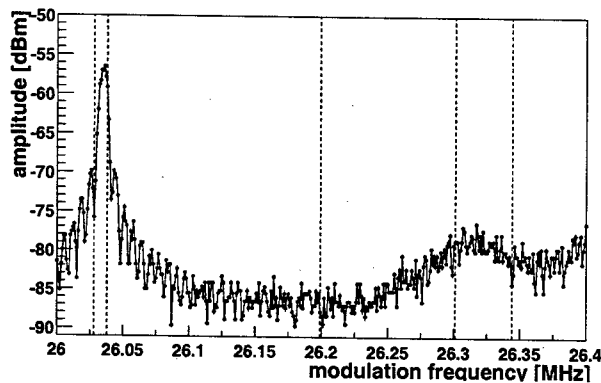
Figure 6: Example of a zoom into Fig. 5 (lower plot) where the amplitude of the vertical beam oscillation versus the modulation frequency is shown. Vertical lines correspond to the frequencies measured with the network analyser.

In the frequency range of Fig. 6, three of five expected modes have a high impedance $Z = (R/Q) \cdot Q_{ext}$, as it is shown in Fig. 7. Two are dipole modes (at approx. 2.573 GHz, marked with larger triangles) and one is a quadrupole mode (at approx. 2.3 GHz, the second from the left). The decay time of both dipole modes is about 1 μs and they are not seen in the scan of the frequency modulation. The only enhanced and remaining peak is the quadrupole mode which has a decay time of about 100 μs. The damping of both dipole modes was confirmed with the decay of output signals from the HOM couplers. The other two expected modes shown in Fig. 7 were not excited due to their low impedance. The search of other high (R/Q) modes has been performed in similar way.
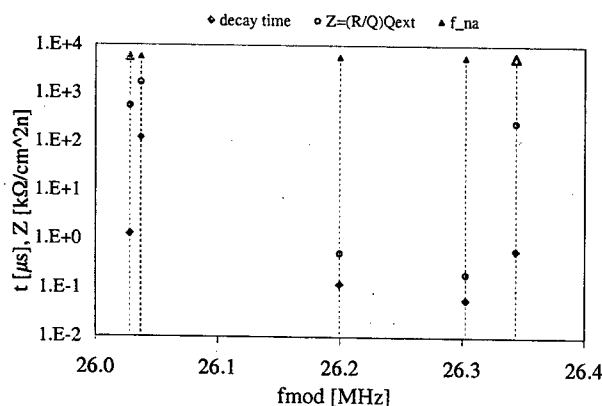
Figure 7: Decay time τ and impedance Z of modes shown in Fig. 6 (vertical lines).

CONCLUSIONS

The investigations on the HOM damping of the super-structures with modulated beam together with two other

methods described in [5, 6] have proven that all dipole modes relevant for the TESLA collider (up to 2.58 GHz) are well damped by at least a factor of 5 better than specifications ($Q_{ext} \leq 10^5$). Four modes out of 420 measured modes were found to have a large Q_{ext} of 10^7 to $2 \cdot 10^8$. These modes are in the 5th dipole passband at about 3.08 GHz. Their (R/Q)s are almost zero and therefore they do not degrade the quality of the TESLA beam.

ACKNOWLEDGMENT

REFERENCES

[1] S. Fartoukh; "A new method to detect the high impedance dipole modes of TESLA cavities", Saclay Preprint, DAPNIA/SEA-98-18 and TESLA 98-13 (1998).

[2] R. Brinkmann, K. Flöttmann, J. Rossbach, P. Schmüser, N. Walker and H. Weise (eds.); "TESLA Technical Design Report, Part II The Accelerator", DESY 2001-011, Hamburg, 2001.

[3] J. Sekutowicz et al.; "Superconducting superstructure", Proc. of LC'97, Zvenigorod, 1997.

[4] J. Sekutowicz et al., "Superconducting superstructure for the TESLA collider; A concept", PR-ST A.B, 1999.

[5] J. Sekutowicz et al.; "Cold- and beam test of the first prototypes of superstructure for the TESLA Collider", Proceedings of the PAC 2003, Portland, 2003.

[6] J. Sekutowicz, A. Gössel, G. Kreps, S. Zheng; "Active HOMs excitation in the first prototype of superstructure", Proceedings of the PAC 2003, Portland, 2003.

[7] S. Fartoukh et al.; "Evidence for a strongly coupled dipole mode with insufficient damping in TTF first accelerating module", Proceedings of the PAC 1999, New York, 1999.

[8] Ch. Magne et al.; "Measurements with beam of the deflecting higher order modes in the TTF superconducting cavities", Proceedings of the PAC 2001, Chicago, 2001.

[9] S. Schreiber for the TESLA Collaboration; "Performance status of the RF-gun based injector of the TESLA Test Facility Linac", Proceedings of the EPAC 2000, Vienna, 2000.

[10] S. Schreiber, D. Sertore, I. Will, A. Liero, W. Sandner; "Running experience with the laser system for the RF gun based injector at the TESLA Test Facility", NIM A445 (2000) 427-431.

OPERATION OF THE LEP CW KLYSTRONS IN PULSED MODE

Daniel Valuch, CERN, Geneva 23, CH-1211, Switzerland

Abstract

For possible future accelerator projects, as, e. g., the Super-Conducting Proton Linac, SPL, at CERN, it would be desirable to reuse as much of the LEP/RF equipment as possible. In the SPL, as in other proposed proton linacs, pulsed operation is required with RF pulse-lengths varying between 1 and 3 ms and a pulse repetition rate of 50 Hz. The LEP klystrons are equipped with a modulation anode by means of which their beam current and hence the output power can be controlled. In LEP the klystron output power had to be varied very slowly when the energy was ramped. In order to keep a high efficiency also in pulsed mode the rise- and fall-time of the beam pulse in the klystron should be considerably less than $100\mu s$. This goal was achieved by modifying the tetrode modulator, the HV line between modulator and klystron, and the filter network of the HV power supply.

SPICE simulations were performed to evaluate the optimum values of capacitors and inductors in the HV filtering network of the LEP 100kV, 40A power converter when a specified DC pulse shape is required and up to eight klystrons are to be powered by one HV supply. These simulations are presented, together with the experimental results obtained on a modified LEP klystron/power converter assembly.

INTRODUCTION

For reasons of economy, the power converters for the LEP klystrons have been designed such that two klystrons could be operated by one high voltage (HV) unit. The rated output of this power converter is 100kV and 40A. In order to generate 1.3MW of RF power from a LEP 2 klystron, an operating voltage of 100kV and a beam current of 20A was required.

Each LEP klystron is equipped with a modulation anode (MA). By means of the MA voltage, the klystron beam current and hence its output power can be varied.

In LEP operation, the klystron output power was only varied during beam energy ramping. The ramping from injection to top energy lasted a few minutes during which the klystron power had to be increased from about 50kW to 1MW.

In pulsed operation the requirements for the modulation anode circuitry, with respect to the LEP operation mode, change dramatically in that its time constant must be lowered by about a factor of one hundred.

HV 100kV/40A power supply

One HV supply module was designed to power 2 klystrons in parallel, which means output voltage up to 100kV and output current up to 40A.

The power supply consists of four modules:

1. 18kV/1kV step-down extended-delta transformers. There are two transformers used, of which the first one shifts the phase between primary and secondary by +30 degrees, and the second one by −30 degrees. By this phase shift, 3 input phases are converted into 6 phases at the 1kV output side.
2. Two 3-phase thyristor bridges which are working in parallel. The control of the power converter output voltage is done in this module.
3. Two 1kV/50kV step-up transformers.
4. Rectifier and filtering choke. Both step-up transformers are connected in series to obtain output voltage from zero to 100kV DC. There is a 5H filtering choke installed in same the oil tank as the diode rectifier bridge.
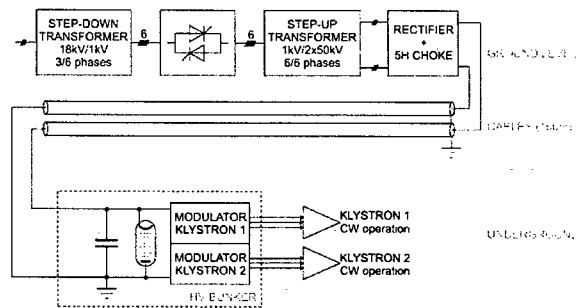
Figure 1: LEP HV system configuration

Each of these modules with the exception of the thyristor bridges is housed in a separate oil-tank.

Two-way rectification of each phase results in a 12 pole system with a 600Hz ripple, which lowers the requirements for output filtering choke and capacitor.

The power converters have been installed at the surface, and connected to HV interface bunkers by up to 600m long HV cables. The fire-proof HV bunkers, which were located next to the respective klystrons, housed the modulators, the $2\mu F$ decoupling capacitor, thyratron crowbar and HV commutator switch (see figure 1).

Modulation anode power supply

The LEP klystrons have been equipped with a modulation anode. By varying its voltage the klystron beam current, and hence its output power can be controlled while keeping RF drive level and operating voltage constant.

In LEP an adjustable resistive voltage divider was used (see figure 2). The variable resistor consisted of a TH5186 tetrode. Since only slow changes of MA voltage were needed in LEP, the tetrode was used in triode mode requiring less electronics. Less equipment in oil and at high-voltage potential gives higher reliability.
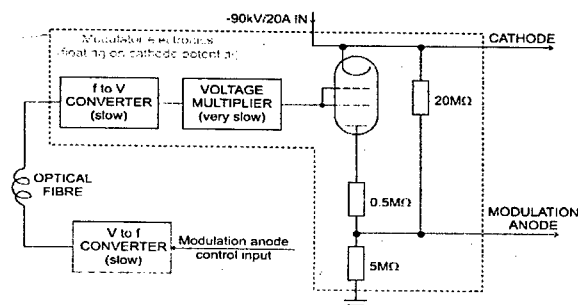
Figure 2: LEP klystron modulator circuitry

The resistors forming the MA voltage divider have had relatively high values to keep the thermal power dissipation in the oil tank as low as possible.

The HV cable connecting the modulator tetrode with the klystron modulation anode was 25m long, representing a total capacity of 5nF. Together with the tetrode anode resistor of 5MΩ, this capacity fixes the time constant of the modulation anode system to 25ms.

Because the tetrode is at cathode potential, all control signals must be galvanically insulated. For this reason an optical fibre was employed. A signal, the frequency of which was proportional to a control signal, was sent via the optical fibre to the electronics of the tetrode grid.

For pulsed operation with millisecond pulses, the time constants of the system must be reduced significantly. This requires a complete redesign of the tetrode modulator circuitry.

PULSE OPERATION OF LEP CW SYSTEM

In order to operate the LEP/RF CW system in pulsed mode the following items must be modified or rebuilt:
- The modulator
- The interconnection between modulator and klystron
- The HV power supply filtering network

For economy, it is envisaged to re-use as many LEP RF components as possible.
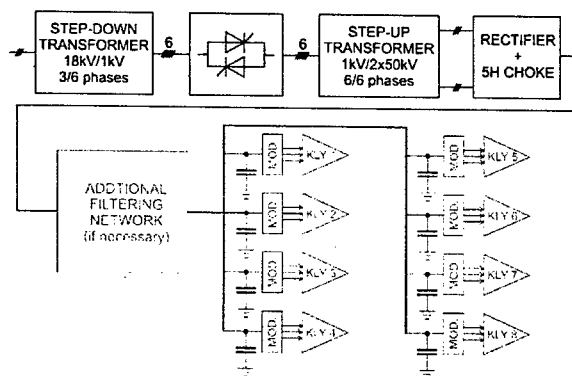
Figure 3: HV system for pulsed operation of the klystrons

Modulator modifications

As discussed earlier, the modulator electronics and the cable connection to the klystron determine the speed of the whole circuit.

First, the tetrode electronics was redesigned. To increase its current capability, the short circuit between screen and control grid was removed enabling operation of the tube in tetrode mode. An additional stabilized power supply for the biasing of the screen grid had to be installed.

The voltage multiplier for the control grid was replaced by a stabilized power supply with a fast linear voltage regulator. With these modifications, 70kV pulses with rise and fall times of 100µs at the modulator output could be generated.
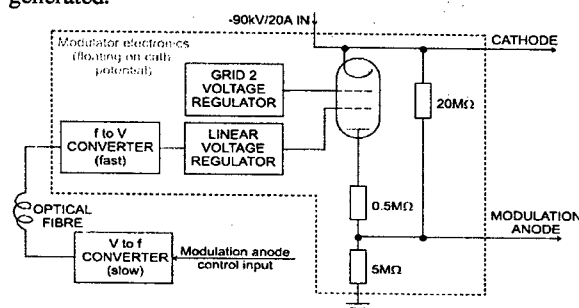
Figure 4: Modified modulator circuitry

The anode resistor has been lowered by a factor of more than three to its final value of 1.5MΩ. The lower limit for the anode resistor value is determined by the maximum acceptable power losses in the modulator tank. At R_A=1.5MΩ and U_{CATH}=90kV more than 5.5kW are dissipated which must be extracted by a oil-to-water heat exchanger.

HV interconnection cable between modulator and klystron

The capacity of the HV cable used in LEP is 200pF per meter, and the input capacity of the modulation anode is 130pF. These capacities are the main limitations for short rise and fall times of the modulation anode pulses. The only possibility to reduce the capacity of the link between modulator and klystron was to make the HV cable as short as possible and remove its shielding.

By shortening the cable to 3 meters, and removing the shielding, a rise time of 600µs and a fall time of 100µs were achieved.

It would be desirable to integrate the tetrode with the HV resistors in the oil tank attached to the klystron gun. However, this would require a bigger oil tank.

High voltage feeding system modifications

The filtering network of the LEP 100kV/40A power converter consisted of a 5H choke and a 2µF capacitor. In order to operate klystrons in pulsed mode with a power supply designed for continuous mode a special filtering network must be installed. This network must isolate as far as possible the varying load from the power supply.

For that reason, most of the pulse energy must be stored in capacitors located close to the klystron. These capacitors provide the peak current required for the pulsing of up to eight 1.3MW klystrons, and are charged by the rated current of the power supply (40A) during the idle period.

The filtering choke together with the capacitor form an L-C network, which tends to oscillate when operated in pulsed mode. These oscillations could cause voltage overshoots, which are dangerous for the klystrons. Special care must be taken in designing an appropriate filtering network.

SPICE simulations were used to find the voltage drop and circuit current during the pulse as a function of capacity installed per klystron. Results are shown in table 1 and pictures 5,6 and 7 (conditions for simulations – U_{CATH}=90kV, 6 klystrons, 20% duty cycle, 50Hz repetition rate).

Table1: SPICE simulated currents and voltages

Capacity per klystron	Cathode voltage		Klystron current	
	U_{avg} (kV)	Ripple (kV)	I_{avg} (A)	Ripple (A)
2μF	90	29.2	25.8	15.9
2.6μF	90	21.2	26.2	11.2
3.3μF	90	16.8	26.4	8.6
4μF	90.1	13.7	26.5	6.9
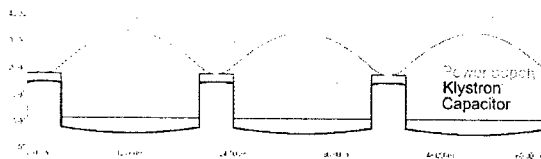
Figure 5: Circuit currents
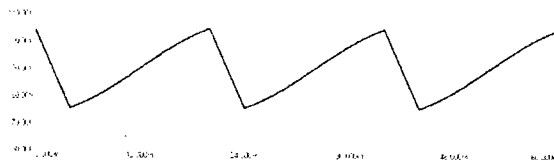
Figure 6: Klystron cathode voltage
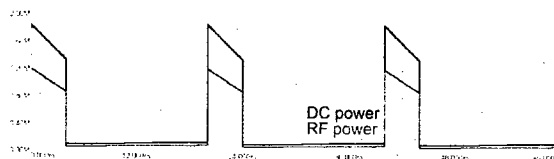
Figure 7: Klystron DC and RF power

MEASURED RESULTS

Measurements were done in view of a possible application in SPL, i.e. at a pulse repetition rate of 50Hz and pulse width of 5ms up to a peak power level of 850kW. No warming up of the oil-insulated capacitors could be observed. The output RF pulse followed the pulse supplied to the modulation anode of the klystron (see figures 8-11).
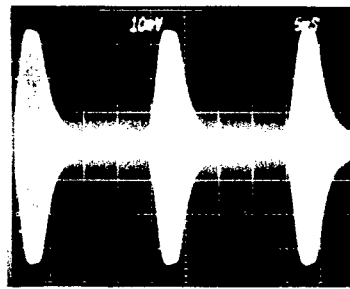
Figure 8: Shape of the RF pulses using LEP modulator
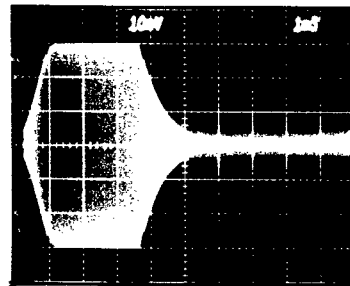
Figure 9: Detail of the pulse generated by the LEP modulator
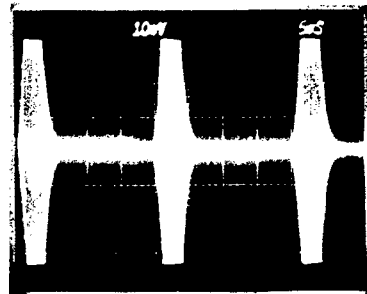
Figure 10: Shape of the RF pulses using modified modulator
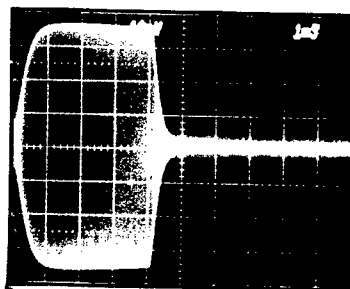
Figure 11: Rise and fall times of the RF pulse provided by the modified modulator

ACKNOWLEDGEMENTS

FERRITE EVALUATION FOR AHF PROTON SYNCHROTRONS*

J. T. M. Lyles[†], L. J. Rybarcyk, LANSCE, J. F. Bridges, TechSource,
Los Alamos National Laboratory, Los Alamos, NM 87545, USA

Abstract

The Advanced Hydrotest Facility (AHF) proton synchrotrons are likely to use parallel-biased, Nickel-Zinc ferrite cores in accelerating cavities. The Booster frequency is anticipated to be in the range of 0.32 – 1.25 MHz, depending on the choice of final energy and design, while the 50 GeV Main Ring (MR) frequency range is 4 – 5.03 MHz. Experiments were conducted to characterize the response of large rings of Ferroxcube 4M2, 4B3 and 8C12 ferrites over these frequency ranges. Testing of 4M2 for the Booster revealed degraded performance due to the nonlinear response of incremental permeability at elevated flux densities [1]. This constrains the operating voltage to a range well below the thermal power limits of the material. The 4M2 and 4B3 material appears to be satisfactory for the MR. The 8C12 material is satisfactory for the Booster if it is operated below the threshold of a high loss effect. The final cavity designs will be based upon the results of ferrite measurements from the test cavity, for the requirements of the AHF accelerators. Testing methods, analysis and results will be presented.

ADVANCED HYDROTEST FACILITY

The AHF will allow for quantitative proton radiography for hydrodynamic tests and dynamic experiments in support of the stewardship of the nuclear weapons stockpile. The proton accelerators are comprised of an H-injector linac, a Booster synchrotron and a 50 GeV MR. The LANSCE 800 MeV proton linac or a new 157 MeV linac are being considered for the injector. Also under consideration is either 4 or 9 GeV (h = 1 or 2) booster design. A significant portion of AHF consists of beam transport lines with splitters and multiple imaging systems at hydrotest firing sites.

Radio Frequency Systems

The Booster designs under consideration cover a frequency range of 0.32 to 1.25 MHz, with maximum voltages of 39 to 72 kV/turn. The MR frequencies range from 4 to 5.03 MHz, depending on the Booster injection energy. The maximum voltages are from 170-210 kV/turn.

It is expected that the RF cavities will use conventional Ni-Zn ferrite cores in a parallel biased arrangement. The ferrite will be arranged around the beam tube inside the coaxial cavity, in a foreshortened $\lambda/4$ transmission line structure. A capacity-loaded gap completes the LC resonant circuit. This type of cavity is commonly used for proton synchrotrons in this range of frequencies. Co-

located drivers will use tetrodes to provide the RF excitation to the cavities.

FERRITE TESTING

We investigated three compositions of ferrite from Ferroxcube. Ferrite types 4M2, 4B3 and 8C12 are all candidates for the two machines, and pairs of large sample cores with 0.5 m outer diameters were obtained. A table-top cavity was constructed to drive several cores of ferrite at realistic magnetic flux densities. This cavity is a coaxial enclosure made from rolled and welded sheet aluminum. It has a short aluminum tube for a center conductor with a thin copper disk at the upper end. This disk connects a ring of radially-oriented ceramic or mica RF capacitors attached to the outer walls of the cavity. RF voltages are developed across these low loss capacitors. Several matching networks were constructed to provide approximately 50Ω impedance to the power amplifier at either 1 or 5 MHz. Power amplifiers of up to 1 kW output power have been used. All testing was done at room temperature without supplemental cooling, by keeping the operating RF pulses under five seconds at a very low duty cycle. Fig. 1 shows a simplified diagram of the test cavity with associated RF instrumentation.
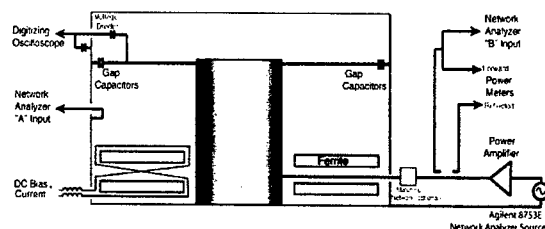
Figure 1: Diagram of Ferrite Test Setup

In the test cavity the RF magnetic flux density (B_{rf}) is in the same direction in both cores by way of RF current in the center post, while the DC bias winding uses a 'figure-of-eight' configuration for opposite sense in each core. The RF current induced in each bias winding is cancelled at the common leads. Residual current due to asymmetry of the layout and lead pickup is blocked with a low-pass filter. Multiple bias windings around the cores provide up to 1110 Amp-turns with a compact lab current source. Susceptibility to stray resonances is a disadvantage of having a multi-turn bias winding. In general these were located above the fundamental resonance and therefore not a problem for our tests.

In figure 2, Agilent network analyzers and the cavity with matching networks are seen left of center; power meters and data acquisition system are on the right. Several high power amplifiers are located on the far right.
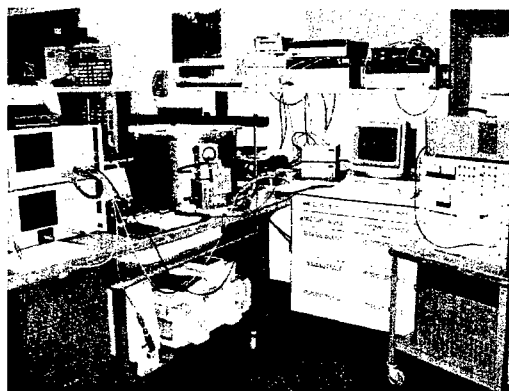
Figure 2: Photograph of Ferrite Test Setup

Determination of u', Q and u'Qf

We developed a data-reduction method to extract the desired ferrite parameters from the RF measurements. The quantities of interest are the relative permeability (μ'_r) of the ferrite, the quality factor (Q) of the ferrite, and $\mu'Qf$. We benchmarked our results against published measurements of 4M2 ferrite at 2 MHz with no bias [2]. The results showed excellent agreement.
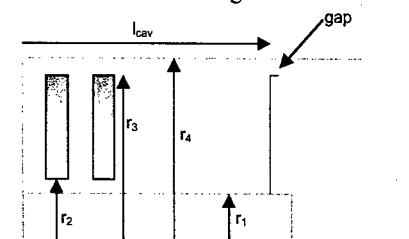
Figure 3: Axially Symmetric Model of Cavity

A physical model of the electrically-short cavity (fig. 3) was used to derive an expression (eq. 1) for μ' for the ferrite cores:

$$\mu'_r = 1 + \frac{l_{cav}}{N \cdot t_{core}} \left(\frac{1}{\frac{\mu_0}{2\pi} \cdot \ln\left(\frac{r_4}{r_1}\right) \cdot l_{cav} \cdot C_{tot} \cdot (2\pi f)^2} - 1 \right) \left(\frac{\ln\left(\frac{r_4}{r_1}\right)}{\ln\left(\frac{r_3}{r_2}\right)} \right) \quad (1)$$

The total capacitance was determined from a fit of the resonance data using several known capacitors across the gap using equation 2.

$$L_{tot} \cdot (C_{ext} + C_{stray}) = \frac{1}{(2\pi f)^2} \quad (2)$$

To determine Q and u'Qf, the equivalent shunt impedance is found by measuring the voltage and power, while ignoring cavity wall losses. The ferrite Q is then deduced from cavity Q and the ratio of inductances (eq. 3):

$$Q_{ferr} \cong \frac{\frac{V^2}{2P}}{2\pi f L_{total}} \cdot \frac{L_{ferr}}{L_{total}} \quad (3)$$

The total (ferrite) inductance is derived from the expression for the magnetic flux in the cavity (cores).

Results with Ferrite 4M2, 4B3 and 8C12

Ferrite types 4M2 and 4B3 were evaluated for both the MR and Booster frequency bands. 8C12 was evaluated only for the Booster frequency band due to its high permeability. A summary of the results are shown in Fig. 4 through 9:
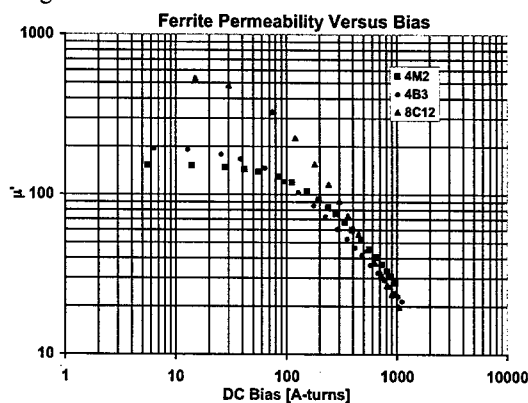
Figure 4: Permeability vs. Bias with ≈ 10 mW RF
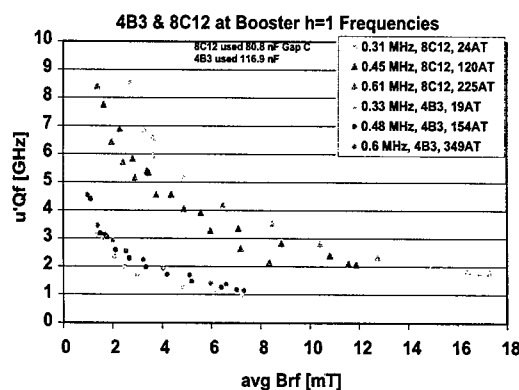
Figure 5: μQf vs. Magnetic Flux Density
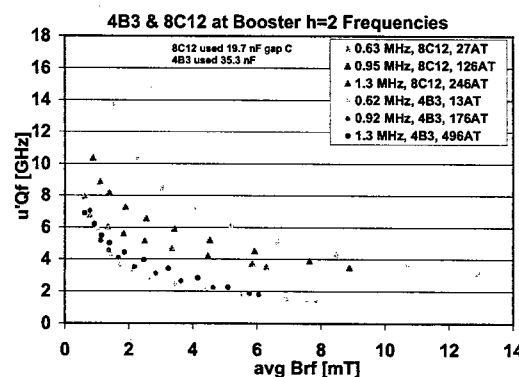
Figure 6: μQf vs. Magnetic Flux Density
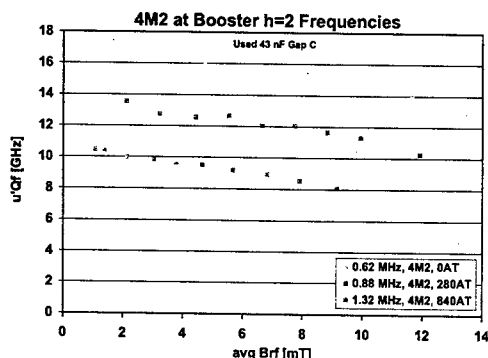
Figure 7: μQf vs. Magnetic Flux Density
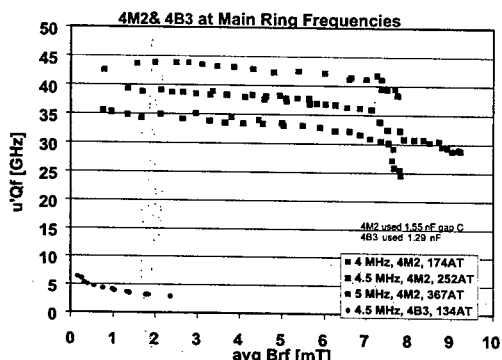
Figure 8: μQf vs. Magnetic Flux Density
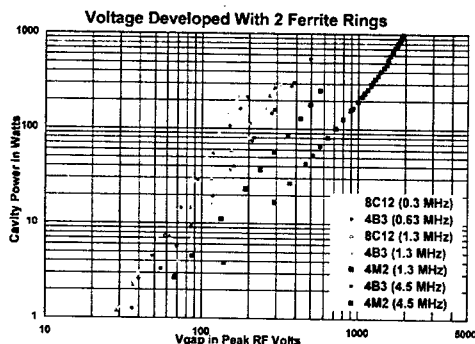
Figure 9: Power vs. Voltage for Various Ferrites

For the 9 GeV h=1 Booster frequencies, the higher B_{rf} drove the 4M2 material into a nonlinear regime in which the observed resonance curve became distorted (left in fig. 10). This effect is caused by the location of the minor BH_{rf} loop inside the major bias BH loop [1]. It would be problematic for control loops for the RF system, as gain would rise steeply around resonance in a phase detection process. The same plot shows the response at lower flux density. 4B3 and 8C12 also show evidence of this nonlinearity, but the effect is shunted by the lower ferrite Q. 4M2 is acceptable for the MR, but was eliminated from further consideration for the Booster. 4B3 is acceptable as a lower Q alternative (more power required) for the MR, but μ may be too low for the lower frequency booster design. Material 8C12 is suitable for both Booster designs.
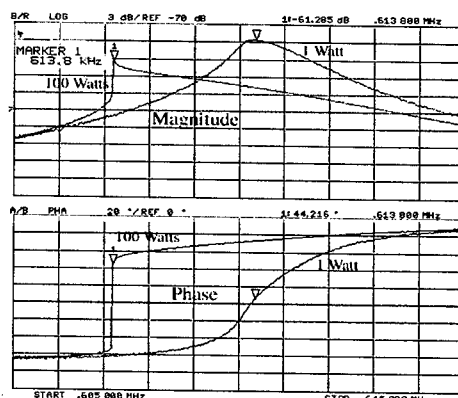
Figure 10: Amplitude/Phase Responses of 4M2 Ferrite at 0.614 MHz, with High and Low B_{rf}

We observed a high loss effect in the 8C12 ferrite, occurring when the flux density was high at certain bias conditions. It is related to stored energy in the ferrite [3] and was manifested as noise on the gap voltage and a significant drop in voltage during long pulses of RF. This can be problematic where the bias is held constant, such as during a plateau of the frequency program. Dynamic losses have not been determined at this time, but will be measured when a suitable bias ramping scheme is incorporated into the setup. All three of these anomalies must be well characterized and mitigated before designing full-sized cavities.

SUMMARY

We have developed an accurate measurement methodology to fully characterize ferrite cores for the design of cavities for the AHF Booster and MR. Three types of ferrite have been tested, and a summary of the results are presented. Material 4M2 or 4B3 appear satisfactory for the MR while 8C12 would be suited for the Booster cavities.

ACKNOWLEDGEMENTS

REFERENCES

[1] G. Rakowsky and A. Tranis, "Nonlinear Effects in Linear Ferrites at High RF Fields", IEEE Trans. Nucl. Sci., NS-16, p. 543-5, June, 1969.

[2] Y. Tanabe, et. al., "Dependence of RF Characteristics on AC Bias Current for Large-Sized Ferrites", Electrical Eng Japan, Vol. 127, No. 4, 1999.

[3] J. Griffin and G. Nicholls, "A Review of Some Dynamic Loss Properties of Ni-Zn Accelerator RF System Ferrite", IEEE Trans. Nucl. Sci., NS-26, p. 3965-7, June, 1979.

THE SNS LINAC HIGH POWER RF SYSTEM DESIGN, STATUS, AND RESULTS*

D. Rees, J. Bradley III, K. Cummings, T. Hardek, M. Lynch, W. Roybal, P. Tallerico LANL, Los Alamos, New Mexico, 87544 USA

Abstract

The Spallation Neutron Source being built at the Oak Ridge National Lab in Tennessee requires a 1 GeV proton linac. Los Alamos has responsibility for the RF systems for the entire linac. The linac requires 3 distinct types of RF systems: 2.5-MW peak, 402.5 MHz, RF systems for the RFQ and DTL (7 systems total); 5-MW peak, 805 MHz systems for the CCL and the two energy corrector cavities (6 systems total); and 550-kW peak, 805 MHz systems for the superconducting sections (81 systems total). The design of the SNS Linac RF system was presented at the 2001 Particle Accelerator Conference in Chicago. Vendors have been selected for the klystrons (3 different vendors), circulators (1 vendor), transmitter (1 vendor), and high power RF loads (3 different vendors). This paper presents the results and status of vendor procurements, test results of the major components of the Linac RF system and our installation progress.

SNS HIGH POWER RF EQUIPMENT

A summary of the status of each of the high power RF components and a description of the problems encountered is provided below.

Klystrons

The SNS klystrons are supplied by three manufacturers. The specifications for each type of SNS klystron are given in Table 1. The 2.5-MW, 402.5 MHz klystrons are supplied by E2V Technologies (formerly Marconi & EEV). The 5.0-MW, 805 MHz klystrons are supplied by Thales (formerly Thomson). The 550 kW, 805 MHz klystrons are supplied by two manufacturers, CPI (formerly Varian) and Thales. A photograph of the 402.5 MHz klystron installed at Los Alamos is included in Fig. 1 and a photograph of the CPI 550 kW klystron and the Thales 5 MW klystron side by side is shown in Fig. 2. The klystrons operate in a vertical orientation with localized shielding and are mounted into a socket attached to the lid of an oil tank. They are protected from high reflected power by a circulator. The 805 MHz klystrons have a separate magnet while the 402.5 MHz klystron has an integral magnet.

402.5 MHz, 2.5 MW Klystrons

As of the end of March 2003, eight 402.5 MHz klystrons have been delivered by E2V Technologies. Of these 8 klystrons five have passed a site acceptance test, one is currently in test, one developed a vacuum leak

during the site acceptance tests, and one developed a vacuum leak in shipping.

We accepted the first two klystrons at a reduced power (approximately 1.7 MW instead of the required 2.5 MW) to make schedule progress and because the first 2 sockets for the RFQ and DTL-1 required less than 1 MW of RF

Figure 1: 402.5 MHz, 2.5 MW Klystron

Figure 2: CPI 805 MHz, 550 kW klystron on left and Thales 805 MHz, 5 MW Klystron on right.

Table 1: SNS Klystron Specifications

Vendor	E2V	Thales	CPI/Thales
Peak Power	2.5 MW	5 MW	550 kW
Test Power	2.75 MW	5.5 MW	605 kW
Frequency	402.5 MHz	805 MHz	805 MHz
Duty Factor	8 %	8 %	9 %
PRF	60 Hz	60 Hz	60 Hz
Efficiency	58 %	55 %	65 %
Beam Voltage	125 kV	140 kV	75 kV
Bandwidth	1.0 MHz	2.6 MHz	2.6 MHz
Height	13 ft	13 ft	9 ft

power each. All other accepted klystrons have met all requirements. However, each of these klystrons has required modification by E2V based on the site acceptance tests. We have had a klystron which passed the factory acceptance tests not able to make power at Los Alamos because of a tuning change of unknown origin in the second harmonic cavity. All of the klystrons received have required modifications in the RF joint between the coaxial output and the coax to waveguide transition. The shielding has had to be modified to reduce the x-ray level to a value consistent with the specification. There have been problems with the load on the second cavity being undersized, failing, and in once instance causing a vacuum leak. And we have had problems with the lead shielding shorting out the magnet coils. Fortunately, most of these problems have been external to the vacuum envelope and have been repaired successfully on site.

Three of these klystrons are already installed at SNS and the fourth is in progress. These klystrons have been very easy to install and remove and very easy to condition and operate. They arrive from the factory with all lead shielding and waveguide in place, so that these klystrons are quickly installed and made operational. These klystrons can typically be brought up to the full peak and average power while maintaining a very low ion pump current value (less than 1 uA) in less than 1 hour. They have also demonstrated a very low gun and RF arc rate. We execute a 96 hour burn-in test on these klystrons as part of the site acceptance and at the conclusion of this period the arc rate is typically less than 1 event in 24 hours.

The contract for this klystron allowed for a 14 month development. The first klystron was delivered about 11 months late.

805 MHz, 5 MW Klystrons

The first of nine 5 MW klystrons has been delivered by Thales and subsequently failed the site acceptance test at Los Alamos. Thales is currently making design modifications external to the vacuum envelope and we will retest the klystron in June. When this klystron was factory tested at Thales they filled their waveguide system with sulfur hexaflouride (SF6) which is required for their RF load and the tests were executed with SF6 in the air

side of the output window and output transition of the klystron. When the tube was operated at Los Alamos without the SF6 as called for in the tube specification, the output window and transition experienced severe RF arcing at approximately 1/3 the required peak power. Unfortunately, the output transition was not designed for long term operation with SF6. There was no o-ring seal or barrier window to keep the SF6 from leaking out of the transition and the SNS waveguide system is not filled with SF6. We were able to do a temporary field modification to include a capton window at the output of the klystron waveguide and to install o-ring seals between the transition and RF window. With the application of liberal amounts of silicon gel, were able to temporarily fill the output transition with SF6 and continue testing.

Thales is only able to test to a pulse width of approximately 400 usec at the factory yet the klystron is required to operate with a cathode pulse of 1300 usec. The combination of the long pulse with the high peak power is one of the most technically challenging aspects of this tube so we were anxious to validate the long pulse performance. We operated this tube for one month at Los Alamos and for short periods of time (4 to 6 hours) were able to achieve the full peak and average power. The efficiency of our testing and conditioning was impaired by a number of failures. This is the highest peak and average power klystron of the SNS RF system and we had been awaiting its arrival to prove out the performance of many of the waveguide components. With the initial operation of this klystron we discovered design problems with the circulator, the RF load, and the cathode power supply. Temporary and permanent resolutions to these problems impacted the number of hours we could operate the tube. In one month we operated the klystron approximately 112 hours until the cumulative problems in the waveguide systems and transition caused us to suspend testing until permanent repairs and design changes could be made. Testing will resume in June, 2003. With 112 hours of conditioning, the arc rate of the klystron was still high. We averaged either an RF arc or gun arc about every two hours. The tube must demonstrate less than 2 arcs in 24 hours of full power operations before we will accept it.

This klystron is not delivered as an assembled unit. The output transition and most of the lead shielding need to be installed after the tube is inserted in the socket. The insertion and assembly of the first article shielding took approximately 3 days. The x-ray protection of the lead shielding was also discovered to be inadequate and is currently being redesigned by Thales. The contract for this klystron required a 14 month development and this first klystron was delivered about 10 months late.

805 MHz, 550 kW Klystrons

Two vendors were selected to produce the 550 kW klystrons. CPI was awarded an order for 75 tubes and Thales was awarded an order for 23 tubes. The contract for these developments also called for the first tube in 14 months. CPI delivered the first tube 4 months late but has

subsequently delivered 15 tubes and has made up most of the schedule delay. They are currently only 1 tube (2 weeks) behind schedule. Thales has yet to deliver the first tube, although it is in transit. They are 11 months behind schedule on the delivery of their first 550 kW klystron.

We have site acceptance tested 11 of the CPI klystrons and have yet to discover a problem. We accepted the first klystron from CPI to a slightly reduced efficiency specification of 63%. Every subsequent tube has exceeded the efficiency specification. We execute a 36 hour burn-in test on these tubes as part of the site acceptance tests. To date we have seen only 2 gun arcs in approximately 400 hours of burn-in testing with these klystrons. These klystrons require minimal assembly in their delivered configuration. Typically, we can remove a tested CPI tube, install and assemble a new CPI tube, restart testing, and have the tube operating at full peak and average power in under 4 hours.

Circulators

All SNS klystrons are protected from reflected power by y-junction circulators supplied by AFT. These circulators are rated to provide 26 dB of reverse isolation at any phase of a full power reflection. We have received all 107 circulators at the two frequencies and three power levels from AFT. We have high power tested five of the 2.5 MW, 402.5 MHz circulators and all have passed. We have also high power tested eight of the 550 kW, 805 MHz circulators and all passed. We have attempted to site acceptance test the first of the 5 MW, 805 MHz circulators. Because of the voltage gradients associated with the high peak power, this circulator is filled with SF6. Capton windows are used to restrict the SF6 to the circulator body. While trying to validate the circulator design under high power, we have had multiple failures and persistent arcing problems of the port 2 capton window. AFT has completed some further modeling on this window design and is implementing a new design for the port 2 window. This design will be high power tested in April 2003.

Loads

All the circulator loads for the SNS RF system are liquid loads where the liquid is the absorptive element. All loads have been delivered. The 402.5 MHz loads, made by Atlantic Microwave, are rated for 2.5 MW of peak power and 200 kW of average power and use a 70/30 water glycol mix. Six of these loads have been high power tested and all have worked perfectly.

The 805 MHz loads at 550 kW and 5 MW are pure water loads. The load for 550 kW application, made by Mega Industires, is rated at 600 kW peak and 60 kW average. We have tested 8 of these loads and all worked perfectly. We tested the prototype load up to a peak power of 1.3 MW and an average power of 200 kW without problem.

The 5 MW peak power, 400 kW average power load, made by Sure Beam, failed high power testing. On the first 2 loads exposed to high power, an o-ring failed due to exposure to the RF and water leaks developed. The damaged o-ring has been replaced with an o-ring material less susceptible to RF heating and these loads are awaiting retest.

RF Windows

LANL is providing the RF windows for the DTL and CCL. We are using planar waveguide windows provided by Thales. The power from the 402.5 MHz klystron passes through a single window into the DTL and the power from the 5 MW, 805 MHz klystron is split and enters the CCL through two windows. All windows have been delivered. We have tested 4 DTL windows and 2 CCL windows. The first pair of DTL windows failed high power testing due to poor RF contacts on the air side of the window. They are being reworked. Thales modified their assembly procedures to correct the problem. A subsequent pair of DTL windows passed the high power testing. A pair of CCL windows has also passed high power testing. Details of the test conditions and the measured performance can be found in reference 1.

Transmitters

The SNS transmitters comprise all of the electronics to operate and diagnose the SNS RF equipment. They are being provided by Titan System Corporation Pulsed Sciences Division. All twenty transmitters for the normal conducting portion of the SNS linac, test stands, and spares have been delivered to LANL and ORNL and are in various stages of installation and operation. Delivery has just begun on the transmitters for the super conducting linac. A description of the transmitter equipment and test results can be found in reference 2.

CONCLUSION

Most of the SNS high power RF hardware has been delivered and good testing progress is being made. The 402.5 MHz RF systems and the 805 MHz, 550 kW RF systems are performing as required. The primary technical risk area is the 5 MW RF systems. Currently the klystrons, loads, and circulators are all being reworked. The arc rate of the klystron is still very high even after over 100 hours of conditioning. This is the area where we will be concentrating our future efforts.

REFERENCES

[1] K. Cummings, "High Power Testing of the 402.5 MHz and 805 MHz RF Windows for the Spallation Neutron Source Accelerator", PAC 2003, May 2003.

[2] J. Bradley III, "Spallation Neutron Source High-Power RF Transmitter Design for High Availability, Ease of Installation and Cost Containment" PAC 2003, May 2003.

JLAB HIGH EFFICIENCY KLYSTRON BASELINE DESIGN FOR 12 GEV UPGRADE*

H. Wang#, L. Harwood, R. Nelson, C. Hovater, J. Delayen

TJNAF, Newport News, VA 23606, USA

Abstract

A computer design of a 13.5 kW, 1497 MHz, CW type, 55% efficiency, 0.8 µP beam perveance, ~40 dB gain, 5-cavity klystron has been developed for the JLAB 12GeV Upgrade project. The design uses TRICOMP codes to simulate the gun, modulating anode section, solenoid focus channel and beam dump. The klystron tube was designed by JPNDISK (1D) code initially and then optimized by MASK (2D) code for the baseline parameters. All of these codes have been bench marked by JLAB 5 kW operational klystrons. The details of scaling laws, design parameters and the simulation results are presented.

INTRODUCTION

The CEBAF energy upgrade from 6GeV to 12GeV at JLab requires that the klystron power (CW type) to be 13kW for the new high gradient superconducting cavity [1]. A new product or design of a high efficiency (>50%) klystron had been specified. In addition to the bidding process with the klystron tube industry and the SBIR development program, we have independently designed this klystron using integrated computer tools. Before proceeding with the new design, we have used these tools to bench-mark our operating 5kW klystron. A possible beam interception in the gun to mod-anode section was found [2]. This problem caused potted ceramic insulators thermal runaway and finally damaged klystrons in the CEBAF machine.

We used TRICOMP (2D) [3] package to design the gun section from cathode to modulation anode, and the focusing channel from anode to beam dump. For the klystron tube design, we used small signal analysis first to get initial design parameters. We then put them into the large signal 1D JPNDISK code to get parameter optimization. These parameters were optimized further by the 2D MASK code to get the transverse space-charge effects. From MASK's result, we finally designed the klystron dimensions with Superfish [4]. We found that a 5-gap klystron is the minimum length structure and can be used as our baseline for a low cost design. In Table 1, we list the design specifications and what we have achieved in our preliminary design. Operation at 1dB below saturation and with a wide bandwidth was based on the CEBAF superconducting cavity's control experience. It

normally contradicts a high efficiency tube design. A new low-level RF control system will be designed to work in conjunction with this new klystron.

Table 1: Specification and achieved design parameters.

Parameters	Specification	Achieved in Design
Frequency	1497MHz	1497MHz
Saturated power	16.4kW	15kW
Operating power	13kW	13.5kW
Saturated gain	40dB	41.8dB
Bandwidth	3dB>6MHz or 1dB>5MHz	3dB: 5.7MHz; 1dB: 3.8MHz
Efficiency	>50%	55%
Beam voltage	<30kV	16kV
Beam current	NS	1.6A
Gradient in gun	<75kV/cm	48kV/cm
Gradient in cavity	<300kV/cm	48.3kV/cm
Magnetic field	<2kGauss	1.7kGauss

DESIGN SURVEY AND SCALING LAWS

To achieve a high efficiency klystron design, the first approach is to lower the beam perveance and to use longer drifting tubes. We have summarized two scaling laws from our achieved data and a survey from the production catalogs of two major klystron vendors.
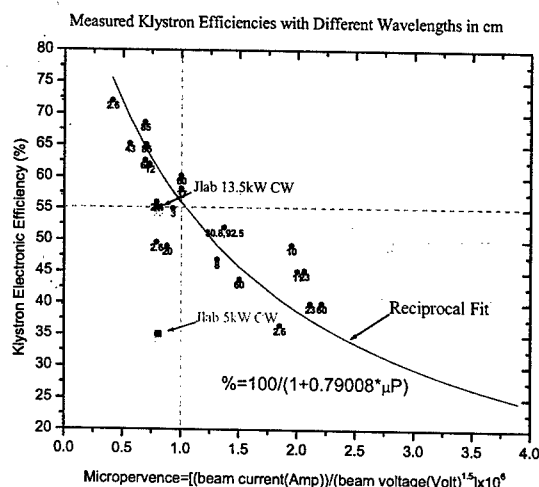
Figure 1: Klystron efficiency vs beam preveance.

Figure 1 shows that a 0.8 µP beam perveance design can achieve our 50% efficiency goal. The efficiency of current JLab 5kW klystron is well below the fitting curve. By the same fitting curve, we did a comparison between the vendor 1 and vendor 2. We found the vendor 1

follows the curve but the vendor 2 is below (Figure 2). Based on the data from vendor 1, the linear fittings can be obtained for different type of klystrons. Each type has a different slope. The PPM has a more effective focusing than the solenoid. The CW klystron normally has a larger beam dump than the pulsed type. The total length does not depend on the operating frequency because it only affects the transverse dimension. The klystron tube length is normally proportional to the plasma wavelength. And the plasma wavelength is $\lambda_p \propto V^{1/4}/j^{1/2}$ (V is the beam voltage and j is the current density) which is space charge and bunching effect related.
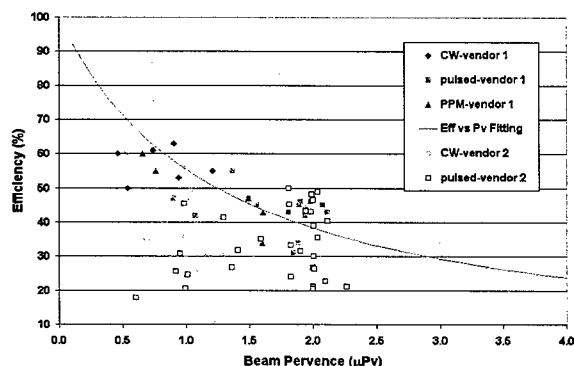
Figure 2: Efficiency vs. perveance to compare between vendor 1 and vendor 2.
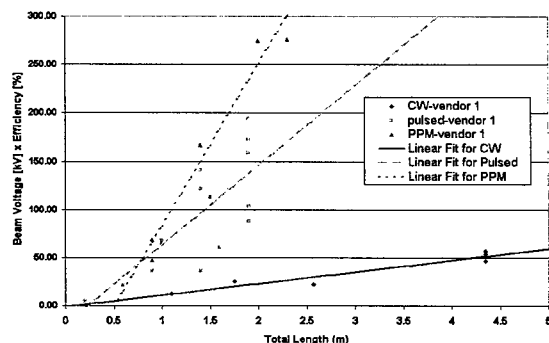
Figure 3: Beam voltage × efficiency vs. total length.

PIERCE GUN AND BEAM DUMP DESIGN

The cathode is a thermionic dispenser type. The current density is $0.4A/cm^2$, low enough for long-life operation. It works at the temperature-limited current emission with the cathode voltage of −16kV and the beam current of 1.6A. The maximum static electric field at the focus electrode is 48kV/cm. With a solenoid field ramping from 300 G at the cathode surface to a flat top of 1700 G at the anode entrance, the beam compresses down to a 5.6mm radius with a scallop amplitude of ~9%. The area compression ratio is 18:1 (Figure 4). With a -4kV mod-anode voltage, the maximum field between the mod-anode cylinder and the ground tube is 24.8kV/cm. The ceramic insulator is going to be air-cooled without potting. With a falloff of 370gauss/cm of the solenoid

field, the full power of the beam can be uniformly dumped.
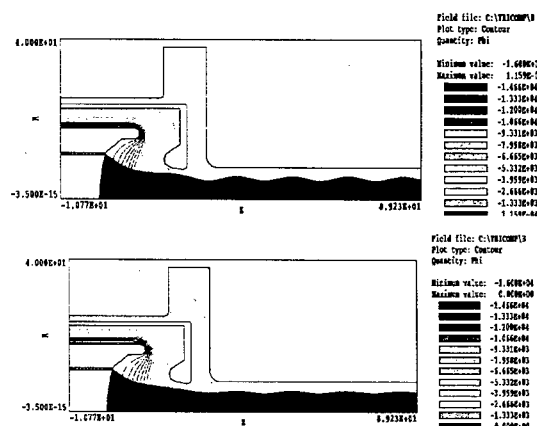
Figure 4: TRICOMP simulations in gun section. The potential at the cathode is −16kV; at the mod-anode is 0kV in top plot and -4kV in bottom plot.

Figure 5: TRICOMP simulation in tube and beam dump.

KLYSTRON TUBE DESIGN

The tube is a 5-gap, single output gap cavity with a long drift from 3rd to 4th gap. The beam pipe radius is 8mm. The beam-filling factor is 70%. The input power for a saturated output is 1.18W. The electronic efficiency is 55% and the kinetic efficiency is 57.2% No second harmonic cavity was used on this design. Table 2 lists the design parameters. The "detune" is the detuned cavity frequency minus operating frequency.

Table 2: Tube design parameters optimized by MASK.

Cavity No.	1	2	3	4	5
Qexts	400	2000	2000	2000	260
R/Qs (Ω)	95.0	95.0	95.0	95.0	95.0
Gaps (mm)	7.5	7.5	7.5	7.5	7.0
Drift pos. (mm)	0	40	78	160	200
Detune (MHz)	0.2	2.7	8.0	10.0	-1.0

We note that there is a small difference between the 1D JPNDISK code and 2D MASK code in the optimized parameters. In Figures 6~9, we show the JPNDISK output plots. Figure 10 is one of MASK output plots.

KLYSTRON CAVITY DESIGN

Since the required cavity's R/Q is relative low, we adopted a pillbox reentrant shape cavity to achieve the desired value. The cavity resonant frequencies can be obtained by adjusting the cavities outer radii. Figure 11 shows the detail dimension calculated by Superfish. The maximum electric field (48.3kV/cm) is at the output gap. The tuners will be radial button type and on all cavities. The input coupler will be inductive loop type. The output

waveguide will be side coupling and bent to interleave with the solenoid pole plate. A detail 3D MAFIA design needs to be developed.
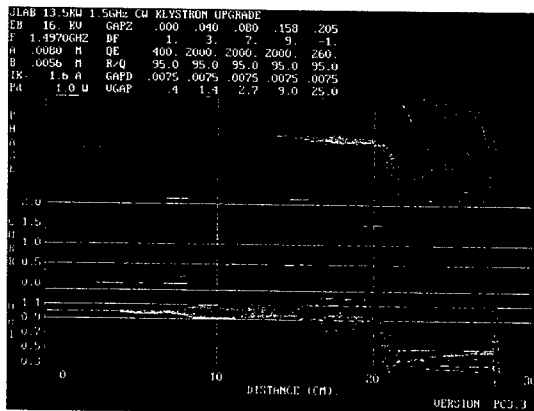
Figure 6: The JPNDIS simulation. Up to down: input parameters, Applegate plot, RF current verse z, velocity spread verse z.
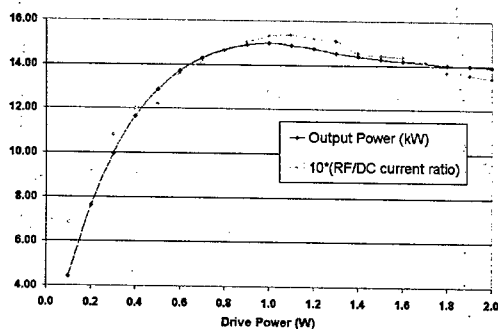
Figure 7: JPNDISK calculated output power verse input.
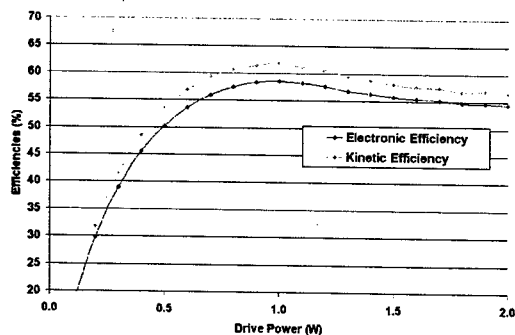
Figure 8: JPNDISK calculated efficiency vs drive power.

SUMMARY

The initial computer design to a 13.5kW RF power and 55% efficiency of a CW klystron for the JLab 12GeV Upgrade has been achieved. Although it is not a best design yet, it should be complementary to a parallel SBIR design [5]. We need to do further on the component designs, mechanical and thermal dynamic simulations. A

prototyping program or an adjoining venture with SBIR is needed in near future.
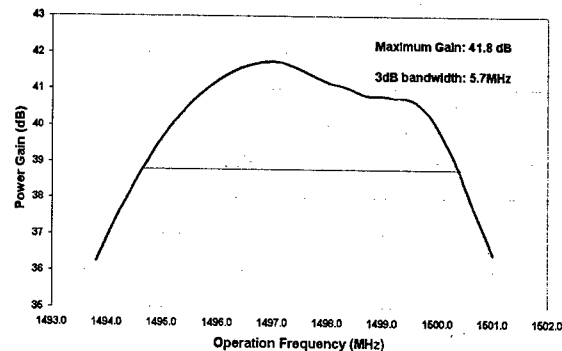
Figure 9: JPNDISK calculated gain and bandwidth.
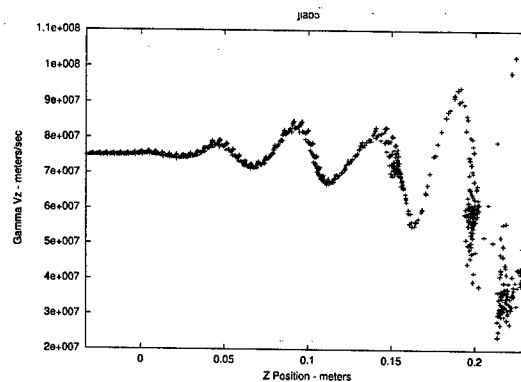
Figure 10: MASK output, transverse velocity verse z position. The gap positions are shown in Table 2.
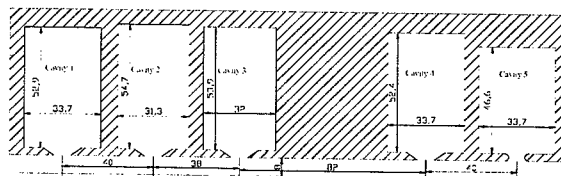
Figure 11: Klystron cavities designed by Superfish. All dimensions are in mm.

ACKNOWLEDGMENT

We would like to thank D. Sprehn of SLAC for the contribution of JPNDISK code.

REFERENCES

[1] 12 GeV RF Parameters Team, Discussions and Figures, Feb-May 2001. AccDev Notes 5/11/01. http://www.jlab.org/~harwood/12GeV/SRF/Alllowed Detuning_13kW.htm.

[2] H. Wang, SRF Institute Seminar, Feb. 26, 2003, transparencies are available as request.

[3] Field Precision, Finite-element Software for Electromagnetics, http://www.fieldp.com.

[4] Los Alamos Code Group, LAACG@LANL.GOV.

[5] M. Read, et al., these proceedings, TPAE028.

ANALYTICAL DESIGN OF A WAVEGUIDE IRIS/STUB TUNING COUPLER TO AN OVERCOUPLED SUPERCONDUCTING CAVITY[#]

Haipeng Wang[*]

TJNAF, Newport News, VA 23606, USA

Abstract

The high RF power test of a superconducting cavity without beam loading requires a variable coupling scheme. For a fixed power coupler and a finite source power, one needs to increase the external Q. A 3-stub tuner placed between the doorknob transition and an iris plate inside of WR975 waveguide has been developed for the SNS cryomodule test facility (CMTF). This paper describes the theoretical analysis, calculation by equivalent circuits and the coupling scale related to the stub tuning and the iris size. A copper model bench measurement and a 3D computer simulation proved the principle and some of the parameters. A factor of 100 over $Q_{ext}=7\times10^5$ has been achieved when implemented in the cryomodule test.

INTRODUCTION

The external quality factor $Q_{s,ext}$ of the fundamental power coupler (FPC) to a superconducting cavity is normally designed much lower than the cavity's intrinsic quality factor Q_s in order to match the input power to the beam load. For example, $Q_{s,ext}=10^5\sim10^7$, $Q_s=10^9\sim10^{10}$. That means the coupling co-efficient $\beta_s=Q_s/Q_{s,ext}$ from FPC to cavity is always heavily over-coupled $\beta_s\gg1$. A common high power type FPC was also designed in a fixed coupling in order to handle a high power and save cost. When the cavity cryomodule is under the final high power test without a beam loading, most of forward power is going to reflect back and to dump into the klystron's circulator. Using a finite klystron power to achieve a high gradient field in the cavity, one needs to increase the equivalent external Q ($Q_{eq,ext}$) by 1~3 order of magnitude, up to a controllable level to microphonics. A simple and common solution is to use a 3-stub tuner on the input power waveguide. Normally this tuning mechanism can only change $Q_{eq,ext}$ about 1 order. By adding an iris plate upstream to klystron, like in the Figures 1& 2, from the following analysis, one can get 2 orders higher. Combining the 3-stub tuning capability, the coupling of $\beta_{eq}=Q_s/Q_{eq,ext}$ can be variable. Here we define loaded $Q_{sl}=Q_s/(1+\beta_{eq})$. This mechanism is very attractive for an energy recovery recirculating linac (ERL). When the beam energy is returned to the cavity, the beam loading is gone. A higher external Q will save more klystron power from its circulator. Using a variable coupling, a same cavity can be used for both beam acceleration and storage. It can also help in helium

processing to bring more power to the cavity for destroying the field emitters. In the CMTF, using a 3-stub tuner only was the usual case for small Q external changes.
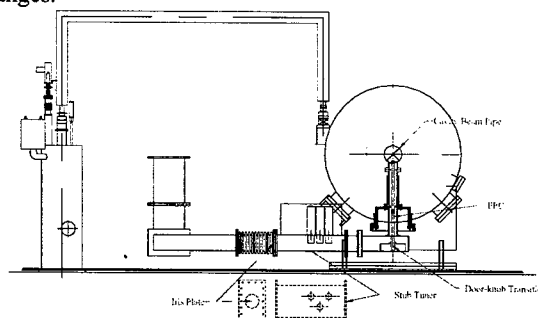
Figure 1: Iris/stub tuner design layout for SNS cryomodule tests.
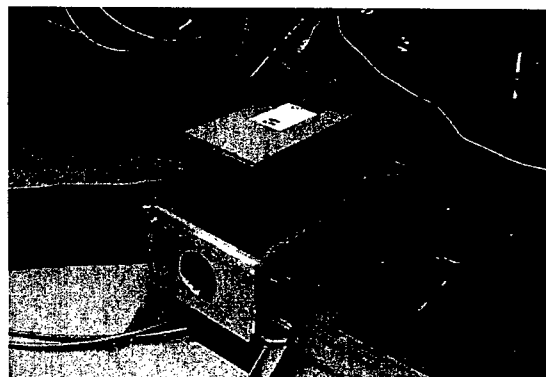
Figure 2: An iris plate installed next to the stub tuner for a 15kW CW klystron system at TJNAF.

EQUIVALENT CIRCUIT ANALYSIS

The waveguide section between the iris plate and the superconducting (sc) cavity detuning short can be treated as a low-Q coupling resonator. The power coupling from klystron to the sc cavity will be two-stage impedance transforming (see Figure 3). The sc cavity loaded Q can be deduced as [1]:
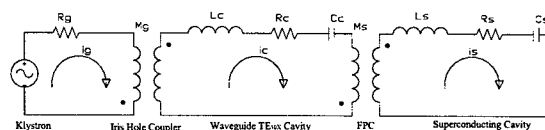
Figure 3: Resonator coupling equivalent circuit.

$$Q_{SL} = \frac{Q_s(1+\beta_g) - Q_s\delta_s + Q_c - Q_c\delta_c}{1+\beta_g + \beta_s - Q_s\delta_s Q_c\delta_c} \qquad (1)$$

Here

$$\omega_c^2 = \frac{1}{L_c C_c} \quad \omega_s^2 = \frac{1}{L_s C_s} \quad Q_c = \frac{\omega L_c}{R_c} \quad Q_s = \frac{\omega L_s}{R_s} \qquad (2)$$

$$\beta_g = \frac{\omega^2 M_g^2}{R_c R_g} \quad \beta_s = \frac{\omega^2 M_s^2}{R_c R_s} \quad \delta_c = 1 - \frac{\omega_c^2}{\omega^2} \quad \delta_s = 1 - \frac{\omega_s^2}{\omega^2} \qquad (3)$$

Using the fact that mostly $Q_s \gg Q_c \gg Q_s\delta_s \gg Q_c\delta_c$. (1) can be simplified as:

$$\frac{Q_{eq,ext}}{Q_{s,ext}} = \frac{\beta_s}{\beta_{eq}} = \frac{1+\beta_g}{1 - \frac{Q_s\delta_s Q_c\delta_c}{\beta_s}} = \frac{1 + Q_c/Q_{c,ext}}{1 - Q_{s,ext}\delta_s Q_c\delta_c} \qquad (4)$$

We define the Q_c is the coupling cavity intrinsic Q. $Q_{c,ext}$ is the iris coupling external Q to the coupling cavity. The relative frequency detuning for sc cavity δ_s is normally limited by the static tuner and microphonics' level. However, stub tuning can change the relative frequency of coupling cavity δ_c, so as to change the $Q_{eq,ext}/Q_{s,ext}$. Note that this detuning requires $Q_{s,ext}\delta_s Q_c\delta_c < 1$. That means stub frequency detuning for the resonance coupling condition has to be:

$$\Delta f_c < \frac{f^2}{4 Q_{s,ext} Q_c \Delta f_s} \qquad (5)$$

Here f is the klystron operating frequency. For example, for a SNS medium beta cavity, $Q_{s,ext} = 7.3 \times 10^5$, f=805MHz, assumed $\Delta f_s = 10$Hz, $Q_c = 1 \times 10^3$. Δf_c must be less than 22MHz. The Q_c determines the sensitivity of stub tuning. If the Q_c can be made high enough, a fast tuner can be used to compensate the Lorenz force detuning and microphonics noise. From Equation (4), we can see that this iris/stub tuning coupler can only increase equivalent external Q or $Q_{eq,ext} > Q_{s,ext}$.

People worry about the power loss of coupling cavity P_c relative to the power loss in the sc cavity P_s. It can be found out [1] that it mainly depends on the sc cavity's microphonics' level. Figure 4 shows this calculation.

$$\frac{P_c}{P_s} = \frac{Q_{s,ext}}{Q_s}\left(1 + 4Q_s^2 \frac{\Delta f_s^2}{f^2}\right) \qquad (6)$$
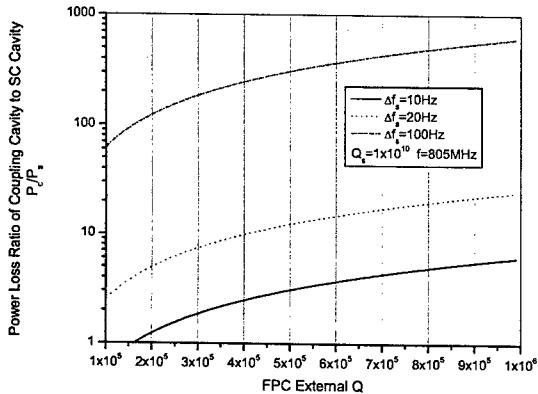
Figure 4: Power loss ratio in the coupling cavity.

The $Q_{c,ext}$ in Equation (4) depends on the iris hole's size, position and thickness. From the analytical calculation of next section, the external Q enhancement factor can be plotted as the function of iris diameter (Figure 5).
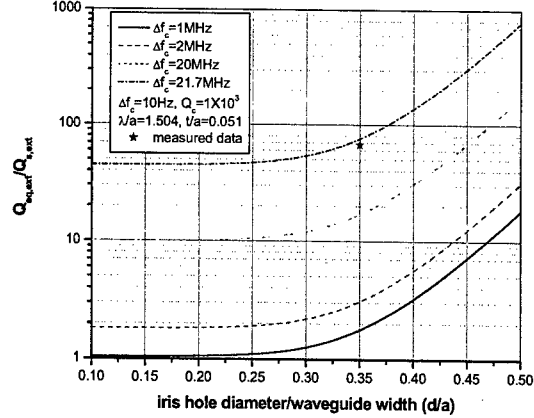
Figure 5: Analytical calculation verse one measured data.

IRIS COUPLING CALCULATION

The iris hole coupling to a rectangular waveguide $Q_{c,ext}$ can be done by a 3D computer simulation like MAFIA or Analyst (Omega3). The first approach I took is the analytical solution by equivalent inductances (Figure 6). The susceptance of an iris inside of waveguide is [2]:

$$\frac{B}{Y_0} = \frac{\lambda_g}{a}\left[\frac{\pi b}{24 d j_1^2} - 1 + A_1 - \left(\frac{a}{\lambda}\right)^2 A_2\right] \qquad (7)$$

With an iris thickness (Figure 6) correction:

$$\frac{B_a}{Y_0} = \frac{B}{2Y_0} + \frac{|Y_0'|}{Y_0}\tanh\frac{\pi t}{|\lambda_g'|} \qquad \frac{B_b}{Y_0} = \frac{|Y_0'|}{Y_0}\csc h\frac{2\pi t}{|\lambda_g'|} \qquad (8)$$

Here Y_0 is the shunt conductance of waveguide. The j_1, A_1, A_2, and Y_0', λ_g' are all the functions of d/a, see Ref. [2] for detail.

Q external of an iris coupling to a TE10x rectangular cavity can be deduced from Ref. [3] by the circuit transformation of Figure 7:

$$Q_{ext} = \left(\frac{B}{Y_0}\right)^2\left[\frac{\pi}{2}\frac{1}{1-(\lambda/2a)^2} + \frac{Y_0}{B}\right] \qquad (9)$$

With an iris thickness correction:

$$Q_{c,ext} = \left(\frac{B_a}{Y_0}\right)^2\frac{\pi}{2}\frac{1}{1-\left(\frac{\lambda}{2a}\right)^2}\left(\frac{B_a + 2B_b}{B_b}\right)^2 \qquad (10)$$

There is another formula from Collin [4] for the case of without iris thickness:

$$Q_{c,ext} = \frac{9}{4\pi}\frac{b^2 c(a^2 + c^2)\lambda}{d^6\sqrt{1 - \left(\frac{\lambda}{2c}\right)^2}} \qquad (11)$$

Here a, b and c is waveguide width, height and length respectively. The d is the iris hole diameter.

In Figure 8, I compare two analytical methods, MIT's Equations (7)~(10) and Collin's Equation (11), with an

1102

Analyst 3D simulation [5]. The simulation used Balleyguier's method [6]. The simulation has confirmed
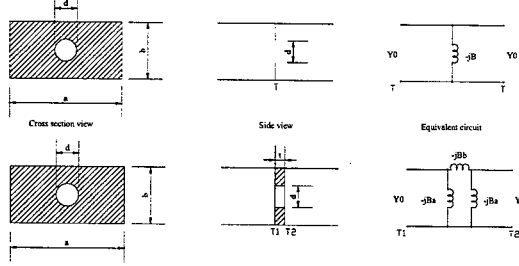
Figure 6: Iris without (top) and with (bottom) thickness simulation inside of a TE10 rectangular waveguide.
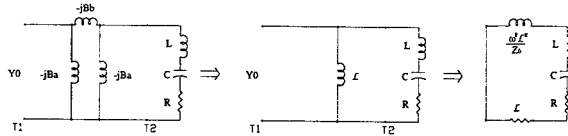
Figure 7: Equivalent circuit transformation from an iris-coupled to a short-circuit waveguide cavity.

that the detail of meshing around the iris hole is important. The thickness of the iris has also a significant susceptance contributed to the $Q_{c,ext}$'s calculation.
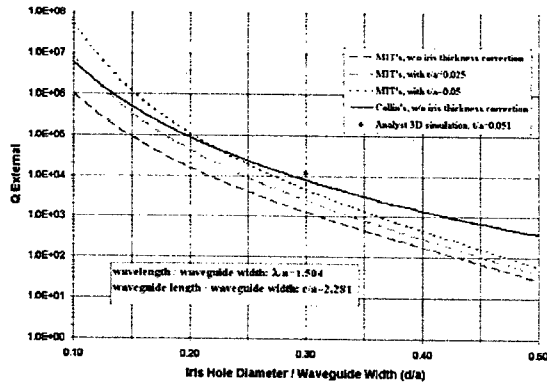
Figure 8: Q external calculation for an iris hole coupling to a TE10x rectangular waveguide resonator.

IRIS POSITION DETERMINATION

The position of the iris plate along the waveguide has to be at the voltage minima of standing wave (SW) when the cavity/coupling system is on resonance. So the iris inductance will be effectively at the maximum SW current position. Also the coupling waveguide will be in the TE01n mode resonant frequency when the waveguide length $c=n\lambda_g/2$. For a waveguide coupling to a normal conducting cavity, like a copper or a room temperature niobium cavity, the "detuned short" position is also the voltage minimum position in resonance. It can be explained by the voltage reflection coefficient, because of $\beta<<1$:

$$\Gamma(\omega) = \frac{\beta - 1 - iQ_0\delta}{\beta + 1 + iQ_0\delta} \qquad \delta = \frac{\omega}{\omega_0} - \frac{\omega_0}{\omega} \qquad (12)$$

When the cavity changes from normal conducting state to superconducting state, the coupling coefficient changes from $\beta<<1$ to $\beta>>1$. The voltage minimum position at resonance will be changed by $\lambda_g/4$ (90°). It is important to incorporate this change in the design. For the SNS medium beta cavity coupling, the iris position was determined by a computer 3D simulation, then by a bench measurement on a model. Using a slot-line waveguide (or a hole array on the centerline) coupled to a copper cavity, I measured the SW profile. From the plot in Figure 9, I got that the distance from the doorknob center to the first V_{min} is 52.6cm. The HFSS simulation from Y. Kang is 52.7cm [7]. Both of them are for the copper cavity. The iris position in the actual design was pulled back by $3/4\lambda_g$.
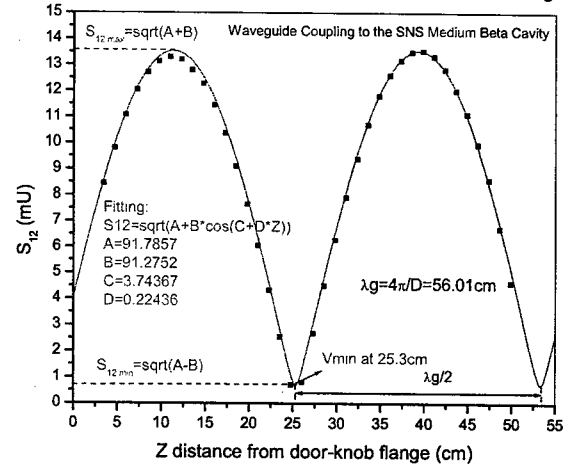
Figure 9: SW profile measured on WR975 waveguide.

SUMMARY

The combination of iris plate and 3-stub tuner can be used as a variable coupler. It increases the equivalent external Q of an over-coupled superconducting cavity by two orders of higher. More measurement needs to be done to verify this analysis when the CMTF is available for this study.

I would like to thank R. Sundelin, L. Phillips, C. Reece, and J, Delayen, I. Campisi and Y. Kang of ORNL for the fruitful discussions during the course of this work.

REFERENCE

[1] I. Ben-Zvi, SUNYLAC Internal Report, April 1980.
[2] Waveguide Handbook, edited by N. Marcuvitz, MIT Radiation Lab, 1986 edition, p238~240, p327, p408~409.
[3] Principle of Microwave Circuits, edited by C. Montgomery, R. Dicke, E. Purcell, MIT Radiation Lab, series 1948, p231~234.
[4] Field Theory of Guided Waves, second edition, R. Collin, p523~531.
[5] Private communication with J. DeFords of STAR, Inc.
[6] P. Balleyguier, LINAC98 proceedings, MO4037.
[7] Private communication with Y. Kang of ORNL.

HOM DAMPING PERFORMANCE OF JLAB SL21 CRYOMODULE[#]

H. Wang[*], I. Campisi, K. Beard, R. Rimmer, C. Thomas[+], J. Mammosser, J. Preble

TJNAF, Newport News, VA 23606, USA

Abstract

The SL21 cryomodule is a first 1.5GHz, 12.5MV/m, 7-cell cavity, 8-cavity string superconducting accelerator module produced at JLab. The first two passbands of TE111 and TM110 high order modes (HOM) have to be damped to avoid beam breakup problems at 460µA current. External Q's of the HOM couplers and waveguide were measured on a copper model, on cold niobium cavities in vertical tests and finally in the cryomodule without beam. This paper presents all HOM data and general measurement techniques. A threshold current predicted by MATBBU code based on these data and the 6GeV machine beam optics is 10mA.

INTRODUCTION

The new SL21 cryomodule is the first example of a 7 cells/cavity, 8-cavities/string superconducting accelerator module developed for the JLab 12GeV Upgrade project. The specified accelerating gradient is 12.5MV/m to achieve total voltage of 70MV. It replaced a 5MV/m, 5 cells/cavity, 8-cavities/string old CEBAF cryomodule in the South Linac tunnel No.21 slot. Adding two more cells in each cavity to gain more beam voltage was the original design goal. The cavity cell shape remained the "Original Cornell" (OC) design. The cavity irises and beam pipe radii are 35.3mm. The HOM couplers resemble the DESY welded type. Two are attached at one end of the cavity outside the tuner hub, separated azimuthally by 115°. The couplers' center is 80mm from the first end cell edge. A λ/4-stub fundamental power coupler (FPC) waveguide is located at the other end of cavity (see Figures 1&2). Without changing the tuner design, the HOM couplers could not be brought closer to the end cell or moved to the other side of cavity.

MAFIA SIMULATION

A MAFIA 2D(R, Z) simulation was preformed for this "OC" shape with ~1mm mesh steps and double precision. Up to 50 monopoles and 50 dipoles were calculated in the frequency domain. The TE111 and TM110 dipole modes are the first two HOM passbands above the TM010 fundamental passband. Those with high R/Q values were identified as potentially dangerous modes for the beam breakup (BBU) problem in the CEBAF accelerator. The R/Q was calculated for each mode at 1cm off-axis distance and normalized in Table 1. It agrees with an early URMEL calculation [1]. One mode in the TE112
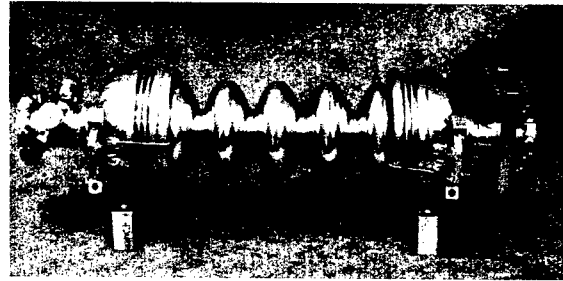
Figure 1: JLab "OC" shape, 1.5GHz, 7-cell niobium cavity with helium vessel removed.
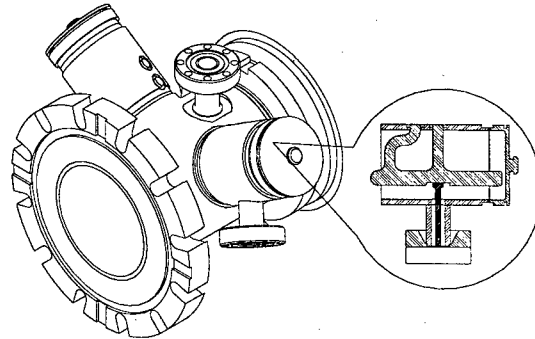
Figure 2: HOM coupler design adopted from DESY.

Table 1: MAFIA R/Q calculation for "OC" shape with a 9cm-long beam pipes and the electric boundary on each end. Here k=2π/λ, a=off-axis distance. Shaded rows are high R/Q modes dangerous for BBU problem.

Frequency [MHz]	R/Q [Ω/cm²]	(R/Q)/(ka)² [Ω]
1725.3	0.03	0.3
1746.4	0.005	0.04
1780.2	0.56	4.0
1824.0	0.37	2.5
1874.3	13.3	85.9
1926.0	10.1	61.9
1991.5	0.47	2.7
2000.6	2.93	16.7
2068.6	0.35	1.9
2089.2	5.73	29.9
2102.5	5.59	28.8
2109.7	0.03	1.4
2113.5	0.005	5.2
2113.9	0.56	0.7
2953.1	11.38	29.7

passband was also found to have a high R/Q. It is included in the last row of Table 1. We did not calculate the Q externals of HOM couplers with MAFIA. They were determined by measurements on a copper model.

COPPER MODEL MEASUREMENT

The HOM coupling was measured on the bench by using a calibrated network analyzer to get two-port S parameters. Port 1 is the launching electric antenna, Port 2 is the HOM coupler pickup in which the Q external to be determined. To get more accurate data when $Q_{ext} \gg Q_0$ for room temperature copper, a good launching position to get nearly critical coupling $\beta_1 = 1$, and less perturbation to the intrinsic cavity field is preferred. An array of small holes along the cavity wall from irises to equators at different azimuths was drilled, so an optimum hole with a minimum antenna insertion can be chosen. Q external can be calculated from the S parameters as follows.

$$\beta_1 = \frac{|1 \mp S_{11}|}{|1 \pm S_{11}|} \quad \beta_2 = \frac{|1 \mp S_{22}|}{|1 \pm S_{22}|} \quad (1)$$

$$Q_{ext,trans} = \frac{4\beta_1}{1+\beta_1+\beta_2} Q_{load} \times 10^{\frac{|S_{21}|(dB)}{10}} \quad \text{(Transmission)} \quad (2)$$

$$Q_{ext,refl} = Q_{load} \frac{1+\beta_1+\beta_2}{\beta_2} \quad \text{(Reflection)} \quad (3)$$

Here, Q_{load} is measured at –3dB bandwidth of S_{21}. In Equations (1), upper signs are for under coupling $\beta<1$, lower signs are for over coupling, $\beta>1$. In the case of $\beta_2 \ll 1$, Equation (1) gives a large error. Equation (4) can be used instead.

$$\beta_2 = |1 - S_{22}/S'_{22}|/|1 + S_{22}/S'_{22}| \quad (4)$$

Here S_{22} is at resonance and S'_{22} is at off-resonance where there is nearly full voltage reflection. In this case, transmission method Equation (2) will give a more accurate result with a careful cable calibration. In Figure 3, the port-dependent Q externals were plotted.

For the positive mode identification and the electric field profile, a bead-pull system with a dielectric bead passing through the cavity off-axis was integrated with this bench setup.
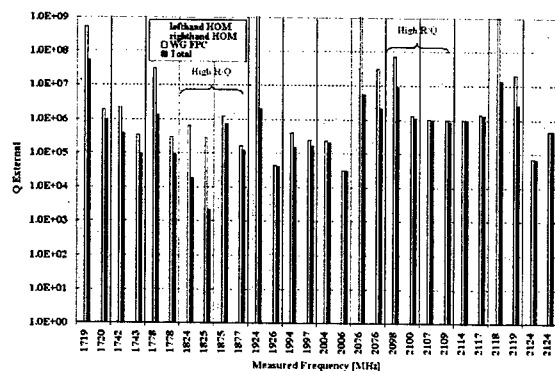
Figure 3: Q external measurement on a copper model.

VERTICAL COLD TEST

Five of eight niobium cavities in the SL21 cryomodule were tested at our Vertical Test Area (VTA) with the both HOM couplers and the Field Probe (F.P.) installed and

with their cable connections up to the warm interface. The waveguide (WG) is at bottom and shorted with a niobium blank. The whole assembly including HOM couplers at the top can be cooled to a temperature of 2K. The power coupling port is at the bottom beam pipe flange with a Q external of the TM010 π mode $\sim 10^9$. The S_{21} measurement was done from this port 1(PC) to the F.P. port 2. A phase shifter was used with its input connected on each HOM coupler warm connector. So the –3dB frequency bandwidth of Q load can be minimized (Δf_L) to get the highest Q'_L by adjusting the phases with the shifters' outputs shorted (or open), see Equation (5). When a 50Ω load is put on one of the shifters' outputs, for example, on HOM coupler 1. The loaded Q is changed as Q_L in Equation (6). So the Q external of HOM coupler 1 $Q_{ext,HOM1}$ can be determined by the new bandwidth (Δf_L) from Equation (7). Here the f is the resonance frequency when the 50Ω load is put on. The condition of approximation is when $Q'_{ext,HOM1} \gg Q_{ext,HOM1}$. That means the loss in the standing wave at lossy cable and joints has to be much less than the loss to the 50Ω load. We found that when the Q external of the HOM coupler is very high ($>10^8$), this method doesn't apply. The power transmission method, Equation (2), could be used instead.

$$\frac{1}{Q'_L} = \frac{1}{Q'_{ext,HOM1}} + \frac{1}{Q'_{ext,HOM2}} + \frac{1}{Q_0} + \frac{1}{Q_{ext,PC}} + \frac{1}{Q_{ext,F.P.}} \quad (5)$$

$$\frac{1}{Q_L} = \frac{1}{Q_{ext,HOM1}} + \frac{1}{Q'_{ext,HOM2}} + \frac{1}{Q_0} + \frac{1}{Q_{ext,PC}} + \frac{1}{Q_{ext,F.P.}} \quad (6)$$

$$Q_{ext,HOM1} \approx \frac{1}{1/Q_L - 1/Q'_L} = \frac{f}{\Delta f_L - \Delta f'_L} \quad (7)$$
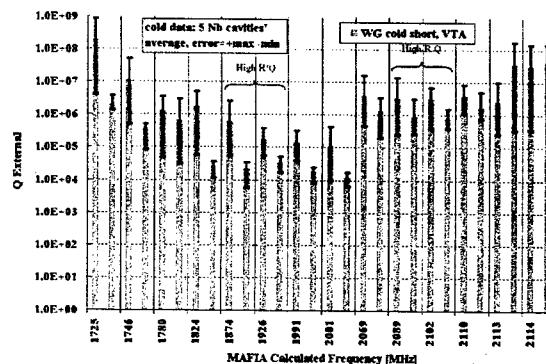
Figure 4: Q external measurement in vertical tests.

When the damping by the HOM couplers was found to be limited, a separate cavity vertical test was carried out with the WG connected to a warm load through a warm window. The result [2] indicates that the waveguide has a limited damping which is different from an early measurement [1] done on a horizontal test bed (HTB). This result was confirmed by the later cryomodule tests.

CRYOMODULE COLD TEST

After the SL21 cryomodule was cooled down to 2K and before the waveguides were connected to the high power

source in our Cryomodule Test Facility (CMTF), we were able to measure the loaded Q of the HOMs by the transmission from HOM1 to HOM2 with the "WG short" and the "WG load" conditions. The "WG load" is a low power waveguide load with a tapered RF absorber inside. We found out from a separate measurement that the VSWRs of this load within the HOM spectrum are between 1.07:1 and 1.34:1. When the cryomodule was finally installed in the CEBAF tunnel, 8 HOM waveguide filters were installed in a "T" joint with the high power waveguides. Gamma Microwave made these filters in 1990. The specification range of the VSWRs in the HOM spectrum is 2.0~3.0:1. In Figure 5, we summarize all data in the cryomodule measurements. The error bars in this plot represent the range's values among the 8 cavities in the module. The difference of data between the "WG short" and the "WG load" in CMTF should indicate the additional waveguide damping to the HOM couplers. "WG HOM filter" data is the end performance of HOM damping at the SL21 cryomodule in CEBAF tunnel. We have also searched for the 2953MHz mode. It mixes up within monopole and quadruple modes. So we measured all Q loads in the frequencies around 2953 MHz. No modes with more than 1.0×10^6 Q external were found in any cavity even with the waveguide shorted.
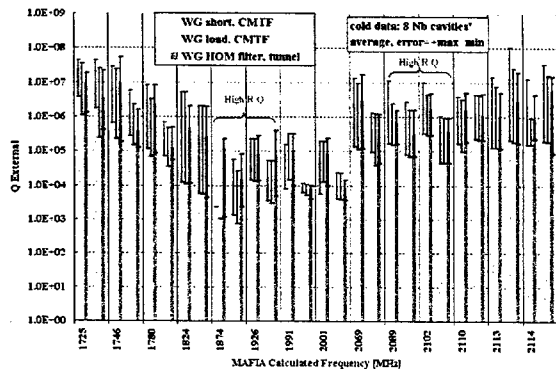
Figure 5: Q external measurement in cryomodule.

MATBBU SIMULATION

The MATBBU is a code for calculating beam breakup threshold current in a re-circulating linac [3]. The Q external data of "WG short, CMTF" were input into the MATBBU with the current beam optics of 6GeV machine. The predicted lowest threshold current is 10mA, which is limited by two high R/Q modes in the TE111 passband. All other modes have higher threshold currents. Figure 6 shows the final results, where the beam impedance is normalized by $(R/Q)Q_{ext}/(ka)^2$. The data points are averaged beam impedance pre cavity. The error bars indicate the frequency spread range over the 8 cavities within the module.
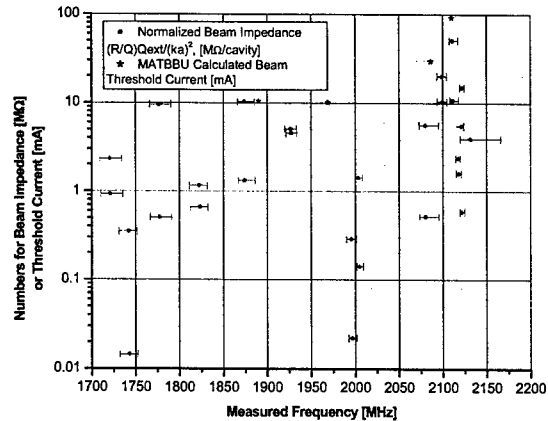
Figure 6: SL21 beam impedance and threshold current for 6GeV CEBAF machine.

SUMMARY

All HOM data measured for SL21 cryomodule without beam indicate that the TE111 and TM110 mode damping is sufficient for the 12GeV Upgrade machine (460 μA). To improve other performance, two types of 7-cell cavities for the Upgrade [4] have been developed.

It was found out by MATBBU that the SL21 damping was not sufficient for a high current (>10mA) FEL's etc. In order to improve the HOM damping to the $Q_{ext}=10^3 \sim 10^4$ level, some trials were done on this copper model by extending the HOM coupler antenna tip or putting an extra elliptic coupler at the FPC side. No significant improvement was possible without a major redesign of the end groups and tuner. No further attempt was done on this structure. Instead a 2×5-cell Superstructure type cavity was proposed [5].

ACKNOWLEDGMENTS

We would like to thank all JLab staff who dedicated to this work and A. Sun from ORNL who took some of data. We particularly appreciate J. Sekutowicz from DESY for his advice during the course of this work.

REFERENCES

[1] B. Yunn, JLAB tech note, 01-028, June 25, 2001.
[2] C. Thomas, JLAB tech note, 02-048, December 2002.
[3] K. Beard, et al. TOP D006, these proceedings.
[4] J. Sekutowicz, et al. TPAB085, these proceedings.
[5] J. Sekutowicz, et al. TPPE013, these proceedings.

ON CREATION OF A CATHODE UNITS FOR THE X -BAND KLYSTRON

A.N. Dovbnya, N.I. Aizatsky, V.N. Boriskin, V.V. Zakutin, V.A. Kushnir, V.A. Mitrochenko,
N.G. Reshetnyak, V.G. Romas'ko, Yu.Ya. Volkolupov, M.A. Krasnogolovets, NSC KIPT, Ukraine

Abstract

The reports presents the results from studies, performed at the SRC "Accelerator", on development of units for the X-band klystron with an output power 1÷2 MW and at a voltage 50÷100 kV. A magnetron gun with a cold secondary-emission metallic cathode is supposed to be used as an electron source.

INTRODUCTION

Creation of small-scale resonance linear electron accelerators is very important for solving a number of applied problems - interoscopy (custom control), medicine (radiation therapy), technological treatment of food products etc. In this connection, the development of linear electron accelerators with an X-band operating frequency is a high-priority task. A main problem for carrying out the works in this direction is a choice of a powerful microwave source that would be capable to provide a compactness of an accelerator. The most acceptable microwave source for the small-size accelerator is an amplifier klystron with an output power 1÷2 MW, a voltage up to 50 kV and an operating

large diameter is used, one can apply the structure based on annular (coaxial) resonators as a resonance system. Just this type of a resonance system was chosen for the X-band low-voltage klystron that is under development at the NSC KIPT. Development of the klystron includes two stages: development of an electron source and development of a resonance system.

A main problem of the resonance system development is a possibility of a "parasitic" relation between the coaxial resonators due to the TEM wave excitation. However, by a special selection of the external and internal radii of resonators it is possible to provide the TEM mode suppression in the structure. Our preliminary calculations and experimental studies have showed that the connection/junction between resonators separated by the drift region can be made rather small in the system without beam. At the same time, the estimations showed that to increase the efficiency of the bunched beam interaction with the resonance structure, the latter should include the sections comprising several connected resonators excited at the π-mode of oscillations. The layout of the bunching resonance system of the klystron under development is presented in fig.1.

Figure 1: The layout of the bunching resonance system

frequency of 11.4 GHz (fourth harmonics of the SLAC klystron frequency of the S-band). Considering that the typical value of the klystron efficiency lies within 30 ÷50 %, the pulse power of the electron beam should be 3 - 4 MW, i.e. at a voltage of 50 kV the beam current should be 60 ÷ 80 A. The use of such a beam with a high perveance is connected with a particle bunching deterioration caused by the decrease of the wavelength of plasma oscillations in the beam with particle density increasing. One of the methods applied to decrease the beam density and to decrease the spatial charge force influence on the klystron bunch is the use of a hollow beam having a large diameter. As is shown in [1] when a hollow beam with a

As a source of the annular beam in this klystron, a secondary-emission magnetron gun with a cold metallic cathode will be used [2]. One of its advantages is a potentially long-term lifetime and a high beam density. The magnetron gun was investigated at the experimental installation with an 8-channel sectionalized Faraday cup and a computer information measuring system. It allows measuring the voltage amplitudes, beam current, as well as investigating the azimuthally charge distribution in each selected time interval during the current pulse.

EXPERIMENTAL RESULTS AND DISCUSSION

The performed investigations showed that the beam generation is stable during 32 pulses measured by the help of an information measuring system. For example, for one of operating modes at a cathode voltage of 26 kV, a beam current of 52 A and a magnetic field 2500 G, the current instability of each of Faraday cup's sections at a cathode voltage instability of 1.8% was not higher than 4.5%. In another case at a cathode voltage of 27 kV, a beam current of 49A and a magnetic field of 2300 G the instability of each of beams getting the Faraday cup's sections at a cathode voltage instability of 1.7% was 1.8÷2.9 %. The investigation demonstrated that such a beam shapes a tubular beam with an external beam diameter of 43 mm, internal diameter of 41 mm. The duration of the beam current pulse was ~5 μs, the repetition rate was 15 Hz, the pulse power of a beam was ~ 1.5 MW with the microperveance ~10.
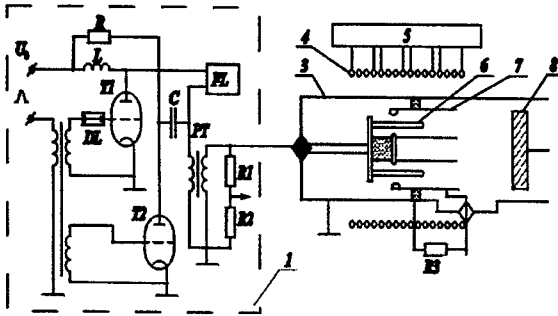
Figure 2: The layout of the experimental installation

The measurement of the beam density distribution on the azimuth showed that this uniformity has a significant non-uniformity. Fig.3 presents the distribution of the beam charge from each of eight Faraday cup's sectors (channels 4 and 10 are not connected to the system).
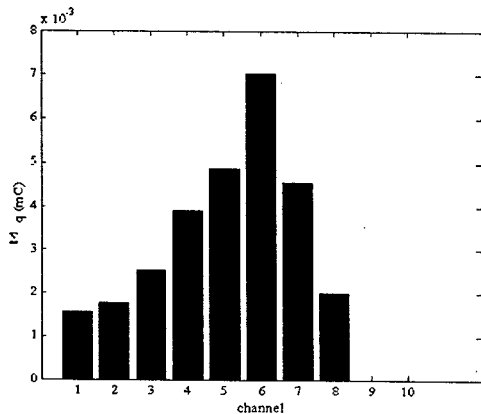
Figure 3

From the figure it is seen that the charge distribution on the azimuth is non-uniform and the non-uniformity

amounts 400 %. The non-uniformity of the azimuthal distribution within (200 – 400)% was observed for different parameters of the high-voltage supply of the gun and for different values of the magnetic field. Moreover, it has been established that there exists also a significant asymmetry in the spatial particle distribution, i.e. the annular beam as a whole displaces relatively to the gun axis. In some cases this displacement on the collector was 8 mm. As is shown, the azimuthal distribution of the beam density and its position at the collector plane are depending on the magnetic field direction. Changing the magnetic field direction leads to the beam displacing in the opposite direction that is illustrated in figures 4 and 5 respectively.
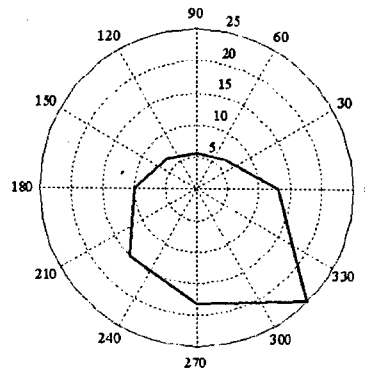
Figure 4
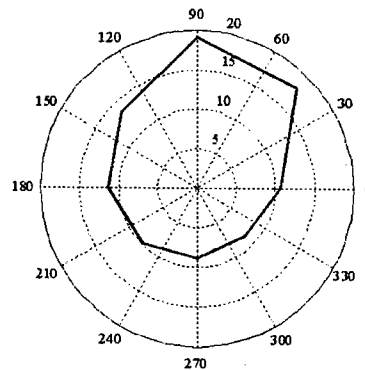
Figure 5

The detailed investigation of the magnetic field topology showed that the magnetron source axis at the experimental installation was deviated from the solenoid axis (the deviation from the axis in the collector point was ~5 mm, in the cathode connection point was ~2 mm, the tilt was ~ 1°). Probably, this circumstance can be a cause of the asymmetry in the azimuthal particle density distribution and beam displacement. This may be explained by misalignment of magnetic and geometrical axises of the system or by development of diocotron

instability of the beam [3].Thus, the experiments showed that the electron source with a secondary-emission cathode has a rather high stability. However, to define the conditions of obtaining the high azimuthal uniformity of the beam it is necessary to carry out supplementary investigations.

CONCLUSION

Our investigations have demonstrated the possibility of a stable generation of electron beams in the magnetron gun with a cold secondary-emission cathode. It is shown that the stability of the beam current amplitude is ~ 2÷3% and under optimum conditions can reach ~ 1%.

REFERENCES

[1] M. Friedman, J. Pasour and D. Smithe, Appl. Phys. Lett. 71(25), 22 December 1997, p. 3724 - 3726.

[2] Volkolupov Yu.Ya., Dovbnya A.N., ZakutinV.V. et al. Zhourn.Tekhn.Fiz.2001. V.71. N.2. P.98-104 (in Russian).

[3] V. Zakutin, N. Ajzatsky, V. Boriskin et al. Abstr. Broch. of the 8th Europ. Part. Accel. Conf., Paris, France, 3-7 June 2002, p.146.

[4] A.N.Dovbnya, N.G.Reshetnyak., V.P.Romas'ko et al., Proc. of the Part. Accel. Conf., Chicago, USA, 18-22 June.2001, V. 5., p. 3759-3761.

DESIGN OF AN X-BAND, 50 MW, MULTIPLE BEAM KLYSTRON

Liqun Song, Patrick Ferguson, Lawrence Ives, George Miram, David Marsden and Max Mizuhara
Calabazas Creek Research, Inc.

Abstract

Calabazas Creek Research has designed a 50 MW, multiple beam klystron (MBK) with eight separate electron beams operating at 11.424 GHz with an efficiency of 54%. The MBK will be integrated with an electron gun in development on a current U.S. Department of Energy grant. The gun is being fabricated and will be tested in July, 2003. During the initial MBK development, several circuits capable of generating an RF output power of 50 MW were investigated. These circuits included ring resonators, hybrid cavities and standard reentrant cavities. The final design included an optimized, high efficiency (54%), eight cavity, interaction circuit, consisting of a mutually coupled set of input cavities, five discrete hybrid cavities for each circuit and a mutually coupled output cavities combined to transmit the RF power through a single window.

INTRODUCTION

Design of the klystron required a number of advanced computer simulation tools. The electron gun was originally designed using TOPAZ, and this design was verified using OMNI TRAK, both 3D codes. The circuits were simulated using KLSC, a 2 1/2D large signal code and MAGIC, a 3D, particle-in-cell (PI C) code.

The electrical and mechanical design parameters for a single circuit and for the MBK are listed in Table 1.

Description	Single Circuit	MBK
Peak RF output power	6.75 MW	54 MW
Center frequency	11.424 GHz	11.424 GHz
Instantaneous bandwidth	80 MHz	80 MHz
Efficiency	52%	52%
Electron beam voltage	190 kV	190 kV
Electron beam current	66 A	66 A
Beam perveance	0.8 μ pervs	0.8 μ pervs
Pulse width	3.0 μ s	3.0 μ s
Pulse repetition rate	120 Hz	120 Hz
Duty	0.036%	0.036%
Average RF output power	2.35 kW	18.8 kW
Average beam power	4.52 kW	36.2 kW

CIRCUIT DESIGN

As originally envisioned, the MBK would use ring resonators for all cavities. This configuration offered the potential to simplify the introduction of RF power into the MBK and the extraction of the RF output power. Figure 1 shows a cross section of the arrangement.
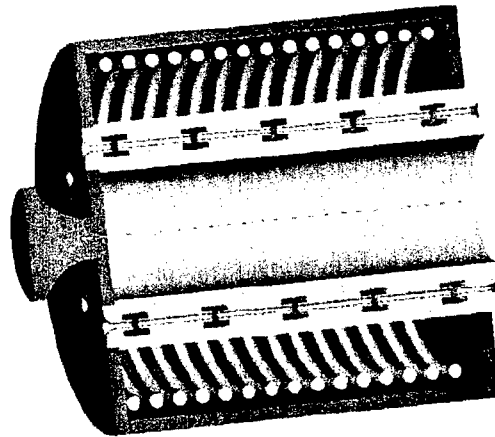
Figure 1. Solid model of multiple beam klystron with ring resonator cavities.

Simulation of a single input resonator where eight ports were introduce to accommodate the eight beams determined that the distributed shunt impedance and electric field were reduced significantly. Consequently, the effective wave-beam interaction was considerably less than the interaction for a single cavity. Extending this result to all ring resonators indicated that the saturated gain would be too low for efficient operation. Redefining the geometry increased the interaction strength but resulted in the introduction of higher order modes in the ring resonator. Adding loss to the resonator to suppress these modes was considered but rejected due to the complexity of the structure. A much simpler arrangement involves splitting the input power four times via three dB couplers and then dividing this power into two cavities. Figure 2 shows the input cavity assembly with four coax-waveguide transformers. Note that each input drives two klystron input cavities and thus the power at each port is divided to give equal power with constant phase at each beam tunnel.
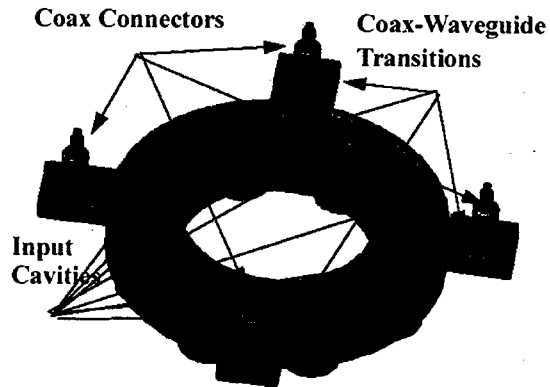
Figure 2. Input cavity assembly showing four coaxial inputs to waveguide transitions.

Bunching Circuit

The bunching circuit consists of eight sets of input cavities and five reentrant cavities. An exploded view of the bunching circuit is shown in Figure 3. The cavities and cooling holes are shown in the sections.
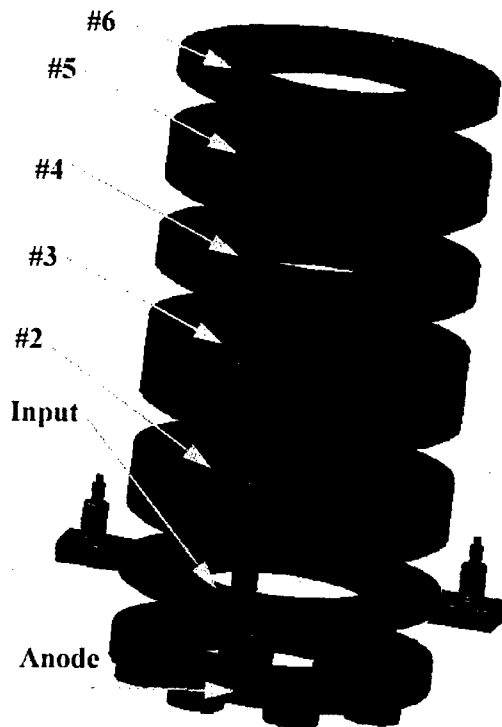
Figure 3. Exploded view of circuit assembly for first six cavities

Output Cavities

In order to extract the RF power in phase efficiently from each of the eight outputs, two different configurations were analyzed. The first configuration utilized a compact waveguide twist [1] for each cavity, each twist feeding into a common circular guide, as shown in Figure 4. An evaluation of the power handling capability of the waveguide twists is being finalized. An alternate arrangement is shown in Figure 5. This arrangement combines the RF power from each output cavity into a TM_{040} cavity, which is then coupled to a TM_{010} cavity. The RF power is then extracted into two normal waveguide twists coupled into a TE_{01} waveguide.
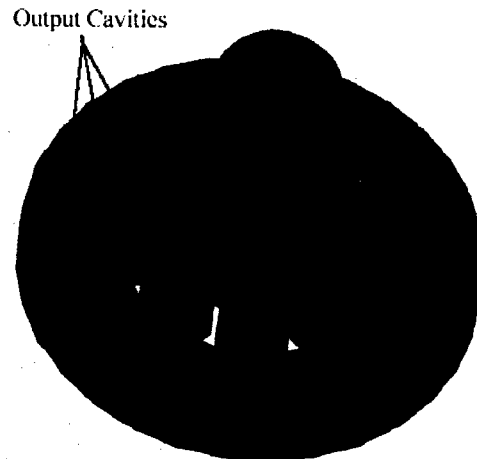
Figure 4. Output waveguide system consisting of eight waveguide twists, a TE_{01} circular waveguide, and the TE_{01} window
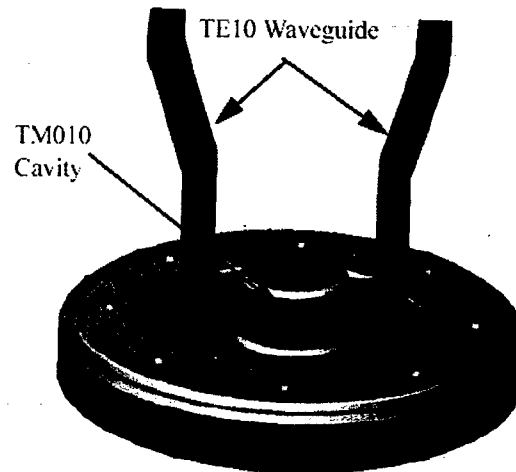
Figure 5. Output configuration consisting of TM_{040} cavity coupling to TM_{010} cavity.

A complete cross-section of the MBK with the first output circuit configuration and TE_{01} high power window is shown in Figure 6. Also shown are two individual circuits and a common electron beam collector.

Window

Collector

Output
Waveguide

Circuit
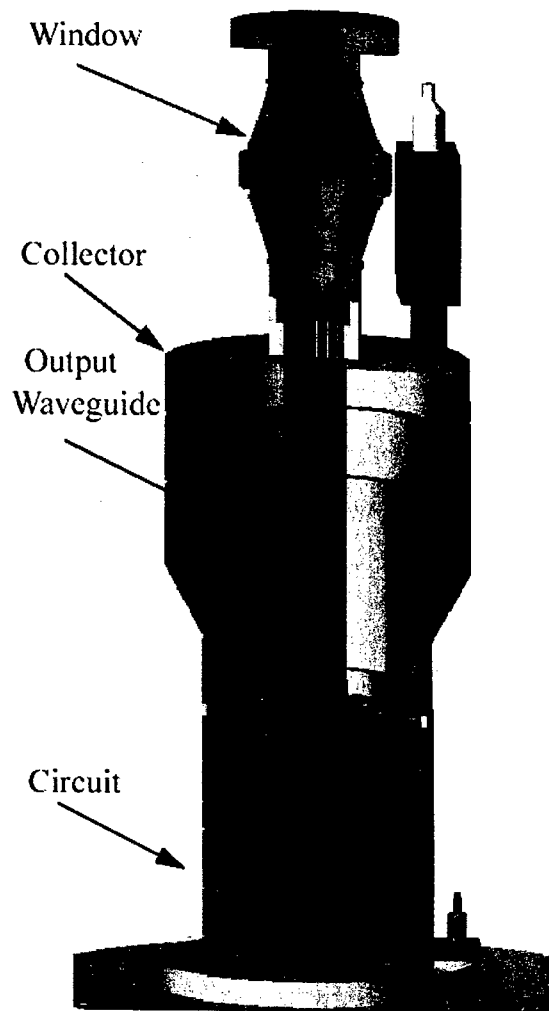
Figure 6: Cross-section of MBK

SUMMARY

Initial design was completed for a 50 MW multiple beam klystron at 11.424 GHz. The klystron is designed to incorporate and eight beam gun currently being constructed. The predicted performance of the klystron meets or exceeds the goals of the program. Successful construction and test of this klystron would represent a significant advance in RF source technology and could facilitate the development of new accelerator and collider systems.

REFERENCES

[1] Uwe Rosenberg, Jens Bornemann, Smain Amari, "A compact and Broadband 90-Degree Waveguide Twist Transformer for Integrated Waveguide Systems," http://www.ece.uvic.ca/~jbornema/Conferences/087-01eumc-rba.pdf

DEVELOPMENT OF IMPROVED CATHODES FOR
HIGH POWER RF SOURCES

L. Ives, G. Miram, M. Read, M. Mizuhara, Calabazas Creek Research, Inc., Saratoga, USA
Philipp Borchard, Lou Falce, Consultants
Kim Gunther, HeatWave Laboratories, Inc.

Abstract

All high power RF sources start with an electron beam generated by a cathode. The quality of this cathode directly impacts the performance of the RF device. Typically, dispenser cathodes heated to approximately 1000 C provide the electrons constituting the electron beam that is subsequently used to drive an RF circuit. A number of high power devices recently suffered significant performance degradation due to nonuniform emission from the cathode surface. Nonuniform emission can be caused by variations in termperature or work function across the cathode surface. Research is underway to determine the causes of both temperature and work function nonuniformity and derive improved construction and processing techniques and procedures to reduce of eliminate the problems. This information will be provided to cathode vendors and users to improve the future performance of these devices. This paper presents results of research to date as well as experimental measurements of cathode performance.

INTRODUCTION

High power RF sources are in development worldwide for the next generation of accelerators and colliders. Typically, RF power for accelerators is provided by klystrons. A number of novel devices are being considered, however, including gyroklystrons, multiple beam klystrons and sheet beam klystrons. Irrespective of the type RF device, the starting point for RF power production is generation of a high quality electron beam. The quality of the electron beam is determined by the optical design of the gun and the quality of the cathode. Unfortunately, RF engineers have insufficient control of cathode quality.

Most klystrons and traveling wave tubes use solid electron beams generated by Pierce-type cathodes operating space charge limited. Gyroklystrons and gyrotrons use annular electron beams created with a magnetron injection gun (MIG) operating temperature limited, which means the emission current is a function of the local temperature. Consequently, gyro device operation is more sensitive to temperature variations across the cathode surface. Efficient operation of gyrotrons and gyroklystrons require a high-quality electron beam with low-velocity spread and uniform current density around the circumference of the beam. Advances in computer modeling allow design of electron

guns with velocity spreads less than 8%, which is adequate for efficient operation; however, there is substantial evidence that large azimuthal asymmetries in current emission often occur. Communications and Power Industries, Inc. (CPI), the U.S. and world leader in gyrotron production, reports azimuthal variations in the power density of the electron beam in the collector[1]. Because these devices are operating close to the thermal limit, any localized increase in the power density, such as occurs with azimuthally asymmetrical emission, can lead to overheating of the collector surface and eventual failure. Failures of this type have occurred.

The beam-RF interaction in the circuit depends on beam current, and azimuthal variations in current implies that all portions of the beam are not operating with optimal conditions, which can result in a substantial loss of efficiency. Research is underway at the University of Maryland to quantify this effect[2]. The Plasma Science and Fusion Center a the Massachusetts Institute of Technology performed experimental research on existing guns to measure the asymmetry. Asymmetries in a MIG for a coaxial gyrotron produced a 6:1 variation in current with regard to the angular position[3]. When the electron gun was replaced with one having more uniform emission (1.2:1), the output power in the gyrotron doubled.

Nonuniform temperature problems can be overcome with space charge limited cathodes by increasing the cathode temperature until all areas are operating sufficiently above the temperature limited regime. This can solve problems with nonuniform emission, however, the increased operating temperature can significantly reduce cathode life. It can also result in excessive barium evaporation to surrounding surfaces, leading to arcing.

Nonuniform cathode emission is typically caused by temperature or work function variations across the surface. Since gyro devices are more sensitive to these type variations, this program is performing detailed analysis of gyrotron cathodes to address both the temperature and work function problems. Improvements in work function uniformity will also have an impact on space charge limited cathodes, since it will allow reduction in the operating temperature.

Calabazas Creek Research, Inc. (CCR) is funded by the U.S. Department of Energy to improve the emission uniformity of magnetron injection guns for high power

RF sources for accelerator applications. CCR is addressing this effort in the following ways:

- New, innovative heater designs are under investigation to improve temperature uniformity. This includes improved geometrical design of heat shields, heater supports, potting, and surrounding thermal surfaces,

- Causes of nonuniform work function are being investigated. Once causes are determined, modifications to materials, processes, techniques, or procedures will be explored, in association with cathode manufacturers, to eliminate the causes of work function variation.

- A test facility is under construction to allow precise, detailed measurement of emission uniformity across the surface of magnetron injection guns. Precise measurement of temperature is also being developed. This will allow identification of problem areas for nondestructive or destructive analysis to identify the causes of emission uniformity or to evaluate the effectiveness of manufacturing improvements.

THERMAL DESIGN OF MIGS

Detailed, 3D thermal analysis was performed on a MIG displaying temperature variation to determine the root cause. For this cathode, the gap between the heater lead the heater coil resulted in an unacceptable temperature variation. A plot from one of the analyses is shown in Figure 1.
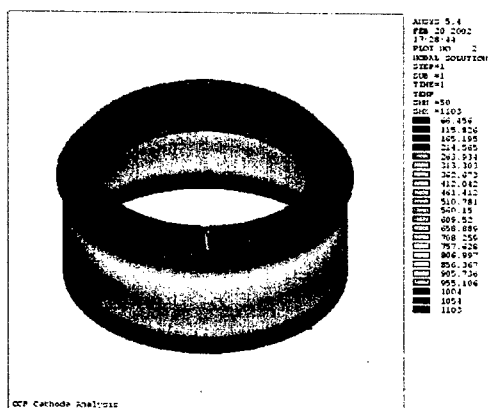
Figure 1. 3D thermal analysis of magnetron injection gun

As a result of this analysis, two improved designs were developed. The first design employs a variation in the heater winding pitch in the vicinity of the heater lead gap. The second design uses a "bombarder" cathode, where a space charge limited cathode generates an annular electron beam that heats the primary cathode by electron impact. Because the space charge limited cathode is generating little total current and operating in the space charge limited regime, it should exhibit less emission variation as a function of temperature. The uniform electron beam will then become the heating source for the primary, high current, temperature limited cathode emitter. Both these designs will be built and tested during the coming year.

WORK FUNCTION CONSIDERATIONS

The surface of a dispenser cathode typically consists of a large number of small openings on a tungsten substrate. The shape of these openings is highly irregular with random spacings. Several cathode specialists hypothesized that if the pores had a uniform shape and spacing, the barium flow and surface coverage would be uniform as well, resulting in reduced emission spread. During Phase I of this program, a cathode exhibiting nonuniform emission was donate by Communications and Power Industries, Inc. This cathode was tested in a special chamber designed to measure emission at 64 positions over the surface. The test chamber is shown in Figure 2.
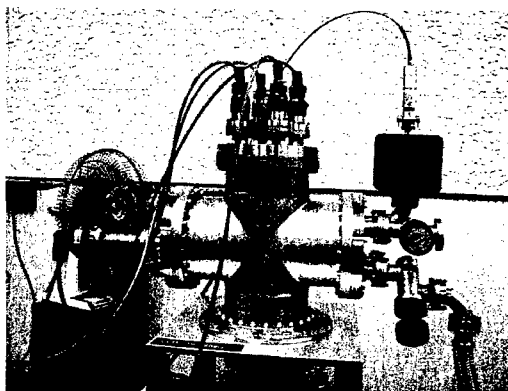
Figure 2. Test Chamber for measuring emission current

Measurements indicated that the emission was varying by a factor of two across the cathode surface. The areas of reduced emission were identified and the surface examined optically at high magnification. Figure 3 shows two regions of the surface with significantly different emission. The image on the left shows a large number of pores in a region with good emission, while the image on the right shows a region with reduced pores and emission. It would appear in this case that a variation in the pore distribution was a contributing factor to the nonuniform emission, however these results are not conclusive and additional testing is scheduled.

The research will continue to examine this cathode until a definitive cause is found for the nonuniform emission. CCR scientists and engineers will then work with the

cathode vendor to address this issue in the manufacturing process.

Figure 3. Magnified optical images of two regions on the cathode surface

As additional defective cathodes become available, they will also be tested. A new test chamber is currently under construction that will allow more rapid and accurate measurement of cathode emission at considerably higher resolution. A photograph of the chamber being assembled is shown in Figure 4. The chamber will include an electron beam scrubber for improved vacuum and will be adaptable to various sizes of magnetron injection guns. It is anticipated that the chamber will be available for pretesting cathodes prior to installation into tubes to avoid costly rebuilds from defective cathodes.
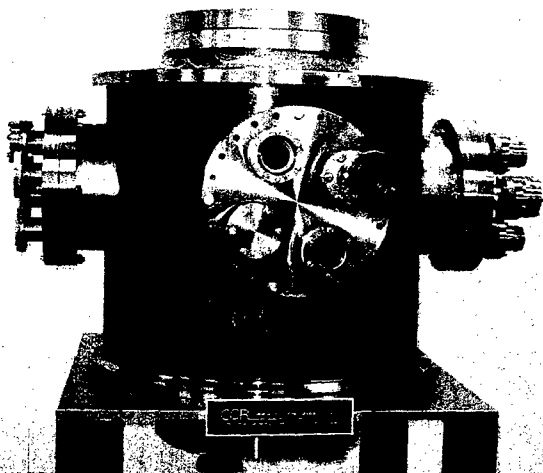
Figure 4. Test chamber for measuring emission uniformity of magnetron injection guns

SUMMARY

A research effort is underway to determine causes of nonuniform current emission in dispenser cathodes and eliminate them. The program is working primarily with magnetron injection guns operating in the temperature-limited regime. These guns are more sensitive to thermal variation than space charge limited cathodes; however, the improvements in work function uniformity will be directly applicable to space charge limited operation. Increased uniformity of the work function will allow reduction in cathode temperature with a subsequent increase in cathode life.

The program is also exploring improved designs for heaters for magnetron injection guns. Variable pitch and bombarder cathodes will be built and tested in the program. The program is also exploring improvements in heat shield configurations, potting, heater supports, cathode support, and manufacturing processes and procedures. Many of these will be applicable to both space charge limited and temperature limited cathodes.

Improve cathodes will result in improved electron beams for a wide variety of RF sources. This will ultimately result in increase efficiency, greater yield, improved performance, and lower cost for these devices.

ACKNOWLEDGEMENT

REFERENCES

[1] K. Felch, M. Blank, P. Borchard, P. Cahalan, S. Cauffman, T.S. Chu, C. Dubrule, "Results of 10-sec Pulse Tests on a 110 GHz Gyrotron," Intern. Vacuum Elec. Conference 2000, Monterey, CA, May 2000.

[2] Wesley Lawson, personal communication, January 2001.

[3] R. Advanti, S. Korbly, K. Kreischer, M. Shapiro, and R. Temkin, "Multi-Megawatt Gyrotrons for ECRH," *24th Intern. Conf. Infrared & Millimeter Waves*, Monterey, CA, September 1999.

MULTIPLE BEAM GUNS FOR HIGH POWER RF APPLICATIONS

L. Ives, G. Miram, M. Read, M. Mizuhara, Calabazas Creek Research, Inc., Saratoga, USA
Philipp Borchard, Lou Falce, Consultants
Kim Gunther, HeatWave Laboratories, Inc.

Abstract

The U.S. Department of Energy is funding development of multiple beam electron guns for high power RF sources. The advantage of multiple beam devices is that the operating voltage can be significantly reduced from that required for a single beam. In a multiple beam device, the beam power is divided into a multiplicity of smaller beams that traverse the RF circuit in individual beam tunnels. This dramatically reduces the space charge forces that drive the beam voltage requirement. The reduced operating voltage significantly reduces the cost of the power supply system, improves efficiency, reduces the device length, lower the magnetic field required for confinement, reduces radiations hazards, and increases the bandwidth. This paper describes an eight beam gun designed to produce 100 MW of beam power for a multiple beam klystron.

INTRODUCTION

Multiple beam guns (MBGs) are finding increased application in different types of microwave tubes. The advantages of having MBGs in a microwave tube, for example, in a klystron (MBK), is a decrease of beam voltage, reduced power densities and lower voltage gradients. Another advantage is increased bandwidth and lower x-radiation production. A detailed description of multiple beam devices and their advantages and applications was recently described in a publication by from the Naval Research Laboratory[1].

At present most MBKs use Brillouin focusing where the cathode is shielded from the magnetic focusing field. This type focusing is seldom used in the single beam, high power klystrons due to inferior beam transmission as compared to the confined flow focusing. Presently available MBK tubes typically have beam transmission of 90% or less. In fact most of them have transmission less than 80%, some even operate with less than 70% transmission. In comparison most high power, single beam klystrons have transmission around 99%.

MBKs with confined flow magnetic focusing will be capable of much higher values of RF power. The objective of this program is to demonstrate confined flow focusing in a multiple beam gun applicable to a 50 MW klystron at X-Band.

The main objective of this program is to design multiple beam guns with confined flow focused beams off axis on a radius determined by the RF cavity design.

This is not a trivial task, because in this type of gun, the magnetic flux reaching the cathode is no longer symmetric with the cathode center. If left uncompensated, the radial divergence in the magnetic field will distort the shape and size of the beam and prevent adequate transmission.

COMPUTER SIMULATION TOOLS FOR 2-D AND 3D INVESTIGATIONS

The geometry of multiple beam guns requires advanced 3D simulation tools. A number of the required tools were developed during the course of this research. The program extensively utilized a number of commercial 2D and 3D computer codes, including EGUN, TRAK, Maxwell 2D and 3D, and MAFIA. Principle code for modeling the electron beam optics was TOPAZ, a computer code developed by Valentin Ivanov at Stanford Linear Accelerator Center. Additional information on this code is available from another paper being presented at this conference[2].

MULTIPLE BEAM GUN DESIGN

The beam requirements were determined for a multiple beam klystron producing 50 MW of RF power at 11.424 GHz. The initial circuit design was performed in parallel by scientists in the United States and Russia. Both organizations arrived at the same circuit design and beam specifications, providing high confidence that the beam specifications were correct. Subsequently, U.S. Department of Energy funding was provided to perform more research on the klystron relevant to the gun produced here, and that program successfully produced a 50 MW klystron design. That design is also being presented at this conference[2].

Each of the eight beams is designed to provide approximately 12.5 MW of beam power with an operating voltage of 175 kV. The beam voltage was chosen to be consistent with currently available solid-state power supplies. The radial position of the electron beams is at the approximate position of the third radial maximum of the TM_{03} mode at 11.424 GHz. This is 6.3 cm from the central axis of the gun.

Initially, a 12.5 MW electron gun was designed on axis to determine the geometrical requirements for generating the correct perveance and beam size. The magnitude and shape of the magnetic field was also determined for the

on-axis gun and was used as the goal configuration for the off-axis guns.

Following design of the 12.5 MW gun on axis, the geometry was shifted 6.3 cm from the axis and duplicated to generate eight electrons guns about the primary axis of the gun. At this point, 3D simulation was required to design electrical and magnetic structures to generate the goal magnetic field about the local axis of each of the eight beams. It was necessary to simulate all beams in order to properly account for the additional space charge in the cathode-anode regions and the self magnetic fields of all the beams. Principle design tools were MAFIA, to generate the electrical and magnetic fields and TOPAZ to propagate the electron beams through the device geometry. Figure 1 shows the predicted performance for one of the eight electron beams.
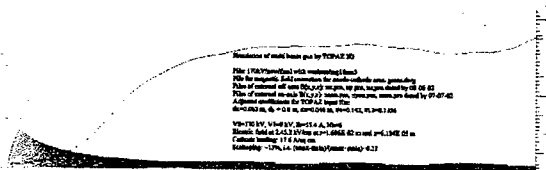
Figure 1. TOPAZ simulation of one of the eight multiple beams

The principle challenge in designing confined flow multiple beam guns is controlling the magnetic field in the cathode-anode region. Without correction, the field will radially diverge as it exits from the beam openings in the magnetic polepiece. During the program, iron structures were designed to surround the individual cathodes and force the magnetic field to be symmetric about the local axis of each cathode.

Another challenge is to design the electric and magnetic field structure to counteract any tendency of the electron beams to spiral about the primary axis of the gun. It was determined that azimuthal correction to the field structure was required to generate beams that did not spiral. Figure 2 shows the iron structure used to provide the required field correction.
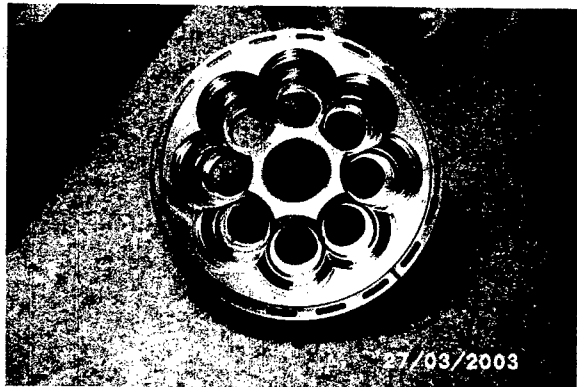
Figure 2. Field shaping iron in cathode-anode region

The gun is designed for testing in a special beam analyzer, also being developed on this program. The beam analyzer will allow testing of the gun at reduced voltage and current so that the current profile of an electron beam can be measured at various axial positions. Consequently, the prototype gun will be tested at approximately 12 kV. Stepper motors will transport a Faraday probe across the electron beam to generate a transverse profile of the beam current. The probes can be located at several axial positions to measure beam scallop and detect any spiraling motion.

A solid model of the prototype electron gun is shown in Figure 3. Because the gun will operate a significantly reduced voltage from the design value, it can be operated without a high temperature bake. The gun will be connected to vacuum pumps through conflat flanges and will be demountable from the beam analyzer. The gun is designed so that critical surfaces can be readjusted, and the gun retested. It should be noted that the computer tools used for the design are, themselves, untested against actual measurements. Not only will the test results characterize the operation of the gun, they will also be used to validate the accuracy of the computer tools. This will facilitate design of additional 3D devices and development of more advanced multiple beam guns.
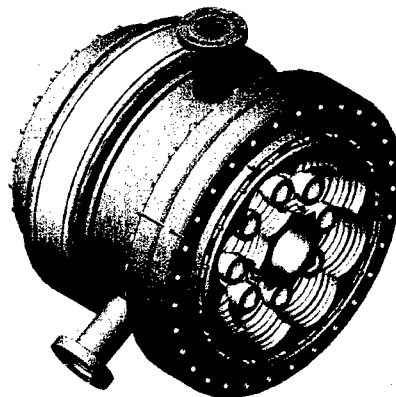
Figure 3. Solid model of eight beam electron gun

ELECTRON GUN AND PROGRAM STATUS

The design for the electron gun is complete and construction is underway. Figure 4 shows the eight electron guns mounted in the high voltage assembly. All parts for the gun are in stock, and the assembly should be completed in June 2002.

A beam analyzer is being constructed to measure the performance of the gun. A current probe will measure the transverse current profile at various distances from the cathode. This will allow determination of the beam size, scallop, current profile, and any spiraling of the beams. The beam analyzer is scheduled for completion at the end

of June. The power supply system is already in place and the control software is almost complete.

Following successful completion of the development of this gun, a doubly convergent gun will be designed. That gun will allow an increase in the total beam power with a decrease in the cathode current emission density.
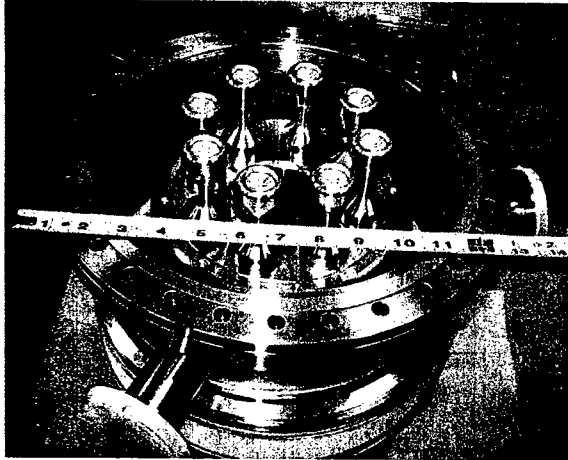
Figure 4. Eight beam, multiple beam gun under construction

SUMMARY

A multiple beam gun is currently being constructed to provide approximately 100 MW of beam power for an X-Band klystron. The gun consists of eight cathodes and field shaping iron to provide a high quality beam without spiraling. If successful, the gun will be capable of powering a 50 MW klystron with a beam voltage of less than 200 kV.

ACKNOWLEDGEMENT

REFERENCES

[1] G. Nusinovich, B. Levush, D. Abe, "A Review of the Development of Multiple-Beam Klystrons and TWTs," Naval Research Laboratory Memorandum NRL/MR/6840--03-8673, March 2003.

[2] V. Ivanov, A. Krashykh, et. al., "3D Modeling Activity for Novel High Power Electron Guns," 2003 Particle Accelerator Conference, Portland, OR, May 2003.

[3] L. Song, P. Ferguson, R.L. Ives, "Development of a 50 MW Multi-Beam Klystron at 11.42. GHz," 2003 Particle Accelerator Conference, Portland, OR, May 2003.

10 MW, 91 GHZ GYROKLYSTRON FOR HIGH FREQUENCY ACCELERATOR RESEARCH

R.L. Ives, J.M. Neilson, M. Read, M. Mizuhara, T. Robinson, D. Marsden, Calabazas Creek Research, Inc.
Wesley Lawson, Bart Hogan, Institute for Research in Electronics and Applied, University of Maryland

Abstract

Calabazas Creek Research, Inc. is developing a gyroklystron amplifier for W-Band linear accelerator applications. The device will be available for testing W-Band accelerator components and systems. The gyroklystron will operate at 91.392 GHz and is predicted to produce 10 MW of RF power with an efficiency greater than 38% and a gain of 55 dB. The design uses the second-harmonic mode to reduce the magnetic field requirement and use available TWT drivers. The current circuit design employs six cavities consisting of an input cavity, four buncher cavities and a final output cavity. The output mode is a hybrid TE_{01}/TE_{02} mode which facilitates transmission with reduced loss and flexibility for incorporating bends in the transmission system. The device is capable of depressed collector operation. The gyroklystron is fully assembled and ready for high power testing.

INTRODUCTION

Calabazas Creek Research, Inc. (CCR) is funded by the U.S. Department of Energy to develop a high efficiency gyroklystron amplifier for W-Band linear collider applications. This research supports an international effort to design the next generation of linear electron-positron colliders with anticipated center of mass energies of 0.5 TeV and beyond. In particular, this program supports development of a W-Band accelerator being investigated by the Stanford Linear Accelerator Center. CCR is developing a 91.392 GHz gyroklystron to produce 10 MW of RF power with efficiency greater than 40% and a gain of 55 dB. Achievement of 10 MW of peak power would advance the state of the art for W-Band amplifiers by two orders of magnitude and potentially lead to other applications, including land- and ship-based radar, medical accelerators, and materials processing.

GYROKLYSTRON DESIGN

The design uses the second-harmonic mode to reduce the magnetic field requirements and use available TWT drivers. The current circuit design employs six cavities consisting of an input cavity, four buncher cavities and a final output cavity. A schematic of the circuit is shown in Figure 2. The input cavity is a fundamental cavity operating with the TE011 mode and uses radial coupling to the input rectangular waveguide. The first buncher cavity is operated in the fundamental TE011 mode. The following buncher cavities operate with the TE021 mode and are stagger-tuned to improve efficiency and bandwidth. The output cavity operates in the TE021 mode and has smooth-wall transitions along with a non-linear output taper to minimize mode conversion.
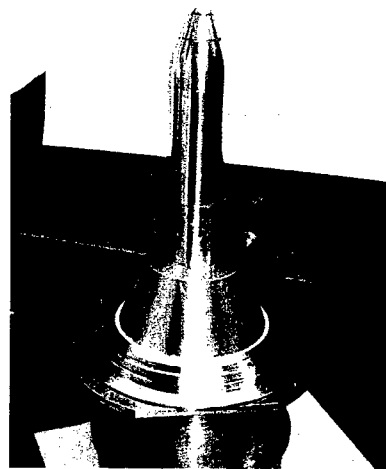
Figure 1: Gyroklystron gun stem.

Following the circuit, a large radial gap is introduced in the output waveguide to allow voltage depression of the beam collector to increase the overall efficiency. A hybrid mode is used (TE01/02) to maximize transmission across the gap. An internal elbow is included to prevent beam bombardment of the output window.
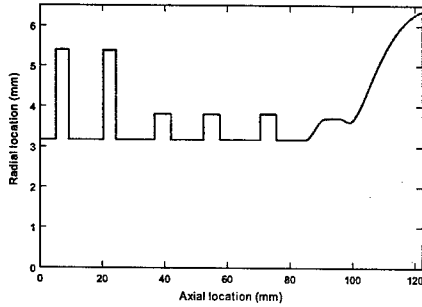
Figure 2: Schematic of gyroklystron circuit.

The output window is a single disk alumina ceramic. The predicted RF performance is shown in Figure 3.
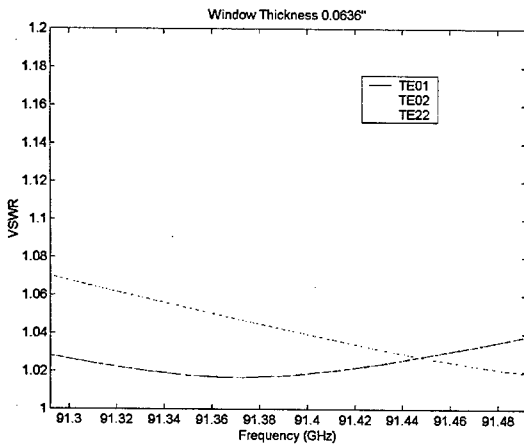
Figure 3: Predicted performance of gyroklystron window.

The gyroklystron uses a superconducting magnet manufactured by Cryomagnetics Corporation. There are also three room temperature collector coils to help distribute the spent beam power. Two TWT drivers are available for testing.

A layout drawing of the gyroklystron is shown in Figure 4 and a photograph is shown in Figure 5. Table 1 and Table 2 summarize the system parameters and current results.
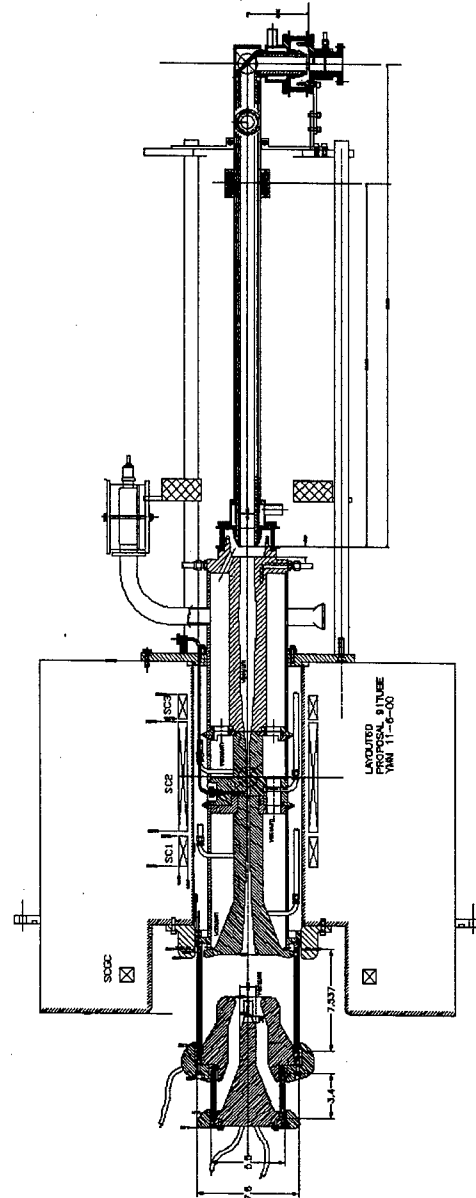
Figure 4: Layout drawing of the 10 MW, 91.4 GHz, second-harmonic gyroklystron.

Table 1: Gyroklystron Parameter

System Parameters	Value
Beam Voltage (kV)	500
Beam Current (A)	55
Average velocity ratio	1.6
Average beam radius (mm)	1.62
Peak magnetic field (kG)	28
Drive frequency (GHz)	45.696
Drive power (W)	17

Table 2: Design results achieved in simulations

System Parameter	Value
Electronic efficiency (%)	38
Gain (dB)	58
Output power (MW)	10.5
Axial velocity spread (%)	4.4

SUMMARY

A 10 MW, 91 GHz is assembled and ready for final testing. Following successful completion of testing, it will be available for high power component and system research.

ACKNOWLEDGEMENTS
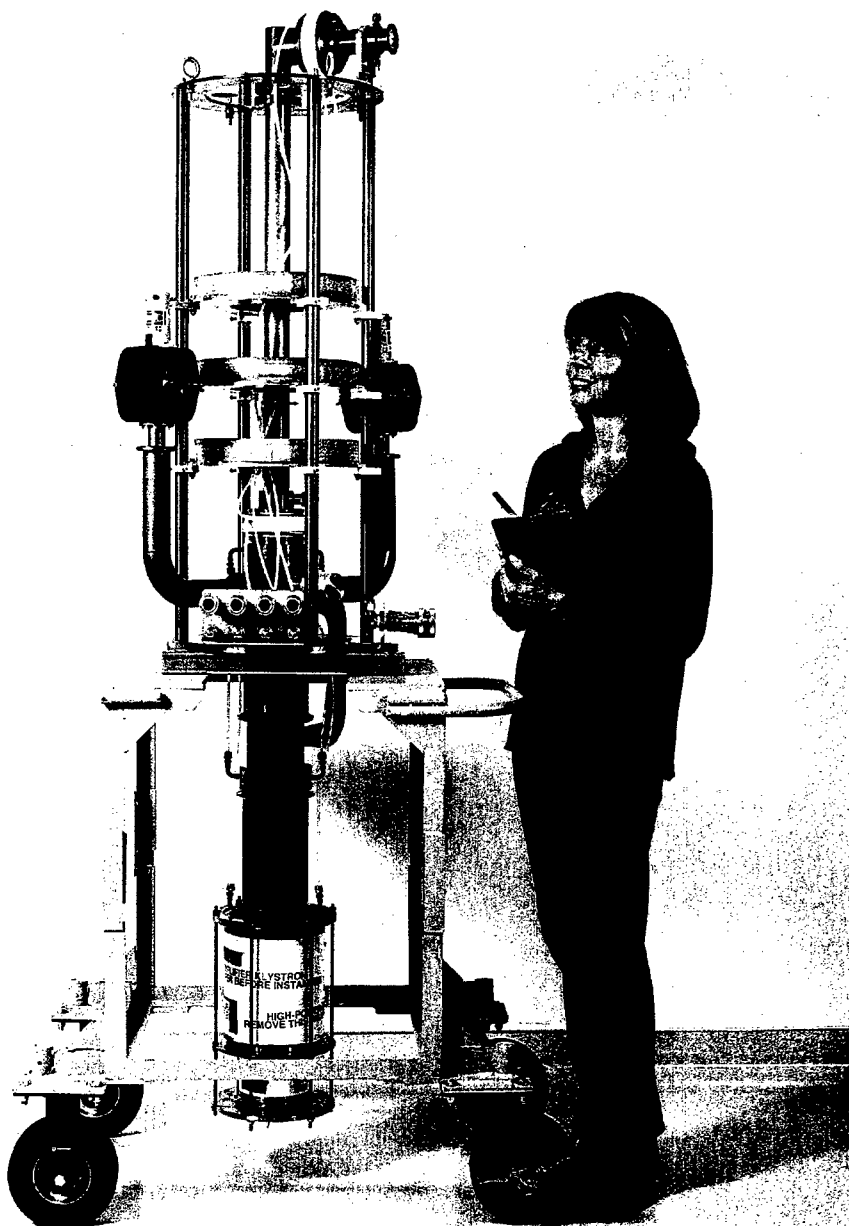
Figure 5: 10 MW, W-Band Gyroklystron.

DEVELOPMENT OF AN 805-MHZ, 550 KW PULSED KLYSTRON FOR THE SPALLATION NEUTRON SOURCE*

S. Lenci, E. Eisen, and B. Stockwell, CPI, Palo Alto, CA, USA

Abstract

The Spallation Neutron Source (SNS) is an accelerator-based neutron source being built in Oak Ridge, Tennessee, by the U.S. Department of Energy. The SNS will provide the most intense pulsed neutron beams in the world for scientific research and industrial development. CPI is supporting the effort by providing 550 kW pulsed klystrons for the super-conducting portion of the accelerator. The primary output power requirements are 550 kW peak, 49.5 kW average at 805 MHz, with an electron beam-to-rf conversion efficiency of 65% and an rf gain of 50 dB. A total of 73 units are on order. Through April 2003, eighteen units have been factory-tested. Performance specifications, computer model predictions, and operating results will be presented.

INTRODUCTION

CPI, formerly the of the Electron Device Group of Varian Associates, has a long history of building high-power pulsed UHF klystrons for many applications. This 550 kW pulsed klystron will be used in the Superconducting linac of SNS. Up to 12 klystrons will be powered from a single power supply. Since the klystrons do not have a modulating anode, the cathode voltage will determine the beam current. The system must accommodate variation in klystron perveance as well as end of life operation. The result is the klystron with the highest cathode voltage requirement will determine the operating level of the entire group of klystrons.

Although the peak and average rf power requirements are fairly modest, the combination of high efficiency (65%) and high gain (50 dB) provided quite a challenge. The additional constraint on beam operation and microperveance limited design options.

A total of 73 of the 550-kW tube, VKP-8291A, have been ordered. The prototype unit had low efficiency, but all subsequent tubes have met all the specification requirements. Through April 2003, a total of eighteen units have been factory tested. The contractual delivery rate is 2 per month with the 73rd unit being delivered in December 2004.

DESIGN

Electrical Design

The electron gun design is primarily performed using XGUN, starting with the electrostatic beam optics. Once the performance is satisfactory, the design is refined with magnetic field is applied. Care is taken to evaluate and minimize the beam scallop down the drift tunnel. Analyses are performed at various operating conditions. The voltage gradients of the gun electrodes are analyzed with a goal of a maximum gradient of 60 kV/cm for this long pulse device. Great care is taken to ensure a well-behaved beam is obtained. The peak cathode loading is 0.6 Amps/cm2, which yields a predicted cathode life in excess of 100,000 hours.
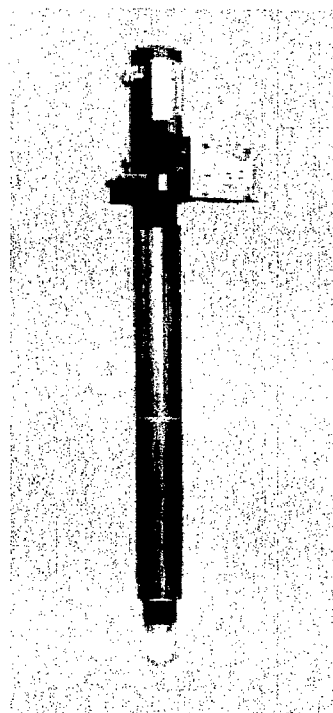
Figure 1: VKP-8291A Klystron

The baseline for the electrical design was our 700 MHz, 1 MW CW klystron built for the APT project at LANL, which also had to meet a 65% efficiency requirement. The rf-circuit contains six cavities, including one tuned slightly below the second harmonic of the operating frequency. The design is optimized to provide the required efficiency and gain without compromising bandwidth. The first two cavities are staggered around the operating frequency to provide the bandwidth. Next is the second-harmonic cavity followed by two inductively tuned cavities to optimize the electron bunching. The output cavity then extracts energy from the beam.

The rf-circuit is designed using 1-D and 2-D particle-in-cell codes developed at CPI. Many years of benchmarking the codes to measured results has lead to high confidence in the results. SUPERFISH is used for cavity design, while HFSS and MAFIA are used for the output cavity and output window design.

Mechanical Design

The klystron is required to operate vertically with the gun down and is shown Figure 2. The two buncher cavities and the two inductively tuned cavities have stainless steel walls with copper endwalls, with cavities 4 and 5 copper plated to reduce resistive loss. The second harmonic and output cavities have OFE copper walls. The 550-kW tube incorporates diaphragm tuners in the cavities for adjusting the frequency.
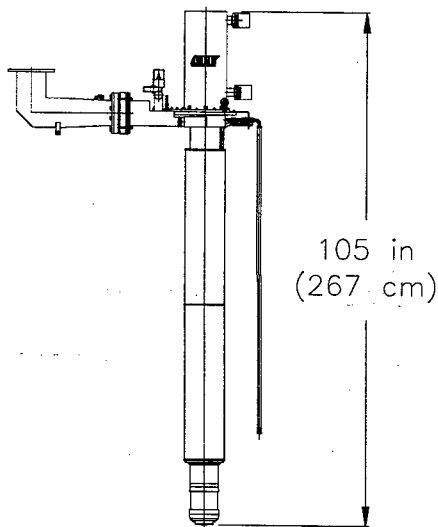
Figure 2: VKP-8291A Klystron Layout

The rf energy is extracted through a single window with an alumina ceramic. The pillbox window is designed around WR-975 wavguide.

The collector is designed to dissipate the entire beam energy. It is made from thick-walled copper with grooves milled into the outer wall for the coolant to pass. The water-jacket is part of the brazed collector assembly. The proof test pressure is 200 psi (13.6 bar).

TEST RESULTS

The prototype met all performance specifications except for the efficiency. Only 62.3% was achieved instead of 65%. The specification efficiency could be achieved when the magnet power was increased above the allowable limit. Modifications to the rf circuit were implemented to correct this deficiency. See Table 1 for the performance summary.

Table 1: VKP-8291A Performance Summary

	VKP-8291A Specification	VKP-8291A Typical
Frequency	805 MHz	805 MHz
Peak Cathode Voltage	75 ± 1.5 kV	75 kV
Peak Beam Current	11.5 Amps max	11.2 Amps
Perveance	.55 nom	.54
Peak Output Power	550 kW min	560 kW
-1 dB Bandwidth	± 1.3 MHz min	± 2 MHz
Efficiency	65 % min	67 %
RF Duty Cycle	9 %	9 %
RF Pulse Length	1.5 msec	1.5 msec
Peak RF Drive Power	5.5 Watts	4.3 Watts
Gain	50 dB min	51dB

The transfer and bandpass curves of all 18 units, along with the simulation predictions, have been plotted together for comparison as seen in Figures 3 and 4. The prototype klystron stands out as the only unit that did not meet the efficiency requirement. Otherwise the variation among the units is quite reasonable.
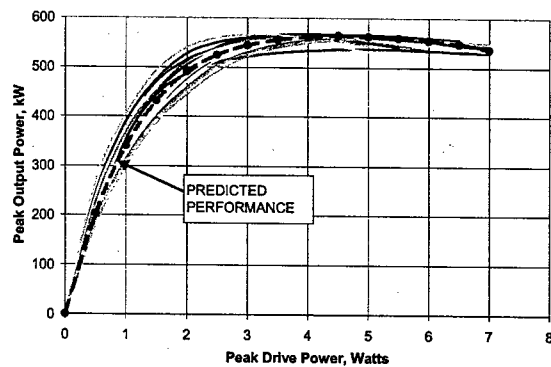
Figure 3: VKP-8291A Transfer Curves
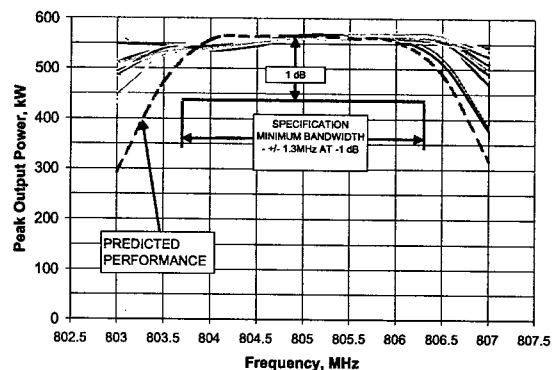
Figure 4: VKP-8291A Bandpass Curves

Each klystron has to demonstrate stable performance and achieve 80% of its rated power at six equally spaced positions of a 1.2:1 mismatch. Figure 5 plots a set of transfer curves at different mismatch positions and into a matched load for S/N 015.
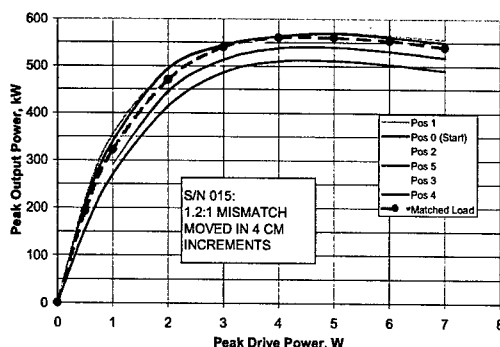
Figure 5: Performance into a 1.2:1 VSWR

The Phase Transfer Characteristic (the insertion phase of the klystron) is required to be a smoothly varying, monotonic function as the drive power is increased from 20% to 100% of the saturated drive, and is measured on each unit. Samples of the input and output power were processed through an Analog Devices AD8302 RF/IF Gain and Phase Detector. The phase detector output voltage was observed on a scope and averaged over many pulses. The phase shift was measured in 0.5 dB increments as the drive power was reduced from saturated output (0 dB) to −13.5 dB (4.5% of saturated drive).
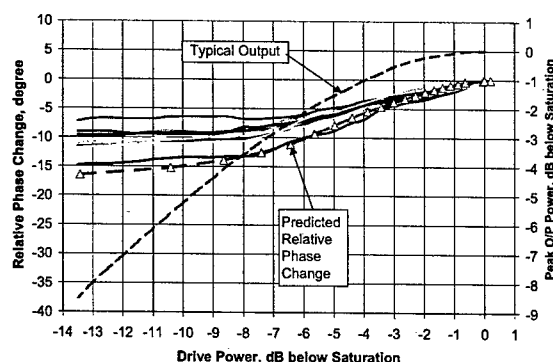
Figure 6: Relative Phase Change vs. Drive Power

The production rate to support this contract has provided an opportunity to evaluate operational and performance variation. Some of the variation is due to manufacturing tolerances, such as spacing in the gun that directly influence the microperveance, and some are due to optimizing performance at test. The gain and bandwidth are greatly influenced by the cavity tuning. We found if the gain is too high, the tube is much closer to instabilities should the magnet settings or beam voltage drift. Our goal is to set the gain just below 51 dB to provide margin.
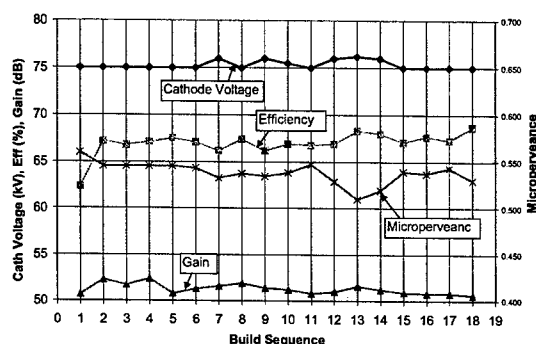
Figure 7: Summary of Performance in Build Sequence

CONCLUSIONS

The measured results instill high confidence in our simulation codes. The tube also demonstrates a high degree of stability under various operating conditions. Although the prototype 550-kW klystron did not meet the efficiency specification, all subsequent tubes have met all aspects of the specification.

ACKNOWLEDGEMENT

The authors would like to thank their co-workers at CPI for their contributions throughout the development of these products. They would also like to thank the CPI management team for their support. Finally many thanks go to the technical leaders and their colleagues at Los Alamos National Lab, in particular Dan Rees and Paul Tallerico.

DESIGN AND TEST OF A 100MW X-BAND TE$_{01}$ WINDOW

Jeff Neilson and Lawrence Ives
Calabazas Creek Research, Inc.
20937 Comer Dr, Saratoga, CA 95070
Email: jeff@calcreek.com

Sami G. Tantawi
Stanford Linear Accelerator Center
P.O. Box 4349, Stanford, CA 94309

Research at Stanford Linear Accelerator Center (SLAC) is in progress on a TeV-scale linear collider that will operate at 5-10 times the energy of present-generation accelerators. This will require development of high power X-Band sources generating 50 -100 MW per source. Conventional pillbox window designs are capable of transmitting peak rf powers up to about 30 MW, well below the desired level required for the use of a single window per tube. SLAC has developed a 75 MW TE$_{01}$ window [1] that uses a 'traveling wave' design to minimize fields at the window face. Irises match to the dielectric window impedance, resulting in a pure traveling wave in the ceramic and minimum fields on the window face. The use of the TE$_{01}$ mode also has zero electric field on the braze fillet. Unfortunately, in-band resonances prevented this window design from achieving the desired 75MW power level. It was believed the resonances resulted from sudden steps in the circular guide to match the 38mm input diameter to the overmoded (TE$_{01}$ and TE$_{02}$ mode propagating) 65 mm diameter of the window ceramic.

Calabazas Creek Research Inc. is currently developing a traveling wave window using compact, numerically optimized, parabolic tapers to match the input diameter of 38mm to the window ceramic diameter of 76mm (Figure 1). The design is projected to handle 100 MW of pulse power with a peak field at the window face of 3.6 MV/m.

Cold test of the window has shown the return loss to be better than -25 dB over a 100 MHz bandwidth and to be resonance free (Figure 2). The window is scheduled for high-power testing in July 2003 at the SLAC.
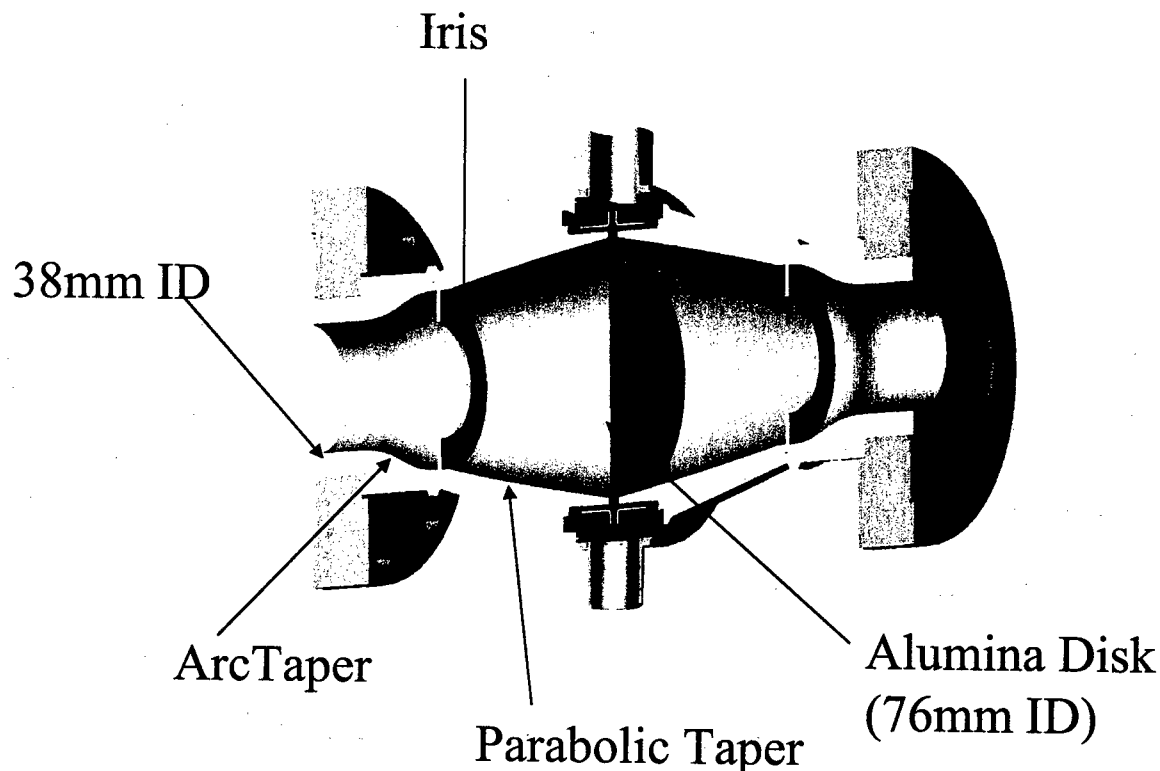
Figure 1. Cross section of high power X-Band window.
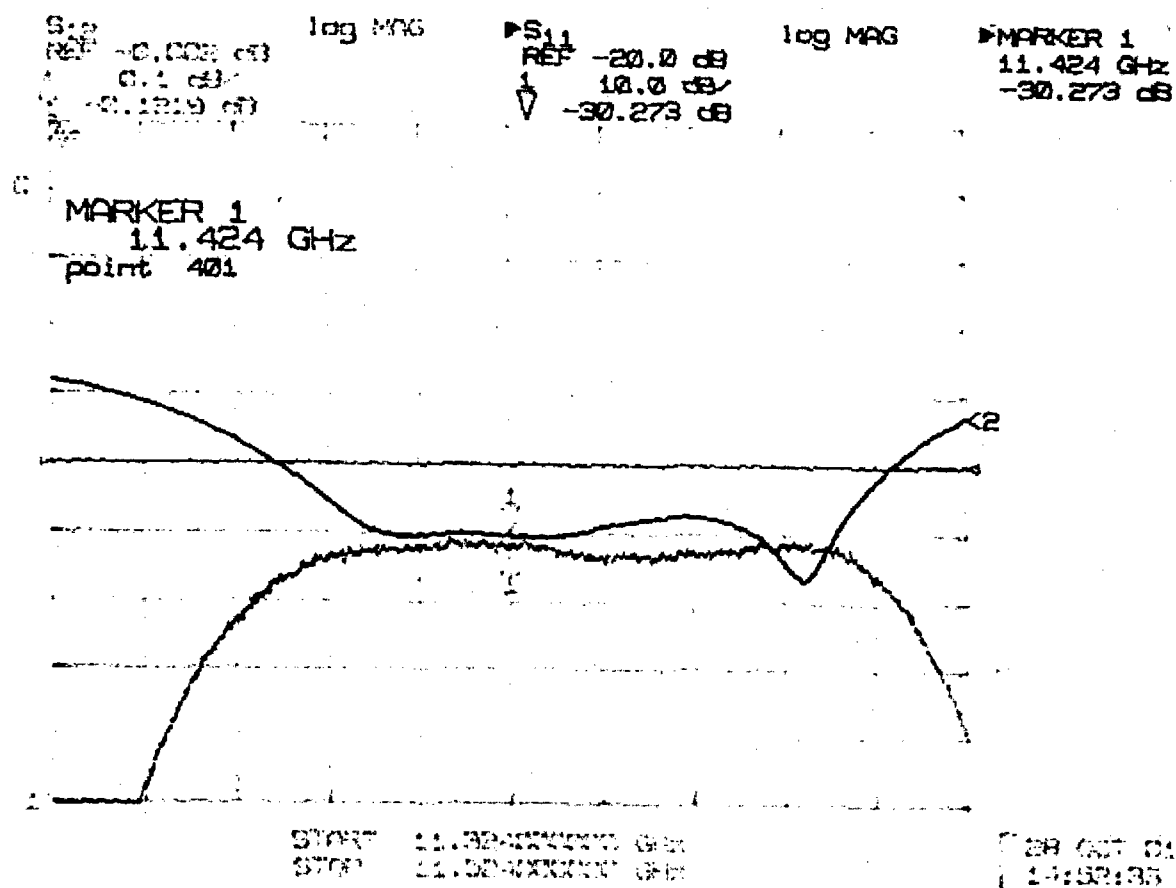
Figure 2. Crossection of high power X-Band window.

REFERENCE

1. W.R Fowkes, R.S. Callin, E.N. Jongewaard, D.W. Sprehn, S.G. Tantawi, A.E. Vlieks, "Recent advances in high power RF windows at X band", AIP Conf.Proc.474:289-295,1999

DEVELOPMENT OF A MULTI-MEGAWATT CIRCULATOR FOR X-BAND

Jeff Neilson and Lawrence Ives, Calabazas Creek Research, Inc., Saratoga, CA 95070
Sami G. Tantawi, Stanford Linear Accelerator Center, Stanford, CA 94309

Research is in progress on a TeV-scale linear collider that will operate at 5-10 times the energy of present-generation accelerators. This will require development of high power RF sources generating of 50 -100 MW per source. Transmission of power at this level requires overmoded waveguide to avoid breakdown. In particular, the TE_{01} circular waveguide mode is currently the mode of choice for waveguide transmission at Stanford Linear Accelerator Center (SLAC) in the Multimode Delay Line Distribution System (MDLDS).

A common device for protecting an RF source from reflected power is the waveguide circulator. A circulator is typically a three-port device that allows low loss power transmission from the source to the load, but diverts power coming from the load (reflected power) to a third terminated port. To achieve a low loss, matched, three port junction requires nonreciprocal behavior. This is achieved using ferrites in a static magnetic field which introduces a propagation constant dependent on RF field direction relative to the static magnetic field.

Circulators are currently available at X-Band for power levels up to 1 MW in fundamental rectangular waveguide; however, the next generation of RF sources for TeV-level accelerators will require circulators in the 50-100 MW range. Clearly, conventional technology is not capable of reaching the power level required.

In this paper, we discuss the development of an X-Band circulator operating at multi-megawatt power levels in overmoded waveguide. The circulator will employ an innovative coaxial geometry using the TE_{01} mode. Difficulties in maintaining mode purity in oversized rectangular guide preclude increasing guide area to allow increasing the power level to the desired 50-100 MW range.

The TE_{01} mode in circular waveguide is very robust mode for transmission of high power in overmoded waveguide[2]. The mode is ideal for transmission of high power microwaves because of its low-losses, zero tangential field on the guide (which minimizes arcing problems) and reduced propensity for mode conversion compared to non-asymmetric circular waveguide modes. Unfortunately, no current designs exist for circulators using the circular TE_{01} mode.

The basic building block for all low-loss circulators and isolators is a nonreciprocal element with a phase shift dependent on the propagation direction in the guide. Such an element can be constructed by placement of a hollow ferrite rod in a cylindrical waveguide. An inner conductor placed inside the ferrite rod conducts a current pulse that induces an azimuthal magnetic field inside the ferrite. This configuration is depicted in Figure 1a. An alternate configuration using permanent magnets is shown in
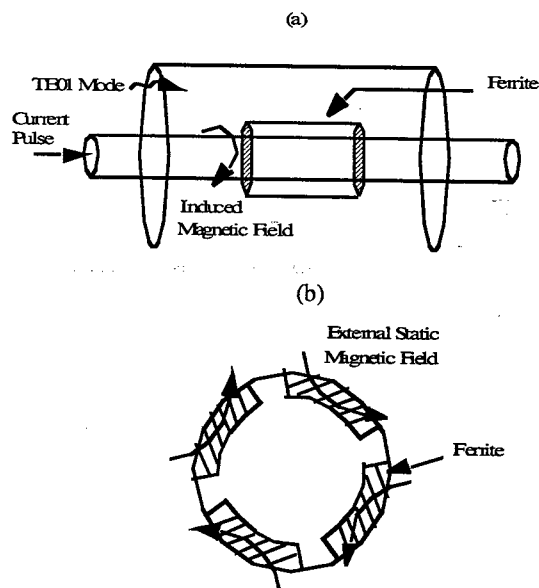
Figure 1. Configurations for nonreciprocal element for TE01 mode in circular waveguide. (a) Inner cylindrical placement of ferrite with azimuthal field induced by current pulse through conductor inside ferrite. (b) Transverse cross section of cylindrical guide with ferrites on outer radius guide with azimuthal field induced by external permanent magnet field.

Figure 1b. Either of these configurations will create a different phase shift for waves propagating in opposite directions along the waveguide axis. This feature can be used to develop a high power circulator.

We are currently testing a TE_{01} nonreciprocal phase shifter in a 50 MW test stand. This device is in the configuration shown in Figure 1a. The induced differential phase shift and loss will be measured and compared to calculations.

1. P.B. Wilson, "RF power sources for 5-15 TeV linear colliders," Intern. workshop on pulsed RF sources for linear colliders, Shonan Village, Japan, April 1996.

2. Theodore Moreno, *Microwave Transmission Design Data*, Dover Publications, New Your, NY, 1948.

PERFORMANCE OF X-BAND PULSED MAGNICON AMPLIFIER*

O.A. Nezhevenko,[1] V.P. Yakovlev,[1] J.L. Hirshfield,[1,2] E.V. Kozyrev,[1,#]
S.H. Gold,[3] A.W. Fliflet,[3] and A.K. Kinkead[4]
[1]Omega-P, Inc., New Haven, CT 06511 USA
[2]Physics Department, Yale University, New Haven, CT 06520 USA
[3]Beam Physics Branch, Plasma Physics Division, Naval Research Laboratory, Washington, DC 20375, USA.
[4]LET Corp., Washington, DC 20007, USA.

Abstract

A frequency-doubling magnicon amplifier at 11.4 GHz has been developed and built as the prototype of an alternative microwave source for the Next Linear Collider, and to test high power RF components and accelerating structures. The tube is designed to produce ~60 MW, in ~1.2 μsec pulses at 58% efficiency and 59 dB gain, using a 470 kV, 220 A, 2 mm-diameter beam. Recent results of the tube performance are presented in this paper. Operation of this magnicon has established a research facility located at NRL as only the second laboratory in the USA, after SLAC, where high-power microwave development at the NLC X-band frequency can take place.

INTRODUCTION

This paper describes the current experimental status of the 11.424 GHz Omega-P/NRL magnicon amplifier [1], that is under development as an alternative RF source for a future electron-positron linear collider. The magnicon [2] is microwave amplifier tube that combines the scanning beam synchronism of the gyrocon [3] with a cyclotron resonant interaction in the output cavity. This synchronism makes possible high efficiencies and, with larger cavities than in klystrons, allows higher powers at high frequencies than comparable klystrons [2,4].

A schematic layout of the Omega-P/NRL magnicon is shown in Fig. 1. The tube consists of an electron gun, ~6.5 kG solenoid, RF circuit and collector insulated from ground. The 500 kV diode gun provides the required 100 MW of power, and a 2 mm diameter beam in the solenoid which corresponds to a beam area compression of 1400:1 [5]. The RF circuit has six 5.712 GHz TM_{110} deflection cavities (a drive cavity, three gain cavities and two penultimate cavities), followed by an 11.424 GHz TM_{210} output cavity. In contrast to the magnicon described in ref. [4], the two penultimate cavities are not coupled and operate in the angle summing mode, in order to suppress an instability that limits the pulse width [6]. To extract RF power there are two output apertures at the downstream end of the output cavity, separated by 135°, that couple to WR-90 waveguides.

The magnicon design parameters for the measured 2-mm beam diameter [5] are summarized in Table 1 and general view of the tube is shown in Fig.2.
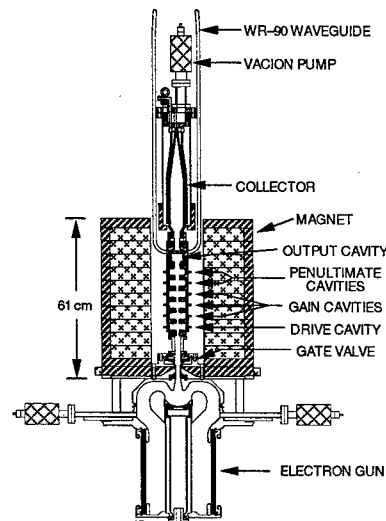
Figure 1. The magnicon schematic.

Table 1. Design parameters of the X-band magnicon.

Frequency, GHz	11.424
Power, MW	60
Efficiency, %	58
Pulse duration, μsec	1
Maximum repetition rate, Hz	10
Gain, dB	59
Drive frequency, GHz	5.712
Beam voltage, kV	470
Beam current, A	220
Perveance, A-V$^{-3/2}$×10^{-6}	0.68
Beam diameter in magnet, mm	2

EXPERIMENTAL RESULTS

1. Operation of the Omega-P/NRL magnicon has established an 11.424 GHz high power accelerator test facility at NRL. During 2001-2002, the facility was used to carry out two separate collaborative experimental programs, namely study of high-power active microwave
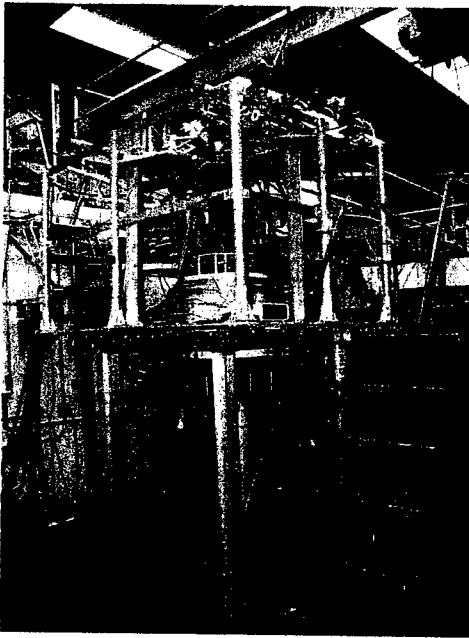
Fig. 2. General view of 11.424 GHz magnicon.

pulse compressors and high-gradient dielectric-loaded accelerating structures [7]. In 2002 high-power ceramic windows were installed at the magnicon output waveguides. These windows, built by Calabazas Creek Research, Inc. [8], allow one to change the test experimental configuration without breaking vacuum in the tube. Starting in February 2003, the magnicon underwent an extensive three-month cycle of rf conditioning.

2. After this cycle of conditioning, the output power remained limited to a level of 26 MW in a 200 ns pulse. Oscillograms are shown in Fig. 3.
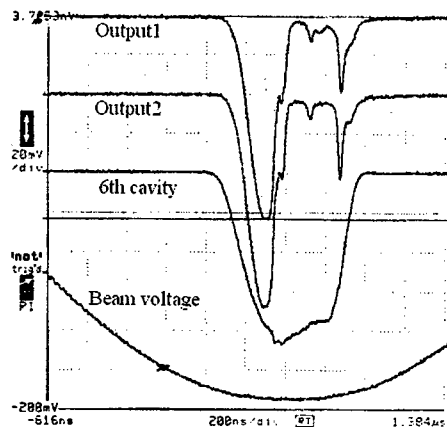
Fig. 3. Oscillograms of both output signals, and signal from the penultimate (6th) cavity. Beam voltage pulse is shown also..The output power is about 13 MW in each output, the beam voltage is 490 kV and surface rf field in cavity 6 is about 600 kV/cm.

One can see that both output signals look similar, and that the output pulse width is limited by effects in the output cavity but not in the deflection system. Pulses from both penultimate cavities have the full width (signal from cavity 6 is shown in Fig.3) compared to the shortened output pulses. The output power was measured calorimetrically in both output waveguides. The measurements show that the output powers in the waveguides are equal to within a few percent over a wide range of output power.

3. The dependences of signals from the last three deflection cavities, as well as output power *vs.* input power, are shown in Fig. 4.
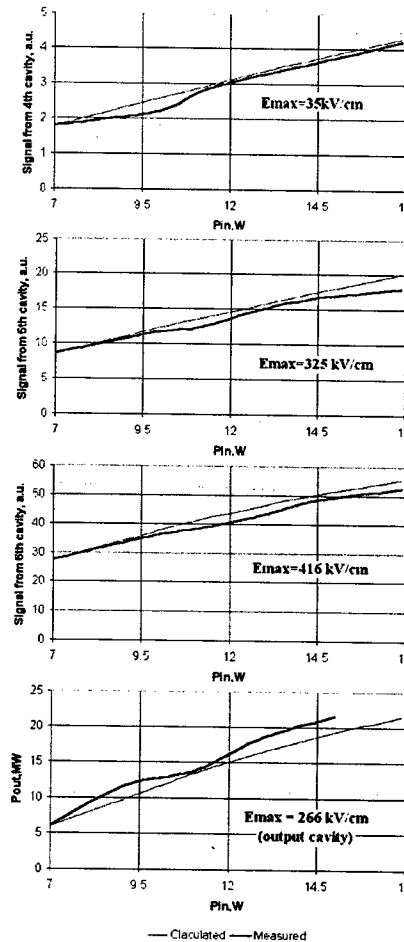
Fig. 4. Signals from the last three deflection cavities and the output power *vs.* the input power.

One can see that behavior of the measured curves is in good agreement with the simulation results. The maximum surface electric fields are given in Fig. 4 as well. One can see that these fields are well below the breakdown limit. Note, that the maximum achieved surface electric field in cavity 6 (Fig. 3) is about 600 kV/cm, which is higher than the value required for magnicon operation at a full power of 60 MW. The

curves in Fig. 4 are plotted against the measured input power, which is higher than the calculated value, mostly due to a shift in the first cavity frequency, which leads to strong reflections from the input port.

4. The shape of the shortened output signals and relatively low surface electric field in the magnicon cavities (Fig. 4) strongly suggest that the reason for the pulse shortening is not breakdown, but multipactoring. It was also found that pulse shortening is accompanied by a pressure increase in the tube collector. In an attempt to understand the possible cause of the observed problems, measurements of microwave signals from the collector have been made. The results of these microwave measurements are shown in Fig. 5 and Fig. 6. The oscillograms in Fig. 5 are taken in the regime of relatively low power, when there is no pulse shortening. The collector signal measurement was made with shorted slotted line, and the shape of the signal is very similar to that from cavity 6. The frequency measurements were made with both the slotted line and a heterodyne method. The measured frequency is exactly equal to the magnicon drive signal (~5712 MHz). Up to the certain level of power the amplitude of the collector signal scales smoothly with the magnicon input signal. When the input power is increased, pulse shortening in the collector signal is observed, and this begins at a power level that is lower than the level when output pulse shortening begins. These observations suggest excitation of a resonant mode in the collector, with efficient
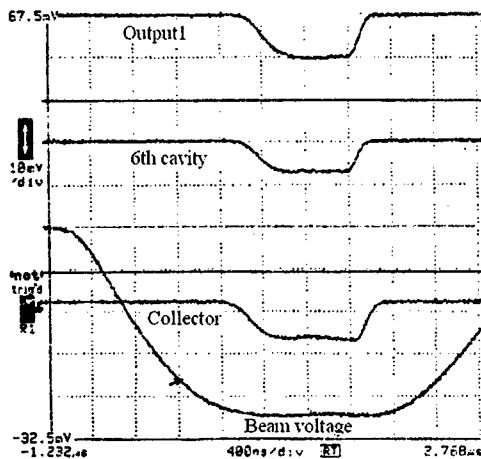
Fig.5. Magnicon signals for low power.

interaction of the gyrocon/magnicon type [2,3]. At the maximum power level, the collector signal drops to low amplitude, and one can see a peak in the midst of the collector signal (Fig. 6). The frequency of the signal in the peak is about 6.7 GHz. This signal is not synchronous with the magnicon drive or output frequencies and most probably is the result of self-excitation.

Thus, one is led to conclude that effects leading to output pulse shortening originate in the collector. The collector plasma cannot play a significant role in the interaction between the collector and the output cavity,

because the plasma drift time would be too long and the time difference between these two effects is too small. Most probably, electrons from multipactoring in the collector drift along the magnetic field into the output cavity, thereby triggering multipactoring therein.
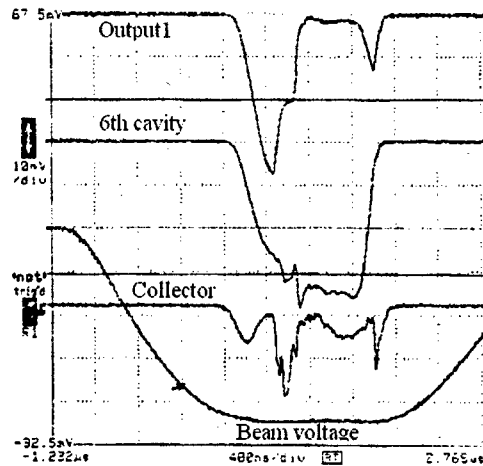
Fig.6. Magnicon signals for high power.

CONCLUSION

Future plans include design and fabrication of a new collector, based on the design of the collector built for the 34 GHz Omega-P magnicon [9]. This latter collector does not incorporate a large internal chamber that could support a spurious resonant mode, but also allows external damping to be inserted around the collector insulator in case oscillations do arise. It is anticipated that use of a re-designed collector will allow the 11.424 GHz magnicon to reach its design output power in a full-width pulse.

REFERENCES

[1] O.A. Nezhevenko, et al., PAC2001, Chicago 2001, p.1023.

[2] O.A. Nezhevenko, *IEEE Trans. On Plasma Sci.,*, vol. 22, p. 765, 1994.

[3] G.I. Budker, et. al., *Part. Accel.*, vol. 10, p.41, 1979.

[4] E.V. Kozyrev, et. al., RF98 Workshop, AIP **474**, p.187.

[5] O.A. Nezhevenko, et al., *IEEE Trans. On Plasma Sci.*, vol. 30 , p. 1220, 2002.

[6] O.A. Nezhevenko and V.P. Yakovlev, *IEEE Trans. On Plasma Sci.*, vol. 28, p. 542, 2000.

[7] S.H. Gold, et al., AAC2002, AIP **647**, p.439.

[8] http://calcreek.com

[9] O.A. Nezhevenko, et al., AAC2000, AIP **569**, p. 786.

34 GHz, 45 MW PULSED MAGNICON: FIRST RESULTS*

O.A. Nezhevenko,[1] M.A. LaPointe,[1,2] V.P. Yakovlev,[1] J.L. Hirshfield [1,2]

[1]Omega-P, Inc., New Haven, CT 06511 USA

[2]Physics Department, Yale University, New Haven, CT 06520 USA

Abstract

A high efficiency, high power magnicon at 34.272 GHz has been designed and built as a microwave source to develop RF technology for future multi-TeV electron-positron linear colliders. To develop this technology, this new rf source is being perfected for necessary tests of mm-wave accelerating structures, RF pulse compressors, RF components, and to determine limits of breakdown and metal fatigue. The description of this magnicon and first experimental results are presented in this paper.

INTRODUCTION

One of the attractive candidates for the role of rf source for a new generation of particle accelerators is the magnicon, a microwave amplifier employing circular deflection of an electron beam [1]. Magnicons have shown great potential with both high efficiency and high power. A first magnicon to have demonstrated these qualities was build and tested in the 80's in Novosibirsk. A power of 2.6 MW was obtained at 915 MHz with a pulse width of 30 μsec and an electronic efficiency of 85% [2]. In experimental tests also at Budker INP [3], a second harmonic magnicon amplifier operating at 7.0 GHz achieved an output power of 55 MW in a 1.1 μsec pulse, with a gain of 72 dB and efficiency of 56%. Another frequency-doubling magnicon amplifier at the NLC frequency of 11.424 GHz has been designed and built in a collaboration between Omega-P, Inc and NRL. The tube is designed to produce ~60 MW at 60% efficiency and 59 dB gain, using a 470 kV, 220 A, 2 mm-diameter beam [4]. At present, the tube is conditioned up to power level of 25 MW for 0.2 μsec pulse widths [5].

In order to develop RF technology in the millimeter wavelength domain for a future multi-TeV electron-positron linear collider, it is necessary to test accelerating structures, RF pulse compressors, RF components, and to determine limits of breakdown and metal fatigue. A high efficiency, high power magnicon at 34.272 GHz has been designed and built as the basis for a test facility dedicated to carrying out these aims.

THIRD HARMONIC MAGNICON AMPLIFIER

In scaling magnicon amplifiers to higher frequencies (consequently, smaller physical dimensions), a few design problems arise at high power due to the limitations imposed by cathode loading, rf breakdown and pulse

heating of the cavity walls. The concept of a third harmonic magnicon amplifier is introduced to overcome these limitations [6,7].

In general, a magnicon (as a klystron) consists of four major components, namely an electron gun, magnet, RF system and beam collector. The electron gun injects a 500 kV, 215 A beam with a diameter of about 1 mm into a chain of cavities forming the RF system. The deflection system consists of a drive cavity, three gain cavities and two "penultimate" cavities (working in "angle summing" mode [8]). The external magnetic field provides both beam focusing and coupling between the electrons and the RF fields in the cavities. The electron beam is radially deflected by the RF magnetic fields of rotating TM_{110} modes in the deflection system cavities. The scanning beam rotates at the frequency of the drive signal (11.424 GHz), then enters the output cavity and emits radiation at three times the drive frequency (34.272 GHz) by interacting with the TM_{310} mode. Fig. 1 shows the required magnetic field profile (top) and the superconducting coil configuration and iron yoke geometry to achieve this profile (bottom). For effective deflection, the magnetic field in the deflection system should be such that $\Omega/\omega \sim 1.5$, where Ω is the cyclotron frequency and ω is the drive frequency. In the output cavity, however, for efficient extraction of energy, the magnetic field should be chosen such that $\Omega/3\omega \sim 0.9$ [7].

The design parameters of this amplifier are given in Table 1.
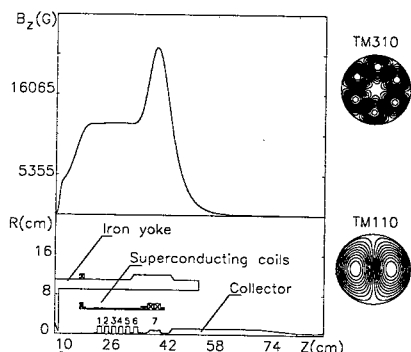
Fig. 1. Required axial magnetic field profile (top), and superconducting coil and iron yoke layout (bottom). Cavity chain and collector are also shown. Inserts at the right show RF field patterns for cavities #1-6 of deflecting system (TM_{110} mode at 11.424 GHz), and for the output cavity (TM_{310} mode at 34.272 GHz).

The gun design [9] calls for a cathode current density of 12 A/cm^2, and a maximum surface electric field strength of 238 kV/cm on the focus electrode. It is found in this design that 95% of the current is within a diameter of 0.8 mm [9] in the magnet.

TABLE 1. 34.3 GHz magnicon parameters.	
Operating frequency, GHz	34.272
Output power, MW	44-48
Pulse duration, μs	1.5
Repetition rate, Hz	10
Efficiency, %	41-45
Drive frequency, GHz	11.424
Drive power, W	150
Gain, dB	54
Beam voltage, kV	500
Beam current, A	215
Beam diameter, mm	0.8-1.0
Magnetic field, deflecting cavities, kG	13.0
Magnetic field, output cavity, kG	22.5

An engineering design drawing of the complete 34.272 GHz magnicon is presented in Fig. 2.
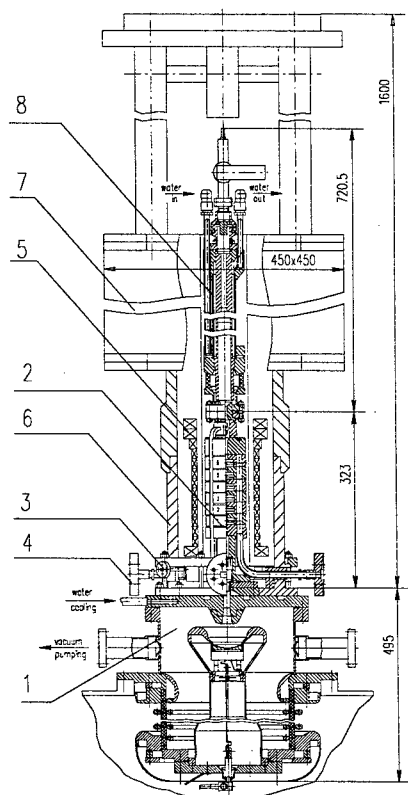
Fig. 2. 34.272 GHz magnicon amplifier tube: *1*-electron gun, *2*-RF system, *3*-output waveguide (WR28), *4*-WR90 waveguide, *5*-superconducting coils, *6*-iron yoke, *7*-cryostat, *8*-beam collector.

The RF system consists of seven cavities: one drive (#1) three gain (#2-4), two "penultimate" (#5-6), and one output cavity (#7). The shapes and dimensions of the cavities are chosen to avoid monotron self-excitation of axisymmetric modes, and of harmonic frequency modes [7]. All cavities of the deflection system are about 1.25 cm long and their diameters are about 3.0 cm. There are four WR90 waveguides built in the body of the deflecting system. One is for the drive cavity, and the rest are for diagnostic measurements in cavities #3, 5 and 6. These waveguides are also used for pumping. The length of the output cavity (3.15 cm) and its shape were optimized to achieve maximum efficiency, absence of parasitic oscillations, and acceptable surface electric fields [7]. The diameter of the output cavity is about 1.75 cm. Power is extracted through four WR28 waveguides having an azimuthal separation $\Delta\theta = \pi/2$ that couple to both field polarizations [7]. Only one of the four is shown in Fig. 2. The RF system is built as a brazed monoblock that allows baking up to 400° C.

EXPERIMENT

Before assembling the full magnicon, the gun and beam collector were assembled and tested up to the design power of 100 MW in μsec pulses [9]. Initial conditioning up to ~515 kV was carried out without beam current. To achieve this, a matched load was connected to the primary of the pulse transformer. After cold conditioning, the gun was conditioned and tested hot up to ~480 kV and ~200 A. The measured beam current is in excellent agreement with the design value, with a measured error no greater than ±2%.

The magnicon was then assembled, cold tested and baked out in 2002. The cryomagnet was installed only later, after making modifications necessary to achieve the required axial symmetry of the magnetic field.

The general view of the fully assembled tube is shown in Fig. 3.

Preliminary tests of the tube were conducted for only a few days prior to PAC2003. Oscillograms of the measured input and output signals are shown in Fig. 4. The beam voltage for this experiment was 450 kV, beam current was 185 A, and drive frequency was 11.428 GHz. After a few days of conditioning at a repetition rate of 1 Hz, the output signal had not yet stabilized, and in the process of conditioning a rise of pressure is observed. Preliminary calibration shows about 1 MW of output power in one output and consequently, about 4 MW in total.

CONCLUSION

The 34 GHz magnicon amplifier is assembled and first tests have been conducted. To date the measured output power is about 4 MW.

The program of future experimental work on the 34 GHz magnicon test facility includes:

1132

a) Experimentation on metal fatigue caused by pulse heating, and consequently determination of accelerating structure longevity.

b) Development high-power components, including output windows, mode converters, phase shifters, power splitters and power combiners, low-loss transmission lines, etc.

REFERENCES

[1] O. A. Nezhevenko, *IEEE Trans. Plasma Sci.*, **22**, 1994, pp. 756-772.

[2] M.M. Karliner, *et. al.,* Instrum. Methods Phys. Res. A **269**, p. 459 (1988)..

[3] E.V. Kozyrev, *et. al.,* EPAC98, Stockholm, 1998, p.1897.

[4] O.A. Nezhevenko, *et al., IEEE Trans. Plasma Sci.,* **30**, 2002, pp. 1220-1230.

[5] O.A. Nezhevenko, *et al.,* Present Conference, TPAE022.

[6] O.A. Nezhevenko, *et al.,* PAC97, Vancouver, 1997, p. 3156.

[7] O.A. Nezhevenko, *et al.,* AAC2000, AIP **569**, p. 786.

[8] O.A. Nezhevenko, and V.P. Yakovlev, *IEEE Trans. Plasma Sci,,* **28**, 2000, pp 542-549.

[9] V.P. Yakovlev, *et al.,* PAC2001, Chicago 2001, p. 1041.

Fig. 3. The general view of the fully assembled tube.

Fig.4. The oscillograms of the measured input and output signals. The upper curve represents output power and the lower curve is incident input signal.

EQUILIBRIUM TRANSPORT OF SHEET ELECTRON BEAMS IN SOLENOIDAL FOCUSING FIELDS*

R. Pakter[#]

Instituto de Física, Universidade Federal do Rio Grande do Sul, Brazil

Abstract

The transport of sheet electron beams is an important issue in the development of high-power RF generators because large amounts of current can be achieved at reduced space-charge density. In this paper we analyze equilibrium configurations for the transport of sheet electron beams in tapered solenoidal focusing fields. In particular, we use the generalized envelope equations obtained for the evolution of space-charge-dominated beams propagating through a general linear focusing channel [R. Pakter and C. Chen, Phys. Rev. E, 62, 2789 (2000)] to derive an optimal focusing field profile for sheet beam transport. Analytic solutions based on multi-time scale perturbation theory are found and compared to numerical simulations.

INTRODUCTION

The improvement of high-power vacuum microwave sources plays a crucial role in the development of the new generation of high-gradient, high-frequency particle accelerators [1]. As scaling up the microwave sources to higher frequencies, a significant difficulty is the need to transport intense beams through decreasing aperture sizes, because the RF circuit dimensions decrease with the wavelength. In this regard, the use of sheet electron beams seems a promising concept, since larger amounts of current can be transported at lower current densities by increasing the width of the beam, while keeping its height of the order the RF wavelength [2-4]. The main drawback on the use of sheet beams in comparison to the usual round beam is that the sheet beam may be more vulnerable to some instabilities in ordinary solenoidal focusing channels [5].

In this paper, we analyze the transport of sheet electron beams in solenidal focusing systems. In particular, we consider the case of tapered focusing fields, and search for field profiles leading to equilibrium solutions for the transport. Use is made of the generalized envelope equations obtained for the evolution of intense beams in general linear focusing systems [6] to derive an equation for the magnetic field profile as a function propagation distance.

MODEL AND THE GENERALIZED ENVELOPE EQUATIONS

In this section we review the generalized envelope equations [6], specializing to the transport in solenoidal focusing fields. Let us consider a thin, continuous, space-charge-dominated beam propagating with constant axial velocity $\beta_b c \hat{\mathbf{e}}_z$ through a solenoidal focusing field. Here, c is the speed of light in vacuum. The focusing magnetic field is approximated by

$$\mathbf{B}_0(\mathbf{x}) = B_z(s)\hat{\mathbf{e}}_z - \frac{1}{2}B_z'(s)(x\hat{\mathbf{e}}_x + y\hat{\mathbf{e}}_y) \qquad (1)$$

where $s = z = \beta_b ct$ is the axial coordinate, and the prime denotes derivative with respect to s.

It has been shown in the paraxial approximation that there exists a class of solutions to steady-state cold-fluid equations [6], which, in general, describes corkscrewing elliptic beam equilibria for, space-charge-dominated beam propagating through the applied focusing magnetic field defined in Eq. (1). The generalized beam envelope equations are [6]

$$a'' + \left(\frac{b^2(\alpha_x^2 - 2\alpha_x\alpha_y) + a^2\alpha_y^2}{a^2 - b^2} - 2\alpha_y\sqrt{\kappa_z(s)} \right)a - \frac{2K}{a+b} = 0 \qquad (2)$$

$$b'' - \left(\frac{a^2(\alpha_y^2 - 2\alpha_x\alpha_y) + b^2\alpha_x^2}{a^2 - b^2} + 2\alpha_x\sqrt{\kappa_z(s)} \right)b - \frac{2K}{a+b} = 0, \qquad (3)$$

$$\frac{1}{b}\frac{d}{ds}\left\{b^2\left[\alpha_x + \sqrt{\kappa_z(s)}\right]\right\} - \frac{a^3(\alpha_x - \alpha_y)}{a^2 - b^2}\frac{d}{ds}\left(\frac{b}{a}\right) = 0, \qquad (4)$$

$$\frac{1}{a}\frac{d}{ds}\left\{a^2\left[\alpha_y + \sqrt{\kappa_z(s)}\right]\right\} - \frac{b^3(\alpha_x - \alpha_y)}{a^2 - b^2}\frac{d}{ds}\left(\frac{a}{b}\right) = 0, \qquad (5)$$

$$\frac{d\theta}{ds} - \frac{a^2\alpha_y - b^2\alpha_x}{a^2 - b^2} = 0. \qquad (6)$$

where $\sqrt{\kappa_z(s)} = qB_z(s)/2\gamma_b\beta_b mc^2$ is the focusing parameters for the solenoidal and qudrupole-focusing magnetic fields, $K = 2q^2 N_b / \gamma_b^3 \beta_b^2 mc^2$ is the normalized self-field perveance, $a(s)$, $b(s)$, and $\theta(s)$ are the major radius, the minor radius, and the angle of rotation with respect to the laboratory frame of the ellipse that describes the cold-fluid corkscrewing elliptic beam equilibrium density illustrated in Fig. 1, and the variables $\alpha_x(s)$ and $\alpha_y(s)$ specify the corresponding equilibrium flow velocity as defined in Refs. 6. Here, m and q are the rest mass and charge of the particle, N_b is the number of particles per unit axial length, and $\gamma_b = (1 - \beta_b^2)^{-1/2}$ is the relativistic mass factor.

In general, the envelope equations (2)-(6) are used to determine beam evolution for a given external focusing field. In the case of sheet electron beams in solenoidal focusing field to be discussed in the next section, we apply the generalized envelope equations to determine field profiles that lead to equilibrium beam transport, given the required constrains on the beam evolution.
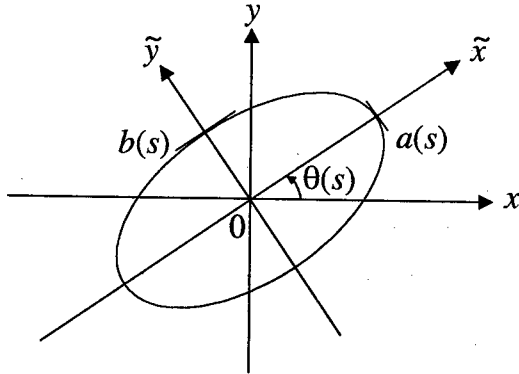
Figure 1: equilibrium density profile in the laboratory and rotating coordinate systems.

SHEET BEAM TRANSPORT IN SOLENOIDAL FIELD

In the case of sheet electron beams, the ellipse that describes the equilibrium beam density has one of the axis much greater than the other, i.e. $a >> b$, and its is required that the beam does not rotate, such that the conditions $\theta(s) = 0$, $d\theta(s)/ds = 0$ must be satisfied throughout the focusing channel. From Eq. (6) it is seen that this condition implies that $a(s)$, $b(s)$, $\alpha_x(s)$ and $\alpha_y(s)$ are not independent anymore, but must satisfy

$$a^2\alpha_y^2 = b^2\alpha_x^2 \qquad (7)$$

for all s. Therefore, the task that we propose here is to determine a solenoidal focusing field profile that guarantees the condition imposed by Eq. (7).

Using Eq. (7), and keeping only the leading order terms of a/b, the generalized envelope equations can be written as

$$\frac{d^2a}{ds^2} - \frac{(\alpha_x + \Omega_L)b^2\alpha_x + 2K}{a} = 0, \qquad (8)$$

$$\frac{d^2b}{ds^2} - \Omega_L\alpha_x b = \frac{2K}{a}, \qquad (9)$$

$$\frac{d}{ds}\left[b^2(2\alpha_x + \Omega_L)\right] = 2\alpha_x b\frac{db}{ds}, \qquad (10)$$

$$\frac{d}{ds}\left(a^2\Omega_L\right) + 4\alpha_x b\frac{db}{ds} = 0 \qquad (11)$$

where $\Omega_L(s) = 2\sqrt{\kappa_z(s)}$ is the Larmor frequency, which is proportional to the focusing field strength. The set of equations (8)-(11) describe the evolution of a nonrotating

sheet beam, where, specifically, the field profile $\Omega_L(s)$ is determined by Eq. (11).

Examining Eqs. (8)-(11) one notices that the large disparity in the transverse beam length scales along the major and minor axis, $a >> b$, also leads to a large disparity in the longitudinal length scales involved in the evolution of the envelope variables. In particular, equations (9) and (10) describe *fast* variations for $b(s)$ and $\alpha_x(s)$, whereas, equations (8) and (11) describe *slow* variations for $a(s)$ and $\Omega_L(s)$ [7]. Therefore, we can obtain approximate solutions to the envelope equations by first integrating the fast equations in time scales where the variations of the slow variables are negligible, and then solving the slow equations by averaging over the fast time scales.

Assuming Ω_L constant, we directly integrate Eq. (10) to obtain

$$b(\alpha_x + \Omega_L) = \text{const.} \qquad (12)$$

In principle, the above constant could vary on the slow-time scale, however more detailed calculations show that it is a real constant. Physically, this constant is related to the differential rotation between the internal beam particle flow given by α_x (see Ref. 6) and the Larmor frequency. Here, we are interested in typical cases where the particles move with the Larmor frequency, such that the constant in Eq. (12) is equal to 0.

Using Eq. (12) and assuming a and Ω_L constants, we can solve Eq. (9) to find

$$b(s) = A\cos(\Omega_L s + \phi) + \frac{2K}{\Omega_L^2 a} \qquad (13)$$

which gives the evolution for the ellipse minor radius. From Eq. (13) we notice that the fast-time scale is governed by the local Larmor frequency Ω_L.

Using Eqs. (12) and (13) in Eqs. (8) and (11), and averaging over the fast time scales, we obtain

$$\frac{d^2a}{ds^2} - \frac{2K}{a} = 0, \qquad (14)$$

$$\frac{d}{ds}\left(a^2\Omega_L\right) = 0. \qquad (15)$$

Many aspects of sheet beam evolution in solenoidal focusing can be understood from Eqs. (14) and (15). First, the evolution of the slow variables is completely independent of fast variables, such that, as long as the two-time-scale analysis is valid, the field profile and the major ellipse radius will be the same irrespective to the minor radius and internal beam flow detailed characteristics. Second, the focusing field strength must be proportional to the inverse of the square of the major radius in order to preserve the sheet beam from rotating. In fact, from Eq. (15) we obtain

$$\Omega_L(s) = \frac{a_o^2\Omega_{Lo}}{a^2(s)}, \qquad (16)$$

where $a_o = a(0)$ and $\Omega_{Lo} = \Omega_L(0)$ are the initial conditions at the entrance of the focusing channel. Third,

the major radius evolution is governed exclusively by space-charge forces which are always defocusing. Hence, to increase the interaction region its is convenient to inject a converging beam with $a'_o \equiv da/ds|_{s=0} < 0$. The particular value of a'_o for a specific arrangement can be calculated with the aid of Eq. (14). Multiplying Eq. (14) by da/ds and integrating leads to

$$\frac{1}{2}\left(\frac{da}{ds}\right)^2 - 2K \ln a = \text{const.} \tag{17}$$

Let us consider a case where we inject in the focusing channel a beam with major radius a_o, let the beam converge to a minimum major radius a_{min}, and extract the beam when its major radius returns to its initial value; i.e., $a(S) = a_o$, where S is the length of the focusing channel. In this situation, the required initial beam convergence is given by Eq. (17) as

$$a'_o = -2\left(K \ln \frac{a_o}{a_{min}}\right)^{1/2}. \tag{18}$$

Fourth, the focusing channel length S can also be estimated from Eq. (14) as

$$S \approx \left(\frac{a_o^2 - a_{min}^2}{K}\right)^{1/2}. \tag{19}$$

In reality, S is a measure of the slow time scale associated with the dynamics of $a(s)$ and $\Omega_L(s)$. Recalling that the fast time scale is governed by the Larmor frequency, the condition of validity for the multiple time-scales analysis applied here is $\overline{\Omega}_L S \gg 1$, with the bar indicating average values. Using Eq. (19) the condition roughly leads to

$$K \ll \overline{\Omega}_L^2 \overline{a}^2, \tag{20}$$

which informs that for a given focusing field and beam size, there is a limit in the total beam intensity. In practice this is not a strong constrain because the whole purpose of using sheet beams is being able to reduce beam intensity by spreading it over larger sizes by increasing the ellipsis major radius. Finally, using Eqs. (14) and (16) we can write down

$$\frac{d^2\Omega_L}{ds^2} - \frac{3}{2\Omega_L}\left(\frac{d\Omega_L}{ds}\right)^2 + \frac{4K\Omega_L^2}{a_o^2\Omega_{Lo}} = 0 \tag{21}$$

which gives the optimal solenoidal focusing field profile $\Omega_L(s)$ that leads to an equilibrium nonrotating sheet beam propagation.

The above results were tested against solutions obtained by numerically integrating the generalized envelope equations using the focusing field profile prescribed by Eq. (21). A good agreement was found between the numerical solutions and the estimates from the multiple-time-scale analysis. In particular, considering moderately intense sheet electron beams with $K \sim 10^{-2}$ and major radius of a few centimeters, transported along the typical longitudinal length scales of high-power vacuum microwave sources (on the order of 30 cm), presented very small rotation angles on the order of 10^{-4} rad.

CONCLUSIONS

We have analyzed equilibrium configurations for the transport of sheet electron beams in tapered solenoidal focusing fields. In particular, using the generalized envelope equations obtained for the evolution of space-charge-dominated beams propagating through a general linear focusing channel, we derived an equation that provides an optimal focusing field profile for nonrotating sheet beam transport. Analytic solutions based on multi-time scale perturbation theory were found and compared to numerical simulations.

REFERENCES

[1] Special Issue on High-Power Microwave Generation, edited by J.H. Booske, T.A. Spencer, and J.P. Verboncoeur, IEEE Trans. Plasma Sci., 28 (2000).
[2] D.J. Radack, J.H. Booske, Y. Carmel, and W.W. Destler, Appl. Phys. Lett., 55, 2069 (1989).
[3] D. Yu and P. B. Wilson, in Proceedings of 1993 Particle Accelerator Conference, p. 2681 (1993).
[4] J.H. Booske, A.H. Kumbasar, and M.A. Basten, Phys. Rev. Lett., 24, 3979 (1993).
[5] C. C. Cutler, J. Appl. Phys. 27, 1028 (1956).
[6] R. Pakter and C. Chen, Phys. Rev. E62, 2789 (2000).
[7] Perhaps the most appropriate would be denoting as short and long longitudinal variations, instead of slow and fast variations, however since s and time are closely related by $s = \beta_b ct$, we decided to use the more usual terms slow and fast time-scales.

A GRIDDED ELECTRON GUN FOR A SHEET BEAM KLYSTRON

M. E. Read, G. Miram, and R.L. Ives, Calabazas Creek Research, Inc., Saratoga, CA, 95070-3753
V. Ivanov and A. Krasnykh, Stanford Linear Accelerator Center, Menlo Park, CA 94025

Abstract

This paper describes the development of an electron gun for a sheet beam klystron. Initially intended for accelerator applications, the gun can operate at a higher perveance than one with a cylindrically symmetric beam. Results of 2D and 3D simulations are discussed.

Calabazas Creek Research, Inc. (CCR) is developing rectangular, gridded, thermionic, dispenser-cathode guns for sheet beam devices. The first application is expected to be klystrons for advanced particle accelerators and colliders.[1] The current generation of accelerators typically use klystrons with a cylindrical beam generated by a Pierce-type electron gun. As RF power is pushed to higher levels, space charge forces in the electron beam limit the amount of current that can be transmitted at a given voltage. The options are to increase the beam voltage, leading to problems with X-Ray shielding and modulator and power supply design, or to develop new techniques for lowering the space charge forces in the electron beam.

In this device, the beam has a rectangular cross section. The thickness is constrained as in a normal, cylindrically symmetric klystron with a Pierce gun; however, the width of the beam is many times the thickness. The resulting cross sectional area is much larger than in the conventional device. This allows much higher current and/or a lower voltage before space charge forces become too high.

The current program addresses issues related to beam formation at the emitter surface and implementation of shadow and control grids in a rectangular geometry. It is directed toward a robust, cost-effective, and reliable
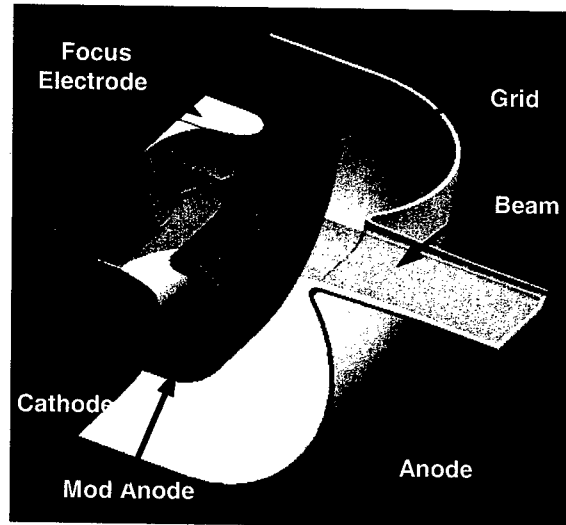
Figure 1. Geometry of the sheet beam gun. One quarter of the gun is shown, with the cathode on the left and the axes of symmetry toward the top and left. The mod anode is included to grade the field and minimize the possibility of an arc directly from the cathode to the anode.

mechanical design. A prototype device will be developed at 415 kV, 250 A for a 40 MW, X-Band, sheet-beam klystron. The cathode will have 100 cm^2 of cathode area with an average cathode current loading of 2.5 A/cm^2. For short pulse formation, the use of a grid was chosen. The geometry of the gun is shown in Figure 1.
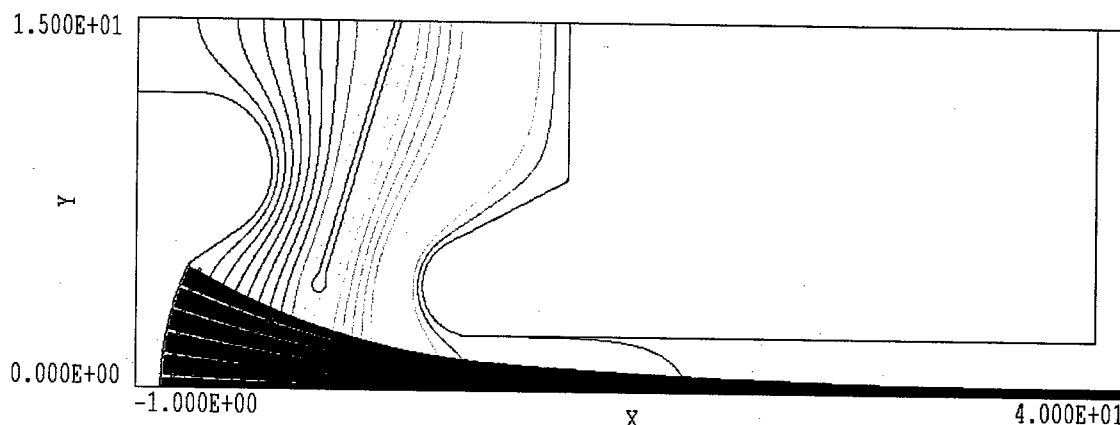
Figure 2. Trajectories from a 2D simulation using TRAK, including the shadow grid. Dimensions in cm.
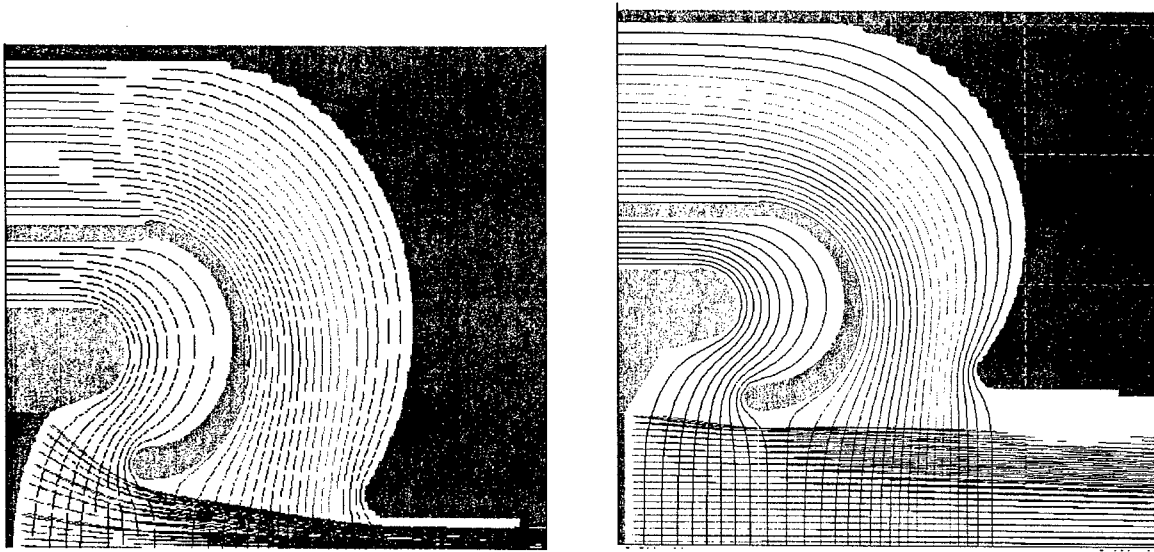
Figure 3. Trajectories as calculated using the 3D code OmniTrak. Cross sections near the axes of symmetry for two planes normal to the direction of propagation.

The gun is being designed with a combination of 2-D and 3-D codes. 2-D codes were used to determine the starting point for the electrodes to produce the compression (which is in only one direction.) These results showed that a very high quality beam could be achieved even in the presence of the shadow grid. A plot of the 2-D results is shown in Figure 2.

The 3-D design is done using the codes TOPAZ and OmniTrak.[2] Both codes include relativistic effects and self magnetic fields of the beam. OmniTrak uses a structured grid, while the grid in TOPAZ is unstructured. Examination of initial designs showed good agreement between the codes.

Initial results from OmiTrak are shown in Figure 3. The beam is compressed only in one dimension. Compression from the 8.4 cm high cathode to close to the desired 8 mm thickness is shown in the left. There is almost no compression in the other plane; however, in the

plane of compression, trajectories originating close to the edges of the cathode are over compressed. This is shown in Figure 4. The additional compression occurs because electrons near the cathode edge see the effect of the focusing electrodes in both transverse planes. Efforts are continuing to reshape the corners of the focus electrodes to eliminate this effect.

Self-fields were found to be very important for this geometry. Figure 5 shows the trajectories in the plane of compression calculated without the self magnetic field. The compression is reduced to the point that a substantial interception of the beam by the anode. Clearly, designing the electrodes without consideration of the self-fields would result in over compression of the beam.

A DC power supply will drive the gun, with the grid being used to pulse the beam. While this approach allows sharper pulse formation than can be achieved with a cathode pulser and is potentially less expensive, it does
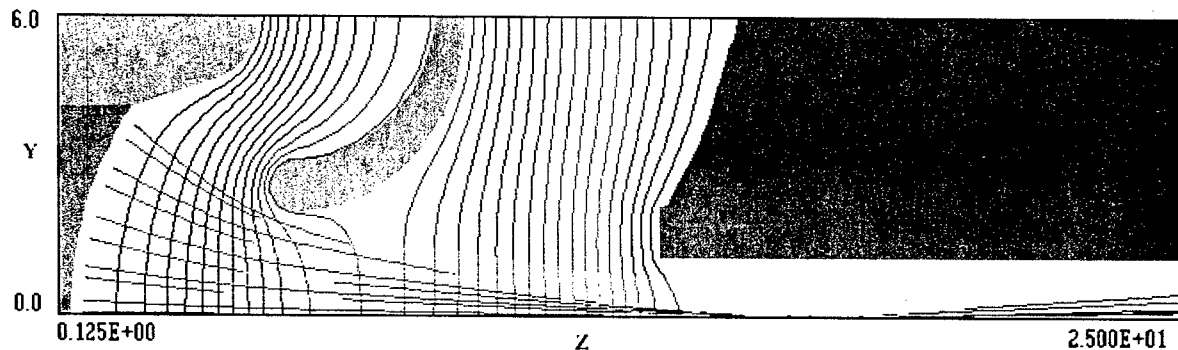
Figure 4. Trajectories (darker lines) near the "X" edges of the cathode. The solution space has been shrunk from that of Figure 1 by applying potentials determined from the electrostatic solutions of Figure 1 to the upper boundary of this solution.
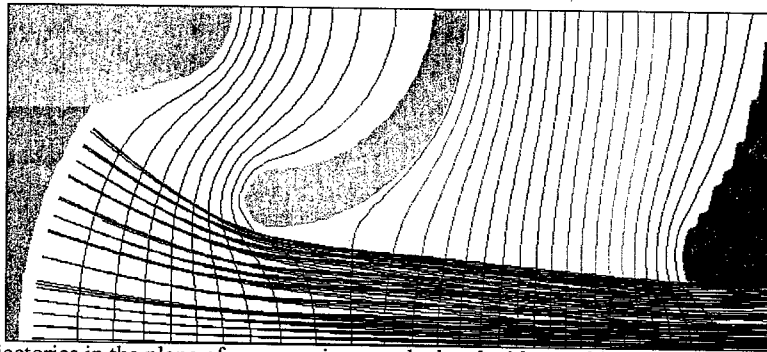
Figure 5. Trajectories in the plane of compression as calculated without taking into account self magnetic fields.

place stricter limits on the field gradients, both in vacuum and in the oil of the high voltage tank. The design goal is to limit the vacuum fields to less than 75 kV/cm on the beam formation electrodes and 40 kV/cm elsewhere. In the oil, the goal is approximately 20 kV/cm.

A drawing showing both the triode region and the insulator is shown in Figure 6.

ACKNOWLEDGEMENT

REFERENCES

1. P.B. Wilson, "RF power sources for 5-15 TeV linear colliders," Intern. workshop on pulsed RF sources for linear colliders, April 1996.

2. S. Humphries, www.fieldp.com, 2003

~ 1m
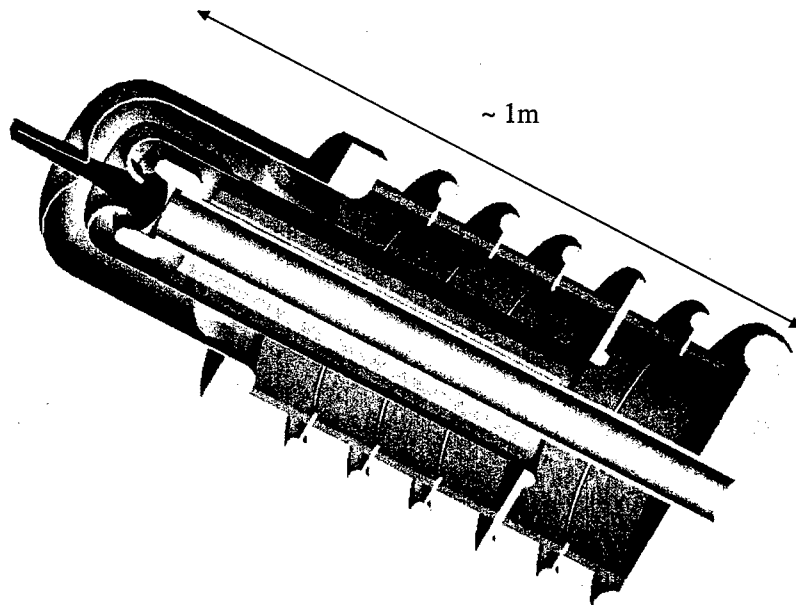
Figure 6. Cut-away solid model of the sheet beam gun.

A MAGNETRON INJECTION GUN WITH INVERTED GEOMETRY FOR AN 80 MW GYROKLYSTRON

M.E. Read, R.L. Ives and G. Miram, Calabazas Creek Research Inc., Saratoga, CA 95070-3753
G. Nusinovich, W. Lawson and V.L. Granatstein, IREAP, University of Maryland, College Park, Maryland

Abstract

A 500 kV, 500 A magnetron injection gun (MIG) is being developed for the University of Maryland Ku-band, coaxial gyroklystron. The gun will have three electrodes, with the cathode at a larger diameter than the intermediate electrode, thus being an inverted form of the normal geometry. This allows the gyroklystron's inner conductor to be supported through the electron gun, eliminating the need for the beam-intercepting supports and facilitating cooling. It also allows for adjustment of the coax position external to the vacuum. Details of the design, including modeling of the beam trajectories, are discussed.

GEOMETRY

The gun is a replacement for the MIG used in the University of Maryland. Gyroklystron[1] shown in Figure 1. With a conventional MIG, the inner conductor must be supported from the collector and/or beam-intercepting pins in the cavity region. Due to the use of the collector as the output waveguide, pins are the only supports in the existing experimental device. This limits the pulse repetition rate. Even if this restriction is removed by extracting the RF via the side of the gyroklystron, supporting the inner conductor from only the collector

requires an undesirable reversal of the cooling flow. Replacing the gun with the cathode on the outside, in an inverted geometry as shown in Figure 2, allows the inner
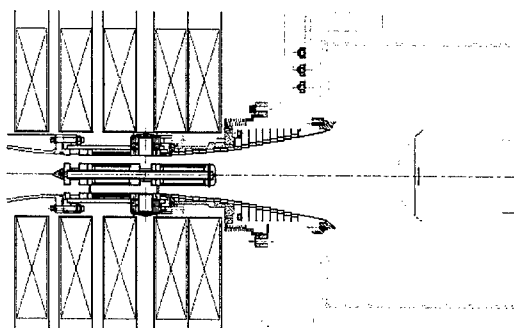
Figure 1. University of Maryland gyroklystron with a conventional MIG

conductor to be supported by the "modulating anode" of the gun. The mod anode is at ground potential, allowing it to be supported from the outer, grounded shell by two posts. This arrangement allows for coolant for the inner conductor to flow in one direction. The posts can be sealed to the vacuum envelope by bellows, allowing fine
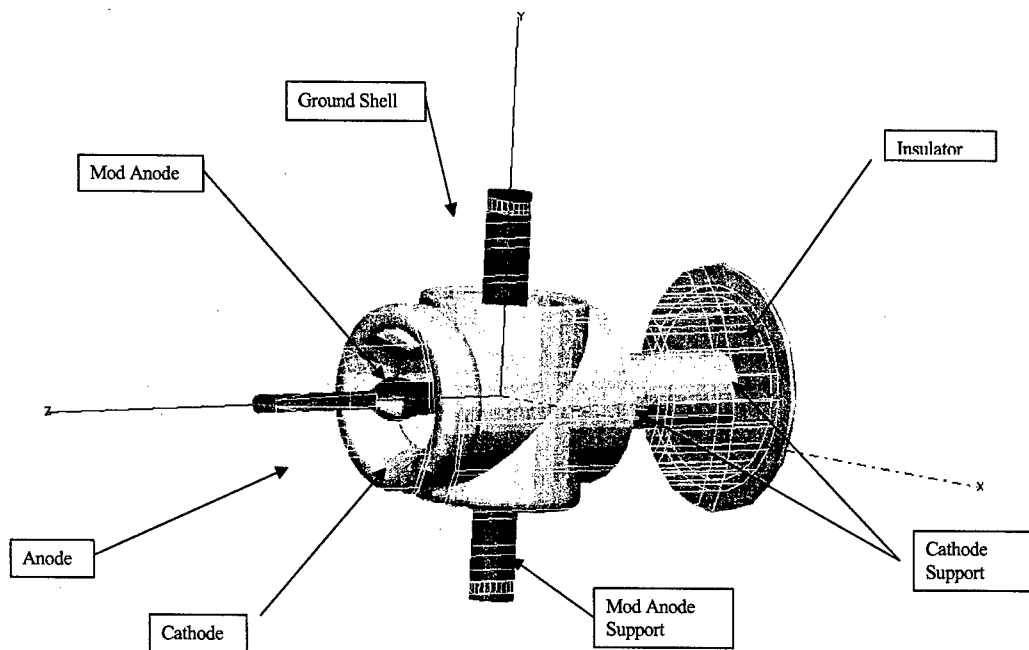
Figure 2. Geometry of the inverted MIG.
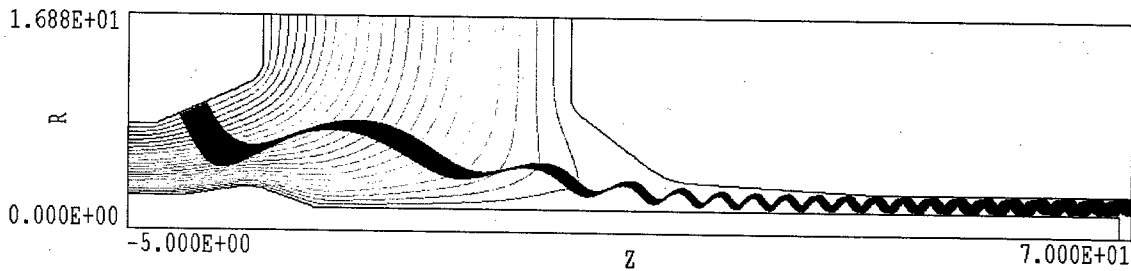
Figure 3. Trajectories of the inverted MIG as calculated using TRAK. Dimensions are in cm.

adjustment of the position of the mod anode, and hence the inner conductor, if needed.

BEAM SIMULATIONS

Simulations of the beam trajectories were done using TRAK[2] This code is well documented and has been used for a number of gun simulations by the authors. It agrees very well with EGUN [3] and has the advantage of a variable mesh that allows modeling of the problem without continuations, as would be required in EGUN to handle the small orbits of the fully compressed beam. The results of a TRAK simulation are shown in Figure 3. For a beam current of 550 A, an average ratio of perpendicular to parallel velocities, alpha, of 1.49 was achieved with a spread in the perpendicular velocities of 0.6%. The spread in parallel velocities was 1.3%. These spreads are due to the optics only, and thermal and surface roughness contributions will decrease the beam quality. The optics-determined values are significantly lower than those achieved with the conventional design, where the spread in parallel velocities was about 7%.

The dependences of alpha and the velocity spreads on the beam current are shown in Figure 4. The design is clearly optimized for about 525 A, with the velocity spread rising for both lower and higher currents. The design could be optimized for another current. In this design, the parallel velocity spread is less than 2.1% over the range of 100 A – 600 A.

It is important to include not only space charge effects, but also self magnetic fields in the calculation. With inclusion of the latter, alpha rises to 1.7 and the parallel velocity spread is 1.5%.

A disadvantage of the inverted geometry is that the fields on the mod anode higher than normally found in gyrotrons to obtain the electric fields at the cathode required for proper beam formation. The fields for the current design are shown in Figure 5. The peak field on the mod anode is 150 kV/cm. This is high for a CW gun, but is not high for a ~1 microsecond pulse gun, particularly considering that mod anode is a positive electrode.
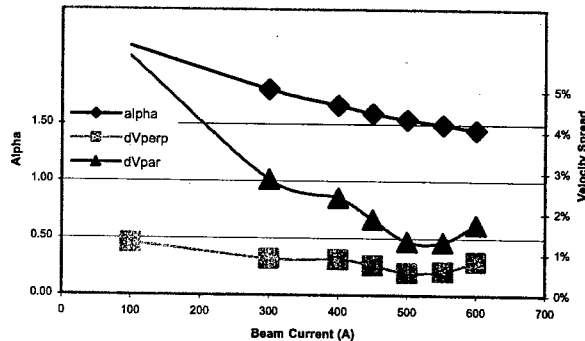
Figure 4. Ratio of perpendicular to parallel velocities, alpha and velocity spreads as functions of beam current.
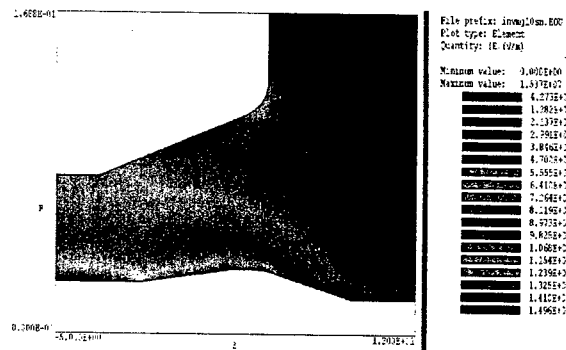
Figure 5. Electric field magnitudes.

ACKNOWLEDGEMENT

REFERENCES

1 . V. L. Granatstein and W. Lawson, IEEE-PS, v. 24, p. 648, (1996).
2. S. Humphries, www.fieldp.com (2003).
3. W.B. Hermannsfeldt, SLAC Report 226, Sanford, CA, Nov, 1979.

DEVELOPMENT OF A 19 KW CW, L-BAND KLYSTRON FOR THE CONTINUOUS ELECTRON BEAM ACCELERATOR FACILITY

M.E. Read, A. Mizuhara, G. Miram, L. Song, and R.L. Ives, Calabazas Creek Research, Saratoga, CA, 95070-3753

Abstract

This document describes the design of a klystron for the RF system upgrade of the Continuous Electron Beam Accelerator Facility (CEBAF) at the Thomas Jefferson National Accelerator Facility. The klystron will produce 19 kW of saturated CW power at 1497 MHz with an efficiency of 59%.

DESIGN PARAMETERS

The design parameters of the klystron are shown in Table 1.

Table 1. Klystron parameters.

Frequency	1497 MHz
Saturated Power	19 kW (max)
Operating Power	15 kW
Power Range	50% - 100%
Voltage	18.8 kV
Current	1.76 A
Small Sig. Gain	56 dB
3 dB Bandwidth	5.8 MHz
Efficiency	59%

CIRCUIT DESIGN

As shown in Figures 1 and 2, the klystron will have 6 "race-track" cavities, one of which operates at the second harmonic to enhance the bunching. Design of the klystron follows conventional procedures plus the use of 2.5D and 3D codes for calculating the performance. The output power and gain, as calculated using MAGIC, are shown in Figure 3.
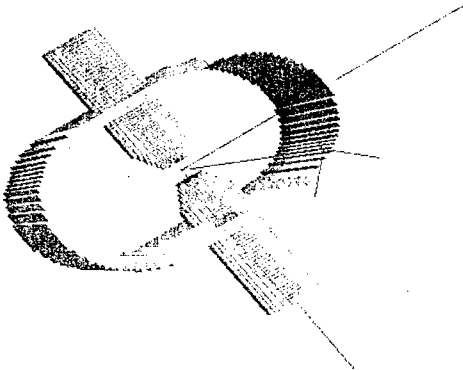
Figure 1. Race-track cavity.
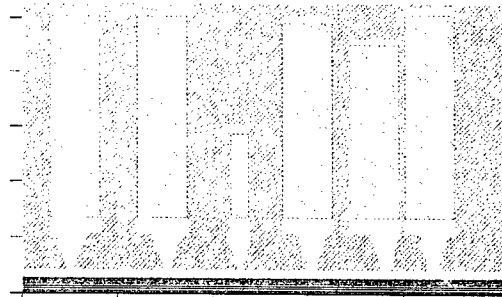
Figure 2. Cross section of the cavities and beam (crosshatch represents surface covered with loss coating).
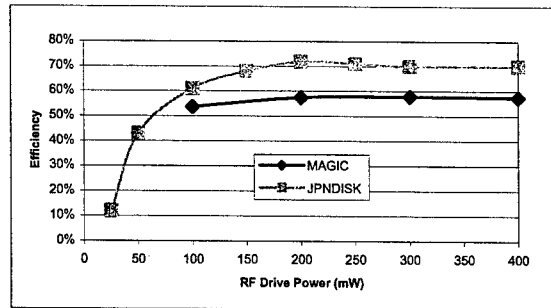
Figure 3. Output power and gain of the klystron, as calculated using MAGIC.

Figure 3 compares the results of the MAGIC simulation with those of the large signal code JAPANDISK. The efficiency predicted by JAPANDISK is about 10% higher than predicted by the more accurate MAGIC simulation. This is about the same difference observed between the efficiency predicted by other similar large signal codes and that obtained in actual operation.

ELECTRON GUN

The beam is generated using an immersed Pierce gun in a solenoidal magnetic field. Figures 4 and 5 show predicted performance of the gun using the 2.5D computer code TRAK. The design includes a modulating anode to reduce the current when less than the maximum power is required from the tube. This insures that the efficiency drops only to 47% at ½ the maximum operating power.
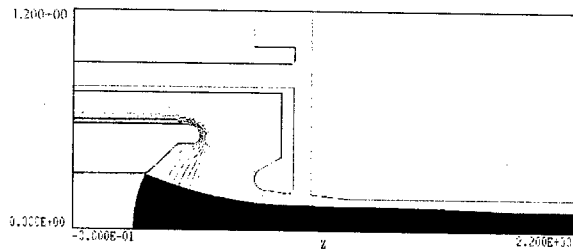
Figure 4. Electron gun for the klystron.

Reliability is critical since the tube is for use in a large accelerator. consequently, conservative values were used for the gun electric fields, the cathode current density and the collector power density. These are 83 kV/cm, 1 A/cm^2, and 500 W/cm^2, respectively.

STATUS

The tube design is complete, and a solid model of the klystron is shown in Figure 6. As soon as additional funding is approved, two prototype klystrons will be built and tested. These will then be delivered to the Thomas Jefferson National Accelerator Facility.
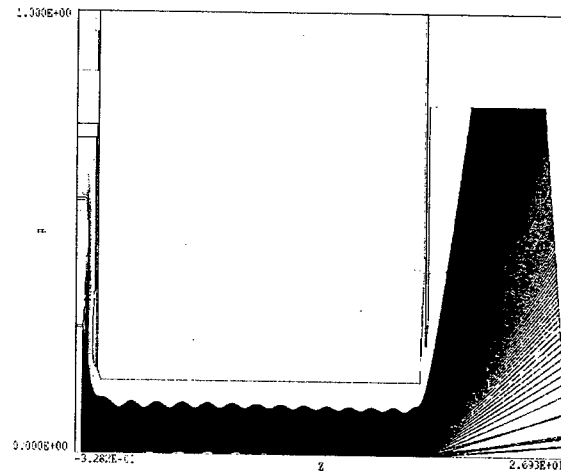
Figure 5. Beam for the klystron. The radial scale is enlarged to show detail. The scallop amplitude is 6.4%.

ACKNOWLEDGEMENT
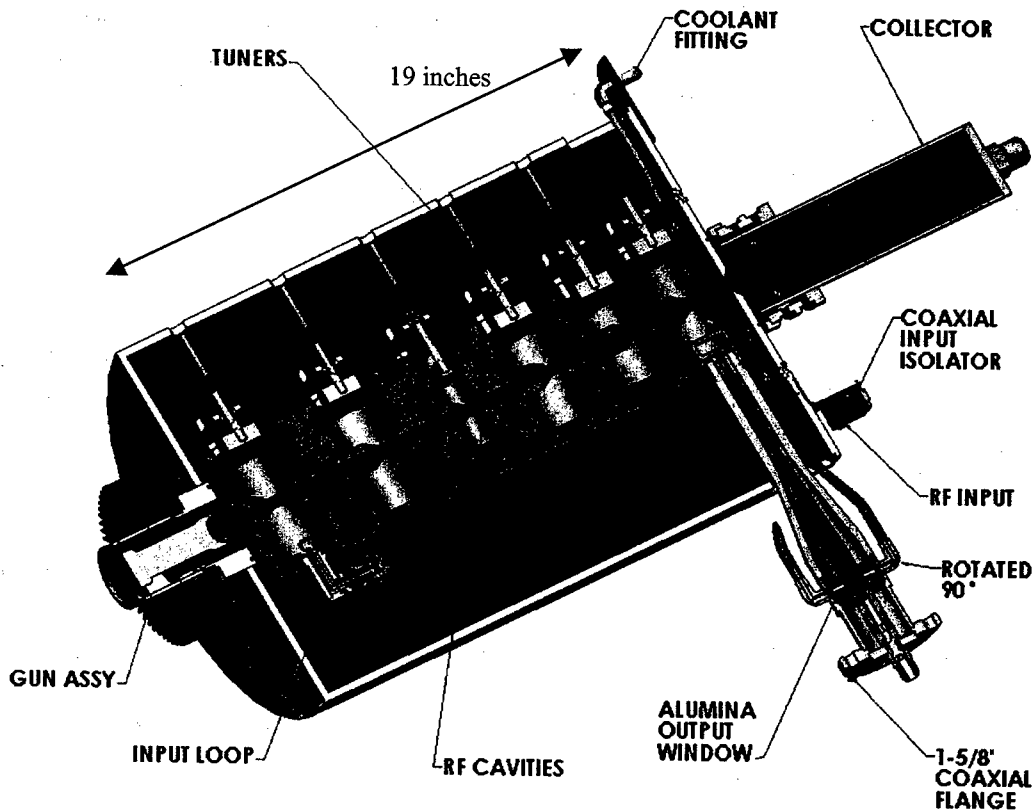
Figure 6. Solid model of the klystron.

DEVELOPMENT OF A 10-MW, L-BAND, MULTIPLE-BEAM KLYSTRON FOR TESLA*

E. Wright, A. Balkcum, H. Bohlen, M. Cattelino, L. Cox, M. Cusick, L. Falce, F. Friedlander, B. Stockwell and L. Zitelli, Communications and Power Industries, Microwave Power Products Division, 811 Hansen Way, M/S B-450, Palo Alto, CA 94303-0750

Abstract

A high-efficiency, Multiple-Beam Klystron (MBK), designated the VKL-8301, is being manufactured for the DESY Tera Electron volt Superconducting Linear Accelerator (TESLA) in Hamburg, Germany. There are a number of excellent reasons for using an MBK for this application. The primary reasons are reduced size and lower operating voltage with respect to the conventional, single beam counterparts. Once this decision has been made, the class of MBK must now be selected. MBK's can be divided into two categories: Fundamental Mode (FM) and Higher-order Mode (HM) devices, distinguished by the interaction mode of the cavity resonators. Each class has inherent advantages and disadvantages dependent upon end-user requirements. For the 10 MW, 1.3 GHz TESLA application the HM-MBK is the clear choice. The primary factor influencing this choice was operational life, since the accelerator will require approximately 600 MBK's. The advantage of the HM approach is low cathode loading. Our cathode loading design goal of 2 A/cm^2 or less has been achieved. For this application the HM-MBK cathode loading is a factor of four lower than competing FM-MBK designs and a factor of three lower than the SLAC 5045 design. The VKL-8301 will use six off-axis electron beams interacting with a combination of TM$_{010}$ and hybrid TM$_{020}$ cavities. These six beams are equally spaced on a diameter of approximately 25 centimeters. Because of the large beam-to-beam separation, individual high-area convergence guns can be utilized versus the single multi-emission-site gun used in FM-MBK's. This solution requires a sophisticated focusing system that is relatively difficult to realize, compounded by our use of confined-flow focusing. Newly developed, state-of-the-art three-dimensional electromagnetics codes have been used to design the novel electron-beam-focusing system and microwave cavity geometry. Modeling and simulation results will be presented, hardware will be shown, and a description of the FM- versus HM-MBK selection process will be discussed.

BACKGROUND

Last year we reported on the progress developing the TESLA MBK and provided a description of the CPI approach [1]. This paper is intended to supplement the original, updating our progress, and more importantly describe the thought process involved when selecting the HM-MBK for this application. All of the large, next-
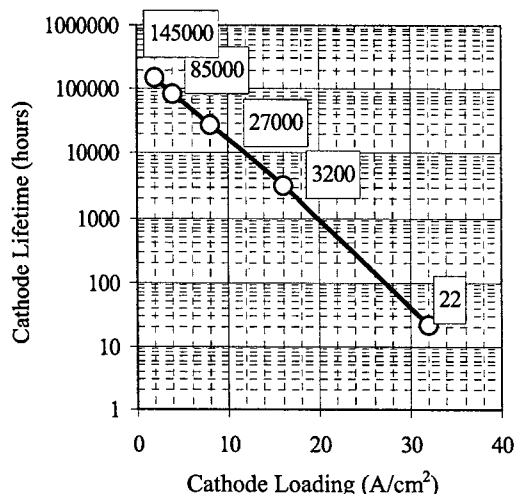
Figure 1. Life versus loading for an M-type dispenser cathode, space charge limited operation, 40 °C above the knee.

generation linear colliders considering the use of klystrons as their high-power rf source should consider, as DESY has, the FM-MBK approach. The merit of the approach is a result of one of the most important parameters for a practical system, LIFE.

For any mature, well-designed tube the primary mode of failure is cathode end-of-life, a result of barium depletion. So, what factors influence cathode life? There are primarily two: Temperature and Pressure. Today's manufacturing techniques provide products operating with exceptionally low pressure, so for a well-designed product this is no longer a major issue. What's left is temperature. However we will use current density, rather than temperature, because most tube engineers can readily quote cathode loading for a given design.

Cathode lifetime as a function of cathode current density can be seen in Figure 1, and is based on a compilation of measured data taken within the past 30 years. This curve is in excellent agreement with measured average lifetimes for klystrons and CCTWT's installed in mature systems, with current densities in the 2 A/cm^2 to 8 A/cm^2 range. This curve plays a pivotal role in selecting the appropriate class of MBK for this application, as will be shown.

MBK DESIGN

Classification

There are two classes of MBK's, differentiated by the rf cavity mode used: FM- and HM-MBK's [2][3]. These can be further subdivided by the proximity of neighboring electron beams and the number of cathodes used.

Clustered Emitters (CE) are single-cathode guns with multiple emission sites designed to form clusters of electron beams in close proximity to one another. The primarily advantage of this approach are the large instantaneous bandwidths that can be achieved with the use of single gap or inductively coupled, multiple gap TM_{01} resonator. All large instantaneous bandwidth FM-MBK's use this approach, however narrow bandwidth FM- and HM-MBK's equally benefit. The disadvantage of this approach is the cathode current density is constrained, proportional to the square of frequency, as will be shown.

Distributed Emitters (DE) are multiple cathode guns with single emission sites from each of the cathodes, are used when large beam-to-beam separation is desired, and are only used for HM-MBK's. The HM-MBK is a narrow band device due to the proximity of neighboring resonator modes, perfectly suited for high-power scientific applications. One key advantage to this approach is the cathode loading is unconstrained. The system designer needs to be aware that this tradeoff exists when developing MBK based systems, particularly those intended for high-power scientific applications requiring a large number of MBK's.

FM-MBK Cathode Loading

When a single-cathode, multi-emission site gun is proposed for a given design, cathode loading must be considered. As such, we need a way of estimating the cathode loading, which in turn can be used to determine tube life. Conversely, one can approach the problem from the other direction: What life/loading is considered acceptable?

$$J_C = \frac{576}{7\pi c^2} I_o f^2 \qquad (1)$$

In order to keep the rf interaction within the cavity uniform, in-general the diameter of the beam cluster must fall within $\lambda_o/4$, or less. This condition forces the individual cathode emitters to follow suit, i.e. they must be concentric to their respective drift tubes. One can readily see there is a connection between cathode loading and frequency. Let's explore this. Assume there are seven emission sites with close-packed hexagonal geometry (or choose a number of emitters suitable for your specific application). Individual emitters would have one third the total interaction diameter, or $\lambda_o/12$. Computing the area of these seven emitters and dividing the total beam current by that value will give you the best-case current density for a given frequency of operation (1); the value obtained
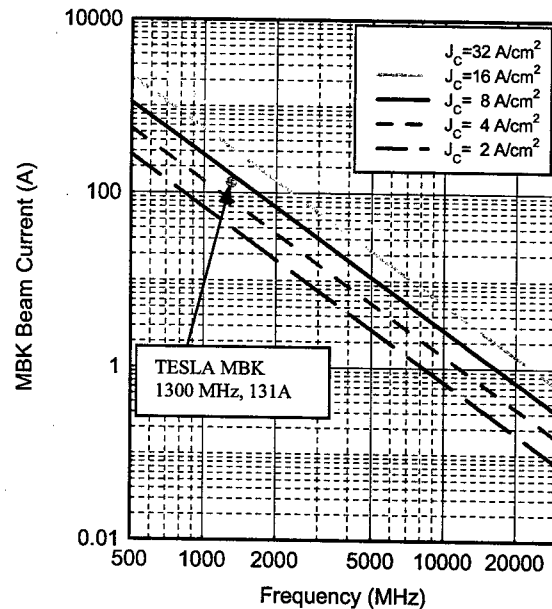
Figure 2. Total current versus frequency for the CE gun geometry.

is best case because it assumes zero thickness separating the individual emitters. A plot of this function for the cathode loading values given in Figure 1 can be seen in Figure 2.

Table 1: Klystron Typical Operating Parameters

Parameter	Value	Units
Peak Output Power	10	MW
Average Output Power	150	KW
Beam Voltage	114	KV
Beam Current	131	A
Efficiency	65-67	%
Frequency	1300	MHz
Pulse Duration	1.5	Ms
Saturated Gain	47	DB
Number of Electron Beams	6	
Number of Cavities	6	
Cathode Loading	<2.5	A/cm^2
Solenoid Power	4000	W, max.

The TESLA MBK

The operating parameters for the TESLA MBK can be seen in Table 1. For this analysis the key parameters are the operating frequency of 1300 MHz and the total device current of 131 Amperes. This data point has been placed on the graph, Figure 2. For this application the CE-gun average cathode loading is 7 A/cm^2, minimum. For practical gun designs, i.e. a gun with separation between adjacent emitters, this value is at least 8 A/cm^2. From the graph of Figure 1 we estimate the average lifetime of the CE-gun to be approximately twenty seven thousand hours, or less than three years.
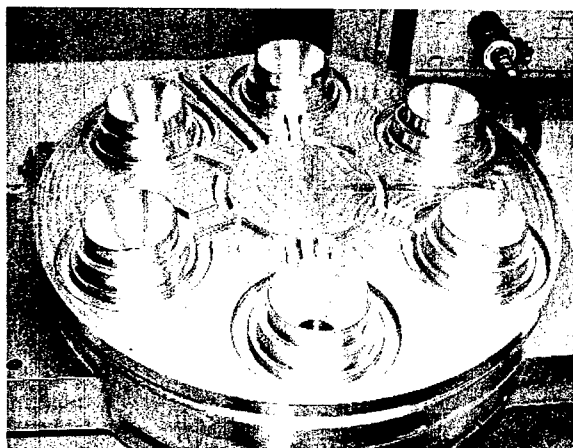
Figure 3. Aluminum output cavity model during rf cold testing.

CPI has recommended the HM-MBK base primarily on the increased life these products would have due to their use of the DE-gun. Since the HM approach imposes no restrictions on cathode loading, we can select a value suitable for long-life operation. We selected 2 A/cm^2 because this value will provide average lifetimes of 145,000 hours (or sixteen years!) and also for ease of manufacture.

This may seem like we're getting something for nothing, which is certainly not the case. An HM-MBK will be more expensive to produce than an equivalent FM-MBK. However when these units are mass-produced the difference in price will be small, on the order of 15% to 30% more. However the long-term benefit resulting from reduced life-cycle costs are orders of magnitude greater than this difference. For this particular application the FM-MBK is the desired approach. Let say the desired

frequency were halved, or 650 MHz. At 131 A of total current, either approach would provide excellent life.

PROGRESS UPDATE

We have entered into the build phase of this program. All the material, except for the input and output cavities, has been issued to the assembly floor and manufacturing has begun. The raw material for the higher-order mode TM_{020} input and output cavities has been received, however we have additional rf cold test to perform to fine-tune these resonators before we start the final machining. Full-size aluminum cold test cavity models have been received for the input and output, Figure 3. We have spent considerable time cold testing these cavities measuring frequency, Q-factors, and gap-to-gap electric field (intensity) and phase uniformity. We will finish these tests by the end of May 2003.

Another important milestone will be reached when we receive the magnet in early June 2003. At that time the critical step of measuring, verifying, and fine-tuning the magnetic field will begin. Once this step is complete the MBK will be sealed in, exhausted, dressed and tested. Testing is schedule to start the beginning of August 2003.

REFERENCES

[1] E. Wright, et al., "Development of a 10 MW, L-Band, Multiple-Beam Klystron for TESLA", EPAC'02, Paris France, May 2002, p. 2337-2339.

[2] Edward A. Gelvich, "Multi-beam amplifiers", NRL Sponsored MBK symposium, 2001.

[3] G. Nusinovich, B. Levush, D. Abe, "A Review of the Development of Multiple-Beam Klystrons and TWT's", NRL/MR/6840--03-8673.

FIRST HIGH-POWER EXPERIMENTS ON A TWO-CHANNEL X-BAND ACTIVE RF PULSE COMPRESSOR*

A. L. Vikharev,[1,2] O. A. Ivanov,[1,2] A. M. Gorbachev,[1,2] V. A. Isaev,[1,2] S. V. Kuzikov,[1,2]
S. H. Gold,[3] A. K. Kinkead,[4] O. A. Nezhevenko,[1] and J. L. Hirshfield[1,5]
[1]Omega-P, Inc., New Haven, CT 06511
[2]Institute of Applied Physics, Nizhny Novgorod, 603600 Russia
[3]Plasma Physics Division, Naval Research Laboratory, Washington, DC 20375
[4]LET Corporation, Washington, DC 20007
[5]Physics Department, Yale University, New Haven, CT 06511

Abstract

A brief report is presented on experiments carried out at the NRL X-band magnicon facility on a two-channel X-band active rf pulse compressor that employs plasma switches. Experimental evidence is shown to validate the basic goals of the project, which include: simultaneous firing of plasma switches in both channels of the rf circuit, operation of quasi-optical 3-dB hybrid directional coupler, coherent superposition of rf compressed pulses from both channels, and operation of the X-band magnicon directly into the rf pulse compressor. For incident 1.2 μsec pulses in the range 0.63-1.35 MW, compressed pulses of 5.7-11.3 MW were obtained, corresponding to power gain ratios of 8.3-9.3. Insufficient bakeout and conditioning of the high-power rf circuit prevented experiments from being conducted at higher rf input power levels.

INTRODUCTION

Active rf pulse compressors are nowadays commanding interest for use in a future electron-positron collider [1,2]. Here, results are given of the first high-power experiments on a two-channel X-band active rf pulse compressor that employs gas discharge switch tubes as active elements. The experiments can be understood by reference to Fig. 1, a schematic diagram of the set-up for tests conducted at the X-band magnicon facility at the Naval Research Laboratory. Critical elements in the set-up include the Omega-P/NRL X-band magnicon (2), the quasi-optical 3-dB hybrid directional coupler (3), and the two channels of the compressor itself (1). Each compressor channel consists of a TE_{01}-mode energy-storage cavity, and an input/output coupler cavity containing a gas-filled switch tube that can be externally discharged by application of a high-voltage pulse. Both channels function as active Bragg compressors (ABC), with synchronized input-output switchable reflectors. The detailed design of ABC [2] and low-power test measurements on it [3] have been reported previously. In the two-channel compressor scheme (ABC-2), the 3-dB hybrid coupler allows the input drive pulse from the magnicon to be split, with half the power directed to each channel. Upon firing, composite compressed pulses from the two channels are

superimposed in the hybrid, and directed to a high-power load (7). In practice, the load would be replaced by an accelerator section. Two channel ABC-2, in comparison with one channel, allows (i) isolation of the magnicon from power reflected during energy storage, (ii) operation of both channels into one load, (iii) increase in efficiency, and (iv) operation with lower electric field in the gas discharge tube region with a resulting increase in the margin-of-safety against self-breakdown of the plasma switch. Non-vacuum prototypes of ABC-2 tested at low-power levels showed good pulse-to-pulse reproducibility in the shape and amplitude of the compressed pulse, and coherent addition of compressed pulses from the channels [4].

In this brief report, results of preliminary high-power experiments are reported that validate the main goals of the project, which include: (i) simultaneous firing of
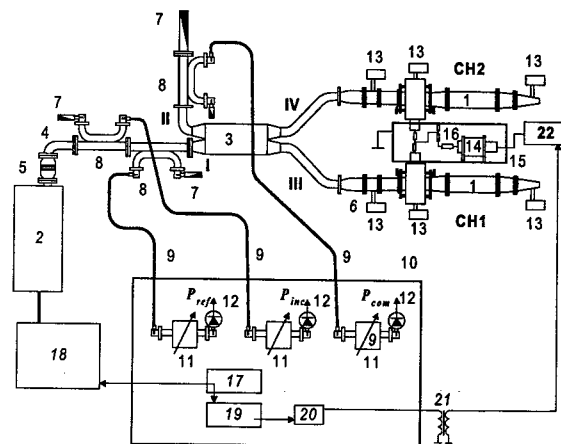
Figure 1. Schematic diagram of the experimental set-up for high-power test of two-channel compressor: 1 – single-channel compressor, 2 - magnicon, 3 – quasi-optical 3-dB directional coupler, 4 – waveguide line, 5 – output window, 6- phase rotator, 7 – matched load, 8 – 55.5-dB directional coupler, 9 – coaxial waveguide, 10 – screen room, 11 – attenuator, 12 – detector, 13 – ion pump, 14 – high-voltage pulse generator, 15 – shielding box, 16 – divider, 17 – trigger generator, 18 – modulator, 19 – delay generator, 20 – trigger amplifier, 21 – pulse transformer, 22 – high-voltage power supply.

plasma switch tubes in both channels of the compressor, (ii) operation of the quasi-optical 3-dB hybrid directional coupler, (iii) coherent superposition of rf compressed pulses from the two channels, and (iv) feeding one output arm of the X-band magnicon directly into the rf pulse compressor while the second arm was terminated in a match load. Unfortunately, insufficient time for component bakeout and rf conditioning during the brief first experimental campaign prevented operation at input power levels higher than about 1.5 MW. In the next campaign scheduled to begin in June 2003, tests with higher power input pulses are planned, and more time is to be allotted for bakeout and conditioning.

EXPERIMENTS

Examples of some results of high-power experiments are shown in Figs. 2-5. Fig. 2 shows the frequency characteristic of the quasi-optical 3-dB hybrid coupler with arms III, and IV terminated in reflecting shorts, and arm II terminated in a matched load. In evidence are balanced splitting of the incident signal at 11.424 GHz from arm I into arms III and IV, and small reflection back into arm I. This is the first high-power operation of this type of quasi-optical 3-dB directional coupler that operates on the principle of image multiplication in oversized rectangular waveguide [4].
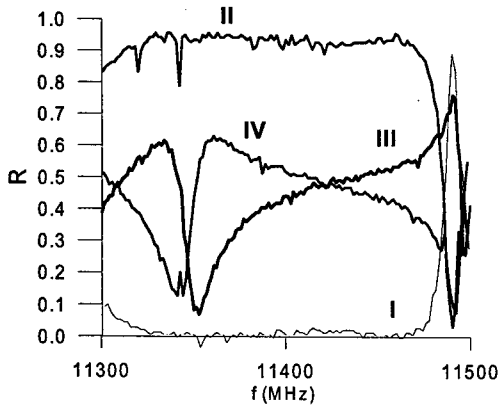
Figure 2. Measured frequency characteristic of the 3dB quasi-optical directional coupler. Note balanced splitting between arms III and IV at 11.4 GHz, as well as low reflection back into arm I.

Fig. 3 shows compressed pulses obtained in each arm individually, when the plasma switch in the opposing arm is not fired. While not identical, the two results show compressed pulses with peak powers of about 2 MW, for an incident pulse of about 1 MW. Fig. 4 shows incident, reflected and output power pulses for the two-channel configuration when the plasma switch tubes are not fired. The difference between incident and output pulses is the energy stored in the ABC-2 compressor. In this example, 61% of the incident rf energy is stored, with the balance being reflected into the output arm of the 3-dB hybrid, mainly during the first half of the pulse. This value of efficiency of energy accumulation is higher than in the

single-channel ABC [3]. Fig. 5 shows three examples of compressed pulses obtained when the plasma switch tubes in both channels are fired simultaneously, using an 80 kV trigger pulse of duration 100 nsec. The maximum power of the compressed pulses reached 11.3 MW within a pulse duration of about 70 nsec.
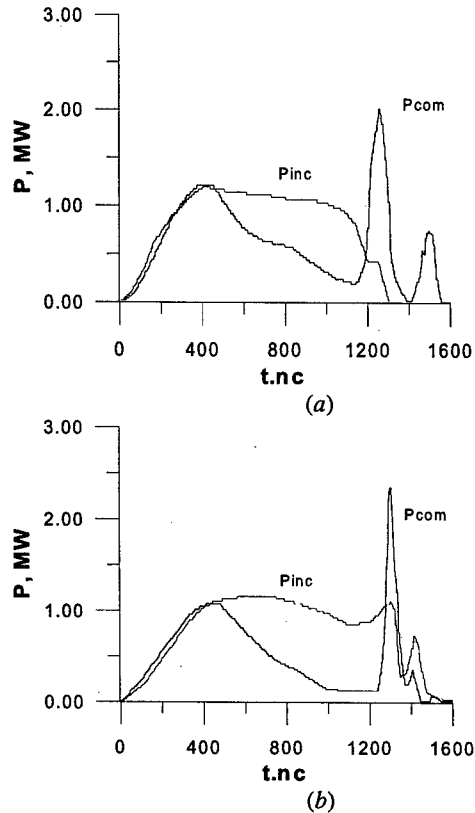
Figure 3. Traces of the compressed pulses obtained separately from each of the compressor channels: (a) channel I; (b) channel II.
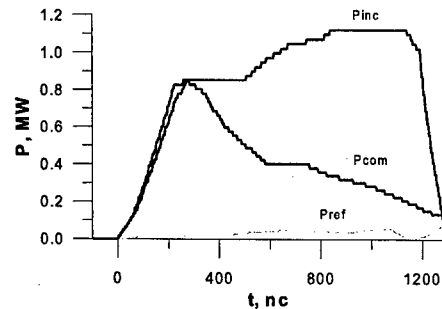
Figure 4. Traces of the incident P_{inc}, reflected P_{ref} and output pulses P_{com} without discharge of plasma switch.

CONCLUSIONS

1. Coherent superposition of compressed pulses from both channels was demonstrated, as seen by comparing Figs 3 and 5. Compressed pulses with powers of 9–11 MW and

durations of 50–70 nsec were observed, corresponding to power gain ratios k in the range 8-9.

(a)

(b)

(c)
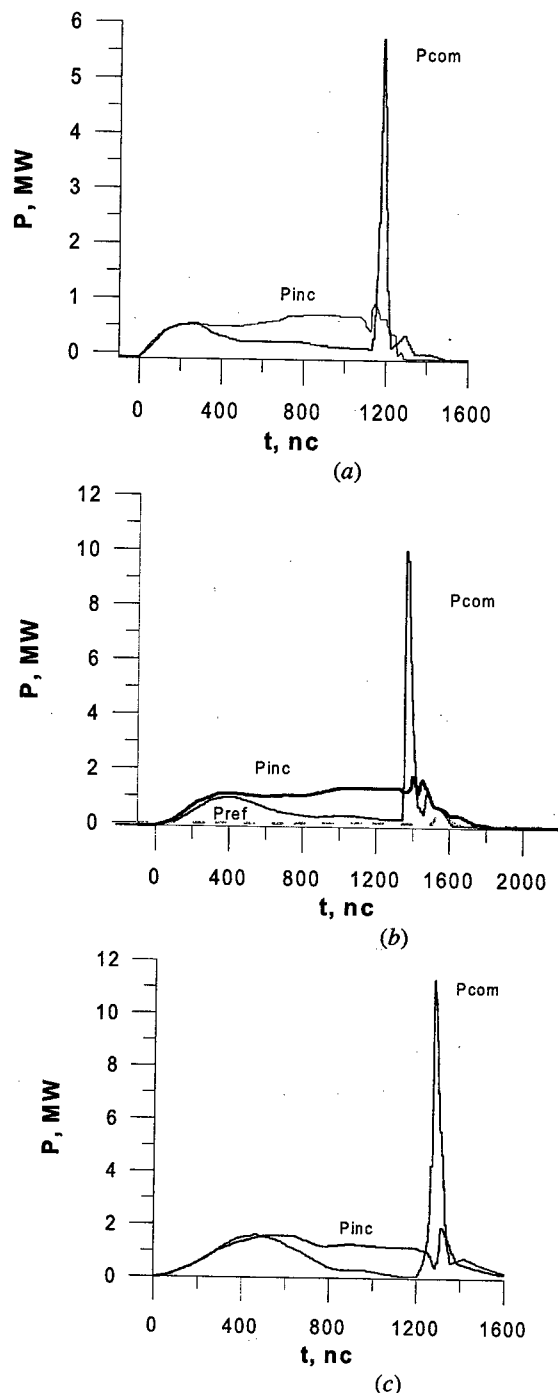
Fig. 5. Oscillogram traces of compressed pulses with external firing of the plasma switches at different values of incident power. The gas pressure in the tubes was $(2-5)\times10^{-2}$ Torr.

2. The use of incident power levels <1.5 MW to drive the compressor ABC-2 was required by the appearance at higher powers of microwave breakdowns evidently in the 3-dB directional coupler and the waveguide feed to the compressor. These breakdowns were probably caused by insufficient baking and degassing of the waveguides. Bakeout was not carried out at temperatures >100°C, nor was prolonged rf conditioning carried out thereafter. Operation with an incident power level of about 12 MW is seen to be required to obtain the 100 MW compressed output pulses that are a goal of this program. At this power level, rf fields in the compressor would be about three times greater than those in the experiments reported here. After full conditioning, each output arm of the magnicon is expected to supply about 25 MW.

3. The need for operation of both channels of the compressor with equal cavity resonant frequencies and equal Q-factors has been shown to require a means for circuit monitoring at high power, and for effective external tuning of the cavities. In the experiments reported here, such tuning could only be performed at low power, but detuning due to mechanical movement during pump-down required time-consuming iterations before near equal tunings could be achieved. It is planned to implement a modified tuning procedure during the forthcoming experimental campaign to overcome these difficulties.

REFERENCES

[1] S.G.Tantawi, R.D.Ruth, A.E.Vlieks and M.Zolotarev, "Active high power rf pulse compression using optically switched resonant delay lines," Advanced Accelerator Concepts, 7th Workshop, Lake Tahoe, CA, 1996. AIP Conf. Proc., **398**, 813 (1997)

[2] A.L.Vikharev, A.M.Gorbachev, O.A.Ivanov, V.A.Isaev, S.V.Kuzikov, A.L.Kolyslo, A.L.Litvak, M.I.Petelin, and J.L.Hirshfield, "Active microwave pulse compressors employing oversized resonators and distributed plasma switches," Advanced Accelerator Concepts, 8th Workshop, Baltimore, MD, 1998. AIP Conf. Proc., **472**, 975 (1999).

[3] A.L.Vikharev, A.M.Gorbachev, O.A.Ivanov, V.A.Isaev, S.V.Kuzikov, A.L.Kolyslo, A.L.Litvak, M.I.Petelin, J.L.Hirshfield, O.A.Nezhevenko and S.H.Gold, "100 MW active X-band pulse compressor," Proc. of the 1999 Particle Accelerator Conf., NY, IEEE Conf. Proc., **1-5**, 1474 (1999).

[4] A.L.Vikharev, A.M.Gorbachev, O.A.Ivanov, V.A.Isaev, V.A.Koldanov, S.V.Kuzikov, A.L.Litvak, M.I.Petelin, J.L.Hirshfield and O.A.Nezhevenko, "Two-channel active high-power X-band pulse compressor," Advanced Accelerator Concepts, 9th Workshop- Santa Fe, NM, 2000. AIP Conf. Proc., **569**, 741 (2001).

ACTIVE RF PULSE COMPRESSOR WITH A FERROELECTRIC SWITCH*

V.P. Yakovlev[1], O.A. Nezhevenko[1], and J.L. Hirshfield[1,2]

[1]Omega-P, Inc., New Haven, CT 06511, USA, Physics Department,
[2]Yale University, New Haven, CT 06520, USA

Abstract

Principles and preliminary design for a microwave active pulse compressor using an electrically-controlled ferroelectric switch are presented. The design of an 11.4 GHz, 500 MW pulse compressor with a pulse width of about 50 nsec and a compression ratio of 10 is described. It is planned to drive the compressor using the Omega-P/NRL X-band magnicon.

INTRODUCTION

The current design for the linear collider NLC [1] relies on pulse compression to achieve the high peak rf power levels required to drive the accelerator structures (500 - 600 MW in ~ 400 nsec pulses). A number of rf pulse compression systems have been under consideration recently including versions of the Delay Line Distribution System (DLDS) [2], Binary Pulse Compression (BPC) [3], and SLED-II [4]. The mechanisms upon which these compressors operate are *passive*, in that no element in the compressor structure has time-dependant properties. Common limitations of these systems are their relatively low compression ratio (~4:1), and/or their very long runs (100's of km) of low-loss vacuum waveguide [5]. In an attempt to circumvent these limitations, various concepts of *active* rf pulse compression have recently received attention, involving switches with optically-varied silicon mirrors [6], ferromagnetic elements [7], PIN diode arrays [8], and plasmas [9]. To date, none of the tested versions of these active pulse compressors achieved high enough power levels for use with NLC.

In the present paper, an active pulse compressor with a resonance switch based on use of electrically–controlled ferroelectric elements is presented.

GENERAL

1. Ferroelectric elements have an E-field-dependent dielectric permittivity $\varepsilon(E)$ that can be very rapidly altered by application of a bias voltage pulse. The switching time in most instances would be limited by the response time of the external electronics that generates the high-voltage pulse, and can therefore be in the nsec range. Modern bulk ferroelectrics, such as barium strontium titanate ($Ba_xSr_{1-x}TiO_3$, or BST), have high enough dielectric breakdown fields (100-200 kV/cm) and do not require too high a bias electric field (~20-50 kV/cm) to effect a significant change in ε [10]. Ferroelectrics are already successfully used in rf communication technology, radar applications, etc. Euclid Concepts, LLC recently developed and tested a bulk ferroelectric based on a

composition of BST ceramics, magnesium compounds, and rare-earth metal oxides that has a permittivity $\varepsilon = 500$, and -20% change in permittivity for a bias electric field of 50 kV/cm. The loss tangent already achieved is close to 1.5×10^3 at 11 GHz [11]. Development of production techniques for this material continues, with the expectation of further lowering the loss tangent to the values of less than 1×10^3. High breakdown fields, fast switching time, and already achieved low losses make ferroelectrics attractive elements for using in high-power microwave switches.

2. In active pulsed compressors with resonance switches, the rf source supplies electromagnetic energy to fill a low-loss storage cavity coupled through an electrically-controlled resonance switch to a load (the accelerating structure). Compressor operation involves two steps: *first*, that of energy storage when the coupling to the storage cavity is small in order to provide good efficiency of filling; and *second*, that of energy extraction when the coupling is high to provide fast energy discharge into the accelerating structure. The coupling of the storage cavity with the rf source is controlled by changing the resonance frequency of the switch cavity. In general, it is possible to provide a fast change of resonance frequency of the cavity by rapidly changing the rf properties of an active element situated within the cavity. A schematic diagram of a proposed active pulse compressor is shown in Fig. 1. This example is based on the design of Omega-P's two-channel Active Bragg Compressor (ABC) [12] that employs resonance plasma switches. As shown in Fig. 1, two cylindrical TE_{01}-mode storage cavities (8) are each
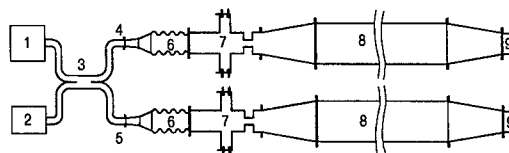
Figure 1. Schematic diagram of the two-channel ABC.

terminated with an adjustable short (9) at one end, and an electrically-controlled switch cavity (7) at the other end. Waveguides (4 and 5) are fed from the rf source (1) after the source power is split using a 3-dB hybrid coupler (3). Mode converters (6) transform the mode from TE_{10}-rectangular to TE_{01}-circular. Compressed output pulses are combined and absorbed in the load (2). This scheme is similar to SLED [13] but for the addition of active elements (i.e., the switch cavities). Employment of the Omega-P/NRL X-band magnicon [14] that is designed for a maximum output power of about 50 MW in a 1 μsec pulse as a power source feeding the active pulse compressor described here allows one to anticipate a

maximum output power of 500 MW in the compressed pulse. The main design parameters of the proposed active pulse compressor are given in Table I.

Table I. Parameters of the active pulse compressor.

operating frequency f_0	11.424 GHz
input power P_o	50 MW
input pulse duration t_f	1 μsec
power gain k	10
peak output power $P_{out} = kP_o$	500 MW
output half-height pulse duration $t_{0.5}$	~40 nsec

3. To determine the switch cavity parameters, it is necessary to calculate optimal coupling of the storage cavity in both operating regimes, namely in the energy storage regime and the energy extraction regime. All calculations have been carried out for the existing ABC storage cavities [12], even though superior performance could be anticipated from improved design of the cavities. The TE_{01} energy storage cavities have lengths of about 2 m including tapers and diameters of 8 cm; their measured self quality factors Q_o are 110,000. Optimal coupling in the energy storage regime is determined by maximizing the filling efficiency. The efficiency η for energy transfer to the storage cavity is [15]

$$\eta = \frac{2\beta\tau_o}{t_f(1+\beta)^2}\left(1-\exp\left(-\frac{t_f(1+\beta)}{\tau_o}\right)\right)^2, \quad (1)$$

where β is the coupling, and $\tau_o = 2Q_o/\omega$ is the self time constant for the storage cavity. For parameters listed in Table I, the optimal coupling β is 4.2, which corresponds to a maximum efficiency of 64%. The coupling in the energy extraction regime is found to be

$$\beta_{out} = \frac{1}{2\eta}\frac{P_{out}}{P_o}\frac{\tau_o}{t_f} = \frac{k}{2\eta}\frac{\tau_o}{t_f}. \quad (2)$$

For the case considered here, $\beta_{out} = 25$. The time constant τ_{out} in the energy extraction regime is $\tau_{out} = \tau_o/(1+\beta_{out}) = 123$ ns, and the half-height pulse duration $t_{0.5}$ in this case is 43 nsec. The switch cavity is a two-port element inserted between the storage cavity and the mode converter; it is characterized by transmission coefficient T, that is related with the coupling β in the following way:

$$T^2 = \beta\frac{4L}{v_{gr}\tau_0}, \quad (3)$$

where v_{gr} is the average group velocity in the storage cavity, L is the storage cavity length. In the case considered ($L=2$ m and $v_{gr} \sim c$), $T^2 \approx 9\cdot10^{-3}\beta$. Thus, the switch cavity transmission should be –14 dB in the energy storage regime, and –6.5 dB in the energy extraction regime.

4. As a result of simulation of the model switch cavity partially filled with ferroelectric (as shown in Fig. 2) two mode families were found. The first family, which are labeled "vacuum modes," are exemplified by tuning curves #1 in Fig. 3; these have a small electric field in the ferroelectric, and thus their resonance frequencies don't depend sensitively on ε. The second family, which are labeled "ferroelectric modes," are exemplified by curves
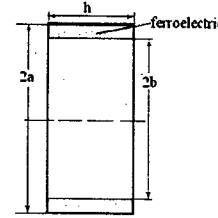
Fig. 2. The model switch cavity schematic.
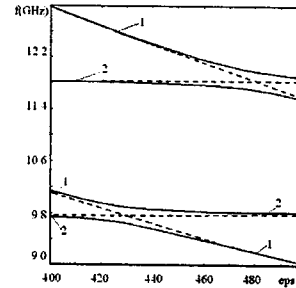
Fig. 3. The model cavity spectrum *vs.* ferroelectric permittivity ε for a=56 mm, b=53 mm and h=20 mm.

#2 in Fig.3; these have high electric field in the ferroelectric and thus, their resonance frequencies exhibit a strong dependence of the frequency on ε. One can see that the resonance frequencies on curve #2 change by ~10% when ε changes by 20%. Consequently, the ferroelectric mode could be controlled with weaker applied electric field than the vacuum mode.

5. For the proposed 500 MW, 11.424 GHz active pulse compressor, where an available ferroelectric with $\varepsilon = 500$ [11] is to be used, the resonance frequency of the switch cavity for the ferroelectric mode changes by ~1 GHz while ε changes from 400 to 500, but the resonance frequency for the vacuum mode changes by only ~70 MHz. Unfortunately, the maximum electric field in the
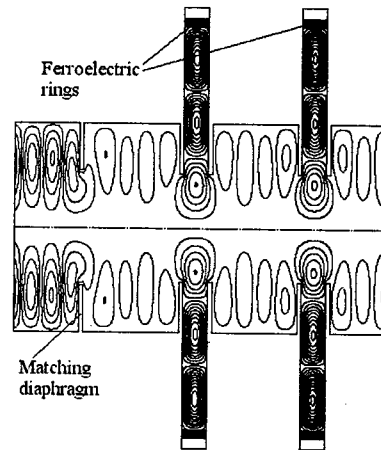
Fig. 4. The switch conceptual layout.

ferroelectric for the ferroelectric mode would be about 350-370 kV/cm, which is much higher than the field for

vacuum mode (15-20 kV/cm), and far above the breakdown limit of ~100 kV/cm. As a consequence, the vacuum mode is the only choice to be the operating mode for this type of active pulse compressor. Parameters found for the switch cavity are listed in the Table II.

Table II. Parameters of TE_{031} switch cavity.

operating frequency, GHz	11.424
operating mode	TE_{031}
cavity length, mm	20
coupling iris diameter, mm	30
coupling diaphragm thickness, mm	3
ferroelectric ring length, mm	20
ferroelectric ring inner diameter, mm	106
ferroelectric ring thickness, mm	3
transmission in energy extraction regime ($\varepsilon = 400$), dB	0
transmission in energy storage regime ($\varepsilon = 500$), dB	-4
maximum electric field in ferroelectric in energy extraction regime, kV/cm	20
maximum electric field in ferroelectric in energy storage regime, kV/cm	10
maximum electric field in vacuum in energy extraction regime, kV/cm	865
maximum electric field in vacuum in energy storage regime, kV/cm	675

The entire proposed ferroelectric switch arrangement is shown in Fig. 4, including the matching diaphragm and two TE_{031} switch cavities with ferroelectric rings, because in the switch containing only one cavity the electric field in the ferroelectric is still too high even for the vacuum mode. .
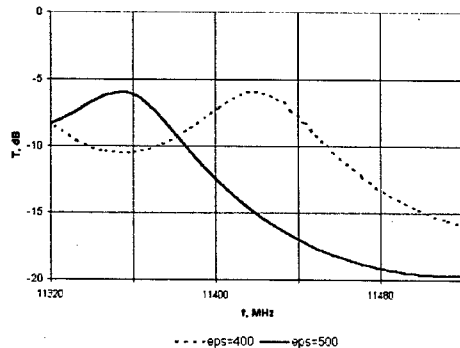
Fig. 5. Transmission T vs. frequency in the energy storage regime (solid curve), and the energy extraction regime (dashed curve).

The diameter of the matching diaphragm (see Fig. 4) is 30 mm and its thickness is 3 mm, to provide -6.5 dB isolation in the energy extraction regime. The frequency dependences of transmission for the energy storage and energy extraction regimes for the entire system that includes the matching diaphragm and the two switch cavities are shown in Fig. 5. The solid curve corresponds

to the energy storage regime, when both switch cavities have resonance frequencies of about 11.350 GHz, and transmission at the operating frequency is about –14 dB. In the energy extraction regime (dashed curve), the ferroelectric permittivity of the switch cavities is decreased from 500 to 400, and the resonance frequencies are close to the operating frequency. At resonance the self transmission of both cavities is close to 0 dB, and the matching diaphragm provides the desired transmission of –6.5 dB at 11.424 GHz. The bias pulse electric field of 50 kV/cm is applied to the ferroelectric ring along the axial direction. The switching time in the compressor is limited by the time which is necessary to charge the capacitance of the ring and surrounding structure up to the full voltage of 100 kV. This capacitance is in range 180 – 220 pF for $\varepsilon = 400 – 500$. So, in order to get a rise time of about 10 ns for a capacitance of 200 pF, the biasing generator impedance should be about 25 Ohms.

DISCUSSION

A new ferroelectric switch has been designed for installation in the existing double-channel Active Bragg Compressor structure already built by Omega-P for evaluating plasma switches [12], and which is installed at the NRL X-band magnicon test facility.

In addition to the main goal of achieving a compression ratio higher than that available with passive compressors, this new switch could also allow rapid variations, during both the incident and compressed rf pulses, in the coupling between an rf energy storage cavity, the load and the rf source. This attribute would lead to an increase in energy efficiency, and an improved shape of the output pulse, compared to a switch with only binary coupling coefficients.

Authors would like to thank Anatoly Vikharev for useful discussions.

REFERENCES

[1] International Linear Collider Technical Review Committee, 2^d Report, SLAC-R-606, SLAC2003
[2] H. Mizuno and Y. Otake, KEK 94-112, Oct. 1994.
[3] Z.D. Farkas, IEEE Trans. MMT-34, 1986, pp. 1036.
[4] P.B. Wilson, et al, SLAC-PUB-5330.
[5] S. Tantawi, SLAC-PUB-8582.
[6] S. Tantawi, et al, SLAC-PUB-7368.
[7] S. Tantawi, PAC2001, Chicago, pp. 1216.
[8] F. Tamura and S. Tantawi, LINAC 2000, pp. 751-753.
[9] A.L. Vikharev, et al, AIP **472**, p. 975.
[10] Sengupta L.C. et al, IEEE Trans. on Ultrasonics, Ferroelectrics and Freq. Control, v.44, p.792, 1997.
[11] E.A. Nenasheva, et al, Int. Conf. on Electroceramics, MIT, Cambridge, MA, 2003. (To be published).
[12] A.L. Vikharev, et al, AIP **569**, p. 741.
[13]. Z.D. Farkas, et al, Proc. 9th Int. Conf. On High Energy Accelerators. SLAC, 1976, p.576.
[14] O.A. Nezhevenko, et al, PAC2001, p. 1023-1025.
[15] M.M. Karliner, et al. Preprint INP 86-146.

PBG CAVITIES FOR
SINGLE-BEAM AND MULTI-BEAM ELECTRON DEVICES*

A. Smirnov, D. Newsham, D. Yu

DULY Research Inc., Rancho Palos Verdes, CA 90275

Abstract

PBG cavity having one or six defects is studied in the frequency domain. External Q-factors are found numerically for different portal configurations. A new type of hybrid HOMs with coupled monopole and multipole field patterns is found. A novel radial transmission line method is introduced to evaluate the external Q-factor of modes with quasi-absorbing external boundary. A flat-field, rectangular cavity loaded with linear arrays of rods and defects is designed and compared with the planar barbell cavity. Loss-factor and modal spectra are compared with conventional cavities for both circular and planar PBG cavities.

INTRODUCTION

Photonic Band Gap (PBG) structures for accelerator applications have been studied in the last few years by several research groups [1,2,3,4,5]. We consider the rod-loaded configurations as a new class of microwave structures having periodic boundary in the transverse dimensions. The PBG acronym for such generalized rod-loaded structures may better stand for Periodic Boundary in a Gap. For most classical accelerator physics applications, an infinite lattice is not required, and the essence of such structures is the fields defined by the metallic (or dielectric) rods in discrete modes useful to the specific application. They can be cavities (usually a single-gap) or waveguides (multi-gap in the longitudinal direction). We present some of the new features found for metallic single-defect and 6-defect cavities as well as novel multi-cell [6] and planar designs.

SINGLE- AND 6-DEFECT CAVITIES

The common property of the PBG structures is that the modal spectrum is much denser than that for the conventional pillbox structure. Along with trapped (defect) and global (non-local) modes [4], we have found and identified new hybrid modes for the metal PBG cavities. These hybrid modes are a result of the coupling between monopole and multipole modes in the lattice.

In Figure 1 we compare the modal spectrum (TM modes) and bunch energy loss for a single-defect PBG cavity with those of a cylindrical pillbox cavity having about the same gap, fundamental mode frequency and r/Q-value. For the PBG the loss-factor is about the same (or higher) as for the pillbox cavity. This result is in agreement with comparison made for PBG and TESLA cavities [2], and also with the fundamental nature of structure-dominated waveguides and cavities [7].
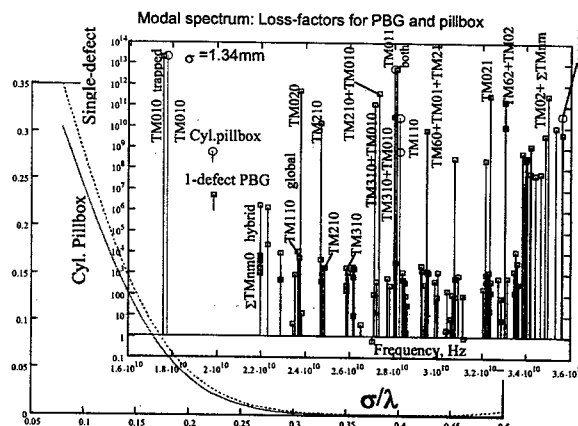
Figure 1: Gaussian bunch TM HOM normalized losses *vs* rms normalized bunch length (solid line: pillbox cavity; dashed: 1-defect cavity). Inset: spectral losses (J-s/C²) *vs* frequency (Hz) for pillbox (circles) and 1-defect cavity (boxes).

As an example of a multi-defect PBG cavity [6], a 6-defect cylindrical cavity with 55 rods (Figure 2, a) is found to have a high efficiency: r/Q = 5.25 kΩ/m per defect at f = 16.7 GHz, Q = 5491 for a gap of 6.91 mm. Thus in total, r/Q = 5.25 × 6 = 31.5 kΩ/m, which is very close to a simple TM_{01} pillbox cavity having an r/Q of 32.2 kΩ/m at f = 17 GHz, and a Q of 5525 for the same gap. Unlike single-defect PBG and most non-PBG structures, a sextupole mode has about the same r/Q as the fundamental one. Moreover, dipole and quadrupole degenerate modes for some of the defects give even higher values of r/Q (by ~1.5 to 2 times, depending on the mode).
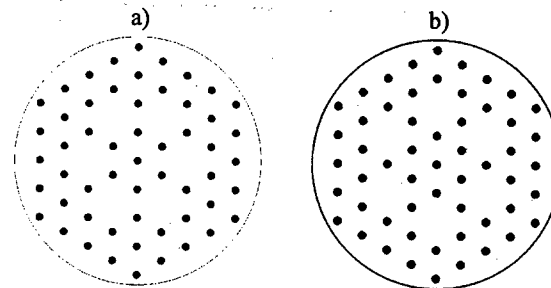
Figure 2: Two lattice configurations for a typical 6-defect, 4th order PBG structure.

Like the 1-defect case, most of the non-trapped HOMS are hybrid in the 6-defect case. The classification of hybrid modes (e.g. those in Figure 3) is more difficult in

this case since they can combine some of the local and trapped modes along with global modes.
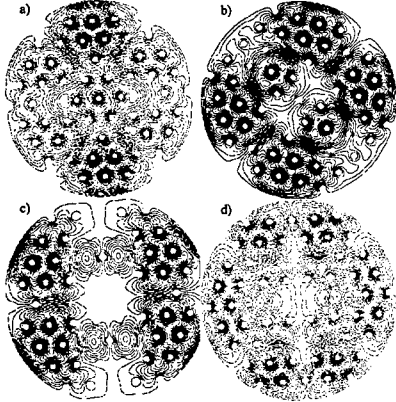
Figure 3: Hybrid modes of a 6-defect PBG cavity: a) coupled monopole and global quadrupole modes; b) global dipole and local sextupole modes; c) trapped and global quadrupole modes; d) sextupole and dipole modes – both global and trapped.

Several coupling schemes for the 6-defect cavity (see Figure 2, b) are considered using frequency detuning methods [8,9]. Calculated outcoupling coefficients β_c for TM_{02} mode in a configuration with two or three rectangular waveguides on the periphery are 1.2 and 1.7, respectively.

Another configuration is a cylindrical pipe of $\varnothing 6.6$ mm attached to an additional, center defect. From the results given in Table 1 one can see that the TM_{02} mode is suppressed completely, dipole modes are overcoupled, and the fundamental mode is strongly overcoupled.

Table 1: Central coupling characterization.

Mode	f, GHz	Q_{ext}	β_c
TM_{02}, next monopole	18.78	1.71	6130
TM_{31}, sextupole	18.62	10^6	$7.2 \cdot 10^{-3}$
TM_{21}, quadrupole next	18.44	12750	0.544
TM_{21}, quadrupole	18.41	16940	0.4
TM_{11}, dipole next	18.09	1176	7.4
TM_{11}, dipole	18.05	1102	7.8
TM_{01}, fundamental	18.02	347	20

Next we introduce a simple numerical method of calculating the external Q-factor for a cavity with a perfect, peripheral absorber. Instead of performing extensive, time-domain simulations with a real absorber [10], we consider the entire circular periphery as a moveable boundary within the framework of a frequency detuning method [8]. The peripheral boundary is extended to include an outer radial waveguide (radial transmission line) where there are no rods. The results are given in Table 2 for a 4th order lattice with 55 rods (in the brackets); a smaller 3rd order lattice with 31 rods; and a bigger 5th order lattice with 85 rods.

The results show that the lattice order has a dramatic influence on the external Q-factor of the major modes (up to 1-2 orders). This is quite understandable: the group velocity is always lower for more closed/loaded structures. The Q-factor reduction observed in a test at MIT [11] qualitatively confirms our simulation results, which show an ~1.5 order of magnitude reduction (see Table 2 for the 3rd order lattice). Table 2 is also in good correlation with the results of a 7×7 rectangular-lattice PBG structure [3], its Q-factor being reduced with peripheral absorber by 2 orders for the next (after the fundamental one) monopole TM_{02}-like mode.

Table 2: Radial line outcoupling characterization.

Mode	f, GHz	Q_{ext}	β_c
TM_{02}	23.04	(272) 632	(~21) 8.92
TM_{31}	17.85	2086 ($>10^5$)	3.6 (<0.08)
TM_{21}	17.59	3973	1.8
TM_{21}	17.58	(171) 3346 (89000)	(40) 2.11 (13)
TM_{11}	17.094	2228	2.84
TM_{11}	17.095	(~70) 2181 (8900)	(90) 2.9 (0.71)
TM_{01}	16.85	(~69) 1959 (77000)	(82) 2.9 (0.07)

FLAT-FIELD, ROD-LOADED CAVITY

A rectangular cavity loaded by finite rows of rods (and defects) can have a very high vacuum conductance. Since the fields diminish rapidly away from the rods, the cavity can take on a large volume, which can easily facilitate insertion of non-evaporative getter (NEG) modules with high pumping speed, diagnostic ports or laser beams (to illuminate, e.g., a photocathode at optimal angles). The field flatness in a structure with a row of defects between several rows of rods can be adjusted with just a slight shift of one or few side rods. Such a flat-field PBG cavity is depicted in Figure 4. The performance of the fundamental mode is nearly identical to the barbell cavity [12] (see Figure 5). The effective aspect-ratio [13] of both cavities is high and lies in the range of 11-12 to fit the typical needs of, for example, a sheet-beam klystron.
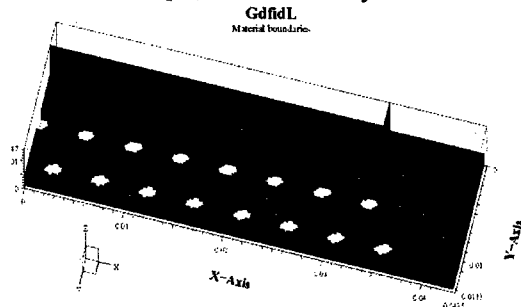
Figure 4: One eighth of an X-band, planar PBG structure with 2 rows of rods on each side of a sheet beam.

Figure 6 shows the modal spectrum and HOM losses for the vertical TE mode. In spite of very different modal spectra for the barbell and the rod-loaded cavities, the losses are essentially the same with the exception of extremely short and long bunches.

For the coupler design of a flat-field cavity, the major difficulty is that significant coupling dramatically affects the flatness. Several coupling schemes were examined for an X-band, flat-field PBG cavity. We found that a cavity with only 1 + 1 rows of rods worked quite well with inductive slots (parallel to the beam) made in both side walls as depicted in Figure 7. The coupling for the fundamental mode is characterized in Table 3 in which dimensions of the slot gap are varied with respect to the WR90 pipe vertical height; $<\Delta f/f>$ is the averaged relative frequency deviation from an analytical fit [8,9].
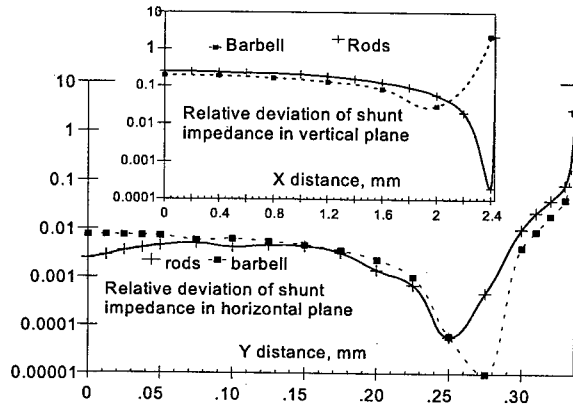
Figure 5: Relative non-flatness of shunt impedance of two planar cavities for the fundamental TM_{11} mode: barbell (dashed), and one loaded by 2+2 rows of rods (solid line).
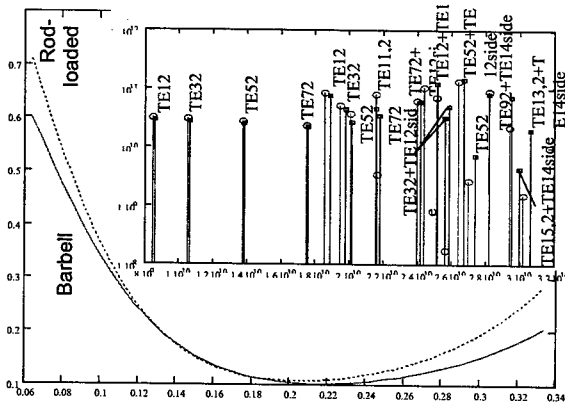
Figure 6: Relative contribution of vertical TE losses of displaced bunch $\Delta y=0.43$mm vs its relative length for barbell and rod-loaded structures. Inset: loss-factor modal spectrum (J-s/C^2) vs frequency (Hz) for vertical dipole symmetrical TE modes in barbell (circles) and rod-loaded (boxes) planar structures at $\sigma=1.6$mm.

Table 3. Coupling characterization for planar PBG cavity.

Slot WR90	f, GHz	Q_o	Q_{ext}	β_c	$<\Delta f/f>$
1/5	11.11	5643	7084	1.01	$2 \cdot 10^{-5}$
1/4	11.04	8026	2278-2018	3.07-3.48	$1.5 \cdot 10^{-4}$
1/3	11.5	7115	~330	~25	$1.5 \cdot 10^{-4}$
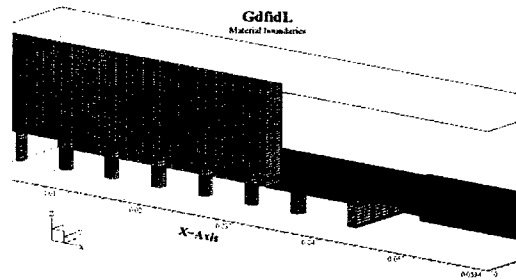
Figure 7: One eighth of a planar PBG structure with 1+1 rows of rods coupled with a WR90 waveguide.

APPLICATIONS

As noted, the relatively open nature of the planar PBG structure gives it several advantages. Planar PBG cavities can be used in a sheet beam klystron (SBK) or a planar lasertron (see Figure 5) to modulate a high current, moderate voltage, ribbon beam, and to generate high rf power from a bunched beam. A planar lasertron which requires only a simple output circuit would be more compact than an SBK, with an additional advantage of excellent pumping.
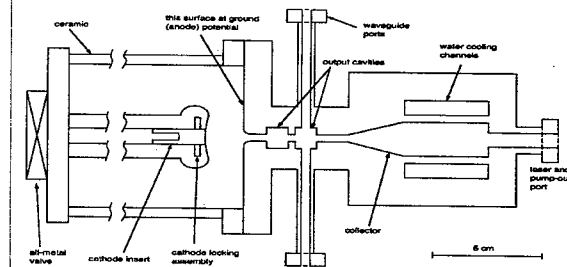
Figure 8: Schematic of a planar, X-band lasertron ("long" dimension into paper).

REFERENCES

[1] N. Kroll et al., AAC92, AIP 279, 1993, p. 197.

[2] D.R. Smith et al., AAC94, AIP 335, 1995, p. 761.

[3] D.R. Smith et al., AAC96, AIP 398, 1997, p. 518.

[4] M.A. Shapiro et al., Phys. Rev. Special Topics – Accelerators and Beams, Vol. 4, 042001 (2001).

[5] M.A. Shapiro, et al., PAC99 p 833.

[6] D. Yu et al., AAC02, AIP 647, 2002, p. 394.

[7] L.A. Vainshtein, Open Resonators and Open Waveguides, Izdatelstvo "Sovetskoe Radio", Moscow, 1966.

[8] J.C. Slater, Microwave Electronics, D. Van Nostrand Co. Inc, Princeton, NJ. 1959.

[9] N. Kroll and D. Yu, Particle Accelerators, V. 34 (1990) 231.

[10] L. Derun et al., AAC96, AIP 398, 1997, p. 528.

[11] E.I. Smirnova et al., AAC2002, AIP 647, 2002, p. 383.

[12] R. Merte et al., PAC99, p. 815.

[13] D. Yu et al., PAC2001, p. 3855.

CONSTRUCTION AND TESTING OF A 21 GHZ CERAMIC BASED POWER EXTRACTOR*

D. Newsham, A. Smirnov, D. Yu, *DULY Research Inc, Rancho Palos Verdes, CA 90275*
W. Gai, R. Konecny, W. Liu, *ANL, Argonne, IL*
H. Braun, G. Carron, S. Doebert, L. Thorndahl, I. Wilson, W. Wuensch
CERN, Geneva, Switzerland

Abstract

A ceramic based power extractor [1] operating at 21 GHz was built by DULY Research Inc. and tested at CTF2, the CERN Linear Collider (CLIC) Test Facility. The structure includes a ceramic extractor section, a 2-output-port, circular-to-rectangular waveguide coupler, and a 3-port rectangular waveguide combiner that provides for a single output waveguide. Results of cold tests and full beam tests are presented and compared with theoretical and numerical models.

INTRODUCTION

The dielectric based rf power extractor [2] shows great promise for use in a power source of a two-beam collider, having superior performance and a simpler design when compared to conventional high-power sources. As a first test of the power that can be extracted at high frequency from a dielectric structure, DULY Research has manufactured a 21-GHz ceramic power source [1] which was full-beam tested at CTF2. Data was taken for both single-bunch and multi-bunch train operation.

Because of the strict time constraints imposed by the impending shutdown of CTF2, cold test measurements were performed at CERN and ANL after the full beam test was performed. Based on the data from the full-beam experiment along with the measured S_{21} from the cold test, the peak power produced by the power extractor with a 275 nC bunch train is estimated to be ~50 MW, and is consistent with theory.

FABRICATION

Figure 1 shows a 3D cut-away model of the power extractor with the primary sections split open indicating the internal structure of the separate pieces. The inner diameter of the ceramic tube was 10 mm, and was a compromise between the size of the electron beam (≥ 6 mm), and the thickness of the wall of the ceramic tube (1.465 mm). The full length of the ceramic section was 33 cm and consisted of 4 ceramic tubes. Three of the tubes were 9 cm each and the final tube was tapered to minimize reflection from the end.

The extractor was constructed of OFHC copper and brazed to two NW40 flanges for mating to the coupler and to the CTF2 beam line. After brazing, the center hole was precision honed such that the ceramic tubes just slipped through without binding. The ceramic was held in place

by copper spacers that are part of the flange connections. The waveguide side slots in the coupler and WR42 flange pieces were EDM cut. The assembly was brazed to form a choke joint in the central hole at the downstream side of the coupler, which includes 2 output waveguides and proper flanges for attachment to the extractor and the CTF2 beam line. The WR42 waveguides between the coupler and the combiner were bent and cold tested for equal phase length at CERN and shipped to DULY for brazing to the flanges. The combiner was constructed from two pieces of 304 SST. Two 90°-arc grooves were machined into one of the pieces. The slots were plated with copper, and then the 2nd SST piece was brazed on top of the grooved piece to close the waveguide. After brazing, the required flange faces were machined.
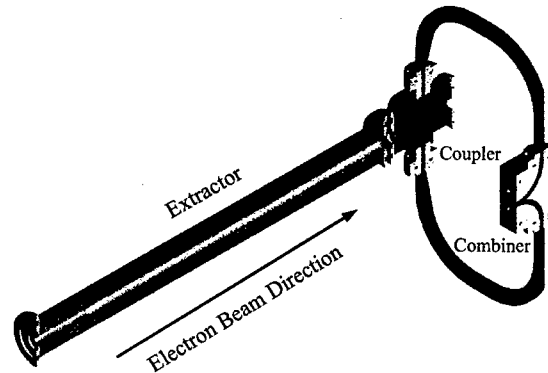
Figure 1: 3D split model of the 21 GHz ceramic based rf power extractor.

THEORETICAL MODEL

The theoretical model [1] for the Cherenkov radiation produced in the ceramic by the passing electron beam was modified to include the effects of reflections at both ends of the ceramic lined tube. This model assumed that there were no reflections at the interfaces between the individual ceramic tubes, that there was no mode conversion within the structure (the coupler could easily cause mode conversion), and that the reflection coefficients at the two ends were constant over the range of study in both time and frequency. Reflections induced by the coupler, choke, or combiner were assumed to be part of the reflection at the end of the extractor tube. The circulating power stored in the cavity is given by:

$$P_{Intra}(t) \approx \left| \frac{1 - (\Gamma_0 \Gamma_L)^{1+[t/2t_f]}}{1 - \Gamma_0 \Gamma_L} \right|^2 P_1, \qquad (1)$$

where t_f is the filling time, Γ_0 and Γ_L are the complex reflections at the beginning and end of the ceramic tube, and P_1 is the power generated by the ceramic in the absence of any reflections [1]. Two typical cases of Eq. (1) correspond to destructive and constructive interference. Destructive interference occurs for $|1-\Gamma_0\Gamma_L| > 1$ and the power circulating in the cavity is identical to the power generated by the electron beam P_1. This condition occurs over a wide phase range: $|\arg(\Gamma_0\Gamma_L)| > \text{Arccos}(|\Gamma_0\Gamma_L|/2)$. Constructive interference occurs when $|1-\Gamma_0\Gamma_L| < 1$, and the power will build up during the pulse, and the peak power circulating in the cavity will occur when the reflection phase is approximately zero, $\arg(\Gamma_0\Gamma_L) \approx 0$. From 3D electromagnetic simulations using CST Microwave Studio, the reflection at the beam entrance is $|\Gamma_0| = 0.992$.

Ultimately, the power that exits the structure is delivered to the load at the power combiner and is determined by S_{21} assuming no losses in the cavity and the power only exits out the combined port:

$$P_{Out} \cong S_{21}{}^2 P_{Intra} . \tag{2}$$

COLD TESTS

Cold tests of the power extractor were performed at CERN and ANL after the full beam tests. Early on during the beam tests, it was noticed that strong reflections were taking place within the structure. A circular mode launcher was designed and constructed at CERN specifically for launching/receiving the test signal at the beginning of the ceramic pieces, and a second launcher was built to match the entrance of the coupler. In addition to the circular launchers, absorbing loads and a single WR42 high power load were used for the cold tests.

A measurement launching from the beginning of the first ceramic tube and ending at the combiner output waveguide resulted in a transmission coefficient: $S_{11} = -12\text{dB}$ (ANL measured -14dB). This number will be used with the measured rf output power in the full beam test to determine the power generated in the extractor.

Subsequently, the coupler was tested separately. With the signal launched at the upstream beam opening, the insertion loss to one of the output flanges (with an absorber in the other one) was -12.5 dB, not the -3 dB that was expected. Finally, the phase difference between the two WR42 output ports on the coupler was 120° instead of the 180° required for correct operation of the power combiner. This mismatch could potentially be used to advantage by trapping more power than generated in the extractor (with constructive interference) to test the ceramics breakdown.

FULL BEAM TESTS

Full beam tests were performed at CERN on CTF2 during the first week in October 2002. Both a single electron bunch and multi-bunch electron trains were used. In all cases, the output rf signal was mixed with a local

oscillator (f_{LO}) and displayed on a digital oscilloscope, where both down-mixed time signal and the FFT spectrum of that signal were displayed. Based on the value of the attenuators, the power calibration (on the time scale display) was 35 kW for a 0.1 V (zero-to-peak) signal. The charge of the electron bunches varied (2.5 – 5.7 nC per bunch), but the bunch length was between 5 and 6 ps FWHM, and assumed Gaussian.

Single Electron Bunch

Single bunch experiments were first performed using a bunch charge up to 5 nc. Figure 2 shows the results from a single electron bunch test. Figure 3 shows the results of the theoretical model with similar input parameters and numerically mixed with a local oscillator at 23 GHz, the same as the experimental data.
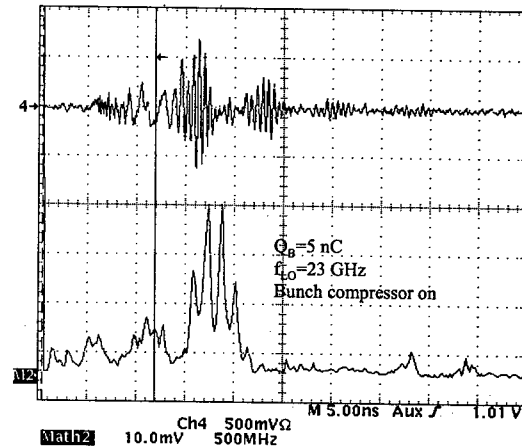
Figure 2: Experimental results of the CTF2 single bunch test. The upper trace is the mixed output time signal; the lower trace is the frequency spectrum of the time signal.
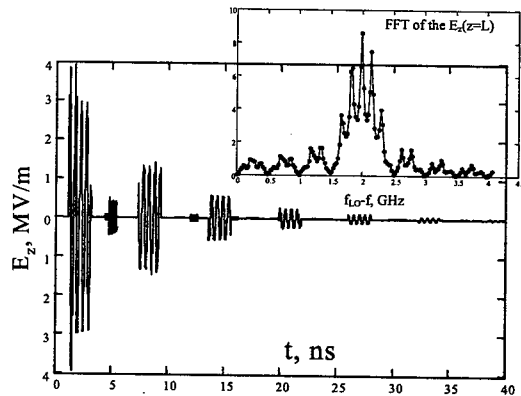
Figure 3: Simulated extractor signal for a single electron bunch mixed with a local oscillator time signal. The insert is the FFT spectrum of the simulated time signal.

Both the experimental and theoretical data for single bunch excitation show the following spectral characteristics:

- The main peak is split into several peaks spaced by approximately 0.16 GHz, which corresponds to

1157

approximately the inverse of twice the filling time, caused by reflections within the length of the ceramic structure.

- Large satellite peaks separated from the main peak by approximately 0.5 GHz, which correspond to the inverse of the rf pulse length of the signal produced by a single bunch (drain time).

Multiple Bunch Train

Electron bunch trains consisting of 48 bunches per macro pulse were the primary focus of study at CFT2. The results were studied for several values of the total charge. Because higher charge resulted in an electron beam that was larger than the beam aperture, multi-bunch operation was functionally limited to a total charge of 275 nC, or, 5.7 nC/bunch. Radioactivity measurements after the beam test corroborated that there was beam interception at the entrance of or inside the power extractor tube. The bunch spacing of 0.33 ns was based on the linac frequency (3 GHz), and the extractor was designed to operate at 7 times the linac frequency. Figure 4 shows a sample experimental time signal and frequency spectrum.
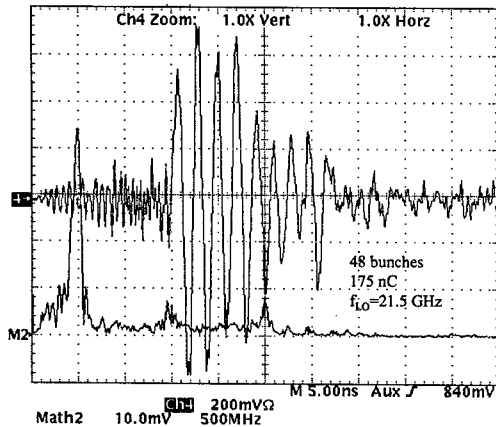
Figure 4: CTF2 results for a multi-bunch electron train.
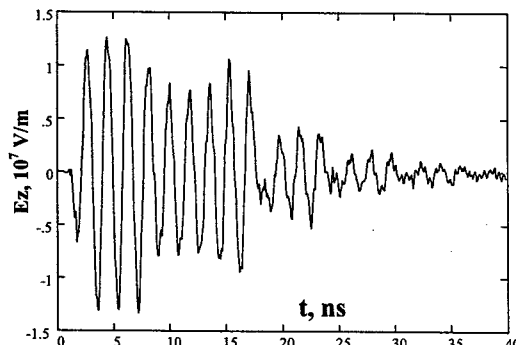
Figure 5: Simulated time signal for the case shown in Figure 4 (different time scale).

Figures 5 and 6 show the analytical calculations for a bunch train with a total charge that is the same as the experimental data, with a local oscillator frequency is 21.5 GHz, the same as the experiment.

The results of the cold test data gave a transmission loss of -12 dB, thus the power generated in the cavity can be calculated by inverting Equation 2: $P_{Intra} \cong 15.8\, P_{out}$. The apparently low power output is a result of the poor output coupling and is not an indication of low power generation. Figure 7 shows a summary of all the experimental data taken for the multiple bunch train measurements at CTF2 along with a theoretical curve [1] that contains no free parameters. Endoscopic examination after the beam testing revealed signs of damage in the last ceramic tube.
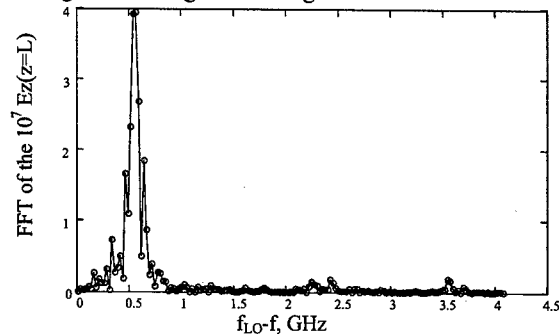
Figure 6: FFT of the simulated time signal shown in Figure 5 (see Figure 4 for comparison with measurement).
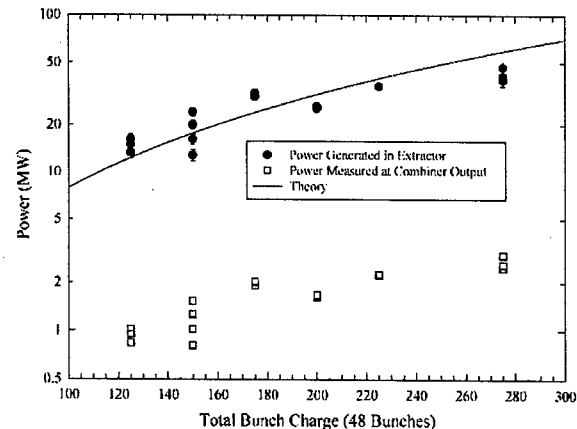
Figure 7: Power generated in the 21 GHz ceramic based power extractor for various values of the total beam charge (48 bunches per pulse).

CONCLUSIONS

A ceramic based rf power extractor generated almost 50 MW of power at 21 GHz. Despite some experimental difficulties and fabrication errors, this value for the generated power matched quite well with the anticipated power level. The measured spectra correlate well with the spectra extracted from a theoretical model with simple reflections at the ends of the ceramic extractor.

REFERENCES

[1] D. Yu, D. Newsham, A. Smirnov, Proc. 10th Adv. Accelerator Workshop, AIP 547, pp. 484-505, 2002.

[2] W. Gai and P. Schoessow, Nuclear Instruments and Methods A459, pp. 1-5, 2001.

USING FERRITE AS A FAST SWITCH FOR IMPROVING RISE TIME OF IPNS EXTRACTION KICKER *

L.I. Donley, J.C. Dooling, and G. E. McMichael Argonne National Laboratory, Argonne, IL 60439

Abstract

The Kicker system [1-2] is used to extract beam from the Rapid Cycling Synchrotron (RCS). The Kicker consists of four identical pulse circuits, each providing over 3.8 kA to each magnet winding. The magnet length is restricted to the space between vacuum bellows attached to the ring magnets. This leaves 0.89m for the magnet. To keep the voltage low the magnet conductor is broke up into 4, ¼-turn magnet windings. Each pulse circuit consists of a Pulse Forming Network (PFN) that is charged to 50 KV. The PFN is discharged through a thyratron into a 6.3-ohm transmission line to one of the magnet windings. Our system has always had marginal rise time of around 100 ns. Although the thyratron switching time is much faster than this, losses in the transmission lines cause the slower response. By using ferrite to make a fast switch between the transmission lines and the magnet, the rise time in the magnet can be reduced. To make a fast ferrite switch, the saturation point must carefully be chosen. Parameters related to choosing the proper ferrite to provide fast saturation, at the correct current will be discussed.

INTRODUCTION

The Intense Pulsed Neutron Source [3] RCS delivers 450-MeV protons in a 70 ns pulse at 30Hz to a heavy-metal target to produce spallation neutrons for material science research. The average current is 15 µA with a peak intensity of 10 Amps. The kicker system is used for single turn extraction from the RCS. The RCS extraction kicker current has always had a slower rise time than desired; historically, it has been greater than 100 ns. Up to now, the rise time has not presented a problem other than to restrict the tuning range available to the operators. At extraction, the cycle time of the h=1 bunch is 194 ns of which 70 ns contains 98 percent of the beam. Therefore a 100 ns rise time leaves a 20-25 ns window for manual tuning. However, with the installation of a third cavity [4-5] operating at the second-harmonic to raise the current limit, the kicker tuning window will be consumed. A shorter rise time will be necessary to take full advantage of second harmonic operation.

Operationally, the previous coaxial cable used in the PFNs and transmission lines to the magnets failed frequently. When our supply of cable ran low, we decided to purchase a different type of line. The new line is much more robust, but pulse rise time is slower. The rise time for the new cable was initially measured at 115-120ns. This caused beam loss to go up in the RCS. We needed to improve the kicker rise time, but due to the radiation levels in the RCS tunnel, the project needed to be done with minimal time in the tunnel. Also, limited space is available in the RCS tunnel by the kicker magnets for additional components.

TEST SETUP AND RESULTS

We are in the process of developing a new kicker system that will use CX-1725 thyratrons, replacing the CX-1175 devices currently in use. The new thyratrons offer longer lifetime and cheaper replacement cost. A test stand has been constructed to evaluate a new switch circuit using the CX-1725. With the exception of the magnet, a prototype system is presently operating as it will be used in the RCS. The transmission lines for the prototype are terminated in a 6.5-Ω load. The kicker test stand provides an excellent place to test ideas that might improve the overall extraction system.

Employing the nonlinear saturation effect of ferrite, [6-8] the rise-time of the current in the kicker magnets can be lowered. Ferrite toroids are placed on the conductor between the end of the transmission line and the load. The square cross section toroid dimensions are 2.9-in. (7.37 cm) O.D. by 1.5-in.(3.81 cm) I.D. with a thickness of 0.5-in. (1.27 cm). The ferrite toroids used here are composed of Ni-Zn and are commercially available (Fair-Rite Products, Corp., Type 43, PN: 5943011101). The initial permeability of the Type 43 material is 850. Figure 1 shows the double exposure of a pair of oscilloscope waveforms. The signal displayed on channel 1 comes from one turn on a single ferrite toroid. Channel 3 monitors the current using a current transformer (CT). The "A" traces are the result of having only one toroid on the conductor; whereas, the "B" waveforms are with 14 toroids on the same conductor. Fig. 1 shows that the current pulse through the CT has an 18 percent shorter rise-time using the 14 toroids.

Voltage across the toroid stack can be estimated by multiplying the voltage across one toroid by the total number of ferrite pieces. The voltage across one toroid is greater than 2000 V at the peak and drops to less than 500 volts in 18 ns, a 1500 V change. The
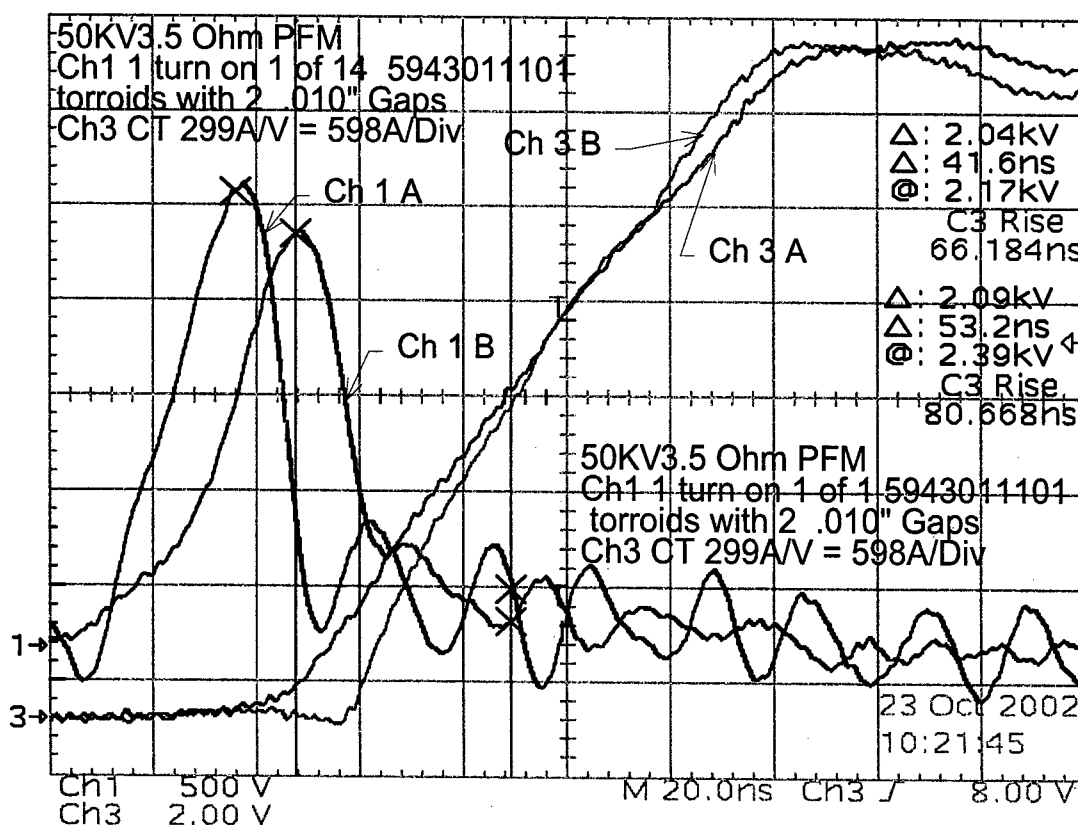
Figure 1 Scope trace from test stand. Ch 3 A is with only one toroid and Ch 3 B is with 14 toroids.

total voltage exceeds 20 KV in less than 20 ns for the 14-toroid stack. Because of the low quality factor for the coax cable transmission line, much of this voltage rise is not seen by the load and is instead dropped across lossy components in the transmission line. Magnet load termination is also an important factor in determining kicker current rise time. Load termination will be discussed in the next section.

The ability of the toroids to improve rise time is a function of their ability to store energy. In this application they will be operated with current passing through them in only one direction. Under this condition, the ferrite tends to become a permanent magnet. The field that remains at the beginning of the pulse, decreases the amount of field change the ferrite can accept before the it goes into saturation. By gapping the ferrite, the residual magnetic field can be reduced. This increases the energy that can be stored each pulse. Figure 2 shows effect of adding a gap to the Ni-Zn toroids mentioned above. Several factors must be considered when choosing a toroid and gap thickness. The ferrite must have a frequency response capable of handling the pulse rise-time being sought. Under high bias conditions, the upper frequency limit of ferrite can be increased slightly. Frequency response requirements limit the permeability of the ferrite to less than 1000. The rise-time of the current is limited by the inductance of the

toroids until saturation is reached. This requires the ferrite to go into saturation at a current low enough not have a significant effect on the circuit. The assumption is made that if the saturation current is below 5% of the peak current, the added inductive loading would not cause a problem for the beam for the one pass through the magnet before extraction. This requires the toroids to saturate at less than 200 A. Figure 2 plots Volt-seconds verses Amps for gapped and ungapped Type 43 toroids. Figure 2 shows that saturation of the gapped toroids occurs between 100 and 200 amperes.

Reading from the graph, each toroid can block the current from rapid rise for about 55 V-μs before going into saturation. During the time before the toroids saturate, the current is being limited by the ferrite and the transmission line voltage is approaching its full voltage. When the toroids saturate their inductance will drop to near zero and the transmission line voltage will be applied to the magnet load system.
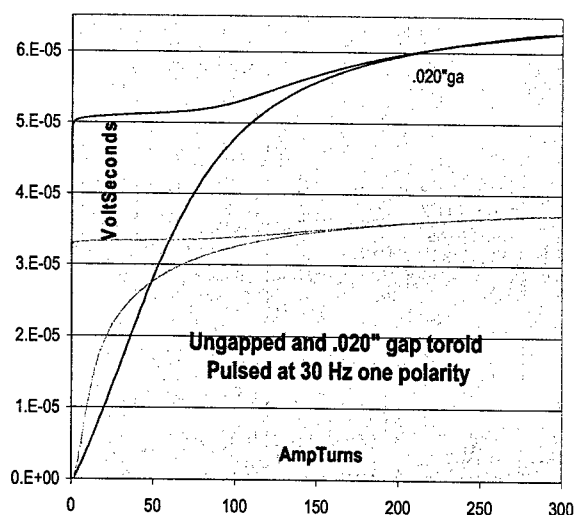
Figure 2 Measurements on 5943011101 toroid shows how many volt seconds can be applied before the toroid saturates.

RCS KICKER SYSTEM

A block diagram of the kicker transmission line, magnet and load shows the new components and where they are installed. The capacitance, C_{Trans}, at the end of the transmission line is 800 pF and C_{Load} is 7500 pF. Five toroids are present on the load capacitor line and nine are placed on the lead between the transmission line and the magnet. In the block diagram all of the circuitry before the feed end of the transmission line has been omitted because of space.

CONCLUSION

It is harder to evaluate the effect on the system that is in operation because of radiation levels and the time required to make changes and take data but improvements have been seen. Initially all of the toroids were between the end of the transmission line and the magnet. Tests showed better results with some of the toroids on the capacitor lead. When considering how many toroids to put on the capacitor lead both the current in the load and the toroid current go through the

magnet. Magnet current should be less than 5% of flat top when the toroids go into saturation. By putting a loop of high voltage wire through one of the toroids the voltage can be measured. The voltage across the toroids on the capacitor lead is lower than the other toroids. There was some overshoot of the current pulse but the rise time of the pulse is faster and the top is flatter after some load tuning. More time will be spent when the new CX1725 system is installed.
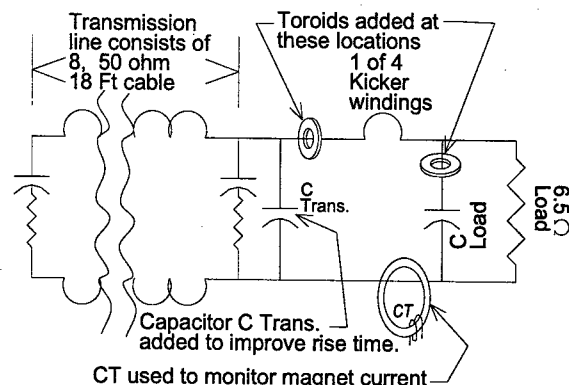
Figure 3 Block diagram of Kicker system including only components from transmission line through load.

REFERENCES

1. D Suddeth, IEEE Trans. Nucl. Science, NS-26, (3024)1979
2. D Suddeth, IEEE Trans. Nucl. Science, NS-28, (3017)1981
3. http://www.pns.anl.gov/
4. J Dooling, Particle Accelerator Conference, New York 1999 p.2274
5. M Middendorf, Particle Accelerator Conference, Chicago 2001 p. 834
6. A. Bruckner, CERN Rept. 68-25 (1968).
7. A. Bruckner, IEEE Trans. Nucl. Sci., NS-18, 976 (1971).
8. G. Nassibian, IEEE Trans. Nucl. Sci., NS-26, 4018 (1979).

THE LHC INJECTION KICKER MAGNET

L. Ducimetière, N. Garrel
CERN, AB Division, CH-1211 Geneva 23, Switzerland

M.J. Barnes, G.D. Wait
TRIUMF, 4004 Wesbrook Mall, Vancouver, B.C., Canada V6T 2A3

Abstract

Proton beams will be injected into LHC at 450 GeV by two kicker magnet systems, producing magnetic field pulses of approximately 900 ns rise time and up to 7.86 µs flat top duration. One of the stringent design requirements of these systems is a flat top ripple of less than ±0.5%. Both injection systems are composed of 4 travelling wave kicker magnets of 2.7 m length each, powered by pulse forming networks (PFN's). To achieve the required kick strength of 1.2 Tm, a low characteristic impedance has been chosen and ceramic plate capacitors are used to obtain 5 Ω. Conductive stripes in the aperture of the magnets limit the beam impedance and screen the ferrite. The electrical circuit has been designed with the help of PSpice computer modelling. A full size magnet prototype has been built and tested up to 60 kV with the magnet under ultra high vacuum (UHV). The pulse shape has been precision measured at a voltage of 15 kV. After reviewing the performance requirements the paper presents the magnet design, emphasizing several novel design features, and discusses the test results.

INTRODUCTION

CERN, the European Laboratory for Particle Physics, is constructing the Large Hadron Collider (LHC), which will bring protons into head-on collisions at an energy of 14 TeV, and heavy ions at 1148 TeV.

The LHC will be located in the 27 km long tunnel that previously housed the Large Electron Positron Collider (LEP), and be filled at 450 GeV through a chain of injector machines. Two counter-rotating beams, which can collide in up to 4 interaction points, will circulate in two horizontally separated channels. Each beam channel will be filled by 12 batches of protons from the Super Proton Synchrotron (SPS), injected successively along the machine circumference from a dedicated injection point. Injection is carried out in the horizontal plane by means of a septum magnet followed by a vertical fast pulsed kicker system.

INJECTION REQUIREMENTS

The beam to be injected approaches the kicker system at an angle of 0.8 mrad, requiring a total kick strength of 1.2 Tm for deflection onto the central machine orbit. The reflections and the flat top ripple of the field pulse must be lower than ±0.5%, a very demanding requirement, to limit the beam emittance blow-up due to injection oscillations. The pulse repetition time is imposed by the duration of the SPS acceleration cycle which is about 18 s. The LHC will be filled with 12 batches of either 5.84 µs or 7.86 µs duration each, to be deposited successively on the machine circumference. This leaves 11 gaps of 0.94 µs to account for the kick rise time and one gap of 3.0 µs for the kick fall time. The latter gap will also be used for the rise time of the beam dumping kickers. Table 1 summarizes the main parameters of the injection kicker system.

Table 1: System requirements and parameters

Number of magnets per system	4	
Kick strength per magnet	0.3	T.m
Magnet beam aperture (diameter)	38	mm
Characteristic impedance	5	Ω
Operating charging voltage (PFN)	54	kV
Field flat top ripple	< ±0.5	%
Field flat top duration	up to 7.86	µs
Field rise time 0.5%-99.5%	0.9	µs
Field fall time 99.5%-0.5%	3.0	µs
Magnet length	2.7	m

MAGNET DESIGN AND CONSTRUCTION

General

A carefully matched high bandwidth system is needed to obtain the stringent pulse response requirements. The system is therefore composed of a multi-cell PFN and a multi-cell travelling wave kicker magnet, connected by a matched transmission line and terminated by a matched resistor. A low system impedance (Z) of 5 Ω has been chosen [1]. Fig. 1 gives the basic circuit diagram.
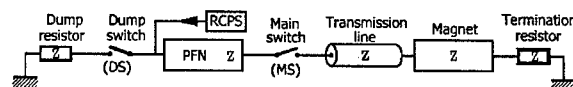
Fig. 1: Schematic circuit of system.

The design voltage is 60 kV, as in most SPS kicker installations, allowing the use of several proven components such as transmission line, connectors and termination resistors. The voltage on the magnet is half of the PFN voltage: allowing for overshoot, the design voltage of the magnet is 35 kV.

Design strategy

The ferrite cores of the kicker magnet have a C-configuration to allow earthing of the coaxial cable input

connection and the output connection to the termination resistor. To achieve a characteristic impedance of 5 Ω, ceramic plate capacitors with contoured rims have been used inside the magnet. The kicker magnet consists of 33 cells, which is a compromise between the bandwidth and the cost. The cell size allows an optimum filling of the 540 mm diameter vacuum tanks reused from the LEP separators. The nominal self-inductance and capacitance of each cell is 101 nH and 4.04 nF, respectively.

In order to minimize beam impedance, while allowing a fast field rise time, a ceramic pipe with silver stripes on its inner wall is placed within the aperture of the magnet. The stripes provide a path for the image current of the beam and screen the ferrite against induced heating [2]. The stripes are directly connected to the standard vacuum chambers of the machine at one end and via a decoupling capacitance of 300 pF at the other end.

Modeling

The electrical circuit of the complete kicker system, including PFN, thyratrons, coaxial cables, kicker magnet and terminators has been optimised using PSpice [3]. The voltage dependency of the terminating resistor has also been modelled. The PFNs were optimised to obtain the required rise time, flattop, fall-time and post pulse field quality, first with an ideal transmission line magnet modelled, and then with a realistic model of the kicker magnet including all known parasitic elements. An input RC network and a capacitor in parallel with the terminating resistor were added and optimised to obtain the required field quality.

Some damping is necessary to minimize the pulse ripple. The ferrite has a quality factor (Q) of 5, but it cannot be considered as being the Q factor of the cell inductance because the latter is defined by the aperture of the magnet. This has been verified by measurement and damping resistors of about 30 Ω have been connected in parallel with each cell inductance to reduce the effective Q. A more efficient damping would affect field rise time.

The mathematical model also includes beam impedance stripes mutually coupled to the self-inductance of the corresponding cell of the magnet [1]. This allows the effect of the stripes upon the field quality to be included.

The predicted magnetic field for the prototype PFN and prototype kicker magnet constructed at CERN was well within the specification, providing allowance for real pulses. The dump switch was turned on during the simulation to define the duration of the field pulse. The predicted rise-time was approximately 820 ns, and the corresponding fall time 2.2 μs. The field flat top varied by almost ±0.3%, a result of already known variations in the diameter of the prototype PFN coils [4]. Detailed measurements made on the series of nine PFNs manufactured at TRIUMF [5] have shown that this problem has been overcome.

Construction

Each of the 33 cells includes 2 ceramic plate capacitors with diameter 210 mm, to arrive at the capacitance of 4.04 nF, including the plate end effect. The capacitors are mounted between the high voltage and ground plates and the connections are ensured by toroidal spring contacts all around the capacitor rims. This electrical contact is critical and depends strongly on a good rim geometry. The high voltage and ground plates are spaced by three ceramic-metal insulators, which together compose an independent cell assembly. Careful design of the mechanical components (distances and radii) aimed at maintaining electrical fields below 5 MV/m.

Fig. 2 shows a schematic cross section of a magnet cell with C-shaped ferrite yoke and 2 ceramic matching capacitors mounted between high voltage and ground plates, and Fig. 3 shows the magnet during assembly.

Ground plate
High Voltage Plate
Matching Capacitors
Vacuum tank ⌀540
Ground Conductor
Metallized Ceramic Tube
Damping Resistor
High Voltage Conductor
Ferrite C-Core
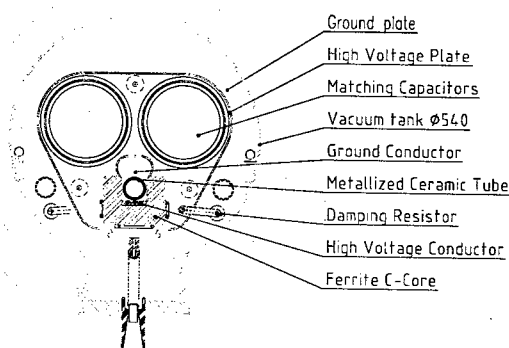
Fig. 2: Kicker magnet cross section
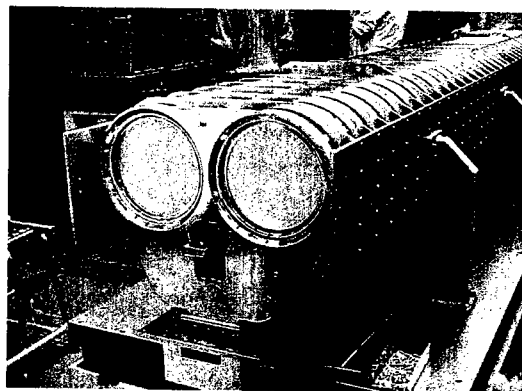
Fig. 3: Prototype kicker magnet during assembly

For stability reasons capacitors are made of class 1 ceramic with relative permittivity between 75 and 90, consisting of a monolithic ceramic with silver layers for the electrodes. Three manufacturers have been qualified in Europe.

Outgassing tests have shown that these ceramic capacitors can be used in UHV. However, their high-voltage behaviour was unexpectedly poor under vacuum, with surface flash-over problems, calling for challenging development work to achieve a reliable operation at full voltage. Successful test results have finally been obtained

1163

by improving two important aspects that drastically affect the voltage holding:

a) The geometry of the transition between the connecting plates and the capacitor has been studied in detail with finite element computer codes. Deflector parts have been implemented to eliminate the electrical field at the triple junction; in addition high voltage and ground plates have been electropolished.

b) The vacuum quality has been improved by bake out at 300°C and vacuum firing on most of the parts of the magnet. Therefore, the magnet has been designed to be bakeable and made of stainless steel, aluminium being unsuitable for such temperature cycles.

Low inductance damping resistors have been developed for UHV compatibility. They consist of two counter-wound Kanthal© wires on a ceramic rod.

The ceramic pipe inside the aperture of the magnet is made from a 3 m long extruded ceramic tube with a wall thickness of 4 mm. The stripes are produced using a printed circuit board technique, but complicated by the access to the inside of the tube. Two layers of silver painting are first applied uniformly inside with bake out at 800°C after each layer. The mask is maintained against the inner wall by vacuum while UV light is passed through the pipe. The decoupling capacitor at one end is obtained using the ceramic tube itself as dielectric. The tube extends outside the magnet on which the outer surface is uniformly silver painted over 200 mm and the inner covered by the stripes, thus giving the capacitance between each stripe and the outer layer. The outer layer is to be connected to the metallic beam tube of the machine.

Test results

A prototype magnet has been built. The vacuum level after bake out was as low as $3 \cdot 10^{-11}$ mbar. The magnet has been successfully tested with $4 \cdot 10^5$ pulses at 60 kV PFN voltage with only two non-destructive breakdowns.
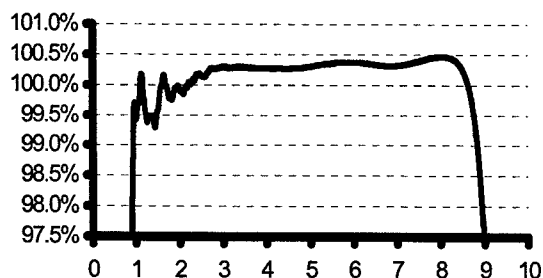
Fig. 4: Measured magnetic field (horiz. scale μs)

After these tests in UHV, the magnet has been pulsed in air at reduced voltage (15 kV) for precision magnetic measurements in the aperture. The measurements have been carried out by means of an inductive loop probe with a precision better than 0.1% [6]. The metallization being not yet realized on the full length ceramic pipe, a metallised mylar film with the final stripe geometry has been installed and connected adequately to represent the final coupling. Fig. 4 shows that the resulting field pulse

just fulfils the stringent requirement. The measured rise and fall times, with dump switch triggered, are 880 ns and 2.7 μs, respectively.

CONCLUSIONS

A large and relatively strong fast pulsed magnet has been designed for the LHC injection and constructed for its specific requirements. The simulation results have shown that it is theoretically possible to achieve the required magnetic field pulse. The mechanical design has been complicated by the need to bake-out the full magnet due to the ceramic capacitors. A prototype of the whole system has been built and tested at CERN at full voltage with the magnet under UHV. Although some parasitic effects have not been identified and incorporated in the equivalent circuit, the magnetic field waveform is within specifications.

The design thus validated, the series construction has been launched and most of the components are in production in industry. The injection test in LHC with beam, using 4 kicker magnets, is foreseen in spring 2006.

ACKNOWLEDGEMENTS

We would like to remember our late colleague John O. Pearce who initiated the mechanical development of this magnet. Many thanks to M. Mayer and B. Riffaud who brought the mechanical design to its final state, to J. Bertin, J. Hurte and J. M. Dury who contributed in the construction and test of the prototype, to E. Carlier and his team who provided the electronics and controls, and to J. H. Dieperink and J. Uythoven for the development of the probe and magnetic measurement method.

REFERENCES

[1] L. Ducimetière, U. Jansson, G.H. Schröder, E.B. Vossenberg, M.J. Barnes, G.D. Wait, "Design of the injection kicker magnet system for CERN's 14 TeV proton collider LHC", 10th IEEE Int. Pulsed Power Conference, Albuquerque, June 1995, pp 1406-1411.

[2] R.L. Gluckstern, L. Vos, B. Zotter, "Shielding Particle Beams by Thin Conductors", CERN-SL-2002-014-AP, May 2002.

[3] Cadence, 2655 Seely Av., San Jose, CA 95134, USA.

[4] M.J. Barnes, G.D. Wait, TRIUMF, E. Carlier, L. Ducimetière, G.H. Schröder, E.B. Vossenberg, "Construction and 60 kV tests of the prototype pulser for the LHC injection kicker system", 12th IEEE Int. Pulsed Power Conference, Monterey, June 1999, pp 777-780.

[5] M.J. Barnes, G.D. Wait, L. Ducimetière, "Low voltage measurements on nine PFNs for the LHC injection kicker systems", 8th EPAC, Paris, June 2002, pp 2520-2522.

[6] J. H. Dieperink, J. Uythoven, "CERN High precision magnetic field measurements of fast pulsed magnets", 12th International Magnet Measurement Workshop, Grenoble, October 2001.

SWITCHING POWER SUPPLY FOR THE PFL KICKER MAGNET

H. Sato, E. Nakamura, S. Murasugi, S. Yamanaka and T. Kawakubo, S.Igarashi, KEK-PS

T. Hatano and N. Shimizu, NGK Insulators LTD, Nagoya
And
A. Tokuchi, Nichicon Corporation, Kusatsu

Abstract

SI-thyristor is expected as a solid-state high power switching semi-conducting device for the kicker magnet in the circular accelerator. Current rise has reached to 100kA/µs. We noticed this characteristic and tried the use it for the pulse forming line(PFL). Preliminary results of the proto-type power supply of 20kV-120ns, with various impedance, although the intention is 75kV-100ns, are presented.

1 INTRODUCTION

Static Induction type semi-conductors were invented by Dr.J.Nishizawa in 1970's [1,2] for diode and transistor. Static induction thyristor (SI-thyristor) is recently noticed as it's superior characteristics for high voltage and high current applications such as,

(1) A low "ON state voltage drop" characteristics.
(2) The high speed switching and low loss characteristic.
(3) The high blocking voltage.
(4) High current rise rate.
(5) High current characteristics.

As consideration these caharacteristics, SI-thyristor is expected as a solid-state high power switching semi-conducting device for the kicker magnet in the circular accelerator. We noticed this characteristic and tried to use it for the pulse forming line (PFL). Although the intention is 75kV-100ns as shown in Table 1, preliminary test of the proto-type power supply of 20kV-120ns with various impedance, has been performed[3].

A solid-state switch is also implemented as the high power switch for the KEKB injection kicker magnet power supply and one of the thyratrons has been replaced to the SI-thyristor [3,4]. The switch has been successfully operated at 20kV voltage, 1.3kA peak current and 2 µsec pulse width under 50 Hz repetition rate.

The use of the solid-state switch in the pulsed magnet must be considered seriously under heavy duty repetition and consideration of the equipment life. Recently research and development using SI-thyristor started in the accelerator field, such as high power switch for the driver of the klystron pulse modulators [5].
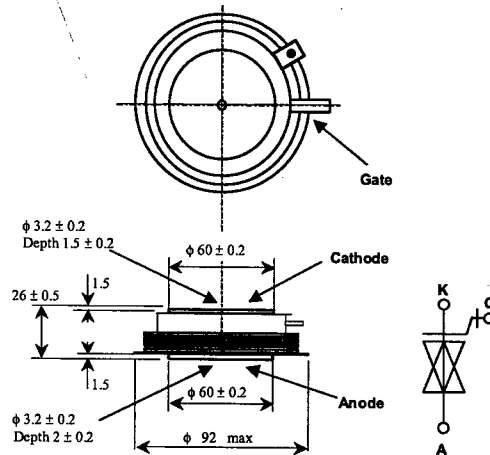
Repetitive peak off-state voltage: 4000V
Reverse conducting type
Non-alloyed Flat-wafer pellet
Press-pack ceramic housing
On-state current: 600A(RMS)
Peak one cycle surge on-state current: 5500A
Critical rate of rise of on-state current: 150kA/µs

Figure 1: Reverse Conducting Static Induction Thyristor Type PS1600PA4071

2 PROTO-TYPE SWITCHING POWER SUPPLY FOR THE PFL KICKER MAGNET

Specification of the kicker magnet parameter for the several hadron accelerator are shown in Table 1. First of all, we performed the test of current rise using a sample, RT103, Toyo-Denki-NGK. Although the catalogue data is 100kA/µs, the current rise was made sure up to 283kA/µs. A 45kV modulator using this device for klystron [5] had been done in advance and we tried to test for the PFL kicker using this module [6]. After the good results, we set about making a R&D module for exclusive use to test the PFL kicker using new type of RS1600PA40T1-NGK as shown in Fig.1. Following the specification as shown in table 1, aim of the proto-type power supply are set as, 70kV of charged voltage, 7kA of output current, 5Ω of impedance, less than 120ns of rise time and 1.1µs of pulse width, but first goal was set as, 20-40kV of charged voltage and current depend on

the impedance between 10 Ω to 50 Ω. Over view of the demonstrated modulator is shown in Figures 2 and 3. Figure 4 shows a schematic drawing of the test circuit of SI-thyristor unit. Deterioration in current rise was observed. This may be considered by the inductance around load resistor and CT and the modification trial using head-up condensers of various capacitor. Results of the load current waveforms, as shown in Figure 5, are satisfy except of the charged voltage. After that, we are going to make the modulator for the 50GeV abort kicker.

Table 1

Pulsed Power Supply for the Kicker Magnet at the KEK-PS and JHF

	Extraction Kicker KEK-12GeV PS	Extraction Kicker 500MeV BSTR	Extraction Kicker JHF-3GeV-RCS	Injection Kicker JHF-50GeV-PS	Abort Kicker JHF-50GeV-PS
Voltage(kV)	+70~-40	65	80	80	40
Current(kA)	+6~-3	1.3	8	8	8
Pulse width(μs)	1.1	0.12	1.2	1.2	6
Current Rise(ns)	80	40	80	70	1,100
Field Rise(ns)	150	70~80	250	250	1,100
Field Fall(ns)		70~80			
Flatness(%)	±1	±1	±1	±1	
Repetition(Hz)	1/2.2	20	25	25pps x 4bursts	1/3.6
Impedance of magnet (Ω)	12.5	25 (distributed magnet)	10 (lumped magnet)	10	2.2μH / 5Ω
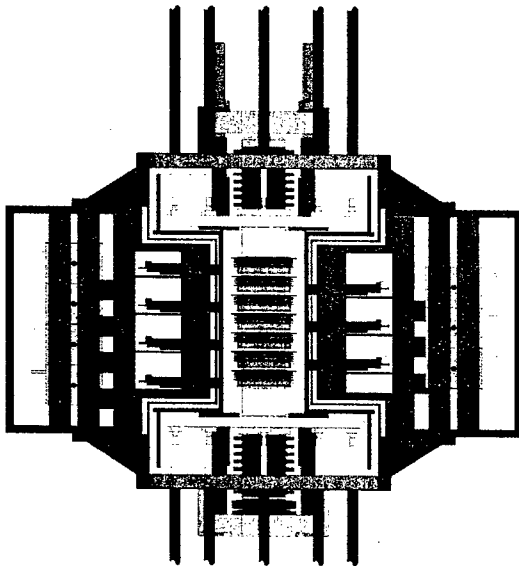
Figure 2: Drawing of seven series SI-thyristor stack.
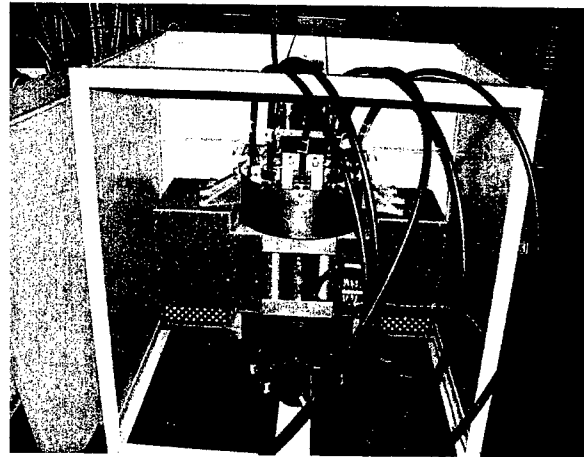
Figure 3: Picture of SI-thyristor module and PFL cable.

* Simple lines with floated cathode SI-thy. unit.
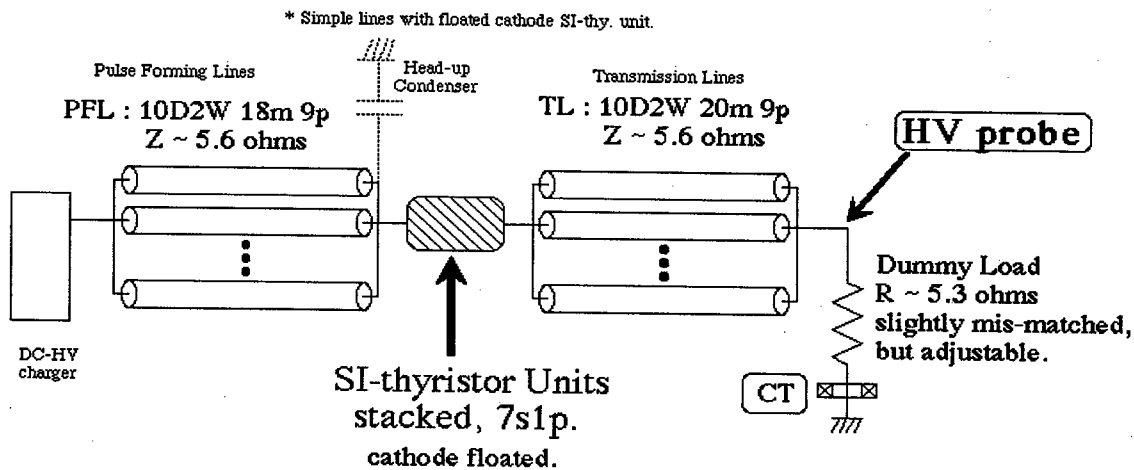
Figure 4: Schematic drawing of test circuit of SI-thyristor.
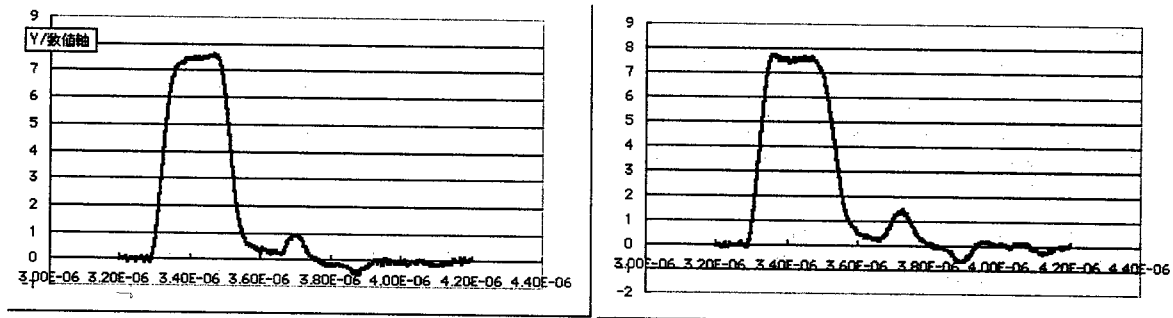
Figure 5: Load current waveforms mearsured by CT
Left: no capacitor, Right: 349PF co-ax. Cables attached

3 CONCLUSION

Prototype power supply for the trapezoidal waveform PFL kicker magnet of 20kV SI-thyristor switch has been successfully performed. Deterioration in current rise due to the inductance around load resistor and CT are improved by using the speed up capacitor. System has been operated under various cable impedance.

In this prototype power supply, SI thyristors are covered by cylindrical cupper and it is hard for maintenaunce. Then, improved type power supply has just made in order to replace the broken SI-thyristor easily and will be tested.

Authours are going to aim the application for the J-PARC 50GeV abort kicker power supply with high speed diode to cut the reflection.

REFERENCES

[1] J.Nishizawa, "Static Induction Devices", Japanese patent. No. 1793126, 1977

[2] J.Nishizawa et al., "Field-Effect Transitor Versus Analog Transistor", IEEE Trans. On Electron Devices ED-22(1975)185-197

[3] H.Sato et al., "Pulsed Power Supply for Kicker Magnet with SI-Thyristors", Proceedings of the International Workshop on Recent Process in Induction Accelerators (RPIA2002), October 29-31, 2002, Tsukuba, Japan. To be printed in KEK-Proceedings #.

[4] T.Mimashi et al, "KEKB Injection kicker magnet system", Proceedings of the EPAC'2000, Vienna, Austria, June 2000

[5] M.Akemoto et al., "High-Power Switch with SI-thyristors for klystron Pulse Modulators", Conference Record of the 2000
Twenty-Forth International Power Modulator Symposium, Norfolk, Virginia,USA (2000) 205.

[6] "Stacked SI-Thyristor Trial to m sec-PFL swiching", ASN-441, March 21 2002, Circular in KEK-PS, written in Japanese

NEUTRON-INDUCED FAILURE TESTS OF 3300-V IGBTS FOR THE SPALLATION NEUTRON SOURCE ACCELERATOR*

D. L. Borovina[#], J. T. Bradley III, M. Pieck, R. S. Przeklasa, T. W. Hardek, M. T. Lynch, D. E. Rees, P. J. Tallerico, W. A. Reass, S. A. Wender, B. E. Takala S. C. Ruggles, LANL, Los Alamos, NM 87545, USA

Abstract

The RF transmitters for the 1-GeV Spallation Neutron Source (SNS) linear accelerator are powered by 15 converter-modulator stations. Each converter-modulator provides pulses up to 11 MW peak power with a 1.1 MW average power to a multiple-klystron load. A low-voltage switching network, comprised of three sets of four IGBTs in an 'H-bridge' configuration, is used to generate the 20 kHz drive waveform components for the three step-up transformer primaries. This setup brings the total number of 3300-volt semiconductor IGBTs operating within the accelerator at 180. When biased to operating voltages of 1500 V or greater, all IGBTs are inherently sensitive to neutron interactions caused by background cosmic ray radiation.

The project described used neutrons produced by proton spallation (with a similar spectrum as cosmic ray neutrons) to gain knowledge of failure mechanisms of the SNS IGBTs. These tests were performed using the highly accelerated neutron flux generated at the Weapons Neutron Research facility at the Los Alamos National Laboratory.

The results of these experiments have shown the existence of a critical threshold voltage that lies within the operational range beyond which the IGBTs are no longer effective. This threshold varied with each brand of IGBT tested. Statistical failure times have also been projected for all brands of IGBT tested under normal biased operation with the SNS accelerator given natural neutron flux in Oak Ridge, TN.

HIGH POWER IGBTS IN THE SNS ACCELERATOR

The RF transmitters for the 1-GeV Spallation Neutron Source (SNS) linear accelerator are powered by 15 converter-modulator stations. Each converter-modulator provides pulses up to 11 MW peak power with a 1.1 MW average power to a multiple-klystron load, as required for the acceleration of the beam.

A low-voltage switching network, comprised of three sets of four Insulated-Gate Bipolar Transistors (IGBTs) in an 'H-bridge' configuration, is used to generate the 20 kHz drive waveform components for the three step-up transformer primaries in each converter-modulator. This setup brings the total number of IGBTs operating at any time to 180.

The operation of each of these IGBTs can be interrupted by random collisions with cosmic-ray-produced neutrons when subjected to the high electric field (collector-emitter voltages) required for their operation. Because of the H-Bridge design, conduction of one IGBT caused by random neutron interaction at the time the opposite IGBT is normally conducting will cause a direct discharge of all capacitor bank energy through both IGBTs, causing a disastrous failure, or a 'shoot-through' fault, as shown in Figure 1.

Figure 1: Example of IGBT failure during recent acceptance tests.

Any such interruption will take down the entire accelerator, causing costly down time for the entire facility.

The converter-modulator is designed to not permit accidental turn-on of adjacent IGBTs. A random turn-on, however, caused by a high-energy cosmic neutron will not be detected. The current passing through each IGBT is also monitored, and the control system is designed to shut down all power and discharge the capacitor bank if an anomaly is detected. However, because of its reactive

nature, this system will not protect the IGBTs, but merely avoid secondary damage.

It was therefore imperative that the impact of random neutron interactions with various IGBT systems and a predicted failure behavior be studied in depth.

COSMIC-RAY-INDUCED NEUTRONS AND HIGH-POWER SEMICONDUCTORS

Solar and galactic cosmic rays collide with nuclei in Earth's upper atmosphere and create a shower of subatomic particles, including neutrons. A small percentage of these neutrons can penetrate the atmosphere and reach low altitudes, where they can interfere with operating semiconductor electronics. These effects are noticeable especially for miniature devices on one end and high-power semiconductors on the other.

In high-power devices, such as the SNS IGBTs, a neutron interaction with the semiconductor material produces one or more charged particles, which are accelerated by the high electric field and create secondary charged particles, causing a particle avalanche which allows the device to draw large currents and be destroyed. The failure rate increases dramatically above a critical threshold voltage that is significantly lower than the rated voltage of the device.

Weapons Neutron Research (WNR) Facility: The ICE House

Because neutrons are produced at the WNR LANSCE Facility by the same basic process as in the atmosphere (proton spallation), the neutron spectrum is similar to the neutron spectrum produced by cosmic rays in the atmosphere, as shown in Figure 2.
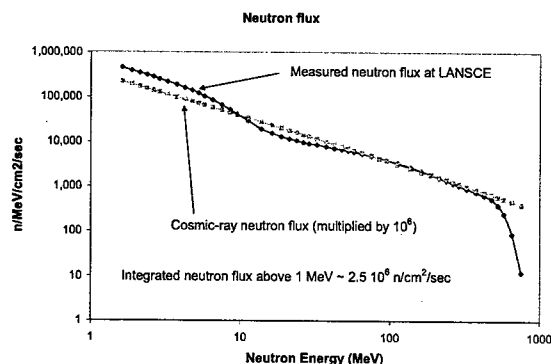
Figure 2: A graphical comparison of cosmic neutron spectrum vs. LANSCE spallation-produced spectrum.

Because ICE House beam intensity is approximately 10^6 times greater than the flux at aircraft altitudes, one hour of testing is equivalent to over 100 years of natural flux testing. The neutron beam used for these experiments consists of 625-microsecond pulses at 100 Hertz and covers an 8-cm diameter area, enough to shower an entire IGBT uniformly. Thanks to the design of the testing facility at WNR, all IGBTs tests were performed in air within easy reach of data acquisition equipment.

TEST SETUP AND DATA ACQUISITION

The objective of the experiment was to use neutrons produced by proton spallation (similar to the process taking place in the atmosphere by cosmic rays) to gain knowledge of failure mechanisms of the SNS IGBTs at a highly accelerated neutron flux.

During the experiment, we monitored and recorded:
- leakage current, collector-emitter voltage, heat sink temperature, neutron beam energy;
- the time to failure for identical IGBTs at a full range of collector-emitter voltages;
- the time to failure (single effect gate rupture) for different manufacturers' IGBTs subjected to different operational voltages;
- current spikes as precursors to gate rupture, using current detectors and digital oscilloscopes.

The IGBTs being tested were placed directly into the path of the neutron beam, and a voltage differential applied between the collector-emitter gap of up to 3000 V, simulating normal operation. All parameters and data were monitored continuously and stored into a hard disk for later reduction.

The neutron flux was monitored using a thin film detector as well as directly by monitoring the neutron interactions inside the IGBT. Figure 3 displays a direct measurement of the neutron interaction inside the semiconductor (top trace) and signals from the monitoring chamber (bottom trace), which was used statistically to predict neutron density.
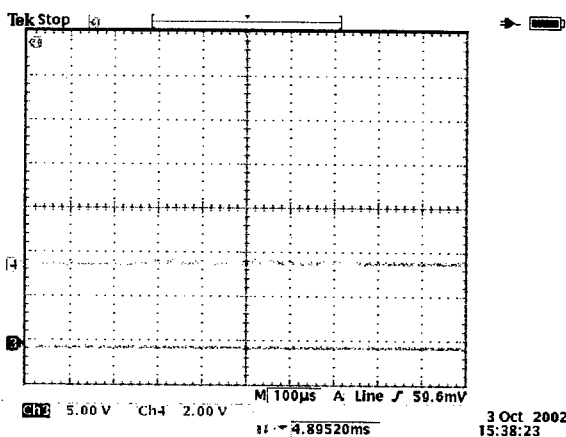
Figure 3: A direct measurement of neutron interactions inside the IGBT (top) and the detector chamber (bottom).

When charges caused by one or more interactions were accelerated by the electric field, starting an avalanche, a noticeable drop in power supply voltage and a corresponding rise in current were observed, signaling the shorting of the IGBT and its final failure. In these experiments, the power supply was current limited, limiting the physical destruction of the IGBT, but at full

operational current, the damage created would closely resemble that pictured in Figure 1.

The IGBTs tested were multiple elements of the following types:

- Dynex Semiconductor DIM1200ESM33-A000,
- Mitsubishi CM1200HB-66H,
- EUPEC FZ 1200 R 33 KF2,
- EUPEC FZ 1200 R 33 KL2 and KL2 ENG.

TEST RESULTS

Failure curves were obtained for each device by monitoring the time to failure at increasing bias voltages. Multiple IGBT test subjects showed great consistency, providing a minimum failure voltage above which the H-field across the emitter-collector gap is large enough to accelerate randomly-created charges to avalanche speed, destroying the device. An example of one such failure curve is shown in Figure 4. These findings indicate that during operation above this threshold the IGBTs are susceptible to random cosmic neutron interactions.
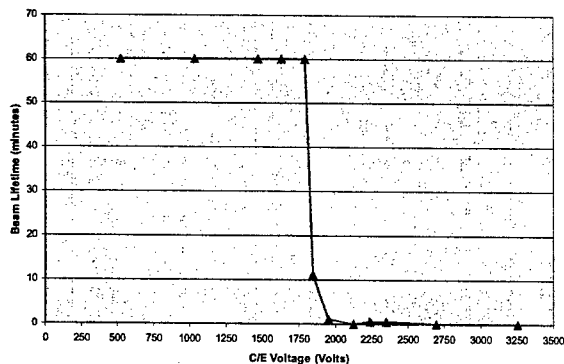
Figure 4: A failure curve for one of the brands of IGBTs tested.

Similar tests were performed while the IGBT cooling plate was artificially heated to normal operational temperature (60°C). No difference was observed in the resulting failure curve.

Consistent failure curves were obtained for all types of IGBTs available, and specific thresholds were obtained for each, all within a bias voltage range of 1500 V to 2300 V, well within their operational specifications.

Lifetime Projections for SNS-Specific Operation

Given the known neutron flux in the WNR beam, its ratio with the flux of natural cosmic-ray induced neutrons, and the average flux at the SNS site in Oak Ridge, Tennessee, lifetime predictions were obtained to assist in the maintenance procedures and expectations.

When the converter-modulator capacitor banks are charged, the IGBTs are biased to full voltage and susceptible when not switching. Since regular IGBT operation for all SNS Converter-Modulators takes place at up to 1,200 V, there are no expectations of reliability problems, as long as the voltage stays below the knee of the curve.

However, during a typical pulse, because of the H-bridge design for the IGBT switching network, each IGBT is biased to twice the voltage for periods of 25 microseconds (or less), at 20 kHz, during each 1.3 ms SNS 60-Hz pulse. During regular, full-power (5-MW klystron) operation, the duty factor for exposure to potential neutron damage at 2400V is 3.9%. In other words, every 100 minutes of normal pulsed operation the IGBTs get 3.9 minutes of double-voltage exposure.

From the data obtained in these experiments, lifetime expectancies of each IGBT during normal SNS pulsed operation ranged between 13 and over 2500 calendar days. This means that, with the best device tested, reliability calculations project that, due to the multiple converter-modulators having multiple IGBTs, a random failure is expected statistically about every 90 calendar days, unrelated to ageing of the devices or any other failure mechanisms.

CONCLUSIONS

The failure curve for the lifetime vs. voltage was established for each available IGBT. The failure rate increases very dramatically past a certain voltage within the operational range.

It was established that the IGBT device least susceptible to cosmic-ray induced neutrons is the EUPEC KL2. Based on these results, SNS IGBT selection has already been changed to the KL2.

Statistical lifetime projections for normal operations of the SNS accelerator were obtained, given no other failure modes.

REFERENCE

B. Takala, S. A. Wender, "Accelerated Neutron Testing of Semiconductor Devices", http://int.lanl.gov/orgs/nmt/news/index.shtml.

ELECTRICAL BREAKDOWN STUDIES WITH MYCALEX INSULATORS*

W. Waldron, W. Greenway, S. Eylon, E. Henestroza, S. Yu
Lawrence Berkeley National Laboratory, Berkeley, CA 94720, USA

Abstract

Insulating materials such as alumina and glass-bonded mica (Mycalex) are used in accelerator systems for high voltage feedthroughs, structural supports, and barriers between high voltage insulating oil and the vacuum beam pipe in induction accelerator cells. Electric fields in the triple points should be minimized to prevent voltage breakdown. Mechanical stress can compromise seals and result in oil contamination of the insulator surface. We have tested various insulator cleaning procedures including ultrasonic cleaning with a variety of aqueous-based detergents, and manual scrubbing with various detergents. Water sheeting tests were used to determine the initial results of the cleaning methods. Ultimately, voltage breakdown tests will be used to quantify the benefits of these cleaning procedures.

INTRODUCTION

Glued Mycalex insulators have been used in the induction cells and the injector column of the second axis of the Dual Axis Radiographic Hydrodynamic Test (DARHT) facility at Los Alamos National Laboratory [1,2]. Mycalex samples were tested in vacuum to determine the electrode geometry and the acceptable fields at the insulator triple points. The effect of oil contamination on voltage holding, and cleaning methods have also been considered.

HOCKEYPUCK TESTS

Test #1

The pulser used for these tests was an RC discharge circuit with a time constant of 24 ms. In this configuration, the insulators were glued between "flowerpot" electrodes to lower the fields at the insulator triple points (Figure 1). For a peak test voltage of 90 kV, the peak field at the electrode is 125 kV/cm (Figure 2). The observed voltage breakdowns around 90 kV were between the two electrodes (0.48" gap) and not along the insulator surface. The electrodes did condition to hold 90 kV.
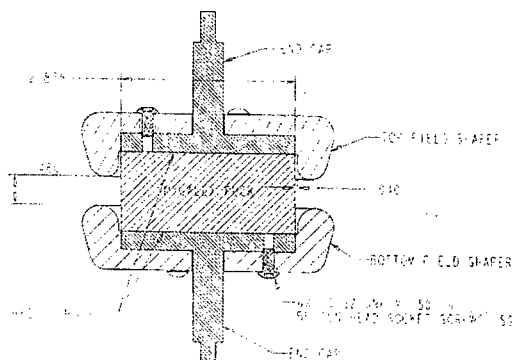
Figure 1: Test #1 insulator and electrode configuration.
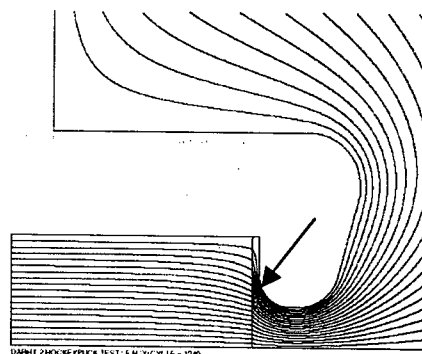
Figure 2: Test #1 electric field distribution with the arrow pointing to the highest field region.

Test #2

In this configuration, the insulators were glued between flat electrodes which created a uniform field of 30 kV/cm on the insulator surface for a 100 kV test voltage. The insulator held above 100 kV and there were no breakdowns.

Test #3

In this configuration, the insulators were glued between rectangular electrodes which hung over the insulator sample to create a triple point with a field of 200 kV/cm for a 110 kV test voltage (Figure 3). This sample was tested to 110 kV without any voltage breakdowns.
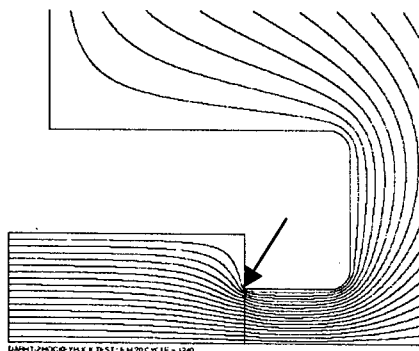
Figure 3: Test #3 electric field distribution with the arrow pointing to the highest field region.

Test #4

In this configuration, the insulators were glued between shaped electrodes which hung over the insulator sample to create a triple point with a field of 110 kV/cm for a 40 kV test voltage (Figure 4). This sample broke down above 40 kV.
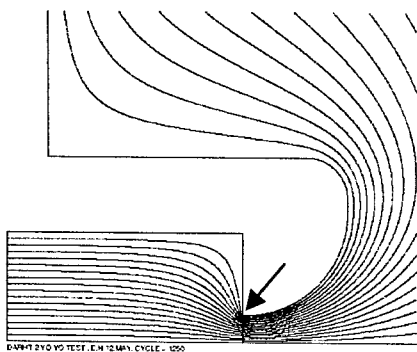
Figure 4: Test #4 electric field distribution with the arrow pointing to the highest field region.

CLEANING PROCEDURES

A variety of cleaning methods were tested to remove Shell Diala AX transformer oil from Mycalex insulators. An in situ approach was developed for large insulators which are part of an assembly and an approach involving the removal, cleaning, and replacement was developed for small removable insulators. Aqueous-based cleaners were chosen for their ease of use, safety, and effectiveness [3,4].

Manual In Situ Procedure

Contaminated insulator samples were scrubbed for three minutes with clean 3M Scotchbrite maroon pads

that were wetted with the detergent being tested. During three minute cleaning cycles, additional detergent was added to the pad as needed to maintain effectiveness. After 3 minute cleaning cycles, the samples were rinsed with 18 Mohm deionized water and checked for beading or sheeting on the surface. If beading was noted (oil still present on surface), the cycle was repeated until sheeting was present. Sheeting of the 18 Mohm deionized water was used as the main criteria for cleaning effectiveness. Fresh Best N-Dex Nitril gloves and Scotchbrite pads were used for each cleaning cycle to eliminate cross contamination. Pads were not dipped in detergent mix but were sprayed to eliminate cross contamination. Detergents were heated to approximately 135 degrees F for the cleaning cycle. The Wyndotte 909 detergent was more effective than the Metalube BlueGold detergent and the VWR Labtone detergent. On average, the Wyndotte 909 detergent took three cleaning cycles compared to four cleaning cycles for the other detergents.

Ultrasonic Cleaning Procedure

The contaminated insulator samples were placed in a beaker with heated detergent and run for 15-30 minutes in the ultrasonic bath. After the cleaning cycle, the samples were removed with tongs and rinsed with deionized water and checked for sheeting. The cycle was repeated until sheeting was noted on sample. As before, the Wyndotte 909 detergent was more effective than the Metalube BlueGold detergent and the VWR Labtone detergent. On average, three cleaning cycles were required using the Wyndotte 909 detergent.

FUTURE HIGH VOLTAGE TESTS

Grade 400 Mycalex cylinders and cones have been purchased and will be tested for voltage breakdown after the various cleaning procedures have been performed. The cylinders have a 1" diameter and are 1" tall. The cones are 1" tall and have a 3.75" diameter on one end and 0.6" diameter on the other end. The surface of the cone is at a 30 degree angle. Cylinders and cones will be tested to quantify the "angle effect" on voltage holding. Using a 50 ohm thyratron-switched pulse forming network into a 1:8 step-up transformer with a matched resistive load, high voltage testing will be done to quantify the benefits of the various cleaning procedures. The maximum test voltage is 160 kV for a 700 ns pulse (FWHM) (Figure 5). 160 kV will produce peak fields of 63 kV/cm on the cylindrical sample and 260 kV/cm on the conical sample. Voltage flashovers across the insulator surface will be detected using the voltage waveforms and the vacuum gauge.
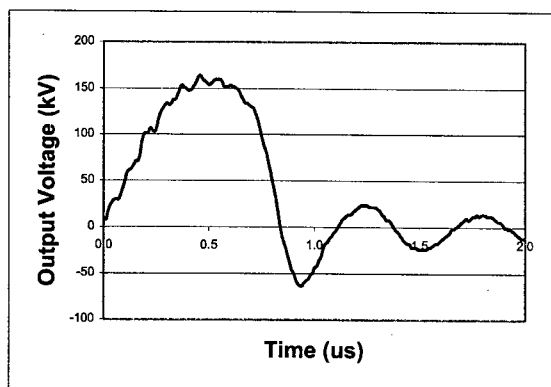
Figure 5: Output voltage for breakdown tests.

These insulators will be contaminated with Shell Diala AX transformer oil and will be cleaned using the various procedures. The insulators will then be glued to stainless steel disks using Hysol EA 9359.3 epoxy. By gluing the insulators to these "disposable" disks which insert into the high voltage electrodes, the need to polish the large electrodes between insulator tests will be eliminated (Figures 6 and 7). This configuration also tests the performance of insulator glue lines.
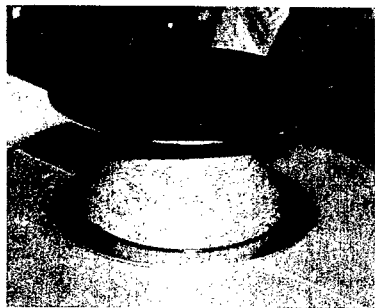
Figure 6: Mycalex cone glued to "disposable" stainless steel disks.

Figure 7: Mycalex cylinder between test electrodes.

CONCLUSION

In the most successful geometries, the Mycalex hockeypuck insulators achieved between 110 kV/cm and 200 kV/cm fields at the insulator triple points without voltage breakdown. These numbers were unexpectedly high and may not hold when tested for better statistics. Both manual and ultrasonic insulator cleaning procedures after oil contamination were established. Wyndotte 909 detergent was the most effective per the sheeting tests. Future high voltage breakdown tests will quantify the electrical benefits of the various cleaning methods.

REFERENCES

[1] C. Ekdahl et al., "DARHT II Commissioning Results", proceedings from this conference.
[2] Mycalex is the trade name for glass-bonded mica made by Spaulding Composites Co.
[3] J. Shoemaker et al., LLNL report UCRL-ID-115831 (1994).
[4] J. Geurtin, internal LBNL document (1994).

A CRITICAL ANALYSIS OF IGBT GEOMETRIES, WITH THE INTENTION OF MITIGATING UNDESIRABLE DESTRUCTION CAUSED BY FAULT SCENARIOS OF AN ADVERSE NATURE*

G. E. Leyh, SLAC, Menlo Park CA 94304 leyh@slac.stanford.edu

Abstract

Megawatt class Insulated Gate Bipolar Transistors [IGBTs] find many uses in industrial applications such as traction drives, induction heating and power factor correction. At present, these devices are not optimized for higher speed pulsed-power applications, such as kicker magnets or klystron modulators.

This paper identifies fundamental issues that limit the dI/dt performance of standard commercial packages, and investigates several IGBT design optimizations that significantly improve high-speed performance at high peak power levels.

The paper presents design concepts, results of electromagnetic simulations, and performance data of actual prototypes under high dI/dt conditions.

INTRODUCTION

The prototype 8-Pack modulator for the Next Linear Collider employs an array of commercial 3.3kV IGBT's [Mfr 'A'] for the primary drive stages. Early prototype testing has shown that these IGBTs are susceptible to damage from hard arcs in the 500kV output circuit. A number of failed IGBT's were carefully dissected and analyzed, in order to determine the mechanisms of failure.

Datasheet specifications for the Mfr 'A' IGBT:

V_{CES}	3300V
I_C	800A
I_C [1mS]	1600A
I_{SC} [10uS]	4000A [at 15V V_{GE}]
$V_{CE\ sat}$ [800A]	3.40V

Measurements have shown that peak IGBT currents can exceed 15kA during an arc, with risetimes greater than 10kA/uS. Ideally, the IGBT is supposed to come out of saturation around 4000A (with 15V gate drive) and self-limit its fault current to somewhere around that level.

ANALYSIS OF THE IGBT GEOMETRY

In order to cleanly open the failed units for inspection, an arbor press was used to separate the outer casing from the internal IGBT structure, using a machined support fixture to preserve the internal die substrate and the busbars of the IGBT.

The Mfr 'A' IGBT design employs 16 total IGBT dies and 8 anti-parallel diodes. **Figure 1** shows the placements of the dies. Four separate 'rafts' carry 4 IGBT dies and 2 diode dies each. Positions indicated by 1A - 4D are the

IGBT dies, and the 8 blank squares show the anti-parallel diode locations. The emitter and collector busbars connect to the 4 die rafts at points marked by 'E' and 'C'.
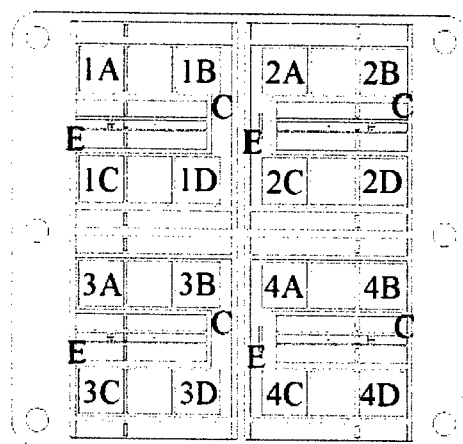
Figure 1: Internal Layout of the Mfr 'A' IGBT.

The points of failure on the actual dies are readily observable. In several cases the entire die is fragmented and blown clear of the pad. The failed die positions are summarized in **Table 1** below, for six failed units:

Table 1: Damage Summary

Die Position	# Of Observed Failures
1C	5
2C	4
3A	2
4C	2

Several patterns are readily apparent in the die failures:

- Dies tend to fail closest to the Emitter terminal.
- Dies tend to fail on the lower half of the raft.
- Dies tend to fail in the upper half of the IGBT.

It is also important to note that on **every** damaged die found, the point of failure was located in the half of the die closest to the emitter busbar.

Each of these four tendencies has the potential for reducing the available silicon by up to 50% during a fault. The aggregate reduction of available silicon from all four effects could therefore be as high as 87.5%. Such an acute constriction of the IGBT's active silicon area would in effect violate the Short Circuit Safe Operating Area by many times during a fault.

EM CURRENT DENSITY SIMULATIONS

Figure 2 shows two EM simulations, with current density profiles for the Mfr 'A' and Mfr 'B' internal IGBT bonding wires and busbars during fast dI/dt conditions. The conductivity of copper is assigned to all conductors. A thin red rectangle around a conductor path indicates where the specified dI/dt is injected. Only half of each complete IGBT module is modeled here, since each module uses two identical sections. The typical matrix computation time for each simulation was approximately 4 hours.

The 8 IGBT dies shown in the Mfr 'A' IGBT have emitter-bonding wires daisy-chained across them, towards the busbars at the center. The hot spots of calculated current density seen on the bonding wires appear to correlate well with the observed damage locations outlined in Table 1 and Figure 1. The simulation also predicts that the portions of the dies closest to the emitter busbars carry the greatest load, by a wide margin.

MAXWELL 3D POST PROCESSING
MFR 'A' 400A BUSBAR ASSEMBLY

G. LEYH 21 AUG 02

dI/dt = 7578A/uS

MAXWELL 3D POST PROCESSING
MFR 'B' 400A BUSBAR ASSEMBLY

G. LEYH 21 AUG 02

dI/dt = 7564A/uS
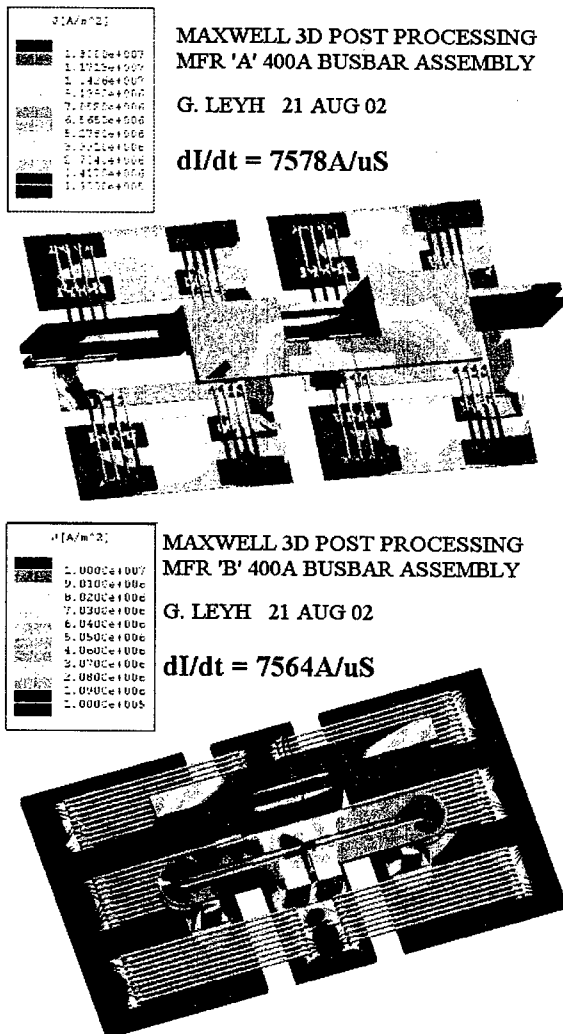
Figure 2: IGBT Mfr 'A' and 'B' current density patterns.

The centralized emitter plate and the long bonding wires of the Mfr 'B' IGBT greatly enhance its current uniformity, as seen in the simulation. Unfortunately this particular IGBT employs a PT silicon technology with a long turn-off tail -- too slow for the NLC application.

A number of design ideas naturally flow from these results. One is a radially symmetric geometry, with a low inductance buswork. **Figure 3** shows the simulated performance of this design. Note that the range of current densities in the bonding wires is less than a factor of two.

MAXWELL 3D POST PROCESSING
RADIAL 3.1 RAFT/BUSBAR ASSEMBLY

G. LEYH 21 AUG 02

dI/dt = 9347A/uS
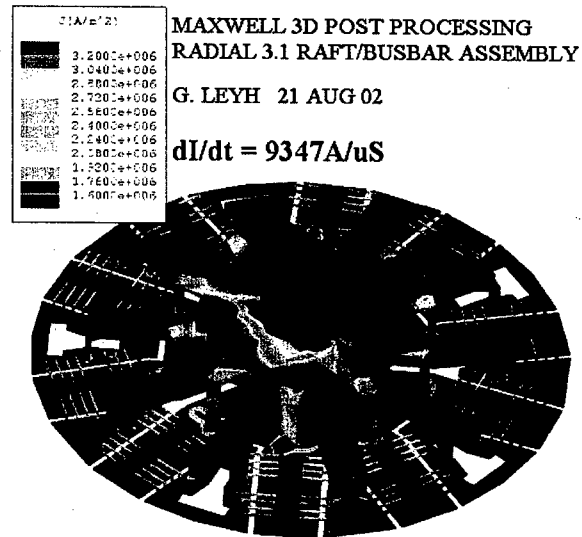
Figure 3: Radial IGBT current density patterns.

Another design concept, though not quite as optimized as the radial approach, is the rectilinear arrangement shown in **Figure 4.** This design has the advantage of improved manufacturability, and compatibility with existing IGBT module footprints. As can be seen, the loss of current sharing performance is minimal. The large blue rectangle in the center is a central emitter summing plate. The green bar represents a parallel plate feed line.

MAXWELL 3D POST PROCESSING
RECTILINEAR 5.2 RAFT ASSEMBLY

G. LEYH 21 AUG 02

dI/dt = 9263A/uS
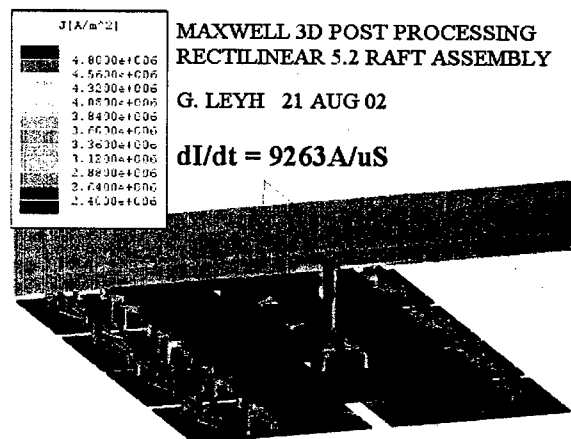
Figure 4: Radial IGBT current density patterns.

PROTOTYPE DESIGN

To evaluate real-world performance parameters, SLAC produced a number of IGBT module prototypes based on the rectilinear concept, using both 3.3kV and 6.5kV IGBT dies provided by Mfr 'A'. The mechanical design of the die substrates, buswork and packaging was performed in-house, based on the simulation results. **Figure 5** shows an exploded isometric view of the prototype IGBT module.
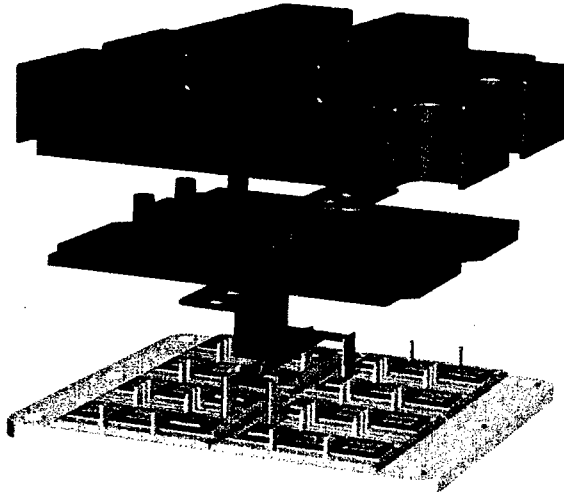
Figure 5: Rectilinear Prototype IGBT assembly.

This design features a number of optimizations for surviving high dI/dt fault events. The emitter bonding wires leave the dies to each side symmetrically and terminate at a single point, minimizing voltage gradients across the die. The large emitter summing plate (green) equalizes the emitter branch inductances. Singular main terminals for the emitter and collector minimize the effects of external circuit current paths on the internal distribution of currents. High-speed active clamp circuitry located at each raft stabilizes the gate voltages against the Miller capacitance during a severe fault.

PROTOTYPE EVALUATION

The test fixture for evaluating IGBT fault performance utilizes a large tape-wound magnetic core with a single turn winding as the test load. A secondary winding attached to a resistive load sets the nominal output pulse current. The core is biased to saturate at some point during the output pulse, thereby producing a near short-circuit condition.

Figure 6 shows the response waveforms for the Mfr 'A' IGBT. The steep rise in current [green] marks the onset of core saturation, about 3uS into the pulse. The IGBT should self-limit to about 2000A at this gate drive level, but internal effects such as the unbalanced emitter bus inductances and the current pinch effects mentioned earlier force the internal gate voltages to vary widely, resulting in a very non-uniform response of each internal die to the fault currents.
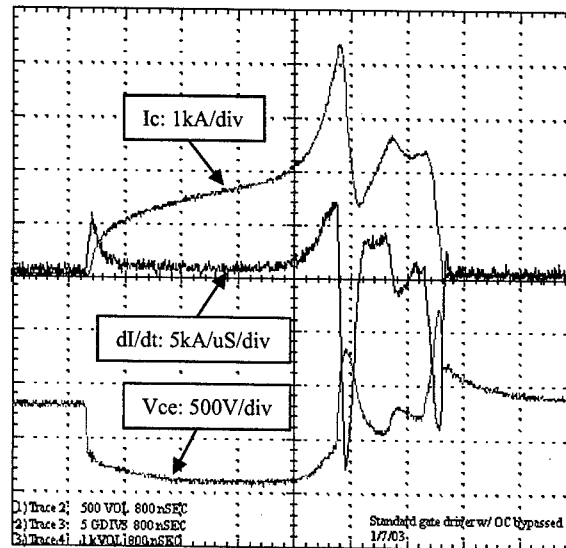
Figure 6: Fault waveforms for the Mfr 'A' IGBT.
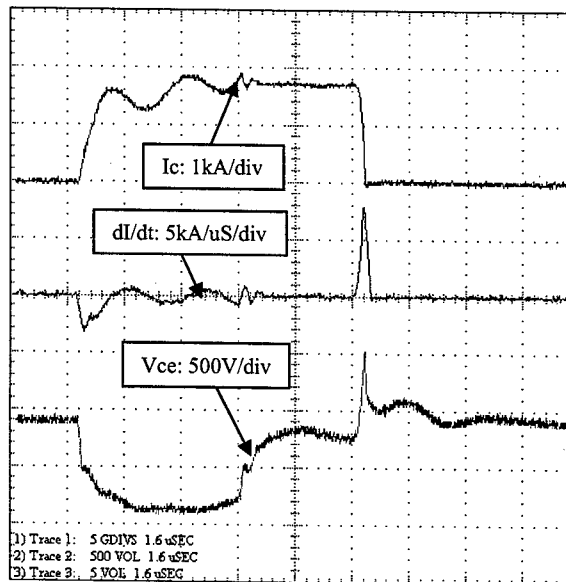
Figure 7: Fault waveforms for the SLAC Prototype IGBT.

Figure 7 shows the prototype IGBT operating at roughly the same Vce and output current. The core saturates around 4uS, as can be seen by the rapid rise in Vce [red]. As the impedance of the load approaches a short circuit, the IGBT current flattens around 1800A and Vce approaches the bus voltage. The current overshoot is minimal, owing to the more even current distribution in the emitter buswork and the placement of active gate clamping circuits directly at each of the four internal rafts.

ACKNOWLEDGEMENTS

FAST-FERRITE TUNER OPERATION ON A 352-MHZ SINGLE-CELL RF CAVITY AT THE ADVANCED PHOTON SOURCE*

D. Horan, E. Cherbak

Argonne National Laboratory, Argonne, IL 60439

Abstract

A 352-MHz fast-ferrite tuner, manufactured by Advanced Ferrite Technology, was tested on a single-cell rf cavity at the Advanced Photon Source. Low-power rf testing was performed on the tuner-cavity combination to evaluate tuning range, bandwidth, stability, and compatibility with existing Advanced Photon Source low-level rf hardware. The test system comprises a single-cell copper rf cavity, a bipolar DC bias supply for the ferrite tuner, a water flow and temperature metering and interlock system, and a low-level rf cavity tuning loop consisting of an rf phase detector and a PID amplifier. Test data will be presented.

INTRODUCTION

A 350-MHz fast-ferrite tuner, manufactured by Advanced Ferrite Technology, was purchased by the Advanced Photon Source (APS) RF Group in 1996 for evaluation as an rf cavity tuning device. Several potential applications for this tuner were considered, based on the fast tuning speed that such a device could deliver. Two of the main applications involved using the fast tuner in conjunction with a standard motor-driven piston tuner, thereby gaining the following advantages: [1] eliminating unnecessary rapid motion of the mechanical tuner, reducing the wear on mechanical tuner components and improving their operational lifetime, and [2] providing compensation for fast beam-loading effects. Operational experience with the APS rf systems has shown that both advantages factor more in the operation of the 7-GeV booster synchrotron 5-cell cavities than in the case of the storage ring single-cell cavities. Software controls were implemented in the mechanical tuner drive systems to eliminate unnecessary motion over the synchrotron ramp, but severe beam loading at injection is still a performance issue with the APS booster synchrotron. Improving control of cavity phase during the injection period would enhance capture and injection efficiency [1]. A fast-ferrite tuning device could be used in conjunction with the existing mechanical piston tuners to glean both advantages.

The ferrite tuner internal design consists of a ferrite-loaded, short-circuited coaxial transmission line, where the electrical length of the tuner is controlled by the amount of magnetic bias field impressed on the ferrite material. This bias field is generated by a combination of permanent and electromagnetic sources, with the electromagnetic bias coils consisting of parallel AC and DC paths. The tuner has a power handling capability of 150 kilowatts, and full tuning range can be achieved by varying bias current over a range of ±100 amperes.

LOW-POWER RF TEST CONFIGURATION

The ferrite tuner test setup is shown in Figures 1 and 2. A 352-MHz, single-cell, copper cavity, identical to cavities used in the APS storage ring, was fitted with a conventional mechanical piston tuner (manually adjusted for coarse tuning adjustments) and two one-turn coupling loops. One loop is used to couple incident power to the cavity and is adjusted for best match into 50 Ω (Zo). The other loop couples the ferrite tuner to the cavity and is adjusted to be perpendicular to the cavity fundamental mode magnetic field to achieve maximum coupling. Both coupling loops are identical to those used in the APS storage ring, designed to form immediate transitions to a WR2300-half-height waveguide. Waveguide-to-N-type coaxial transitions are used on both cavity coupling loop waveguide flanges to allow a coaxial connection to incident power and the ferrite tuner. For high-power rf applications, the rf connection to the ferrite tuner is made utilizing 6-1/8″ coaxial line (see Fig. 1). However, to facilitate low-power rf testing, the opposite end of the directional coupler was fitted with a 6-1/8″-to-N-type transition to allow for a manual coaxial phase shifter to be installed between the tuner and the cavity (see Fig. 2).
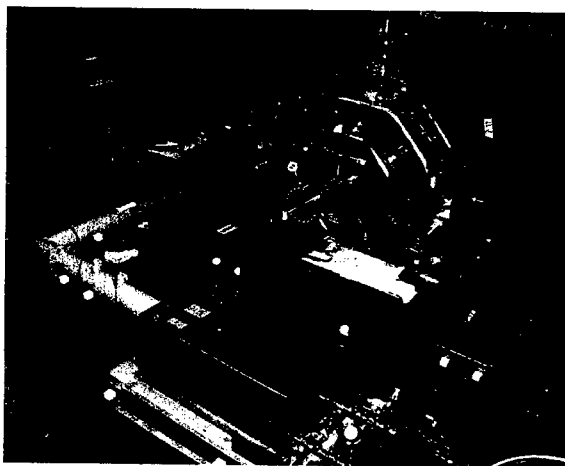
Figure 1: Photo of test setup.
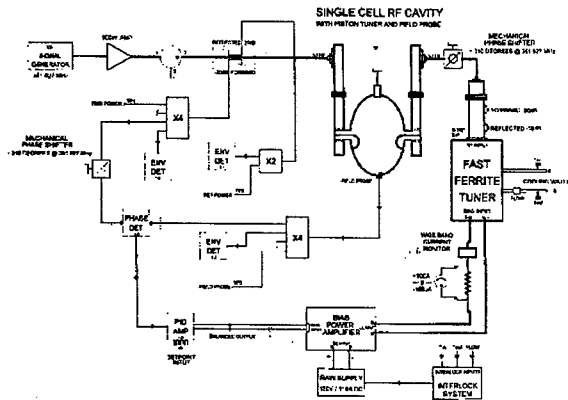
Figure 2: Schematic of test setup.

The test setup low-level rf system utilizes standard VXI-based rf components, identical to those used in the APS 350-MHz rf systems. An analog rf phase detector and PID amplifier are used to form a tuning loop across the cavity to maintain a constant phase relationship between the cavity forward power and field probe output. The output of the PID amplifier is used as the input control signal for the ferrite tuner bias supply. A 100-W, 350-MHz rf amplifier is used to develop sufficient input power for the cavity. The ferrite tuner bias current is generated using a model 232P power amplifier manufactured by Copley Controls Corporation, which can deliver ±120 amperes continuous output current and has a 3-dB bandwidth in current mode of 5 kHz. The power amplifier is supplied raw DC power from a regulated DC power supply capable of 100 amperes @ 150 volts DC. An rf and DC interlock system, necessary for high-power rf operation, is used to protect the tuner against rf arcing, insufficient cooling water flow, insufficient cooling air flow, and excessive return water temperature.

TEST RESULTS

The first test involved using a control system analyzer to measure the ferrite tuner relative rf phase shift while modulating the tuner bias current with a frequency-swept sinusoid stimulus signal, without the tuner being connected to the cavity. For this test, a 100-W, 350-MHz power amplifier was used to drive the tuner rf input at approximately 50 watts. The relative amount of rf phase shift generated by the tuner was detected using a resistive splitter to combine the forward and reflected signals from a directional coupler in-line with the tuner input, then peak-detecting the output of the splitter. The ferrite tuner bias supply was operated with a raw DC input of 90 volts, and the bias current was sine-modulated by the control system analyzer from 100 Hz to 10 kHz for the swept-frequency measurement. The sinusoidal stimulus signal amplitude for the test was 1.75 volts peak, an amplitude which produced ±50 A peak of tuner current when applied to the bias supply input under DC conditions, ±1.75 V. The results of this test are shown in Fig. 3. The upper trace (channel 1 input) is the tuner bias current, and the lower trace (channel 2 input) is the resulting rf phase shift

generated by the tuner. These tests indicate that the tuner phase shift frequency response is being limited to some degree by the slew rate of the bias supply, as the inductance of the tuner bias windings is approximately 400 µH @ 1 kHz. The same measurement sweeping from 10 Hz to 100 Hz was flat to within 1 dB on both traces.
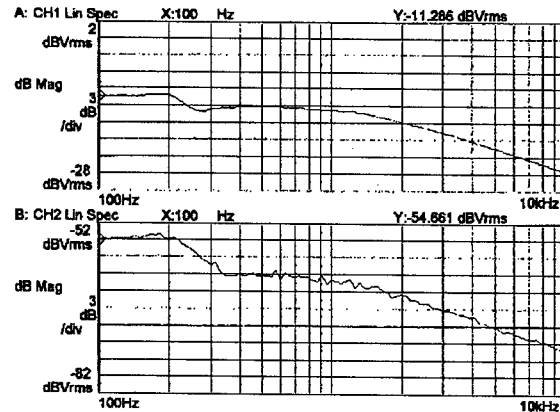
Figure 3: Phase shift and current response plots. The upper trace is tuner bias current, and the lower trace is relative rf phase shift.

Tuning tests with the single-cell cavity were conducted after determining the optimum electrical length between the ferrite tuner and the cavity, which resulted in a cavity tuning range of approximately 25 kHz. This range was necessary to allow the ferrite tuner to operate alone in maintaining cavity resonance during the low-power tests. A manual phase shifter with approximately 310 degrees of range at 351 MHz was used in this adjustment, and the system was set for best compromise between overall tuning range and effect on the cavity input coupler match. This resulted in a variation of loaded cavity Q from approximately 16,000 to 18,000 at tuner bias currents of +100A and −100A respectively, apparently caused by cable losses in the manual phase shifter assembly. The PID amplifier was adjusted for a proportional gain of 4, with integral and derivative values both set at minimum. The tuner bias raw DC power supply was 100 volts DC. This arrangement was maintained for all further low-power rf tests.

Figure 4 shows the result of a closed-loop frequency-response test of the cavity tuning loop configuration using the ferrite tuner to shift the cavity phase. A frequency-swept sinusoid loop stimulus signal of 1 volt peak was used, an amplitude which produced ±30A of tuner current when applied to the bias supply input under DC conditions, ±1 volt. The sinusoid stimulus signal was mixed with the tuning loop PID amplifier output using an isolation amplifier, and was also applied to the channel 1 input of the control system analyzer as the measurement reference. Figure 5 indicates the tuner response to a step-change in the cavity tuning loop setpoint. The scope traces shown are tuning loop signals, from top to bottom, setpoint voltage (trace #1), phase detector output (trace #2), PID amplifier output (trace #3), and ferrite tuner

1178

current (trace #4, 100 A/div). The horizontal time base is 2 ms/division. It can be seen that the cavity reached a tuned condition at the new setpoint value in approximately 6 ms, with the tuner current changing from approximately −85 A to +10 A. The PID amplifier output momentarily clipped at the positive rail during this period due to the slew-rate limitations of the bias power supply.
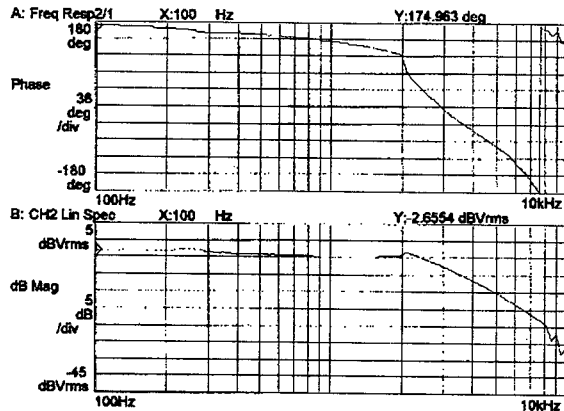
Figure 4: Cavity tuning closed-loop frequency response.
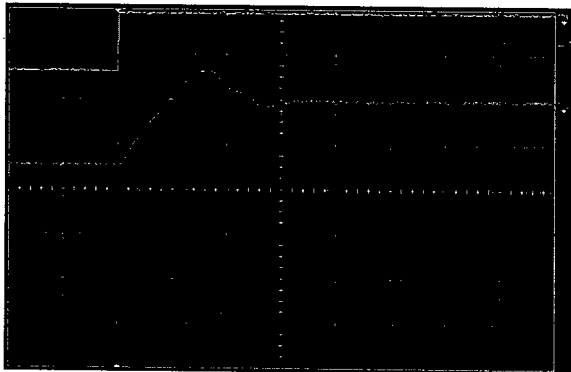
Figure 5: Scope trace of loop setpoint step-change response. Top to bottom, the traces are tuning loop setpoint voltage (#1), loop rf phase detector output (#2), loop PID amplifier output (#3, 5 V/div), and tuner bias current (#4, 100A/div). The horizontal time base is 2 ms/div.

CONCLUSION

The fast-ferrite tuner proved to be effective in tuning a 350-MHz, single-cell rf cavity. It provided much-improved tuning speed over the standard mechanical tuner and was easy to implement in a tuning loop made up of existing APS low-level and high-level rf hardware. The

tuner demonstrated the bandwidth necessary to be effective in reducing mechanical tuner motion and tracking relatively fast beam loading phase effects in the booster synchrotron. However, for best results in a practical application, the ferrite tuner should be used in conjunction with a standard mechanical piston tuner to maintain cavity resonance under all operating conditions. In such an arrangement, the mechanical tuner would be used to compensate for slow cavity effects, such as beam loading and temperature changes, while the ferrite tuner could compensate for faster phase distortions. In this way, the ferrite tuner coupling to the cavity could be optimized for a more narrow tuning range. Measurements also indicate that using 6-1/8″ rigid coax to connect the tuner to the cavity resulted in less degradation of cavity Q, with loaded Q values of 22,063 and 22,263 at tuner bias currents of +100A and −100A, respectively.

Optimizing transmission line length between the ferrite tuner and the cavity for this compromise could be made more practical by the addition of a mechanical phase shifter capable of full-power operation. Such a configuration is being considered for future high-power rf tests on this tuner, as space restrictions inside the APS rf test stand bunker severely restrict adjustments in transmission line length.

FUTURE PLANS

Further low-power rf tests are planned to study the effects of optimum transmission line length between the ferrite tuner and the test cavity. The ferrite tuner assembly will then be installed on a 350-MHz, single-cell test cavity in the APS rf test stand, where it will be tested at power levels up to 150 kW CW. Possible further high-power rf tests of the ferrite tuner on a 350-MHz, 5-cell cavity is being considered for booster synchrotron applications. This work is tentatively scheduled for the summer of 2003.

ACKNOWLEDGEMENTS

REFERENCES

[1] N. Sereno, "Advanced Photon Source Booster Synchrotron RF Capture Design," these proceedings.

MECHANISMS LIMITING HIGH GRADIENT RF CAVITIES

J. Norem*, A. Hassanein, I Konkashbaev, ANL, Argonne IL 60439 USA

Abstract

The specific mechanisms responsible for breakdown of rf cavities have been widely debated. A large number of different processes are thought to be involved, including field emission, surface contamination, mechanical stresses, plasma effects, explosive electron emission, a variety of heating mechanisms, mechanical imperfections, surface structure and chemical composition. We are attempting to model the surface effects that limit the operation of high gradient rf cavities using the HEIGHTS package. Models of individual processes are being developed and compared, in an attempt to evaluate the relative importance of these effects, specifically for the case of low frequency (200 - 800 MHz.) copper cavities, but probably applicable to other materials and frequencies.

INTRODUCTION

Although breakdown has been studied for many years, the problem seems to be complex and have many causes. In analyzing the data from experiments done by the Muon collaboration in Lab G, we have found that the dark current spectrum can give useful information on the field emitters, and these field emitters can likewise provide useful information on the sources of breakdown. We have begun to model breakdown mechanisms with the ultimate aim of producing predictions that can be compared with experimental measurements.

BREAKDOWN MODELS

An enormous amount of data has been collected on rf and dc breakdown over the past century. This work has been summarized in a number of books and papers[1, 2, 3]. The basic mechanism, described by Dyke and Trolan, who used "lightning rod" shaped probes against ground planes, is that high current densities heat up probe tips and evaporation and ionization then produce breakdown[4]. Additional detail in this model was supplied by Knobloch, who modeled the formation of plasma and the ionization and heating of the surface by the plasma in a high electric field[5].

A number of sources of field emission have been discovered. Dust, inclusions, debris from past breakdown events, voids, grain edges, and distortions of the surface have been seen and identified as possible emission sites. Dust, which is composed of silicon and aluminum oxide, is difficult to completely eliminate from most surfaces. Voids, grain edges and distortions are to some extent the

---
#norem@anl.gov

byproduct of the cleaning and annealing process and are being actively studied. In addition the surface of most metals is covered with an oxide layer. The behavior of the oxide layer in an electric field can be complex. Oxides, while normally good insulators, can form conducting paths when exposed to electric fields, and these conducting paths remain after the removal of the electric field[6].

In addition, grain edges and inclusions are found to be the sites of breakdown events, possibly because they contain foreign material and structures. Arcing is seen to take place preferentially at grain boundaries.

While the causes of breakdown events are studied extensively, any breakdown model must explain how very low breakdown rates can exist. Many old linacs with large areas of very damaged copper structures, such as the 50 MeV IPNS system, seem to operate at accelerating gradients where they produce some dark currents and x rays, but do not break down at a significant rate. There is evidence, however, that breakdown rates and dark current production are related[7]. An example of this is shown in Fig. 1.
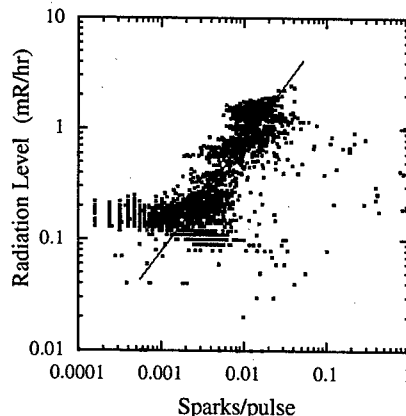
Fig 1. Sparking vs. Field Emission

TENSILE STRESS

Much of this work was heavily influenced by measurements made on 805 MHz open and closed cell copper cavities in Lab G of Fermilab for the Muon Collaboration[8][9].

This work seemed to indicate that the mechanism for breakdown was related to the tensile stress exerted by the electric fields, and the tensile strength of the wall material.

The basic argument is: 1) field emission describes emitter properties, and 2) the properties we infer are very close to mechanical failure of the structure. We assume that dark currents we see produced in the cavity are the

result of field emission as described by the Fowler Nordheim (FN) expression. We denote this current density by $i_{FN}(E)$, where E is the local electric field. Measured dark currents as a function of electric field can then provide rough estimates of the emitter area and the enhancement factors required to produce the 5 - 10 GV/m gradients required by the FN parameterization of field emission. The argument is shown in Fig. 2, which relates measured dark current production with the FN parameterization. There are basically two variables, the emitter area and the enhancement factors that can be determined from the data. There is a small correction (~0.1) that converts rf field emission values to dc field emission .

HEIGHTS package[9]. The HEIGHTS package was originally developed for studying plasma-wall interactions in the fusion program, and has been extended to consider a large number of problems where materials are subjected to exotic environments.
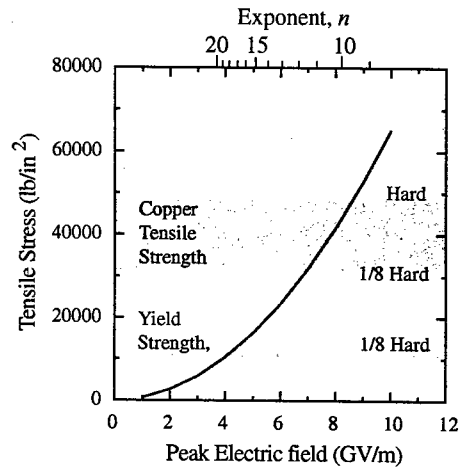
Figure 3. Copper stress

Fig 2. Dark currents and the Fowler-Nordheim model.

The local electric fields inferred from this analysis are very large. These fields are associated with process are very large and the stresses associated with the fields, $p = 0.5\varepsilon_0 E^2$, where E is the electric field and ε_0 is the capacitance of free space, are also very large. This is shown in Fig. 3, for copper. As the field inferred from the dark current measurements increases towards 8 - 10 GV/m, the associated tensile stresses approach 40,000 - 50,000 lb/in^2, which is the tensile strength of hardened copper.

We assume an initial failure of the structure, perhaps on the edge of a crater on a protrusion, might look something like Fig. 4. Such a fragmentation of a crystalline sample would tend to leave sharper corners that could then produce further fragmentation as shown in Fig. 5. We have begun numerical simulation of these processes using the

Figure 4. Initial breakup of a copper surface.
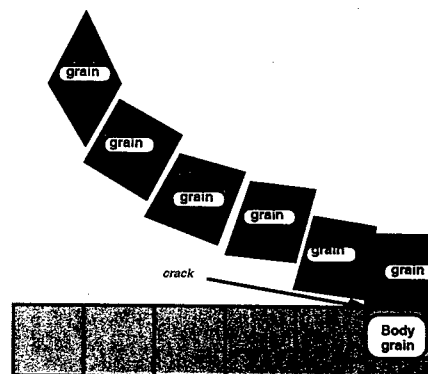
Figure 5. Destruction of surface layer.

Copper grains can be heated ohmically by dark current beams within the structure, or by ionization heating from accelerated dark current beams when the copper grains have detached from the structure. When the grains are coupled to the wall, ohmic heating power increases the temperature. This power is equal to IV, where I is the dark current and V the resistive voltage drop across the grain. On the other hand, when the grains are detached from the wall the absorbed power, IV, can be much larger, since the relevant voltage in now the accelerating voltage seen by accelerated electrons, $V = Edz$ with an electric field E and separation dz. This energy, can be many orders of magnitude larger than the ohmic power. Since the grains have lost thermal contact with the wall there will also be no conduction losses. Thus detached grains in space can be heated much faster than grains coupled to the wall. Modeling is underway to determine the rates at which all these processes can occur in real systems to compare with experimental data.

It is also useful to look at the limits of this mechanism in detail to determine how much of the observed behavior is compatible with this mechanism. On the other hand, there are many phenomena that are not obviously explained by the field induced stress on the surface. These include breakdown at inclusions and grain boundaries, repetitive breakdown at similar field conditions and wall damage due to high currents. It is not clear how widely this mechanism applies.

MODELING

Although we are just beginning, we have some initial results on the size limit for grains, frequency dependence of breakdown the motion of electrons in the cavity and the effects of secondary emission. We intend to expand this effort and look at the time development of the breakup, ionization and rf breakdown process in the coming months.

ACKNOWLEDGEMENTS

REFERENCES

[1] H. Padamsee, K. Knobloch, T. Hays, *RF Superconductivity for Accelerators,* John Wiley and Sons, Inc., New York (1998)

[2] R. Latham ed., *High Voltage Vacuum Insulation,* Academic Press, London (1995).

[3] http://www-project.slac.stanford.edu/lc/wkshp/

[4] W. P. Dyke, and J. K. Trolan, Phys. Rev., **89** (1953) 799.

[5] http://www.lns.cornell.edu/public/CESR/SRF/dissertations/knobloch/knobloch.html

[6] E. L. Cook, J. of Appl. Phys., **41** (1970) 551.

[7] T. Kroc, Fermilab, Private Communication, (2001).

[8] http://www-mucool.fnal.gov/mcnotes/public/pdf/muc0235/muc0235.pdf

[9] J. Norem, P. Gruber, A. Bross, S. Geer, A. Moretti, Z, Qian, D. M. Kaplan, Y. Torun, R. Rimmer, D. Li, M. Zisman. This conference.

[10] A. Hassanein and I. Konkashbaev, J. Nucl. Matl. **273** (1999) 326

DARK CURRENT AND X RAY MEASUREMENTS
OF AN 805 MHZ PILLBOX CAVITY

J. Norem[#], ANL, Argonne Il 60439 USA
P. Gruber, CERN, Geneva, Switzerland
A. Bross, S. Geer, A. Moretti, Z Qian, FNAL, Batavia IL 60510 USA
D. M. Kaplan, Y. Torun, IIT, Chicago IL 60616 USA,
R. Rimmer, Jefferson Laboratory, Newport News VA 23606 USA
Derun Li, M. Zisman, LBNL, Berkeley CA 94720 USA

Abstract

The muon cooling systems proposed for neutrino factories require low frequency (201 MHz) RF cavities with Be windows, at high gradient ($E_{acc} \sim$ 16 MV/m), in strong solenoidal magnetic field (~ 5 T). For the proposed Muon Ionization Cooling Experiment (MICE) [1], an experimental demonstration of cooling, we have an additional constraint that we must operate sensitive particle detectors very close to the RF cavities, which produce backgrounds from dark currents and x rays. To understand the processes involved in cavity conditioning and operation near particle detectors, we have constructed a test facility at Lab G of Fermilab, where a 5 Tesla superconducting solenoid, a 14 MW peak power klystron and a pillbox test cavity at 805 MHz are available. We present measurements of dark currents, x rays and surface structure from the pillbox cavity, with both copper and beryllium endplates, and discuss the interaction between surface structure and radiation backgrounds produced.

INTRODUCTION

Muon cooling systems are necessary for both muon colliders and muon based neutrino beams. While extensive modeling has been done on the design of these systems, the experimental program to study how well the components will operate is just beginning. This paper reports results from tests of an 805 MHz prototype rf cavity for a cooling channel.

Muon cooling systems consist of alternating liquid hydrogen absorbers and rf cavities. Since multiple scattering tends to heat rather than cool the beam, and muon beams do not interact strongly with matter, we have assumed that the rf cavities could use windows of beryllium, which produces a higher accelerating field for a given surface field. In order to test how cavities of this type would operate, we have constructed an 805 MHz pillbox cavity with removable end windows in which Be and other materials can be tested. The cavity is basically a cylinder, powered through an arc shaped slot near the outer radius. There is an inner pair of windows that defines the rf properties of the system and an outer pair of windows that maintains the vacuum. A variety of windows have been used on the cavity.

[#] norem@anl.gov

We are looking at a number of issues. We want the maximum gradient we can obtain in these cavities, particularly with Be windows, and the minimum flux of dark current electrons and x-rays that can be produced. We are also interested in how Be windows perform and in information on how 201 MHz cavities will operate with real beams.

DESCRIPTION

The cavity is shown in Figure 1. The parameters of the different windows are given in the following table and in ref [2].

Figure 1. The pillbox cavity.

Window configurations are shown in the table below:

Rf window	Cu	Cu	Be
Thickness	0.200"	0.015"	0.01"
(g/cm^2)	4.55	0.342	0.045
Vacuum window	SS	Ti	Ti
Thickness, (g/cm^2)	15	0.091	0.091
E_{rf}/V_{probe} (MV/m/V)	1.49	1.28	1.16
Max. grad. (MV/m)	34	23	16
E_{surf}/E_{acc}	1.01	1.01	1.01

Timeline

The timeline for experiments with the closed cell cavity is given below. The cavity was first operated with thick rf and vacuum windows. The rf components were replaced with thin copper, then Be windows.

1/4/02	Open Cell cavity removed from the Magnet
3/13/02	Begin conditioning with thick Cu plates
	Eventual operation at 34 MV/m, little sparking
7/16/02	Removal of thick Cu plates, little damage
7/30/02	Conditioning with thin Cu plates to 24 MV/m
9/27/02	Operation in B Field, high BG, E_{max}=16 MV/m
	Improvements from conditioning with B=0
12/5/02	Removal of thin plates, considerable pitting
12/19/02	Conditioning of TiN/Be windows to 21 MV/m
2/10/03	Begin conditioning with B field
	Conditioning to 17 MV/m, stable at 14 MV/m
4/22/03	Replacement of Be windows

EXPERIMENTAL RESULTS

The experimental program has been defined by the particular plates which were installed in this cavity and the electric and magnetic fields used. Conditioning periods with a new surface averaged about a month.

Copper and Be Windows

With copper windows we were able to reach 34 MV/m acceleration gradient without a solenoidal field, with very low x-ray, dark current and sparking rates, indicating that the cavity could easily have operated at higher field. Both thick and thin copper plates operated similarly.

When a magnetic field was applied, dark currents, x-ray and sparking rates increased. Fig. 2 shows the measured dark current before the magnet was turned on (bottom band), after the magnet was turned on (top band) and after the magnet was turned off (middle band). These results seem to show that some permanent damage was produced on the windows of the cavity that did not immediately condition away. On the other hand, more extensive conditioning over a one month period with no magnetic field was able to reduce the fluxes of dark currents and electrons to levels seen before the magnetic field was applied.

The Be windows were fabricated by Brush-Wellman. A thin Be foil was supported by a ring of Be. The ring applied a prestress to allow for some heating of the foil without deformation. After annealing, the unit was coated with TiN coating, nominally 150 Angstroms thick, but perhaps thicker. The Be windows conditioned to 16 MV/m but over a period of weeks the dark current and sparking rates slowly increased so that it was difficult to return to the initial high accelerating fields.
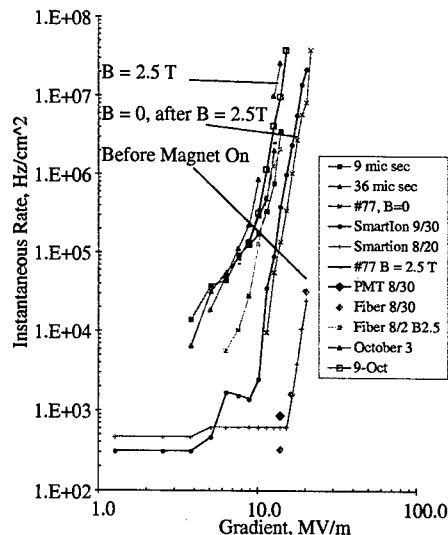
Figure 2. Background rates with copper windows.

Pictures of the dark current transmitted through the windows were recorded on glass slides, polaroid film and photographic paper. The glass and polaroid pictures show the beams near the window in the homogeneous field, and the photographic paper shows how the beams diverge with the fringe fields of the magnets. See a paper by Gruber et al[3].
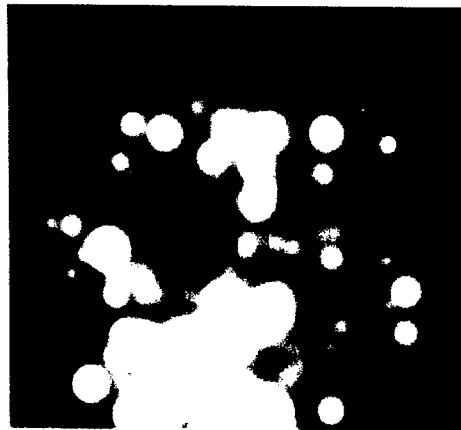
Figure 3. Dark current with 2.5T solenoidal B field.

X ray Spectra

The spectra of photons were measured with an ORTEC Ge detector, calibrated with Co60 and Cs137. The spectra were obtained at fairly low accelerating fields because the busy gate on the qVt pulse height module was comparable to the length of the rf pulse, so it was not possible to count photons at a rate of more than 1/rf pulse. The spectrum is somewhat more steep than would be produced from first generation bremsstrahlung, which might indicate that the x-ray energy is being attenuated by scattering.
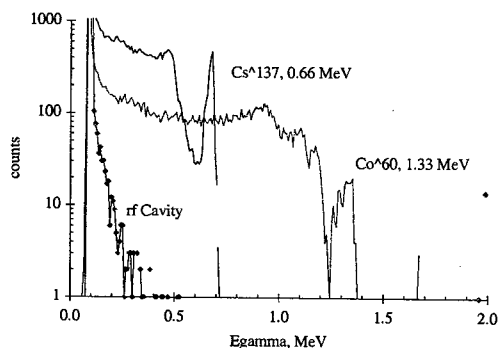
Figure 4. Energy spectra of x rays.

The appearance of the Be windows was quite different. Visually, the dark TiN coating seemed unbroken, and this seems to be confirmed with electron and optical microscopy, The surface was covered, however, with copper particles. An electron microscope picture of the surface, Fig. 7, shows some of the typical structures. With irregular copper blobs are visible on an otherwise unbroken Be surface. The TiN covered Be shows marks evidently made during rolling. Almost all damage seems to be due to copper deposition, which can be irregular, circular or linear. The Cu surfaces show admixtures of Fe at the 2.5% level when EDX analysis is done, trace amounts of Fe were in the Be. We also saw deposits of what may have been dried machining or cleaning fluid.

Surface Damage in Cu and Be

Surface damage on the Cu plates consisted of pits on the order of 100 - 400 μm in diameter and occasional splashes where liquid copper drops had evidently splashed and adhered to the surface.

Example of this damage are shown in Fig. 5 and Fig. 6. An electron microscope picture shows a typical sharp edged crater in an otherwise smoothly machined surface. The pits show sharp edges which are consistent with the field emission we see with films and radiation monitors.
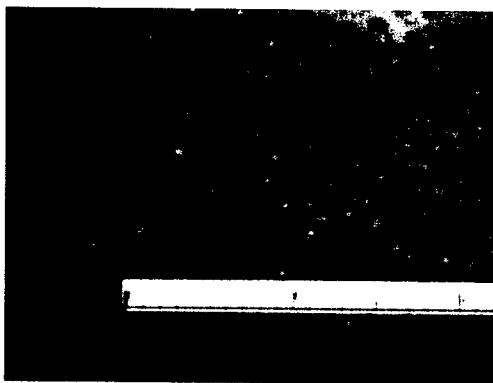
Fig. 5. Optical image of copper plate, (scale in cm).

Figure 6. SEM image of copper plate.

Figure 7. SEM image of Be Windows showing copper.

CONCLUSIONS

We have built an rf cavity which can be used to study the use of beryllium rf windows which are needed in low frequency cavities for muon cooling We have found that copper cavities seem to produce acceptable background rates at 8 MV/m, however strong (~2.5 T) magnetic fields can produce problems which require long conditioning periods. The dark current performance of Be windows seemed to degrade with time. A preliminary analysis of the windows themselves, however, using SEM and optical microscopy, shows that all the damage seems to be due copper contamination, and little or no significant damage has been done to the TiN coated Be windows. This work was done as part of the MUCOOL experimental program and was supported by the USDOE and the State of Illinois.

REFERENCES

[1] http://mice.iit.edu/cooldemo/.
[2] D. Li et al, Tests of an 805 MHz Pillbox Cavity at Lab G of Fermilab, this conference.
[3] P. Gruber, et al. Beam Photography: A Technique for imaging Dark Currents, this conference.

HOM DAMPED NC PASSIVE HARMONIC CAVITIES AT BESSY*

W. Anders, P. Kuske, BESSY, Berlin, Germany

Abstract

HOM damped normal conducting passive harmonic cavities are developed and installed at the BESSY II storage ring. The mechanical and electrical parameters and the operation modes are described. The operational parameters are presented, showing good agreement of bunch lengthening, synchrotron frequency shift and increase of Touschek lifetime. Measured data of the transient shift of the synchronous phase driven by the harmonic cavities are presented. Due to the HOM dampers no coupled bunch modes of the beam are driven by the harmonic cavity.

INTRODUCTION

BESSY II is a high brilliance 3rd generation synchrotron light source running with electrons at 1.7 GeV. Typical lifetime at a current of 250 mA is in the order of 6-8 hours, depending on the settings of the insertion devices and the vacuum conditions. The lifetime is mostly dominated by the Touschek scattering driven by the small bunch volume. Small transversal beam dimensions are desired, but Touschek scattering can be reduced also by increasing the bunch length without influence on the measurements of the synchrotron light users.

Basic Ideas:

The bunch length is proportional to the square root of the gradient of the rf voltage at the position of bunch. By adding a harmonic voltage of the rf voltage, the gradient can be changed (Fig.1).
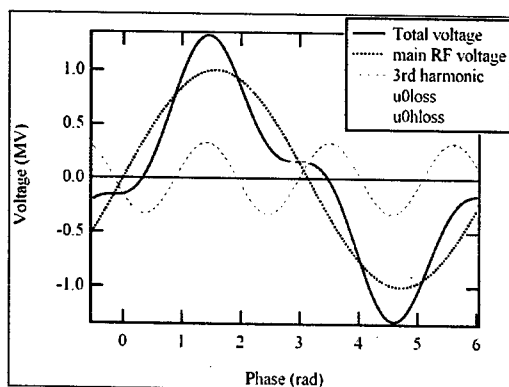
Figure 1. Plot of the voltages in the 500 MHz main cavities and in the 1.5 GHz cavities, summing up a zero slope to the beam at the synchronous phase.

When using a passive cavity at a harmonic frequency of the main rf (3rd harmonic at BESSY) the beam induces the

voltage in the harmonic cavity having no accelerating fields at the position of the bunch. By tuning the resonance of the harmonic cavity little above or below the harmonic of the main rf, the phase of the harmonic voltage is changed ±90° resulting in decreasing (resonance above harmonic) or increasing gradient of the sum voltage leading to bunch lengthening or bunch shortening. The voltage in the passive harmonic cavity depends on the beam current (beam spectrum) and can be controlled by the resonance of the harmonic cavity using a plunger for tuning.

Harmonic Cavities with uneven Bunch Filling

With harmonic cavities the gradient of the rf can be made flat at the position of the bunch and lifetime increase up to a factor of 3 can be calculated [1] assuming even bunch filling. First tests with harmonic cavities at BESSY [2] and ALS showed much lower values. This is now well understood. When running the storage ring with an asymmetric filling the voltage of harmonic cavities increases while electron bunches are passing and decreases in the gaps of the filling. This results in varying gradient of the synchronous phase during a revolution. Taking this in account, the achievable gain in lifetime reduces. The parameters are calculated in a tracking code [3] and are in quite good agreement with the measurements.

Landau Damping with Harmonic Cavity

The gradient in synchronous phase gives a decoupling of the bunches and can be used for supressing coupled bunch modes [4]. At the BESSY storage ring all cavities are equipped with HOM dampers. Therefor no coupled bunch modes have to be supressed.

PARAMETERS OF THE HARMONIC CAVITIY

Mechanical Parameters
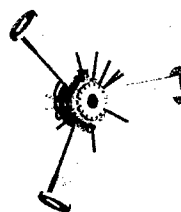
Figure 2 HOM damped cavity body

The harmonic cavity is a further development of the non damped cavities [2]. The cavity has a pillbox shape and three wave guides with cut off 1.85 GHz (Fig.2). The beam tube diameter is 60 mm and the total length is 200 mm. The cavity body is made from HC copper with inter-

nal cooling channels. The typical water flow is 15 l/min. The copper plated stainless steel wave guides are half size wave guides at the corner of the body expanding to full size at the flanges with vacuum ferrite [5] for higher order mode damping. Because of space requirements the waveguides are bent to one side of the cavity. There are two plungers for tuning (only one necessary) and two diagnostic loops to do S_{12} measurements with beam for adjusting the resonance in respect to the beam harmonics .

Electrical Parameters

The main parameters of the cavity are given in table 1:

Parameter	Value	Unit
fundamental frequency	1,499	MHz
R/Q	62	Ohm
Q_o	13,900	
R_{eff}	860	k Ohm
typical operation voltage	60	kV/cavity
length of cavity	20	cm
number of installed cavities	4	

Table 1: Electrical Parameters of Cavity (measurements)

The cavity was cross checked by a mafia calculation to adjust the cut off of the wave guides. For reasons of symmetry only two wave guides were calculated. A prototype cavity was built and the length of the wave guides and the exact diameter of the body evaluated. The shunt impedance of the cavity was measured by bead pull measurement. The Q value and the higher harmonic modes were investigated by S_{12} measurements with a
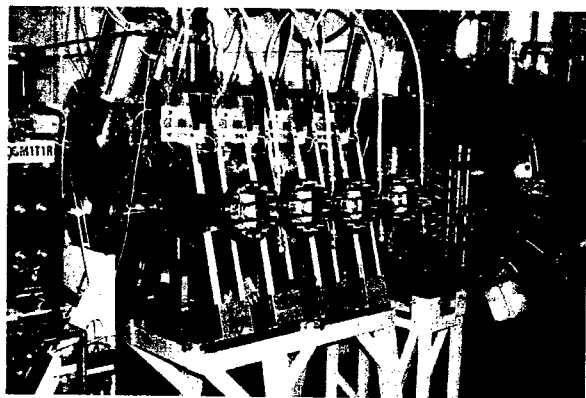
Figure3: Four harmonic Cavities installed at BESSY II

network analyser and cross checked by measurements with beam in single bunch mode. The Q value of the most powerfull TM011 is about Q=150. The TE111 mode has a moderate high Q=1,000 HOM near the cut off of the wave guides, but shunt impedance is low and the beam is not excited by this mode.

OPERATING MODES

The harmonic cavities are controlled by the EPICS control system. The operator can choose between four operation modes. The harmonic number h of the 3rd harmonic of the main rf is h=1200.

1. *Parking Position:* In this mode the plunger drive to a fixed position so that the resonance of the cavities is in the middle of two revolution harmonics, for example on harmonic number h=1195.5

2. *Set Mode:* Set mode is dedicated to machine studies. Both plungers can be driven to positions given by sliders on the control system.

3. *Lengthening Mode:* Lengthening mode is the standard mode in user operation. The resonance is tuned for decreasing the gradient of the total rf voltage for lengthening the bunch and increasing the lifetime of the beam. One plunger is on fixed position while the other is controlled by a voltage loop. The loop is programmed as a slow PI-loop on the EPICS control system. To avoid the cavity going to resonance and inducing very high voltages, the range of the position of the plunger to drive is limited to about 250 kHz to 750 kHz above 3rd harmonic of main rf corresponding to harmonic number h=1200.2 to h=1200.6. By limiting the range of the resonance, at low currents the desired voltage can not be achieved. This is no problem, because touschek scattering is reduced by low currents as well and lifetime is high enough.

4. *Shortening Mode:* This operation mode is a voltage loop similar to the lengthening mode, but the resonance of the harmonic cavities is set to values below the 3rd harmonic of the main rf to harmonic numbers of h=1199.4 to h=1199.9 giving a bunch shortening.

OPERATIONAL RESULTS

Four harmonic cavities are installed in the BESSY II storage ring (figure 2) and operated normally in bunch lengthening mode. The operational voltage per cavity of 55-60 kV means a sum voltage of 230 kV while the sum voltage of the accelerating 500 MHz rf cavities is 1.3 MV. Lifetime and bunch length were measured (figure 4) using a Hamamatsu C5680 streak camera. harmonic voltage decreases at currents lower than 150 mA due to the tuning limit of the plungers controlled by the voltage loop. The increase of the bunch length is measured as $\sigma=15.6$ ps going to $\sigma=20.5$ ps (30%). The synchrotron frequency shift fit to those data. The increase of toushek lifetime is 30% as well and in agreement with the increase of bunch length. Considering a gas scattering lifetime of 25 h at the time the measurements are done the total increase of lifetime is 20%. There is no heating of the beam by HOM´s driven by the harmonic cavities. The TE111 mode can be seen on the beam spectrum but due to its low shunt impedance there is no influence on beam stabilty. Bunch shortening has been demonstrated in machine shifts in low alpha optic for generating coherent radiation with very short bunches.
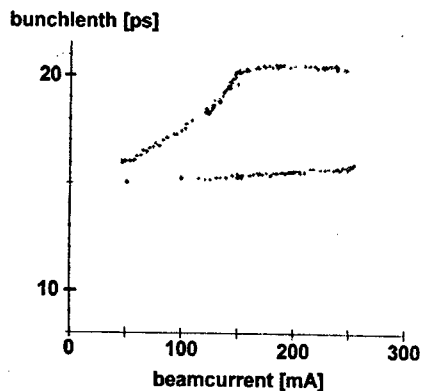
Figure 4: Bunch length with harmonic cavities at 225 kV (lengthening mode) and lower 30 kV (parking position). Main rf voltage is 1.3 MV. For beam currents lower than 150 mA the harmonic voltage decreases due to the tuning limit.

BESSY II is an electron storage ring. For ion clearing not all the 400 buckets of the ring are filled but a bunch train of 360 bunches and a ion clearing gap of 80 ns is used. The asymmetric filling produce a modulation of the harmonic voltage resulting in a change of the synchrounous phase of the bunches in respect of the position of the bunch (figure 5). The phase detector of the longitudinal feed back has a detection range of 30° phase, so the clearing gap has to be kept short.
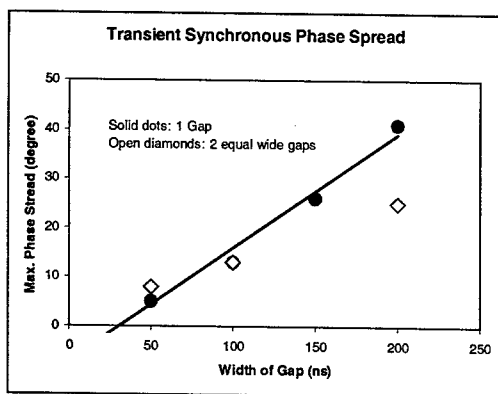
Figure 5: Transient phase shift of synchronous phase of the bunches due to influence of harmonic cavities at BESSY II. Total harmonic voltage is 225 kV, voltage of the fundamental rf cavities is 1.3 MV. Solid dots are measurements with one bunch train and one gap, open diamonds are measured using two symmetrical bunch trains and two gaps

Outlook

The voltage in the harmonic cavities is still below the optimum voltage. The harmonic voltage is limited by the power capacity of the cavities and the installation length in the storage ring. To achieve a higher voltage and hav-

ing lower phase transients a super conducting harmonic cavity is ordered at ACCEL company and will be delivered this year. The SC cavity is a passive 1.5 GHz scaled version of the cornell type CESAR cavity. The design voltage is up to 500 kV and the length of the cryostat is 80 cm flange to flange. This is the same length as the four normal conducting cavities so that the cavities can be replaced on the same installation place of the storage ring.

Conclusion

Four passive 3rd harmonic HOM damped cavities are installed and operated without problems in the BESSY II storage ring resulting in a lifetime improvement of overall 20% in normal user operation of the storage ring.

Acknowledgement

REFERENCES

[1] J-M-Byrd, K.Baptiste, S.De Santis, S.Kosta, CC.LO, D.Plate, R.A.Rimmer, M.Franks *Design of a higher harmonic RF system for the Advanced Light Source* Nucl. Instr. and Meth. Phys. Res. A 439; 15-25 (2000)

[2] M.Georgson, W.Anders, D.Krämer, J.M.Byrd *Design and commissioning of 3rd harmonic cavities at BESSY II* Nucl. Instr. and Meth. Res., Sect. A **469**, 373-381 (2001)

[3] J. M. Byrd, S. De Santis, J. Jacob, and V. Serrie *Transient beam loading effects in harmonic rf systems for light sources* Phys. Rev. ST Accel. Beams 5, 092001 (2002)

[4] Å. Andersson, *A landau-cavity at MAX,* Max Lab report NTMX-7009 1988

[5] Walter Hartung, *The Interaction Between a Beam and a Layer of Microwave-Absorbing Material,* Ph.D. Cornell University (1996)

IMPEDANCE MEASUREMENTS
OF A HOM-DAMPED LOW POWER MODEL CAVITY*

F. Marhauser, E. Weihreter, BESSY II, Berlin, Germany
C. Weber, TU Berlin, Germany

Abstract

In the frame of a European Community funded project a higher order mode (HOM) damped normal conducting 500 MHz cavity is under development optimized for the use in 3rd generation storage ring light sources. The relevant HOM-impedances have been measured with a fully scaled low power model made from aluminium. By using a cutoff frequency of 615MHz for the damping waveguides we have found a good compromise between the preservation of the accelerating mode impedance and the efficient broadband damping of HOM's. Detailed experimental results are presented and compared with numerical simulations.

1 INTRODUCTION

In undulator dominated 3rd generation storage rings the beam induced coupled-bunch instabilities driven by the narrowband HOM's of rf-cavities can severely limit the quality of the photon beams. Thus strong damping of all relevant cavity HOM's is a straight forward solution to avoid such instabilities. Based on numerical simulations [1] a cylindrically shaped 500MHz HOM-damped cavity was optimized with special emphasis on conceptual simplicity, low investment cost and a compact layout for compatibility with such cavities in existing storage ring tunnels (see Fig. 1). Detailed measurements have been performed for a fully scaled aluminium cavity to verify the promising impedance estimates of the simulations. A high power prototype cavity made from OFHC copper is under fabrication designed for 100kW input power [2] and for a max. gap voltage of 850kV.

2 CAVITY DAMPING SCHEME

The prototype cavity uses three tapered circular double ridged waveguide to coaxial transitions (CWCT's) as HOM-couplers [3]. They are spaced by 120° around the cavity circumference to facilitate the energy extraction of differently polarized transverse HOM's and shifted away from the cavity equator in axial direction to enable coupling to both symmetric and anti-symmetric HOM-field distributions (with respect to the longitudinal midplane). In this manner all critical beam induced HOM's couple to the 1st waveguide mode (TE$_{11}$-like) of the CWCT's. The CWCT internal ridge profile is shaped such that a constant cutoff is maintained all along the tapered section (see Fig. 2), which provides a broadband transmission characteristic with negligible mode conversion [3]. A cutoff frequency of f_c=615MHz has been chosen finally as a compromise between a high

damping efficiency for the low frequency HOM's and a high shunt impedance for the fundamental accelerating mode.
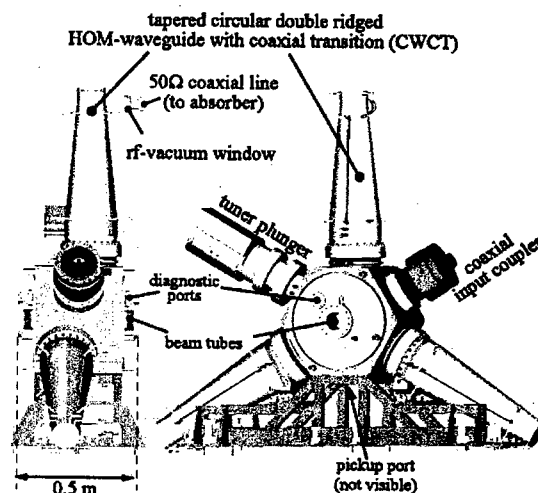
Figure 1: The 500MHz HOM-damped cavity assembly.

At the end of the tapered waveguide the TE$_{11}$-like mode is transformed to the TEM-mode of a 7/8" EIA standard 50Ω coaxial line by means of a transformer section. Thus HOM-energy can be extracted from the cavity and dissipated efficiently up to the relevant beam tube cutoff (f_{TM01}=3.1 GHz) by means of external 50Ω absorbers, which are separated from the vacuum via broadband ceramic rf-windows.
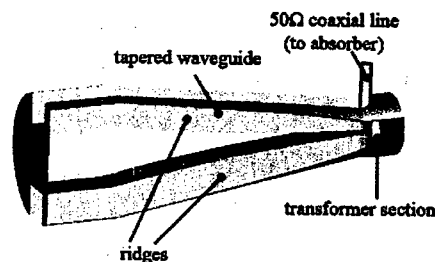
Figure 2: Schematic view inside a CWCT.

The length of the CWCT's has been chosen to limit the fundamental mode power leakage to about 1kW per absorber at 100kW cavity input power. This has been

---

verified by measurements for the low power model scaling the result to this power level and taking the higher copper conductivity into account. Additional power originating from HOM's has been assessed analytically to be well below 1kW [4] for different design currents and fill patterns of modern storage rings. Thus commercially available 50Ω absorbers can be used as loads.

3 OPTIMIZATION STRATEGY

3.1 Simulations

Extensive numerical work has been done to optimize the cavity shape and the location of the damping waveguides [5] using MAFIA 3D time domain (T3) calculations to enable the simulation of broadband external damping measures [6]. Results have been improved iteratively by means of the beam coupling impedances, which can be evaluated from a Fast Fourier Transform of the computed wake potential induced behind the leading charge. However, the enormous amount of different optimization steps prevented from modelling the complex CWCT shapes, which would have led to prohibitively long calculation times. Homogeneous double ridged dampers were used instead (*simplified model*) with an ideal absorbing boundary at the end of the waveguides, i.e. $S_{11}=0$ just for the 1st propagating TE_{11}-like mode to resemble the CWCT characteristic as close as possible. Simulations indicate that HOM impedances can be reduced to a level of 2kΩ and 50kΩ/m for longitudinal and transverse HOM's respectively based on this damping scheme [1].

3.2 Initial Experimental Results

For the low power prototype cavity CWCT's with a cutoff of f_c=650MHz have been used initially. Impedance measurements up to 1.6 GHz were carried out applying a "bead pull" method to probe the electric field of critical HOM's [7]. The TM_{011}-like mode (f=699 MHz) with the usually highest R/Q-factor of all monopole HOM's could be damped down to a level of 1.7kΩ. However, a coexisting TM_{011}-like "persistent mode" (*PM*) has been measured with a prohibitively high impedance of 36kΩ at 654 MHz not predicted by the *simplified model*.

Table 1: Measured persistent mode parameters

f_c [MHz]	f [MHz]	Q_l	R/Q [Ω]*	R [kΩ]*
650	654	1290	28.2	36.4
625	639	820	12.7	10.4
615	634	383	10.0	3.8

*$R=U_{eff}^2/2P_V$ with U_{eff}=effective voltage, P_V=power loss

It has been verified, that the *PM* does not exist in the cavity with closed HOM-ports and is due to the damping waveguides themselves. As the *PM* "sticks" to the cutoff, the energy propagation to the external loads is reduced causing a relatively high loaded quality factor (Q_l) and

consequently a higher impedance $R=(R/Q)*Q_l$. Therefore we lowered the CWCT cutoff and hence the *PM* frequency with the aim to convert the field pattern to a more TE_{111}-like nature, as such modes resonate at lower frequencies and exhibit much lower R/Q-factors. In fact the *PM* impedance could be reduced to 3.8kΩ resonating at 634MHz with a final choice of f_c=615MHz as summarized in Table 1.

4 FINAL RESULTS

The unexpected persistent mode phenomenon has shown that the use of CWCT's as HOM-couplers can lead to results significantly apart from the predictions of the *simplified model* as the amount of HOM-energy that can be extracted from the cavity is reduced by the tapered waveguides. To evaluate the related impedance increase, extensive measurements have been carried out for the low power model cavity with the final choice of f_c=615MHz. In addition long term MAFIA T3 calculations have been performed for a more realistic model, this time including the complex CWCT shape (*"realistic model"*).

In Fig. 3 the measured impedances are presented together with the calculated impedance spectra for the *simplified* and *realistic model* respectively. Measurements reveal that a broadband damping efficiency of all HOM's is provided with impedances reduced to a level of 4kΩ and 170kΩ/m for the most dangerous longitudinal and transverse HOM's respectively.

4.1 Numerical and Experimental Issues

For the *realistic model* ~18 million mesh points (applying one symmetry plane) have been used exploiting our PC capabilities, but the complex CWCT shapes might still not be discretized satisfactorily to avoid numerical artefacts especially at higher frequencies. Actually some of the higher impedances could not be confirmed by the measurements as indicated in Fig. 3. Nevertheless the *realistic model* has predicted impedances in principal agreement with experimental results, also confirming the relatively high impedance of the persistent mode.

As all HOM's are strongly damped, the accuracy of the measurements suffers from overlap of adjacent modes. E.g. for the monopole HOM at 2.64 GHz with a relatively high longitudinal impedance we have observed large field amplitudes in the beam tubes, which belong to a propagating TE-like dipole mode in the vicinity measured at the same time. The use of pick-up probes with loose coupling therefore is essential for the measurement, which compromises however the signal-to-noise ratio. Major inaccuracies were found for HOM's with rather low impedances fortunately out of interest. Due to the broken symmetry of the cavity, the electrical and geometrical (beam) axis can differ considerably depending on the HOM field pattern. Hence transverse modes can exhibit significant longitudinal field components on the beam axis, which has been verified experimentally. Transverse HOM's with such behaviour

have been included in the longitudinal impedance spectrum. Measurements were also complicated by many low impedance HOM's excitable by the pick-up probes but not relevant for the beam even when left undamped. Actually 3D eigenmode calculations with Microwave Studio [8] up to 1.6GHz (full model, but no damping measures possible in frequency domain) revealed the existence of about 100 modes. In that spectral region all critical HOM's could be identified unambiguously by comparing measured and calculated field patterns. This also gives confidence in experimental results at higher frequencies not surveyed by eigenmode calculations.
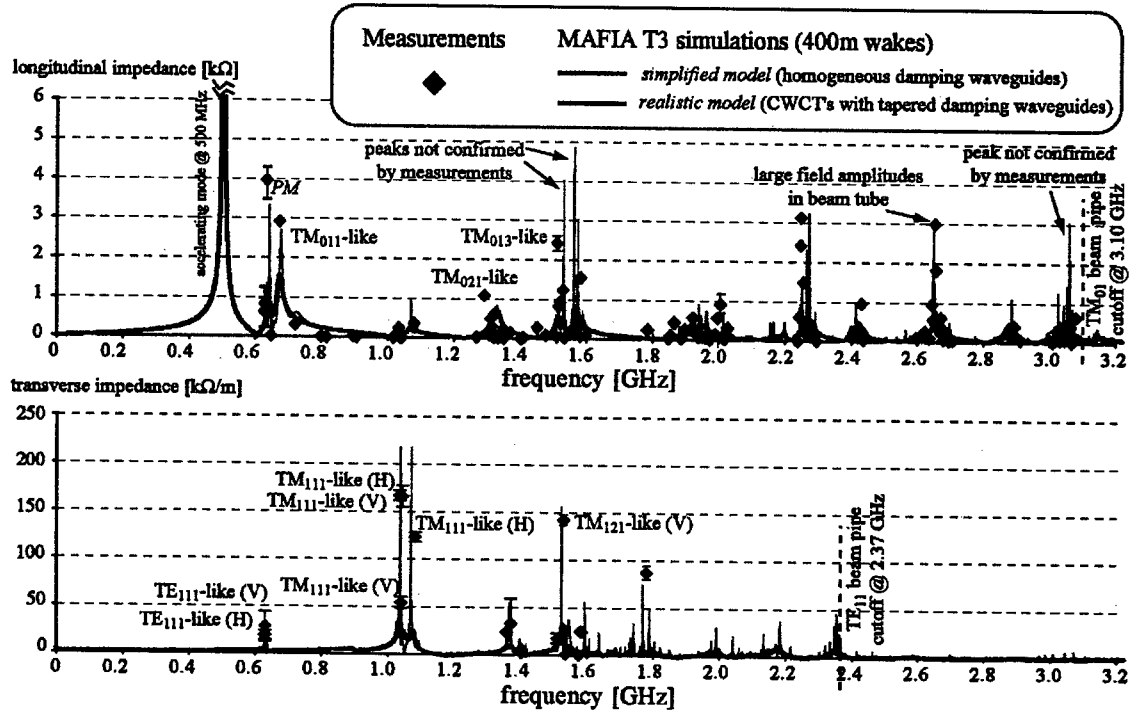
Figure 2: Measurement results (diamonds) for longitudinal (top) and transverse impedances (bottom) together with the predicted impedance spectra (lines) of the *simplified* and *realistic* MAFIA T3 *model* respectively. The European definition of the shunt impedance $R=U_{eff}^2/2P_V$ is assumed with U_{eff}=effective voltage, P_V=power loss.

5 CONCLUSION AND OUTLOOK

Detailed impedance measurements have been performed for a 500MHz low power HOM-damped cavity, which makes use of tapered CWCT's as HOM-couplers. With these couplers the HOM's are damped down to a level of 4kΩ and 170kΩ/m for the most critical longitudinal and transverse HOM's respectively. The measurement results are in principal agreement with numerical estimates for the *realistic model*. A first high power prototype cavity made of OFHC copper is under manufacturing encouraged by the promising results. Benchmark measurements for the most critical HOM's, high power conditioning, and first beam tests in the DELTA ring in Dortmund/Germany are scheduled for the second half of 2003.

In parallel investigations are performed to design a more homogeneous damping waveguide with internal loads as an alternative to the CWCT's. The aim is to a) closer resemble the *simplified model*, which indicates that longitudinal and transverse HOM's can be further damped to a level of 2kΩ and 50kΩ/m respectively and b) to reduce the investment costs for the HOM-couplers.

6 REFERENCES

[1] F. Marhauser, E. Weihreter, D.M. Dykes, P. Mc-Intosh, Proc. of 19th PAC 2001

[2] C.L. Hodgkinson et al., Proc. of 19th PAC 2001

[3] E. Weihreter, S. Küchler, Y.C. Tsai, K.R. Chu, Proc. of 6th EPAC, Stockholm, Sweden, 22-26. June 1998, vol. 2, p. 2065

[4] F. Marhauser, BESSY-013-march-2001, Internal Report

[5] F. Marhauser, E. Weihreter, BESSY-016-July-2001, Internal Report

[6] X.E. Lin, K. Ko, C.K. Ng, Proc. of 16th PAC, Dallas (Texas), USA, 1-5 May 1995, pp. 1744-1746

[7] F. Marhauser, E. Weihreter, C.C. Yang, Proc. of 8th EPAC, Paris (France), 3-7 June 2002

[8] Microwave Studio (PC release 3 RC1), CST, Darmstadt, Germany 2000

RADIO FREQUENCY CONTROL SYSTEM FOR THE DUVFEL

J. Rose*, A. Doyuran, W. Graves, H. Loos, T. Shaftan, B. Sheehy, Z. Wu,

BNL, Upton, NY 119733, USA

Abstract

A new RF control system was designed and implemented to support short pulse High Gain Harmonic Generation (HGHG) experiments, which require sub-picosecond synchronization between the laser and the accelerating RF fields[1]. This control system consists of a 81MHz crystal oscillator to drive both the Ti::Sapphire laser and a 2856 MHz synthesizer, direct vector modulators that control the amplitude and phase of the klystron drive and vector de-modulators for amplitude and phase measurement. RF and electron beam based measurement results of the RF to laser jitter are presented as well as experimental results of synthesizing the RF directly from the 81.6 MHz pump laser pulse train.

INTRODUCTION

The DUVFEL linac is composed of four travelling-wave 2856 MHz accelerator tanks injected by a 1.6 cell photo-cathode gun, a magnetic chicane for bunch compression, and a 10 m undulator. The accelerator tanks are driven by three Thompson 2128 klystrons capable of 40 MW each. The first klystron output is split with 10 MW going to the gun and 30 MW divided between accelerating tanks one and two. Tank one is the reference tank with no high power phase or amplitude control. The gun and tank two have high power phase shifters and attenuators for control. The remaining two klystrons drive tanks three and four directly. A magnetic chicane between tanks two and three is used for electron bunch compression. At the end of tank four there is an analysing spectrometer magnet and a YaG screen beam position monitor (BPM) for measuring electron beam energy. The HGHG FEL operates by seeding the electron bunch by overlaying a laser pulse on the compressed electron bunch. The laser pulse induces energy modulations in the bunch which are converted into spatial modulation in a undulator. This spatial modulation produces coherent lasing in the final undulator. As the electron and seed laser pulses reach sub-picosecond lengths, timing jitter becomes a limiting factor in HGHG FEL performance.
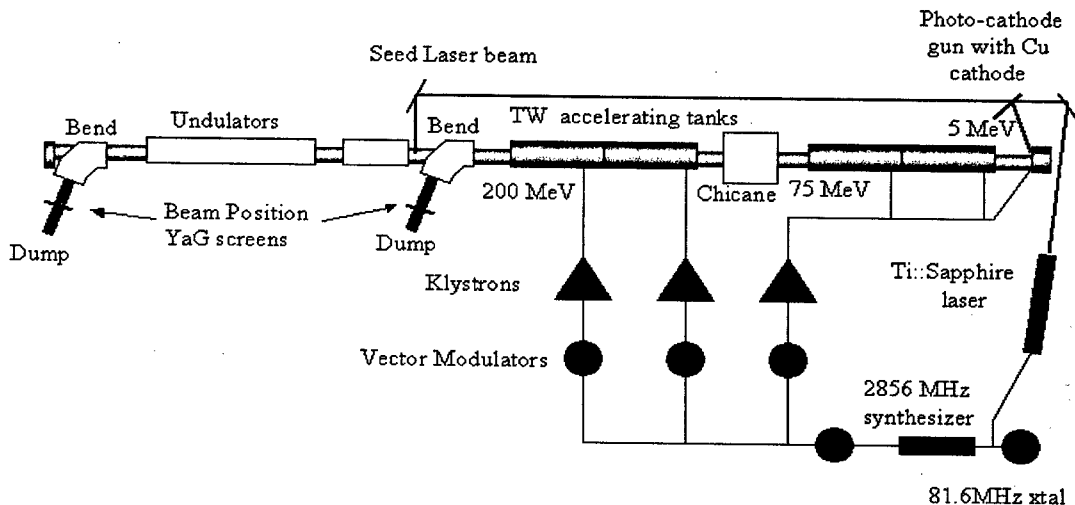
Figure 1. DUVFEL Facility Layout

RF SYSTEM DESCRIPTION

The layout of the DUV-FEL is shown in Figure 1. A 81.6 MHz crystal oscillator drives both the Ti::Sapphire pump laser and a 2856 MHz coaxial dielectric resonator synthesizer for the RF system. The synthesizer output is split to drive the 3 klystrons and provide the LO for phase measurements. A new Quadrature Vector Modulator developed at the DUV-FEL provides the amplitude and phase control. It utilizes a new communications chip by RF Micro-devices Inc., the RF2480 Direct Quadrature modulator. This device is specified to operate with an LO between 800 and 2500 MHz, and baseband I/Q channels from DC to 250 MHz. The 250 MHz modulation bandwidth will allow feedforward during the 2-microsecond rf pulse for pulse shaping, if required in the future. As-built the modulators have approximately a 5% amplitude ripple and 4-degree phase accuracy. In order to improve this each modulator is calibrated by recording the I and Q set

points required to step the phase in 10-degree steps and maintain uniform amplitude. A polynomial fit to the calibration data is stored in the EPICS control system to drive the I and Q channels. After calibration the phase and amplitude variations are brought to 1 degree and 1 % as the phase is varied from 0 to 360 degrees. At very small amplitudes, ~1% of full power, the phase error approaches 10 degrees. In principle this could be corrected by calibrating over several amplitude ranges but this has been enough of a problem in normal operations to warrant the effort. The modulators have been installed and operating for over a year without any failures. They have proven to be extremely stable against thermal drift and noise since the entire modulator is on a single piece of GaAs.

A vector de-modulator has been prototyped using the Analog Devices AD8347 integrated circuit. Like the RF2480 this IC was designed for use in wireless communications systems with an RF bandwidth 800 to 2700 MHz. The baseband output bandwidth of 65 MHz easily accommodates the 2-microsecond pulse width of the klystrons. For testing an Agilent 8357 Network Analyzer (NA) provided the LO input to both the modulator and the demodulator. The modulator output signal was split to provide the transmission (S21) return signal to the NA and RF input to the demodulator. A LabView program was written to command the I/Q modulator in one-degree steps and provided an external trigger to the NA for each step. Figure 2 shows the input phase vs. the reconstructed output phase of the AD8347.
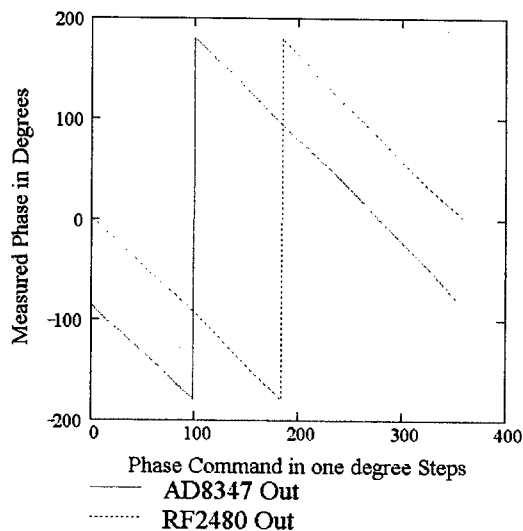
Figure 2. Phase Output of Vector Modulator as measured by Network Analyser and AD8347 de-Modulator

PHASE NOISE CHARACTERIZATION

The timing jitter between the electron beam and seed laser is critical for ultra-short pulse and cascaded HGHG FEL operation. The stability of the rf to laser system, and the

shot to shot stability of the electron beam was characterized. Based upon the results of this system characterization an improvement in the rf to laser jitter was implemented.

Beam Jitter Measurements

The final electron beam energy is related to the field strength and timing jitter of the accelerating fields as

$$E_f(t) = \sum_i E_i(\cos(t + \Delta\phi_i))$$

where i denotes the ith rf system. The laser to RF jitter dominates the jitter between the seed laser and the electron bunch, in particular at the photo-cathode gun. Since we are measuring E_f which is a function of energy and phase there is a contribution of tanks 2 and 3 amplitude jitter that "hides" the actual measured value of γ_{rf}. In order to separate this effect from others we have performed the following measurements.

The jitter was measured using the first bending magnet as a spectrometer and measuring the beam position on a YaG screen, similar to zero-phasing bunch measurements[2]. For these experiments the nominal beam energy was 60.6 MeV. The gun phase was set to 30 degrees, tank 1 on crest, tank two 23 degrees off crest and tank three was phased so as to cancel the energy chirp of tank 2, near 90 degrees phase. The beam was centered on the YaG screen downstream of the first spectrometer magnet. The phase of the rf system with respect to the laser system can be adjusted with an I/Q modulator just after the rf synthesizer. This was used to introduce a +3 degrees and − 3 degrees phase shift to calibrate the beam position on the YaG screen in degrees of RF or time. Figure 3 shows the jitter in picoseconds of the nominal and +/- 3-degree calibration electron beams.
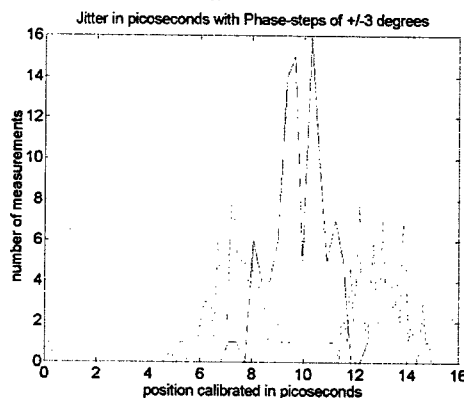
Figure 3. Beam jitter as measured by position on YAG screen after spectrometer magnet.

This measurement was repeated but with the variable being the klystron 2 voltage. A 10^{-3} relative klystron voltage shift on tank 3 is shown in Figure 4. The klystron 2 PFN voltage was measured with an oscilliscope and varied shot-to-shot by 10^{-4} rms. This voltage variation is not enough to explain all of the jitter in figures 3 and 4.
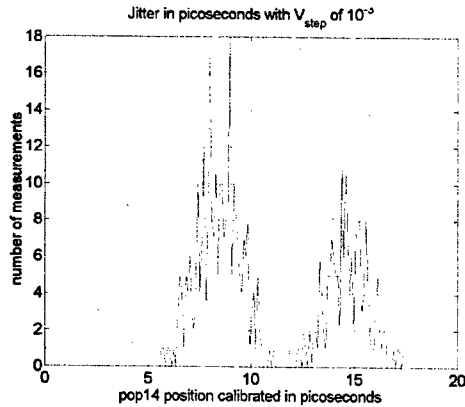
Figure 4. Beam position with 10^{-3} relative voltage step on tank 3 klystron. The standard deviation of the tank 3 klystron voltage was measured to be 1×10^{-4}.

Laser to RF Phase Jitter

The phase jitter between the laser and RF system was measured by monitoring a sample of the Ti::sapphire laser output with a fast (10 GHz bandwidth) diode detector. The 35th harmonic at 2856 MHz was filtered, amplified and compared against the 2856 MHz synthesizer output in a mixer. The error signal was low pass filtered at 300 kHz, and amplified. This signal was analysed with a Dynamic Signal Analyser (DSA). The I/Q modulator was used to calibrate the data by introducing a +/- 3-degree phase shift. The results are shown in Figure 5.
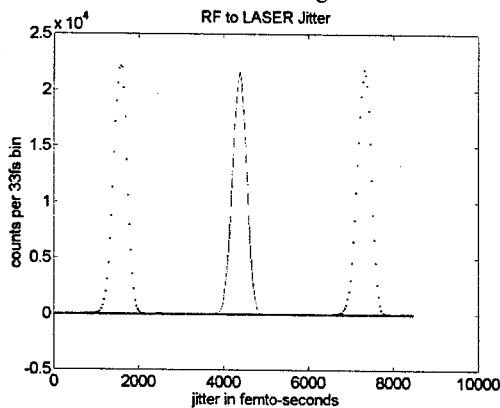
Figure 5. Laser to RF jitter in an 8 second histogram length with +/- 3-degree calibration traces.

In order to reduce the jitter between the laser output pulse and the 2856 MHz accelerating field methods of locking the rf to the laser oscillator pulse train were investigated. Since the rf is the 35th harmonic of the 81.6 MHz finding an IF frequency for a conventional loop[3] required division by an odd integer. Although possible, odd division is difficult to perform without adding additional noise. It was decided to use the laser oscillator to derive the rf frequency directly. The laser oscillator output pulse train at

81.6 MHz was detected with a photodiode with 10 GHz bandwidth, and 3 Amp/W sensitivity. The 35th harmonic was filtered out with a bandpass filter resulting in –30 dBm signal strength. This signal was amplified to 0 dBm and sent to the low level RF system, as described above. The RF to laser jitter measurement was repeated and is shown in Figure 6. Each trace represents a histogram of the phase detector output with a 3.8microsecond sample time and an 8 second histogram length. The right trace is a +2-degree calibration taken by stepping the I/Q modulator phase that is inside the measurement loop. The 2-degree step is nearly the minimum step size that produces sufficient accuracy for reliable calibration with our current set-up. The Digital to Analog Convertors (DAC'S) that drive the quadrature modulators are only 12 bit and produce quantization of the phase steps below 1 degree in some quadrants.
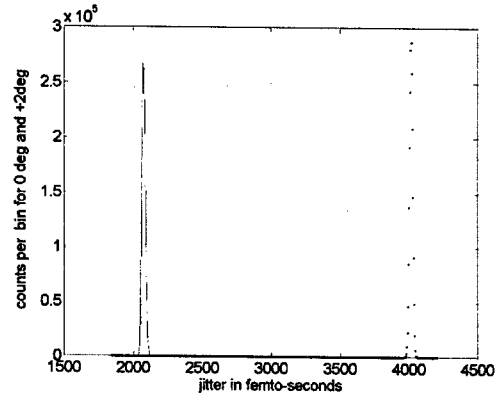
Figure 6. Laser to RF jitter in 8-second histogram length when RF is driven by laser output. A +2-degree calibration trace is on the right, second calibration trace omitted to improve scale for clarity.

CONCLUSIONS

Driven by the need for sub-picosecond jitter between a photo-cathode laser and the linac rf system a program of improvements to the rf system has been undertaken. Implementing a new vector modulator enabled accurate and repeatable phase and amplitude control. Measurements of the laser and rf have identified specific problem areas producing this jitter. Operation with a laser driven rf source has greatly reduced the front-end jitter of this system, from 400fs FWHM to <40fs FWHM

REFERENCES

[1] A. Doyuran et al, Saturation of the NSLS DUV-FEL at BNL, these proceedings

[2] D.X. Wang et al, Phys Rev. E Vol 57, No. 2 Feb 1998

[3]F.B. Kiewiet et al, NIM PR A 484(2002) 619-624

PROGRESS IN THE DEVELOPMENT OF HIGH LEVEL RF FOR THE SNS RING*

A. Zaltsman, M. Blaskiewicz, J. Brennan, J. Brodowski, J. Butler, M. Meth, F. Severino, K. Smith, R. Spitz

BNL, New York 11973, USA

Abstract

A High Level RF (HLRF) system consisting of power amplifiers (PA's) and ferrite loaded cavities is being built by Brookhaven National Laboratory (BNL) for the Spallation Neutron Source (SNS) project. Four cavities were built and are being tested. Each cavity has two gaps with a design voltage of 10 kV per gap and will be driven by a PA directly adjacent to it. The PA uses a 600kW tetrode to provide the necessary drive current. All the PA's were built and are being tested at BNL prior to shipping to ORNL. A dynamic tuning scheme used to help compensate for the effect of beam loading was implemented and tested.

1 INTRODUCTION

Main tasks of the HLRF system for the SNS ring are to capture proton beam during 1 ms injection from the 1GeV linac and to maintain a gap for the rise time of the extraction kicker. The HLRF system consists of three harmonic one cavities running at 1.05 MHz and one harmonic two cavity at 2.1 MHz.

The HLRF is required to operate at wide dynamic ranges of the gap voltage (20 dB) and from no beam loading at the beginning of the cycle to the heavy beam loading (75 Amps peak current) at the end.

This paper will describe progress in the development and testing of all the key components of the HLRF system.

2 SYSTEM PARAMETERS

High beam loading and reliability of the system were the determining factors for the system configuration and parameters.

To achieve these requirements, a set of parameters was developed. These parameters take into consideration beam loading, reliable high voltage design, availability of components (ferrites, tubes, etc.), space in the ring and maintainability.

System parameters are tabulated in Table I.

Table I

RF system type	Dual harmonic
Cavity length	2.3 m
Accelerating gaps per cavity	2
Harmonic 1 frequency	1.058 MHz
Number of harmonic 1 cavities	3
Harmonic 1 total voltage	40 kV
Harmonic 2 frequency	2.115 MHz
Number of harmonic 2 cavities	1
Harmonic 2 total voltage	20 kV
Beam loading compensation	Dynamic tuning and feed forward
Harmonic 1 cavity shunt impedance	800 Ω

3 CAVITY AND POWER AMPLIFIER

Reliability, conservative design and easy maintainability were the prime consideration in the development of the SNS RF system.

Small samples, as well as full size ferrite rings, were evaluated for power dissipation, permeability and instabilities. The best choice for the ferrite for this application was Philips 4M2. The highest flux density is at the lowest frequency and on the inner surface of the ferrite ring. Each gap consists of 21 rings, and each ring measured 50cm O.D x 25cm I.D. x 2.72cm thick.

$$V_{gap} = 2 \cdot \pi \cdot f \cdot B_{rf} \cdot l \cdot a \cdot \ln(b/a)$$

$$B_{rf\,max} = \frac{10^4}{6.28 \cdot 1.05 MHz \cdot 21 \cdot .0272 \cdot .125 \cdot \ln\frac{50}{25}} = 310 \cdot Gauss$$

Tests of the ferrite showed no instabilities at flux density in excess of 400 Gauss.

In our design, four capacitors of 750 pF each provide a total gap capacitance of 3 nF. Because removing 3 of 4 gap capacitors from the h=1 cavity will

---

convert it to h=2 cavity, we are able to utilize the same cavity for both systems.
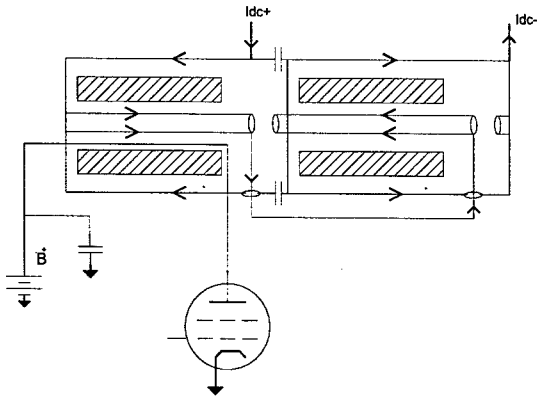
Figure 1

Figure 1 shows a functional diagram of the RF cavity and the PA. Ferrite rings are dc biased whereas the outer can, beam pipe and the gap connecting buswork form a single turn bias winding. Because two halves of the cavity are in series to the dc bias, but in parallel to the RF drive, the RF will be cancelled (figure eight).

At the present time two out of four cavities were fully tested to 11 kV peak and are ready to ship to ORNL. The other two are fully assembled and ready for testing. Two amplifiers are fully tested and the remaining two are being assembled.

The amplifier is magnetically coupled to the cavity. B^+ link is inserted along the beam pipe. This technique eliminates the need for a plate choke. To reduce the downtime in case of the failure of this link a second one was installed and tested to the full RF voltage.
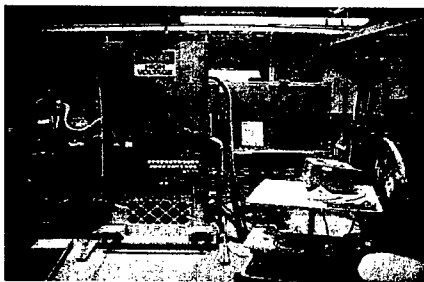
Cavity and the PA under test

4 DYNAMIC TUNING

The beam current in the accumulator ring is in quadrature with the generator current. During the accumulation the average beam current increases from 0 to 35 amperes. The peak amplitude of the first harmonic component is 50 amperes per gap with total 100 amperes per cavity.

$$I_b = 2 \cdot 10^{14} \, ppp = 35 A_{dc} = 55 A_{pk}$$

By optimizing the resonant frequency of the cavity, the PA current may be reduced to the unloaded value.

Set the gap voltage to $V(t) = V_{rf} \sin(\omega t)$ and the PA current to $I_{pa}(t) = \left(\dfrac{V_{rf}}{R}\right) \sin(\omega t)$.

The beam current is $I_B = I_b \cos(\omega t)$.

The total driving current is the sum of the beam and PA contribution and is equal to the sum of the currents in the resistor, capacitor and inductor of the cavity.

$$\frac{V_{rf}}{R} \sin(\omega t) - I_b \cos(\omega t)$$

$$= \frac{V_{rf} \sin(\omega t)}{R} + \left(\omega C - \frac{1}{\omega L}\right) V_{rf} \cos(\omega t)$$

$$\text{so,} \quad I_b = V_{rf}\left(\frac{1}{\omega L} - \omega C\right)$$

The inductance is varied according to:

$$-\frac{\Delta L}{L} = \frac{(R/Q) \cdot I_b}{V_{rf} + (R/Q) \cdot I_b} \quad \text{where} \quad \left(R/Q = \frac{1}{\omega C}\right)$$

$$\frac{\Delta L}{L} = .35 = 35\%$$

$$\frac{\Delta f}{f} = -\frac{1}{2}\left(\frac{\Delta L}{L}\right) = 17\%$$

At 1.05 MHz it would represent 170 kHz frequency difference between the drive frequency and the resonant frequency of the cavity. The loaded Q of the cavity is 50 at tube quiescent current of 5 amperes, and drops to 38 at 10 amperes.

To simulate this mistuned condition the frequency was swept from 1.05 MHz to 1.22 MHz, while keeping the cavity tuned at the 1.05 MHz by the constant tuning current. AGC kept the voltage on the gap constant at 7 kV. (Figure 2)
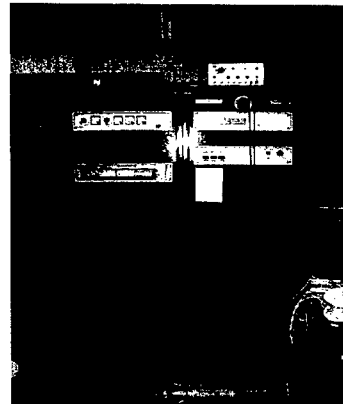
Dynamic tuning PS
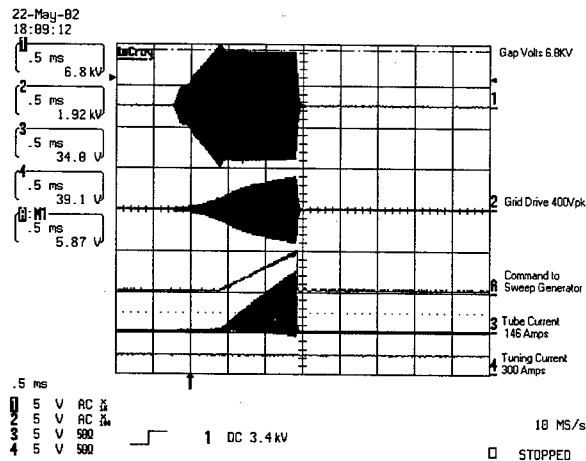
Figure 2

To reduce the effect of beam loading Dynamic Tuning was implemented. Dynamic tuning is a feed forward correction, which is perfect for the SNS application since the repetition rate of the machine is 60 Hz, and the beam intensity doesn't change from cycle to cycle. Tuning current will be changing at 60 Hz (or a multiple of it) by +/-450 amperes peak around the dc component needed to tune the cavity without the beam loading.

The results were great, and a full power tuning supply was built to test on the final cavity.
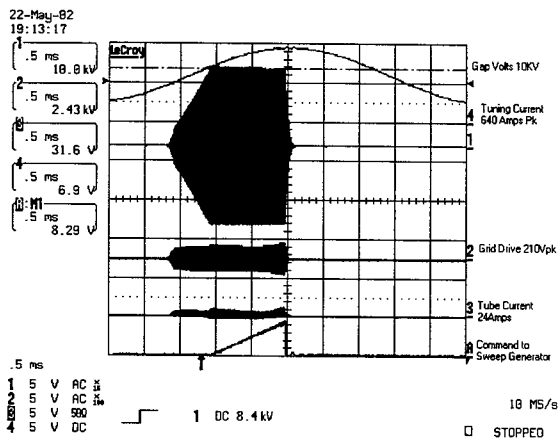
Figure 3

Fig. 3 shows a dynamically tuned cavity at 10 kV on the gap with the tube current less than 30 amperes. The tube current and the grid drive are drastically reduced.

5 POWER SUPPLIES

The beam accumulation in SNS lasts mS, and if we add mS for pre tuning the cavities to the nominal voltage, the duty cycle of the HLRF system does not exceed 12%. A pair of 12 kV, 3.5 amp charging power

supplies in parallel, charging a 70uF capacitor bank was chosen for the anode supply. To switch the tube on and off we used fast (1 MHz) grid bias power supply that switches the bias between the shut-off (-700 volts) and 20 amperes of quiescent current.

Anode, screen, grid and 3 out 4 tuning power supplies are at BNL being tested. 500 watt drivers were successfully tested and being ready to ship to ORNL.

6 CONCLUSIONS

Two cavities, two power amplifiers and a set of power supplies were rigorously tested and operated at BNL at the gap voltages exceeding the design values and are being packaged for shipment to ORNL

The system was designed conservatively with an eye on reliability, ease of operation and troubleshooting in a high radiation environment. All the components used were rated with comfortable safety margins.

7 REFERENCES

[1] M.Blaskiewicz, et all, 2001 Particle Accelerator Conference, Chicago

[2] F.Pederson, IEEE, TNS, Vol. NS-22, No.3, pg 1906, (1975).

[3] D.Boussard, CERN 91-04 (1991)

[4] M.Meth, A.Zaltsman, Stability and Neutralization of SNS RF Power Amplifier, SNS tech note #68, 1999.

[5] A.Zaltsman, et all, 2002 European Particle Conference, Paris

BUNCHER CAVITY FOR ERL

V. Veshcherevich[†] and S. Belomestnykh
Laboratory for Elementary-Particle Physics, Cornell University, Ithaca, NY 14853, USA

Abstract

Design of the buncher cavity for Cornell/JLab ERL project is presented. This is a reentrant spherical copper cavity at a frequency of 1300 MHz. It will be installed between a 500 keV electron gun and superconducting accelerating sections in the injector part of ERL. The cavity has Q of 20,000 and a shunt impedance of 2.1 MOhm. For a design cavity voltage of 200 kV, power dissipated in cavity is as much as 9.6 kW. The cavity has a coaxial loop coupler and will be driven by a 17.5 kW klystron. The estimates of cavity influence on beam dynamics are also discussed.

1 INTRODUCTION

The project of a 100 MeV, 100 mA Energy Recovery Linac (ERL) is in the R&D stage at Cornell University and Jefferson Laboratory [1], [2], [3]. To obtain the required beam properties, bunching of the beam produced by the gun is necessary. Therefore a buncher cavity will be built and installed between the electron gun and the first accelerating section of ERL injector. It will produce an energy spread of about 10 keV in a $\sigma = 12$ ps, 500 keV bunch coming from the gun so that the bunch will be shortened to $\sigma = 2.3$ ps in the drift space between the buncher cavity and the first injector cavity.

2 CAVITY DESIGN

The frequency of the buncher cavity is equal to the frequency of injector and main ERL linacs (1300 MHz). The maximum RF voltage that the buncher cavity should provide is 200 kV. This voltage is relatively small. Therefore there is no reason to build a superconducting cavity despite the fact that other accelerating structures of the ERL are superconducting. The buncher cavity is a copper cavity that has a spherical reentrant shape, which was optimized using the SLANS computer code [4]. Its geometry is shown in Figure 1. Table 1 summarizes main cavity and cavity-related parameters.

Figure 1: Geometry of the ERL buncher cavity.

The cavity has four 40 mm diameter ports: a port for input coupler on the cavity top, a pump-out port on the cavity bottom, and two ports in the horizontal plane for tuners. There is also a small 15 mm port for the field probe.

3 INPUT COUPLER

The cavity has a water-cooled coaxial loop type coupler (see Fig. 3). However, the coaxial part is short and ends with a coax-to-waveguide transition with a ceramic window similar to the warm window of the TTF III coupler for TESLA cryomodule [5]. The coupling can be

Table 1

Energy of electrons, E	500 keV
Velocity of electrons, v/c	0.863
Beam current, I_0	100 mA
Resonance frequency, f	1300 MHz
Q	20,000
Shunt impedance, $R = V^2/2P$	2.1 MOhm
Nominal operating voltage, V	120 kV
Maximum accelerating voltage, V_m	200 kV
Maximum dissipating power, P_m	9.6 kW
Peak surface electric field, E_p	8.8 MV/m
Cavity detuning by beam current, ψ	73°

† vgv@lepp.cornell.edu
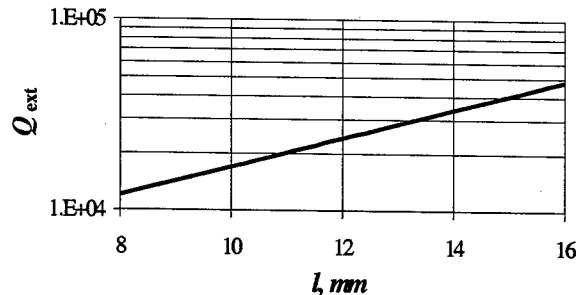
Figure 2: Dependence of Q_{ext} of the cavity on the distance between the coupling loop and the port opening.
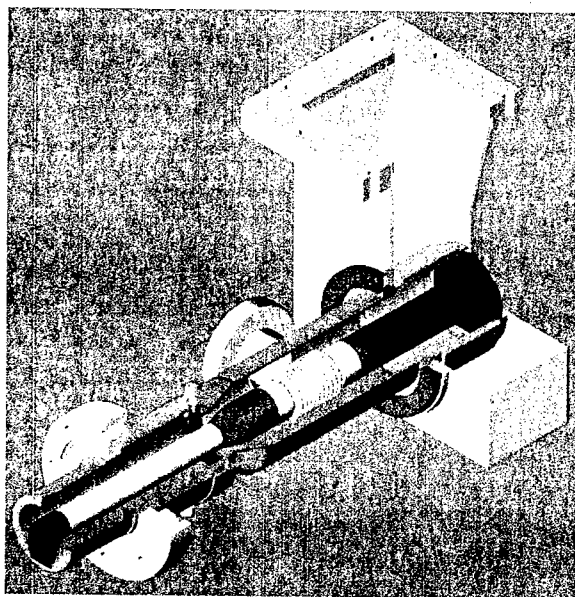
Figure 3: Design of the input coupler.
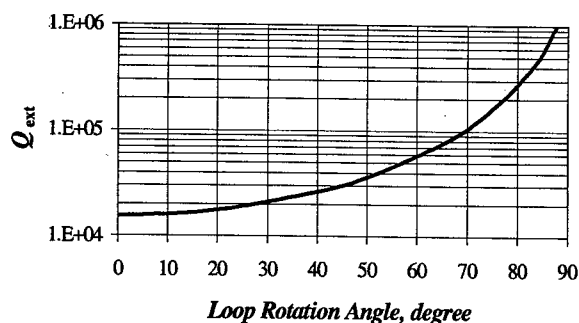
Figure 4: Dependence of Q_{ext} of the cavity on the coupling loop rotation.

Figure 5: Tuning the cavity frequency by a plunger tuner.
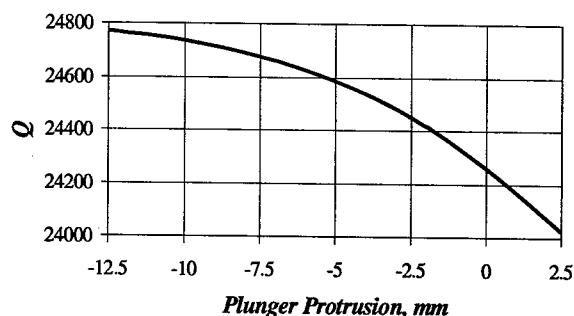
Figure 6: Cavity Q as a function of tuner position.

adjusted by rotation of the coupling loop. Figure 2 shows the dependence of Q_{ext} of the cavity on the distance l between the loop and the port opening; Figure 4 shows the dependence of Q_{ext} on the loop rotation for $l = 10$ mm.

The average RF power delivered by buncher cavity to the beam is zero. Therefore no overcoupling is necessary and the Q_{ext} of the input coupler should be equal to $Q_0 = 2.0 \times 10^4$.

The RF power that goes trough the coupler to the cavity during routine operation is 3.4 kW and is 9.6 kW during operation at highest voltage (see Table 1). However, for the fast beam turn-on an operation with pre-detuned cavity (73° off resonance) will be necessary that requires a higher RF power of 12 kW at high reflection. Similar power requirements are valid for operation with a discontinuous electron beam. For operation at the highest voltage with a discontinuous beam the RF power goes up to 23 kW that is higher than the klystron power (17.5 kW). In this case the cavity will be operated halfway detuned.

4 TUNERS

The cavity has two plunger type water-cooled tuners. Two tuners provide a better field symmetry on the beam axis. Only one tuner is used for routine operation, the other one is used for preliminary frequency adjustment. Figures 5 and 6 show how the cavity frequency and Q depend on tuner position. These results were calculated by the 3D computer code CST Microwave Studio® [6].

During operation, the tuner has to compensate thermal effects (roughly 400 kHz from cold cavity to maximum voltage) and beam detuning (108 kHz). That corresponds to plunger travel of 2.5 mm. The full stroke of one tuner is 10 mm that gives a tuning range of 1.6 MHz.

5 FIELDS ON BEAM AXIS

The cavity has to have very low transverse fields on the beam axis. Therefore we try to symmetrize perturbations of an ideal cavity shape: there are two tuners symmetrically placed in the horizontal plane and in the vertical plane the input coupler is balanced by a pumping port optimized to minimize the vertical kick on the electron beam.

Figure 7 presents transverse fields on the beam axis calculated by CST Microwave Studio®. Using these data, transverse kicks were calculated:

$$\frac{V_x}{V_{acc}} = \frac{\int_{-l}^{l} (E_x \sin kz + vB_y \cos kz)dz}{\int_{-l}^{l} E_z \cos(kz)dz} = 2.3 \times 10^{-4} / mm,$$

$$\frac{V_y}{V_{acc}} = \frac{\int_{-l}^{l} (E_y \sin kz - vB_x \cos kz)dz}{\int_{-l}^{l} E_z \cos(kz)dz} = 3.5 \times 10^{-4}.$$

(The horizontal kick was calculated for the difference of positions of two tuners of 1 mm).

The values of kicks are small, they are an order of magnitude smaller than the ERL requirement (1.6×10^{-3}) [7].

Figure 8: Calculated impedances of higher order modes.
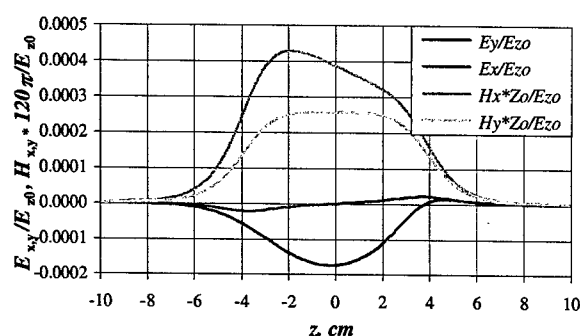
Figure 7: Transverse fields on the cavity axis for 1 mm difference of positions of two tuners.

6 HIGHER ORDER MODES

Higher order modes of the cavity were calculated and the results are presented in Figure 8 (the modes having frequencies above cut-off frequencies of the beam pipe and being able to propagate along the beam pipe are not shown). In the ERL machine electron bunches will pass the cavity at the rate of 1300 MHz. Accordingly, only modes with resonance frequencies multiple of 1300 MHz can be dangerous for the beam stability. The dashed lines in Figure 8 correspond to harmonics of 1300 MHz. As one can see, there are a few modes that seem to be close to these frequencies but they are at least 20 MHz away from dangerous harmonics. Therefore no dedicated HOM dampers are provided in the buncher cavity.

7 CONCLUSION

A preliminary design of the buncher cavity for Cornell/JLab ERL project has been done. The cavity was optimized for getting a minimal wall loss and low transverse kick.

REFERENCES

[1] S. M. Gruner and M. Tigner (editors). "Study for a Proposed Phase I Energy Recovery Linac (ERL) Synchrotron Light Source at Cornell University". CHESS Technical Memo 01-003, JLAB-ACT-01-04, 2001.

[2] I. Bazarov, et al., "Phase I Energy Recovery Linac at Cornell University," Proc. of the 8th European Part. Accel. Conf., (Paris, France, 2002), p. 644.

[3] G. Hoffstaetter, et al. "The Cornell ERL Prototype Project". This Proceedings, report TOAC005.

[4] D. G. Myakishev and V. P. Yakovlev. "The new possibility of SUPERLANS Code for Evaluation of Axisymmetric Cavities". Proc. of the 1995 Part. Accel. Conf. (Dallas, TX, 1995), Vol. 4, p. 2348.

[5] B. Dwersteg, et al. "TESLA RF Power Couplers Development at DESY". Proc. of the 10th Workshop on RF Superconductivity, Tsukuba, Japan, September 2001.

[6] CST GmbH, Darmstadt, Germany.

[7] S. Belomestnykh, et al. "High Average Power Fundamental Input Couplers for the Cornell University ERL: Requirements, Design Challenges and First Ideas". ERL 02-8, Cornell University, 2002.

INPUT COUPLER FOR ERL INJECTOR CAVITIES*

V. Veshcherevich[†], I. Bazarov, S. Belomestnykh, M. Liepe, H. Padamsee, and V. Shemelin
Laboratory for Elementary-Particle Physics, Cornell University, Ithaca, NY 14853, USA

Abstract

A conceptual design of the input coupler for superconducting injector cavities of Cornell/JLab ERL project is presented. The injector cavities are two-cell structures operating at 1300 MHz in CW mode. The coupler has a symmetric design to accommodate requirements for small transverse kick, high RF power delivery to the cavity, and high input coupling value. Therefore it consists of two identical antenna type couplers symmetrically attached to a beam pipe of the cavity. Each coupler delivers 50 kW of CW RF power to the beam. The coupler has a variable coupling. Q_{ext} should be varied from 4.6×10^4 to 4.1×10^5. The symmetric design of the coupler dramatically reduces the transverse kick, a critical requirement for the ERL project. Estimates of the influence of coupler induced fields on beam dynamics are given.

1 INTRODUCTION

The project of Energy Recovery Linac (ERL)—a challenging ultra-high brightness X-ray source of a new generation—is in the R&D stage at Cornell University and Jefferson Laboratory [1], [2], [3]. It should be a CW 100 MeV machine with high average current (100 mA). Superconducting 1300 MHz RF structures will be used in the main linac and injector of this project. A goal of the ERL project is achieving a 2 µm emittance for a bunch charge q of 77 pC and 0.2 µm for 8 pC at the undulator location. This implies emittances of about 1 µm and 0.1 µm in the injector for the two different bunch charges.

A high brightness injector [4] is a key element of this machine. It includes a 500 keV DC photoemission electron gun, a conventional buncher, and five two-cell superconducting RF cavities. The injector cavities should accelerate the beam to a nominal energy of 5.5 MeV (1 MeV per cavity) with minimal emittance dilution. It requires delivering 500 kW power to the beam (100 kW for each cavity). Operation with acceleration to about 15.5 MeV (3 MeV per cavity) is also planned at a reduced average current (33 mA), limited by the total RF power available. All five two-cell cavities will be mounted in a single cryomodule [5].

2 REQUIREMENTS TO THE INJECTOR CAVITY COUPLER

The parameters of the injector cavities are summarized in Table 1. The injector cavity coupler has to deliver

Table 1: Parameters of the injector cavities

Energy of electrons, E	0.5 to 5.5 (15.5) MeV
Beam current, I_0	100 (33) mA
Frequency, f	1300 MHz
Number of cells per cavity, N_c	2
Q_0	$\geq 5 \times 10^9$
Q_{ext}, nominal	4.6×10^4
Q_{ext}, range	4.6×10^4 to 4.1×10^5
R/Q	218 Ohm
Cavity voltage, V	1 (3) MV
RF power per cavity, P	150 kW

100 kW of RF power to the beam and provide matching conditions for a cavity gap voltage of 1 through 3 MV and corresponding beam currents of 100 through 33 mA. Thus the external Q factor range is 4.6×10^4 to 4.1×10^5 or a factor of 9. This coupler should be designed to withstand an RF power up to 150 kW CW in traveling wave (TW), the installed RF power per cavity.

The main design challenges to RF power coupler of the injector cavity are:

- High average RF power (up to 150 kW TW)
- Very strong coupling ($Q_{ext} = 4.6 \times 10^4$)
- Wide range of variable coupling (factor of 9)
- Minimizing transverse kick to the beam to avoid emittance growth
- Multipacting-free (or almost multipacting-free) design

3 COUPLER DESIGN

We considered different options of the coupler design [6]. Finally, we chose a twin coaxial coupler [7], [8]. It consists of two identical antenna type couplers symmetrically attached to a beam pipe of the cavity (see Fig. 1). With this approach only a half of the full RF
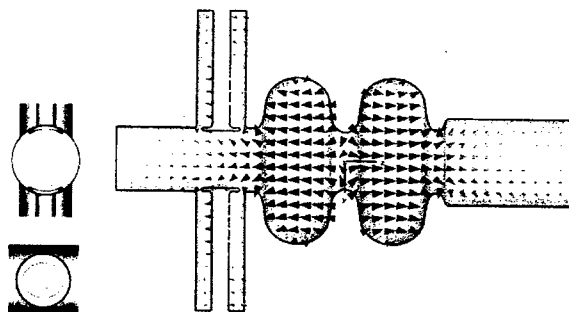
Figure 1: Input coupler in the injector cavity.

power goes through a single coupler and twice as less coupling is necessary ($Q_{ext} = 9.2 \times 10^4$). Another excellent feature is a good transverse field symmetry, which is very important for the ERL requirements—no more than 10% of the emittance growth due to injector cavities.

As individual couplers we decided to use the TTF III couplers [9] modified to meet our requirements. It is rather natural because we plan to use TESLA cavities and cryostats in the main linac structure. We took into account some of the B. Dwersteg's advices given in [10].

The cold part of the original coupler was completely redesigned. Instead of a 40 mm 70 Ω coaxial line, a 62 mm 60 Ω line was chosen for getting a stronger coupling and better handling the high power. It is also multipacting-free in the full power range [7]. The coupler has a larger profiled antenna tip to provide a strong coupling. The travel range of the antenna was increased to 15 mm for getting the required coupling variation (see Fig. 2). In the cold window a bigger ceramic cylinder is used (similar to the one used in the warm window but with a reduced height). The weakest points of the TTF III coupler at high power levels are the bellows in the warm coaxial line. At the power of 50 kW the bellows temperature would reach 400 K on the outer conductor and 375 K on the inner conductor. This problem is solved in the new design by providing air cooling of both bellows of the warm coax line. For realizing the cooling of the outer conductor bellows, an additional edge-welded bellows unit is added to the design. It encloses the regular bellows and an air flow is established in the space between the two bellows. The general design of the coupler is shown in Figure 3.

The coupler has to deliver RF power to a superconducting cavity, i. e. it is a part of the cryogenic system. Table 2 shows the values of heat loads of a single coupler to the cryogenic system.
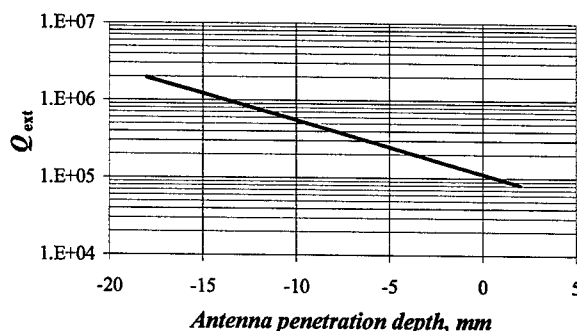
Figure 2: Dependence of Q_{ext} of a single coupler on the penetration of the antenna tip into the cavity beam pipe. The Q_{ext} of a twin coupler is twice as low.

Table 2: Injector cavity coupler heat loads.

	Static	At 50 kW (CW, TW)
To 1.8 K	0.05 W	0.2 W
To 4.2 K	0.30 W	2.0 W
To 70 K	6.80 W	31 W

4 FIELDS SYMMETRY AND BEAM DYNAMICS

The twin coupler design gives an excellent transverse field symmetry on the beam axis. There can be only residual transverse fields due to antennae position errors and errors of power and phase balance between two single couplers.
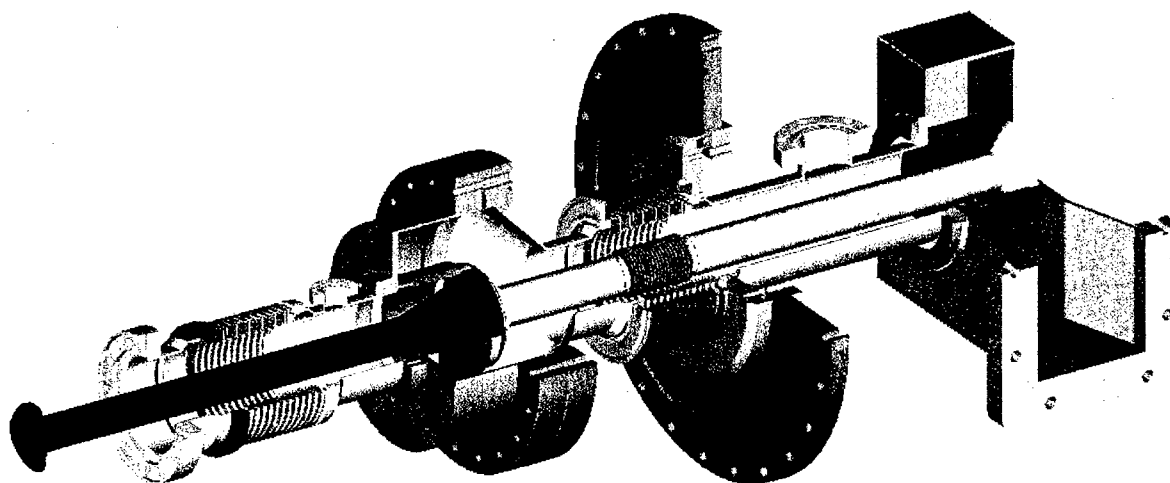
Figure 3: View of the injector cavity coupler.

Figure 4 shows the distribution of transverse fields along the beam axis for 1 mm difference of antenna penetration depths of two couplers (for the strongest coupling where the response to position errors is maximal). The 3D computer code CST Microwave Studio® [11] was used for field calculations. The fields are normalized to the maximum accelerating field E_{zm} on the axis. Integrating the fields, one can calculate the transverse kick for different coupler errors [7], [8]. The results are summarized in Table 3. For a comparison, the transverse kick of a single coupler is also presented in the table.

Figure 4: Normalized transverse fields on the axis of the injector cavity for a relative penetration depth error of 1 mm. The coordinate $z = 0$ corresponds to the cavity center. E_{y1}, B_{x1} and E_{y2}, B_{x2} were calculated respectively for shorted and open coupler.

Table 3: Relative transverse kick (normalized to the maximum accelerating voltage) due to twin coupler errors.

Error in:	Error value	Transverse kick
Relative penetration depth	1 mm	8.0×10^{-4}
Relative phase	1°	5.0×10^{-4}
Relative power	1%	4.5×10^{-5}
Single coupler		3.0×10^{-3}

The influence of an injector cavity on beam dynamics was simulated using the 3D computer code ASTRA [12]. The results are shown in Table 4.

Table 4: Beam emittance growth due to RF focusing and kick in the injector cavity with a single coupler and with a twin coupler.

	q [pC]	V_{acc} [MV]	ε_0 [μm]	σ_z [mm]	σ_x [mm]	emittance growth
single input coupler	77	1	1.0	0.6	2.0	6%
	77	3	1.0	0.6	0.9	3%
	8	1	0.1	0.6	0.6	16%
	8	3	0.1	0.6	0.3	28%
twin input coupler	77	1	1.0	0.6	2.0	4%
	77	3	1.0	0.6	0.9	1%
	8	1	0.1	0.6	0.6	4%
	8	3	0.1	0.6	0.3	1%

One can see from these estimates that coupler kick contribution is not important for nominal bunch charge of 77 pC but becomes noticeable in the case of ultra-low 0.1 μm emittances. For cavity with the twin coupler the emittance growth governs solely by RF focusing.

5 CONCLUSION

A preliminary design of the input coupler for the Cornell/JLab ERL injector cavity has been done. Based on the TTF III TESLA coupler design, it is developed for a much higher CW power operation. A twin coupler design has a very good field symmetry and meets stringent requirements of the ERL project.

REFERENCES

[1] S. M. Gruner and M. Tigner (editors). "Study for a Proposed Phase I Energy Recovery Linac (ERL) Synchrotron Light Source at Cornell University". CHESS Technical Memo 01-003, JLAB-ACT-01-04, 2001.

[2] I. Bazarov, et al. "Phase I Energy Recovery Linac at Cornell University," Proc. of the 8th European Part. Accel. Conf., (Paris, France, 2002), p. 644.

[3] G. Hoffstaetter, et al. "The Cornell ERL Prototype Project". This Proceedings, report TOAC005.

[4] C. Sinclair and I. Bazarov. "High Brightness, High Current Injector Design for the Cornell ERL Prototype". This Proceedings, report WPAB013.

[5] M. Liepe, et al. "Overview of the Cornell ERL Injector Cryomodule". This Proceedings, report TPAB052.

[6] S. Belomestnykh, et al. "High Average Power Fundamental Input Couplers for the Cornell University ERL: Requirements, Design Challenges and First Ideas". ERL 02-8, Cornell University, 2002.

[7] V. Shemelin, S. Belomestnykh, and H. Padamsee. "Low-Kick Twin-Coaxial and Waveguide-Coaxial Couplers for ERL". SRF 021028-08, Cornell University, 2002.

[8] V. Shemelin, et al. "Dipole-Mode-Free and Kick-Free 2-Cell Cavity for the SC ERL Injector". This Proceedings, report WPAB012.

[9] B. Dwersteg, et al. "TESLA RF Power Couplers Development at DESY". Proc. of the 10th Workshop on RF Superconductivity, Tsukuba, Japan, 2001.

[10] B. Dwersteg. "Couplers for Superconducting Cavities at 1.3 GHz High CW Power," presented at the Workshop on 1.3 GHz Couplers for CW Operation at Power Levels between 10 and 100 kW, ACCEL Instruments GmbH, Bergisch Gladbach, Germany, April 9, 2002.

[11] CST GmbH, Darmstadt, Germany.

[12] P. Piot. Private communication.

LINEARIZATION OF THE FERMILAB RECYCLER HIGH LEVEL RF*

J. Dey[#], S. Dris, T. Kubicki, J. Reid, FNAL, Batavia, IL 60510, USA

Abstract

In studying the Recycler high level RF, it was found that at 89 kHz, the lowest frequency required by the system, some nonlinearities in magnitude and phase were discovered. The visible evidence of this was that beam injected in a barrier bucket had a definite slope at the top. Using a network analyzer, the S-parameter S_{21} was realized for the overall system and from mathematical modeling a second order numerator and denominator transfer function was found. The inverse of this transfer function gives our linearization transfer function. The linearization transfer function was realized in hardware by summing a high pass, band pass and low pass filter together. The resulting magnitude and phase plots, along with actual beam response will be shown.

INTRODUCTION

The recycler high level RF system [1] has four stations producing a total of 2000 peak accelerating volts. Each station consists of a broadband 3.5 kilowatt RF (10 KHz-100 MHz) solid-state amplifier, 50Ω ferrite loaded cavity, and a feedforward circuit that is used to compensate for the droop induced by the AC coupled amplifiers and the low frequency response of the cavities. It was discovered through beam studies that the beam profile exhibited a slope from unequal beam charge distribution between a barrier bucket (Fig. 1.) After some investigation, a small parasitic 89 KHz (h =1 harmonic component) sinusoidal component was found imposed on the RF vector sum of all four RF stations.
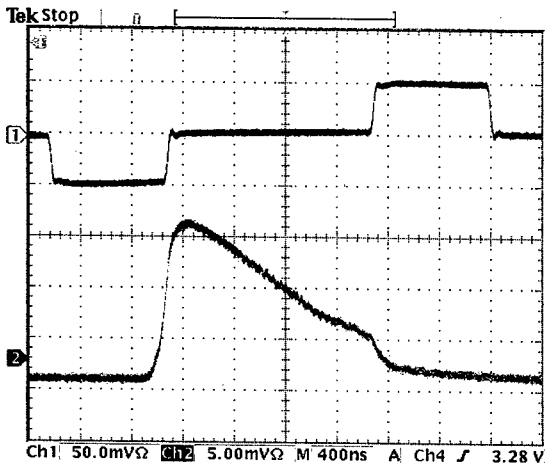
Figure 1: Recycler Barrier Bucket (blue) and Beam Profile (red) before Compensation

LINEARIZATION
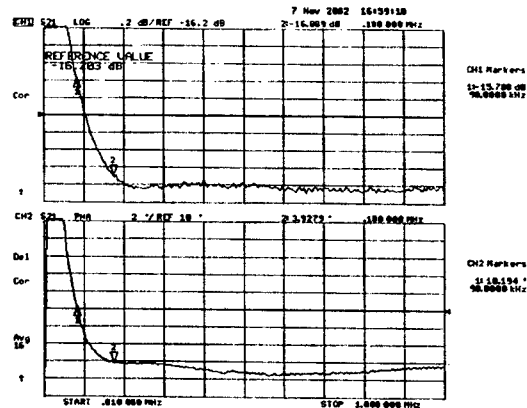
Figure 2: Nonlinear Region of the Recycler High Level RF

Using an Agilent 8753 ES Network Analyzer, the system's frequency response was measured using the vector RF sum signal from four cavities and is shown in Figure 2. The nonlinearity in magnitude and phase was found to be 1.1 dB and 6.26° in phase from 90 kHz to 180 kHz. Most of the error in flatness is due to the Amplifier Research 3500A100 Broadband RF Amplifier. The goal was to linearize the frequency in the region from 90 kHz to 1 MHz with a flatness in amplitude of 0.26 dB and 1.8° in phase. Using the program Filter Light® 2.1, we were able to quickly realize that a second order high pass Chebyshev 1 Filter (Eq. 1) was a close approximation to the transfer function shown in Figure 2.

$$\frac{s^2}{s^2 + 9.7 \times 10^4 s + 4.5 \times 10^{10}} \qquad (1)$$

Taking the inverse of transfer function Equation 1 yields transfer function Equation 2, a good starting point in creating a compensation network that would flatten out the low-end response.

$$\frac{s^2 + 9.7 \times 10^4 s + 4.5 \times 10^{10}}{s^2} \qquad (2)$$

Error-based Optimization

Taking the 801 S_{21} points (10 kHz to 999.6 kHz) from the Network Analyzer and multiplying them by the linearizing function for each frequency, gives the compensated response. These results were analyzed at 90 kHz intervals from 90 kHz to 990 kHz to find the smallest root mean square percentage error. By iteratively making changes to the linearizing function, a new linearizing function (Eq. 3) was found that gave the smallest compromise in magnitude and phase for the root mean square percentage error.

$$\frac{s^2 + 1.8 \times 10^5 s + 6.2 \times 10^{10}}{s^2 + 1.26 \times 10^5 s + 4 \times 10^9} \quad (3)$$

By breaking the transfer function (Eq. 3) into three parts, using the same common denominator, three filters could be constructed and summed together. The s^2 term in the numerator is a Second Order High Pass Bessel Filter (Fig. 3.) The s term in the numerator is a First Order Band Pass Butterworth Filter (Fig. 4.) The constant term in the numerator is a Second Order Low Pass Matched Filter (Fig. 5.)

0.5369uF

232.8uH

$$\frac{s^2}{s^2 + 1.26 \times 10^5 s + 4 \times 10^9}$$
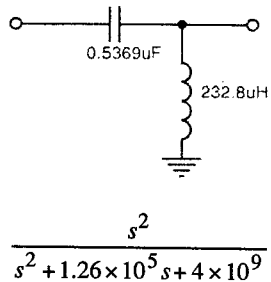
Figure 3: Second Order Term Filter

0.315uF   793.7uH

$$\frac{1.26 \times 10^5 s}{s^2 + 1.26 \times 10^5 s + 4 \times 10^9}$$
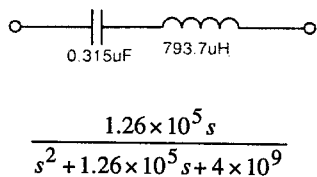
Figure 4: First Order Term Filter

2.684mH

0.1863uF

$$\frac{4 \times 10^9}{s^2 + 1.26 \times 10^5 s + 4 \times 10^9}$$
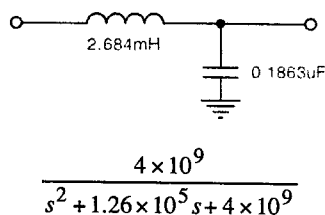
Figure 5: Constant Term Filter
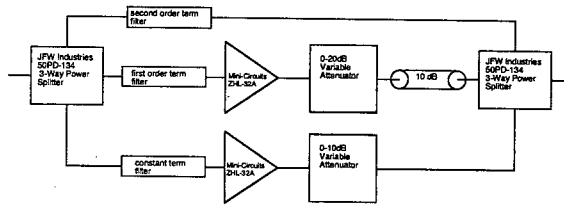
Figure 6: Block Diagram of Linearizing Circuit

IMPLEMENTATION

The filter program was used to implement the individual parts of the transfer function. Each section was found by applying the appropriate filter type that would implement each numerator term. Once this was found, the filter program allowed the user to change the values of the capacitors and inductors. The program has the capability of generating a new transfer function from these values of components. This transfer function was compared to the theoretical model. It was necessary to find three separate functions that implemented the numerator term over a common denominator. Coefficients in front of the different terms were corrected by the appropriate amount of gain (Fig. 6.)

The theoretical values of the phase obtained from the mathematical modeling of each part of the compensation transfer function were used as a basis to compare how well the real circuit approximates the ideal circuit. The phase component of each part was calculated at 89 kHz and up to the 11th harmonic. Measurements of each part of the compensated transfer function's phase were compared to the ideal phase results. The capacitor and inductor component values were changed to better approximate the ideal case for each part. This iterative process was used until the best approximation of the ideal transfer function was found for each case. The circuits were built using surface-mounted capacitors and inductors. Using surface-mounted parts enabled a closer approximation of ideal component values, since parasitic lead inductances are much less.

The construction of the compensation circuit required the use of two 3-way resistive power dividers/combiners, amplifiers, fixed value and variable attenuators, and the filter circuits to realize the function. The second order high pass filter for the s^2 term requires no gain adjust. The First Order Band Pass Butterworth filter required 3.1 dB of gain to realize the s-term part of the compensated transfer function. The Second Order Low Pass Matched filter required 23.8 dB of gain to realize the constant term of the compensated transfer function. The amplifiers used were Mini-circuits ZHL-32A with 25 dB of gain. Variable attenuators were placed at the output of both amplifiers, while an additional 10 dB attenuator was placed with the amplifier and variable attenuator that controlled the gain for the s-term of the compensated transfer function.
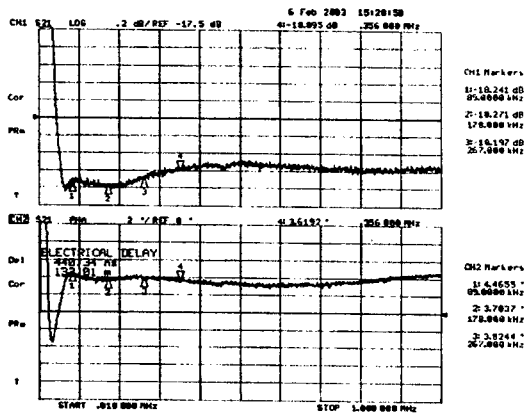
Figure 7: System's Response after Compensation

Figure 8: Recycler Barrier Bucket (blue) and Beam
Profile (red) after Compensation

Phase matching of each section is very important to
ensure that the individual transfer functions add up
algebraically. Otherwise, the compensation transfer
function will be a vector sum of all the components, and
this would not realize the correct compensation transfer
function. Figure 7 is the final compensated system
response using the new linearizing circuit. The
improvement in magnitude and phase at 90 kHz is readily
apparent when compared to Figure 2.

CONCLUSION

Final adjustments to the system were made with beam
(Fig. 8) in the Recycler. While looking at the beam in the
Recycler, the slope in the beam profile can be corrected
by using the variable attenuators. The variable
attenuators provide the flexibility to simultaneously
compensate for the magnitude and phase response that
will ensure a linear beam profile. In the event that
components in the high level RF Recycler system need to
be changed, the compensation network can be quickly
adjusted to account for any differences. Long-term
stability looks good, as no major adjustments have been
necessary to date. Further operational experience will
determine long-term stability.

REFERENCES

[1] J. E. Dey, D. W. Wildman, "Wideband RF System
for the Fermilab Recycler Ring," 1999 PAC, p. 869,
New York City, March 1999.

COUPLER DESIGN FOR NLC/JLC ACCELERATING STRUCTURES

I. Gonin, D. Finley, T. Khabiboulline, N. Solyak
FNAL, Batavia, IL 60510, USA

Abstract

In the framework of the NLC/JLC collaboration, Fermilab is working on developing the technology for X-band accelerating structures. One key element of a structure is the input/output coupler. The coupler should provide not only good power transmission from the waveguide to the structure, but also should not limit the high gradient performance of the accelerating structure itself. There are other special requirements for designing high power input/output couplers: reliability; cost; sensitivity to errors; trapped HOM; etc. In this paper we discuss the HFSS simulation of different types of couplers for JLC/NLC accelerating structures. We compare the surface electric and magnetic fields, field asymmetries, pulsed heating, presence of trapped modes and the complexity of production. Results of RF measurements and high gradient tests show good agreement with the design parameters.

INTRODUCTION

The emphasis of our present study at FNAL is on the production of two series of traveling-wave structures (FXB and FXC) required for tests at the NLCTA, the operation of the 8-Pack project, and the study of breakdown issues. The FXB structures have 60cm length, synchronous phase advance $5\pi/6$, average ratio $a/\lambda=0.18$, with an initial $v_g/c=0.03$. The FXC structures have a decreased ratio of $a/\lambda=0.17$, and all features for damping of HOM (slotted cells, HOM manifolds, etc.). Previous to FNAL's involvement in the process of conditioning the structures at SLAC, two main reasons of RF breakdown were discovered: in or near the input coupler, and the first few cells. RF breakdowns were associated with surface damage in areas of maximum surface electric field, and in areas of high magnetic field leading to plastic deformations due to pulse heating. We decided to design the FNAL structures with two different types of couplers that address the problems mentioned above instead of using the previous coupler design [1]. FXB002 and 003 used the "fat lip" coupler, a modification of the standard coupler made by rounding the coupling slot irises to minimize the surface magnetic field. For FXB004-006 and for all FXC structures, we will use waveguide couplers. This paper discusses the different aspects of coupler designs.

COMPUTATIONAL MODEL

The optimization cycle used to process each coupler design is shown in Fig.1. Solid models of different couplers are presented in Fig. 2. We match the "fat lip" coupler by varying the coupler cell diameter, the diameter of the coupler cell iris, and the width of the coupling slot. We match the waveguide coupler by varying the iris diameters of the coupler and matching cells, the coupler iris thickness, and the matching cell diameter and length.
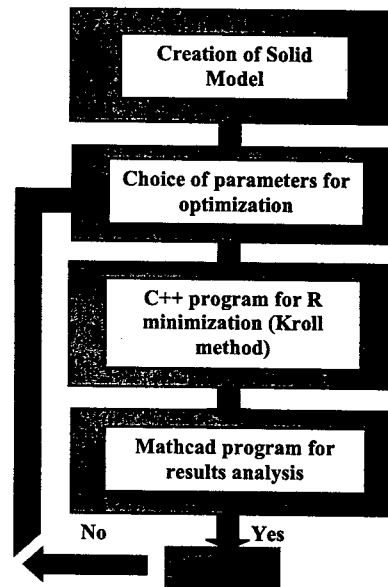
Fig.1: The optimization cycle

The main program of the optimization cycle is based on the procedure described in [2]. For each step of the cycle, the program calculates the reflection coefficient in the regular cells of the structure based upon two selected coupler parameters. Depending on the gradient direction, the program defines each parameter's new value. This procedure is iterated until the residual value of the reflection coefficient is small enough.

As well as the reflection coefficient minimization, other coupler parameters including amplitude and phase distribution, electric and magnetic surface fields should also meet the design requirements. We use a Mathcad program to help us analyze some of those requirements. If some of the parameters are unsatisfied, the computation can be restarted with new initial values.

This procedure is repeated until all of the main coupler parameters reach an acceptable range.
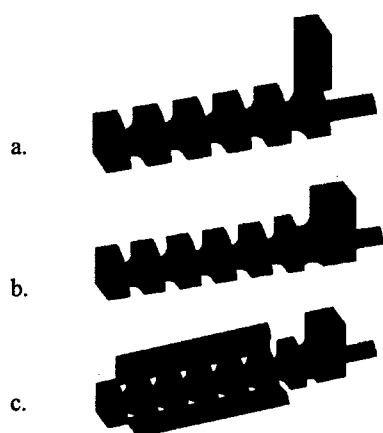
Fig.2: a. Solid model of the FXB "fat lip" coupler.
   b. Solid model of the FXB waveguide coupler.
   c. Solid model of the FXC waveguide coupler.

DISCUSSION OF DESIGN RESULTS

Using the procedure described above, three sets of input and output couplers for FXB and FXC structures were designed. FXB "fat lip" and waveguide couplers were produced and tuned. Designed and measured amplitudes of electric fields on the coupler's axis and in the first few regular cells are shown in Fig.3. Good agreement between designed and measured values is shown.

The electric and magnetic fields for both kinds of couplers are shown on fig. 4. There is a difference in surface field between waveguide and "fat lip" couplers. The maximum of both electric and magnetic fields in the waveguide coupler and the matching cell are less than in regular structures. The electric and magnetic fields are about 10% and 15% lower respectively. The surface electric field in the "fat lip' coupler can be decreased, compared with regular structures, by a proper choice of coupler dimensions. For the given design, the maximum field in a coupler cell is 10% lower. However, the surface magnetic field on the slot iris (see Fig.4 b.) is greater by about 30% than the maximum value in a regular cell.

ANSYS simulations of thermal-stresses on the coupler surfaces are presented in the table in Fig.5. The temperature and stresses are calculated for a 400 ns power pulse, for a given distribution of density of power dissipation on the surfaces (HFSS simulation).
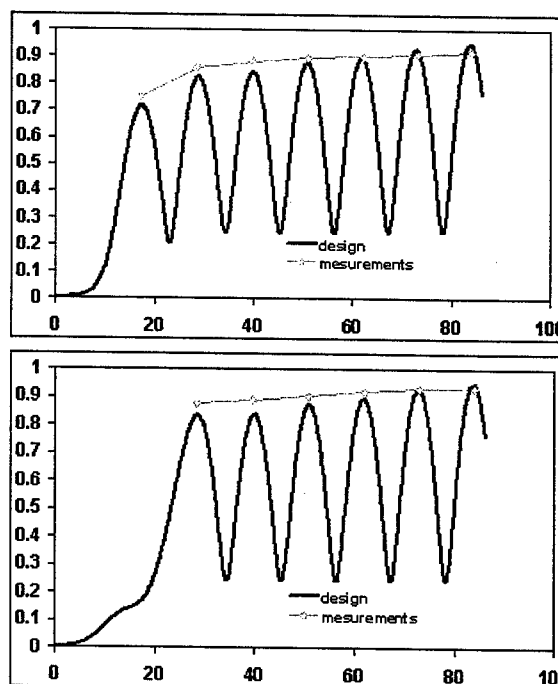
Fig.3: The designed and measured amplitude of electric field distribution for FXB "fat lip" (upper) and waveguide (lower) couplers
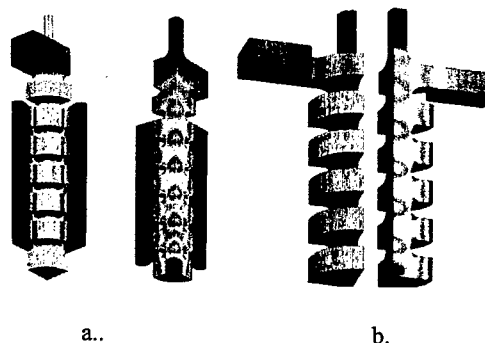
Fig. 4: Magnetic and electric fields in couplers and the first few cells.
   a.   FXC waveguide input coupler.
   b.   FXB "fat lip" input coupler.

H, A/M	P/S, VA/m**2	T, C	EQV. stress, Mpa
3.0E+5	1.26E+9	24	42
3.3E+5	1.52E+9	30	50
4.0E+5	2.23E+9	44	74
5.0E+5	3.49E+9	70	120

Fig. 5: Maximum values of temperatures and equivalent stresses for a given level of magnetic field.

For FXB structures with waveguide couplers, the maximum value of the magnetic surface field inside the regular part of structure is about $3.0*10^5$ A/m (~24°C). For FXB structures with "fat lip" couplers, the maximum value in the coupler coupling slot iris is about 30% higher, and the maximum temperature is about 40°C. For FXC structures, the magnetic field reaches a maximum value of $3.5*10^5$ A/m on the rounded coupling slots. This field level correspond to a temperature of ~34°C. For all cases the maximum value of equivalent stress is less than the yield point of copper, about (~70Mpa).

TRAPPED HOM's IN STRUCTURES

To control multi-bunch instabilities caused by high order modes (HOM's) in NLC accelerating structures, the design incorporates detuning as well as damping through slots into manifolds along most of the structure. One or possibly a few cells near the coupler might be uncoupled from the manifold. If for some reason, HOM's are trapped in these uncoupled cells, the transverse wake fields compared to those in the original design can increase considerably. All coupler designs were inspected for possible trapped HOM's. As an example, Fig.6 shows the spectrum of HOM's for the matched FXC structure with waveguide couplers (Fig. 2c).
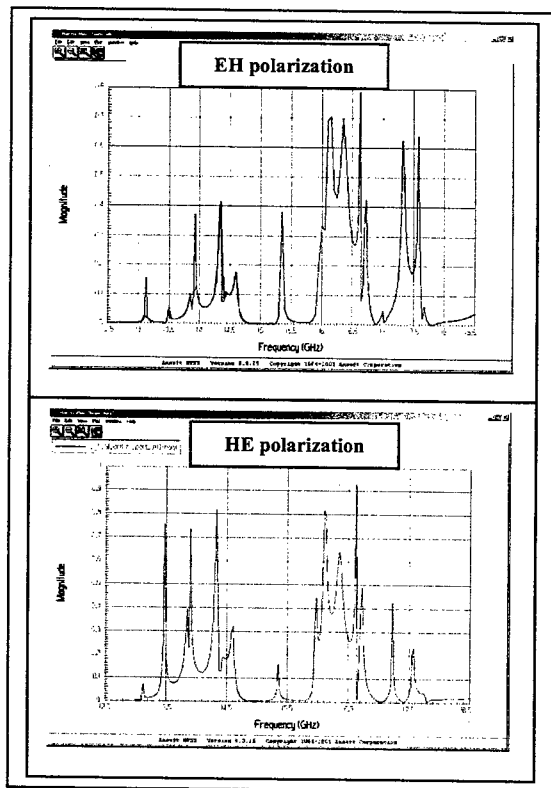
Fig. 6: HOM's spectrums for FXC structure.

Both polarizations were studied, with EH and HE boundary conditions. For each resonance peak, the E-field pattern was investigated. We have no indication of any trapped HOM's in this particular structure.

COUPLER PRODUCTION

All designed couplers are precision machined at Medco and LaVezzi Inc., our two major suppliers. The "fat lip" input coupler is shown in fig.7.
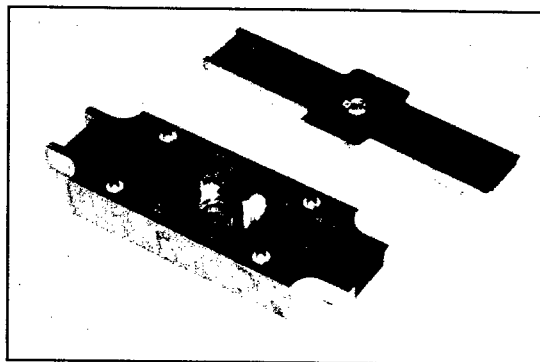
Fig. 7: "Fat lip" input coupler main body and plate.

By simplifying the design and lowering tolerance requirements, the waveguide coupler is, according to our estimation, about 25% less expensive than the "fat lip" coupler.

CONCLUSIONS

A procedure for quick and accurate coupler design is presented. Three series of couplers for structures for tests at the NLCTA were designed and produced. FXB structures with "fat lip" couplers were tuned and tested. See [3] for more details. FXB structures with waveguide couplers were tuned and will undergo high power processing in June 2003. Waveguide couplers for FXC structures have been designed.

We would like to thank V. Dolgashev (SLAC) for providing software and for useful discussions.

REFERENCES

[1] G. Bowden et al, "A compact RF power coupler for the NLC linac", PAC99, New York, 1999.
[2] N.M. Kroll, et al, "Applications of time domain simulation to coupler design for periodic structures", Proc. Linac 2000, Monterey, USA, 2000.
[3] T. Arkan, et al, "Development of X-band accelerating structures at Fermilab, PAC2003, Portland, 2003.

DEVELOPMENT OF X-BAND ACCELERATING STRUCTURES AT FERMILAB

T. Khabiboulline, T. Arkan, E. Borissov, H. Carter, D. Finley, C. Boffo, I. Gonin,
G. Romanov, B. Smith, N. Solyak, Fermilab, P.O.Box500, Batavia, IL 60510, USA.

Abstract

The RF Technology Development group at Fermilab is working together with the NLC and JLC groups at SLAC and KEK on developing technology for room temperature X-band accelerating structures [1] for a future linear collider. We have built a few 60cm long, high phase advance, detuned structures (HDS or FXB series). These structures have 150 degrees phase advance per cell, and are intended for high gradient tests. The structures were brazed in a vacuum furnace with a partial pressure of argon, rather than in a hydrogen atmosphere. We have also begun to build 60cm long, damped and detuned structures (HDDS or FXC series). Our goal is to build many structures for the 8-pack test at SLAC by the end of 2003, as part of the JLC/NLC effort to demonstrate the readiness of room temperature RF technology for a linear collider. This paper describes the design, fabrication techniques, RF measurements and tuning, as well as the initial results from high gradient testing of an FXB structure.

INTRODUCTION

The first structures built at Fermilab were proposed and designed by SLAC RF group [2]. The initial goal of the Fermilab group was industrialization of NLC type structures. Subsequently, the RF group was formed and we developed extensive infrastructure (clean room, RF Lab, vacuum furnaces, chemistry, tooling etc...), and we have started to participate more deeply in structure development. We developed initial production techniques by making short 20cm long FXA structures, and we further honed the technology by building numerous 60cm long detuned structures (FXB series, or H60VG3S18) for high gradient testing. Two FXB's were successfully tested at SLAC/NLCTA. We are now developing the FXC structure, which will incorporate damping and thus will have every feature needed for an NLC ready structure. Our goals include: verification of SLAC's cell dimension table, design of input/output couplers, development of mechanical quality assurance, and RF quality control on each step of production including final tuning. Also, some effort will be spent on R&D on movable supports (girders), which constitute the basic cell in the main linac. Temperature stability and vibration measurements together with FEA simulations are ongoing activities on the subject.

STRUCTURE DESIGN

For the FXB structure we designed two different types of couplers: the conventional "fat lip" coupler, and a waveguide coupler. Results of simulations of the input

and output couplers and HOM simulations of trapped modes are reported elsewhere at this conference [3].

STRUCTURE FABRICATION

The RF structures are fabricated in the "RF Structure Factory", an infrastructure built at the Fermilab Technical Division [4]. The RF structures group's goals for the RF Factory are: RF Design, RF Disk Fabrication & Quality Assurance (QA), RF Structures Fabrication & QA, and Infrastructure Setup for all of the above. Major infrastructure of the factory consists of two clean rooms (Room A is class 3000 and Room B is class 1000); two vacuum furnaces inside a soft-sided clean room, a clean room leak detector, a turbo pump station, a residual gas analyzer, anaerobic chambers etc.
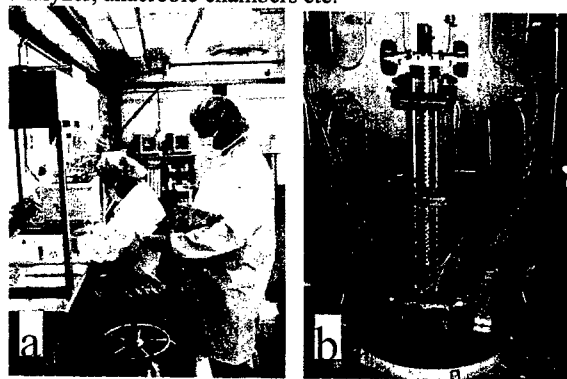
Fig.1. Clean room B (a), and an FXB structure in the large vacuum furnace (b).

The structures group's original mission was to develop industrialization of the structure manufacturing process. This included developing vendors to supply structure component parts and developing vendors to supply assembled structures. The mission has evolved into the above, plus as a higher priority, the group is to supply test structures in support of the Eight Pack Program at SLAC. Structure production started with 20-cm long traveling wave structures. We have produced three structures: FXA-001, FXA-002 and FXA-003. The RF design is identical to the SLAC T20VG5 structure. However, FXA structures are all brazed; no diffusion bonding used. The RF disks are precision machined; no diamond turning is done. Couplers are precision machined with some diamond turned RF surfaces in the iris area. FXA-003 was totally brazed and fabricated at Fermilab using the small and large vacuum furnaces. FXA structures were not high power tested.

We are currently producing 60-cm long traveling wave FXB structures. The design is identical to SLAC H60VG3N structure except for brazing grooves in the

disks. Disks and couplers are precision machined at Medco and LaVezzi Inc., our two major suppliers. The outer diameter of FXA disks is 45 mm, and that of FXB disks is 61 mm. The 60-cm structure length for FXB's required new tooling. Fat-lipped and wave-guide couplers were designed in order to reduce pulsed heating. Disks and couplers were chemically etched with the SLAC C01 procedure to remove any surface impurities. FXB-002 and FXB-003 were high power tested at the NLCTA at SLAC. The FXB-002 accelerating gradient was acceptable, although the processing of this structure was not finished. FXB-003's breakdown rates are lower than FXB-002. FXB-004 was totally fabricated in the RF Factory using proper clean room handling and furnace procedures. It is currently at the NLCTA and it will be tested in June 2003. We will produce two more FXB structures. All successful FXB structures can be used for the Eight Pack Test.

After completing the FXB structures, we will produce five 60 cm long FXC structures. These will have High Order Mode (HOM) manifolds on the RF disks and HOM couplers on the RF structures. Fermilab waveguide design (FWG) couplers will be used. The successful FXC structures will also be used for the Eight Pack Test. The design is identical to SLAC H60VG3S17 structure except for the brazing grooves in the disks. We will continue with the "all brazed" assembly approach. We redesigned the braze groove due to HOM manifolds in the disks.

RF CELL QUALITY CONTROL

To verify the accuracy of machining the cell parts, we do a so-called "single cell microwave QC" [5]. The particular design of our single cell QC set-up has been determined by the fact that the cells are machined in the form of "cups" to allow room for tuning holes. So we need an additional half-cell to measure the frequencies of "0"-like and "π"-like modes.

The "cup" shape of cell parts and the tapering of structures have resulted in the impossibility of performing direct absolute frequency measurements. We have to make a large number of very fine simulations of set-ups, prepare and verify master cups for comparison, and perform control measurements of short stacks every time we get a different cell design in order to avoid possible systematic errors.

Basically, the set-up consists of two flat ground blocks with a cup and a half-cell in between them. We decided to use a replaceable half-cell part despite the additional contact surface in order to facilitate the use of different half-cells for different cup designs. The ground blocks have offset antenna axes that permit the measurement of both the fundamental modes and the HOM frequencies. Fig.2 shows the set-up.

During the measurements the network analyzer is operated and controlled by a PC, or more precisely, by a program written in LabView. The program has a simple and convenient interface, which permits the online control of all parameters being measured and saves the result as a file, which can be opened by Excel.
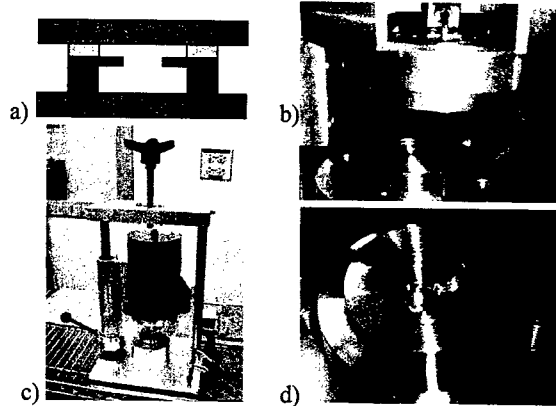
Fig.2. a) Schematic view. b) Bottom block and upper floating block. c) General view of set-up. d) Cup and half-cell installed on bottom block.

We have achieved an accuracy ± 0.2 MHz (random errors) for frequency measurements and ±3% for Q-factor measurements. One cup can be measured (four modes) in 35 seconds, but the necessity of careful handling and visual inspection of cups increases the time to 1-1.5 minutes per cup.

Fig. 3 shows the typical results of cell quality control.
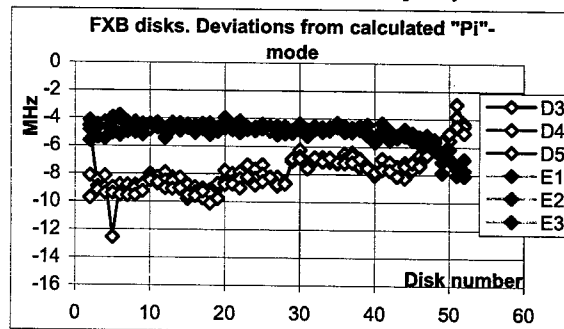
Fig.3. The cell quality control of six disk sets from two vendors. D3-D5 - machined at Medco, E1-E3 - machined at LaVezzi Inc.

BEAD-PULL MEASUREMENTS AND STRUCTURE TUNING

After final brazing, the structure needs to be tuned to the working frequency. Bead-pull measurements, which are based on the non-resonant perturbation method [6], are used for measurements of the accelerating field amplitude and phase distribution along the structure axis. Continuous nitrogen flow through structure is applied during whole tuning process; Fig.4 shows the bead-pull setup. Operating frequency calculations take into account air pressure, structure temperature and frequency shift due to the fishing line, which holds the metal bead. To minimize the error due to fishing line nonuniformity, we used the difference of two measurements: with and without the bead.

Fig. 5 shows the results of the Lab View program, which acquires the Network Analyzer data and displays
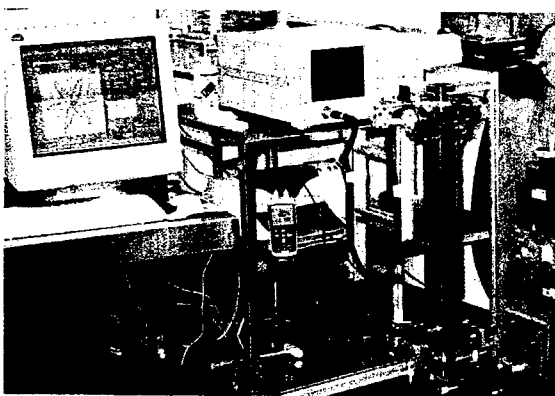
Fig.4. Bead-pull set-up in clean room A.

The reflection coefficient S11 during the pulling of the bead along the structure axis. The structure tuning technique [7] calculates forward and backward waves in different parts of the structure. For output coupler tuning we use minimization of the backward wave in the last cells. As the last step we tune the input coupler and 1-st cell to minimize the power reflected from the structure. After tuning, the SWR in the structure is less than 1.06 (Fig. 6) and the phase error is less than 2 degree (Fig.7).
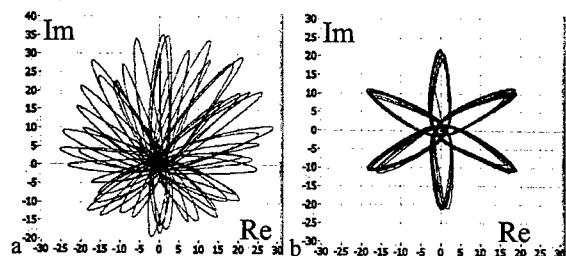
Fig.5. S11 trajectory during bead-pull before (a) and after (b) RF tuning of FXB-004.
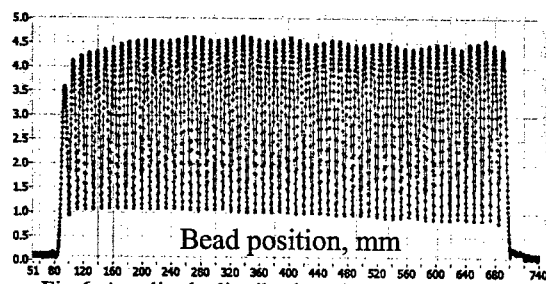
Fig.6. Amplitude distribution along tuned FXB-003.

HIGH GRADIENT TEST

Two FXB structures were high power tested at the NLCTA at SLAC. The first structure (FXB-002) reached a 65 MV/m accelerating gradient with a 400 nsec pulse length after 300 hours of processing. After testing, a visual boroscope inspection showed small breakdown spots in the surface of irises 2 to 20 but nothing in the input and output couplers. Bead-pull measurements did not show any degradation in the accelerating field distribution after the high power (HP) test as shown in Fig.7.
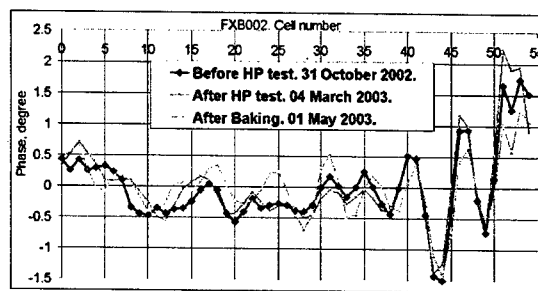
Fig.7. History of the phase distribution in FXB-002.

Fig. 8 shows the first 50 hours of high power testing of the second structure (FXB-003) and it looks pretty good [8]. Further FXB-003 HP processing is continuing with a pulse length of 400 nsec and accelerating field of 70-75 MV/m, which meet the NLC specifications.
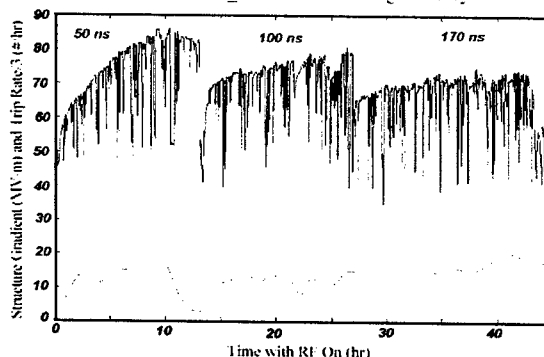
Fig.8. FXB-003 High Power processing. First 50 hours.

SUMMARY

We have developed at Fermilab the infrastructure and design and fabrication capabilities to allow us to built one accelerating structure per month for R&D toward the NLC. We have produced many 60-cm detuned structures and have started fabrication of 60-cm detuned damped NLC ready structures for the 8-pack test. High gradient tests at the NLCTA have demonstrated very good performance of the Fermilab built structures.

REFERENCES

[1] www.slac.stanford.edu/grp/ara/structures_meeting/.
[2] Z. Li et al., "Optimization of the X-band Structure for the JLC/NLC", PAC2003, Portland, 2003.
[3] I. Gonin et al, "Coupler design for NLC/JLC accelerating structures", PAC2003, Portland, 2003.
[4] T. Arkan, "X-band RF structure fabrication at Fermilab", http://lcdev.kek.jp/ISG/ISG9.Arkan.pdf
[5] H. Carter et al, "Automated microwave low power testing techniques for NLC", LINAC02, Seoul, 2002
[6] Charles W. Steele, "A nonresonant perturbation theory", IEEE Trans., Vol. TT 14, No 2, 1966.
[7] T. Khabiboulline et al, "Tuning of a 50-cell constant gradient S-band traveling ..." DESY M-95-02, 1995.
[8] http://www-project.slac.stanford.edu/lc/local/notes/ rf_process/RF_Processing_Breakdown.

DEVELOPMENT OF THE THIRD HARMONIC SC CAVITY AT FERMILAB

N. Solyak, I. Gonin, H. Edwards, M. Foley, T. Khabiboulline, D. Mitchell, J. Reid, L. Simmons,
Fermilab, P.O. Box 500, Batavia, IL 60510, USA.

Abstract

The third harmonic 3.9 GHz superconducting cavity was recently proposed by DESY for a new generation of high brightness photo-injector (TTF photoinjector-2) to compensate nonlinear distortion of the longitudinal phase space due to RF curvature of the 1.3 GHz TESLA cavities [1,2]. Installation of the 3rd harmonic cavity will allow us to generate ultra-short (<50 μm rms) highly charged electron bunches with an extremely small transverse normalized emittance (<1 μm). This is required to support a new generation of linear colliders, free electron lasers and synchrotron radiation sources. In this paper we present the current status of the 3rd harmonic cavity being developed at Fermilab. We discuss the design procedure, the building and testing of the copper and niobium half-cells and components, the design of input and HOM couplers.

INTRODUCTION

The design philosophy of producing highly charged bunches is based on using a long laser pulse to pull a long bunch from the photocathode and thereby reducing the deleterious space charge effect. However, in the accelerating section, the sinusoidal accelerating field profile distorts long bunches. The purpose of the 3rd harmonic de-accelerating section is to compensate for this distortion. In this manner, the injector should generate nC-bunches at an emittance that is four times lower than what existing injectors typically produce.

Fermilab, as part of the TTF collaboration, participates in developing and testing 3rd harmonic cavities at the existing FNPL photoinjector [3]. A number of USA institutions have expressed interest in specific facets of the photoinjector program and intend to form a collaboration to build and operate a 100+ MeV high-brightness electron photoinjector at Fermilab.

CAVITY DESIGN

Design parameters

The first design of the 3.9 GHz cavity was proposed by DESY[4]. The cavity consists of nine cells with an elliptical cup shape with a 30mm diameter iris and a 40mm diameter beam pipe. However, Fermilab calculations done for this design show that the coaxial input coupler has to be mounted very close to the end cell to provide the necessary coupling. In an improved design, the iris diameter of the end-cell was increased to 40mm with increased distance from the end-cell to the input coupler (Table 1). This leaves more space for welding and mounting of the helium vessel flange. The field distribution in the half-cavity is shown in Fig.1. The design parameters of the 3rd harmonic section are presented in Table 2.

Table 1: Geometry of the cups.

Dimensions in mm	mid-cell	end-cell
Iris radius, a	15.0	20.0
Equator radius, b	35.787	35.787
Half-cell length, h	19.2167	19.2167
Curvature at:		
Equator–horz/vert semi-axis	13.6/15.0	14.4/15.0
Iris - horz/vert. semi-axis	4.5/6.0	4.5/6.0
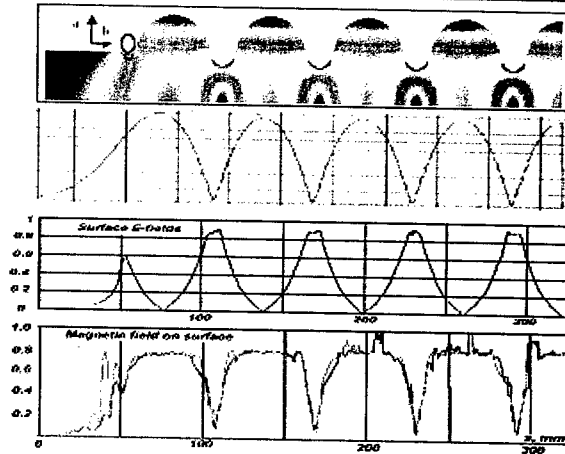
Fig.1. E-field (from the top: in cavity, on axis and on surface) and H-field on surface (bottom). HFSS.

Table 2: 3.9 GHz section parameters.

Number of cavities		4
Active Length	m	0.346
Gradient	MV/m	20
Phase	degree	-179
R/Q	Ohm	375
Q$_{ext}$ for accelerating mode		9.5e+5
BBU limit for HOM, Q		<1.e+5
Total energy	MeV	20
Beam current	mA	9
RF power/per cavity	kW	11.5

Lorentz forces

Lorentz forces, caused by electromagnetic fields, may change frequency during the RF pulse. An ANSYS analysis, made for niobium half-cells with fixed boundaries, shows frequency shift of 90Hz for a 2.8-mm thickness and ~200Hz for a 1.5mm thickness. (Fig.2). Electric and magnetic surface fields were taken from HFSS calculations. If free boundaries are assumed, then the frequency shift will be one order of magnitude higher. However, comparison calculations with the experimental results for TESLA and CKM cavities show, that the fixed

boundaries assumption is more realistic. These calculations show that the rigidity of the cavity, fabricated from 2.8mm thick niobium is high enough, even without stiffening rings.
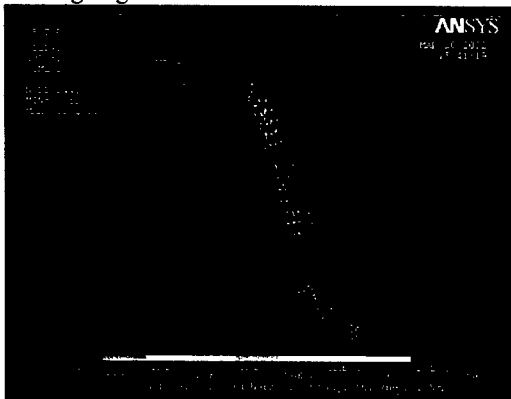
Fig.2. Distribution of surface displacement.

FABRICATION OF COMPONENTS

Forming of half-cells

For cup production two different processes are under development. For the conventional deep drawing process, we built a set of dies, machined from 7075-T6 aluminum alloy and formed the cups, using 2.8-mm-thick niobium (RRR 300+) or copper blanks. (Fig.3). To get the required curvature at the iris, the nose of the cup is then coined [5]. An alternative process is hydro-forming of the cups. Advanced Energy Systems, Inc. is developing this process for the 3rd harmonic and CKM cavities.
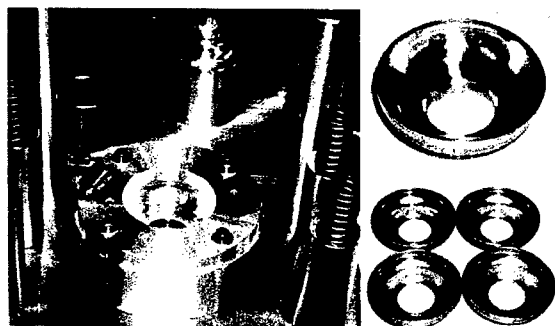
Fig.3. Tooling. Copper and niobium half-cells.

Using the deep drawing technology, many copper and niobium cells have been produced. The shape was carefully monitored on a CMM machine. First results show large profile errors of ~200μm, predominately near the iris, where the radius of curvature is only 4.5 mm. This deviation causes a frequency error of ~15 MHz. The best and repeatable results were achieved by intermediate annealing followed by re-coining and re-stamping (Fig4.). All 22 copper and 6 niobium cups, produced with this improved technology, have < 1MHz dispersion in frequency. The actual frequency is well correlated with the length of the cell.
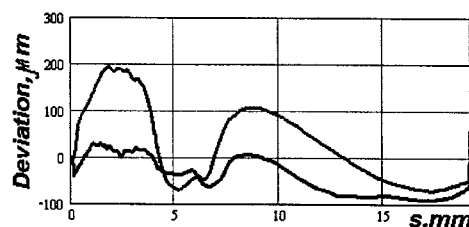
Fig.4. Deviation from design shape after drawing+coining (red), and following annealing+coining+drawing (blue).

Welding of Dumbbells

Twelve niobium cups were formed to help develop the forming and welding technology. Electron-beam welding parameters were optimized for iris and equator welds (Fig.5). The measured weld shrinkage was ~0.3mm/joint at the iris and ~0.2mm/joint at the equator with deviation of ±10%. Annealed half-cells had higher shrinkage, but more tests are needed to finalize EBW characteristics.
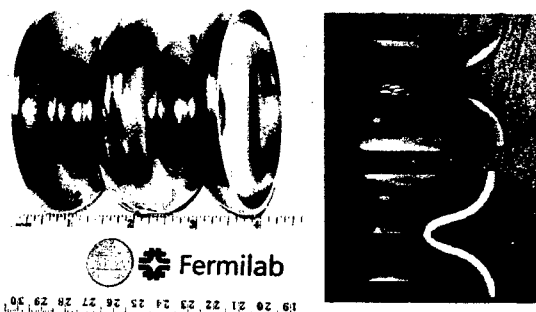
Fig.5. Welded dumbbells

Cavity tuning

After fabrication, the cavity has to be tuned to obtain the design frequency and field flatness. Limitations in the space between cup pairs, makes it difficult to use a conventional tuning system. A more adequate solution is obtained by squeezing the equator diameter instead of changing the cell length [6]. This type of tuner was designed, built and tested (Fig.6). The tuning clamp consists of 8 curved steel sectors, sliding on a chain. The chain length can be adjusted by a screw. Since the inner surface of this clamp conforms to the cell shape, longitudinal lengthening of the cell is minimal. During the test, a niobium cell was easily tuned up to 35 MHz, which is a higher than our goal.
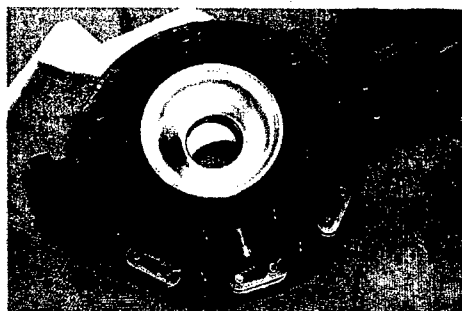
Fig.6. Frequency tuning device.

Copper model

Building a copper model is the first step in developing fabrication, tooling, RF control and tuning. Copper and niobium have similar mechanical properties, but copper is cheaper and has a higher conductivity at room temperature. A general view of the copper model and some components are shown in figure 7.
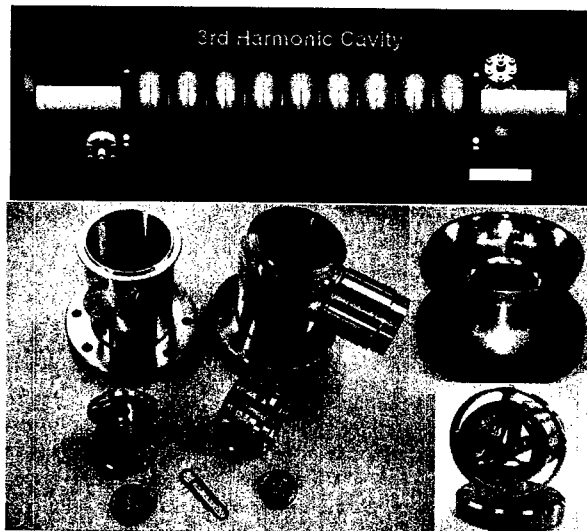
Fig.7. Cavity, end-tubes, dumbbells and HOM couplers.

End-tubes are decoupled from the cavity body to give us the ability to rotate or replace components if needed. HOM couplers are also rotatable. Measured RF properties of the coupler are in a good agreement with the calculations. All components are brazed, tested and ready for final brazing.

Input coupler

Fig.8 shows the design of the coaxial, adjustable input coupler, we are developing for 3.9GHz cavity. This is 50Ω coaxial line with a 30mm outer diameter to prevent the excitation of asymmetrical modes. For the cold window, we adopted the cylindrical ceramics of TESLA's coupler. For the warm window we are planning to use a standard waveguide window designed by CPI for a 3.9 GHz klystron.
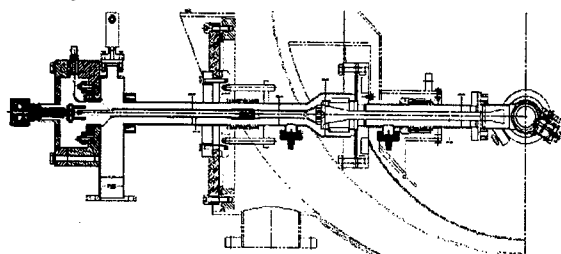
Fig. 8. Coaxial input coupler.

The coupler has pick-ups and light detection and is designed with DC biasing to suppress multipactor (MP). A lower power level should facilitate MP problems, but we need more detailed calculations to prove this

statement. Bellows, in the assembly, allow us to move the antenna back and forth (±2.5mm) and adjust Qext by a factor of five. The current design is quite complicated and after a discussion with W.D. Moller, we are working on a simple non-adjustable version of this coupler.

HOM analysis

Trapped High Order Modes (HOM) may excite BBU instability in the accelerator. Beam dynamics analysis gives us an upper limit of Qext (Table.2). Using HFSS, we have analyzed high order modes in 2-D model (R/Q calculations) and 3-D (R/Q and $Q_{external}$) up to 9 GHz [7,8]. 3-D geometry includes the input coupler and two HOM couplers with mirrored symmetrical antennas. The cavity in this model is excited by the beam with 2 mm vertical or horizontal off-sets. Analysis shows that if we apply electric or magnetic boundaries at the end of cavity, then few modes in the third passband have Q_ext above the BBU limit. For a more realistic assumption, "open" boundaries, all dipole modes in three first pass-band will be significantly damped with the maximal Q_{ext}=2400 (figure 9).
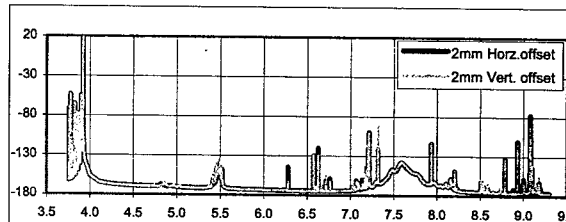
Fig.9. Field amplitude in cavity (dB) vs. frequency (GHz).

CONCLUSION

Fermilab is making good progress in developing a superconducting 3.9 GHz accelerating cavity [9].

REFERENCES

[1] M.Ferrario et al., "Conceptual Design of the XFEL Photoinjector", TESLA-FEL-01-03.

[2] F.Floettmann et al.,"Generation ultrashort electron bunches by cancellation of nonlinear distortions in the longitudinal phase space", TESLA-FEL-01-06.

[3] J-P.Carniero et al., "First results of the Fermilab high brightness RF photoinjector", Proc. PAC'99, p.2027.

[4] J.Sekutowicz et. al.,"A design of a 3rd harmonic cavity for TTF2 Photoinjector". TESLA-FEL, 2002-05.

[5] H. Padamsee et al., "RF superconductivity for accelerators", 1998.

[6] H.Kaiser, "New approaches to tuning of TESLA resonators", Proc. 9th Workshop on RFSC, Santa Fe, Nov.1999.

[7] T. Khabibouline et.al., "Higher Order Modes of a 3rd harmonic Cavity with an increased end-cup iris", preprint FNAL,2003.

[8] W.F.O.Muller et.al., This conference, RPPB071.

[9] http://www-td.fnal.gov/lc/sc/lc.html

MULTI-HARMONIC RF CONTROL SYSTEM FOR J-PARC RCS

Fumihiko Tamura, Masanobu Yamamoto, JAERI, Tokai, Japan
Alexander Schnase, Forschungszentrum Juelich, Juelich, Germany
Chihiro Ohmori, Akira Takagi, Tomonori Uesugi, Masahito Yoshii, KEK, Tsukuba, Japan

Abstract

The RF cavity of J-PARC Rapid Cycling Synchrotron (RCS) has a low Q value and a wide band which covers the frequency from the accelerating frequency to the second harmonic frequency. The cavity is driven by a composite signal of the fundamental RF and the second harmonic RF. The system acts as a bunch shaping system as well as an accelerating system. In this presentation, a multi-harmonic RF control system is studied. The signal processing is based on a combination of digital hardware like 16 bit multipliers, arithmetic units, and FPGAs with commercially available signal processors. The beam loading compensation is a critical issue because of the high beam-current in the ring. The RF feedforward compensation system is discussed. Also the stability is discussed under the beam feedback loops.

INTRODUCTION

Japan Proton Accelerator Research Complex (J-PARC) is a project of a high-intensity accelerator complex which consists of 400 MeV linac, 3 GeV rapid cycling synchrotron (RCS), and 50 GeV synchrotron (MR).

The RCS accelerates the beam from 180 MeV (will be 400MeV) to 3 GeV in 20 msec. The harmonic number of the RCS is 2, and the number of the bunches in the ring is 2 for RCS users and 1 for the MR injection. The fundamental accelerating frequency varies from 0.94 to 1.67 MHz. The maximum accelerating voltage is 435 KV by 12 RF cavities. The average circulating beam current is from 3.8 amperes at the injection and 6.7 amperes at the extraction.

Since the beam current is high, the bunching factor must be as large as possible to alleviation the space charge effects. We employ two techniques as following; (1) the momentum-offset multi-turn injection scheme and (2) making a wide potential well by superposing the second-harmonic ($h = 4$) RF voltage. At the injection, the second harmonic voltage is relatively high as $V_2/V_1 > 0.5$ where V_1 and V_2 are the fundamental and the second harmonic RF voltage respectively, to make the bunch shape flatten effectively (as shown in Figure 1). The fundamental and the second harmonic RF voltages are fed into the same cavity. We employ a magnetic-alloy (MA) loaded cavity without a tuning loop to realize a high accelerating voltage. Hence, the cavity must be wide-band and must have a low Q-value to cover the frequency range from the fundamental to the second harmonic frequencies. The Q-value of the RCS cavity is to be about 2.

The LLRF controls for this multi-harmonic system are discussed. Also, a scope of multi-harmonic beam loading is
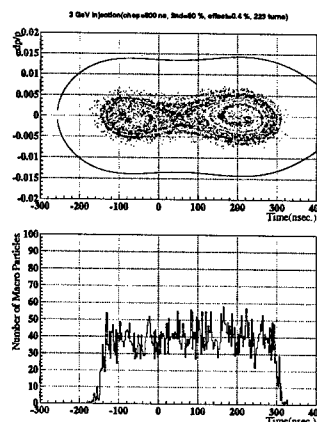
Figure 1: A simulated flat bunch generated by using the momentum-offset injection scheme and applying the second-harmonic voltage ($V_2/V_1 = 0.8$).

taken into account and the means of loading compensation are discussed.

MULTI-HARMONIC LLRF SYSTEM

The LLRF block diagrams for the J-PARC ring RF are shown in Figure 2 and 3. The whole system is based on digital signal processing with digital hardwares like 16 bit multipliers, arithmetic units, and FPGAs with commercially available signal processors.

The core of the system is the Direct Digital Synthesis (DDS) technology. By using DDS, the multi-harmonic signals are directly generated without PLL, and the signals are easily synchronized. In the RCS LLRF system, the phase-counter block accumulates the phase by proper steps corresponding to the frequency pattern, and generates sawtooth (phase) waves of the harmonics of $h = 1, 2, 3, 4, 5$. The fundamental ($h = 2$) and the second-harmonic ($h = 4$) phases are used for the generation of accelerating signal, for the feedforward, and for the phase-loop. The other harmonics ($h = 1, 3, 5$) are used only for the feedforward. We discuss on the feedforward beam loading compensation in the later section.

The feedback loops are common one. The radial loop, the phase loop and the AVC (Auto Voltage Controller). Note that there is no cavity tuning loop since the cavity is an MA-loaded one without tuning. The radial loop controls the frequency and the phase loop gives the offset of the phase. In the second-harmonic phase loop, the phase offset

1216
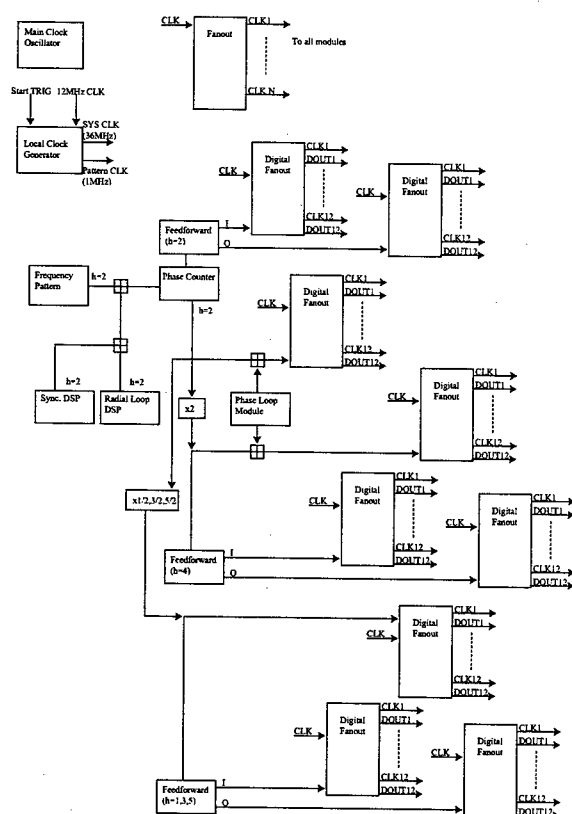
Figure 2: Block diagram of LLRF system.

Figure 3: Block diagram of LLRF signal control unit for each cavity.
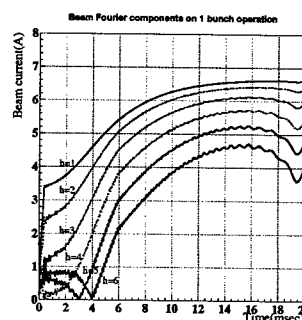
Figure 4: Fourier components of the beam current.

is determined by the difference between the fundamental cavity RF phase and the beam phase, so that the fundamental and the second harmonic signals follow the beam with perfectly synchronized steps and the composite of the RF bucket keeps the sharpe.

Each of the 12 cavities has own phase pattern and the amplitude pattern to compensate the amplifier gain difference and cavity impedance, and also to realize the counterphasing between each cavity.

BEAM LOADING COMPENSATION

The circulating beam current in the RCS is fairly high and the beam loading effects have to be carefully considered. In the RCS, the parameters are chosen so that relative loading factor Y is less than 1, except near the injection and the extraction[5], while the beam current is as same as the generator current during acceleration. Y is fairly higher than 1 at the extraction because the RF voltage is small to match the RF bucket with MR RF bucket. The phase of the fundamental accelerating voltage in the RF cavities goes far from the correct phase without compensation. The beam loading must be compensated for stable acceleration.

Furthermore, since the cavity has a low Q-value, the higher harmonic voltages are induced in the cavity. Figure 4 shows the Fourier components of the beam current. The

induced higher-harmonic voltages cause the bucket distortion. The distorted RF buckets during the acceleration and near the extraction are illustrated in Figure 5. The figure shows that the bucket distortion is not very crucial when the relative loading is not very high. However, one can see that the bucket is seriously distorted when Y is large. In order to suppress this bucket distortion, the beam loading compensation of higher harmonic component is necessary [6]. In the two-bunch acceleration case, $h = 2, 4...$ components must be compensated. Additionally, $h = 1, 3, 5...$ components also have to be cancelled when the ring accelerates the one-bunch beam for the MR injection. A particle tracking simulation result in the case of two-bunch acceleration is shown in Figure 6. The results show that the bucket distortion is not very serious and no strong emittance blow-up occurs, if up to the second harmonics ($h = 4$) are cancelled by a feedforward system.

A prototype feedforward module has been designed and built [7]. A test with real beam signals of KEK-PS MR has been performed in December 2002. We tried to pick up only the accelerating frequency (6.02 MHz) signal from the beam signal including revolution frequency components at
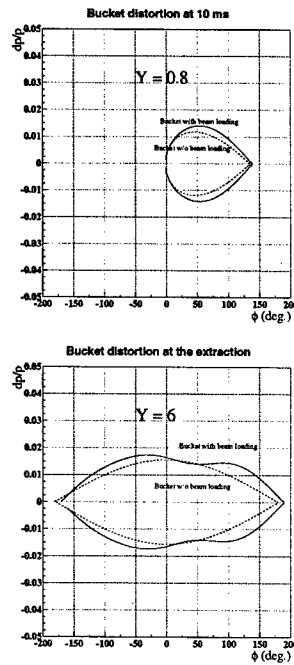
Figure 5: Distorted buckets during the acceleration and near the extraction (two-bunch operation case).
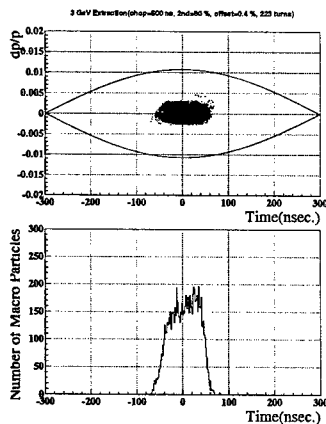
Figure 6: Particle tracking simulation results with $h = 2, 4$ feedforward, in the case of two-bunch acceleration.

the injection period. The results are shown in Figure 7. A 20 dB separation was achieved. Since 6 MHz is more than the second harmonic frequency of J-PARC RCS, the basic configulation of the module has a feasibility to the application for the real J-PARC RCS.

SUMMARY

We summarize the presentation as below.

- In the J-PARC RCS, an MA-loaded low-Q cavity is
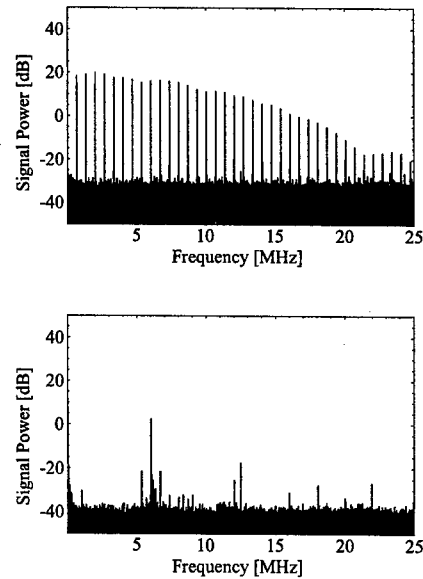
Figure 7: Spectrum of the beam signal at the injection (top) and the output of the feedforward module, center frequency is 6.02 MHz (bottom).

employed to realize the multi-harmonic drive. The system acts as a bunch shaping system as well as an accelerating system.

- The multi-harmonic LLRF system is based on the DDS technology.
- An RF feedforward system is to be employed to compensate the beam loading. In the case of the single-bunch operation, the components of $h = 1, 3, 5$ must also be cancelled as well as the cavity-drive components ($h = 2, 4$).

REFERENCES

[1] "Accelerator Technical Design Report for High-Intensity Proton Accelerator Facility Project (TDR)", KEK-Report

[2] JHF Project Office, "JHF Accelerator Design Study Report", KEK Report 97-16 (JHF-97-10)

[3] F. Pedersen, "Beam Loading Effects in the CERN PS Booster", IEEE Trans. Nucl. Sci. vol. NS-22 No.3, p1906, 1975

[4] R. Garoby, "LowLevel R.F. Building Blocks", in the proceedings of CERN Accelerator School, CERN92-03

[5] M. Yamamoto et al, "Longitudinal Beam Dynamics in JKJ 3 GeV Synchrotron", in the proceedings of the Eighth European Particle Accelerator Conference, Paris, 2002

[6] K. Saito et al., "Higher Harmonic Beam Loading Compensation for Broad Band MA-loaded RF Cavity", in the proceedings of the First Asian Particle Accelerator Conference, 1998

[7] F. Tamura et al., "Digital RF Feedforward Systems for Beam Loading Compensation in JKJ Synchrotrons", in the proceedings of the Eighth European Particle Accelerator Conference, Paris, 2002

DESIGN OF 20 MEV DTL FOR PEFP

Y. S. Cho[#], B. H. Choi, J. H. Jang, H. J. Kwon, M.Y. Park, PEFP / KAERI, Daejeon, Korea

Abstract

We have designed a conventional 20MeV drift tube linac (DTL) for the Proton Engineering Frontier Project (PEFP) as a low energy section of 100MeV accelerator. The machine consists of four tanks with 152 cells supplied with 900kW RF from 350MHz klystron. We have also studied beam dynamics in this structure and designed focusing quadrupole magnets. The details of the DTL design are reported.

INTRODUCTION

In this paper, we have designed a conventional drift tube linac (DTL) to accelerate proton beam of 20 mA from 3 MeV to 20 MeV. The input beam for the DTL comes from the radio frequency quadrupole (RFQ) which is designed to produce the 3 MeV proton beam of 20 mA from the 50 keV beam of 23 mA. The normalized rms emittance in the phase space are given as 0.23 ≺ mm-mrad for transverse direction and 0.15 deg-MeV for longitudinal direction.

The following sections include the general features of our DTL such as cavity design, beam dynamics, and quadrupole magnet (QM) design.

DESIGN LAYOUT

Structure

The available structures for the 20 MeV proton accelerator are a coupled cavity DTL (CCDTL), a super-conducting cavity linac, and a conventional DTL. The CCDTL has a merit that the QM can be located at the outside of cavity. Since the high shunt impedance structure should be operated at the higher frequency than that of RFQ, a matching section is necessary to compensate the structure/frequency change and the cavity becomes longer. For the super-conducting cavity, more R&D is necessary for lower beta region. Therefore the most suitable choice is the conventional DTL in spite of its disadvantage that the QM has to be installed even inside the short first drift tube in the first tank.

Frequency

The operating frequency of RFQ is 350 MHz and the conventional DTL is also working at the same frequency in order to make the matching easy between RFQ and DTL.

RF Power

The 20 MeV accelerator should be constructed within next 2 years, and should deliver the proton beam to users. With this schedule, the RF system for 20 MeV DTL should be separated from the other parts of the 100 MeV accelerator. From the construction cost viewpoint, one RF system for the DTL is preferred. The RF power is limited to 900 kW.

CAVITY DESIGN

To get the optimised information of DTL cavity, we use the DTLfish code which is an automated tuning program included in the Poisson/Superfish code group [1].

We have calculated the effective shunt impedance as a function of $\updownarrow$ (= v/c) under varying each parameters in order to get their optimal values to give the maximum shunt impedance. Table 1 and Figure 1 show the final design values of the geometrical parameters for the DTL cavities and the resulting plot of the effective shunt impedance under the selected parameter values. In this work, the tank diameter is determined after compensating the frequency increase by the stem effects.

Table 1. DTL design parameters

Parameter	Value
Tank diameter	54.44 cm
Drift-tube diameter	13 cm
Bore radius	0.7 cm
Drift-tube face angle	10 degrees
Drift-tube flat length	0.3 cm
Corner radius	0.5 cm
Inner nose radius	0.2 cm
Outer nose radius	0.2 cm
Stem diameter	2.6 cm
Frequency tolerance	0.001 MHz
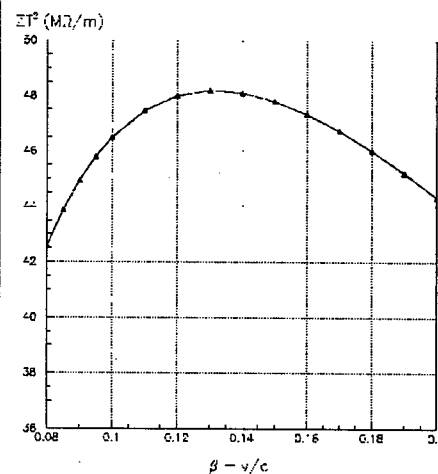
Figure 1. Effective shunt impedance

[#]choys@kaeri.re.kr

Table 2. DTL parameters for each tank

	Tank 1	Tank 2	Tank 3	Tank 4
Energy range (MeV)	3.00 ~ 7.18	7.18 ~ 11.50	11.50 ~ 15.80	15.80 ~ 20.00
Number of cells	51	39	33	29
Tank length (cm)	443.1	464.9	475.5	477.6
Total power (kW)	225	225	224	221
Synchronous phase (deg.)	30	30	30	30
Quad. gradient (kG/cm)	5.0	5.0	5.0	5.0
Effective Quad. length (cm)	3.5	3.5	3.5	3.5
E_0 (MV/m)	1.30	1.30	1.30	1.30
Transit time factor	0.83	0.83 ~0.81	0.81 ~ 0.79	0.79 ~ 0.77

BEAM DYNAMICS

We use the PARMILA code [2] to simulate the proton beam going through the DTL structure.

DTL Geometry

Our DTL has been designed to accelerate proton beam of 20 mA from 3 MeV to 20 MeV via 4 tanks. The inter-tank length is 1 ↑ℓ. Table 2 shows the design results for each DTL tank. The cell number of each tank is determined by requiring that they use similar amount of RF power which is less than 225 kW. In the power estimate, we use the reduced values of the shunt impedance by the factor of 0.8. The largest cell number is 51 of the first tank which is a reasonable value for easy tuning process.

We select FOFODODO lattice structure where every drift tube includes one QM. The structure allows weak focusing magnet at the cost of large beam size.

We don't adopt the ramping in the accelerating field and the synchronous phase since the peak current is relatively low in this design. The magnitude of the peak surface electric field is designed to be lower than 0.9 times Kilpatrick field.

For frequency tuning and field stabilization, we will use the 8 slug tuners for each tank and one post coupler for every 3 drift tubes (tank1) and 2 drift tubes (tank 2, 3,4).

Result

Figure 2 shows the tendency of the emittance growth in the transverse and longitudinal directions. There is no serious change in the emittances.

The maximum and rms beam size in the transverse direction are given in figure 3 which shows the betatron oscillation.

The zero-current phase advance per focusing period should be less than 90~ in order to avoid the envelop instability. In our case, it is designed for the phase advance to be below 75~ as shown in figure 4.

Figure 5 represents the output beam distribution at the end of the fourth tank. Even though we don't carefully consider the missing RF region between tanks, the plot shows that there is no abnormal signature such as large tail outside the beam core.
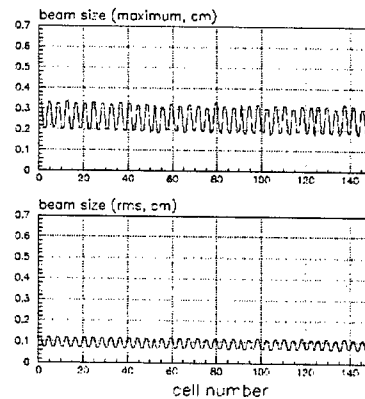
Figure 3. beam size in transverse direction

Figure 2. Transverse and longitudinal emittance profile
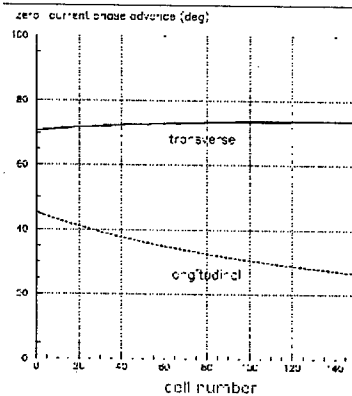
Figure 4. zero-current phase advance per focusing period
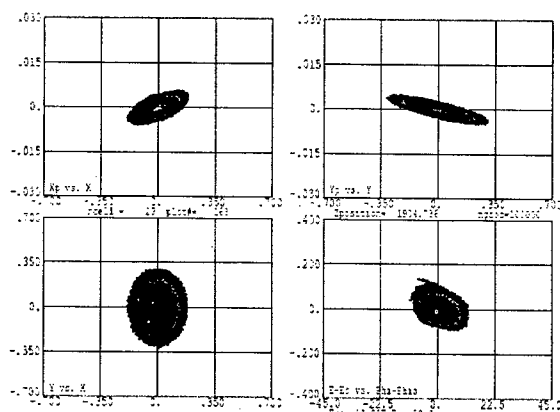
Figure 5. Configuration plot of the beam at the end of 4th tank

Table 3. EMQ parameters

Parameter	value
Strength (GL)	20 kG/cm cm
External diameter	110 mm
Bore Diameter	20 mm
Pole length	30 mm
Good field diameter	14 mm (1%)
Multipole fraction	< 1%
NI for 20 kG	2,200 AT
Conductor	3 3 mm
Number of turns	8
Joule dissipations	600 W

QUADRUPOLE MAGNET

The type of the QM installed in drift tubes can be either electromagnet or permanent magnet. Since our DTL will be operated with varying current from 0 to 20 mA, we choose the electromagnet where the focusing strength can be changed.

The required quadrupole strength GL is 17.5 kG/cm m. With 10% safety margin, we choose it as 20 kG/cm cm.

The first cell length is about 6.9 cm corresponding to one $\updownarrow\ell$. Considering fabrication of QM, its occupation rate in the drift tube can be 60% of the cell length. This means that QM should be shorter than 4 cm for the first drift tube. So, the special care should be required for the quadrupole design.

There are two different methods to overcome the limited space. One is using the electroformed hollow coil with water-cooling system which is developed in KEK[3]. This method is too expensive and complex to use it for our DTL. The other is using the transformer coil with external cooling system which is suggested in CEA[4]. Even though it isn't realized until now, we select the latter method since it is simple to make it.

Since the machining of the ideal hyperbolic pole shape for the QM is too complicated and expensive, we choose a circular pole which is optimised so that a good field aperture within 1% error occupies more than 70 % of the pole region and the multi-pole components in the good field region is less than 1% of the quadrupole component.

The figure 6 shows the optimised field profile in the quadrupole calculated by using the POISSON code [1]. We confirm that the iron core isn't saturated and the design is satisfied with the requirement for the good field region and multi-pole components.

Table 3 shows the main parameters of the designed electromagnetic quadupole (EMQ). The EMQ will be installed in every drift tube. Due to pool type cooling, we choose the thin conductor in order to secure the larger surface for cooling. However we have to study the thermal properties of this thin conductor and solve the heat problem under high current.

We will use 1010 low carbon steel for the iron core and use the discharge-machining method for manufacturing the pole shape. The transformer coil used as the conductor will be directly wounded on the iron core. After inserting EMQ into the drift tube, the OFHC copper end caps will be welded onto the drift tube by using the e-beam.

In conclusion, this article is a brief summary of a conventional DTL design for PEFP. The more detail of the design can be found in Ref 5.

REFERENCES

[1] J. H. Billen and L. M. Young, "POISSON / SUPERFISH", LA-UR-96-1834, LANL, 1996.
[2] H.Takeda, "Parmila", LA-UR-98-4478, LANL, 1998.
[3] K. Yoshino, et. al, Proceeding of Linac 2000.
[4] P.E. Bernaudin, et al, "Design of the IPHI DTL", Proceeding of PAC 2001.
[5] Y.S. Cho, et al, "PEFP DTL (3~ 20 MeV) preliminary design report", PE-30000-DD-P001, 2002.

Figure 6. Quadrupole magnet field profile

THE RF POWER DELIVERY SYSTEM DESIGN AND ITS COMPONENT CHARACTERIZATION FOR PEFP DTL

H. J. Kwon[#], Y. S. Cho, K. K. Jeong, J. M. Han, B. H. Choi, PEFP, KAERI, Daejeon, Korea

Abstract

The PEFP (Proton Engineering Frontier Project) was started at September 2002 whose main goals are to construct 100MeV proton accelerator and develop beam utilization areas. In this project, 20MeV DTL is scheduled to be constructed and tested within three fiscal years. The RF power delivery system for 20MeV DTL was designed and its components were characterized at PEFP, KAERI. The RF power from a 350MHz, 1MW klystron is split into four legs to drive four tanks of the 20MeV DTL. Each leg has a phase shifter to adjust the phase of the RF field in each tank. The design of the RF power delivery system of the 100MeV accelerator will be based on experiences of the 20MeV DTL RF system development.

1 INTRODUCTION

The 100MeV, 20mA proton accelerator is being developed in Korea as a part of the "21C Frontier R&D program" launched by government [1][2]. As a low energy part of the accelerator, 20MeV DTL was designed and being constructed at PEFP [3]. The DTL consists of 4 tanks to accelerator proton beams from 3MeV to 20MeV. As described earlier, the DTL should be constructed within next 2 years and deliver the beam to the users. With this time table, the RF system for 20MeV DTL is preferred to be separated from the other accelerators up to 100MeV. The most suitable RF system for the 20MeV DTL is the similar one to the RFQ RF system [4]. From the viewpoint of construction cost, one RF system for 20MeV DTL is preferred. Therefore, one of the major design issues of DTL was to restrict the required RF power well below 1MW in order to drive the DTL with one klystron. In addition, the number of cells in each tank was determined from the consideration of the nearly equal distribution of the RF power in each tank.

2 DTL RF SYSTEM OVERVIEW

The required RF power for the 20MeV DTL is described in Table 1, which is an output results of the PARMILA code considering 25% power margin from the SUPERFISH code input data. The total required power is about 900kW which can be covered with one 1MW klystron. The power distribution in each tank is within ±1%. The schematic of RF power delivery system is shown in Figure 1. The RF power from one 1MW klystron is split into four legs by magic tee to drive four DTL tanks respectively. Each leg has a phase shifter to adjust the phase of the RF field in each tank. With this type of power distribution, the amplitude of the RF field in each tank can be maintained within ±1% of the design value in spite of feeding equal power into each tank.

Table 1: Required RF power for 20MeV DTL

Tank #	Cu power (kW)	Beam power (kW)	Total power (kW)
1	141.6	83.4	225.0
2	138.8	86.2	225.0
3	138.3	85.7	224.0
4	137.1	83.9	221.0
Total (kW)	555.8	339.2	895.0
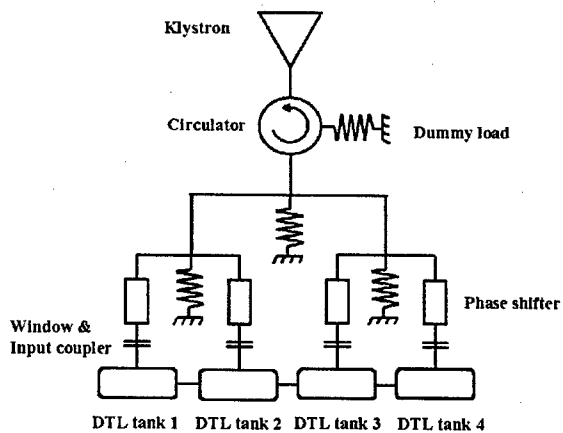
Figure 1: Schematic of RF power delivery system for 20MeV DTL

3 SYSTEM COMPONENTS

Klystron

A TED (THALES Electron Devices) TH2089F klystron which was used as a RF source for 3MeV RFQ will be also used for 20MeV DTL. It is a slightly modified model of the 352MHz, 1.1MW klystron used at CERN. The klystron has a modulating anode to control the beam current and is capable of dissipating the full beam power up to 1,800kW. The klystron is scheduled to be delivered to PEFP site at Jan. 2004.

[#]hjkwon@kaeri.re.kr

High voltage power supply

The requirements of the high voltage power supply are 100 kV, 20 A with the conditions that both the voltage ripple and regulation are less than 1 %, and energy deposition in the klystron at the tube arc is less than 20 J. A three phase AC voltage controller type using thyristor is used. The thyristor controller is located at low voltage side and control the output voltage by adjusting the conducting angle of the 12 pulse AC power. A device which limits the load arc energy is important component because it should limit the deposition energy into the klystron below 20J at klystron arc condition otherwise the klystron has permanent damage. An opening switch which consists of IGBTs is used for that purpose. The switch is now developed by POSCON. The modulating anode power supply comprised of voltage dividing resistors and tetrode will be used. That type was successfully operated as a modulating anode power supply of the 3MeV RFQ klystron. The voltage can be adjusted by controlling the grid voltage of the tetrode. The schematics of the high voltage power supply and modulating anode power supply are shown in Figure 2 and Figure 3 respectively.
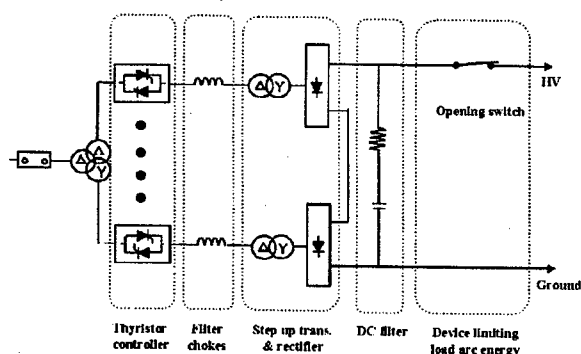
Figure 2 : Schematic of high voltage power supply
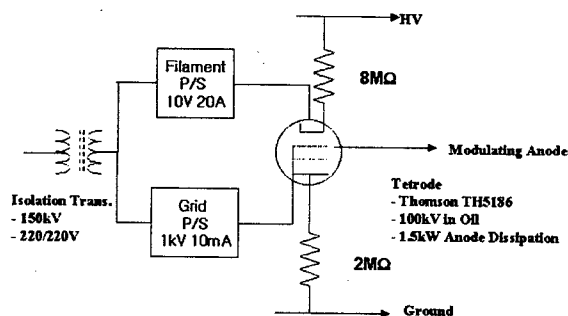
Figure 3 : Schematic of mod. anode power supply

Circulator

An AFT (Advanced Ferrite Technology) circulator which was also used for RFQ RF system will be used for 20MeV DTL RF system. It is a Y-junction type circulator which can deliver 1.3MW RF power for forward direction and permit 1.3MW reverse power at any phase. It uses temperature compensating system to compensate the temperature dependent ferrite saturation magnetization. The circulator is scheduled to be delivered to PEFP site at the end of this year.

RF dummy load

In addition to the role of RF station to the accelerator, the high power RF system for 20MeV DTL has also the role of a high power test stand of various RF components including klystron, circulator, window and so on. Because there is no additional space for high power test in the present site. Under this situation, to test a klystron, a shorting plate is installed between circulator and DTL tank, then all the RF power reflected from the shorting plate is directed to the dummy load located at one side arm of the circulator and dissipated. For this reason, the dummy load at the one side arm of the circulator can dissipate the full power from klystron. A dummy load which is cooled by the water and MEG (Mono - ethyleneglycol) mixture will be used.

Waveguide system

The components of the waveguide system include power divider, phase shifter, harmonic filter, E & H bends, full height to half height transition and so on. The full and half height WR2300 waveguide components will be used. The power balance of the divider should be less than ±1% in order not to use an amplitude adjuster in each waveguide leg. But the power balance of the general divider is less than ±0.25dB. Therefore, precisely balanced power divider or general power divider plus amplitude adjuster structures are required in our case. The phase shifter should have the full range of phase shift above 45° because the phase difference between the waveguide arms for low energy side tanks and for high energy side tanks are nearly 45°. The phase shifter which has three stub tuners and ±45° tuning range is considered for that purpose.

Input coupler

The RF input coupler is one of crucial components in accelerator development. Generally, two types of couplers are used, one is loop type and the other waveguide type. In spite of the cooling difficulty. the loop type coaxial coupler is considered for DTL input coupler because of its easy matching. Among several types of coaxial loop coupler, the one with cylindrical window and half height waveguide to $\lambda/4$ coaxial transition is selected primarily, because of the relatively easy fabrication method. This type of coupler is very similar to the input coupler of the spoke cavity in Accelerator Driven Test Facility at LANL [5]. In addition to the development of reliable window, the potential difficulty of this coupler in our case is the multipacting in the coaxial line. The single point multipacting level follows the scaling law : $P_{one-point} \sim (fd)^4 Z$, where f is the RF frequency, d is the diameter of the outer conductor and Z is the impedance of the coaxial line [6]. According to the data from the paper [5], the single point multipacting level for several geometries can be estimated from the scaling law and is shown in Figure

4. The operating power level is also shown in the Figure. With these data, several geometries are currently investigated (inner diameter of the outer conductor of the coaxial line : 100mm, 103mm, line impedance : 50ohm, 75ohm). As a start up for the development of the input coupler, a cylindrical window was fabricated to verify the fabrication processes including material, machining, brazing, coating as shown in Figure 5. The inner diameter of alumina ceramic (purity : 95%) is 130.1mm and thickness 4.8 mm. The ceramic was brazed into 1.5mm thick copper sheet, which was e-beam welded into the copper-stainless steel flange. The window will be TiN coated and installed in the coupler section to check vacuum tight and low level RF properties.
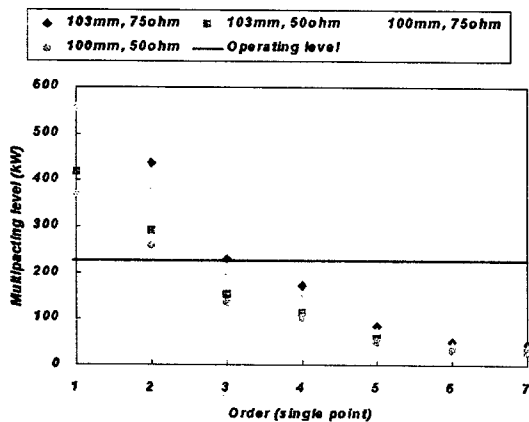
Figure 4 : Single point multipacting level for various coaxial geometry
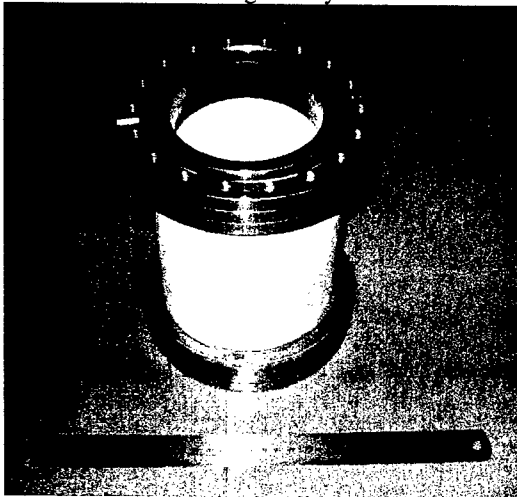
Figure 5 : Cylindrical window for vacuum and low level RF test

4 CONCLUSIONS

The high power RF system for PEFP 20MeV DTL was described. Some components such as klystron, circulator, high voltage power supply are now in purchase or development stage, and others require more detailed information about the specification before setting up the purchase order. The development of the input coupler is the first trial in our group. The estimated potential difficulties are loop cooling, window failure at high power condition and multipacting in the coaxial line at operating condition. Some modifications and improvements of the 20MeV DTL RF system which are based on the experiences on the operation of the 3MeV RFQ RF system will be carried out. The R&D on the high power RF system of 3MeV RFQ and 20MeV DTL will be a valuable experience for developing RF system for 100MeV accelerator.

ACKNOWLEDGEMENT

REFERENCES

[1] B. H. Choi, et al., "High Power Proton Linac Program in Korea", Proc. of XXI International LINAC Conference, Gyeongju, Korea, 2002.

[2] Y. S. Cho, et al., "Development of 100MeV Proton Accelerator", Proc. of XXI International LINAC Conference, Gyeongju, Korea, 2002.

[3] Y. S. Cho, et al., "PEFP DTL (3MeV~20MeV) Preliminary Design Report",PE-30000DD-P001, 2002.

[4] H. J. Kwon, et al., "RF System for RFQ", Proc. of XXI International LINAC Conference, Gyeongju, Korea, 2002.

[5] E. N. Schmierer, et al., "Design of the Spoke Cavity ED&D Input Coupler", Proc. Of 10th Workshop on RF Superconductivity, Tsukuba, Japan, 2001.

[6] E. Somersalo, et al., "Analysis of Multipacting in Coaxial Lines", Proc. Of 1995 Particle Accelerator Conference, Dallas, Texas,1995.

R & D STATUS OF C-BAND ACCELERATOR UNIT FOR SUPERKEKB

T. Kamitani*, T. Suwada, for the KEK electron/positron Injector Linac and
the Linac Commissioning Group, KEK, Tsukuba, Japan

Abstract

In an extensive luminosity upgrade of the KEK-B factory, considered as a future plan, the injector linac has to increase the positron acceleration energy from 3.5 GeV to 8.0 GeV. In order to double the acceleration field (from 21 to 42 MV/m), a design study of the C-band accelerating unit has been started. This paper reports on the R & D status of the C-band components for a high-power test and for a beam-acceleration test at the KEKB injector linac.

INTRODUCTION

Recently, the KEK b-factory (KEKB) has surpassed its goal luminosity of $1 \times 10^{34} cm^{-2} sec^{-1}$. Though it is the world-highest luminosity ever achieved, an even higher luminosity ($10^{35} - 10^{36} cm^{-2} sec^{-1}$) is desired for a deeper understanding of a B-meson physics. The design consideration of this extensive upgrade, called "SuperKEKB" [1], started in 2001, and R & D of the components are now underway. One of the major changes in this upgrade is the switch of the beam energies (from 8.0-GeV electrons and 3.5-GeV positrons to 3.5-GeV electrons and 8.0-GeV positrons). Raising the beam energy suppresses the positron beam blow-up caused by the electron-cloud inside the vacuum chamber.

The present KEKB injector linac accelerates electrons up to 8 GeV with 55 accelerator units, including a few stand-by units [2]. The electrons are injected directly into the High Energy Ring. For positron injection, the electrons are accelerated up to 4 GeV in the former half of the linac (26 units), and hit a metal converter target to produce positrons. Those positrons are accelerated up to 3.5 GeV in the latter half (29 units), and are injected into the Low Energy Ring. For the SuperKEKB, positron acceleration energy is required to be increased from 3.5 GeV to 8 GeV. The maximum energy gain by all of the present positron accelerating units is not sufficient (4.8 GeV) for 8-GeV injection. Since the positron intensity is proportional to the primary electron energy, the number of positron acceleration units cannot be increased by changing the target position at the cost of the units for the primary electron. The simplest way to realize this energy upgrade is to increase the acceleration field by about twice. It requires a four-times higher rf input power, if the present S-band accelerating structures are used. It is not realistic based on the limit of the capacity of the present klystron gallery and the input electricity power. Instead, the possibility to use C-band accelerating structures is considered. The upgrade scheme presently considered is shown in Fig.1. A damping

ring (DR) is added for emittance reduction. The accelerator units after the DR are to be upgraded with C-band components to achieve 8-GeV injection. Another upgrade scheme using beam recirculation instead of the C-band units is also considered, but it is not mentioned here.
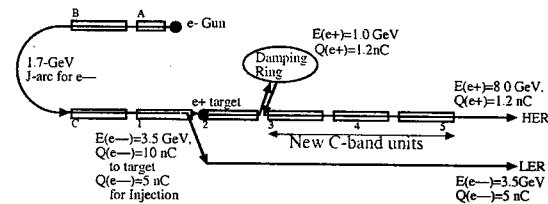
Figure 1: upgraded Linac with C-band units

ACCELERATOR UNIT

The present S-band accelerator unit of the KEKB injector linac involves four 2-m accelerating structures fed by a klystron through a SLED-type rf-pulse compressor. The average accelerating field gradient is 21 MV/m with 41 MW output power of 4 μs pulse duration from the klystron and with rf-pulse compression. The energy gain by a unit is typically 160 MeV. In the upgrade to the C-band, an S-band unit is replaced by two identical sub-units; each is composed of two 2-m accelerating structures fed by a klystron through an rf compressor. The average accelerating field gradient is expected to be 42 MV/m with 40 MW output power of 2 μs duration from the C-band klystron and with a LIPS-type rf-pulse compressor [3]. The total energy gain by two sub-units is 320 MeV.

Compared with the S-band unit, the rf power source is divided into two. It is mainly because there is no C-band klystron available which can supply the 80 MW power necessary for the four accelerating structures. Instead, two 50-MW class klystrons are used. The modulator is also divided into two. A design comparison was made between the single modulator feeding two klystrons and the two modulators feeding a single klystron, respectively. In the case of the single modulator, it becomes too large to re-use the present components, like the capacitors, and requires complete renewal of the design to fit in the present klystron gallery, and costs too much. Finally, we decided to adopt a system composed of the two identical sub-units. It facilitates the design of the modulator and reusing the present components. What is more, by complete isolation of the sub-units, the operation is more flexible, since individual tuning is possible.

RF SOURCE

The present S-band unit uses a 50-MW class klystron (Mitsubishi PV3050 or Toshiba E3730), which supplies 41 MW output power of 4.0 μs rf pulse duration. In the R & D work for the C-band linear collider, a 50-MW class klystron was developed by T. Shintake and H. Matsumoto [4] and is commercially available (Toshiba E3746). It is operated at 5712 MHz with a beam of 358 kV voltage and 320 A current in pulse repetition of 50 Hz. It needs 240 W of drive power and delivers an output power of 53 MW in 2.5 μs duration. In the C-band upgrade of the KEKB linac, this klystron is the first candidate. A klystron of this type has already been fabricated and used in a high-power test in a test stand since December 2002 and will be used in a beam acceleration test scheduled from this September.

The present line-type modulator produces a 4.0 μs long (flat-top) 306 kV high-voltage pulse for the klystron at a repetition rate of 50 Hz. In the upgrade to the C-band unit, two modulators for the two klystrons must be installed in the same space of the klystron gallery, as shown in Fig.2. To make the modulator more compact, the present high-voltage dc power supply and the charging circuit will be replaced by a compact inverter-type power supply. To generate a flat high-voltage pulse of 4.0 μs duration, two pararell pulse-forming-network (PFN) circuits, each composed of 20 capacitors (0.0146 or 0.0155 μF) and 20 inductors (0.67 μH), are used in the present modulator. In the C-band modulator, a pair of PFN circuits (14 capacitors and 14 inductors) is used to generate a pulse of 2.0 μs duration. Most of the components in the S-band modulators, like PFN capacitors, thyratrons, cabinets, pulse transformers and oil-tanks can be reused, which contributes to reduce the cost of the upgrade.
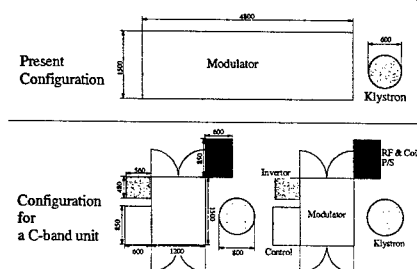
Figure 2: Modulator/Klystron layout

In the present rf drive system, an rf signal of 2856 MHz is transmitted from the main drive system to each sub-booster through phase-stabilized optical fibers. In the sub-booster, the signal is amplified by a 60-kW klystron and distributed to eight klystrons. In the sub-booster of the C-band unit, the frequency is doubled with a multiplier to 5712 MHz. Concerning the sub-booster klystron, instead of designing a brand-new one, an available 200 kW klystron operated in 5.3 GHz for radar (Mitsubishi PV-5101) is modified for 5712 MHz operation.

ACCELERATING STRUCTURE

The accelerating structure used in the present S-band unit is a 2-m long, disk-loaded, traveling-wave structure operated at 30.0 deg C. The structure is composed of 54 regular cells and two (input, output) coupler cells, and the phase advance per cell is $2/3\pi$. The iris diameter is decreased linearly cell-by-cell to achieve a quasi-constant field gradient. The typical size of the iris diameter is 24.275 - 20.300 mm from the entrance to the exit. A total of five variant types of structures which have different iris sizes are used to distribute the deflecting mode of the cavities and prevent a beam break up from occuring during long-pulse operation. As shown in Fig.3, the first prototype C-band 1-m accelerating structure is designed as a scale-down model of the present S-band 2-m structure, which has the largest iris diameter within the five variants. The dimen-
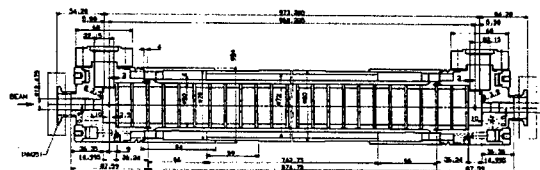
Figure 3: 1-m long C-band Accelerating structure

sions of the regular cells can be scaled precisely to half that of the S-band structure. They are already processed and the phase advances in respective cell are adjusted to 120 degree within an error of 2 degrees with the nodal-shift measurement. As has been done for the S-band structure, the disks and the cylinders processed individually are formed into an integral structure by an electroplating technique. Unlike the regular cells, the coupler dimensions (the iris width and the coupler cell diameter) have to be modified because the dimension of the wave-guide, which is connected to the coupler, is not scaled. The coupler dimensions are roughly optimized with the MAFIA-3D code to achieve the proper coupling strength and the minimum reflection, and further finely adjusted by milling and lathering step-by-step with the feedback from the measurement of the rf property. Fabrication of the couplers for high-power operation and electroplating of the regular cells are in progress. The couplers and the regular cells are to be connected later by electron-beam welding, and will be finished by the end of June.

RF COMPONENTS

In place of the WR-284 (WRJ-3) standard wave-guide (inner dimension; 72.1 mm × 34.0 mm) used in the S-band unit, the WR-187 (WRJ-5) standard wave-guide (inner dimension; 47.55 mm × 22.15 mm) is adopted for the C-band unit, considering the power loss and the contamination of the higher-order mode. An Merdinian-type flange for the wave-guide is designed and used at the test stand.

As an rf window to separate the vacuum of the accelerating structure and that of the region close to the klystron,

a pillbox-type window is already available, which has been developed as a component of the C-band klystron. However, its maximum transmission rf power is 25 MW. A new type of an rf window, which can transmit 50 MW, is being developed to simplify the system in the C-band unit. Unlike the pill-box type window, it uses a mixture of two modes (TE11 and TM11) to generate a traveling-wave in the ceramic of the window. It lowers the electric field strength at the edge of the ceramic and reduces the electron emission, which results in a breakdown of the ceramic. With the high-power test performed using a resonant ring at the test stand, the new rf window has been confirmed to work without any problems at 160 MW rf power and a 2 μs duration at 50 Hz repetition.

A 3-dB high-power rf divider of the C-band has been designed by simulations using the HFSS code to determine the approximate dimensions. It does not have a button inside, which is often used for a fine adjustment to reduce the reflection, but sometimes causes discharging. Instead, the inner dimension is finely optimized by measuring the rf transmission properties of 16 candidate low-power test modules. Modules for high-power operation are under fabrication.

A high-power dummy load to fit for the WR-187 waveguide is being designed. Inside the wave-guide of the dummy load, cylindrical SiC blocks of 12 mm diameter stand in line with the gradually growing heights to absorb the rf-power uniformly. The heights and the positions of the blocks are optimized using the HFSS code. They are further optimized to achieve the least reflection by an rf-measurement using a low-power test module, in which the blocks are changeable and the positions are variable. The modules for high-power operation are being fabricated.

The rf pulse compressor for the C-band is still in the stage of conceptual design. Since the SLED-type cavity using TE015 mode [2] does not give a sufficient Q-factor and field multiplication at a frequency of C-band, an LIPS-type cavity using the TE038 mode [3] is being considered. A low-power prototype cavity will be fabricated this summer to optimize the coupling hole dimensions.

TEST STAND AND BEAM ACCELERATION STUDY

For rf-conditioning and high-power test of the C-band components, setting up of a test-stand started in December 2002. The test stand has been used for conditioning the S-band accelerating structure, which is to replace the damaged structure after long use in the linac. The stand has also been used for a high acceleration field study of the S-band structure, which recorded a field of 40 MV/m with 41 MW supplied into a single 2m-long structure through a SLED-type rf compressor cavity. The stand has been re-arranged for a C-band study as shown in Fig.4. A unit test of the modulator, began in January 2003 with a coaxial dummy load. Initial tuning and the trouble shooting of the modulator has been performed. Later, a C-band klystron has been

connected to the modulator as a proper load. After conditioning, a 43 MW output power of 2.0 μs duration from the klystron at 50 Hz repetition was achieved in April.

The accelerating structure, the 3-dB high-power divider and the SiC dummy loads will be installed in the test stand in June. Their rf-conditioning and a high-power test will be performed in July and August. In mid of August, the components of the C-band accelerator unit will be moved from the test stand to the location of the "4-4" unit in the KEKB linac, which is temporarily vacant. The energy gain and the average acceleration field will be evaluated by measuring the beam energies of the electrons and the positrons in the beam study from September.

Figure 4: C-band High-power Test Stand

REFERENCES

[1] "Expression of Interest in A High Luminosity Upgrade of the KEKB Collider and the Belle Detector", By I. Abe, *et al.*, January 2002
http://www-kekb.kek.jp/SuperKEKB/Document/EoI.pdf

[2] "The KEKB injector linac", By I. Abe, *et al.*, Nuclear Instruments and Methods in Physics Research Section A, Volume 499, Issue 1, 21 February 2003, Pages 167-190

[3] "Design Consideration, Construction and Performance of a SLED Type Radiofrequency Pulse Compressor using very high Q Cylindrical Cavities" By A. Fiebig, R. Hohbach, P. Marchand, J.O. Pearce (CERN). CERN-PS/87-45, Mar 1987. 3pp. Presented at 1987 Particle Accelerator Conf., Wash., D.C., Mar 16-19, 1987.

[4] "Development of C-band 50 MW pulse klystron for e+ e- linear collider", By T. Shintake, N. Akasaka, H. Matsumoto, Y. Ohkubo, H. Yonezawa, KEK Preprint 97-47, Presented at 1997 Particle Accelerator Conference, Vancouver, BC, Canada, May 12-16, 1997

IMPROVEMENTS IN THE RF SYSTEM
FOR THE PHOTON FACTORY ADVANCED RING (PF-AR)

S. Sakanaka[*], K. Ebihara, E. Ezura, S. Isagawa, T. Kasuga, H. Nakanishi, M. Ono, M. Suetake, T. Takahashi, K. Umemori, S. Yoshimoto, High Energy Accelerator Research Organization (KEK), Tsukuba, Ibaraki 305-0801, Japan

Abstract

The Photon Factory Advanced Ring (PF-AR) is a 6.5-GeV synchrotron light source at KEK. An rf system for the PF-AR can provide an rf accelerating voltage of about 16 MV. During an upgrading project for the PF-AR, we carried out some improvements in the rf system. This paper reports these improvements, as well as the present operation status of the system.

INTRODUCTION

The PF-AR is a 6.5-GeV dedicated synchrotron light source at KEK. An rf system for the PF-AR comprises two 1-MW klystrons, an rf distribution network, and six accelerating cavities [1, 2]. Each cavity is an alternating periodic structure (APS) [3], having eleven accelerating cells and ten coupling cells. This cavity can produce high accelerating voltages with small space. Two and four cavities are housed in the east and the west rf sections, respectively. A block diagram of the west rf station is shown in Fig. 1. Typical rf-related parameters are listed in Table 1.

An upgrading project [4] for the PF-AR was carried out during 2001. As one of the goals of this program, we anticipated to increase the beam current from 40 mA to 60-70 mA. To this end, we made some improvements in the rf system, which includes: 1) remodeling the crowbar circuit in the klystron power supply, 2) temperature stabilization of the cavity cooling water, 3) reinforcement of higher-order-mode (HOM) loads for the cavities, and 4) renewal of the control system.
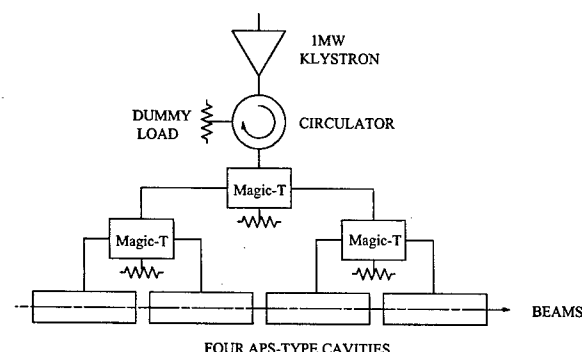
Table 1: Principal parameters of the PF-AR rf system under user operation (6.5 GeV) and at injection (3 GeV).

Beam energy	E	6.5 GeV	3 GeV
Typical rf voltage	V_c	16 MV	3.3 MV
Radiation loss/turn	U_0	6.66 MeV	302 keV
Transverse damping time	τ_x	2.5 ms	25 ms
Longitudinal damping time	τ_z	1.2 ms	12 ms
Synchrotron frequency	f_s	42.6 kHz	29.8 kHz
Total klystron power	P_k	982 kW	43 kW
Total beam power	P_b	400 kW	18 kW
Dissipated power/cavity	P_{c1}	94 kW	4 kW
Typical rf frequency	f_{rf}	508.567 MHz	
Harmonic number	h	640	
Momentum compaction	α	0.01264	
Maximum beam current	I_0	60 mA (at present)	
Shunt impedance/cavity	R_{sh1}	75.6 MΩ	

IMPROVEMENTS IN RF SYSTEM

Improvement in Crowbar Circuit

Higher beam currents require us to operate the klystron at higher voltages of more than 80 kV. In such cases, high reliability of the crowbar circuits [2], which are used to protect the klystrons under discharges, is particularly important. In order to achieve higher reliability, we improved the crowbar circuit in the klystron power supply.

The crowbar circuit is relatively sensitive to some electrical noise since it is triggered by a signal from a fast-response current transformer. From a long-term experience at KEK, we were convinced that the primary source of wrong triggers should be due to some noises which were caused by corona discharges in the circuit case. In order to prevent such corona discharges, we remodeled the crowbar circuit so that all high-voltage components, such as ignitrons, resistors and a discharger, were placed in insulating oil. In addition, the main part of the circuit was housed in a separate tank from the other parts. Thus improved crowbar circuit has been operated very well for more than one year without any wrong triggers.

Stabilization of Cooling Water Temperature

Each cavity is cooled by a water flow of about 250 lit./minute. Since the higher-order-mode frequencies of the cavities can be affected by the cooling-water temperature, it is desirable to stabilize the temperature in order to avoid cavity-induced coupled-bunch instabilities. For this purpose, a temperature stabilization system was constructed in fiscal year 1997. This system (see Fig. 2)

FOUR APS-TYPE CAVITIES

Figure 1: Block diagram of the west rf station.

* shogo.sakanaka@kek.jp .

can stabilize the temperature of the cooling water by exchanging its heat with separate cold water. The cold water is provided by two chillers. Because each cavity has a separate heat exchanger, we can set up the water temperature for each cavity independently. This function is very useful for finding an optimum set of temperatures during operations. Since the beams are injected at lower energies (2.5-3 GeV), it is essential to optimize various operating conditions under injection. A typical tuning range of the water temperature is about 23-29°C.
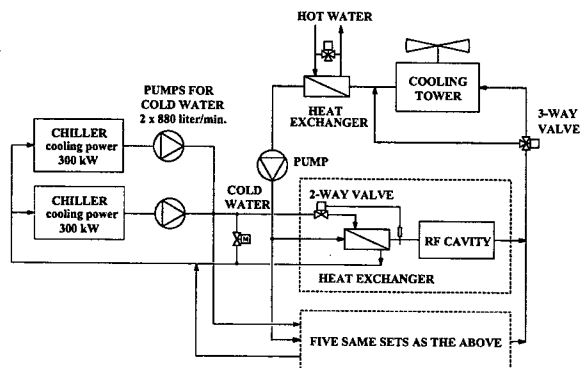
Figure 2: Temperature stabilization system for the cavity cooling water. Blue lines indicate a cold water route.

Reinforcement of Cavity HOM Loads

Each cavity is equipped with twelve higher-order-mode (HOM) couplers [5] which can damp some harmful HOMs. Each HOM-coupler was terminated by an air-cooled, 1-kW dummy load. Since we anticipated higher HOM power after the upgrade, we replaced all 70 dummy loads to water-cooled, 3-kW ones.

Because these loads are installed in the ring tunnel under high x-ray backgrounds, they should be highly resistant to radiation, as well as to flame. Direct water-cooled mechanism, which is adopted in some commercially available loads, are not suitable because the radiation can easily damage rubber seals for the cooling water. We therefore adopted indirect water-cooled loads, which were newly developed in Nihon Koshuha Co., Ltd.

A drawing of the new 3-kW load is shown in Fig. 3. The heart of the load is three beryllium-oxide (BeO) plates having resistive-stripe coatings on them. Input HOM power is dissipated in these resistive stripes. The BeO plates touch tightly to a water-cooled copper block via a thermally conductive compound. These resistive stripes are connected in series by copper bridges.

The voltage standing-wave ratio (VSWR) of the completed dummy loads were less than 1.5 within a frequency range of 0.5-1.5 GHz, and less than 2.0 within 1.5-2 GHz. We installed these dummy loads on the top of the cavities. The waterway of six dummy loads was connected in series, and a water flow of 15 lit./minutes was supplied per each route. Figure 4 shows the installed dummy loads.

These HOM loads have been working very well after the commissioning. Typical dissipated power per load was about 560 W under the beam current of 57 mA and the beam energy of 6.5 GeV.
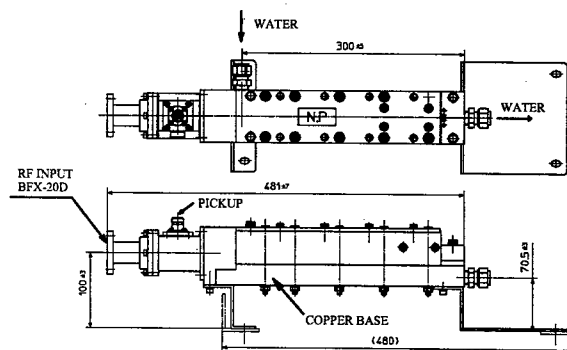
Figure 3: Drawing of the 3-kW broadband dummy load.
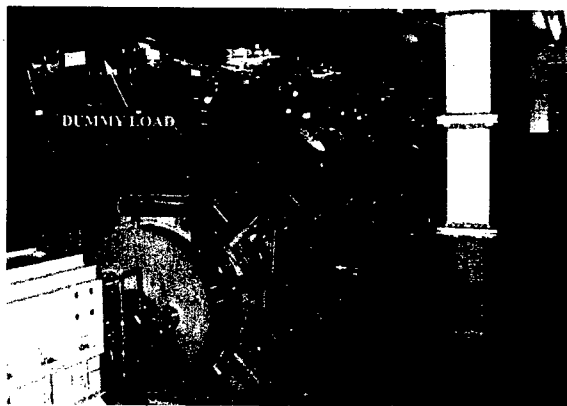
Figure 4: New higher-order-mode loads as installed on the top of the cavities.

EPICS-Based Control System

The control system for the rf system was fully upgraded to a new one which is based on the Experimental Physics and Industrial Control System (EPICS) [6]. Figure 5 shows an outline of the new control system. Most of the rf equipments are controlled by an I/O Controller (IOC) through original CAMAC interfaces. Some of the instruments, such as a master oscillator and data loggers, are controlled by another IOC through GPIB interfaces. Operator-interface (OPI) programs run on the workstations. We developed both an EPICS database and OPI programs. There were about 600 incoming signals from the equipments, and about 600 outputs to them. We then defined about 1200 database records which correspond to these signals. Some sequence controls were realized using record links and state programs for the EPICS sequencer. The OPI programs were developed using both a SAD/Tkinter script language and the Python/Tkinter language.

Using this system, we can control all parameters of the rf system, such as the rf voltage, the phases, and the cooling water temperatures. It also allows us to condition the cavities automatically before storage-ring operations.

WORKSTATIONS for OPI

CONTROL NETWORK

IOC RF EAST

IOC RF WEST

LAN-GPIB GATEWAY

GPIB DEVICES

CAMAC RF WEST — WEST LOW-LEVEL CONTROL SYSTEM

CAMAC RF EAST — EAST LOW-LEVEL CONTROL SYSTEM
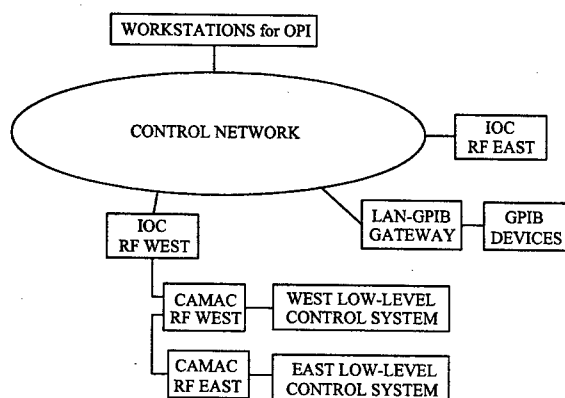
Figure 5: New control system for the rf system.

PF-AR RF STATUS

| | Total Vc = | 16.29 | MV | frf | = | 508.568 005 | MHz | |
| | Energy = | 6.50 | GeV | Current = | 56.95 | mA | | |

	LV	HV	RF	Pk (kW)	Pd (W)	Vc (MV)	ALC	PLL	Local
EAST	ON	ON	ON	354.7	3.96	5.25	OK	OK	R
WEST	ON	ON	ON	712.4	3.63	11.04	OK	OK	R

	Vk (kV)	Ib (A)	Va (kV)	Ia (mA)	Vh (V)	Ih (A)	Heater	Local
EAST	70.0	10.0	40.3	0.30	11.1	23.5	OK	R
WEST	83.2	14.7	52.3	0.44	11.0	23.4	OK	R

Cavity CCG (V)   Cavity water temp. (deg.)   Klystron power (kW)   High voltage (kV)
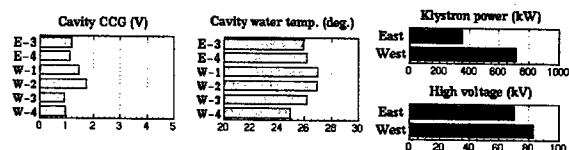
Figure 6: One of the control panels showing typical rf parameters under operation.

COMMISSIONING AND OPERATIONS

The PF-AR was recommissioned smoothly in January, 2002. During a half year after the commissioning, the maximum beam current was limited to about 40 mA due to some collective effects. We could then gradually increase the beam currents to about 60 mA. This was achieved by raising the injection energy from 2.5 GeV to 3 GeV, and by investigating optimum conditions for beam injection. The PF-AR is currently operated with the maximum currents of 50-60 mA with single bunch.

Figure 6 shows one of the control panels, indicating typical rf parameters during operations. It shows such parameters as the output power from the klystron (P_k), the drive power for the klystron (P_d), the cavity voltage (V_c), the cathode voltage (V_k), the beam current of the klystron (I_b), the voltage and the current of the klystron anode (V_a and I_a), the voltage and the current of the klystron heater (V_h and I_h), and so forth. Because an equal rf-power is fed to each cavity, the east klystron provides about a half power of the west one. In a case of Fig. 6, the output powers from the east and the west klystrons were about 350 kW and 710 kW, respectively, under the beam current of 57 mA. Because there is some margin in the rf power, we continue to make efforts for increasing the beam current to the target value of 70 mA.

CONCLUSION

During the upgrading project of the PF-AR, we carried out some improvements in the rf system. The improved rf system was commissioned very smoothly, and it has been working very well for more than one year. The stored current was gradually increased from 40 mA (before upgrade) to about 60 mA under routine single-bunch operations.

REFERENCES

[1] K. Akai et al., "RF System with Room-Temperature Cavity of the TRISTAN e^+e^- Storage Ring", Proceedings of the 13th International Conference on High Energy Accelerators, Novosibirsk, U.S.S.R., 7-11 August, 1986, p. 303.

[2] M. Ono et al., "TRISTAN RF System with Normal Conducting Cavity", KEK Internal 87-6 (1987).

[3] T. Higo, Y. Yamazaki, T. Kageyama, M. Akemoto, H. Mizuno, K. Takata, "Development of an APS Cavity for TRISTAN Main Ring", IEEE Trans. on Nucl. Sci. NS-32 (1985) 2834.

[4] K. Ebihara et al., "Present status of PF-AR", in these proceedings, PAC2003, Portland, U.S.A., May 12-16, 2003.

[5] Y. Morozumi, T. Higo and Y. Yamazaki, "Higher Order Mode Damper with Self-Cooled Coupler", Part. Accel. 29 (1990) 85.

[6] L.R. Dalesio, M.R. Kraimer, A.J. Kozubal, "EPICS Architecture", Proc. ICALEPCS'91, KEK, Tsukuba, Japan, 1991, p. 278.

RADIO FREQUENCY ACCELERATION SYSTEM FOR 150MEV FFAG

Akira Takagi[#], Yoshiharu Mori, Joe Nakano, Tomonori Uesugi, Masahiro Sugaya

KEK, Tsukuba, Japan

Abstract

An rf cavity for 150MeV FFAG(Fixed Field Alternating Gradient) proton synchrotron has been developed. The rf cavity consists of four pieces of MA(Magnetic Alloy) core. These MA cores are indirectly cooled by thermally conductive spacers and cooling plates. One piece of MA core (Wide:1700mm, Height:950mm, Length:25mm) is mechanically supported by a cooling plate. The range of acceleration frequency is 1.5MHz to 4.6MHz. The acceleration voltage of 19kV and the acceleration cycle of 250Hz are required. A couple of rf stations are proposed to install in the 150MeV FFAG. Recent developments on the radio frequency acceleration system for 150MeV FFAG proton synchrotron are presented

INTRODUCTION

The fist acceleration of protons in the 500keV FFAG proton synchrotron (PoP=Proof of Principle FFAG) was demonstrated at KEK in March 2000 [1]. After this successes, the design and the construction of a 150MeV FFAG proton synchrotron has been started [2] The 150MeV FFAG is a prototype FFAG to investigate the possibilities of various applications such as proton beam therapy [3].

Since the magnetic field in the FFAG is static, therefore the acceleration cycle depends only on the sweep rate of the accelerating rf frequency. A high gradient rf cavity using the "FINEMET" MA (magnetic alloy) cores [4], has been developed at KEK [5]. With this new type of rf cavity, the acceleration cycle of the synchrotron can become very high, 1kHz or more, which is more than 100 times of the ordinary synchrotron cycle. Thus, the FFAG is an attractive machine for accelerating intense beams.

The rf cavity consists of four MA (Magnetic Alloy) cores. These MA cores are indirectly cooled by thermally conductive spacers and cooling plates. An MA core (Wide:700mm, Height:950mm, Length:25mm) is mechanically supported by the cooling plate. The rf acceleration parameters of the 150MeV FFAG are listed in table 1

Table 1: RF acceleration Parameters of 150MeV FFAG

Acceleration cycle	250Hz
Harmonic Number	1
RF frequency	1.5MHz~4.6MHz
Total acceleration voltage	19kV(peak)
Number of cavity	2

CAVITY DESIGN

The metal water-cooled plates adopted on the one side of MA cores. A thermally conductive spacer [6] is inserted between the MA core and the cooling plate. The effect of thickness was measured for a small sized MA core (O.D.=340mm, I.D.=140mm, L=25mm). Figure 1 and Figure 2 show the cavity impedances as a function of rf frequency with the different thickness of cooling spacers with and without metal plate.

It was found that the "parallel inductance" of the core was strongly disturbed by the gap between the MA cores and the metal plate as shown in figure 2. The shorter gap between core and metal plate causes severe additional capacitive component. By these results, as a thermally conductive spacer, the thickness of 3mm is adopted to the full-scale design of cavity cooling plate.
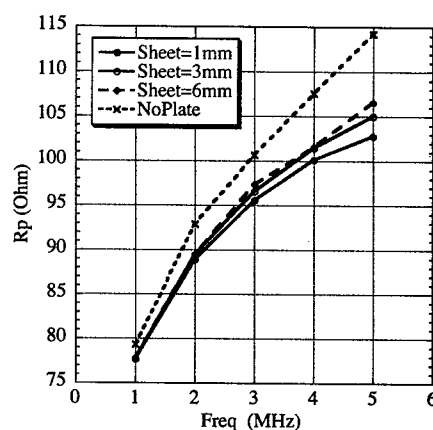
Figure 1: Shunt impedance v.s. rf frequency.
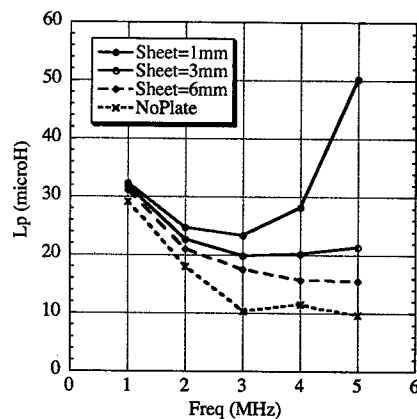
Figure 2: Parallel inductance v.s. rf frequency.

[#] akira.takagi@kek.jp

LARGE MA CAVITY

The full-scale cavity design is base on the rf cavity of PoP FFAG [7]. The horizontal dimension of vacuum duct is very large because of the orbit excursion of the FFAG is very large. By this reason, core size of 150MeV FFAG has a very large horizontal dimension. The mechanical dimensions of large MA core are listed in table 2.

Table 2: Mechanical dimension of large MA core

Core material	FINEMET(FT-3M)
Outer size	1700x950 mm
Inner size	980x230 mm
Aperture of metal frame	940x190 mm
Core Length	25 mm

The MA cores are indirect cooled by aluminum water cooled plates with the thermally conductive spacer (DENKA, FSL-B: 3W/mK). Total of four cores were installed in a cavity. When the power loss in a MA core is about 15tW/core, the estimated power density is about 1W/cm^3 in a MA core.
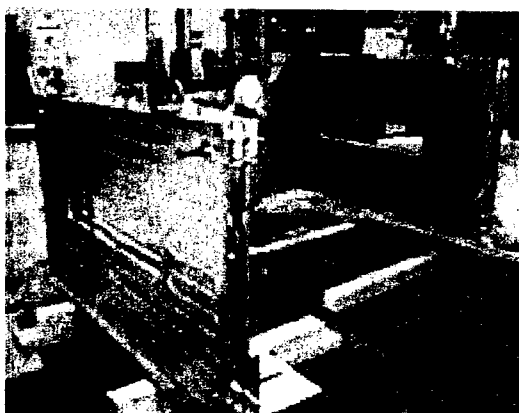
Figure 3: Photograph of cooling plates and MA cores
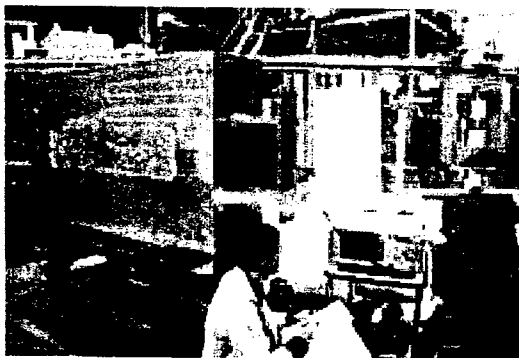
Figure 4: Photograph of the 150MeV FFAG cavity.
(After a vacuum duct with a ceramic gap was inserted)
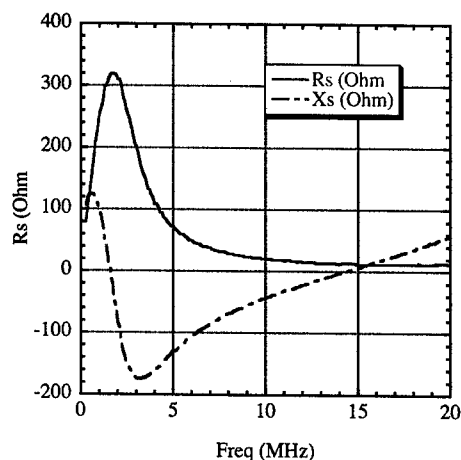
Figure 5: Measured values of the cavity impedance.
(Rs is real part and Xs is imaginary part)
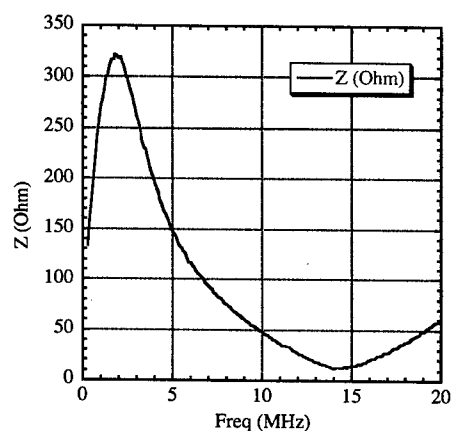
Figure 6: Measured values of the cavity impedance.
(Z is the impedance magnitude)

Total cavity cooling water flow rate of 70 litter/min is required. Figure 3 shows a photograph of cooling plates and MA cores during assemble a cavity.

Actual impedance of cavity is strongly affected by additional stray capacitance from the cavity components such as a ceramic gap, cooling plates and so on. The rf cavity is connected with the vacuum tubes of a high power rf amplifier. The cavity impedance with vacuum tubes was measured by using the network analyzer. Figure 4 and 5 show the results of these measurements.

It was found that the big capacitance components cause the reduction of cavity impedance. The measured impedances (Z) of 320~170Ω are correspond to the acceleration frequency range of 1.5~4.6MHz. We prepared one set of rf station (cavity & amplifier) only, The second rf station of 150MeV FFAG will be newly designed after actual operation of this rf system.

WIDE BAND AMPIFIER

The radio frequency high power amplifier supplies rf power to the cavity. Specifications of the rf wideband amplifier for the 150MeV FFAG proton synchrotron are listed in table 3.

Table 3: Specifications of the rf amplifier

RF frequency	1.5 MHz~4.6 MH
RF voltage	0.5 kV(peak)
RF output power	55 kW
Class	B class, Push-pull
Power Tube	4CW25000Ax 2

Several types of wide band rf power amplifiers was developed at KEK [8],[9].

The first is the direct loop couple method by using an anode wire. Second is the choke couple method with dc cut capacitors. A schematic diagram of choke coupling circuit is shown in figure 7. A practical choke circuit is shown in figure 8. This second method has an advantage about the voltage holding in the cavity circuit. But the defect is that the choke has some resonance mode.

The 2nd resonance of the choke is the serial resonance mode. As this serial resonance makes the short circuit to the anode potential, the fr voltage at the anode of the tube is eliminated by the second resonance.
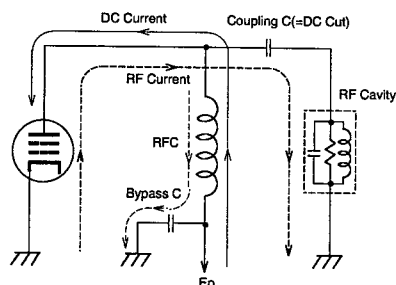
Figure 7: Diagram of the output circuit with RFC (Radio Frequency Choke) and the dc cut capacitor.
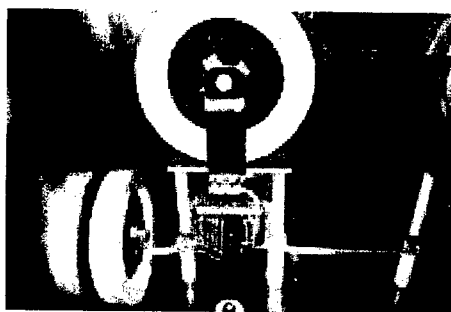
Figure 8: Photograph of the output circuit in the rf power amplifier. An RFC and dc cut capacitor are connected by the large sized cooper bus bar. RFC is winding on three pieces of toroidal cores.

Figure 9 shows origins of these resonances in the anode choke coil. The 1st resonance is a parallelresonance, this resonance mode has not severe effect. The measured 2nd resonance frequency of the actual choke coil was about 12MHz. This higher frequency of 2nd resonance is achieved by using special toroidal cores.

(a)   (b)
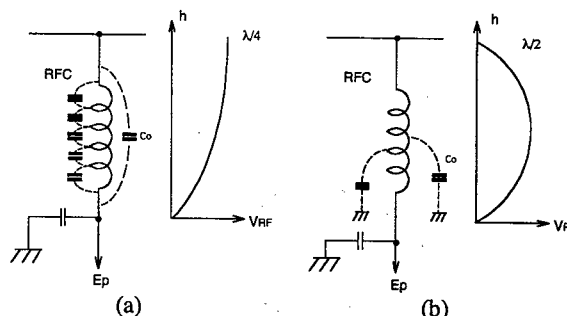
Figure 9: Resonance modes of anode RFC coil.
(a) 1st resonance (=parallel resonance).
(b) 2nd resonance (=serial resonance).

SUMMARY

A wideband rf acceleration system for the 150MeV FFAG proton synchrotron has been developed at KEK. The indirect cooling core cooling method was developed with a special thermally conductive spacer sheet. An anode choke coil shows good quality by using special toroidal cores.

REFERENCES

[1] M. Aiba et al., "Development of a FFAG proton synchrotron", EPAC2000, p. 581.
[2] T. Adachi et al., "A 150MeV FFAG synchrotron with return-yoke free magnet", PAC200, p. 3254.
[3] http://hadron.kek.jp/FFAG/.
[4] Hitachi Metals, Ltd., FINEMET: FT-3M.
[5] Y. Mori et al., "A new type of rf cavity for high intensity proton synchrotron using high permeability magnetic alloy", EPAC98, p. 299.
[6] DENKA, Ltd., General type: FSL-B.
[7] Y. Mori et al., "Multi-beam acceleration in FFAG synchrotron", PAC2001,p. 588.
[8] C. Ohmori et al., "A wide band rf cavity for JHF synchrotron", PAC97, p. 2993.
[9] Y. Sato et al., "Wide-band push-pull amplifier for high gradient cavity", PAC99, p. 1007.

DIRECT-COOLING MA CAVITY FOR J-PARC SYNCHROTRONS

T. Uesugi*, Y. Mori, C. Ohmori, A. Takagi, M. Yoshii, KEK, Tsukuba, Japan

M. Yamamoto, F. Tamura, JAERI, Tokai, Japan

and A. Schnase, COSY, Juelich, Germany

Abstract

The first rf cavity for the J-PARC(Japan Proton Accelerator Research Complex) 50GeV synchrotron has been developed. In the cavity, magnetic-alloy(MA) cores are cooled by water directly. With the cavity, we have accomplished an acceleration field of more than 50 kV in 1.776 m cavity length. We show the design of the rf cavity and results of high-power tests.

1 INTRODUCTION

In the J-PARC project[1], a proton beam will be accelerated from 181 MeV to 3 GeV in the rapid cycle synchrotron(RCS), and then up to 50 GeV in the main ring(MR). The parameters of the synchrotrons are listed in Table 1. In both synchrotrons, an accelerating field of about 30 kV/m is required. In order to realize such a high field-gradient, we will employ rf cavities loaded with magnetic-alloy(MA) cores whose impedance is kept high under high magnetic field as 2 kG at least[2]. The average power-dissipation of the cavity, taking the duty factor into account, will become about 120 kW/cav(40 kW/cell) for the RCS and about 240 kW/cav(80 kW/cell) for the MR, respectively.

Because of the high power-dissipation, it is important to cool the cores efficiently. We have developed two types of rf cavities as candidates for the J-PARC synchrotrons; One is indirect-cooling MA cavity, and the other is direct-cooling one. In the indirect-cooling cavity, the MA cores are cooled by cooling-disks indirectly[3]. With the cavity a gap voltage of 10kV was stably obtained in the RCS
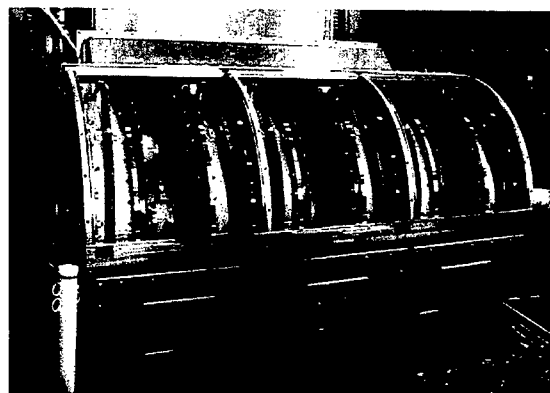
Figure 1: Direct-cooling MA cavity.

Figure 2: Inside the tank.

frequency-band, and the averaged-power of 36 kW/gap was removed by water.

In the direct-cooling cavity, on the other hand, the MA cores are installed in a water-sealed tank and cooled by water directly. This type of cavity is used in the NIRS-HIMAC[5] and in the KEK-PS second-harmonic cavity[6]. In this paper, we report the design and the performances of the direct-cooling MA cavity for the J-PARC synchrotrons.

2 CAVITY DESIGN

Figure 1 shows the picture of the direct-cooling MA cavity. The cavity consists of three identical cells, and each cell has an accelerating gap at the center, three MA cores on both side, and vacuum capacitors for tuning. It has no dynamic tuning system because of the broad-band characteristics of the MA. The accelerating gaps are connected

Table 1: Rf parameters of the J-PARC synchrotrons.

parameter	RCS	MR
circumference	348.3 m	1567.9 m
particle energy	0.181~3 GeV	3~50 GeV
revolution freq.	0.94~1.67 MHz	1.67~1.72 MHz
repetition time	40 msec	~3 sec
harmonic no.	2	9
max. rf-voltage	450 kV	280 kV
duty(power)	~30 %	~60 %
no. of cavities	11	6
cavity length	1.776 m	1.776 m
quality factor	2~3	~10
no. of gaps	3/cavity	3/cavity

* He has moved to NIRS, Inage-ku, Chiba, Japan

with a couple of bus-bars in parallel. The rf power is put by a 1 MW push-pull amplifier with two tetrodes(TH558)[4].

The dimension of the MA cores is 800 mm(OD)-250 mm(ID)-35 mm(TH). The cores are diametrically cut in two by water-jet-cut in order to control the quality factor[5]. The accuracy of the cut-surface is ∼1 mm, which should be improved not to disturb the water-flow there. Three MA cores are piled in a water-sealed tank with FRP-disks inserted between, and fixed by spacers at outer side and the cut-surfaces of the cores(Fig. 2). Those spacers are not only for the core-support but also for excluding a part of water around the core, which causes the impedance reduction due to the dielectric effect of the water(ε ∼80). The band-width, or quality factor(Q) of the cavity in other word, is controlled by changing the thickness of the spacers at the cut-surface; It is 1 mm for the RCS(Q ∼2) and 10 mm for the MR(Q ∼10).

Cooling-water comes from the bottom of the tank and flows upward. The configuration of the core-support pieces on the FRP-disks should be optimized to diffuse the water-flow. In a direct-cooling MA cavity, it is important to protect the cores from rusting or corrosion. We are planning to protect the cores by coating them with epoxy- and then polyester-resin with ∼0.2 mm thickness. According to a small-sample test, the surface of an MA core has survived in a 6 % $FeCl_3$ solution at 50 ℃ over 24 hours.

3 HIGH-POWER TEST

High-power tests of the cavity were carried out with the RCS and the MR setup, respectively.

3.1 cavity impedance

As is written before, the resonant frequency and the band-width of the cavity are determined by the tuning capacitance and gap width of the cut-core. The parameters of the cavity are shown in Table 2. Figure 3 shows the impedance of the cavity measured from the accelerating gap directly. The effects of the capacitance due to the tube and the water are included. In the Fig. 3, the dashed line shows the case where three cells are filled with the cores and connected to the amplifier, and rigid ones show only one cell is connected. Three cells impedance for the RCS

Table 2: Parameters of the cavity for the RCS and the MR setup.

parameter	RCS	MR	
cut-core gap width	1.5 mm	10 mm	
tuning capacitance	400 pF	1600 pF	
number of cells	1	1	3
peak impedance	837 Ω	786 Ω	263 Ω
resonant frequency	1605kHz	1800kHz	1821kHz
band-FWHM	549 kHz	189 kHz	195 kHz
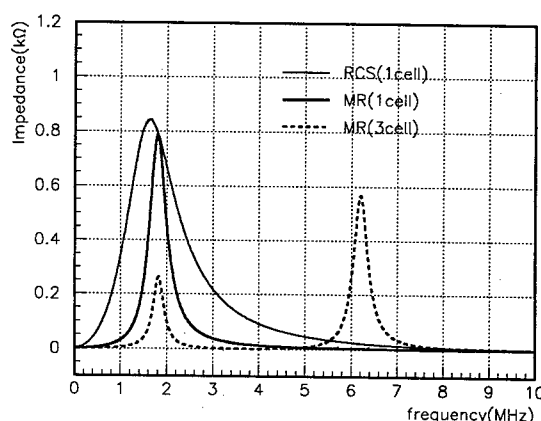
Figure 3: Cavity impedance measured from the gap.

setup is not measured in this moment. Without the water inside the tank, one-cell impedance with the MR setup was 960 Ω at its peak; The impedance reduction due to the water is about 18 %.

As shown in Fig. 3, the band-width with the RCS setup was not enough to cover the required range, because the cut-surfaces of the cores were not flat enough to reduce the Q-value.

There is a parasitic resonance at 6.2 MHz when three cells are loaded. That resonance came from the inductance of the bus-bars and resonant capacitors, and it was found that we could damp it by putting damping resistors on the bus-bar and adding another bus-bar[7]. In addition, another impedance measurement with a conductor wire showed that the parasitic resonance is not observed[8].

3.2 MR setup

We have input an rf-power into just one cell of the cavity with the MR setup. The operating frequency was fixed at 1.785 MHz. A gap voltage of 18 kV was successfully obtained with 50 % duty in 2.0 sec on/off period. The averaged rf-power was calculated to be 103 kW, which was beyond the requirement. The wave-form of the gap voltage looked quite good. The temperature rise of the cooling-water, whose flux was 50 ℓ/min for each tank, was about 15 ℃ ; That value was consistent with the power-dissipation at the cores.

In the next, we have input power into the whole cavity, ie. three-cells cavity. At 1.81 MHz the voltage up to 18 kV/gap was stably obtained for 6 hours. After a 49 hours long run with 17 kV/gap, we opened the water-tanks of the cavity and found no damage on the cores or FRP pieces. The power-test is limited by the water-cooling system of the experimental facility. Thus, the direct-cooling MA cavity has completely satisfied the requirements of high-voltage and high-power performance for the MR.

3.3 RCS setup

Preliminary high-power test for the RCS setup has also been done with the cavity. The rf-power was continuously input into one cell of the cavity. The gap voltage of 12.4 kV was obtained; That corresponds to the rf-power of 90 kW, which is more than twice of the requirement. The temperature rise of the water was 12 ℃.

After 5 hours high-power operation, a part of the cores were damaged by heat at the cut-surface where the heat was concentrated. Because the cores were designed for the MR, the flatness of the cut-surface was not enough and and the coolant is difficult to flow in the narrow-gap case. We are trying to improve the water-flow control by improving the smoothness of the cut-surface.

4 COMPARISON TO THE INDIRECT-COOLING

We compare the direct- and indirect-cooling[3] MA cavities at this moment. With the indirect-cooling cavity with the RCS setup, an rf power of 40kW/cell was succesfully cooled by water. On the other hand, high-power test has not been tried with the MR setup because of the heat concentration at the outside of the MR cores, which was observed in a single-core test in wide gap($\sim$1 cm) condition. In addition, the adhering strength of the insulator between a core and a cooling-disk is important, because a presence of an air-gap between them seriously reduces the local cooling efficiency. A part of the insulators was peeled off by thermal stress under a high-power operation. The cooling efficiency of the direct cooling is better than the indirect one. This is the main reason we decide to use the direct cooling scheme for J-PARC cavity.

The impedance reduction comes from the capacitive effects between cores and other material. It is larger in case of the direct-cooling than that of indirect one because of the high dielectric constant of water. The effect becomes severe at the high frequency region. To reduce the effect, the purity of water is important. It is possible to overcome the disadvantage by using a coolant with lower dielectric constant like fluorinert[6].

There might be a situation where one have to change the gap-distance slightly to readjust the bandwidth of the cavity. In the indirect-cooling cavity, it is easy to push one half of the MA cores to control the gap-distance. However, in the direct-cooling one, we need to open the tanks and fix the cores with a different thickness of the spacers. We need to improve the maintenanceability of the direct-cooling cavity.

5 SUMMARY

We have newly developed a direct-cooling MA cavity for the J-PARC synchrotrons, and examined it with high-power rf. The cavity accomplished the required rf-voltages for the MR and the RCS operations. The cores were cooled well with the MR setup. However, it was not sufficient with the RCS setup with the heavy duty operation(200% of the requirement) where the gap distance was narrower. This problem will be solved by improvement of the cut-surface.

6 REFERENCES

[1] Accelerator group, JAERI/KEK Joint Project Team, 'Accelerator Technical Design Report for High-Intensity Proton Accelerator Facility Project', KEK-report.

[2] Y. Tanabe et al., EVALUATION OF MAGNETIC ALLOYS FOR JHF RF CAVITY, APAC98, Tsukuba, 1998.

[3] C. Ohmori et al., HIGH FIELD GRADIENT CAVITY FOR JAERI-KEK JOINT PROJECT, EPAC2002, Paris, 2002.

[4] M. Yoshii et al., RF Acceleration Systems for the JAERI-KEK Joint Project, EPAC2002, Paris, 2002.

[5] C. Ohmori et al., High Field-Gradient Cavities Loaded with Magnetic Alloys for Synchrotrons, PAC1999, New York, 1999.

[6] M. Yoshii et al., MA RF Cavity for the KEK 12GeV PS, EPAC2000, Stockholm, 2000.

[7] M. Brennan, The Upgraded RF System for the AGS and High Intensity Proton Beams, Dallas, PAC95, 1995.

[8] T. Toyama, private communication.

HIGH POWER TESTING OF THE 402.5 MHZ AND 805 MHZ RF WINDOWS FOR THE SPALLATION NEUTRON SOURCE ACCELERATOR*

K.A. Cummings, J.M. De Baca, J.S. Harrison, M. Rodriguez, P.A. Torrez, D.K. Warner,

LANL, Los Alamos, NM 87544, USA

Abstract

Historically, Radio Frequency (RF) windows have been a common point of failure in cavity input power couplers; therefore, reliable RF windows are critical to the success of the Spallation Neutron Source (SNS) project. The normal conducting part of the SNS accelerator requires six RF windows at 402.5 MHz and eight RF windows at 805 MHz [1]. Each RF window will transmit up to 180 kW of average power and 2.5 MW peak power at 60 Hz with 1.2 millisecond pulses. The RF windows, designed and manufactured by Thales, were tested at the full average power for 4 hours to ensure no problems with the high average power and then tested to an effective forward power level of 10 MW by testing at 2.5 MW forward power into a short and varying the phase of the standing wave. The sliding short was moved from 0 to 180 degrees to ensure no arcing or breakdown problems occur in any part of the window. This paper discusses the results of the high power testing of both the 402.5 MHz and the 805 MHz RF windows. Problems encountered during testing and the solutions for these problems are discussed.

EXPERIMENTAL SETUP

Window Geometry

The 402.5 MHz and 805 MHz windows are planar windows, shown in Figures 1 and 2, respectively. The vacuum side of both windows is copper plated stainless steel waveguide, and the air side is aluminum waveguide. The 402.5 MHz window consists of 1/2 height WR 2100 waveguide on the vacuum side and full height WR 2100 on the air side. The 805 MHz window consists of full height WR 975 waveguide on both the air and the vacuum side. The ceramic in both windows is a high purity alumina ceramic.

Test Stand Configuration and Diagnostics

A 2.5 MW klystron was used as the RF source [2]. Assuming waveguide and circulator losses of up to 8%, 2.3 MW of peak RF power was available in the test area. In a transient condition, 2.5 MW was obtained. The steady state power was 2.3 MW peak power.

High average power testing and high peak power testing require different test configurations. In the high average power testing the forward power is transmitted through the windows into a matched load, as shown in Figure 3. The peak power test setup is the same, but instead of a load a sliding short is used. The windows are

tested at the full average power and duty factor for four hours; and then peak power tested to an effective forward
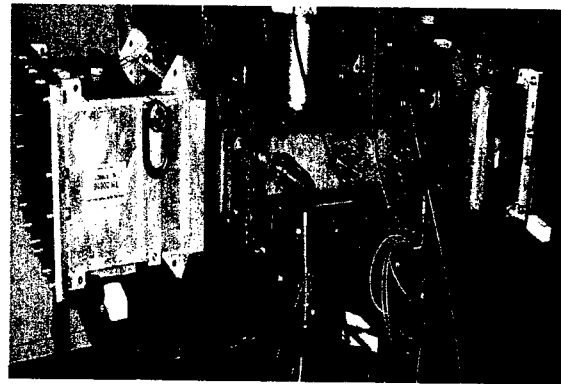
Figure 1: 402.5 MHz Windows and Vacuum Waveguide.
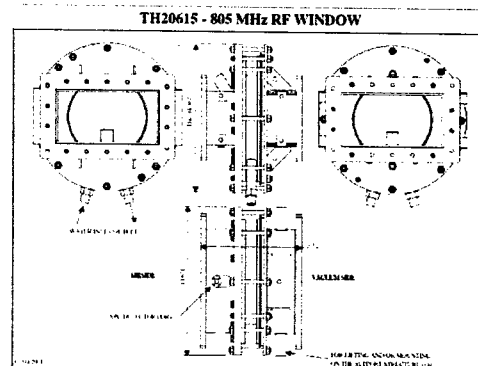
Figure 2: 805 MHz Window Schematic

power level of 10 MW by testing at 2.5 MW forward power into a sliding short and by varying the phase of the standing wave. The sliding short was moved from 0 to 180 degrees to ensure no arcing or breakdown problems occur in any part of the window.

The RF power was measured with four directional couplers, as illustrated in Figure 3. The vacuum pressure was measured with two ion gauges that are interlocked to turn off the RF power if the pressure rises above 1×10^{-7} Torr. The water inlet and outlet temperatures and surface temperatures are also measured. Fiber optic arc detectors are used on both the air side and the vacuum side of the ceramic. If an arc is detected, an interlock turns off the RF power for 1.6 seconds. A LabVIEW data acquisition system is used to monitor, display and record the RF power, pressure, water inlet and outlet temperatures, surface temperatures and the total number of arcs

1237

detected. The control racks for the test stand are shown in Figure 4. The racks are, from left to right, the 805 MHz arc detection rack, two 805 MHz transmitter racks; the computer rack for LabVIEW data acquisition program; a rack containing the HV ready/ crowbar interlock chassis, the ion gauges for the window vacuum; a scope displaying HV pulse waveform, pulse generator and RF signal generator; and a rack with 402.5 MHz arc detectors, the vacuum interlocks and the gate valve controllers.
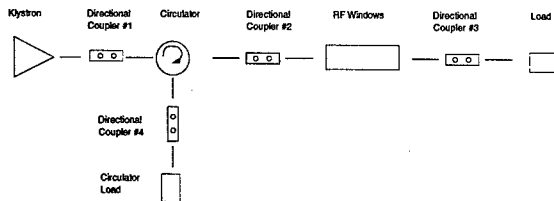
Figure 3: Test Block Diagram for Average Power Testing.
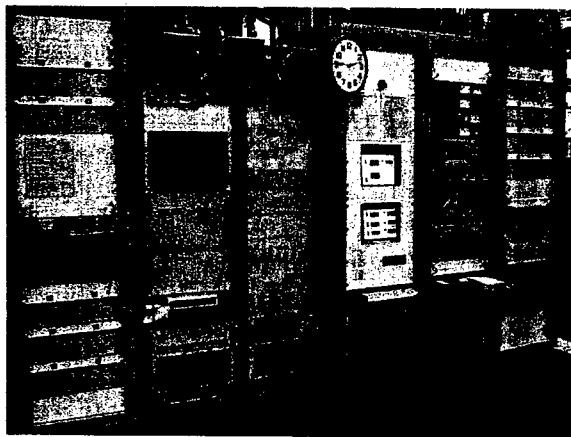
Figure 4: Control Racks for RF Window Test Stand.

EXPERIMENTAL RESULTS

High Temperature Bake Out Results

A high temperature vacuum bake out is done to release particles and water vapor embedded in the ceramic and vacuum waveguide surfaces. During the bake out, the windows are held between 150 ßC to 200 ßC until the pressure drops below 5×10^{-7} Torr as shown in Figure 5 and Figure 6. It typically takes 5 hours for the windows to reach the required temperature. It takes 10 to 15 hours, once the windows are at the required temperature, for the vacuum level to decrease to below 5×10^{-7} Torr. Because of safety regulations, the bake out is not allowed to run unattended. The bake out requires 3 to 4 days.

Experiments done to validate the need for the bake out showed that the bake out is essential to conditioning the windows successfully and expediently. Testing of two unbaked 402.5 MHz windows was attempted, but it was not successful because the vacuum pressure was too high.

These two windows were then baked out and then successfully conditioned and tested. Two 402.5 MHz windows were baked out, vented to nitrogen, exposed to air, and then re-pumped and tested at high power. There was not a second bake out after the windows were exposed to air. The windows were still successfully conditioned and tested.
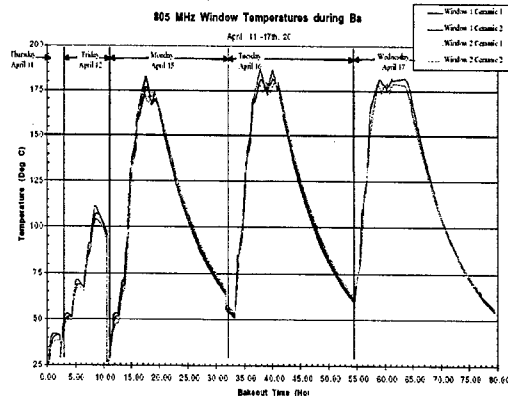
Figure 5: Temperature vs. Time during Bake Out
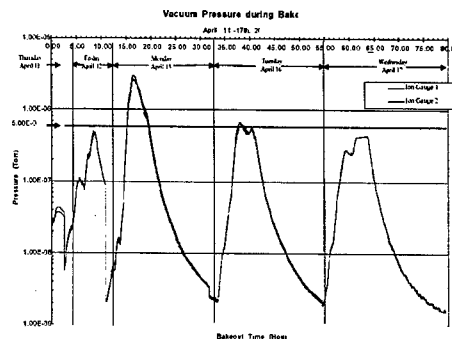
Figure 6: Pressure vs. Time during Bake Out

High Power Test Results

The conditioning procedure consists of beginning with a low duty factor and gradually increasing the power level. Next, the peak power level is lowered, the duty factor is increased and then the peak power level is gradually raised at the new duty factor. For the 805 MHz windows, a graph of the peak power verses time is shown in Figure 8. Once the windows are conditioned, the four hour heat run is done at full power and duty factor, also illustrated in Figure 8. It took about 10 hours to condition the two 805 MHz windows to the full power and duty factor. There were only a few arcs and the conditioning rate was limited by the pressure, as expected.
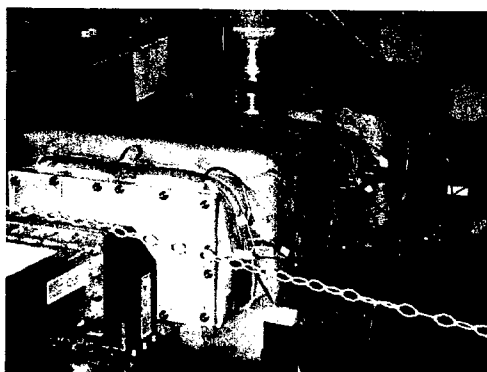
Figure 7: Windows in Heat Blankets during Bake Out.
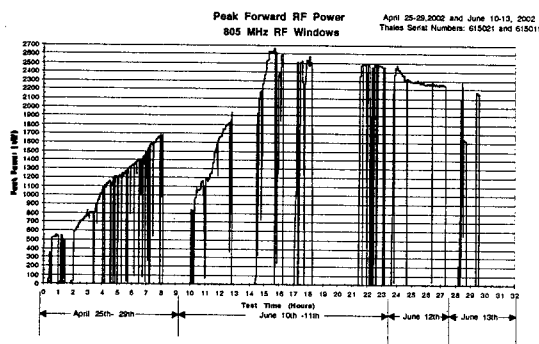
Figure 8: 805 MHz Window Peak Power vs. Test Time

It took 5 hours to condition the first two 402.5 MHz windows to 500 kW. The available power supply voltage was limited, thus they were run at 500 kW for seven more hours. Once the full power supply capacity was available, they were conditioned up to full power in two hours. This results in a total conditioning time of 7 hours. The second two 402.5 MHz windows were conditioned up to 500 kW in 4 hours and then once the full power supply capacity was available, they were conditioned up to full power in 3 hours. Thus, the average conditioning time for all 6 windows was 8 hours.

Problems Encountered during Testing

Two separate problems were encountered while testing the 402.5 MHz windows. The first problem was that a RF leak was found on the top surface of the waveguide in the region of the ceramic. The leak was measured at 9.7 mW/cm^2 at a distance of 10 cm from the surface at 6.4 kW average power. At 2.5 MW peak power and 180 kW average power, this extrapolates to 272 mW/cm^2. This exceeded the specified maximum leak rate of 1 mW/cm^2 at a distance of 10 cm. This window was sent back to Thales, where it was repaired, but has not yet been re-tested. The leak was due to an inadequate RF seal caused by loose bolts around the ceramic, as shown in Figure 9.

The Thales assembly procedure was modified and additional post-delivery inspections were implemented. The second problem encountered during testing is that the second pair of 402.5 MHz windows are arcing during the peak power test with the sliding short. This pair of windows does not arc at all when run into a matched load. When run into a sliding short, both circulator and window arcs occur at the same time. This problem has not yet been resolved and it may be due to arcs in the waveguide run and/or circulator and not due to window arcs. To help isolate the arcing problem, air will be blown through the waveguide to reduce window arcs during the next sliding short window tests.
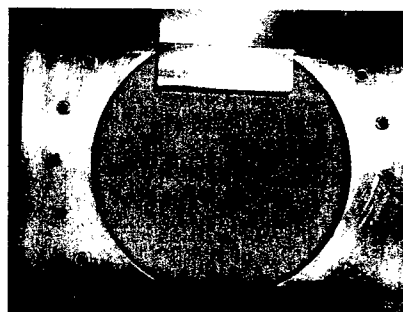
Figure 9: 402.5 MHz Inner Bolt Circle

CONCLUSIONS

Two of the eight 805 MHz windows and four of the six 402.5 MHz windows have been successfully baked out, conditioned and tested. The test results are very important for four different reasons: First, they prove the design concept of the windows. Second, they have shown that the bake out is an essential part of the testing process. Windows could not be conditioned and tested without a bake out. Third, if a window is baked out and then vented to nitrogen, it retains the benefits of the bake out and does not need to be re-baked out. Previous work has indicated that if a window is baked, conditioned, and then vented to air, it can be reconditioned quickly [3]. Fourth, we have learned that the average conditioning time for the windows is 8 hours. Hence it is not feasible to condition windows while conditioning the accelerator. Therefore, the bake out and the conditioning of the windows on the test stand is absolutely essential to the success of the SNS project.

REFERENCES

[1] D. Rees, M. Lynch, P. Tallerico, W. Roybal, K. Cummings, T. Hardek, J. Bradley, W. Reass, A. Regan, "The RF System Design for the Spallation Neutron Source," PAC'01, Chicago, IL, 2001.

[2] D. Rees, "The SNS Linac High Power RF System Design, Status, and Results," PAC'03, Portland, OR, 2003.

[3] K. Cummings, "Theoretical Predictions and Experimental Assessments of the Performance of RF Windows," Ph.D. Dissertation, University of California, Davis, CA 1998.

HOM DAMPERS FOR ALS STORAGE RING RF CAVITIES.

S.Kwiatkowski, K.Baptiste, J.M. Byrd, J.Julian, R.Low, L.Lyn, D.Plate
LBNL, Berkeley, CA 94565, USA*

Abstract

The main source of narrowband impedance in the Advanced Light Source (ALS) are higher order modes (HOMs) of the two main RF and three third harmonic cavities. These HOMs drive longitudinal and transverse coupled bunch instabilities, which are controlled using active beam feedback systems. The dominant longitudinal HOMs in both systems are TM_{011}-like modes with the R/Q factor an order of magnitude higher than all other longitudinal modes. To reduce the growth rates within the range of the longitudinal feedback system (LFB), these modes were tuned away from beam resonances by means of cooling water temperature control (main rf system), and the combination of two tuners (third harmonic system). To improve the reliability of the longitudinal dampening system, we have built and installed E-type HOM dampers for the fundamental and harmonic cavities. We present the design, commissioning and performance of the HOM dampers in this paper.

INTRODUCTION

The ALS storage ring 500 MHz RF system uses two re-entrant accelerating cavities apertures coupled to a waveguides for providing power. Originally, each main RF cavity was equipped with the HOM damper located in this waveguide as shown in Fig. 3, which resulted in moderate damping of some HOMs. From operational experience there were still three HOM main cavity modes that were gave instability growth rates beyond the damping rate of the longitudinal feedback (LFB) system [1] and required careful tuning to maintain beam stability. The most important modes are TM_{011} mode (highest R/Q factor) at 0.81 GHz and two others at 2.35 GHz and 2.85 GHz. The longitudinal symmetry of two out of the three modes of interest (0.81 GHz and 2.85 GHz) were an "odd" type, which indicated that an E-type damper located at the cavity equator was the best choice for a HOM damper (there was one port with the 48mm diameter available for HOM damper installation). In the 1.5 GHz third harmonic cavities, only one longitudinal mode (TM_{011} at 2.32GHz) presented problems. This mode was damped with a similar HOM damper.

E-TYPE HOM DAMPER BASICS

The simplest E-type HOM damper consists of a pick-up probe and resistive termination. The damper will reach optimum performance when $Rd=X_{pr}$ (maximum power dissipated in the termination resistor).

$$P_{n_{MAX}} = \frac{1}{4}I_n^2 \cdot X_{C_{pr}} = \frac{1}{4}I_n^2 \frac{1}{\omega \cdot C_{pr}}$$

In reality some length of the coaxial transmission line has to be introduced between the HOM antenna and the termination resistor. By having the termination load impedance different from the characteristic impedance of the transmission line one can achieve an enhanced damping effect at particular frequencies. The equivalent electrical schematic of the basic E-type damper terminated into resistive load is shown in Fig.1.
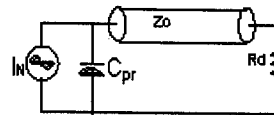
Fig.1

where: C_{pr}-total probe capacitance
I_n – displacement current induced in the HOM antenna for a particular cavity mode (for probe port shorted).

$$I_n = \omega_n \times \varepsilon_0 \iint_S E_n \cdot dS$$

DESIGN PROCESS

MAFIA 3D frequency and time domain processors have been used to determine the required size and the penetration of the HOM antenna into the rf cavity. Our goal was to damp the TM_{011} mode to the level where the growth rate was well within the damping ability of the LFB without dissipating significant fundamental frequency power in the HOM damper. The best damping effect has been achieved with the 19mm copper rod penetrating the rf cavity by 70mm. The "cold model" has been build and installed on the spare cavity in our test stand facility. The cold model was equipped with the sliding piston, which allowed further optimization of the geometry of the damper. Figure 2 shows the dependence of the loaded Q of the TM_{011} mode as a function of the penetration of the antenna into the rf cavity.

The total fundamental frequency power dissipated in the HOM damper for a 70mm antenna penetration is approximately 500W (for 50kW cavity cell power). More than 99.9% of the fundamental frequency losses in the HOM damper are due to eddy current losses induced on the surface of the antenna by the RF cavity field.
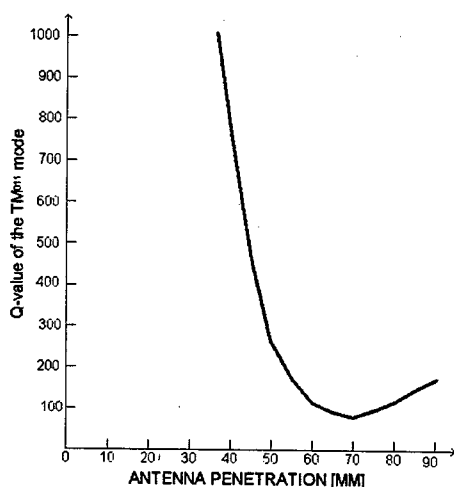
FIG.2

The required power handling capabilities of the termination resistors for the worst scenario of single bunch 30mA circulating current with all HOM modes tuned to the adjacent current spectral lines has been calculated and 150 W termination resistors have been chosen accordingly.

The same technique has been used while designing the HOM damper for the third harmonic cavities. The optimum performance of the third harmonic cavity damper was achieved for an antenna with a 10mm diameter and a 25mm cavity penetration. In this case the loaded Q of the TM_{011} mode dropped from 15000 to 60 with the fundamental frequency losses in the HOM damper of about 100W (for 5kW cavity cell power).

DAMPERS LAY-OUT

The cross-section of the ALS RF main cavity and HOM damper is shown in Fig 3. It consists of 180mm long antenna, supporting coaxial structure, two 50Ω termination ports and the vacuum bellows. The antenna and the two rods connecting the coaxial supporting structure to the vacuum feedthrough are made of OFHC copper. All other parts are made of stainless steel. Additionally, the coaxial supporting structure is nickel plated, to increase the rf losses to the HOM modes, which are not strongly coupled to the dampening resistors. Terminated ports are located 281mm from the shorted end of the HOM main supporting structure ($3/4\lambda$ for TM_{011} mode and 0.5λ for fundamental TM_{010} mode). Vacuum bellows allow us to minimize the coupling of the fundamental mode to the HOM damper, and to optimize the damper performance over all frequency spectra.

The HOM damper antenna and the coaxial supporting stem are water-cooled. The damper is located on the movable table, which allows position of the antenna with all six degrees of freedom. Fundamental frequency coupling factor to the HOM damping port is lower than $-60dB$.

In the third harmonic cavity case the optimization of the position of the antenna in the cavity is not as critical since there is only one monopole mode required to be damped and the cavity cell power is a factor of 10 lower than in the main cavities. For these reasons bellows have been excluded from the damper layout, and the damper is directly attached to the cavity flange without any additional support. Over the next few months we will install a second identical damper on each third harmonic cavity, which will damp the second (horizontal) component of the "odd" dipole modes.
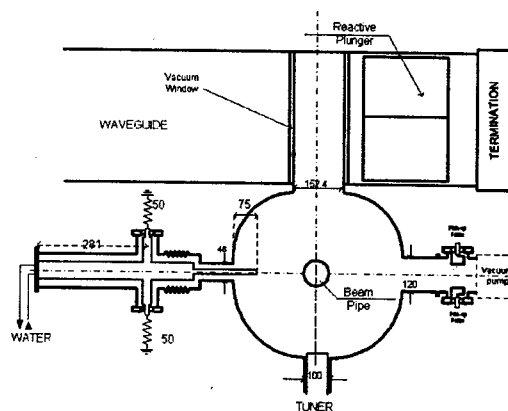
FIG.3

PERFORMANCE

The results of the measurements of the longitudinal HOM spectrum at fundamental frequency cavity before and after damper installation are shown in Table1.

Table 1

Without damper			With damper		
F	Q	R_{sh}	F	Q	R_{sh}
MHz	-	$k\Omega$	MHz	-	$k\Omega$
499.6	40400	5000	499.8	40000	4960
809	**38700**	**1970**	**810.6**	**100**	**5.1**
1026.6	8250	9.9	1027.1	940	5.9
1310.8	10300	159	1327.8	280	4.3
1353.4	4000	39.2	1379.5	110	1.1
1554.1	5600	41.4	1560	940	7.0
1808.5	2850	13.1	1806.5	240	1.1
1883.7	1650	4.6	1886.2	540	1.5
2130.4	16800	58.8	2129.6	7200	25.2
2271.6	1800	6.8	2274.3	1500	6.5
2350	27500	99	2348.1	16300	58.7
2850	33500	142	2850	5360	22.8

We've been investigating an impact of the HOM damper on the few most important dipole modes. The results of the measurements are given in Table2.

Table 2

Mode	Without damper				With damper			
	F_H	Q_H	F_V	Q_V	F_H	Q_H	F_V	Q_V
	MHz	k	MHz	k	MHz	k	MHz	k
1-M-1	707	36.2	708.4	46.5	723	2.8	709	44.2
1-E-1	810	51.1	796	0.9	811	48.3	796	0.9
1-M-2	1122	7.4	1123	38.1	1102	2.1	1123	38.1

One could notice the positive effect of our E-type damper on the horizontal component of the "odd" dipole modes. The dampening effect of the vertical component of the 1-E-1 and some other "even" modes is the result of the "waveguide" type HOM damper installed in the rf power waveguide and coupled to the cavity via rf power coupler.

There is only one "odd" longitudinal mode "trapped" inside the third harmonic cavity (TM_{011} mode), which was effectively damped by single HOM damper installed in April 2003. The cross-section of the ALS third harmonic cavity with two E-type HOM dampers is shown in Fig 4.

FIG.4

REFERENCES

[1] D. Teytelman , J. D. Fox, S. Prabhakar, J. M. Byrd, "Characterization of longitudinal coupling impedances in storage rings via multibunch effects", Phys. Rev. ST Accel. Beams 4, 112801 (2001).

[2] E. Haebel "COUPLERS, TUTORIAL AND UPDATE".

[3] M.Izawa, H. Kobayakawa, S. Sakanaka, S.Tukumoto "Higher-Order-Mode Damping Coupler for Beam Instability Suppression" Japanese Journal of Applied Physics Vol. 26 October 1987.

CONCLUSION

The installation of the HOM dampers on ALS rf cavities was an immediate success. Now, the ALS storage ring can operate with the 312 bunch filling pattern (with help from the third harmonic cavities Landau damping effect) without the Longitudinal Feedback System closed. For the 276 bunch beam pattern due to the significantly higher phase transient effect the LFB system is still required, but it can operate with significantly lower gain.

A 201 MHZ RF CAVITY DESIGN WITH NON-STRESSED PRE-CURVED BE WINDOWS FOR MUON COOLING CHANNELS*

Derun Li[+], A. Ladran, J. Staples, S. Virostek, M. Zisman
Lawrence Berkeley National Laboratory, Berkeley, CA 94720, USA
W. Lau, S. Yang, Dept. of Physics, Oxford University, Oxford, UK
R.A. Rimmer, Jefferson National Accelerator Facility, Newport News, VA, USA

Abstract

We present a 201-MHz RF cavity design for muon cooling channels with non-stressed and pre-curved Be foils to terminate the beam apertures. The Be foils are necessary to improve the cavity shunt impedance with large beam apertures needed for accommodating large transverse size muon beams. Be is a low-Z material with good electrical and thermal properties. It presents an almost transparent window to muon beams, but terminates the RF cavity electro-magnetically. Previous designs use pre-stressed flat Be foils in order to keep cavity from detuning resulting from RF heating on the window surface. Be foils are expensive, and difficult to make under pre-stress to accommodate thermal expansion. An alternative design is to use pre-curved and non-stressed Be foils where the buckling direction is known, and frequency shifts can be properly predicted. We will present mechanical simulations of the Be window designs.

INTRODUCTION

High gradient RF cavities at 201 MHz are required for muon cooling channels in a neutrino factory or a muon collider, and also for a recently proposed muon cooling demonstration experiment at RAL (Rutherford Appleton Laboratory) - MICE (An International Muon Ionization Cooling Experiment). As high as 16 MV/m at frequency of 201 MHz is required, or 1.07 Kilpatrick. Eight 201 MHz cavities are needed for the MICE cooling channels, but the accelerating gradient for MICE will have to be limited to ~ 8 MV/m restricted by budget for RF power sources, not by cavity design. The cavity design supports a gradient of 16+ MV/m. In order to achieve such a high gradient for naturally large dimension muon beams, using conventional open iris structures would inevitably introduce very high peak surface fields, a limiting factor of achievable accelerating gradient. A closed-cell (pillbox like) cavity design was proposed and reported [1] where the beam apertures are electro-magnetically terminated by low Z and thin Be foils. To keep the cavity from detuning by RF heating power, these Be foils are under tension which is introduced by small CTE (coefficient of thermal expansion) difference between the thin Be foils and thick Be window frame during the brazing process. The pre-stressed windows should stay flat up to a certain temperature gradient limit where the pre-tension becomes zero. This temperature gradient limit determines how much heating power it can take for a given window thickness.

Manufacturing of the pre-stressed Be windows is expensive, and predicting the temperature limit is difficult. Predictions on the temperature gradient limit are difficult. Previous Be window designs for the 201 MHz cavity were scaled from the pre-stressed Be windows for an 805 MHz cavity. Recent experimental tests on the 805 MHz cavity found that the cavity frequency started to shift at a lower than predicted temperature gradient on the windows (the frequency shift was quite small and well within the klystron bandwidth). By taking advantage of the pillbox-like profile, non-stressed and pre-curved Be windows should result in smaller frequency shifts with both windows are installed oriented to the same direction in a cavity.

THE 201-MHZ CAVITY

Cavity Profile

The cavity shape has a slightly re-entrant round profile with a large beam aperture of 21 cm in radius. The cavity profile has been updated recently, and a small 2° tilt angle has been added at radius out of iris region to avoid having a two-parallel-plane configuration in consideration of possible multipacting problem, as shown in Figure 1.
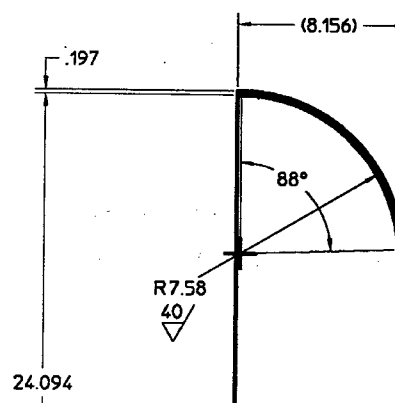
Figure 1: The 201 MHz cavity profile (only 1/8 of the cavity is shown here)

Cavity Parameters

The cavity parameters are listed in Table 1 for Study-II and MICE muon cooling channels.

Table 1: 201 MHz cavity parameters

Name	Study-II	MICE
Length (cm)	43	43
Radius (cm)	61.2	61.2
Accelerating Gradient (MV/m)	16.2	8.0
Voltage on crest (MV)	5.76	2.84
Peak forward power* (MW)	4.63	1.0
Peak surface field (MV/m)	26.5	13.1

* Assumed 3τ filling time and 85% of theoretical Q_0

NON-STRESSED AND PRE-CURVED BE WINDOWS

Window Profile

Experimental studies on pre-stressed flat Be windows have shown that the window started buckling at a limiting temperature gradient where the tension in the foil became zero. The measurements were conducted on 16 cm diameter windows in an 805 MHz cold-test cavity using halogen lamp as a heating source. Both no-stressed Al and pre-stressed Be windows were measured. These measurement results are summarized in Figure 2. It is worth pointing out that it is difficult to predict the buckling direction of the pre-stressed flat windows once the re-tension becomes to zero.
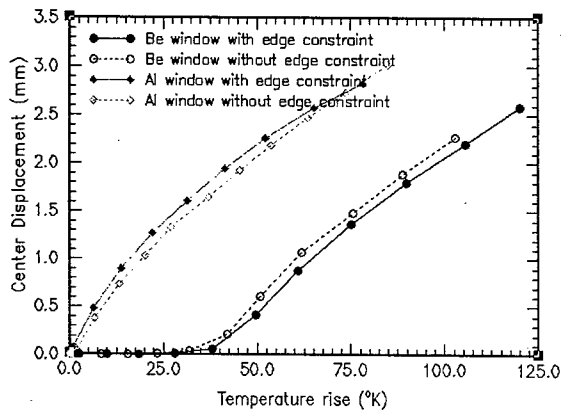
Figure 2: Experimental measurements on pre-stressed Be windows in an 805 MHz cold-test cavity. Temperature rise here is defined as the temperature difference between the window center and window frame. Limited by measurement sensitivity (resolution), a measurable displacement seemed to start at 35 °C.

A non-stressed and pre-curved window design has been developed to replace the pre-stressed flat windows. The following criteria have been considered during the evolution of the window design:

- Low thermal stress within the window for a given temperature gradient
- Out-of-plane window displacement for a given temperature gradient
- Ability for window to deform in a single direction
- Thinner window (less material and less scattering)
- Mechanical stiffness (characterized by mechanical resonant frequency)
- Cost and manufacturing

Figure 3 shows the window profile evolutions during the design process. We started with a single bow (curvature) window and found the thermal stress was too high at the annular frame. Then a new window design is developed to having an intersection between a concave and a convex in a region away from the edge of the frame, which makes the window more flexible and allow for more free expansion. The thermal stress is then further reduced.
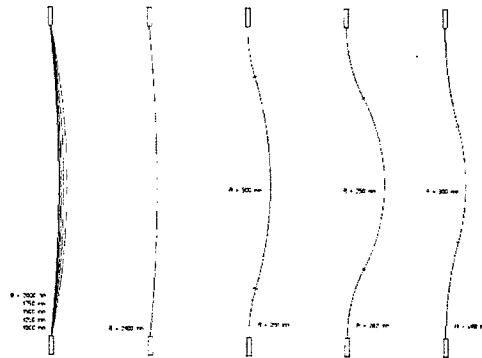
Figure 3: Window cross-section profile evolutions: from one to two curvatures (left to right)

The window thickness has been varied from 0.125-mm to 0.5-mm to study its effect on thermal stress. Since windows thinner than 0.125-mm tend to be more expensive, we chose a window thickness of 0.38-mm as a baseline study parameter for the window with 42-cm diameter.

FEA Modeling

Each window profile configuration has been modeled using FEA (Finite Element Analysis) code ALGOR in 2-D and 3-D. The following temperature distribution is then applied over the window for thermal and mechanical simulations [2].

$$T(r) = T_{max}\left(1 - \left(\tfrac{r}{R}\right)^4\right),$$

where T_{max} is the temperature gradient limit, R the window radius. This temperature distribution is a result of magnetic field distribution of TM_{010} mode in a pillbox cavity and the low radial thermal transfer of thin material. The fact that the window center as the hottest spot is due to the limited thermal conduction within the thin Be foil. As one would expect that T_{max} is proportional to the total RF heating power over the window, and inversely proportional to window thickness. T_{max}=100 °C, which is

higher than the temperature limit for operational gradient of 16 MV/m, have been assumed and used for all the simulations.

Figure 4 shows a 3-D FEA model of the non-stressed and pre-curved Be windows with two curvatures, together with their mechanical resonant frequencies. In this example, two lowest and one higher order mechanical resonant vibration distributions are shown in this figure.

Window thickness: 0.38 mm

1st natural frequency: 609 Hz   2nd natural frequency: 752 Hz
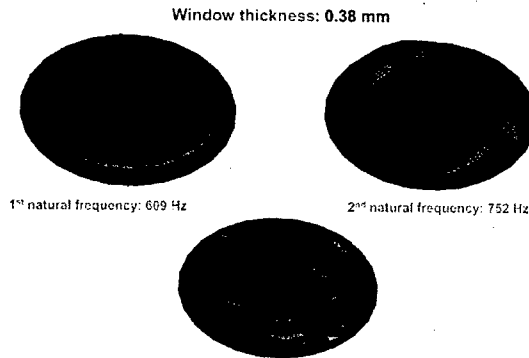
Figure 4: 3-D FEA model of a 42cm diameter, 0.38-mm thick and non-stressed and pre-curved Be window. Vibration distributions and their natural resonant frequencies have also been shown.

Window Displacement

Window displacements of the 42 cm diameter Be foils of different thickness were simulated after applying the above temperature distribution. Table 2 lists the maximum displacement at the window center from its natural position.

Table 2: Be window displacement versus thickness

Thickness (mm)	0.25	0.38	0.50
Displacement (mm)	2.42	2.25	2.13

The amount of the displacement is considered to be acceptable as long as all the windows are installed oriented in the same direction, which also results in minimum frequency shift of the cavity.

Thermal Stress

Similarly, the corresponding stresses due to the thermal load (T_{max}=100 °C) are simulated and their results are listed in Table 3.

Table 3: Thermal stress versus window thickness

Thickness (mm)	0.25	0.38	0.50
Thermal Stress (MPa)	150	169	179

Considering temperature gradient for thicker windows is lower (scaled linearly with d, the window thickness), all the above windows should work, and yet give adequate

safety margin. The thermal stresses are much less than the Be stress limit of ~ 340 MPa.

Window Fabrication

A concept for fabrication of the pre-curved Be window is shown in Figure 5. A smaller window of 16 cm diameter using the same concept will be tested first. This test may be conducted in either room temperature or up to the recommended forming temperature of Be depending on the resulting window profile. We expect that the window may spring back slightly to its natural shape after the forming process. This will be quantified during the tests.
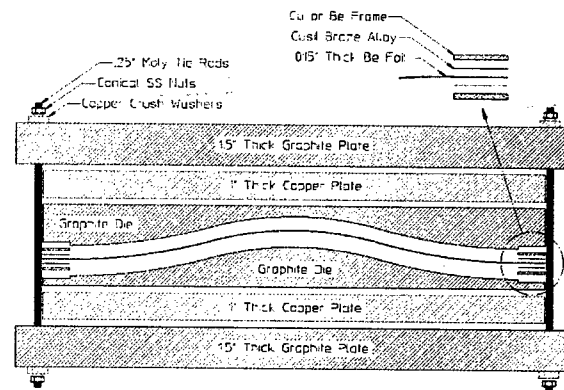
Figure 5: A concept for fabrication of pre-curved Be window.

Future Work

The fabrication concept of pre-curved windows will be realized in 16 cm diameter windows using materials having similar mechanical properties as beryllium. Time domain simulations will be performed to study possible mechanical resonant excitations by RF impulse using operational parameters for Study-II and MICE cooling channels.

CONCLUSION

A non-stressed pre-curved Be window has been designed. FEA simulations show it has more mechanical flexibility and thermal capability to handle the RF heating power while keeping the required cavity performance. Experimental tests and engineering efforts will continue.

REFERENCES

[1] R. Rimmer, *et al.*, "Closed-Cell 201.25 MHz RF Structures for a Muon Ionization Cooling Experiment", EPAC 2002, Paris, France

[2] D. Li, *et al.*, "Temperature Distribution Calculations on Be windows in RF Cavities for Muon Colliders, International LINAC Conference 1998, Chicago, IL, USA

RF TESTS OF AN 805 MHZ PILLBOX CAVITY AT LAB G OF FERMILAB*

Derun Li, J. Corlett, R. MacGill, J. Wallig, M. Zisman, LBNL, Berkeley, CA 94720, USA

A. Moretti, Z. Qian, V. Wu, FNAL, Batavia, IL, USA

R. Rimmer, Jefferson National Accelerator Facility, Newport News, VA, USA

J. Norem, ANL, Argonne, IL, USA

Y. Torun, Illinois Institute of Technology, Chicago, IL, USA

Abstract

We report recent high power RF tests on an 805 MHz RF pillbox cavity with demountable windows over beam apertures at Lab G of Fermilab, a dedicated facility for testing of MUCOOL (muon cooling) components. The cavity is installed inside a superconducting solenoidal magnet. A 12 MW peak RF power klystron is used for the tests. The cavity has been processed both with and without magnetic field. Without magnetic field, a gradient of 34 MV/m was reached rather quickly with very low sparking rate. In a 2.5 T solenoidal field, a 16 MV/m gradient was achieved, following several weeks of conditioning. Strong multipacting effects associated with high radiation levels were measured during processing with the magnetic field. More recently Be windows with TiN-coated surface have been installed and tested with and without the external magnetic field. 16 MV/m gradient without magnetic field was reached quickly as planned. Less multipacting was observed during the conditioning, indicating that the TiN-coated surface on the windows had indeed helped to reduce the secondary electron emission significantly. A gradient of 16.5 MV/m was finally achieved with magnet on in solenoidal mode and the field up to 4 T. Preliminary inspection of the Be window surface found no visual damage, in comparison with Cu windows where substantial surface damage was found. Preliminary understanding of conditioning the cavity in a strong magnetic field has been developed. More thorough window and cavity surface inspection is under way.

INTRODUCTION

Accelerators for intense muon beams call for very high gradient RF cavities at various frequencies. The high gradient is required to manipulate muon beams that are created with a large 6-D phase space, and decay rapidly (muon lifetime is about 2 μs at rest). Any manipulation to the muon beams has to be done quickly, including cooling. For instance, on the muon cooling channel design for Study-II [1] calls for accelerating gradient of ~ 16 MV/m at 201 MHz, compared to ~ 15 MV/m Kilpatrick criterion at the same frequency. Moreover these cavities have to be installed inside a superconducting magnet where magnetic fields are as high as a few Tesla. Therefore normal (warm) conducting RF cavity technology has to be used. Cavity geometry optimization alone is not sufficient to reduce the peak surface field and at the same time provide high shunt impedance with the large beam iris needed for muon beams. Taking advantage of the muon penetration property, a closed cell RF cavity was proposed [2] where the large beam iris may be terminated by thin low Z conducting material. The closed cell cavity resembles a cylindrical pillbox cavity where peak surface field is the same as the peak acceleration field on beam axis. Furthermore such a cavity design allows for arbitrary choices of phase advance per cavity, independent phase control of each cavity, and more freedom for beam dynamics design. Efforts to design such a high gradient cavity have highlighted the engineering challenges on how to incorporate thin Be windows in the cavity. Conditioning and operating a RF cavity in strong magnetic field of a few-T pose potential difficulties in overcoming multipacting zones, surface damage and many possible unknowns. As part of ongoing R&D activity for the high gradient RF cavity for muon beams, we have designed and constructed an 805 MHz pillbox cavity with demountable windows [3]. The cavity design allows for tests of different windows. The cavity has been under high power RF tests at Lab G, FNAL since March 2002. In this paper, we report recent test results and future plans. Preliminary data analysis will be presented. Surface inspection and analysis of windows are being analyzed, and is reported in another paper at this conference [4].

THE 805 MHZ CAVITY

The 805 MHz pillbox cavity was reported previously [3]. The cavity and its power coupler were designed at LBNL using the MAFIA code in frequency and time domain, respectively. Good agreement was achieved between the design values and low power RF measurements. The cavity body was fabricated at the University of Mississippi, with final cavity braze carried out at the Alpha-Braze Company in Fremont, California. Final cavity cleaning, assembly, system integration and vacuum checking were conducted at LBNL. Four pre-stressed flat Be windows were purchased from Brush-Wellman Company in Fremont for tests. The cavity was shipped to Lab G of Fermilab for high power tests in March 2002. Table 1 lists the main RF parameters of this cavity in comparison with the low power RF measurements at Lab G.

Table 1: Main parameters of the cavity in comparison
with low power microwave measurements

Name	Design	Measured	Unit
Frequency	805.00	804.946	MHz
Q_0	18,800	15,080	
Coupling constant	1.0	1.08	
Radius	15.62		Cm
Gap Length	8.1		cm
Window diameter	16		
Be window thickness	0.127		mm
Gradient on axis	30		MV/m
Shunt Impedance[‡]	32		MΩ/m

RF TEST OF THE CAVITY

Test Set Up at Lab G

A 12 MW peak power klystron and a superconducting solenoid magnet up to 5 Tesla are available for the RF tests. The SC magnet can be powered to operate in either solenoidal mode or gradient mode. Figure 1 is a photo taken inside Lab G test cave showing the test set up.
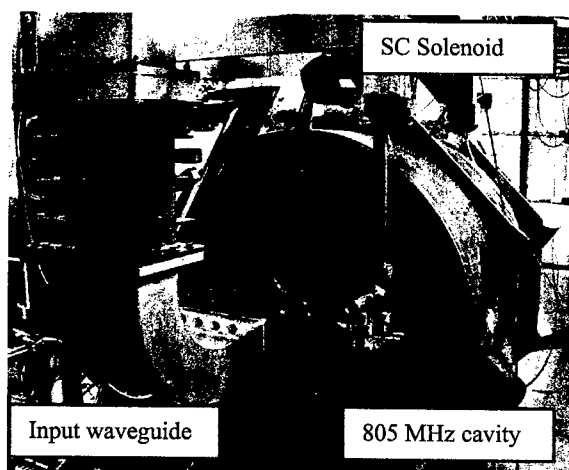
Figure 1: RF cavity inside the SC solenoid at Lab G, FNAL

The 805 MHz pillbox cavity sits inside the center of the warm bore of the superconducting solenoid. All necessary measurement equipment and probes needed for RF, vacuum, x-ray and dark current measurement are available. The RF tests can be set and controlled either by computers or manually.

Test Results

The cavity was first baked up to 115 °C with hot N_2 purge for 2 days and then pumped down to vacuum of order of 10^{-8} Torr before RF conditioning started. We will report the test results according to the timeline. High power RF conditioning was conducted on Cu windows

first, and then followed tests of Be windows with one TiN-coated surface facing RF, with and without magnetic field.

Test of Cu Window without External Magnetic Field

High power RF conditioning started with Cu windows, rather than Be windows initially, without magnet the on. Combinations of different pulse lengths and repetition rates were used in conditioning phases. Multipacting effects were observed at low RF power as expected. Typical two-plate multipacting zones were observed, and passed rather quickly. 34 MV/m accelerating gradient was achieved with low x-rays, low dark current and little sparking. This gradient has exceeded our designed value of 30 MV/m. The cavity was then taken apart for surface inspection on cavity body and windows, no surface damage was found.

Test of Cu Window with External Magnetic Field

The cavity tests resumed with the super-conducting magnet on at 2.5 T in solenoidal mode. The cavity seemed to have lost its conditioning history and behave like a brand new cavity again. More multipacting zones popped up, and they were much harder to pass through. Radiation levels went up by almost 1000 times, compared to the case without the external magnetic field. Details on x-ray, dark current and radiation measurements are reported in [4]. Higher radiation levels and more severe sparking prevented us from pursuing higher accelerating gradients. Nevertheless we found a possible surface *self-healing* effect that appeared during a period of the conditioning. That is, after a period of conditioning with the magnet on, associated with strong multipacting zones and high radiation levels, we turned the magnet off and continued re-conditioning the cavity without magnetic field for one or more days. The dark currents and radiation levels were measured to be dropping continuously with the conditioning time. This process was repeated and verified. Higher or equal gradient was then re-gained at much lower radiation levels. This suggests re-conditioning without the external magnetic fields seem to be able to cure or condition the damaged surface caused with the strong magnetic field.

Experiments indicated that it is difficult to run an RF cavity in a strong magnetic field without extensive conditioning. We are still exploring the best way to condition a cavity in such an environment. In addition to RF fields in the cavity, the external magnetic field (in the longitudinal direction) forms a strong focusing channel for electrons and ions and forces them to orbit within the channel. As this focusing force from the external magnetic field is much stronger then that of RF field, multipacting zones are no longer bound in the region of the two parallel windows at low RF powers only. Multipacting conditions may be satisfied at higher powers and larger radius. Numerical simulations of experimental conditions are required and will be conducted in the near future to further study and understand these effects.

[‡] Shunt impedance definition used here: $ZT^2 = V^2/P$

A modest 18 MV/m accelerating gradient was reached with the Cu windows at 2.5 T magnetic field in solenoidal mode. The Cu windows were taken out for surface examination after reaching this gradient. Surface damage on the windows was apparent, as shown in Figure 2.
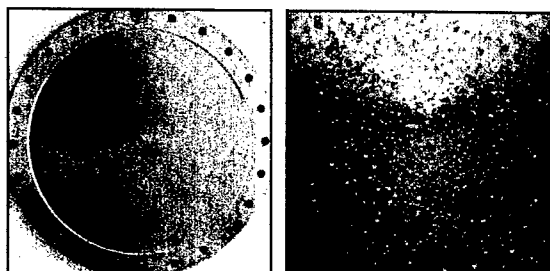
Figure 2: Cu window after RF conditioning with the external 2.5 T magnetic field in solenoidal mode. Surface damage (pitting) can be seen clearly on the photo (right), which is a close-up view of the center region of the same window.

Test of Be Windows with TiN Coated Surface Without External Magnetic Field

Two Be windows with TiN coated surface were installed face-to-face in the cavity. They are pre-stressed flat windows of 0.25 and 0.5 mm thickness, respectively. The coating thickness is ~ 200 A which is intended to suppressing multipacting. As was experienced in previous tests of the Cu windows, conditioning with an external magnetic field results in window surface damage. A modest gradient of 16 MV/m was set for conditioning without magnetic field. The purpose of this test was to make sure that we can condition the cavity with the thin Be windows, and yet not damage the window surface before switching the magnet on. Less multipacting was indeed observed as expected from the TiN-coated surface. The target of 16 MV/m was achieved quickly without difficulty.

Small cavity frequency shifts were measured during the conditioning. This suggested that the pre-stressed thin Be windows may have deformed slightly (lost their tension) or vibrated due to either RF heating or the RF impulse. The frequency shifts were small and slow, and they were well within the bandwidth of the klystron. Conditioning was continued with manual adjustment of the drive frequency.

Test of Be Windows with TiN-coated Surface With External Magnetic Field

The high power tests were resumed with the TiN-coated Be windows with the solenoid magnet on. After weeks of conditioning, only 16.5 MV/m gradient was achieved with the magnetic field up to 4 T. Higher than this gradient would result in more sparking. Fearing possible damage to the Be windows (Be is a health hazardous material), we stopped the test at this gradient and inspected the window surface. Fig. 3 shows a Cu and a Be window side by side after the conditioning, for comparison purpose.
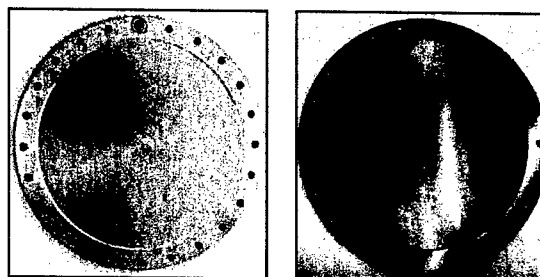
Figure 3: Cu window (left) and Be window (right) after RF conditioning with magnetic field. Deposited Cu particles on the Be window can clearly be seen.

Preliminary surface analysis indicated no surface damage to the Be window. Copper particles or beads were deposited on the Be window surface. This indicated that they must come from cavity body. Further inspection found that there was minor surface damage around the iris area where the Be windows were bolted on. The distribution pattern of the Cu particles (beads) is not well understood, and will be further studied by numerical simulations and experiments in near future.

Future Test Plan

A new pair of Be windows with TiN-coated surface have been installed and are ready for tests to the highest gradient. Bare Be windows will be tested for multipacting studies. Other window options such as pre-curved windows or grids may be designed and tested at Lab G.

CONCLUSION

We have tested the cavity with Cu and Be windows with and without external magnetic fields. 16.5 MV/m was achieved with TiN-coated Be windows with a 4 T magnet on. We believe the gradient is not limited by the Be windows. Preliminary surface analysis indicated no damage on the Be windows which further suggests that Be windows can withstand high RF gradient in a few-T magnetic field. Coating on high field region of the cavity body, say TiN, may reduce multipacting and improve cavity performance.

REFERENCES

[1] M. M. Alsharo'a, et al., "Status of neutrino Factory and Muon Collider Research and Development and Future Plans", PRST-Accelerators & Beams (2002)

[2] W. Turner, et al., "RF System Concept for a Muon Cooling Experiment", EPAC 1998, Sweden

[3] D. Li, et al, "High Power RF Test of an 805-MHz Cavity for a Muon Cooling Channel", EPAC 2002, Paris, France

[4] J. Norem, et al., "Dark Current and X-ray Measurements of an 805 MHz Pillbox Cavity", this conference.

DEFLECTING RF CAVITY DESIGN FOR A RECIRCULATING LINAC BASED FACILITY FOR ULTRAFAST X-RAY SCIENCE (LUX)*

Derun Li[#] and J. N. Corlett
Lawrence Berkeley National Laboratory, Berkeley, CA 94720, USA

Abstract

We report on superconducting deflecting RF cavity designs for a Recirculating Linac Based Facility for Ultrafast X-ray Science (LUX) at Lawrence Berkeley National Laboratory. The deflecting cavities operate in the lowest dipole mode and are required to produce a temporal correlation within flat electron bunches, as needed for x-ray compression in crystal optics. Deflecting voltage of up to 8.5 MV is required at 3.9 GHz. We present a 7-cell cavity design in this paper. Seven such cavities are required to generate the 8.5 MV deflecting voltage. Longitudinal and transverse impedance from LOM's (lower order mode) and HOM's (higher order mode) are simulated using the MAFIA code. Short-range and long-range wakefields excited through these impedances are calculated. Beam loading effects of the deflecting mode and parasitic modes are estimated. Q values of the LOM monopole modes in the cavity need to be damped to be below 10^4-10^5 levels in order to maintain the required energy spread.

INTRODUCTION

Figure 1 shows a layout of the LUX machine at LBNL. The SC deflecting cavities (highlighted with yellow color) are required at the last turn of the flat electron bunch at energy of ~ 3 GeV. More information on the LUX machine can be found in [1].
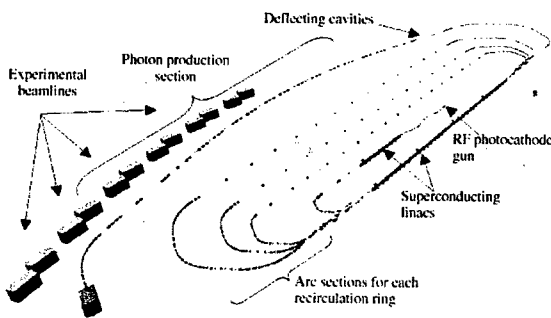
Figure 1: The layout of the proposed LUX machine

RF cavities operating in the lowest dipole mode (TM$_{110}$-like) deflect the head and tail of ~ 3 GeV flat electron bunches to allow for compression of the x-ray pulse in x-ray optics. The center of the electron bunch passes the cavities at *zero* phase of the RF field such that the head

and tail are deflected in opposite directions, and the center of the bunch experiences no deflection. This introduces a correctable divergence into the electrons within a bunch that is much greater than the opening angle of hard x-ray radiation (the radiation opening angle is 7 μrad at 1 Å), and the angular divergence of the electrons (~ 6.4 μrad) in the undulators. The required deflecting voltage is 8 MV at 3.9 GHz for ~ 3GeV beam energy, but we aim at the cavity design for 8.5 MV to allow some head room. Superconducting cavities are a natural choice in obtaining such a high voltage, and the design of a multi-cell structure with large transverse shunt impedance has been developed. A 7-cell π-mode cavity design has been selected. This choice represents a compromise between a large number of cells to increase transverse shunt impedance and reduce the number of cavities required, and smaller number of cells to minimize the number of cavity modes and potential mode coupling. The cavity design is similar to a multi-cell deflecting cavity design for the kaon separation project at Fermilab [2].

THE DEFLECTING CAVITY

The deflecting cavity operates at the lowest dipole mode, or TM$_{110}$-like mode. The field distribution of this mode is
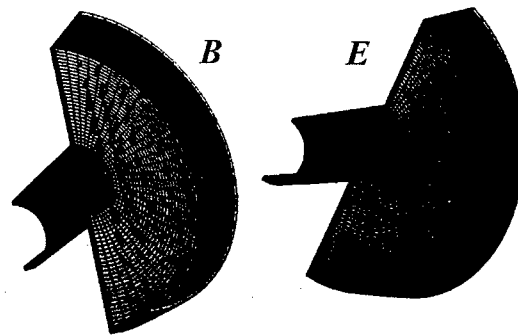
shown in Figure 2 using a single cylindrical pillbox cavity with beam pipe as an example.

Figure 2: Electric (right) and magnetic (left) field distribution of the lowest dipole mode in a cylindrical pillbox cavity. This mode is used for deflecting electron bunches to generate a temporal correlation for x-ray compression.

For cylindrical cavities, dipole modes are degenerate, and two dipole modes have the same field distribution, but with different orientations. In order to obtain the needed polarization, the cavity geometry needs to be perturbed in one plane. Figure 3 shows a concept proposed for KEK-B crab cavity which splits the mode

1249

degeneracy and orients the required mode by using a non-cylindrical geometry [4]. The Fermilab multi-cell deflecting cavity used the similar technique [2].
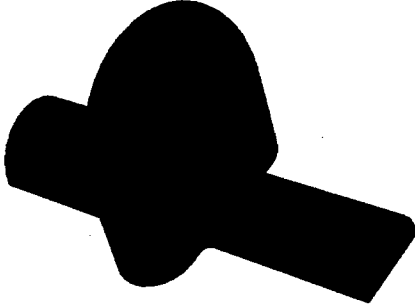
Figure 3: KEK-B Crab cavity with asymmetry to obtain the polarization of the crabbing mode

Electron bunches passing through the deflecting cavity experience transverse forces from both electric and magnetic fields. The cavity shunt impedance definition then has to take this into account.

Shunt Impedance of the Dipole Mode

For the TM dipole mode of an ideal closed cylindrical pillbox cavity, there is no electric field on-axis. Beam passing through such a cavity on-axis would not exchange energy with the cavity and experience a transverse force from the magnetic fields only. However once beam irises are introduced, as it is necessary for a practical cavity, TE-like modes are introduced and mixed with TM modes in the iris (or between cells) and beam-pipe regions. The deflecting mode is no longer a pure TM_{110} mode, but a hybrid of TM_{110} and TE_{111} modes, which is the result of Maxwell equations in order to satisfy the new boundary conditions introduced by the irises and beam-pipes. Even the beam traversing the cavity on-axis, it will not just experience transverse force from the magnetic fields, but also from the transverse electric field. For a cavity with a π phase advance, these two transverse forces add. To calculate the shunt impedance of the deflecting mode, we define the transverse shunt impedance as follows,

$$\left(\frac{R}{Q}\right)_{\perp} = \frac{\left|\int E_Z(r_0)e^{jkz}dz\right|^2}{\omega U(\kappa r_0)^2}$$

where the Panofsky-Wenzel theorem is applied to obtain the deflecting voltage using the off-axis longitudinal electric fields only. $\omega = 2\pi f$ with f as the resonant frequency; U the stored energy of the mode at the resonant frequency; $E(r_0)$ the longitudinal electric field at r_0 over which the longitudinal electric field is integrated along variable z over the cavity length. Note that the unit of this definition for transverse shunt impedance is in Ω, and it implies that the deflecting kick is independent of the beam transverse position within the cavity.

Design of the Multi-Cell Cavity

A 3-D MAFIA model, as shown in Figure 4, was established to simulate the deflecting cavity and the main RF coupler in addition to 2-D simulations reported previously [3]. A 7-cell design is chosen for field flatness, and to avoid mode overlaps and possible trapped modes from large number of cells.
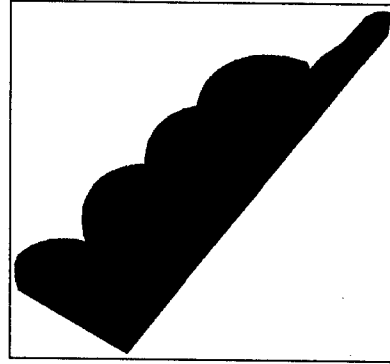
Figure 4: 3-D MAFIA model for the 7-cell deflecting cavity (1/4 of the structure shown here)

One-quarter of the cavity was used for the simulations, combinations of boundary conditions and the geometry symmetry allow us to compute all LOM and HOM modes up to the beam-pipe cut-off frequencies. Table 1 and Table 2 list the dimensions of cavity and performance parameters.

Table 1: Main dimensions of the deflecting cavity

Cavity frequency	3.9	GHz
Phase Advance per cell	180°	Degree
Cavity Equator Curvature	1.027	cm
Cavity Radius	4.795	cm
Cell length	3.846	cm
Iris Radius	1.500	cm
Beam pipe radius	1.500	cm
TM mode cut-off frequency	7.634	GHz
TE mode cut-off frequency	5.865	GHz

Table 2: Main cavity parameters

(R/Q)	350	Ω
Q_0	2×10^9	
Active length/cavity	26.92	cm
Deflecting gradient	5	MV/m
Transverse voltage	1.346	MV
RF power loss at 2 K	2.6	Watts

1250

The 5-MV/m gradient was chosen and determined by limiting critical magnetic fields to be ~ 80 mT, which corresponds to a 25 MV/m accelerating gradient for the TESLA SC cavities.

BEAM LOADING

Beam traversing the deflecting cavity interacts with all of the cavity modes, and the beam may lose energy, and induce a voltage in the cavity. This voltage then acts back on the beam, and may cause energy spread or perturb the deflection along the bunch.

Beam Loading in the Deflecting Mode

The beam induced transverse voltage in the deflecting mode may be written as,

$$V_\perp = \left(\frac{R}{Q}\right)_\perp \frac{Q_0}{1+\beta}(\kappa\Delta r)I \approx 1.1\,\text{kV}$$

where I, κ, Δr and β are beam current, cavity RF wave number, displacement from cavity axis and RF coupling constant, respectively. For the above calculation, we have used $\kappa = 82$, $\Delta r = 0.1$ mm and $\beta \approx 50$ assuming an achievable bandwidth of 100 Hz which corresponds to an external Q of 3.9×10^7. This bandwidth is determined from the requirements for synchronization, microphonics detuning (25 Hz peak). With 2.5 MHz band limited phase noise spectra of mode-locked laser master oscillator at optimum coupling condition, the peak RF power required is less than 200 Watts per 7-cell cavity. Beam current of 10 μA (1 nC charge at 10 kHz repetition rate) was assumed for the above calculation.

Power induced in the deflecting mode is then given by,

$$P_{\text{induced}} = \frac{1}{2}f_{\text{rep.}}^2 q^2 \left(\frac{R}{Q}\right)_\perp^* \frac{Q_0}{1+\beta}(\kappa\Delta r) \approx 5.3\,\text{mW}$$

This is considered to be quite small in comparison with power loss of 2.6 Watts in the cavity.

Beam Loading from Monopole Modes

Longitudinal voltages may be induced by beam through interaction with monopole LOM and HOM modes. It was found that two LOM monopole modes at 2.8581 GHz and 2.8685 GHz contribute ~ 85 % of the total impedance. At steady state the beam induced voltage per cavity can be calculated by,

$$V(\infty) = \sum_{n=1}^{n_r} 2k_n q\left(\frac{2Q_{n,0}}{\omega_n T}\right) \approx 17\,\text{MV}$$

Assuming $q = 1$ nC, 10 kHz repetition rate and $Q_0 = 2\times10^9$ for all the modes

In order to maintain beam energy spread of 10^{-4} at ~ 3 GeV, these modes need to be damped. Their Q values have to be below 10^4-10^5 levels. It is worthy of noting that main RF coupler may provide certain damping to all the HOM and LOM modes, but has not been evaluated yet. Nevertheless a coaxial insert in the beam pipe (proposed for KEK-B crab cavity) may be couple to these monopole modes only and provide required damping [4], but this may add complexity to the cavity.

HOM Dipole Modes

Loss factors of HOM dipole modes were calculated by,

$$k_\perp = \frac{\omega}{4}\left(\frac{R}{Q}\right)_\perp \kappa.$$

Again assuming 2×10^9 of Q for all HOM modes, the total loss factor is only 14 V/(pC-m), compared to 176 V/pC-m) for the deflecting mode. The overall HOM impedance is considered not to be excessive.

CONCLUSION

A 7-cell SC deflecting cavity design has been presented. To provide 8.5 MV deflecting voltage, seven 7-cell cavities are required. LOM monopole modes need to be damped to minimize beam energy spread. Impedance from the HOM dipole modes is not excessive. The main RF coupler may provide extra damping to LOM and HOM modes and will need to be evaluated in the future. RF power requirement is estimated to be less than 200 Watts per 7-cell cavity at optimum coupling (β ≈ 50), a solid state RF power amplifier may be used at this power level. Synchronization requirements may demand increased cavity bandwith, and will be investigated further with the development of the project.

REFERENCES

[1] J. Corlett, et al., "A Recirculating Linac-Based Facility for Ultrafast X-Ray Science, this conference.

[2] L. Bellantoni, et al., "Design and Measurements of a Deflecting Mode Cavity for an RF Separator", PAC 2001, Chicago, IL, USA

[3] D. Li and J. Corlett, "RF Deflecting Cavity Design for Berkeley Ultrafast X-Ray Source", EAPC 2002, Paris, France

[4] K. Akai, "Development of Crab Cavity for CESR-B", Proceedings of PAC 1993, USA

RF POWER DETECTOR/MONITOR UPGRADE FOR THE 500MHZ SYSTEMS AT THE ALS*

K. Baptiste,
LBNL, Berkeley, CA, 94720 USA

Abstract

Several systems rely on the accurate and linear detection of 500 MHz signals, (the fundamental frequency of both the Booster Ring and Storage Ring) over a dynamic range in excess of 25dB. Prior to this upgrade, the detector/monitor was diode based and though this type of detector could handle the dynamic range requirement it could not do so in an accurate and linear manner. In order to meet the requirements, (dynamic range greater than or equal to 25dB, accurate and linear to ±0.25dB over the range, and additional circuitry to interface to the legacy control system and interlocks) a new RF Power Detector/Monitor has been developed using two AD8361, Analog Devices TruRMS Detectors and a fuzzy comparator, which extends the overall detector's range to twice that of the AD8361. Further information is available [www.analogedevices.com/]. Details of the design requirements and the detector/monitor's circuit as well as the performance of the detector will be presented.

INTRODUCTION

In the Advanced Light Source (ALS) Booster Ring and Storage Ring RF Systems there are a total of 16-500 MHz signals of which the signal power level must be measured accurately. The signal levels in these systems can range from tens of watts to 330 kW and via couplers, dividers, attenuators, and cable loss these signals have been attenuated down to a range of –20 to +10 dBm. Once detected, some of the signals are used in a variety of sub-systems, which include control loops, personnel and equipment interlock control chains and they are sent to the computer control system. The old detectors utilized the square-law functionality of a diode detector and though they had a large enough dynamic range they were not accurate or completely linear from device to device. The primary objectives in this redesign are to improve the linearity and accuracy over a minimum dynamic range of 25dB, to interface to the legacy analog loops and control systems, to improve the local meter display capabilities, and to achieve interchangeability amongst the detectors with out the need for recalibration.

DESIGN

The new design, which came from the AD8361 Data Sheet [1], employs a dual channel detector system to extend the dynamic detection range for a given accuracy. The system is built using two AD8361 (Analog Devices TruRMS Detectors). See block diagram in Figure 1.
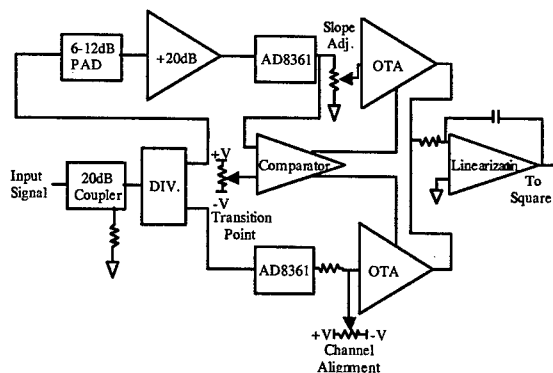
Figure 1: Detector Front End Block Diagram

Dual Channel Detector System

The incoming signal is split into two channels, one for weak signals and the other for strong signals. The weak signal channel has a net gain, which boosts the weak signals up into the usable and accurate range of the AD8361. The circuit utilizes fixed value attenuators to adjust the net gain in the weak signal channel in order to optimize the channel for variations in the amplifiers gain and the detectors sensitivity. This method of optimization proved to be time consuming during the configure and test phase since several of the detector chips had wide variations in gain/sensitivity and accuracy. The strong signal channel has no additional gain.

Cross-Fader & Fuzzy Comparator

The outputs of the two detectors are connected to the input of a cross-fader via a slope-equalization and offset adjustment circuit. Since the detection range of the two detectors overlap, the cross-fader must transition smoothly between the weak and strong signal channels over an approximate 3dB range. This transition is controlled by a fuzzy comparator, which controls the relative gains of the two detected signals thereby providing a weighted dynamic combination of the two detectors as a function of RF input level. As stated in the AD8361 Data Sheet Application section, the cross-fader is comprised of two Operational Transconductance Amplifiers, (OTA), and the comparator is comprised two transistors. The amplifier final stage applies feedback in order to linearize the transfer function of the transconductance amplifiers. A transition point adjustment is provided at one input of the comparator.

User & Legacy Systems Interface

` Additional requirements for the new detector/monitor are to fit into existing Eurocard chassis, provide front panel controls and indicators, and to interface with the existing control system.

The front panel of the module was redesigned to hold an auto ranging digital display, set point set and monitor controls, test/operate controls, and RF and detected signal monitors. The front panel interface is used for local system set-up and monitoring as well as by maintenance personnel for periodic interlock system tests. The legacy control system interface consists of an analog voltage linear in watts, relay contacts for power level interlocks (latching or non latching), open collector interlock for fast response, remote interlock reset, and various analog outputs for feedback loops.

PERFORMANCE

The main reasons to upgrade the power detectors was to increase their linearity and accuracy. The previous detectors were diode based, their linearity was poor therefore, and their accuracy was poor as well. Out of the 12 detectors in service in the ALS Storage Ring RF System only one unit exhibited ±0.5dB linearity over a 20dB range though its absolute accuracy was off by +2.5dB. See Figure 2, which shows the legacy detectors error on a logarithmic scale.
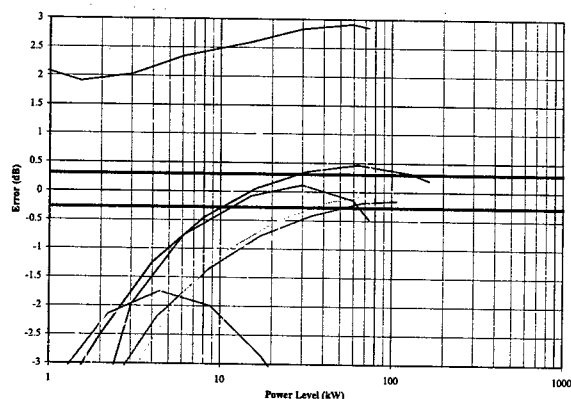
Figure 2: Legacy Detector, Error from Linear Reference vs. Input Level

The redesigned detector, which utilizes the AD8631, is vastly superior in linearity as compared to the diode version. The AD8631 data sheet claims the device has up to 30dB dynamic range however it also states that for ±0.25dB error the range is reduced to 14dB. This limitation is the reason for using a dual channel detection method in order to extend the range while maintaining accuracy. The data sheet also shows a graph of the error from a linear reference versus input power for a large sample of devices at 900MHz. The black upper and lower error bars on Figure 3, which were extrapolated down to 500MHz from the 900MHz data, determine the expected accuracy range. The red bars determine our targeted accuracy range. Of the 26 units measured, (for both

500MHz and 1.5GHz operation) 16 units were within and 10 fell outside of the ±0.25dB accuracy requirement over a dynamic range >25dB. The measurement uncertainty was estimated to be 0.1dB due to temp drift and connections. However, one can see in Figure 3 and 4 that the low-end accuracy is much worse than the high-end accuracy. According to the data sheet for the AD8631, the low-end problems are due to signal offsets in the internal squaring circuits.
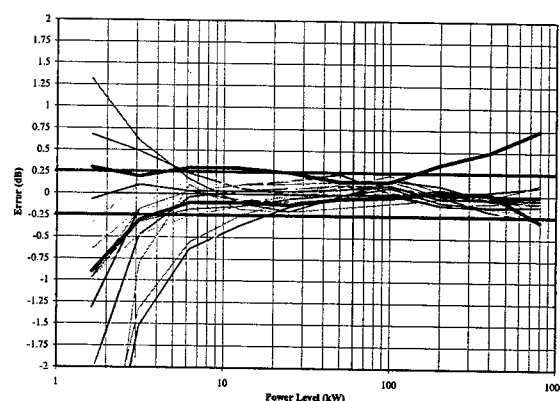
Figure 3: Redesigned Detector (500MHz), Error from Linear Reference vs. Input Level

In order to set-up the two channels slope, offset, and transition point I developed a LabView application, which controlled an ESG Series Signal Source that produced a 100 step linear power ramp and read data from a TDS 744A oscilloscope. See Figure 5 for a partial screen shot of the application. This application allows me to select only the ramp portion of the measured data array, which is then compared to a linear reference to generate the error plot. Due to the low resolution of the digital scope and the inaccuracy of the linear input power ramp from the signal source, the application was used only to initially tune the channels visually by observing the computed error for each power ramp. After the detector was initially set, I measured the accuracy at ten different power levels while making fine adjustments to slope and offset of the two channels.
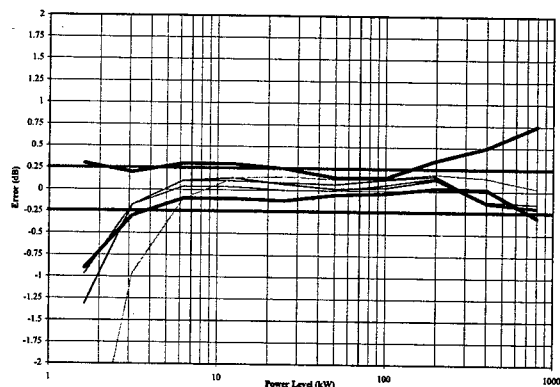
Figure 4: Redesigned Detector (1.5GHz), Error from Linear Reference vs. Input Level
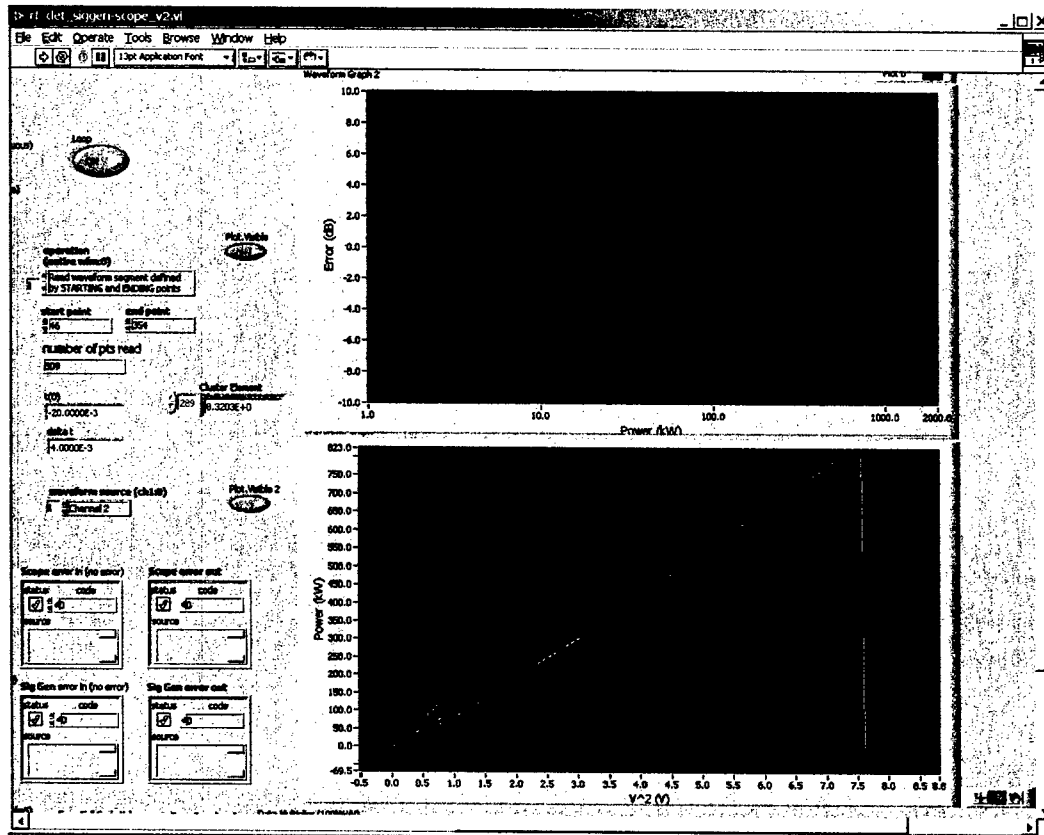
Figure 5: Partial Screen-Shot of LabView Application used to Initially Tune Each Channel.

Operation at 1.5GHz

It was decided to utilize the redesigned detectors at 1.5GHz on ALS's 3rd Harmonic Cavities. The detector was modified by changing the matching networks at the input to the AD8631's and by replacing the directional coupler and power divider with higher frequency devices. Results can be found in Figure 4.

FURTHER IMPROVEMENTS

- As mentioned earlier, it was very time consuming to set the correct net gain value in the weak signal channel by changing fixed attenuators. An improvement would be to use an electronically controlled variable attenuator.
- In order to minimize differences between detector chips one could digitize the outputs of the two AD8631s and once characterized, optimization and cross fading could be applied via programmable logic and software. This would produce more consistency between detectors.
- Installing a digitized temperature sensor would allow for software correction of gain and offset drift as a function of temperature.

- Installing an on board reference, which can be switched in via logic would allow for on board calibration.
- Installing a programmable gain amplifier used to set the analog output's scaling.

CONCLUSION

The redesigned detectors, 12 500MHz and 3 1.5GHz models of which have been installed in the Storage Ring RF and Third Harmonic Cavity Systems have been in service since December 2002 and April 2003 respectively. Four 500MHz detectors are scheduled for installation during an upcoming installation and maintenance period. The performance of the installed units has been as expected based on the bench tests discussed in this paper. The detectors exhibit +0.25dB accuracy, due to their good linearity, and their dynamic range meets our operational requirements. The operational staff now has at their disposal linear and accurate RF power data that they can rely on.

REFERENCES

[1] http://www.analog.com/UploadedFiles/Datasheets/541 602412AD8361_b.pdf.

THEORETICAL ANALYSIS OF OVERMODED DIELECTRIC PHOTONIC BAND GAP STRUCTURES FOR ACCELERATOR APPLICATIONS

M.A. Shapiro, E.I. Smirnova, C. Chen, and R.J. Temkin

MIT Plasma Science and Fusion Center,
Cambridge, MA 02139, USA

Abstract

An overmoded accelerator structure is proposed based on a dielectric photonic-band-gap (PBG) disk-loaded structure. The structure consists of dielectric rods and metal disks with irises. It is advantageous for application in high frequency (17 GHz and higher) linacs because of the large dimensions of the structure. The operating mode is a higher-order TM_{02} mode. One unique feature is that the fundamental TM_{01} mode is not supported by the structure. Along with that, the dipole mode TM_{11} is strongly suppressed. The dielectric PBG structure can also be attractive for application in a dielectric wakefield accelerator.

INTRODUCTION

In recent years major progress in novel accelerating structures using dielectrics has been reported. These experiments include the two-beam dielectric accelerator [1] and the millimeter-wave accelerator on a dielectric substrate [2]. It has been demonstrated that breakdown and charging can be avoided in the dielectric accelerating structures. We have been focused on the electromagnetic properties of dielectric structures for accelerator applications. Using low loss dielectrics, high Q-factor microwave cavities can be built, and, therefore, high shunt impedances can be achieved. The dielectric structures can be designed to be mode selective, providing a high Q-factor of the operating mode along with low Q-factor, high losses for all unwanted modes. These electromagnetic properties of the dielectric structures make them very attractive for accelerator applications because wakefields can be suppressed through the selective excitation of the operating mode.

One possible way to build a mode selective cavity is to utilize a photonic band gap (PBG) structure in the cavity. An example of a PBG structure is a 2D lattice of dielectric or metal rods with a defect (missing one or several rods) in the center [3,4]. The metallic PBG cavity was proposed as an accelerator cell [5]. We have previously reported on the cold test of metallic PBG cavities at X- and Ka-bands [6-8]. Dielectric PBG cavities have been cold tested at a variety of bands including X-band [9]. The dielectric PBG fibers have been proposed for laser accelerators [10].

We propose the dielectric PBG cavity for application as a cell of an accelerating structure. The PBG cell includes the dielectric PBG structure placed between two metal disks. A stack of the PBG cells coupled through the beam holes forms an accelerating structure. We have designed a dielectric PBG cavity operating at 17 GHz (Ka-band) and

at a higher-order mode TM_{02}. The unique feature of this dielectric structure is that the fundamental TM_{01} mode is not confined. This effect could not be observed in a metal PBG cavity where the fundamental mode TM_{01} always exists. The higher-order accelerating mode TM_{02} allows us to enlarge the transverse dimensions of the accelerator, which is advantageous at high frequency operation. Also, the dipole modes are suppressed.

FREQUENCY SELECTIVE CAVITIES UTILIZING DIELECTRIC PBG STRUCTURES
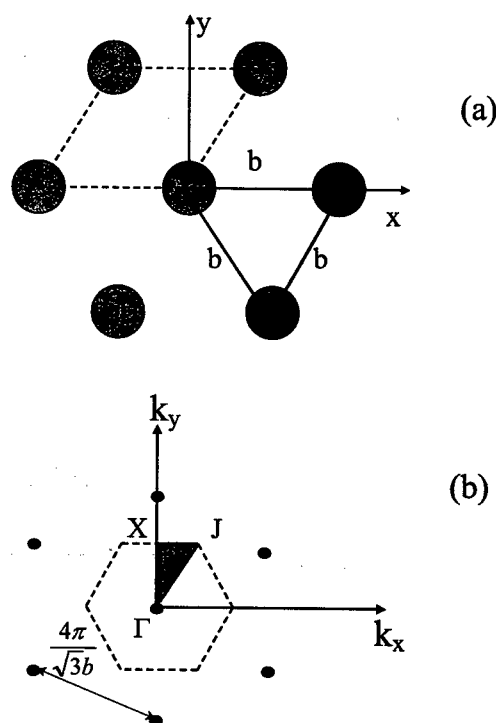
Figure 1: 2D triangular crystal lattice (a) and reciprocal lattice (b).

Band Gaps in a 2D Lattice of Dielectric Rods

Figure 1 (a) depicts a 2D triangular lattice of dielectric rods, and Figure 1 (b) depicts the reciprocal lattice in the wave-vector **k** plane. The hexagon in the k-plane is the first Brillouin zone of the lattice. The shaded triangle in Fig. 1(b) covers the meaningful values of k-vector at which waves propagating in the lattice should be calculated. The result of this calculation is presented in the Brillouin diagram (Fig. 2). The Brillouin diagram indicates the frequencies of the waves propagating in the lattice while the k-vector on the reciprocal lattice (Fig. 1(b)) varies from Γ-point to X-point, from X-point to J-point, and back to Γ-point. The Brillouin diagram plots the normalized frequency $\omega b/c$, where b is the spacing between the rods, and c is the speed of light. The diagram is calculated for the ratio of 0.39 of the rod radius a to the spacing b. The rods are made of alumina Al_2O_3, the dielectric constant $\varepsilon=9.7$.

The important characteristic of the lattice is the band gap. The band gap is marked in Fig. 2 indicating that there is no propagating wave in a certain frequency band. The existence and frequency bandwidth of the gap depends upon the dielectric constant and the ratio a/b. The band gaps in the triangular dielectric lattices are calculated in [11], and the results are plotted in Fig. 3. Two band gaps are contoured in Fig. 3; there is no propagating wave in the lattice if the frequency is inside the contours plotted.

PBG Cavity Design

A triangular lattice of rods with a defect forms a PBG cavity. We remove the central rod and three rows of rods around it (37 rods total) to form the defect. The spacing b is determined such that the operating frequency of 17 GHz falls into the band gap (Fig. 3). The ratio of a/b should be close to 0.4 because the band gap narrows down at this ratio. The cavity mode is a mode confined in the defect (defect mode). If the band gap is narrow, the number of defect modes can be reduced.

The HFSS code [12] has been employed to calculate the PBG cavity modes. Through optimization of the parameters a and b, a well-confined TM_{02}-like mode at the frequency of 17 GHz was found (Fig. 4). Using the calculated field distribution, the acceleration parameters of the PBG cavity are calculated and listed in Table 1. The Q-factor and shunt impedance are calculated for the dielectric loss tangent of $2 \cdot 10^{-4}$, which is the average measured loss tangent of alumina [13]. The cavity axial length of one third of the wavelength is selected.

Note that for the 17 GHz pillbox copper cavity with the fundamental mode TM_{010}, the Q-factor is 6000, and the parameter r_s/Q is 540 Ω/cm. For the TM_{020} mode of the pillbox copper cavity, $Q=8500$ and $r_s/Q=240$ Ω/cm. Therefore, the designed dielectric PBG cavity operating at the TM_{020}-like mode has the Q-factor close to that of the TM_{010}-mode pillbox cavity and the r_s/Q close to that of

the TM_{020}-mode. The Q-factor of the dielectric cavity combines the dielectric side-wall Q-factor calculated using HFSS and the end plates Q-factor calculated analytically assuming it is the TM_{020} mode; both Q-factors are about 12000.
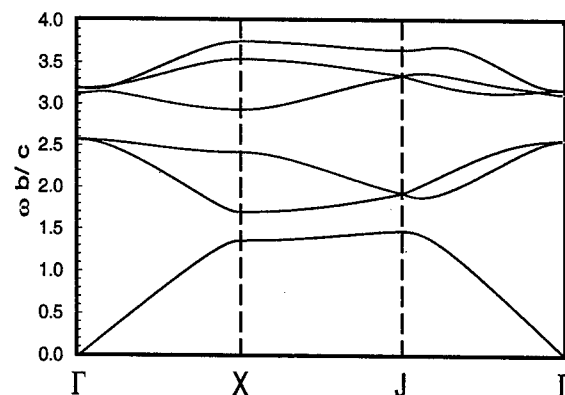
Figure 2: Brillouin diagram for the dielectric triangular lattice of rods. The normalized frequency vs. k-vector is plotted. The k-vector varies around the contour in the reciprocal lattice (Fig. 1(b)). The band gap is marked. The lattice parameters: $\varepsilon=9.7$ (alumina), $a/b=0.39$.

Table 1: Acceleration parameters of a dielectric PBG cavity with the TM_{02} mode

Permittivity, ε	9.7 (Al_2O_3)
Loss tangent, $\tan \delta$	$2 \cdot 10^{-4}$
Lattice spacing b	0.44 cm
Rod radius a	0.17 cm
Ratio a/b	0.39
Minimal radius of defect	1.35 cm
Outer radius	3.5 cm
Number of rods	132
Number of missing rods in defect	37
Axial length	0.58 cm
Mode	TM_{02}
Frequency	17.14 GHz
Ohmic Q-factor	5900
Shunt impedance r_s	1.2 MΩ/cm
Parameter r_s/Q	212 Ω/cm

It is shown that the fundamental TM_{01} as well as dipole TM_{11} modes are not confined in the PBG cavity. This is consistent with the band gap map (Fig. 3): the frequencies

of these modes are not in the band gap. A transverse wakefield mostly formed by the dipole mode is thus suppressed. As shown in Fig. 3, the modes TM_{21}, TM_{31}, and TM_{12} fall into the gap. Only a quadruple TM_{21} mode is well confined in the defect, however this mode is less dangerous than dipole modes.
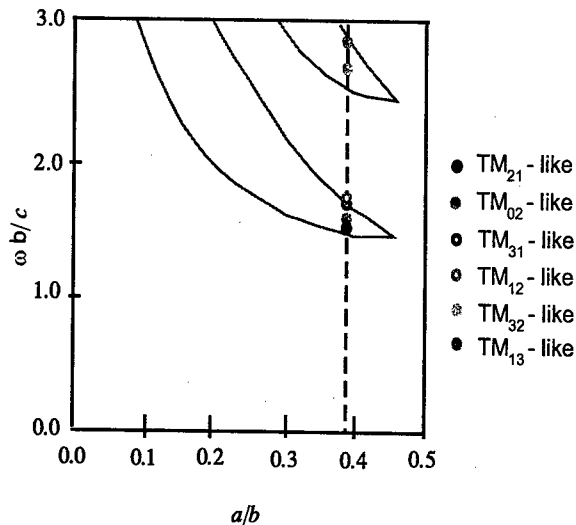
Figure 3: Areas of global band gaps are contoured on the plane of parameters: the normalized frequency and the ratio of the rod radius a to the spacing b. The simulations carried out for a triangular lattice, $\varepsilon = 9.7$. For the design parameter $a/b = 0.39$, the frequencies of the defect modes in the PBG cavity are shown.

Figure 4: Field pattern of the TM_{02}-like mode in a dielectric PBG cavity formed by a 2D triangular lattice of dielectric rods with a defect.

CONSCLUSION

Dielectric PBG structures may allow extension of RF accelerator operation to higher frequencies using higher order modes, without facing the problem of wakefields. Use of dielectric PBG structures may allow construction of a PBG cavity, which selectively confines the TM_{02}-like mode. The design of the accelerator cell has been presented at the operating frequency of 17 GHz.

ACKNOWLEDGMENTS

REFERENCES

[1] W. Gai, M. E. Conde, R. Konecny, J. G. Power, P. Schoessow, J. Simpson, X. Sun, and P. Zou, "Experimental Demonstration of Two-Beam Acceleration Using Dielectric Step-Up Transformer," PAC'2001, Chicago, p. 1880.

[2] M. E. Hill, C. Adolphsen, W. Baungartner, R. S. Callin, X. E. Lin, M. Seidel, T. Slaton, and D. H. Whittum, Phys. Rev. Lett., 87 (2001) 094801.

[3] E. Yablonovitch, Phys. Rev. Lett. 58 (1987) 2059.

[4] J. D. Joannopoulos, R. D. Meade, and J. N. Winn, "Photonic Crystals: Molding the Flow of Light," Princeton: Princeton Univ. Press, 1995.

[5] D. R. Smith, N. Kroll, and S. Schultz, "Study of a Metal Photonic Bandgap Cavity," Advanced Accelerator Concepts, Fontana, WI, 1994, AIP Conf. Proc. No. 335, p. 761.

[6] E. I. Smirnova, M. A. Shapiro, C. Chen, and R. J. Temkin, "Photonic Band Gap Structures for Accelerator Applications," Advanced Accelerator Concepts, Mandalay Beach, CA, 2002, AIP Conf. Proc. No. 647, p. 383.

[7] E. I. Smirnova, C. Chen, M. A. Shapiro, J. R. Sirigiri, and R. J. Temkin, J. Appl. Phys. 91 (2002) 960.

[8] M. A Shapiro, W. J. Brown, I. Mastovsky, J. R. Sirigiri, and R. J. Temkin, Phys. Rev. Special Topics: Accelerators and Beams, 4 (2001) 042001.

[9] D. R. Smith, R. Dalichaouch, N. Kroll, S. Schultz, S. L. McCall, and P. M. Platzman, J. Opt. Soc. Am. B, 10 (1993) 314.

[10] X. E. Lin, Phys. Rev. Special Topics: Accelerators and Beams 4 (2001) 051301.

[11] S. J. Johnson and J. D. Joannopoulos, Optics Express 8 (2001) 173.

[12] Ansoft High Frequency Structure Simulator – User's Manual, Ansoft Corp, 1999.

[13] R. A. Woode, E. N. Ivanov, M. E. Tobar, and D. G. Blair, Electron. Lett. 30 (1994) 2120.

AN 11 GHZ PHOTONIC BAND GAP ACCELERATOR STRUCTURE WITH WAKEFIELD SUPPRESSION

E.I. Smirnova[*], C. Chen, M.A. Shapiro, R.J. Temkin,
Plasma Science and Fusion Center, MIT, Cambridge, MA 02139, USA

Abstract

We report the design and cold test results for an 11 GHz photonic band gap (PBG) cell, which can be utilized as an accelerator cavity with reduced long-range wakefields. The eigenmodes of the two-dimensional (2D) PBG cavities formed by the defect in a triangular array of metal rods were studied numerically. A 2D PBG cavity with reduced HOM content was designed and built. Cold test results proved the suppression of the higher order modes (HOM) in the PBG cavity. A 6-cell 17.137 GHz PBG accelerator structure is proposed and designed.

1 INTRODUCTION

Metallic photonic band gap (PBG) structures have received considerable attention recently, because of their possible applications in rf accelerators and high-power microwave electronics [1-3]. A remarkable property of the PBG structure is its ability to reflect waves in certain ranges of frequencies (called *global band gaps*) while allowing other frequencies to pass through. A defect in periodic structure forms "PBG cavity" in which a mode with the frequency inside the global band gap can be confined under certain conditions. The PBG cavity is advantageous over the conventional pillbox cavity because of its high mode selectivity: only the modes with frequencies within the band gap can be confined.

We investigate the PBG structures based on triangular lattice of metal rods. A cavity is formed with a missing rod and can confine eigenmodes (see Fig. 1). Two important aspects need to be studied in order to facilitate the design of PBG-based cavities. One involves the global band gaps calculation, and the other concerns mode
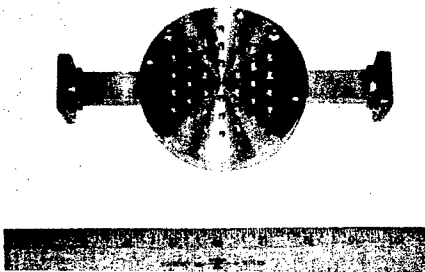
Fig. 1: A PBG resonator built for the cold test. The cavity is formed by a missing rod in a triangular array of copper rods with $a/b = 0.15$.

*E-mail: smirnova@psfc.mit.edu.
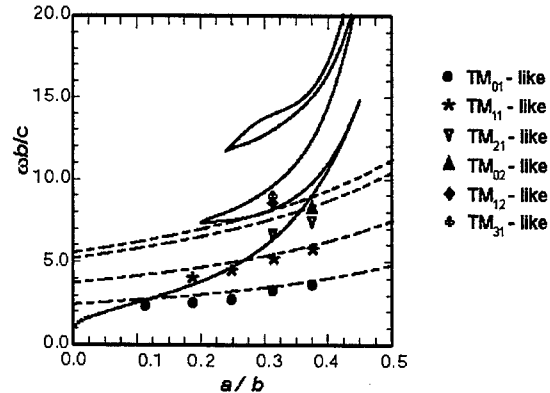
Fig. 2: TM eigenfrequencies of a PBG cavity formed by single rod missing in triangular array of metal rods (solid lines show the boundaries of global band gaps).

confinement in PBG cavity. Global band gaps for two-dimensional (2D) triangular lattice of metal rods have been recently calculated by these authors and reported in [3]. For analysis of PBG resonators, we apply the HFSS code [4].

The PBG cavity supporting a single TM_{01}-like mode is a good candidate for an accelerator cell. A disk-loaded $2\pi/3$ accelerator structure can be built with a stack of PBG cavities set between the disks with the beam holes inserted on axis. A complete design of a 6-cell PBG accelerator structure was performed using the HFSS code [4]. We plan to construct and test a 6-cell PBG accelerator structure.

2 MODES OF A PBG RESONATOR

We studied a 2D PBG resonator formed by a single rod missing in a triangular lattice of metal rods. We kept only three rows of rods and surrounded them by a metal wall. The results of our HFSS computation for the frequencies of eigenmodes are presented in Fig. 2. In Fig. 2 the global band gap boundaries derived in [3] are plotted with solid lines as functions of the ratio of rods radii (a) to the rods spacing (b). The region of frequencies to the right of solid curve corresponds to the global band gap, whereas the frequencies to the left of the curve lie in the pass band. The frequencies of the defect modes are plotted over the band gap picture with dots. Dashed lines in Fig. 2 show the eigenfrequencies of the pillbox cavity with the radius $R=b-a$, which is about the effective radius of the PBG cavity.

It can be seen from Fig. 2 that for $a/b = 0.15$ only a single TM_{01} mode is confined below the cutoff. The field

patterns of two lowest modes in a PBG resonator with a/b = 0.15 are shown in Fig. 3. The TM_{11} mode is confined by the metal wall placed at the periphery of the PBG structure and can be suppressed if we eliminate the wall or put an absorber at the periphery. Thus we can construct a resonator with reduced HOM content on the basis of a PBG structure.

TM$_{01}$ **TM$_{11}$, not confined**
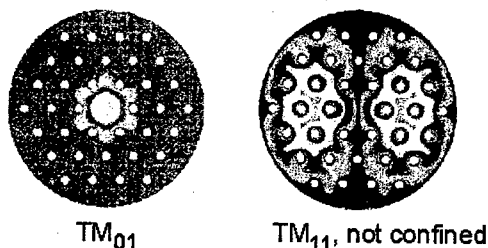
Fig. 3: Modes of a PBG resonator with $a/b=0.15$. TM_{01} mode is confined, TM_{11} mode is not confined.

Table 1. Dimensions of the PBG resonator for cold test.

Rod radius a	0.16 cm
Lattice spacing b	1.06 cm
a/b	0.15
Freq. (TM_{01})	11.00 GHz
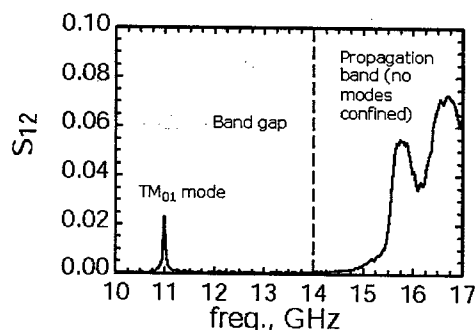
Fig. 4: The transmission curve for a PBG resonator.

3 COLD TEST OF PBG RESONATORS

In order to verify experimentally the suppression of higher order modes in PBG resonators, we constructed a resonator for cold testing. The resonator was made out of brass (see Fig. 1). The dimensions of the resonator are shown in Table 1.

A WR62 waveguide was employed to feed the rf power to the resonator. We measured the S_{12} element of the scattering matrix using the HP8510 vector network analyzer (Fig. 4). We placed the eccosorb at the periphery of the cavity, so that the Q-factors of the modes not confined by the PBG structure were reduced by the factor of 10. The Q-factor of the TM_{01} mode at 11 GHz was not reduced. These results agree with the design. We also measured the S_{11} elements of the scattering matrices and derived from those that the ohmic Q-factor for the TM_{01} mode was about 2000. This was much lower than a
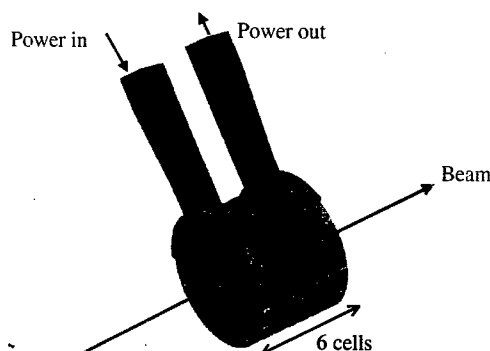
Fig. 5: A 6-cell 2π/3 PBG accelerator structure

theoretically predicted Q of 5300. To resolve this problem we manufactured a second PBG resonator with the same dimensions out of the OFHC copper. Then we brazed the rods into the end plates. This increased the Q-factor up to 4000, which is much closer to the theoretically predicted Q.

4 A 6-CELL PBG ACCELERATOR DESIGN

We have designed and are now building a disk-loaded 2π/3 accelerator structure at 17.137 GHz with a stack of PBG cavities set between the disks with the beam holes inserted on axis (see Fig. 5). A complete design of a 6-cell PBG accelerator structure was performed using the HFSS [4].

Table 2. Dimensions of the 2π/3 PBG accelerator structure.

Rod radius (structure cell) a	1.04 mm
Rod radius (coupler cell) a_1	1.05 mm
Lattice spacing b	6.97 mm
a/b	0.155
Cavity radius	24.38 mm
Cavity length	5.83 mm
Iris radius	1.94 mm
Iris thickness	0.96 mm
Freq. (TM_{01})	17.137 GHz

First, the PBG cell dimensions were calculated and the cells were tuned to 17.137 GHz. Second, the coupler cell was tuned following [5,6]. The dimensions of the structure are listed in Table 2. The coupler cell will have three rods withdrawn and the rods in the coupler cell are 0.01 mm thinner than in traveling wave cells. The dependence of the reflection from the PBG coupler on the coupler's dimensions is shown in Fig. 6. It can be seen from the picture that the reflection is as big as 0.6 to 0.8 if either a rod radius or distance between the rods differs by 0.025 mm from those given in Table 2. This means, that tuning will be needed in order to achieve small reflection from the coupler. Two methods of tuning are considered: putting clips on the rods of the second row and bending the rods.

1259
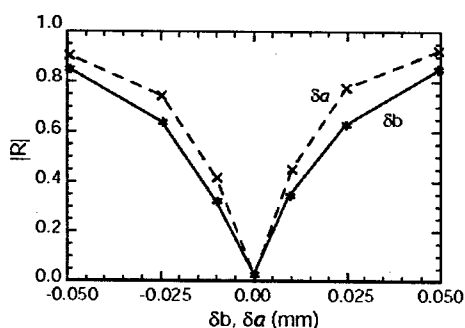
Fig. 6: The reflection from the PBG coupler as a function of deviation of the rods radii (a) and spacing (b) from those given in Table 2.

The accelerator characteristics of the PBG structure were calculated and compared to those of a pillbox structure (see Table 3.). It was discovered that the shunt impedance for a PBG cell is lower than for a pillbox cell. However, the group velocity for a PBG structure is 10% lower than the group velocity for a pillbox structure with the same irises (see Fig. 7). Thus the PBG structure has an average gradient close to that of a pillbox structure.

Table 3. Comparison of acceleration parameters of $2\pi/3$ PBG and pillbox structures.

	Pillbox	PBG
Frequency	17.137 GHz	
Q_w	4188	5618
r_s	0.46 MΩ/cm	0.71 MΩ/cm
$[r_s/Q]$	0.11 kΩ/cm	0.126 kΩ/cm
Group velocity	0.011c	0.012c
Gradient	18.9$\sqrt{P[MW]}$ MV/m	19.4$\sqrt{P[MW]}$ MV/m

5 THE PLAN OF PBG ACCELERATOR TEST

An experiment to test the PBG accelerator is planned at Massachusetts Institute of Technology (MIT). The MIT Plasma Science and Fusion Center currently has a 17.137 GHz accelerator, which was built by the Haimson
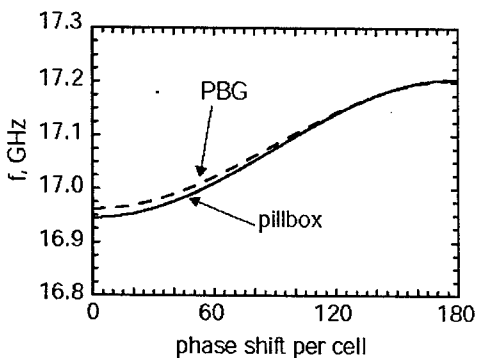
Fig. 7: A comparison of dispersion characteristics for PBG and pillbox accelerator cells with similar irises.

Research Corporation (HRC). We plan to fabricate a 6-cell PBG accelerator section to accelerate a 7 MeV accelerator beam to 8 MeV. The PBG accelerator will be powered with 3 MW coming from the HRC klystron [7]. This will allow us to achieve the acceleration gradient of 32 MV/m.

Finally, the wakefields in PBG structure will be measured in cold-test.

6 CONCLUSION

An extensive research on PBG structures for accelerator applications is underway at MIT. The main advantage of PBG cavities over the conventional pillbox cavities lies in their high mode selectivity. Thus, if applied to the linear accelerators the PBG cavities will sufficiently reduce the long-range wakefields.

We have already studied the bulk properties of the PBG structures [3] and investigated the properties of PBG resonators. We will continue our research towards the constructing and testing a 6-cell $2\pi/3$ PBG accelerating structure.

Additionally, we conduct the investigation of dielectric PBG structures [8]. Use of dielectric PBG structures may allow construction of a PBG resonator, which selectively confines the TM_{02}-like mode. This may allow extension of accelerator operation to higher frequencies using HOM without facing the problem of lower order wakefields.

ACKNOWLEDGEMENT

REFERENCES

[1] D.R. Smith, N. Kroll, and S. Schultz, in *Advanced Accelerator Concepts,* AIP Conference Proceedings 398, p. 761, AIP, New York, 1995.
[2] M.A. Shapiro, W.J. Brown, I. Mastovsky, J.R. Sirigiri, and R.J. Temkin, Phys. Rev. Special Topics: Accelerators and Beams 4, p. 042001, 2001.
[3] E.I. Smirnova, C. Chen, M.A. Shapiro, J. R. Sirigiri, R.J. Temkin, J. Appl. Phys. 91(3), p. 960, 2002.
[4] Ansoft High Frequency Structure Simulator – User's Manual, Ansoft Corp, 1999.
[5] N.M. Kroll, C.-K. Ng, and D.C. Vier, SLAC-PUB-8614, 2000.
[6] V.A. Dolgashev, HFSS User's Workshop, Los Angeles CA, 2001.
[7] J. Haimson, B. Mecklenburg, and B.G. Danly, in *Pulsed RF Sources for Linear Colliders,* AIP Press, 1995.
[8] M.A. Shapiro, E.I. Smirnova, C. Chen, R.J. Temkin, TPAB028, *These Proceedings.*

TRANSVERSE IMPEDANCE BENCH MEASUREMENTS IN NLC/JLC ACCELERATING STRUCTURES*

N. Baboi[#], G.B. Bowden, R.M. Jones, S.G. Tantawi, J.R. Lewandowski,
SLAC, Stanford, CA 94025, USA

Abstract

The wire method is a more rapid and less costly method to measure impedances of RF components compared to methods using a beam. A setup using a single displaced wire to excite and measure transverse resonant modes in accelerating structures for the Next Linear Collider/ Japanese Linear Collider (NLC/JLC) has been built. The RF signal is coupled into and out of the structure using two matching sections with a broadband frequency from 11 to 18 GHz. Their contribution to the scattering parameter is minimized by a calibration technique. A standing wave structure has been measured. Difficulties in accurately predicting the modal loss factors were encountered related to the approximations made and to experimental issues. The measurements are presented and comparisons with simulations are made.

INTRODUCTION

Wake fields in accelerating structures are the main cause of transverse beam emittance growth in high energy accelerators. By appropriate design of the accelerating structures and absorption of electromagnetic energy, they must be brought below a limit where the effect on the beam is acceptable. Therefore their understanding is essential. Although modern computer codes have proved to give reliable results, measurements are important as well.

Direct measurements of wake potentials imply studying their interaction with a beam. Measurements in the time domain have been made for example at the ASSET setup at SLAC on X-band accelerating structures [1], while at TTF at DESY individual dipole modes have been studied [2]. The results of these types of measurements are in good agreement with theoretical predictions [3]. Nevertheless they require long preparation times and costly beam time. Bench-top measurements are made by perturbing the field with a small bead [4] or by propagating RF through a coaxial line made of the structure and one or two thin wires [5].

In this paper we present first frequency-domain measurements using the wire method on a 11.4 GHz standing-wave structure in study for the NLC/JLC [6]. Results are discussed and comparisons with simulations are made.

METHOD

Since their proposal in the 1970s, time domain [7] and frequency domain [8] wire measurements have been made

for various microwave components. In time domain the method requires current pulses of a length shorter or comparable to the length of the bunches used in that structure. Therefore we chose to study individual modes in frequency domain. The wire method theory is rather well established for resistive wall wakefields and modes below cut-off. Several approximations exist for lumped and distributed impedances [9]. Attention must be paid particularly when these conditions are not met.

Setup

The measurement setup is shown in Fig. 1. The signal from a network analyzer is matched to the ports of the structure through two specially designed sections containing adapters from rectangular waveguides (WR62) to coax. These have a broad band from about 11 to 18 GHz. The wire is inserted through the adapter and can be displaced by slightly bending the thin coax tubes. We chose this solution in order to minimize discontinuities in the structure.
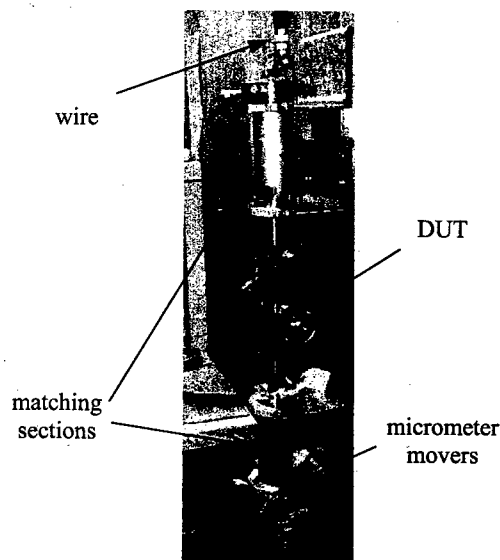
Fig. 1 Wire measurement setup

The wire is made of brass and has a diameter of 300 μm. Compared to previous measurements in single cell cavities, the wire diameter has been increased in order to provide a better contact. This has improved the stability and reproducibility of the transmission curves. For the same reason, the flanges of the matching sections have been modified to eliminate the gaskets. The reflection of the matching sections is better than −30 dB.

TRL calibration

In order to obtain measurements that are hardly affected by the imperfections of the matching sections, we calibrated the measurements at the ports of the matching sections connecting to the device under test (DUT). For this we used a TRL (through-reflect-line) technique in which only a few parameters of the calibration standards need to be precisely known [10]. A delay line and an RF short were required to be built especially for this setup. The third standard is a through measurement. With this method one does not need to know precisely the reflection of the short, or the length of the delay line.

An alternative was to calibrate the network analyzer directly by modifying a calibration kit for a coaxial line to fit the parameters of our setup. Fig. 2 shows the agreement of the calibration results obtained with these two methods. The DUT is here a single cell structure.
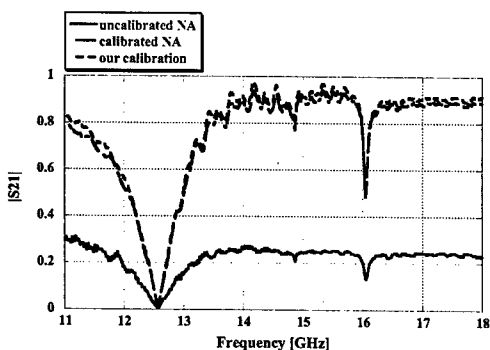
Fig. 2 TRL calibration of measurements on a single- cell structure.

Standing-wave structure

A standing wave structure was measured in this setup (see Fig. 1). It consists of 15 cells which, prior to tuning, are identical. The structure is fed through the middle cell by a symmetrical coupler.

The main contribution to the transverse wake field is given by the first 3 dipole passbands [11]. The setup allows us to measure the first two bands plus the fundamental monopole band.

RESULTS

The two ends of the wire were approximately centered. Then the wire was displaced using two transverse micrometers with respect to this position. Moving the wire rather than measuring at a fixed position allows us to reduce statistical errors. Moreover, one can fit data and ascertain the loss factor in the limit of centered wire [12]. At the same time the alignment of the wire can be based on the dipole signal.

Measurements with various wire offsets

Fig. 3 shows the transmission parameter S_{21} measured on the standing-wave structure for various transverse positions of the wire. One can distinguish the fundamental

monopole passband between about 11.8 and 12.5 GHz. It remains essentially unchanged with changing wire offset.

All modes at higher frequencies are from the first and second dipole passbands in interaction with the TEM coaxial mode. The amplitude of the peaks changes with the wire position. One can see that they are smallest for a wire offset around 0.5 mm. The frequency of the modes also shifts as the displacement of the wire changes. In the limit of zero wire offset, the frequency goes to the frequency of the unperturbed dipole.
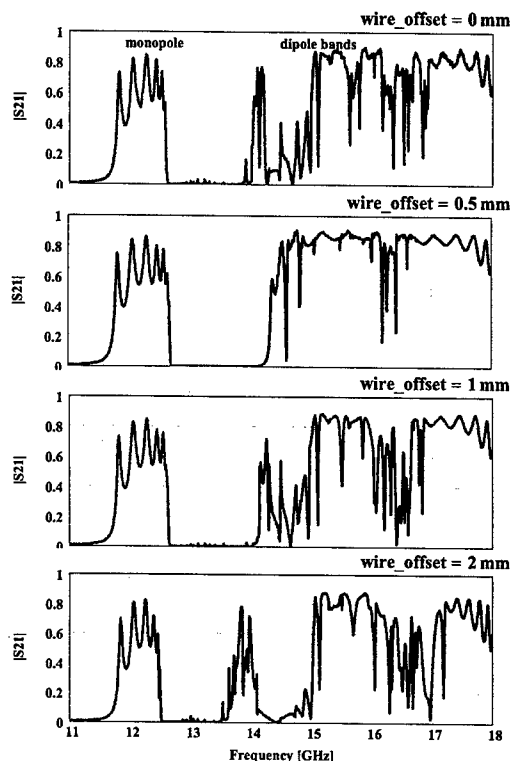
Fig. 3 S_{21} for various transverse positions of the wire.

Comparison to simulations

The properties of the standing wave structure have been simulated with the HFSS code (High Frequency Structure Simulator). The S-parameters of a single cell and of the end cell plus the beam pipe were obtained. A wire with 300 mm in diameter was placed 1 mm off-center. Using a cascading technique, the result for a 15-cell structure was obtained [13].

Fig. 4 compares the simulation with the measurement made for a relative wire displacement of 0 mm which seems to match it best. The agreement for the monopole band is good apart from a frequency shift. This is due to neglecting the input coupler in the simulations. Also the actual structure was tuned to obtain a flat accelerating field.

The dipole bands are more difficult to compare. They depend strongly on the alignment of the wire and clearly

the two curves are not made at the same wire offset. Also it is likely that the wire was tilted with respect to the structure axis and therefore some modes have higher amplitude in the simulation and others in the measurement. The alignment of the structure cells may also play a role.
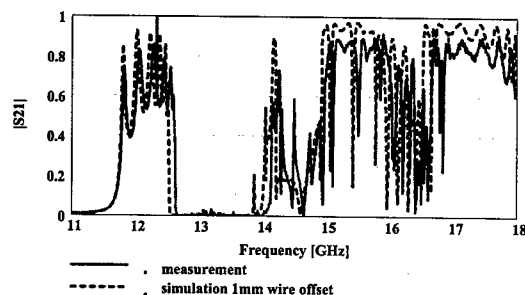
Fig. 4 Comparison of measurement with the wire placed at relative position of 0 mm with simulation for a wire offset of 1 mm.

The coupling impedance and the loss factors of the structure are related to the S-parameters. The correlation is nevertheless not straightforward for accelerating structures. The theory is rather well established for lumped impedances, and for distributed impedances, below cut-off. Further studies are in progress in this sense.

SUMMARY

Initial wire measurements of a NLC/JLC accelerating structure have been undertaken. Special matching sections have been designed and built in order to allow for a relatively easy mounting and displacement of a thin brass wire. A TRL calibration technique gives good results when applied directly on the network analyzer, as well as post-measurement. By moving the wire, excitation of dipole modes was observed. The simulations show good agreement with the measured monopole band, and give a qualitative comparison for the dipole. Nevertheless better wire tilt alignment is needed. Further investigations on inferring the coupling impedance of the dipole bands is under way.

ACKNOWLEDGEMENTS

REFERENCES

[1] C. Adolphsen et al., "Measurement of Wake-Field Suppression in a Detuned X-Band Accelerator Structure", Phys. Rev. Lett. 74, p. 2475 (1995)

[2] P. Castro et al., "Analysis of the HOM Damping with Modulated Beam in the First Prototype of Superstructure", MPPG035, these proceedings (PAC 2003); J. Sekutowicz et al., "Active HOM Excitation

in the First Prototype of Superstructure", TPAB084, these proceedings (PAC 2003)

[3] R.M. Jones et al., "A Spectral Function Method Applied to the Calculation of the Wake Function for the NLCTA", 18th Int. Linac Conf. (LINAC 96), p. 650, Geneva, Switzerland; SLAC-PUB-7287

[4] L.C. Maier, Jr and J.C. Slater, J. Appl. Phys. 23, p. 951 (1952)

[5] F. Caspers in "Handbook of Accelerator Physics and Engineering", World Scientific, Singapore, p. 570 (1998)

[6] N. Phinney (ed.), "2001 Report on the Next Linear Collider", SLAC Report: SLAC-R-571 (2001)

[7] M. Sands and J. Rees, "A Bench Measurement of the Energy Loss of a Stored Beam to a Cavity", SLAC Report: PEP-95 (1974)

[8] A. Faltens et al., "An Analog Method for Measuring the Longitudinal Coupling Impedance of a Relativistic Particle Beam with Its Environment", Proc. 8th Inter. Conf. on High-Energy Accel., Geneva, p. 338 (1971)

[9] H. Hahn, "Validity of Coupling Impedance Bench Measurements", Phys. Rev. ST Accel. Beams 3, p. 122001 (2000)

[10] H.-J. Eul and B. Schiek, "A Generalized Theory and New Calibration Procedures for Network Analyzer Self-Calibration", IEEE Trans. MTT 39, p. 724 (1991)

[11] R.M. Jones et al., "Wakefield Band Partitioning in Linac Structures", 21st Int. Linac Conf. (LINAC 2002), Gyeongju, Korea

[12] N. Baboi et al., "Coaxial Wire Measurements in NLC Accelerating Structures", Proc. Europ. Part. Accel. Conf. (EPAC 2002), p. 1440, Paris, France (2002)

[13] R.M. Jones et al., "Analysis of the Wire Measurement Method of Beam Impedance in Accelerating Structures", TPAB034, these proceedings (PAC 2003)

STATUS OF X-BAND STANDING WAVE STRUCTURE STUDIES AT SLAC

V.A. Dolgashev, C. Adolphsen, D.L. Burke, G. Bowden, R.M. Jones, J. Lewandowski, Z. Li,
R. Loewen, R.H. Miller, C. Ng, C. Pearson, R.D. Ruth, S.G. Tantawi, J.W. Wang, P. Wilson,
SLAC, Stanford, CA 94309, USA

INTRODUCTION

Accelerating gradient is one of the major parameters of a linear accelerator. It determines the length of the accelerator and its power consumption. The SLAC two-mile linear accelerator uses 3 meter long S-band traveling wave (TW) accelerating structures. The average accelerating gradient in the linac is about 20 MV/m. This gradient corresponds to a maximum surface electric field of about 40 MV/m. An operational gradient of 40 MV/m was reported for a 1.5 m constant impedance TW structure for the SLC positron injector. This corresponds to a maximum surface field of 80 MV/m [1]. A typical operational gradient for standing wave (SW) structures of a medical linear accelerator is 30 MV/m, with surface electric fields of 130 MV/m [2] at a pulse width of several microseconds (longer than the working pulse width for SLAC TW structures). SW structures for S-band rf guns routinely operate at maximum surface fields of 130 MV/m ($\sim$2 μs pulse width) [3]. We emphasize an operational gradient with a very low fault rate in comparison to much higher gradients obtained in dedicated high gradient test structures. The operational surface fields in the above mentioned SW structures are obviously higher than in TW, S-band structures.

For the Next Linear collider (NLC) and Japanese Linear Collider (JLC), 1.8 meter long X-Band (11.4 GHz) TW structures were originally considered. Operational tests of these structures showed irreversible damage at an input power levels of $\sim$70 MW and an average gradient of about 45 MV/m (250 ns) [4]. As a consequence, an extensive experimental and theoretical program is underway at SLAC, FNAL and KEK to develop structures that reliably meet the NLC/JLC requirement of 50 MV/m loaded (65 MV/m unloaded) gradient operation [5]. This program includes testing of both TW and SW accelerating structures.

Four pairs of SW structures were built in a SLAC collaboration with KEK and LLNL. Three pairs have been tested to date and one is scheduled to be tested in May - June 2003. Design considerations, results of high power tests and future plans are discussed in this paper.

DESIGN

There are three main design requirements for a linear collider accelerator structure: the ability to sustain the working gradient, acceptable short-range wakefields, and suppressed long-range wakefields.

Other requirements for the NLC/JLC accelerating structures include: operation at 120 Hz with a 270 ns flat top pulse (after the structure is filled with rf energy); no degradation of performance during decades of operation; and less than one breakdown per 10^6 pulses per meter of structure [6, 7]. Single bunch wakefield effects limit the minimum average iris radius (a) of the structures to 4.7 mm, which is 18% of the X-band wavelength (λ= 2.62 cm).

The TW and SW structures under consideration are of the disk loaded waveguide type, are nearly constant gradient, with varying cell dimensions to produce dipole mode detuning. The structures will also include dipole mode damping.

Motivation

It is desirable for the structures to be able to operate at unloaded gradients as high as 100 MV/m, to accommodate an NLC/JLC energy upgrade above 1 TeV using the same tunnel. SW structures may prove better than TW structures in this regard. They will likely have a lower breakdown rate and less breakdown damage due to their reduced maximum surface electric fields and lower rf power absorbed per breakdown than TW structures at the same loaded gradient.

Maximum surface fields are lower in a SW structure due to the fact that the loaded gradient is equal to the unloaded gradient. However, a TW structure could be designed to reduce this difference.

The power absorbed during a breakdown is less in SW structures compared to TW structures for two reasons. It depends, first, on the lower total power fed into the structure and second, on the fact that the response of a SW structure to breakdown currents is different from the response of a TW structure.

The structure input power is determined, roughly by gradient and structure length. Reducing of the TW structure length while keeping the average iris radius 0.18λ reduces the structure efficiency. The efficiency of a SW structure does not depend on its length for the same average iris size. But this length reduction has an obvious drawback — the structure will have more couplers per meter of accelerator.

As for rf energy absorbed in the breakdown, the behavior of SW structures is very different from TW structures [8]. In TW structures during most breakdowns, a large fraction of the incident energy (up to 90%) is absorbed by the breakdown. In SW structures during most breakdowns, most of the rf power is reflected from the structure.

Design considerations

One possible scheme for a SW-based NLC/JLC linac would contain 60-80 cm long superstructures made of 3 or 4 short (20cm, 15 cell) standing wave structures. The structures in the superstructure would be separated by a 6 mm thick cutoff iris with a radius of 4.75 mm. This superstructure has 3 couplers per 60 cm of structure compared to the present NLC TW structure design that has 2 couplers per 60 cm [9]. The structure cells are azimuthally symmetric, without the Higher Order Mode (HOM) damping

Structure name		SW20a375	SW20PI	SW20a565
Iris radius, a	[mm]	3.75	4.75	5.65
Cell diameter, $2b$	[mm]	21.11	21.64	23.04
Iris thickness, t	[mm]	2.6	2.3	4.6
Iris ellipticity		1.69	1	1.48
Filling time	[ns]	120	123	118
Shunt impedance	[MΩ/m]	81.9	68.3	51.1
Q value		$\sim$8600	$\sim$8700	$\sim$8400
E_{peak}/E_{acc}		2.05	2.65	2.12
RF power for $E_{acc} = 50$ MV/m	[MW]	6.0	7.2	10

Table 1: Parameters of 3 types of 20 cm long π-mode SW structures built for high power tests.
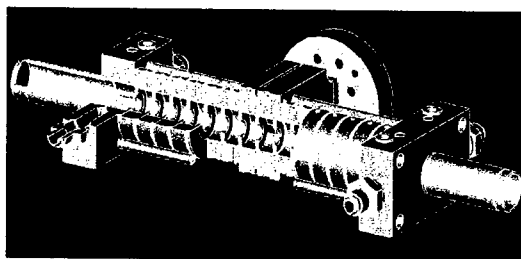
Figure 1: Cutaway view of a 15-cell π-mode SW structure with an iris radius 4.75 mm.

slots and manifolds that are in the TW structure. Long-range wakefield suppression is achieved by detuning the dipole modes within the superstructure and damping them using azimuthially symmetric cells with fundamental mode chokes and internal loads. To sufficiently damp the dipole wakefields, the structure would have one damped cell per 4 regular cells.

Test structures

To test high power performance, 4 pairs of 3 types of SW structures were built. In the test setup, a pair of SW structures is connected to the rf source using a planar 3dB hybrid. With such a connection the rf power reflected from the structures is directed to a high power load (during filling and decay time). Each 20 cm long structure has 14 cells plus a coupler cell. The coupler has two symmetrical waveguide inputs and is located in the middle of the structure. With such positioning of the coupler, the coupling from the rf source to the next-to-π resonance is suppressed. The iris radii of the three SW types are 3.65 mm, 4.75 mm and 5.65 mm. They cover the range required to detune a SW superstructure. The design parameters of these structures are shown in Table 1. Two of the structure types have elliptical iris tips to reduce the ratio of accelerating gradient E_{acc} to peak surface electric fields E_{peak}. The cutaway view of our first SW structure with a=4.75 mm is shown on Fig. 1. The three pairs of structures tested to date have sharp ($\sim$ 80 μm radius) waveguide-to-coupler cell edges. The newest pair of structures ($a = 3.65$ mm), which will be tested soon, have rounded (3 mm radius) waveguide-to-coupler iris edges to reduce the peak rf magnetic field for

reasons discussed below.

HIGH POWER TEST

All SW structure testing has taken place at the Next Linear Collider Test Accelerator (NLCTA). The first pair tested have 4.75 mm iris radii and were designed with critical coupling (coupling $\beta = 1$). The structures were aggressively processed and then run at the loaded NLC/JLC gradient (at that time 55 MV/m) with a 400 ns pulse widths (150 ns structure filling plus 250 ns flat top) at the NLCTA pulse repetition rate of 60 Hz. Under these these conditions, the breakdown rate of the pair was 2-5 per hour. Video images of breakdown events viewed along the beam line axis indicated that most breakdowns were occurring in the coupler. An average of these images shows a distinct enhancement at the azimuthal positions of the waveguide-to-coupler cell edges. After the run, cold-test measurements revealed a π resonance frequency increase of $\sim$ 0.3 MHz. Bead-pull measurements showed that most of the frequency change was in the couplers.

The second pair of structures tested was of the same type as the first but designed to have $\beta = 2$. The experience gained with the first pair prompted us to reduce the field (both magnetic and electric) in the coupler cell (relative to the field in the rest of the cells) by 15%. This was done by tuning the coupler cell frequency down a few MHz. This tuning reduced the external coupling of the structure, so that it ended up at $\beta = 1$. The pair was conditioned with $\sim$2000 breakdowns in three days up 55 MV/m, 400 ns, where it ran with less then breakdown per hour for $\sim$150 hours. The gradient was verified by a measurement of acceleration using the NLCTA electron beam. No detectable damage was found in the structure in after-test measurements.

The third pair of structures tested have the largest radii (5.65 mm) and hence the lowest shunt impedance of the three types. The structures have elliptical iris tips, an improved E_{peak}/E_{acc} ratio and a $\beta = 2$ coupling. Due to an error in coupler cell dimensions, it was not possible to reduce field in the coupler. The structure was processed to 55 MV/m, 400 ns, where the breakdown rate was 6-10 per hour. Video images again indicated that most breakdowns were in the coupler and, similar to first pair, the azimuthal

position of light from the breakdowns correlated with the position of the waveguide-to-coupler-cell edges. A shift in the π resonance of < 0.2 MHz was measured after 4300 breakdowns.

High magnetic fields

During the time of the SW structures tests, several TW structures that were processed also showed an enhancement in the coupler breakdown rate relative to that in the other cells. Measurements of breakdown induced acoustic emission near one of the TW input couplers also suggested that the breakdowns were occurring near the waveguide-to-coupler edges [10]. An autopsy of the TW structure showed that the inner edges (cell side) of the waveguide-to-coupler-cell edges were eroded [11]. Calculations showed that the surface currents peaked at the inner edge of the iris and reached ~ 0.7 MA/m [12]. A simple 1D linear model of rf heating predicts a pulse temperature rise of $\sim 130°$ C. It is unlikely that a temperature rise of of this size can, by itself, produce breakdowns. Some other phenomena must be present to explain the acoustic and video data, and also the large number of breakdown craters observed near the waveguide edges and the on the tips the coupler iris.

When it became apparent that the breakdowns in the couplers were preventing a further increase of the gradient in the third pair of SW structures, we continued an experimental study of the phenomena itself. These experiments showed the following properties of the coupler breakdowns:

1. The breakdown rate is determined by the input rf power and pulse width. It is roughly constant over hours and slowly increases on a longer time scale.

2. The number of pulses without breakdown is roughly independent of the pulse repetition rate.

3. The breakdown rate has a clear correlation with the pulse temperature rise as calculated using a simple model of rf pulse heating. The breakdown rate grows almost exponentially with the temperature as seen in Fig. 2. On a linear scale, it appears like the breakdown rate has a threshold. The threshold temperature varies from 60 to 150° C for the different accelerating structures.

Discussion

Mechanical damage due to pulse heating is discussed in [13, 14] and may be related to the observed breakdown characteristics. The model described in [15] suggests that the mechanical fatigue accumulates with each pulse and (after certain number of pulses) macroscopic change occurs (similar to creation of a dislocation). This model is supported by the experimental data on coupler breakdowns in SW and TW structures with an additional assumption that this macroscopic change triggers the rf breakdown. The mechanism of the surface heating also needs verification, since other effects, like single surface multipactor discharge in strong rf magnetic fields could also increase surface the temperature. Also, more recent TW structure
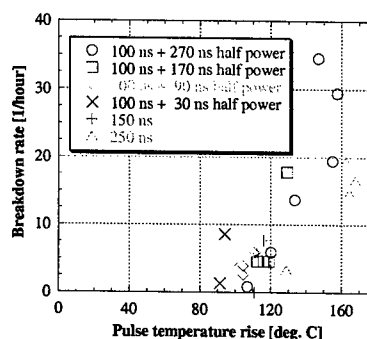
Figure 2: Measured breakdown rates for the SW20a565 structure *vs.* calculated pulse temperature rise on the waveguide-to-coupler iris edges for different shapes of the input rf pulse.

tests showed that some couplers did not breakdown even when the predicted pulse temperature rise was well above 100° C. The absence of breakdown in such cases might be explained by relatively small (~ 1 MV/m) electric field on the iris edge of the coupler without breakdowns in comparison with fields (~ 10 MV/m) in couplers with breakdowns [12].

SUMMARY

Three pairs of SW structures have been tested to date. The performance of two of them was limited to gradients lower than 55 MV/m by breakdowns in the couplers. These breakdowns may be related to the high rf magnetic and moderate rf electric fields on the sharp edges at the waveguide-to-coupler cell opening. Couplers for a new set of structures have been designed to reduce the pulse temperature rise to below 20° C. These structures will be high power tested in May-June 2003.

Despite the potential for coupler breakdowns, one of SW structure pairs tested ($a = 4.57$ mm) did meet NLC/JLC gradient and breakdown rate requirements and had no measurable damage.

REFERENCES

[1] J. E. Clendenin, et al., Part. Accel. 30, 85 (1990).

[2] C. J. Karzmark, et al. " Medical Electron Accelerators," McGraw-Hill, Inc., New York, 1993.

[3] D. T. Palmer et al., SLAC-PUB-7422.

[4] C. Adolphsen et al., TUE01, LINAC2000, 2000, Monterey, CA.

[5] J. W. Wang et al., TH464, LINAC02, 2002, Gyeongju, Korea.

[6] "2001 Report on The Next Linear Collider," SLAC-PUB-R-571, Snowmass, Colorado, 2001.

[7] "NLC Newsletter," July, 2002.

[8] V. A. Dolgashev, et al., FPAH057, PAC2001, Chicago, IL, 2001, pp. 3807-3809.

[9] Z. Li, et al., WPAG027, this conference.

[10] J. Frisch et al., TH484, LINAC02, Gyeongju, Korea, 2002.

[11] F. Le Pimpec et al., MO486, LINAC02, Gyeongju, Korea, 2002.

[12] V. A. Dolgashev, TPAB032, this conference.

[13] O. A. Nezhevenko, PAC97, Vancouver 1997, p.3013.

[14] D. P. Pritzkau, "RF Pulsed Heating," SLAC-Report-577, Ph.D. Dissertation, Stanford University, 2001.

[15] V. F. Kovalenko et al., "Thermophysical Processes and Electrovacuum Devices," Moscow, SOVETSKOE RADIO (1975), pp. 160-193.

HIGH MAGNETIC FIELDS IN COUPLERS OF X-BAND ACCELERATING STRUCTURES*

V.A. Dolgashev,
SLAC, Stanford, CA 94309, USA

INTRODUCTION

Increasing the accelerating gradient is an important issue for linear accelerators. Among phenomena that limit the gradient is rf breakdown in accelerating structures. Breakdowns have been frequently observed in coupler cells of accelerating structures and have been attributed to the electrical field enhancement noted in simulations. Several solutions have been proposed to reduce this enhancement [1, 2]. For example, increasing the group velocity in the coupler and adjacent cells, and shaping of the coupler cell to reduce maximum surface electric fields below the fields in the structure. Little attention was paid to enhancement of the magnetic field in the couplers although the possibility of damage due to pulse heating was mentioned in [3].

The limit imposed by rf pulse heating and thermal fatigue was discussed in [4, 5], but the connection between the high rf magnetic field and coupler breakdowns was realized only recently in high gradient experiments with traveling wave (TW) and standing wave (SW) 11.4 GHz accelerating structures [6, 7, 8]. These experiments are part of extensive experimental and theoretical program underway at SLAC, FNAL and KEK to develop structures that reliably meet the Next Linear Collider and Japanese Linear Collider (NLC/JLC) requirement of 50 MV/m loaded (65 MV/m unloaded) gradient operation.

Experiments There is overwhelming experimental evidence that the waveguide-to-coupler irises in couplers are prone to breakdowns for low group velocity TW and SW structures [9]. The maximum gradient in all of these structures was limited by breakdowns in couplers. The damage was concentrated in input couplers [10].

The breakdowns produce mechanical shock. Shock waves were registered by acoustic sensors installed on the input coupler of a TW structure. The data have shown that the location of the source of the acoustic signal is correlated to the location of waveguide-to-coupler-cell irises [11].

A video-camera was used to obtain images of the arcs in the SW structures. Averaging of more than 100 images again shows that the visible arc location corresponds with the location of the waveguide-to-coupler-cell irises [8].

An autopsy of a TW structure has shown that the inner edges (cell side) of the waveguide-to-coupler-cell irises are eroded while the outer edges (waveguide side) are almost intact. The damage was roughly uniform over the height of the irises [12].

Detailed electrodynamic simulation was made in order to understand the physics underling coupler breakdowns. The simulations and their results are discussed in this paper.

COUPLER SIMULATIONS

A coupler cavity is designed to provide rf power flow from waveguide to the accelerating structure. Design of the coupler is a complex 3D electrodynamic problem. To find the rf magnetic field and calculate the pulse temperature rise the existing couplers had to be modeled with a more accurate code than the code they were originally designed with. Since both TW and SW accelerating structures were tested, couplers for both types were simulated. First, the couplers were matched. The matching procedures for couplers of TW structures and SW structures are different: a TW structure coupler should match waveguide to an infinitely long periodic structure; a SW structure coupler should provide specified loaded Q. Second, the maximum surface rf magnetic field should be determined. In the couplers the field reaches maximum on the edges of the waveguide-to-coupler iris. Then the maximum pulse temperature rise due to the magnetic field is estimated.

Matching of TW structure couplers

An efficient automated procedure has been developed for the simulation of existing TW structure couplers, new couplers designs, and for study of how cell shape effects the magnetic and electric fields. A C++ program optimizes coupler dimensions using the commercial frequency-domain code Ansoft HFSS^{TM}[13]. The matching procedure uses a method based on properties of periodic structures to calculate reflection from the coupler for known on-axis electric field. This method was developed for time domain simulations by N. M. Kroll *et al.* [1]. To find the reflection three points on z axis separated by structure period P were used, with complex electric fields at $E(z - P)$, $E(z)$, and $E(z + P)$. Intermediate quantities are

$$\Delta(z) \equiv (E(z + P) - E(z - P))/E(z),$$
$$\Sigma(z) \equiv (E(z + P) + E(z - P))/E(z).$$

Phase advance per cell ψ is found from equation $\cos \psi = \Sigma(z)/2$. The reflection is

$$R(z) = (2 \sin \psi - j\Sigma(z))/(2 \sin \psi + j\Sigma(z)).$$

Here $j = \sqrt{-1}$. One frequency point calculation of a model made of 4 to 6 cells and one coupler cell gives coupler reflection directly. More than 4 cells is needed if the structure is tapered. Reflection from the excitation port is irrelevant so there is no need for a second coupler. The structure does not have to be symmetrical from beginning to end as in [1]. The following algorithm is executed during coupler matching:

1. The program reads a text file of coupler and cell dimensions and optimization parameters. Then it

writes an HFSS macro that is later executed by post-processor and a macro for 3D modeler to generate the first structure geometry.

2. The program starts HFSS and waits until HFSS has finished calculating and saving $\Re e(E(z))$ and $\Im m(E(z))$ along the z axis of the structure.

3. The program reads the saved fields, calculates $R(z)$ and ψ and then writes an HFSS macro with geometry for the next iteration.

4. The program uses a two parameter optimization algorithm and repeats steps 2 and 3 until the desired coupler reflection is found.

This program can use any structure dimensions in the parameter search, but usually the chosen dimensions are diameter of the coupler cell, opening of the waveguide-to-coupler iris, and diameter of next-to-coupler cell. For typical geometries one such iteration takes from 8 to 30 minutes on a two-processor 900 MHz Pentium computer. More accurate calculations require more time. A typical coupler is matched with an overnight run of the program using lower accuracy faster iterations. Then the match is verified with several more accurate runs, which at the same time provide tolerance analysis for manufacturing. Typical final R achieved is 0.02...0.06.

The whole procedure is robust and never failed to match a coupler. Such sources of error as finite accuracy of field calculation in HFSS or slight variations of tapered structure dimensions from dimensions of an exactly periodic structure do not prevent a good match.

Matching of SW structure couplers

SW π mode structures were recently high power tested at SLAC [8]. Each structure has 14 uniform cells with the coupler cell located in the middle. The coupler matching of such a structure is reduced to adjusting the resonant frequency and loaded Q of the coupler cavity only.

HFSS in eigenvalue mode was used for these calculations. Magnetic boundaries were applied on the interface between coupler and adjacent cells to simulate π mode. Waveguide, connected to the coupler cell, was terminated with a matched load. With these boundary conditions the HFSS eigenvalue solver directly calculates resonant frequency and loaded Q. First, the loaded Q is adjusted with a change of the waveguide-to-coupler cell iris opening; then the coupler is tuned to resonate at the working frequency by changing the coupler cell diameter. Typically 6 to 10 iterations are enough to tune the coupler with total calculation time of one to two hours. The match is verified by calculating the reflection coefficient of the whole structure assuming it is made of copper.

Magnetic fields on sharp edges

The radius of the waveguide-to-coupler cell iris edge was specified on the drawing at $76 \pm 25 \mu m$. Width of the iris is 0.8 mm. Direct calculation of this small rounding is rather time consuming and was done only for several couplers.

For the rest of the couplers, the magnetic field was calculated using an analytical extension of the numerical result.

Usually, the couplers were simulated without the waveguide-to-coupler cell rounding. On a 90° corner the normal magnetic and electric fields have a singularity proportional to $\rho^{-1/3}$, where ρ is the distance to the corner [14]. Fields calculated with HFSS on such a corner will depend on mesh size and will not converge. At the same time, field between the sharp edges will converge. A 2D electrostatic model was built to determine field enhancement on the corner compared to field between edges. A precision 2D boundary-element code was used [15]. Fitting of the results gives the amplification factor $k = 1.04r^{1/3}$ for iris width of 0.8 mm and the edge rounding r [mm]. This factor for 76 μm rounding is ~ 2.5. Direct HFSS calculations of couplers with 76 μm rounding agree with this simple model.

Pulsed heating

RF heating of a metal surface was calculated with a 1D model using calculated tangential magnetic field $H_\parallel$ [5]. The pulse temperature rise ΔT is given by :

$$\Delta T = \frac{|H_\parallel|^2 \sqrt{t}}{\sigma \delta \sqrt{\pi \rho' c_\epsilon k}},$$

where t is the pulse length, σ is the electrical conductivity, δ is the skin depth, ρ' is the density, c_ϵ is the specific heat, and k is the thermal conductivity of the metal. For copper at a frequency of 11.424 GHz the temperature rise $\Delta T = 430|H_\parallel|^2\sqrt{t}$, where ΔT is in °C, $H_\parallel$ in MA/m, and t is in μs. In this simplified model, nonlinearities of the metal's physical properties are neglected.

RESULTS

Coupler breakdowns limited the performance of all recently tested structures with sharp edged couplers. Some of the couplers were cut open after the test. Damage to edges observed on the microscope images was correlated with calculated pulse temperature rise of about 100°C. But to predict the breakdown behavior using the calculated pulse temperature rise was difficult. All structures have shown threshold-like breakdown behavior with the input rf power and pulse width similar to that given in [8]. The calculated pulse temperature rise for the threshold varied between 60 to 150°C, but not all couplers with similar rf magnetic fields where breaking down.

Rounded irises

After the source of coupler breakdowns was traced to high magnetic fields on the sharp edges of the waveguide-to-coupler cell irises, an obvious solution followed: increase the iris rounding to reduce magnetic surface fields. To determine the sufficient rounding one NLC prototype structure was matched by couplers with different iris rounding. That structure is 60 cm long, constant gradient, with initial group velocity (v_g) of 3% of speed of light (c) and 150° phase advance per cell. Several couplers with different rounding were matched. The results for two structures with 70 MV/m unloaded gradient and NLC pulse
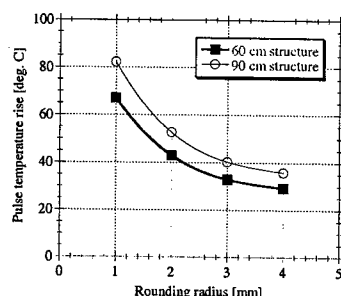
Figure 1: Dependence of maximum pulse temperature rise *vs.* waveguide-to-coupler iris rounding for 60 cm and 90 cm long accelerating structures. Dots — simulation, curves — polynomial fit.

width of 400 ns are shown in Fig.1. The shorter structure needs 70 MW of input power while the longer one needs 96 MW to reach this gradient. The temperature rise for the 90 cm, $v_g = 0.03c$ structure has been scaled up from 60 cm structure results since both structures have the same input couplers. Iris rounding of 3 mm was chosen for the new couplers to keep the pulse temperature rise far below 100° C. Couplers for several structures with such rounding were designed, built and high power tested. Performance these structures was not limited by coupler breakdowns [16]. At the same time, new coupler designs have been developed to considerably decrease the pulse temperature rise and surface electric field [17].

Electric fields

A coupler that had more than 150°C calculated temperature rise but no breakdowns was autopsied. The coupler had damage on the the iris edges. This damage was roughly uniform along the height of the iris but looked very different from damage in couplers with breakdowns. This observation prompted a closer look at the surface electric field.

This edge surface electric field is commonly ignored since it has much lower amplitude than the maximum field in the cell. A real structure with irises and beam pipes always has electric field on outside cell diameters contrary to an idealized case of a pill-box cavity with TM001 mode. The sharp edges on the waveguide-to-coupler iris enhance this field.

Input and output couplers of a 60 cm structure with initial $v_g = 0.03c$ were simulated using HFSS. The couplers were modeled with 80 μm rounding. The surface electric field distribution on the iris edges is shown in Fig. 2. For unloaded gradient of 70 MV/m the input coupler has 13 MV/m maximum field on the edge, the output couplers has $\sim$2 MV/m. The calculated pulse temperature rises are 270° and 160°C respectively. During the high power test the input coupler was breaking down, but output did not.

SUMMARY AND DISCUSSION

After the source of coupler breakdowns was traced to sharp edges of the waveguide-to-coupler irises the problem was solved with new low magnetic field coupler designs.
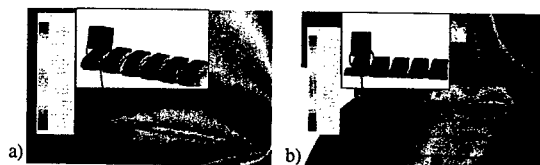
Figure 2: Surface electric field distribution on the edge of 60 cm, $v_g = 0.03c$ structure: a) input coupler, maximum edge field $\sim$13 MV/m; b) output coupler, maximum edge field $\sim$2 MV/m.

The damage observed on the coupler edges and the breakdown behaviour suggests that the breakdown trigger is related to *mechanical fatigue* of the copper surface. In the the model described in [18] the mechanical fatigue accumulates with each pulse and after certain number of pulses a macroscopic change occurs (similar to creation of a dislocation). This model needs an additional assumption that this macroscopic change triggers the rf breakdown. It seems that the moderate electric fields ($\sim$ 10 MV/m) on the edges are an essential part of this trigger. The physics of the surface heating also needs verification, since other effects, like single surface multipactor discharge in strong rf magnetic fields, could increase the surface temperature in addition to the Joule heating due to rf currents.

REFERENCES

[1] N. M. Kroll *et al.*, "Application of Time Domain Simulation to Coupler Design for Periodic Strucutres", LINAC 2000, Monterey, CA, August, 2000.

[2] J. Haimson *et al.*, AAC96, AIP Conf. Proc. 398, p. 898 (1997).

[3] O. A. Nezhevenko *et al.*, PAC01, Chicago, IL, 2001, p. 3492.

[4] O. A. Nezhevenko, PAC97, Vancouver, BC, 1997, p. 3013.

[5] D. P. Pritzkau, "RF Pulsed Heating," SLAC-Report-577, Ph.D. Dissertation, Stanford University, 2001.

[6] J. W. Wang *et al.*, TH464, LINAC02, Gyeongju, Korea, 2002.

[7] V. A. Dolgashev, TU104, LINAC02, Gyeongju, Korea, 2002.

[8] V. A. Dolgashev *et al.*, TPAB031, this conference.

[9] "NLC Newsletter," July, 2002.

[10] C. Adolphsen *et al.*, ROAA003, PAC01, Chicago, IL, 2001.

[11] J. Frisch *et al.*, TH484, LINAC02, Gyeongju, Korea, 2002.

[12] F. Le Pimpec *et al.*, MO486, LINAC02, Gyeongju, Korea, 2002.

[13] http://www.ansoft.com/products/hf/hfss/

[14] R. Mittra and S. W. Lee, "Analytical Techniques in the Theory of Guided Waves", Macmillan, 1971.

[15] V. Ivanov, "Computer simulation the problems of high-current electronics," Proc. 11-th IEEE Int. Pulsed Power Conf., Baltimore, Maryland, June 29- July 2, 1997.

[16] C. Adolphsen, ROPC006, this conference.

[17] C. Nantista *et al.*, TPAB036, this conference.

[18] V. F. Kovalenko *et al.*, "Thermophysical Processes and Electrovacuum Devices," Moscow, SOVETSKOE RADIO (1975), pp. 160-193.

CIRCUIT AND SCATTERING MATRIX ANALYSIS OF THE WIRE MEASUREMENT METHOD OF BEAM IMPEDANCE IN ACCELERATING STRUCTURES*

R.M. Jones, N. Baboi[#], S.G. Tantawi, SLAC, Stanford, CA 94025,
N.M. Kroll, UCSD, La Jolla, CA 92093

Abstract

In order to measure the wakefield left behind multiple bunches of energetic electrons we have previously used the ASSET facility in the SLC [1]. However, in order to produce a more rapid and cost-effective determination of the wakefields we have designed a wire experimental method to measure the beam impedance and from the Fourier transform thereof, the wakefields. In this paper we present studies of the wire effect on the properties of X-band structures in study for the JLC/NLC (Japanese Linear Collider/Next Linear Collider) project. Simulations are made on infinite and finite periodical structures. The results are discussed.

1 INTRODUCTION

The progress of multiple bunches of electrons down several thousand accelerating structures can, at worst, lead to a Beam Break Up instability or at the very least can give rise to a dilution in the emittance of the beam. These affects are driven by both intra-bunch (or short range) wakefields and long-range wakefields. In order to ensure that these effects do not occur it is important to be able to predict and measure the associated beam impedance, loss factor and wakefield for a given accelerator structure in a routine manner. Measurements already made on X-band structures inserted in the 2-mile SLAC linac using the ASSET facility [1] have indicated that theoretical models, give good predictions as to how well the wakefield is damped [2]. However, such measurements are so time consuming and expensive that it is only practical to make this measurement on a very limited number of accelerating structures. The wire measurement technique [3,4,5,6], once perfected, will enable a routine measurement of the impedance of dipole frequency bands. We would envisage having a number of wire measurement setups being available according to the frequency band of interest [7].

The wire measurement method essentially replaces the electron beam with a pulse propagating along a wire placed in the DUT (Device Under Test). In practice, the loss factor is determined through the perturbation of the current due to the DUT [3]. In the frequency domain the transmission factor leads to the impedance [4], while the area under the resonances allows the loss factor to be determined [8]. In this paper we investigate the frequency domain behavior of multiple cell structures. In section 2 the dispersion properties are calculated with the aid of a circuit model. The circuit is developed to model the monopole and first dipole mode regions. In the third section we utilize a matrix cascading technique in order to calculate the overall transmission coefficient of multi-cell structures.

2 CIRCUIT MODEL OF LOWER BAND MODES

We model the interaction between the TEM coaxial mode of a wire inserted on-axis into a cavity with the TM01 mode of the cavity. The cavity consists of two half irises separated from each other by a section of waveguide. This cavity will later be considered to be infinitely repeating in order to obtain the dispersion properties of the system.

The circuit model chosen to model the electromagnetic behavior of a single traveling wave cavity is shown in Fig. 1. The structure is represented by two sections of coax with a parallel resonant circuit connecting the upper conductors of the two sections. The lower conductors of the two sections are connected together directly.
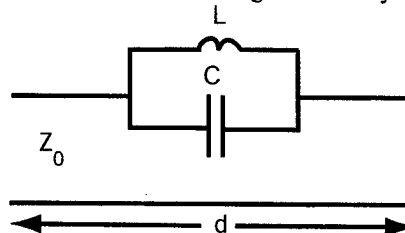
Fig. 1 Circuit model of wire inserted into accelerating cell. The period of the structure is d and the characteristic impedance of the transmission line is Z_0.

For an accelerator made up of an infinite sequence of cavities with identical parameters, the dispersion relation for a structure modeled by the circuit in Fig. 1 is:

$$\cos\psi = \cos\left[\psi_{acc}f/\sqrt{1+b}\right] - \frac{\psi_{acc}bf\sin\left[\psi_{acc}f/\sqrt{1+b}\right]}{2\sqrt{1+b}(1+a^2f^2)}$$

Here ψ refers to a particular phase advance, f is the frequency normalized with respect to the accelerating frequency (11.424 GHz), ψ_{acc} is the characteristic phase advance per cell at the accelerating frequency. The parameters a and b are the accelerating frequency normalized with respect to the cell resonance frequency and, the parallel resonant circuit inductance divided by the coax inductance per unit length multiplied by the cell period, respectively. In practice, these two parameters are obtained such that the dispersion equation identically fits the second 0 mode and the first π mode.

In the limit of small frequencies this dispersion relation yields:

$$1 - \frac{\psi^2}{2} = 1 - \frac{\psi_{acc}^2 f^2}{2}$$

and thus there is a linear relation between frequency and phase. For frequencies close to zero, circuit theory predicts that the mode follows the light line in this region as there is little or no coupling to the monopole or indeed any other modes.

We apply this circuit method to a single cell of the SLAC detuned accelerating structure known as DS2S. Fig. 2 shows the dispersion points for this structure computed with HFSS (High Frequency Structure Simulator) together with the curves obtained from the dispersion equation. The points are seen to be well simulated with the circuit model for all points apart from those in the upper branch close to the π phase advance point. Replacing the L-C circuit with a transmission line may improve this representation. Work is in progress to improve this model in the π phase advance region and also to include the higher order frequency bands.
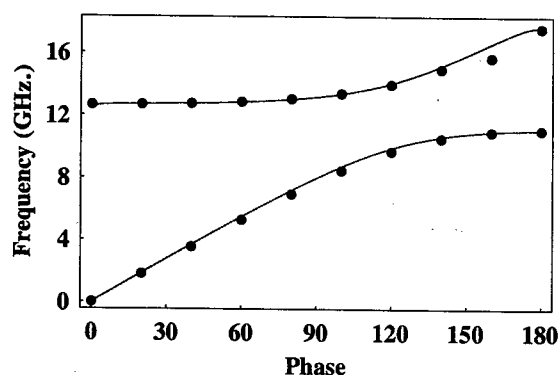
Fig. 2 Dispersion curves for the detuned accelerating structure DS2S. The circuit model is denoted by the curves and the HFSS simulation is given by the points.

3 MATRIX CASCADE SIMULATIONS

In order to determine the impedance or loss factors of various passbands, in the wire method the transmission S_{21} has to be determined. Here we calculate the transmission coefficient of structures consisting of multiple cells in order to facilitate comparison with experimental measurements. We considers the

dimensions of a 11.4 GHz standing wave structure built for the JLC/NLC studies. This accelerator structure, known as SW20PI, is 20cm in length and consists of 15 cells. The cells have an iris radius of 4.75 mm and are all identical prior to tuning the cells (in order to obtain a flat field). The calculations were made with the HFSS code. The walls and the wire are considered to be perfect conductors except where otherwise noted. All curves in the geometry were approximated by straight lines subscribing angles of 10-15 degrees..

Performing simulations of full 3D accelerating structures is computationally expensive in terms of both memory and time. Therefore, we used the technique of cascading scattering matrices to obtain the overall scattering matrix from the individual multi-mode matrices. The scattering matrix of an object is given by:

$$S = \begin{pmatrix} S_{11} & S_{12} \\ S_{21} & S_{22} \end{pmatrix},$$

where S_{12} is in general a matrix relating modes of port 1 to the modes of port 2. The individual elements of the
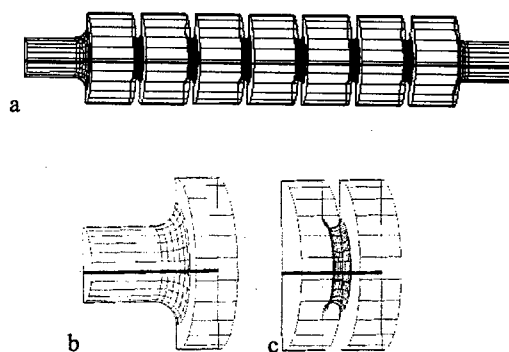
Fig. 3 Structures used for simulation of S parameters: a. full structure; b. and c. geometries used in simulations for cascading

2×2 matrix are themselves matrices as they represent the scattering into higher order modes. However, in calculating the impedance, only the first component of the S_{21} matrix is necessary once the overall scattering matrix has been evaluated.

In order to obtain the scattering parameters for a structure similar to the one illustrated in Fig. 3a, we calculated the S matrix for the end section 3b and a middle section 3c. Six modes were considered in each port. The conductors are assumed to have an infinite conductivity. The wire has a diameter of 300 μm. The global scattering matrix is obtained by cascading two-sections-at a-time using the generalized scattering matrix method [9,10]:

$$S_{11} = S_{11}^A + S_{12}^A \left(I - S_{11}^B S_{22}^A \right)^{-1} S_{11}^B S_{21}^A$$

$$S_{12} = S_{12}^A \left(I - S_{11}^B S_{22}^A \right)^{-1} S_{12}^B$$

$$S_{21} = S_{21}^B \left(I - S_{22}^A S_{11}^B \right)^{-1} S_{21}^A$$

$$S_{22} = S_{22}^B + S_{21}^B \left(I - S_{22}^A S_{11}^B \right)^{-1} S_{22}^A S_{12}^B$$

Here, S^A and S^B represent the matrices of the individual sections. This allows the overall matrix to be determined quite rapidly as the calculation of a single section is very efficient.

In order to verify the accuracy of our cascading, a structure consisting of a limited number of cells (seven for the calculation herein) has been studied. The detailed results are presented in the following subsections. Two cases have been considered: a centered and an offset wire.

Centered wire

For the centered wire we sliced a 10 degrees section of each simulated object in order to reduce the calculation time. An initial comparison of the cascading results to the ones obtained directly by simulating the full length of the structure showed good agreement, except in the region of the cutoff frequencies of higher band modes. The agreement is improved considerably by performing a simulation in which the actual conductivity of copper ($\sigma \sim 5.8 \cdot 10^7 \ \Omega^{-1} \cdot m^{-1}$) is used for the walls of the structure and for the wire. This prevents numerical instabilities occurring as the modes now start to propagate gradually. Excellent agreement is now obtained between the two simulations as seen in Fig. 4a.
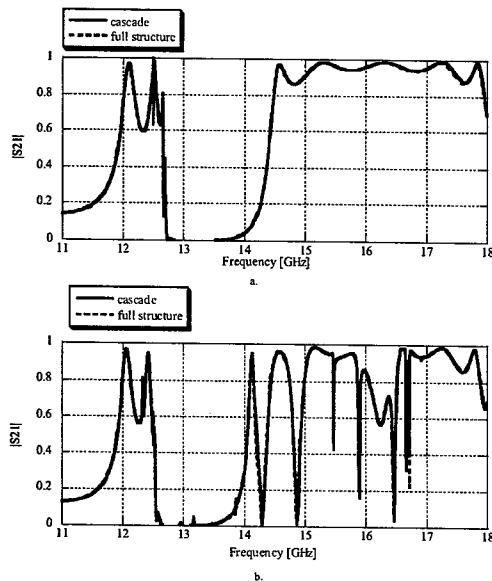
Offset wire

In order to excite dipole modes, the wire is displaced from the axis by 1 mm. Symmetry considerations dictate that half of the geometry is required to be modeled. The walls and the wire are again simulated with the conductivity of copper. The results are compared in Fig. 4b. The discrepancy between the two methods is negligible.

We also note that in Fig. 4 the fundamental monopole band can be distinguished between about 12 and 12.6 GHz. Moving the wire hardly perturbs it. The frequency range above about 13 GHz contains modes of the first and second dipole bands interacting with the coaxial TEM mode. This region is perturbed significantly by moving the wire off-axis.

4 DISCUSSION

The dispersion properties of the wire-loaded accelerating structure have been seen to be quite well modeled with a transmission line and an L-C circuit. Using this circuit for the complete 15-cell structure will also enable the impedance of the structure to be obtained and enable a thorough understanding of the nature of the resonances obtained in the experimental measurement of the transmission coefficient. Work is already ongoing in this area. Further research is in progress on developing the circuit model to include higher order frequency bands.

Application of the generalized scattering matrix method has allowed the overall transmission coefficient to be obtained accurately and efficiently. The monopole frequency band is, as expected, little affected by the movement of the wire whilst dipole resonances are seen to appear as the wire is moved off axis.

5 REFERENCES

[1] C. Adolphsen et al., Phys. Rev. Lett. 74, p. 2475 (1995)

[2] R.M. Jones, et al, Proc. LINAC96, also SLAC-PUB-7287

[3] M. Sands and J. Rees, SLAC Report: PEP-95 (1974)

[4] A. Faltens et al., Proc. 8th Int. Conf. on High-Energy Accel., Geneva, p. 338, 1971

[5] H. Hahn, Phys Rev Special Topics – Accelerators and Beams 3, p. 122001 (2000)

[6] L.S. Walling et al., Nucl. Instr. Meth. A281, p. 433 (1989)

[7] N. Baboi et al., TPAB030, these proceedings

[8] P.B. Wilson, Private communication

[9] R. Mitra and S.W. Lee, 'Analytical Techniques in the Theory of Guided Waves', Macmillan Comp., New York (1971)

[10] G.L. James, IEEE Trans MTT-29, p. 1059 (1981)

Fig. 4 S_{21} obtained with the cascading technique compared to the direct simulation of a complete 7-cell structure, having a wire of 300 μm in diameter placed on-axis (a) and at 1 mm offset (b)

AN AUTOMATED 476 MHZ RF CAVITY PROCESSING FACILITY AT SLAC*

P. McIntosh, A. Hill and H. Schwarz, SLAC, Stanford, CA 94025, USA

Abstract

The 476 MHz accelerating cavities currently used at SLAC are those installed on the PEP-II B-Factory collider accelerator. They are designed to operate at a maximum accelerating voltage of 1 MV and are routinely utilised on PEP-II at voltages up to 750 kV. During the summer of 2003, SPEAR will undergo a substantial upgrade, part of which will be to replace the existing 358.54 MHz RF system with essentially a PEP-II high energy ring (HER) RF station operating at 476.3 MHz and 3.2 MV (or 800 kV/cavity). Prior to installation, cavity RF processing is required to prepare them for use. A dedicated high power test facility is employed at SLAC to provide the capability of conditioning each cavity up to the required accelerating voltage. An automated LabVIEW based interface controls and monitors various cavity and test stand parameters, increasing the RF fields accordingly such that stable operation is finally achieved. This paper describes the high power RF cavity processing facility, highlighting the features of the automated control system and illustrating its operation with some recent high power processing results.

INTRODUCTION

There are currently thirty, 476 MHz RF cavities [1] installed on PEP-II. The ten RF stations are split with 3 powering the LER (Low Energy Ring) and 7 powering the HER (High Energy Ring). HER station configuration typically consists of a single 1.2 MW klystron powering 4 cavities via a circulator and a network of WR2100 waveguide, whereas LER stations have 2 cavities powered by a single klystron. Recently, to enable more of the 1.2 MW of klystron power to be delivered to the beam, newer HER stations are being configured in the 2-cavity mode. More RF stations are to be installed on PEP-II, starting with a 2-cavity HER station this summer and a new LER station expected in the summer of 2004.

SPEAR3 [2], which is currently under construction at SSRL at SLAC, will adopt a 4-cavity HER station for their RF system. The cavities employed will be identical to those used on PEP-II, except that they will be tuned slightly higher in frequency to 476.3 MHz. Construction is scheduled to be completed by the end of September 2003. ACCEL Instruments GmbH in Germany is manufacturing the new cavities for PEP-II and SPEAR3, while accessories such as RF windows, tuners and coupling networks are being fabricated at SLAC.

RF processing of these cavities is initially performed in FM mode, with the RF signal swept in frequency across the fixed tuned cavity, which effectively pulses the RF at

resonance. As the vacuum activity diminishes, the cavity tuner loop can be energized and CW mode processing performed up to a maximum gap voltage (V_{RF}) of 850 kV.

A dedicated test facility is utilized at SLAC to perform the RF processing and it is automated in such a way that the cavity processing can be monitored remotely and should the station trip off for any reason, can be re-energized. This enables the facility to remain on-line for significant periods of time and the RF processing can more effectively continue until the cavity reliably achieves full accelerating field.

TEST FACILITY CONFIGURATION

The 476 MHz RF cavity test facility at SLAC (see Figure 1) consists of a SLAC designed and built, 500 kW CW klystron feeding power via a WR2100 waveguide system through a circulator, to a bunker enclosure which houses the RF cavity. The feeder waveguide penetrates the roof of the bunker and couples to the RF cavity via its coupling network. The bunker itself has been designed to absorb potentially up to 1 MeV of ionizing radiation by way of its concrete walls, roof and sliding, lead lined door.
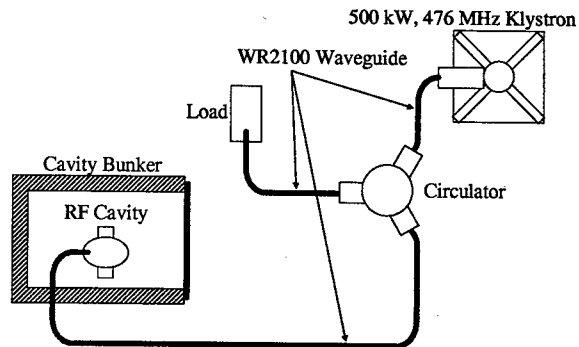
Figure 1 RF Cavity Processing Test Facility Layout

For 850 kV of gap voltage in the cavity, 93 kW of dissipated power in the cavity (P_{cav}) is required for the standard PEP-II type, HOM damped structure. The forward power into the cavity (P_{fwd}) needed to generate this accelerating field is derived from equation 1:

$$P_{fwd} = \frac{(1+\beta)^2}{4\beta} P_{cav} = \frac{(1+\beta)^2}{4\beta} \frac{V_{RF}^{\,2}}{2R_s} \qquad 1$$

Table 1 shows nominal characteristics for the PEP-II RF cavity and from these, one can calculate for a $V_{RF} = 850$ kV, that $P_{fwd} = 145$ kW.

Table 1 PEP-II Nominal Cavity Characteristics

Cavity Characteristics	Value
Frequency (MHz)	476.0
Unloaded Q-factor Q_o	33500
Loaded Q-factor Q_L	6700
Coupling Factor β	4.0
Shunt Impedance R_s (MΩ)	3.9
Effective Impedance R_s/Q_o (Ω)	116.4

A limit is placed on both the maximum cavity input power to the bunker and the peak accelerating voltage generated. These limits are designated as station MPS (Machine Protection System) interlocks. P_{fwd} is limited to 150 kW and is monitored through a WR2100 directional coupler at the entrance to the bunker penetration and the accelerating voltage is limited to 1 MV and is monitored via the cavity coupling loop. The HVPS (High Voltage Power Supply) is shut off rapidly ($\sim 30 \mu s$) should either of these limits be breached during RF processing.

AUTOMATED RF PROCESSING SYSTEM

RF processing of the cavity is performed using the National Instruments, high level graphical programming language - LabVIEW [3], which controls the input power to the cavity whilst monitoring various elements of its operation, such as vacuum pressure, cavity body temperatures, tuner position, resonant frequency, RF window temperature and forward and reverse powers. Other features of the test facility are monitored and interlocked which include; cavity window air side and vacuum side arc detectors, water flow and temperature, reverse power at the cavity as well as the MPS limits previously defined. A CCD camera is located on a cavity inspection port looking at the movable tuner; this is also read back into the LabVIEW system, via an image capturing interface which enables monitoring of breakdown events inside the tuner, should they occur.

A voltage feedback routine controls the cavity accelerating voltage and forward power and if the vacuum in the cavity is below a specified level, the RF power is steadily increased. As more gas is generated from the cavity, its coupling network and the RF window, the vacuum level inside the cavity will increase. If the cavity vacuum exceeds the vacuum limit set for RF processing, then the RF power is reduced automatically until the vacuum in the cavity improves again. The process is then repeated and P_{cav} is increased again until the cavity achieves its maximum defined field level of 850 kV. Typically then the cavity is held at this power level for 1-2 days, as its vacuum activity and stability improves.

The hardware used to perform the readback and control functions are shown in Figure 2. A PC system is configured with 4 National Instruments interface boards; **Board a)** a PCI-GPIB board is used to interface to a Marconi 2019 Signal Generator which controls the drive to the 500 kW klystron in either FM or CW modes. **Board b)** a PCI-6025E data acquisition (DAQ) board which is used to read and write digital I/O (DIO) control

information to and from the test facility. The DIO interlock reads comprise cavity water flow, cavity arc detectors, cavity temperatures and cavity vacuum. The DIO writes include, switching the HVPS on and off, enabling the RF, activating the voltage feedback system and resetting interlocks. **Board c)** the 6025E board also connects to an AMUX-64T analog multiplexer board, which reads 13 temperature sensors positioned at various locations on the cavity body and its coupling network. It also reads the cavity forward and reverse power levels, the gap voltage, the tuner position and the cavity pressure. **Board d)** a PCI-1409 image acquisition board is connected to a CCD camera looking at the cavity movable tuner. The image acquisition (IMAQ) board is triggered from external sources and the images are buffered so that potential breakdown events occurring in the tuner gap can be captured.
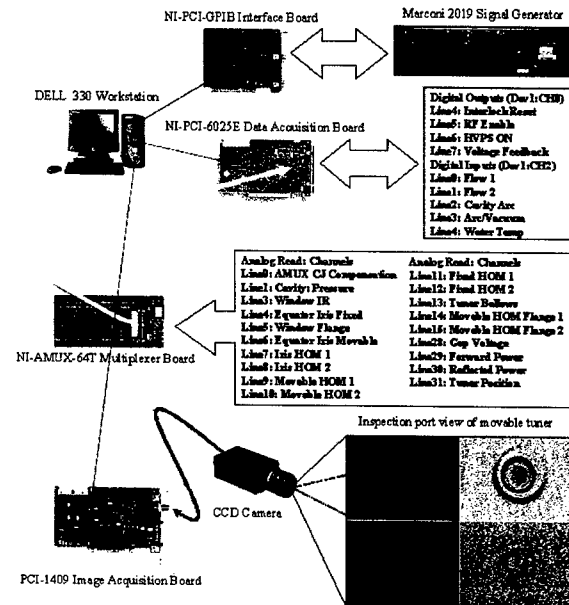
Figure 2 Analog and Digital Diagnostics and Controls

The LabVIEW front panel for the cavity processing or conditioning system allows for easy manipulation of the system controls and diagnostics as shown in Figure 3. It currently comprises 9 sections; **File Acquisition** which identifies the file to which data is being stored, **Interlocks** indicates the current interlock status, **Temperatures** whereby each of the 13 cavity body water cooling circuit temperatures including an infra red temperature reading of the RF window are indicated and limits are set which shut off the HVPS if exceeded, **Cavity Pressure** shows a real time plot of cavity pressure and allows for a pressure limit on cavity processing to be specified, **Misc Parameters** allows the users to monitor in real-time a specific cavity parameter, **RF Power** indicates the current cavity powers along with imposed limits, **Cavity Tuner** shows the tuner position, **Cavity Voltage** graphically shows the cavity voltage and **Voltage Feedback** enables the voltage feedback loop to be closed in order to increase the power

from the klystron, the feedback loop monitors the cavity forward power with respect to its limit as well as the cavity pressure and if either limits are exceeded then the RF input power is reduced via a voltage controlled attenuator on the input to the klystron.
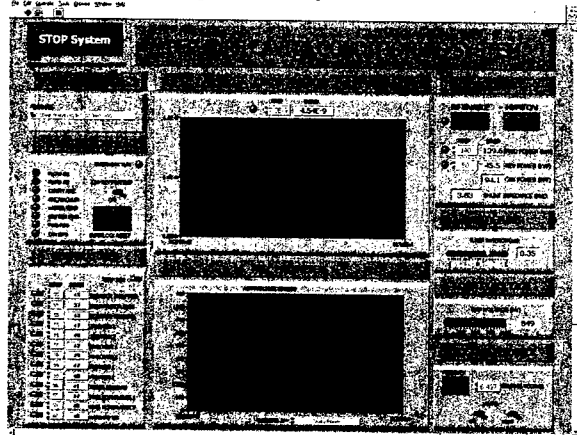
Figure 3 LabVIEW Cavity Conditioning Front Panel

Closed loop operation of this feedback loop has 2 modes; FAST and SLOW, which relates to the rate that each power iteration is made with FAST occurring every ~0.5 seconds and SLOW acting every ~2 seconds. This SLOW provision is implemented to assist in processing through particularly stubborn areas whereby large vacuum spikes would normally inhibit processing in FAST mode.

CAVITY PROCESSING RESULTS
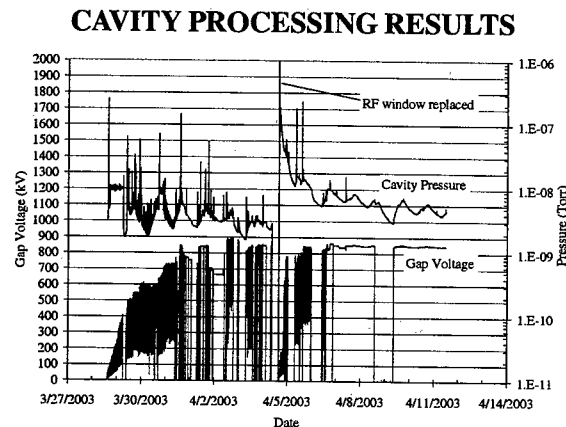
Figure 4 Cavity SP3-01 RF Processing History

A total of 6 PEP-II type cavities have been successfully processed using the system described here. The most recent were 2 cavities completed in March - April 2003 for SPEAR3. Figure 4 shows the 14 day processing history for the first SPEAR3 cavity SP3-01. Processing started in FM mode on 3/28, initially at 300 kHz modulation up to a peak voltage in the cavity of V_{RF} = 850 kV and left to run at this level for several hours, with the vacuum level in the cavity controlled to below 1 x 10^{-8} torr. Processing was then switched to CW mode at 476.3

MHz and the cavity took only 3 hours to process to full field on 3/31.

A problem then arose whereby the cavity could not sustain this level of field and repeatedly tripped off, after ~ 1 hour operation, on the RF window vacuum side arc detector interlock signal (LabVIEW interlock: Cavity/Arc). The imaging camera did not capture any arc or breakdown evidence inside the cavity when this event occurred. After 2 days of attempted processing CW at full field, the station was reverted back to FM processing mode to try and overcome this limit. A peak field of V_{RF} = 900 kV was set and the FM frequency was cycled under LabVIEW control from 150 kHz down to 20 kHz over several hours. Switching back to CW processing mode however did not improve the stability of the cavity at high field and it again repeatedly broke down on vacuum side window arcs.

On 4/04 the cavity was removed from the test facility and the RF window was taken off the coupling network and a pre-baked replacement window re-installed. The removed window was later diagnosed as having faulty copper plating as the cause for the repeated arcing. The cavity was then put back into the test facility bunker and FM processing resumed a few hours later when the vacuum level in the cavity reduced to a reasonable level. After ~24 hours, the cavity had reached V_{RF} = 850 kV at a pressure of 1.3 x 10^{-8} torr. Switching back to CW mode, the cavity reached full field in 2 hours and remained there, following a trip attributed to a circulator arc, for ~41 hours before tripping off again on another circulator arc. Processing was concluded for this cavity with a further ~49 hour run at full field.

CONCLUSIONS

As the RF processing of these accelerating structures up to full accelerating fields takes many days of continuous operation, it becomes necessary to incorporate a control system which can provide an automated mechanism of control. The LabVIEW control system utilised at SLAC allows for a reliable interface to a number of data acquisition and control boards which are configured to monitor system operation and react accordingly to various cavity parameters to ensure that RF processing continues efficiently whilst minimizing downtime due to station trips.

The system has proved invaluable in terms of being able to process these cavities rapidly and also having the inherent flexibility to include sufficient diagnostics that assist in identifying problems that may occur.

REFERENCES

[1] R A Rimmer, "High-Power RF Cavity R&D for the PEP-II B Factory", Proc. EPAC'94, London, June 1994, pp 2101-2103.

[2] See: http://www-ssrl.slac.stanford.edu/spear3/SPEAR3_main_page.htm.

[3] LabVIEW can be obtained from National Instruments Corporation, Austin, Texas, USA.

NOVEL ACCELERATOR STRUCTURE COUPLERS*

C.D. Nantista, V.A. Dolgashev, and S.G. Tantawi, SLAC, 2575 Sand Hill Rd., Menlo Park, CA 94025, USA

Abstract

Recent experience with X-band accelerator structure development has shown the rf input coupler to be the region most prone to rf breakdown and degradation, effectively limiting the operating gradient. A major factor in this appears to be high magnetic fields at the sharp edges of the coupling irises. As a first response to this problem, couplers with rounded and thickened iris horns have been employed, with improved performance. In addition, conceptually new coupler designs have been developed, in which power is coupled through the broadwall of the feed waveguide. A prototype "mode converter" coupler, which launches the TM_{01} mode in circular waveguide before coupling through a matching cell into the main structure, has been tested with great success. With peak surface fields below those in the body of the structure, this coupler represents a break-through in the NLC structure program. The design of this coupler and of variations which use beamline space more efficiently are described here. The latter include a coupler in which power passes directly through an iris in the broad wall of the rectangular waveguide into a matching cell and one which makes the waveguide itself an accelerating cell. We also discuss techniques for matching such couplers.

INTRODUCTION

RF power is typically coupled into accelerator structures by magnetic coupling through a pair of iris apertures in thin-walled interfaces between the ends or narrow walls of rectangular waveguides and a coupling cell [1]. In the development of high-gradient structures for future linear colliders, much attention has been demanded by the limitations imposed by rf breakdown and surface damage [2], [3]. Although high-field regions such as iris tips and slots throughout these structures are vulnerable to breakdown, couplers have been seen to represent a sort of bottleneck. In the past couple of years, this has led us to explore ways of reducing the surface fields in structure couplers. We here present and discuss some solutions to the coupler problem.

FAT-LIPPED COUPLER

Post-processing autopsies of test structures have revealed gross deterioration of the "horns" or ridges of waveguide to coupler cell irises. This confirmed a connection between processing damage and pulsed heating due to large surface currents [4]. The problem was most obvious in structures where the horn edges had been

made sharp (~0.08 mm radii). The most straight-forward remedy to the problem of coupling iris pulsed heating is to round the iris edges with increased radius. Figure 1 shows a coupler geometry of the type which performed poorly and a modified coupler with a 3 mm thick, full-radiused waveguide iris. This redesign reduced the peak surface magnetic field by ~50% and the pulsed heating by a factor of four. The coupler cell wall is given a racetrack shape to compensate for the larger quadrupole distortion of the fields [5].

Figure 1: Quarter cross-section of a) thin-irised coupler and b) fat-lipped coupler with reduced pulsed heating.

MODE-CONVERTER COUPLER

Greater reduction of coupler fields requires a qualitative change of design. The mode-converter coupler was adapted from a set-up designed to test and study single cells of various geometries and materials. To test the performance of these cells without being limited by coupler field enhancement, we had decided to couple on axis from a circular TM_{01} mode waveguide. A TM_{01} launcher was thus designed. Between two such launchers could be inserted a simple, symmetric structure consisting of the travelling-wave test cell sandwiched between two lower-field matching cells.

The TM_{01} Mode Launcher

After electric fields were found to be too high in an initial wrap-around style mode launcher, a simpler design was conceived. It consists of a WR90 waveguide, to be fed symmetrically from both ends, opening through its broad wall into a perpendicular 0.900" diameter circular waveguide. Matching the diameter to the rectangular guide width keeps the fields low while avoiding unnecessary overmoding. The only other propagating mode, the fundamental TE_{11}, even when not excluded by symmetric feeding, is poorly coupled compared to the TM mode. A simple matching element completes this launcher or mode converter. This can be an iris in the circular waveguide or, as shown in Fig. 2, a set of matching bumps (or posts) in the rectangular waveguide.

The edge of the junction, where the walls of the rectangular and circular guides meet, is rounded to minimize electric field enhancement. For the singe-cell tests, a smaller hole, opposite the circular waveguide, opens into a cutoff viewport. In adapting this mode

converter into a coupler for an actual beamline structure, this viewport becomes the beampipe.

Figure 2 shows the geometry of the mode converter with electric and magnetic field plots from HFSS. For a power flow of 50 MW, the peak surface electric field is 35 MV/m and the peak magnetic field is 100 kA/m. The match, quite broad relative to structure bandwidths, is shown in Figure 3.
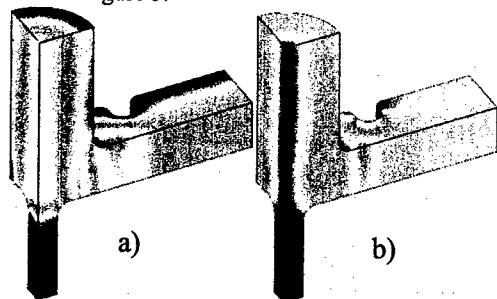
Figure 2: Quarter geometry of TM$_{01}$ mode converter with a) electric field and b) magnetic field plots.
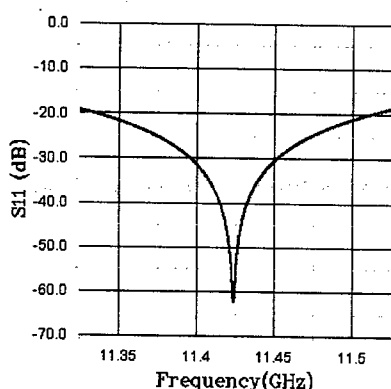
Figure 3: Simulated frequency response of X-band TM$_{01}$ mode converter.

Designing Matching Cells

Use of this universal mode converter in any given input or output coupler requires design of a customized cell to match the circular waveguide into the disk-loaded structure. This cell has fields higher than in the mode converter itself, but can typically be designed to have surface fields below those in the main structure cells, so that the coupler is no longer a weak link. To determine the matching cell dimensions for a travelling-wave structure, one can use the following approach based on symmetrized models and single-mode cascading.

First, one models a symmetric structure composed of one or more structure cells, with the central one symmetrized—for example cells 1, 2, 3, 2, and 1, with the diameter of cell 3 adjusted if necessary to account for the fact that it has the same iris dimension on either side (normally changing in a constant gradient structure). Using a field solver such as HFSS, this model is simulated, with a port at each end of the circular waveguide diameter, to determine the scattering matrix.

This is repeated with the central, symmetric cell doubled and then tripled.

If one converts the scattering matrix to a transmission matrix and cascades it between those of an undetermined matching element and its reflection as $T^{tot} = T^m TT^{m(1\leftrightarrow2)}$, the condition for a match, $T_{21}^{tot} = 0$ (or $S_{11}^{tot} = 0$), yields the following equation for the amplitude of the matching reflection as a function of the phase as seen looking out from the modelled port:

$$\left|S_{22}^m\right| = \frac{\cos\left(\phi_{11} + \phi_{22}^m\right)}{\left|S_{11}\right|} - \sqrt{\left[\frac{\cos\left(\phi_{11} + \phi_{22}^m\right)}{\left|S_{11}\right|}\right]^2 - 1},$$

where the ϕ's are phases of scattering matrix elements.

Plotting the solution to this equation over the ϕ_{22}^m region where it is pure real for the cases of one, two, and three symmetrized cells, one finds that the curves intersect at a unique point. Since this match is independent of the number of central cells, it must be a travelling wave match to the periodic structure represented by that cell. A matching iris can now be designed to give this desired reflection amplitude, and from its simulated reflection phase its proper spacing from the first structure iris can be determined. This defines the matching cell. Figure 4 shows an example with electric fields.

Figure 4: Circular waveguide (left) matched to a TW periodic structure through a matching cell with field plot.

The symmetry technique described here is applicable to more complicated three-dimensional matching problems as well, since the matching element need not be a simple waveguide iris. In practice, this matching method does not always give as small a reflection as desired. It can be used to get close to the desired match. The coupler dimensions can then be optimized using the Kroll method [6], by which the internal reflection from a periodic structure coupler is calculated from the simulated fields in the cells using formulae derived from Floquet's theorem. Since such optimization takes many long field solver iterations, the three iterations (even two would suffice) of the symmetry technique are seen to provide a valuable head start.

BROADWALL (WAVEGUIDE) COUPLER

An undesirable aspect of the mode-converter coupler, where real estate is valuable, is that negligible acceleration is gained over the beamline distance it occupies. This reduces the average effective accelerating gradient of a structure. For use in a linear collider, a more compact coupler is required. With this in mind, it was realized that two matching steps, from rectangular waveguide to circular waveguide and from circular

waveguide to disk-loaded structure, are not necessary. The TM_{01} waveguide can be eliminated by direct electric coupling through a circular iris in the WR90 broadwall into a matching cell. We had wondered how short the circular waveguide section could be made before evanescent modes spoiled the independently simulated matches. With the added design cost of having to simulate 90° wedges of the 2-D accelerator cells due to the coupler symmetry, we could in this way reduce its length to zero. Figure 5 illustrates the broadwall coupler.
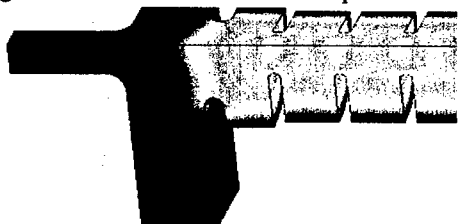
Figure 5: Quarter geometry of a broadwall coupler with electric fields

This single match design also allows the elimination of bumps or posts in the rectangular waveguide ports. The WR90 is then free of obstruction. This is good from the point of view of dipole wakefield damping. One orientation of the lowest TM dipole mode on the coupler axis excites TE_{10} asymmetrically in either arm of the rectangular waveguide; the other excites in-phase TE_{20} waves. Without matching elements, these are free to propagate out, and trapped coupler modes can be avoided.

ACCELERATING WAVEGUIDE COUPLER

Even the broadwall coupler sacrifices some acceleration efficiency for low coupler fields. There is very little field in the waveguide region, and the field in the matching cell may not be quite synchronous. If the couplers represent a small fraction of the structure length and/or allow a higher gradient to be reached in the main cells than otherwise achievable, it may be a viable candidate.

Ideally, however, we would like to reclaim this beamline space for acceleration. This might be accomplished with a more complicated accelerating waveguide coupler similar to that shown in Figure 6. Here partial chokes in the waveguide create a standing wave in the region of the beamline. The height of the waveguide is stepped down to the length of a cell, and the iris coupling it to the main structure is adjusted to achieve the desired phase advance. The waveguide region thus becomes for the beam another cell. The idea is to get significant acceleration here without, in the process, raising field levels at the chokes, or alternative matching elements, back to dangerously high levels.

The waveguide width is also stepped down near the structure axis so that the half guide wavelength $\lambda_g/2$ is equal to the waveguide width. This makes the standing wave field lobe square, eliminating quadrupole asymmetry, which can cause surface electric field

enhancement on the iris and beampipe opening. This is similar to "racetracking" in the fat-lipped coupler. Due to their lower fields, it was considered unnecessary in the mode-converter and broadwall couplers.

Figure 6: Quarter geometry of an accelerating waveguide coupler with electric fields.

CONCLUSIONS

Several innovative coupler design have been presented. The fat-lipped and mode converter couplers were successfully used for the output and input couplers, respectively, of an experimental X-band structure, allowing it to be processed up to 90 MV/m (400 ns pulse). A subsequent set of structures in the SLAC/KEK program will be tested with mode converter couplers to optimize the main structure parameters. Fermilab will provide additional R&D structures with broadwall couplers. The CLIC structure program at CERN has likewise adopted the mode-converter and broadwall coupler designs for 30 GHz test structures [7].

REFERENCES

[1] G. Bowden, et al., "A Compact RF Power Coupler for the NLC Linac," proc. of 1999 Particle Accelerator Conference, March 29-April 2, 1999, New York, NY, USA.

[2] C. Adolphsen, et al., "Processing Studies of X-band Accelerator Structures at the NLCTA," proc. of 2001 Particle Accelerator Conf., June 18-22, 2001, Chicago, IL, USA.

[3] H.H. Braun, et al., "CLIC High-Gradient Test Results,".presented at 21st International Linac Conf., August 19-23, 2002, Gyeongju, Korea.

[4] Valery Dolgashev, "High Magnetic Fields in Couplers of X-Band Accelerating Structures," these proceedings.

[5] J.Haimson, et al., "A Racetrack Geometry to Avoid Undesirable Azimuthal Variations...," proc. of Advanced Accel. Concepts Workshop, October 1996, Lake Tahoe, CA, USA.

[6] N.M. Kroll, et al., "Applications of Time Domain Simulation to Coupler Design for Periodic Structures," proc. of 20th International Linac Conf., August 21-25, 2000, Monterey, CA, USA.

[7] S. Doebert, et al., "Coupler Studies for CLIC Accelerating Structures," proc. of Eighth European Particle Accel. Conf., June 3-7, 2002, Paris, France.

USE OF ACOUSTIC EMISSION TO DIAGNOSE BREAKDOWN IN ACCELERATOR RF STRUCTURES[#]

J. Nelson*, M. Ross, J. Frisch, F. Le Pimpec, K. Jobe, D. McCormick, T. Smith, SLAC, Menlo Park, CA 94025 USA

Abstract

Accelerator structures of a wide variety have been damaged by RF breakdowns. Very little is known about the mechanisms that cause the breakdown and the damage although there has been theoretical work [1,2]. Using an array of ultrasonic acoustic emission sensors we have been able to locate and classify breakdown events more accurately than possible using microwave techniques. Data from the technique has led to improvements in the design of the NLC X-band RF structure. We report results of acoustic emission studies at the DESY TESLA Test Facility and the SLAC NLC Test Accelerator.

INTRODUCTION

The Next Linear Collider (NLC) project requires X-band copper structures capable of operating at accelerating gradients of about 70 MV/m with a breakdown rate less than 0.1/hour. To understand the higher breakdown rates seen, a tool is needed that is able to localize the deposited energy within a few square mm around the iris.

In [1] a breakdown mechanism is proposed which entails a small plasma spot forming near an iris. This model predicts surface melting in the region of the plasma spot as well as energy deposition on an opposing iris. If so, a tool capable of localizing the breakdown should be able to distinguish this phenomenon from a breakdown affecting only one iris.

Acoustic emission sensors (AES) were used to localize breakdowns in multiple scenarios: L-band RF gun and X-band accelerating structures, as well as studying breakdown patterns associated with X-band structure processing.

ACOUSTIC EMISSION SENSORS

Acoustic emission sensors are piezo-electric devices used in industrial non-destructive testing of such things as crack propagation in airplane frames. In the X-band case, heat from the 40 joule RF pulse is absorbed in the structure walls causing thermal expansion which creates sound that we can detect in the 100 kHz – 1 MHz range. We see little attenuation at these frequencies; however, at higher frequencies the attenuation is strongly dependent on crystalline structure. While we don't have an absolute calibration of the amplitude of the vibrations in the copper, one can readily hear breakdowns and even normal events in the structure.

Acoustic waves propagate in annealed copper as bulk shear (s) waves with a speed $v_s = 2325$ m/s, bulk pressure (p) waves, $v_b = 4760$ m/s, or as a slower shear wave [3]. At our detectable frequencies, the shear wave disturbance wavelength is about 10 mm, the characteristic dimension of X-band RF cell widths, but significantly smaller than L-band components.

DATA

L-Band

The TESLA Test Facility (TTF) normal-conducting L-band 1.5 cell RF photocathode gun has exhibited breakdown activity near its peak design power and pulse length [4]. The determination of the breakdown location is more easily done with acoustic sensors than with standing wave microwave localization techniques.

Eight sensors were attached to the copper gun cavity and waveguide with cyano-acrylate glue. The sensors' signals were locally amplified then recorded with oscilloscopes outside the tunnel housing. Figure 1 below shows sensor signals from a typical breakdown event. The breakdown signals are up to 100 times larger than the signals produced on a non-breakdown pulse.
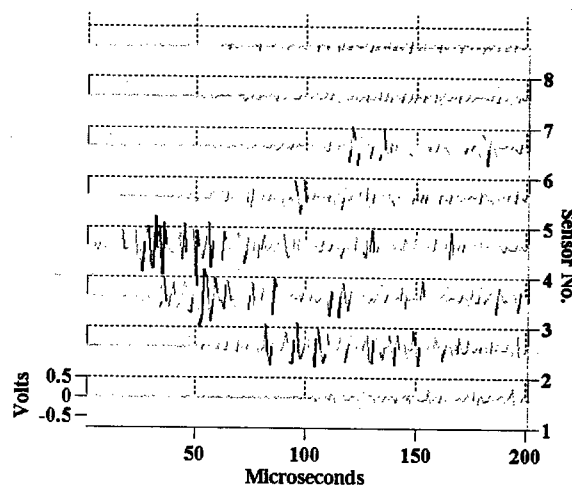
Figure 1: Recorded voltage signals from TTF gun acoustic sensors from a single breakdown event.

In Fig. 1, the breakdown signals that are largest and arrive earliest (sensors 3 and 4) are around the waveguide coupler iris. Those that are small and arrive later (sensors 7 and 8) are attached to the gun's cavity coupler cell and close to the cathode, respectively. The shapes of the envelopes of the signals are not understood.

X-Band

At the NLC Test Accelerator (NLCTA) an aggressive structure testing program is underway to refine structure designs to achieve the NLC required parameters. The structures' achievable gradients are limited by breakdowns and ultimately by the damage they cause [5]. To diagnose this problem, 64 sensors are attached to a copper X-band accelerating structure, typically glued 4 sensors per structure cell, 90 degrees apart. The signals are digitized at 10 MHz. Each waveform contains 100 μs of a sensor's signals from three consecutive RF pulses with the last pulse being the breakdown pulse.

Figure 2 shows two consecutive pulses for 12 sensors (3 cells, 4 sensors per cell). Sensor 6 shows the largest signal, about 30 times larger than the non-breakdown pulse. Adjacent sensors 2 and 10 have relatively small signals, indicating very localized energy deposition at sensor 6.
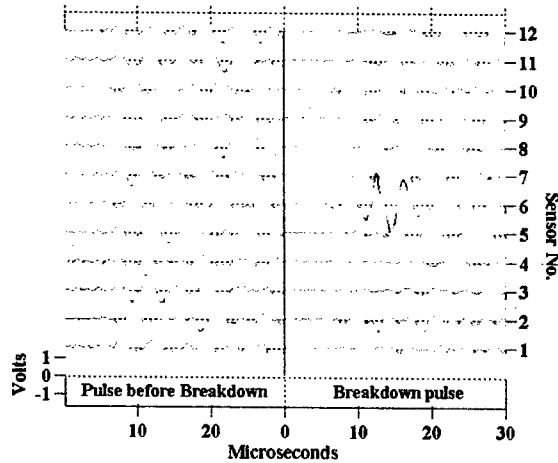
Figure 2: Two consecutive RF pulses in NLCTA. The amplitude of the non-breakdown pulse has been increased 10x.

ANALYSIS

Breakdown Localization

We determine breakdown location using two methods: (1) time of arrival t_0 of the breakdown signal at the sensor and (2) relative amplitude of the sensor signals σ_{norm}.

To identify the time of arrival of the breakdown signal at a given sensor, we first calculate the integrated rms of each sensor's signal,

$$R_n(t) = \sigma_n[V_n(1,2,...t)], \qquad (1)$$

where t is time in 0.1 μs data points, V is the acoustic sensor signal voltage, σ is the rms, and R is the integrated rms from 1 to t. The subscript n denotes the breakdown pulse; subscript $n-2$ denotes the non-breakdown pulse 2 pulses before.

At TTF, the time of arrival was determined as when the integrated rms crossed a threshold, R_0:

$$t_0 = t \text{ when } R(t) > R_0. \qquad (2)$$

For NLCTA, we used:

$$t_0 = t \text{ when } [R_n(t)/R_{n-2}(t)] > R_0. \qquad (3)$$

At TTF the division by R_{n-2} wasn't necessary as the acoustic signals on non-breakdown pulses were so small.

Another way to determine breakdown location is to look at the relative amplitude of the signals seen at the sensors:

$$\sigma_{norm} = R_n(20\mu s)/R_{n-2}(20\mu s). \qquad (4)$$

RESULTS

Particle Contamination in X-band Structures

For one of the NLC test structures, a week's worth of processing, 2366 breakdowns, was analyzed using the σ_{norm} technique. It was discovered that more than 600 breakdowns occurred in one location – the twelfth cell of the structure, a rate six times more than the typical cell average. Of the events in cell 12, 83% showed the highest signal from the sensor on the bottom of the cell. Based on the AES data, the structure was dissected at that cell. We found a 0.5mm by 1mm sliver of aluminum near the location of the largest σ_{norm}. The particle was surrounded by many craters and melted spots.

X-band Structure Input Coupler

AES gave conclusive evidence of breakdown in the low electric field region of the input coupler. This unexpected result prompted the redesign of the coupler to reduce pulse heating (possibly due to high magnetic fields) on the four input waveguide matching irises. This work is summarized in [6,7].

TTF

For the TTF L-band gun the breakdowns were isolated to the input waveguide coupling iris, not the cathode as originally suspected. Typical signals from the 3 sensors on this iris are shown in figure 1 as signals 3, 4, and 5. Using the t_0 technique and given the distance between the sensors and the potential breakdown sources, one can pinpoint the breakdown location between sensors 4 and 5, as well as calculate the speed of the signal's propagation: 3520 ± 810 m/s. This speed is between the p and s wave speeds. The sensors probably see both waves with differing sensitivities.

Multiple-Iris Events in X-band Structures

Given a data set of a few thousand breakdowns for a particular structure from a month's running, we chose to select just the events which appear to be highly localized, namely those meeting the following criteria: for a given sensor, i, and its axial neighbors, $i\pm1$,

$$\sigma_{norm}(i) > 20 \text{ and } \sigma_{norm}(i\pm1) < \sigma_{norm}(i)/2.$$

This selected 15 of the 400 events in the body of the structure. Figure 3 shows a typical event of this type.

This figure shows that the sensors' resolution is less than the distance between the sensors around the cell and about equal to the cell spacing. Using the t_0 technique, we found that the signals from sensors $i\pm1$ arrive at the same time, approximately 1 μs later than the signal from sensor i. Given that the sensors are mounted between the irises,

the breakdown can only be coming from both irises, not just one. This result is consistent with the theory proposed in [1,2].
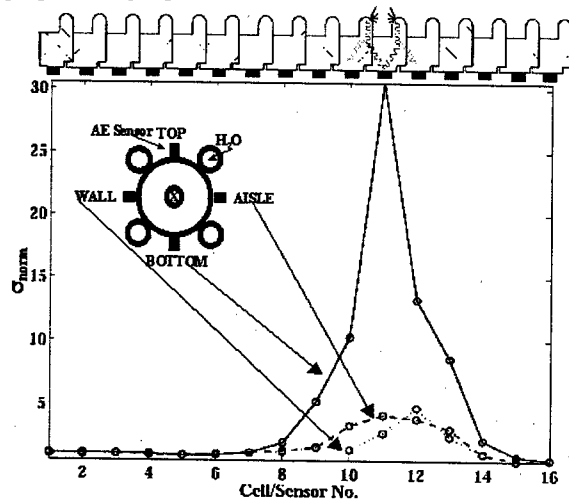
Figure 3: σ_{norm} for a typical multiple-iris event. The solid line connects data from 16 sensors, one per cell, in a row. Along the top is a schematic of the structure, showing the placement of the sensors between the irises as well as a possible path for the sound from the breakdown to travel. The inset shows the sensors mounted around a cell. Of note is the vertical scale: more than 30 times the energy deposited on a non-breakdown pulse is seen by one sensor.

Spitfests in X-band Structures

Another phenomenon seen during processing of the X-band structures in NLCTA is the so-called spitfest –when breakdowns are rare, but clustered in time. For example, there will be no breakdowns for more than 30 minutes, followed by many breakdowns in quick succession, less than two minutes apart. Some of these breakdowns occur at very low voltage. From a two week, steady-state running period with 288 breakdowns, 141 happened within two minutes of the previous event in 62 spitfest groups. Figure 4 below shows the locations of seven breakdowns that happened in one spitfest sequence.

This figure shows that subsequent breakdowns aren't confined to the same location as the first breakdown and actually vary their locations by more than just a few cells. This is inconsistent with the assumption that subsequent breakdowns happen near the surface damage caused by the first breakdown.

CONCLUSIONS

AES have proven uniquely suited to locating breakdowns in RF components. Two analysis techniques provide complementary information: relative signal power and signal timing. Using these two techniques, we have been able to diagnose many problems including particle contamination and high pulse heating regions as well as better understand the multiple-iris breakdown process in

X-band structures and the spitfest phenomenon seen during processing.
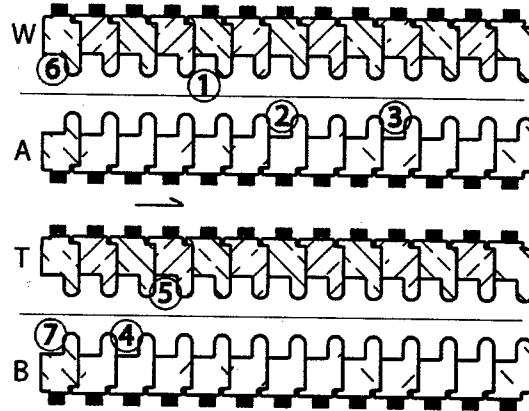
Figure 4: Sketch of a section of a 60-cell X-band structure showing the location of a series of breakdowns in a spitfest. The rows correspond to the rows of sensors on the structure: on the wall, aisle, top and bottom sides.

FUTURE PLANS

Future plans include adding another 80 sensors to give a total of 144. This should help better understand events with multiple breakdowns on one pulse. AES will also be used to diagnose breakdowns in high power components of the 8-pack RF distribution system installation.

ACKNOWLEDGEMENTS

REFERENCES

[1] P. Wilson, "Frequency and Pulse Length Scaling of RF Breakdown in Accelerator Structure," (2001) SLAC-PUB-9114.

[2] P. Wilson, "Gradient Limitation in Accelerating Structures Imposed by Surface Melting," TPAB039, this conference.

[3] J. Nelson and M. Ross, "Studies of TTF RF Photocathode Gun using Acoustic Sensors," (2001) SLAC-PUB-9340.

[4] S. Schreiber, et. al., "First Experiments with the RF Gun Based Injector for the TESLA Test Facility Linac," PAC'99, March 1999, New York, NY.

[5] C. Adolphsen, "Normal-Conducting RF Structure Test Facilities and Results," ROPC006, this conference.

[6] J. Frisch, et. al. "Studies of Breakdown in High Gradient X-Band Accelerator Structures using Acoustic Emission," (2002) SLAC-PUB-9469.

[7] V. Dolgashev, "Experiments on Gradient Limits for Normal Conducting Accelerators," LINAC 2002, August 2002, Gyeongju, Korea.

GRADIENT LIMITATION IN ACCELERATING STRUCTURES IMPOSED BY SURFACE MELTING*

Perry B. Wilson, SLAC, Stanford, CA 94309, USA

Abstract

A rough picture is beginning to emerge of the physics behind the maximum gradient that can be sustained in an accelerating structure without producing surface damage at a level sufficient to cause a measurable change in the rf properties of the structure. Field emission sites are known to trigger the formation of so-called plasma spots in regions of high dc or rf surface electric fields. A single plasma spot has a finite lifetime (~20–50ns) and leaves behind a single crater. In the rf case, some fraction of the electrons emitted from the spot pick up energy from the rf field and back-bombard the area around the spot. Depending on the gradient, pulse length and available rf energy, multiple spots can form in close proximity. The combined back-bombardment power density from such a spot cluster can be sufficient to raise the surface temperature to the melting point in tens of nanoseconds over an area on the order of 100 microns in diameter. This molten area can now support a plasma capable of emitting several kiloamperes of electrons with an average energy of 50–100kV. This is sufficient beam power to collapse the field in a travelling structure in 30 ns or so. The plasma also exerts a tremendous pressure on the molten surface, sufficient to cause a macroscopic amount of material to migrate toward a region of lower surface field. Over time, this process can modify the profile of the iris tip and produce an unacceptable change in the phase shift per cell.

FIELD EMISSION AS A TRIGGER FOR BREAKDOWN

Plasma Spots

The breakdown process begins with the formation of a plasma spot. In measurements on breakdown in a dc field, it is observed that a plasma spot forms only at a previously existing field emission site [1]. Some details concerning the formation and properties of plasma spots are given in [2]. A few of their properties are summarized here. Single dc plasma spots are usually roughly hemispherical in shape, although sometimes elongating toward a mushroom shape. A Langmuir sheath forms at the plasma–metal interface, forming a dc Child's Law diode that subjects the surface to an intense bombardment of ions from the plasma (energy ≈ 20 eV, current density $\approx 10^{12}$ A/m^2). This power density is sufficient to raise the temperature of the metal surface below the spot to the melting point in a nanosecond or so. The molten region expands to a diameter of 5–20 microns during the lifetime

of the spot (30–50ns), leaving behind a crater 'foot print'. The craters produced by spots in both dc and rf fields are remarkably similar, indicating that the physics of the formation and evolution of plasma spots is quite similar in both cases. In a dc field a single plasma spot emits an electron current of 5–50A and an ion current 10–20% of this. In the following, we assume a typical dc single spot current of of 20A.

Field Emission Model for Triggering Plasma Spots

The model assumes that the probability per unit time for triggering the formation of a plasma spot is a function of the field emission current, $I_{FE} \sim \exp(-C/\beta_{FE}E_s)$. Here E_s is the surface electric field, β_{FE} is the electric field enhancement factor at the field emission site and $C = 6.4 \times 10^4$ MV/m for copper. In recent measurements on dark current from traveling-wave (TW) accelerating structures at NLCTA, values for β_{FE} in the range $30 - 40$ have been obtained [3]. The field emission model next assumes that, with some probability, the formation of a plasma spot leads to a full breakdown event (defined by the collapse of the transmitted power in a TW structure). It is observed that the breakdown rate also follows an exponential dependence on $1/E_s$, but that the values for beta (β_{BR}) tend to be about $1/2$ β_{FE} [4]. This indicates that the probability for triggering a plasma spot varies as I_{FE}^2. This variation with current makes sense if adsorbed gas molecules are knocked off the surface by the intense electron back-bombardment near a field emission site, and the resulting gas is then ionized by the field emission current.

The probability of a breakdown per pulse at a fixed gradient will also be a function of pulse length. In our model, we assume this probability is proportional to T^m, where T is the pulse length. Here we will take m as a parameter to be fit by comparison with experiment (in [5] a physical model for m is developed). The net breakdown rate is given by $R = AT^m\exp(-C/\beta_{BR}rG)$, where r is the ratio of the surface electric field to the accelerating gradient. Now introduce normalized time and gradient variables defined by $\tau = T(A/R)^{1/m}$ and $g = Gr\beta/C$, giving

$$g = [m \ln(\tau)]^{-1} \qquad (1)$$

This can be compared with a variation of gradient vs. pulse length parameterized by $g = B/T^n$. By equating the values and derivatives of this expression and Eq. (1), we obtain

$$n = mg \qquad (2)$$

In recent measurements at NLCTA on H90VG3 (r = 2.3), values of β_{BR} = 20 and m in the range 3 to 4 were obtained for gradients in the range 64 to 80 MV/m [4]. Calculating the exponent n at the center of this range using Eq. (2), we obtain n = 0.18. This can be compared with a measured value n $\approx$ 1/6 = 0.17.

ELECTRON MOTION IN AN RF GAP

Particle motion in a gap between two parallel planes is an excellent model for the motion of electrons and ions emitted from a plasma spot in a low group velocity rectangular waveguide. The model is also better than might be expected for the motion of particles emitted near an iris tip in a disk-loaded accelerating structure. This is especially true for electrons that are emitted and then turn back to impact on the emitting surface. The low energy component of these back-bombarding electrons will travel out into the rf field by less than a millimeter. The local surface looks reasonably flat on this scale.

The equations of motion (non-relativistic) for an electron emitted with zero velocity from a plane at y = 0 at a phase angle θ_e with respect to the crest of an rf field with peak value E_0 are

$$y/\lambda = [E_0\lambda/(2\pi)^2 V_e] \, y_n; \quad v/c = [E_0\lambda/2\pi V_e] \, v_n \qquad (3)$$

where y is the distance from the emitting surface, v is the electron velocity, λ is the rf wavelength and $V_e = mc^2/e$ = 511 kV. The parameters y_n and v_n are a normalized distance and velocity given by: y_n = [cos θ_e − cos ωt − (ωt − θ_e) sin θ_e]; v_n = [sin ωt − sin θ_e]. The normalized trajectories for electrons emitted during the positive half of the rf cycle (θ_e = −π/2 to +π/2) are plotted in Fig.1. Electrons emitted in the phase range θ_e = −π/2 to 0 cross the rf gap and eventually hit the opposing surface, no matter how far away. A plane at y_n = 3, for example, corresponds to the distance from one iris tip to the tip of a neighboring iris in an 11.4 GHz, 2π/3-mode accelerating structure operating at a gradient on the order of 70 MV/m. However, the model is very crude in this case because of relativistic effects and the fact that the real field is far from uniform. Of more importance for our purpose here are the electrons emitted in the phase range θ_e = 0 to +π/2. All of these electrons return back to impact on the emitting surface if the normalized gap width is greater than y_n = 2. Electrons emitted at θ_e = 0 venture out to y_n = 2, then return to skim the surface with zero velocity at ωt = 2π. For a very narrow gap, however, most of the electrons in this phase range will impact the opposing surface. As an example, the line at y_n = 0.11 in Fig.1 corresponds to parameters for the "Windowtron" X-band cavity breakdown experiment [6] at SLAC, at a surface field of 500 MV/m (the gap width is 1.9 mm). Even for this narrow gap, a substantial fraction (about 15%) of the emitted electrons still return to the emitting surface to produce local heating near the plasma spot emitter. The velocity (and energy) of

these back-bombarding electrons can be calculated from the slope of the trajectories at y_n = 0.
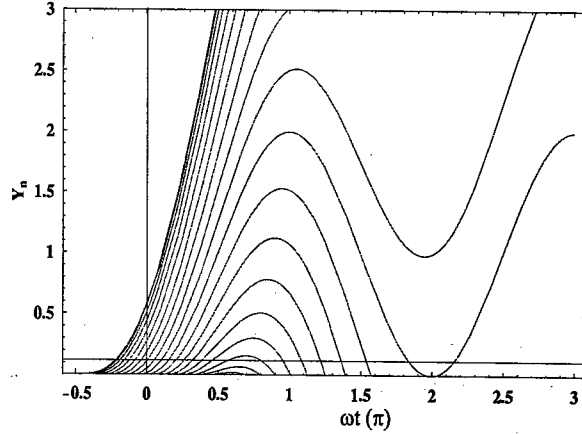
Figure 1: Normalized distance from the emission surface as a function of time for an electron emitted at at various phase angles in a parallel-plane rf gap.

SURFACE HEATING NEAR A PLASMA SPOT

Material Properties Related to Surface Melting

A complicating factor in calculating the temperature rise produced at a metal surface by the impacting electrons is the fact that these electrons can penetrate a substantial distance into the metal for typical impact energies. The penetration depth is given by [7],

$$X_P \, (\mu m) = .0276 \, (A/\rho Z^{0.89})[V(kV)]^{1.67} \qquad (4)$$

where A is the atomic mass, Z is the atomic number and ρ is the density in g/cm³. The energy deposited per unit length is a function that rises from zero at the metal surface, reaches a maximum at about one-half X_P, and then trails off toward zero above X_P. To a first approximation, we can assume that the energy is deposited uniformly to depth X_P and is zero beyond this. As energy is being deposited in the region up to X_P, heat is also flowing out of this region following the equation for heat diffusion. The equation can be solved analytically for the temperature as a function of X and t, but for our purposes here it will be useful to compute the temperature rise in two limits. In the heat diffusion limit, power is absorbed in a relatively thin region close to the surface. The diffusion depth as a function of time is $X_D(\mu m)$ = 1$\times$10⁴ (Dt)$^{1/2}$ where D = K/ρC_S is the diffusivity in cm²/sec, K is the thermal conductivity in W/cm–°C and C_S is the specific heat in J/gm–°C. The surface temperature rise is

$$\Delta T = (2P_A/\pi^{1/2}K)(Dt)^{1/2} \qquad (5)$$

where P_A is the incident power per unit area. In the second limit, we calculate the heating due to electrons that penetrate well beyond the heat diffusion depth, $X_P \gg X_D$. The temperature rise is

$$\Delta T = P_A t/(\rho C_S X_P). \qquad (6)$$

Some useful quantities for calculating material melting are given in Table 1. The last two columns compare the relative melting times in the bulk heating limit for 50 kV electrons, and in the diffusion limit at 30 ns. The actual melting times are given by $t_m = (1/P_A)T_P$ and by $t_m = (\pi/4 \ P_A{}^2)T_D$.

Table 1: Useful Quantities for Calculating Surface Melting

Metal	X_D at 30 ns (μm)	X_P at 50 kV (μm)	Relative Melt. Time T_P at 50 kV	Relative Melt. Time T_D at 30 ns
Cu	1.9	6.7	2.5	16 x 10⁶
Au	1.9	4.0	1.0	8.3
Mo	1.3	6.5	4.4	24
SS*	.04	7.3	4.1	1.2
W	1.4	2.1	1.8	38
Ta	0.8	4.5	3.1	11
Nb	0.8	7.5	4.2	7.2

*304 stainless steel

Surface Temperature Rise

The next step in the model is to calculate the temperature rise due to electron back-bombardment in the region of the plasma spot during a typical spot lifetime of 30 ns. We compare the temperature rise for a copper surface in the two limits discussed above: diffusive heating from low energy electrons that penetrate less than the diffusion depth, and bulk heating from higher energy electrons that penetrate deeper than the diffusion depth. Details of the calculation are given in an expanded version of this paper [5]. We assume a surface field of 150 MV/m at 11.4 GHz. For a typical plasma spot that emits 10 A of electrons during the positive half of the rf cycle, about 6 kW is absorbed in the 2 micron diffusion depth at 30 ns. We also need to know the spot area. Based on an estimate of the transverse velocity component of electrons emitted from the plasma we calculate an impact area of about 3×10^{-4} cm², giving a power per unit area of about 2×10^7 W/cm². Puting this value for P_A in Eq. (5) along with values of D and K for copper, we calculate a temperature rise of about 1000°C at 30 ns. The deeply penetrating back-bombarding electrons have an average energy of about 50kV and penetrate to an average depth of about 7 μm. The total power extracted from the rf field for these electrons is estimated to be about 400 kW. However they travel, on the average, several iris tip diameters away from the emission point and will return to the surface over

a much larger area. A crude estimate gives $P_A \approx 4 \times 10^7$ W/cm². Equation (6) then gives a temperature rise of about 500°C.

We conclude that, in a surface field of 150 MV/m, a single plasma spot can raise the temperature of a copper surface close to the melting point in 30 ns over a region 100–200 μm in diameter.

DISCUSSION

In the model presented above, it was shown that electron back-bombardment can produce substantial heating in the area around a single plasma spot. However, on all surfaces that have been exposed to high surface fields, a multitude of single craters (footprints of plasma spots) are observed with no evidence of surface melting in the surrounding area. This implies that, to produce such melting, a number of plasma spots must be present at the same time within an area on the order of 1×10^4 μm². In [5] it is shown how this might happen through the phenomenon of crater clustering. Once this area has been raised to perhaps twice the melting point (to produce a substantial vapor pressure), we propose that the plasma spots responsible for the melting then coalesce to form a plasma 'cloud' extending over the liquid region. In simulations, Dolgashev [8] has shown that this macroscopic plasma layer is capable of emitting kiloamperes of electrons and tens of amperes of ions. A full breakdown event then follows the formation of this plasma.

ACKNOWLEDGEMENT

REFERENCES

[1] N.S. Xu and R.V. Latham, "Electrical and spatial correlations between direct current pre-breakdown electron emission characteristics and subsequent breakdown events", J. Phys. D: Appl. Phys. 27, 2547 (1994).
[2] P.B. Wilson, "A Plasma Model for RF Breakdown in Accelerator Structures", *Proceedings of Linac 2000*, (SLAC-R-561, SLAC, Stanford, CA (2000) p. 618.
[3] Steffen Doebert, private communication.
[4] Calculated from data supplied by C. Adolphsen.
[5] P.B. Wilson, SLAC/AP–142, SLAC, Stanford, CA (2003). To be issued.
[6] L. Laurent, "A Study of RF Breakdown", Ph.D. Thesis (SLAC, Stanford, CA, 2002).
[7] Electron Microprobe Notes: Electron Interaction with matter, p.4 (http://jan.ucc.nau.edu/~wittke/Interact.html).
[8] Valery Dolgashev, private communication.

TRIUMF ISAC RF SYSTEM IMPROVEMENTS AFTER 2 YEARS OF OPERATIONAL EXPERIENCE

I. Bylinskii[#], Z. Ang, S. Fang, K. Fong, R. Kumaran, J. Lu, R. Poirier,
TRIUMF, 4004 Wesbrook Mall, Vancouver, Canada

Abstract

The TRIUMF ISAC accelerator has been successfully operating since spring 2001 with very little downtime. The machine comprises 16 independent RF systems including a 35 MHz RFQ, a 106 MHz DTL and several sub-harmonic choppers and bunchers. The post stripper DTL enables fully variable output energy up to 1.5 MeV/u for rare isotopes with A/q≤6 in cw mode. This sets rather stringent requirements for the RF system as a whole and the RF controls in particular. A new RF phase measuring system has been commissioned, which together with other modifications has improved machine tunability. During initial operation the DTL frequency tuners and power couplers showed some problems, which could affect the machine reliability. Modifications to these components together with additional diagnostics have solved these problems. In this paper we will describe the overall operation of the RF system and present details of the modifications.

INTRODUCTION

The first stage of a radioactive beam facility at TRIUMF, ISAC-1, was commissioned in 2001 and is routinely producing a variety of beams to low and high energy experiments [1]. The accelerator consists of a 35.36 MHz RFQ, which accelerates beams of A/q $\leq$ 30 from 2 keV/u to 153 keV/u, and a post stripper, 106 MHz variable energy drift tube linac (DTL) [2], comprising 5 interdigital-H accelerating and 3 split-ring bunching cavities to accelerate ions of 3 $\leq$ A/q $\leq$ 6 to a final energy between 0.153 to 1.53 MeV/u. A multi harmonic pre-buncher is part of the low energy beam transport (LEBT) section. The 106 MHz bunch rotator used for focussing, the dual frequency (5.89 and 11.8 MHz) chopper for 85 ns and 170 ns pulse separation, and the 35 MHz rebuncher for DTL matching are the rf structures which constitute the medium energy beam transport (MEBT). The high energy beam transport (HEBT) section consists of 11.8 MHz, low-β and a 35 MHz, high-β bunchers, which are required to maintain a good longitudinal emittance. The rf structures' parameters and commissioning details are reported elsewhere [3].

RESONATORS

Most of the rf structures have been reliably operated since commission with minor maintenance interventions. For example, the RFQ structure required a high power pulse conditioning twice a year to reduce the build up of dark currents. At the same time a lot of effort was

dedicated to the reliable operation of DTL rf amplifiers, couplers, tuners, problem troubleshooting and upgrades. Once a year all the DTL cavities were opened for inspection and assessed for problem. In the DTL tanks #3 and #4, soldering flux patches were observed around the nose cones (see Figure 1). This was traced to be a manufacturing defect, when the flux residuals were trapped in a pocket behind the nose cone and then came out during rf conditioning. Evaporating flux contaminated some critical rf surfaces, including rf coupler window, which eventually overheated and broke. A few attempts were required to clean off the flux residuals from the tank surface.

Figure 1. Soldering flux patch in DTL tank #4

In the beginning we also faced many interruptions caused by spurious vacuum interlock trips. Replacement of ion gauges, installation of screening grids and distancing the ion gauge from the cavity volume by means of extension pipes 200 mm long and 25 mm in diameter did not solve the problem. On the assumption that the problem was caused by a penetration of charged particles ionised and accelerated in the presence of an rf field, extension elbows were installed for all DTL ion gauges and the problem disappeared.

RF couplers

RFQ 150 kW coupler gave us troubles in the beginning due to uneven rf field gradient along a ceramic window, which eventually led to a ceramics overheating. Improved design incorporated cylindrical screening electrodes, which cured the problem. Smaller type (30kW) coupler, installed in most of the other rf cavities (11 units), did not suit such a modification. Over 2 years we had to replace 6

of those. In DTL buncher #2 a silver alloy evaporated from the coupling loop soldering joint (see Figure 2) and coated all the surfaces around including the ceramics (see Figure 3). Three other couplers failed in DTL tank #5 due to overheating, showing darkened ceramics with dramatically degraded isolation properties (DC resistivity dropped from few MOhm down to ~ 30 kOhm).

Figure 2. Buncher #2 coupling loop with a failed soldering joint.
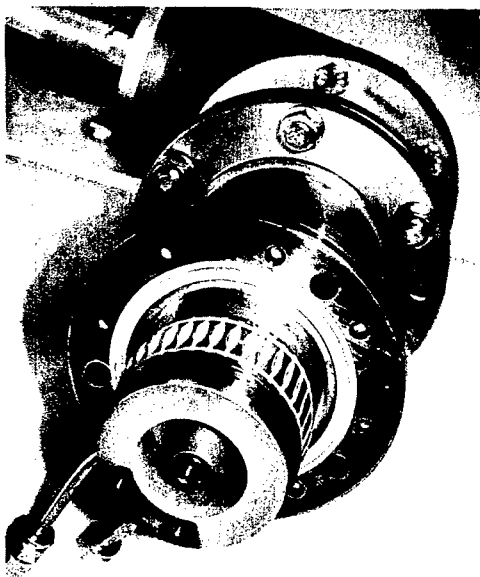
Figure 3. Buncher #2 coupler – silver spattered.

Test studies brought us to a conclusion that in most cases coupler coating is triggered by a secondary electron emission discharge (multipactoring). In DTL tank #5, for instance, it happened during abnormal operation of an automatic starting procedure. After its rf controls operational parameters were readjusted the failure never happened again. To reduce the coupler failure risk some other preventive measures were taken:

- All coupling loops were copper plated to eliminate the soldering alloy exposure to the rf field.

- All couplers were equipped with Omega OS36 infrared thermocouples, which are pointed on the ceramic window.
- High standing wave (VSWR) protection was introduced into rf controls .

An easy and economical restorative solution has been found for the degraded couplers. It involves an abrasive removal of the coating by means of a sand blaster. With this procedure 4 malfunctioning couplers were rebuilt to their original specifications. In future we plan to incorporate a multipactor sensor into coupler design.

Frequency tuners

All DTL systems use capacitive tuners driven by identical drives. The weakest point of this drive appeared to be the rf fingerstock contacts between the moving copper shaft and a ground housing. Inspection has shown almost all shafts being severely scratched with deep cuts. The most damaged MEBT rebuncher tuner shaft is shown in Figure 4.
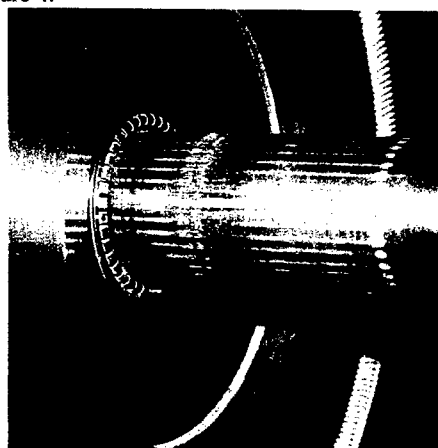
Figure 4. Damaged MEBT rebuncher tuner shaft

The reason for this failure is a constantly moving tuner, which operates in a feedback loop for frequency regulation. The fingerstock cannot stand that heavy load. Operating in vacuum without lubrication they get worn and start scratching the copper shaft. These contacts serve to shield a stainless steel bellow from rf currents, which could result in excessive heat on the bellow. An extensive design review and bench tests were undertaken, which led us to the conclusion that the fingerstock could be removed without causing excessive heat on the bellows. Bench tests showed that 25 W dissipated power caused a bellow temperature rise of up to 100°C without cooling, while application of air cooling allowed 100 W power dissipation with a moderate 40°C temperature rise. Full-scale test on DTL tank #5 confirmed our optimistic assumptions regarding operating the tuner without fingerstock. At a 20 kW power level the bellow temperature rose only by 6°C even without air-cooling. Following this positive outcome, we removed the fingerstocks from all DTL operational tuners.

1286

Subsequently all the modified tuners were equipped with thermocouples to ensure our control over bellow temperature. A few months of operation didn't show any noticeable degradation in system performance.

RF CONTROLS

Linac variable energy capability requires an amplifier operational range of 5 - 100% of output power. The DTL amplifier's phase shift is dependant on the output power and exceeded 45° for the full dynamic range. Since the frequency tuning control is achieved by monitoring the tank rf phase, this phase deviation caused intolerable detuning with power variation. Implementing of a phase compensation circuit, which uses amplifier output sample voltage to modulate the input signal phase, reduced the phase shift down to 5°.

Upgrade work has been done on the input circuits of the control modules in order to increase stability and reduce rf interference between subsystems. We have also completed the installation of all VSWR protection circuits in all the control modules.

All rf control computers have been upgraded from embedded Intel-486 processors to rack-mounted AMD K-7 processors and VXI IEEE-1394 slot 0 controllers, with increased RAM and hard drive capacities. Their firmware and software were upgraded for better flexibility, performance, and reliability. The DSPs are fitted with flash EEPROMs that enable their firmware to be upgraded remotely. The ADCs in the VXI mainframes are now cycled by separate threads, with better performance in the rate of data update.

Phase measuring system

An auxiliary phase measuring system has been developed for the ISAC rf system. It provides precise phase difference measurements between the reference rf source and each individual rf device. The need for this system comes from the operation of a multi-cavity variable energy linear accelerator, which dictates very high tolerance (fraction of a degree) for rf phase stability and reproducibility. The setup includes a frequency synthesizer, an rf switcher and a Hewlett Packard vector voltmeter. The synthesizer is driven by a 5.89 MHz ISAC rf controls reference signal and provides all ISAC rf system harmonics: 5.89, 11.78, 23.57, 35.36, 106.08 MHz with a very good stability (0.2°) with respect to the reference signal. Rf MUX connects voltmeter to the desirable rf cavity and corresponding frequency multiple harmonics from the synthesizer. MACOM SW221 rf switches provide 100% reproducible connection and –75 dB isolation between channels. Vector voltmeter measures amplitudes and phase difference between 2 rf signals of the same frequency. Voltmeter phase resolution is about 0.1°. All the rf signals are canalized through semi-rigid phase stable cables in order to reduce temperature dependence and dielectric aging effect. All hardware was tested and calibrated. An EPICS based control system for this device is being commissioned. In the manual mode this system has already helped us in the troubleshooting of beam instabilities.

AMPLIFIERS

All the DTL rf systems are energized by identical 106 MHz amplifiers based on an EIMAC 4CW25000B tetrode as the final amplifier. Last year most of tubes had reached 10000 hours of operation and a substantial degradation in their performance was observed. One tube showed a grid to cathode short, a filament burnt in another one, and 4 more aged, providing low cathode emission. Five tubes out of 8 tubes in operation had to be replaced. This triggered a detailed investigation on the tube performance. Two major conclusions were derived as a result.

- Hairpin filament structure in a tube of different type 4CW25000A is almost insensitive to thermal deformation, while the tube is warming up, compared to the mesh filament structure (4CW25000B). So application of a type-A tube dramatically cuts down the downtime for system conditioning and reduces the probability of a thermal grid-to-filament short circuit.

- Most of the tubes were running at slightly increased filament voltage, which is good for tube conditioning but not for operation. The supplier claims a 15% reduction in filament voltage should double the tube lifetime.

Based on these findings we decided to gradually replace all B-type tubes in use to A-type tubes. Also, all filament transformers were replaced with new ones with proper voltage taps and all filament operational voltages were reduced by 15% from the nominal values.

Annoying problems were experienced with amplifier screen power supplies. These were commercial switching regulators and their designs were prone to RF interference and were unable to handle transient loads. These had resulted in many spurious amplifier trips. All these power supplies have been replaced with unregulated ones that are more immune to RF interference.

CONCLUSION

The extensive study and upgrade activities performed for the key rf system elements allowed high machine availability (above 90%) and ensure an improved reliability for the future.

REFERENCES

[1] R.E. Laxdal, "ISAC-I and ISAC-II at TRIUMF: Achieved Performance and New Construction", Proc. of the XXI-st Linac Conf. (LINAC2002), Gyeongju, Korea, Aug. 2002

[2] A. K. Mitra et al, "RF Measurement Summary of ISAC DTL Tanks and DTL Bunchers", Proc. of the 2001 Part. Acc. Conf., Chicago, 2001, p. 951.

[3] K. Fong et al, "Commissioning of the TRIUMF ISAC RF System", Proc. of the 2001 Part. Acc. Conf., Chicago, 2001, p. 945.

RF ACCELERATING SYSTEM AT HIRFL-CSR MAIN RING

Wenzhi Zhang, Zhe Xu, Xiaodong Yang, Hongwei Zhao, Wenlong Zhan
Institute of Modern Physics, Chinese Academy of Sciences, Lanzhou 73000 China

Abstract

A heavy ion cooler-storage ring HIRFL-CSR[1] has being constructed at IMP. It consists of a main ring (CSRm) and an experimental ring (CSRe). Two RF cavities will be employed for CSRm. One is for beam acceleration, and another is for beam RF stacking. The accelerating cavity is designed to accelerate the beam from 10-50MeV/u to 400-900MeV/u with harmonic number h=1. The peak RF voltage is 8.0kV and frequency range is from 0.25 MHz to 1.7 MHz. The RF stacking cavity with maximum voltage amplitude of 20kV and tunable frequency range 6.0-14.0 MHz is used to capture the injected bunches from injector SSC (or SFC) and to accumulate the beam to high intensity by RF stacking method. In the present paper, the measured RF parameters and the details of hardware for the RF accelerating system are described.

MAIN RF ACCELERATION PARAMETERS

The specifications for RF acceleration system of CSRm ring are shown in Table 1.

Table 1: RF Accelerating parameters

Injection Energy	10-25 MeV/u
Acceleration energy	900 MeV/u
Momentum spread at injection	$< \pm 0.15\%$
Harmonic Number	1
Acceleration frequency	0.25-1.7 MHz
Maximum RF acceleration voltage	8.0 kV

The Lowest injection energy is 10 MeV/u for $^{238}U^{72+}$ ions among various ions from the injector SSC (or SFC), corresponding to the revolution frequency 0.25 MHz. At the top energy of 900 MeV/u for $^{12}C^{6+}$, the revolution frequency is 1.7 MHz. The harmonic number 1 will be employed to accelerate the ions thus the RF frequency should cover the frequency range from 0.25 MHz to 1.7 MHz. The Maximum acceleration voltage of 8.0 kV is needed for the beam acceleration with $\pm 0.15\%$ momentum spread within acceleration period of 3.0s.

RF CAVITY

The RF cavity has a single-accelerating-gap structure, which consists of two ferrite-loaded quarter-wave coaxial resonators (Fig.1).

We selected the ferrite material 600HH for cavity. The dimension of ferrite rings is 480mm in outer-diameter, 300 mm in inner-diameter and 20 mm in thickness. The ferrite rings are assembled in 4 stacks, 2 stacks for each of the two halves. Totally, 80 pieces of ferrite disks are stacked in whole cavity. Two bias windings had be made, one for two stacks of the cavity. Every winding will have 12 sections, 8 turns in each section. Ends of each turn go outside the cavity wall and are accessible. It is possible to connect the turns in series, in parallel or mixed connection depending on available power supply for biasing of for other consideration. The magnetic permeability can be varied from 600 to 12. There is a margin of 20% for biasing current to compensate for temperature and other instabilities. Maximum value of RF voltage at the winding is lower than 2.5 kV.

The space between electrical conductors of the cavity is filled with silicon hermetic of VIKSINT type. It provides mechanical and electrical stability, better conditions for cooling, and excellent insulation of elements at a high RF electric field.
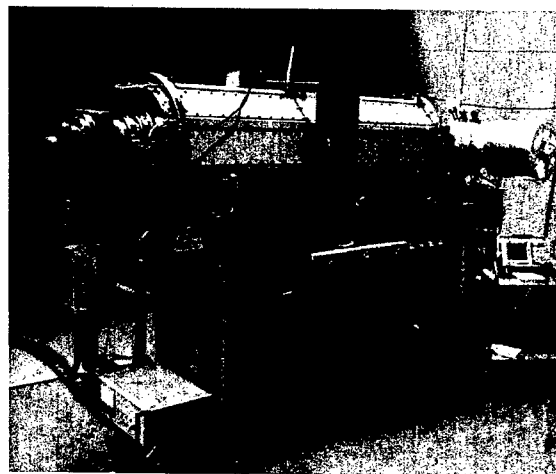
Fig.1 HIRFL-CSR Main ring accelerating cavity

LOW LEVERL RF SYSTEM

The low-level RF electronic system is composed of a Direct Digital Synthesizer (DDS) as the master oscillator and several feedback loops (Fig.2). Three memory modules store the ramping data: frequency, acceleration voltage and bias current as functions of bending-magnet field strength. These pre-set data are put into the DDS, magnitude modulation and bias current power supply respectively. The bias current error obtained from RF signal phase detector which get the deviate of the RF cavity by comparing the plate's and the grid's sampling signal will be used to correct the deviation of the cavity through the auto frequency control (AFC).
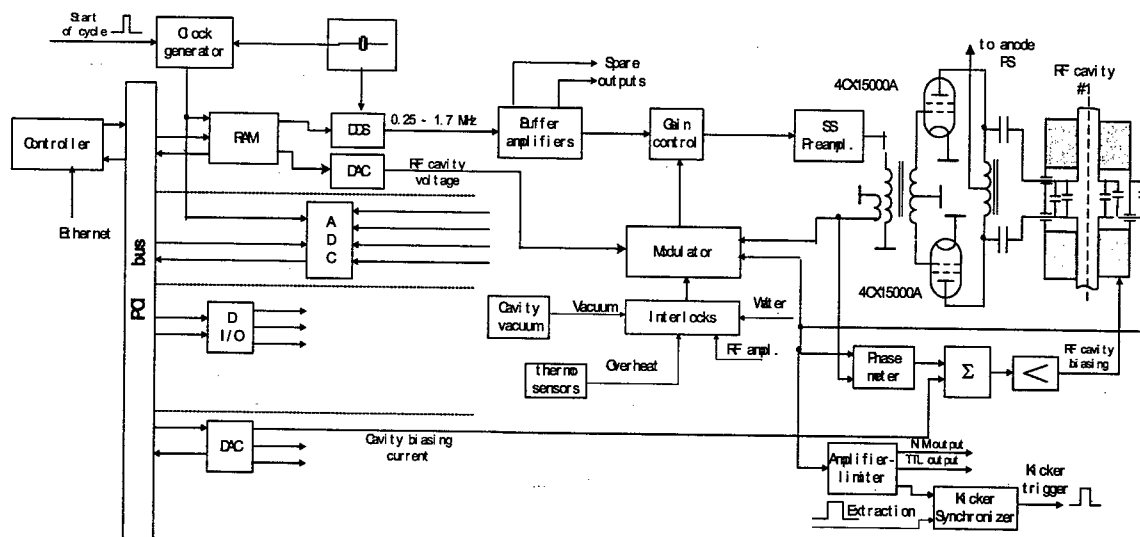
Fig.2 Block Diagram of RF control system for CSR Main Ring accelerating cavity

RF signal control unit is developed as PCI bus based modules. All these modules are independent sub-system, which have their own MCU.

DDS Circuit

The RF signal process applys the advanced DDS plan. The AD's AD9832 is functioned with the 16BIT processor in parallel connect mode to achieve high synthesis updating of signal. The local control processor sends data to DDS chip to release the RF signal. At mean time DDS receives the information from the control system to adjust the outputting frequency.

Phase Loop

Phase loop is used to compensate the deviation between the DDS and cavity voltage, achieving phase lock among RF cavity voltage and cavity voltage phase. All sample signals serving above units come from one identical detector; each of them has its own isolator to proof interference.

Bias Current Control Loop

The signal of V/F converted from the DDS synthesis's RF signal or the signal of D/A converted directly from digital data applying to DDS input is put to FREQ/RES adjusting unit to control the bios current. The offset value from MCU and the signal from phase discriminating between the cavity voltage and grid of the final stage power amplifier are also fed into this unit. The FREQ/RES correction must be a real time analogy circuit to dynamically tune the cavity. The signals after F/V converter that represents the changing of the frequency add one from the phase discriminator. The sum is put into the bios current driver to control the saturation of the ferrite so as to tune the cavity.

MCU/DAC 's data compensates the nonlinear relation between the bios current and the permit of the ferrite and offsets the bios current's initializing value.

RF Frequency Control Loop

RF system requires frequency resolution be less than 100Hz, frequency stability less than 10^{-5} thus requires non less than 16Bits control word and less than 1us update rate of frequency sweeping. The digital dividing PLL may meet the requirement, but it update speed is determined by the frequency resolution. The fact is that the higher the frequency resolution the lower the updating speed. This is determined by the LPF of the PLL loop. Furthermore at high dividing rate 1/N requiring by large frequency range, the loop gain drops to 1/N to damage the loop stability, at this situation the high stability power supply is needed to meet the critical requirement. The advanced DDS tech can resolve this problem.

Applying 16Bit/32Bit MCU or PLD to control the DDS RF signal processing circuit to attain high speed and real time control. 16Bit of amplitude data are also applied to amplitude modulation unit, which also serves as amplitude stability control to achieve 10^{-2}-10^{-3} rates. The bios current data supplying by MCU are converted by DA to feed into the bios current power supply which actuating the coil. Bios current error derived from the deviation of cavity's resonance and DDS frequency tunes the cavity through AFC. MCU connected with PCI bus receives the control word. All DAC and ADC are high-speed products.

The connection between the RF and CSR control bus applies PCI function module and particular parameter and timing network.

TESTING RESULTS

The acceptance testing had been made according to operating cycle of $^{12}C^{6+}$ being accelerated from 25 to 900 MeV/u and $^{238}U^{92+}$ from 10 to 450MeV/u. The maximum RF voltage of 8.25 kV had been obtained in the designed frequency range of 0.25 – 1.7MHz.

REFERENCES

J. W. Xia et al. "HIRFL status and HIRFL-CSR project in Lanzhou". APAC'98, KEK, Tsukuba, Japan, March 1998.

MICROPHONICS MEASUREMENTS IN SRF CAVITIES FOR RIA

M.P. Kelly, K.W. Shepard, M. Kedzie, J.D. Fuerst, S. Sharamentov
ANL, Argonne, IL, 60439, USA
J. Delayen
Thomas Jefferson National Accelerator Facility (JLAB)

Abstract

Phase stabilization of the RIA drift tube cavities in the presence of microphonics will be a key issue for RIA. Due to the relatively low beam currents (≤ 0.5 pmA) required for the RIA driver, microphonics will impact the rf power required to control the cavity fields. Microphonics measurements on the ANL $\beta=0.4$ single spoke cavity and on the ANL $\beta=0.4$ two-cell spoke cavity have been performed many at high fields and using a new "cavity resonance monitor" device developed in collaboration with JLAB. Tests on a cold two-cell spoke are the first ever on a multi-cell spoke geometry. The design is essentially a production model with an integral stainless steel housing to hold the liquid helium bath.

INTRODUCTION

The 400 superconducting (SC) cavities needed for the RIA driver linac[1] and spanning the velocity range $0.02 < \beta < 0.84$ will require a method for compensating for the rf eigenfrequency shifts induced by microphonics. A solution for cavities with frequencies up to 97 Mhz has operated for years in the form of the VCX (Voltage Controlled Reactance). Another established technique overcouples to the cavity using the rf drive probe and uses negative phase feedback to control the cavity fields[2]. Recent results from DESY using a fast piezoelectric tuner[3] suggest that the effects of microphonics may be compensated for without detuning the cavity, possibly resulting in much reduced rf power requirements.

These tests represent the first microphonics measurements on a realistic production model RIA drift-tube cavity. Two-spoke tests were performed horizontally with separate cavity and insulating vacuum spaces, a fully integrated stainless steel jacket for the helium bath and a variable rf power coupler. An understanding of microphonics will be crucial for the proper choice of slow and fast tuner design.

RF INSTRUMENTATION

Microphonics in the single-cell $\beta=0.4$ spoke cavity and the two-cell spoke cavity have been measured using two techniques based on largely independent sets of electronics. One method uses a standard phase-locked loop (PLL) circuit where the phase of an external signal generator is locked in quadrature to the cavity rf phase by means of a feedback or "error" signal. In the second method the cavity is run in a self excited loop and the cavity rf frequency is compared directly to that of a low

noise external generator using a device developed together with JLAB and referred to as a cavity resonance monitor[4] (CRM).

It is critical that such measurements be performed with a low phase noise signal generator since noise in the generator is difficult to distinguish from microphonics. Measurements here were performed with an Agilent 8665B in low noise mode and having less than 1 Hz rms frequency jitter for modulation frequencies in the range of interest. All results here are for the cavities in cw operation, though the CRM may be used during pulsed operation since it is designed to be insensitive to the input signal amplitudes.

MEASUREMENTS

Probability densities for rf eigenfrequency shifts are shown in Figure 1. for the two-cell spoke cavity at T=4.2 K and $E_{ACC}=1$ MV/m. Each data set contains 100 seconds of data. Measurements were first performed based on the phase-locked loop (PLL) error signal and then for comparison performed 5 minutes later using the cavity resonance monitor (CRM). Consistently good agreement between the PLL and CRM measurements is seen. The rms frequency jitter shown here at low field levels is 2.8 Hz.
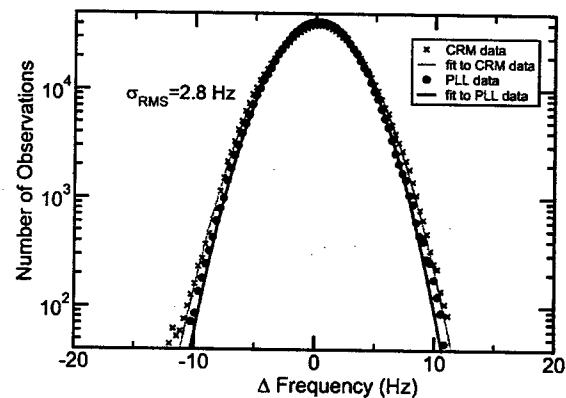
Figure 1. Two methods for measuring rf eigenfrequency shifts (see text) in the two-cell spoke cavity due to microphonics.

The present baseline design for the RIA driver linac calls for operation of the drift-tube cavities at a peak surface electric field 21 MV/m. This corresponds to 6 MV/m accelerating field in the two-cell spoke cavity. Measurements of microphonics levels in the two-cell

spoke cavity have been performed at fields equal to and above this design value.

Figure 2. compares a low field measurement together with a measurement performed at an accelerating field of E_{ACC}=7 MV/m. The input rf power for the two cases is 300 mWatts and 15 Watts respectively. The increase in eigenfrequency excursions by roughly a factor of two for the high-field case is due mostly to low frequency vibrations below about 15 Hertz and may be related to heat dissipation in the helium bath.
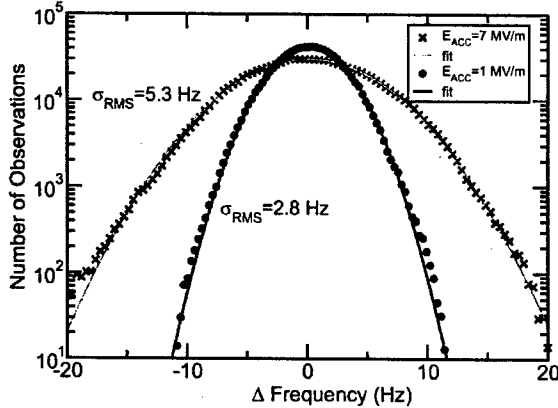
Figure 2. Probability density for double spoke eigenfrequency deviations for cw operation at E_{ACC}=7 MV/m (broad curve) and E_{ACC}=1 MV/m (narrow curve).

The Fourier spectrum of the error signal for the data where E_{ACC}=7 MV/m is shown in Figure 3. The x-axis gives the cavity vibration frequency while the y-axis gives the peak frequency shift in the cavity resonant frequency due to cavity vibrations.
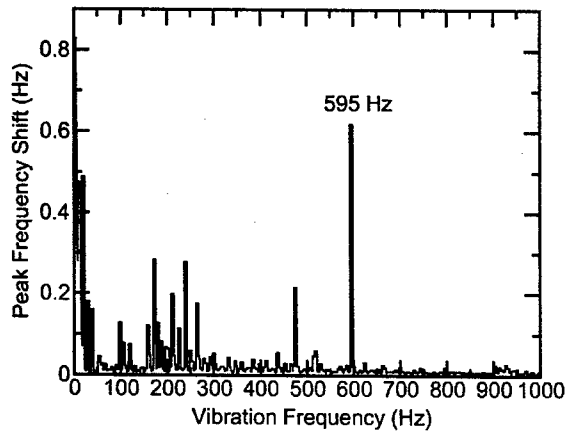
Figure 3 . Frequency spectrum for vibrations in the two-cell spoke cavity running cw at E_{ACC}=7 MV/m.

The peak in Figure 3. at a vibrational frequency of 595 Hz represents the largest contribution to eigenfrequency shifts due to excitation of a natural mechanical mode of the cavity, however, it contributes less than 0.5 Hz rms to the 5 Hz rms total shake. This compares favorably elliptical-cell structures even when structurally reinforced

which typically still have mechanical modes lying well below those observed here. Further analysis of the natural cavity modes using accelerometer measurements and additional finite element analysis calculations is being performed.

Based on measurements like those shown in Figure 3. most of the remainder of the 5 Hz rms cavity shake at E_{ACC}=7 MV/m is due to relatively low frequency oscillations likely from the coupling of pressure changes in the helium bath to the cavity rf eigenfrequency. The dominance of low frequency (helium) vibrations is clearly demonstrated in Figure 4. which shows the integrated total vibration below a given vibrational frequency*. The curve has been normalized to unity for high vibrational frequencies. Clearly 95% of the total amplitude for eigenfrequency excursions is due to vibrations at frequencies below 15 Hz. The two-cell spoke cavity sensitivity to pressure changes in the helium bath has been measured to be +65 Hz/Torr so that the corresponding pressure changes in the helium bath giving rise to the 5 Hz rms shake are likely of the order of 10-100 mTorr. Additional measurements to measure the bath pressure fluctuations directly will be performed.
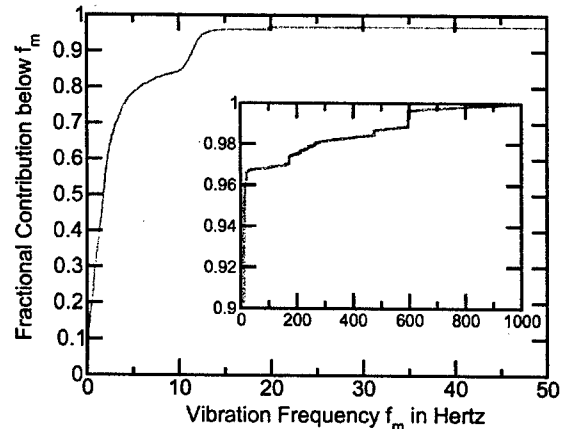
Figure 4 Fractional contribution to the total cavity shake from vibrations at and below the frequency f_m. The inset shows the same curve extended to vibrational frequencies up to 1 kHz. The result is based on the same data as used for Figure 3.

Measurements of the static field Lorentz detuning of the single-cell and two-cell spoke cavities have also been measured as a function of accelerating field gradient as shown Figure 5. Measurements for the spoke cavities were performed with all ports unconstrained and give detuning coefficients of –2 and -3.5 Hz/(MV/m)^2 for the double and single-cell cavities respectively. This indicates that the spoke geometry is roughly an order of magnitude more rigid with respect to Lorentz detuning than a typical unconstrained elliptical cell structure constructed from similar thin wall niobium.

---

* Note that Figure 3. is an amplitude spectrum and must be converted to a power spectrum before integration.

The lower detuning coefficient for the two-cell cavity compared to the single spoke is probably due to the added stiffness of the stainless steel jacket in the former. A given amount of deformation in the end wall of the two-cell cavity will also tend to shift the frequency less than in the single spoke cavity because of the relatively higher stored energy. The single spoke is a bare niobium cavity. Indeed, the frequency shifts induced in the two cavities from pressure changes in the helium reservoir ($\Delta f/\Delta p$) also differ by a factor of two although the shifts are in opposite directions. The values are +55 kHz/atm. and −120 kHz/atm. for the double and single spoke cavities respectively. The difference arises primarily from the different reinforcements on the cavity end walls.
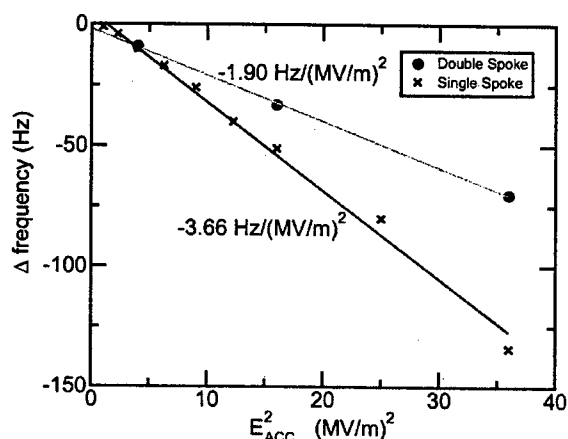
Figure 5 Static field Lorentz force detuning for the single spoke cavity (crosses) and the two-cell spoke cavity (circles) as a function of the square of the accelerating gradient. All ports are unconstrained.

DISCUSSION

The two-cell spoke resonator forms a section of the baseline RIA driver linac where beam loading requirements will already require fairly large rf amplifers. For example, assuming the two-cell spoke is operating at E_{ACC}=7 MV/m and with an effective accelerating length of 39 cm then each cavity provides nearly 3 MV of accelerating potential. The RIA driver baseline proposal calls for 0.5 mA of protons implying beam loading of roughly 1.4 kW per cavity.

Beam loading power may be compared to the additional amount of rf power required to control the cavity fields by overcoupling and assuming the same microphonics levels observed here. An estimate of that power is given by the expression $P = \delta\omega \cdot U$, where $\delta\omega$ is the required tuning window and U is the stored energy of the cavity at the operating field. Assuming σ_{RMS}= 5 Hz and allowing a window of $\delta\omega = 6 \times \sigma_{RMS}$ then the power required required for phase stabilization is roughly 1.4 kW based on the measured cavity stored energy of U_o=0.146 J at E_{ACC}=1 MV/m. In this case rf power requirement needed to compensate for microphonics would roughly double that needed due to beam loading alone.

It is likely that a further reduction in the cavity frequency response to pressure will be achieved through fairly minor design revisions. Even for the present case it will be possible to phase stabilize the cavity fields with presently available rf power of several kilowatts. Such tests will be performed shortly.

CONCLUSION

Microphonics tests on the first multi-cell spoke geometry have been performed in a realistic accelerator conditions on a two-cell spoke cavity with full helium jacket and movable coupler all in a horizontal test cryostat. Results show that the spoke geometry is rigid with respect to microphonics showing only 5 Hz rms shake at an accelerating field of E_{ACC}=7 MV/m. Vibrations of the natural mechanical modes contribute very little to the shake which is due mostly to low frequency pressure changes in the helium bath.

ACKNOWLEDGEMENTS

REFERENCES

[1] K.W. Shepard, in Proceedings of the 21st LINAC Conference, August 19-23, 2002, Gyeongju, Korea, (2002).

[2] J. Delayen, in Proceedings of the 2001 Particle Accelerator Conference, June 18-22, 2001, p. 1146, Chicago, IL (2001).

[3] L. Lilje, S. Simrock, D. Kostin, in Proceedings of EPAC 2002, June 3-7, Paris, France, (2002).

[4] G. Davis, J. Delayen et al., in Proceedings of the 2001 Particle Accelerator Conference, June 18-22, 2001, p. 1152, Chicago, IL (2001).

SUPERCONDUCTING 345 MHZ TWO-SPOKE CAVITY FOR RIA

J.D. Fuerst, M. Kedzie, M.P. Kelly, K.W. Shepard
ANL, Argonne, IL, 60439, USA
E. Peterson, Advanced Energy Systems

Abstract

This paper reports development of a two-cell 345 MHz spoke-loaded superconducting cavity intended for the U.S. RIA Project driver linac. The 3 cm aperture cavity has a useful velocity range 0.3c < v < 0.6c. In initial tests at 4 K the prototype cavity operated cw at peak surface electric fields as high as 40 MV/m, and with 20 Watts of rf input power provides 3 MV of effective total accelerating voltage. As constructed, the niobium cavity shell was fully housed in an integral stainless-steel helium vessel using pure copper braze joints at the niobium to stainless-steel transitions.

1 INTRODUCTION

A superconducting (SC) multi-ion driver linac for the RIA project will consist of nearly 400 SC cavities of several types which span the velocity range $0.02 < \beta < 0.84$. This paper reports the first cold test results on one of these cavities, a fully jacketed two-cell spoke cavity with geometric $\beta = 0.4$. This represents the first test of a multi-cell spoke cavity and continues the development of spoke cavities that began with 350 MHz single-spoke cavities of $\beta = 0.29$ and $\beta = 0.4$ successfully tested at ANL previously[1-3]
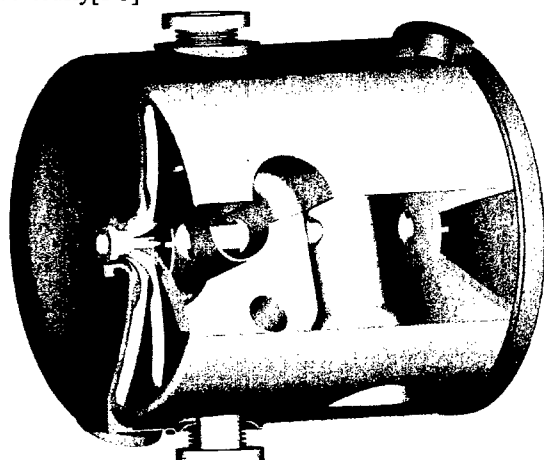
Figure 1: Cut away view of a 345 MHz two-cell spoke cavity. The niobium housing diameter is 48 cm and the active length is 39 cm.

2 FABRICATION

The major niobium components of the two-cell spoke resonator were formed from 3 mm RRR=250 niobium sheet. The transverse spoke elements were die formed in halves (Advanced Energy Systems). The niobium housing was rolled from flat 3 mm sheet. The spherical end walls were die-formed and then stiffened with 12 radial gussets cut from 6.25 mm niobium sheet. The dies constructed would be entirely suited for a production run. Existing dies for the two-cell spoke cavity are suitable for mass production for RIA.

The integral stainless steel helium jacket, shown partially cut away in Figure 1, was rolled from 3mm sheet while the end walls were machined from plate stock. Liquid helium can circulate in the annular space, of about ½ inch, between the niobium cavity and the stainless steel jacket. A niobium to stainless steel transition, using a pure copper braze, was used for the two axial beam ports, of 3 cm diameter, and the three radial coupling ports, of 5.08 cm diameter.
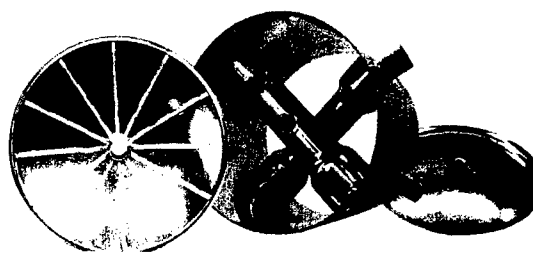
Figure 2: Three pieces of the two-cell spoke cavity after receiving a heavy electropolish.

3 CAVITY TESTING

3.1 Surface Processing

The cavity has no access ports sufficiently large to permit electropolishing of the completed cavity. To enable adequate surface processing while minimizing surface roughness, the niobium elements of the cavity as shown in Fig. 2 were initially processed just prior to the final closure EB welds by a heavy electropolishing which removed 100~150 microns of niobium. The completed cavity was then finally processed by a light, ~10 micron, chemical polish in a solution of 1:1:2 BCP at T = 15 C to remove possible weld residue. This technique greatly reduces the surface roughness that would result from a heavy BCP alone. Following the BCP, the cavity was rinsed and filled with clean deionized water.

The ANL high-pressure rinsing system, consisting of a high-pressure pump and an automated spray wand, was used to remove particulates from the interior cavity

1294

surface prior to final assembly into a test cryostat. The rinsing system supplied 15 liters per minute of ultrapure deionized water through eight 6.1 mm diameter jets at a nozzle pressure of 115 bar. The cavity was rinsed for 80 minutes in a curtained clean room while moving the spray wand in and out along the beam axis several times.

3.2 Clean Assembly

A horizontal test cryostat was built for the two-cell cavity incorporating the following features:

- A cleanable, low-particulate, variable 7 kW rf coupler.

- Clean room assembly of the cavity and rf coupler, the cavity vacuum being sealed prior to installation into the cryostat (See Figure 4.)

- Separate cavity and cryogenic vacuum spaces to maintain cavity cleanliness

- A dedicated connection to the existing ATLAS He refrigeration system which enables long-term tests

- A 7 kW cw 345 MHz rf power source which enables pulse-conditioning and also overcoupling to maintain phase control in the presence of microphonic- induced frequency fluctuations.

3.3 Cold Tests

Tests following the first cooldown to 4.2 K were performed with up to 5.5 kW of rf power for pulse conditioning of surface emitters at the higher fields. The observed Q for low fields was $\approx 1.3 \times 10^9$ corresponding to a residual surface resistance R_S of 17 nΩ. BCS resistivity contributes 38 nΩ at this frequency and temperature. Following rf pulse conditioning, stable cw accelerating

Table I. RF parameters for the β=0.4 two-cell spoke

	Calculated	Measured
frequency	347.072 MHz	347.623 MHz
Active Length =	-	39 cm
β_{Geom} =	0.393	0.393
QR_S =	71	-
U_o^* =	151 mJ	147 mJ
E^*_{peak} =	3.47 MV/m	-
B^*_{peak} =	69 G	-
*At an accelerating field of 1 MV/m		

fields of E_a=11.5 MV/m were reached as shown in Figure 3., which correspond to a peak surface electric field of E_{peak}=40 MV/m. RF parameters for the two-cell spoke cavity are shown in Table I.

Electron loading was observed first at accelerating fields around 5 MV/m as evidenced by x-ray emission, but was reduced by conditioning for with short duration (~10 ms) high-power pulses and with the cavity strongly overcoupled. After several hours of conditioning, no further reduction of electron loading could be obtained.

Figure 4: Clean room assembly of a horizontal test cryostat for the two-cell spoke cavity. The system incorporates separate cavity and cryostat vacuum systems to enhance cleanliness.

Figure 3: The first cold test results of a two-cell spoke cavity at 4.2 K following high-pressure rinse, clean assembly and high-power rf pulse conditioning
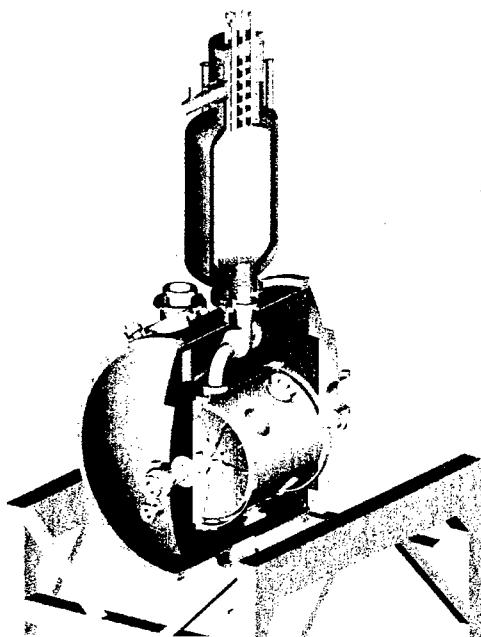
Figure 5: The horizontal test cryostat for the to-cell spoke cavity with separate vacuum systems for the cavity interior and the cryogenic insulating vacuum

3.4 Horizontal Test Cryostat

The present series of tests represent the first tests of a fully-featured SC drift-tube cavity suitable for the RIA linac operated on a refrigerator in a realistic accelerator environment. The two-cell cavity has been tested oriented horizontally as shown in Figure 5. and uses a stainless steel jacket fully integrated with the niobium cavity to house the liquid helium bath. A movable high-power rf coupler was assembled in a clean room together with the cavity and is an integral part of the separate cryostat and cavity pumping systems required to maintain cleanliness for long term operation at high fields.

4 CONCLUSION

The first two-cell spoke loaded SC cavity, which operates at f_o=345 MHz and has β_{opt}=0.4, has been successfully tested at cw accelerating fields up to 11.5 MV/m (E_{PEAK}=40 MV/m). Surface processing using a combination of electropolishing, chemical polishing, and high-pressure rinsing has resulted in a low level Q of 1.3×10^9 at 4.2 K, implying a residual surface resistance of 17 nΩ. As tested, the resonator is in a 'fully dressed' form with forming dies and fabrication techniques suitable for production for the RIA driver linac.

5 ACKNOWLEDGEMENTS

6 REFERENCES

[1] M.P. Kelly, K.W. Shepard, M. Kedzie, G. Zinkann, in Proc. 2001 Particle Accelerator Conf., June 18-22, 2001, Chicago, IL (2001).

[2] T. Tajima et al., Proc. Workshop on Spoke Cavities, http://lib-www.lanl.gov/documents/g/00796120.pdf

[3] K.W. Shepard, M.P. Kelly, M. Kedzie, T. Schultheiss, in Proc. 2001 Particle Accelerator Conf., June 18-22, 2001, Chicago, IL (2001).

SUPERCONDUCTING INTERMEDIATE-VELOCITY CAVITY DEVELOPMENT FOR RIA

K.W. Shepard, M.P. Kelly, J.D. Fuerst, M. Kedzie, ANL, Argonne IL 60439, USA

Abstract

This paper discusses the design and development of two types of intermediate-velocity superconducting cavity and an associated cryomodule for the RIA driver linac. The two cavity types are a 115 MHz, β_{GEOM} = 0.15 quarter-wave resonant (QWR) cavity, and a 173 MHz, β_{GEOM} = 0.26 coaxial half-wave cavity. The useful velocity range of the two cavity types extends from 0.1 to 0.4c. Both cavities are well-corrected for dipole and quadrupole asymmetries in the accelerating field. A cryomodule is being designed to incorporate a separate vacuum system for the cavity vacuum in order to provide a clean, low-particulate environment for the superconducting cavities. This will enable a higher degree of surface cleanliness than has previously been the case for TEM-type, drift-tube-loaded superconducting cavities. The status of prototype cavity and cryomodule construction are reported.

INTRODUCTION

The proposed U.S. Rare Isotope Accelerator (RIA) requires a driver linac formed of several hundred superconducting rf cavities of several different types to span a velocity range $0.02 < \beta < 0.9$. The driver will accelerate uranium ions to 400 MeV/nucleon, and protons to energies of 900 MeV [1].

Existing superconducting RF (SRF) technology is available for both the low-velocity and high-velocity sections of the driver linac. The low-velocity section is formed of cavities similar to the quarter-wave structures in existing heavy ion linacs[2], while the high-velocity section can employ 805 MHz elliptical-cell cavity technology existing already developed at JLAB for the SNS project[3]. The cavities described in this paper fill an intermediate velocity range $0.1 < \beta < 0.4$. They are being designed to be processed with high-pressure water rinse cleaning techniques and to operate in the clean environment supported by separating the cavity and cryogenic vacuum systems.

CAVITY PRODUCTION

Electrical and Mechanical Design

Figure 1 shows the geometry of the two cavities, while Table 1 lists the calculated electromagnetic (EM) parameters. Pro/Engineer software was used to numerically model the mechanical properties of the structures, while the electromagnetic properties were modeled in 3D using CST Microwave Studio (Version 4).

The quarter-wave structure is useful over the velocity range $0.10 < \beta < 0.30$ while the half-wave covers $0.20 < \beta < 0.40$. The drift-tube of the QWR structure is shaped

Table 1: EM Parameters (from Microwave Studio)

	Quarter-Wave	Half-Wave
Frequency [MHz]	115	172.5
β_{GEOM}	0.15	0.26
Length [cm]	25	30
QR$_s$	42	58
At 1 MV/m accelerating field:		
E_{peak} **[MV/m]**	3.2	2.9
B_{peak} **[G]**	57	78
rf energy [mJ]	170	345

to introduce electric dipole fields which largely cancel the beam steering caused by magnetic dipole fields intrinsic to the QWR geometry [4].

Design of the niobium shell and stainless-steel housing of both cavities followed analysis of the mechanical stresses both from helium pressure loads and also from mechanical tuning loads as shown in Figure 2.

Fabrication

The cavities have been designed for mass production.
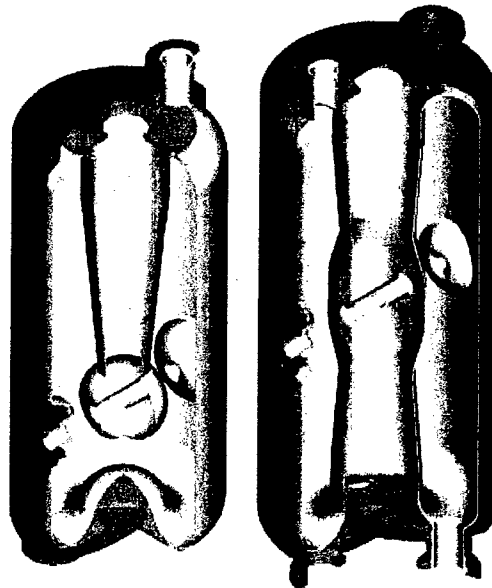
Figure 1: Cutaway views of the quarter-wave and half-wave cavities showing both the niobium cavity and the integral stainless-steel helium vessel.

Figure 2: Numerically modeled displacement under a compressive load for tuning the QWR cavity.
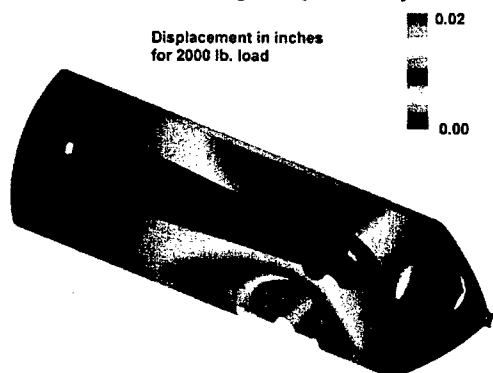
The blended corners and smooth transitions shown in Figure 1 are well suited to hydroforming and other sheet metal working processes, and also facilitate chemical processing and high-pressure water rinsing.

Dies and tooling were tested first on 3 mm aluminum sheet. Once parameters were established, the parts were formed of 3 mm niobium sheet with RRR>250. Figure 3 shows some of the sub-assemblies for the half wave cavity.

Formed parts were finish machined to fit, then joined with electron-beam welds. Figure 4 illustrates a complex weld on the quarter-wave center conductor involving multi-axis control of both gun and table with a varying beam current programmed to achieve optimum results.

These cavities are designed with integral stainless steel helium tanks which requiring joining niobium to stainless steel at the various coupling and beam ports. This was accomplished by brazing with pure copper, which requires neither plating or other surface treatment other than cleaning. Figure 5 shows two prototype braze assemblies. Copper wire is placed in a shoulder machined into the stainless steel and flows into the smooth annular space
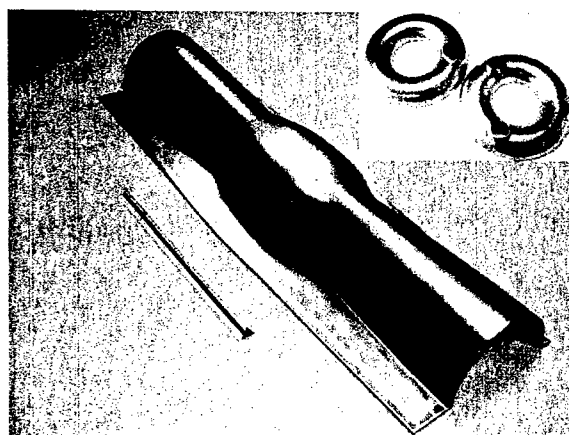
Figure 3: Half-wave resonator parts, as-formed niobium center conductor and (inset) toroidal end-cups with coupling ports.

Figure 4: Setup to electron-beam weld the QWR resonator center-conductor halves together in a single pump-down.

between stainless flange and niobium tube. The mating surfaces are completely wetted and the excess copper forms a fillet on the underside of the joint. Two beam port (30 mm ID) and three coupling port (51 mm ID) transitions of this type are currently in service and operating on a double spoke cavity at ANL [5].

CRYOMODULE

Low-β drift-tube loaded TEM structures extend further vertically than along the beam axis, and can be efficiently housed in a rectangular cryostat geometry. Building on experience with the cryostats for the Positive Ion Injector at Argonne's ATLAS heavy ion linac, a rectangular cryomodule design has been developed [6] that is space-efficient and consistent with the requirements for high-performance superconducting rf surfaces. Features include separation of the cavity and the cryogenic vacuum systems, and top-loading of the cavity-string subassembly which enables hermetic isolation of the cavity string along with assembly in a clean room.

Figure 5 shows three stages of module assembly, from clean-room subassembly to a completed module. The end walls of the vacuum vessel are chamfered in the middle, as shown in Figures 5 and 6, to allow the room-temperature, low-particulate beam-line vacuum valves which seal and isolated the cavity-string assembly, to insert through the cryomodule vacuum wall.

The cryomodule contains an internal magnetic shield as well as a liquid nitrogen cooled thermal shield. Both shields are installed by hanging sheets of copper and/or mu-metal, much like curtains, on the wall of the vacuum vessel, overlapping as required. Cost and installation effort should be reduced compared to more traditional construction methods. Multi-layer insulation (MLI) can be installed due to the independent cavity and cryogenic

Figure 5: Cryomodule assembly sequence. (Top) clean-room assembly of cavity string includes cavity and beamline vacuum and couplers. (Middle) Top flange assembly includes cryogenic systems. (Bottom) Completed cryomodule.

Figure 6: Detail of cryomodule-cryomodule interface. The distance between SC cavity beam-port flange surfaces is 50.8 cm. Some 20.6 cm of beamline between the 4 cm, low-particulate beam-line valves is available for diagnostics, etc.
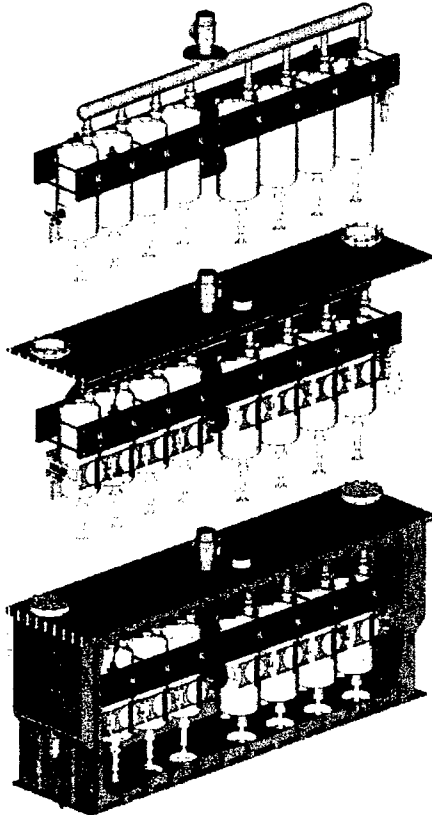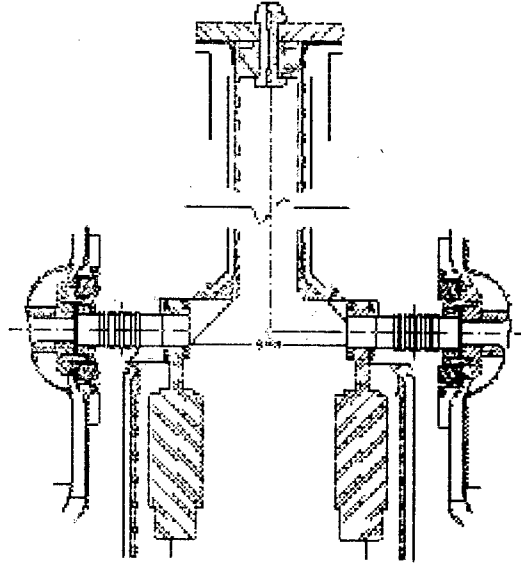
insulating vacuum spaces which ensure a clean cavity space.

ACKNOWLEDGEMENTS

We acknowledge the work of E. Peterson and his coworkers at Advanced Energy Systems, Inc. in designing tooling and forming niobium parts. T. Hejna of Sciaky, Inc developed procedures and performed electron beam welds for the work described in this paper. W. Toter of the ANL central shops developed the copper braze used to join stainless and niobium. Meyer Tool and Manufacturing Co. machined and fit many of the niobium parts.

REFERENCES

[1] C. W. Leemann, in Proc. 2000 Linac Conf., Monterey, California, August 21-25, 2000, SLAC VR-561, p.331 (2000).

[2] K.W. Shepard, Nucl. Intr. Meth. in Phys. Res. A 382, p125-131 (1996).

[3] G. Ciovatti, et al., in Proc. 10th Workshop on RF Superconductivity, Tsukuba, Japan, September 6-11, 2001, edited by S. Noguchi.

[4] P. N. Ostroumov and K.W. Shepard, Phys. Rev. ST AB 4, 110101 (2001).

[5] J.D. Fuerst et al, "Superconducting 345 MHz Two-Spoke Cavity for RIA", in the proceedings of this conference.

[6] J.D. Fuerst and K.W. Shepard, "A Cryomodule for the RIA Driver Linac," ICEC19, Grenoble, July 2002.

DESIGN OF A SUPERCONDUCTING LINAC CAVITY FOR HIGH-CURRENT ENERGY RECOVERY LINAC OPERATION

Dong Wang*, Yongxiang (Joe) Zhao, Ilan Ben-Zvi, Xiangyun Chang, Jorg Kewisch, Christoph Montag (BNL), Jacek Sekutowicz (DESY&JLab) , Carlo Pagani, Paolo Pierini (INFN)

Abstract

The RHIC electron cooler as well as other applications (such as a linac-ring version of eRHIC) require a very high average current CW electron linac in an energy recovery mode. In this paper we present the design of a 5-cell superconducting linac cavity for velocity of light particles. This cavity will operate at 703.75 MHz with a large beam pipe aperture of 19 cm diameter and ferrite HOM absorbers in the beam pipe, in addition to the conventional HOM couplers for low frequency HOMs. We will report the design of the cavity geometry using the BuildCavity and Superfish codes, loss factor simulations with ABCI, detailed HOM simulations with MAFIA (with and without the ferrite absorbers) and beam breakup simulations using the code TDBBU.

INTRODUCTIONS

The main goal of the Relativistic Heavy Ion Collider (RHIC) is to provide head-on collisions at energies up to 100 GeV/u per beam for very heavy ions, which are defined to be gold $^{197}Au^{79+}$, but the program also calls for lighter ions all the way down to protons and polarized protons. Luminosity requirements for the heaviest ions are specified to be in the $10^{26} \sim 10^{27} cm^{-2}s^{-1}$ range. A first upgrade of the luminosity by about a factor four consists of increasing the number of bunches from about 60 to about 120 and decreasing beta* from 2m to 1m. Luminosity can be further enhanced by decreasing the beam emittance by the electron cooling the gold beams at storage energy. With electron cooling the beam emittance can reduced and maintained throughout the store and the luminosity increased until non-linear effects of the two colliding beams on each other limit any further increase (beam-beam limit). The simulations of electron cooling for RHIC show that a high charge electron bunch (10nc) is needed. The resulting average current is about 100mA.

Table 1 Parameters of electron beam for RHIC cooler

Final Beam energy	55MeV
Charge per bunch	10nc
Repetition rate	9.4MHz
Average current	94 mA
Bunch length at Linac	~1cm, rms
Injection energy	2.5 MeV

To accelerate about 100mA electron beam to 55MeV the energy recovery linac (ERL) scheme is proposed to save tremendous power. Beams will go through the linac twice, first to be accelerated up to 55MeV then to be de-accelerated while giving their energy back to the linac. Superconducting radio-frequency cavity technique is assumed in this cw accelerator machine.

* Email: dongwang@rocko.mit.edu

The main issues for the linac cavities are the effects due to the very high current.

1) the power in the HOMs(Higher Order Modes) which depends on the product of bunch charge and the average current.

2) multi-bunch and multi-pass effects which are driven by the high-Q superconducting cavities and limit the average current.

3) effect due to the high charge per bunch (at relatively low energy)

For the RHIC e-cooling project, 1) and 2) are serious concerns and will be discussed in this paper. The cavity-related single bunch effect is discussed in context of linear collider designs. Non-cavity-related single bunch effects (space charge, magnetized beam, etc.) are covered in a separate study.

CAVITY DESIGN

To address above challenging issues a new sc linac cavity is being designed by a collaboration of people from several laboratories.

Frequency

A relatively low frequency, say, 700MHz, is chosen to get a reasonably small loss factor. It also allows a longer bunch and larger transverse aperture is another advantage. On the engineering side the availabilities of cw klystrons and cleaning facilities are also the factors in choosing frequency.

Number of cells

Five-cell structure is adopted since it can keep good acceleration efficiency while making the coupling and propagation of some modes easier, compare to other 7~9-cell structures.

Cavity geometry is designed with the BuildCavity code. Figure 1 shows cavity shape and main parameters.

G	240	Ω
R/Q	710	Ω
Q_{bcs}	4	10^{10}
E_p/E_a	2.1	
H_p/E_a	5.94	mT/MV/m
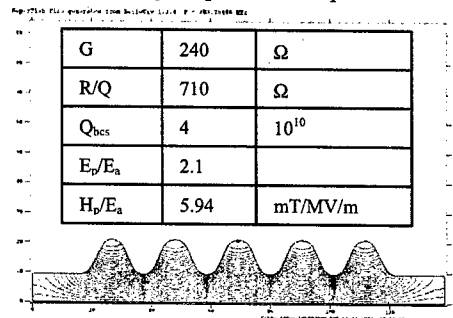
Figure 1: geometry and main parameters of new cavity

The loss factor is calculated by the ABCI. See Figure 2.

ABCI 9.4, Spectrum of Loss Factor
704 MHz 5-cell Cavity
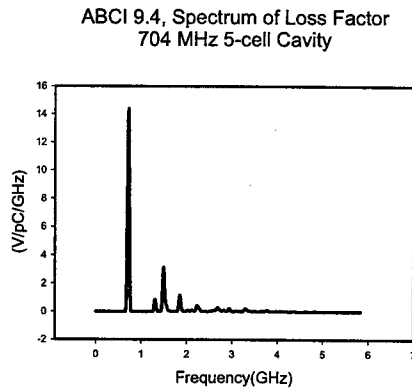
Figure 2: loss factor of new cavity

HIGHER ORDER MODES ISSUE

The HOM (Higher Order Modes) is the key player in the design and operation of this sc cavity. Simulations are carried out with MAFIA. Particularly the low frequency dipole modes are of importance to the instability issues in the linac. Table 2 shows the 30 modes with the lowest frequencies.

Table 2 major dipole higher order modes

	Frequency(GHz)	R/Q (ohm)
1	7.489798350E-01	0.109982526E-02
2	7.569791871E-01	0.136660994E+00
3	7.570094240E-01	0.274434304E-02
4	7.711698536E-01	0.184679902E+01
5	8.032362047E-01	0.305099726E+01
6	8.246061998E-01	0.129250653E+01
7	8.252309047E-01	0.711581113E-01
8	8.401347490E-01	0.484628264E+02
9	8.773347638E-01	0.461812638E+02
10	8.822060575E-01	0.707655746E+01
11	9.214217593E-01	0.308168408E+01
12	9.214559575E-01	0.119930774E+01
13	9.524008689E-01	0.177325199E+00
14	9.567931457E-01	0.312298753E+01
15	9.639985747E-01	0.125690626E+02
16	9.709637992E-01	0.500794841E+01
17	1.010896594E+00	0.143507816E+01
18	1.011128111E+00	0.604053638E-05
19	1.089125001E+00	0.143106632E+01
20	1.089888247E+00	0.367335628E-03
21	1.170296440E+00	0.885562614E+00
22	1.177597825E+00	0.521756140E+00
23	1.210143769E+00	0.219157590E-03
24	1.250641137E+00	0.306075197E-01
25	1.280658315E+00	0.594297261E-03
26	1.310722096E+00	0.142675869E+00
27	1.351442021E+00	0.285837611E-01
28	1.390585487E+00	0.434743738E-01
29	1.420472371E+00	0.419089300E+00
30	1.420472371E+00	0.419089300E+00

Among these dipole modes some may have frequencies below the beam pipe (assuming equal to the iris of the cavity or a little bit larger) cutoff. Electromagnetic fields of these modes are calculated by the MAFIA. See Figure 3 to 11.

Figure 3: TE111, 750 MHz

Figure 4: TE112, 772 MHz

Figure 5: TE113, 803 MHz

Figure 6: TE114, 840 MHz

Figure 7: TE115, 877 MHz

Figure 8: TM11x, 952 MHz

Figure 9: TM11x, 956 MHz

Figure 10: TM11x, 964 MHz

The outer sections of beam pipe are enlarged from 19 cm to 24 cm diameter (about 20cm away from the end cells). From mode analysis and observations some modes may not propagate well through the pipes.

A detailed study is done with method in Ref. [3] to estimate the external Qs of the modes.

Table 3 External Qs of some dipole modes

Mode	Frequency (GHz)	Field Pattern*	R/Q (Ohm)	Qext
1	7.504E-01	TE111	0.001	7600
2	7.722E-01	TE112	1.9	1033
3	8.035E-01	TE113	2.8	258
4	8.404E-01	TE114	48	99
5	8.776E-01	TE115	46	26-29
6	9.520E-01	TM11x	0.16	large
7	9.566E-01	TM11x	2.9	large
8	9.641E-01	TM11x	13	large

The calculations suggest that TM11x modes might have quite high Qs (exact amount are not available with the

method) or are difficult to propagate in the pipes. To solve the problem in propagating those modes both the CESR 'flute' structure or larger pipes might be needed.

HOMS WITH FERRITE ABSORBERS

Ferrite absorbers have been successfully used in other high current cw RF cavities in colliding beam accelerators like CESR and KEK-B for single cell sc cavities to damp HOMs and absorb huge power up to a few tens of kW.

An attempt to apply the same technology to the multi-cell linac cavity is made in our design. The preliminary simulations are performed with E-module in the MAFIA. Two ferrite absorbers are placed on each side of the beam pipe, a few tens of centimeters from the cavity cells as ferrite sections are in room temperature. Each ferrite absorber has 5 mm thick layer with tapered ends. The eigenmodes are calculated with MAFIA as a lossy problem. By carefully matching the MAFIA options and properties of ferrite materials [5][6] (some permittivity and permeability values may fail) the Qs of monopole and dipole modes can be calculated with high precision (~1E-6). Fig. 11 and Table 4 show the fields and Qs of some major dipole modes. HOM coupler is also planned as it will provide a lot of more flexibility in locations of ferrite absorbers, pipe diameter and cryogenic system designs. To reflect the real environment in the linac the time-domain solutions are being sought in collaboration with other labs to better understand the issue.
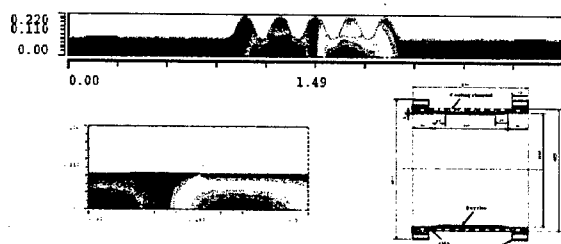
Figure 11: Simulation with ferrite absorbers
Top, field of TM11x mode, in cavity and pipes,
Lower left, local field near ferrite, Lower right, ferrite absorber (used in B-Factories)

Table 4 Dipole modes with ferrites absorbers
Eps=10.0,-1.0 Mu=2.0, -0.5,
(modes with high R/Q are selected)

Mode	Freq.(Re) (MHz)	Freq.(Im) (MHz)	Q with Ferrite
A	877.3	0.1981	4428
B	882.2	0.2094	4212
C	956.7	0.001521	628533
D	963.8	0.02025	47595
E	971.2	0.04392	22112
F	1016	6.741	151
G	1273	7.732	164
H	1311	7.248	181

In a high current superconducting, energy recovery linac machine like RHIC e-cooler there are a number of collective effects that may potentially limit the maximum current. The multi-bunch multi-pass effects which are mainly driven by the high-Q s.c. cavities are our major concerns, particularly the transverse Beam Break-Up(BBU), which results from the interaction of the beam with cavity Higher Order Modes. A preliminary study is performed to investigate the effect of HOMs of newly designed 700 MHz, 5-cell sc cavities on the cumulative Beam Break-Up. The analytical formula of the threshold current exists only for the specific mode in the simplified case. The precise evaluation calls for the numerical method. In our study so far the computer simulation code TDBBU developed in the Jefferson Lab is used. The circumference is around 251 rf wave length, about 108 meters. The bunch repetition rate is 9.4 MHz. The simple transverse optics is assumed as the design of the cavity and transport are still underway. R/Q and Q values of major HOMs with ferrite HOM absorbers are from preliminary MAFIA calculations. Qs are same for both polarizations since there is no fundamental or HOM waveguide coupler in our calculations. The threshold current can be about 500 mA for a uniform distribution of frequencies of the HOMs in all cavities.

SUMMARY

A design of a 700MHz, 5-cell superconducting cavity is performed for the use of high current Energy Recovery Linacs(ERL). Primary concern has been the HOM issue due to very high beam current. Most important deflecting modes with low frequencies are studied by several different methods. Simulations of the cavity with ferrite absorbers are done with MAFIA as a lossy eigenmode problem. Preliminary results are quite interesting. More calculations especially with time-domain method are underway. Design of main and HOM coupler is also going on mainly by J. Sekutowicz.

ACKNOWLEDGMENTS

REFERENCES

[1] M. Tigner, Nuovo Cimento, 37, 1228(1965)
[2] I. Ben-Zvi et al., these proceedings
[3] P. Pierini, BuildCavity manual
[4] P. Balleyguier, p 133-5, LINAC'98, Chicago, IL, 1998
[5] A. Chao, M. Tigner, Handbook of Accelerator Physics and Engineering, 1997
[6] W. Hartung, PhD Thesis, Cornell University, 1996

EXPERIMENTAL RESULTS ON 700 MHz MULTICELL SUPERCONDUCTING CAVITY FOR PROTON LINAC

B. Visentin[#], J.P. Charrier, D. Roudier, F. Simoens, E. Jacques, A. Aspart,
Y. Gasser, J.P. Poupeau, P. Sahuquet, D. Braud,
CEA-Saclay, DSM/DAPNIA/SACM - 91191 Gif / Yvette Cedex - France
H. Saugnac, Ph. Szott, S. Bousson, J.L. Biarrotte, T. Junquera, S. Blivet,
IPN-Orsay, Accelerator Division - 91406 Orsay Cedex - France

Abstract

The first five-cell niobium superconducting cavity (700 MHz, β=0.65) has been successfully tested in the horizontal cryostat CryHoLab. Technological choices like equipment with stainless steel helium vessel and flanges appeared to be viable for the future. Preceding this test, several operations have been performed: field flatness adjustment, chemical etching, heat treatment and RF measurements in a vertical cryostat. Good performances for a multicell cavity were obtained. However, field emission and not yet elucidated phenomenon limit the accelerating field around 16 MV/m.

1 INTRODUCTION

The R&D collaboration on 700 MHz superconducting radio frequency (SCRF) cavities between CEA-Saclay and IPN-Orsay started few years ago in the context of the French ASH (Superconducting Accelerator for Hybrid reactor) project, aborted since then.

Nevertheless, the developments of this kind of cavities are still a topical subject because of its involvement in any linear proton accelerator requiring a high energy section. Such projects, using a high intensity beam, are dedicated to produce radioactive ion beams, neutrons for nuclear waste transmutation, or particles for muon colliders and neutrino factories.

Currently, the French SCRF proton cavities research is related to the European projects XADS (eXperimental Accelerator Driven System) and EURISOL (EURopean Isotope Separation On-Line). The linac design and the beam dynamics studies defined modules made of five-cell SCRF cavities with several β values (0.47, 0.65, and 0.85). Our first goal was to manufacture and test a 5-cell prototype (β=0.65) in a horizontal cryostat to validate the design and the technological choices. A second step will be to experiment its associated components: the cold tuning system and the power coupler.

2 CAVITY CHARACTERISTICS

The five-cell A5-01 niobium cavity, manufactured by CERCA, was designed on the basis of RF codes simulations [1] and after validation through the results achieved with the A1-05 monocell cavity in a vertical cryostat (Fig.1) [2]. This cavity is characterized by:

- ratios of E_{peak}/E_{acc} and B_{peak}/E_{acc} surface peak to accelerating fields, respectively about 2.32 and 4.48 mT/(MV/m),
- no stiffening rings between cells,
- two lateral ports used for the input coupler and the transmitted power pickup probe,
- an asymmetry in the beam tube diameters (RRR 30 niobium),
- Conflat® CF flanges, bellow and liquid helium vessel, made with 316 L stainless steel, which are copper-brazed on niobium,
- the Nb cells material supplied by Wah Chang (4 mm sheets - RRR>250)

3 FIELD FLATNESS TUNING

To ensure the electric field flatness on the beam axis, it is necessary to pre-tune the multicell cavity, at the room temperature. The tuning procedure consists into a mechanical deformation of each cell by means of steel plates to squeeze or stretch it. The field profile is measured by the perturbation method induced by a small metal bead moving along the beam axis [3].

Three pre-tunings were necessary to improve the field flatness up to E_{min}/E_{max}=92% from the initial values: on receipt of the cavity from CERCA (24%) and after new degradations resulting from the first important chemical etching (75%) and from the heat treatment (65%).

4 CAVITY PREPARATION

4.1 Chemistry

All along RF tests, the cavity has been treated several times by a "Buffered Chemical Polishing", HF/HNO$_3$/H$_3$PO$_4$ acid mixture (1:1:2). To limit the acid volume required for dunk chemistry, the chemical treatment was only made in the inner part of the cavity. The cavity apertures were closed by PolyVinylChloride flanges and Viton® O'ring seals protect brazes from the acid attack. A first hard etching of the surface removed a 170 μm thickness. Then several slight chemistries (20 μm) were made to prevent possible surface contamination after each cavity handling (field flatness tuning, heat treatment and helium vessel welding).

Unfortunately, during one chemistry a bad adjustment of the O'ring protection seal caused the acid attack of the

[#] bvisentin@cea.fr

copper braze at one axial flange. A vacuum leak occurred that was temporarily sealed in using a Stycast® epoxy compound. This cure has been effective until now: even after several thermal cycles, we did not observe any leak on the cavity immersed in He II bath.

4.2 Heat Treatment for Q-Disease

To avoid the important Q-disease effect (curve 2 on Fig.2), due to hydride formation around 100K and observed during a slow cool-down, the cavity has been annealed under vacuum (1.10^{-7} mbar) for one day in the CERN furnace. This treatment is required before the test in horizontal cryostat because in that case a fast cooling down is impossible, the pre-cooling being necessarily carried out by liquid nitrogen at 77K.

During this treatment, we have verified the hydrogen removal from the bulk material with a rare gas analyzer. A 650°C temperature has been chosen, instead of the usual 800°C, to prevent the stainless steel CF flanges brittlement that could appear at low temperature during subsequent RF tests and to preserve the cavity stiffness. The curve 3 on Fig.2 proves the efficiency of the heat treatment at low temperature, an observation already mentioned in an earlier experiment [4].

4.3 Helium Vessel

After heat treatment, the helium vessel [6] was attached to the multicell niobium cavity by TIG welding. An ultimate field flatness check and a new test in a vertical cryostat showed that cavity performances were unchanged by the stainless steel helium tank welding and that the cavity was then ready for horizontal tests in CryHoLab.

5 RF MEASUREMENTS

5.1 Tests in Vertical Cryostat

For the first test, the 5-cell cavity (curve 1 on Fig.2) shows a similar behavior to the A1-05 monocell (Fig.1) with a multipacting barrier around 10 MV/m; but, instead of the limitation by quench at 25 MV/m, we were surprisingly limited at 15 MV/m without any of the usual causes, quench or electrons. We observed and did not find yet an explanation, that when E_{acc} exceeds 15 MV/m the incident power P_i is partially reflected at the cavity entrance, after a time Δt (Fig.3). We suspected a coupling problem and decided, for next vertical test, to change the RF antenna position and put them on the beam axis, instead of lateral ports.

During the second test (curve 3 on Fig.2), after the annealing of the cavity, we noted the electron production by field emission and we observed the same limiting phenomenon at 15 MV/m. This was in spite of the new antenna position. The phenomenon study shows that if we switch off the RF power between each data point, during the "RF-off" time τ, we can extend the Δt time enough to make the RF measurements.
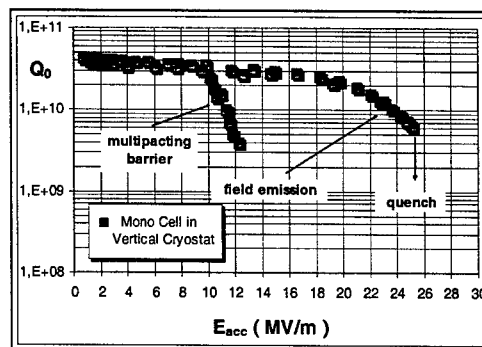
Figure 1: Q_0 vs E_{acc} for the mono-cell cavity (A1-05), in vertical cryostat at 1.7K
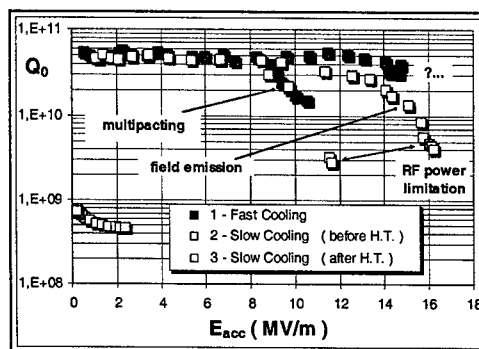
Figure 2: Q_0 vs E_{acc} for the 5-cell cavity (A5-01), in vertical cryostat at 1.7K.
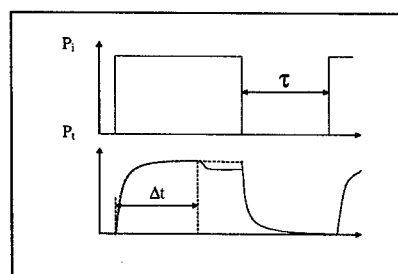
Figure 3: Schematic traces of incident P_i and transmitted P_t powers versus time during the observed phenomenon with $\Delta t = f(1/E_{acc}, \tau)$

By this way, it was possible to exceed the 15 MV/m limit and we then met a more usual "RF power supply limitation" due to the electron emission at 16 MV/m. On the curve 3 (Fig.2) we can see the shift ($\leftrightarrow$) for the two last data points if we do not switch off the RF power between the measurements. When the E_{acc} value increases, Δt decreases so a longer "RF-off" time is necessary. The τ value, about two minutes, suggests a long relaxation time for the limiting phenomenon. In spite

of these difficulties the RF results show good performances for our 5-cell cavity if we compare them with similar multicell cavities [4-5].

5.2 CryHoLab Horizontal Test Facility

For the first time CryHoLab (french acronym of "CRYostat HOrizontal de LABoratoire") is running with a cryogenic generator [7] (compressor, 120 l/h liquefier-cold box, 2000 l buffer-dewar), instead of liquid helium containers. The pumping system allows the helium bath temperature to decrease down to the working value (1.8 K).

The 5-cell cavity is the first one tested in such conditions. The dynamic cryogenic power consumption of the whole installation at 1.8 K (cryostat, cavity, transfer lines and He bath pumping) is around 20 W (29 l/h). Figure 4 shows the A5-01 cavity, inside CryHoLab, wrapped in super-insulation layers as thermal shielding.

Figure 4: The 5-cell cavity inside CryHoLab.
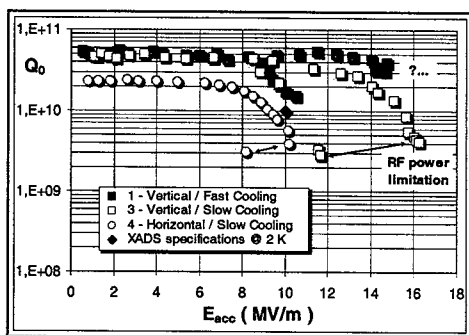
Figure 5: Comparison of the RF tests in vertical and horizontal cryostats

5.3 Tests in Horizontal Cryostat

To be able to make a real comparison between vertical and horizontal tests, and in spite of the electron emission, the cavity is tested without a new cleaning stage. Curve 4 on Fig.5 shows the RF horizontal results with a slight decrease in the Q_0 value at low accelerating field from 4.6

to $2.3 \cdot 10^{10}$ due to the change of the residual resistance resulting from the difference of the magnetic field shielding between vertical and horizontal cryostats (from 2 to 20 mG). The same phenomenon in the input power limitation is also observed in CryHoLab but from only 8 MV/m. Using the same "RF-off" method than in the vertical cryostat, it is possible to reach 10 MV/m. But we did not succeed to go through the multipacting barrier, even after we attempted to make a cell by cell RF formation using other fundamental modes than π-mode. It is necessary to carry on the investigations of the limiting phenomenon and to check a possible connection with the lack of stiffeners between the cavity cells.

6 CONCLUSION

The first preliminary results of the multicell cavity allowed to:
- show the good performances of the cavity, above the XADS specifications, in spite of field emission,
- reinforce the technical options and particularly the use of stainless steel helium vessel,
- validate the horizontal RF test facility CryHoLab and the cryogenic fittings.

The five-cell cavity being characterized all along the different stages of its preparation, up to the final RF test in the horizontal cryostat, our priority now is to understand and to solve the experimental event that limits the intrinsic performances of this cavity.

In parallel, we will improve the CryHoLab magnetic shielding and we will clean again the cavity to suppress the electron emission, probably linked to a surface contamination due to pollution in the rinsing water system.

7 REFERENCES

[1] J.L. Biarrotte et al., "704 MHz Superconducting Cavities for a High Intensity Proton Accelerator", 9th Workshop on RF Superconductivity, Santa Fe - USA (1999), Vol.II, p.384 – CDROM: WEP005.

[2] S. Bousson et al., "700 MHz Superconducting Proton Cavities Development and ...", 8th EPAC Paris FRANCE 2002), p.2211 – EPAC 2002: THPDO036.

[3] F. Simoens et al., "A Fully Automated Test Bench...", 8th EPAC, Paris - FRANCE (2002), p. 963 - EPAC 2002: THPLE033.

[4] G. Ciovati et al., "Superconducting Prototype Cavities for the SNS Project", 8th EPAC, Paris - FRANCE (2002), p.2247-EPAC 2002: THPDO015.

[5] T. Tajima et al., "Developments of 700 MHz 5-cell superconducting cavities for APT", 19th PAC, Chicago USA(2001), p.1119 – PAC 2001: MPPH145

[6] H. Saugnac et al., "Preliminary Design of a Stainless Steel Helium Tank ...", 10th Workshop on RF Superconductivity, Tsukuba - JAPAN (2001), – SRF2001: PT022

[7] H. Saugnac et al., "Cryogenic Installation Status of the Cryholab Test Facility", 10th Workshop on RF Superconductivity, Tsukuba - JAPAN (2001), – SRF2001: PZ007

USING PASSIVE CAVITIES FOR BUNCH SHORTENING IN CESR*

S. Belomestnykh[†], R. Kaplan, J. Reilly, J. Sikora, and V. Veshcherevich
Laboratory for Elementary-Particle Physics, Cornell University, Ithaca, NY 14853, USA

Abstract

Passive (beam-driven) superconducting cavities can be used in storage rings for bunch shortening when necessary high RF voltage can be achieved only by using multiple cavities, but the beam power consumption does not justify using all of them in the active mode, powered by klystrons. An example is the e^+e^- collider CESR running with a beam energy below 2.5 GeV as a charm-tau factory (CESR-c) [1]. A short bunch length of about 10 mm is required for obtaining higher luminosity, while maximum beam power is only 160 kW. Theoretical and experimental studies are in progress at CESR to investigate the collider performance at low energy in preparation for its conversion to CESR-c. In the course of these studies we looked at possible impacts of using passive cavities on the accelerator performance. The results are presented.

1 MOTIVATION FOR USING PASSIVE CAVITIES

CESR [1] is a single-ring e^+e^- collider operating in the energy range from J/Ψ (1.55 GeV) through Υ resonances (E $\approx$ 6 GeV). In the past CESR has operated mainly at 5.3 GeV and achieved peak luminosity well above 10^{33} $cm^{-2}s^{-1}$. Its operation range was extended recently to lower energies of charm/tau region. The low energy mode of operation, called CESR-c, utilizes short bunches and high synchrotron frequency and requires high total RF voltage (see Table 1). By raising operating gradient on some of the existing cavities and replacing others with new/refurbished cryomodules we will attain the RF voltage increase [2].

However, while the required RF voltage is high, the beam power demand is very modest and does not justify using three transmitters as in the present RF system configuration. Even one klystron is more than adequate to supply necessary power. To significantly reduce RF system power consumption and to ease stability requirements to RF controls we had proposed operating some of CESR superconducting cavities in a passive mode. A proof-of-principle experiment was performed to check feasibility of this mode of operation [3]. Measured dependence of the synchrotron frequency on the beam current was in good agreement with calculations. In this paper we present further studies of passive cavity operation in CESR-c including first experimental high-energy physics (HEP) run results.

Table 1: Selected parameters of CESR-c

Energy [GeV]	1.55	1.88	2.5
No. of cavities	4	4	4
Gradient [MV/m]	6.25	8.33	10
Voltage [MV]	7.5	10	12
Beam power [kW]	40	90	160
Beam current [A]	0.26	0.36	0.46
Synch. frequency [kHz]	41	43	41
Bunch length [mm]	9.9	10.2	10.2

2 RF SYSTEM CONFIGURATION AND PARAMETERS FOR CESR-C

CESR RF system consists of four single-cell superconducting cavity cryomodules. The cryomodules are installed in pairs in the East (E1 and E2 locations) and in the West (W1 and W2) RF straight sections of CESR. Two East cavities have individual klystrons while two West cavities share RF power from one klystron (see Figure 1).
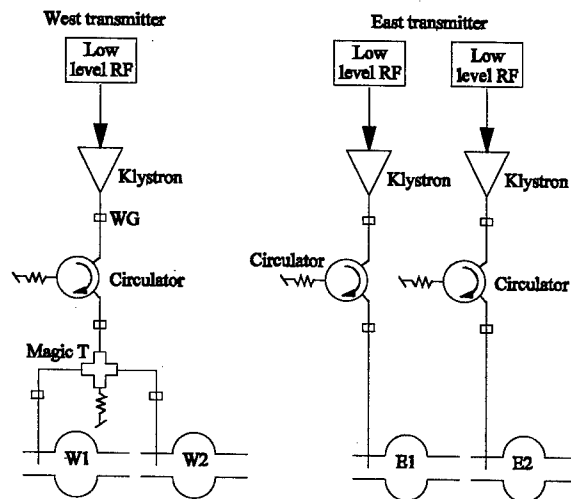
Figure 1: RF system configuration.

The proposed scheme [2] is to operate two West cavities in an active mode and two East cavities in the passive mode with the external Q factor in the range between 1×10^6 and 3×10^6. We will retain klystrons connected to the passive cavities for RF processing purposes and for CESR operation at high energy for synchrotron radiation user facility.

Requirements to the CESR-c RF system were analyzed elsewhere [2, 4]. Table 2 compares RF parameters for

different number of active and passive cavities and different cavity coupling at 1.88 GeV. First set of parameters is for the configuration with four active cavities with $Q_{ext} = 2.0 \times 10^5$, the same as we have at present. Most efficiently RF system is operating though when matched conditions are reached at the maximum beam current (second set). For CESR-c this means operating at high values of Q_{ext}, which will significantly increase the beam loading parameter Y. In the past CESR typically operated with $Y \approx 9$, which is considered heavy beam loading [4]. Using two passive cavities will alleviate the beam loading problem as well as significantly reduce power consumption (third and forth sets of parameters in Table 2).

Table 2: Comparison of RF parameters at 1.88 GeV

No. of active + passive cavities	4+0	4+0	2+2	2+2
No. of klystrons	3	3	1	1
Q_{ext} active	2.0×10^5	3.1×10^6	6.1×10^5	1.0×10^6
Q_{ext} passive	–	–	1.0×10^6	3.0×10^6
$Y = V_{br}/V_c$	2.6	40.0	7.8	13.2
Synchr. phase	83.7	88.6	86.3	87.8
P_{RF} [kW]	398	90	230	137
P_{AC} [kW]	1150	810	470	370

The beam acts as a transmission line between the source of RF power (active cavity) and the load (passive cavity). At a constant passive cavity voltage the power transmitted via beam stays constant. Hence the voltage seen by the beam as it passes the beam-driven cavity will depend on the beam current and will be maximal at the lowest beam current (threshold current, see next section). For example, for 1.88 GeV conditions the voltage seen by the beam would reach 1.4 MV at the beam current of 50 mA, cavity voltage of 2.5 MV and passive cavity $Q_{ext} = 1.0 \times 10^6$. Energy kick due to this high voltage can create orbit perturbation (dispersion function is non-zero at the cavities' location in CESR) that may worsen machine performance. This was the reason to include two sets of parameters for passive cavities. While operating at $Q_{ext} = 1.0 \times 10^6$ is better because of the smaller beam loading, higher external Q reduces the energy kick. One can improve beam loading in the latter case by operating active cavities at lower than optimal Q_{ext}.
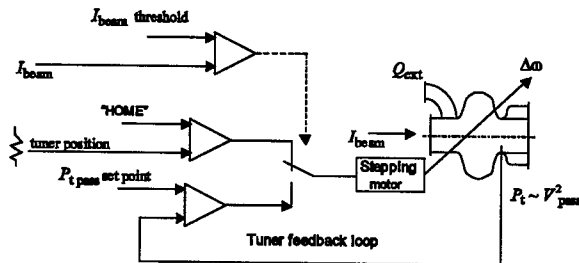
Figure 2: Passive cavity block diagram.

3 PASSIVE CAVITY SETUP

RF control electronics of the E2 cavity has been modified to allow operation in the passive cavity mode. Figure 2 presents the block diagram for this regime. Initially, when the beam current is below the pre-set threshold, the cavity is parked in a "HOME" position off resonance. As soon as the beam current exceeds the threshold, the tuner feedback loop is turned on and tunes the cavity frequency to keep the beam-induced voltage equal to its set point. The set-up works only on one side of the cavity resonance. One needs to change the sign of the loop gain to operate on the other side. For bunch shortening the cavity resonance frequency must be below the operating harmonic of revolution frequency. The cavity voltage set point cannot exceed $I_{beam} R/Q \cdot Q_{ext}$.
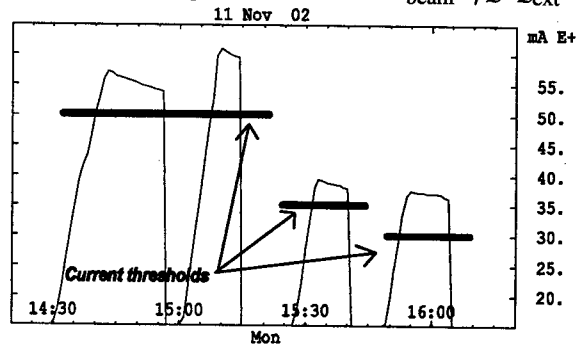
Figure 3: Beam current during first experiment.
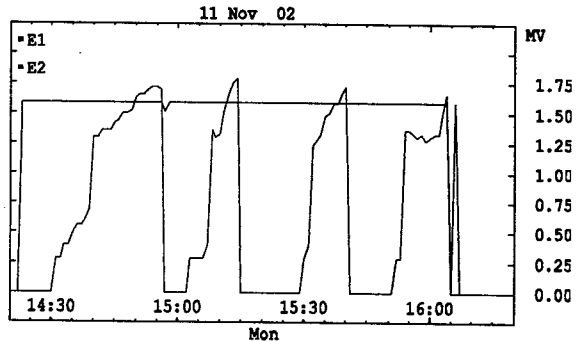
Figure 4: RF voltages during first experiment.
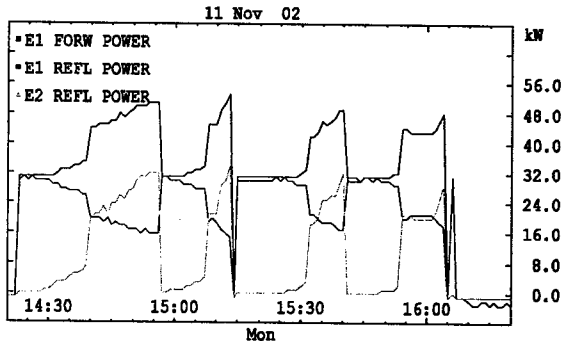
Figure 5: RF power during first experiment.

4 EXPERIMENTAL RESULTS

Passive cavity experiments were performed when CESR was operating at the beam energy of 1.84 GeV using only two cavities. The first experiment was to check operability of the passive cavity setup. E2 cavity has been switched to passive mode and its external Q was adjusted to 1×10^6. E1 cavity remained active at 1.59 MV, West transmitter was not used at that time and both W1 and W2 cavities were detuned and parked off resonance. We injected positron beam to a current level slightly above the pre-set threshold and observed feedback loop operation. Then we slowly raised passive cavity field set point until RF trip due to passive cavity vacuum (Figures 3 and 4). This was repeated several times. In all cases RF tripped as soon as E2 cavity voltage reached approximately 1.9 MV. We have concluded that the trips were associated with the cavity quench and the cavity would have to be processed to operate at this level. Figure 5 illustrates how the passive cavity is loading the active one via beam current. One can see that difference between forward and reflected power on E1 cavity matches reflected power on E2 cavity.

During the second experiment RF system was switched again to one passive and one active cavity to check how passive cavity would affect luminosity during high-energy physics run. E1 (active) cavity voltage was set to 1.75 MV, E2 (passive) cavity voltage was set initially to 1.55 MV at first and later in the run was changed to 1.3 MV. The beam current threshold was set to a total beam current of 30 mA. History plots of the beam currents and passive cavity voltage are shown in Figures 6 and 7 correspondingly. The luminosity was quite respectable (in comparison with normal RF setup of two active cavities) while the passive cavity voltage was set to 1.55 MV though it degraded somewhat when the voltage was lowered. Figure 8 presents comparison of luminosity obtained with passive cavity with luminosity during one of the normal HEP runs.

5 SUMMARY

Experimental results obtained with one passive and one active cavity in CESR-c conditions confirm feasibility of using such a scheme. The plan is to use two passive cavities in CESR-c for more efficient running of the RF system. More experiments will be performed to study passive cavity operation at higher voltages and effects of passive cavities on beam dynamics. We hope to switch to a routine operation with two passive cavities later this year.

6 REFERENCES

[1] D. Rice, "CESR-c – a Frontier Machine for QCD and Weak Decay Physics in the Charm Region," *Proc. of the 8th EPAC*, pp. 428-430 (2002).

[2] S. Belomestnykh, "Requirements to the CESR-c RF system," Cornell LEPP Report SRF020918-06 (2002).

[3] S. Belomestnykh, et al., "Superconducting RF System Upgrade for Short Bunch Operation of CESR," *Proceedings of the PAC'01*, pp. 1062-1064.

[4] S. Belomestnykh, et al., "Superconducting RF Control Issues at CESR," *Proceedings of the PAC'01*, pp. 1065-1067.
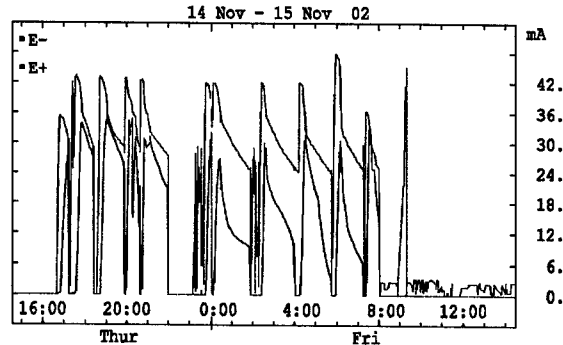
Figure 6: Beam currents during HEP run.
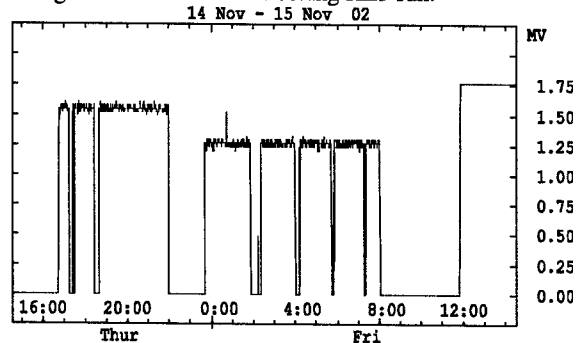
Figure 7: Passive cavity voltage during HEP run.
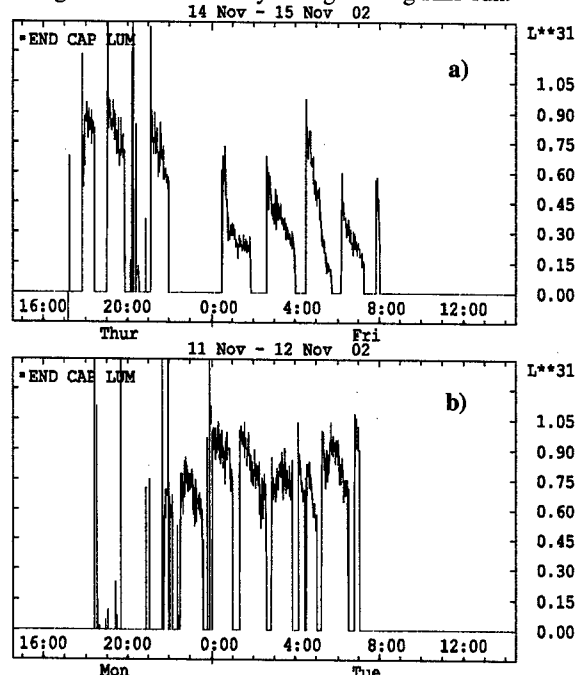
Figure 8: Luminosity during passive cavity experiment (a) and during one of the normal HEP runs (b).

FIRST RF TEST AT 4.2K OF
A 200MHZ SUPERCONDUCTING NB-CU CAVITY*

R.L. Geng[†], P. Barnes, D. Hartill, H. Padamsee, J. Sears, LEPP, Cornell Univ., Ithaca, NY 14853, USA
S. Calatroni, E. Chiaveri, R. Losito, H. Preis, CERN, Geneva, Switzerland

Abstract

A 200MHz single cell elliptical Nb-Cu cavity has been fabricated and tested at 4.2 K and at 2.5 K in a vertical dewar fitted in a radiation shielded pit, 5 m deep and 2.5 m in diameter. The low field Q_0 reached 1.5×10^{10} at 4.2 K. Two multipacting barriers show up at $E_{acc} = 3$ MV/m and 1 MV/m. Helium processing is effective to reduce field emission and improve accelerating gradients by a factor of as much as 2. E_{acc} reached 11 MV/m at a Q_0 of 6×10^8. The Q-drop is observed but shows a stronger field dependence as compared to expected Q-slope typical for Nb-Cu cavities.

INTRODUCTION

The proposed neutrino factory and muon collider ask for RF cavities operating at a frequency near 200 MHz for rapid acceleration of muons [1]. One scenario is to use superconducting RF cavities [2]. The desired accelerating gradient is at least 15 MV/m at a Q_0 of 6×10^9. Since there is no superconducting RF experience at 200 MHz, R&D in this regime should be started early. Cornell and CERN collaborated to fabricate and test of a 200 MHz single cell elliptical Nb-Cu cavity.

FABRICATION

The prototype cavity is fabricated at CERN with the standard film niobium sputtering technique that has been used for manufacture of LEP2 cavities. Due to its gigantic dimensions at such a low frequency, it would have been too expensive and inefficient to build the 200 MHz cavity with bulk Niobium. The shape of the prototype cell is the result of a trade-off between the optimization of RF parameters ($E_{pk}/E_{acc}, B_{pk}/E_{acc}, R/Q$) and the geometry imposed by the requirements for film deposition of Niobium using the technique of DC Magnetron Sputtering. The diameter of the cell measures 1370 mm, while the diameter of the cut-off tubes is 400 mm. The ratio between these diameters is higher than usual to reduce the risk of leak problems at the end flanges. The consequences are a higher R/Q but also a higher value for the ratio of E_{pk}/E_{acc}. On the other hand having the possibility of enlarging the radius gives more flexibility to optimize the shape for sputtering, and a next version of the cavity should certainly address such a problem. RF parameters are listed in Table 1.

Table 1: RF parameters

Parameter	Value	Unit
G	250	Ω
R/Q	121	Ω
E_{pk}/E_{acc}	1.69	-
B_{pk}/E_{acc}	4.34	mT/(MV/m)
$E_{acc}/\sqrt{U}$	0.518	(MV/m)/$\sqrt{J}$

Once the geometry has been fixed, the minimum thickness to avoid collapse under the atomspheric pressure has been calculated by simulating the structure with ANSYS. The two half cells were formed by spinning two 8 mm thick OFE copper sheets. We removed electrolytically 400 μm from the surface to reduce the imperfections induced by the mechanical process. The cavity was then welded by ACCEL with an electron beam from the inside, to avoid welding projections inside the cavity. Further mechanical smoothing has been done at CERN by grinding locally all the sharp points of the internal surface. Chemical polishing (SUBU) was performed twice on the whole cavity to remove 20 μm + 20 μm, the standard value to prepare the copper surface before the deposition of the niobium film. Fig. 1 shows the photo of a half cell under rinsing.

The deposition was made by using the existing infrastructure of the LEP2 cavities. The cavity was rinsed at 100 bars with ultra pure water on the automatic programmable machine. A special vacuum valve was installed on the cavity to insulate the cavity from the outside after drying the cavity. The cavity, filled with dry and dust-free N2, was then sent by airplane and truck to LEPP.

Figure 1: A half cell that is being rinsed.

Figure 2: 200MHz cavity on a horizontal supporting frame.

Figure 3: First test results.

PREPARATION

After arriving at LEPP, the cavity was rolled into the clean room for installation of the input coupler and for pump down. Fig. 2 shows a photo of the cavity when it was in the clean room.

Facilities at LEPP have been upgraded to allow vertical tests of this 2 m long cavity. A 72 inch diameter dewar, manufactured by Cryofab, is fitted into a pit of 5 m deep and 2.5 m in diameter. The pit is lined with low-carbon steel sheets and the earth magnetic field is attenuated to 200 mGauss. The radiation from the test pit is shielded by an 80-ton movable block. Up to 2 kW RF power (CW) at 200 MHz range is available from a solid state amplifier manufactured by QEI. High power RF cables are all fitted with LC connectors or 7/8″ flanged coax connectors. The 2 kW input coupler, manufactured by Ceramaseal, is fitted with a bellow allowing an adjustable Q_{ext} (from 10^9 to 10^{10}). Fixed couplers (connector DN16 type 7/16) rated at 500 W, obtained from CERN, are also used. A new 200 MHz RF electronics system was built. Home molded foam (Versi-Foam from RHH Foam System) blocks are installed around the cavity to displace space and save usage of LHe. In addition, we pre-cooled the LHe vessel and the foam ballast with LN2 before starting LHe transfer.

VERTICAL TEST

TEST-I

During the first test in June 2002, there was a very steep Q drop at 3 MV/m, accompanied with strong X-ray bursts (100 R/h measured on beam axis, 1 m above the cavity equator). Signatures of the reflected power signal was suggestive of multipacting. Simulations confirmed the existence of a two-point multipacting at the observed gradient. RF processing was pursued but the effort was stopped due to damage occurred to the cable connector underneath the feed-through at the dewar top plate. Condensed water vapor formed a thin layer of ice at the interface between connector dielectric (Teflon) and the cable dielectric (foam), which caused impedance mismatch. This resulted excessive heating at the interface and the foam was burnt into
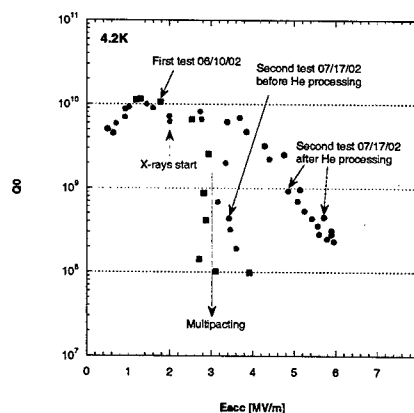
carbon, which in turn shorted the inner and out conductors.

The cavity was then warmed up to room temperature and the cable connector was shifted to the outside of the dewar. The second test was again limited by a barrier at 3 MV/m. Extended RF processing only yielded small improvement. Helium processing was then performed and gradual improvement was obtained. After about 4 hours of helium processing, the accelerating gradient was boosted to 6 MV/m from 3.5 MV/m. A decrease in x-ray flux rate was observed during helium processing. Ultimately the radiation level reached 100 R/h at 6 MV/m. We concluded that the limiting mechanism was field emission. These test results are summarized in Fig. 3. It is noted that the low-field Q is already 1×10^{10} at 4.2 K, indicating an encouraging film quality.

TEST-II

After justification of good film quality and conclusion of the field emission limiting mechanism, the cavity was sent back to CERN for another high pressure water rinsing. A fixed input coupler was installed at CERN following cavity rinsing. This practice eliminated further exposure of the cavity inner surface and would be beneficial in reducing particulate contamination, source of field emission, on the RF surface.

As with Test-I results, the multipacting barrier at 3 MV/m was observed again. A breakthrough was achieved after a cumulative 3.5 hours of RF processing (in CW mode). The gradient jumped from 3 MV/m to 7 MV/m! The radiation level was 40 R/h at 7 MV/m, in contrast to 100 R/h at 6 MV/m in Test-I. This indicates that the extra rinsing indeed reduced the number of field emitters. RF processing continued for 4.5 hours, but in a pulsed mode in order to relieve the ceramic of the fixed input coupler from being over heated. Altogether, the accelerating gradient rose from 7 MV/m to 9.5 MV/m. At this point, the forward power was over 1000 W, which is already twice as high as the coupler power rating. At 9.5 MV/m, the radiation level settled at 30 R/h. Test-II results are summarized
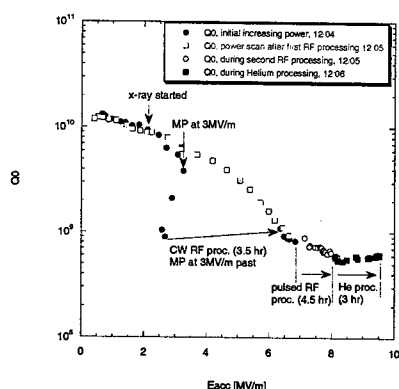
Figure 4: Second test results.

in Fig. 4.

TEST-III

Test-III was pursued at reduced temperatures. Results are given in Fig. 5. At 2.5 K, the low-field Q_0 reached
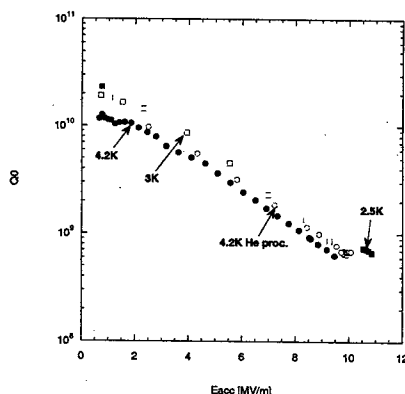
Figure 5: Third test results.

2×10^{10} and the accelerating gradient reached 11 MV/m. Ultimately, the damage power threshold (1.3kW at 200 MHz) of the input coupler was reached. For that reason, the data for the measurement at 2.5 K are obtained only at the two extreme field regions.

MULTIPACTING

Besides the multipacting barrier at 3 MV/m, a second barrier at 1 MV/m was also observed. These two barriers show themselves in Fig. 5 as two dips at the corresponding gradients in the $Q(E_{acc})$ curve for 4.2 K. The radiation level also showed peaks at these two gradients. They were sometimes shown as two switches in the reflected power signal (Fig. 6) after RF is turned off. Simulations with the code MULTIPAC [3] confirmed the existence of a multipacting barrier at 3 MV/m (2-point, first-order). But no barrier is predicted at 1 MV/m, even with an artificially
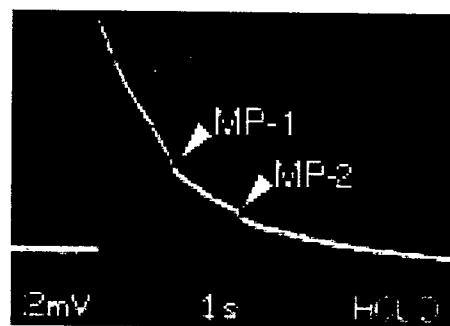
Figure 6: Two multipacting barriers show themselves as two switches, indicated by arrows MP-1 and MP-2, in reflected power signal.

inflated secondary emission coefficient. Nevertheless, the second-order 2-point multipacting is expected at 1 MV/m, since the power level of 2-point multipacting has an order dependence of 1/(2N-1).

As already shown, these multipacting barriers can be processed through within a few hours. In principle, they are not expected to limit the cavity gradients. However, these barriers may become hard and require much longer processing if the cavity surface is contaminated, as evidenced in a recent test of another 200MHz cavity.

Q-SLOPE

As shown in Fig. 5, Q_0 has a strong field dependence. This slope is a result of residual field emission and some intrinsic film characteristics. The fact that Q_0 changes with temperature indicates that the latter dominates. Analysis, in which field emission contribution is subtracted, shows that the intrinsic Q-slope is steeper than the projected value by an order of magnitude.

CONCLUSION

A 200 MHz sputtered Nb-Cu has been successfully fabricated and tested. The low field Q_0 reached 1.5×10^{10} at 4.2 K. E_{acc} reached 11 MV/m, limited by the input coupler. Multipacting barriers at 3 MV/m and 1MV/m can be processed through within a few hours. The film has a stronger Q-slope than projected. This effect needs to be understood in the future.

REFERENCES

[1] Feasibility Study-II of a Muon-Based Neutrino Source, ed., S. Ozaki, R. Palmer, M. Zisman, and J. Gallardo, BNL-52623 (2001).

[2] H. Padamsee, Proceedings of the 9th workshop on RF superconductivity, 587(1999).

[3] P. Ylä-Oijala, D. Proch, Proceedings of the 10th workshop on RF superconductivity, Tsukuba, Japan (2001).

A 1500 MHZ NIOBIUM CAVITY
MADE OF ELECTROPOLISHED HALF-CELLS*

R.L. Geng[†], A. Crawford, G. Eremeev, H. Padamsee, J. Sears
LEPP, Cornell University, Ithaca, NY 14853, USA

Abstract

A 1500 MHz niobium cavity has been fabricated with two half-cells, which are pre-electropolished with a very simple and compact system. In this paper, we present half-cell electropolishing, cavity fabrication and first test results.

INTRODUCTION

Electropolishing of niobium cavities is proving to yield consistently better performance than chemical polishing thanks to the persistent effort by KEK [1]. However, an electropolishing system for a multi-cell structure can become complicated and expensive. An alternative, economic way is to electropolish half-cells or dumbells before they are welded into a cavity. This method has been tried at DESY [2], but the results were reported to be unpromising. The cavity surface was compromised by the niobium vapor and spatter during electron beam welding. We have taken a second look at the principle of half-cell electropolishing by improving the electron beam welding procedure with an EB welder in our facility. A 1500 MHz niobium cavity has been fabricated with two half-cells, which are pre-electropolished with a very simple and compact system.

HALF-CELL ELECTROPOLISHING

1500 MHz cups were formed by deep drawing with 1/8″ thick RRR250 niobium sheets with MK-III dies. The inside surface of these cups was electropolished for a surface removal of 160 μm (This was done in March, 2000). The electropolishing set-up is similar to the one illustrated in Fig. 1. The cup is filled with a mixture of HF(49% wt.) and H_2SO_4(96% wt.) at a volume ratio of about 1:10. The mushroom-shaped cathode is made of aluminum. A voltage-regulated DC power supply is used. The normal voltage across electrodes is 10 - 15 V. The cup is cooled by bath water. Acid was agitated through a magnetic stirrer driven spin bar placed inside the acid and at the bottom of the cup. A laminar circulating acid flow is formed when the spinning speed is adjusted to the optimal value [3]. A continuously oscillating current is obtained and can be maintained for more than 2 hours. It is believed that in this CW current oscillation mode, a dynamic balance is
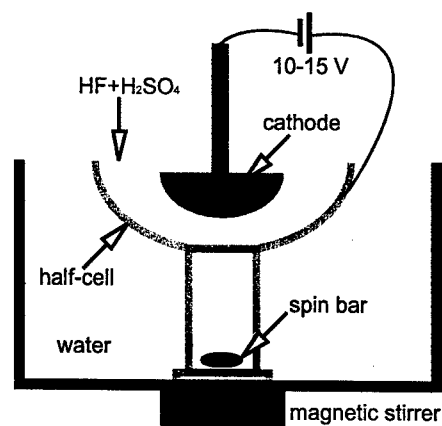
Figure 1: Sketch of the half-cell electropolishing setup.

reached between the niobium oxidization and dissolution of the oxide.

After electropolishing, the cups were trimmed at its iris and equator and then beam tubes were welded to the half-cells.

HALF-CELL PURIFICATION

The two beam-tube-welded half-cells were paired together and Ti purified in our furnace. The outside surface of the half-cells is taken care of by the Ti liner of the furnace and the inside surface by a cylindrical-shaped Ti box centered inside the cell.

An optimal heat treatment recipe [4] was used, namely 2 hours at 1300°C followed by 4 hours at 1200 °C. This recipe allows gettering of oxygen with limited Ti diffusion ($< 16\,\mu m$) into the bulk of niobium. The RRR is boosted to over 500 from 250, as measured with the witness samples treated in the same batch as the half-cells.

ELECTRON BEAM WELDING

The equator end of half-cells was dipped in cold BCP for 20 minutes to remove possible Ti trapped along the corner of the weld-preps. This was followed by another cycle of electropolish (Fig. 1) for an inside surface removal of about 30 μm to remove the Ti diffused layer of the RF surface. EBW of the equator was done with a special jig, made of niobium, running across the two irises as shown in Fig. 2. The jig has a maximum allowable diameter to
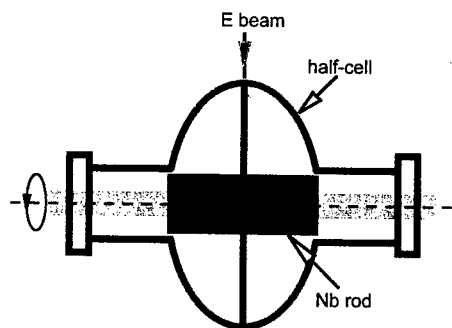
Figure 2: EBW pre-electropolished half-cells with a Nb vapor interceptor.

intercept niobium vapor and spatter so as to minimize contamination to the pre-electropolished surface.

The exterior surface of the welded cavity was etched with cold BCP for a surface removal of 3 μm to eliminate the titanized surface layer so as to improve heat transfer across the interface between the niobium and LHe during cavity test. The final step of the cavity treatment was a brief etching with cold BCP for a surface removal of 4.5 μm (inside and outside). Then the cavity was rinsed with high pressure water and mounted to the test stand.

CAVITY TEST RESULTS

First cavity test at 1.5 K yielded a Q_0 of 5×10^9 for Epk $\leq$ 15 MV/m as shown in Fig. 3. Above 15 MV/m, Q_0 dropped down to 6×10^8 at 20 MV/m. No x-ray was observed at the highest field and the limitation was due to the power from the amplifier.

Thermometry system revealed that there was a temperature rise within a band in the bottom half of the cavity. The boundary of the band is $1''$ and $3/4''$ away from the equator and the lower iris respectively. The center of the band does not corresponds to the peak magnetic field region. The na-

Figure 3: First test results.

ture of this increased losses is not fully understood yet. But residual Ti due to insufficient etching after purification is suspected.

The cavity was etched with cold BCP for another 7.5 μm of surface removal (inside and outside) and tested again. The overall BCP surface removal after EBW reached 13 μm for the inside surface and 16 μm for the outside surfacerespectively. This time, a surprising high Q_0 of 6×10^{10} was measured at low fields. This high Q is retained up to Epk = 25 MV/m. At this field, a Q-switch was observed. The Q_0 jumped to 2×10^{10} and Epk backed off to 20 MV/m. When the input power was raised further, Q started to drop down. Finally the cavity quenched at Epk = 30 MV/m. Again, no x-ray was observed for the entire field range. When the input power was decreased, Q switched back to 6×10^{10} at 20 MV/m.

Thermometry system revealed that at the switching field, a hot spot appeared near the equator. Also above 20 MV/m, the lower half of the cavity still showed relatively higher temperature rise within the same band observed during the previous test. The cause for the Q-switch at 20 - 25 MV/m is under investigation. A niobium blister from weld spatter is suspected.

REMARKS

Our first 1500 MHz half-cell electropolished has been fabricated and cavity test has started. First test showed encouraging high Q at low field and no field emission was observed up to a Epk of 30 MV/m. It is essential to remove a surface layer of at least 13 μm after EBW in order to achieve a high Q. Further investigations on Ti purification and welding procedures are needed to reach a higher accelerating field.

REFERENCES

[1] K. Saito, Proceedings of the 10th Workshop on RF Superconductivity, Tsukuba, Japan, 288(2001).

[2] L. Lilje, in The Workshop on Single-Cell Cavity R&D, ed. H. Rissen, TESLA Report, 2002-07, (2002).

[3] R.L. Geng et al., Proceedings of the 9th Workshop on RF Superconductivity, Santa Fe, New Mexico, USA, 238(1999).

[4] H. Safa et al., Proceedings of the 7th Workshop on RF Superconductivity, Gif Sur Yvette, France, 649(1995).
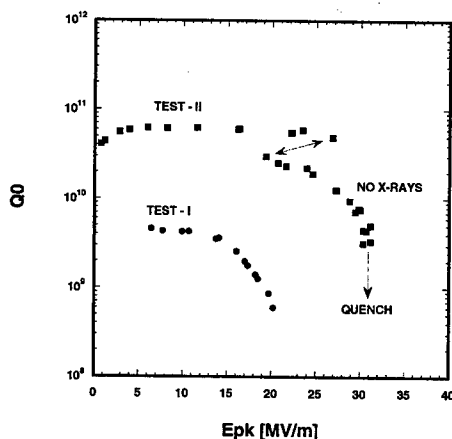
AN OPTIMIZED SHAPE CAVITY FOR TESLA: CONCEPT AND FABRICATION[#]

V. Shemelin*, R. L. Geng, J. Kirchgessner, H. Padamsee, J. Sears
Laboratory for Elementary-Particle Physics, Cornell University, Ithaca, NY 14853

Abstract

The accelerating gradient performance of superconducting niobium cavities is rapidly progressing as a result of reduced field emission due to improvement in surface preparation techniques. Beyond the field emission limitation, there exists a fundamental limit imposed by the critical magnetic field of niobium. One way to tackle this limit is to reduce the ratio of the peak magnetic field to the accelerating gradient so that a higher accelerating gradient is possible while the cavity is still superconducting. New cavity shapes of reentrant type have been proposed and optimized [1]. A single cell 1300MHz cavity of this new class of shapes has been fabricated. Because of the reentrant geometry, the fabrication and surface cleaning of the cavity becomes challenging. In this paper, we present some calculation prerequisites and the fabrication and preparation results for this new cavity.

1 INTRODUCTION

In deciding on a cell shape of a SC accelerating section, it is necessary to ensure both electric and magnetic strength. For comparison of different shapes one can use the ratios of the peak electric and magnetic field strength on the cell surface to the acceleration rate achievable in the given cell:

$$\frac{E_{pk}}{E_{acc}} = \frac{E_{pk}}{\Delta W/L} = \frac{E_{pk}}{2\Delta W/\lambda}, \quad \frac{H_{pk}}{E_{acc}} = \frac{H_{pk}}{2\Delta W/\lambda}.$$

Here ΔW is the energy gain (in volts) obtained at the cell length L equal to half wavelength (π-mode). For the TESLA accelerating cavity these values are [2]:

$$E_{pk}/E_{acc} = 2.0, \quad H_{pk}/E_{acc} = 42 \text{ Oe/(MV/m)}.$$

We will compare values of calculated fields with these values and introduce for this purpose the normalized peak electric and magnetic fields:

$$e = \frac{E_{pk}}{2E_{acc}}, \quad h = \frac{H_{pk}}{42E_{acc}}.$$

For the regular TESLA cells [2]

$$e = 1, \quad h = 1.$$

We believe that for superconducting cavities it is more important to reduce H_{pk} on the surface, even if we increase E_{pk}. This is because the critical magnetic field is a hard limit at which superconductivity fails and the cavity quenches; whereas E_{pk} is a soft limit: field emission can be decreased by maintaining better cleanliness and by high power processing.

2 THE CODE AND GEOMETRY FOR CALCULATIONS

We used for optimization the SLANS code [3]. This code has better accuracy in comparison with earlier URMEL code used for calculation of TESLA cavities. With SLANS we can expect accuracy better than 0.1 %.

The profile line of the original TESLA cell is constructed as two arcs: elliptic and circular, and a segment of a conjugated straight line between them (the dashed line in Fig. 1). It is felt that more intricate line could give better values of e and h.

Between other approaches we examined [1], one was done with use of two elliptic arcs. The problem of a cavity electric strength led to the iris edge in a shape of an ellipse long ago [4]. This type of cavity has several features important for superconducting Nb cavities [5]. Let us apply an ellipse to the inductive part of the cell because now we have a problem of *magnetic* strength.

After some optimization of the original geometry, the length of the straight interval conjugated to both ellipses appeared to be zero. So, we could describe the shape of the regular cell as two conjugated elliptic arcs. The aperture was taken as in the TESLA cell, $R_a = 35$ mm.
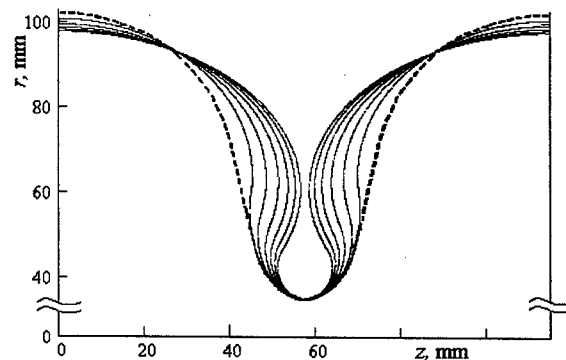
Fig. 1. Optimization of the TESLA regular cell shape. Dashed line – the present shape, solids – optimization with 2 elliptic arcs, δe = 0, 10, ..., 50 %.

3 RESULTS OF CALCULATIONS

The process of optimization consists in searching a cell shape with a minimal value of the peak normalized surface field e in this cell. The result of optimization should be a function $h(e)$, which should be a monotonous function, and from physical reasons it should be decreasing.

We turn to maximal electric strength as a special case: maximal electric strength is achieved with the shape corresponding to the leftmost point on the curve $h(e)$.

The results obtained by optimization can be used at any operation frequency because the values of e and h depend on the shape, not on the dimensions of the cavity. On the other hand, the value of the critical field H depends on the frequency and the choice of the working point on the curve of Fig. 2 can be different for different frequencies.

h goes down for lower ratios of the beam pipe radius to the wavelength (R_a/λ, Fig. 2). However, it is preferable to keep the same R_a to preserve low wakefields.

The data presented on the Fig. 2 correspond to the regular cell of the structure. The end cells have somewhat different dimensions and their optimization should be discussed separately.
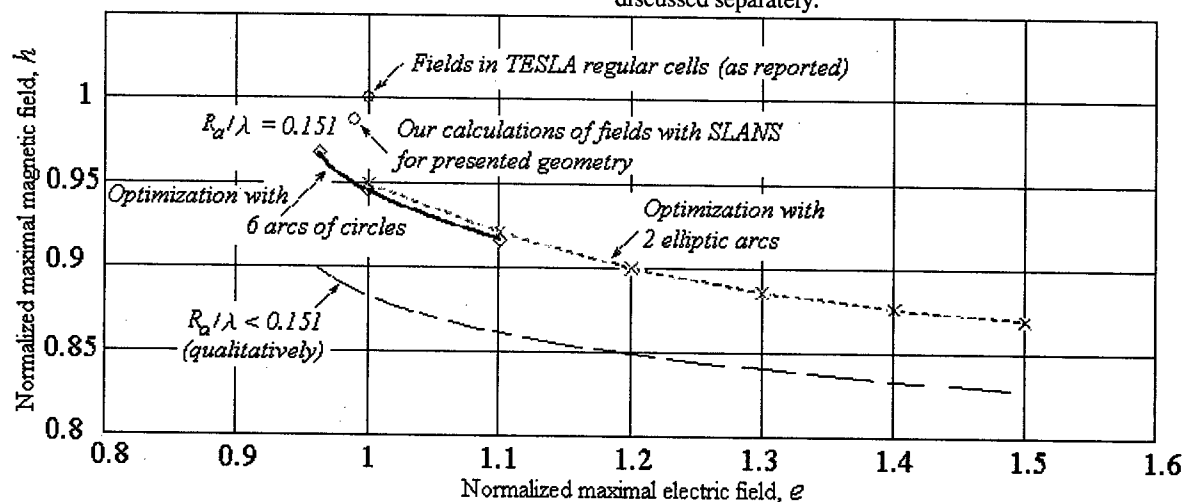
Fig. 2. Optimization curve for TESLA-like geometry.

Our calculations showed that for the TESLA regular cell geometry [2] maximal fields differ slightly from the values of fields presented also there: the electric field is 1.2 % below and magnetic field is 1.3 % below for the regular cells (see Fig. 2). The coupling coefficient k is obtained nearly the same: 1.87 %.

For comparison the results are summarized in the Table. Values of cell-to-cell coupling and iris thickness are also presented. This thickness (d) becomes small for the biggest δe that can be a technological problem.

Distribution of the cell area over the electric field is presented in Fig 3 for the original TESLA shape and for the shape with 10 % less magnetic field.

The parts of the curves corresponding to the field within 90 ... 100 % of the maximal value are shown. The area under each curve corresponds to the portion of the whole cell surface having the given value of field. One can see, for example, that 1.6 % of surface has electric field within 99.5...100 % of the maximal value in case of the optimal cell. The original cell has 2.8 % of surface within the same range of the relative value of field. However, the maximal field is 1.2 higher in the case of optimized field. The consequence of this is a higher field emission current in spite of less area. For example, for the field enhancement factor $\beta = 200$ and accelerating field $E_{acc} = 35$ MV/m the total field emission current will be 2.7 times higher for the optimized cell. This is a payment for a lower magnetic field.

With the simulation code MultiPac [6], it was shown that multipacting characteristics of the new cavity shape are not worse than of the original TESLA shape.

Table. δe, δh – change of normalized electric and magnetic fields by optimization with two elliptic arcs, k – coupling coefficient, d – minimal distance between the walls of cells.

δe, %	δh, %	k, %	d, mm
0	-5.07	1.90	24.80
+ 10	-7.92	2.10	18.30
+20	-10.00	2.38	12.52
+30	-11.36	2.64	8.14
+40	-12.30	2.88	4.74
+50	-12.99	3.06	2.18
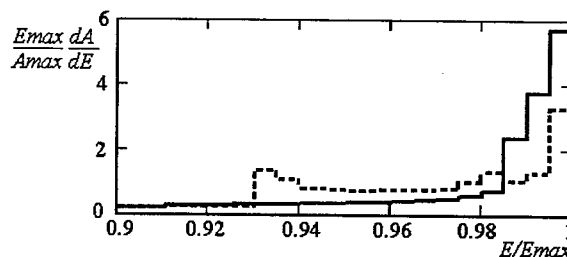
Fig. 3. Distribution of the cell surface area over the electric field. Solid line is for the original TESLA shape, dashed line – for the optimized cell with 10 % lower magnetic and 20 % higher electric field. A_{max} is the total surface area of the cell.

4 FABRICATION

Reentrant cups were successfully formed by deep drawing 3 mm thick RRR300 sheet niobium. It was critical to hold down the niobium blank sheet to the

1315

female die with a right torque. A center hole (an inch in diameter) on the blank was found beneficial to achieve better material flow in the critical reentrant section. No intermediate annealing was done to the cups. Very good contour of the reentrant section was achieved by using the coining technique, although the reentrant section was not pushed deep enough after the first stamping step. In order to reduce the chances of cavity quench at high gradients, cups were purified with yttrium [7] to drive out oxygen and improve niobium thermal conductivity. Heat treatment was done at 1200°C for 4 hours with distributed yttrium foils in the vicinity of niobium surface. The RRR value was boosted to 500 after this purification. The cups were trimmed with standard milling process. Fig. 4 shows a pair of the trimmed niobium cups to be welded to beam tubes. We plan to electropolish the half-cell before the final equatorial weld. This desire has driven us to switch from our traditional "step weld" of 1/16" material to "butt weld" of thicker, 0.11", material. A new set of EBW

parameters has been successfully developed and a very high quality weld with a negligible underbead was obtained. This is achieved by opening a small compensating groove on the inner surface at the equator, which holds the molten niobium and maintains its tensioned surface at the right place. Beam tubes are welded to the half-cells first. The welded parts would then go through heavy electropolish for a surface removal of more than 120 microns. This "half-cell electropolish" is the same as what we have done to some 1500 MHz cavities and half-cells [8]. The final equatorial weld of electropolished half-cells is done from outside and at full penetration with a niobium rod running across irises, which serves to intercept niobium vapor and spatter and prevents contamination to polished surface. The cavity would receive a light BCP, for a surface removal of about 10 microns, before high-pressure water rinsing, following which will be RF tests.

Fig. 4. 1300 MHz reentrant cavity cups. Left cup: outside surface view, right cup: inside surface view.

5 CONCLUSIONS

The presented results can be used for an increase of accelerating rate of the TESLA structure where the hard limit for this increase is the surface magnetic field. One can, for example, sacrifice 20 % of electric field to gain 10 % in magnetic field.

Calculations show that the new shape should be free of multipacting.

The change of the shape leads to some technological complications. Reentrant cups were successfully formed, heat-treated and prepared to electropolishing and welding.

6 REFERENCES

[1] V. Shemelin, H. Padamsee, R.L. Geng. Optimal cells for TESLA accelerating structure. Nucl. Instr. Methods Phys. Res.-A, 496, pp. 1-7, 2003.

[2] TESLA Test Facility Linac – Design Report. Editor D.A. Edwards. DESY Print, March 1995, TESLA 95-01.

[3] D.G. Myakishev, V.P. Yakovlev. The new possibilities of SuperLANS code for evaluation of axisymmetric cavities. 1995 PAC and Int. Conf. on High-Energy Accel. May 1-5, 1995. Texas. Pp. 2348-2350.

[4] M.M. Karliner, O.A. Nezhevenko, B.M. Fomel, V.P.Yakovlev. On the problem of comparison of accelerating structures operated by stored energy. (In Russian). Preprint of INP 86-146, Novosibirsk, 1986.

[5] P. Kneisel, R. Vincon and J. Halbritter, First results on elliptically shaped cavities. Nucl. Instr. Methods Phys. Res., 188, p.669-670, 1981.

[6] P. Ylä-Oijala et al. MultiPac 2.1. Rolf Nevanlinna Institute, Helsinki, 2001.

[7] H. Padamsee, IEEE Trans. Magn., 21, 1007 (1985).

[8] R.L. Geng et al., A 1500 MHz niobium cavity made of electropolished half-cells. This Conference, report TPAB050.

OVERVIEW OF THE CORNELL ERL INJECTOR CRYOMODULE

H. Padamsee, B. Barstow, I. Bazarov, S. Belomestnykh, M. Liepe, R. L. Geng, V. Shemelin,
C. Sinclair, K. Smolenski, M. Tigner and V. Veserevich
Laboratory for Elementary-Particle Physics, Cornell University, Ithaca, NY 14853

Abstract

The Laboratory for Elementary-Particle Physics, Cornell University, in collaboration with Jefferson Lab is exploring the potential of a Synchrotron Radiation User Facility based on a multi-GeV, low emittance, Energy-Recovery Linac (ERL) with a 100 mA CW beam[1]. The ERL injector will accelerate bunches from the electron source from 0.5 MeV to 5 MeV with minimal emittance growth. The injector and main linac of the ERL will be based on superconducting RF technology to provide CW operation. There will be one cryomodule with five 1300 MHz 2-cell cavities, each providing one MV of acceleration, corresponding to an accelerating field of about 4.3 MV/m in CW operation. Besides standard features such as an integrated helium vessel and mechanical tuner, each cavity has two input couplers, symmetrically placed on the beam pipe to cancel kicks due to coupler fields. For a 100 mA maximum injected beam current, each coupler must deliver 50 kW of beam power leading to a Qext of 4.6×10^4 for matched beam loading conditions. Antenna- and loop-based HOM couplers can disturb beam emittance through kicks. We plan to avoid the use of such couplers. Following the strategy for B-factory SRF cavities, the beam pipe aperture has been enlarged on one side to propagate all higher order modes out to symmetric ferrite beam pipe loads. These are positioned outside the helium vessel and cooled to liquid nitrogen temperature. Ferrite properties at 77 K have been measured and the corresponding damping evaluated. To explore the full capabilities of the injector, energy gains up to 3 MV per cavity will be considered at lower beam currents. For this flexibility, the input coupling needs to be adjustable by a factor of 9.

1 INTRODUCTION

Before committing to specific designs for a full energy ERL (a large machine with significant investment), it is essential that accelerator and technology issues be explored on a high current prototype machine. The first stage of the ERL project would be a 100 MeV, 100 mA (CW) prototype machine to study the energy recovery concept with high current, low emittance beams [2]. In the injector, a bunched 100 mA, 500 keV beam of a DC gun will be compressed in a normal-conducting copper buncher and subsequently accelerated by five superconducting (SC) 2-cell cavities to an energy of 5.5 MeV.

One attractive feature of a future linac-based light source is the low emittance beam from a high-brightness photo-emission electron gun. But the emittance must be preserved while the injector and main linac accelerate the beam. The goal is to have a beam with a normalized emittance of 2 mm·mrad. The injector system needs to deliver 500 kW to the beam through input coupling devices, typically antennae that protrude into the beam pipe. More than a hundred watts of beam induced power must be removed through HOM couplers. Both power delivery and extraction must be accomplished without introducing emittance-diluting asymmetries. At the same time, flexibility is necessary so that RF focusing and RF bunching can be accomplished without destroying space charge compensation. The high current beam must also remain stable against transverse and longitudinal multibunch instabilities. High average current and short bunch length beams excite significant higher order modes (HOMs) which result in cryogenic load. Our design goal is to allow a maximum emittance growth of no more than 10% total for five injector cavities [3].

The proto-ERL will require operation of superconducting cavities in two extreme regimes. In the injector, the high beam loading in the superconducting cavities requires a strong coupling to the fundamental mode coupler for high power transfer to the beam. In the main linac, the decelerated, re-circulated beam cancels the beam loading of the accelerated beam. Accordingly the main linac cavities must operate at a high external quality factor to minimize the RF power requirements.

To explore whether energy recovery is more favorable for smaller ratios of final and input energies, the injector cavities will be also be operated at three times the nominal gradient to deliver 15.5 MV total, but at lower current. Such studies will also open the possibility of better emittance preservation in the low energy part of the accelerator.

2 INJECTOR CAVITIES

Table 1 lists the properties of the superconducting 2-cell niobium structures, and Fig.1 shows the basic cavity/coupler design. The cavity design is fully discussed in [4].

One source of the emittance dilution is through interaction of the beam with high Q transverse higher-order modes (HOMs). Especially dangerous are the lowest frequency dipole modes with frequencies below the cut-off frequency of the beam pipes. With the cavity shape proposed, even the lowest dipole mode propagates into the beam pipe where it can be adequately damped by ferrite absorbers lining the beam pipe. The frequencies of

all dipole and monopole modes are at least 10 MHz higher than the appropriate cut-off frequency of the beam pipe. Cornell [5] and KEK-B [6] employ a similar strategy against HOMs.

Table 1: RF properties of 2-cell superconducting cavities.

Frequency	1300 MHz
Number of cells	2
R/Q	218 Ohm
E_{pk}/E_{acc}	1.94
H_{pk}/E_{acc}	42.8 Oe/(MV/m)
Coupling cell to cell	0.7 %
Q_0 at 2 K	$> 5 \times 10^9$
Twin-Input coupler Q_{ext}	$4.6 \times 10^4 / 4.1 \times 10^5$
Accelerating voltage	1 MV / 3 MV
Max. power transferred to beam	100 kW

Despite the presence of a large beam pipe to propagate out HOMs, the main cavity parameters are similar to those of the TESLA cavity. This was accomplished through the additional freedom of the cell length. The injector cavity has a thicker iris than in TESLA. The resulting cell-to-cell coupling is weaker (0.7 %), but still sufficient for two-cells.

The simulation code MultiPac [7] was used to check multipacting characteristic of the optimized cavity. This cavity shape is free of one-point multipacting. The familiar two-point multipacting exists but it is weak since the electron energies are about 35 eV.

3 INPUT COUPLER

The external Q factor must be variable through the range from 4.6×10^4 to 4.1×10^5. Such strong coupling usually demands a deep insertion of the antenna into the beam pipe, which enhances the kick problem. A twin-coaxial coupler [9] for the 2-cell SC cavities offers two advantages: (1) Ideally there is zero transverse kick to the beam traveling along the cavity axis and (2) it reduces the power load for each of its arms by a factor of two. The outer diameter of the coaxial line is 62 mm and the impedance 60-Ohm to minimize heating of the inner conductor. The geometry of the antenna tip (Figure 1) is optimized to minimize penetration into the beam pipe.

One of the possible sources of emittance dilution is a kick caused by non-zero on-axis transverse electromagnetic fields of fundamental power couplers in superconducting cavities. This effect is especially strong in the injector cavities, where a high average RF power per cavity must be coupled to a vulnerable low-energy

beam. The requirements here are far more demanding than in any existing system. A twin-input coupler reduces the kick ideally to zero. For a one mm offset between the two antenna locations, the kick is still more than a factor of 10 lower than the kick produced by a single coupler. Simulations show that a kick of this magnitude will be harmless to a low emittance beam [8].

A full description of the coupler is presented in [9]. The coupler will have two ceramic windows. One window is cold, tied to 80 K shield. This window with the "cold" part of the coaxial line will be attached to the cavity in a clean room thus sealing the cavity vacuum space. The "warm" coaxial line, waveguide-to-coaxial transition, and the "warm" ceramics will be attached in a process of the cryomodule assembly.
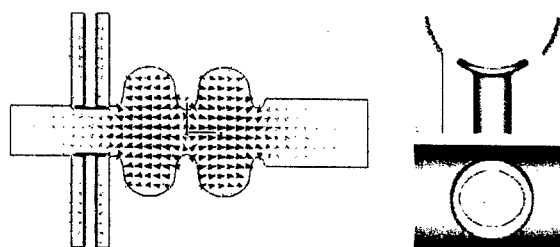
Fig. 1. Geometry of the cavity with the fundamental mode excited in it and details of the coupler.

4 HIGHER MODE COUPLERS

With the method described in detail in [4] and extended for circular waveguides, the value of Q_{ext} of the lowest frequency dipole mode was found as $Q_{ext, p} = 250$ for the parallel polarization. Due to the presence of the input couplers, the transverse polarization has lower frequency than the parallel one, but still propagates into the beam pipe and has $Q_{ext, t} \sim 1000$.

Strong damping of the HOMs is essential for beam stability and to reduce the HOM losses to a few hundred watts per meter. To achieve this demanding goal we plan to place RF absorbing material in the beam tubes between the cavities in the linac. However, this will require operating the HOM absorbers at temperatures below 80 K to simplify the thermal transition to the cavities at 2 K with low static losses to 2 K. One possible material candidate is ferrite, as it is used at room temperature in the HOM absorbers in the SC CESR cavities. Experiments performed to study the RF absorption properties of ferrite at cryogenic temperatures in the frequency range from 1 GHz to 15 GHz show that the material is even more lossy than at room temperature.

Using these ferrite properties in CLANS, first results show that the monopole HOMs are damped to Q values of less than 1000 with the exception of two modes near 5 GHz [10].

5 CRYOMODULE

For the injector cryomodule, our plan is to closely follow the design of the TESLA cryomodule. Constraints for the input coupler design will be similar to those of the TTF3 coupler. There will be heat intercepts at 4.2 K (cold He gas) and 80 K (either liquid nitrogen or cold He gas). The interface flanges, the length of the coupler as well as some other design features will be similar to the TTF3 coupler design.

6 REFERENCES

[1] Study for a proposed *Phase I Energy Recovery Linac (ERL) Synchrotron Light Source at Cornell University*, ed. by S. Gruner and M. Tigner, CHESS Technical Memo 01-003 and JLAB-ACT-01-04 (July 4, 2001).

[2] I. Bazarov, et al., "Phase I Energy Recovery Linac at Cornell University", *Proceedings of the 8th European Particle Accelerator Conference*, Paris, France, June 2002, pp. 644-646.

[3] S. Belomestnykh, et al., "High Average Power Fundamental Input Couplers for the Cornell University ERL: Requirements, Design Challenges and First Ideas," Cornell LEPP Report ERL 02-8 (September 9, 2002).

[4] V. Shemelin, S. Belomestnykh and H. Padamsee, "Low-kick Twin-coaxial and Waveguide-coaxial Couplers for ERL", Cornell LEPP Report SRF 021028-08 (November 28, 2002), and V.Shemelin et al, this conference.

[5] H. Padamsee et al., "Accelerating Cavity Development for the Cornell B-Factory, CESR-B", *Proceedings of the PAC'91*, pp. 786-788.

[6] S. Mitsunobu et al., "Superconducting RF Activities at KEK", *Proceedings of the 5th Workshop on RF Super-conductivity*, Hamburg, Germany, 1991, pp. 84-94.

[7] P. Ylä-Oijala et al. MultiPac 2.1. Rolf Nevanlinna Institute, Helsinki, 2001.

[8] I. Bazarov (private communication in minutes of the Cornell SRF meeting, and Z. Greenwald, this conference.

[9] V. Veserevich et al., this conference.

[10] M. Liepe et al., this conference.

FIRST STUDIES FOR A LOW TEMPERATURE HIGHER-ORDER-MODE ABSORBER FOR THE CORNELL ERL PROTOTYPE*

M. Liepe[†], B. Barstow, H. Padamsee, Cornell University, Ithaca, NY 14853, USA

Abstract

Cornell University, in collaboration with Jefferson Laboratory, has proposed the construction of a prototype energy-recovery linac (ERL) to study the energy recovery concept with high current, low emittance beams [1]. The beam with a current of up to 100 mA will excite significant higher-order-mode (HOM) power in the superconducting (s.c.) RF cavities with frequencies up to 100 GHz. Strong damping of the HOMs is essential for beam stability and to reduce the HOM losses to a few hundred Watts per meter. To achieve this demanding goal we plan to place RF absorbing material in the beam tubes between the cavities in the linac. However, this will require operating the HOM absorbers at temperatures below 80 K to simplify the thermal transition to the cavities at 2 K with low static losses to 2 K. One possible material candidate is ferrite, as it is used at room temperature in the HOM absorbers in the s.c. CESR cavities. In this paper we present experiments performed to study the RF absorption properties of ferrite at cryogenic temperatures in the frequency range from 1 GHz to 15 GHz. First results are shown and the resulting HOM damping is evaluated and discussed.

INTRODUCTION

In high current storage rings strong broadband HOM damping in superconducting cavities has been achieved by using beam-pipe ferrite loads, located at room-temperature; see [2] for CESR and [3] for KEK-B. Adopting the same damping concept for the ERL with RF absorbers between the cavities in a cavity string will require to operate the absorbers at a temperature of about 80 K. This temperature is high enough to intercepted HOM power with good cryogenic efficiency, and 80 K is low enough to simplify the thermal transitions to the cavities at 2 K. However, the electro-magnetic properties of possible absorber materials like the ferrite TT2-111R [4] were not well known at cryogenic temperatures. Therefore we started a measurement program at Cornell to answer the question if ferrite remains lossy at cryogenic temperatures.

FERRITE RF PROPERTIES AT 110 K

The complex ϵ and μ properties of a ferrite material called TT2-111R were measured at room temperature and at approximately 110 K in the frequency range 1 to 15 GHz. These properties were measured with a vector network analyzer using a technique suggested by Nicholson and Ross [5] and documented by Hewlett Packard [6].
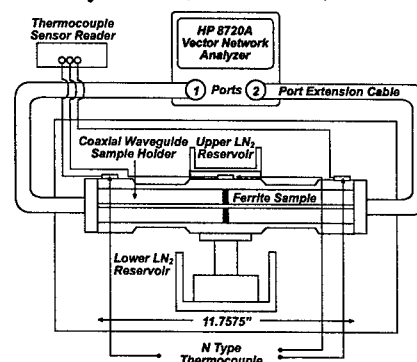
Figure 1: Schematic of low temperature EM properties measurement apparatus.

Measurement Setup

High frequency voltages were applied to a ferrite sample and the amplitude and phase of the reflected and transmitted waves were measured with a vector network analyzer. The normalized amplitude and phase of these waves are called the *S parameters*. From these S parameters the complex ϵ and μ values of the sample were inferred. A schematic of the experiment is shown in Figure 1. A 12 inch long coaxial waveguide with an outer conductor diameter of 7 mm and inner conductor diameter of 3 mm was used to hold the ferrite sample. A coaxial line, unlike a rectangular waveguide can support a wide range of radiation frequencies in a single propagation mode. Our 7 mm coaxial line can support radiation in a single frequency mode up to 18 GHz. To ensure that the microwave reflections from the interface between the cables and waveguide sample holder were minimized, the connector interfaces on the end of the sample holder were carefully machined.

A cooling clamp was attached to the center of the sample holder where the sample is situated. A finger protrudes from the clamp into a bath of liquid nitrogen to cool the sample. ANSYS and analytical calculations indicated that the center of a 12 inch long sample holder may have a temperature close to that of the liquid nitrogen bath ($\approx -165°C$) while the ends would be closer to room temperature ($\approx -60°C$) . This temperature gradient ensured that no damage occurred to the dielectric filled flexible cables that took microwave power from the network analyzer to the sample. It also minimized thermal deformation of the metallic connectors, ensuring minimal change of their physical state from the one they were calibrated at. To prevent ice formation on any of the cooled electronics, the experiment was housed under positive pressure in a nitrogen atmosphere.

Ferrite Samples

High quality material samples were needed to achieve reproducible, results with low systematic errors. It is necessary to have very good contact between the ferrite beads and the inner and outer conductors of the coaxial line. Several ferrite beads were carefully fabricated from tiles of TT2-111R. Those that most closely matched the dimensions of the sample holder were selected and used in the experiment.

Beads with an inner diameter slightly too small for the inner conductor were preferred. The inner conductor of the sample holder was cooled with LN_2 and the bead was forced along the line to its center. This ensured good contact between the sample and holder at 100 K and excellent contact at room temperature.

Calibration

The built in full 2 port calibration algorithm was used to calibrate the network analyzer. The isolation calibration routine was not used because of anecdotal evidence [7] suggesting that the network analyzer set up becomes overly sensitive to movements of the cables when this calibration is performed. It is necessary to correct the phase of the S parameters recorded by the network analyzer due to additional phase picked up as the microwaves propagate along the sample holder away from the sample. To do this one must know precisely the distance of the sample from the phase reference planes established during the network analyzer calibration. This distance was first measured approximately using a depth gauge. The insertion distance was then refined by comparing the phases of the reflected signals measured at either port of the network analyzer. The two phases should be identical, so the difference between them was minimized by varying the assumed insertion distance of the sample.

Measurements and Results

A number of room temperature S parameter data sets were then acquired. Gaseous nitrogen was pumped into the box. LN_2 was then poured into the reservoirs. The temperature of the middle of the line, where the sample is held, and the ends of the lines were measured. The measurement apparatus was then allowed to cool to its final, quasi equilibrium temperature before S parameter measurements were taken again.

Due to finite propagation time of signals in the setup and the wide frequency range over which the S parameters were measured it was found that the network analyzer receiver fell out of phase with the transmitter, resulting in an artificially attenuated transmission. To avoid this problem, a wide receiver bandwidth of 3 kHz and slow sweep over a short frequency range were used. Two data sets were taken, with 801 frequency points from 1 to 10 GHz, followed by another 801 frequency points from 8 to 18 GHz. The two data sets were merged following collection of the data. Good continuity was found between the data sets. It is believed that the presence of the ferrite sample in the line

caused excitation of higher order modes above 15 GHz, invalidating all measurements of the S parameters above this frequency.

The S parameters were converted to complex ϵ and μ values following the algorithm outlined by Hartung [8]. Multiple S parameter data sets spanning the range 1 to 18 GHz were collected at room temperature and $\approx$ 110 K. The different data sets were then averaged and filtered to smooth out ringing due to microwave reflection from the ends of the sample holder. The final results are shown in Figure 2 (next page).

EVALUATION OF HOM DAMPING

A Simple RF Absorber Model

For a first evaluation of the efficiency of the investigated TT2-111R ferrite, we used the simple planar absorber model shown in Figure 3. It is assumed that a TEM incident wave is propagating in positive z-direction towards the ferrite material (which extends to infinite in x- and y-direction). Based on the measured ferrite properties at 110 K, an absorber efficiency $\eta = P_{absorbed}/P_{incident}$ can be calculated, see Figure 4. As can be seen, the absorber is highly efficient at low temperatures in the frequency range in which the material properties have been measured so far.
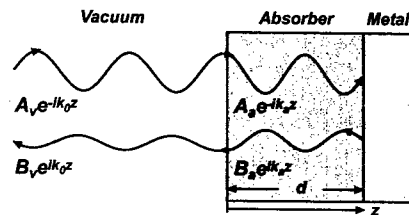
Figure 3: Absorber model.
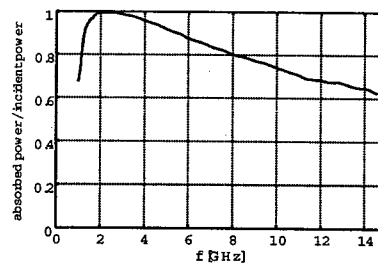
Figure 4: Absorber efficiency for a TT2-111R absorber with $d = 2$ mm thickness at 110 K.

ERL Injector Cavities

The finite element code CLANS has been used to calculate the damping of monopole modes by the ferrite absorbers in the injector cavities of the Cornell ERL prototype (refer to [9] for details). CLANS uses a complex eigen solver to calculate modes in an RF structure in the presence
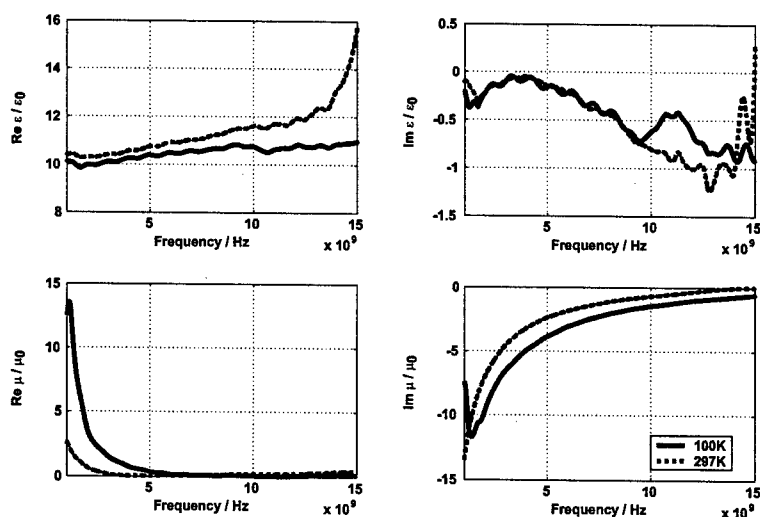
Figure 2: Complex ϵ and μ values of TT2-111R.

of an RF absorbing material. The measured complex ϵ and μ values of TT2-111R at 110 K were input into CLANS to describe the absorber properties in the numerical calculations. In the ERL injector the beam will be accelerated by five 2-cell cavities [10]. The presence of a 10 cm long ferrite ring-absorber between each cavity and at the ends of the cavity string was considered in the simulations. The obtained damping factors, represented via the quality factor $Q = \omega U/P_{diss}$, are shown in Figure 5. As intended, the fundamental mode passband is not propagating through the tubes, thus the fields at the absorbers are small and these modes are not significant damped by the ferrites. However, all other TM monopole modes are propagating, and their low quality factors show the strong damping by the absorber material.

FUTURE PLANS

We will extend the measurement of the absorber properties to 40 GHz by using rectangular waveguides as sample holders. Using different size waveguides will ensure that only one propagation mode is supported during a measure-
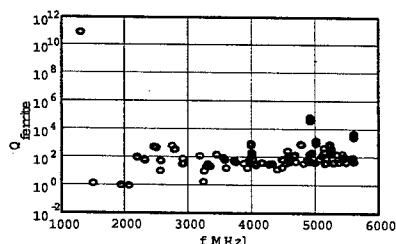
Figure 5: Calculated damping of TM monopole modes by ferrite ring-absorbers in the superconducting injector cavities of the ERL prototype.

ment in a certain frequency range. Absorber samples made of different ferrite types have been ordered and their RF losses will be compared to find the optimal broadband RF absorber for the Cornell ERL prototype.

CONCLUSIONS

The EM properties of the ferrite TT2-111R have been measured at 110 K and 300 K in the frequency range 1 to 15 GHz. In this frequency range TT2-111R is even more lossy at cryogenic temperatures than at room temperature, and therefore is a promising material for an RF absorber in the Cornell ERL prototype.

ACKNOWLEDGEMENTS

REFERENCES

[1] Study for a proposed Phase I ERL Synchrotron Light Source at Cornell University, ed. by S. Gruner and M. Tigner, CHESS Tech. Memo 01-003, JLAB-ACT-01-04 (July 2001).

[2] D. Moffat et al., in Proceedings of the 1993 Particle Accelerator Conference, Washington, DC, p. 977 (1993).

[3] KEKB B-Factory Design Report, Technical Report 95-7, KEK, Tsukuba, Japan, 1995.

[4] Product of Trans Tech, Adamstown, MD 21710, USA.

[5] A.M. Nicholson and G.F. Ross, IEEE Trans. Instrum. Meas. IM-19, p. 377-382 (1970).

[6] HP Product Note 8510-3: Measuring the dielectric constant of solids with the HP 8510 network analyzer, Hewlett Packard (1985).

[7] S. Ganchev, private communication.

[8] W.H. Hartung, Ph.D. thesis, Cornell University, Ithaca NY (1996).

[9] H. Padamsee et al., this conference, paper TPAB052.

[10] V. Shemelin et al., this conference, paper WPAB012.

NEW POSSIBILITIES FOR SUPERCONDUCTING CAVITY TESTING AT CORNELL UNIVERSITY*

M. Liepe[†], P. Barnes, I. Bazarov, S. Belomestnykh, R.L. Geng,
H. Padamsee, J. Sears, Cornell University, Ithaca, NY, 14853, USA
J. Knobloch, BESSY, D-12489 Berlin, Germany

Abstract

Cornell is testing superconducting cavities for many different purposes: system development for CESR, supporting technology transfer of CESR SRF systems to storage ring light sources around the world, collaboration with the world-wide TESLA project, collaboration with Muon Collider/Neutrino Factory projects, developing an Energy Recovery Linac (ERL) based synchrotron light source in collaboration with TJNAF, and basic cavity R&D in the areas of high Q, high field Q-slope and field emission.

For this Cornell has upgraded its preparation and test facilities and now has the capabilities to test s.c cavities with frequencies between 200 MHz and 3 GHz. Three radiation-shielded test pits have been built. The largest pit has a size of 2.4 m diameter by 4.4 meter deep. In addition to the existing RF test system at 500 MHz, 1.3 GHz and 1.5 GHz, a 200 MHz low power (2 kW) RF test system has been completed [1]. The high-power 1.3 GHz test system as well as the cavity preparation facility are presently being upgraded to incorporate TESLA 9-cell cavities. A new 1000 sq ft clean room is in operation for improved cavity preparation.

NEW FACILITIES

In a two year effort Cornell University has upgraded its cavity preparation and test facilities. A new clean room and cavity test pits give the unique capability to test superconducting RF cavities with frequencies as low as 200 MHz or a length of more than 2 m.

Cavity Test Pits

In a new cavity test area three test pits of different sizes have been excavated.

- Small test pit: 1 m diameter by 2.9 m deep for 1.5 GHz and higher frequency cavity tests.

- Medium test pit: 1.6 m diameter by 3 m deep for 500 MHz and 1.3 GHz cavity tests. A waveguide can be connected to the 1.3 GHz insert for pulsed high power tests.

- Large test pit: 2.4 m diameter by 4.4 m deep for 200 MHz and 1.3 GHz multicell cavity tests. Also this pit can be connected to the 1.3 GHz klystron for pulsed high power tests.

The small and large size pits are shown in Figure 1. A radiation shielding block with 90 tons of high density concrete can be moved over a selected pit during cavity test while the other two pits are accessible for cavity installation or removal. Up to three cavity tests within one week have been done with this new test facility.
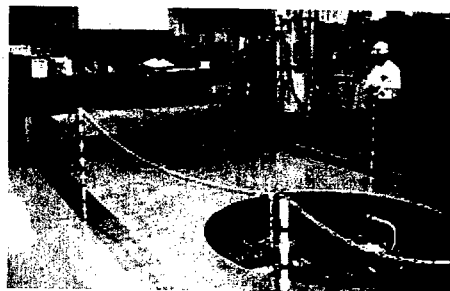
Figure 1: Test pits for various size cavities. Shown is the small and the large pit. Not shown is the medium size pit.

Clean Room

For improved cavity preparation a new clean room with a total size of about 1000 sq ft has been installed; see Figure 2. With 262 sq ft of class 1,000 area and 704 sq ft of class 100 area this clean room allows to prepare cavities for cw performance tests and to assemble whole cryostats with a length up to about 5 m. A high temperature high vacuum furnace for cavity post-purification and a high-pressure rinsing system for cavity cleaning are placed inside the clean room.
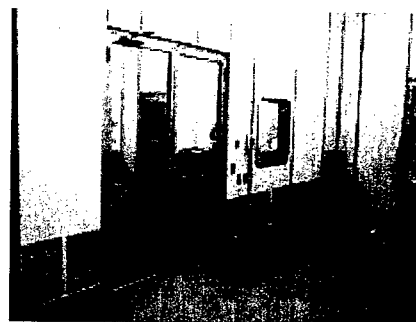
Figure 2: New 1000 sq ft clean room.

HPR System

A new high-pressure (up to 900 psi) water rinsing system has been built and installed in a class 100 area of the new clean room; see Figure 3. While the cavity is moving up or down, a nozzle head rotates to clean the inner cavity surface. Ultra-clean water is filtered once more directly before the nozzle head by a 0.1 μm teflon particle filter. The rinsing system has been designed to incorporate cavities from 1.5 GHz up to 500 MHz. With a travel range of about 120 cm, multicell cavities like a TESLA 9-cell cavity can be rinsed in one step.

Figure 3: New high-pressure water rinsing system.

CAVITY TEST SYSTEMS

200 MHz

The proposed neutrino factory and muon collider ask for RF cavities operating at a frequency near 200 MHz for rapid acceleration of muons [2]. One scenario is to use superconducting RF cavities [3]. The desired accelerating gradient is 17 MV/m at an unloaded quality factor of $6 \cdot 10^9$. Since there was no superconducting RF experience at 200 MHz, an R&D program was started. Two 200 MHz single cell elliptical Nb sputtered Cu cavities have been fabricated by CERN at tested at Cornell University. Figure 6 shows a 200 MHz cavity mounted on the test insert for a cw cavity performance test in the large test pit. A 2 kW cw RF amplifier is available to power the cavity during test. Several tests have be done so far; refer to [1] for details.

500 MHz

The 500 MHz cw cavity test insert with a cavity mounted is shown in Figure 6. A 500 W cw amplifier is used to drive the cavity during a performance test. In the past years this insert was used for cavity qualification tests prior to the installation of a cavity in a cryostat. In the future we plan
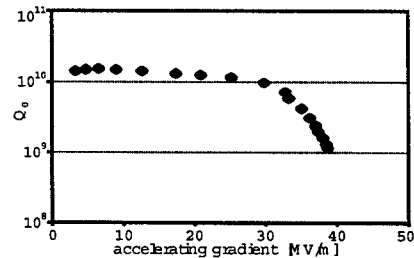
Figure 4: Cw performance of a 1.3 GHz electropolished single-cell cavity (EP done at CERN).

to test Nb sputtered 500 MHz cavities to continue the work on sputtered SRF cavities.

For a full system test a 500 MHz horizontal cryostat test facility is in operation with a 600 kW cw klystron to power the cavity. All CESR cryostats are tested to verify their performance before installing them in the CESR ring.

1300 MHz

About 10 years ago the work on s.c. 1.3 GHz cavities for the proposed TESLA linear collider was started at Cornell. A cavity test insert for low power cw test and high power pulsed test was built, see Figure 6. Via a waveguide the cavity under test can be powered from a cw 200 W amplifier or a 2 MW pulsed klystron. High peak power processing allowed to reach record high fields in the early days of these studies. Today's improved cavity preparation allows to reach high fields during a performance test without any X-rays, see for example Figure 4.

Since the "old" 1.3 GHz insert is limited to 1 to 5 cell cavities a new 1.3 GHz cavity insert with waveguide coupler is under construction; see Figure 5. This new setup will allow to test cavities with a length of up to 2 m, e.g. TESLA 9-cell cavities.
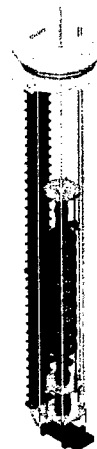
Figure 5: Sketch of the 1.3 GHz cavity insert under construction.

1324
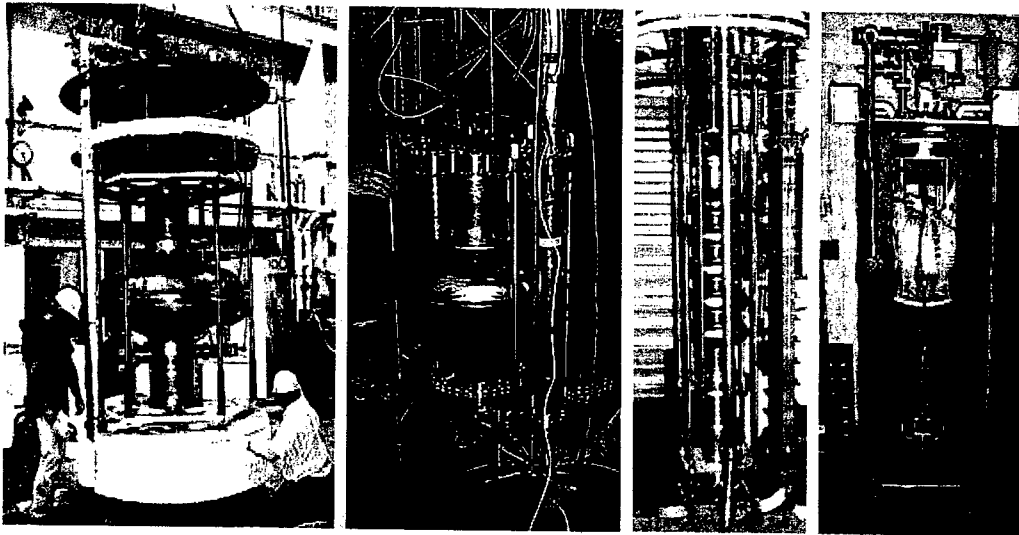
Figure 6: Cavity test inserts for various frequencies. From left to right: 200 MHz system, 500 MHz system, 1300 MHz system and 1500 MHz system.

1500 MHz

The 1500 MHz single-cell cw test system (see Figure 6) is used frequently for basic cavity R&D. With its temperature mapping system [4] it provides a powerful tool to study the high field behavior of SRF cavities. Recent studies focused on the high-field Q-drop and electropolished cavities [5].

FUTURE PLANS

Cornell will continue its work in basic SRF cavity R&D as well as in RF system development. While in the last years the primary effort of the SRF program was the development, construction, installation and operation of the 500 MHz CESR SRF system, in the upcoming years we will broaden our high gradient, high Q cavity studies for future light sources and the proposed TESLA linear collider. Cornell University, in collaboration with TJNAF, has proposed the development and construction of an Energy Recovery Linac (ERL) based synchrotron light source [6]. Such a machine offers superior x-ray beams compared to storage ring sources due to a significantly better beam quality. In order to develop the required technology and to demonstrate the feasibility of a high current, low emittance ERL we are proposing the construction of an 100 MeV, 100 mA ERL prototype at Cornell [7]. Central parts of this machine are the superconducting injector linac with 2-cell cavities and the main linac with energy recovery. Many challenges like the cw cavity operation at high gradients, HOM damping, emittance preservation, high cw power input couplers and RF field control needs attention to develop the SRF system for the ERL prototype. With the new SRF facilities we have the infrastructure to address these challenges, and work is in progress; refer to [8, 9, 10, 11, 12, 13, 14, 15].

REFERENCES

[1] R.L. Geng et al., this conference, paper TPAB049.

[2] Feasibility Study-II of a Muon-Based Neutrino Source, ed., S. Ozaki, R. Palmer, M. Zisman, and J. Gallardo, BNL-52623 (2001).

[3] H. Padamsee, SRF for muon colliders, Proceedings of the 9th workshop on RF superconductivity, 587 (1999).

[4] J. Knobloch, Ph.D. thesis, Cornell University, CLNS thesis 97-3 (1997).

[5] R.L. Geng et al., this conference, paper TPAB050.

[6] Study for a proposed Phase I ERL Synchrotron Light Source at Cornell University, ed. by S. Gruner and M. Tigner, CHESS Tech. Memo 01-003, JLAB-ACT-01-04 (July 2001).

[7] C. Sinclair et al., this conference, paper TOAC005.

[8] H. Padamsee at al., this conference, paper TPAB052.

[9] V. Veshcherevich, this conference, paper TPAB009.

[10] V. Veshcherevich, this conference, paper TPAB008.

[11] V. Shemelin et al., this conference, paper WPAB012.

[12] M. Liepe and S. Belomestnykh, this conference, paper TPAB056.

[13] M. Liepe et al., this conference, paper FPAB027.

[14] M. Liepe et al., this conference, paper TPAB053.

[15] Z. Greenwald, this conference, paper WPAB011.

MICROPHONICS DETUNING IN THE 500 MHz SUPERCONDUCTING CESR CAVITIES*

M. Liepe[†] and S. Belomestnykh, Cornell University, Ithaca, NY 14853, USA

Abstract

The RF system of the Cornell Electron Storage Ring (CESR) consists of four superconducting (s.c.) 500 MHz cavities. For a charm-tau upgrade (CESR-c, see [1]) we plan to drive two cavities by one klystron and to operate some cavities in passive mode [2].

During the previous high energy run the RF system performance was not significantly affected by microphonic cavity detuning, since the cavities were operated under strong beam loading with a low loaded quality factor of $2 \cdot 10^5$. However, in low energy CESR-c operation with increased loaded Q-factor the RF system becomes less tolerant to microphonics, especially when two cavities are driven by one klystron. In order to address this potential problem we have studied microphonics in the CESR cavities in detail. Significant improvements have been achieved by reducing major contributions to the detuning. For further improvements we plan to study the performance of an active microphonics compensation scheme, which is based on a fast piezoelectric-driven frequency tuner.

INTRODUCTION

Environmental microphonic noise can cause fluctuation of the cavity resonance and as a result produce amplitude and phase modulations of the cavity field, which then can affect beam quality or RF system performance. This is especially true for high-Q superconducting cavities. Though this noise was an issue when the very first s.c. cavity has been installed in CESR [3], it was drastically reduced later and is not considered a limiting factor in the present configuration of the CESR RF system with external cavity quality factors of approximately $2 \cdot 10^5$.

However, as CESR is being modified for operating at lower energies, there will be changes in the RF system parameters and configuration [4]. First of all, two out of four s.c. cavities will be operated in a passive mode (i.e. driven only by the beam current) at high voltage and external quality factor [2]. Second of all, the remaining two active cavities will have to operate at significantly higher Q_{ext} ($6 \cdot 10^5$ to $1.2 \cdot 10^6$) than at present. Hence we need to reassess the influence of microphonics.

Microphonics influence on the beam quality via the active cavities should be negligible as RF feedback loops are taking care of the cavity field stability. The issue here is the RF system performance. Bigger RF power overhead is required to compensate for the microphonics detuning. Suppose the cavity is tuned to compensate the reactive beam loading, then the required forward power P_f from the klystron is

$$P_f = \frac{V_c^2}{4\frac{R}{Q}Q_{ext}} \left\{ \left[1 + \frac{I_b \frac{R}{Q} Q_{ext}}{V_c} \cos \phi_s \right]^2 + \left[\frac{2Q_{ext}\delta\omega_m}{\omega} \right]^2 \right\} \quad (1)$$

Here V_c is the cavity voltage, I_b is the average beam current, ϕ_s is the synchronous phase, $\delta\omega_m$ is the amplitude of the microphonic noise, and ω is the RF frequency. At full beam loading (i.e. matching conditions) the relative contribution of the microphonics to the power demands is then

$$\frac{\delta P_f}{P_f} = \left(\frac{Q_{ext}\delta\omega_m}{\omega} \right)^2 \quad (2)$$

Accordingly 42 Hz microphonics at the external Q of $1.2 \cdot 10^6$ results in 1% of forward power fluctuation. Since a fluctuation of a few percent can be tolerated, keeping the peak microphonic detuning below 100 Hz is desirable for the CESR-c cavities.

In the passive cavities microphonic noise will cause amplitude and phase modulation of the cavity voltage [5], which in turn will affect the bunch length. While phase modulation for the CESR-c conditions is reasonably small, the voltage amplitude modulation can be significant. In passive operation the cavities are detuned by several bandwidths ($\Delta\omega \gg$ cavity bandwidth) [2], and for this condition the field amplitude modulation due to microphonics is given by

$$\left| \frac{\delta V_c}{V_c} \right| \approx \frac{2V_c}{I_b \frac{R}{Q}} \frac{\delta\omega_m}{\omega}. \quad (3)$$

We find that a microphonics amplitude of 30 Hz gives a 1 % voltage amplitude fluctuation. A fluctuation of a few percent can be tolerated with respect to the resulting bunch length modulation. Accordingly keeping the peak microphonic detuning below 100 Hz is desirable also for the passive cavities in CESR-c.

MICROPHONICS STUDIES AND REDUCTION

Since microphonic cavity detuning is a potential limiting factor during CESR-c operation, we started a measurement program to study the microphonics levels in the CESR cavities in detail. A typical measured fluctuation of the 500 MHz mode frequency of a CESR cavity (cavity E2) is shown in Figure 1. We identified two significant contributions to the measured fluctuation of the accelerating mode frequencies:

- The slow frequency tuner excites vibration of the cavity. The tuner is driven by a stepping motor and is

used to compensate slow drifts of the cavity eigen frequency. A sequence of steps of the stepping motor has a step frequency of several 10 Hz. If this frequency matches a mechanical resonance of the cavity-cryostat system, strong mechanical vibrations can be excited, which then can result in a modulation of the 500 MHz electrical resonance frequency; see Figure 1 and Figure 2. In the example shown, a mechanical resonance at about 75 Hz is excited by a sequence of motor steps; see also Figure 6.

- The second contribution to the measured cavity microphonics is not due to vibration of the cavity itself, but results from a phase modulation of the 500 MHz CESR reference signal; see Figure 3. Cleary visible are sidebands at frequencies $f = 500 \text{MHz} \pm n \cdot 120 \text{Hz}$. Since the RF feedback loops measure the phase of the RF field with respect to the 500 MHz reference signal, it appears as if the 500 MHz electrical cavity resonance frequency is fluctuating with frequencies $f = n \cdot 120 \text{Hz}$; see Figure 2.

Figure 2: Measured microphonics spectrum. Top: Fourier transform of the cavity detuning signal shown in Figure 1 (before improvements have been made). Bottom: Fourier transform of the cavity detuning signal shown in Figure 4 (after improvements have been made).

Figure 1: Top: Fluctuation of the 500 MHz mode frequency of cavity E2 before improvements have been made. The peak cavity detuning is 150 Hz, the fluctuation is 27 Hz rms. Bottom: Stepping motor activity of the slow frequency tuner during the same time interval. Each impulse marks a motor step.
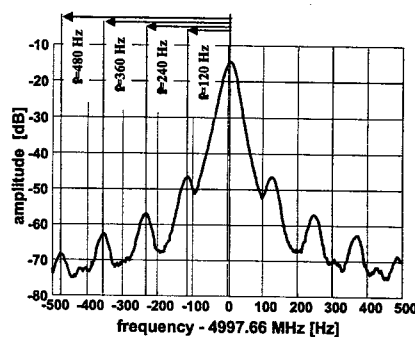
Figure 3: Spectrum of the 500 MHz CESR reference signal before improvements have been made.

The microphonics measurements showed rms amplitudes of 20 to 30 Hz and peak microphonics amplitudes of about 150 Hz for the four CESR cavities. The peak values are above our 100 Hz goal for the low energy CESR-c operation, and a reduction of the microphonics levels was needed. Since we had identified two major contributions to the cavity microphonics, a logical step was to reduce these sources. To avoid vibration excitation by the slow frequency tuner the step sizes of the motor have been reduced. As a result of this, the cavity is now tuned smother with a faster sequence of smaller steps, and the excitation of mechanical resonances is reduced significantly; see Figure 4.

The sidebands of the 500 MHz reference signal were eliminated by improving the grounding of the RF signal generation hardware; see Figure 2. Due to these steps the microphonics levels in the CESR cavities were reduced by about a factor of two. Typical rms values are now 15 Hz with peak microphonics amplitudes of about 60 Hz, i.e. well below the CESR-c requirements.

FUTURE PLANS

After eliminating major sources of the microphonic cavity detuning, further reduction of the frequency fluctuation can be achieved by using a fast active compensation scheme. Piezo-electric elements are frequently used for vibration damping, and have been used to drive a fast cavity frequency tuner [6]. To investigate a fast frequency tuning scheme for the CESR cavities, piezo-elements have been integrated into the tuning frame of the slow stepping-motor driven frequency tuner; see Figure 5. In order to design a feedback loop for fast detuning compensation, it
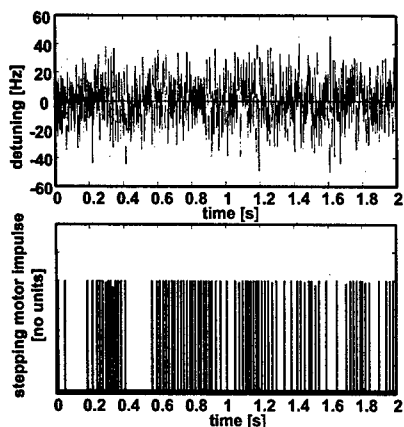
Figure 4: Top: Fluctuation of the 500 MHz mode frequency of cavity E2 after improvements have been made. The peak cavity detuning is 60 Hz, the fluctuation is 14 Hz rms. Bottom: Stepping motor activity of the slow frequency tuner during the same time interval. Each impulse marks a motor step.

Figure 6: Transfer function from the piezo drive signal to the cavity detuning measured at cavity E2. Top: amplitude. Visible are mechanical resonances above 40 Hz. Bottom: phase.

is essential to identify the dynamics of the system. Figure 6 shows the measured transfer function from the piezo drive signal to the cavity detuning measured at cavity E2. Clearly visible are mechanical resonances above 40 Hz, with the strongest resonance at about 75 Hz. Note that the 75 Hz resonance is excited by the steps of the slow frequency tuner during the microphonics measurement shown in Figure 1 and 2. Because of the low frequency resonances feedback control will be challenging and a complex control algorithm will be required. A digital control system is presently under development [7] and will provide the needed computational capacities for a digital controller. Once the hardware is finished we plan to study the performance of a fast microphonics compensation controller. Beside a further reduction of the microphonic cavity detuning at the CESR cavities, we hope to benefit from this experience when designing a fast frequency tuner for the cavities of the proposed Cornell ERL prototype [8, 9], where low microphonics amplitudes are essential [10].

CONCLUSIONS

For the low energy CESR-c operation microphonics amplitudes in the four s.c. cavities below 100 Hz are desirable. Detailed studies of the microphonics levels and frequency spectrum enabled us to identify major contributions to the frequency fluctuation. Eliminating these sources reduced the microphonics amplitudes by a factor of two to a level well below the CESR-c requirements. Further reduction appears feasible by using a fast active detuning compensation scheme based on a piezo-electric driven frequency tuner.

ACKNOWLEDGEMENTS

REFERENCES

[1] D. Rice, Proceedings of the European Particle Accelerator Conference 2002, Paris, June 2002, p. 428.

[2] S. Belomestnykh et al., this conference, paper TPAB048.

[3] S. Belomestnykh et al., Proceedings of the 2001 Particle Accelerator Conference, Chicago, IL, June 2001, p. 1065.

[4] S. Belomestnykh, Report SRF020918-06, Cornell Laboratory for Elementary-Particle Physics (2002).

[5] S. Belomestnykh, et al., Proceedings of the 2001 Particle Accelerator Conference, Chicago, IL, June 2001, p. 1062.

[6] M. Liepe et al., Proceedings of the 2001 Particle Accelerator Conference, Chicago, June 2001, p. 1074.

[7] M. Liepe et al., this conference, paper FPAB027.

[8] Study for a proposed Phase I ERL Synchrotron Light Source at Cornell University, ed. by S. Gruner and M. Tigner, CHESS Tech. Memo 01-003, JLAB-ACT-01-04 (July 2001)

[9] C. Sinclair et al., this conference, paper TOAC005.

[10] M. Liepe et al., this conference, paper TPAB056.

Figure 5: CESR cryostat with piezo frequency tuner.

RF PARAMETER AND FIELD STABILITY REQUIREMENTS FOR THE CORNELL ERL PROTOTYPE

M. Liepe*and S. Belomestnykh, Cornell University, Ithaca, NY, 14853, USA

Abstract

Cornell University, in collaboration with Jefferson Laboratory, has proposed the construction of a prototype energy-recovery linac (ERL) to study the energy recovery concept with high current, low emittance beams [1, 2]. The ERL will require the operation of superconducting cavities in two extreme regimes. In the injector a multi-mA beam is accelerated to several MeV energy. The resulting high beam loading in the superconducting cavities requires a strong coupling of the fundamental mode coupler and a high power transfer. The dominating sources of field perturbation in the injector cavities are beam transients and beam current fluctuations. In the main linac the decelerated recirculated beam cancels the beam loading of the accelerated beam. Accordingly these cavities are operated at a high external quality factor to minimize the RF power requirements. Microphonic cavity detuning and path length fluctuations significantly increase the RF power demands. In this paper an overview of the prototype RF system is given and the RF power demands and field stability requirements are discussed in detail.

OVERVIEW

The schematic of the injector RF system is shown in Figure 1 (see also [3]). A bunched 100 mA, 500 keV beam of a DC gun will be compressed in a normal-conducting copper buncher and subsequently accelerated by five superconducting (s.c.) 2-cell cavities to an energy of 5.5 MeV.

The main linac with energy recovery is based on five superconducting 9-cell cavities, each with its own field control system and klystron; see Figure 2.

INJECTOR CAVITIES

Buncher Cavity:

The buncher cavity is a normal-conducting single-cell cavity made of copper. It is used to produce a correlated energy variation of about 10 keV along a $\sigma_{gun} = 12$ ps, 500 keV bunch coming from the gun. This will shorten the bunch to $\sigma_{inj} = 2.3$ ps in a drift space between the buncher cavity and first superconducting cavity. The RF properties [4] of the buncher cavity are listed in Table 1.

Power requirements: In order to maximize the energy variation along the the bunch at a given cavity accelerating voltage V_{acc}, the beam passes the buncher cavity $-90°$ off-crest, i.e. during zero-crossing. The RF power required to maintain a constant field in the cavity is then given by

$$P_g = \frac{V_{acc}^2}{\frac{R}{Q}Q_0} \frac{(1+\beta)^2}{4\beta} \left\{1 + \frac{Q_0^2}{(1+\beta)^2}\left(\frac{\omega_c}{\omega} - \frac{\omega}{\omega_c} - \frac{R}{Q}\frac{I_b}{V_{acc}}\right)^2\right\},$$

(1)

* mul2@cornell.edu
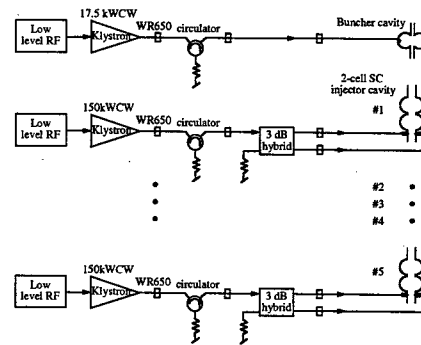
Figure 1: Schematic view of the ERL injector RF system.
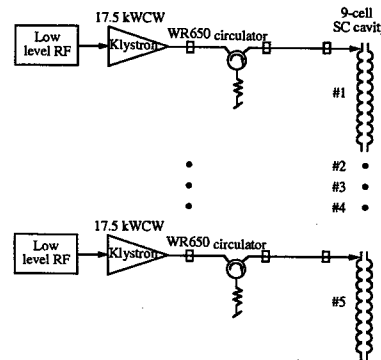
Figure 2: Schematic view of the ERL main linac RF system.

where $\beta = Q_0/Q_{ext}$ is the coupling factor of the input coupler, ω_c is the cavity eigenfrequency and ω is the RF frequency of the driving power. It is desirable to minimize the required RF drive power with and without beam passing the cavity. The short ion-clearing gaps in the beam train will not allow to retune the cavity for beam/ no beam conditions. In both cases a minimum RF power of 5.2 kW is required, if the frequency of the cavity is tuned to 1.3 GHz + 57 kHz, and if the coupling factor of the input coupler is

Table 1: RF properties of the ERL cavities.

	buncher cavity	2-cell injector	9-cell main linac
Frequency	1300 MHz	1300 MHz	1300 MHz
Num. of cells	1	2	9
R/Q	210.5 Ω	218 Ω	1036 Ω
Q_0	20,000	$> 5 \cdot 10^9$	$> 1 \cdot 10^{10}$
Q_{ext}	9,900	$4.6 \cdot 10^4$ ($4.1 \cdot 10^5$)	$2.6 \cdot 10^7$
Acc. voltage	120 kV	1MV (3MV)	$\approx 21 MV$

$\beta = 2.02$. To account for waveguide losses and power overhead for control we shall add 30 % to this number. Thus the required unsaturated output power of the klystron driving the buncher cavity is 6.8 kW.

2-Cell S.C. Cavities:

Downstream of the copper buncher the beam will be accelerated by five superconducting 2-cell cavities (see [5]) to 5.5 MeV (up to 15.5 MeV for special studies). The beam passes these cavities on-crest at small bunch charges and slightly off-crest (up to 15°) for a 77 pC bunch charge to compensate space charge effects. The RF properties of the s.c. injector cavities are summarized in Table 1.

Power requirements: With optimized (matched) input coupler coupling the required RF drive power for a superconducting injector cavity is simply given by the power transferred to the beam: P= $V_{acc}I_b = 1$ MV $\cdot$ 0.1 A = 100 kW. Increasing this number by 30 % for waveguide losses and control overhead yields 130 kW as required klystron output power per cavity. As mentioned above, this requires matched coupling of the input coupler with

$$Q_{opt} = \frac{V_{acc}}{\frac{R}{Q}I_b \cos\phi_b}. \qquad (2)$$

Assuming on-crest acceleration this gives $4.6 \cdot 10^4$ for the baseline energy gain of 1 MeV per cavity and $4.1 \cdot 10^5$ for a 3 MeV operation with 33 mA beam current. These relativly low values reflect the strong beam loading in the injector cavities. Because of the resulting large bandwidth, microphonics cavity detuning (usually well below 50 Hz) will give no significant increase in the RF power demand.

Stability Requirements:

Amplitude fluctuations of the buncher cavity voltage will affect the resulting bunch length. It is desirable that the bunch length does not fluctuate more than 0.1 ps (rms). This results in a modest amplitude stability requirement of $8 \cdot 10^{-3}$ (rms).

The intra-bunch energy spread behind the injector is about $\sigma_{inj} = 10$ keV for 5.5 MeV, 77 pC bunches (dominated by space charge effects [6]). It is desirable for the bunch-to-bunch energy fluctuation (bunch centroid energy) at the end of the injector to be well below the intra-beam energy spread. Then the total energy spread of the beam is dominated by the latter. The gun laser timing jitter, the buncher cavity as well as the five superconducting injector cavities contribute to a bunch-to-bunch energy variation in the injector. We have to separate between uncorrelated and correlated (from cavity to cavity) errors. For the ERL injector cavities the 100 mA beam loading will be dominating field perturbation, which will cause correlated field errors. Accordingly, we shall consider correlated field errors in the injector cavities. A stability of 2 ps rms is achievable for the gun laser timing jitter. This jitter is compressed by the buncher cavity to 0.1 ps (0.047° phase error at 1.3 GHz). The resulting energy error in the buncher and the five SC

injector cavities (for 15° off crest acceleration) is 0.87 keV. We require that the bunch-to-bunch energy fluctuation is increasing the total energy spread at the injector by less than 20%, i.e. to a total of 12 keV rms. Accordingly, the maximum bunch-to-bunch fluctuation is 6.6 keV. Quadratically subtracting 0.87 keV contribution of the gun timing jitter will allow for 4.7 keV energy spread contribution of the phase errors and amplitude errors each. Considering that the phase errors of the buncher cavity and the five injector cavities contribute equally, this gives a maximum allowable energy fluctuation of 2.35 keV rms from phase errors. Table 2 summarizes the resulting stability requirements in the injector. For more details refer to [7].

S.C. MAIN LINAC CAVITIES

In the main linac a 100 mA beam is accelerated by five superconducting 9-cell TESLA-style cavities (baseline layout) to a final energy of about 105 MeV (assuming 5.5 MeV injection energy), while the recirculated beam is decelerated from 105 MeV to 5.5 MeV. Each cavity is operated at an accelerating cw gradient of about 20 MV/m. The RF properties of the linac cavities are summarized in Table 1.

Depending on the machine-operating mode, the beam will pass these cavities on-crest or slightly off-crest [6]:
(1) Minimum energy spread operation: On-crest beam acceleration results in a minimum intra-bunch energy spread of $\sigma \approx 50$ keV.
(2) Low emittance operation: Off-crest acceleration by about $-15°$ gives minimum CSR emittance growth.
(3) Short-bunch operation: Off-crest acceleration by about 15° for bunch compression in the Bates magnets results in a bunch length of about 100 fs.

Power requirements: Since the beam loading of the accelerated and decelerated beam cancel, ideally there is no effective beam loading for the accelerating cavity mode. The required RF power to maintain a given accelerating voltage V_{acc} is then

$$P_g = \frac{V_{acc}^2}{4\frac{R}{Q}Q_{ext}}\left\{1 + \left(\frac{\Delta\omega 2Q_{ext}}{\omega_c}\right)^2\right\}. \qquad (3)$$

We see that the maximum power is determined by the peak microphonics cavity detuning $\Delta\omega = \omega_c - \omega$ during cavity operation; see Figure 3. Therefore passive and active

Table 2: RF stability requirements in the injector and resulting energy spread.

	gun timing jitter	buncher cavity	s.c. cavities
Ampl. stab. (rms)	-	$8 \cdot 10^{-3}$	$9.5 \cdot 10^{-4}$
Phase stab. (rms)	2ps	0.1°	0.1°
Contrib. of ampl. fluct. to energy spread	-	-	4.7 keV
Contrib. of phase fluct. to energy spread	0.87 keV	2.35 keV	2.35 keV
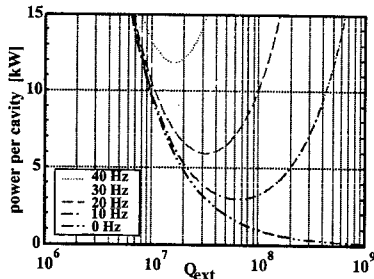
Figure 3: Required RF power to maintain an accelerating gradient of 20 MV/m in a 9-cell main linac cavity as function of the coupler external quality factor for different peak microphonic detunings.

Figure 4: Required RF power to maintain an accelerating gradient of 20 MV/m in a main linac cavity in presence of a phase error of the recirculated beam. Also shown is the optimum detuning needed to minimize the RF power demands. The accelerating phase is $-15°$.

reduction of the cavity vibration is desirable to further improve the efficiency of an ERL. From equation 3 one finds for the optimum external quality factor of the input coupler

$$Q_{opt} = \frac{1}{2} \frac{\omega_c}{\Delta\omega}. \qquad (4)$$

Note that the optimum external quality factor is determined only by the peak cavity detuning. If we assume a peak detuning of 25 Hz, we find $Q_{opt} = 2.6 \cdot 10^7$. According to equation 3 the required RF power is then $P_g \approx 8$ kW per 9-cell cavity with $V_{acc} = 21$ MV.

While beam loss within reasonable limits gives no significant increase in RF power demands, a small phase error $\delta\phi$ of the recirculated beam does. Ideally the recirculated beam is decelerated at an RF phase shifted by 180° relative to the phase at which the initial beam is accelerated. Any deviation $\delta\phi$ form this ideal condition results in a effective beam current in the main linac cavities (complex vector representation)

$$I_{eff} = I_{acc}(1 - e^{i\delta\phi}) \approx -iI_{acc}\delta\phi, \qquad (5)$$

where I_{acc} is the average current of the accelerated beam. As a result of a non-zero current, the required RF power to maintain a given field increases; see Figure 4. Proper cavity detuning is required to minimize the RF power demand. Path length errors of the recirculated beam and a phase slip along the linac due to a not fully relativistic beam will contribute to a phase error $\delta\phi$ of up to 1° in some cavities.

Stability requirements: In short bunch operation the beam is accelerated off-crest by about 15° and subsequently the bunches are compressed from $\sigma = 2.3$ ps to $\sigma \approx 100$ fs in bending magnets [6]. We shall require that the timing jitter of the bunch-centroids after the compression should not exceed the length of a single bunch. This translates to a required bunch-to-bunch energy stability of $2 \cdot 10^{-4}$ or 20 keV at the end of the linac ($R_{56} = 15$ cm). A bunch-to-bunch energy fluctuation of less than 30 keV is also desirable for on-crest operation, because then the total beam energy spread is dominated by the intra-bunch energy spread of $\sigma \approx 50$ keV.

We may neglect contributions from the injector cavities to the energy spread in the following. Further, we can neglect contributions resulting from the timing jitter of the
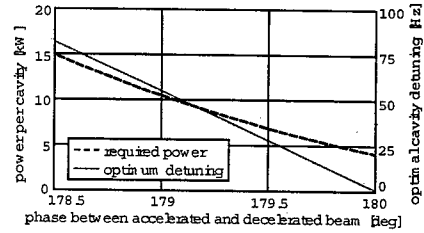
bunches after the injector; see [7]. Microphonics cavity detuning will be one of the major field perturbations in the ERL main linac, and previous measurements at the Tesla-Test-Facility linac indicate that this effect is not correlated between the cavities. Therefore we will assume non-correlation for the field errors in the five main linac cavities. It should be noted that this assumption has to be verified at the ERL prototype, since it has major impact on the field stability requirements in a large scale facility. Assuming further equal contributions ($20keV/\sqrt{10} \approx 6$ keV per cavity) from amplitude and phase errors we find an rms amplitude stability requirement of (15° off crest acceleration)

$$\frac{\sigma_A}{A} = \frac{\sigma_E}{eV_{acc}\cos\phi_b} = \frac{6keV}{e21MVcos(15°)} \approx 3 \cdot 10^{-4} \quad (6)$$

for the field in the main linac cavities. The required rms phase stability is

$$\sigma_\phi = \frac{\sigma_E}{eV_{acc}\sin\phi_b} = \frac{6keV}{e21MVsin(15°)} \approx 0.06°. \quad (7)$$

CONCLUSIONS

The RF power demands and field stability requirements have be estimated for the Cornell ERL prototype. The stability requirements are demanding, and a fast digital RF controller is under development to address these challenges [8].

REFERENCES

[1] Study for a proposed Phase I ERL Synchrotron Light Source at Cornell University, ed. by S. Gruner and M. Tigner, CHESS Tech. Memo 01-003, JLAB-ACT-01-04 (July 2001)

[2] C. Sinclair et al., this conference, paper TOAC005.

[3] H. Padamsee at al., this conference, paper TPAB052.

[4] V. Veshcherevich, this conference, paper TPAB008.

[5] V. Shemelin et al., this conference, paper WPAB012.

[6] I. Bazarov, private communications.

[7] S. Belomestnykh, M. Liepe, Cornell ERL Note 2003-01.

[8] M. Liepe et al., this conference, paper FPAB027.

SUCCESSFUL BEAM TEST OF THE HOM FREE SUPERCONDUCTING SOLEIL CAVITY PROTOTYPE AT THE ESRF

J. Jacob, D. Boilot, ESRF, Grenoble, France
S. Chel, P. Bosland, P. Brédy, CEA, Saclay, France
E. Chiaveri, R. Losito, CERN, Geneva, Switzerland
J.-M. Filhol, M.-P. Level, P. Marchand, C. Thomas-Madec, SOLEIL, Saclay, France

Abstract

A cryo-module housing two strongly HOM damped 352 MHz superconducting (SC) cavity cells has been developed within the framework of the SOLEIL project design phase. In 2002, the prototype was installed in the ESRF storage ring and tested with beam in the accelerating regime with the cavities cooled down to 4.5 K by means of liquid helium from Dewars. Four series of tests have been carried out at the end of scheduled shutdowns. In order not to disturb the ESRF machine performance during the user mode of operation, the cavities were maintained detuned at room temperature. In this passive regime, they remained transparent to the beam with less than 100 W of heat deposited by the beam and evacuated by a warm helium gas flow.

Up to 170 mA of beam could be accelerated with a peak RF voltage of 3 MV and a power of 360 kW from the SC module. This corresponds to the performance required for the first SOLEIL operation phase. The concept of effective HOM damping was validated up to the maximum ESRF intensity of 200 mA. A few week points already identified at previous CERN tests were confirmed: high static cryogenic losses, poor cooling of one HOM coupler and too high fundamental power through the dipolar HOM couplers.

INTRODUCTION

In June 1996, a collaboration project between CEA, CNRS, CERN and ESRF was launched to develop, build and test a strongly HOM damped SC cavity for the SOLEIL project [1]. The frequency of 352.2 MHz was chosen in order to benefit from a possible transfer of CERN technology, including the coupler design, and to open the possibility of a future implementation at the ESRF. The prototype was successfully tested at CERN in December 1999 up to 7 MV/m of accelerating gradient [2].

In December 2001, the SOLEIL module was installed in the ESRF storage ring for a period of one year, in order to validate the design with a high intensity beam [3]. For the limited test period, it was decided to feed the cryostat with liquid helium (LHe) from Dewars. Tests with the cavity at 4 K have been carried out following the four shutdowns of March, May, August and October 2002. After one week of pre-cooling with cold helium gas, the first machine restart days were dedicated to the tests at 4 K. The cavity was then warmed up, kept in the ring at room temperature (300 K) and cooled with warm helium gas for the normal user operation, its resonance being thermally shifted off beam harmonics.

The successful operation at 300 K with high beam intensity - not initially foreseen in the cavity design - opens the possibility of increasing the availability of SC RF systems if the ring can be operated with a reduced number of modules.

The cooling with LHe from Dewars was also a success: during the four series of tests, the cavity was kept stable at 4 K between 17 and 20 hours. With the resonance detuned from the main RF frequency, 200 mA could then be stored without any sign of HOM excitation. The SOLEIL cavity module was successfully operated in the accelerating regime as well: with 3 MV of accelerating voltage, a maximum of 360 kW could then be transferred into 170 mA of beam.

In December 2002, the cavity module was removed from the ESRF storage ring as the space was required for a new beam line. Taking into account the results of the test, it is now planned to modify the existing prototype and to prepare it for the first commissioning phase of the SOLEIL storage ring starting in April 2005.

It is also planned to build a second unit, which is required and will be installed in the SOLEIL ring for a second phase in order to reach full performance of the machine in 2006: 500 mA at 2.75 GeV, the ring fully equipped with insertion devices.

TEST OF THE HOM DAMPED SC SOLEIL CAVITY AT THE ESRF

Figure 1 shows the SC HOM-free SOLEIL prototype module in the ESRF storage ring. The module, the test configuration at the ESRF and the cooling plant have already been described extensively [1, 2, 3].
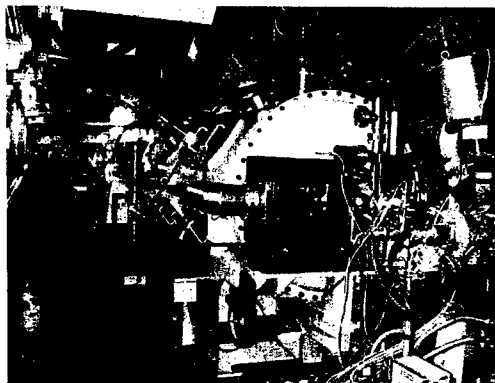
Figure 1: SOLEIL SC module in the ESRF storage ring

The main design aspects that have been optimised for a reliable HOM-free operation in high intensity rings [1, 2, 3] are briefly reminded below:

- On the 400 mm diameter beam tube connecting two cells in a single cryostat, the HOMs are effectively coupled with conventional coaxial couplers, which extract the power from the structure. As no ferrite absorbers are needed in the beam tubes, possible vacuum contamination is avoided.

- The open structure exhibits an excellent conductance for a very efficient vacuum pumping directly on the main tapers at each side.

- A high reliability is thus expected, which is essential for light sources with an expected MTBF better than 50 hours and more than 96 % beam availability [4].

- The CERN technology using niobium coated copper cells has been adopted for the SOLEIL cavity. It is the first application to a cavity designed for high beam current.

The cooling circuit, the vacuum configuration as well as the connection to the 3rd RF transmitter of the ESRF were thoroughly described in [3].

ACHIEVEMENTS

As already reported in [3], 5700 litres of liquid helium from three Dewars were sufficient to cool down and operate the SC module at 4 K for about 17 to 20 hours.

Passive Operation at 300 K

During normal user operation of the storage ring, the SC module was kept at 300 K by means of a 15 m^3/h flow of helium gas (GHe) circulating through the cryostat. Less than 100 W of heat load from the beam had to be removed from the accelerating structure, naturally detuned by *1204 kHz = 3.4 f$_{revolution}$* at 300 K [3]. This is slightly less than the worst case computations, which had predicted between 200 and 300 W of heat load.

A maximum HOM power of 50 W was measured on monopole HOM couplers in 16 bunch filling at 90 mA and no HOM driven coherent multibunch instability was ever observed up to the maximum ESRF intensity of 200 mA. The system proved to be very reliable and transparent to machine operation, causing only three beam trips over a full year, which could not clearly be attributed to the cavity itself.

Passive Operation at 4 K

In passive operation at 4 K, as at 300 K, the cavity remained transparent to the beam and no instability was detected up to 200 mA: along with the experience at 300 K, this demonstrates the validity of the concept for an effective HOM damping.

RF Voltage Conditioning at 4 K

The SOLEIL prototype module had already been powered in the CERN teststand prior to its installation at the ESRF, and it was relatively easy and fast to recondition the couplers up to the nominal total voltage of 4 MV in CW and up to 5 MV in pulsed mode.

After the second test window at 4 K in May 2002, a problem with the HOM coaxial feed-throughs was encountered, which limited the maximum voltage [3]. It turned out that the brazing joints close to the external RF connectors, between atmosphere and insulation vacuum, were leaking. As a consequence, some glow discharges occurred inside the coaxial lines and limited the voltage due to the spurious coupling to the fundamental mode. Once identified, the leaks were easily repaired. One of the coaxial lines showing strong traces of the discharges was cleaned up. At the August test, a decade was gained in the insulation vacuum and the accelerating voltage of the module could be raised to its nominal value.

The dipolar HOM couplers which are located close to the accelerating cells are equipped with notch filters for the rejection of the fundamental mode coupling. Due to an incorrect tuning of these filters and to the resulting spurious coupling to the fundamental mode, at 4 MV in CW, the extracted power was as high as 1650 W. Moreover, the LHe circuits feeding the HOM couplers are not yet fully optimised and the cooling efficiency is only moderate. Altogether this lead to strong overheating of the HOM couplers at high accelerating voltage and was probably the reason for some quench-like events, with pressure bursts on the LHe tank.

At 4 MV, the total cryogenic losses were evaluated around 140 W, which is slightly above the already high static losses of ca. 117 W measured in previous tests [3].

Some multipacting was also observed in the main RF couplers around 4 MV, eventually leading to some pressure bursts on which the RF was tripped. The fast vacuum interlock had been implemented to protect the ceramic against sputter deposition of copper. It is expected that further conditioning of the couplers will help to overcome multipacting.

Beam Acceleration at 4 K

With 5 MeV energy loss per turn at the ESRF, a minimum of 7 MV of RF voltage is necessary for stable storage of a high intensity beam. At the end of the 4th test window, in October 2002, 170 mA of beam could be stored, achieving 30 hours of lifetime with 3 MV from the superconducting SOLEIL module and 4 MV from the existing normal conducting ESRF cavities. This corresponds to 360 kW of power transferred from the SC cavity module into the beam and meets the requirements for the commissioning of the SOLEIL ring with one module. Surprisingly, only little time was needed for conditioning so that the beam intensity and the beam loading of the module could be ramped within a few hours.

A run test of one hour was carried out at the end of the last test period, with a smooth beam decay from 155 to 149 mA, demonstrating that more than 300 kW can be fed to the beam over a longer period of time, without any thermal run away.

HIGHER ORDER MODE INVESTIGATION OF SUPERCONDUCTING CH STRUCTURES AND STATUS OF THE CH PROTOTYPE CAVITY *

H. Podlech, H. Deitinghoff, H. Liebermann, H. Klein, U. Ratzinger, A. Sauer, X. Yan
Institut für Angewandte Physik (IAP), University of Frankfurt, Germany

Abstract

H-Mode cavities (IH-DTL, IH-RFQ, 4-Vane-RFQ) have been developed sucessfully during the last decades for a large variety of applications in the field of ion acceleration [1]. The CH- or Crossbar H-structure is a new H-Mode drift tube structure operating in the TE_{210} mode. This structure is currently under development at the IAP in Frankfurt, Germany. This type of cavity is an excellent candidate for the use in future high current applications like IFMIF or XADS with beam currents of up to 125 mA [2][3]. For these applications superconducting operation is very attractive. The overall plug power consumption is lower and the use of larger apertures can reduce the risk of activation significantly. Due to the possible superconducting operation it is important to investigate the higher order modes (HOM) in such a cavity. In this paper, we present the first results of the HOM analysis and give a status of the development of the superconducting CH cavity prototype.

Figure 2: View into the CH copper model. The characteristic crossed stem construction of the CH cavity is clearly visible.

possible. The reasonable energy range is between 3 and 150 A·MeV and a frequency between 150 and 800 MHz can be used.

Figure 1 shows the prototype of a 19-gap superconducting CH-structure which is presently under construction. The operating frequency is 352 MHz and the β is 0.1.

HOM ANALYSIS

Theory

Inside a cavity the beam can gain energy due to longitudinal electric on axis fields. On the other side, every higher order mode with electric field on or near the axis could in priciple be excited by the beam. Higher order mode excitation can lead to beam instabilites and to additional power losses. Besides the frequency of the higher order modes the R/Q value is one of the most important quantities:

$$R/Q = \frac{\left| \int E_z(z) \exp \left(i\omega z/\beta c \right) dz \right|^2}{\omega W}, \quad (1)$$

where W is the stored energy. The geometric shunt impedance R/Q measures the level of excitation of higher order modes. For cw applications, significant voltages can be generated only if a Fourier beam component is within the bandwidth of HOM.

Simulation and Measurements

For future high current applications it is necessary to determine all of the potentially dangerous modes with respect

Figure 1: View of the prototype of the superconducting CH cavity which is presently under construction.

INTRODUCTION

Existing H-Mode cavities can be operated only at room temperature. Many future projects require cw operation. Normal conducting structures are limited in the gradient because of power losses.

Due to its mechanical rigidity the CH-structure can be realized for room temperature as well as for superconducting operation. Together with the use of the KONUS beam dynamics [4] long lens-free sections and therefore superconducting multicell structures like the CH-cavity become

Figure 4: Distribution of the electrice field of the first 12 eigenmodes of the CH copper model.

to R/Q values, frequencies and additional power losses. In a first step we simulated a CH-cavity with Microwave Studio [5] to identify the higher order modes and to dertermine their frequencies. A copper model of this cavity has been built to validate the simulations. It is a 19-gap copper model with a measured frequency of the basic mode of 289 MHz and with a β of 0.08. Figure 2 shows a photograph of this model resonator. The measurements have

Table 1: Measured and simulated parameters of the CH copper model

Parameter	Simulation	Measurement
f (MHz)	285	289
length (cm)	104	104
diameter (cm)	34	34
gap number	19	19
β	0.08	0.08
R_a/Q (Ω)	1668	1690

been performed using the bead perturbation method. A metallic bead with a diameter of 4.75 mm has been pulled through the resonator. The Figure 3 shows the experimental setup. Unlike to elliptical cavities, it is sufficient to measure on axis because every mode produces a longitudinal on axis electric field in CH-cavities. Due to the fixed velocity profile of CH-structures one has to determine the R/Q value only for the design β. In a first step the R_0/Q_0 values of the first 15 modes up to a frequency of 1 GHz could be determined. The agreement between the simulations and the measurements was excellent. The Figure 4 shows the measured and simulated field distributions of the first 12

modes. Table 1 shows the measured and simulated parameters of the model resonator. So far, the investigation shows that the simulations are accurate enough to determine potentially dangerous higher order modes in CH cavities. We found an interesting and potentially dangerous mode. Figure 5 shows the simulated field distribution of the basic mode (f=285 MHz) and of the 28th mode (f=1235 MHz). Both modes have a similar field distribution although the 28th mode has a frequency of almost 4.3 times the basic frequency. The investigation of the properties of this mode are still under way.
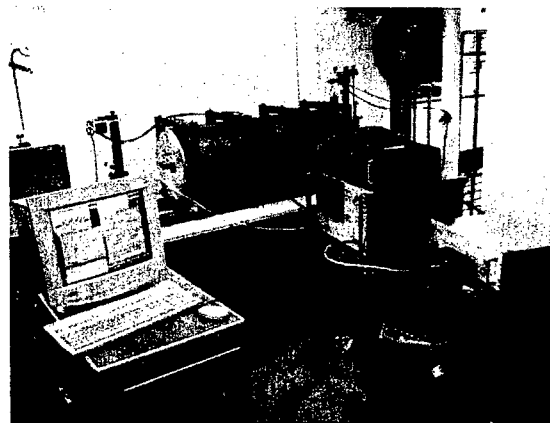
Figure 3: Photograph of the experimental setup. In the center the CH r.t. model is visible.

Comparing between basic mode and 28th
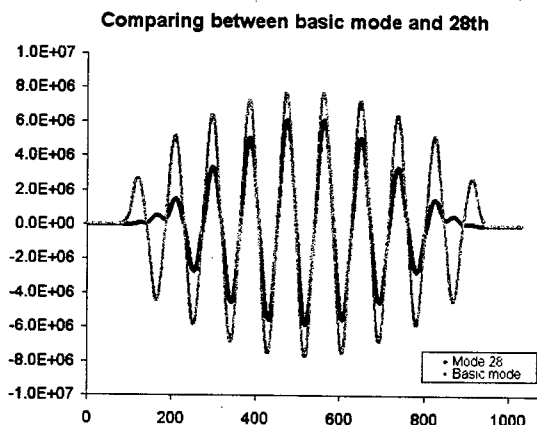
Figure 5: Comparison of the field distribution of the basic mode (285 MHz) and the 28th mode (1235 MHz).

Table 2: Parameters of the superconducting CH cavity prototype

f [MHz]	352
β	0.1
length [cm]	104.8
diameter [cm]	28
number of gaps	19
R_a/Q_0 [Ω]	1610
G [Ω]	56
E_p/E_a	6.59
B_p/E_a [mT/MV/m]	7.29
E_p @ E_a=3.2 MV/m [MV/m]	21
B_p @ E_a=3.2 MV/m [mT]	23.3
W [mJ/(MV/m)^2	155
W @ E_a=3.2 MV/m [J]	1.58
Q_0 (BCS, 4K)	$1.6 \cdot 10^9$
Q_0 (R_s=100 nΩ)	$5.6 \cdot 10^8$
P @ E_a=3.2 MV/m [W]	13

Figure 6: The 3 m long vertical cryostat (center) and the class 100 laminar flow box (right) in the new cryogenic laboratory in Frankfurt.

PROTOTYPE STATUS

The cavity parameters have been optimized using Microwave Studio. The major issue was to minimize the electric and magnetic peak field to reduce the risk of field emission and thermal breakdown [6]. This type of cavity will be limited most likely by the electric fields whereas the magnetic peak fields have very moderate values. Table 2 summarizes the most important parameters of the superconducting prototype.

A design and engineering study has been performed in close cooperation with industry (ACCEL) to show the feasibility of the production of superconducting CH structures. After a call for tenders, the cavity has been ordered. The

production of the cavity has already started, the used material is high RRR bulk niobium. After fabrication the cavity will be treated with Chemical Buffered Polishing (BCP) and High Pressure Rinsing (HPR). It is expected that the cavity will be delivered in January 2004.

The cavity will be tested in the new cryogenic laboratory at IAP in Frankfurt. The lab has been equipped with a 3 m long vertical cryostat and a class 100 laminar flow box (see fig. 6), a magnetic shielding, a helium recovery system and two 250 l transport dewars.

OUTLOOK

It is planned to continue the HOM analysis and to determine the Q_{ext} for different modes. A mechanical analysis using the program COSMOS will be performed to investigate the mechanical vibrations of the cavity. The setup for the cryo tests is beeing equipped and the rf control system is under development. In addition, investigations of a mechanical tuner have started.

REFERENCES

[1] U. Ratzinger, Nucl. Physics A, 701 (2002) 614c

[2] A. Sauer, R. Eichhorn, R. Tiede, H. Deitinghoff, H. Klein, U. Ratzinger, Beam Dynamics Design of a Superconducting 175 MHz CH-Linac for IFMIF, Proceedings of the EPAC 2002, Paris, France

[3] Requirements for the XADS Accelerator & Technical Answers, DAPNIA-02-302, September 2002, France

[4] U. Ratzinger, Nucl. Inst. Meth., A 415 (1998) 229

[5] http://www.cst.de

[6] H. Liebermann, H. Podlech, U. Ratzinger, A. Sauer, Design of a superconducting CH-cavity for Low and Medium β Ion and Proton Acceleration, these proceedings

HIGH POWER RF TESTS ON INPUT COUPLERS FOR 972MHZ SUPERCONDUCTING CAVITIES IN THE J-PARC PROJECT

E. Kako,[†] S. Noguchi and T. Shishido
KEK, 1-1 Oho, Tsukuba, Ibaraki 305-0801 JAPAN

H. Asano, E. Chishiro, M. Matsuoka, H. Suzuki and M. Yamazaki
JAERI, Tokai, Ibaraki 319-1195 JAPAN

Abstract

Prototype coaxial input couplers with a planar rf window and a high power test stand were designed and fabricated. The high power tests with a 972MHz pulsed klystron had been successfully carried out. Input rf power of 2.2MW in a pulsed operation of 0.6msec and 25Hz (370kW in 3.0msec and 25Hz) was transferred to the input couplers without any problem.

1 INTRODUCTION

In the KEK-JAERI joint project named J-PARC (Japan Proton Accelerator Research Complex), a superconducting linac is required to boost the energy of the H^- beam from 400MeV to 600MeV. The 600MeV beam will be used for ADS (accelerator-driven system) experiments in the second phase of the J-PARC project. In the present system design of the superconducting linac [1], eleven cryomodules containing two 972MHz 9-cell niobium cavities will be installed in the linac tunnel. The accelerating gradient has been set at about 10MV/m, and the operating temperature is 2K. A prototype cryomodule with $\beta=0.725$ (424MeV) was designed last year. The construction of the prototype cryomodule has been just started for an essential R&D work. Two input couplers are needed for installation in the cryomodule. Prototype 972MHz input couplers were fabricated in order to test the high power capability and reliability. The experimental set-up, the processing procedure and the test results with high rf power are described in this paper.

2 INPUT COUPLERS

Input couplers are used for transferring rf power to superconducting cavities. Basic design of the 972MHz input coupler was carried out with referring the 508MHz input coupler for the TRISTAN superconducting cavities [2]. Similar design is also found in the KEKB and SNS superconducting cavities [3, 4]. Heat load dissipated at copper surface and a ceramic disk is considerably reduced due to a pulsed operation, in comparison with the 508 MHz coupler in a cw operation. On the other hand, heavy irradiation caused by an intense proton beam has to be taken into consideration in the design. A fundamental specification of the 972MHz input coupler is summarised in Table 1. The required input rf power is 300kW for a

beam current of 30mA at the operating accelerating gradient of 10MV/m. Detailed dimensions of a 972MHz coaxial window with a choke structure and the calculated rf characteristics are shown in ref. [5]. The ceramic disk is made of Al_2O_3 with the purity of 95%, and the thickness is 7.0mm. Coating with TiN on the surface of the vacuum side was carried out. The rf window is connected with a coaxial line ($\phi80$) of 50Ω. The inner conductor made of a cupper pipe is equipped with a built-in cooling channel. The projection length of the antenna tip was determined to obtain the external Q value of 5×10^5 [5]. As shown in Figure 1, the high power test stand consists of two doorknobs connected to the WR975-waveguide system, two coaxial input couplers with a planar rf window and a pair of coupling waveguide with a pumping port.

Table 1: Specification of the 972MHz input couplers

External Q value	5×10^5	
Input rf power	300 kW,	(I_b= 30 mA)
Pulsed operation	3.0 msec,	25 Hz

3 EXPERIMENTAL SET UP

The input couplers and the coupling waveguides were carefully rinsed with ultra-pure water. They were dried for one day and were assembled in a clean room. Then, pumping was carried out by a vacuum system composed of a turbo molecular pump of 500 l/s and a rotary pump of 16000 l/h. The input coupler system was baked out at 120°C for 24 hours prior to rf processing. The vacuum
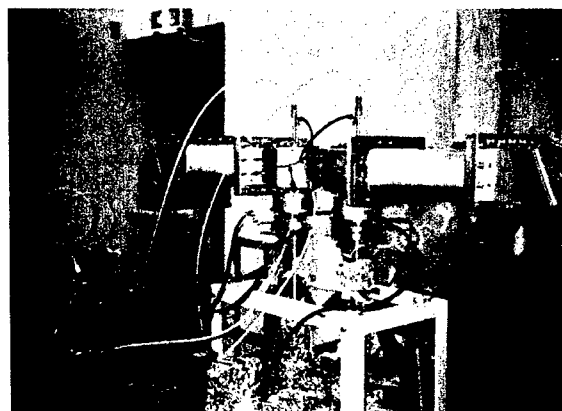
Figure 1: High power test stand

[†]eiji.kako@kek.jp
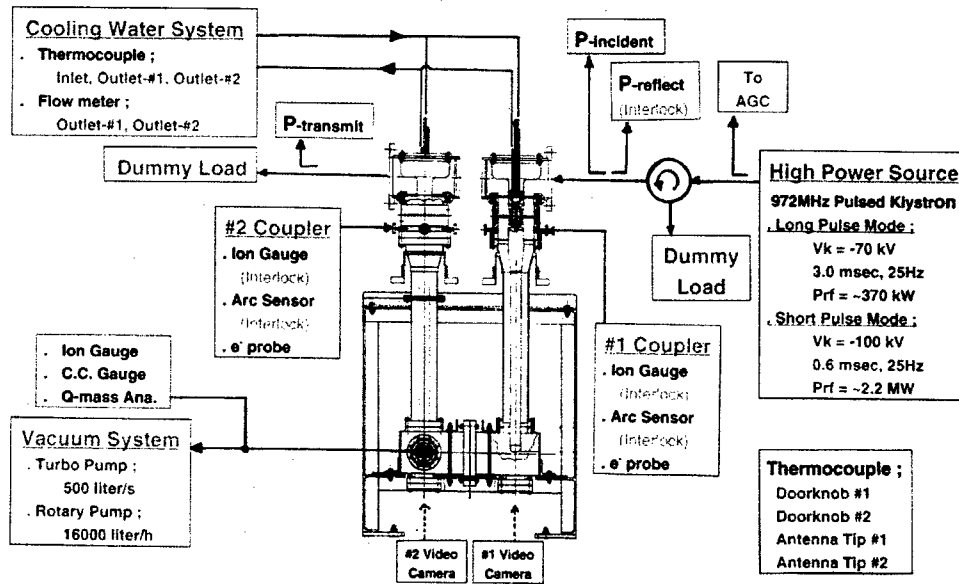
Figure 2: Experimental instrumentation for high power tests

pressure at room temperature has reached to about 1×10^{-6} Pa. An experimental instrumentation for high power tests is shown in Figure 2. An ionization gauge, a cold cathode gauge and a residual gas analyser are installed in the vacuum system. An ionization gauge, an arc detector and an electron pick-up probe are attached at three small ports close to the rf window of each input coupler. These monitoring instruments are very important to prevent a fatal sparking discharge around the rf window. Two video cameras locating at the bottom of the coupling waveguide can observe visible lights like a glow discharge by multipacting. A water-cooling system for the inner conductors is equipped with thermocouples and flow meters, which are used for a calorimetric measurement of the rf loss. A 972MHz pulsed klystron is a prototype for normal conducting cavities aiming at performances of 0.6msec, 50Hz and the maximum power of 3.0MW [6]. A longer pulsed operation is required for superconducting cavities. Therefore, modification in the rf control system and adjustment of the DC power supply system were carried out. In the present operated condition, the maximum available rf power is 370kW in the long pulse mode of 3.0msec and 2.2MW in the short pulse mode of 0.6msec.

4 HIGH POWER TESTS

Up to the present, high power tests had been carried out four times, as summarised in Table 2. The initial rf processing was started with a low duty factor of 0.1msec and 10Hz. The interlock level of vacuum pressure at the rf window was set to 5×10^{-4} Pa. The first deterioration of the vacuum pressure was observed at 30kW. As seen in Figure 3, the input rf power had been carefully increased, and the processing time up to 300kW was 22 hours. With gradual increment of the duty factor, the maximum rf power of 350kW in the long pulse mode of 2.45msec was

transferred. There was no work of interlocks due to vacuum burst or arc detection during the processing. The maximum average rf power was 21kW. The temperature rise to about 100°C was observed at the antenna tip in the initial test without cooling water. Therefore, the necessity of forced cooling in the inner conductor was concluded, and the water-cooling was started in the successive processing. Rf loss at the rf window and the inner conductor was measured in various power levels by a calorimetric method. The rf loss was about 0.2% of the average input rf power [7]. In the third test, finally, 2.2MW in the short pulse mode of 0.6msec was fed to the input couplers without any trouble. However, degradation of the vacuum pressure had been still observed between 400kW and 800kW even after processed up to 2.2MW, as shown in Figure 4. The vacuum degradation in this power range was simultaneously accompanied with detection of electrons by the pick-up probe and observation of lights

Table 2: Procedure of rf processing

Test	Pulsed operation	Max. rf power	
1. Initial Tests:			
	0.1msec, 10Hz	300kW	(Fig. 3)
	2.45msec, 25Hz	350kW	
2. Exposure to N_2 gas:			
	0.1msec, 10Hz	300kW	(Fig. 5)
	2.45msec, 25Hz	350kW	
	0.6msec, 25Hz	1100kW	
3. Kept for one month without pumping:			
	0.1msec, 25Hz	1700kW	(Fig. 5)
	0.6msec, 25Hz	2200kW	(Fig. 4)
	Standing Wave	650-800kW	(Fig. 6)
4. Exposure to air:			
	0.1msec, 25Hz	360kW	(Fig. 5)
	3.0msec, 25Hz	370kW	(Fig. 4)
	Standing Wave	370kW	

by the video camera. The cause must be due to multipacting at the rf window or coaxial line. Main residual gas components desorbed by multipacting were H_2 and N_2+CO [7]. In order to investigate memories of the rf processing effect, the input couplers were exposed to N_2 gas and air for a few days, (and residual gases in vacuum without pumping for one month). Baking at 120°C for 24 hours was always carried out after the exposure. As seen in Figure 5, the processing time up to 300kW was less than two hours in any case. Therefore, no major influence due to the exposure was observed.

RF processing in the standing wave was carried out, just after processed at 2.2MW in the travelling wave. Figure 6 shows the results in various phase conditions performed by successively changing the short-end position by 1/8 λg. Since the distribution of electromagnetic fields along the coaxial line of the couplers changes with the phase, the resonant condition of multipacting has shifted in each phase. The observation of the vacuum deterioration above 50kW suggests careful rf processing is needed in couplers installed in the actual cavities, even if processed up to 2.2MW in the test stand.

Figure 3: Rf processing logs in the initial test

Figure 6: Rf processing in the standing wave

5 SUMMARY

Input rf power of 2.2MW in a pulsed operation of 0.6msec and 25Hz (370kW in 3.0msec and 25Hz) was transferred to the input couplers. Multipacting level was observed between 400kW and 800kW. There was no influence in the processing time due to exposure to N_2 gas and air.
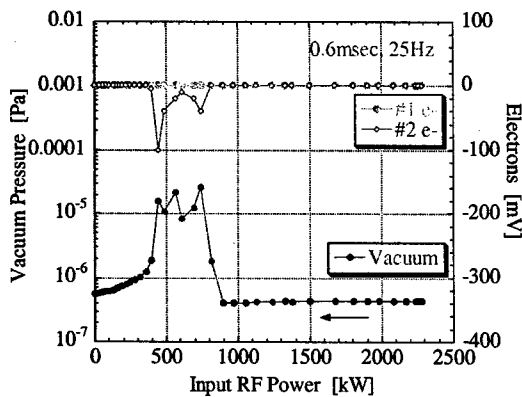
Figure 4: Vacuum pressure and electron activities after processed up to 2.2 MW

6 REFERENCES

[1] S. Noguchi, "SRF System in the JAERI - KEK Joint Project", Proc. of 10th Workshop on RF Superconductivity, Tsukuba, Japan (2001) p302-307.

[2] S. Noguchi, E. Kako and K. Kubo, "Couplers – Experience at KEK", Proc. of 4th Workshop on RF Superconductivity, Tsukuba, Japan (1989) p397-412.

[3] Y. Kijima et al., "Conditioning of the Input Couplers for KEKB Superconducting Cavities", ibid. [1] p565-569.

[4] I.E. Campisi, "Fundamental Power Couplers for Superconducting Cavities", ibid. [1] p132-143.

[5] E. Kako and S. Noguchi, "RF Design of a 972MHz Superconducting Cavity for High Intensity Proton Linac", Proc. of EPAC2002, Paris, France (2002) p2244-2246.

[6] E. Chishiro et al., "Development of 972MHz Klystron for High-Intensity Proton Accelerator Facility", Proc. of LINAC2002, Gyeongju, Korea (2002) TU459.

[7] E. Kako et al., "High Power Test of the 972MHz Input Couplers for Proton SC Cavities", Proc. of Workshop on HPC2002 at JLab, Newport News, Virginia, USA (2002), to be published.

Figure 5: Effect after exposure to N_2 gas and air

RESULTS OF TWO LANL β = 0.175, 350-MHZ, 2-GAP SPOKE CAVITIES*

T. Tajima[†], R. L. Edwards, R. C. Gentzlinger, F. L. Krawczyk, J. E. Ledford, J.-F. Liu, D. I. Montoya, R. J. Roybal, D. L. Schrage, A. H. Shapiro, LANL, Los Alamos, NM 87545, USA,
D. Barni, A. Bosotti, C. Pagani, INFN/Milano, Italy,
G. Corniani, E. ZANON, S. P. A., Italy

Abstract

Two β = 0.175, 350 MHz, 2-gap superconducting (SC) spoke cavities were fabricated in industry under the Advanced Accelerator Applications (AAA) project for the transmutation of nuclear waste. These cavities are promising candidates for the accelerating structures between a RFQ and the elliptical SC cavities for proton and heavy ion linacs. Since their delivery in July 2002, they have been tested in terms of mechanical properties, low-temperature performance, i.e., Q_0-E_{acc} curves at 4 K and 2 K, surface resistance dependence on temperature and for multipacting (MP). The two cavities achieved accelerating fields of 13.5 MV/m and 13.0 MV/m as compared to the required field of 7.5 MV/m with enough margin for the quality factor. These cavities seem to need more time to condition away MP than elliptical cavities, but MP does not occur once the cavity is conditioned and kept at 4 K. The length of the 103 mm-diameter nominal coupler port was found to be too short for the penetrating field.

INTRODUCTION

The spoke cavity was invented by Delayan and Shepard in the late 80s [1]. It is a half-wave resonator, but has a capability of having multi spokes so that the real estate gradient can be higher. Although this structure has not been used in a real accelerator yet, it has been proven from past bench tests that this structure can be an excellent candidate to support the velocity range of β<0.5 [2], and it could compete with well established elliptical cavities at even higher β [3].

At LANL, we modified our facility to test spoke cavities and successfully tested a spoke cavity on loan from ANL. The result was excellent and we then designed our own cavity at β =0.175. Two prototype cavities, named EZ01 and EZ02, were fabricated at Zanon, Italy, and have been tested at LANL since July 2002. As shown below, the results have been excellent and proved our capability of designing cavities to a predicted level of performance.

DESIGN OF THE CAVITY

A RF and mechanical design using MAFIA, Microwave Studio (MWS) and MICAV has been performed [4]. Figure 1 shows cut-away design views (top) and the fabricated cavity made of niobium (bottom). The cavity diameter is ~ 40 cm, which is about half the size of elliptical cavities of the same frequency. The detailed dimensions can be found in Ref. [5].
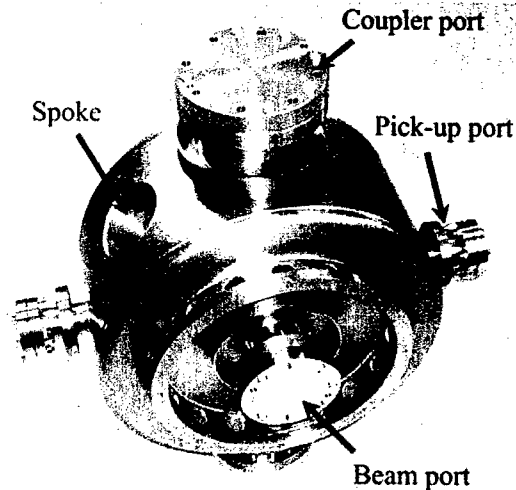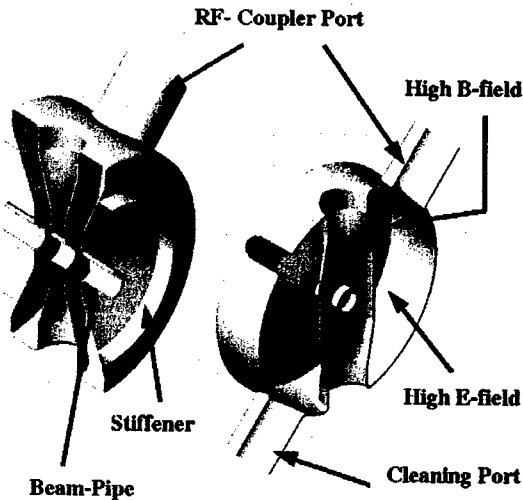
Figure 1: Cut-away design views (top) and the fabricated LANL β=0.175, 2-gap spoke cavity made of niobium (bottom).

Table 1 shows the RF parameters. The E_{peak}/E_{acc} and B_{peak}/E_{acc} ratios have been well optimized as shown in the Table.

Table 1: Design RF parameters [6]

Q_0 (4 K)	1.05E+09 (for 61 $n\Omega$)
T (β_g)	0.7765 (β_g=0.175)
$T_{max}(\beta)$	0.8063 (@ β=0.21)
G	64.1 Ω
E_{pk}/E_{acc}	2.82
B_{pk}/E_{acc}	7.38 mT/MV/m
P_{cav} (4 K)	4.63 W @ 7.5 MV/m
R/Q	124 Ω

Table 2: Summary of the LANL/AAA spoke cavities test results at 4 K.

Cavity	EZ01	EZ02
Low-field Q_0	1.74E+9	1.04E+9
$E_{acc, max}$ (MV/m)	13.5	13.0
Q_0 at E_{acc}=7.5 MV/m	8.6E+8	1.06E+9
$E_{p. max}$ (MV/m)	38.0	36.6
$B_{p. max}$ (mT)	99.4	95.8
Field limitation	Quench	Quench

TEST PREPARATIONS

The detail of the preparation is described elsewhere [5]. We performed standard 1:1:2 buffered chemical polishing (BCP) of 150 microns. We then high-pressure rinsed (HPR) the cavity with ultra-pure water at ~1200 psi for ~ 40 minutes in a class-100 clean room

After setting the cavity on the cryostat insert and pumping it down, we bake the cavity at ~110 °C for 2-3 days. The typical cavity vacuum monitored at the cryostat lid are 7E-9 to 3E-8 Torr at room temperature after baking, 5E-9 to 1E-8 Torr after pre-cooling and 2E-9 to 5E-9 Torr during the 4 K and 2 K tests.

TEST RESULTS

4 K Tests

Figure 2 shows the $Q_0 - E_{acc}$ curves of two cavities at 4 K and Table 2 summarizes the results. After the first test in August 2002, we disassembled the cavity EZ02 and high-pressure rinsed again and tested in March 2003. Both Q_0 and E_{acc} improved as shown in Fig. 2.
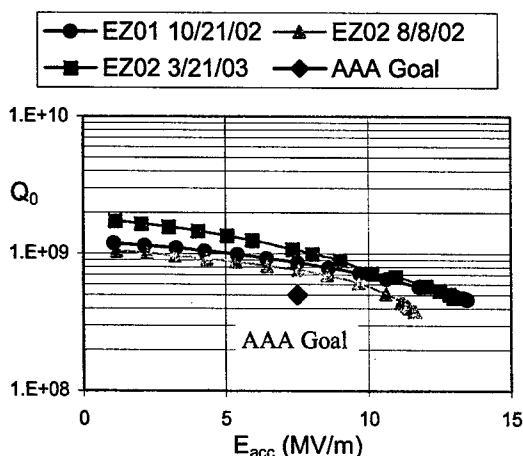
Figure 2: Q_0-E_{acc} curves of the two LANL/AAA cavities at 4 K. Test dates are written in the legend. Repeated high-pressure rinse and helium processing improved the EZ02 result in the second test.

2 K tests

Figure 3 shows the results of 2 K tests together with 4 K results. The quench level of the EZ01 at 2 K was the same as that at 4 K, but that of EZ02 was slightly higher than that at 4 K. The data of EZ02 also show the effect of helium processing. A short period (~12 minutes) of processing improved the performance drastically.
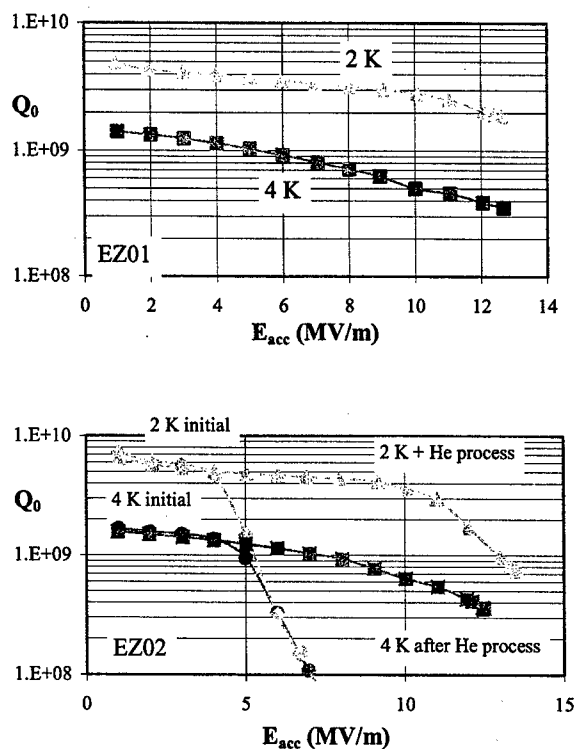
Figure 3: Q_0-E_{acc} curves at 2 K together with 4 K data. The EZ02 data also include the curves before helium processing. After ~12 minutes of helium processing the performance improved drastically.

Residual resistance

We measured Q_0 at E_{acc}~1 MV/m during the cooldown from 4 K to 2 K. By fitting the surface resistance, $R_s=G/Q_0$, as a function of $1/T$, we determined the residual resistance of EZ01 and EZ02 to be 12 $n\Omega$ and 10 $n\Omega$, respectively.

ISSUES FOR FUTURE DEVELOPMENTS

Penetrating field at the nominal coupler port

It was found during our tests that the length (9.2 cm) of the 103 mm-diameter nominal coupler port was too short to avoid penetrating field. The results shown above were measured with niobium (Nb) blank flanges attached on these ports. When we tested with one stainless steel (SST) flange on one of these ports and one Nb blank on the other, the Q_0 was ~ 80 % lower as shown in Fig. 4.
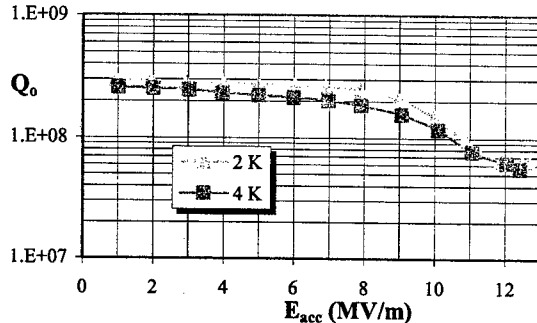
Figure 4: The Q_0-E_{acc} curves at 4 K and 2 K of the cavity EZ01 with one stainless steel flange attached on the 103-mm-diameter nominal coupler port. The small increase of the Q_0 from 4 K to 2 K indicates the loss being dominant at the SST flange.

A simulation using MWS with the real configuration, i.e., a SST flange and a copper gasket, predicted Q_0 of 2.4E8 in good agreement with the measured 2.6E8.

To know the port distance required to avoid the field penetration, a model that has a 10 cm long spool piece made of SST terminated with a Nb plate attached on the coupler port was generated as shown in Fig. 5. Figure 6 shows the cavity Q_0 calculated with different additional port length. An extension of 5 cm was determined to be enough to avoid the effect of the penetrating field.
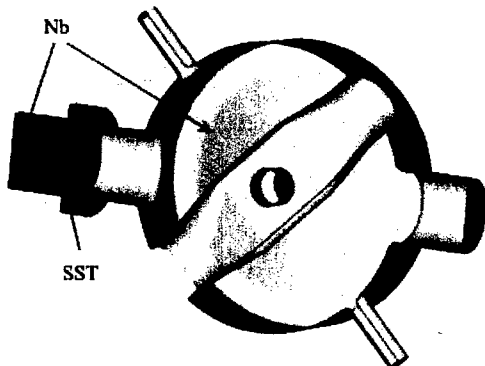
Figure 5: A model for the Microwave Studio calculations. A spool piece made of SST and ended with a Nb plate was added to one of the nominal coupler ports and the cavity port length was changed.
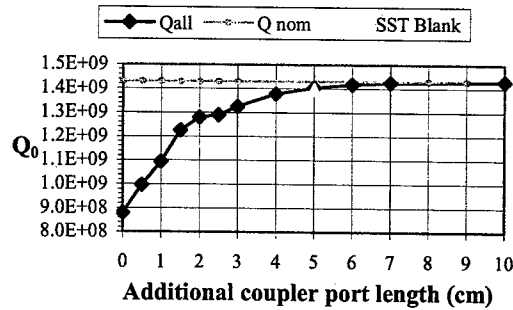
Figure 6: The MWS calculation of Q_0 as a function of the additional port length. This shows that the penetrating field will not affect Q_0 with > 5 cm extension.

Multipacting(MP), field emission and quench

We have encountered the situation where we need conditioning for a few hours to process the MP. This usually occurs the first time we cooldown the cavity to 4 K and after warming up to room temperature. The persistent MP levels are at E_{acc}=1-2 MV/m and 4-6 MV/m.

Regarding field emission, according to the X-ray data taken using a NaI detector put on the cryostat lid, EZ01 and EZ02 started showing some X-rays caused by emitted electrons from E_{acc} = 10.7 MV/m and 9.4 MV/m, respectively, after helium processing.

Both cavities quench at similar gradients. Whether this was caused by field emitted electrons or defect(s) is unknown and remains to be identified as well as the quench locations.

SUMMARY

The two LANL designed spoke cavities have shown excellent results, encouraging us to strive for multi-spoke cavities for better real estate gradients as well as the development of the nominal coaxial power couplers.

ACKNOWLEDGEMENT

REFERENCES

[1] J. R. Delayen, Nucl. Instrum. Meth. B40/41 (1989) 892.
[2] T. Tajima et al., Proc. PAC2001 (2001) 903.
[3] K. W. Shepard et al., Proc. LINAC2002 (2002).
[4] F. Krawczyk et al., 10th Workshop on RF Superconductivity, Tsukuba, Ibaraki, Japan, Sep. 6-11, 2001. http://laacg1.lanl.gov/scrflab/pubs/spoke/LA-UR-01-4989.pdf
[5] T. Tajima et al., Proc. LINAC2002 (2002).
[6] F. Krawczyk et al., Proc. EPAC2002 (2002) 272.

Q DISEASE ON 350-MHZ SPOKE CAVITIES*

T. Tajima[†], R. L. Edwards, J. Liu, F. L. Krawczyk, D. L. Schrage, A. H. Shapiro, LANL, Los Alamos, NM 87545, USA

Abstract

Q disease, i.e., an increase of RF surface resistance due to hydride precipitation, has been investigated with 350-MHz spoke cavities. This phenomenon was studied extensively in the early 1990s with cavities at frequencies >1 GHz. This is possibly due to the fact that the lower-frequency cavities were believed to show insignificant effect. However, early 500-MHz KEK elliptical cavities and JAERI 130-MHz quarter wave resonators have shown significant Q degradation, suggesting that this disease can be a serious problem with lower-frequency cavities as well. Since there were no quantitative data with 350-MHz cavities, we decided to measure our two spoke cavities. Our spoke cavities were made of RRR~250 niobium and were chemically polished ~150 microns. A few series of systematic tests have shown that our spoke cavities do not show any Q_0 degradation after up to ~24 hours of holding the cavity at 100 K. However, it starts showing degradation if it is held for a longer time and the additional loss due to the Q disease increases linearly. It was also found that our spoke cavity recovers from Q disease if it is warmed up to 150 K or higher for 12 hours.

INTRODUCTION

Q disease would pose a serious problem in the system where superconducting (SC) cavities cannot be cooled down in a short time. Although degassing hydrogen at >600 °C and careful surface treatment can cure this problem, heat treatment costs a significant amount of money and the niobium (Nb) softens. Thus, understanding the mechanism of Q disease and developing a way of treating the SC cavities without heat treatment will be beneficial. We have been investigating the Q disease using our 350-MHz spoke cavities named EZ01 and EZ02 [1, 2].

The first systematic test of checking the holding temperature range in which Q disease occurs suggested that the Q disease might occur after some time even if it does not occur during the first 12 hours [2]. This paper presents recent findings on the Q disease of the LANL 350-MHz spoke cavities.

TEST PROCEDURE

We took the Q_0-E_{acc} curves after warming up the cavity from 4 K to an intermediate temperature (70 – 150 K), holding it there for 12 hours and cooling it down to 4 K again. The detailed time evolution of the temperature during the test can be found elsewhere [1, 2]. When we tested the dependence on the holding time at 100 K, we repeated this procedure and used an accumulated time as the holding time, assuming the effect is the same as that of

holding the cavity at 100 K continuously.

RESULTS

Since we found that the Q disease occurs in our spoke cavities [1, 2], we started checking the temperature range of this occurrence by holding the cavity at temperatures starting from 70 K through 150 K every 10 K for 12 hours. However, it was found after a series of tests that the Q disease does not occur within 24 hours at any temperature for our spoke cavities. We then started to test more prolonged holding times at 100 K, expecting from the past tests with longer holding times that the Q disease should occur

Holding time dependence

Figure 1 shows a collection of Q_0-E_{acc} curves after every 12 hours of holding at 100 K up to 120 hours for our two spoke cavities EZ01 and EZ02. These two cavities were fabricated from the same Nb sheets of RRR~250.
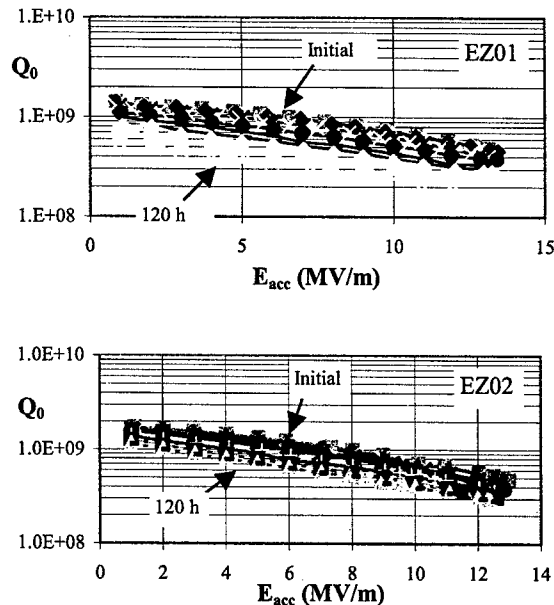
Figure 1: A collection of Q_0-E_{acc} curves of the cavities EZ01 (top) and EZ02 (bottom) measured at 4 K after every 12 hours of holding the cavity at 100 K up to 120 hours.

As one can see, the Q disease occurred on both cavities, but the amount of degradation was different.

Figure 2 shows the additional surface resistance as a function of the accumulated holding time with 0 being the initial value. It was found that the additional surface

resistance starts increasing at ~24 hours and it increases linearly. This linear increase is consistent with published data [3].
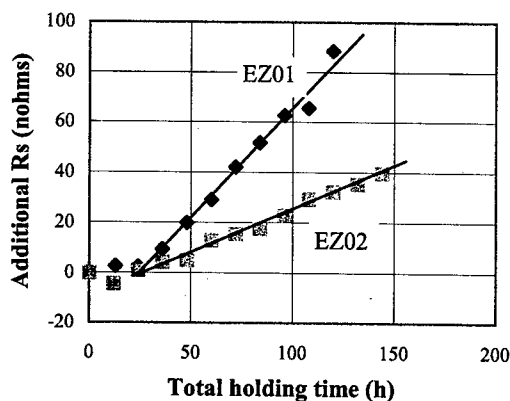
Figure 2: Additional surface resistance due to Q disease as a function of accumulated holding time at 100 K. The data was taken at E_{acc}=4 MV/m.

Surface resistance vs. temperature

Figure 3 shows the surface resistance R_s of the initial cavity (top) and the Q-degraded cavity (bottom). It was found that there is a kink at ~2.18 K in the Q-degraded cavity, below which the R_s gets lower more rapidly. This suggests the existence of a weak superconductor that has a T_c of ~2.18 K.
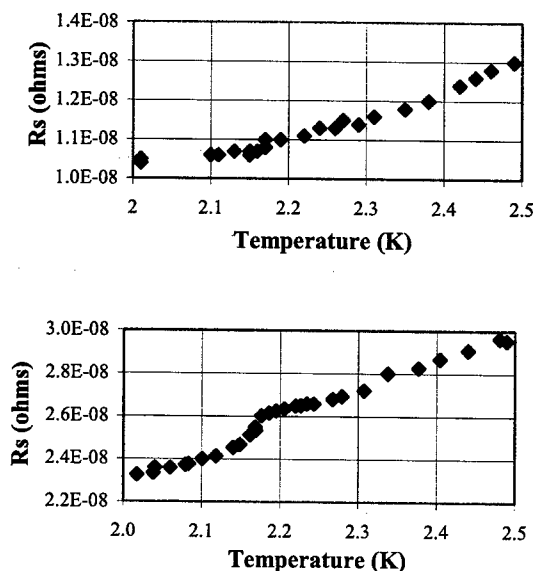
Figure 3: Surface resistance R_s as a function of temperature of the initial (top) and Q-degraded cavity EZ02 (bottom).

Very low field behavior

We checked the Q_0 at field levels lower than E_{acc}=1 MV/m that corresponds to a peak magnetic field B_{peak}=7.38 mT. Figure 4 shows a Q_0-E_{acc} curve at 2 K, including those data, with the cavity EZ02 that was held at 100 K for a total of 180 hours. It was found that the slope of the curve is steeper at these field levels, and the Q_0 increases as the field gets lower. This steep Q_0 drop at E_{acc}<1 MV/m means a rapid increase of RF losses at these low field levels, i.e., there exists some mechanism that causes it such as a superconductor that has a low critical magnetic field or an increase of so-called weak links [7].
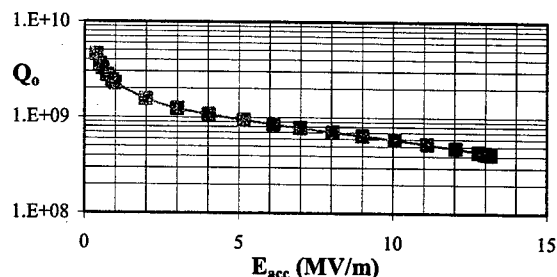
Figure 4: Q_0-E_{acc} curve at 2 K of the Q-degraded cavity EZ02. This cavity was held at 100 K for a total 180 hours. The Q_0 at the lowest measured E_{acc}=0.37 MV/m was 4.54E9, which was still lower than the initial value of ~6E9 of the non-degraded cavity.

Temperature to recover the Q disease

To determine the temperature at which the Q disease recovers, we tried to warm up the degraded cavity EZ02 from 4 K to 150 K and held it at 150 K for 12 hours and took the Q_0-E_{acc} curve after cooling down to 4 K again. The performance recovered to the initial level. Then, we tried to degrade the cavity again and repeated this procedure at 130 K and 140 K. There was no change from the degraded performance. Therefore, it was concluded that the Q disease heals by warming up the cavity to 150 K, but not 140 K or lower for our spoke cavity EZ02. We have not tested this transition temperature with the cavity EZ01. It might be higher since this transition temperature depends on the concentration of untrapped hydrogen [3].

Hydrogen content in the material

A preliminary measurement on the content and the depth profile of hydrogen (H) was performed using ERDA (Elastic Recoil Detection Analysis). The following 3 Nb samples were tested: A) an untreated Nb that was taken from the Nb sheet that was used to fabricate the spoke cavities, B) chemically polished 155 microns from sample A and C) chemically polished 193 microns from sample A. The chemical polishing was done simulating our standard procedure, i.e., buffered chemical polishing (BCP) using a mixture of $HF:HNO_3:H_3PO_4$=1:1:2 by volume and keeping the solution temperature at <15 °C.

Regarding the depth profile, the H is concentrated within 100 nm from the surface, which is consistent with the data in [4]. As to the amount of integrated content of H, there is only relative comparison at the time of writing. The result was that the 155-micron chemically polished sample showed the least and it was 54 % less than the untreated sample. This may confirm the hypothesis that proper BCP can reduce the amount of H content [5]. The 193-micron polished sample showed an increase of H content by 57 % compared to the 155-micron polished sample. This may indicate that the prolonged chemical polishing might increase the H content. It should be noted, however, that this experiment was the very first attempt and the result is preliminary.

DISCUSSIONS

A superconductor having T_c of 2.18 K?

The R_s versus T curve shown above suggests the presence of a superconductor that has a T_c of 2.18 K. Carefully looking at a figure (Fig. 4) in a past paper [6] that shows similar data with a 4 GHz Q-degraded cavity, one can find a similar change of slope at the same temperature, although this was neglected in the paper because there was another kink at 2.8 K in the figure and it seemed more pronounced. We did not find any change of slope at 2.8 K in our cavity. Producing a model that could explain the phenomenon with a thin layer of a weak superconductor having $T_c = 2.18$ K is under way.

Difference between the two cavities

As shown above, the amount of Q degradation was found to be different between the two spoke cavities tested. This may indicate that the H content of EZ01 is higher than that of EZ02. To the best of our knowledge, the two cavities were fabricated from the Nb sheets taken from the same lot. The possibilities of H uptake are the conditions of, BCP, rinsing after BCP, and during high-pressure rinsing with ultra-pure water. At the time of writing, the thorough analyses of these conditions have not been done yet and it might be difficult due to lack of detailed data.

SUMMARY AND FUTURE PLAN

We have tested two 350-MHz spoke cavities to investigate the occurrence of Q disease. The following summarizes the findings.

- The Q disease does not occur if the cavity was held in the dangerous temperature range within 24 hours, but it occurs for a prolonged holding time.
- Once the Q disease occurs, the additional R_s increases linearly with the total holding time.

- Q-degraded cavities show a change of slope in the R_s at 2.18 K, which suggests the presence of a weak superconductor having a T_c of 2.18 K.
- One of our cavities showed a full recovery from Q disease by warming up the cavity to 150 °C or higher for 12 hours. The transition temperature was determined to be 140 °C $<T<$ 150 °C, but it may be different depending on the H content.
- A preliminary test on the H content has shown that our standard procedure of 150 micron BCP could reduce the H content by ~ 54 %, although further BCP might increase it again.

Although there is no immediate plan, it would be interesting to see the results of similar 350-MHz spoke cavities being developed elsewhere.

ACKNOWLEDGEMENT

REFERENCES

[1] T. Tajima et al., "Q_0 degradation of LANL 700-MHz β=0.64 elliptical cavities and ANL 340-MHz spoke cavities," EPAC2002, Paris, France, p. 2286.

[2] T. Tajima et al., "Results of Q disease tests with 350-MHz spoke cavities," International Workshop on Hydrogen in Materials & Vacuum Systems, JLAB, Newport News, VA, November 11-13, 2002. www.jlab.org/intralab/calendar/archive02/hydrogen.

[3] R. W. Roth, "Islands or films? - New aspects of the NbH$_x$ puzzle," Proc. 6th Workshop on RF Superconductivity, CEBAF, Newport News, VA, USA, October 4-8, 1993, p. 1126.

[4] C. Z. Antoine et al., "The role of atomic hydrogen in Q degradation of niobium superconducting RF cavities : Analytical point of view," Proc. 5th Workshop on RF Superconductivity, DESY, Hamburg, Germany, August 19-23, 1991, p. 616.

[5] T. Higuchi and K. Saito, "Hydrogen absorption in electropolishing of niobium," ibid [2].

[6] B. Aune et al., "Degradation of niobium superconducting RF cavities during cooling time," Proc. 1990 Linac Conference, Albuquerque, NM, Sept. 10-14, 1990, p. 253.

[7] J. Halbritter et al., "Additional losses in high purity niobium cavities related to slow and hydrogen segregation," ibid [3], p. 617.

UPDATE ON RF SYSTEM STUDIES AND VCX FAST TUNER WORK FOR THE RIA DRIVER LINAC*

B. Rusnak, S. Shen, Lawrence Livermore National Laboratory
Livermore, CA 94550, USA

Abstract

The limited cavity beam loading conditions anticipated for the Rare Isotope Accelerator (RIA) create a situation where microphonic-induced cavity detuning dominates radio frequency (RF) coupling and RF system architecture choices in the linac design process. Where most superconducting electron and proton linacs have beam-loaded bandwidths that are comparable to or greater than typical microphonic detuning bandwidths on the cavities, the beam-loaded bandwidths for many heavy-ion species in the RIA driver linac can be as much as a factor of 10 less than the projected 80–150 Hz microphonic control window for the RF structures along the driver, making RF control problematic. While simply overcoupling the coupler to the cavity can mitigate this problem to some degree, system studies indicate that for the low-β driver linac alone, this approach may cost 50% or more than an RF system employing a voltage controlled reactance (VCX) fast tuner. An update of these system cost studies, along with the status of the VCX work being done at Lawrence Livermore National Lab is presented here.

INTRODUCTION

The Rare Isotope Accelerator, as it is presently envisioned, is a heavy-ion accelerator capable of efficiently accelerating all stable or near-stable isotopes from protons to uranium. To meet the nuclear physics objectives of producing proton- and neutron-rich nuclei far from stability, the machine would be used to drive either heavy nuclei into a fast-fragmentation target or protons into an isotope separator on-line (ISOL) target. The specification of 1 puA of 400 MeV/nucleon U-238 on target is needed to obtain the largest isotope range out of the fragmentation target and is limited by the current available from an electron cyclotron resonance (ECR) source. Using protons to drive the ISOL targets bounds the light end of the ion spectrum and requires the cavities to accommodate a very large velocity range and acceleration rate. By utilizing short, low-frequency RF cavities between 57–345 MHz on independently-phased RF generators, large cavity velocity acceptances can be realized. This is achieved by using a combination of superconducting accelerating structure types that are common to the heavy ion superconducting RF (SRF) accelerator community and span quarter-wave, half-wave, and spoke, as well as elliptical, cavities [1]. The combination of light and varying beam loading (~10's–100's of uA) and very high cavity quality factor ($Q \sim 10^9$)

provides an engineering challenge as how one can most efficiently couple RF power into the cavities, thereby minimizing capital and operating costs.

RF CONTROL REQUIREMENTS

In any RF accelerator, it is desirable to optimally and efficiently couple RF energy into the beam-loaded resonator. In normal conducting accelerators, the power dissipated in the cavity walls plays a significant role in setting the loaded Q_l bandwidth of the cavity, since these losses are generally comparable to or greater than the beam power in the cavity. In superconducting accelerators, the extremely low loss and resulting high unloaded Q_0 of a cavity changes the RF control situation appreciably. The first consequence is that even modest beam current completely dominates the Q_l bandwidth of the structure. The second consequence is that the cavity is vulnerable to slight mechanical deformations that can appreciably change the resonant frequency of the cavity. Since superconducting niobium cavities are typically made of high-purity niobium sheet metal, this makes them prone to micro-scale deflections from vibrations, cryogenic pressure variations, and ponderomotive detuning.

For beams where the current is appreciable (>1 mA), setting the RF coupler for matched coupling to the beam results in a loaded cavity bandwidth of many 100's of Hertz or more. Bandwidths in this range are usually sufficient to mask the effects of microphonic detuning on a cavity. When beam loading becomes lighter (~10's to 100's of uA), the matched beam-loaded bandwidth becomes comparable to or less than the bandwidth of the microphonic excitations. This leads to significant low-level RF control problems since the cavity resonant frequency is moving around the linac set point frequency by multiples of a cavity resonant bandwidth.

To maintain stable accelerating voltage in the cavity, three basic strategies are available: 1) Beam-match couple to the cavity and attempt to adapt to the microphonic-driven detuning by rapidly driving in increased generator power when the cavity detunes in a localized microphonic excursion; 2) greatly overcouple the cavity beyond beam match with the drive coupler to increase the bandwidth; or 3) try to reduce the microphonic-driven detuning bandwidth directly. The first two approaches result in wasted RF power and larger capital costs for installed capacity, while the third requires some sort of fast tuner. The situation is shown graphically in Fig. 1 for a 345-MHz two-gap spoke resonator. The case where the cavity

is overcoupled would be for a Q_x a factor of 10 below ~1.3×10^7, and for the beam-match coupled case the dashed curve would be the generator power needed to maintain cavity fields with microphonics.
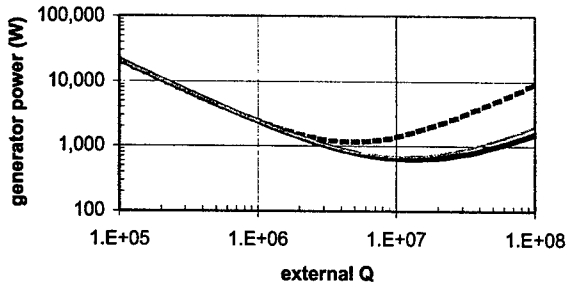
Fig. 1. Plot shows the RF generator power needed t maintain cavity fields at the desired level for a 345–MH spoke cavity with 413 uA of beam current. The uppe dashed and lower light-weight line indicate the powe needed for minus and plus 40 Hz of microphoni detuning, respectively. The heavier solid bottom curve i for beam-induced detuning as well as the fast-tune compensated microphonics case.

Microphonics

The issue of what constitutes a reasonable microphoni window is rather complicated and difficult to establish On lightly beam-loaded heavy-ion superconducting accelerators like ATLAS, control windows for microphonics are quoted as being around 150 Hz [2]. Discussions at recent workshops [3][4][5] have indicated that while measured microphonic excursions by a given cavity may only be 5–15 Hz, having a factor of 10 on the overall control window for the system of cavities on the linac is necessary, since the actual spread of detuning across a distribution of cavities will be larger than it is for a singular cavity. This methodology of having a modest actual detuning range, multiplied by a margin factor, shall be used for the comparisons presented in this paper.

RF SYSTEM LAYOUTS AND COST BASIS

Two conceptual RF system designs were developed for comparison purposes. The first system used overcoupling to increase the bandwidth to ameliorate the effects of microphonics. The second used some form of fast tuner to significantly reduce the microphonic-induced detuning window.

In the assessment, components were chosen appropriate to the operating conditions anticipated. In the overcoupled case, transmission lines, power couplers, and circulators needed to handle infinite voltage standing wave ratio (VSWR) conditions on a continuous wave (CW) basis. This case also required larger RF amplifiers to drive the system. The fast-tuner system was similar, except the overall system power was substantially less, thereby lessening the power handling requirements on these components and decreasing the generator size. The fast-

tuner assembly and impacts on the cryogenic system were also taken into account.

The conceptual designs for the respective RF systems were significantly affected by the large variation in component choices between the 500 W and 20 kW power ranges. A survey of four companies was carried out to determine component prices, which were used to establish a credible representative market price for each system. Fig. 2 shows the variations average cost in CW RF amplifiers at low power. The staircase effect suggests one would like to choose amplifier sizes to maximize cost efficiency. Fig. 3 shows how the data extends to higher power ranges using a more conventional dollar-per-Watt metric.
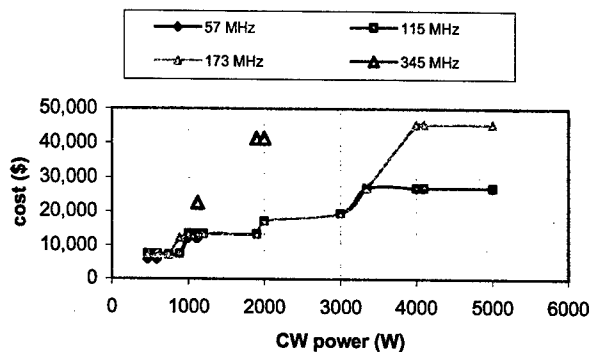
Fig. 2. Cost data for narrow-band RF amplifiers as a function of output power. The amplifiers were either Class A or AB.
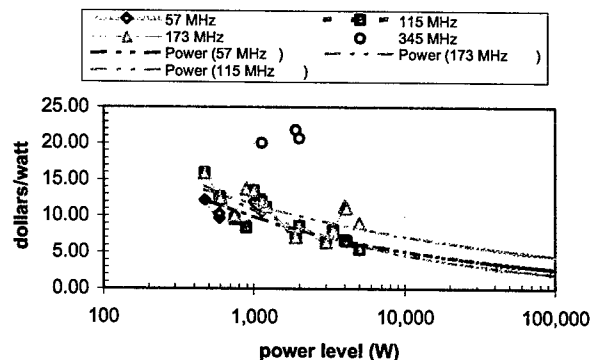
Fig 3. Cost data expressed in dollars per Watt as a function of power level. Power-function fits show how the data scales to higher power values consistent with $3–5 /Watt.

COST COMPARISONS

Applying the cost data to the two RF architecture concepts, a cost comparison was done between fast-tuning and overcoupling-compensated microphonic cases. Table 1 shows that utilizing a form of fast tuning can reduce the installed RF power required by as much as a

factor of 3 and reduce the capital cost by a factor of 1.5, potentially saving on the order of 6 million dollars.

Cavity Type	Overcoupled Case		Fast-Tuner Compensated	
low β (MHz)	installed RF power (W)	section cost (k$)	installed RF power (W)	section cost (k$)
57.5	160,000	2,155	30,000	1,160
115	225,000	2,424	45,000	1,576
172.5	520,000	7,522	104,000	3,642
345	160,000	5,508	160,000	5,098
totals:	1,065,000	17,609	339,000	11,476

Table 1. Results of a cost comparison exercise between overcoupled and fast-tuner compensated approaches for handling microphonic detuning on the low-beta section of the RIA driver linac. In the 345–MHz case, while the installed power is the same, the costs differ since the RF match is better, resulting in lower VSWR operation.

Evaluations were also made on the impacts of using fast tuning on the elliptical cavity portions of the linac, which indicate a potential reduction in installed RF power of a factor of 5.1, and a cost savings on the order of 11 million dollars could be realized. Further development would be needed to extend the present work to 805 MHz elliptical cavities.

FAST TUNING

The potential for appreciable cost savings using fast tuning on the RIA driver linac, combined with improved efficiency of the machine resulting from better coupling, is motivating work on advancing the design of the voltage controlled reactance (VCX) fast-tuner concept that was originally developed and applied on ATLAS at Argonne [6]. The original Argonne approach utilized 10 PIN-type RF-switching diodes combined with lumped inductive and capacitive elements, all immersed in liquid nitrogen, to change the reactive impedance of the cavity to effect a rapid change in the resonant frequency of the system of the cavity plus tuner. By switching the PIN diodes from full conduction to full isolation at 25 kHz, the desired precise accelerator frequency can be approximated by the vector sum of the cavity voltages corresponding to the on and off state of the tuner. To compensate the observed microphonic detuning windows on ATLAS, 15–20 kVAR (voltage-ampere reactive) of reactive power was switched.

This approach has worked for over 20 years on ATLAS at up to 97 MHz. To extend the technology to higher frequency and reactive power ranges, a different design approach is being developed and evaluated that utilizes distributed inductive and capacitive elements in a transmission-line configuration, but keeps the same proven lumped-element, high-power PIN diodes used originally. The new configuration offers the possibility of being more broadband for higher frequencies than an approach relying on lumped elements and is also potentially extendable to switching reactive power levels up to 75–100 kVAR by readily adding larger numbers of PIN diodes. A drawing of the distributed element approach being investigated is shown in Fig 4.
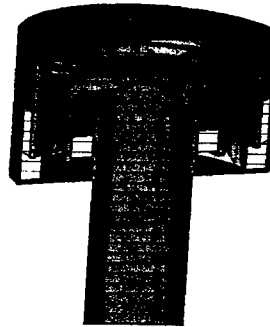
Fig 4. Drawing of a distributed element approach for a high-frequency VCX. The light components are ceramics acting as capacitors, and the PIN diodes are the circumferentially distributed cylinders. The region where the PINs are located would be filled with liquid nitrogen.

CONCLUSIONS

The light beam loading conditions envisioned on the RIA driver linac offer unique challenges and opportunities in efficiently coupling RF power into superconducting cavities. Studies have shown that appreciably less installed RF power is needed when a fast tuner is used to compensate microphonics. This benefit is motivating work on advancing the design of a higher frequency, higher power version of the original VCX tuner concept used on ATLAS.

ACKNOWLEDGEMENTS

The authors would like to thank Ken Shepard, Gene Clifft, Gary Zinkann, and Sergey Sharamentov for their assistance and fruitful discussions on this work.

REFERENCES

[1] K. Shepard et al, "SC Driver Linac for a Rare Isotope Facility," Proc. of the 9th Workshop on RF Super-conductivity, Santa Fe, NM, Nov. 1–5, 1999, p. 345.

[2] N. Added et al, "Upgraded Phase Control System for Superconducting Low-Velocity Accelerating Structures," LINAC 1992, Ottawa, Canada, Aug 24–28, 1992, p. 181.

[3] LLRF Control Workshop, Jefferson Lab, Newport News, VA, April 25–27, 2001.

[4] Spoke Cavity Workshop, Los Alamos National Lab, Los Alamos, NM, Oct. 7–8, 2002.

[5] Second RIA Driver Linac Workshop, Argonne National Lab, Chicago, IL, May 22–24, 2002.

[6] J.M. Bogaty et al, PAC 1989, Chicago, IL, March 20–23, 1989, p. 1978.

CRYOMODULE DESIGN FOR THE RARE ISOTOPE ACCELERATOR*

T.L. Grimm[†], W. Hartung, M. Johnson, R.C.York

National Superconducting Cyclotron Laboratory, Michigan State University, E. Lansing, MI, USA

P. Kneisel, L. Turlington

Thomas Jefferson National Accelerator Facility, Newport News, VA, USA

Abstract

The Rare Isotope Accelerator (RIA) driver linac will produce >400 MeV/u proton through uranium beams using many types of superconducting accelerating cavities such as quarter wave, spoke, and elliptical cavities. A cryomodule design that can accommodate all of the superconducting cavity and magnet types is presented. Alignment of the cold mass uses a titanium rail system, which minimizes cryomodule size, and decreases both the tunnel cross-section and length. The titanium rail is supported from the top vacuum plate by an adjustable tri-link, which is similar to existing Michigan State University magnet technology. A prototype cryomodule is under construction for testing 805 MHz, v/c=0.47, six-cell niobium cavities in realistic operating conditions. Details of the design and progress to date are presented.

INTRODUCTION

The Rare Isotope Accelerator (RIA) driver linac is designed to accelerate heavy ions to 400 MeV/u (β=v/c=0.72) with a beam power up to 400 kW [1]. To obtain these intensities, partially stripped ions are accelerated in a 1400 MV superconducting linac. A design based on the 80.5 MHz harmonic requires six cavity types as shown in Table 1 [2]. The first and last cavity types were developed for other linacs and the remaining four are variants of these two.

A rectangular cryomodule design with cryogenic alignment rail that can accommodate all of the superconducting cavity and magnet types is proposed for RIA. This type of module has been used at Michigan State University (MSU), TESLA, INFN Legnaro and Argonne National Laboratory. In particular, a prototype cryomodule for the elliptical cavities with geometric β, β_{geo}, of 0.47 (optimum β, β_{opt}, of 0.49) is presented and easily extends to the other cavity types. While the Spallation Neutron Source (SNS) has already developed a cryomodule that could be used for the elliptical cavities of RIA [8], it would be inappropriate for the drift tube cavities, and significant simplifications and cost savings are possible with the rectangular cryomodule due to RIA's continuous, relatively low power beam.

Table 1. Overview of RIA Driver Linac Cavities (80.5 MHz harmonic).

β_{opt}	f(MHz)	Type	Status
0.041	80.5	$\lambda/4$	Developed for INFN Legnaro [3]
0.085	80.5	$\lambda/4$	Prototype in Fall 2003 [4]
0.160	161	$\lambda/4$	Prototype in Summer 2003 [4]
0.285	322	Spoke $\lambda/2$	Demonstrated in 2002
0.49	805	6-cell Elliptical	Demonstrated in 2002 [5]
0.63	805	6-cell Elliptical	Developed for SNS [6]

DESIGN

Beam dynamics simulations for efficient beam transport with minimal emittance growth have shown that four β=0.47 cavities per cryomodule with cavity alignment tolerances of ±1-2 mm are acceptable [9]. Figure 1 shows the rectangular cryomodule with four 805 MHz β=0.47 six-cell cavities, and Table 2 shows the main parameters.

The cavity with titanium helium vessel, power coupler and tuner are shown in Figure 2. The first transverse mechanical mode of the cavity is damped by attaching the center of the cavity to the helium vessel with titanium spokes. A titanium to stainless transition is used to attach the cavity to the helium manifold. No higher-order-mode dampers are required due to RIA's relatively low beam current [10]. An external room-temperature frequency tuner is used for improved reliability and maintainability. An external actuator can also be used to damp microphonics.

The input rf power is less than 10 kW for beam loading and microphonics control. The same ceramic window as SNS is used and transitioned to a smaller diameter vacuum coax for capacitive coupling to the cavity [11, 12]. The outer conductor does not require helium gas cooling which greatly simplifies the cryoplant. The thermal load from the power coupler to the helium system was calculated assuming 10 kW of rf power and a center conductor at room temperature. The outer conductor is 0.89 mm thick stainless steel with 8 microns of RRR=10 copper. Figure 3 shows the temperature
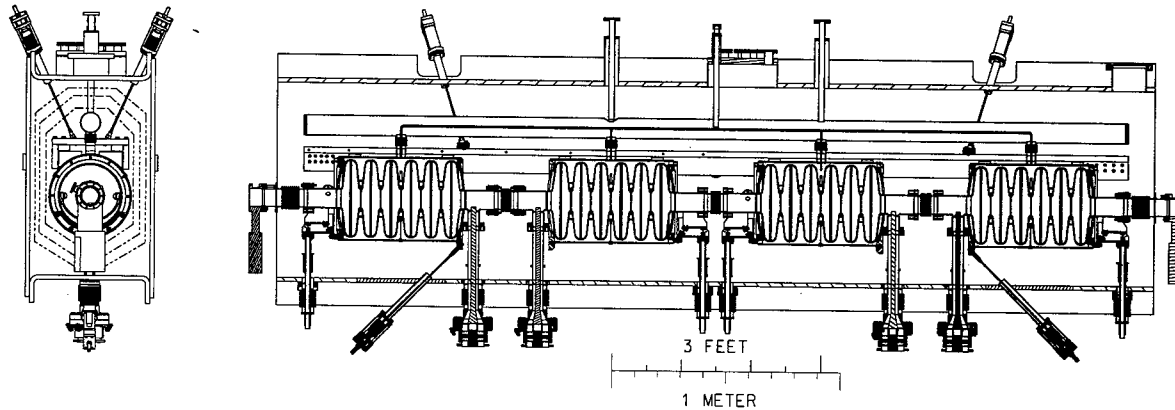
Figure 1. RIA Cryomodule with four β=0.47 elliptical cavities (side and end view).

profile along the outer conductor, which has a liquid nitrogen intercept. The helium and nitrogen load are 1.6 and 4 W per coupler respectively. Operation with 50 K helium gas in lieu of liquid nitrogen would further decrease the helium load.

Table 2. Design specifications of RIA cryomodule.

Cavity	
Frequency	805 MHz
v/c = β	0.47
He Vessel Diameter	0.362 m
Total Mass	71.6 kg
Beam Aperture	0.075 m
Design Q	5×10^9
V_{acc}	4.2 MV
RF loss	22 W
Input RF power	<10 kW
Cryogenic Module	
Length	4.0 m
2K Cold Mass	400 kg
Total Module Mass	3000 kg
# Bayonets	4
# Support Links	6
2K Heat Load	
Power Coupler	1.6 W/ea
Tuner	0.8 W/ea
Total / RF OFF	15 W
Total / RF ON	103 W
Shield Heat Load	<100 W
Pressure Rating	
2K System	3 bar
Thermal Shield	10 bar

All four cavities are rigidly aligned on a titanium rail with optical fiducials at the ends and center of the rail that can be viewed when cooled to 2 K to verify alignment. The 2 K cold mass is assembled in a Class 100 cleanroom as shown in Figure 4. The cavities are aligned using push-pull mechanisms and shims outside the cleanroom.

The 2 K cold mass is supported with six nitronic links. The link forces are monitored using strain gauges. Two magnetic shields and a 77 K thermal shield are supported by the helium distribution and thus mechanically isolated from the 2 K cold mass. The vacuum vessel is made from low carbon steel plate. During transportation pins secure the cold mass to the vacuum vessel, and a stiffener is inserted into the power coupler. The most sensitive component to shock is the power coupler's inner conductor, which will plastically deform above 4.6g.
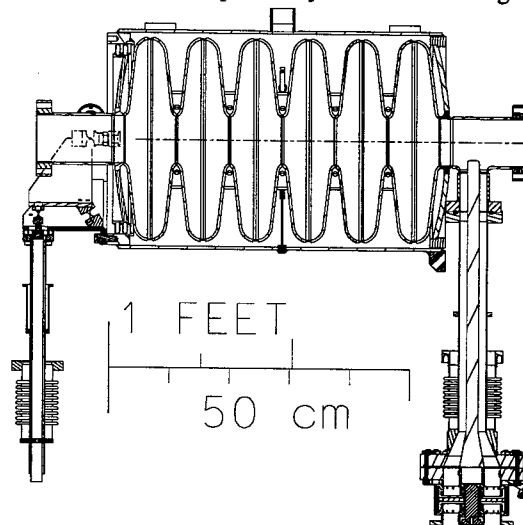
Figure 2. Cavity with helium vessel, power coupler and tuner.

The cryogenic distribution system houses the control valves and heat exchangers to simplify the cryomodule and allow commissioning of the cryogenics before installation of the cryomodule.

The rectangular cryomodule with titanium rails offers several advantages over that used for the SNS. The rectangular design concept can be used for all of the RIA superconducting cavities and superconducting magnets. The module will cost less than half that of SNS. The

smaller helium vessel simplifies construction and processing of the cavities, and decreases the cryomodule width, thereby decreasing the tunnel width. Also, the
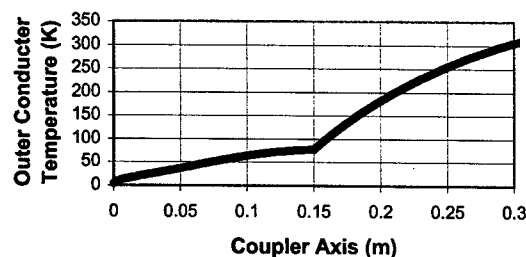
Figure 3. Temperature profile along outer conductor of the power coupler.

titanium rail and small helium vessel simplify fixturing and alignment of the cavities. The lower power rf couplers do not require helium gas cooling which simplifies the coupler and cryoplant, thereby decreasing the module and tunnel length. With the cryogenic controls adjacent to the module, the room temperature slot length for diagnostics and focusing elements can be reduced, again decreasing the tunnel length. The cavity tuner is removed from the cold mass and operated at room temperature for improved reliability and maintainability.
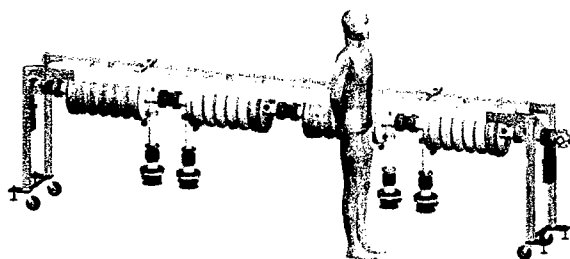
Figure 4. Clean room assembly of 2 K cold mass.

CONSTRUCTION AND TEST PLANS

A two cavity version of the rectangular cryomodule is under construction to demonstrate performance and costing. The cavities shown in Figure 2 are complete and will be tested in a vertical dunking Dewar in the summer of 2003. Next the 2 K cold mass will be assembled and then installed inside the cryomodule for testing by the end of 2003. Once the design has been demonstrated for elliptical cavities, a low beta version for the quarter-wave and half-wave cavities will be constructed.

ACKNOWLEDGEMENTS

REFERENCES

[1] "The Rare-Isotope Accelerator (RIA) Facility project", C.W. Leemann, in *Proceedings of the XX International Linac Conference*, Monterey, CA (2000).

[2] *Proceedings of the RIA Driver Workshop II*, Argonne, IL (May 2002).

[3] "Completion of the LNL Bulk Niobium Low Beta Quarter Wave Resonators", in *Proceedings of the 9th Workshop on RF Superconductivity*, Santa Fe, NM (1999).

[4] To be presented at the 11th Workshop on RF Superconductivity, Lubeck/Travemunde, Germany, September 2003.

[5] "Experimental Study of a 322 MHz v/c=0.28 Niobium Spoke Cavity", T.L. Grimm, J. Bierwagen, S. Bricker, C.C. Compton, W. Hartung, F. Marti, and R.C. York, *these proceedings*.

[6] "Status Report on Multi-Cell Superconducting Cavity Development for Medium-Velocity Beams", W. Hartung, C.C. Compton, T.L. Grimm, R.C. York, G. Ciovati, P. Kneisel, *these proceedings*.

[7] "Superconducting Prototype Cavities for the Spallation Neutron Source", P. Kneisel, G. Ciovati, K. Davis, K. Macha and J. Mammosser, in *Proceedings of the 8th European Particle Accelerator Conference*, Paris (2002).

[8] "Design of the SNS Cryomodule", W.J. Schneider, I.E. Campisi, E.F. Daly, T. Hiatt, J. Hogan, P. Kneisel, D. Machie, J. Preble, C.H. Rode, T. Whitlatch, M.A. Wiesman, K. Matsumoto and R. Mitchel, in *Proceedings of the 2001 Particle Accelerator Conference*, Chicago (2001).

[9] "The Beam Dynamics Studies of Combined Misalignment and RF Errors for RIA", X. Wu, D. Gorelov, T. Grimm, W. Hartung, F. Marti and R. York, *these proceedings*.

[10] "Input Coupling and Higher-Order Mode Analysis of Superconducting Axisymmetric Cavities for the Rare Isotope Accelerator, T.L Grimm, W. Hartung, F. Marti, H. Podlech, R.C. York, J. Popielarski, C. Wiess, L. Kempel, G. Ciovati and P. Kneisel, in Proceedings of the 8th European Particle Accelerator Conference*, Paris (2002).

[11] "The Prototype Fundamental Power Coupler for the Spallation Neutron Source Superconducting Cavities: Design and Initial Test Results", K.M. Wilson, I.E. Campisi, E.F. Daly, G.K. Davis, M. Drury, J.E. Henry, P. Kneisel, G. Myneni, T. Powers, W.J. Schneider, M. Stirbet, Y. Kang, K. Cummings, T. Hardek, in *Proceedings of the 10th Workshop on RF Superconductivity*, Tsukuba, Japan (2001).

[12] "Design and Fabrication of Input RF Coupler Windows for the SNS", Q. Sheng, J. Susta, G. Cheng, S. Einarson, T.A. Treado, W.C. Guss and M. Tracy, in *Proceedings of the Workshop on High-Power Couplers for Superconducting Accelerators*, Newport News VA (2002).

EXPERIMENTAL STUDY OF A 322 MHz v/c=0.28 NIOBIUM SPOKE CAVITY*

T.L. Grimm[†], J. Bierwagen, S. Bricker, C.C. Compton, W. Hartung, F. Marti, R.C.York
National Superconducting Cyclotron Laboratory, Michigan State University, E. Lansing, MI, USA

Abstract

The Rare Isotope Accelerator (RIA) will accelerate heavy ions to >400 MeV/u using an array of superconducting cavities. A proposed linac design based on harmonics of 80.5 MHz will require six cavity types to cover the entire velocity range: three quarter wave resonators, one spoke cavity (half wave resonator), and two 6-cell elliptical cavities. A prototype 322 MHz niobium spoke with optimum velocity of 0.28c has been fabricated. Each spoke would generate over 1 MV at 4 K for acceleration from v/c=0.20 to 0.40. Details of the design and experimental study are presented.

INTRODUCTION

The Rare Isotope Accelerator (RIA) driver linac is designed to accelerate heavy ions to 400 MeV/u (β=v/c=0.72) with a beam power up to 400 kW [1]. To obtain these intensities, partially stripped ions are accelerated in a 1400 MV superconducting linac. A design based on the 80.5 MHz harmonic requires six cavity types as shown in Table 1 [2]. Two of the cavity types were developed for other linacs and the remaining four are variants of these two. This paper presents the design and experimental results of the 322 MHz niobium spoke cavity with an optimum β, β_{opt}=0.28.

Table 1: Overview of RIA Driver Linac Cavities (80.5 MHz harmonic).

β_{opt}	f(MHz)	Type	Status
0.041	80.5	λ/4	Developed for INFN Legnaro [3]
0.085	80.5	λ/4	Prototype in Fall 2003 [4]
0.160	161	λ/4	Prototype in Summer 2003 [4]
0.285	**322**	**Spoke λ/2**	**Demonstrated in 2002**
0.49	805	6-cell Elliptical	Demonstrated in 2002 [5]
0.63	805	6-cell Elliptical	Developed for SNS [6]

DESIGN AND FABRICATION

Figure 1: Cross section of spoke

The spoke cavity (or half-wave resonator) design is based on coaxial tubes that are formed using dies and mandrels. Sheet and plate niobium of RRR>150 was used. The inner and outer tubes, 24 cm and 10 cm inner diameter, are formed from 2 mm sheet. The beam ports and rf coupling ports are identical and at the median plane, which requires capacitive coupling for the rf. The beam aperture is 3 cm. These four ports are the only access to the cavity for chemistry and high-pressure rinse. They are indium sealed providing beamline and cryostat vacuum isolation. No helium vessel is required for this prototype to quickly verify electromagnetic performance and address multipacting and microphonic issues. Lorentz detuning is not a concern for RIA since it is a cw machine.

Table 2: Design parameters of spoke

Design Specifications	
Type	λ/2
β_{opt}	0.285
f (MHz)	322
V_{acc} (MV)	1.04
T (K)	4.2
Q_o	2.5×10^8
P_o (W)	21.8
U (J)	2.68
R/Q (Ω)	199
R_s (nΩ)	244
E_{peak} (MV/m)	16.5
B_{peak} (mT)	45.3

Table 2 shows the electromagnetic design parameters of the cavity [7]. A single-spoke cavity with two accelerating gaps was chosen to cover the velocity range from v/c=0.20 to 0.40. While multi-spoke structures could decrease the number of units, it would require more than one cavity type of increased complexity [8]. Figure 2 shows the effective accelerating voltage of the driver linac cavities through the acceleration chain.
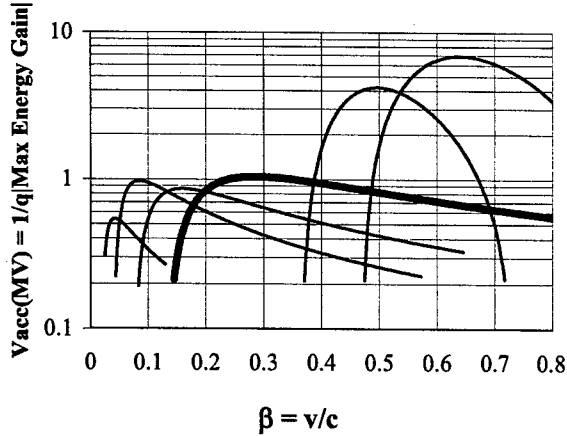
Figure 2: Effective accelerating voltage of driver linac cavities. The 322 MHz spoke is shown boldfaced/blue.

Electron beam welding with pressure less than 3×10^{-5} torr was used to join the niobium parts. All parts were etched >10 μm prior to welding. Figure 3 shows all of the niobium parts before final electron beam welding. After welding was complete, a final etch of 120 μm using pumped and chilled 1:1:2 buffered chemical polish was performed. Next the cavity was high-pressure rinsed for an hour and allowed to dry in a Class 100 cleanroom. Finally the vacuum ports and antennae were attached and the cavity installed on the dunking Dewar insert prior to testing as shown in Figure 4 [9].
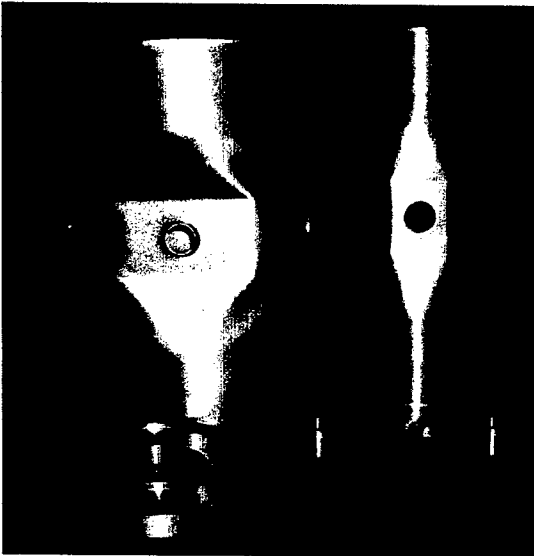
Figure 3: Niobium parts before final welding.

Figure 4: Spoke cavity on the dunking Dewar insert.

EXPERIMENTAL RESULTS

The electric field profile along the beam axis was measured using a bead pull technique and is shown in Figure 5. The field unflatness was relatively small at 2.5 %. During the first test in December 2002, the input and pickup couplers were fixed with coupling strengths, Q_{ext}, of 1.4×10^{9} and 1.6×10^{11} respectively.
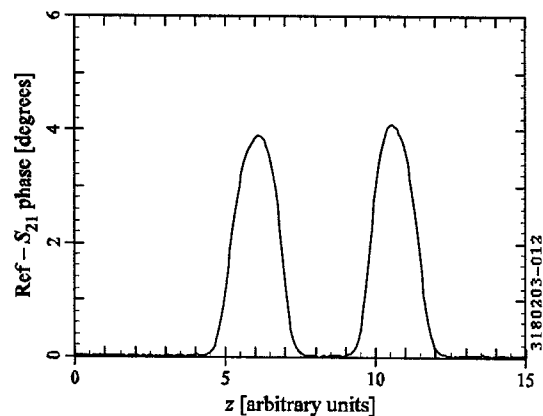
Figure 5: Bead pull measurement showing the electric field profile along the beam axis.

No bakeout of the cavity was performed and the base pressure was 1.6×10^{-8} torr at which point the cavity was cooled to 4.3 K. Conditioning took about 1 hour to remove multipacting barriers at peak electric fields, E_p, of 0.25-0.45 MV/m. These barriers were consistent with calculations showing one-point multipacting on the outer conductor at the high electric field region.
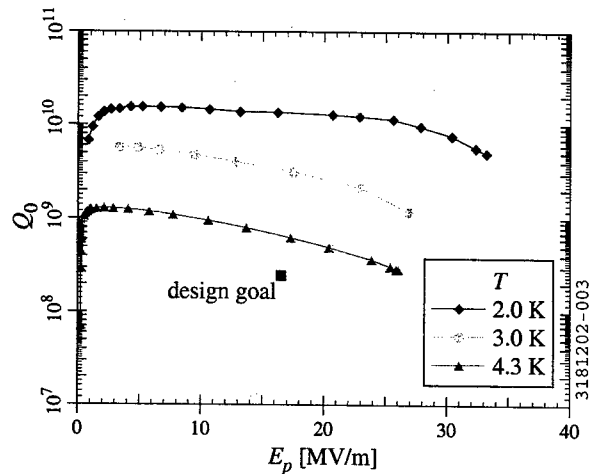
Figure 6: Cavity quality factor versus peak electric field.

Designs are underway to incorporate a titanium helium vessel, tuner and high power coupler, and test the cavity under realistic operating conditions in a RIA horizontal cryomodule. A prototype cryomodule is under construction for the RIA 6-cell structures that can be modified for the spoke cavity [10]. To date, four of the six cavity types for the 80.5 MHz RIA driver linac have been demonstrated and the remaining two should be tested in 2003.

ACKNOWLEDGEMENTS

The cavity quality factor, Q_0, was measured versus peak electric field at 2-4.3 K and shown in Figure 6. The design goal for operation at 4.3 K is also shown in Figure 6 with performance significantly exceeding it. In March 2003, the cavity was retested with a higher input Q_{ext} of $5x10^9$. Similar peak fields were obtained, and a residual surface resistance of 5 nΩ was confirmed.

Measurements of frequency detuning due to microphonics, pressure and the Lorentz force were made. Since the helium vessel will further stiffen the cavity, the values reported here are upper limits to those anticipated in an operating linac. The pressure detuning was −264 Hz/torr, and the Lorentz detuning coefficient (in terms of E_p) was −1.56 Hz/(MV/m)^2. Microphonics measurements show a total frequency shift of ±4 Hz due to several driving terms such as the cleanroom blowers with vibrations at 14 and 50 Hz, and the turbo pump at 458 Hz.

CONCLUSION/FUTURE PLANS

The 322 MHz spoke has significantly exceeded design specifications at 4.3 K of Qo>$2.5x10^8$ and peak electric fields greater than 16.5 MV/m. An extremely low residual surface resistance of 5 nΩ was measured which opens up the possibility of economically operating this cavity at less then 4 K. Multipacting barriers were easily conditioned without baking or adjustable power couplers. Measured frequency detuning due to microphonics, pressure and Lorentz force were at acceptable levels for RIA and would likely be smaller once a helium vessel is added.

REFERENCES

[1] "The Rare-Isotope Accelerator (RIA) Facility project", C.W. Leemann, in Proceedings of the XX International Linac Conference, Monterey, CA (2000).

[2] Proceedings of the RIA Driver Workshop II, Argonne, IL (May 2002).

[3] "Completion of the LNL Bulk Niobium Low Beta Quarter Wave Resonators", A. Facco and V. Zviagintsev, in Proceedings of the 9th Workshop on RF Superconductivity, Santa Fe, NM (1999).

[4] To be presented at the 11th Workshop on RF Superconductivity, Lubeck/Travemunde, Germany in September 2003.

[5] "Status Report on Multi-Cell Superconducting Cavity Development for Medium-Velocity Beams", W. Hartung, C.C. Compton, T.L. Grimm, R.C. York, G. Ciovati, P. Kneisel, these proceedings.

[6] "Superconducting Prototype Cavities for the Spallation Neutron Source (SNS) Project", G. Ciovati, P. Kneisel, K. Davis, K. Macha and J. Mammosser, in Proceedings of the 8th European Particle Accelerator Conference, Paris (2002).

[7] Analyst, Simulation Technology and Applied Research, Inc., WI (http://www.staarin.com).

[8] "The RIA Driver Linac", K.W. Shepard, in Proceedings of the XXI International Linac Conference, Gyeongju, Korea (2002).

[9] "Superconducting RF Activities at NSCL", T.L. Grimm, W. Hartung, H. Podlech, and R.C. York, in Proceedings of the 10th Workshop on RF Superconductivity, Tsukuba, Japan (2001).

[10] "Cryomodule Design for the Rare Isotope Accelerator", T.L. Grimm, M. Johnson, R. C. York, P. Kneisel and L. Turlington, these proceedings.

X-RAY TOMOGRAPHY OF SUPERCONDUCTING RF CAVITIES*

S.E. Musser[†], T.L. Grimm, W. Hartung,

National Superconducting Cyclotron Laboratory, Michigan State University, E. Lansing, MI, USA

Abstract

Field emission loading limits the performance of a significant fraction of the cavities in existing superconducting accelerators. The field emission produces an additional load to the cryogenic system; it is a source of dark current and background radiation in the accelerator; and it can lead to RF breakdown if the cavity is pushed to its limits. The field-emitted electrons are accelerated by the RF field and strike the cavity wall, generating Bremsstrahlung x-rays. The regions of x-ray emission (intensity and energy spectrum) can be located by using a collimated NaI detector placed outside the cryostat and radiation shield. The x-ray emission sites can be reconstructed using tomographic techniques. Particle tracking simulations can be used to trace the field emission electrons back to their source in order to help identify the locations of the surface defects.

INTRODUCTION

Field emission (FE) in superconducting radio frequency (SRF) cavities is a primary factor that limits the surface electric field. Sources of field emission include surface roughness, dust or micro-particles, grain boundaries, adsorbed gas and impurities in the metal itself. Additional sources of electrons such as antenna discharge and multipacting can also limit cavity performance.

FE is normally a steady state phenomenon, but RF breakdown can occur when regular FE currents increase exponentially. RF breakdown further limits the operation of accelerators and can cause irreversible damage to their physical structures. The sequence of events leading to RF breakdown is varied, but typically when under high gradient operation dark current, x-rays, pressure and temperature changes appear before a structure begins to break down.

The field-emitted electrons are accelerated by the RF field and strike the cavity wall, generating Bremsstrahlung x-rays. The x-rays have been detected on general radiation monitoring systems and coincide with a fall of the quality factor (Q) value while the electric field is increased [1]. Though a good determination of cavity performance, the location of the x-rays and the possibility of multiple sources cannot be determined.

X-ray images of a single-cell cavity were taken through a Dewar and magnetic shield using a lead "pinhole camera" and high sensitivity re-useable x-ray film [2]; this approach has proven successful but lacks three-dimensional and energy information.

Carbon resistors placed on the cavity wall have been used for thermometric diagnostics of cavities in identifying the actual electron impact location(s). Field emission simulations are used to locate the source of the field-emitted electrons [1,3]. This system has proven successful also, and has been used by several labs.

In utilizing x-ray tomography, the regions of x-ray emission (intensity and energy spectrum) can be located by using a collimated sodium iodide (NaI) detector placed outside the cryomodule and radiation shield. By positioning the detector in each plane a tomographic image of the cavity can be reconstructed. The image will accurately locate the source(s) and energies of x-rays in SRF cavities being tested or in operation. Knowing the location of the x-rays and the maximum electron kinetic energy, field emission simulations can be used to determine the location of the source of electrons and thus surface defects. Other than FE from the cavity wall the electron source may be discharge from the antenna, multipacting, discharge from the window, residual gases (plasma) in the cavity or residual gases in the cavity that adsorb to micro-particles and change the potential barrier.

When successful, x-ray tomography should make it easier to identify defects and greatly facilitate superconducting radio frequency research and development.

DESIGN

A horizontal test of the $\beta_g=0.47$ 6-cell cavity for the Rare Isotope Accelerator (RIA) is being planned [4]. This provides good opportunity for x-ray imaging, as the detector assembly can be placed within 50mm of the cryomodule wall. This will provide good spatial resolution of the cavity inside.

A detector with slit collimation, moving perpendicular to slit orientation along the entire cavity length, will locate the source of x-rays in one plane (see Fig. 1a). A 1.5mm slit collimator through 102mm of lead will provide full width half maximum horizontal resolution of 3.3mm to 8.4mm.

The slit will then be replaced with a parallel hole collimator and positioned at the plane of the x-ray source. An angular scan over the cavity diameter will locate emission along a chord (see Fig. 1b). Additional scans will provide three dimensional or tomographic imaging and resolve multiple sources (see Fig. 4). A parallel seven-hole collimator with 1.5mm hole diameter and 1.8mm septa thickness through 102mm of lead will provide full width half maximum resolution of 9.9mm to 15.0mm.

a)

Detector alignment rails

Lead shield

NaI Detector

Slit collimator

b)

Lead shield

NaI Detector

Parallel hole collimator
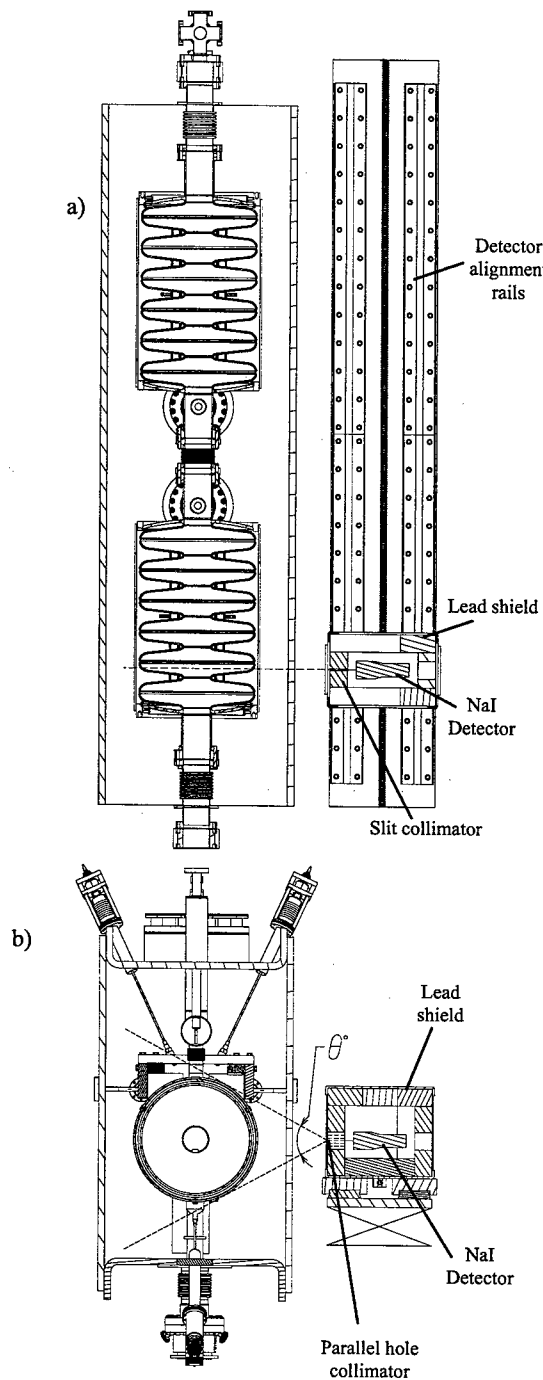
Figure 1: (a) Top view of slit collimator scanning the cryomodule in the horizontal direction [4,5]. (b) End view of parallel hole collimator scanning the diameter of the cavity [4,5].

Detector

The x-ray spectrum is measured with an ORTEC 50mmx50mm integral sodium iodide (NaI) crystal and photomultiplier tube (PMT). Sodium iodide was chosen as the scintillator since it provides adequate energy resolution and good efficiency. Sodium iodide can be obtained in almost any shape and size so it is possible to arrange an array of detectors along the scintillator to form a gamma camera [6].

Data Acquisition

Data is acquired with a digiDART portable multi-channel analyzer (MCA). The portable MCA is connected to a host computer via a universal serial bus (USB) port. The host computer, running a MAESTRO-32 software package, emulates an MCA and is used to display and archive the spectra.

Data Analysis

Energy spectra from a $\beta=0.47$ single cell cavity [7] inside a dunking Dewar that was housed in a 0.8m concrete walled bunker were measured. A typical energy spectrum measured with an unshielded, non-collimated Bicron 76mmx76mm integral NaI crystal and PMT located on top of the Dewar lid is shown in Figure 2. An energy spectrum of x-rays decreases monotonically as photon energies increase, and goes to zero at the energy of the electrons generating the x-rays. That is, measuring the x-ray spectrum and locating the endpoint energy determinations the maximum electron kinetic energy. This energy can be compared to that which is predicted.
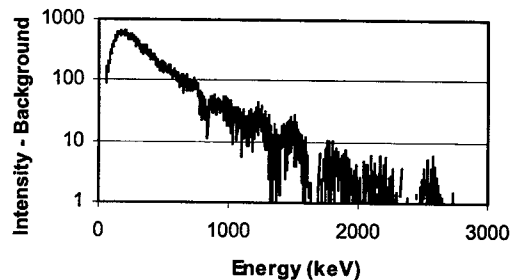
Figure 2: A typical x-ray energy spectrum from a $\beta=0.47$ single cell cavity measured on top of the Dewar lid [2]. The peak electric field level in the cavity was 21.88MV/m and the maximum electron kinetic energy 1200keV.

The regions of x-ray emission (intensity and energy spectrum) for the 6-cell $\beta_g=0.47$ cavity will be located from outside the cryomodule [4]. Compton scattering will be the predominant x-ray interaction for the range of energies expected and cryomodule materials. When an x-ray is Compton scattered only a fraction of its energy is imparted to an electron. The x-ray travels on in the material at a lower energy and on a different trajectory. The electron travels a short distance losing energy in ionizing and radiative collisions. Therefore Compton

1357

scattering increases the intensity of x-rays in low energy channels at a higher rate than the reduction in higher energy channels. Thus binning of the data is necessary to distinguish an actual x-ray source from Compton scattered x-rays. The detector assembly will be placed in a lead housing to essentially eliminate many of the low energy scattered x-rays. A lead filter in front of the detector will allow x-rays above a certain energy to pass and attenuate those below that energy.

Energy spectra from the β=0.47 single cell cavity were measured through a 0.8m concrete wall. The shielded Bicron 76mmx76mm integral NaI crystal and PMT was slit collimated. The slit was moved horizontally, perpendicular to the slit orientation. When the x-ray source was out or range of the slit resolution the intensity of x-rays in the low energy bins increased at a higher rate than the reduction of intensity in higher energy bins due to Compton scattering (see Fig. 3).
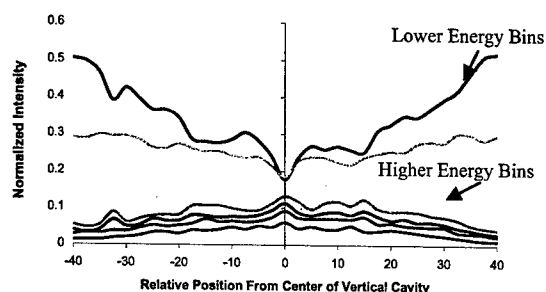
Figure 3: Binned and normalized x-ray energy spectrum from a β=0.47 single cell cavity measured through 0.8m of concrete [2]. The peak electric field level in the cavity varied between 38.22-38.48MV/m.

Image Reconstruction

The initial horizontal scan of the cryomodule, with a slit-collimated detector, will determine the plane where the x-ray source(s) reside. Tomography reconstruction expresses the x-ray emission as a set of pixels covering some mesh. Each pixel then corresponds to a function that is dependent upon position and ΔI, where I is x-ray emission intensity in an energy bin (see Fig. 4).
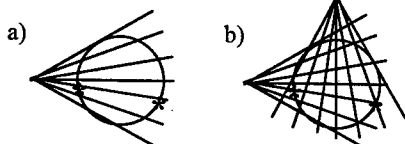
Figure 4: (a) Angular view in one position showing two x-ray sources. (b) An additional view will provide three dimensional information and resolve multiple sources.

Field Emission Simulation

Multipacting/field emission simulation software [3] is used to trace the source of electrons, producing the Bremsstrahlung x-rays, to their point of origin. The

software not only predicts the trajectories of field-emitted electrons, but their impact locations, impact energies and the resulting power deposition along the inner surface of the cavity as well (see Fig. 5).
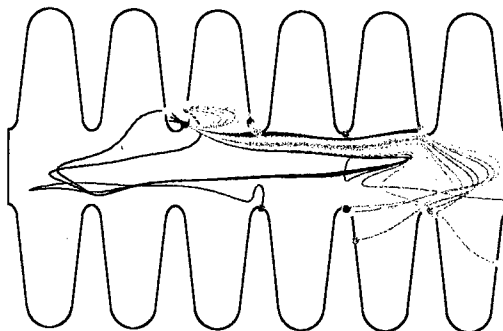
Figure 5: Field emission simulation. The electron emission site is near the iris in the third cell. Primary clusters of electron impact, or primary x-ray emission sources, are seen in the third and fifth cells [3].

FUTURE PLANS/STATUS

When successful, x-ray tomography will make it easier to identify defects and greatly facilitate superconducting radio frequency research and development. The alignment rails and the detector angle positioner are projected for assembly in September 2003. Calibration measurements and data acquisition tests with known sources will follow around November 2003. Test of the 6-cell cavities in the cryomodule is planned for 2004 [4,5]. X-ray tomography will be demonstrated at that time.

REFERENCES

[1] H. Padamsee, J. Knobloch, T. Hays, *RF Superconductivity for Accelerators*, John Wiley & Sons, Inc., 1998.

[2] T.L. Grimm et al., in *Proceedings of the Tenth Workshop on RF Superconductivity: Tsukuba 2001*, KEK, Tsukuba, Japan, 2003, p. 86-90.

[3] H. Padamsee et al., in *Proceedings of the 1987 IEEE Particle Accelerator Conference*, IEEE Publishing, New York, 1987, p. 1824-1826.

[4] T.L. Grimm, M. Johnson, R. York, "Cryomodule Design for the Rare Isotope Accelerator," these proceedings.

[5] W. Hartung et al., "Status Report on Multi-Cell Superconducting Cavity Development for Medium-Velocity Beams," these proceedings.

[6] E. Seeram, *Computed Tomography: Physical Principles, Clinical Applications, and Quality Control*, W.B. Saunders Co., 2001.

[7] C.C. Compton et al., in *Proceedings of the 2001 Particle Accelerator Conference*, IEEE Publishing, Piscataway, New Jersey, 2001, p. 1044-1046.

MECHANICAL PROPERTIES, MICROSTRUCTURE, AND TEXTURE OF ELECTRON BEAM BUTT WELDS IN HIGH PURITY NIOBIUM

H. Jiang[*], T.R. Bieler[*], C. Compton, T.L. Grimm

*Chemical Engineering and Materials Science, National Superconducting Cyclotron Laboratory
Michigan State University, East Lansing, MI 48824, USA

Abstract

The effects of Electron Beam Welding on solidification microstructure, texture, microhardness and mechanical properties were investigated in high purity Niobium weld specimens. The welds have an equiaxed microstructure with a 1 mm grain size in the fusion zone, 100 μm in the heat affected zone (HAZ) and 50 μm in the parent metal. The fusion zone had slightly higher microhardness values despite having a large grain size, while the unaffected material had the lowest microhardness. The texture in the weld consisted of a strong {111} fiber texture in the center and a mix of {111} - {100} components on the surface. Tensile tests of specimens gave $\sigma_y = 60$ MPa, but the UTS and elongation for weld specimens were lower than the parent material (137 vs. 165 MPa, 32% vs. 58%). The properties and microstructure of the weld are discussed in terms of optimizing the SRF cavity.

INTRODUCTION

Superconducting radio frequency (SRF) cavities made from high purity niobium are often fabricated using deep drawing metal forming processes to make parts that are subsequently welded together [1,2]. Electron beam welding (EBW) is used to obtain high quality welds that maintain the high purity required for superconductivity. Studies of EBW on pure metals have shown that properties of the weld material are comparable to the parent metal [3,4] although ductility was reduced and the grain size increased in Mg [3], and caused intergranular failure due to N segregation to boundaries in Mo [4]. However, little is known about how the electron beam weld affects the microstructure and properties that are important to high purity Nb SRF cavities.

Also, there is little published information on formability of pure niobium, but information on interstitial free (IF) or extra-low carbon steels [e.g. 5] may be transferable to pure niobium. Optimal processing for deep drawability in steels without developing undesirable surface roughness called "orange peel" involves rolling and recrystallization schedules that develop a very strong γ fiber texture, i.e. {111} ‖ sheet normal direction. This texture and a fine grain size minimizes the "orange peel" surface roughness which can be a source of flow instability that degrades formability [6]. Thus, this study is an initial investigation of interrelationships between welding and formability relevant to high purity niobium used for SRF cavities.

EXPERIMENTAL PROCEDURES

The niobium specimens used in this investigation were extracted by electro discharge machining (EDM) from 2 mm thick high purity niobium (RRR=150) sheet from Tokyo Denkai LTD. Two plates were butt welded together shown in Figure 1 using an electron beam weld procedure (1.7×10^{-5} torr, 50 kV, 46 mA, 5 mm/s, 1mm diameter, 1.5 mm circular oscillation). For one sheet, normal cleaning procedures were used [2] (ultra-sonically degreased ~20-30 min + cleaned in 60°C ultra-pure water ~45 minutes, dried in clean room, bagged with N_2; etched in BCP 5-7 min, rinsed in ultra-pure water just before welding), and in the less clean specimen, the final chemical etch was not done. Three 20 mm long samples were cut along the line indicated in Figure 1, and polished using standard techniques. Optical microscopy using a Nikon Epiphot 200 inverted microscope provided digital images from which the average grain size of the samples was determined using the linear intercept method and a known scale. Microhardness measurements were made using a LECO M-400-G1 hardness tester machine.

Figure 1: Welded plate and tensile specimens
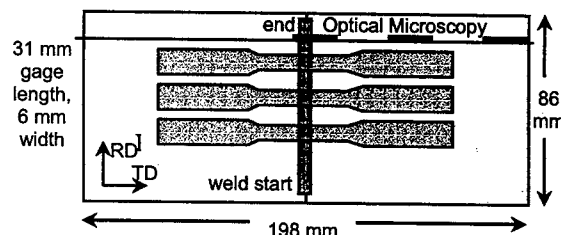
Samples for texture measurements were prepared from as-received material to measure texture on the surface and near the midplane using a Scintag XDS 2000 diffractometer and popLA software for post processing the data [7]. The spatial distribution of texture through the thickness of weld samples was investigated with a *hkl Technologies* electron backscattered diffraction pattern mapping system in a Camscan 44FE microscope, using a 25-kV beam and a specimen current of about 2.3 nA. The data were further analyzed using TexSEM Laboratories Orientation Imaging Microscopy (OIM) Analysis software version 3.0. Maps of crystal orientations covered the full 2 mm thickness of the specimen at several locations in the heat affected zone and unaffected parent material. Due to the large grain size in the weld region, 25 mm long line scans were made along sections parallel to the weld direction near the surface and in the center of the sheet to measure a statistically significant number of grain orientations.

Tensile tests were conducted according to guidelines in ASTM E8 standard test methods. The weld material

tensile specimens were machined so the tensile axis was transverse to the weld direction, and the weld was parallel to the rolling direction (RD). The EB weld region is about 5.6 mm wide, ~20% of the specimen's 31 mm gage length. Specimens of the parent material were also deformed in the same conditions to compare with the weld specimens. The tensile tests were performed on a series 4200 Instron testing machine, model number 43K2. Deformation of weld specimens was periodically stopped to measure the actual thickness and width at several locations along the gage length.

RESULTS

Figure 2 shows the fusion zone of the weld. The lighting used illustrates solidification ridges and a large grain size in the weld. From optical micrographs, the grain size decreased with the increasing distance from the weld as shown in Figure 3.

Figure 2: The 5.6 mm wide EB weld shows grain boundaries on the left side and solidification ridges on the right.
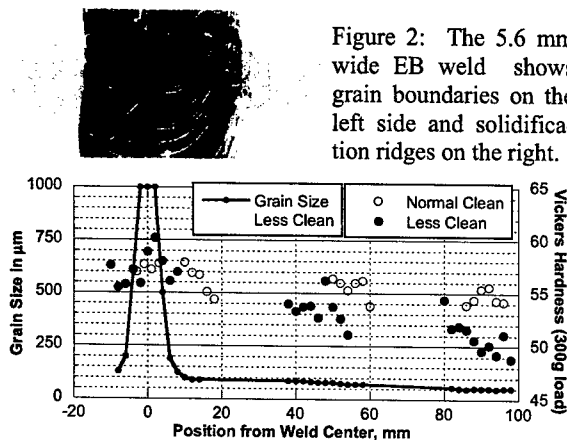
Figure 3: Grain size and Vickers Microhardness

Microhardness

The weld fusion zone has the highest microhardness value of ~57 H_V, and it decreased with increasing distance from the weld (Figure 3). The higher individual hardness values were correlated with indents on or near grain boundaries and the lower values were in the middle of a grain. Both samples show the same hardness in the weld fusion zone, but they have different rates of decreasing hardness with distance away from the weld.

Tensile Tests

The tensile properties of the as-received Niobium are comparable with prior work [2,8] and butt-weld specimens are illustrated with two specimens in Figure 4. The yield strength of as-received specimens was slightly higher than the butt-weld specimens, but the UTS of as-received specimens was ~30 MPa higher than butt-weld specimens, and the elongation was ~25% higher. The normal cleaning process caused a slight improvement in UTS and elongation of the weld specimens, but it may not be statistically significant.

The tensile tests were periodically stopped to measure the current width and thickness of the specimen in the

weld and HAZ regions. Deformation in these samples was predominantly in the width direction, and the thickness strain was nearly unchanged with strain after a small initial reduction, but it thinned during the final necking process prior to fracture. All of the weld specimens failed between the center and edge of the fusion zone, with orange-peel in the HAZ and very heterogeneous deformation shown in Figure 5. The analytically determined true stress-strain curve for the as-received parent material, and at three positions in the weld specimen (based upon the known loads and measured area changes) and the engineering stress-strain curves are plotted in Figure 4. The flow behavior in the weld fusion zone and the HAZ 10 mm from the center show the same yield stress values, but the fusion zone showed a lower strain hardening behavior, such that it became weaker
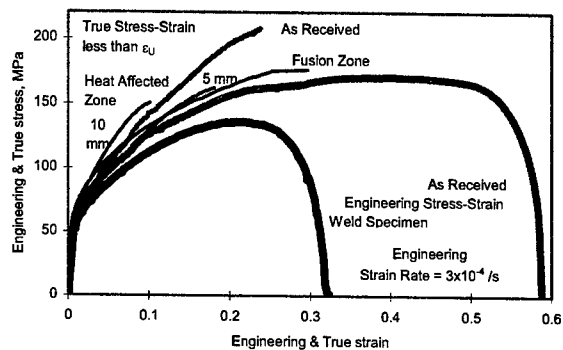
than the as-received material at a true strain of about 0.07.

Figure 4: Stress-Strain of weld and parent material
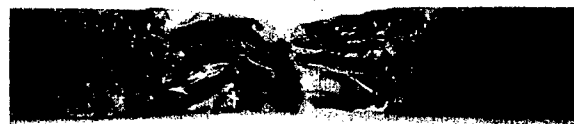
Figure 5: Fracture of weld specimen

Texture Analysis

The parent material texture in Figure 6 is shown as recalculated pole figures from the sample orientation distribution obtained using procedures given in [7]. The sheet center has a strong {111}<110> texture, but the near surface layer has a much weaker {111}<110> texture.
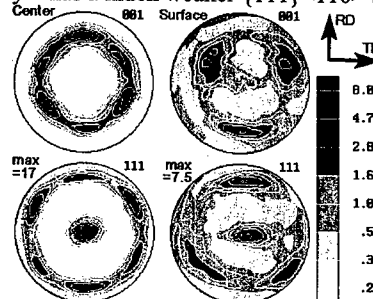
Figure 6: X-ray pole figure of parent material texture

Using OIM, microstructure and texture information were obtained simultaneously, as shown in the parent material scan in Figure 7. The orientations at the center show primarily <111> crystal directions aligned with the sheet normal direction, but the surface region has a variety of orientations, including <100> || sheet normal. The pole figures obtained from OIM are consistent with the x-ray data, as shown in Table 1. Pole figures from the HAZ and the weld also show similar trends, indicating that solidification in the weld followed the texture in the parent material.

500.0 µm = 50 steps   Black = <100> // ND, White = <111> // ND ◄——►
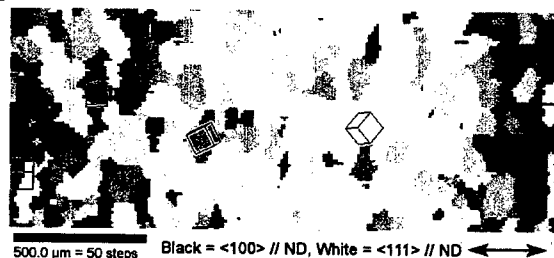
Figure 7: OIM scan of parent material; the full 2 mm sheet thickness is horizontal (sheet normal direction)

Table I: Maximum {111} Pole Figure Texture, x random, from OIM; surface / through thickness / center

Weld center	5mm HAZ	13 mm HAZ	Parent
10/-/14	13.9/13/18.2	6.2/8.3/14.1	5.4/8.0/12.2

DISCUSSION

The mechanical properties of the weld and HAZ are different from the parent material (Figure 4), due to differences in microstructure and impurity atom content. A slight increase in impurities in the weld is likely due to adsorbed water and oxygen on the surface. In the fusion zone, impurities would be well mixed since diffusion is rapid in the liquid phase. In the HAZ 5 mm from the center, where the grain size is large, there was probably about 10 seconds near the melting temperature, allowing for about 0.2 mm characteristic diffusion distance (x = $\sqrt{Dt}$; D = $0.586\exp(-13188/T)$ mm^2/s, t=10s, 2741K [9]), so there was less mixing of oxygen in the HAZ than the fusion region, and even less diffusion into the material 10 mm from the center. Table II shows how the combination of impurity atom concentration and grain size based upon the Hall-Petch equation for the yield stress, $\sigma_y = \sigma_0 + kd^{-1/2}$ (k is a material constant and d is the grain size) may account for the observed flow in the weld specimen.

Texture measurements show that as-received niobium has very strong {111} texture in the center of samples, and some near-{100} texture near the surface of samples, similar to recrystallized IF steels [5]. The fact that the texture in the weld is similar to the texture in the parent material implies that resolidification occurred epitaxially with the existing grains in the solid adjacent to the melt pool. The large equiaxed grains in the weld and immediately adjacent HAZ imply that grain growth took place while the weld was cooling. The increasing intensity of the {111} texture as one gets closer to the weld is due to the increasing grain size.

The strong {111} texture is desirable for good formability because it provides a high "R" value for sheet metal forming and deep drawing [5]. This texture resists thinning, as indicated in the lack of thinning in the weld. This retention of the {111} texture in the weld is beneficial since even though a weld may be weaker than the parent material; its resistance to thinning will prevent unstable deformation in a welded structure.

The concerns important for applications to SRF cavities are the large grain size, the mixed surface texture components, and absorption of impurities. Impurities are known to disrupt the superconducting behavior, and the large grain size causes much greater orange peel effects if subsequent plastic deformation is required. The large grain size leads to surface roughness if any plastic deformation is imposed, due to the orange peel effect [6]. The different grain directions normal to the surface cause differential etching rates that lead to ledges at grain boundaries that can disrupt the superconducting state due to local aberrations in the magnetic field. Furthermore, the work function is a strong function of crystal orientation, so that electron emission will occur most on {100} oriented grains, and least on {110} grains [10]. Impurities can locally poison the superconducting state, leading to localized heating and electric field anomalies. All of these issues will assist quenching of the electric field due to emission or field disturbances. Thus, obtaining a material with surface texture that has no {100} fiber texture would be a desirable outcome for optimized high purity niobium for SRF cavities.

Table II: Impurity and Grain Size (GS) Effects

Location	Comments; n = $d\ln\sigma_T/d\ln\varepsilon_T$ (hardening rate), σ_y = yield stress, MPa, σ = flow stress
Parent	n=0.4, σ_y=60; Smallest GS => high n, lowest impurities => low σ
10 mm HAZ	n=0.4, σ_y=61; Smaller GS => high n like parent; some impurities => higher σ_y and σ
5 mm HAZ	n=0.4, σ_y=58; Larger GS => reduces σ_y, but higher impurities => higher σ_y
Fusion zone	n=0.3, σ_y=59; Largest GS => lowest n, σ, σ_y, but highest impurities => higher σ_y

REFERENCES

[1] F Smith, J Milewski, Welding Journal (USA) 80 (2001) 43.

[2] H Padamsee, J Knobloch, T Hays, in RF Superconductivity for Accelerators, Wiley & Sons, NY, (1998), p. 105.

[3] T Asahina, H Tokisue, Materials Transactions (Japan) 42 (2001) 2345.

[4] F Morito, Journal de Physique (France) 51 (1990) 281.

[5] N Hashimoto, N Yoshinaga, T Senuma, ISIJ International (Japan) 38 (1998) 617.

[6] R Orsund, O Lohne, Mater. Sci. Forum 94 (1992) 753.

[7] JS Kallend, UF Kocks, AD Rollett, H-R Wenk, Materials Science and Engineering A132 (1991) 1.

[8] MG Rao and P Knesisel, Mechanical Properties of high RRR Nb, DESY Print, TESLA 95-09, March 1995.

[9] Smithells Metals Reference Book, 7th ed., Butterworth Heinemann, Oxford, 1992, p. 13-90.

[10] CRC Handbook of Chemistry and Physics, 73rd ed., 1992, pp. 12-108f.

1361

STATUS REPORT ON MULTI-CELL SUPERCONDUCTING CAVITY DEVELOPMENT FOR MEDIUM-VELOCITY BEAMS*

W. Hartung, C. C. Compton, T. L. Grimm, R. C. York
National Superconducting Cyclotron Lab, Michigan State University, East Lansing, Michigan, USA
G. Ciovati, P. Kneisel
Thomas Jefferson National Accelerator Facility, Newport News, Virginia, USA

INTRODUCTION

The Rare Isotope Accelerator (RIA) is being designed to supply an intense beam of exotic isotopes for nuclear physics research [1]. Superconducting cavities are to be used to accelerate the CW beam of heavy ions to 400 MeV per nucleon, with a beam power of up to 400 kW. Because of the varying beam velocity, several types of superconducting structures are needed [2].

Since the RIA driver linac will accelerate heavy ions over the same velocity range as the Spallation Neutron Source (SNS) proton linac, the 6-cell axisymmetric 805 MHz cavities and cryostats of SNS can be used for part of the RIA linac. Prototypes for both SNS cavities ($\beta_g = 0.61$ and $\beta_g = 0.81$) have been tested [3]. (Herein, β is the particle velocity divided by c and β_g is the geometric β.)

The SNS cavity design is being extended to lower velocity ($\beta_g = 0.47$) for RIA [4, 5]. Other single-cell cavities for $\beta = 0.47$ to 0.5 have also been prototyped at various laboratories [6, 7, 8]; in all cases, gradients and Q's have exceeded the design goals. A 5-cell $\beta = 0.5$ cavity has also been prototyped at JAERI [9].

This paper covers the fabrication of three prototype RIA 6-cell $\beta_g = 0.47$ cavities and the RF tests on the first and second of these cavities.

CAVITY DESIGN

The SNS $\beta_g = 0.81$ and $\beta_g = 0.61$ cavities are the basis for the RIA $\beta_g = 0.47$ cell shape [4, 5]. The beam tube is enlarged on one side of the SNS cavities in order to provide stronger input coupling. Less coupling is needed for RIA, so no enlargement of the beam tube is needed for the $\beta_g = 0.47$ cavity [10]. This simplifies the cavity fabrication and yields a slight improvement in the RF parameters. Selected cavity parameters are given in Table 1. In Table 1, E_p and B_p are the peak surface electric and magnetic field, respectively, and E_a is the accelerating gradient (transit time included) for a particle travelling at the design velocity.

An analysis was done of the excitation of higher-order modes (HOMs) in the cavity by the beam and coupling of the HOMs to the input coupler and pick-up antenna. This analysis indicates that HOM couplers are not required for operation of the $\beta_g = 0.47$ cavity in RIA, allowing for further simplification of the system [10].

Table 1. Parameters of the symmetric 6-cell $\beta_g = 0.47$ cavity; R_s is the shunt impedance (linac definition). RF quantities were calculated with SUPERFISH [11].

Mode	$TM_{010}\pi$
Resonant frequency f	805 MHz
Cell-to-cell coupling	1.5%
E_p/E_a	3.34
cB_p/E_a	1.98
R_s/Q	173 Ω
Geometry factor	155 Ω
Active length	527 mm
Inner diameter at iris (aperture)	77.2 mm
Inner diameter at equator	329 mm

SINGLE-CELL CAVITY PROTOTYPING

Two single-cell prototypes of the $\beta_g = 0.47$ cavity were fabricated and tested. The highest gradient reached in the first round of tests [4] was about 15 MV/m. The Q values at 15 MV/m were about 10^{10}; the low-field Q values were between $2 \cdot 10^{10}$ and $4 \cdot 10^{10}$. These measurements were done at 2 K in a vertical cryostat at Jefferson Lab.

Additional tests were done on the second of the two single-cell cavities while commissioning the facilities at NSCL for etching, high-pressure rinsing, clean assembly, RF testing, and helium processing of superconducting cavities. The highest gradient reached in these tests was about 18 MV/m, albeit with a slightly lower Q; however, the Q still exceeded 10^{10} at the design gradient of 8 MV/m [12].

MULTI-CELL CAVITY PROTOTYPING

Cavity Fabrication and Preparation

Sheet Nb 4 mm in thickness with a nominal Residual Resistivity Ratio (RRR) of 250 was used for the 6-cell cavities. The forming and joining of half-cells were done by the standard deep drawing and electron beam welding techniques used for SNS cavity fabrication. As with the SNS cavities, Nb-Ti flanges and Al alloy gaskets were used for the vacuum seal on the beam tubes.

The first 6-cell cavity (Figures 1a and 1b) was a simplified version without stiffening rings, dishes for attachment of the helium vessel, or side ports for the RF couplers; these features were included in the second and third cavities (Figures 1c and 1d).

The first cavity was etched with a Buffered Chemical Polishing solution to remove about 100 μm from the inside surface. The cavity was then fired in a vacuum furnace
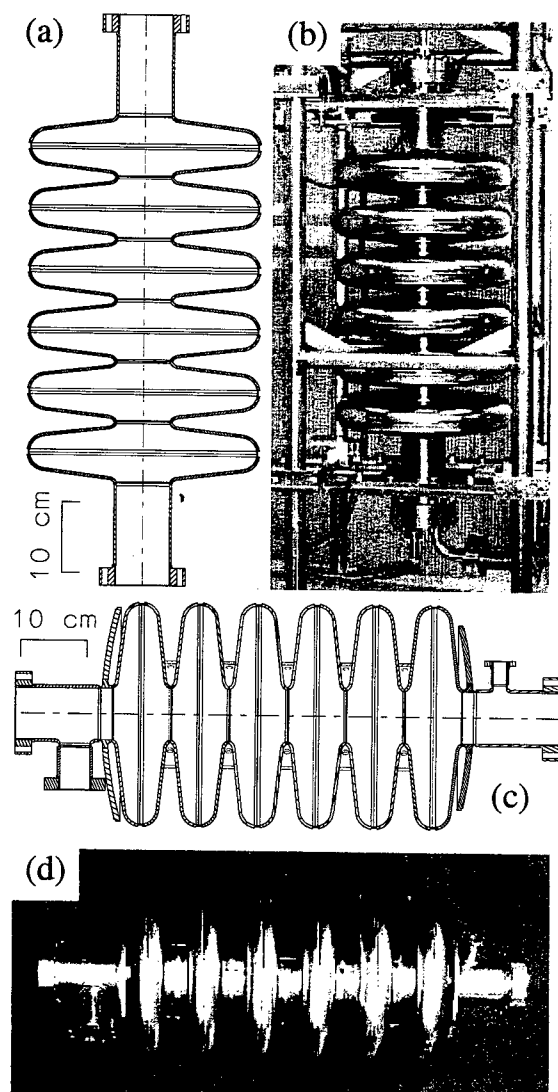
Figure 1. (a) Drawing of the first six-cell $\beta_g = 0.47$ Nb cavity and (b) photograph of the cavity on the RF test stand. (c) Drawing and (d) photograph of the second cavity.

for 10 hours at 600°C to inoculate it against the "Q disease." The pressure in the furnace was $\leq 10^{-6}$ torr during the heat treatment. Field flatness tuning was done next (see below). The final preparation steps were etching of an additional 60 μm from the inner surface and high-pressure rinsing with ultra-pure water in a clean room to remove particulates from the inside surface of the cavity.

The second cavity was etched to remove 150 μm and rinsed with the high-pressure water; it was not fired.

Tuning

Field flatness tuning was done on the first two niobium 6-cells; ancillary tuning was also done on a 5-cell copper model. The goal was a field unflatness parameter ($\Delta E/E$) of 10% or less. The first cavity and the copper model were tuned with a tuning jig designed for the SNS cavities. After tuning, $\Delta E/E$ was 7% for the Cu cavity and 12% for the

Nb cavity. The second Nb cavity was tuned with a new custom-built jig for the $\beta_g = 0.47$ cavity. This made the tuning easier; a $\Delta E/E$ of 5% was reached in one iteration (see Figure 2).

First RF Test on the First Cavity

A vertical RF test was done on the first 6-cell cavity in September 2002. The cryostat was cooled down rapidly to 4.2 K and then pumped to 2 K. As shown in Figure 3 (squares), the low-field Q was about $2 \cdot 10^{10}$ and the Q remained above 10^{10} up to $E_a = 11$ MV/m approximately. A gradient of about 16 MV/m was reached. The test was stopped at that field due to the failure of an RF cable. Some x-rays were observed at high field, indicating that the decrease in the Q at high field was likely due to field emission. Modest RF conditioning was required in order to reach a gradient of 16 MV/m. A small leak into the cavity vacuum manifested itself when the cryostat was cooled down; the pressure in the cavity was about 10^{-6} torr at 2 K.

Follow-Up RF Tests on the First Cavity

The failed RF cable was replaced, the leak in the cavity vacuum was fixed, and the cavity was retested 1 week after the first RF test (without exposure of the inside of the cavity to air). A gradient of about 7 MV/m was reached. It was thought that helium processing might be beneficial, but the test had to be stopped early due to scheduled maintenance of the cavity testing facility.

The next opportunity for an RF test was in January 2003. In between tests, the cavity was etched again to remove another 50 μm from the inner surface and the high-pressure water rinsing was repeated. The final filter on the high-pressure rinsing system (between the pump and the nozzle) was temporarily unavailable at the time of this rinse.

The results of the January 2003 test are shown in Figure 3 (circles). The low-field Q was smaller than in the first test, although the difference is within the margin of reproducibility for the measurement. A gradient of about 11 MV/m was reached. The decrease in Q between 9 and 11 MV/m is likely due to field emission; the x-ray signals were larger than those seen in the first RF test. Thus the differ-
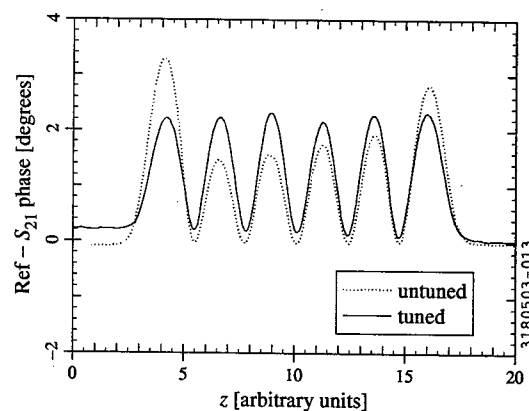
Figure 2. Bead pulls for the second six-cell niobium cavity.
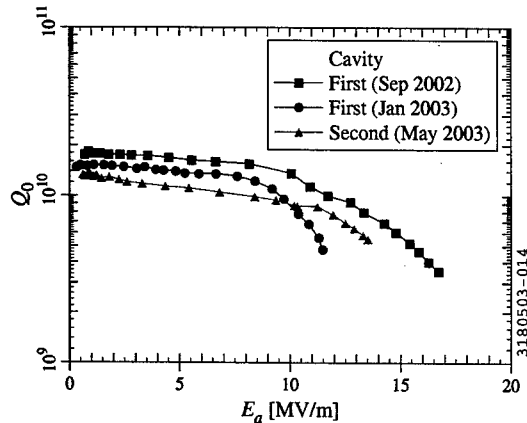
Figure 3. Measured dependence of the quality factor on the accelerating gradient at 2 K for the first and second 6-cell cavities.

ence between the September 2002 and January 2003 tests could be due to particulate contamination during the high-pressure rinse without the final filter. Although the field level was not as high as in the first test, the design goal of 8 MV/m was nevertheless reached with a Q in excess of 10^{10}.

In the January 2003 tests, measurements of Q as a function of gradient were done at several different temperatures. The low-field Q at 1.8 K was higher ($2 \cdot 10^{10}$) than at 2 K, which indicates that the BCS losses are still contributing to the surface resistance. However, the maximum gradient at 1.8 K was only slightly higher than at 2 K. A value of $Q = 2 \cdot 10^{10}$ corresponds to a surface resistance of 8 nΩ.

RF Tests on the Second Cavity

Vertical RF testing on the second cavity was done in May 2003. In the first RF test, a gradient of 8 MV/m was reached at 2 K. The Q was a bit low ($8 \cdot 10^9$) and some Q-switching was seen, indicating that more etching was needed.

In preparation for a second RF test, another 150 μm was removed from the inner surface, and the high-pressure rinse was repeated. Results from the second RF test are shown in Figure 3 (triangles). A gradient of 13 MV/m was reached. The Q was 10^{10} at the design gradient of 8 MV/m. The field was limited by the available RF power (the input coupling was weaker than planned).

MICROPHONICS AND MULTIPACTING

Microphonics are more serious for RIA than for SNS due to the lower RIA beam current. The lateral brace and stiffening rings of the SNS $\beta_g = 0.61$ cavity will be used on the $\beta_g = 0.47$ cavity to reduce microphonic excitation. The RIA cavities will be over-coupled in order to ensure that the gradient can be maintained in the presence of microphonics [10]. Some microphonic measurements were done on a single-cell cavity [12]. Modelling of the vibrations in multi-cell cavities is in progress. The predictions will be compared with measurements on the 6-cell cavity.

The RF tests on single-cell cavities showed that there

are no hard multipacting barriers. A soft barrier was seen occasionally at very low field. Multipacting simulations [5, 13] also indicate that there should be no hard barriers in the single-cell cavities. Likewise, no multipacting problems were encountered in the tests on the two 6-cell cavities.

CONCLUSION

RF tests have been done on two single-cell $\beta_g = 0.47$ cavity prototypes and two 6-cell cavities with encouraging results: all of the cavities exceeded the desired accelerating gradient, with a $Q \geq 10^{10}$ at the design gradient of 8 MV/m. The first 6-cell and both single-cell cavities exceeded the design gradient by a factor of 2; the second 6-cell reached 13 MV/m. Two niobium multi-cells and one copper multi-cell have been tuned for field flatness. The next step will be a horizontal test of 2 fully-equipped $\beta_g = 0.47$ cavities in a prototype cryomodule [14].

REFERENCES

[1] C. W. Leemann, in *Proceedings of the XX International Linac Conference*, Report SLAC-R-561, 2000, p. 331–335.

[2] K. W. Shepard *et al.*, in *9th Workshop on RF Superconductivity: Proceedings*, Report LA-13782-C, LANL, Los Alamos, New Mexico, 2000, p. 345–351.

[3] G. Ciovati *et al.*, in *Proceedings of the Eighth European Particle Accelerator Conference*, 2002, p. 2247–2249.

[4] C. C. Compton *et al.*, in *Proceedings of the 2001 Particle Accelerator Conference*, p. 1044–1046.

[5] D. Barni *et al.*, Tech Note JLab-TN-01-014, Jefferson Lab, Newport News, Virginia (2001).

[6] W. B. Haynes *et al.*, in *Proceedings of the Eighth Workshop on RF Superconductivity* Report LNL-INFN (Rep) 133/98, LNL, Legnaro, Italy, 1998, p. 523–533.

[7] Kenji Saito *et al.*, *Ibid.*, p. 534–539.

[8] Carlo Pagani *et al.*, in *Proceedings of the 2001 Particle Accelerator Conference*, p. 3612–3614.

[9] N. Akaoka *et al.*, in *9th Workshop on RF Superconductivity: Proceedings*, Report LA-13782-C, LANL, Los Alamos, New Mexico, 2000, p. 450–458.

[10] T. L. Grimm *et al.*, in *Proceedings of the Eighth European Particle Accelerator Conference*, 2002, p. 2241–2243.

[11] K. Halbach & R. F. Holsinger, *Part. Accel.* **7**, p. 213 (1976).

[12] Terry Grimm *et al.*, in *Proceedings of the Tenth Workshop on RF Superconductivity: Tsukuba, 2001*, KEK, Tsukuba, Japan, 2003, p. 86-90.

[13] W. Hartung, F. Krawczyk, & H. Padamsee, *Ibid.*, p. 627–631.

[14] T. L. Grimm *et al.*, "Cryomodule Design for the Rare Isotope Accelerator," these proceedings.

SIMULATION OF QUENCH DYNAMICS IN SRF CAVITIES UNDER PULSED OPERATION*

Sang-ho Kim, SNS/ORNL, Oak Ridge, TN 37830, USA

Abstract

As has been well verified both theoretically and experimentally in steady state, the thermal stability of SRF (superconducting radio-frequency) cavities strongly depends on the material properties of niobium such as RRR (residual resistivity ratio) and the presence of material defects on the surface. Recently, SRF technology has been chosen for pulsed machines such as the Tesla Test Facility (TTF), the Spallation Neutron Source (SNS), and the European Spallation Source (ESS). In order to guide the selection of operational limits and materials, an understanding of dynamics of quenching in pulsed operation is important. For this purpose, a universal thermal stability analysis algorithm is set up. With the help of 3D FEM codes, a series of transient, non-linear and self-correlated analyses are carried out. This scheme may be used for any stability analysis in SRF cavities with arbitrary conditions such as 3D structure, varying material properties, transient behavior, non-linear material properties, etc.

INTRODUCTION

Thermal breakdown in SRF cavities is one of the major factors that limit the maximum achievable accelerating field and accordingly the operating point. Considerable effort has been made to better understand this topic both theoretically and experimentally. The effects of related parameters on the thermal stability have been systematically quantified [1]-[6].

As the interests for SRF technology in pulsed machines increase, there is need to have more understanding of the dynamics of thermal stability in connection with all the parameters, which include 3D structure, varying material properties, non-linearity of material properties, transient behaviors, realistic thermal loads along with the rf surface dissipations, etc.

In this paper the simulation algorithm of dynamic thermal stability, taking into account general relations among the parameters, and some examples by taking the realistic situation are briefly shown.

PHYSICAL PARAMETERS AND THEIR RELATIONS TO THERMAL STABILITY

The general relations of parameters that determine the thermal stability in SRF cavities are shown in Fig.1. As can be seen, many parameters are correlated and some parameters such as RRR (residual resistivity ratio), Kapitza resistance, etc, should have experimental verification. As an example, the power dissipation per unit area due to the surface rf current is expressed via $P = \frac{1}{2} R_s H^2$,

where, Rs is the surface resistance in Ohm, and H is the magnetic field strength on surface in A/m. The surface resistance is, however, a strong function of temperature as seen in Fig.2 and the temperature is actually the final determining factor of the thermal stability, results from all relations of parameters such as RRR. RRR is one of the most importance material properties for the thermal stability. The thermal conductivity k versus temperature data for various RRR's in Fig.3 are taken from [1], [3], and [4], in which the RRR values from RRR1 through RRR8 are 40, 270, 525, 90, 250, 400, 140, and 840 respectively. The k is known to have an approximate relation with RRR, which is k=RRR/4 at 4.2 K. But it is difficult to apply the same rule to k's of the higher temperature that are actually more important for the thermal stability. The k dependence on RRR should be carefully checked experimentally.
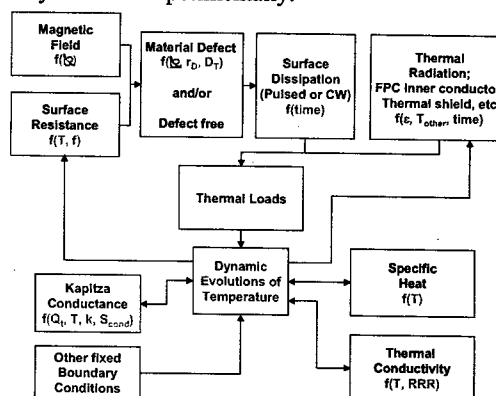
Figure 1: Parameter relations for the thermal stability. (f: function of; $\underline{V}$: location; r_D: defect radius; D_T: defect type; ε: emissivity; T_{other}: temperatures of other structure; RRR: residual resisvity ratio; Q_t: thermal flux; f: frequency; k: thermal conductivity; S_{cond}: surface condition; T: niobium temperature which is also a function of location)
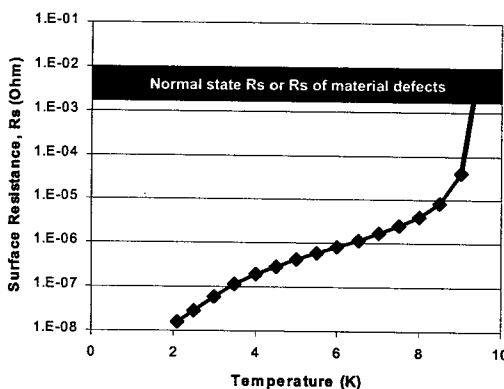
Figure 2: Surface resistance of Nb at 805 MHz. 10 nΩ of residual resistance is assumed.
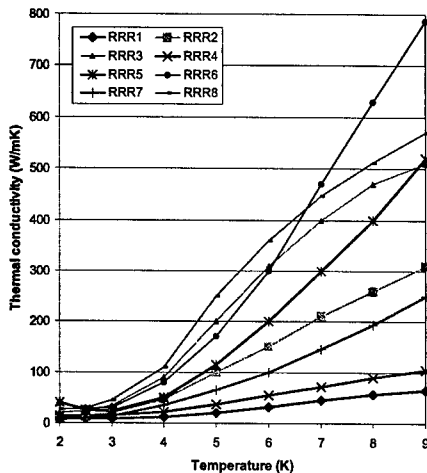
Figure 3: Thermal conductivities for various RRR's

Kapitza resistance is a function of many factors, one of which is the specific surface condition followed by different surface treatments [6]. The simulations shown in the following used the Kapitza resistance as expressed in [7]. The specific heat is a sort of pure thermodynamic property, which is taken from [8].

QUENCH DYNAMICS: EXAMPLES

By taking into account all the relations explained in Fig.1 and with the help of a 3D FEM code (ANSYS) incorporated with script programs correspond to blocks and arrows in Fig.1, a series of algorithms for 3D, transient, non-linear, self-correlated and coupled field problem has been set up. For benchmarking, comparisons have been done with steady state results [1] and show good agreement.

A series of systematic simulations have been carried out in terms of Nb thickness, k, magnetic field strength, etc, which gives proper guidance not only for the material selection and the thermal design, but also for operation regimes. The details of these analyses are planned to be reported in a separate paper.

One example introduced in this paper contains an explanation regarding quenching dynamics. The typical temperature evolutions in the thermally stable system are shown in Fig.4. The test sample used here is 2 mm thick niobium
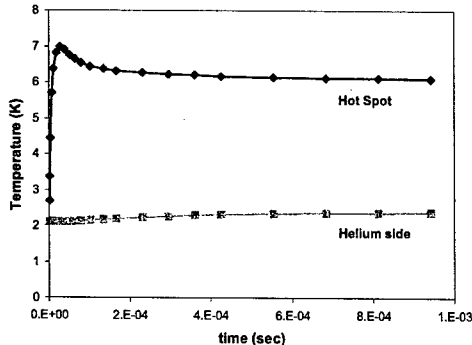
Figure 4: Typical example of the temperature evolution when a SRF cavity system is thermally stable (stabilized).

having RRR2 as in Fig.4 on which a 70 mT field was applied and a material defect corresponding to 0.05 W was introduced. Fig. 5 and 6 show the temperature evolutions and the corresponding snapshots when a system is thermally unstable. In this example, a material defect of 0.1 W is used under the same conditions. Though the time scale of quenching development depends especially on the field and k, quenching develops with the following sequences.

Phase I; Surroundings are still keeping SC state. Hot region is very small. Thermal conduction is weak. The main heat dissipation areas are only the places very near the material defect.

Phase II; Only small adjacent regions near the material defect becomes normal state. Hot spot size is still small, so the thermal conduction (diffusion) is very weak, which results in the steep temperature increment.

Phase III; Surroundings become hotter but still keep SC state except the hot spot at the material defect and small adjacent region. Main quench propagation does not start yet. Thermal conduction is better than region II, that's why there's some decrement in the hot spot temperature. The duration of this meta-stable phase is a function of k, defect size, magnetic field strength, etc. A certain combination of parameters could sustain this phase during a long pulse or CW.

Phase IV; Normal regions are expanding. Growth rate of surface dissipation is much larger than that of thermal diffusion to the bulk Nb and eventually to helium. Quenching propagates.
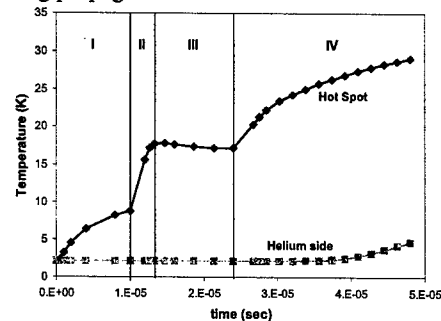
Figure 5: Typical example of the temperature evolution when a SRF cavity system is not thermally stable (thickness; 2mm, 70 mT, RRR2 in Fig. 3, 0.1W material defect).
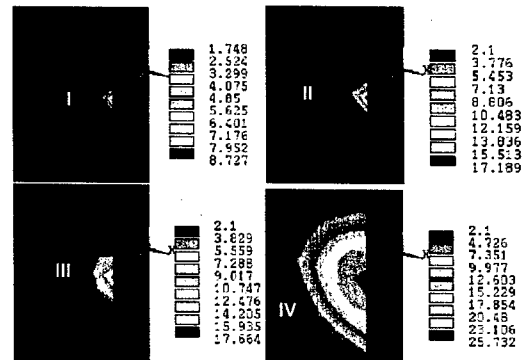
Figure 6: Snapshots of each phase in Fig.5.

The following example is for a cavity end group at the side of coaxial fundamental power coupler where low RRR materials are used and no active cooling exists. The schematics and the surface magnetic field strength along the inner surface of an SNS medium beta cavity are shown in Fig.7. This example contains several special features such as thermal radiation from the inner conductor of the power coupler, varying material properties of niobium, different boundary conditions, full 3D structure, and pulsed operation. Fig.8 is an example where a defect equivalent to 0.1 W is introduced 5 mm from the cell end in order to have clear pictures at the nominal operating condition of SNS. Since the magnetic field strength is small, the quenching propagation is quite slow as can be seen in Fig.8. It is noticeable that the operation for certain duration could be done even after main quenching, but a full recovery is not accomplished during the gap between pulses in this example. The material selections and preparations, surface conditions of niobium and inner conductor, operation conditions such as pulse length, repetition rate, rf power through coupler, etc was found through a series of systematic analyses using this simulation method.
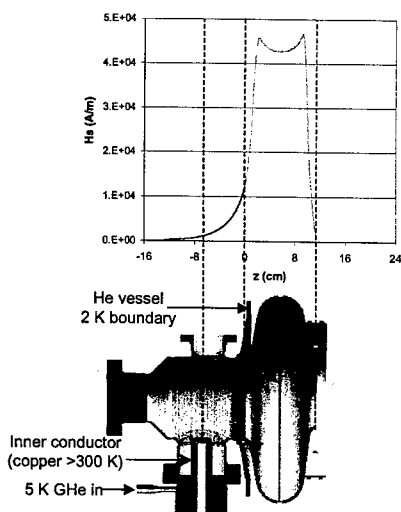
Figure 7: Surface magnetic field along the end group and end cell of the SNS medium beta cavity.

Figure 8: Hot spot temperature evolution through time in 1.5 ms, 60 Hz pulsed operation. A material defect equivalent to 0.1 W is introduced at the distance of 5 mm from the end cell.

SUMMARY

- General algorithms for thermal stability analysis have been set up.
- Benchmarking showed good agreement with the steady state calculation. A series of systematic analysis has been done, which guide the operational limits and material selection. (to be reported in a separate paper)
- Dynamics of the thermal stability are explained.
- Application of the simulation algorithm to the end-group of the SRF cavity is introduced.
- This scheme may be used for any stability analysis in SRF cavities with arbitrary conditions such as 3D structure, varying material properties, transient behavior, non-linear material properties, etc.

ACKNOWLEDGEMENTS

REFERENCES

[1] H. Padamsee et al., *RF Superconductivity for Accelerators*, John Wiley & Sons, New York, New York (1998).

[2] J. Knobloch, *Advanced Thermometry Studies of Superconducting Radio-Frequency Cavities*, Ph.D Thesis, Cornell Univ (1997).

[3] D. Reschke, "Thermal Model Calculations for 1.3 GHz TTF Accelerator Cavities," Proc. of 8th Workshop on RF Superconductivity, pp.385-396, Padova, Italy, Oct. 6-10 (1997).

[4] M. Fouaidy, "Kapitza Conductance and Thermal Conductivity of Materials Used for SRF Cavities Fabrication," Proc. of 9th Workshop on RF Superconductivity, TUP028, Santa Fe, NM, Nov. 1-5 (1999).

[5] J. Lesrel et al., "Study of Thermal Effects in SRF Cavities," Proc. of 8th Workshop on RF Superconductivity, pp.372-384, Padova, Italy, Oct. 6-10 (1997).

[6] J. Amrit et al., "On Intrinsic Thermal Limitations of superconducting Cavities: Kapitza Resistance," Advances in Cryogenic Eng., Vol. 47, pp.499-506 (2002).

[7] K. Mittag, Cryogenics, Vol.13, p.94 (1973)

[8] R. P. Reed et al., *Materials at Low Temperature*, ASME (1983)

THE NUMERICAL ANALYSIS OF HIGHER-ORDER MODES FOR SUPERCONDUCTING RF CAVITY AT SRRC

P. J. Chou[*], SRRC, Hsinchu, Taiwan

Abstract

The beam current in the storage ring at Taiwan Light Source (TLS) is limited by the longitudinal coupled-bunch instabilities [1] and the available rf power. Two Doris cavities are currently used for particle acceleration in the storage ring at TLS. The higher-order modes (HOMs) from Doris cavities are the major source of longitudinal impedance in the storage ring at TLS. In order to increase the electron beam current in the storage ring, a superconducting (SC) rf cavity developed by Cornell University will be installed to replace those two Doris cavities. The property of HOMs of SC rf cavity is obtained from numerical simulations by using a three-dimensional parallel code GdfidL [2]. The preliminary results show that the storage ring at TLS will not suffer from the longitudinal coupled-bunch instabilities for a beam current not exceeding 450 mA.

INTRODUCTION

The TLS is a third-generation synchrotron radiation facility serving broad scientific community in Taiwan. The storage ring at TLS has encountered longitudinal coupled-bunch instabilities since the commissioning in 1994. The maximum beam current is limited to 200 mA in daily operation. The dominant source of longitudinal coupled-bunch instabilities is contributed by the HOMs of two Doris cavities in the storage ring. At present the technique of rf voltage modulation and detuning of cavity HOMs are applied to stabilize the beam in the storage ring [1]. To raise the flux of photon beams, the maximum beam current has to be increased and HOMs to be damped.

The SC rf cavity developed at Cornell University is chosen for the upgrade of storage ring at TLS [3]. The SC rf cavity of CESR-III type has the same operating frequency as the Doris cavities currently in use at TLS. The fabrication of two SC rf cavities is contracted to ACCEL Instruments GmbH in Germany. The cryogenic system is contracted to Air Liquide in France. The high-power tests of SC rf cavities are conducted at Cornell University. One SC rf cavity will be installed to replace those two Doris cavities in the storage ring at TLS in 2003.

A three-dimensional model of SC rf cavity is built based on the mechanical drawings obtained from Cornell University and modifications required for operating the SC rf module at TLS. The design of taper has been modified to fit into the vacuum chamber of storage ring at TLS. The SC rf cavity will be cooled in a liquid helium bath of 4.5°K. The layout of SC rf module used in the

numerical simulations is shown in Fig. 1. The relevant accelerator parameters used in the analysis of longitudinal coupled-bunch instabilities are listed in Table 1. The numerical simulations for SC rf module are performed with a 3D electromagnetic code GdfidL on a Linux PC cluster at TLS.

Table 1: Accelerator parameters used in the analysis of longitudinal coupled-bunch instabilities for TLS storage ring operating with a SC rf cavity of CESR-III type.

Accelerator Parameters	CESR-III type SC rf cavity
beam energy [GeV]	1.5
rf frequency [MHz]	499.666
harmonic number	200
revolution period [ns]	400
rms bunch length [mm]	6.5
momentum compaction factor α_c	0.00678
synchrotron frequency (rf voltage at 1.6 MV) [kHz]	37.8
radiation damping time [ms] longitudinal: horizontal: vertical:	5.668 6.959 9.372
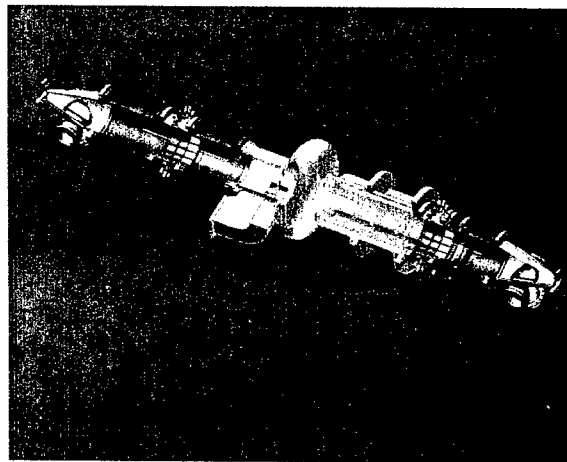
Figure 1: Layout of SC rf module used in the numerical simulations for the HOM studies at TLS. The taper design has been modified in order to fit into the vacuum chamber of storage ring at TLS.

*pjchou@srrc.gov.tw

Because the cross section of beam pipe is smaller than the CESR beam pipe, there are still few resonant modes above 4 GHz in the simulated impedance spectrum of SC rf module at TLS. Those resonant modes have a loaded quality factor on the order of a thousand. For the worst estimate, we assume the storage ring to be evenly filled with 200 bunches. The growth time of longitudinal coupled-bunch instabilities will equal to the radiation damping time at a beam current of 450 mA. Since the storage ring is operated with a gap of 40 bunches in routinely operation, the threshold current of longitudinal coupled-bunch instabilities is expected to be higher than 450 mA.

LONGITUDINAL HIGHER-ORDER MODES

The impedance spectrum of SC rf module is obtained from the Fourier transform of wakepotentials computed in time domain. A Gaussian shaped beam is sent through the SC rf module as the source to excite wakefields in the structure. The maximum relevant frequency f_{max} of excited wakefields is [4]

$$f_{max} = \frac{c}{2\pi\sigma_z} \qquad (1)$$

where c is the speed of light in vacuum, and σ_z is the rms bunch length of Gaussian beam. Since the computed wakepotential is excited by the frequency contents of source beam, the impedance spectrum is less reliable above the maximum relevant frequency f_{max}. The lowest cutoff frequency of longitudinal waveguide modes in the beam pipe of TLS storage ring is 4.712 GHz. The rms bunch length used in time-domain simulations should not be larger than 10 mm for TLS SC rf module.

In the case of shorter bunches and longer structures the mesh size of numerical models should satisfy [4]

$$\Delta_z < \sqrt{\frac{\sigma_z^3}{L_z}} \qquad (3)$$

where L_z is the structure length. The structure length of SC rf module as shown in Fig. 1 is 3.0165 m. In numerical simulations, straight elliptic beam pipes of 10 cm were attached to both ends of tapers. The actual structure length used in numerical simulations for TLS SC rf module is 3.2165 m. The relation of maximum step size vs. rms bunch length used in simulations for reliable wakepotentials is shown in Table 2.

Table 2: The relation of maximum step size vs. rms bunch length used in simulations for reliable wakepotentials of SC rf module at TLS.

rms bunch length (mm)	maximum step size (mm)
7	0.38
10	0.58

Impedance and Instability Growth Time

The results of simulated wakepotentials depend strongly on the property of C48 ferrite. The C48 ferrite is less lossy at higher frequencies [5]. Therefore, the longitudinal HOMs are less damped by C48 ferrite at higher frequencies. For the worst estimate, the longitudinal wakepotential of SC rf module was calculated with the property of C48 ferrite set at 4750 MHz. The corresponding impedance spectrum is shown in Fig. 2. The simulated impedance spectrum was fit with Lorentzian distributions. The fit results give the HOMs of SC rf module as shown in Table 3. Because of the limitation imposed by available computing resources at TLS, results in Fig. 2 and Table 2 are calculated with a mesh size of 2 mm and rms bunch length of 4 cm respectively.

Table 3: The worst estimate of longitudinal HOMs of SC rf module. The growth time of longitudinal coupled-bunch instability is calculated for a completely filled storage ring at a beam current of 400 mA.

frequency [MHz]	loaded shunt impedance R_s [Ω]	loaded Q-factor Q_L	instability growth time [ms]	instability mode number μ
4127.2	875.9	1267	6.37	52
4209.6	678.5	698	8.20	85
4259.6	738.5	1327	7.46	105
4574.4	481.7	1037	11.36	31
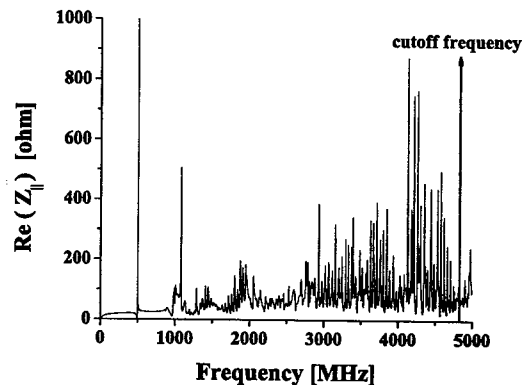
Figure 2: The real part of longitudinal impedance spectrum of SC rf module obtained from numerical simulations for TLS storage ring. The property of C48 ferrite tiles is set at a frequency of 4750 MHz.

Loss Factor and Power Dissipation

The calculated loss factors $K_{||}$ for conducting materials operating at different temperatures are listed in Table 4. The dependence of calculated loss factors on the mesh

1369

size of numerical models is shown in Table 5. From those results shown in Table 4, we find that the calculation of loss factors is less sensitive to the operating temperature of conducting materials used in SC rf module. The loss factor is more sensitive to the property of C48 ferrite used to absorb those HOMs in SC rf module.

Table 4: The calculated loss factors of SC rf module with Niobium and Copper operating at different temperatures. The mesh size and rms bunch length used in simulations are 0.5 mm and 10 mm respectively.

Frequency of C48 ferrite [MHz]	$K_{\|}$ (V/pC) Nb=293K, Cu=293K	$K_{\|}$ (V/pC) Nb=4.5K, Cu=293K	$K_{\|}$ (V/pC) Nb=4.5K, Cu=60K
975	0.993	N.A.	N.A.
1950	0.939	0.939	0.939
4750	0.799	0.799	0.799

Table 5: The calculated loss factors of SC rf module with Niobium and Copper operating at 293°K. The rms bunch length used in simulations is 10 mm. The property of C48 ferrite is chosen at 975 MHz.

mesh size (mm)	$K_{\|}$ (V/pC)
0.5	0.993
1	1.052

The parasitic energy loss ΔE for a beam bunch passing through the SC rf module is

$$\Delta E = q^2 K_{\|} \tag{4}$$

where q is the charge of beam bunch. We calculate the total loss factor of SC rf module by using the property of C48 ferrite at 975 MHz. The total loss factor is 1.854 V/pC for an rms bunch length of 7 mm. Supposed that the storage ring is evenly filled with a beam current of 400 mA for 160 bunches, the energy loss per bunch is 1.854×10^{-6} J. Using a bunching period of 2 ns, we get an estimate for the average power dissipation in the SC rf module as 927 W.

TRANSVERSE HIGHER-ORDER MODES

Preliminary results of vertical impedance obtained from numerical simulations are shown in Fig. 3. The SC rf module does not have reflection symmetry because of the coupling hole for rf input power. The lowest cutoff frequency of vertical waveguide modes for the beam pipe is 2.237 GHz. The vertical wakepotentials are calculated for a beam offset of 15 mm and –15 mm respectively. There is noticeable difference in the vertical impedance spectrum for beam offset of opposite sign. The detailed analysis of vertical HOMs is in progress.
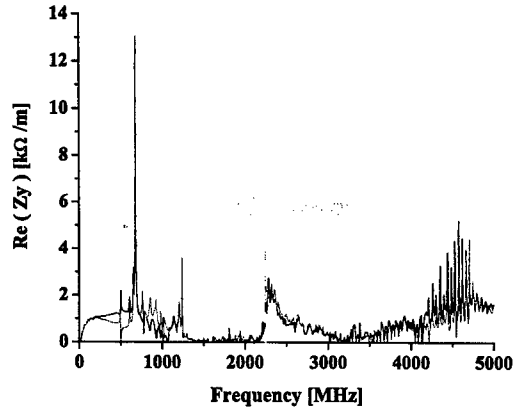
Figure 3: The vertical impedance spectrum calculated with vertical beam offset of 15 mm (black) and –15 mm (red) respectively. The lowest cutoff frequency of the transverse waveguide modes in the vertical direction is 2.237 GHz.

CONCLUSION

The longitudinal HOMs of SC rf module are obtained by fitting the impedance spectrum simulated with GdfidL. From those fit results, we find that the storage ring at TLS will not encounter the longitudinal coupled-bunch instability for a beam current less than 450 mA. If there is other source of resonator impedance not previously known in the storage ring besides the rf cavity, this prediction will need to be modified.

REFERENCES

[1] P.J. Chou and A.W. Chao, IEEE PAC'01, Chicago, June 2001, p. 1978.

[2] W. Bruns and H. Büssing, EPAC'02, Paris, France June 2002, p. 1619.

[3] Ch. Wang, et. al., Proc. 10th Workshop on RF Superconductivity, Tsukuba, Japan, 2001, paper ID TL010.

[4] A.W. Chao and M. Tigner (eds.), Handbook of Accelerator Physics and Engineering (World Scientific, Singapore, 1999), p. 201.

[5] ACCEL GmbH, Germany (private communication).

EFFECTS OF MATERIAL PROPERTIES ON RESONANCE FREQUENCY OF A CESR-III TYPE 500 MHZ SRF CAVITY

M.C. Lin*, Ch. Wang, L.H. Chang, G.H. Luo, NSRRC, Taiwan
M.K. Yeh, National Tsing Hua University, Taiwan

Abstract

A simulation that links the calculation of mechanical structure and of radio frequency electromagnetic field with the finite element code ANSYS® is employed in this study. Both efficiency and accuracy of the calculation are thus improved over those of the conventional computation that builds separate models with different codes for each computed domain because information related can be internally transferred between the different computation domains. The resonance frequency changes associated with mechanical properties of niobium are examined. The computed results indicate that the coefficient of thermal expansion significantly affects the shift in resonance frequency that occurs when the cavity is cooled from room temperature to liquid helium temperature. Young's modulus and Poisson's ratio have minor effects.

INTRODUCTION

As a major upgrade, one CESR-III 500 MHz SRF module will be installed in the electron storage ring at the National Synchrotron Radiation Research Center, Taiwan, to double the stored electron beam and consequently the synchrotron light density, as well as to eliminate the higher order mode (HOM) effects [1]. This SRF cavity is thus examined herein.

The shell-like cavity inside this SRF module is made of 3mm-thick bulk niobium sheets. This cavity is immersed in liquid helium to be maintained in a superconducting state. The saturation temperature of He^4 at 1 atm (101.33 kPa) is 4.22 K. The mechanical properties of niobium at room temperature and at cryogenic temperature have been tested [2,3] to some extent, and found to depend very strongly on purity, manufacture, and the post treatment, like heat treatment. However, the cavity structure shrinks as it is cooled down to cryogenic temperature by liquid helium. Consequently the resonance frequency of the accelerating mode, the TM_{010}-like mode, raises primarily because it is inversely proportional to the radius of the cavity. Besides thermal contraction, the SRF cavity is also loaded by external pressure, since it has an ultra-high vacuum inside while the liquid helium applies external pressure. Hence the resonance frequency shift is a total effect of cooling and pressuring.

A coupled domain simulation can predict the RF characteristics after cooling. The commercially available finite element code ANSYS® has provided the capability to link the high-frequency electromagnetic computation with structure computation. Such a linked simulation is efficient because compatible models of these two domains can be established and integrated using this software. The related calculated data can then be transferred since the meshes of models employed at these two domains are compatible with each other.

The technique is applied herein to predict the RF characteristics of the CESR-III 500 MHz SRF cavity when cooled and externally loaded. This study focuses mainly on the variation of the electromagnetic resonance frequency. For simplicity, the RF input coupler structure is not considered. The effects of material properties on the electromagnetic resonance frequency are examined. At first, the deflection is determined using a shell structure model. The coordinates of all the surface nodes in the electromagnetic model are updated with the displacements of corresponding shell structure nodes. Then the electromagnetic characteristics of the deflected cavity are computed.

NUMERICAL MODELING

In calculating the electromagnetic resonance frequency using ANSYS®, a good mesh has been demonstrated to reduce the numerical error in the calculated resonance frequency of a 500 MHz cylindrical pillbox cavity to within 0.1% of theoretical result [4]. This fact helps the arrangement of the mesh herein. The cavity wall is modeled using shell elements Shell93 for mechanical behavior analysis because it is curved and its thickness is much less than the main dimensions of the cavity. And the brick element HF120 is used in electromagnetic computations because it is appropriate for modeling solids with curved surfaces. The mapped mesh established using the commercial code MSC.PATRAN allows full control of its size and shape.
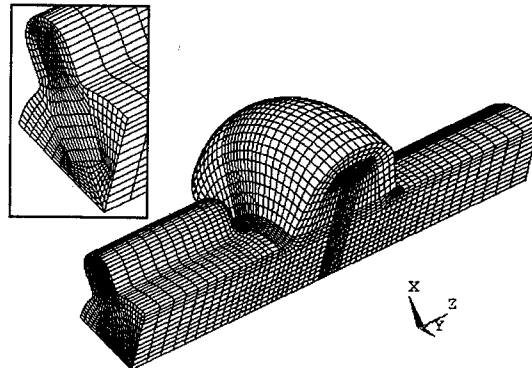
Figure 1: FEM model of the CESR-III 500 MHz SRF cavity.

* chyuan@srrc.gov.tw

Only one quarter of the cavity was modeled because both the structure and the interested electromagnetic fields are symmetric. Figure 1 shows the mesh of the FEM model. This model is comprised of 29474 HF120 elements, 2422 SHELL93 elements, and 126170 nodes. The meshes used in structural and electromagnetic computations are mutually compatible and allow computing information to be transferred between these two computation domains. Both the calculation efficiency and accuracy are thus improved.

In calculating the deflection due to cooling and pressuring, the assigned nodal displacements are the boundary conditions of the fixed end at the round beam tube (RBT) and symmetrical edges at the longitudinal boundaries of the shell model. Additionally, all the nodes at the flute beam tube (FBT) end are constrained to yield the same longitudinal displacement. The applied forces are the pressures on the inner and outer surfaces of the cavity wall and the temperature change.

In calculating the electromagnetic resonance frequency, only the first order transverse magnetic mode, the TM_{010}-like mode, is considered. Thus, the boundary condition of $A_X = 0$ is implied at cavity surfaces and both RBT and FBT ends, where A_X is the covariant components of the electric field

COMPUTED RESULTS

During cooling from room temperature to 4.22 K, the SRF cavity is loaded with a temperature change and a pressure difference, so the material properties of interest herein are the coefficient of thermal expansion, Young's modulus and Poisson's ratio. At room temperature, Young's modulus of niobium is 105 GPa; its Poisson's ratio is 0.38, and the coefficient of thermal expansion is 7×10^{-6} K^{-1}. With all these material constants applied and internal vacuum and external pressure of 1 atm, the computed resonance frequency is 500.559 MHz for a CESR-III type 500 MHz SRF cavity at 300 K.

At cold, only the equivalent state is interested herein. From the available data [2, 3], a coefficient of thermal expansion of 4.94×10^{-6} K^{-1}; Young's modulus of 125 GPa, and Poisson's ratio of 0.38 were selected as the default niobium properties for numerical computation at 4.22 K in this work, where no other values are specified.

Coefficient of Thermal Expansion

The coefficient of thermal expansion is an important property when the temperature change is not negligible. This coefficient declines as the temperature falls for most materials. The equivalent coefficient of thermal expansion is determined as the total thermal contraction ratio over the entire range of temperature change considered. This definition simplifies the numerical computation to avoid incremental computation. The equivalent coefficient is expected to strongly affect both the deflection and the resonant frequency of the SRF cavity.
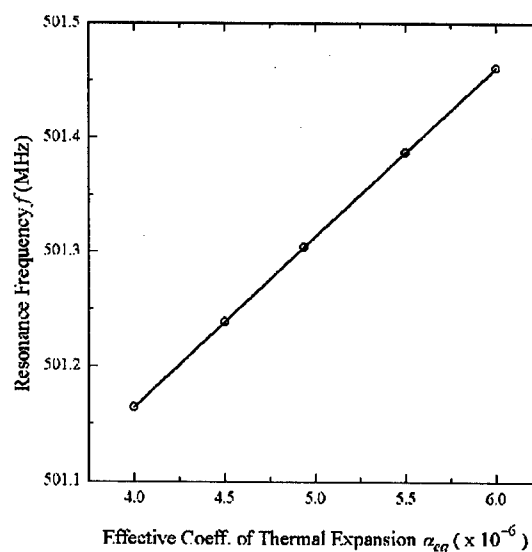
Figure 2: Variation of computed resonance frequency of a CESR-III 500 MHz SRF cavity with various equivalent coefficients of thermal expansion at 4.22 K.

With an internal vacuum and an external pressure 101.33 kPa, Fig. 2 shows that the resonance frequency of the CESR-III 500-MHz SRF cavity increases linearly from 501.164 MHz to 501.461 MHz as the equivalent coefficient of thermal expansion increases from 4.0×10^{-6} K^{-1} to 6.0×10^{-6} K^{-1}. A cavity with a higher coefficient of thermal expansion shrinks more when cooled down, and thus has a higher resonance frequency. The variation of computed resonance frequency is approximately +/-150 kHz given a +/-20% variation in the equivalent coefficient of thermal expansion of around 5.0×10^{-6} K^{-1}. Accordingly precise data on the thermal contraction of cavity material at cryogenic temperatures can improve the prediction of the cavity's resonant frequency at a cryogenic temperature.

Young's Modulus

Briefly, a higher Young's modulus implies greater structural stiffness and, thus, a smaller deflection of a structure under external loading. According to the experiment of Rao and Kneisel [1], Young's modulus of a high-purity niobium sheet is about 125 GPa at 4.2 K. They also stated that the measured Young's modulus of each niobium sheet from different suppliers or undergone different heat treatments varies widely.

Figure 3 plots the variations in the resonance frequency of the CESR-III 500 MHz SRF cavities with various Young's modului given an internal vacuum and an external pressure of 101.33 kPa. The cavity's resonance frequency is shown to increase with the Young's modulus at both 300 K and 4.22 K. This indicates a higher Young's modulus implies greater structural stiffness and thus a smaller deflection and frequency shift. However,
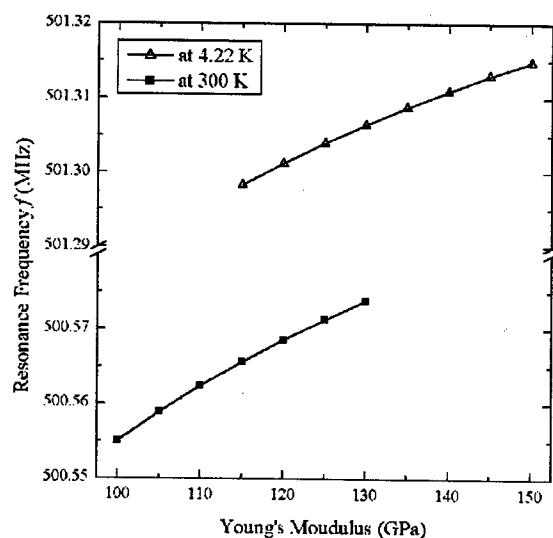
Figure 3: Variation of computed resonance frequency of a CESR-III 500 MHz SRF cavity with various Young's modulus.

over the computed range of Young's modulus, the frequency variation is below 20 kHz at both 300 K and 4.22 K

Poisson's Ratio

Poisson's ratio is defined as the negative of the ratio of lateral strain to the stretched longitudinal strain. According to the theory of elastic mechanics, Poisson's ratio is between 0 and 0.5. Figure 4 shows the variation of the computed resonance frequency of the CESR-III 500 MHz SRF cavity at 4.22 K, under loading conditions of an internal vacuum and an external pressure of 101.33 kPa, as Poisson's ratio changes from 0.1 to 0.5. Although the resonance frequency decreases as Poisson's ratio increases, the total frequency shift is below 4 kHz in the computed range of Poisson's ratio, as shown in Fig. 4. Thus Poisson's ratio is a minor factor in determining the resonance frequency.

CONCLUSIONS

A structure-RF coupled computation process with single code is herein used to predict the characteristics of the CESR-III 500 MHz SRF cavity cooled down to liquid helium temperature. The mechanical properties of niobium are examined to find their effects on the resonance frequency of TM_{010}-like mode. According to the computed result, the electromagnetic resonance frequency increases when the SRF cavity is immersed in a liquid helium bath, due to thermal contraction of the cavity. The coefficient of thermal expansion strongly
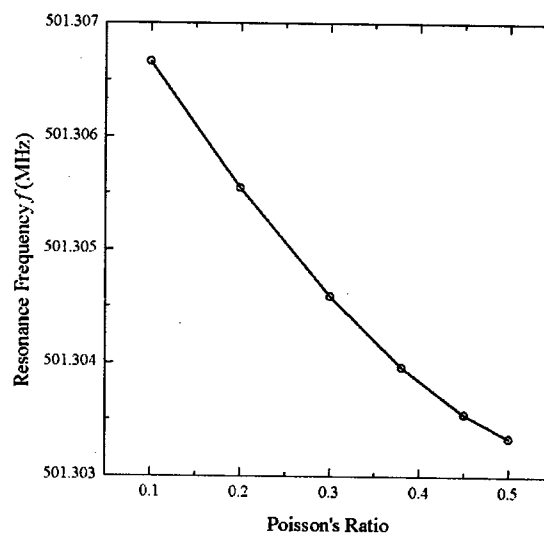
Figure 4: Variation of computed resonance frequency of a CESR-III 500 MHz SRF cavity with various Poisson's ratio at 4.22 K.

affects the shift in resonance frequency when the cavity is cooled from room temperature to liquid helium temperature, whereas Young's modulus and Poisson's ratio have minor effects.

ACKNOWLEDGEMENT

REFERENCES

[1] Ch. Wang, et al., "Superconducting RF Project at the Synchrotron Radiation Research Center," Proceedings of the 10th Workshop on RF Superconductivity, Tsukuba, Japan, 2001, paper ID TL010.

[2] M. G. Rao and P. Kneisel, "Mechanical Properties of High RRR Niobium," Advances in Cryogenic Engineering, 1994, Vol. 40, pp. 1383-1390.

[3] K. Ishio, et al., "Fracture Toughness and Mechanical Properties of Pure Niobium and Welded Joints for Superconducting Cavities at 4K," Proceedings of the 9th Workshop on RF Superconductivity, Santa Fe, New Mexico, USA, 1999, paper ID TUP042.

[4] M. C. Lin, et al., "A Coupled-Field Analysis on RF Cavity," Proceedings of the 2001 Particle Accelerator Conference, 2001, pp. 1207-1209.

PRELIMINARY STUDIES OF ELECTRIC AND MAGNETIC FIELD EFFECTS IN SUPERCONDUCTING NIOBIUM CAVITIES*

G. Ciovati[†], P. Kneisel, G. Myneni, J. Sekutowicz, TJNAF, Newport News, VA 23606, USA
A. Brinkmann, W. Singer, DESY, 22603 Hamburg, Germany
J. Halbritter, FZK IMF I, 76021 Karlsruhe, Germany

Abstract

Superconducting cavities made from high purity niobium with RRR > 200 often show pronounced features in the Q vs. E_{acc} dependence such as a peak at low gradients, a B^2-slope at intermediate fields and a steep degradation of Q-values ("Q-drop") at gradients above $E_{acc} \sim 20$ MV/m without field emission loading.

Whereas the B^2-slope is in line with 'global' heating [2] there are still different models to explain the observed "Q-drop". The model of ref. [1] is based on magnetic field enhancements at grain boundaries in the equator weld region of the cavity and local heating. These grain boundaries become normal conducting, when their critical magnetic field is reached and contribute gradually to the losses in the cavity as long as they are thermally stable.

The model proposed in ref. [2] is based on effects taking place in the metal-oxide interface on the niobium surface. The major contribution to the RF absorption is coming from interface tunnel exchange between electronic states of superconducting Nb with their energy gap and localized states of the dielectric Nb_2O_5.

An experimental program was started at JLab to settle the mechanisms behind B^2-slope and the Q-drop. A modified CEBAF single cell cavity is excited in either TM_{010} or TE_{011} modes and the Q vs. E_{acc} dependences are measured as a function of various surface treatments such as BCP, electropolishing, high temperature heat treatment and "in-situ" baking. In addition, a special two-cell cavity was designed, which allows the excitation of the 0 – and π – modes of the TM_{010} passband, which "scan" different areas of the cavity surface with high electric and magnetic fields, respectively. This contribution reports about the design and first measurements with both types of cavities.

ELECTROMAGNETIC DESIGN

Other than the mode TM_{010}, used to accelerate a charged particles beam, the resonant mode TE_{011} in a cylindrical structure has the property of having a purely azimuthal electric field configuration, providing a way of measuring only the effect of the magnetic field on the surface resistance. A CEBAF single cell cavity with side-port coupling can be excited in both TM_{010} and TE_{011} modes by using a properly shaped inductive loop. The basic properties of these modes have been computed with SUPERFISH and are summarized in Table 1. Figure 1 shows the field distributions along the cavity surface. It can be seen that the magnetic field in the TE_{011} mode is

localized in a region next to the cavity's iris. The shape of the loops used as an input coupler and a field probe for both modes have been optimised through few iterations.

Table 1: Electromagnetic parameters of the TM_{010} and TE_{011} modes for a CEBAF single cell.

	TM_{010}	TE_{011}
Frequency [MHz]	1472.599	2830.723
$E_{peak}/\bullet U$ [(MV/m)/$\bullet$J]	24.1	0
$B_{peak}/\bullet U$ [mT/$\bullet$J]	60.7	70.4
G $(=R_sQ_0)$ [Ω]	271	701
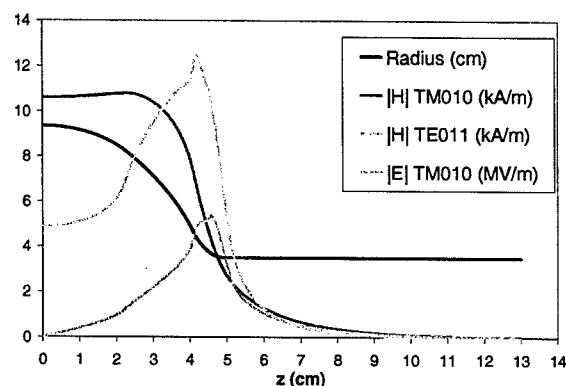
Figure 1: Surface fields for the two modes for 50mJ stored energy and cavity profile.

In addition to the CEBAF single cell, a two cells cavity was designed so that one mode would have a high ratio of peak magnetic to peak electric field and one that would have both high peak electric and magnetic fields. It was decided to have these two modes as close in frequency as possible, to reduce the effect of the frequency dependence of surface resistance.

The cavity was designed with the FEM code described in ref. [3] and the field configurations of choice are the TM_{010}-0 and -π modes. Their features are a large beam pipe that allows a large cell-to-cell coupling and steep curvatures at the equators and middle iris, confining the peak fields in these regions.

The electromagnetic parameters of the modes are indicated in table 2, while figures 2 and 3 shows the field distributions on the cavity surface.

Table 2: Electromagnetic parameters of the TM_{010}-0 and TM_{010}-π for the 2-cells cavity.

	TM_{010}-0	TM_{010}-π
Frequency [MHz]	1381.848	1494.574
$E_{peak}/\bullet U$ [(MV/m)/$\bullet$J]	2.92	11.26
$B_{peak}/\bullet U$ [mT/$\bullet$J]	23.0	24.5
$G (=R_s Q_0)$ [Ω]	406	426
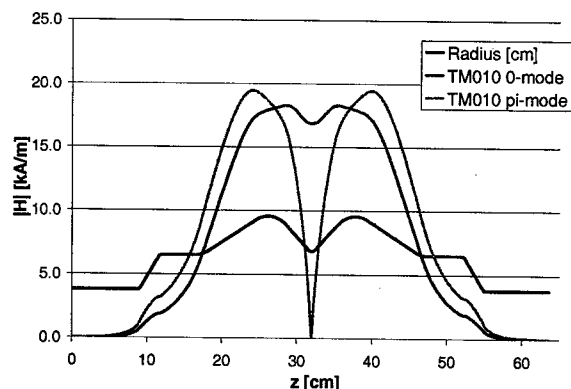
Figure 2: Surface magnetic fields in the TM_{010}-0 and π modes for 1J stored energy.
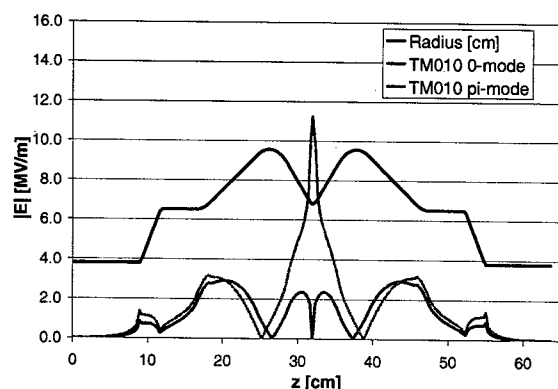
Figure 3: Surface electric fields in the TM_{010}-0 and π modes for 1J stored energy.

It can be seen that the combination of the TM_{010} modes offers the possibility of having high electric and magnetic fields mainly in the area where the electron beam welds are located.

Calculations with the FEM code MULTIPAC showed that the conditions for multipacting are not met for this cavity shape.

Both cavities were fabricated with RRR>250 niobium, using the standard procedure of deep-drawing half-cells followed by electron beam welding. The CEBAF single cell cavity has niobium flanges with indium seal, while the 2-cells cavity has Nb55Ti flanges with AlMg3 gaskets. The preparation for the vertical tests consists of buffered chemical polishing (BCP) with a mixture of HF, HNO_3, H_2PO_4 in a 1:1:1 ratio, removing a total amount of about 150μm from the internal surface. After drying, the cavities

are assembled in a class 100 clean room and attached to the vertical stand where they are evacuated to about 10^{-8} mbar prior to cooldown.
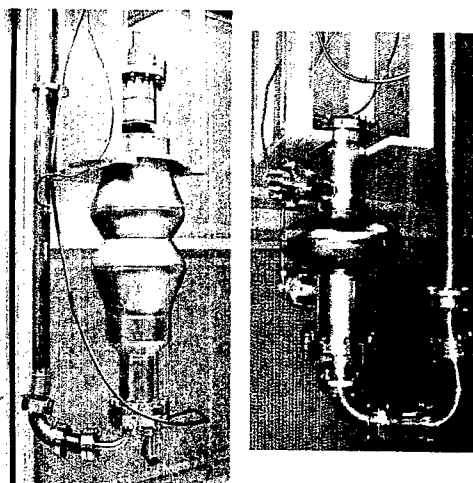
Figure 4: 2-cells cavity (left) and CEBAF single cell (right) on the vertical test stand.

The measurement of the CEBAF single cell cavity in the vertical test (Fig. 5) showed a Q-drop in the TM_{010} mode starting at a peak magnetic field of about 110mT without field emission, but in the TE_{011} mode the cavity quenched at that field level. The surface resistance between 4.2K and 2K was measured and then fitted to the BCS theory to obtain values of residual resistance, mean free path and energy gap.
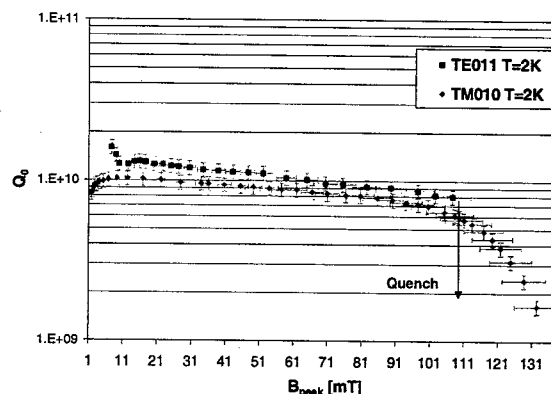
Figure 5: Q vs. B_{peak} in the TM_{010} and TE_{011} modes at 2K.

Subsequently the cavity was "in situ" baked for 20hr at 100C and tested again. The results are shown in figure 6. In the TM mode a strong Q-slope starting at a peak magnetic field of about 38mT was observed, while the test in the TE mode showed the same Q vs. field behavior as before baking, with a quench at 97mT. After baking, the residual resistance increased in both modes, together with a decrease in mean free path, whereas the BCS part of the surface resistance had changed to a lower value as typically observed.
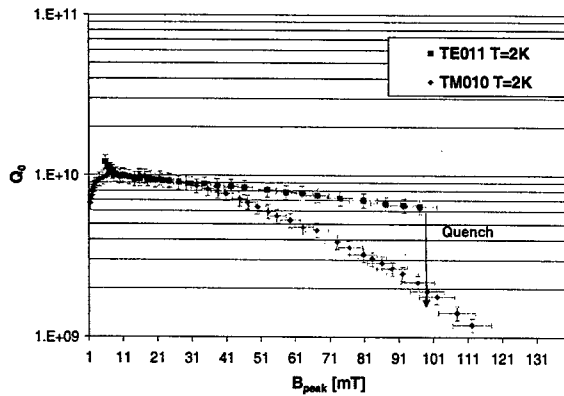
Figure 6: Q vs. B_{peak} at 2K after 100C, 20hr baking.

Figure 8: Q vs. B_{peak} at 2K after 80C, 20hr baking.

The results of the vertical test of the 2-cell cavity are shown in figure 7. Both -0 and -π mode show the same field dependence with Q-drop without field emission starting at a peak surface magnetic field of about 75mT. The maximum field of 100mT corresponds to a peak surface electric field of about 45MV/m in the -π mode, but it's only 13MV/m in the -0 mode. The residual resistance is extremely low in both modes. In a previous test, multipacting was seen at $B_{peak} = 10$mT in both modes and processed after about 30min of applying RF power to the cavity.

Figure 7: Q vs. B_{peak} in the TM_{010} modes at 2K.

The cavity was baked under vacuum at 80C for 24hr by a stream of heated nitrogen gas to avoid oxidation of the cavity outer surface. It was then tested again at 2K (figure 8) showing an increased residual resistance, reduced mean free path and a strong Q-slope beginning at very low fields. The field behavior of the two modes is again very similar. These results remain after warming up to room temperature and cooling down again to 2K. The same results were obtained in a previous test when the cavity was baked at 100C for 24hr.

DISCUSSION

We believe that the quench in the TE_{011} mode is related to a surface defect and does not appear in the TM_{010} because of the different field location of the magnetic field. We plan to improve the quench behavior of the cavity by both "guided repair" and post purification of the niobium material. The Q vs. B_{peak} curves after baking were unexpected. In the single cell cavity the TE_{011} mode still presents a "normal" heating effect ($R_S(B_{peak}) \propto B_{peak}^2$) but the TM_{010} shows an exponential increase of surface resistance with B_{peak} above about 30mT. This was seen in both modes of the 2-cell cavity. The results on the TE/TM modes seem to be consistent with the model in ref. [2], however some ambiguity remains since the H-field limit in the TE_{011} mode happened close to the field level where the Q-drop happened in the TM_{010} mode. The results from the 2-cell cavity seem to indicate a magnetic field effect. The areas where the welds are located are high magnetic field regions and their large grain structure might play an important role. To better investigate this possibility, three seamless hydroformed NbCu 2-cell cavities have been made at DESY. Further tests on the single cell and 2-cell cavity will include high temperature heat treatment and electropolishing.

ACKNOWLEDGEMENT

We would like to thank C. Roncolato for initial calculation of the TE_{011} mode properties in the single cell cavity.

REFERENCES

[1] J. Knobloch et al., "High Field Q Slope in Superconducting Cavities due to Magnetic Field Enhancement at Grain Boundaries", 9[h] RF Superconductivity Workshop, Santa Fe, USA, 1999.

[2] J. Halbritter et al, "Electric Surface Resistance $R_E(T,f,E)$ of Nb/Nb$_2$O$_{5-y}$-interfaces and Q-drop of Superconducting Nb Cavities", IEEE Trans. Appl. Supercond., 11, 1864 (2001).

[3] J. Sekutowicz, "2D FEM Code with Third Order Approximation for RF Cavity Computation", LINAC 1994, Tsukuba, Japan, 1994.

IMPROVED PROTOTYPE CRYOMODULE FOR THE CEBAF 12 GEV UPGRADE[*]

E. F. Daly[#], I. E. Campisi, J. Henry, W. R. Hicks, J. Hogan, P. Kneisel, D. Machie, C. E. Reece, T. Rothgeb, J. Sekutowicz, K. Smith, T. Whitlatch, K. M. Wilson, M. Wiseman, Thomas Jefferson National Accelerator Facility, Newport News, VA 23606

Abstract

In order to provide a higher performance building block cryomodule for the CEBAF 12 GeV upgrade, modifications have been made to the design of the Upgrade Cryomodule. The prototype cryomodule will be completed in 2004 and be installed for operation in CEBAF. Design changes enable the use of higher gradient cavities to achieve greater than 100 MV per cryomodule while not exceeding the budgeted cryogenic load of 300 W during steady-state operation. They also include refinements based on experience gained during the construction of the first generation upgraded cryomodules as well as the prototype cryomodule for the Spallation Neutron Source. Two cavity designs will be used in the prototype, one optimized for E_{peak}/E_{acc} ratio, and the other optimized for minimum cryogenic load. The input waveguides, thermal shield and piping have been redesigned to accommodate the higher expected heat loads. The vacuum connections consist of niobium-titanium flanges, aluminum-magnesium seals and stainless steel clamps to provide reliable UHV sealing. The cavity tuner features one cold motor and two piezoelectric actuators to provide coarse and fine tuning respectively.

INTRODUCTION

A series of three cryomodules (CMs) is being constructed as part of JLab's efforts to increase the machine availability and reliability, provide additional acceleration for the Free Electron Laser (FEL) and produce prototypical CMs for the 12 GeV Upgrade of CEBAF. The first two CMs constructed are based on the initial "Upgrade CM" design [1,2]. The first of these has been completed, installed and commissioned in the SL-21 zone of the south linac of CEBAF, and the second, "FEL03," is planned for installation into the JLab FEL in late 2003. Both modules contain 7-cell cavities based on the original CEBAF cavity cell shape and are expected to exceed 70 MV of acceleration. The third module, dubbed "Renascence," incorporates several design changes in order to provide more than the 108 MV capability required by present plans for the 12 GeV upgrade of CEBAF [3]. It is planned for installation into CEBAF in late 2004, serving both as a reliability improvement for continuing 6 GeV operation, as well as a prototype for the 12 GeV upgrade.

To obtain the required level of HOM damping while revising the cavity cell shape to improve performance, it is necessary to move the coaxial HOM couplers closer to the cells. This displaced the tuner mount, requiring a new tuner design. Also, the input waveguide thermal engineering had to be revisited to avoid conducting too much heat to 2 K via the cavity input coupler flange. Anticipating continued progress in controlling field emission in niobium cavities, a development effort was started to design a heat-load optimized structure for CEBAF, referred to as the Low Loss (LL) cavity. This is being performed in parallel with the previously designed High Gradient (HG) cavity that minimizes the E_{peak}/E_{acc} ratio to reduce the risk of field emission performance limitations. The prototype CM *Renascence* will comprise a mixture of the LL and HG structures. Each cavity has four TTF-style HOM couplers. Specific details of the cavity designs can be found elsewhere [4].

Experience with construction of the first Upgrade CM also indicated a need to improve the flange seal designs, particularly those on the beam line. New solutions are included in plans for *Renascence*.

CRYOMODULE REQUIREMENTS

The performance requirements for the improved prototype are identical in many ways to the initial prototypes in areas such as cavity tuning, alignment and overall dimensions. Only a few key requirements have been changed. A comparison between the first upgrade prototype and the improved prototype CM is given in Table 1. To attain 108 MV, each cavity must achieve a gradient of 19.2 MV/m. The concomitant requirements of high quality factor (Q) and high accelerating gradient are very challenging. In addition, cw operations and the narrow bandwidth of 75 Hz place high demands on the mechanical tuner design.

Table 1: Cryomodule Comparison

Parameter	70 MV CM [1,2]	12 GeV CM
Average cavity gradient (MV/m)	12.5	19.2
Q_{cavity}	6 E+09	8 E+09
$Q_{external}$	2 E+07	2 E+07
Klystron power, cw (kW)	8	13
2K RF heat load (W)	140	240
50K RF heat load (W)	120	104

The estimated and budgeted heat loads are listed in Table 2. These heat loads are significantly higher than what was planned for with the initial prototypes. Changes in the header piping are required to accommodate the higher heat loads.

Table 2: Estimated & Budgeted Heat Loads

	2K Heat Load (W)	50 K Heat Load (W)
Static	< 25	180 - Shield 56 - Coupler
Dynamic (8 cavities)	240	108
Total	275	340
Budget	300	400

DESIGN IMPROVEMENTS

The initial design effort for the upgrade CM was significant and resulted in an integrated solution that considered these key areas: the cavity structure, beam line interfaces, RF power coupling, cavity tuning, and cavity suspension and alignment. Based on experience with the first prototype as well as added experience with the SNS CM design, most of these key areas were studied again in an effort to improve upon the existing design where possible. In addition, the thermal shield and header piping was re-designed to improve clearances for thermal performance, reduce the manufacturing cost and simplify the assembly sequence. In all cases, design improvements that minimally impacted the CM cost were carefully considered. Each of the improvements is discussed in detail.

Cavity Flanges

In order to package 108 MV of acceleration into 5.6 meters of active length within the existing CEBAF slot length, there are no beam line bellows in the cavity string assembly. There is very little axial beam line space available for installing and tightening fasteners. The cavity beam line flanges are sealed with crushable aluminum-magnesium seals like those developed for the TESLA cavities and adopted for the SNS cavities.
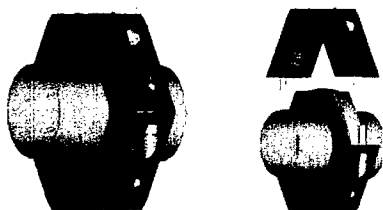
Figure 1: Radial Wedge Flange Clamp – Assembled (left) and Partially Disassembled (right)

To provide the high sealing forces required in limited axial space, a new flange clamping mechanism is used for the cavity beam line flanges. The design (Fig. 1) is called a radial wedge flange clamp [5] and is based on using multiple flat wedges within a set of self-centering clamps to transmit high clamping forces needed for metal-to-metal seals. The clamp and seal assembly has been successfully leak tested while at 2K in separate tests with a Conflat® copper gasket as well as an aluminum-magnesium metal gasket.

Sealing the rectangular waveguide flange with anything other than indium has proven difficult. Efforts to develop an alternative using an aluminum-magnesium seal or other materials are proceeding. If no alternative is found, these flanges will be sealed with an indium gasket.

13 kW Fundamental Power Coupler Waveguide

The original upgrade waveguide design was capable of transmitting 6 kW of RF power to the cavity [6]. The waveguide for *Renascence* is capable of transmitting up to 13 kW of RF power to the cavity [7]. For the prototype, an additional heat station (Fig. 2, shown in red) from the waveguide to the thermal shield is required to transmit the required power while managing the thermal load to the primary helium circuit. The heat load conducted to the cavity end group is large, nearly 4 W (Fig. 2). An additional 60K heat station (Fig. 2, blue curve) was chosen for this prototype for cost reasons. The waveguide design for the production CMs will have an intermediate 300 K heat station (Fig. 2, red curve) since it is a more efficient design solution. The FPC end group on the cavity is fabricated from niobium with RRR > 250 in order to avoid overheating during RF operations.
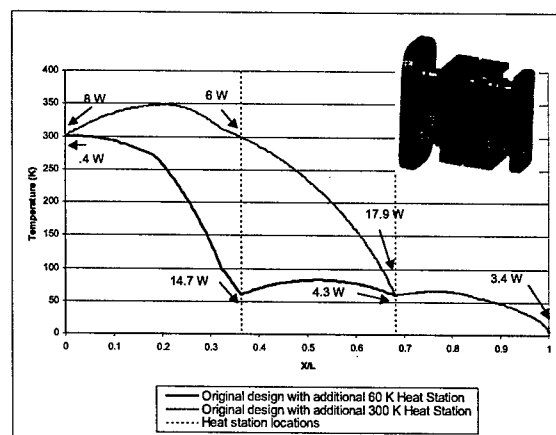
Figure 2: 13 kW Waveguide Thermal Profile

The plating thickness for the waveguides has been increased. The upgrade specification had been 1.6 μm nominal thickness with a range of -20% to +30%. The range was based on achievable limits quoted by the vendor. The specification was changed to 4.5 ± 1.5 μm to avoid inadequate copper plating coverage.

Thermal Shield

The thermal shield intercepts the radiative heat loads and conductive heat loads from both heat stations on the FPC waveguide. More thermal straps have been included on the thermal shield to transport the additional heat deposited in the FPC waveguide during high power operations. There are six straps on the inner heat station and ten straps on the outer heat station

In order to simplify the piping design, only a single pass from the supply to the return is included. The thermal straps are attached to the shield near the cooling line. A helium mass flow of 8 gram/sec is required to remove the budgeted heat load of 400 W with a temperature rise from 35 to 45 K.

Helium Vessel and Headers

The titanium helium vessel consists of two heads, two bellows and a cylindrical shell. The heads are welded to a niobium-titanium transition ring, which is part of the cavity end group. The bellows are located near the helium vessel head opposite the FPC and enable cavity tuning. The helium vessel heads are added to the cavity after any high temperature baking in order to avoid embrittlement of the titanium.

The dynamic heat load per cavity is estimated at 30 W. In superfluid helium the maximum critical heat flux is conservatively 1 W/cm^2 [8], requiring a 30 cm^2 cross-section to support the heat flow into the return header. The vertical piping connections between the helium vessel and the return header have been increased from 1-½" IPS to 2" IPS to avoid exceeding the critical heat flux.

Cold Tuner

The tuner system consists of a coarse mechanical tuner and a fine piezoelectric tuner and satisfies the same design requirements as the first prototype tuner (Table 3). This tuner mechanism differs significantly from the first prototype because all of the components are cold, including the motor, harmonic drive and piezoelectric actuators. This design approach, adopted from the TESLA design and applied to the SNS design, relies on the component evaluation tests that were conducted to prove out the SNS tuner system. The range and resolution goals are derived from these tests.

Table 3: Tuner Requirements and Design Goals

Parameter	Requirement	Design Goal
Coarse Range (kHz)	> 400	> 600
Coarse Resolution (Hz)	< 100	< 3
Coarse Backlash (Hz)	< 25	< 10
Fine Range (Hz)	1000	> 2000
Fine Resolution (Hz)	< 1	< 1

Alignment

The overall alignment requirements are identical to not only the first prototype but also the original CEBAF CMs; the cavities are aligned to the ideal beam line reference within 2 mrad RMS. A pair of fiducial rings, which are machined into the end plates prior to cavity assembly, defines the cavity mechanical centerline. The eight-cavity string is positioned relative to the nominal beam centerline via Nitronic stainless steel rods within the spaceframe. The cavity flanges have compliance that, when combined with the relatively flexible FPC end group, enables lateral adjustment of the cavity ends without the need of inter-cavity bellows [9]. The alignment scheme uses the same techniques employed to acceptably align the cavity string for the first prototype CMs.

SUMMARY

The design of the improved prototype CM is underway. The design effort is proceeding more rapidly than for the first prototypes because the majority of the interfaces between components have been defined.

Prototype cavities have been constructed. The new tuner design is complete and in fabrication. Detailed designs for other components such as the thermal shield and helium vessel are in progress.

Cavity, helium vessel and tuner testing is planned for this coming summer. The cavity string assembly is planned for the end of 2003. The completed CM, with a mixture of high gradient and low loss cavities, is scheduled for mid-spring 2004 with testing completed by fall 2004.

ACKNOWLEDGEMENTS

REFERENCES

[1] J. R. Delayen et al., "Upgrade of the CEBAF Acceleration System," Proc. PAC99, p. 3498.

[2] J. P. Preble et al., "Cryomodule Development for the CEBAF Upgrade," Proc. PAC99, p. 934.

[3] L. Harwood and C. Reece, "CEBAF at 12 and 25 GeV," Proc. 2001 SRF Workshop, http://conference.kek.jp/SRF2001/pdf/TA008.pdf.

[4] J. Sekutowicz et al., "Cavities for Jlab's 12 GeV Upgrade," published in these proceedings.

[5] U.S. Patent No. 6,499,774, See for example: www.jlab.org/~ksmith

[6] T. Hiatt et al., "Cryogenic Testing of the Input Waveguide Coupler for the CEBAF Upgrade Cryomodule," Proc. PAC2001, p. 1155.

[7] R. Hicks and E. Daly, "13 kW Waveguide Design," JLab Tech. Note TN-02-040.

[8] S. W. Van Sciver, Helium Cryogenics, Plenum Press, New York, 1986, pp 146-147.

[9] K. M. Wilson et al., "Mechanical Cavity Design for 100MV Upgrade Cryomodule," published in these proceedings.

LORENTZ DETUNING OF SUPERCONDUCTING CAVITIES WITH UNBALANCED FIELD PROFILES *

J. R. Delayen[#], Thomas Jefferson National Accelerator Facility, Newport News, VA 23606, USA

Abstract

Tests on the prototype SNS medium beta cryomodule showed a strong correlation between the flatness of the field profile and the Lorentz detuning coefficient (both static and dynamic). We present an analytical model for the enhancement of the Lorentz detuning as a function of the flatness of the field profile resulting from a spread of the frequencies of the individual cells of the cavity.

INTRODUCTION

Lorentz detuning of superconducting cavities is the change of frequency associated with the deformation of the geometry induced by the radiation pressure of the electromagnetic field. In all practical applications, this detuning is proportional to the square of the amplitude of the electromagnetic field. Measurements on the SNS prototype cryomodule have shown large variations of the Lorentz coefficient –by more than a factor of 2– between supposedly identical cavities [1,2]. There seemed to be, however, a correlation between the flatness of the field profile and the Lorentz coefficient. In this paper we calculate analytically and numerically the change of the Lorentz detuning coefficient associated with the flatness of the field profile.

TWO-CELL CAVITY MODEL

We represent a 2-cell cavity as two coupled harmonic oscillators of frequencies ω_1 and ω_2 with a coupling strength $k\omega_0^2$. This coupled system is represented by

$$\begin{cases} \ddot{x}_1 + \omega_1^2 x_1 = k\omega_0^2 x_2 \\ \ddot{x}_2 + \omega_2^2 x_2 = k\omega_0^2 x_1 \end{cases}.$$

The two eigenvalues (frequencies of the resonating modes) and eigenvectors (amplitudes of the fields in the cells) are

$$\omega_{a,b}^2 = \frac{\omega_1^2 + \omega_2^2 \pm \left[\left(\omega_1^2 - \omega_2^2\right)^2 + 4\omega_0^4 k^2\right]^{1/2}}{2}, \quad (1)$$

$$\frac{x_1}{x_2} = \frac{2k\omega_0^2}{\omega_1^2 - \omega_2^2 \mp \left[\left(\omega_1^2 - \omega_2^2\right)^2 + 4\omega_0^4 k^2\right]^{1/2}}. \quad (2)$$

Cavities are usually operated in the π-mode where the amplitudes have opposite signs in the two cells. This implies choosing the upper sign in the above equations. If we assume that the frequencies of the two cells have

different values such that $\omega_1^2 = \omega_0^2(1+\alpha)$ and $\omega_2^2 = \omega_0^2(1-\alpha)$, then the frequency of the "π-mode" is $\omega_\pi^2 = \omega_0^2\left[1+\left(\alpha^2+k^2\right)^{1/2}\right]$ and the ratio of the amplitudes in the two cells is $\dfrac{x_1}{x_2} = \dfrac{k}{\alpha-\left(\alpha^2+k^2\right)^{1/2}}$.

Often, the operating gradient of an accelerating cavity is defined not in terms of the actual voltage provided, which is not directly measurable in the absence of a beam, but through the intermediary of the energy content. The relationship between energy content and gradient is obtained and defined for a well-balanced structure. Thus, a comparison of the Lorentz detuning between a balanced and unbalanced structure will be made first at constant energy content *i.e.* we will assume that $x_1^2 + x_2^2 = 2$. With this assumption, the amplitudes in the two cells of an unbalanced structure are

$$x_1 = \frac{k}{\left(\alpha^2+k^2\right)^{1/4}\left[\left(\alpha^2+k^2\right)^{1/2} - \alpha\right]^{1/2}},$$

$$x_2 = \frac{\alpha-\left(\alpha^2+k^2\right)^{1/2}}{\left(\alpha^2+k^2\right)^{1/4}\left[\left(\alpha^2+k^2\right)^{1/2} - \alpha\right]^{1/2}}. \quad (3)$$

We now introduce Lorentz detuning by assuming that the frequencies of the two cells change by amounts proportional to the square of their amplitudes:

$$\omega_1^2 = \omega_0^2\left(1+\alpha-\beta x_1^2\right), \quad \omega_2^2 = \omega_0^2\left(1-\alpha-\beta x_2^2\right).$$

We assume that the changes in frequency induced by Lorentz detuning are small enough that the amplitudes are still given by Eq. (3). From Eq. (1), and using the upper sign, the frequency of the "π-mode" is

$$\omega_\pi^2 = \omega_0^2\left\{1-\beta+\left[\alpha^2\left(1-\frac{\beta}{\left(\alpha^2+k^2\right)^{1/2}}\right)^2+k^2\right]^{1/2}\right\},$$

and the ratio of Lorentz-induced frequency shift with and without asymmetry between the two cells is

$$\frac{\Delta\omega_\pi^2(\alpha \neq 0)}{\Delta\omega_\pi^2(\alpha = 0)} = \frac{\beta - \left[\alpha^2\left(1-\dfrac{\beta}{\left(\alpha^2+k^2\right)^{1/2}}\right)^2+k^2\right]^{1/2}+\left(\alpha^2+k^2\right)^{1/2}}{\beta}$$

$$= 1 + \frac{\alpha^2}{\alpha^2+k^2} \cdot \frac{2-\dfrac{\beta}{\left(\alpha^2+k^2\right)^{1/2}}}{1+\left[1-\dfrac{\alpha^2\beta}{\left(\alpha^2+k^2\right)^{3/2}}\left(2-\dfrac{\beta}{\left(\alpha^2+k^2\right)^{1/2}}\right)\right]^{1/2}}.$$

Thus the enhancement due to asymmetry $(\alpha \neq 0)$ should always be less than 2. In fact, if we make the realistic assumption that the Lorentz detuning at the operating field is much less than the cell-to-cell coupling $(\beta \ll k)$ the enhancement simplifies to

$$\frac{\Delta\omega_\pi^2(\alpha \neq 0)}{\Delta\omega_\pi^2(\alpha = 0)} = 1 + \frac{\alpha^2}{\alpha^2 + k^2} = 1 + \frac{\varepsilon^2}{1 + \varepsilon^2}, \qquad (4)$$

where $\varepsilon = \alpha / k$

These results apply to identical "assumed" gradients; actually they are at identical energy content and the actual gradient will be less than the "assumed" gradient. With the above notations and with $y_i = |x_i|$, at an energy content $y_1^2 + y_2^2 = 2$, the energy gain in a balanced structure will be $y_1 + y_2 = 2$. In an unbalanced structure, the real energy gain at the same energy content will be

$$y_1 + y_2 = \frac{1 - \varepsilon + \left(1 + \varepsilon^2\right)^{1/2}}{\left(1 + \varepsilon^2\right)^{1/4}\left[\left(1 + \varepsilon^2\right)^{1/2} - \varepsilon\right]^{1/2}} < 2.$$

In the case of extreme field unbalance, only one cell will be energized and the actual energy gain will be $\sqrt{2}$ instead of the assumed 2.

When comparing the Lorentz detunings at identical real gradients, the result of Eq. (4) needs to be multiplied by

$$\frac{4}{\left(y_1 + y_2\right)^2} = 2\frac{\left(\alpha^2 + k^2\right)^{1/2}}{1 + \left(\alpha^2 + k^2\right)^{1/2}},$$

and the detuning enhancement at constant real gradient is

$$\frac{\Delta\omega_\pi^2(\alpha \neq 0)}{\Delta\omega_\pi^2(\alpha = 0)} = \frac{2}{1 + \left(1 + \varepsilon^2\right)^{1/2}}\frac{1 + 2\varepsilon^2}{\left(1 + \varepsilon^2\right)^{1/2}}. \qquad (5)$$

The field flatness can be defined simply in a 2-cell structure as

$$\Phi = \frac{|y_1 - y_2|}{\dfrac{y_1 + y_2}{2}} = 2\frac{1 + \varepsilon - \left(1 + \varepsilon^2\right)^{1/2}}{1 - \varepsilon + \left(1 + \varepsilon^2\right)^{1/2}}. \qquad (6)$$

The Lorentz detuning enhancement at constant energy content and at constant energy gain given by Eqs. (4) and (5), respectively, are shown in Fig. 1 as function of the field flatness defined by Eq. (6).

When the cells are almost identical (i.e. when their frequency difference is much less than the cell-to-cell coupling), the enhancements at constant energy content and constant energy gain are $1 + \Phi^2$ and $1 + 1.25\Phi^2$, respectively. In the case of extreme difference between the two cells the enhancement at constant energy content is 2, while, at constant energy gain, it is 4.
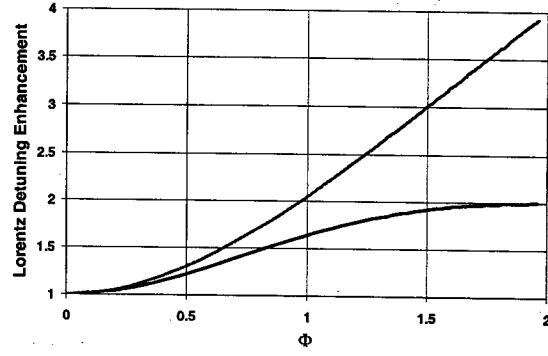
Figure 1: Lorentz detuning enhancement for a 2-cell structure as a function of field flatness between the two cells. Blue curve is at constant energy content; red curve is at constant energy gain.

MULTI-CELL CAVITIES

In the case of cavities with a large number (N) of different cells, the modes frequencies and amplitudes, and the Lorentz detuning coefficient cannot be obtained analytically and a numerical analysis is required. Additionally there are several ways of defining the field flatness, and there is no one-to-one relationship between any of those and the Lorentz detuning enhancement.

One way of defining the field flatness is

$$\Phi_1 = \frac{\max(y_i) - \min(y_i)}{\langle y \rangle}. \qquad (7)$$

Another way is through a standard deviation

$$\Phi_2 = \left(\frac{N}{N-1}\right)^{1/2}\left[\sum\frac{\left(y_i - \langle y \rangle\right)^2}{\langle y \rangle^2}\right]^{1/2}. \qquad (8)$$

It can be noted that, for a 2-cell structure, these two definitions are identical to each other and to that given by Eq. (6); and that, in the case of extreme field unbalance where only on cell is energized, we have $\Phi_1 = \Phi_2 = N$.

We have analyzed numerically a large number of multi-cell structures with random deviations of the frequencies of each individual cells from an average. This amounts to finding the eigenvalues and eigenvectors of tridiagonal $N \times N$ matrices to obtain the frequencies without Lorentz detuning, and then solving the problem again where the frequency of each cell has been changed further by an amount proportional to the square of the amplitude in that cell. The change in frequency of the "π-mode" is then compared to the one that would occur in a similar structure where all the cells are identical.

Results for 6-cell structures are shown in the Figures 2-6. The same numerical analysis was applied to 2-cell structures and the analytical results of section 2 were recovered.
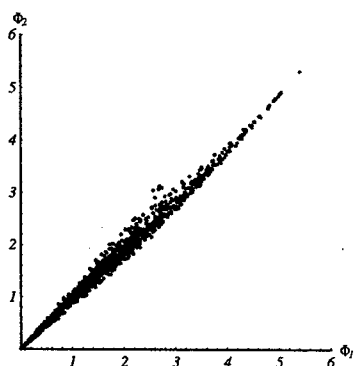
Figure 2: Correlation between the field flatness defined by Eqs. (7) and (8).
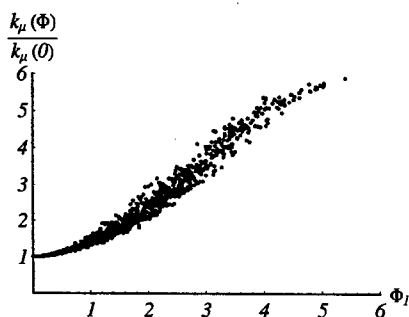
Figure 3: Lorentz detuning enhancement at constant energy content for field flatness defined by Eq. (7).
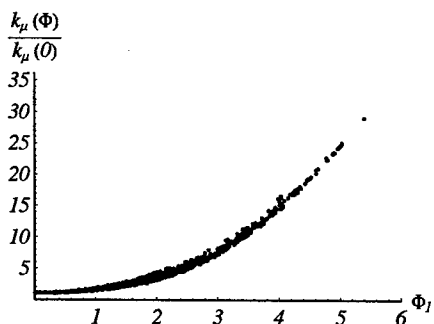
Figure 4: Lorentz detuning enhancement at constant energy gain for field flatness defined by Eq. (7).

DISCUSSION

During the measurements on the SNS prototype cryomodule, Lorentz detuning coefficients of the three cavities were measured. Variations of more than a factor of 2 were observed and seemed to be correlated with the flatness of the field profile, which, when measured at room temperature, was up to 70% according to definition given by Eq. (7). The present analysis supports this correlation but cannot explain such a large difference, if
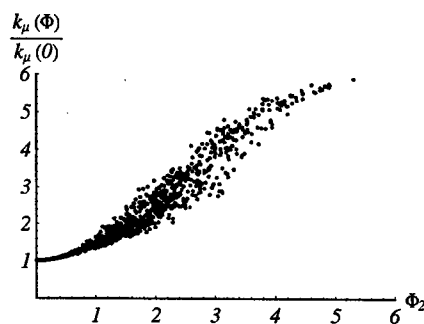
Figure 5: Lorentz detuning enhancement at constant energy content for field flatness defined by Eq. (8).
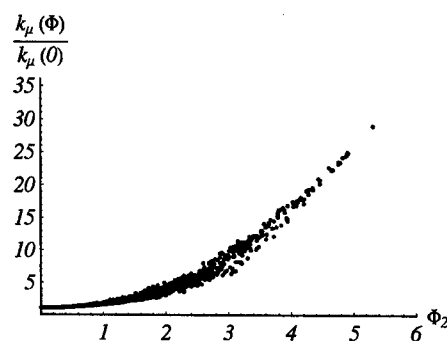
Figure 6: Lorentz detuning enhancement at constant energy gain for field flatness defined by Eq. (8).

the field flatness remained the same during cooldown, and other factors may have contributed.

Analysis of a large number of cavities with random perturbation of the cell frequencies show similar correlation between the two definitions of the field flatness and the Lorentz coefficient enhancement. Definition (7) seems to be better correlated with the detuning enhancement for large flatness coefficients, while, for low values of the flatness coefficient, there is a better correlation with the flatness defined by Eq. (8).

REFERENCES

[1] Jean Delayen, Ed Daly, Kirk Davis, Steve Smee, "Frequency Measurements on the Prototype SNS Medium-β Cryomodule Under Pulsed and CW Operation," JLab Tech Note 02-049.

[2] I. Campisi, G. Ciovati, G. K. Davis, J. R. Delayen, M. Drury, L. W. Funk, J. Mammosser, T. Powers, J. Preble, C. E. Reece, C. H. Rode, M. Stirbet, H. Wang, T. Witlatch, K. M. Wilson, M. Wiseman, "The SNS Prototype Cryomodule: Testing and Performance," these proceedings RPAB065.

PIEZOELECTRIC TUNER COMPENSATION OF LORENTZ DETUNING IN SUPERCONDUCTING CAVITIES *

G. K. Davis, J. R. Delayen[#]

Thomas Jefferson National Accelerator Facility, Newport News, VA 23606

Abstract

Pulsed operation of superconducting cavities can induce large variations of the resonant frequency through excitation of the mechanical modes by the radiation pressure. The phase and amplitude control system must be able to accommodate this frequency variation; this can be accomplished by increasing the capability of the rf power source. Alternatively, a piezo electric tuner can be activated at the same repetition rate as the rf to counteract the effect of the radiation pressure. We have demonstrated such a system on the prototype medium beta SNS cryomodule [1] with a reduction of the dynamic Lorentz detuning during the rf pulse by a factor of 3. We have also measured the amplitude and phase of the transfer function of the piezo control system (from input voltage to cavity frequency) up to several kHz [2].

Figure 1: Dynamic Lorentz detuning during pulsed operation

DYNAMIC LORENTZ DETUNING

SNS will be the first large-scale use of superconducting cavities in a pulsed accelerator. Although the cavities will be strongly beam-loaded the dynamic Lorentz detuning is expected to be a substantial fraction of the bandwidth and the phase and amplitude control under these conditions will require additional amounts of rf power. During tests of the SNS prototype cryomodule [1,2], the dynamic behavior of the frequencies of the 3 cavities was measured and the use of a piezo tuner for its compensation was evaluated.

The measurements were made with a cavity resonance monitor (CRM) [3]. The CRM has a 50 dB dynamic range, so it can measure the cavity frequency during the rise and decay of the fields, but we do not have, at present, the ability to measure the frequency between pulses. This would require maintaining a small but finite rf field in the cavity.

A typical measurement of the dynamic Lorentz detuning for an "SNS" pulse is shown in Fig. 1. In that figure, and all similar ones, the transients at the beginning and the end are associated with the phase-lock loop acquiring and losing lock and are not significant.

PIEZO TUNER TRANSFER FUNCTIONS

The transfer function (phase and amplitude) from input voltage of the amplifier driving the piezo to cavity frequency was measured. This was done by sweeping the frequency of the drive modulation, and measuring

simultaneously the phase and amplitude of the frequency modulation.

For cavity 2 we measured the transfer function for the two extreme positions of the slow mechanical tuner (Fig. 2). Subtle but real differences in the responses were observed
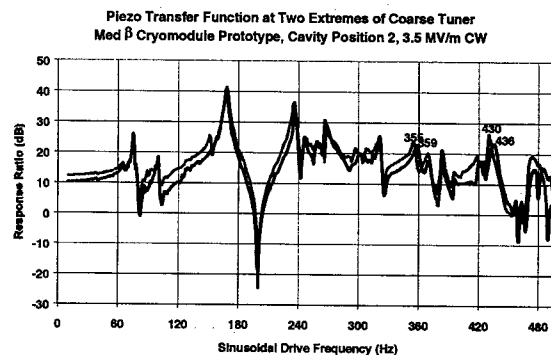
Figure 2: Amplitude of the piezo transfer function in cavity 2 for the two extreme positions of the coarse mechanical tuner. Blue: 804.612MHz; Red: 805.06 MHz

The behavior of the piezo tuner transfer function was somewhat unexpected and is not, at present, fully understood. First, the transfer functions of the 3 cavities were substantially different one from the other; some strong resonances that were present in one cavity were absent in others (Fig. 3). Most surprising was the large amount of phase shift as the modulation frequency was increased; more than 20π had accumulated at 500 Hz. It should be pointed out that the transfer function includes the driver amplifier for the piezo, the piezo itself, and the

mechanical modes of the cavity. Separation of the various contributions will require further testing.

Cavity Pos 1, Piezo Transfer Function

Cavity Response to Piezo, Swept Sinudoid, Drive Amplitude = 26Vpp
Med B Cryomodule Prototype, Cavity Position 2, 804.812MHz, 3.5 MV/m CW

Cavity Position 3, Piezo Transfer Function

Figure 3: Phase and amplitude of the piezo transfer functions for the 3 cavities.

A complete transfer function to 3.2 kHz was measured for cavity 3 (Fig. 4). Note the continuous accumulation of phase shift and the broad peak around 2 kHz.

PULSED OPERATION OF THE PIEZO TUNER

The length of the rf and piezo pulses are much shorter than the period of the dominant mechanical modes so it would be expected that the detail of the pulse shape would have relatively little effect on the dynamic behavior of the cavity. Furthermore the decay time of the dominant modes is much larger than the spacing between

the pulses, thus it would be expected that the cavities would be in a perpetual state of "ringing. This is

Cavity Position 3, Piezo Transfer Function

Cavity Position 3, Piezo Transfer Function

Cavity Position 3, Piezo Transfer Function
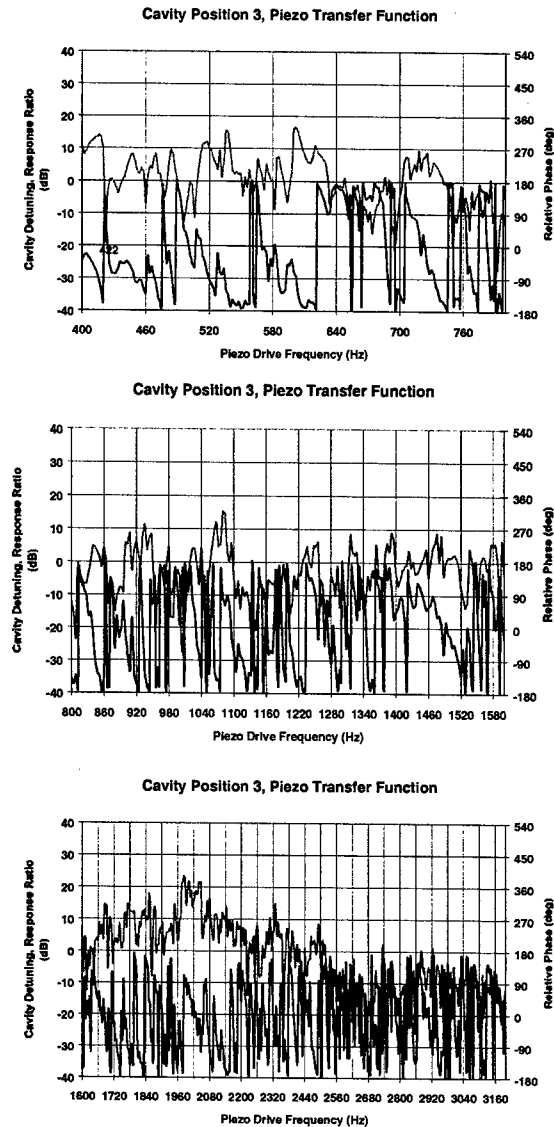
Figure 4: Amplitude and phase of the piezo transfer function for cavity 3 from 400 to 3200 Hz. Results up to 400 Hz are shown in Fig. 3.

demonstrated in the following Fig. 5. Cavity 2 was operated cw and the piezo tuner was activated at 60 Hz, in a similar fashion and amplitude that would be needed to compensate for the Lorentz detuning. The response of the cavity frequency was relatively insensitive to the rise time of the piezo pulse, but it was also essentially periodic. It is for this reason that, for the short duration of the rf pulse, the piezo pulse can be used to compensate for the Lorentz detuning which would have a similar complex, but periodic, behavior by carefully adjusting the timing between the two.

Cavity Position 2 Response to Piezo Pulses at 1.28 ms
pulse width; 160 usec rise time; 60 Hz
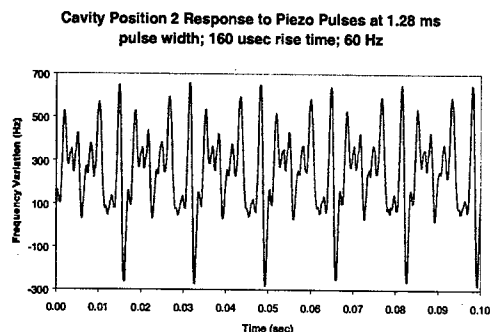
Figure 5: Cavity frequency variation induced by a 60 Hz excitation of the piezo tuner similar to that which would be needed to compensate for the rf-induced Lorentz detuning.

Of concern for use of the piezo tuner to control microphonics is the amount of microphonics that it can generate during activation. The frequency of cavity 2 was measured while activating the piezo tuner with a slow (1 or 2 Hz) trapezoidal signal with rise time of 0, 5, 10, and 20 msec. A square wave (0 rise time) generates microphonics of the same order of magnitude as the steady state displacement it induces; these microphonics then decay in about 400 msec (Fig. 6). In order for the microphonics to be less than 50 % of the steady state displacement, the ramp time of the trapezoidal drive must be at least 5 msec.

Cavity Pos. 2 Piezo Response, 1 Hz Square Wave
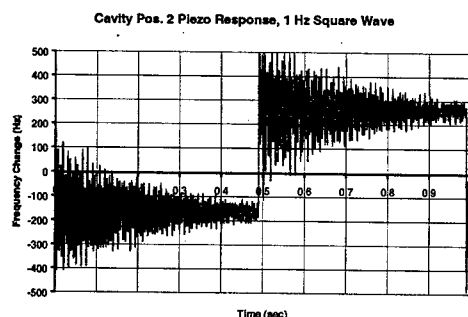
Figure 6: Cavity frequency response to square-wave excitation of the piezo tuner.

PIEZO TUNER COMPENSATION OF DYNAMIC LORENTZ DETUNING

The effectiveness of the piezo tuners in compensating for the Lorentz detuning is shown in Fig.7. A reduction by a factor of 3 was easily achieved. The critical parameter was the timing between the rf pulse and the piezo pulse. Similar reduction was achieved by changing the polarity of the piezo drive signal by adjusting the timing. It should be noted that this compensation takes place only during the short rf pulse. Although we do not have the ability to measure it, it is likely that the cavity

frequency undergoes large transients between the rf pulses.

Cavity # 2 @ 10 MV/m, with and without piezo compensation
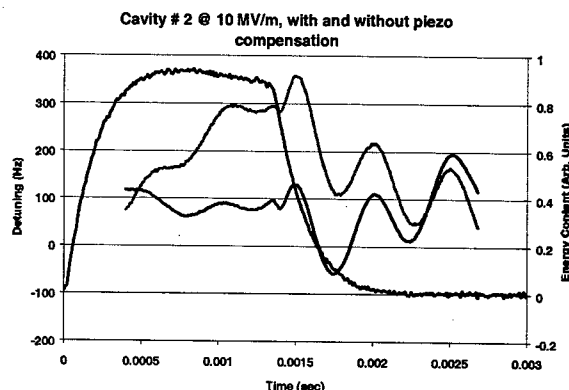
Figure 7: Cavity frequency without (red) and with (blue) piezo tuner compensation. Green: energy content

DISCUSSION

We have demonstrated a reduction by more than a factor of 3 of the dynamic Lorentz detuning of the SNS medium-β prototype cryomodule during pulsed operation. While this more than exceeds the SNS requirements further reduction is possible with better optimization.

The transfer function between piezo actuation and cavity frequency revealed a complex behavior that varied from cavity to cavity. Large-scale use of piezo tuners for control of microphonics during cw operation will have to include sufficient adaptability and flexibility to accommodate this variability.

REFERENCES

[1] Jean Delayen, Ed Daly, Kirk Davis, Steve Smee, "Frequency Measurements on the Prototype SNS Medium-β Cryomodule Under Pulsed and CW Operation," JLab Tech Note 02-049.

[2] I. Campisi, G. Ciovati, G. K. Davis, J. R. Delayen, M. Drury, L. W. Funk, J. Mammosser, T. Powers, J. Preble, C. E. Reece, C. H. Rode, M. Stirbet, H. Wang, T. Witlatch, K. M. Wilson, M. Wiseman, "The SNS Prototype Cryomodule: Testing and Performance," these proceedings RPAB065.

[3] G. Kirk Davis, Jean Delayen, Michael Drury, Thomas Hiatt, Curt Hovater, Thomas Powers, Joseph Preble, "Microphonics Testing of the CEBAF Upgrade 7-Cell Cavity," PAC 2001, Chicago, IL, 18-22 June 2001.

INVESTIGATION INTO THE EFFECTIVENESS OF THE JLAB HIGH PRESSURE RINSE SYSTEM*

J. Mammosser[#], T. Rothgeb, T. Wang, A.T. Wu, Jefferson Lab, Newport News, VA 23606, USA

Abstract

As part of a study to reduce field emission in Superconducting radio frequency cavities, an investigation into the effectiveness of the Jefferson Lab's High Pressure Rinse (HPR) system is underway. This paper describes discoveries from this investigation, the procedural changes made during this investigation, current vertical test results and further plans for improvements and monitoring.

CAVITY PERFORMANCE ISSUES

After the vertical dewar qualifying tests on the South Linac 21 (SL21) cavity string, an effort was renewed to reduce field emission and improve cavity performance. Many of the cavities tested for the SL21 string were field emission limited. The average gradient for field emission onset during vertical tests of these cavities was 8.5 MV/m. Testing of these same cavities in the SL21 cryomodule showed better performance in both Q-value and gradient, with the average field emission onset gradient being 13 MV/m. Early field emission onset in the vertical tests, led to the need to repeat many of the cavity qualification tests. The immediate focus for process improvement was on the HPR system and the Deionised (DI) water plant that supports it. The HPR represents the final cleaning step in our assembly process and understanding its effect on cavity performance may indicate avenues for further improvements.

JLAB'S PRODUCTION HPR SYSTEM

Jefferson Lab's production HPR system consists of a high-pressure pump (ceramic plunger style) pumping ultra pure DI water through a wand, a linear actuator for moving the wand, and a rotary table for rotation of the cavity. Typical cavity process parameters are:

Flow rate	18.9 l/min (5.0 gpm)
Wand velocity	0.3048 m/min (12 in/min)
Wand motion	Reciprocating
Rotational speed	1 rpm
Water pressure	8.27 mPa (1200 psi)
Rinse duration	Typically 1 hour

The spray wand has nine 0.4 mm (0.016") nozzles located around the head of the wand. Three of the nozzles are pointed up at a 45° angle, three are pointed down at a 45° angle and the remaining three spray out horizontally. The nozzles are aligned vertically and spaced around the head 120° apart. The HPR system is contained in a cabinet that is located in a Class 100 cleanroom.
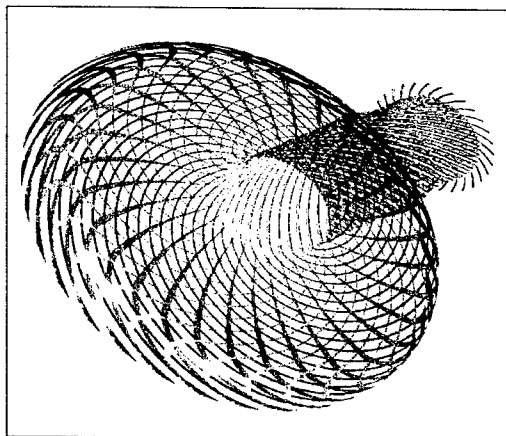
Figure 1: HPR spray impact path for 30 passes all 9 nozzles on an SNS medium beta cavity cell.

A simulated pattern of the HPR spray impact path as mapped out on the SNS medium beta cavity cell surface is shown in Figure 1. These simulated impact paths for all 9 nozzles cover approximately 12% of the cavity surface per pass. From this pattern it is easy to deduce that the impact path of the water yields many areas of light coverage on the surface, which miss the direct force of the water stream.

Analysis of Process DI Water Quality

Water system quality was sampled prior to making any changes to the system in order to establish a baseline. Two sample locations were used, at the HPR outlet and after the final 0.1 µm filter at the DI plant. The water was tested for bacteria, total oxidizable carbon (TOC), dissolved silica, total silica, anions, cations and 68 trace elements. Table I compares the results of the tests with the original pure water specifications and guidelines (from 1988) [1]. Only those results that did not meet the requirement are shown here. These data show that the number of particulates coming out of the HPR was much higher than that of the DI plant, and could be a significant contributor to poor cavity performance.

Along with the tests mentioned above, water samples were collected for Scanning Electron Microscopy (SEM) studies. The results of these tests showed bacteria as well as filter media particulates coming from the HPR system. The filter in the HPR was comprised of borosilicate glass with a 0.2 µm pore size. It was removed and particulates from it were analysed. Two sampling ports were added to the HPR water path, one just before entering the cavity wand (inlet) and a second (drain) to collect rinse water draining from the cavity during processing. Samples were taken during SNS medium β cavity HP rinses and these showed high particle counts on the inlet. Approximately

Table 1 - HPR Specifications and Results

	Limit [2]	HPR	Final Filter
Bacteria	1 cfu	>500	*
TOC	5 ppb	*	*
Dissolved Silica	1 ppb	16	17
Total Silica	1 ppb	15	17
Chloride	0.02 ppb	0.05	0.07
Sodium	0.01 ppb	0.85	0.03
Potassium	0.02 ppb	0.86	*
Magnesium	0.02 ppb	0.12	*
Calcium	0.02 ppb	0.42	*
Barium	0.001 ppb	0.18	*
Boron	0.05 ppb	4.0	4.4
Magnesium	0.002 ppb	0.11	*
Manganese	0.002 ppb	0.006	*
Nickel	0.004 ppb	0.027	*
Potassium	0.1 ppb	0.6	*
Rubidium	0.001 ppb	0.003	*
Silicon	0.5 ppb	7.6	8.0
Sodium	0.007 ppb	0.55	0.023
Strontium	0.001 ppb	0.003	*
Zinc	0.005 ppb	0.74	*

* not detectable

300 particulates were counted during a 20-minute sample and significantly fewer counts of 83 from the drain sample near the beginning of the run and 60 at the inlet, near the end of the run. Most of the elements identified were also identified in the filter media analysis. Figure 2 shows the relative amounts of analyzed elements from the HPR filter.

The DI water plant filters were replaced and the plant was sanitized and flushed to kill and remove bacteria. Afterwards, a new 0.1μm membrane HPR filter was installed and a 1.5 l/min trickle flow of DI through the HPR system was added to reduce bacteria growth in the filter media and pump when the system was idle. A laser water particle counter was added at the HPR wand inlet sample location to monitor particulates during rinses. Figure 3 shows the water particle counts during a typical cavity HPR after the DI water system was sanitized.

Particulate Collection and Analysis From Cavities

Particulate samples were collected from cavities that showed heavy field emission during vertical tests and from vacuum piping and pumps on one of the production vertical test stands for comparison to water particulates collected. Cavity and vacuum system samples were collected using double sided carbon tape by blotting the end flange and beam-tube surfaces and bagging in clean nylon bags. Figure 4 shows analysis of the particulates found in an SNS medium beta cavity after a failed vertical

test at the beginning of this investigation. Figure 5 shows the particulates collected from cavity JL009 after a failed vertical test. JL009 test was near the end of the SL21 qualification testing and before any changes to the DI water system.

Particulates were also collected from the vacuum system piping on the vertical test stand and the roughing pump was opened and samples collected and analyzed. The particles in the cavity samples analyzed showed were consistent with those elements found in the water and HPR analysis yet there were some that could not be explained, such as Au. In the vacuum system many particulates had collected in the lower portions of the vacuum system piping and consisted of many of the elements found in the DI water and HPR analysis. Many of the metals that make up the stand components, such as Cu, Fe, Cr and Ni were also found. From all the particulate analyses it became clear that silicon was present in large quantities in the water plant from both the HPR and in cavity samples.
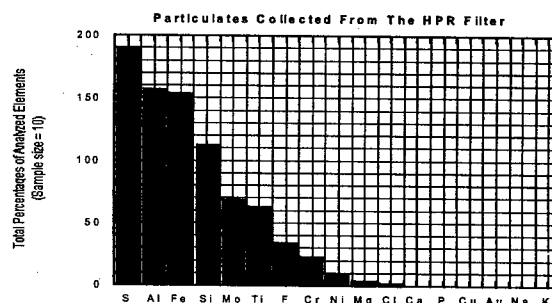
Figure 2. Relative population of HPR filter particulates by element.
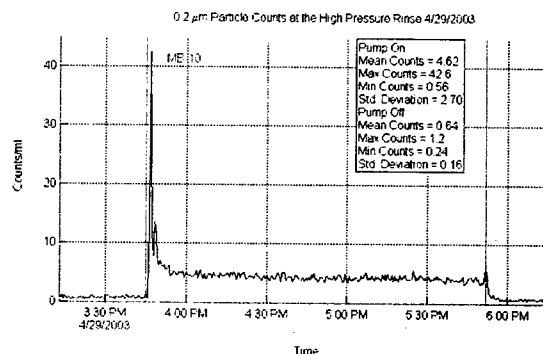
Figure 3. Counts of 0.2 μm sized particles during a typical HPR

PROCESS PROCEDURAL CHANGES IMPLEMENTED

One additional concern was that with only one hour of high pressure rinsing, that the cavity surfaces might not be cleaned well enough, even if the water system was

improved. The problem with increasing the amount of high pressure rinsing was the DI water storage capacity
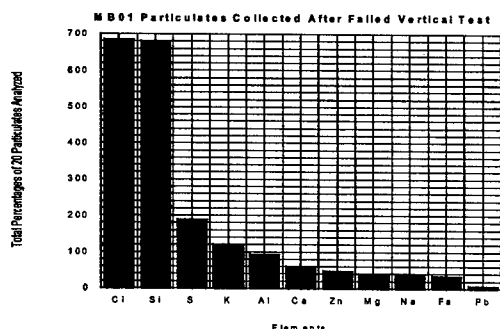
Figure 4. Particulates Collected From MB01

and make-up rate, which were only 8000 litres and 8 l/min, respectively. This allowed for only a single two-hour high pressure rinse per day. A new reverse osmosis system was installed to provide a make up rate of 20 l/min. Along with doubling the time for cavity rinsing, this allowed a second two-hour rinse cycle to be added for cavities after they had most of their test hardware assembled to the flanges. Only the bottom evacuation flange connection was not assembled for the second rinse cycle. This second cycle allowed the cavity and the test hardware to be cleaned in the same way, and to minimize the assembly steps needed for completion of the hermetic sealing of the cavity. The cavity is rinsed and dried vertically in the HPR cabinet overnight and the bottom flange blanked off for removal and assembly of the evacuation flange.

A study into the effect of field emission onset due to the location of particulates from the cavity drying position is also underway. As part of this study, four of the eight cavities for the Free Electron Laser (FEL) string were dried horizontally before vertical tests.

COMPARISON OF FIELD EMISSION ONSET FOR SL21 AND FEL3 CAVITIES

Upon the completion of the FEL3 vertical cavity qualification tests, it was apparent that field emission onset performance had improved. These cavities are the same shape and configuration as those for SL21. The only significant difference was changes to the processes used and to the facilities. Figure 6 shows that the average onset of field emission had increased by 4.3 MV/m for FEL3 cavities, but with a larger range. The last four cavities that were dried horizontally had the best performance, with an average field emission onset of 17.5 MV/m, and a standard deviation of 1.75MV/m.

CONCLUSION

Many changes over the last year have been made to both procedures and processing facilities. Some improvements to performance are being observed from

vertical test data. It is however difficult with the present limited statistics to determine which changes had the most significant impact on performance. Future plans are to continue analysis and monitoring of the DI and HPR systems and improve the surface coverage of cavities during high pressure rinsing by modifying the current programs, to come to a better understanding of the drying process, and to continue tracking vertical test cavity performance.

ACKNOWLEDGEMENTS

We would like to thank Jim Henry for modelling the HPR spray impact path.

REFERENCES

[1]   T. Meltzer, High-Purity Water Preparation For The Semiconductor, Pharmaceutical and Power Industries (1997) p.19.

[2]   S. Schoen Balazs Analytical Services report dated September 19, 2002.
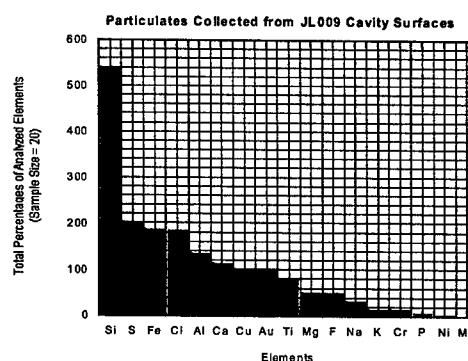
Figure 5. Particulates collected from JL009 after a failed vertical test.
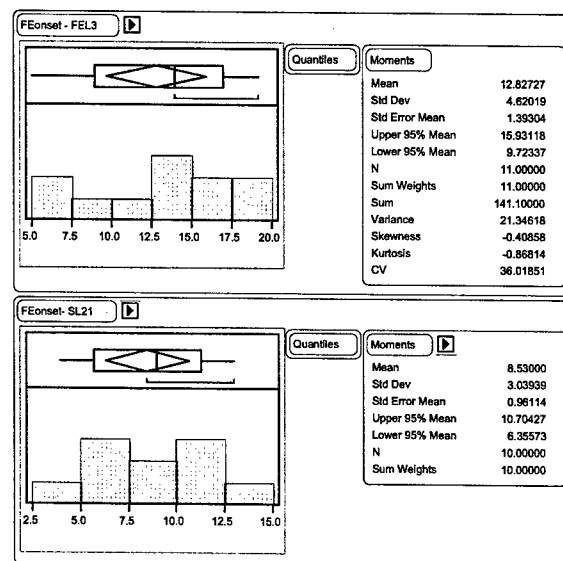
Figure 6. Vertical Test Field Emission Onset Comparison

TOWARDS STRONGLY HOM-DAMPED MULTI-CELL RF CAVITIES*

R. Rimmer*, H. Wang, G. Wu, JLAB, Newport News, VA, USA

D. Li**, LBNL, Berkeley, CA, USA.

Abstract

This paper discusses the prospects for very strong HOM damping in multi-cell RF cavities. There has been much progress in recent years towards "HOM-free" single-cell cavities. Many examples are now operating in high current storage rings around the world. There have also been successes in broad-band damping of multi-cell structures to levels appropriate for linear colliders and low average current applications. We describe the use of modern simulation tools to explore the potential for applying these techniques to multicell structures. Such cavities would be useful for high-current, high-power applications such as high luminosity collider storage rings, damping rings, energy recovered linacs and injector systems. These methods may be applicable in to both room temperature and superconducting cavities.

INTRODUCTION

Strong HOM damping in accelerator RF cavities has become increasingly important. Storage rings for light sources and colliders now routinely operate with strongly HOM damped single-cell cavities. Linear colliders are proposed that rely upon large numbers of multi-cell cavities with moderate HOM damping. Next generation light sources based on energy recovering linacs (ERL's) require a combination of high-gradient multi-cell structures and strong HOM damping. We study some of the factors that influence the ultimate performance of multi-cell structures using numerical simulations.

SIMULATION METHOD

We used the time domain module in MAFIA with a simulated bunch to excite the cavity either on or off axis [1]. By recording the wake potential behind the bunch and taking a Fourier transform we were able to calculate the broad-band impedance spectrum. We used the waveguide boundary condition to terminate the beam pipes and any damping apertures. We have not attempted to model the small coaxial DESY type couplers with this method.

BROAD-BAND DAMPING METHODS

The simplest method of HOM damping is to enlarge the beam pipe on one or both sides of the cavity so all harmful HOMs may propagate away, figs. 1a, 1e, [2]. A modification of this is the fluted beam pipe fig. 1b, used by Cornell [3]. Waveguide dampers in the beam pipe just outside the cavity, fig. 1c, have been used in CEBAF [4].

Fig.1a. enlarged beam pipe 1b. fluted beam pipe

1c. waveguide dampers 1d. coaxial beam pipe

1e. 2 enlarged beam pipes 1f. multiple coaxial loops
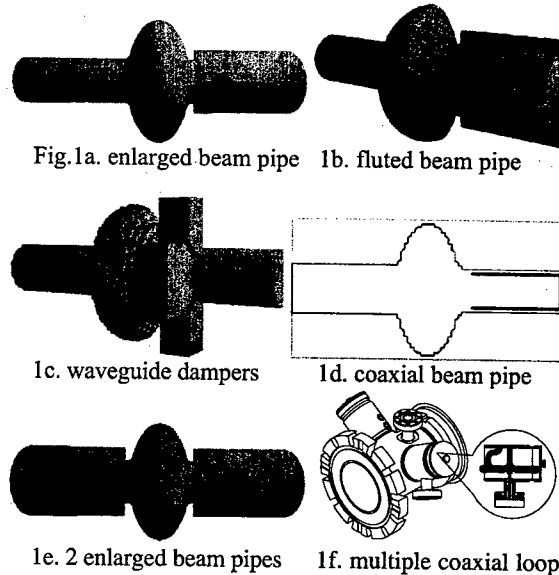
A coaxial insert in the beam pipe, fig. 1d, with a choke to reject the fundamental mode, has been proposed for low-order mode damping in deflecting cavities [5]. Coaxial HOM couplers fig. 1f, are already widely used and can give strong coupling if placed appropriately. Normal conducting cavities use openings directly into the accelerating cells for strong HOM damping but this is not normally used for SCRF cavities and is not studied here.
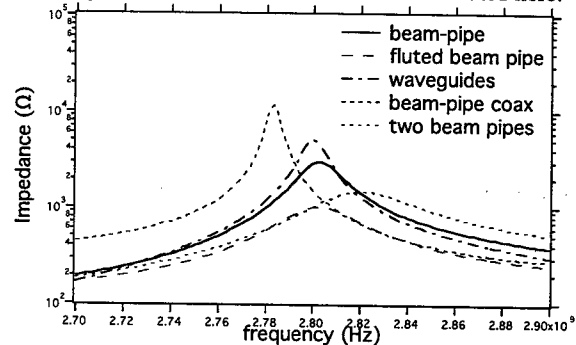
Figure 2. TM_{011} mode with various damping schemes.

We applied the beam pipe, waveguide and beam-pipe-coaxial damping methods to a MAFIA model of a single-cell 1.5 GHz cavity. Figure 2 shows the calculated spectra and table 1 lists the resulting loaded Q's and impedance for the strongest monopole HOM (TM_{011}). The beam-pipe damping on one or both sides or with flutes is very effective. The waveguides also give very good damping and the beam-pipe coaxial load is not far behind. Table 2 lists the results for the first two dipole HOMs (TE_{111}, TM_{110}). Strong damping is also evident in all cases.

Table 1. TM_{011} mode for various damping methods

	freq MHz	Q	R* (Ω)	R/Q (Ω)
b-pipe	2803	252	3001	11.9
flutes	2803	137	1010	7.3
wguide	2800	353	5040	14.3
bp-coax	2783	725	11879	16.4
2xbp	2822	121	1481	12.2

$$*R=V^2/2P$$

Table 2. Dipole modes for various damping methods

	TE_{111} f,MHz	TE_{111} Q	TE_{111} R*, (Ω)	TM_{110} f, MHz	TM_{110} Q	TM_{110} R* (Ω)
b-pipe	1853	83	246	2028	130	1567
flutes	1857	79	239	2029	130	1479
w-guide	1867	553	1594	2027	1131	14419
coax	1924	341	1496	2065	502	5150
2xbp	1830	37	192	2018	53	192

*R calculated at 25mm offset in the cavity

MULTI-CELL STRUCTURES

To study the dependence of damping on the number of cells we calculated the monopole and dipole spectra with from one to seven cells per cavity, with open beam pipes on both ends. Figure 3 shows the impedance spectra for the TM_{011} passband. Tables 3 and 4 list the values for the strongest peak in each passband. Figures 4 and 5 show how the Q and impedance vary with number of cells. The strength of the highest mode in each passband increases with number of cells slightly faster than linearly. The TM_{011} and TE_{111} mode Q's rise with number of cells, the TM_{110} Q's are higher for even numbers of cells than odd numbers, however the impedance climbs monotonically.
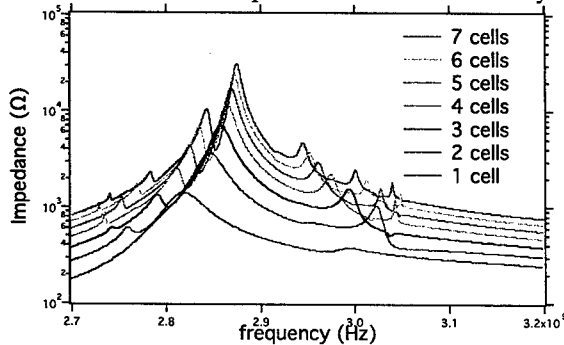
Figure 3. TM_{011} passband mode vs # cells

These results suggest that shorter structures might give better overall HOM performance than long ones, however the overhead in length from each HOM load or set of loads may decrease the average "real-estate"gradient. This might be offset by sharing HOM loads and power couplers between adjacent cavities in "superstructure" assemblies [6]. The maximum number of cells at a given frequency may also be influenced by infrastructure constraints, or limits on window or HOM load power.

Table 3. Strongest TM_{011} passband mode vs # cells

#cells	freq MHz	Q	R* (Ω)	R/Q (Ω)
1	2822	121	1481	12.2
2	2848	167	3856	23.0
3	2860	219	7369	33.7
4	2866	295	12140	41.1
5	2870	362	17795	49.1
6	2873	455	24360	53.5
7	2876	527	31463	59.7

$$*R=V^2/2P$$

Table 4. Strongest TE_{111}/TM_{110} passband modes vs # cells

#cells	TE_{111} f,MHz	TE_{111} Q	TE_{111} R*, (Ω)	TM_{110} f, MHz	TM_{110} Q	TM_{110} R* (Ω)
1	1830	37	192	2018	53	735
2	1907	46	569	2101	2641	10103
3	1940	45	1193	2093	2023	14362
4	1867	94	1844	2101	4058	29270
5	1892	121	3232	2097	3233	40923
6	1910	139	4859	2102	5029	46740
7	1922	135	6088	2099	4177	72101

*R calculated at 25mm offset in the cavity

Figure 4. Loaded Q vs # cells, beam-pipe damping.
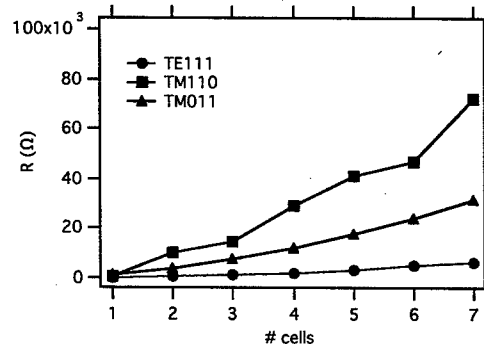
Figure 5. R vs # cells (R at 25mm for dipole modes).

To study the effect of cell shape and coupling strength we compared seven-cell cavities with the original Cornell (OC), high gradient (HG) and low loss (LL) cell shapes [7]. Figure 6 shows the monopole spectrum, while tables 6 and 7 list the peak values for the three passbands. The

TM_{011} mode response is similar for the OC and HG shapes, while the LL peak is lower in frequency but similar in amplitude (within about a factor of three). The dipole passbands show three distinct spectra and about a factor of two spread in amplitude for the TE_{111} mode and about a factor of four in the TM_{110} mode. There does not appear to be any correlation between HOM strength and cell-to-cell coupling in these results. In an operating accelerator the exact mode spectrum could make orders of magnitude difference in BBU threshold and HOM power, so cell profile may be important in this regard.
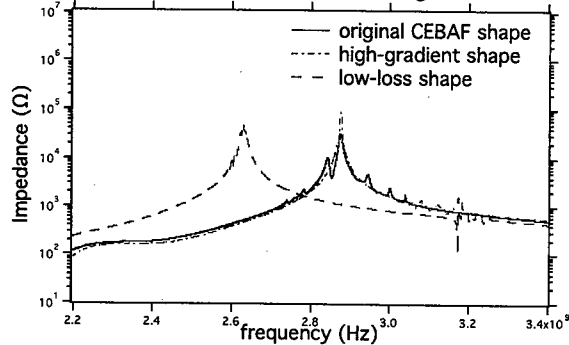
Figure 6. TM_{011} band, OC, HG, LL shapes, 7-cells.

Table 5. TM_{011} mode data for multi-cell cavities.

	#cells	Freq,MHz	Q	$R^\dagger$ (Ω)	R/Q (Ω)
OC	7	2876	527	31463	59.7
HG	7	2876	1348	90380	67.0
LL	7	2629	985	53556	54.4
OC*	5	2871	707	35453	50.1
DESY**	4	910	600		

*waveguide damped. **500 MHz cavity, meas. Q. $^\dagger R=V^2/2P$

Table 6. TE_{111}/TM_{110} mode data for multi-cell cavities.

	# cells	TE_{111} f,MHz	TE_{111} Q	TE_{111} $R^\dagger$, (Ω)	TM_{110} f, MHz	TM_{110} Q	TM_{110} $R^\dagger$ (Ω)
OC	7	1922	135	6088	2099	4177	72101
HG	7	2014	185	11359	2156	5694	146409
LL	7	2021	490	14107	2209	2071	39510
OC*	5	1894	956	22949	2103	3274	47064
DESY	4	650	4000		716	6000	

*waveguide damped. †R calculated at 25mm offset in cavity.

EXAMPLES

Figure 7 shows a five cell structure with waveguide damping. The highest peaks in each passband are listed in tables 5 & 6 (row 4). The TM_{011} peak is about a factor of two stronger for the waveguide damped cavity than for the beam pipe loaded one (table 3 row 5). For the TE_{111} mode (table 4 row 5), the factor is about eight but for the strongest dipole (TM_{110}) mode they are about the same The waveguide dampers take up very little beam line space compared to the beam pipe loads and can transport HOM power to room temperature loads if required.

Included in tables 5 & 6 are data for a four-cell 500 MHz DESY cavity damped by three coaxial HOM couplers [8]. The TM_{011} Q is very similar to the waveguide loaded cavity while the TE_{111} Q is a factor of four higher and the TM_{110} is only up about a factor of two. All of these examples are in the range suitable for next generation high current ERL's
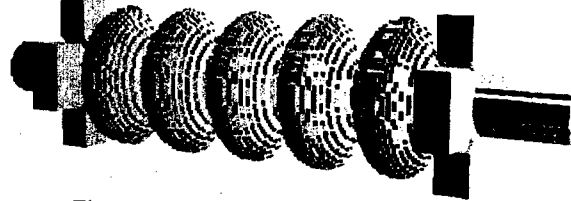
Figure 7. Waveguide damped 5-cell structure.

Other factors such as distortion due to tuning and field tilt might contribute to higher Q's. Having dampers at both ends of the cavity should help. Having symmetrically arranged couplers so that no transverse kick is imparted to the passing beam is also desirable.

CONCLUSIONS

We have shown that strong broad-band HOM coupling techniques used on single-cell cavities can plausibly be applied to multi-cell cavities. None of the schemes described here have been optimized but all show promise. The ultimate limit may be the rate at which energy can propagate through the cavity. To go significantly further we may want to look at more open structures. We would like to thank Jacek Sekutowicz for useful discussions on this topic.

REFERENCES

[1] "Beam Impedance Calculation and Analysis of Higher Order Modes (HOMS) Damped RF Cavities Using MAFIA in Time Domain", Derun Li , Robert A. Rimmer, Proc. PAC 2001, Chicago.

[2] "A Prototype Module of Superconducting Damped Cavity for KEKB" T. Furuya et. al., Proc. EPAC96, Barcelona, Spain.

[3] S. Belomestnykh et. al. "Commissioning of the Superconducting RF Cavities for the CESR Luminosity Upgrade", Proc. PAC99, New York.

[4] J.C. Amato, Proc. third Workshop on RF Superconductivity, Argonne, IL, USA. ANL-PHY-88-1, Vol.1., p 589, 1988.

[5] K. Hosoyama et al., "Crab Cavity for KEKB", Proc. 7th Workshop on RF Superconductivity (1995).

[6] "Superstructures for High Current FEL Application". J. Sekutowicz et.al., these proceedings

[7] "Cavities for JLAB's 12 GeV Upgrade"J. Sekutowicz et.al., these proceedings

[8] "Superconducting Cavities for HERA", B. Dwersteg et.al., Proc. 3rd Workshop on RF Superconductivity, Argonne, IL, USA. ANL-PHY-88-1, Vol.1., 1988.

ACTIVE HOMS EXCITATION IN THE FIRST PROTOTYPES OF SUPERSTRUCTURE

J. Sekutowicz, A. Gössel, G. Kreps, DESY, 22603 Hamburg, FRG

S. Zheng, Tsinghua University, 100084 Beijing, China

Abstract

An alternative layout of the TESLA collider [1], based on superstructures [2], reduces investment cost for the main accelerator due to a much lower number of input couplers and resulting from that, a simplification in the RF distribution system. In May 2002, two first Nb prototypes of the superstructure (P1, P2) were installed next to the injector in the TESLA Test Facility linac (TTF) at DESY to verify experimentally the predicted RF-properties. Part of the experimental program was devoted to the damping of Higher Order Modes (HOM). Good suppression of HOMs in both prototypes has been achieved with HOM couplers based on the coaxial line technique [3]. A several methods have been applied to measure impedances $Z=(R/Q) \cdot Q_{ext}$ of parasitic modes. We report here mainly on results of the active mode excitation method and the measurements of HOMs' parameters by means of a Network Analyzer, which we performed on cold- and on warm prototypes. The other method, HOMs excitation by charge modulation, is reported in more detail in [4].

INTRODUCTION

The superstructures, chains of superconducting multi-cell subunits connected by $\lambda/2$ long tube(s), have been proposed as a replacement for the standard 9-cell TESLA structures. At present, the 2x9-cell (Fig.1) superstructure is seen as the most attractive version, compromising: reduction of cost and an improvement of the performance and being moderately demanding on the production [5]. This version was studied at the time when manufacturing of the subunits of the first original 4x7-cell version was well advanced. In Fall 2001, the decision was made to build, for the test in the TTF linac, two prototypes of a 2x7-cell superstructure instead of one 4x7-cell prototype. The RF-properties of the 2x9-cell and the 2x7-cell versions are very similar as confirmed by the HOMDYN [6] simulation. The acceleration process of the TESLA beam (old or new set of parameters) showed the same, very small bunch-to-bunch energy variation for both versions [7]. Since the scheme of the HOM suppression in both versions is also very similar, we conclude that a beam test of the 2x7-cell prototypes will deliver enough data to verify the superstructure concept.
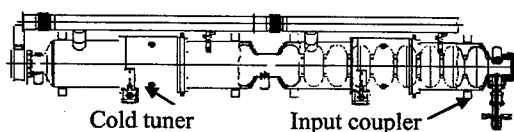
Each prototype has three HOM couplers attached to the end beam tubes and to the interconnection (Fig. 2). The diameter of the interconnecting tubes for all versions of the superstructure has been chosen to keep the accelerating mode well below the cut-off frequency of the tubes. This allowed to avoid heating of HOM couplers attached at the interconnecting tubes by the magnetic field of the accelerating mode. Although the superstructure is made of many cells, the damping is better than for a standard multi-cell cavity with the same number of cells, since pairs of HOM couplers can suppress parasitic modes of much shorter subunits. The attached couplers were of the same type as those used for standard 9-cell TTF cavities. We should mention here that the 2x9-cell version has four cells more than the tested prototypes and an additional HOM coupler will be attached at the interconnection to compensate for that. Both prototypes were examined for the RF-properties of HOMs prior to their assembly in the cryomodule. We will show examples of the measured results in the next section. The discussion here is limited to the dipole modes, since these are relevant for the TESLA beam quality.
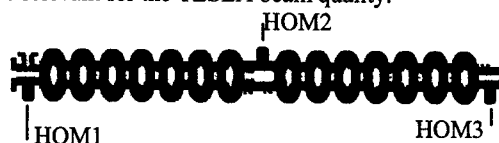
Figure 2: Prototype of 2x7-cell superstructure with three attached HOM couplers: HOM1÷HOM3.

HOM MEASUREMENTS AT 300 K

The computed dipoles of the 2x7-cell prototypes, with significant (R/Q), are listed in Table 1. When compared to the dipoles of a standard 9-cell cavity or to the dipoles of 2x9-cell superstructure, the average impedance per cell is almost the same. This is why the damping specification, $Q_{ext} \leq 10^5$, for these modes holds for all three cases. We have measured frequency, Q_{ext}, and if it was possible, the field profile and angular orientation of both polarizations for each of these modes. The last two measurements were performed by means of the perturbation method. The frequency change was measured vs. the longitudinal position or vs. the angular position of a dielectric perturbing bead. In case of many modes these measurements were impossible due to very strong overlapping of modes and/or difficulty in modes excitation. As an example, the measured profiles of one polarization of the mode No. 45 are shown in Fig. 3 (P1) and in Fig. 4 (P2). The field profile in P1 is similar to the theoretical one. The energy is stored in both subunits. The

Figure 1: 2x9-cells: The left subunit is shown in He vessel with a cold tuner. The right one is shown with only one input coupler needed to transfer power to 18 cells.

Table 1: Computed dipoles, 2x7-cells

Mode No.	f [MHz]	(R/Q) [Ω/cm^2]
11	1717.658	17.0
12	1722.436	13.9
14	1757.921	12.1
21	1858.651	5.2
24	1871.893	10.3
45	2574.259	27.0
47	2641.672	4.4

Figure 5: The lowest frequency is measured at the angle when the perturbing dielectric bead is placed in the highest electric field.

actual (R/Q) in this case is well estimated by its computed value. Unlike this, for P2, the measured field showed that frequencies of subunits differ for this mode and the energy is stored in one subunit only. Although this happened the damping of a parasitic mode can still be provided since HOM couplers are attached at both ends of a subunit. This situation is similar to that of a standard multi-cell cavity. The actual (R/Q) value is near to its computed value for a single 7-cell structure. For these measurements we defined an angular orientation of dipoles as a direction parallel to the maximum of electric field in the x-y plane. In this measurement a dielectric bead was moved angularly in the mid plane of a cell having maximum stored energy. The measurement was done for both subunits in a prototype. For each bead position (increment of 30°) we measured the frequency of the mode. Fig. 5 shows the result measured for mode No. 11 (lower polarization) of prototype P1. The angular position of the electric field maximum (minimum frequency) is the same in both subunits. This means that coupling between subunits does not cause additional angular rotation of the dipole. We observed this, within an accuracy of ± 15°, for other modes which have almost the same stored energy in both subunits. However, when only one subunit has stored energy, the angular position of the mode is determined by irregularities of the shape in this subunit only.
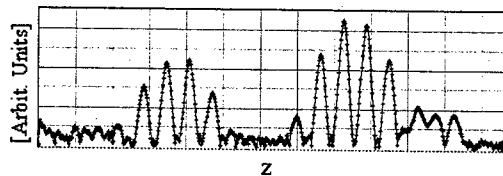
Figure.3: Prototype P1. Field profile of the lower polarization of dipole No. 45, f = 2568.558 [MHz].
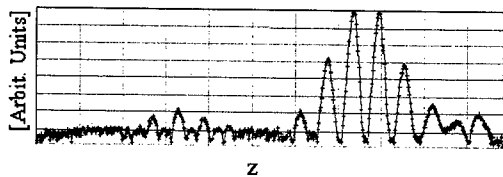
Figure.4: Prototype P2. Field profile of the higher polarization of dipole No. 45, f = 2568.471 [MHz].

HOM MEASUREMENTS AT 2K

At first we measured for both cold prototypes, by means of Network Analyzers, f and Q_{ext} of modes up to 3.2 GHz. In total, 420 modes have been investigated. This data gave us a first estimation of Z and was used to identify dipoles, which interaction with the beam should be measured by the active excitation method to verify their impedance. The sketched setup used for the active mode excitation method is shown in Fig. 6. A chosen dipole mode was excited via one of the HOM couplers with a continuous wave amplifier. Transversal fields of the mode caused sweeping of the on axis injected beam, whose position was measured by a BPM 15 m downstream from the cryomodule. Knowing the RF power coupled into the superstructure one can estimate the amplitude of the deflection. It depends on this power, on the impedance of the mode, on the beam energy and on the distance between the structure and the BPM. The position of the beam in the BPM also shows angular orientation of the mode. One can apply the active method to modes which couple well to HOM couplers. Forty seven modes were measured in this way. An example of measured BPM signals is shown in Fig. 7a,b. In this particular case one polarization of the dipole No. 45 was excited with 20 W forward power. The damping of this mode was good. Its Q_{ext} was $2.1 \cdot 10^4$ (5 times below the spec). We measured the deflection in both planes for 32 bunches (2 nC) in 32 μs long pulses. Ten consecutive pulses are shown in each figure. The strong oscillation of the beam position was
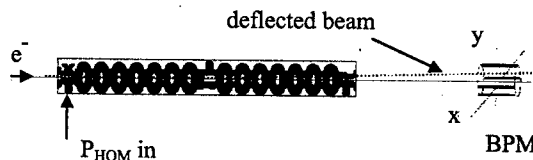
Figure 6: The setup (not in scale) for the active mode excitation. P_{HOM} is the forward power delivered by the

amplifier. BPM measures position of the beam, both in vertical (y) and in horizontal (x) directions.

observed when the power was applied (Fig. 7b). The mode has been tested six times, for various settings of the optics and for various HOM couplers used to transfer RF-power into the cavity. The computed (R_comp) and the measured deflections are presented in Fig. 8, among these values for other modes of prototype P1. The differences between computed and measured deflection were mainly due to the optics setting and due to direct coupling of a part of the RF-power into the beam line [8]. This happens for propagating modes when an external HOM coupler is used as the input port. Fig. 9 shows the measured polarization. Here the differences were due to calibration errors of the BPM signals. Nevertheless, the measured deflection gave the estimation of Z, which in the worst case would be 2 times higher than expected from the Network Analyzer measurements; however it still is harmless to the TESLA beam. The measured polarization showed that this mode, when excited by the accelerated beam, will deflect it almost horizontally.

We measured other modes in a similar way, however not all showed such a deflection as the mode 45 described above. The method still needs further development. All applied methods to measure the HOM damping have
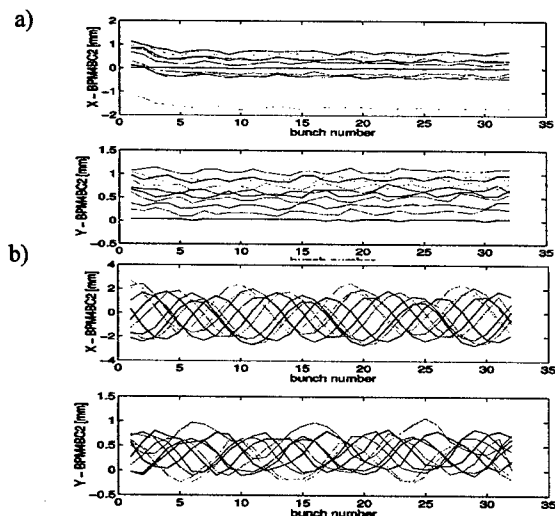
Figure 7: BPM signals without (a) and with (b) the excitation of the dipole mode.
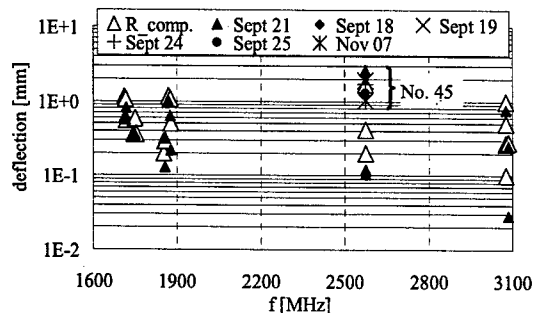
Figure 8: Computed (R_comp) and measured amplitudes of the deflection for dipole modes of the P1 prototype.
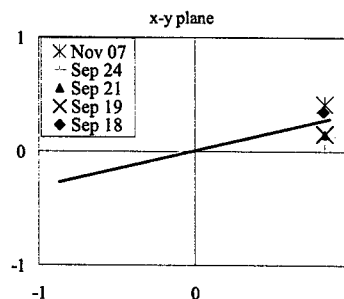
Figure 9: Normalized position of the deflected beam in the x-y-plane. The line shows polarization.

verified the good suppression of dipoles in both prototypes of the superstructure. A summary of the measurements is shown in Fig. 10. After the beam test we are more convinced that the 2x9-cell version should not have a major problem in regard to the HOM damping.
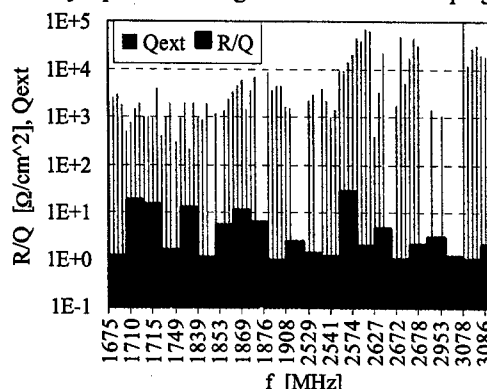
Figure 10: Damping of dipole modes with $(R/Q) \geq 1\Omega/cm^2$.

ACKNOWLEDGMENTS

We would like to express our gratitude to the TESLA collaboration group for many helpful discussions.

REFERENCES

[1] R. Brinkmann et al., "TESLA TDR, Part II: The Accelerator", DESY 2001-011, Hamburg; 2001.

[2] J. Sekutowicz et al, "Superconducting Superstructure for the TESLA Collider; A Concept",PR-ST A.B,1999. [3] J. Sekutowicz, "Higher Order Mode Coupler for TESLA",SRF Work., Newport News,October 1993.

[4] P. Castro et al, "Analysis of the HOM Damping with Modulated Beam in the First Prototype Superstructure" PAC03, Portland, May 2003.

[5] M. Ferrario et al., "Multi-Bunch Energy Spread Induced by Beam Loading in a Standing Wave Structure", Particle Accelerator, Vol. 52, 1996.

[6] J. Sekutowicz et al., "Cold- and Beam Test of the First

CAVITIES FOR JLAB'S 12 GEV UPGRADE*

J. Sekutowicz, G. Ciovati, P. Kneisel, G. Wu, TJNAF, Newport News, 23606 VA, USA
A. Brinkmann, DESY, 22603 Hamburg, FRG
W. Hartung, MSU, East Lansing, Michigan, USA
R. Parodi, INFN Genoa, 16146 Genoa, Italy
S. Zheng, Tsinghua University, 100084 Beijing, China

Abstract

The future 12 GeV upgrade of CEBAF requires new cryomodules in both linacs to increase the energy gain per pass to 1090 MeV [1]. Until recently, the design of new cryomodules, which should deliver on average operational voltage of 70 MV each, was based on 7-cell superconducting cavities that are an extended version of the 5-cell structures currently used in the machine. The 5-cell cavities were constructed 20 years ago at Cornell University (Original Cornell-shape) for the Cornell Electron Storage Ring (CESR). The geometry of these structures [2] met specifications at the time CESR was constructed but is not optimized for the future operation of CEBAF. Two improved cavity shapes have been proposed. This contribution presents the RF features of both new shapes and discusses advantages for the machine operation resulting from the improvement. In addition, we comment on the measurements on copper models of both new cavities and present results of the multipacting calculations.

INTRODUCTION

High Gradient and Low Loss Shapes

The High Gradient (HG) shape has been optimized to lower the ratio of E_{peak}/E_{acc}, keeping in mind that the limitation in the performance of superconducting cavities is in most cases field emission [3]. This phenomenon leads very often to electron showers captured by accelerating fields and/or to strong radiation increasing cryogenic loss and possibly causing a quench. By reducing this ratio one gains in the operational accelerating gradient even without any improvements in surface cleaning procedures.

The Low Loss (LL) shape has been optimized to increase both the characteristic impedance ((R/Q)) and the geometry factor (G) [4]. The improved parameters for this cavity result in less stored energy and less wall loss, at a given accelerating gradient, compared to the two other cavities. The reduced cryogenic load makes the nominal operation less expensive and opens the possibility to reach higher end energy of CEBAF within an available cryogenic budget.

COMPARISON OF INNER CELLS

In a multi-cell ß=1 elliptical structure the RF properties of the accelerating mode are mainly determined by the geometry of the inner cells. The difference in the current and the proposed cells' shape can be seen in Fig. 1. Their parameters are listed in Table 1.
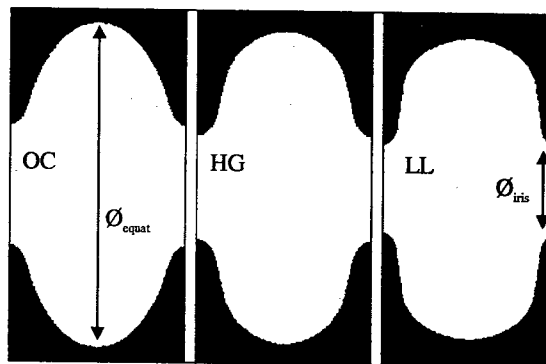
Figure 1: Geometry of three inner cells.

Table 1. Parameters of inner cells

Parameter		OC	HG	LL
$\emptyset_{equator}$	[mm]	187.0	180.5	174.0
$\emptyset_{iris}$	[mm]	70.0	61.4	53.0
k_{cc}	[%]	3.29	1.72	1.49
E_{peak}/E_{acc}	[-]	2.56	1.89	2.17
B_{peak}/E_{acc}	[mT/(MV/m)]	4.56	4.26	3.74
R/Q	[Ω]	96.5	111.9	128.8
G	[Ω]	273.8	265.5	280.3
R/Q·G	[Ω·Ω]	26422	29709	36103

Cell-to-cell coupling, k_{cc}

The LL-shape has the smallest diameter of the equator and of the iris. The small aperture increases (R/Q) and G, but makes cell-to-cell coupling, k_{cc}, weaker. This increases the sensitivity of the field profile of the accelerating mode to frequency errors of individual cells. The measure of the sensitivity is the ratio: $N^2/(k_{cc})$, where N is the number of cells in a structure. This ratio, which one likes to keep low even if k_{cc} is small, can be in a

practical range by reducing the number of cells in a cavity. The upgrade cavities will be made of 7 cells. The ratio for the three upgrade shapes stays below the value for the 9-cell TESLA cavities (k_{cc} = 1.9 %), of which almost 60 were manufactured up to now [5]. Their final field profile flatness, better than 95 %, was maintained without additional technical complications. The large iris of the OC cavity makes the coupling unnecessarily large causing other of its parameters to become unfavorable. The HG-shape is already more progressive here and closing the iris results in better (R/Q) and better E_{peak}/E_{acc} of this shape.

E_{peak}/E_{acc} ratio

Shape optimization with respect to this parameter is very important if cavities are operated at high gradients. However, when final preparation of the superconducting surface and the assembly in cryostat are properly done, the emission phenomena and the resulting radiation can be eliminated to a large degree. The design accelerating gradient for the upgrade has been set to $E_{acc} \approx 20$ MV/m and $Q_o = 8 \cdot 10^9$ at 2 K. The nominal gradient needed to reach 12 GeV of the end energy (with all cavities on) is E_a=17.7 MV/m. The possible operation of new cavities at higher accelerating field is limited by the cryogenic load budget. The maximum possible gradient is 18.3 MV/m, 19.3 MV/m and 21.3 MV/m for OC-, HG- and LL-shape respectively. Thus the maximum possible E_{peak} is limited to: 47 MV/m for the OC-shape, 36 MV/m for the HG-shape and 46 MV/m the for LL-shape. All shapes stay well below technically possible achievements, demonstrated for example, by many multi-cell TESLA cavities and many tests of single cell cavities worldwide.

B_{peak}/E_{acc} ratio

Defects (e.g. residual Ta or embedded impurities) in the Nb surface can limit cavity performance and usually lead to quenches. It has been demonstrated that an additional chemical treatment or mechanical grinding which removes defects in the material can be a remedy to reach higher E_{acc}. Local heating in the defect which eventually causes a quench, is proportional to its size, its surface resistance and the square of the local magnetic field. Therefore it is obvious, that for the same material quality and at a given gradient, cavities with lower magnetic field at the wall are favorable. The potential gain in E_{acc} offered by the LL-shape as compared to the OC-shape and to the HG-shape is 22 % and 14 % respectively. However for the limitation in gradient discussed above, B_{peak} of all shapes remains below 85 mT, a value routinely reached in tests of various Nb cavities.

(R/Q) and geometric factor G

As already mentioned, (R/Q) and G determine the wall loss P_{wall}. When the surface resistance (R_S) and the gradient are given increasing the product (R/Q)·G makes the wall loss lower:

$$P_{wall} = R_s \cdot (E_{acc} \cdot L_{cell})^2 / (G \cdot (R/Q))$$

where L_{cell} is the length of a cell. The LL-shape has the smallest wall loss. The loss of the OC-shape and of the HG-shape is higher by 35 % and 21 %, respectively.

The second advantage of an increased (R/Q) is a lower value of the matched Q_{ext} and thus a widening of the resonance width. This makes the cavity less sensitive to microphonics.

7-CELL CAVITIES

Accelerating mode

Table 2 shows (R/Q) values for all three 7-cell cavities and their parameters for the nominal operation. The value of the matched quality factor, $Q_{matched}$, is computed for the total beam current of 460 μA but without microphonics. The last row gives the optimized quality factor $Q_{microphonics}$. It minimizes additional RF power needed to compensate for the maximum expected frequency mismatch of 25 Hz which may result from the microphonics and the resolution of a cold tuner [6].

Table 2. (R/Q) and parameters at E_a = 17.7 MV/m.

Parameters		OC	HG	LL
R/Q	[Ω]	678	773	877
Q_o		$8 \cdot 10^9$	$7.8 \cdot 10^9$	$8.3 \cdot 10^9$
Dynamic RF- loss at 2K	[W]	28	25	21
E_{peak}	[MV/m]	45	33	38
B_{peak}	[mT]	81	75	66
$Q_{matched}$	[10^7]	4.0	3.5	3.1
$Q_{microphonics}$	[10^7]	1.6	1.5	1.4

The multipacting phenomenon can limit the performance of superconducting cavities. Both new shapes have been examined for this phenomenon with codes used at DESY, MSU and at INFN Genoa. All three codes proved that both shapes can be safely operated at gradients as high as 25 MV/m with no danger of multipacting. We will verify this result very soon with the first Nb prototypes of both new cavities.

Damping of HOMs

Dipole modes can degrade the quality of the CEBAF beam. Computed dipoles with high (R/Q) of both new cavities are listed in Table 3. The required suppression of these modes was computed with the help of the TDBBU code [7]. The results confirmed that the previous specification, $Q_{ext} \leq 1 \cdot 10^6$, as computed for the OC shape [8] holds for the new cavities also. The new cavities will have four HOM couplers, two at each beam tube (see Fig. 2). The couplers are based on the coaxial line technique and are similar to those used for the TTF cavities [9]. We tested this suppression scheme on copper models of new cavities. The results are shown in Fig. 3

Table 3. Dipoles of new cavities .

No.	HG		LL	
	f [MHz]	R/Q [Ω/cm^2]	f [MHz]	R/Q [Ω/cm^2]
1	1980.27	15.9	1978.94	6.8
2	2017.60	15.2	2013.55	10.1
3	2060.48	3.0	2136.47	2.6
4	2143.71	4.1	2170.61	7.2
5	2150.87	7.5	2191.31	15.1
6	2155.11	1.9	2207.37	8.2
7	3004.67	18.9	2893.92	38.1
8			2900.13	4.0
9			2911.06	2.8
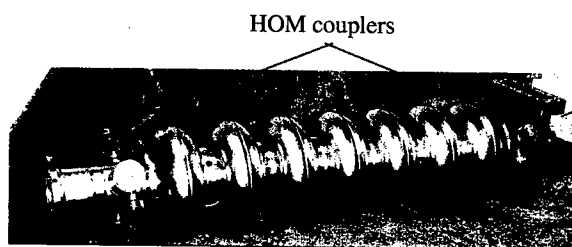
Figure 2: Nb prototype of HG cavity with four HOM couplers.
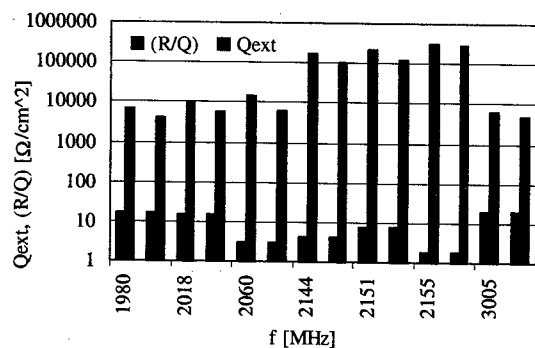
Figure 3: HG cavity. Measured damping of dipoles.
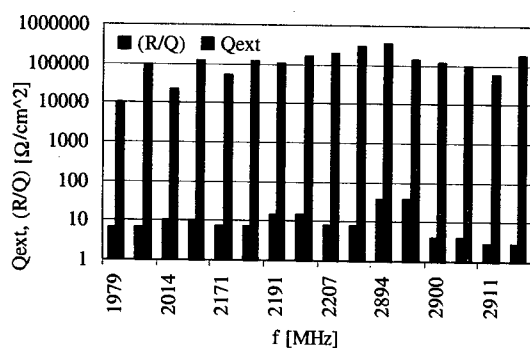
Figure 4: LL cavity. Measured damping of dipoles.

and Fig. 4 for the HG- and the LL-cavity respectively. The LL cavity has weaker cell-to-cell coupling for the parasitic modes than the HG cavity. Their field profile are more sensitive to imperfection in shape and, in case of propagating modes, to the frequency of a neighboring cavity. We have investigated the damping of the propagating dipole No. 7 of LL cavity vs. various standing wave patterns in the interconnecting tube [10]. Except for the one case, when the frequency and the polarization of both cavities were exactly the same, we could still obtain enough damping of this mode. The unfavorable situation is very improbable and no special means have been undertaken to avoid this situation [11].

SUMMARY

Two new cavity designs with improved properties have been completed for the CEBAF upgrade. A prototype of each has been manufactured and will be tested in the near future. The design of new test cryomodule, housing four cavities of each type, is in progress [12]. We are planing to perform the beam test to verify RF properties of the proposed cavities in 2004.

ACKNOWLEDGMENTS

REFERENCES

[1] Interim Point Design for the CEBAF 12 GeV Upgrade, CEBAF, May 1999.

[2] P. Kneisel et al. , " Performance of SC Storage Ring Cavities at 1500 MHz", IEEE Trans. On Magn., MAG-21 (2), 1985.

[3] G. Ciovati et al. , "An Improved Cavity Design For The CEBAF Upgrade", JLAB-TN 01-015, 2001.

[4] J. Sekutowicz et al., "Low Loss Cavity for the 12 GeV CEBAF Upgrade", JLAB TN-02-023, June 2002.

[5] E. Haebel et al., "Cavity Shape Optimization for a Superconducting Linear Collider", HEACC, Vol. 2, Hamburg, 1992.

[6] L. Harwood et al. , "CEBAF at 12 and 24 GeV", SRF Workshop, Tsukuba, September 2001.

[7] K. Beard, private communication

[8] B. C. Yunn, "Dipole HOM Damping Requirement of New 7-Cell Cavity for the 12 GeV CEBAF Upgrade", JLAB-TN 01-028, June 2001.

[9] J. Sekutowicz, "Higher Order Mode Coupler for TESLA", SRF Works., Newport News, October 1993.

[10] G. Wu et al., "HOM Damping Measurements on HG and LL Copper Models", JLAB-TN 03-012, 2003.

[11] C. Reece, private communication.

[12] E. Daly et al., " Improved Prototype Cryomodule for the CEBAF 12 GeV Upgrade", this Proceedings.

FIELD EMISSION STUDIES FROM NB SURFACES RELEVANT TO SRF CAVITIES*

T. Wang[†], C. Reece, R. Sundelin, Jefferson Lab, Newport News, VA 23606, USA

Abstract

Enhanced field emission (EFE) presents the main impediment to higher acceleration gradients in superconducting rf (SRF) niobium (Nb) cavities for particle accelerators. A scanning field emission microscope was built at Jefferson Lab with the main objective of systematically investigating the sources of EFE from Nb surfaces. Various surface preparation techniques and procedures, including chemical etching, electropolishing, ultrasonic water rinse, high pressure water rinse, air-dry after methanol rinse, air-dry after water rinse in Class 10 cleanroom, were investigated. The capability and process variables for broad-area Nb surfaces to consistently reach field emission free or near field emission free performance at ~140 MV/m have been experimentally demonstrated using the above techniques/procedures.

INTRODUCTION

Enhanced field emission is a fundamental limitation in a wide range of high-voltage vacuum devices, for instance, x-ray tubes, electron microscopes, power vacuum switches, klystrons, and high-field SRF Nb resonators for particle accelerators [1][2][3]. When electrons tunnel through the surface barrier of a metal into a vacuum under a high electric field, field emission of electrons occurs. This emission was explained by Fowler and Nordheim in terms of a quantum mechanical tunneling effect in 1928 [4][5]. The result is the so-called Fowler-Nordheim (F-N) law:

$$j = \frac{A \times E^2}{\phi} \times \exp(-\frac{B \times \phi^{\frac{3}{2}}}{E}), \qquad (1)$$

with $A = 1.54 \times 10^{-6}$, $B = 6.83 \times 10^{7}$, current density j in A/cm^2, electric field E in V/cm, and work function ϕ in eV. In practice, FE current is measured at fields much lower than that described by the F-N law, and this phenomenon is termed enhanced field emission. In order to interpret EFE, a field enhancement factor β (> 1) is introduced and usually leads to a good approximation by the modified F-N law [6][7].

Focusing on the material used for SRF cavities, Nb, and other relevant material, a number of institutions have conducted research in FE [8][9][10][11]. Their results show that EFE sources are localized micron or submicron sites that appear to be particles or scratches. Most emitters contain foreign elements, although the types of elements differ. The density of emission sites varies significantly on samples, possibly due to nonstandard preparation and

handling procedures. Lack of consistency in FE performance is also the dominant problem in current SRF cavities. The University of Wuppertal's findings suggest that emitter density increases with material bulk impurity content [12], however, all of their localized emitters were particles containing Nb and Fe. Aimed at addressing some of the above issues, this work was undertaken with the objectives of establishing a standard preparation procedure for maximal and consistent suppression of FE, and investigating the intrinsic FE limit imposed by grain boundary and material bulk impurity in currently employed Nb. As a result, FE sources from Nb were investigated with respect to a variety of preparation techniques, i.e., chemical etching, electropolishing, ultrasonic water rinse, high pressure water rinse, with and without methanol rinse before air-dry.

EXPERIMENTAL APPARATUS AND PROCEDURES

We designed and built an apparatus to scan and locate FE sources on material surfaces, named a scanning field emission microscope (SFEM). The detail of the apparatus was previously described by the authors [13]. The SFEM is a UHV device (~10^{-9} Torr), attached to an existing Amray scanning electron microscope (SEM 1830) with a nominal resolution of several nm. Samples are loaded via the SEM, and can be transferred under vacuum to other chambers. Within the SFEM chamber, samples slightly larger than 25-mm diameter can be moved in Cartesian x, y, and z directions under an anode tip by a high-precision sample manipulator (resolution: 2.5 μm). An anode of 150 μm radius (cylindrical tip) and anodes of 10- and 1-μm tip curvature radius (paraboloid shaped) can be selected for coarse, medium, and fine scans. After emitters are accurately located by the SFEM, the sample is transferred to the SEM and emitters are then relocated with the aid of artificial markings on surface for emitter characterization. The SEM is equipped with an energy dispersive x-ray spectrometer (EDS) capable of windowless operation for light-element sensitivity. The apparatus is located in a Class 1000 cleanroom to reduce the risk of contamination.

The electronic circuit for the experiment is illustrated in Figure 1. The high-voltage power supply is controlled by a computer to output a voltage ramp from 0 up to 40 kV in steps of +200 V, until a FE current threshold, usually set at 1–2 nA, is detected by a picoammeter. Hence, detection of both strong and weak emitters is accomplished in a single scan. The gap between the anode tip and the sample is usually set at 100–200 μm, with the accuracy maintained at ± 10 μm. At an individual emission center, the gap and electric field can be

calibrated, and field enhancement factor β can be extracted [13][14].

FE FROM CHEMICALLY ETCHED AND ELECTROPOLISHED NB

In the same manner as is done with Nb cavities, a number of Nb samples made from high-purity sheets (as used in SRF cavities, RRR~300, where RRR is the ratio of resistance at room temperature to that at low temperature (normal state)), were chemically-etched by BCP (buffered chemical polish, HF (49%):HNO$_3$ (69%) :H$_3$PO$_4$(85%)=1:1:1) to remove the machining-damaged layer. To remove acid residue and particles on samples, ultrasonic cleaning in deionized water was performed in a Class 1000 cleanroom immediately following BCP. The samples were then methanol (electronic grade) rinsed to displace water from the surface before being placed on a filtered laminar-flow bench in the cleanroom for a few minutes to dry.

More than 20 samples were studied, and they exhibited inconsistent FE performance and often a large number of FE sites [14]. Through trial and error, the preparation and handling procedure was significantly modified. The performances from the final set of samples are illustrated in Table 1, with a consistent 0 or near 0 emitter density achieved at ~140 MV/m. The emitters identified in this series of tests are all external particles. SEM picture of a selected emitter is shown in Figure 2. The established procedures, as listed below, proved critical in achieving the final results.

- Material inspection: choose Nb sheet free of scratches and pits using examination lens.
- Sample machining: use a designated clean area, use only plastic fixtures to minimize surface damage, change machine tools frequently to avoid embedding impurities from dull tools.
- BCP: avoid any contact with sample surfaces during BCP and sample removal from bath. Stirring of the acid is often necessary.
- Rinse and transfer: avoid any contact with the surface. Frequently replacing water during ultrasonic cleaning may be necessary. Minimize air exposure in Class 1000 cleanroom after drying.
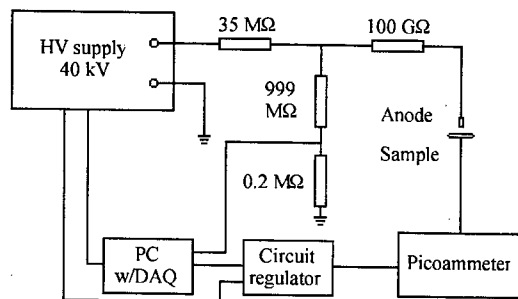
Figure 1: Experimental circuit diagram.

Table 1: FE results at ~140 MV/m scanning field from the final set of BCP-etched samples. (Indicated fields are the fields that yield 2-nA FE current. The scan area for each sample is 25-mm diam. #75-2 (300 μm), for instance, is for sample #75 after the 2nd surface removal, and the combined removal is 300 μm.)

Tests	No. of field emitters
#75-1(250 μm)	1 [35 MV/m (Nb, Fe, Ti, Ca)]
#75-2(300 μm)	2 [99 MV/m (Nb), 103 MV/m (Nb)]
#72-1(250 μm)	0
#72-2(300 μm)	0
#76-1(250 μm)	0
#81-1(200 μm)	0
#83-1(200 μm)	0

Another set of samples was BCP-etched, and then electropolished to remove an additional ~40 μm from the surface. The electropolishing (EP) method developed by Siemens, often used for Nb cavities [15], is used here for samples. The electrolyte formula consists of 850-ml sulfuric acid (96%) and 100-ml hydrofluoric acid (40%). Rinse and drying was done in the same way as previously described. Table 2 shows the FE scan results. Compared to the surface conditions obtained by BCP, the resulting Nb surface is very smooth at grain boundaries [16]. The only emitter found in these tests, which caused a vacuum microdischarge, is an external particle containing Nb, Fe, and Cr. Its SEM picture is shown in Figure 2. As with
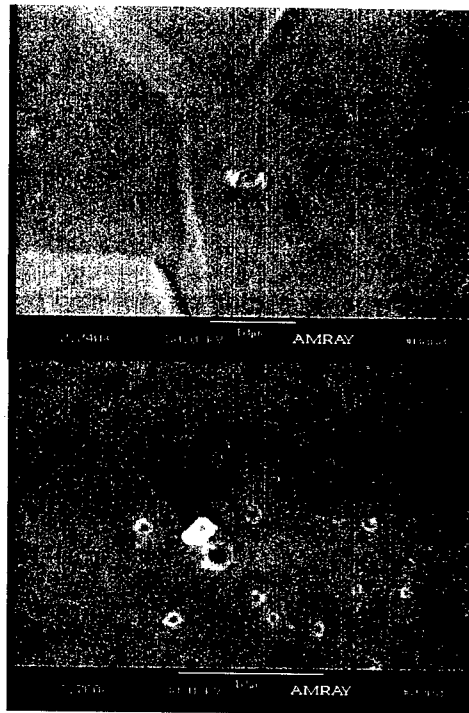
Figure 2: SEM photographs of emitters. Top: #75-1 (site 1), BCP-etched, containing Nb, Fe, Ti, Ca, E=35 MV/m. Bottom: #65-4, electropolished, containing Nb, Fe, Cr, E=105 MV/m. The craters are caused by microdischarge.

Table 2: FE results at ~140 MV/m scanning field from electropolished samples.

Tests	No. of field emitters
#65-4 (440 µm by BCP + 40 µm by EP)	1 [105 MV/m (Nb, Fe, Cr)]
#61-1 (330 µm by BCP + 40 µm by EP)	0
#63-3 (410 µm by BCP + 40 µm by EP)	0

BCP-processed samples, this emitter may have been a contaminant deposited from stainless-steel machining tools based on its composition. Other possible sources for the remaining emitters are dust particles from inside the vacuum chamber and airborne dust particles in the cleanroom. The emitter density is similar for BCP and electropolished samples, and no difference caused by chemistry has been observed. An intrinsic FE limit imposed by grain boundary or native material impurity has not been observed up to 140 MV/m.

EFFECT OF DRYING PROCESSES

For cavities, different labs have employed various approaches for drying after standard processing, e.g., using filtered N_2 gas to blow dry, pumping out the vapor while applying heat, air-drying at Class 10 cleanroom with or without methanol/ethanol rinse. Among them, air-drying without methanol/ethanol rinse raised the concern that water may attract dust, react with residual chemicals, produce acid by dissolving carbon dioxide from air and cause corrosion, any of which could create FE sites. Therefore, a comparative study was done to investigate the effect. Three samples were BCP-etched, ultrasonically rinsed (UR), then methanol rinsed (MR) as previously described and then scanned for FE. Subsequently they were subject to high pressure water rinse (HPR)[17] before methanol rinse and a short air-drying in Class 10 cleanroom. Finally they were high pressure rinsed again and placed in Class 10 for an extended period without methanol rinse. The results, as shown in Table 3, indicated that no significant degradation in FE is observed by slow air-drying in Class 10, provided the time duration can be controlled to be as short as possible. However, this conclusion is not expected to be applicable to a less clean environment, for instance Class 1000 or even Class 100, due to airborne dust. EDS didn't detect any foreign elements at these micron sites possibly due to its relatively large probing depth of several µm.

Table 3: Number of FE and microdischarge sites identified by 140 MV/m scan for study of drying processes.

Samples	UR+MR	HPR+MR	HPR+ n hrs. in Class 10
#71	N/A	0	1 (67 hrs.)
#72	1	0	1 (67 hrs.)
#84	1	2	4 (90 hrs.)

SUMMARY

We have observed no significant difference in FE performance from BCP-etched and electropolished Nb samples, nor an intrinsic FE limit imposed by grain boundary or native material bulk impurity, up to 140 MV/m. Minimizing FE lies in minimizing contamination to Nb throughout the machining, chemistry and handling processes, as illustrated by this work. Extended air-drying in Class 10 cleanroom without methanol rinse didn't significantly degrade FE performance, however, this conclusion may not be applicable to a less clean environment.

REFERENCES

[1] H. Padamsee, J. Knobloch, and T. Hays, *RF Superconductivity for Accelerators* (Wiley and Sons, New York, 1998).

[2] *Proc. of the 7th Workshop on RF Superconductivity*, Gif sur Yvette, (1995).

[3] *Proc. of the 8th Workshop on RF Superconductivity*, Padova, (1997).

[4] R. H. Fowler and L. Nordheim, Proc. Roy. Soc. London A **119**, 173 (1928).

[5] L. Nordheim, Proc. Roy. Soc. London A **121**, 626 (1928).

[6] R. J. Noer, Appl. Phys. A **28**, 1 (1982).

[7] R. V. Latham, *High Voltage Vacuum Insulation* (Academic Press, London, 1981).

[8] P. Niedermann, Ph. D thesis, University of Geneva, 1986.

[9] E. Mahner, G. Muller, H. Piel, and N. Pupeter, J. Vac. Sci. Technol. B **13** (2), 607 (1995).

[10] J. Tan, *Proc. of the 7th Workshop on RF Superconductivity*, Gif sur Yvette, p. 105 (1995).

[11] D. Moffat, et al., *Proc. of the 5th Workshop on RF Superconductivity*, Hamburg, p. 245 (1991).

[12] N. Pupeter, A. Göhl, T. Habermann, A. Kirschner, E. Mahner, G. Müller, and H. Piel, *Proc. of the 7th Workshop on RF Superconductivity*, Gif sur Yvette, p. 67 (1995).

[13] T. Wang, C. E. Reece, and R. M. Sundelin, Rev. Sci. Instru., **73 (9)**, 3215-3220 (2002).

[14] T. Wang, C. E. Reece, and R. M. Sundelin, J. Vac. Sci. Technol. B, (2003), to be published.

[15] H. Diepers, O. Schmidt, H. Martens, and F. S. Sun, Phys. Letter. **37A**, 139 (1971).

[16] R. Sundelin, et al., IEEE Transactions on Nuclear Science **3**, Vol. NS-20, 98 (1973).

[17] P. Bernard, et al., *Proc. of the 1992 European Particle Accelerator Conference*, p. 1269 (1992).

NIOBIUM THIN FILM PROPERTIES AFFECTED BY DEPOSITION ENERGY DURING VACUUM DEPOSITION

G. Wu[†], L. Phillips, R. Sundelin, A-M. Valente

Jefferson Lab*, 12000 Jefferson Avenue, Newport News, VA 23606, USA

Abstract

In order to understand and improve the super-conducting performance of niobium thin films at cryogenic temperatures, an energetic vacuum deposition system has been developed to study deposition energy effects on the properties of niobium thin films on various substrates. Ultra high vacuum avoids the gaseous inclusions in thin films commonly seen in sputtering deposition. A retarding field energy analyzer is used to measure the kinetic energy of niobium ions at the substrate location. A biased substrate holder controls the deposition energy. Transition temperature and residual resistivity ratio (RRR) of the niobium thin films at several deposition energies are obtained together with crystal orientation measurements and atomic force microscope (AFM) inspection, and the results show that there exists a preferred deposition energy around 115eV (the average deposition energy 64 eV plus the 51 V bias voltage).

INTRODUCTION

The successful running of LEP2 using a Nb/Cu technique demonstrated the significant advantages of niobium thin film technology in particle accelerators [1]. Due to the huge cost savings, a future accelerator for muon/neutrino physics calls for accelerating structures made using thin film technology [2]. While the advantages of a thin film cavity make it very attractive to future accelerator applications, the current magnetron sputtered Nb/Cu cavity has much lower Q value comparing to solid niobium cavities at higher field, [3] which limits the broader adoption for particle accelerators.

Different processes are being tried to improve niobium thin films, including post-deposition laser annealing [4], DC post-magnetron sputtering deposition [5], biased DC magnetron sputtering [6] and vacuum arc deposition [7-8].

For the aspect of thin film growth, the higher surface adatom mobility [9] and the vacuum condition are believed helpful to get better film quality as required for superconducting material like niobium. For a niobium thin film on a copper substrate, increasing the substrate temperature is not an option to achieve greater surface adatom mobility. Some processes such as ion-assisted deposition, biased magnetron sputtering, ionized magnetron sputtering, vacuum arc deposition and energetic cluster deposition, are expected to have higher impact energy during film growth, thus increasing the surface adatom mobility. These techniques either require a working gas or entail risk of microparticle contamination and lack good control of the deposition energy.

To take advantage of the high vacuum condition and the capability of controllable deposition energy, the electron cyclotron resonance (ECR) plasma metal ion source is selected as an energetic deposition system to study the niobium thin film deposition at different deposition energies. To better control the substrate quality, sapphire substrate is used for most of the films. For niobium thin films deposited at different energies, transition temperature and residual resistivity ratio (RRR) are measured. Crystal orientation is checked through X-ray diffraction and film surfaces are inspected by an Atomic Force Microscope (AFM).

THE ENERGETIC DEPOSITION SYSTEM

The metal ion source can be achieved by applying ECR to an evaporated or sputtered metal flux [10-11]. To generate refractory metal ions such as niobium inside a vacuum condition, a thermionic electron gun is used to create the neutral niobium flux, and an ECR chamber is used to convert the neutral niobium atoms to niobium plasma. The energetic niobium ions are extracted to a biased substrate [12]. The niobium ion energy distribution under certain plasma conditions is measured by a retarding field energy analyzer at the substrate location. The result is shown in figure 1.

The vacuum pressure before the deposition is as low as 9.0×10^{-8} torr, changes to 1.0×10^{-6} torr during the film deposition in the vacuum chamber and will be significantly lower in the ECR chamber. The majority of the residual gas is hydrogen. The deposition rate averaged 4 Å/s.

TRANSITION TEMPERATURE MEASURED BY AC INDUCTION

The transition temperature is obtained through magnetic shielding ability measured by the AC induction method. Care has been taken to minimize the edge effect and the driven signal is at low voltage magnitude as shown in figure 2 (2 volts over 100 Ω current limiting resistor).

The transition temperature for films deposited at different bias voltages are shown in figure 3. The transition width result is shown in figure 4.
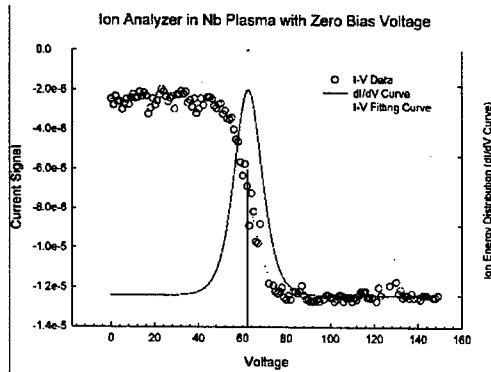
Fig. 1: The ion energy analyzer measurement result for niobium ions at the substrate without bias voltage
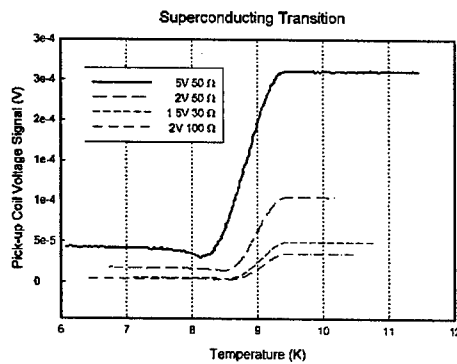
Fig. 2: T_c curve measured by an induction coil set with different driving signal voltage levels.
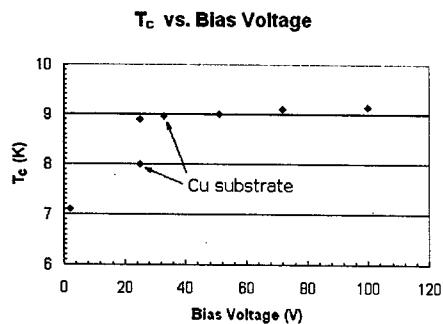
Fig. 3: Bias voltage effect on transition temperature, measured by an inductive method. Substrate is A-cut sapphire unless noted otherwise.
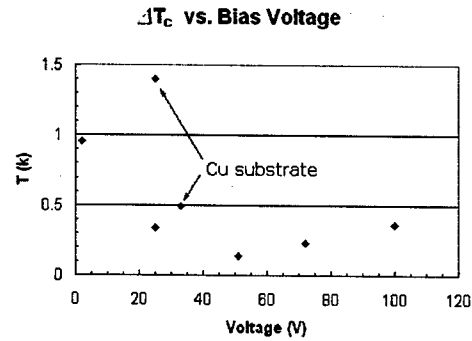
Fig. 4: Bias voltage effect on transition width. Substrate is A-cut sapphire unless noted otherwise.

RRR

The RRR value has been measured with a four-point resistive method and is defined as the ratio of resistivity at 300 Kelvin to the resistivity at 10 Kelvin. Table 1 shows the RRR result together with the film thickness. The lowered RRR values are likely caused by the increased electron resistance by electron boundary scattering in those very thin films [13].

Table 1: RRR and thickness for different films

Film batch started with bias voltage number	RRR	Thickness (nm)
02-SA	2.31	68.2
25-SA	6.8	126
51-SA	2	74.1
51-SA	50.2	235
72-SA	26.7	181
100-SA	4	79

X-RAY DIFFRACTION AND AFM SURFACE INSPECTION

X-ray diffraction has been used on the films. The full width of half magnitude (FWHM) value of the diffraction signal for the Nb-110 crystal plane is shown in table 2.

Table 2. Crystal orientation spread by X-ray diffraction

Film batch started with bias voltage number	Angle FWHM value of X-ray diffraction signal
02-SA	10-15
25-SA	3-4
51-SA	<1
72-SA	5-6
100-SA	5

The film deposited at negative 51V substrate bias was checked by an AFM. The surface morphology shows unusually long narrow grains compared with the round dome-shaped grains seen in films at lower substrate bias voltage.

CONCLUSION

From the results shown in this report, it is concluded that a reasonably high RRR niobium thin film with excellent superconducting transition temperature and width can be achieved through controlled energy deposition in high vacuum. The RRR appears to be more closely related to the film thickness than to the deposition energy. Deposition energy around 115 eV is believed to be the preferred value based on the transition width, the crystal orientation spread, and the AFM results. The AFM surface inspection shows that the surface morphology is affected by the ion impact energy. The X-ray diffraction analysis shows the niobium thin film has a preferred crystal orientation when deposited on sapphire.
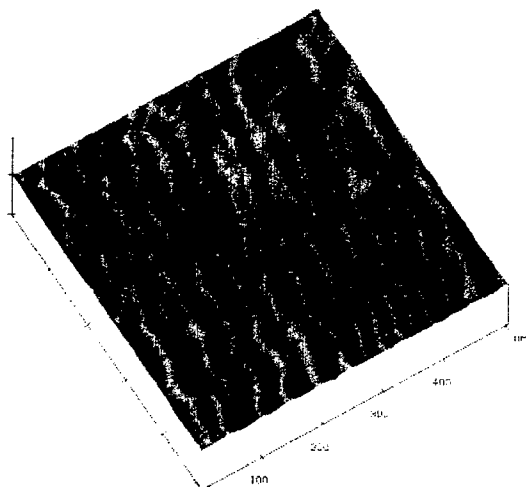
Fig. 5: Long continuous grains of niobium film on sapphire deposited at negative 51 V substrate bias.

ACKNOWLEDGEMENT

REFERENCES

[1] P. Brown, et. al., 9th Workshop on RF Super-conductivity, Santa Fe, (1999), edited by B. Rusnak, Los Alamos National Laboratory, Los Alamos, 1, (1999).

[2] H. Padamsee, 2001 PARTICLE ACCELERATOR CONFERENCE, Chicago, Illinois U.S.A., (2001), edited by P. Lucas, S. Webber, Institute of Electrical and Electronics Engineers, Inc., Piscataway, NJ 08855, (2001).

[3] V. Arbet-Engels, et al., Nucl. Instrum. Methods Phys. Res. A 463, 1-8 (2001).

[4] E. Radicioni, et al., Nucl. Instrum. Methods Phys. Res. A 365, 28-35 (1995).

[5] V. Palmieri, et al., Proc. of 7th workshop on RF superconductivity, Gif-sur-Yvette, 485, (1995), edited by B. Bonin.

[6] K. Zhao, et al., 9th Workshop on RF Super-conductivity, Santa Fe, (1999), edited by B. Rusnak Los Alamos National Laboratory, Los Alamos, 70, (1999).

[7] Y. Igarashi and M. Kanayama, J. Appl. Phys. 57(3), 849-854 (1985).

[8] R. Russo, et al., 10th Workshop on RF Super-conductivity, Tsukuba, Japan, (2001), edited by S. Noguchi KEK, Tsukuba, Japan, (2002).

[9] J. A. Thornton, J. Vac. Sci. Technol. 11, 666 (1974).

[10] W. M. Holber, et al., J. Vac. Sci. Technol. A 11, 2903 (1993).

[11] S. M. Rossnagel, et al., J. Vac. Sci. Technol. B 12, 449 (1994).

[12] G. Wu, et al., 10th Workshop on RF Super-conductivity, Tsukuba, Japan, (2001), edited by S. Noguchi KEK, Tsukuba, Japan, (2002).

[13] H. M. Rosenburg, Low Temperature Solid State Physics (Oxford University Press, 1963)

RF CONTROL SYSTEM FOR ISAC II SUPERCONDUCTING CAVITIES

K. Fong, S. Fang, M. Laverty, TRIUMF, Canada,
Q. Zheng, IMP, China

Abstract

The RF Control system for the superconducting cavities of the ISAC II project is a hybrid analogue/digital system. Each system consists of a self-excited feedback loop with phase-locked loops for phase and frequency stabilization. Amplitude and phase regulation, as well as tuning control, are performed using digital signal processors. Special pulsing circuitry is incorporated into the system for fast punching through multipactoring. This paper describes the RF control system, the characteristics of the feedback loops, and the experience gained in operating this system.

INTRODUCTION

The design of the RF system is based on a self-excited oscillating loop, where the self-excited frequency is determined solely by the loop phase. The system oscillates at a frequency that results in a loop phase that is an integer multiple of $360°$. This frequency is locked to an external reference by regulating the phase shift within the self-excited loop. The system is operated at a coupling strength of approximately 100 to have a manageable bandwidth. The phase difference between the input and output of the cavity is used to drive a mechanical tuner to minimize the drive power required.

RF CONTROL SYSTEM

A block diagram of the RF control system is presented in Fig. 1. The system consists of two main parts: The first is the RF Module, where the RF signal is processed and converted into baseband. The second is the DSP Module, where the baseband signal is converted into digital form and processed by a Digital Signal Processor, then re-converted back into analogue form for modulation of the RF module. Up to 4 pairs of modules can be housed in a C-size VXI mainframe, which is controlled by a PC via an IEEE 1394 interface.

System Hardware

The RF control system hardware consists of a rack mounted PC, a VXI slot zero control module, the RF Module, and the DSP Module housed in a VXI mainframe. These function together to provide three main regulation loops: the amplitude loop, the quadrature phase/frequency loop, and the tuning loop. The primary amplitude detector is a synchronous demodulator, in which an internal PLL supplies an amplitude-stabilized reference to be multiplied with the RF input. The product is filtered, sampled and digitized at 40 k samples/sec and processed by a Motorola DSP56002 DSP. A lower than normal sampling rate is used because of the long time constant of the cavity when it is superconducting. The DSP is configured as a Proportional-Integral controller,

providing amplitude regulation. The internal PLL output is also compared with an external master frequency source using a square wave phase/frequency detector from Analog Devices (AD9901). A different channel of the same DSP processes this phase error. The output of this channel is used to control the quadrature part of the amplifier output, providing phase regulation. Another phase detector measures the phase lag of the cavity. An edge-triggered JK flip-flop, which is constructed out of 8 ECL NAND gates, is used for this purpose. The phase shift is processed by a separate DSP to drive the mechanical tuner and keep the cavity in tune with the external master frequency. The complete tuning system is described in another paper[1].
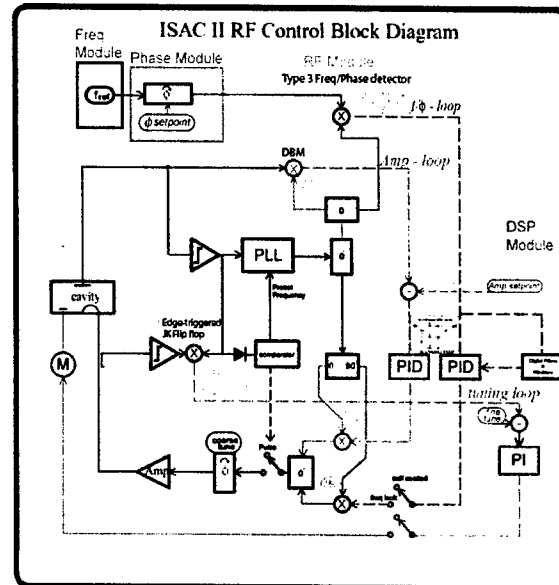
Figure 1. Block Diagram of RF Control

During pulsing on power-up, the phase detector in the internal PLL is disconnected from the VCO. The VCO is then driven directly by a voltage source so that the output frequency matches the resonant frequency of the cavity. This frequency is pulsed by hardware with a pulse width of 256 µs and a period of 35 ms. The coupling loop is moved inward to lower the loaded Q in order to decrease the rise time of the voltage. A Schottky diode detector provides fast cavity voltage detection. When the cavity voltage rises above the multipactoring threshold, the diode detector enables the PLL and switches the system into CW mode automatically, as illustrated in Fig. 2.

A rack-mounted PC provides supervisory control and data acquisition. Communication between the PC and the VXI mainframe is done via a FireWire (IEEE 1394) interface. A National Instruments GPIB interface card

enables the PC to act as a controller for other GPIB-enabled instrumentation, including a frequency counter, a RF power meter and a digital oscilloscope.
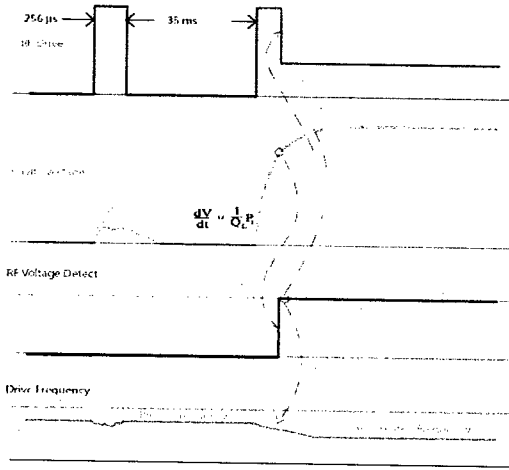
Figure 2. Power-up sequence

System Software

There are three main functions of the system software:
- Control of the superconducting cavity.
- Data acquisition and calculation.
- Communication with the central control system.

The control system can be sub-divided into supervisory tasks and online feedback control. Supervisory tasks, which require low signal bandwidth but relatively complex decision logic, are performed with the rackmount PC. The supervisory PC performs the tasks of setting feedback loop parameters, local status display, and communication with the EPICS-based master control system. These high level controls are written using 32 bit C++ with Windows API's.

The low-level feedback control requires higher signal bandwidth and is performed with DSPs and FPLAs. The DSPs perform digital filtering, open and closed loop regulation, output limiting, low-level decision making as well as exchanges of status information with the supervisory PC. For speed and compactness this software is hand coded in assembler. This code is stored in flash EEPROM, and can be changed remotely. Other logic functions that require still faster response are performed with FPLA's. These include power-up sequencing and fault-detection.

Communication between the PC and the central control system is done via an EPICs IOC server running in the same PC.

SYSTEM MODEL

Using a similar method as in [2], but ignoring beam loading and assuming perfect alignment in static loop phase, we get a transfer function representation of the system:

$$\begin{bmatrix} \delta V \\ \delta \Omega \end{bmatrix} = \begin{bmatrix} G_{aa} & G_{ta} \\ G_{a\omega} & G_{t\omega} \end{bmatrix} \begin{bmatrix} \delta v_i \\ \delta v_q \end{bmatrix} \tag{1}$$

where

$$G_{aa} = \frac{\gamma}{1 + \tau s}, \qquad G_{ta} = 0,$$

$$G_{a\omega} = -\frac{1}{v_i} \frac{\Omega}{(1 + \tau s)}, \qquad G_{t\omega} = \frac{1}{v_i \tau} \equiv \eta,$$

$$\tau = \frac{2Q}{\omega_c} \text{ is the time constant of the cavity,}$$

$\Omega = \omega - \omega_c$ is the detuning of the cavity,

with γ is the voltage transformation ratio, ω_c the natural resonance frequency of the cavity and Q the loaded cavity quality factor. Eq. 1 states that while the cavity voltage is a simple lag response to the input voltage, the cavity frequency varies instantaneously to the input phase.

Fa Gaa	Amplitude regulation loop
1/s Fo Gtω	Quadrature loop
1/s Fo Gta Fa Gaω	Cross talk due to misalignment
Ft Gu	Tuning loop
-Ft Gu	Tuning loop
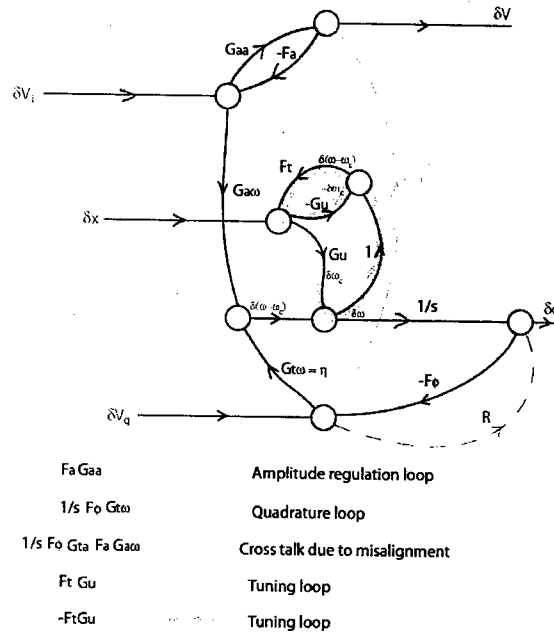
Figure 3. Signal Flow Graph of the Amplitude, Phase and Tuning Loops

Eq. 1 is used to form the signal flow graph of the complete RF control system in Fig. 3, where F_a, F_ϕ and F_t are the amplitude, quadrature and tuner feedback coefficients, respectively. Also the sensitivity of frequency to tuner movement is given by

$$G_u = \frac{\partial \omega_c}{\partial x}$$

and depends only on the geometries of the cavity and the tuning mechanism. From the figure, since the phase-to-

amplitude cross coupling term G_{ta}, drawn in lighter color, is zero, the amplitude loop is independent from the phase and tuning loops.

From the signal flow graph we get the various closed loop gains of the feedback system:

$$\frac{\delta V}{\delta v_i} = \frac{G_{aa}}{1 + F_a G_{aa}} \approx \frac{1}{s\tau + 1 + F_a},$$ (2)

$$\frac{\delta \phi}{\delta v_q} = \frac{\eta(1 + F_t G_u)}{s + F_\phi \eta(1 + F_t G_u)},$$ (3)

$$\frac{\delta \phi}{\delta x} = \frac{G_u}{s + F_\phi \eta(1 + F_t G_u)},$$ (4)

$$\frac{\delta v_q}{\delta x} = \frac{F_\phi G_u}{s + F_\phi \eta(1 + F_t G_u)}.$$ (5)

From Eq. 2, 3 and 4 we see that if one requires zero steady-state errors for both amplitude and phase in response to step inputs, then one requires at least a pole at the origin, i.e. an integration, in both F_a and F_ϕ. To minimize RF power, one also requires the steady-state error for quadrature drive be zero. Given that F_ϕ has one integration, Eq. 5 then requires F_t to have also one integration. Thus PID controllers are used in the amplitude, phase and tuner loops.

SYSTEM PERFORMANCE

Fig. 4 shows the Bode plot of the amplitude loop. The feedback parameters are adjusted such that the dominant pole due to the cavity response is almost cancelled by the zero from the proportional gain. The result agrees with that predicted by theory.
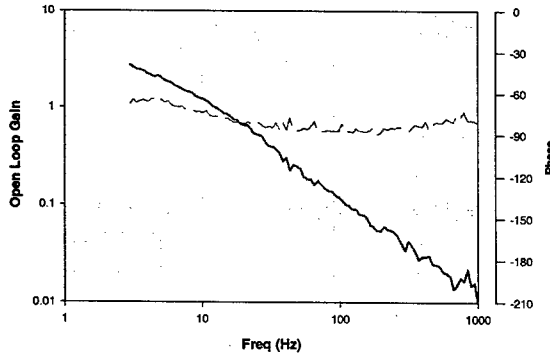
Figure 4. Open Loop Frequency Response for Amplitude Loop

Fig. 5 shows the Bode plot for the quadrature phase loop without tuner feedback. At low frequencies the result is in agreement with theory, but at higher frequencies it shows the behavior of a non-minimum phase system. System stability is seriously degraded with a zero on the

right hand side of the complex plane at 100
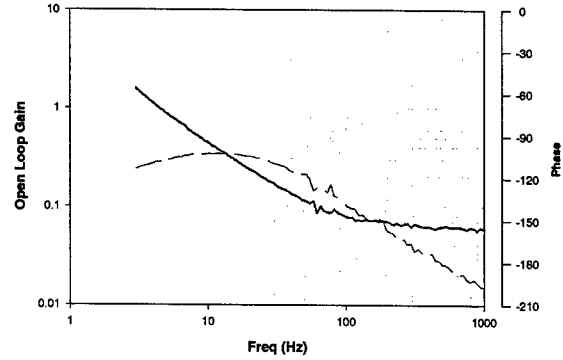
Figure 5. Open Loop Frequency Response for Phase Loop showing Non-minimum phase characteristics

Hz. A crystal ladder network with a Q of 10^5 was used in trying to locate the source of this zero, which was not predicted by theory. Referring back to Fig. 3, if we include the leakage path R, then the phase open loop response is

$$\left(\frac{1}{s}\eta + R\right)F_\phi.$$ (6)

The residue R is found empirically to have the form

$$R = -Av_i e^{ik},$$ (8)

where $A \geq 0$ and $k \approx 0$ are variables that depends on the layout of the RF Module and cabling, resulting in a zero on the right hand side of the complex plane at

$$s = \frac{1}{\tau A}.$$ (7)

To prevent instability in operation due to this zero, we have to operate the phase feedback loop at a lower feedback gain and resulted in a reduced bandwidth.

CONCLUSION

The prototype RF control system for the superconducting cavity has been operated in many cold tests. It has been found to be able to provide amplitude, phase and tuning regulation to within the specifications. The power-up circuit has provided reliable way to punch through multipactoring, even when the cavity is not well conditioned. A parasitic leakage path in the phase feedback loop has caused a reduced operational bandwidth and is being investigated.

REFERENCES

[1] T. Ries et al , "A Mechanical Tuner for the ISAC-II Quarter Wave Superconducting Cavities", This proceeding.

[2] J.R. Delayen, "Phase and Amplitude Stabilization of Beam-Loaded Superconducting Resonators", Proc. Linac 92, p. 371.

MAGNETOSTRICTIVE TUNERS FOR SRF CAVITIES[1]

A. Mavanur[2], C-Y Tai, C. H. Joshi, Energen, Inc. Lowell, MA 01854 USA
T. Grimm, NSCL, MSU, E. Lansing, MI 18824 USA

Abstract

Energen, Inc. has demonstrated two new tuners to address slow and fast SRF cavity tuning requirements. The slow tuner uses a linear stepper motor to deliver high-force, sub-micron linear motion of tens of millimeters at cryogenic temperatures resulting in hundreds of kilohertz tuning range. A separate actuator delivers fast tuning capability for microphonics and Lorenz detuning compensation. These tuning systems are based on magnetostrictive actuators that can deliver high force precision motion at cryogenic temperatures. Performance and capabilities of this prototype SRF cavity tuner will be reported.

1 BACKGROUND

Since 1997, Energen has been working with engineers and scientists at Jefferson Laboratory, The National Superconducting Cyclotron Laboratory and the Spallation Neutron Source to develop and demonstrate several tuning mechanisms for elliptical, superconducting RF cavities.

Energen has built a fine-tuning mechanism for a Jefferson Lab SRF cavity, which provided 2 kHz of tuning range on a 1497 MHz resonant frequency. Details about the tuner and it performance were reported previously[1].

Subsequently, Energen began developing a new tuning system that would replace the entire mechanical tuner system and eliminate the rotating mechanical feed through the vacuum system of the cryomodules. The details of the tuner design are reported in a paper presented at PAC01[2].

The present paper reports on the detailed testing of that tuner and its capabilities along with a new fast tuning actuator that is used for active microphonics control and Lorentz detuning compensation. The technology underlying all of these devices is cryogenic magnetic "smart" materials.

1.1 Magnetic "Smart" Materials (KelvinAll)

Magnetic "smart" materials (MSM) change their shape (elongate) in a predictable and reversible manner when exposed to a magnetic field. The amount of elongation at saturation is the most fundamental measure of a magnetostrictive material.

The most widely available MSM, $Tb_{0.3}Dy_{0.7}Fe_2$ (Terfenol-D) does not work at cryogenic temperatures

because of temperature-dependent changes in its magnetic characteristics. For cryogenic applications, the U. S. Navy has developed a TbDyZn alloy which exhibits much higher elongation than $Tb_{0.3}Dy_{0.7}Fe_2$ but has a Curie temperature around 150 K. TbDyZn is only available in small quantities through custom fabrication and is therefore, very expensive.
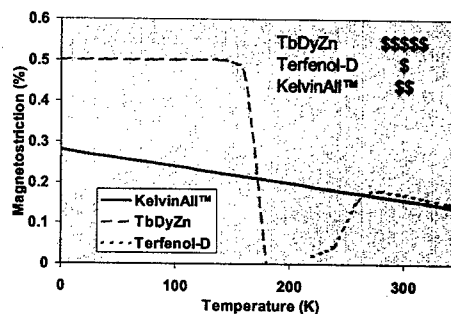
Figure 1 - Temperature dependent magnetostriction for several materials and their relative costs.

Through extensive materials research and development, Energen has developed KelvinAll, a new MSM that has excellent performance over a broad range of temperature from above room temperature to near absolute zero. Figure 1 shows a comparison of the saturation magnetostriction of the three MSM materials[3].

1.2 Actuators & Linear Motors

In its simplest configuration, an MSM-based actuator consists of a rod of MSM surrounded by a coil. When current passes through the coil, the rod elongates and the motion can be used to do useful work. These devices are ideal for applications where short stroke, high force and rapid response are needed.

Linear motors are capable of delivering long range high force motion. Detailed information about the stepper motor operation has been presented previously [4]. The control electronics provide manual and computerized control capability for the linear motors.

2 SLOW TUNER SYSTEM

2.1 Cavity Interface

Under a Cooperative R&D Agreement (CRADA) between Energen and Jefferson Laboratory, Energen

1407

obtained a 5-cell SRF cavity from Jefferson Laboratory for the testing of the tuner. The Energen tuner is designed to be a replacement for the mechanical tuner that is currently used providing the added benefit of better tuning resolution.

A drawing of the tuner connected to the cavity is shown in Figure 2 below. The end cells of the cavity are attached to cell holders. The inactive cell holder (shown on the right side) is rigidly connected to the end plate by four connecting rods. The active cell holder (shown on the left side) is free to move axially. The end plate and the active cell holder are connected to a lever arm by stainless steel wire ropes. The linear stepper motor is mounted on a
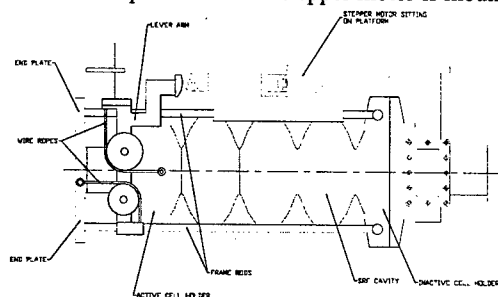
Figure 2 – Geometry of the Energen SRF cavity tuner.

platform beside the SRF cavity. When activated it pulls a cable connected to the lever arm. The rotation of the lever arm pulls the active cell towards the endplate stretching the cavity along its axis thereby changing its resonant frequency.

2.2 Advantages

This type of tuning system has several distinct advantages, it:

- Eliminates sliding or rotating penetrations through the vacuum cryostat
- Simplifies cryostat design and assembly
- Delivers both coarse and fine tuning in a single device
- Can be used for fast tuning (microphonics)
- Locks in position when powered off

2.3 Measurements

The tuning range of the cavity was tested at 77 K in a liquid nitrogen bath at Energen facilities. For these tests, the SRF cavity was evacuated to 10 mTorr. The resonance was measured using a network analyzer, which indicated a resonance at 1,497 MHz. The linear motor was then operated and the frequency shift was measured as a function of lever displacement. As the motor advances, the force required to elongate the cavity increases. This result of the increased load on the stepper motor was a decrease in the step size. At the end of its travel, the step size is reduced to zero. The force

generated by the stepper motor is estimated to be approximately 2600 N.

Figure 3 shows the resonance peak shift near 1497 MHz at the beginning of the test and after the motor was advanced to the farthest distance. The frequency shift of 160 kHz is equal to the capabilities of the existing Jefferson Laboratory mechanical tuner.
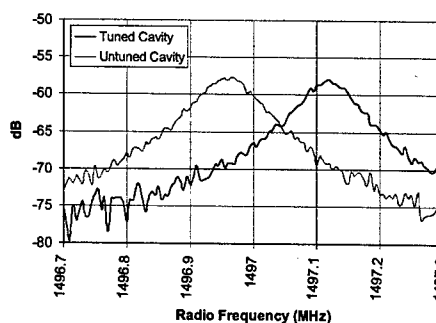
Figure 3 - Resonant frequency range of the slow tuner mechanism.

The slow tuner system was tested at 4 K at the National Superconducting Cyclotron Laboratory located at Michigan State University in a 35 in (0.89 m) diameter Dewar. There were some difficulties encountered during the tests such as vacuum leaks and a limited time available for conducting the tests. During the testing, were able to successfully demonstrate that the tuner system is capable of changing the resonant frequency of the cavity by 60 kHz. When the tuner is adjusted, there is a slight relaxation that occurs in the tuner system causing a frequency shift of approximately 25 Hz. Thereafter, the tuner demonstrated a stability of better than 5 Hz on a resonant frequency of 1497 MHz. – 3.3 ppb.

3 FAST TUNER

3.1 Actuator Design

A short stroke fast responding high force actuator is needed to damp out vibrations due to microphonics and Lorenz detuning. Figure 4 shows the actuator designed for this purpose. The MSM and the superconducting coil are enclosed in a laminated Silicon-steel housing. The coil
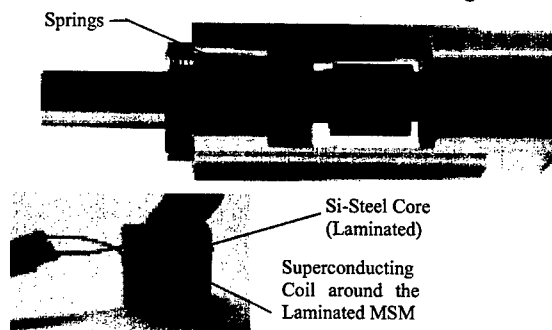
Figure 4 – The Fast tuner

1408

is made of Nb_3Sn as it has a comparatively high critical temperature (18 K), low filament coupling and hysteresis losses. The core concentrates the magnetic flux in the MSM and provides partial magnetic shielding as well. A superconducting niobium shell, not shown in Figure 4, shields the entire actuator. The MSM and the silicon steel housing are laminated to reduce eddy current heat generation and to achieve fast response. Belleville springs are used to preload the MSM.

Analyses of the magnetic design were performed on the active element to optimize the geometry of the coil, the Si-Steel core and the flux distribution in the MSM. The geometric configuration was then refined using 3-D magnetic analysis, to get more accurate field distribution plots, stray magnetic field numbers and the coil inductance.

A superconducting shield is used to minimize stray magnetic fields. The field leakage values obtained from the 3-D analysis are used as inputs in the Bean's model to determine the thickness of superconductor required to shield the field.

Since the fast tuner will be installed in the vacuum space surrounding the helium vessel, providing a conduction path for the small amount of heat generated in the actuator is critical to stable operation. Heat generated in the actuator is due to 1) eddy currents 2) AC operation of the coil 3) hysteresis losses in magnetic materials manifested as heat. The heating due to eddy currents was estimated using a 3-D dynamic analysis and is calculated to be 0.04 Watts. The heating in the coil and due to hysteresis losses is estimated to be 0.05 W and 0.01 W respectively. So the total heat generated is of the order of 0.1 W

3.2 Laboratory Testing

.The fast tuner was tested under the operation conditions for stroke, ramp rate and stray magnetic fields. Figure 5 is a plot of the fast tuner stroke verses the input current and shows the linearity of the actuator.

Figure 6 shows the current ramp rate in the coil. It is seen that the current can be ramped in the coil from 0 to maximum in the required 130 Microseconds.

An open ended Niobium cup is used to shield the stray magnetic field. The magnetic field at a distance of 30 mm from the surface of the actuator is found to be 50 mG. Efforts are on to fabricate a more complete Niobium enclosure to bring down this number. Tests are also being performed to determine the heat generated.

3.3 Advantages

The advantages of the fast tuner include:
1) Very fast response and can be operated at frequencies as high as 2 kHz
2) Sub-micron precision motion.
3) High Force generation
4) Can be operated under extreme conditions
5) Long life.
6) Compact reliable and robust
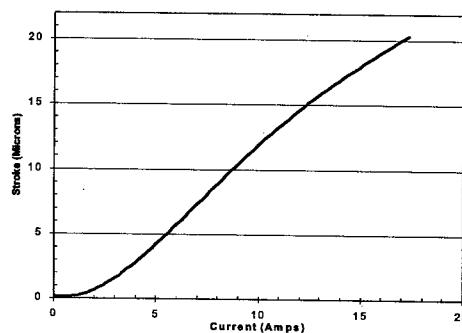
Figure 5: The linearity of the fast tuner
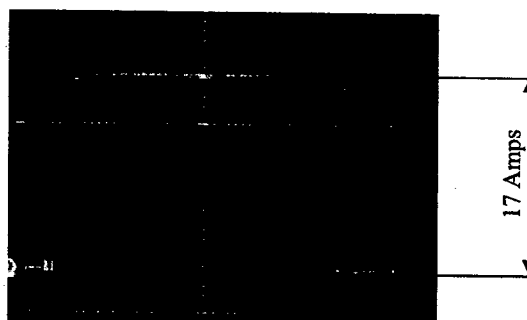
Figure 6: Response of the coil to a step input.

4 FUTURE DESIGNS

Future tuner designs where in both the fast and slow tuners are integrated into a complete tuning system are being considered. More compact fast tuners are being designed and fabricated for custom applications. The smallest one is 62mm x 50mm and 22mm deep. Smaller configurations are possible as the active element is only 25 mm wide, 26 mm high and 17 mm deep.

5 CONCLUSIONS

Energen Inc. has demonstrated a comprehensive tuning system performing both slow and fast tuning for SRF cavities. High-force, compact, magnetostrictive actuators are capable of precisely positioning stiff objects. Reliable and robust operation under extreme conditions of temperature and pressure has been demonstrated.

REFERENCES

[1] Joshi, et al, "A Magnetostrictive Tuning Mechanism For SRF Cavities," PAC 1999.
[2] Joshi, et al, "Progress In The Development Of SRF Cavity Tuners Based On Magnetic Smart Materials," PAC 2001.
[3] http://www.EnergenInc.com
[4] Joshi et al, "High Force, Precision Positioning Using Magnetic Smart Materials," RF Superconductivity Workshop, Santa Fe, NM, Nov. 1-5, 1999.

FABRICATION, TEST AND FIRST OPERATION OF SUPERCONDUCTING ACCELERATOR MODULES FOR STORAGE RINGS

S. Bauer, M. Pekeler*, M. Peiniger, H. Vogel, P. vom Stein,
ACCEL Instruments GmbH, D-51429 Bergisch Gladbach, Germany
S. Belomestnykh, H. Padamsee, P. Quigley, J. Sears,
Cornell University, Ithaca, NY 14853, USA

Abstract

The production of 6 superconducting 500 MHz modules for Cornell University, the Taiwan Light Source and the Canadian Light Source is almost finished. We summarize the vertical cavity test results and report on cold module tests. Operational experience with the delivered modules is also presented. Furthermore a 1.5 GHz superconducting Landau module is under production at ACCEL. The status of this project will be discussed

1 INTRODUCTION

ACCEL is currently producing superconducting 500 MHz modules for Cornell University [1], the Taiwan Light Source SRRC [2] and the Canadian Light Source CLS [3]. The design of that module was developed at Cornell. The possibility to accelerate high current at high gradients together with a very effective damping scheme of the higher order modes makes them attractive for all kind of high current storage ring applications [4].

Figure 1: Schematic view of the superconducting module

ACCEL also supplies the SRF Electronics and the cryogenic distribution boxes to SRRC and to CLS.

Figure 2: First superconducting accelerator module for the Taiwan Light Source with valve box (left) and SRF electronics (right)

2 STATUS OF PRODUCTION

- All single components are produced
- All cavities passed successfully the vertical test.
- All RF windows have been successfully tested.
- One module for Cornell University has been successfully tested with high power RF and is operating in the synchrotron CESR successfully for more than 8 months. The second module for Cornell University is delivered and will be tested with high power RF within the next month.
- One module for Taiwan Light Source has been tested at Cornell University with high power RF. The gradients reached during this test exceeded the design specifications by more than a factor of two. However it was discovered, that this module can not be operated with sufficient high power, because it has the wrong external Q factor of the input coupler. We are currently investigating the source for the wrong external Q.
- One module for the Canadian Light Source was recently delivered and is currently under test at the CLS.
- The electronics for all the 6 modules are finished.
- The valve boxes for the Taiwan Light Source and the Canadian Light Source are delivered.

Figure 3: Assembly area of the SRF modules at ACCEL. In the upper right part the clean room class 100 can be seen where the modules need to be assembled in whenever the cavity vacuum is touched.

3 CAVITY TESTS

The infrastructure at ACCEL allows state of the art cavity preparation. A closed loop chemistry plant (BCP 1:1:2) and a high pressure water rinsing system is available and shown in Fig. 4.
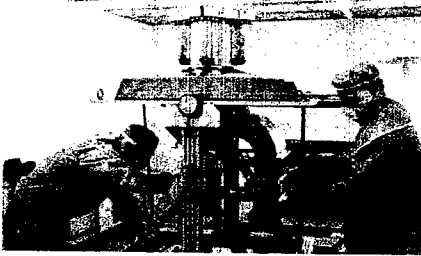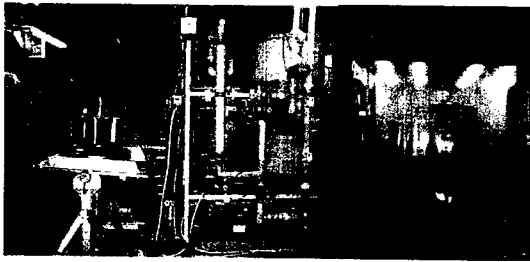
Figure 4: Preparation of a 500 MHz cavity for a vertical test at ACCEL. Up left: closed loop BCP, up right: high pressure rinsing, below: clean room assembly
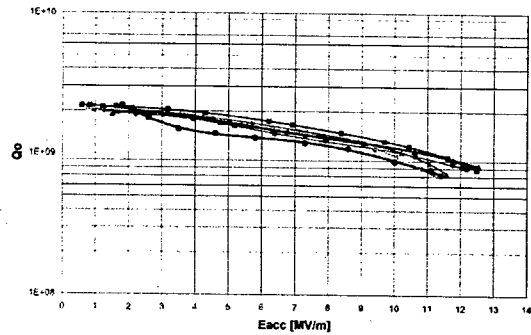
Figure 5: Cavity test results

Figure 5 shows the test results of the six cavities produced for Cornell, SRRC and CLS. All Cavities reached more than 11 MV/m. The highest field observed was 12.6 MV/m. All cavities were limited by available RF power (200 W). No quenches were observed. It is remarkable that the results were achieved consecutive without a unsatisfactory result in between. This indicates a very reliable cavity preparation.

4 MODULE SHIPMENT

For the transportation of the modules from ACCEL to our customers overseas a special shipping frame was designed. It protects the modules from shocks and vibrations during transportation by air and truck. Additionally all transports are controlled by shock detectors attached to the module.
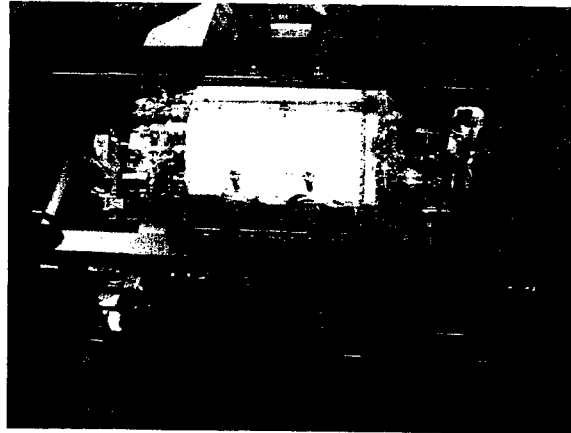
Figure 6: Completed module installed into shipping frame.

5 MODULE TEST AND OPERATIONAL EXPERIENCE

The first delivered module for Cornell University was tested at Cornell University with high power RF in a dedicated test area before installation into the storage ring. After movement to the processing area the module was cooled down and the RF power was increased

continuously. By measuring the cryogenic losses of the module, the quality factor could be calculated for different field levels. The test result is summarized in figure 7 and compared to the vertical test result of the cavity. A field of 9 MV/m was measured with a Q above 1E9. In pulsed mode fields up to 13.3 MV/m were measured.
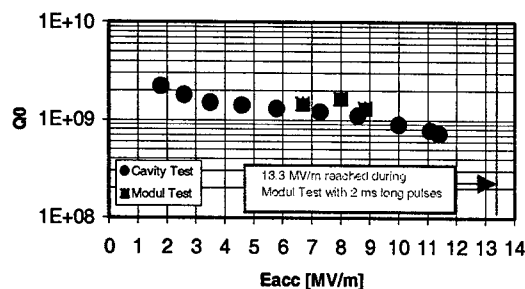
Figure 7: Test result of Cornell module #1

The module performance was comparable with the vertical test result. Due to safety reasons, the fields were limited to below 9 MV/m in cw operation with high power RF. After high power RF test the module was installed into the storage ring and is working there for more than 8 months now without any problems.

6 SUPERCONDUCTING LANDAU ACCELERATOR MODULE

ACCEL currently fabricates a superconducting 3rd harmonic accelerator module for BESSY II [5]. The cavity design is based on a scaled CESR Phase- II cavity operating at 1.5 GHZ.
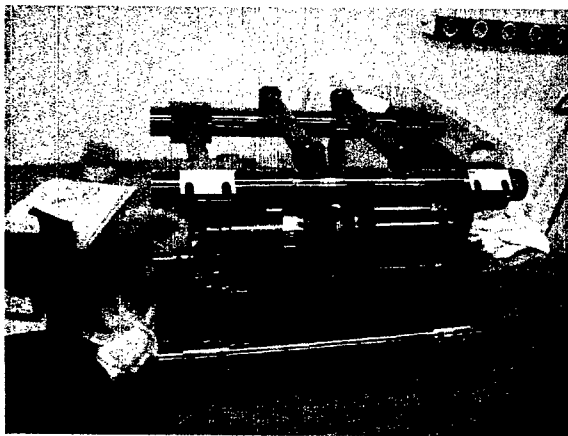
Figure 8: Landau Cavity in handling frame
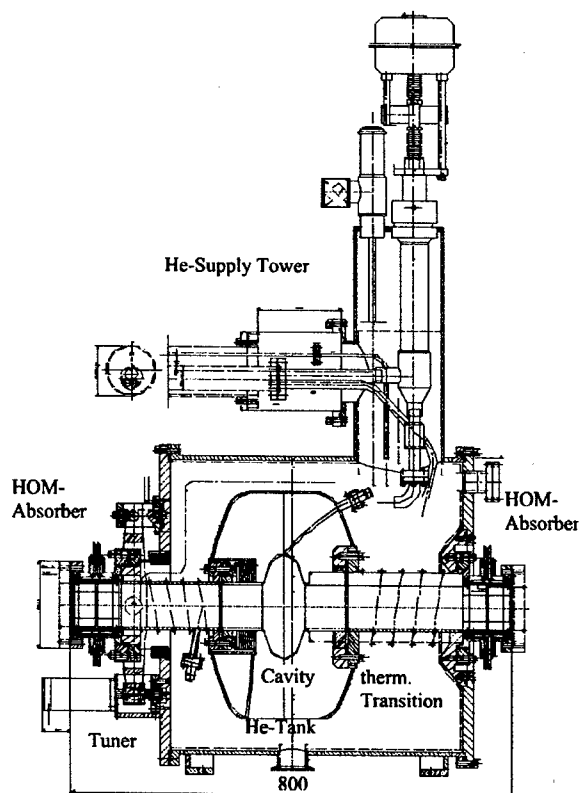
Figure 9: Layout of the Landau Module

The cavity provides strong damping of higher-order modes by ferrite loads on the beam tubes. A new module, constrained to fit into a very limited space at BESSY, was designed.

Meanwhile the fabrication of all major subcomponents is finished. The reworked cavity (s. fig. 8) was submitted to a cold test at DESY reaching 7 MV/m limited by rf power.

REFERENCES

[1] R.C. Sah, et al.,"Status of the Taiwan Light Source", PAC 99, New York, April 1999.

[2] S. Belomestnykh, et al., "Operating Experience with Superconducting RF at CESR...", 9th Workshop on RF Superconductivity, Santa Fe, Nov. 1999

[3] H.Padamsee, "The Future of SRF in High Current Rings", 9th Workshop on RF Superconductivity, Santa Fe, Nov. 1999

[4] Les Dallin, "The Canadian Light Source", PAC 2003, Oregon 2003

[5] P. vom Stein et al., "A Superconducting Landau Accelerator Module for BESSY II", PAC 2001, Chicago 2001

BEAM PHOTOGRAPHY: A TECHNIQUE FOR IMAGING DARK CURRENTS

P. Gruber*, CERN, Geneva, Switzerland
Y. Torun, Illinois Institute of Technology, Chicago, IL, USA

Abstract

Dark currents are unwanted electron currents that stem from surface electrons emitted in rf cavities and accelerated in their electric field. This paper describes a novel technique to produce a 2D-image of dark currents and presents some results.

Ordinary black and white photographic paper was exposed to dark current electrons coming out of an 805 MHz cavity in the Lab G facility at Fermilab. This is a copper pillbox cavity in a 2.5 T solenoidal field parallel to the electric field. Thin rf and vacuum windows allow the electrons to exit the cavity. Due to the focusing effect of the magnetic field, a sharp picture of the dark currents sources is obtained. Single emitters, surrounded by regions of virtually no dark current, can be clearly identified.

INTRODUCTION

Dark currents are formed by electrons which are released from a cavity surface through field emission and which are subsequently accelerated in the cavity's electric field.

Dark currents have been studied in the context of the international Muon Ionization Cooling Experiment (MICE)[1], which is an accelerator R&D experiment for ionization cooling at a future neutrino factory[2]. Ionization cooling is a two step process in which muons are first sent through an absorber (mostly liquid hydrogen) in order to reduce both the transverse and the longitudinal momentum. In the second step, the particles are re-accelerated in an electric field parallel to the beam axis and the longitudinal momentum is restored. The net effect is a reduction of the beam divergence and – as the focusing is kept constant – a reduction of the normalized emittance.

MICE has three main components: an incoming spectrometer, the cooling apparatus with absorbers and cavities, and an outgoing spectrometer. The emittance before and after cooling is measured on a particle-by-particle basis in the spectrometers. The layout of MICE in Fig. 1 shows how close the sprectrometers are to the cavities. In fact, they are only separated by the 35 cm of liquid hydrogen absorber. This makes the measurement vulnerable to dark currents and to x-rays produced by dark current electrons and explains the interest of MICE in controlling dark current emissions.

* peter.gruber@cern.ch
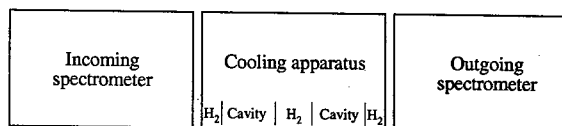
Figure 1: Layout of the MICE experiment. A differential measurement is performed between the two spectrometers. In the middle, there is the cooling apparatus with two cavities and three liquid hydrogen absorbers. The whole experiment is embedded in a fine-tuned set of solenoid magnets.

Frequency	805 MHz
Accelerating gradient	13 MV/m
Total accelerating voltage	1.04 MV
Magnetic field	2.5 T

Table 1: Operating parameters of the cavity and magnet.

EXPERIMENT SETUP

The MUCOOL collaboration operates an 805 MHz test cavity at the Fermilab Lab G[3]. This cavity has been specially designed to study dark currents and x-rays emitted from rf cavities. It features a pair of very thin windows, allowing the dark current electrons to exit the cavity. These windows can be changed. All measurements presented here have been performed with a 200 μm Cu rf window and a 200 μm Ti vacuum window.

The cavity is immersed in a superconducting solenoidal magnet with fields up to 5 T. All measurements except the one reported at the end were performed at a magnetic field of 2.5 T. The cavity operting parameters can be found in Tab. 1. To make the comparison easier, all measurements were performed at 13 MV/m field gradient.

METHODOLOGY AND MATERIAL

Ordinary photographic paper for black-and-white enlargements was used to detect the electrons. The paper was wrapped in contractor-grade black plastic foil to prevent exposure to ambient light. It was placed perpendicular to the beam axis at different distances to the cavity window, exposed for 30 s to 9 hrs and subsequently developed. The exposure time was adapted to the observed flux.

The advantages of photographic paper are its moderate speed (slower than polaroid paper, yet results are obtained in minutes), the low cost, its high grain and the large sizes available. The details of the material are outlined in Tab. 2.
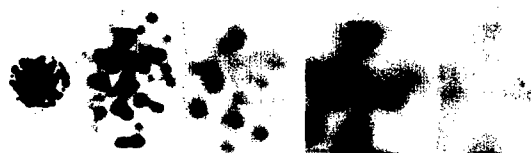
Figure 2: Distance series of photographic paper, taken at various distances of from the cavity window. The exposure time was 1 min for the first three pictures and 3 min for the latter two. All pictures are on the same scale.

Photographic paper	ILFORD® Multigrade IV, FB Fiber, MGF.5K [4] sizes 8x10 in and 11x14 in (20x25 cm and 27.5x35 cm)
Developer	Ilford Multigrade Paper developer, 1+9 diluted, 2 min
Fixer	Ilford Rapid fixer, 1+9 diluted, 2min

Table 2: Specifications of the photographic material used

After the development, the photographic paper was scanned using a Canon 20LIDE scanner with 300 dpi and 16 bits. To calibrate the scans, a sample white and black point was scanned with each picture. The levels of grey expressed at points of interest in percentage points were then extracted using a picture editing program. It was assumed that the level of grey is roughly proportional to the dose for levels of grey of up to 75%.

DISTANCE MEASUREMENT SERIES

A series of pictures were taken on the solenoid axis at varying distances from the cavity windows. The results are shown in Fig. 2. The first picture was taken at a distance of 1 cm from the cavity window, well inside the solenoid. The second picture was taken at the solenoid's end. The other three pictures were taken in the fringe field of the solenoid at distances of 20 cm apart.

The pictures show that the black spots seen on the first plane dilute and grow as the fringe field of the solenoid opens up. This picture makes it clear that the pattern of dark spots is really induced by electrons and not by x-rays, which are also emitted from the cavity.

The last two pictures illustrate very well how the electrons follow the magnetic field lines of the fringe field and how they get diluted in this process. This is important for the MICE experiment, because there is a flip in the field direction between cavity and spectrometers for most configurations. As seen in Fig. 2, the dark current electrons follow the field lines and virtually none will reach the spectrometer.

EXPOSURE TIME SERIES

At a fixed position at the end of the solenoid (this compares to the second position in Fig. 2) a time series of exposures was taken. The exposure times were: 30 s, 45 s, 1 min, 2 min and 5 min. The results, shown in Fig. 3, indicate a background rate that varies highly with the location. One can imagine dark current "beamlets" that stem each from a single emitter.

Combining different exposure times makes it possible to extend the dynamic range of the photographic paper. If one looks at the 30 s picture, there is a spot that is completely black (marked with a dotted circle), while another area (marked with a dotted triangle) is still completely white. After 10 times the exposure time (300s), the region marked with a triangle is 10% grey. If one spot is only 10% grey after 10 times the exposure time, one can conclude that different beamlets vary at least $10 \cdot 10 = 100$ times in intensity.

PHOTOGRAPHIC RANGE TELESCOPE

A photographic range telescope was built with six layers of photographic paper separated by layers of 1.6 mm aluminum each. To be able to see high-energy particles with low rates and attenuated x-rays, the exposure time was extended to 9 hrs. It was thus expected that the first sheet of paper, which is not protected by the aluminum, would be completely black.

The image series is shown in Fig. 4. The light grey ring is due to a mounting device, that cast a shadow on the calorimeter. The active area of sheet no. 0 is completely black, as expected. The most energetic electrons penetrate the first layer of Al and can be identified on sheet no. 1. No electrons are seen after the second layer of Al on sheets no. 2 and beyond; only a uniform x-ray background can be identified.

This result is perfectly compatible with a MARS[5] simulation, that shows that for 1.2 MeV electrons, 20% survive one Al layer, and less than 10^{-4} survive two layers.

The x-ray background shows the expected attenuation pattern, with slightly lower intensities after each layer of Al.

MEASUREMENTS WITHOUT MAGNETIC FIELD

For comparison purposes, one exposure was carried out with no magnetic field. The photographic paper was located at the end of the solenoid. The exposure time was extended to 30 min.

No structure whatsoever could be detected. The photographic paper showed a uniform level of grey of 60%. This translates into an exposure time of 50 min for full black, a factor of 100 more than the darkest spots *with* magnetic field at the same location.

Figure 3: Time series of photographic paper, located at the end of the solenoid, exposed 30 s, 45 s, 1 min, 2 min and 5 min. The individual pictures have been taken during the course of a day. The image is remarkably stable in this time frame.
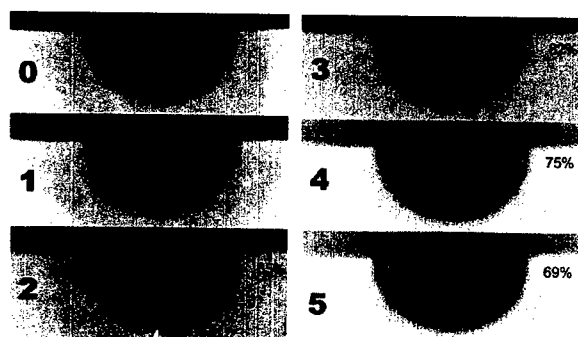
Figure 4: Image series of the photographic range telescope. The first image was directly exposed, then there was a shielding of 1.6 mm Al between each plate. The exposure time was 9 hrs.

CONCLUSIONS

For the **beam photography method** , one can conclude:

- Beam photography is capable of producing accurate 2D-images of dark currents.

- This method works only, if thin windows allow the dark current electrons to exit the cavity and if a magnetic field parallel to the beam axis guides the dark current filaments.

- X-rays are normally not detected, as they produce a signal that is a factor of 500 weaker than the electrons' signal.

Following facts about **dark currents** produced by the Lab G cavity have been revealed:

- About 50 different individual emitters have been identified.

- The pattern of these emitters does not change on the timescale of several days, even after breakdowns.

- The intensity of individual dark current filaments varies by a factor of more than 100,

leading to these conclusions for the **MICE experiment**:

- A field flip at the location of the absorber solves the problem of low-energy electrons, as these follow the field lines and are lost.

- Without field flip, the dark current filaments follow the field lines and reach the spectrometer. There, the local background rate varies by a factor of more than 100. When analyzing background effects in the spectrometers, it is not enough to consider the average background rate.

ACKNOWLEDGEMENTS

REFERENCES

[1] D. Kaplan, this conference.

[2] P. Gruber (ed.), The Study of a European Neutrino Factory Complex, CERN/PS/2002-080.

[3] J. Norem, this conference.

[4] http://www.ilford.com/html/us_english/ prod_html/multifb/multi_iv_fb.html

[5] N. V. Mokhov, The Mars Code System's User Guide, Fermilab-FN-628 (1995).

REBUILDING WR-340 AND WR-284 WAVEGUIDE SWITCHES TO MEET HIGHER POWER AT THE ADVANCED PHOTON SOURCE*

S. W. Berg, D. Bromberek, J. Gagliano, A. E. Grelick, G. Goeppner, A. Nassiri, T. Smith
Advanced Photon Source, Argonne National Laboratory, Argonne, IL 60439 USA

Abstract

The high-power S-band switching system for the Advanced Photon Source (APS) linear accelerator (linac) provides for a hot spare for two of the four S-band transmitters. The system utilizes four-port S-band switches of aluminum construction that are pressurized with sulfur hexafluoride during normal operation and are commercially available. A high-power S-band transmitter test stand at the APS linac has shown that processes that include the hand working and electropolishing of sharp edges internal to the aluminum construction of these switches have measurably improved power handling characteristics.

INTRODUCTION

The rf power for the APS linear accelerator is provided by Thales model TH2128 klystrons, rated at 35-MW peak power, and TH2128D klystrons, rated at 45-MW peak power. The ongoing process of upgrading new and rebuilt klystrons to model TH2128D continues as the lower-grade klystrons are retired or rebuilt with the power upgrade [1]. Of the six klystrons in the APS linac gallery, L1, L2, L4, and L5 are used for normal storage-ring injection. A sixth klystron, the TH2128D model, has been installed in the gallery and serves as a test stand for high-power testing and conditioning of components. This test stand is currently being redesigned to accommodate the high-power rf acceptance testing of S-band SLEDs (SLAC Energy Doublers). The switching system provides for uninterrupted rf power to the APS linac in the event that a klystron needs to be replaced [2].

TOPOLOGY

Figure 1 shows an overhead WR-340 waveguide run that supports the 2856-MHz signal from spare klystron L3. This run (labeled 'From L3') has been installed at an elevation of 14'6" to provide for clear passage of forklifts, thereby accommodating the removal of and replacement of klystrons. Figure 1 illustrates how the two WR-340 switches shown can lead to four scenarios. 1) The L3 rf signal can substitute for L1, providing rf power to the tunnel thermionic gun, which is used for normal storage-ring injection. 2) The L3 rf signal can be used to power the photocathode gun used for low-energy undulator test line (LEUTL) studies. 3) The L3 rf signal can, via a third switch in the linac tunnel, be directed to a test room [3]. 4) The L3 rf signal can be directed to a vertical water load

termination for conditioning. The WR-340 waveguide was used for two reasons. First, it exhibits less return loss than does the WR-284 waveguide. Over the frequency range which the waveguide is designed to support, the WR-340 copper waveguide is 0.261 to 0.363 dB loss per 100 feet while the WR-284 copper waveguide is 0.508 to 0.742 dB loss per 100 feet. The second reason the WR-340 waveguide is used is to handle more power in the pressurized portion of the waveguide. Another switching arrangement has been installed at L2 whereby the spare klystron L3 can replace rf from klystron L2 if klystron L2 becomes temporarily disabled.
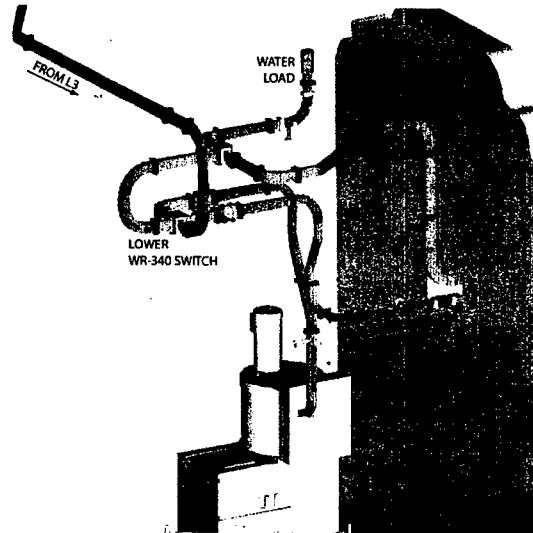
Figure 1: Switching at L1.

COMPONENTS

Measurements to date have determined that the loss from L3 to the photocathode rf gun over a distance of 150 feet is 0.84 dB. This overall loss is influenced by the number of flange joints, which is perhaps greater than ideal because the waveguide straights were limited to six feet due to the brazing furnace size. Windows and transition pieces, which make the size transition from WR-284 waveguide to WR-340 waveguide, contribute to the waveguide losses. The waveguide transitions are machined externally to a tapered shape prior to an internal wire EDM (electrical discharge machine) operation and have an overall length equal to 21.25". A goal of 40-dB return loss was chosen as one of the criteria for the WR-340 windows developed at the APS [4].

The WR-340 flanges and gaskets are unique to the APS switching system, having been upgraded from the WR-284 merdinian male and female flanges developed at SLAC. Construction of the WR-340 waveguide is 0.25" wall OFHC copper. This makes for a heavy waveguide that demands significant attention to safety in installation and support. The heavy wall limits the elastic deflection of the broad wall from applied pressure or vacuum so that deflection is similar to that demonstrated by the proven 0.173" wall WR-284 waveguide. More costly brazed stiffeners to the WR-340 broad walls were thus not needed.

The nominal operating pressure of the SF_6 is 32 psig. Two pressure switches in parallel are installed at each zone to serve as rf interlocks, and they signal local cabinet displays if the pressure falls below 29 psig. An overpressure system for safety purposes incorporates a 35-psig burst disc and pressure relief valve built into the main manifold. There are no temperature stability water traces brazed to the WR-340 waveguide (excepting the WR-340 windows), since the entire WR-340 waveguide subsystem lies ahead of the sampling port, which is used for closed-loop phase regulation in each case.

Provisions have been made to monitor the moisture content of the SF_6, and a future SF_6 recovery system is planned to reclaim 97% of the SF_6 and provide for a scrub, clean, and dry process. Yet, the current SF_6 system is static with minimal moisture content monitoring. For the purposes of maintaining the waveguide and adding new components to the system, the SF_6 is vented completely from a zone. Although SF_6 recovery is not employed, during the SF_6 venting it is automatically tested for the presence of breakdown byproducts SO_2 (1 in 60 ppm) and HF (1 in 120 ppm). Following maintenance activities, the selected waveguide zone is evacuated to 10 mTorr and the zone is refilled from one of two cylinders holding fresh SF_6 pressurized at 400 psig. Automatic SF_6 switchover occurs when one cylinder pressure falls below 120 psig. The two larger zones (6 cubic feet each) have performed for a year without maintenance activity and therefore without SF_6 refreshment.

This describes the static SF_6 system that has performed well for five years. On one occasion, which involved the small zone at the L6 test stand using a 2856-MHz, 41-MW pulse with a 2-μs duration, severe arcing occurred causing SF_6 decomposition. This happened during testing of the prototype WR-340 window, which was afterward redesigned to handle higher power [5]. The arc residue on the SF_6 side of the ceramic contained neither of the more hazardous byproducts, SO_2 or HF. The residue deposited on the gas side of the window was found to be copper fluoride and copper fluoride hydroxide, indicating that the HF reacted with the copper. No other occurrence of SF_6 breakdown has been observed.

PRESSURIZED RF SWITCHES

Early testing at SLAC [6] was significant because WR-284 switches manufactured by Sector Microwave were seen to exhibit return loss characteristics at least commensurate with a more expensive brand of manufacturer. A decision was made to purchase fourteen Sector Microwave 340 size and four Sector Microwave 284 size switches. A more recent purchase order for additional switches has followed. The return loss of the WR-284 switch had been measured at SLAC to be 22 dB using the test setup described in [6]. More recent measurements at the APS using a network analyzer have indicated that WR-340 switches can be fine-tuned to 40 dB, whereas the acceptance criteria requires no return loss less than 36 dB. The network analyzer measurements indicate that the WR-284 switches can be expected in general to exhibit 31- to 35-dB return loss.

Fine-tuning the WR-340 switch in an attempt to reach 40 dB involves removing the electrical switch head to expose a round cover plate, as shown in Figure 2. For illustration purposes, the mitered rotor is raised. The round cover plate (labeled port 1) contains the index blind hole. This cover plate can be rotated slightly in reassembly to change indexing of the switch head and the position of the switch bearing (arrow in picture) relative to the aluminum channel piece (fixed to the rotor axis). This alters slightly the rotation of the rotor and the alignment of housing openings to rotor edges, thus influencing the return loss of the switch.
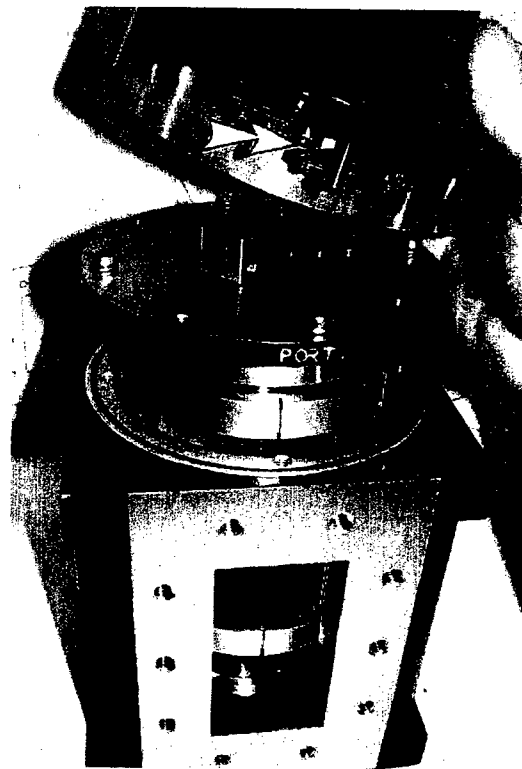
Figure 2: Switch head bearing and channel piece.

High-power testing of WR-284 switches to the extent that results are repeatable has not yet been performed. The great majority of testing has been with WR-340 switches. A factory WR-340 switch sometimes exhibits arcing at peak levels as low as 35 MW, such as the serial number 15 (SN 15) WR-340 switch at the APS. In order to improve this performance, the edges of the aluminum rotor and housing were hand-worked using extremely fine emery cloth backed by flexible lexan. Prior to this rework, the factory irridite finish (shown as silvery in Figure 2) and enamel are removed. Rotor edges that have been reworked are shown in Figure 3, though housing edges were also smoothed. Measurements using an optical comparator indicate that factory edge radii range from 0.002" to 0.008", while handworking increased these radii from 0.014" to 0.030". Following this handworking, the rotors and housing are electropolished to further smooth the edges. This process removes an additional 0.001" to 0.002" from the aluminum surface and thus opens the difference between rotor outer diameter and housing inner diameter 0.004" to 0.008".
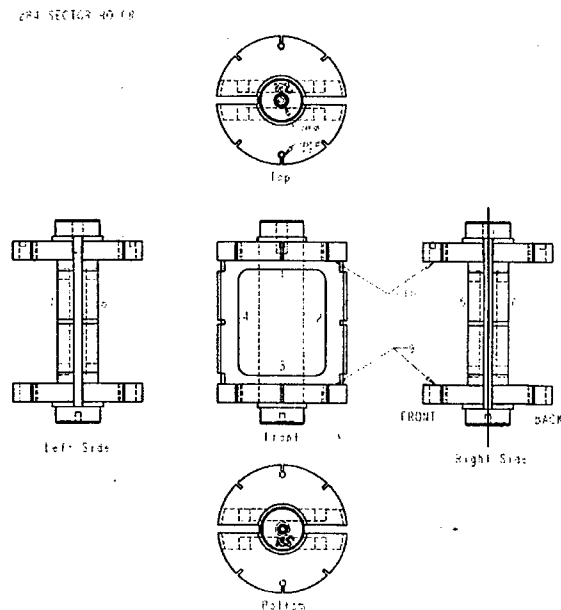
Figure 3: WR-284 rotor edges that are handworked.

Following this rework, the aluminum rotor and housing are irridited with a dark irridite process, and the rotor and housing are reassembled and optimized in alignment. The quality of the new irridite finish on the rotor and housing is more durable and more gold in color than the factory finish, because it follows an electropolish process. Eventually it was determined that the electropolishing and irridite finish alone allowed a WR-340 switch to reliably achieve 45-MW peak with 4-μs pulse, noting that not all factory-grade WR-340 switches are as poor in characteristics as was the SN 15 switch.

CONCLUSIONS

More extensive peak power testing of WR-284 switches is viewed to be necessary. Future purchase orders for WR-340 switches may be similar to the most recent, where the manufacturer supplied matched rotors and housings disassembled and unfinished. That arrangement allowed rework without disassembly of the factory unit. A more efficient option would be for the manufacturer to perform acceptable factory electropolishing and irridite finishing. The electropolish and irridite processes are believed to improve the peak power handling performance of the WR-340 switch by at least 10%. Data for WR-340 switches indicate that handworking offers only a few percent further improvement. At present, only the WR-284 switches receive the laborious handwork process (since operating them at 35 MW constitutes a greater field strength stress than is produced by 45 MW in WR-340).

REFERENCES

[1] A.E. Grelick et al., "Testing and Implementation Progress on the Advanced Photon Source (APS) Linear Accelerator (LINAC) High Power S-Band Switching System," Proceedings of the XX International Linac Conference, Monterey, CA, pp. 983-985 (2000).

[2] A.E. Grelick et al., "A High Power S-Band Switching System for the Advanced Photon Source (APS) Linear Accelerator (Linac)," Proceedings of the XIX International Linac Conference, Chicago, IL, pp. 914-916 (1999).

[3] J.W. Lewellen et al., "The Advanced Photon Source Injector Test Stand," Proceedings of the 2001 Particle Accelerator Conference, Chicago, IL, pp. 2212-2214 (2001).

[4] A.E. Grelick et al., "Testing and Operation of the WR340 Waveguide Window in the APS Linac," Proceedings of the XXI International Linac Conference, Gyeongju, S. Korea (2002), to be published.

[5] S. Berg et al., "Development of the Low Return Loss 340-Size Ceramic Window at the APS Linac," Proceedings of the 2nd International Workshop on Mechanical Engineering Design of Synchrotron Radiation Equipment and Instrumentation, Argonne, IL, pp. 50-57 (2003).

[6] A. Nassiri et al., "High Peak Power Test of S-Band Waveguide Switches," Proceedings of the 1997 Particle Accelerator Conference, Vancouver, BC, Canada, pp. 3174-3176 (1998).

CONDUCTING RESEARCH AND OPERATOR TRAINING WHILE MAINTAINING TOP-UP RELIABILITY USING THE ADVANCED PHOTON SOURCE LINEAR ACCELERATOR*

S. Pasky† and R. Soliday
Argonne National Laboratory, Argonne, IL 60439, USA

Abstract

In recent years many changes have been made to the Advanced Photon Source (APS) linear accelerator (linac) to support multiple tasks. The primary purpose of the linac is to provide beam to fill the APS storage ring, which is done using thermionic cathode rf guns. At the same time we provide support for research projects, including a new facility that will be used for future operator training and testing of injector components. With each task requiring a different lattice and timing configuration, while at the same time using common rf systems, the complexity of operations has increased significantly with even greater demands being made on reliability and performance. In addition, personnel safety and equipment protection concerns have become more complex. We approached these challenges by developing three new subsystems: a highly automated linac operation using APS's Procedure Execution Manager (PEM) software; a new interlock system based on programmable logic controllers; and an automated S-band rf switching system. In this paper, we discuss how these developments have improved the flexibility and reliability of the APS linac, and how we intend to conduct operator training and test new injector components while maintaining storage ring injections.

INTRODUCTION

The Advanced Photon Source at Argonne National Laboratory is a high-brightness, third-generation synchrotron light source. It is operated in top-up mode 75% of the time, which entails injecting beam every two minutes to maintain a current of 102 mA to 1% tolerance. When top-up is not being performed, the ring is filled twice per day. In either mode, the APS linac is now configured to support multiple functions, accomplished by the addition of three new subsystems: an interlock system based on programmable logic controllers (PLCs), an automated S-band rf switching system, and a graphical user interface called the Procedure Execution Manager (PEM).

LINAC AUTOMATED OPERATIONS

The APS linac is made up of five modulators and klystrons, three SLEDs, three electron guns, and a complex diagnostic and lattice arrangement. In addition, there are subsystems, such as water, vacuum, and timing that are incorporated into operating screens that hold hundreds of read-backs and controls for every aspect of operation.

Originally, when making changes in the linac, the operators had to switch back and forth among many control screens and perform procedures from memory or with the aid of written procedures. To say the least, this was a very time-consuming and error-prone task.

The use of PEM software procedures [1,2] for equipment start-ups, lattice reconfigurations, and changes to the rf power system in the event of a failure has proven to be most beneficial. The main difference is that PEM has the ability to repeat steps faster, more consistently, and with less possibility of error.

Complex PEM procedures are constructed by combining simpler PEM procedures in a series and/or parallel fashion. The PEM interface is expandable, simple, and consistent, so operators often do not need to learn anything new in order to correctly use a new procedure. Using the PEM's ability to execute steps in parallel can decrease the execution time and further enhance productivity. In addition, the PEM has error trapping and reporting to help machine managers and software developers diagnose and respond to errors.

As an example, a PEM would be used in the event of an rf system failure. Selecting the Linac_Switch Mode PEM from the operation dialog screen (Fig. 1) will automatically remove the failed rf source and, in parallel, switch to the back-up rf source. Prior to starting this procedure the operator is required to select a snapshot file that will be restored at the end of the switching mode change. A snapshot file (Fig. 2) is a database file that includes all the settings necessary to reproduce the conditions existing when the snapshot was recorded. Once executed, the PEM procedure opens another display window that shows each step as it occurs and reports procedure status (Fig. 3).

There are two principal difficulties with the PEM process. First, changes in the controls system or hardware can cause the procedures to fail. This problem has been managed by the use of administrative controls and a device layer between the PEM procedures and EPICS. Second, thorough testing of these procedures requires

machine time, which is in very high demand for storage ring top-up and experimental programs.
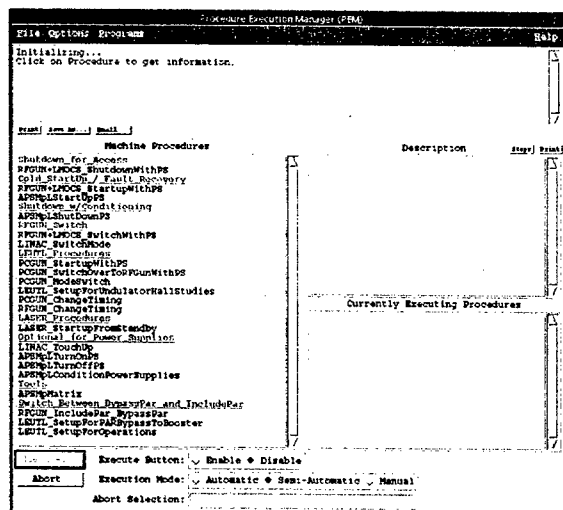
Figure 1: Procedure Execution Manager for the APS linac.
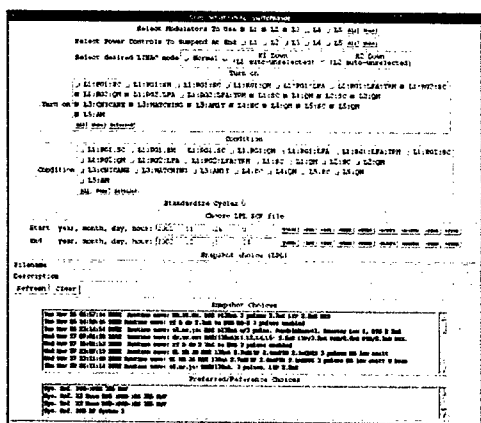
Figure 2: Initial dialog screen.
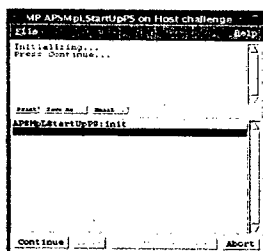
Figure 3: Status monitor.

NEW SUBSYSTEM INTERLOCKS

Interlock Support

New interlock systems have been designed to support various klystron operations. The main responsibility of

the interlock system is to provide machine protection, which depends on vacuum, SF6 pressure and water flow to function properly. The interlock logic generates *Permit* signals specific to each subsystem (vacuum, pressure, and water flow.) These permits are connected in series to permit rf power to be generated from any one of five klystrons.

A milestone was reached in December of 2002 with the completion of the programmable logic controller (PLC)-based interlock protection system. The original interlock system for the linac was a hard-wired, relay-based one that was, for the most part, very reliable. However, adding new interlocks to the old system proved to be very time consuming, and it was unable to communicate with newer PLC-based systems.

PLC Selection

The 205 Direct Logic Controller, known as the world's most powerful micromodular PLC, was found to meet or exceed all our requirements. This Direct Logic Controller uses a remote master eight-slot I/O crate with a DL250 controller-processing unit. Using this type of system has saved money in equipment costs and many hours not only during the initial installation of the hardware but also in programming and debugging time. The DL250 was found to also interface very well with our EPICS system in that it provided additional diagnostic information to the control room via standard control screens.

Interlocks Interfaced with MEDM Displays

In EPICS, equipment is controlled from workstations that communicate over a network of local computers called input/output controllers (IOCs). All systems in the linac that require or use interlocks for equipment or personnel safety protection require a latching function independent of the IOCs. Once a latch has been made, operator intervention is required to reset the interlock.

Using the PLC's ability to monitor each interlock signal separately, the MEDM screen developer is now able to design a thorough diagnostics display for operations and maintenance personnel. In the event of a trip or component failure, a quick glance at this screen shows the general source of the problem in an easily understood graphical fashion.

RF SWITCHING SYSTEM

As a result of top-up operation, the requirements for reliability and availability of the linac are even greater now than in the past. In addition, linac systems are under greater stress due to continuous operation, making failures more likely. The first part of the linac, consisting of the rf guns and four accelerating structures, requires two klystrons (designated K1 and K2) for normal operations. In the event of the failure of either K1 or K2, a third klystron (K3) would be used. Klystron three is also used to support experimental research equipment as well as a test stand. To do this, the system relies on S-band,

1420

electropolished switches, 340 pressurized waveguides, [3,4], and a PLC-based switching controller.

Switching System Description

The linac rf switching control system is responsible for monitoring and controlling eight rf switches connected to various waveguide sections in the low-energy section of the linac (sectors L1 through L3). The switches are used to reconfigure the operation of the linac, or mode change, with respect to gun operation and klystron sources. The switching system communicates to a variety of field devices including switch-mode interfaces, modulator interlocks, VSWR fault switching, sector interlocks, and Bitbus (via serial BUG).

In general, the switching system will monitor the rf switch position, command the switches to move when a mode or gun change is selected, and provide the proper handshaking signals to insure that no damage to equipment will occur due to an improper switch configuration or uncommanded switch motion. The switching system will also notify each individual sector interlock system of the switch configuration in order to route faults to the proper destination.

Modes

The following mode descriptions are used:

Mode 0 – K3 Down   Mode 1 - K1 Down
Mode 2 - K2 Down   Mode 3 - Test Room
Mode 4 - Normal

Using Mode 1 as an example, Figure 4 assumes klystron one (K1) has failed and is no longer able to support its normal operating functions. In this case, K1 Down Mode, when selected, reconfigures the switching system to direct klystron three (K3) output power to drive the selected load.
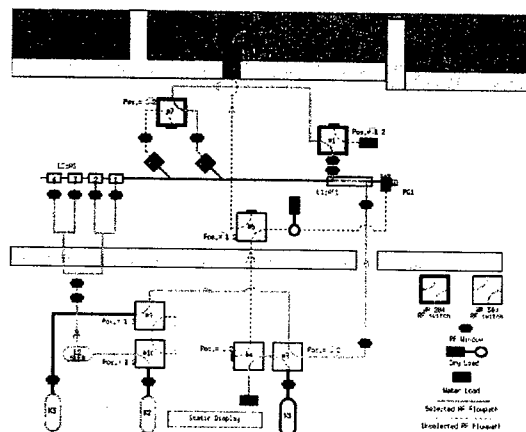
Figure 4: Mode 1 –K1 Down display.

LINAC TEST STAND AND OPERATOR TRAINING

The injector test stand was originally developed for the purpose of testing and commissioning new thermionic rf guns and injector components. Over time, the room evolved into a mini linear accelerator. The test stand holds similar components and in many ways mirrors the main linac injector. For example, control screens and machine protection systems are the same. As you might expect, having an area like this with similarities of the main injector would be ideal for operator training and testing, especially when the main injector is used 95% of the time for top-up operations.

Component Testing

To date, three new thermionic rf guns have been commissioned, and preparations are now being made to test a new gun, designed by John Lewellen, called the bunch ballistic compression (BBC) rf gun. This gun uses three independently powered and phased rf cavities, and either a thermionic cathode or a photocathode.

CONCLUSION

The new linac interlock upgrade and the use of the PEM procedures for equipment startup and configuration switching have proven to be very reliable, making the job of the control room operator much easier. In addition, this work has contributed significantly to the success of experimental programs component testing and will soon contribute to operator training.

ACKNOWLEDGMENTS

REFERENCES

[1] M. Borland, "The Procedure Execution Manager and its Application to Advanced Photon Source Operation," 1997 Particle Accelerator Conference, pp. 2410-2412 (1998).

[2] R. Soliday et al., "Automated Operation of the APS Linac using the Procedure Execution Manager," XX International Linac Conference, SLAC-R-561, pp. 524-526 (2001).

[3] A. Nassiri, A. Grelick, R. L. Kustom, M. White, "High Peak Power Test of S-band Waveguide Switches," 1997 Particle Accelerator Conference, pp. 3174-3176 (1998).

[4] A. E. Grelick et al., "Testing and Implementation Progress on the Advanced Photon Source Linear Accelerator High-Power S-Band Switching System," XX International Linac Conference, SLAC-R-561, pp. 983-985 (2001).

BIDIRECTIONAL COUPLER OPTIMIZATION IN WR284-TYPE WAVEGUIDE*

T.L. Smith[†], G. Waldschmidt, A. Grelick, S. Berg
Advanced Photon Source, Argonne National Laboratory
9700 South Cass Avenue, Argonne, Illinois 60439 USA

Abstract

In the Advanced Photon Source linac gun test area at Argonne National Laboratory a new S-band ballistic bunch compression (BBC) gun is being tested [1]. It was determined that a WR284 waveguide bidirectional coupler with a directivity of greater than 30 dB and a coupling of −57 ± 1 dB was desired for evaluation of waveguide rf power conditions. Numerical simulations were performed using the High Frequency Structure Simulator (HFSS) [2] and experimental models were built to determine the optimal dimensions of the bidirectional coupler assembly and the orientation of the loop coupler element. Magnetic and electric fields in the coupler were adjusted by modifying the coupling of the fields as well as the capacitance of the coupling loop.

INTRODUCTION

The rf operating frequency of the APS linac is 2.856 GHz [3] with waveguide peak power greater than 200 MW. The WR284 bidirectional coupler used is a high-power, high-vacuum design commercially obtained. The coupler is being redesigned in order to improve performance in the linac gun test area, to gain better control of the performance of the directional couplers used for linac operation, and to acquire proper knowledge to fabricate future bidirectional waveguide couplers in WR340-type waveguide.

MEASUREMENT SETUP AND PROCEDURE

The tests were performed using an HP8510 network analyzer. The test setup consisted of two WR284 waveguide-to-N-type transitions, two WR284 waveguide straight pieces, and a 6.5-inch waveguide adapter piece shown in Fig. 1. The waveguide straight pieces were inserted between the directional coupler and the transitions to ensure that any residual fields in the coax-to-waveguide transition would not be included in the measurements. Network Analyzer calibration and proper rf measurement techniques are essential to achieve accurate data results [4].

The 99.5% pure alumina ceramic windows that were used had a permittivity of 9.6 and very low loss. For test purposes, the windows were not brazed in the housing to facilitate changes made to the coupler assembly. If an unbrazed window moves during the rf measurements, the

data may be inaccurate and nonrepeatable. Therefore a spring assembly, shown in Fig. 2, was devised to temporarily hold the windows and the coupler elements in place and to ensure good electrical contact during the rf measurements.
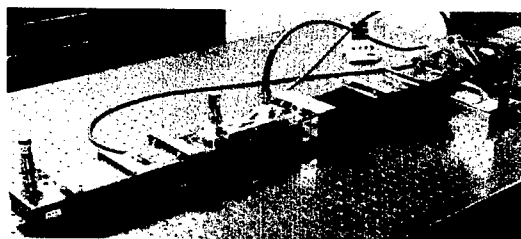
Figure 1: The rf measurement setup.
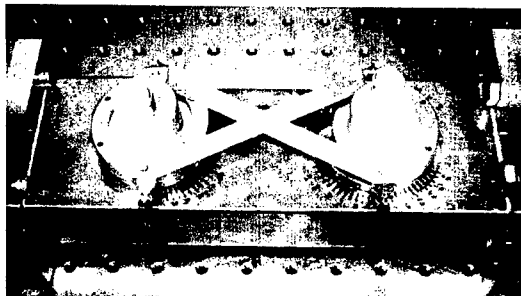
Figure 2: Coupler with spring assembly.

COUPLER PARAMETERS

In the process of tuning the coupler assemblies for maximum performance, a number of parameters were adjusted, as shown in Fig. 3. The resultant change in the coupler was evaluated as a function of these variables.

The rf data were taken after the following changes were made to the directional coupler assembly (see Fig. 4): iris diameter was enlarged, different disc thicknesses were placed under the ceramic window to vary the iris height, different spacer thicknesses were placed above the ceramic window to change the pickup height, different coupling elements were used, and element coupling loops were bent to different angles.

The directivity of the coupler is most dependent upon the orientation of the coupler element with respect to the transverse plane of the waveguide. In the test set-up, the coupler element may be freely rotated within the window assembly. It was determined that the best isolation occurred when the pickup bend was oriented approximately 10° from the transverse plane toward the direction of power flow. However, the precise angle is dependent upon the permittivity of the ceramic window

that is used. In the case where a vacuum seal is not necessary and an air dielectric is essentially all that separates the coupler element from the waveguide, a 28° angle produced the best results.

The coupling is moderately dependent upon the iris height and pickup height. It varies about 1 dB per 0.01 inches for the iris height and about 0.5 dB per 0.01 inches for pickup height. However, the coupling is mostly dependent upon the iris diameter. The iris diameter does not strongly affect the directivity and, as a result, may be adjusted nearly independently of the directivity.

For optimal tuning, the pickup distance, pickup height, and iris height were modified to observe trends. In some cases, their effect on the overall operation was found to vary depending on the exact orientation of the coupler element, as will be discussed in the next section.

MEASUREMENT AND SIMULATION DATA

Since the coupling does not vary as substantially as the isolation when the coupler is rotated, the angle producing maximal isolation also creates maximal directivity. However, the response is very sharp and requires precise positioning. The process of tightening the coupler can make perceptible changes in these values, and care must be taken to limit the error. Figure 5 shows a plot of the measured and simulated directivity for 180° of rotation of the coupler element. The angle is calculated from the axis of the pickup to the transverse plane of the waveguide.

The original coupler assemblies produced a coupling value that was lower than the required level. Increasing the housing iris diameter in both ports by 10%, from 0.312 inches to 0.345 inches, increased the coupling by approximately 4 dB.

Figure 3: Electric field magnitude in coupler element. Parameters associated with the simulations and measurements are defined as follows: PH: Pickup Height, PD: Pickup Distance, ID: Iris Diameter, IH: Iris Height.
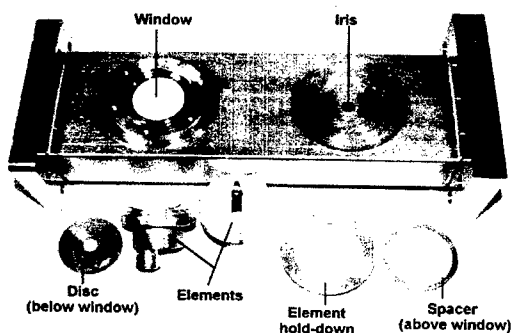
Figure 4: Coupler components.
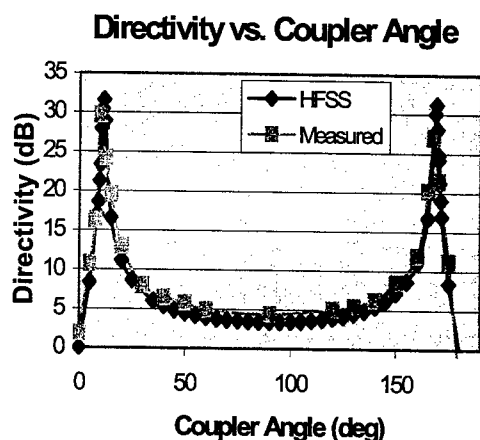
Figure 5: Directivity with respect to element angle of rotation from simulated and measured data.

Adding discs under the window to change the iris height did not make large changes to the directivity. However, adding several 0.006-inch spacers above the window caused substantial changes in the directivity as shown in Table 1.

Table 1: Effect on the Directivity Due to Increase in Pickup Height above the Nominal Value of 0.265 inches

Spacer	Directivity
No spacer	30.3 dB
0.006″	31.4 dB
0.012″	33.2 dB
0.018″	**36.2 dB**
0.024″	31.6 dB
0.030″	29.4 dB

Simulation results found that the effects of the pickup distance and the pickup height were dependent on the orientation of the coupler element. If the coupler element was imprecisely oriented by more than half of a degree, some of the parameters shown in Fig. 3 produced differing effects.

For precisely aligned coupler elements, an increase in the pickup height was found to increase the directivity up to 6 dB. A change in the pickup distance showed little change in directivity once a minimum distance was reached and before the distance became too great. For coupler elements that were slightly off the optimal orientation, an increase in the pickup height had little effect. Also, the directivity became much less uniform and began to degrade as the pickup distance was adjusted.

Optimized dimensions for the directional coupler assembly are shown in Table 2. A plot of the surface current can be seen in Fig. 6. The coupler element is rotated to achieve maximum isolation from forward-directed power traveling into the page. In this figure, the waveguide is, in fact, excited with a field traveling out of the page. The field plot shows the coupling of the fields into the large signal port and the small resistive port.

Table 2: Optimal Parameters Determined from Simulations with HFSS

Parameter	Dimension
Angle	11.75°
Iris Diameter	0.4 in
Pickup Distance	0.025 in
Iris Height	0.065 in
Pickup Height	0.286 in
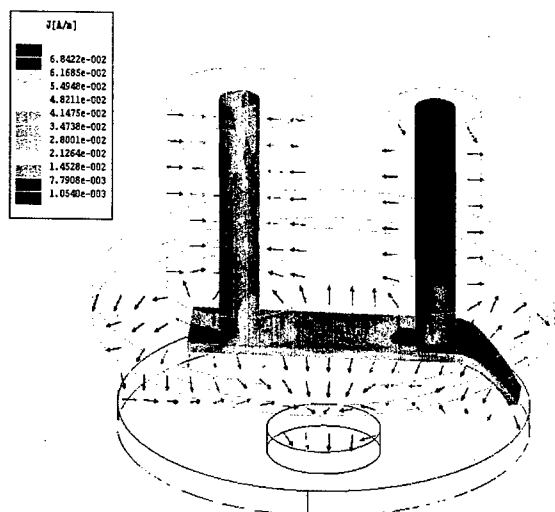
Figure 6: Surface currents on the pickup and inner conductors, and electric field vectors along a cross section of the coupling element.

CONCLUSIONS

Opening the iris diameter was necessary to achieve the desired increase in coupling. The iris diameter does not strongly affect the directivity and, as a result, may be adjusted nearly independently of the directivity. It was found that the coupler is highly sensitive to the orientation of the pickup loop and must be precisely aligned. In addition, the location of the pickup above the coupling iris was a major contributing factor to optimizing the performance of the coupler. The experimental and simulation results that were presented will also aid in the future development of bidirectional couplers in the WR340 waveguide.

ACKNOWLEDGMENTS

REFERENCES

[1] J.W. Lewellen et al., "A Flexible Injector Test Stand Design," these proceedings.

[2] Ansoft HFSS, version 8.5, Ansoft Corporation, Pittsburgh, PA, USA, June 2002.

[3] M. White et al., "Construction, Commissioning and Operational Experience of the Advanced Photon Source (APS) Linear Accelerator," Proc. XVIII Int'l Linear Accelerator Conf., Geneva, Switzerland, August 26-30, 1996, pp. 315-319, 1996.

[4] Agilent Technologies AN 1287-1, Understanding the Fundamental Principles of Vector Network Analysis, August 2000.

CALIBRATION OF RHIC ELECTRON DETECTORS*

P. He†, H.C. Hseuh , D. Gassner, J. Gullotta, D. Trbojevic , S.Y. Zhang
Collider-Accelerator Department, BNL, Upton, NY 11973, USA

Abstract

To characterize the electron cloud in RHIC, eleven custom electron detectors have been designed, fabricated and installed at a few RHIC warm-bore vacuum sectors for data collection during FY2003 runs. Prior to installation, the transmission and collection efficiencies of these detectors at various grid and collector bias voltages were measured using an electron gun with energy up to 1500 eV. This paper describes the design of the detector and the test system set-up, and summarizes the calibration results. In addition the calibration of a commercial micro-channel plate is also reported.

INTRODUCTION

The Brookhaven Relativistic Heavy Ion Collider (RHIC) consists of two counter-rotating rings, labeled Blue and Yellow. During the FY2001/2002 physics runs, which included gold on gold and gold on protons, unwanted vacuum pressure rises occurred as the beam intensity increased (the number of ions per bunch was continually increased up to the design value of 10^9) in both 55-bunch and 110-bunch filling patterns [1]. These pressure "bumps" primarily occurred in the warm bore sectors, most notably at the interaction regions. The observed relevant factors include bunch intensity, bunch spacing, beam loss, and less understood, the locations. Electron multi-pacting appears to be the dominant mechanism and diagnostics are needed to correlate these vacuum pressure bumps with the electron cloud. Since no dedicated electron detectors were available in the RHIC FY2001 run, the coherent tune shift along the bunch train was used to detect the electron cloud density [2]. Some complications, however, may make this approach less reliable. The more straightforward way to detect the electron cloud will the use of electron collectors placed at the intersection region or at the warm bore. These electron detectors allow the measurement of both the electron line density and the energy spectrum of the collected electrons. A comparison between electron density and the observed pressure rise can provide valuable information in understanding the pressure rise.

For this goal, eleven custom electron detectors are installed in the RHIC tunnel for data collection during FY2003 runs. The majority of electron detectors were installed at IR12, IR2 (interaction region) and adjacent insertion sections, where most vacuum bumps occurred (Fig.1). Prior to installation, the transmission and collection efficiencies of these detectors at various grid and collector bias voltages were measured using an electron gun with energy up to 1500eV. This report will present the design of the detector, the laboratory test set-up, and the preliminary bench test results.
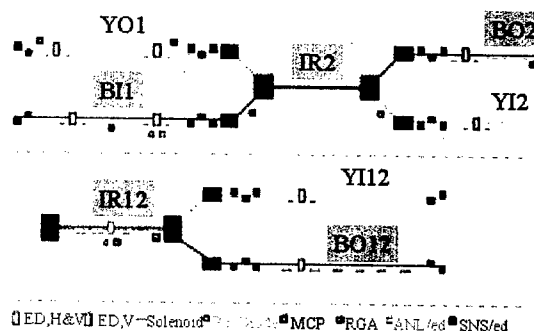
Figure 1. Electron detectors located at RHIC warm bore.

INSTRUMENTATION

Two types of electron detectors were evaluated, the BNL design and a commercial micro-channel plate.

BNL Electron Detector(ED)

An electron detector, similar to ANL's Retarding-Field Analyzer(RFA) [3], was developed to measure the electrons produced at RHIC. A schematic of the electron detector is shown in Fig.2.
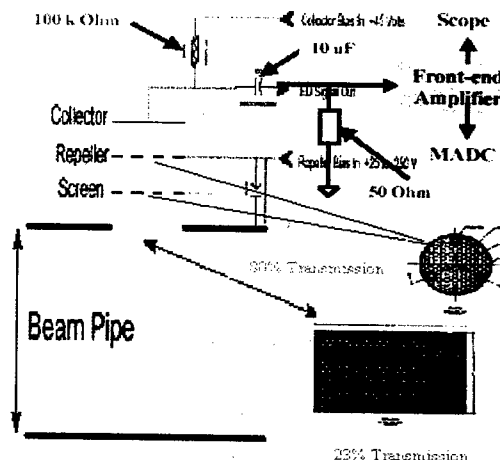
Figure 2. Schematic diagram of the electron detectors.

The detector, mounted normal to the beam line, consists of three layers, two 118mm diameter mesh grids (stainless steel with ~80% transmission) and a collector plate of equal diameter. Additionally, the mounting port is RF-

shielded, as are all beam-line ports and bellows in RHIC, using a grounded screen with 23% transmission to allow for the passage of beam image currents. The outermost grid is grounded to present a uniform field to the incoming electrons while the second grid can be used to impose a retarding or repelling field by applying a bias voltage (Vs) to scan electron energy. The collector is biased at a DC voltage +45V with a battery to increase the collection efficiency. The assembled detector was mounted on a 6 ¼-inch Conflat flange with four SHV feedthroughs.

Microchannel Plate (MCP)

The other type of electron detector uses a microchannel plate (MCP) to obtain a high gain output signal. The MCP (Fig.3) is a 1mm-thick sheet of lead glass with a honeycomb pattern of 25µm-diameter holes. It has ~ 10^6 channels, with a glass surface area of ~1m². The length/diameter aspect ratio of each channel is 40. The electron gain at 900 volts is > $4x10^3$. The MCP is vacuum compatible, but requires a long pump down period. The CEMA Model 6025MA detector assembly contains one MCP and a metal anode readout mounted using stainless steel hardware. The assembly is bakeable to 300°C. The specifications are shown in Table 1.
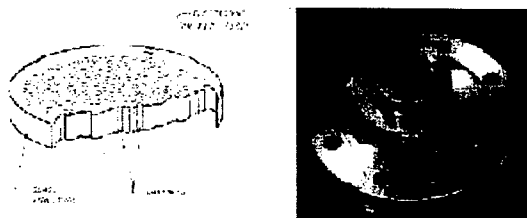
Figure 3. MCP and MCP-anode assembly.

Table 1. Electrical Characteristics of Detector

Electron Gain@900 Volts:	$4x10^3$ Minimum
Bias Current@900 Volts:	3~125 µA
Resistance:	7~30 MΩ
Dark Noise:	$5x10^{-12}$ A Max.
Linear Output Current Density:	Typically 10% of
(µA/cm²)	Bias Current Density

BENCH MEASUREMENTS

For bench measurements, each detector was installed in a vacuum chamber tee with a 127mm diameter, the same as RHIC warm-bore beam pipe. The vacuum chamber tee includes the RF screen required for RHIC beam lines. The test chamber set-up is shown in Fig.4. The electron gun was mounted opposite the detector with the electron beam impacting normal and approximatelynon-divergent. The distance from chamber center to collector is 84mm.
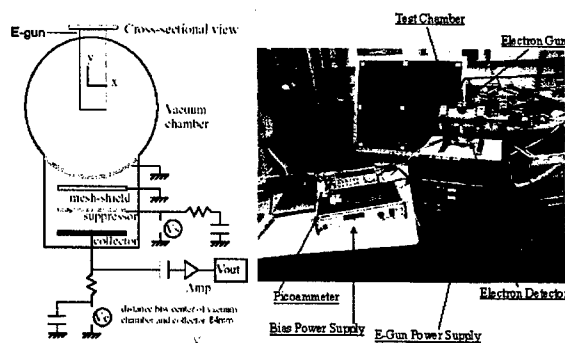
Figure 4. Bench test system set-up.

BNL Electron Detector

The first test measured the collector current as a function of electron energy. Measured results were similar to manufacturer's published values (Fig.5).

Typical Performance(Manual)　　　Bench Test Results(Measured)

Source Current= 1.72 A; Source Voltage = 1.52 V
Working Distance = 30 mm
Chamber Pressure = 3.0 x10(-6) Torr

Source Current = 1.65 A; Source Voltage = 1.40 V
Working Distance = 84 mm
Chamber Pressure = 1.3 x10(-7) Torr
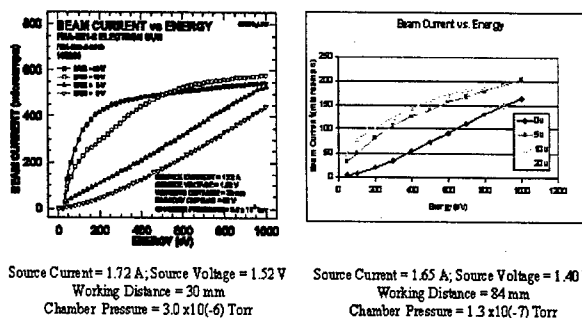
Figure 5. Beam current vs energy.

The second test characterized the filtering ability of the device by measuring the collector current while varying the grid bias voltage (V1g) for primary electron energies (Ue) of 5, 20, 50, 100 and 500 eV. The device shows good resolution, even at the low electron energies produced by electron clouds. The output is reasonably flat, as expected, where V1g < Ue, with good drop-off for
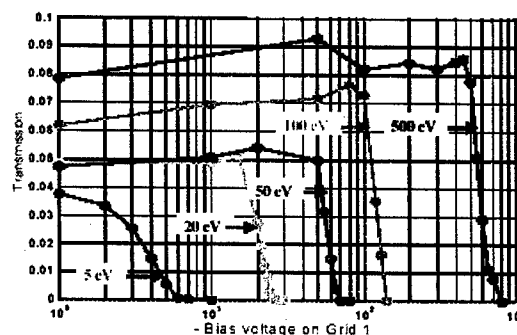
Figure 6. Current obtained as a function of V1g

Vg1 > Ue, at which point electrons are unable to pass the grid and reach the collector.

MCP-Anode Assembly

Due to saturation effects, the CEMA Model 6025MA detector assembly only works with pulsed beams. Unfortunately, the existing electron gun (FRA-2X1-1) does not have a pulse mode option, so a pulse generator is used to power a small light source. The visible blue light passes through a quartz view port to the MCP's anode plate. The test chamber is evacuated to 2.0×10^{-6} Torr and held for 15hours to thoroughly degass the assembly. Upon initial start-up, the CERA model electrical test procedure [4] is followed with the typical wiring diagram shown in Fig.7. Fig.8 gives the output signal of the MCP for selected voltages of Va=0.9kV and Vo=1.0kV. The plot of anode current vs Va (maintaining Vo=1.0kV) is shown in Fig.9.
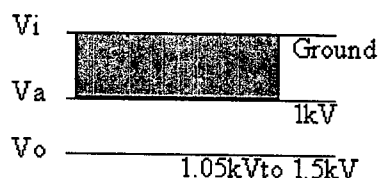
Figure 7. Typical bias settings for MCP.

MCP Output Signal
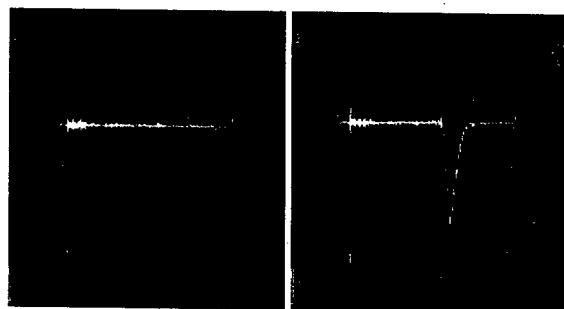
Figure 8. MCP output signal for two voltage (Va ,Vo) settings.
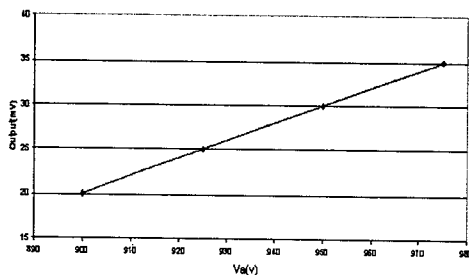
Figure 9. Output current vs Va.

SUMMARY

Two types of electron detectors were evaluated for use in studying electron cloud effects in RHIC. Bench testing was used to make preliminary measurements. Results

show the transmission of the BNL electron detector is between 0.04~0.08 over a wide range of energies. Varying the grid voltage will repel low energy electrons, allowing measurement of the energy spectrum of collected electrons. Also a commercial MCP-anode assembly has been tested and by selecting the appropriate voltages of Va and Vo, a reasonable output signal can be observed.

Eleven electron detectors and one MCP-anode assembly have been installed in RHIC warm bore sectors and will be used to characterize the RHIC electron cloud during the FY 2003 run.

ACKNOWLEDGEMENTS

REFERENCES

[1] S.Y. Zhang, BNL Report No. C-A/AP/67, 2002
[2] W. Fischer, J.M. Brennan, M. Blaskiewicz, and T. Satogata, Phys. Rev. ST-AB, Vol.5, 124401(2002).
[3] R.A. Rosenberg and K.C. Harkay, Nucl. Instr. Meth., A453, 507(2000)
[4] http://www.burle.com/cemastart.htm

INTEGRATION OF THE BEAM SCRAPER AND PRIMARY COLLIMATOR IN THE SNS RING

H. Ludewig, N. Simos, D. Davino*, S. Cousineau+, N. Catalan-Lasheras**, J. Brodowski,
J. Touzzolo, C. Longo, B. Mullany, and D. Raparia
Brookhaven National Laboratory, Upton, New York, 11973, USA
*Univesita' del Sannio, Benevento, Italy
+Oak Ridge National Laboratory, Oak Ridge, Tennessee, USA.
** CERN, 1211 Geneva 23, Switzerland

Abstract

The collimation system in the SNS ring includes a two-stage collimator consisting of a halo scraper and an appropriate fixed aperture collimator. This unit is placed between the first quadru-pole and the first doublet in the collimation straight section of the ring. The scraper is situated at the exact mid-point between these two magnets, and the fixed aperture collimator fills the space between the scraper and the doublet magnet. The scraper and collimator are surrounded by an outer shield structure. The downstream dose to the doublet and the attached corrector magnet will be estimated for normal operating conditions. In addition, the cooling water activation will be estimated. Finally, the dose at the flange locations will be estimated following machine shutdown.

INTRODUCTION

A two-stage halo cleaning system, consisting of a beam scraper and primary fixed aperture collimator are placed between the first quadru-pole and the first doublet in the collimation straight. Halo particles that are intercepted by the scrapers undergo sufficient Coulomb scattering to either deflect them directly into the primary collimator or one of the other collimators in the collimation straight. If the scattered particles are not intercepted on the first pass they will generally be intercepted within the next few circuits around the ring. The scraper is placed at the mid-point between these magnets, and the collimator is placed between the scraper and the doublet. A schematic of the configuration described above is shown on Figure 1. The scrapers will be placed at approximately 140 πmm-mrad, and the fixed aperture of the collimator will be at approximately 300 πmm-mrad. The beam shape at this position is highly elliptical, and thus the beam tube of the collimator will be elliptical with y/2=48 mm, and x/2=79 mm, respectively. The length of the elliptical section of the collimator tube is 1.8 m, and the overall length including transition pieces and end shielding is 2.463 m.

All flux, and heat deposition were determined by the MCNPX code [1]. The activation estimates were carried out using fluxes determined by MCNPX, nuclear data from the CINDER90 library [2], and transmutation determinations by a suitably modified version of the ORIGEN code [3].
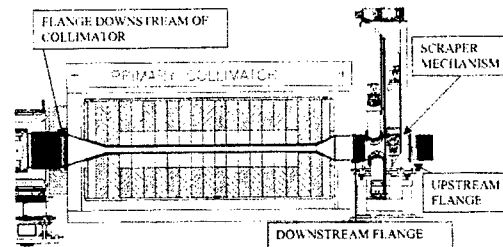
Figure 1: Beam scraper and fixed aperture primary collimator

The scraper consists of tantalum pieces 0.5 cm thick in the direction of the beam, 1.0 cm high, and 5.0 cm wide. This piece is welded to a water-cooled copper block, which in turn is attached to a mechanism to allow motion in and out of the beam. Figure 2 shows a detail of the scraper mechanism. The four scraper surfaces, chain drives, motors, and vacuum chamber can be seen. The scraper mechanism is mounted on three pins, which in turn are attached to a pedestal. Each scraper is individually cooled, and the water temperature, flow rate, and pressure are monitored. The fixed aperture collimator consists of a double walled Inconel-718 [4] tube, surrounded by a water-cooled bed of stainless steel spheres, which in turn is surrounded by a stainless steel shield. This entire configuration is contained in a pressure vessel. Cooling water flows through the particle bed cooling both the spheres and the outer surface of the outer Inconel-718 collimator tube. The space between the inner and outer Inconel-718 tubes is filled with pressurized helium and a copper wire wrap. The scraper mechanism and the collimator will be mounted on a common pedestal in order to ensure alignment, regardless of floor motion. Both components are enclosed in an outer iron shield that reduces dose to the tunnel environment during operation. Due to the proximity of the shield to the magnet, non-magnetic material must be used in this location.

The loss distribution of scattered particles along the inner surface of the collimator tube is required to determine the resulting doses to surrounding components and is given as a percentage of the particles lost on the tube surface in
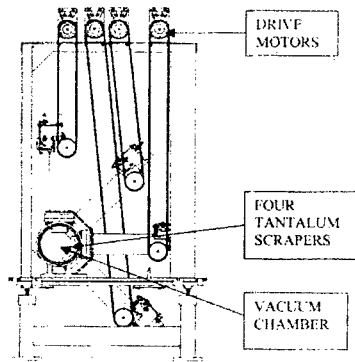
Figure 2: Beam scraper mechanism

Figure 3. It is seen that there is a relatively high loss (~ 10 %) at the entrance to the collimator, and the bulk of the collimator has a relatively constant loss of ~ 4.4 %. This loss profile is used as input to the Monte Carlo code MCNPX.
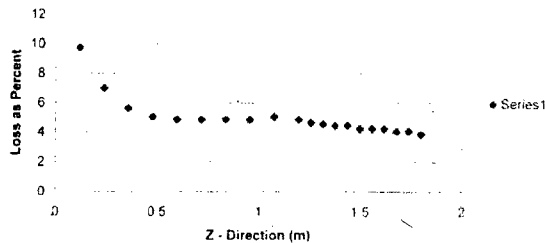
Figure 3: Primary collimator loss profile

RESULTS

In this section we will discuss the estimated results of doses to the flange areas on either side of the collimator and scrapers, to the scraper drive motors, and the downstream magnets. In addition the activation of the components, and subsequent dose to the flange areas due to decay gamma-rays following machine shutdown, will be estimated. The loss fraction under normal operating conditions in the ring is assumed to be 0.001 of the circulating beam; of this, 5% is lost on the scrapers, and 30% is lost on the inner surface of the primary collimator. Thus, the loss fraction on the scrapers is 0.00005, and the loss fraction on the collimator is 0.0003. Furthermore, the assumption will be made that the machine is operating at 2 MW for one year (defined as 250 days, or 2.16×10^7 seconds).

During normal operation of the machine the dose for one year is given below at the four locations of interest.

Table 1: Dose to Flanges while Machine is Operating (rad/yr)

Location Description	Collimator Dose	Scraper Dose	Total Dose
Flange upstream of scraper	1.20(5)*	1.71(6)	1.83(6)
Flange downstream of scraper	4.87(5)	7.54(6)	8.03(6)
Flange downstream of collimator	2.47(7)	~	2.47(7)
Magnet downstream of collimator	4.83(7)	~	4.83(7)

$*1.20(5) = 1.20 \times 10^{15}$

Assuming that the magnet insulation is Kapton, and assuming that its life is approximately 2(9) rads, then the magnet life under normal conditions should be ~ 40 years. Assuming that the entire ring loss fraction takes place in the primary collimator, or the overall ring loss increases by approximately a factor of three, the dose to the magnet increases to 1.6(8) rads, and the implied life of the magnets would be reduced to ~ 12 years.

Following machine shutdown the level of radiation at the flanges is of interest, since they may have to be accessed for maintenance purposes. An estimate was made of the potential dose at the flange locations following one year of operation. The estimated dose at the four locations described above, immediately following shutdown, are given below.

Table 2: Dose to Flanges Following Machine Shutdown

Location Description	Dose (mrad/hr)
Flange upstream of scraper	84
Flange downstream of scraper	5025
Flange downstream of collimator	490
Magnet downstream of collimator	790

It is seen that the dose to the flange located between the scraper and the collimator is quite high, and a decay period would be advisable before maintenance activities are carried out. If the loss in the ring were concentrated at the primary collimator the dose values would increase by approximately a factor of three.

An estimate of the reduction in the above values following a decay period can be obtained by determining the reduction in activation for both the tantalum scrapers and the stainless steel collimator components. The normalized activation decay for representative volumes of these two components is given below.

1429

Table 3: Decay of Activation of Tantalum and Stainless Steel Following Machine Shutdown

Material	Time following machine shutdown				
	0.0	4 hrs.	1 day	7 days	30 days
Stainless Steel	1.0	0.776	0.677	0.537	0.328
Tantalum	1.0	0.462	0.284	0.125	0.061

These estimates indicate that the collimator will decay at a much slower rate than the scrapers. However, if a decay period of approximately one day is allowed in the maintenance schedule, then the dose should be reduced by ~ 50 %.

The dose to the scraper drive motors while the machine is operating is of concern, since eventually a high enough dose will compromise the motor insulation. Estimates of dose at the motor location were made, assuming that 5 % of the loss occurs on the scrapers, and an iron shield was inserted between the scraper mechanism and the motors. Two values for the shield thickness were assumed, and the corresponding doses estimated. Results are given below, and indicate that an iron shield of nominal thickness implies an acceptable motor life, assuming the same radiation damage resistance as that given above for the magnets. If the loss increases to the maximum ring loss, the dose values increase by a factor of 20, and the condition of the drive motors should be monitored.

Table 4: Dose to Scraper Drive Motors

Iron Shield Thickness (cm)	Dose (rad/yr)
15	1.1(5)
30	5.5(4)

An estimate was made of the residual activity in the collimator and scraper cooling water immediately after shutdown and following 4 hours of decay time. These estimates assume that the ring loss is confined to the primary collimator and the machine operation for one year. The scraper activity is estimated by scaling off the values obtained for the collimator. Immediately following shutdown, the activity is dominated by the short half-lived isotopes O-15, N-16, C-11, and B-12. After a 4 hour decay period the dominant contributors to the activity are Be-7, and C-14. Note is also taken of H-3, although its total activity is low, and its contribution to the overall activity marginal.

Table 5: Residual Activity of Collimator Cooling Water Four Hours after Machine Shutdown (Curies)

Isotope	Activity
Tritium (H-3)	2.6(-8)
Beryllium (Be-7)	6.1(-2)
Carbon (C-14)	2.2(-5)

Scraper cooling water activity is a fraction of the above collimator cooling water activity. A direct scaling of the activity by the loss fraction would result in a reduction of the above values by a factor of six. However, this reduction is optimistic, since the collimator water is exposed to the high-energy particles while in the scraper the geometric arrangement essentially precludes this interaction.

CONCLUSIONS

The following conclusions can be drawn from this study:

1) The loss profile along the fixed aperture collimator is biased to the upstream end, and thus affects the flange between it and the beam scraper.

2) Dose estimates while the machine is operating will require the exchange of the downstream magnets at least once during the life of the machine.

3) Dose to the scraper drive motors is likely to be low enough to ensure that they will operate for the machine life.

4) Maintenance work on the flanges will best be carried out following a decay period of at least one day to one week, in order to reduce the dose to the workers.

REFERENCES

[1] *MCNPX Users Manual-Version 2.1.5*, L.S. Waters, ed., Los Alamos National Laboratory, Los Alamos, NM, TPO-E83-G-UG-X-00001 (1999).

[2] W.B. Wilson, "Accelerator Transmutation Studies at Los Alamos with LAHET, MCNP, and CINDER-90," Los Alamos National Laboratory, Los Alamos, NM, LA-UR-93-3080 (1993).

[3] A.G. Croff, "ORIGEN2 – A revised and updated version of the Oak Ridge isotope generation and depletion code," Oak Ridge National Laboratory, Oak Ridge, TN (1977).

[4] W. Sommer, R. Werbeck, S. Maloy, M. Borden, and R. Brown, "Materials selection and qualification processes at a high-power spallation neutron source," Materials Characterization, 43, 97 – 123 (1999).

ACKNOWLEDGEMENTS

VIBRATION STUDIES ON A SUPERCONDUCTING RHIC INTERACTION REGION QUADRUPOLE TRIPLET *

C. Montag[†], G. Ganetis, L. Jia, W. Louie, BNL, Upton, NY 11973, USA

Abstract

Mechanical vibrations of the superconducting interaction region triplets have been identified as source of horizontal beam jitter around 10 Hz in the Relativistic Heavy Ion Collider (RHIC). Therefore, cold masses inside one triplet cryostat have been equipped with accelerometers to further investigate the phenomenon. Additionally, helium pressure transducers have been installed to determine helium pressure oscillations as a possible primary vibration source. Recent results will be reported.

INTRODUCTION

The Relativistic Heavy Ion Collider (RHIC) consists of two superconducting storage rings ("Blue" and "Yellow") that intersect at six equidistantly-distributed locations around the 3.8 km machine circumference, as shown in Figure 1. During machine operation, horizontal orbit jitter at frequencies around 10 Hz can be detected in both rings [1]. The amplitude of this beam oscillation corresponds to $5 \ldots 10$ percent of the rms beam size for a 6σ normalized emittance of $\epsilon = 10\,\pi\,\mathrm{mm}\,\mathrm{mrad}$ at any BPM around the ring, pointing at multiple noise sources. A spectral analysis of this orbit jitter also revealed that spectra in both beams are practically identical, see Figure 2, indicating common vibration sources in both rings.

Since the two RHIC rings share only very few common magnetic elements IRs while the D0 dipoles and the arcs are completely independent (Figure 3), it was soon found that the beam jitter was caused by mechanical vibration of the interaction region triplets which are separate for both beams but share a common cryostat. Figure 4 shows simultaneously measured spectra of horizontal orbit jitter in the "Yellow" ring and of the mechanical vibration of the 4 o'clock triplet. Taking into account the RHIC optics it was shown that the observed jitter amplitudes cannot be explained by the amplitudes measured on the triplet cryostats, but are rather caused by independent vibration of the various cold masses within the cryostat [2].

Since this beam jitter may potentially lead to emittance growth and therefore luminosity degradation due to modulated beam-beam offsets at the interaction points, it is very desirable to find and eliminate its source. We therefore calculated and measured mechanical vibration frequencies of a triplet, and investigated helium pressure oscillations in
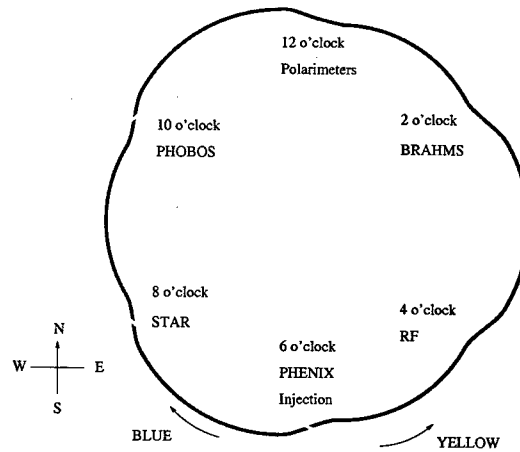
Figure 1: Schematic overview of RHIC with its six interaction regions.

the cryogenic system as a possible source.

MECHANICAL RESONANCES

Each RHIC triplet cryostat contains the cold masses of three quadrupoles (Q1, Q2, and Q3) and one dipole (D0) per ring, eight cold masses in total. Each cold mass is suspended on two posts, which for mechanical considerations are regarded as springs, see Figure 5. The connection between cold masses is designed to allow independent transverse motion, while it is stiff in the longitudinal direction [3]. Coupled motion of the cold masses can therefore be neglected.

The configuration with two posts allows for two oscillation modes per cold mass, a dipole mode with resonance frequency $f_d = \sqrt{2D/m}$ and a quadrupole mode with resonance frequency $f_q = \sqrt{2Ds^2/\Theta}$. Here, D denotes the spring constant of the posts, m the mass of the cold mass, s the distance from the center of the cold mass to the location of the post, and Θ the moment of inertia of the cold mass. The latter can be calculated as

$$\Theta = \frac{mR^2}{4} + \frac{mL^2}{12}, \tag{1}$$

where the cold mass is modelled as a solid cylinder with length L and radius R. The parameters of the various quadrupole cold masses as well as the resulting resonance frequencies f_d and f_q of the two modes for a spring constant of the posts of $D = 1.0 \cdot 10^7\,\mathrm{N/m}$ are listed in Table 1. As this shows, mechanical resonance frequencies are
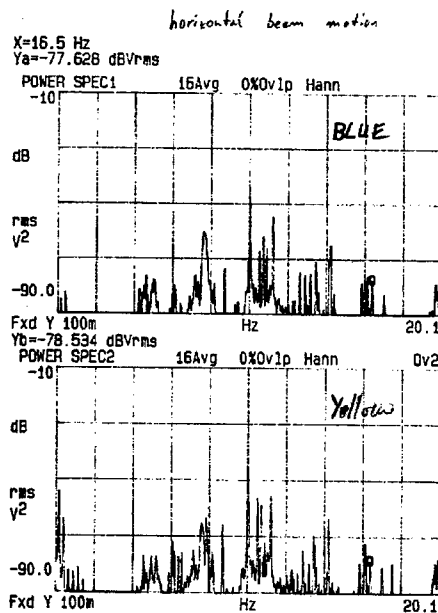
Figure 2: Simultaneously measured horizontal orbit vibration spectra in the BLUE (top) and YELLOW (bottom) RHIC rings.

	Q1	Q2	Q3
m/kg	1130	2580	2260
R/m	0.35	0.35	0.35
L/m	2.24	4.90	4.37
l/m	1.44	3.39	2.10
k/m^{-2}	$-5.76 \cdot 10^{-2}$	$5.61 \cdot 10^{-2}$	$-5.57 \cdot 10^{-2}$
s/m	0.49	1.44	1.19
Θ/kgm^2	481	5182	3614
β/m	404	551	248
f_d/Hz	21.2	14.0	15.0
f_q/Hz	15.8	14.3	14.1

Table 1: Mechanical parameters of the quadrupole cold masses in the triplet, together with the corresponding β-functions, magnetic lengths l, and magnet strengths k for $\beta^* = 2$ m at the IP.

close to those observed on the beam and on the outside of the triplet cryostats. It was therefore attempted to directly measure the mechanical resonance frequencies of the cold masses by attaching an accelerometer to the inside of the beam pipe and measuring the frequency response to a mechanical excitation. This measurement revealed dominant frequency lines at 9.75, 14.0, 16.0, and 19.5 Hz. Except for the lowest frequency at 9.75 Hz, these frequencies are consistent with the mechanical resonances calculated earlier.
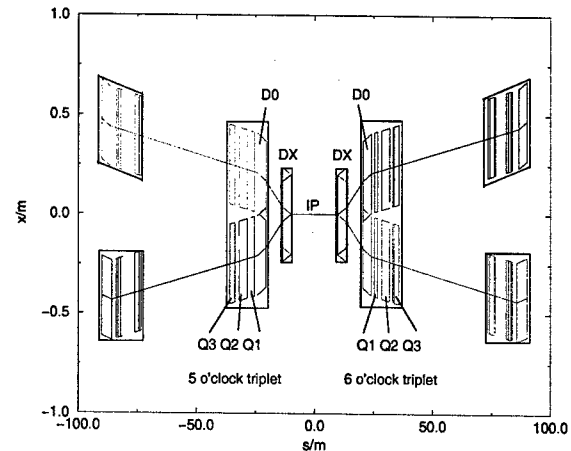
Figure 3: Schematic view of a RHIC interaction region lattice. Both beams collide head-on at the interaction point (IP) and are separated by the DX dipoles. Both orbits are bent back to an almost parallel direction by the D0 dipoles. Strong focusing is provided by superconducting triplets consisting of the quadrupoles Q1, Q2, and Q3.

HELIUM PRESSURE OSCILLATIONS

To investigate the origin of the observed triplet vibrations, helium pressure oscillations in the RHIC cryogenic system were measured. Pressure transducers were installed in the five helium transfer lines (supply (S), return (R), utility (U), heat shield (H), and magnet (M) line, see Figure 6) at the "6 o'clock" valve box and at the six power lead ports of the "6 o'clock" quadrupole triplet crystat.

The magnet line (M) showed a helium pressure oscillation at 10.7 Hz, Figure 7, while no significant oscillations could be detected at the other lines. This frequency was also measured at the power lead ports at the triplet cryostat. This pressure oscillation is caused by the helium recirculator and vanishes when the circulator is turned off. However, though the frequency of this oscillation is very close to the mechanical vibration detected on the triplet cryostat as well as the orbit jitter frequency of the RHIC beam, it could not yet be positively confirmed as the root cause of the magnet vibration and the resulting orbit oscillations.

REFERENCES

[1] C. Montag, M. Brennan, J. Butler, R. Bonati, P. Koello, Measurements of Mechanical Triplet Vibrations in RHIC, Proc. EPAC 2002, Paris

[2] C. Montag, M. Brennan, J. Butler, R. Bonati, P. Koello, Observation of Mechanical Triplet Vibrations in RHIC, Proc. 26th Advanced ICFA Beam Dynamics Workshop on Nanometre-Size Colliding Beams, Lausanne, 2002

[3] J. Sondericker, private communication
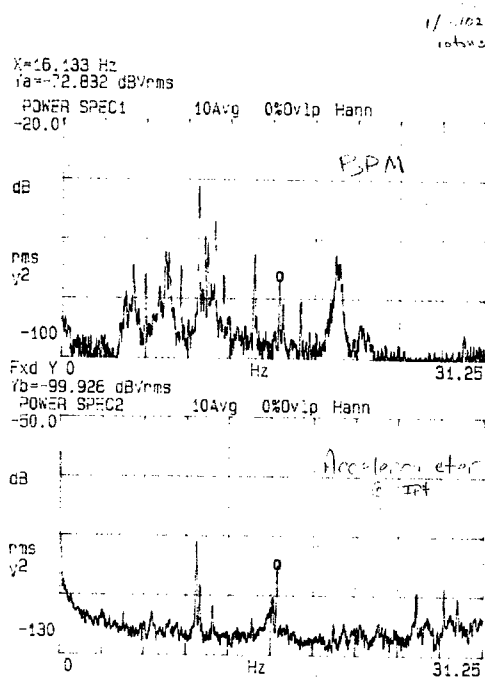
Figure 4: Simultaneously measured beam orbit vibration spectra in the YELLOW RHIC ring (top) and the 4 o'clock triplet acceleration (bottom).

Figure 6: Schematic drawing of the RHIC cryo system. Helium pressure transducers are installed in the five transfer lines, namely the supply line (S), the return line (R), the utility line (U), the heat shield (H), and the magnet line (M). Only three of the six power leads at the quadrupole triplet cryostat are shown, labeled A, B, and C.
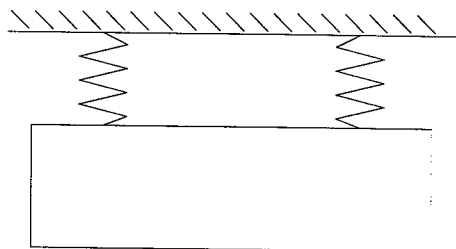
Figure 5: Mechanical model of a quadrupole cold mass suspended on two posts, indicated as springs here.
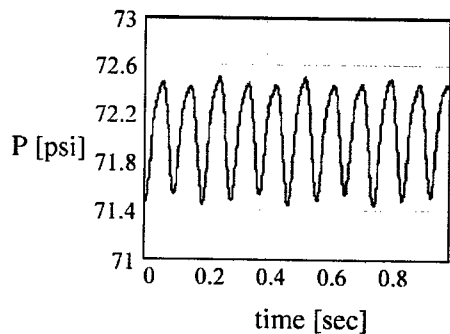
Figure 7: Measured helium pressure P in the magnet line ("M") vs. time. A spectral analysis of this signal reveals a dominating frequency of 10.7 Hz.

MECHANICAL DYNAMIC ANALYSIS OF THE LHC ARC CRYO-MAGNETS

K. Artoos, N. Bourcey, O. Calvet, O. Capatina, C. Hauviller, CERN, Geneva, Switzerland

Abstract

The arcs of the Large Hadron Collider (LHC) will contain around 1700 main superconducting dipoles and quadrupoles. The long and heavy magnets are placed on fragile composite support posts inside a cryostat to reduce the heat in-leak to the magnets super fluid helium bath. The presence of such fragile components like the support posts, the beam position monitors and the corrector magnets make the cryo-magnets very difficult to handle and transport. Furthermore, keeping the geometry of the cryo-magnets unchanged (in the range of 0.1 mm) throughout the various transports and handling is essential for the good functioning of the future LHC.

A detailed dynamic analysis was performed to determine the behavior of the cryo-magnets under all the handling and transport conditions and to choose the related optimum parameters. The results of finite element modal calculations as well as experimental modal analyses are presented and compared. The maximum accelerations admissible during transport with several types of vehicle were computed. The accelerations experienced by both types of cryo-magnets were measured during real transport with different vehicles. The dynamic deformation of the support posts in the cryo-dipole was also measured. The methodologies of these analyses and their results are reported as well as the resulting specification for the transport during the LHC installation.

INTRODUCTION

The arcs of the LHC will contain a large amount of superconducting dipoles and quadrupoles. The arc dipoles installed into their cryostats, hereafter called cryo-dipoles, are 15 m long and have a mass of about 33 ton. The so-called short straight sections (SSS) include main quadrupoles together with their correctors and the beam position monitors. The SSS are about 6 m long and have a mass of about 8 ton.

All those cryo-magnets contain fragile components, such as the thin-walled support posts made of glass fiber reinforced epoxy, to reduce environmental heat in-leak to the magnets super fluid helium bath. The position of the magnet inside its cryostat (in the range of 0.1 mm) as well as the integrity of all its components are compulsory factors for a good functioning of the future LHC.

The cryo-magnets dimensions and weight, the geometric constraints, as well as the fragile components, make them very difficult to handle and transport.

Understanding the cryo-magnets dynamic behavior is needed to avoid potential malfunctions provoked by vibrations during transport and handling.

METHODOLOGY

Important tools to assess the dynamic behavior of the cryo-magnets are numerical models of the cryo-dipole and the Short Straight Section. The models were first built with estimated parameters and then validated by measurements.

Calculations

The cryo-magnets were modeled with the finite element code Ansys™ (ref. [1], [2] and [3]). Components significant for the vibration behavior, i.e. cold mass, support posts, vacuum vessel and transport restraints, were detailed to a sufficient level.
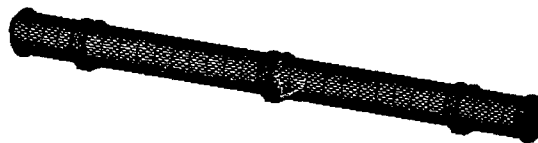
Figure 1: Cryo-dipole finite element model.

Several modal analyses were performed using the cryo-magnet finite element models together with different boundary conditions representing surface, road and tunnel handling and transport equipments.

Measurements

Two types of measurements were performed:
- modal analysis of cryo-magnets on concrete blocks
- cryo-magnet dynamic behavior during transport with different types of vehicles

The natural frequencies and the mode shapes of the cryo-magnets were determined with free (impact) and forced vibration. The harmonic and random forced excitation was applied by an electrodynamic shaker (see Figure 2) via an impedance head. Tri-axial PCB-ICP™ accelerometers measured the accelerations of the cryo-magnet components during the modal analysis.
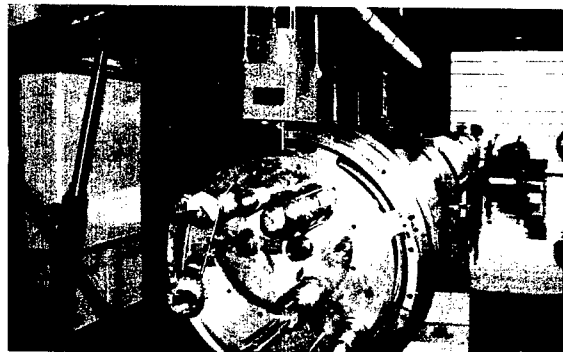
Figure 2: Cryo-dipole on concrete blocks modal analysis.

During handling and transport, the same accelerometers were used together with LVDT gauges that measured the tri-axial dynamic deformations of the support posts.

Calculations and measurements were then combined to specify the maximum allowable accelerations during different types of handling and transport.
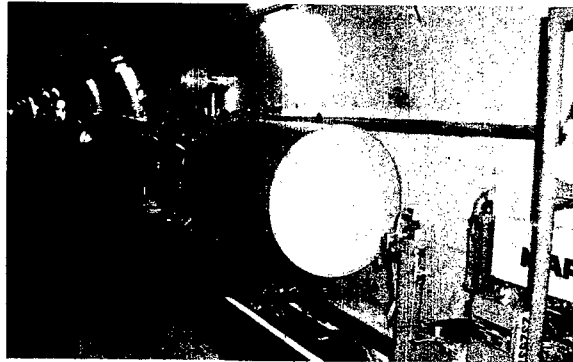
Figure 3: SSS on tunnel vehicle.

Figure 3 shows an acceleration and support post deformation test of a SSS during a transport in the LHC tunnel.

RESULTS

Modal analysis

Several cases were treated with the methods mentioned above. Experimental cryo-dipole and SSS modal analyses were performed. The natural modes were determined for three directions (lateral, vertical and longitudinal) up to 50 Hz, with the cryo-magnets installed on concrete blocks (i.e. the boundary conditions during storage).

The natural frequencies and the modal shapes obtained permitted to validate the finite element models.

Table 1 gives an example of the comparison between tests and calculations, for the first four vertical modal shapes and natural frequencies of the cryo-dipoles installed on concrete blocks.

Table 1: Example of cryo-dipole on concrete blocks modal analysis results - comparison tests/calculations:

Cryo-dipole vertical modal shape	Frequency	
	Tests	Calculations
	8 Hz	10 Hz
	16 Hz	17 Hz
	28 Hz	32 Hz
	36 Hz	34.6 Hz

The complete modal analysis of cryo-dipole and SSS are reported in [2], [3], [4] and [6].

The validated finite element models were then used to compute the cryo-magnets behavior, when installed on various types of transport units. The new modal schemes were calculated for the cryo-magnets under transport conditions, by replacing the "concrete blocks" boundary conditions by appropriate new boundary conditions. For each type of boundary conditions, corresponding to a given transport vehicle, a new finite element modal analysis was performed.

As an example, the first four vertical modes of the cryo-dipole installed on a vehicle for road transport are presented in Table 2.

Table 2: Example of cryo-dipole on a road vehicle modal analysis results:

Vertical modal shape	Calculated frequency
	1.9 Hz (rigid body motion)
	2.9 Hz (rigid body motion)
	13.7 Hz
	18.3 Hz

For each identified modal shape, the maximum admissible acceleration at a specific point of the magnet was calculated from the specified maximum deformations of the support posts. This specific point is the point where accelerometers will be installed during the transport.

Behavior during transport

Accelerations as well as support post deformations were measured during several cryo-magnet transports with surface, road and tunnel vehicles.
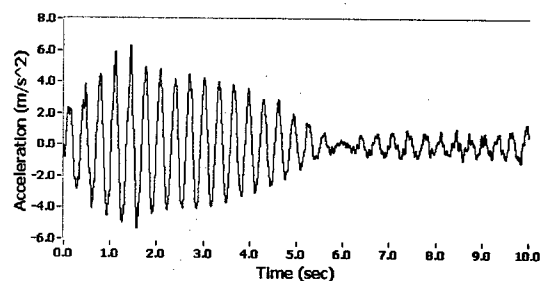
Figure 4: Event recorded in vertical direction during road transport of a cryo-dipole.

For the cryo-dipole road transport, the most important vibration amplitudes in the vertical direction were observed at a frequency of 3 Hz, corresponding to the second mode identified in Table 2.

The modes with the most important amplitudes were identified for the three directions. For an exhaustive list, please refer to [4], [5] [6] and [7]. The measured accelerations and support post deformations were coherent.

1435

Knowing the modes that are excited during a given type of transport, and knowing the corresponding acceleration limits at a given point of the cryo-magnet, global accelerations limits were defined for each type of transport.

The accelerations measured at the extremity of the dipole cold mass and the support post deformations during road transport are presented in Table 3. They are compared with the maximum allowed values.

Table 3: Maximum admissible and measured accelerations for a cryo-dipole road transport

		Lateral	Vertical	Longitudinal
Accelerations (m/s²)	Limits	5	7	4
	Tested	3.2	6.5	1.1
Deformations (mm)	Limits	0.42	0.16	0.42
	Tested	0.05	0.12	0.05

Table 3 shows measured values in the vertical direction close to the admissible limits.

SERIAL TRANSPORT

More than 1200 cryo-dipoles and more than 350 SSS will have to be transported and handled several times, and with different vehicles and handling devices, during the installation phase of the LHC. All these operations are critical. Table 3 indicates that the measured values in the vertical direction, during cryo-dipole road transport, are close to the limits.

A geometry and integrity check of the cryo-magnets is not possible in the tunnel, prior to installation. Localizing and removing a damaged cryo-magnet installed in the tunnel, would be an important time-consuming operation. A detailed qualification of all the vehicles and handling devices that will be used during the LHC installation is hence needed. Each transported and handled cryo-magnet will also be monitored to ensure that the acceleration limits presented in the precedent paragraph have not been exceeded. A tri-axial acceleration-monitoring device will be placed at a specified position on each transported cryo-magnet.

CONCLUSIONS

A detailed dynamic analysis was performed to determine the behavior of the cryo-magnets under all the handling and transport conditions.

Finite element calculations and experimental modal analyses of cryo-magnets under storage conditions (placed on concrete blocks) were performed up to 50 Hz. The calculations and test results were compared and the finite element models were validated.

The finite element models were then used to calculate the modal scheme of the cryo-magnets under various transport and handling conditions. The dynamic behavior of the cryo-magnets during handling and transport was also tested, and energetic modes were identified. From both, calculations and test results, the maximum accelerations admissible during transport with several types of vehicles were specified.

The accelerations experienced by both types of cryo-magnets were measured during real transport with surface, road and tunnel vehicles. The dynamic deformations of the support posts were also measured. Accelerations and dynamic deformations were coherent.

The tests have shown that it is possible to handle and transport the cryo-magnets without damage. Several measured accelerations were however very close to the limits. Each transported and handled cryo-magnet must hence be monitored to insure that the specified acceleration limits have not been exceeded, to avoid installation of damaged cryo-magnets.

REFERENCES

[1] https://edms.cern.ch/file/332842/1.0/TN02_11.pdf, O. Calvet, C. Hauviller; "Analyse du comportement mecanique des cryodipoles du LHC - 1ere partie: Statique"; LHC-CRI Technical Note 2002-11

[2] O. Calvet, C. Hauviller; "Analyse du comportement mecanique des cryodipoles du LHC – 2ème partie: Dynamique"; LHC-CRI Technical Note 2002-12

[3] https://edms.cern.ch/file/352974/1/2002-003.pdf, P. Cupial, J. Snamina; "The verification of the computational models of the LHC Short Straight Section"; Technical Note EST-ME/2002-003

[4] https://edms.cern.ch/file/348871/2/TN02_07.pdf, K. Artoos, O. Calvet, O. Capatina; "Experimental modal analysis and acceleration measurements during surface transport of a LHC cryodipole"; LHC-CRI Technical Note 2002-07

[5] https://edms.cern.ch/file/350433/1.0/TN02-13.pdf, K. Artoos, N. Bourcey, O. Capatina; "Acceleration and support posts deformation measurements during surface transport of a LHC cryodipole", LHC-CRI Technical Note 2002-13

[6] https://edms.cern.ch/file/347269/2.1/TN02_06.pdf, K. Artoos, O. Capatina; "Experimental modal analysis and acceleration measurements during transport of a LHC Short Straight Section", LHC-CRI Technical Note 2002-06

[7] K. Artoos, O. Capatina, "Acceleration and support posts deformation measurements during surface and tunnel transport of a LHC Short Straight Section"– to be published

DIGITAL CRYOGENIC CONTROL SYSTEM FOR SUPERCONDUCTING RF CAVITIES IN CESR*

P. Quigley#, S. Belomestnykh, R. Kaplan, Cornell University, Ithaca, NY 14853, USA

Abstract

Effective cryomodule control and monitoring are essential components to successful operation of CESR (Cornell Electron Storage Ring). The ability to quickly diagnose system problems can have a dramatic effect on machine down time. The CESR SRF Digital Cryomodule control system, employing a PC and a commercial PLC and user interface, is presented. With these tools, system status is available at a glance or, if needed, detailed system information can be displayed. Straightforward configuration of PID (Proportional Integral Derivative) control loops, safety interlocks, signal display, and data acquisition is the main feature of the system. The SRF cryomodules have several modes of operation. For example, under normal machine running conditions, liquid helium level is regulated using a liquid-level signal as the process variable (PV). For cryostat cool-down, the flow rate of cold helium gas returning to the refrigerator directly reflects cryomodule cooling rate and is a more useful process variable. Both these operational modes use the same control variable (CV): the liquid helium supply valve control signal. Other operational modes include warm-up and RF processing. This control system can be reconfigured quickly to meet the conditions of different operational modes.

INTRODUCTION

Previous SRF cryomodule monitoring and control at Cornell's Laboratory for Elementary-Particle Physics (LEPP) [1] has been implemented using discrete controllers for each loop. All control settings were entered at the front panel and loop behavior was also monitored there. The computer interface for these controllers was via RS232 computer interface at a one-minute data rate. Vacuum and cryogenic temperature monitoring was done with commercial vacuum controllers and in-house built signal processing printed circuit cards. Interlocks were implemented with a combination of fast switching circuitry and hardware relay logic.

This discrete module control system was failure prone and lacked full remote capability. It has been replaced with a programmable logic controller (PLC) crate with ten modules, described in Table 1.

Before SRF cryomodules are installed in CESR, they are tested in the high power test area. Because much experience has been gained cooling down and warming up CESR cryomodules in this test area, it was chosen as a good place to revamp the cryogenic control system. PLCs are widely used for industrial applications and have

proved to be reliable for controlling CESR Klystron HV power supplies.

Table 1: CESR's ControlLogix Crate

Slot	Module	Part #	Description
0	Logix5550 Processor	1756-L1M1	512KB Memory
1	Ethernet	1756-ENET/B	Ethernet Bridge
2-5	Analog Input	1756-IF16	16 Channel Non-Isolated Voltage/Current Analog Input
6	Analog Output	1756-OF8	8 Channel Non-Isolated Voltage/Current Analog Output
7	Relay Output	1756-OX8I	8Point 10V-265V AC, 5V-150V DC Isolated Relay N.O./N.C.
8-9	Digital Input	1756-IB16I	16 Channel 10V-30V DC Isolated Input, Sink/Source

HARDWARE

Break-Out Box

The cryomodule break-out box serves as the interface between the module and the control rack. The box houses DC power supplies for all cryomodule signal processors. It also houses the signal processors for cryogenic linear temperature sensors (CLTS), thermocouples, water flow, and linear variable displacement transducers (LVDT), as well as housing differential amplifiers. All but a few signals port through the break-out box. Standard twisted pair and coaxial cables link the break-out box with the control rack.

Programmable Logic Controller (PLC)

The hardware interface of the digital control is the Allen Bradley ControlLogix PLC [2]. The PLC crate has 10 slots for modules. ControlLogix crates also require an attached power supply.

The computer network portion of the system uses the Ethernet protocol and is set up as an independent subnetwork for RF cryogenic control. This network is referred to as a Virtual Local Area Network (VLAN), and the network architecture provides a means for qualified PCs to communicate while isolated from non-RF system

computers but maintains administrator-level access to the VLAN.

Each signal is processed before it reaches the PLC. All system connections with the exception of vacuum pump power supplies and some RF field signals are made through a break-in panel with pluggable connectors. From the break-in panel, vacuum and liquid helium signals go to their respective commercial controllers for processing. The analog outputs for these, along with the signals that are processed by the break-out box, are then routed to a series of multilevel terminal blocks. These terminal blocks serve as an intermediate distribution point between the PLC modules and the rest of the system.

Each PLC module is also fitted with a removable terminal block. This second group of terminal blocks can be bench-wired and then plugged into the front of their respective modules. Each removable terminal block and module can be manually keyed to insure a correct match. The manufacturer claims that removal and installation of these terminal blocks can be done under power, but they caution that if field side power is applied, this can cause arcing at the contact point, which can result in a build-up of contact resistance.

The control rack is designed to be completely portable, thus facilitating off-site rack fabrication and, if needed, installation following acceptance tests.

The PLC has the added advantage that it can run independently of the user interface should network or PC problems arise.

SOFTWARE

All programs in this system are running on a PC with a Windows 2000 operating system.

Ethernet

The Ethernet network interface was chosen for its speed, low cost, and broad applications to general computer system hardware throughout the commercial market.

Digital Interface and Control Software

Three principal sets of software are at work here: Allen Bradley's RSLogix 5000, Kepware's KepServerEX, [3] and National Instruments Lookout [4].

PLC Software

RSLogix 5000 is the programming software for the ControlLogix PLC. With this software one can configure the I/O modules and program the PLC with a ladder logic editor. Through a series of dialogue boxes, one can configure I/O modules for current or voltage, communication mode, data rate, fault reporting, among other things. Through the ladder logic editor, the user programs the PLC with familiar terminology. One can choose from a variety of instructions ranging from basic And/Or to complex mathematics, PID, and motion control. Once the program is complete, it can easily be verified prior to implementation. The program and configuration can then be downloaded to the PLC.

Some additional PLC software features include fault reporting for the crate controller and modules, and wire-off detection for the individual module channels.

OPC Server

Communication between the PLC and the network requires linking software. KepServerEX provides this link between the PLC and the user interface at the PC. This link is an industry open-specification standard, generally known as OPC (Object Linking and Embedding for Process Control), that was developed to provide a means for different manufactures of hardware and software to work together in a seamless manner [5]. Although Allen Bradley makes an application called RSLINX that provides similar connectivity, KepServerEX was chosen due to CESR's previous experience with it and its low cost.

National Instruments Lookout

For this system, Lookout is the user interface, commonly referred to as a human-machine interface (HMI) with supervisory control and data acquisition (SCADA) capabilities. Lookout is object based, that is, it uses object linking and embedding (OLE) to make connections to and from memory locations, which are referred to as tags. Once Lookout is able to communicate with the PLC, building the user interface is simple. Lookout connects to the PLC through an OPC client object. Once this object is created, all appropriate tags are visible in the Lookout object explorer. For example, to create a display for temperature, one opens the object explorer and moves down the file tree to the tag that will be displayed, then selects the item by right-clicking and dragging it to the area of display. Several display methods are available; in this case, one would use the default which is numeric display. This object can also be copied and morphed into another type of display, such as a potentiometer or bar graph.

The SRF cryogenic system status panel is the heart of the user interface, shown in Figure 1. From this panel, one can view the entire system and its health. Detailed system information that can be displayed encompasses: cryogenic system parameters, including liquid helium level, helium bath pressure, cryogenic and thermocouple temperatures in and on the cryomodule, cryogenic transfer line temperature and pressure; vacuum status, including cold cathode and Convectron (760 Torr to 1 mTorr); and system interlocks.

Another feature of Lookout is that rendered AutoCAD drawings arranged in layers provide a mechanically accurate path to view, for instance, historical data and alarms for system components.
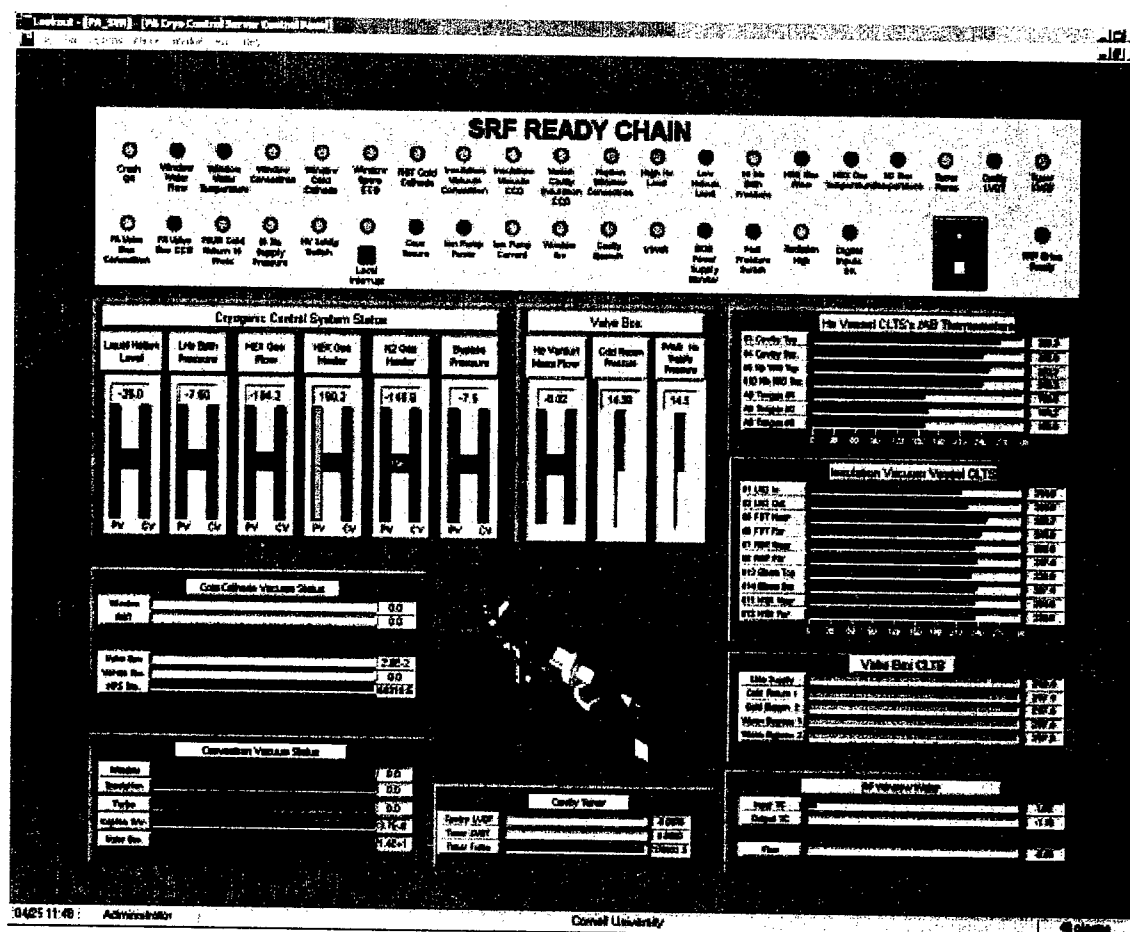
Figure 1: Cryomodule Root Control Panel

CONCLUSIONS

The digital cryogenic control system now being used at CESR has several advantages over its predecessor.

The small footprint of the hardware interface is convenient. Off-site assembly of the control rack and open access to test points makes for easy maintenance of the system. The layout of the multilevel terminal blocks allows ready access for trouble shooting and general testing. It also allows for any reconfiguration or modification of the system as CESR's superconducting program develops.

Once the developer becomes familiar with the software, building the user interface can be done in a timely manner. The HMI is an excellent tool to understand the status of the cryomodule because it allows the user to locate problem areas quickly. As the cryogenic system complexity increases, the graphical user interface provides visual information that is quickly comprehended by the experienced and by those less familiar with the SRF cryomodule.

REFERENCES

[1] S. Belomestnykh et al. "Operating Experience with Superconducting RF at CESR and Overview of other SRF Related Activities at Cornell University" Proceedings of the 9th Workshop on RF Superconductivity, Santa Fe, NM. November 1999, vol. 1, pp. 24-30.
[2] http://www.ab.com/catalogs/b113/controllogix/
[3] http://www.kepware.com/OPC_Server.html
[4] http://www.ni.com
[5] http://www.opcfoundation.org/

AUTOPSY RESULTS OF FAILED LITHIUM COLLECTION LENSES AT THE FNAL ANTIPROTON SOURCE*

P. Hurh#, A. Leveling, FNAL, Batavia, IL 60510, USA
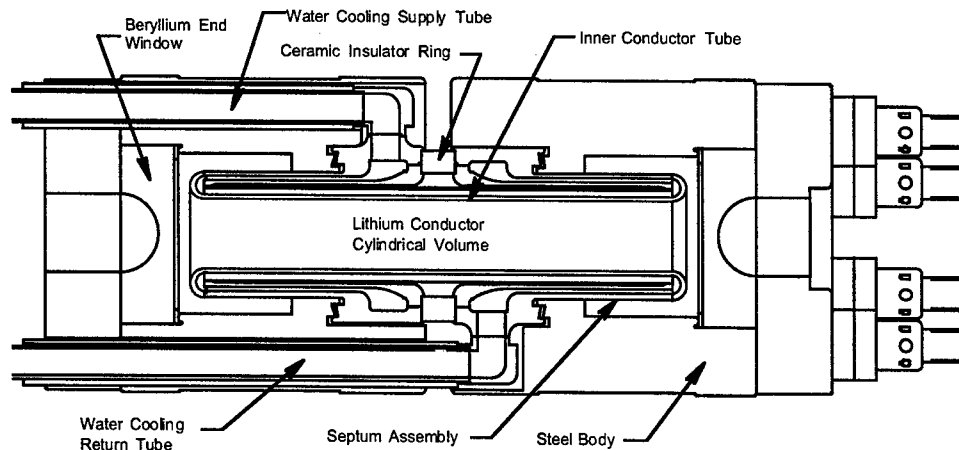
Figure 1: Cross-section diagram of Collection Lens Device. Septum conductor tube is shown in blue.

Abstract

A lithium lens focusing device is used at the FNAL Antiproton Source to collect antiprotons immediately downstream of the production target. Recently developed methods of removing lithium from old collection lens devices have enabled the dissection and autopsy of several failed lenses. Examination reveals longitudinal fatigue cracks in the titanium alloy (6 Al- 4V) cooling jackets. A finite element analysis to estimate stress intensity factors expected in the cooling jackets is presented and compared to the crack propagation and fracture toughness thresholds for Ti 6Al-4V. Results presented indicate that crack initiation and propagation at the currently estimated service loads are unlikely without additional material degradation mechanisms at work.

INTRODUCTION

Failures of Collection Lens devices at the AP-0 P-bar Target Hall in the past have generally been left un-inspected due to the level of residual radioactivity and the semi-hazardous nature of lithium metal. Recently however the passage of time and development of methods to safely remove lithium from a Lens assembly have allowed failure investigation [1]. Five Lens assemblies have been so 'unfilled' and unassembled. However only two assemblies (numbered 20 and 21) have been examined in detail. Both Lenses were constructed in 1993 and failed in service (in 1995) after only a few hundred thousand pulses each, both much earlier than what would be expected from previous Lenses (lifetimes of several

million pulses). Both Lenses appeared to fail due to breaches in the titanium alloy (Ti 6Al-4V) cooling jacket (historically called the septum).

The cross-section of the Lens assembly and septum is shown in Figure 1. The septum of a Collection Lens serves two functions. Firstly, it contains the structurally soft lithium in the cylindrical shape of the central conductor. Secondly, it cools the central lithium conductor by removing heat deposited by the current pulse and the beam pulse from the conductor into a Low Conductivity Water (LCW) system.

The most highly stressed part of the septum is the conductor tube. Stresses arise from several loading sources such as thermal expansion from the current pulse (nearly 500 kA at operating gradient) and the beam pulse, magnetic forces from the current pulse, and structural loading from clamping bolts and lithium filling pre-load. This tube directly contacts the lithium central conductor cylinder on its inner radius surface (1 cm radius) and directly contacts longitudinally flowing LCW on its outer radius surface. The conductor tube wall thickness is 1 mm. It is this conductor tube of each Lens that was the subject of this investigation.

FAILURE DESCRIPTION

Conductor tubes of both Lenses appeared to fail due to a single longitudinal crack through the wall thickness of each tube. This breaching of the septum in each case allowed LCW to come in contact with the lithium. Since lithium and water react to form lithium hydroxide and hydrogen gas exothermically, considerable damage to the conductor tube could occur (especially during subsequent current pulses). This damage could obscure features of the initial tube failure.

1440

Fig. 2: Lens 21 septum conductor tube showing longitudinal crack and melted through area.

Fig. 3: Lens 20 conductor tube crack profile. ID surface at bottom of picture. Tube wall thickness: 1 mm.
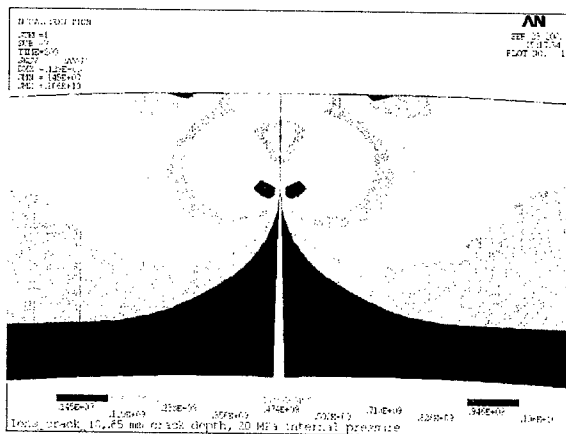
Fig. 4: Von Mises stress equivalent in crack area of ANSYS® model.

In addition, the exit of lithium from the cylindrical conductor volume could create voids which may promote localized areas of extreme heating or even arcing. Finally, both Lenses were stored for long periods of time before dissection. Lithium hydroxide solution, present in the

Lenses over the 6 year period between failure and unfilling, may have corroded or otherwise affected septum surfaces.

Macroscopic Features

Figure 2 shows the conductor tube from Lens 21 with the longitudinal crack which is presumed to have occurred first. In addition Figure 2 shows a badly burned and, in places, melted region at one end of the longitudinal crack. The region is continuous around the circumference of the tube. The tube wall is actually bulged out in this damaged region presumably from internal pressure or a small explosion. The titanium alloy appears to have local areas of melting (Ti 6Al-4V melting point is 1650 °C). The conductor tube from Lens 20 appears very similar to that of Lens 21 (including the longitudinal crack) except for the absence of the bulged out region.

Crack Cross-sections

The conductor tubes of both Lenses were prepared into cross-section samples. Figure 3 shows a typical profile of the through wall crack. Most of the profiles studied show two distinct crack propagation regimes, a region of seemingly brittle cyclic crack propagation near the ID surface and a region of ductile fracture near the OD surface. This indicates that the crack originated on the ID surface and progressed cyclically outward. Once the crack had progressed far enough to weaken the wall sufficiently, the crack progressed rapidly in a ductile fashion to the OD surface. In addition in many of the profiles, some reduction of area (or necking) can be observed at the OD surface indicating considerable plastic deformation before complete failure.

Estimations of the loading just prior to the final ductile failure can be made by observing the remaining wall thickness just before final rupture. Using a 2-D ANSYS® [2] finite element model and a crack depth of 0.65 mm, various load magnitudes were investigated. Figure 4 shows the equivalent stress in the crack area of the model under 20 MPa of internal pressure (equivalent to 200 MPa of hoop stress). The stress pattern and deformation shape are in agreement with the photographed cross-sections. Using an ANSYS® routine, KCALC, the stress intensity factor for this geometry and loading was calculated to be 64.5 MPa-m$^{-1/2}$. This can be compared to the fracture toughness of mill annealed titanium alloy (6Al-4V) of 64.9 MPa-m$^{-1/2}$[3]. For comparison, hoop stress in the conductor tube pulsed at normal operating gradient (745 T/m) predicted by a full Lens FEA [4] is 343 MPa.

Although loads predicted by FEA are large enough to agree with observations of the final ductile failure, they are not high enough to explain the initial, brittle crack propagation. The threshold stress intensity factor for Ti 6Al-4V below which fatigue crack propagation does not occur is 7 MPa-m$^{-1/2}$. Using a similar FEA crack model, it is predicted that an initial crack would have to be 0.15 to 0.25 mm deep before propagating at a rate high enough to fail in the 10E6 cycles range.

Micro-cracks

The cross-section samples were examined under high magnification. Micro-cracks on the order of 10 to 20 microns deep can be seen in Figure 5. The cracks appear to be inter-granular and fairly blunted. In addition, there are locations near the opening of the large, through crack that appear pitted with rice grain shaped voids. All of the micro-cracks are on the ID surfaces of the samples.

The cause of these micro-cracks is not readily apparent, although the role they play in initiating fatigue failure may be critical. Their appearance may indicate some sort of corrosive or embrittlement mechanism, however drawing conclusions from such minute indications is difficult. In fact the micro-cracks may have been caused by chemical reaction and/or electrical arcing after the failure of the septa.

Fracture Surfaces

The fracture surfaces of Lens 20 were examined with a SEM. Figure 6 shows a portion of surface in the brittle fracture zone. Note the extremely stratified appearance and pervasive micro-cracking. Figure 7 shows a portion of the surface in the ductile fracture zone. Note that the characteristic ductile dimples are disrupted with a maze of micro-cracks. These surfaces appear to be abraded or corroded after the original failure, possibly by pulsing, arcing, or chemical reaction. Future studies are planned to explain these curious features.

CONCLUSION

The examinations of failed Collection Lenses 20 and 21 have revealed that the Lenses' septa failed due to fatigue failure. However, fracture features indicate that loads at final failure were not great enough to initiate and propagate small cracks from the ID surface. Thus the loading conditions must have been much more severe earlier in service and/or the fatigue was assisted by degradation of the structural integrity of the Ti 6Al-4V septa material (such as hydrogen embrittlement, stress

corrosion cracking, or liquid metal embrittlement). In addition, small micro-cracks were found on the ID surface of the septa conductor tubes which support the latter possibility. Autopsies of this type will be conducted on several other failed lenses and should include fracture toughness testing to identify material degradation. These topics are discussed in greater detail in a Fermilab MSD Note [5].
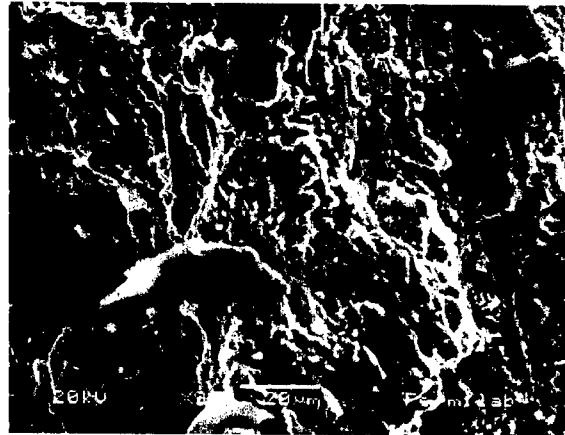
Fig. 6: Lens 20 conductor tube brittle fracture surface.
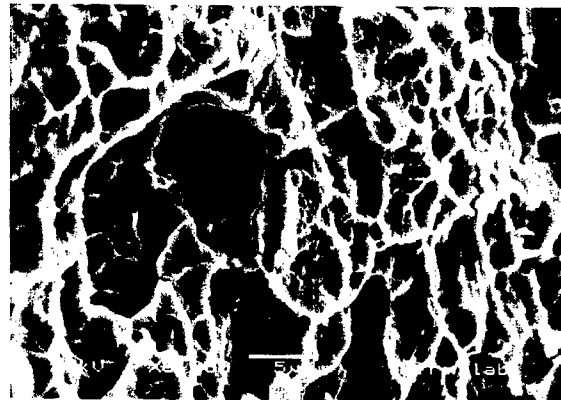
Fig. 7: Lens 20 conductor tube ductile fracture surface.

REFERENCES

[1] A. Leveling, Fermilab P-bar Note #664 (2001).

[2] ANSYS® is a registered trademark of SAS IP Inc.

[3] Materials Properties Handbook: Titanium Alloys, edited by R. Boyer, G. Welsch, E.W. Collings, ASM International, Materials Park, p. 582 (1994).

[4] P. Hurh & S. Tariq, "Comprehensive Electro-Magnetic, Thermal, and Structural Finite Element Analysis of the Lithium Collection Lens at the FNAL Antiproton Source", ROPB011,PAC 2003, Portland (2003).

[5] P. Hurh, "Examination Results of Failed Collection Lens Septa 20 and 21", Fermilab MSDNote #MSDN-ME-000022 (2002).

Fig. 5: Lens 21 conductor tube crack profile. Shows micro-cracking on ID surface. 1000x.

THE DESIGN OF A DIFFUSION BONDED HIGH GRADIENT COLLECTION LENS FOR THE FNAL ANTIPROTON SOURCE*

P. Hurh#, J. Morgan, R. Schultz, FNAL, Batavia, IL 60510, USA

Abstract

Advances in metal joining technology have made it possible to manufacture a one piece lithium lens design utilizing diffusion bonding rather than the current multiple piece, electron beam welded lithium lens design. Advantages of the new design include fewer lithium seals, incorporation of heat treatment with the bonding cycle, vastly simpler assembly requirements, and decreased cost and manufacturing time. Fatigue testing results are presented which indicate that the diffusion bonded joints are just as strong as the parent material. Results from a first prototype of this new design are presented as well as the design of a second prototype.

INTRODUCTION

The antiproton source incorporates a lithium lens to greatly improve the transmission efficiency of antiprotons into the Debuncher ring. A lithium lens is ideally suited for capturing the highly divergent antiproton beam emanating from the target into a phase space that can be transported through a beam-line with magnets of conventional dimensions. The lens has a large axial current passing through a solid lithium cylinder that produces a strong magnet field approximately proportional to the radius. The lens also has the advantage that it focuses in both transverse planes. The design gradient of the 1 cm radius lithium lens was 1,000 T/m (10 Tesla surface field). However, operational lenses have

Fig. 1: Lens gradient vs. Antiproton yield (predicted and measured) for various transverse acceptances.

not been able to sustain the design gradient for enough pulses to be practical. Lenses at the design gradient have failed within days or weeks due to mechanical failures of the titanium tube that contains the lithium. Peak stresses in the titanium rise rapidly as joule heating is increased. Running lenses at reduced gradient has allowed them to survive for an acceptable length of time, millions of pulses and an operational life of greater than 6 months. The penalty for lowering the gradient is less antiproton yield due to the reduction in focusing strength. The operational gradient of the lithium lens is 745 T/m, which is a compromise between service life and performance.

Beam models and measurements indicate that the antiproton yield can be increased by running the lithium lens at an increased gradient. Figure 1 shows the predicted relationship between antiproton yield and lithium lens gradient as a function of transverse acceptance. The ideal gradient is dependent on the optics and acceptance of the AP-2 line, but in most cases is around the design of 1,000 T/m. Operating at 1,000 T/m instead of 745 T/m is expected to increase the antiproton yield by about 10% with the present AP-2 and Debuncher acceptance, and up to 17% after the acceptance is doubled.

Figure 2 shows a cross-section schematic of the currently operating Lens design. The central lithium conductor volume is bounded by the Ti 6Al-4V cooling jacket (historically called the septum), two beryllium end windows and two steel body halves. The entire assembly is held together by highly pre-loaded Ti 6Al4V bolts which provide sealing force to the critical lithium seals between the end windows, the body halves and the septum. The cylindrically shaped Lens assembly is clamped within an 8 to 1 transformer so that it makes up the single, secondary circuit. Current enters the lens assembly from the transformer contact fingers at the outer diameter of the steel bodies. Current passes through the steel body into the dumbbell shaped lithium buffer regions external to the septum where it is directed into the central lithium conductor by the septum.

The most highly stressed part of the septum is the conductor tube. Stresses arise from several loading sources such as thermal expansion from the current pulse (nearly 500 kA at operating gradient) and the beam pulse, magnetic forces, and structural loading from clamping bolts and lithium filling pre-load. This tube directly contacts the lithium central conductor cylinder on its inner surface (1 cm radius) and directly contacts longitudinally flowing low conductivity water on its outer surface. The conductor tube wall thickness is 1 mm. Failures of past Lenses have generally involved the failure of this septum conductor tube [1]. The septum is constructed through a painstaking electron beam welding process that involves several steps of machining, cleaning, etching, baking, and
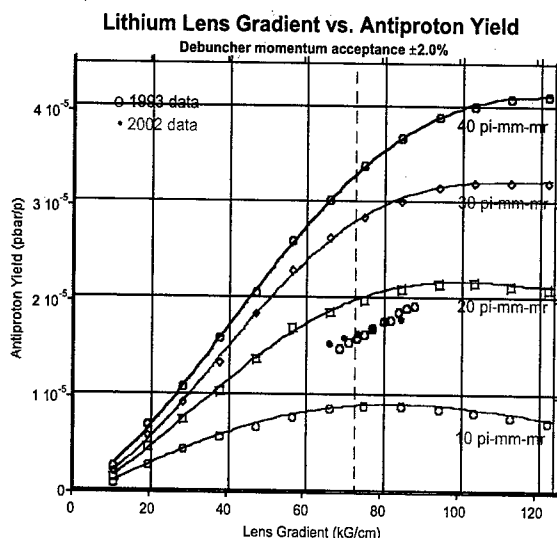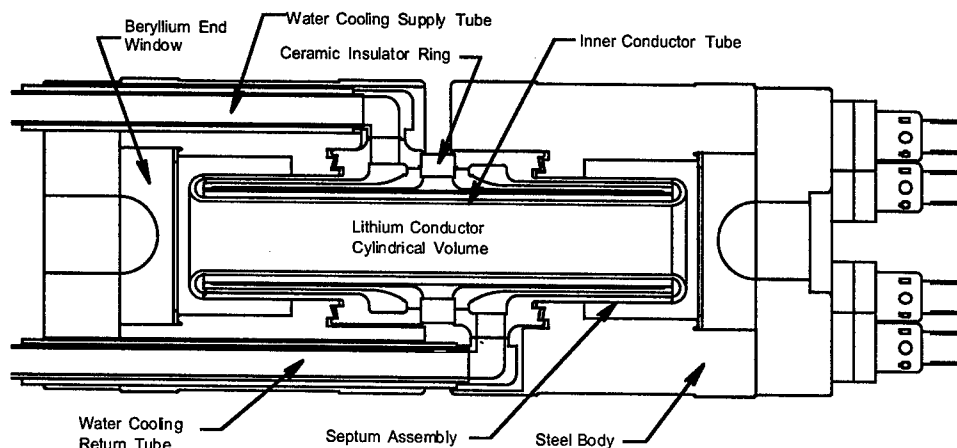
Figure 2: Cross-section diagram of Collection Lens Device. Septum conductor tube is shown in blue.

radiographic NDE for each weld. This, in conjunction with the custom fitting of seal interfaces and the lithium filling process, make the construction of the current Lens design a lengthy (8-10 months at best) process.

The goal of designing an improved Lens is to reliably construct Lenses capable of a 1,000 T/m focusing gradient over a 1 cm radius aperture in a beam environment of 5E12 protons on target per pulse (at 0.5 Hz pulse frequency) without failing in less than 10E6 pulses. Practical considerations also limit the geometrical size of the Lens assembly such that it fits within the existing transformer. It is also desired to increase the ease of manufacture and assembly to improve cost, schedule, quality assurance and reliability.

HIGH GRADIENT LENS FEATURES

At the time of this writing, several design features for a high gradient Collection Lens design are being researched for possible inclusion in a full-scale, operable prototype Lens, hoped to be constructed within the next year.

Diffusion Bonding

Diffusion bonding is a process of joining suitably active
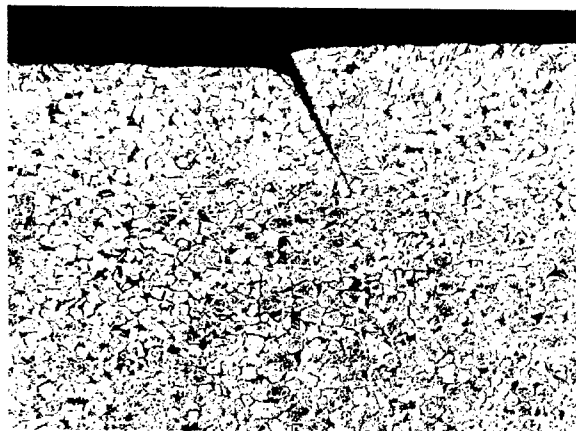
Fig. 3: Diffusion bond joint in Ti 6Al-4V (100x).

metals using pressure and high temperature in a vacuum environment. Figure 3 shows a micrograph of two titanium alloy (Ti 6Al-4V) blocks diffusion bonded together. Away from the edge of the blocks, grain growth across the bond line has been achieved such that material strength in the bond area should be that of the parent material. Advantages of diffusion bonding in a Collection Lens design include ease of construction (one bonding step versus many electron beam welds), elimination of critical lithium seals (body halves and septum can be of one piece construction), and incorporation of water cooling into the body halves themselves. Disadvantages include precision machining requirements (both pre- and post-bond), possibly decreased fatigue strength, and the fact that it is an untried technology for this application.

In order to explore these advantages and disadvantages two identical proof-of-principle, small prototypes were constructed which utilized diffusion bonding. One was cut open to examine bond quality (Figure 4), while the other is currently being assembled and filled with lithium for test pulsing. In addition, several samples of the central critical joint (in the septum conductor tube) were fatigue tested and compared to un-bonded parent material samples of identical geometry. The diffusion bonded samples were found to exhibit fatigue endurance limits equal to the un-bonded parent samples (approx. 60 ksi, R=0.1, greater than 10E7 cycles). Thus diffusion bonding is deemed to be a highly promising technology to be incorporated in the full-scale prototype.

For one piece diffusion bonding construction, the Lens body halves must be made of titanium alloy rather than carbon steel. Although titanium is significantly more resistive than steel, diffusion bonding allows the easy inclusion of water passages within the body halves for increased cooling. Also, the dumbbell shaped lithium buffer regions are eliminated in a diffusion bonded Lens. This may help constrain the lithium from extruding out of the central conductor volume during the magnet pinch, but may increase pressure upon the end windows. These
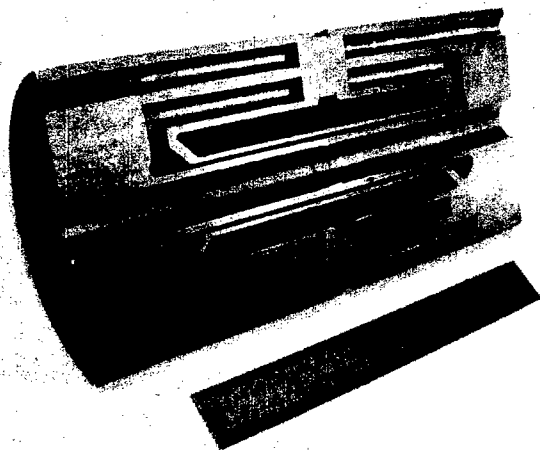
Fig. 4: Bonded Lens, before post-bond machining.

issues will be explored by utilizing finite element analysis (FEA) techniques currently being developed [2].

Material Upgrades

A near-beta titanium alloy (Ti 10V-2Fe-3Al) is being investigated as a replacement for the currently used alloy (Ti 6Al-4V). Ti 10-2-3 possibly possesses significant improvements in fatigue endurance limit and fracture toughness over Ti 6-4. Solution and age heat treatment can be easily incorporated with the diffusion bond process to develop optimal properties. Currently fatigue test results confirm that the Ti 10-2-3 endurance limit is at least 105 ksi (R=0.1, greater than 10E7 cycles) after the diffusion bond heat schedule. This can be compared to the 60 ksi value for Ti 6-4 cited earlier. If diffusion bonding of Ti 10-2-3 can be developed to preserve this 175% advantage, then significant gains in Lens lifetime may be achieved.

Also being investigated is replacement of conventional alumina ceramic insulators with yttria partially stabilized zirconia ceramic.(YTZP). In the past, time intensive hand lapping of alumina ceramics was required. Preliminary tests using YTZP (with its increased flexural strength) have shown that these fitting procedures can be entirely eliminated. Some disadvantages of YTZP are decreased
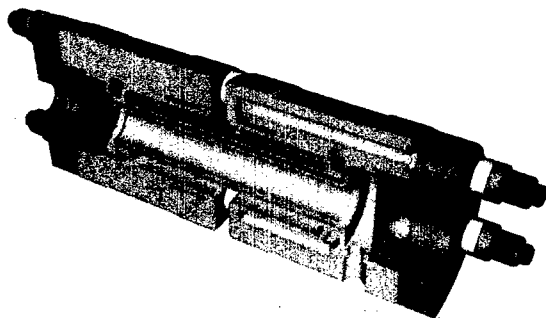
Fig. 5: Conceptual drawing of high gradient Lens prototype.

resistivity (especially at high temperature, 300 - 500 °C) and de-stabilization in humid, moderate temperature environments (200 °C). For Lens operations, temperatures will need to be controlled below these limits.

Protective Coatings

Autopsy results of failed Lenses have indicated that fatigue failure of the septum conductor tube may be aided by some material degradation mechanism such as hydrogen embrittlement or stress corrosion cracking [1]. In order to protect the critical inner surface of the conductor tube from contaminants, an anodizing process is being investigated. It is hoped the anodized surface will provide a barrier to degradation and simplify assembly procedures. Tests are underway to gauge the effect of the coating on fracture toughness and fatigue endurance limit.

Geometrical Changes

Geometrical changes to the structural components are being considered to reduce stresses in critical locations. One obvious structural component is the septum conductor tube. Increasing its thickness may reduce stresses at the expense of higher temperatures in the lithium. Unfortunately, preliminary FEA results [2] indicate that temperatures in the lithium, during high gradient pulsing, near lithium's melting point (180.6 °C). Thus, increasing conductor tube wall thickness is not a viable option. Other changes, such as shape and size of lithium buffer regions are similarly being investigated.

FUTURE STUDIES

Figure 5 shows a conceptual design of a high gradient diffusion bonded Lens that incorporates some of the features described above. Also several improvements are being considered that improve efficiency, lower cost and increase quality (such as seal re-design and improvements to the lithium fill procedure).

Future research includes using FEA methods to tweak Lens geometry, fatigue testing of diffusion bonded and anodized Ti 10-2-3 samples, and diffusion bonding a YTZP insulator ring directly into the Lens assembly (bypassing costly machining steps). The small, proof-of-principle prototype Lens is currently undergoing final preparations for filling with lithium and should be on the test stand during summer '03. Hopefully lessons learned from building and testing it will provide us with the knowledge and confidence to design and build the full-size high gradient Collection Lens prototype this fall.

REFERENCES

[1] P. Hurh, "Examination Results of Failed Collection Lens Septa 20 and 21", Fermilab MSDNote #MSDN-ME-000022 (2002).

[2] P. Hurh & S. Tariq, "Comprehensive Electro-Magnetic, Thermal, and Structural Finite Element Analysis of the Lithium Collection Lens at the FNAL Antiproton Source", ROPB011,PAC 2003, Portland (2003).

BEAMLINE DESIGN FOR PARTICLE PRODUCTION EXPERIMENT, E907, AT FNAL*

C. Johnstone[#], C. Brown, D. Carey, M. Kostin, R. Raja, FNAL, Batavia, IL 60510, USA

E. Hartouni, LLNL, Livermore, CA 94551, USA

Abstract

Experiment 907 at Fermilab will be conducted in the Meson Center beam enclosure. The purpose of this experiment is to measure cross sections for hadron production from nuclear interactions using pions, kaons and proton beams in the momentum range from 5 to 120 GeV/c. Light to heavy targets will be used to study the scaling laws of hadronic fragmentation and light meson and baryon spectroscopy. Design aspects for the experiment's beamline are presented. The lattice, in particular the secondary beamline design, the primary target, and the collimation system are covered.

INTRODUCTION

MIPP (FNAL E-907) stands for Main Injector Particle Production Experiment. A low-cost experiment, it uses existing hardware to measure particle production off hydrogen and other nuclear targets including the NuMI targets, with excellent initial and final state particle identification. The resolution and statistics projected for the experimental data represent a significant improvement over existing measurements. Analysis of the experimental results will provide:

- A test of the accuracy of and energy range over which a general scaling law of fragmentation applies given each particle type,
- A measurement of particle production off NuMI targets with sufficient accuracy to predict the neutrino spectra at the near and far detectors in MINOS,
- A starting point for the study of the dynamics of non-perturbative QCD and its associated resonances,
- A better understanding of the propagation of particles in nuclei.
- Improvement in the predictions of atmospheric neutrino fluxes,
- Advance the design of accelerator-based neutrino factories,
- Improvement of hadronic shower models in collider simulation programs (GEANT and MARS, for example).

A key feature of this experiment is the high-precision identification of the produced particle species across the entire kinematic range that can be accessed using the 120-GeV primary proton beam from the Fermilab Main Injector. Precise particle identification is critical to accomplish the goals stated above. The experiment achieves nearly complete resolution for π, K, and p at a the secondary energy from 0.1-120 GeV/c by measuring energy loss in a TPC, threshold Cerenkov radiation combined with ring-imaged Čerenkov radiation, and time of flight.

Most the experimental beamtime will be spent in survey mode running. The secondary beamline (in Meson Center) will allow acquisition of data at one rigidity for K, and p simultaneously for one sign of the charge. The incident secondary beam species will be tagged by threshold Čerenkov counters upstream of the 1% interaction length experimental (or secondary) target. In 126 hours of beamtime, one million events will be acquired per incident particle species. The momentum range from 5-110 GeV/c will be scanned over a set of experimental targets that span the periodic table from hydrogen to lead.

Further primary data will be acquired at 120 GeV/c by directing the Main Injector primary beam directly onto the NuMI targets. In this way, the pion production spectrum can be measured to 1% across the entire range relevant for MINOS, which is 1-50 GeV/c. Since kaons are produced at approximately 10% of the rate for pions, and both exhibit a fairly flat longitudinal spectrum, particle identification across this momentum range is critical for the measurement.

THE PRIMARY AND SECONDARY BEAMLINES

The length available to the experiment for primary beam control and the secondary beamline totals only 128m, with 41m reserved for the threshold and ring-imaging Čerenkovs. Due to enclosure restrictions and the need for primary beamline magnets in this section (no superconducting magnets are used), the primary portion must remain at least 20 m long. Less than 100 meters is left to accommodate the necessary secondary line optics—optics appropriate for momentum selection and which also meet the beam envelope and divergence criteria for the experiment. A picture of the physical layout of both lines, plan and elevation view, is given in Figure 1.

Primary Beamline Layout

The primary beamline extends for well over a thousand meters through various beam splits back to the Main Injector. Control over primary beam characteristics is

established through a focusing quadrupole doublet and adjustable collimators located roughly 300 and 200 m upstream of the primary target, respectively. Intensity on

Beam Chambers
trims
Beam Cerenkovs
Quadrupole(4Q)
Quadrupole(3Q)
Dipole
Collimator

Beam Chambers
trims
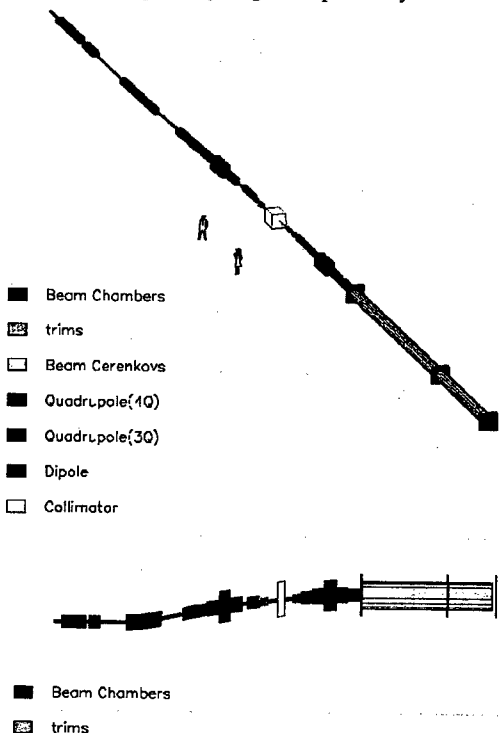
Figure 1. The plan and elevation view of the MIPP primary and secondary beamlines.

the primary target will be attenuated by adjusting both beam optics and the collimator aperture to achieve 10^{11} protons/spill, or less, with a spill occurring about every sec into this line from the Main Injector. Control over primary optics combined with collimator aperture is necessary for proper secondary beamline operation—a spot size of ±2 mm (95%) at the primary target must be maintained. (This requirement will be discussed further in the following section.) The primary line will be tuned and collimated accordingly to maintain a consistent spot size over a large range in primary intensity. The primary intensity will depend on the secondary beam energy and desired event rate.

Secondary Beamline

Several considerations challenged the design of the secondary beamline, a beamline which must accommodate both the demanded momentum resolution and the precision in particle identification. The former requires the momentum-dispersed beam size to be larger than the transverse beam size and the latter requires low divergence at the Čerenkov detectors. At the experimental target dispersion must be cancelled to contain the spot size on the secondary target and associated detectors.

The challenge in meeting the required momentum resolution arose from the fixed civil construction of the experimental and beamline enclosures. The primary and secondary beamlines are straight horizontally with only a slight increase in elevation at the experiment of 0.86 m relative to the primary beamline. Significant dipole bend fields, or weaker fields but longer distances, are required to produce significant separation of beam momenta. In the absence of either, only small separation of particles of different momentum can be achieved; in the case here only 0.3 m of vertical dispersion could be installed in the secondary line and still respect the length and height constraints. In order to make an accurate momentum cut, the transverse beam size must be smaller than the desired momentum resolution otherwise particles with momenta outside the cut overlap spatially. For this experiment a desired momentum resolution was needed of about 1%. When combined with the low value of dispersion (a 1% change in momentum represents only a 3 mm shift in the in particle coordinates), this implied the transverse beam size at the momentum cut or collimator must be less than or comparable to this shift. Hence, the beam spot size at this point must be ~3 mm across, which is less than or comparable to the primary target beam size. This criterion implies point to point focusing, or slight demagnification of the primary beam spot, further implying a strong sensitivity to the actual transverse size of the beam on the primary target.

Due to the limitations in length of the secondary beamline, the quadrupole focusing in the secondary line is strong and achromatic. With a focal length of only about 10 m at 100 GeV/c, most of the quadrupoles must operate at or near their peak fields to achieve the beam sizes depicted in Figure 2. The resulting large chromaticity of the line limits the momentum window to about 2-3% in practice.

Beamline Lattice Functions
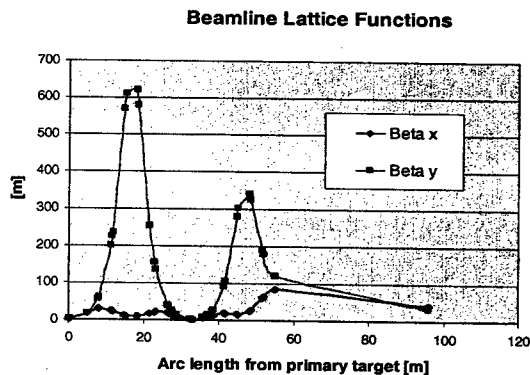
Figure 2. Beamline lattice functions: beam size is determined using an emittance of 3-5π mm-mr.

Accurate particle identification further restricted the divergence of the secondary beam to about 0.3-0.5 mr in the region of the Čerenkov. When coupled with a beam size at the experimental target of about 1 cm in radius, the beam emittance which produces an acceptable beam envelope is about 3-5π mm-mr. To restrict the beam

envelope it was found necessary to scrape the emittance of the secondary beam just after the primary target, and before the momentum collimator to this value. The effect of secondary absorbers was to reduce significantly the ratio of background to signal at the secondary target, although at a price of reduced secondary beam intensity. The results of extensive simulations of this beamline are given in the next section.

BEAMLINE SIMULATION

The primary and secondary beamline were designed using MAD[1] given the specific beam spot size at the primary target and a phase ellipse constrained by the needs of the experiment at the Čerenkov and secondary targets of 3-5π mm-mr. However, collimators, momentum selection and actual performance of the secondary line were simulated in the MARS code[2] using the primary beam distribution and secondary particle production. The secondary particle distribution is ray-traced through the entire beamline locating high loss points for radiation shielding design and showing the effect of collimation and the size and divergence of the beam as it progresses along the secondary line. This proved to be a very effective approach to verification of the optics design of the line. The histograms in Figure 4 show the performance of secondary beamline for a large momentum bite, and for a more restrictive one which involves additional phase space collimation.
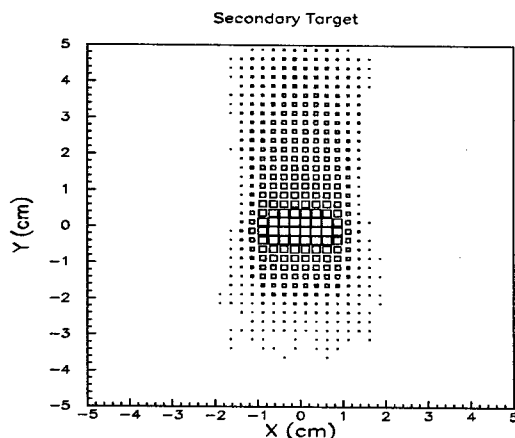
Figure 3. Beam profile on the 1-cm radius secondary target as simulated by MARS[2]

It is interesting to note the effect of a tighter momentum bite and scraping or secondary collimation of the beam to the design ellipse is to reduce the signal to background significantly at the expense of secondary intensity for a given primary intensity. Since we are not currently at intensity limits for the primary beam, more severe cuts are not a problem.
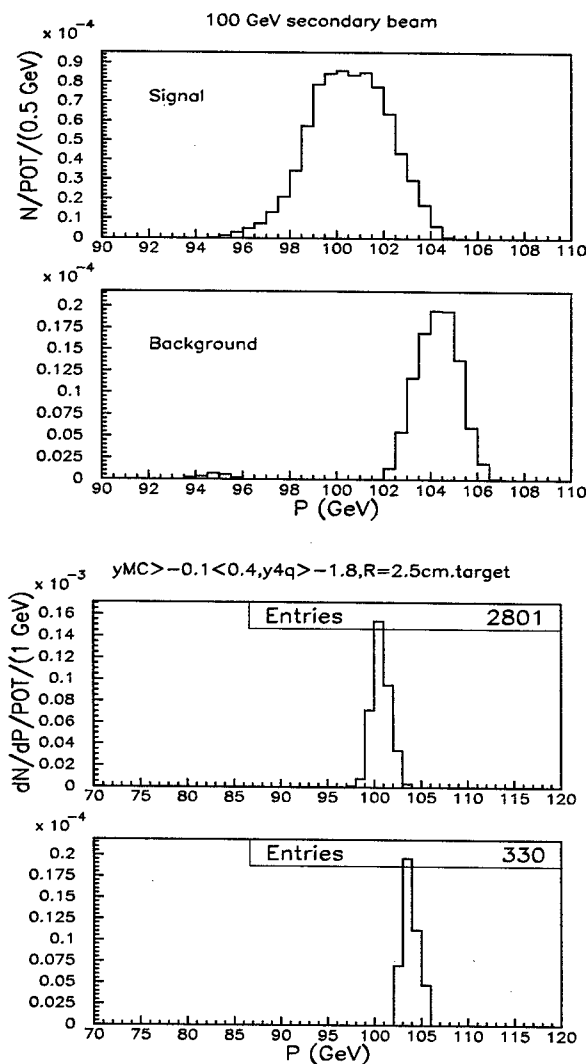
Figure 4. Histograms showing the performance of the secondary beamline and target for a ±5% dp/p at the momentum collimator: the signal and background events for a 1 cm radius detection area at the secondary target and no secondary collimation (8 x 10^{-4} signal protons and 10^{-4} background protons are detected for every proton on the primary target). The second set of histograms show a more restrictive, ±1% dp/p momentum cut, and additional collimation in the secondary line.

REFERENCES

[1] Hans Grote and F. Christoph Iselin, ``The MAD program "Methodical Accelerator Design", CERN/SL/90-13.

[2] N.V.~Mokhov, "The MARS Code System User's Guide", Fermilab-FN-628 (1995); N.V.~Mokhov, O.E.~Krivosheev, "MARS Code Status", Proc. Monte Carlo 2000 Conf., p. 943, Lisbon, October 23-26, 2000; Fermilab-Conf-00/181 (2000); http://www-ap.fnal.gov/MARS/.

Balbekov, V. 1751, 2014, 2017

Balkcum, A. 1144

Ball, M.J. 1996

Balleyguier, P. 2053, 2458, 2601, 2799

Bandelmann, R. 467

Bandura, L. 1999

Bane, K. 126, 3126, 3252

Banna, S. 722, 1879

Bao, X. 2357

Baptiste, K. 869, 1240, 1252

Bär, R. 694

Barber, D.P. 372

Barletta, W.A. 186, 923

Barlow, D. 702, 1664

Barnard, J.J. 1521, 1990, 2658

Barnes, B. 1736

Barnes, C.D. 1530, 1933, 2101

Barnes, M.J. 1162

Barnes, P. 1309, 1323

Barni, D. 1341, 1506

Barov, N. 1870, 2682

Barr, D. 2512

Barr, G. 1987

Barstow, B. 192, 1317, 1320

Barsz, T. 2029

Bartolini, R. 914, 2077, 3285

Barton, D. 1637

Barty, C.P.J. 95

Baskiewicz, M. 302

Batchelor, K. 541

Batrakov, A. 250

Batygin, Y.K. 2751, 3548

Baudrenghien, P. 1718, 3050

Bauer, P. 1730, 1972, 3359

Bauer, S. 1410, 2887

Baum, D. 2527

Baynham, D.E. 1987

Bazarov, I. 192, 842, 848, 1201, 1317, 1323, 2062

Beard, K. 195, 332, 1104, 1575

Beaudoin, B. 426, 2312, 2571

Beche, J.-F. 2530

Bechstedt, U. 598, 3428

Bechtold, A. 1062

Beck, M. 2189

Beckert, K. 434

Beckman, L. 3389

Beczek, K. 2038

Beebe, E. 89

Beebe-Wang, J. 51, 1706

Beinhauer, W. 3551

Belgroune, M. 896

Bellavia, S. 1542

Bellenger, D.W.J. 1527

Beller, P. 434

Bellodi, G. 1527

Bellomo, P. 235

Bellucci, S. 917, 986

Beloglasov, V.I. 2878

Belohrad, D. 2461

Belomestnykh, S. 192, 1198, 1201, 1306, 1317, 1323, 1326, 1329, 1410, 1437, 2059, 3347

Beltran, C. 326, 3086

Bender, H. 558

Benedetti, G. 366, 2279, 2945

Benedetto, E. 1727, 3053

Benedikt, M. 1548

Bengtsson, J. 195

Benjamin, J. 1715

Bennett, J.R.J. 1527

Bennett, S.L. 189

Ben-Zvi, I. 39, 92, 944, 1300, 1909, 2005, 3186

Berden, G. 519

Berenc, T. 1736, 3362

Berg, J.S. 1804, 1816, 2002, 2210, 2213, 2216, 2219, 3413, 3485

Berg, S. 1416, 1422, 2029, 2038

Berg, W.J. 2417, 2420

Bergqvist, M. 2321

Berio, R. 989

Berkaev, D.E. 372

Berkvens, P. 854

Berman, L. 241

Bernal, S. 426, 1673, 1676, 2312, 2571, 2574, 2577, 2673

Bernard, A. 195

Bernardin, J. 1461

Bernaudin, P.-E. 2799

Bernstein, L. 989

Bertolucci, S. 3285

Bertrand, P. 2802, 3488

Bessonov, E. 1963

Bhashyam, S. 1966

Bhat, C.M. 514, 1769, 2345, 2348, 3180

Bhatt, R. 2643

Biagini, M. 366, 914, 2077, 2279, 2297, 2300, 2945, 3285

Biallas, G. 2123, 2135, 2183, 2186, 2189

Biarrotte, J.L. 1303, 2802

Biasci, J.C. 854

Bieler, T.R. 1359

Bieniosek, F.M. 98, 275, 312, 536, 1518, 2524, 2619, 3297

Bierwagen, J. 1353

Bilderback, D. 192

Bilheux, H. 998

Billen, J. 1461, 1515, 2844, 3518, 3521

Biller, E.Z. 1605, 2878

Billing, M. 3059

Binello, S. 1542, 1703

Bini, S. 917

Binkley, M.E. 2497

Biocca, A. 3374

Birkel, I. 893, 3273, 3276

Biryukov, V.M. 917, 986, 1655, 1691

Biscardi, R. 241

Biscari, C. 335, 366, 684, 2279, 2742, 2945, 3285

Bishofberger, K. 57, 1778, 1781

Bisognano, J.J. 3147

Bizen, T. 487

Björkhage, M. 1590

IV

Elioff, T. 235
Elleaume, P. 854
Ellis, S. 2841
Emamian, M. 2273
Emery, L. 256, 283, 833, 2261, 2330, 2423, 2438, 3461, 3464, 3470, 3473, 3476
Emhofer, S. 2869, 2872
Emma, P. 211, 423, 914, 926, 965, 1530, 1933, 3126, 3129, 3138
Endo, K. 1071, 1074
Eng, W. 743, 770, 1542, 2144
England, R.J. 3258
Enomoto, A. 2838
Erdelyi, B. 1760, 1772, 3542
Erdem, O. 1933
Eremeev, G. 1312
Erickson, R. 2297
Eriksson, L. 644
Eriksson, M. 2318, 2321
Ernst, D. 2174
Erokhin, A. 2769
Errede, D. 983, 1999
Esarey, E. 719, 734, 1885
Escallier, J. 164
Eschke, J. 467
Espinoza, C. 1664
Esposito, A. 3285
Esser, F.M. 598
Estrada, J. 1763
Evangelakis, G. 1709
Evans, I. 235
Evans, L.R. 19
Evans, R. 1485
Eversole, S. 558
Eylon, S. 98, 558, 1171, 2533, 2616, 2619, 2622, 2625, 2628, 2646, 3098
Ezura, E. 860, 1228
Faatz, B. 467
Fabbricatore, P. 1987
Fabris, A. 878
Facco, A. 470
Falabella, S. 563

Falce, L. 1113, 1116
Faltens, A. 536, 1990
Fan, L. 815
Fan, M. 1560, 3506, 3509
Fan, T.C. 1041, 1047
Fang, J.-M. 1882, 1924
Fang, S. 1285, 1404
Fang, Z. 1071, 1074
Fann, C.-S. 767
Fantini, A. 3285
Farinon, S. 1987
Farkhondeh, M. 956, 959, 980, 2324
Farrell, J.P. 541
Farrow, R.C. 189
Fartoukh, S. 2225
Farvacque, L. 854, 3189
Faucett, J. 2354
Faure, J. 1840
Faus-Golfe, A. 2240
Favale, A. 92
Fawley, W. 186, 558, 923, 959, 3098
Fedotov, A. 39, 117, 383, 1572, 2589, 2592, 2598, 3032
Fedurin, M. 1053, 2382, 2892
Feher, S. 1969
Feigerle, C.S. 617
Feikes, J. 845, 3023
Felden, O. 598
Feldman, D. 426, 3323
Feldman, R. 426
Fellenz, B. 2348, 2491
Ferguson, P. 1110
Ferianis, M. 214
Ferioli, G. 307
Fernow, R.C. 2002
Ferracin, P. 170, 1984
Ferrari, A. 45, 684
Ferrario, M. 467, 914, 2077, 2080, 2730, 3285, 3548
Fessenden, T.J. 2533
Fessia, P. 1942
Filhol, J.-M. 229, 1332
Filip, C.V. 1873

Findlay, A. 2461
Findlay, D.J.S. 2542
Finley, D. 1207, 1210, 1813
Fiorito, R. 1497, 2712
Fischer, R. 2476
Fischer, W. 51, 54, 135, 476, 794, 797, 1625, 1697, 1706, 1754, 2222, 2228, 3026, 3029
Fisher, A. 2285, 2297, 2300
Fisher, M. 887, 2303
Fittinghoff, D.N. 95
Fitzgerald, D. 508, 2521, 3089, 3455
Fitzgerald, J. 1781
Flanagan, J.W. 2503
Flanz, J. 690
Fliflet, A.W. 1128
Fliller III, R. 272, 1685, 1691, 1706, 2904
Floettmann, K. 965, 2114, 3500, 3548
Flora, F. 3285
Flora, R. 2491
Foley, M. 983, 1213
Folwell, N. 2664
Fong, K. 601, 1285, 1404, 1488
Fontenille, A. 2799
Fontus, R. 138
Forchi', V. 3395
Ford, R. 1652
Forest, E. 397, 1023, 2249
Foster, G.W. 323, 1649, 1766
Fox, B. 1688
Fox, J. 2297, 2300, 3141, 3389
Fox, W. 1461, 2841
Frak, B. 1715
Franchetti, G. 129, 589
Francis, V. 1029
Franczak, B. 589
Franklin, W.A. 2324
Franzke, B. 434
Frawczyk, F.L. 2083
Frayer, D. 558

Gorelov, D. 2805, 2849, 2972

Gössel, A. 467, 1086, 1392

Gottschalk, S.C. 1909

Gould, H. 1837

Gould, O. 794, 3282

Gounder, K. 2928, 3434, 3437

Gourlay, S.A. 42, 170, 1032, 1984

Grabosch, H.J. 2114

Graef, H.-D. 3551, 3569

Graham, D. 89

Granata, V. 1945

Granatstein, V. 1140

Grau, M. 2444

Graves, W.S. 217, 329, 956, 959, 980, 1192

Gray, J.W. 1527

Green, M.A. (LBNL) 186, 1834, 1987

Green, M.A. (SRC) 887, 929

Greenwald, Z. 2056

Greenway, W. 1171

Grelick, A. 1416, 1422, 2029, 2038

Grenoble, C. 457

Gribble, R.F. 553

Grice, W. 1524, 2706

Griep, B. 2887

Grier, D. 1724

Griffin, J. 1554, 2922

Grimm, T. 1350, 1353, 1356, 1359, 1362, 1407, 2849, 2972

Grippo, A. 1485

Grisham, L. 2661, 3309

Grishin, V. 1007, 1010

Grote, D.P. 70, 275, 1518, 2637, 2673

Grote, H. 3497

Gruber, P. 1183, 1413

Gruner, S. 192

Gu, A. 2580

Guan, C.Y. 815

Guenzel, T. 854

Guerra, A. 195

Guethlein, G. 563

Guetz, A. 2664

Guidi, V. 917, 986, 1655

Guiducci, S. 366, 914, 2077, 2279, 2945, 3285

Guignard, G. 665

Guilhem, D. 2601

Guimbal, Ph. 2053, 2458

Gullotta, J. 54, 794, 1425, 2444, 2694

Gung, C. 1990

Gunther, K. 1113, 1116

Gupta, R. 42, 164, 1748, 1936, 1939

Guy, F.W. 2889

Gyr, M. 1646

Ha, K.M. 2857

Ha, W. 1861

Haase, M. 1724

Haber, I. 426, 511, 536, 1673, 2312, 2574, 2577, 2673, 3156, 3297

Haberer, Th. 694

Habs, D. 112, 2869, 2872

Hacker, K. 423

Hafalia, R.R. 170, 1984

Hafizi, B. 716, 1846

Hafz, N. 1849

Haga, K. 860

Hahn, A. 2488, 2491

Hahn, H. 39, 1625, 1706, 2147, 3035

Hahto, S.K. 3309

Hahto, S.T. 3309

Haimson, J. 2095

Hajima, R. 3443, 3446, 3449

Halaxa, E. 3297, 3300

Halbritter, J. 1374

Hall, R.P. 3300

Hamatsu, R. 2709

Hamm, R.W. 1563

Hammons, L. 1542, 1691

Han, J.H. 2114

Han, J.M. 1222, 2539, 2832, 2857, 2884

Han, S.H. 2539, 2832

Han, Y.J. 1470, 2857, 3114, 3383

Hanaki, H. 2838

Hanft, R. 1730, 1972

Hanna, B.M. 2497

Hanna, S.M. 1077

Hannink, R. 2625

Hannon, F.E. 1029

Hansen, R.W.C. 929

Hansen, S. 323

Hara, M. 250

Hara, T. 487

Harada, K. 857, 860, 3201

Hardek, T. 553, 1095, 1168, 1458, 1461

Hardekopf, R. 1461, 1661

Harding, D. 1730, 2168

Hardy, L. 854

Harkay, K. 508, 592, 2438, 3008, 3011, 3014, 3183

Harris, J. 426, 2312, 2571, 2577

Harrison, J. 558, 1237

Harrison, M. 39, 42, 164, 1748

Hartemann, F. 95, 938

Hartill, D. 1309, 2339

Hartline, R.E. 1792

Hartman, S. 752, 2270, 2273, 2482

Hartouni, E. 1446

Hartrott, M.v. 2114

Hartung, W. 1350, 1353, 1356, 1362, 1395, 2849, 2972

Harvey, M. 1715

Harwood, L. 586, 992, 1098

Hasegawa, K. 1509

Hashemi, H. 238

Hashiguchi, E. 1978

Hashiguchi, Y. 902, 3270

Hassanein, A. 1180

Hassanpour, N. 3389

Hassanzadegan, H. 238

Hassenzahl, W. 2162

Hatano, T. 1165

Hauviller, C. 1434

Hawkey, T. 547, 1500

McDonald, K.T. 1628, 1631, 1634, 1709

McGahern, W. 2390

McGee, M. 2020

McIntosh, P. 235, 1273, 3141

McInturff, A.D. 170, 1984

McIntyre, G. 39, 1691, 2904

McKinney, W. 869

McManamy, T. 1572

McMichael, G.E. 592, 1159

McNeil, B.W.J. 189, 950, 953

Mc Nerney, A. 746, 1542

Mead, J. 524, 2444, 2697

Mecklenburg, B. 2095

Medici, G. 3285

Medjidzade, V. 167, 2399

Medvedko, A. 2769

Medvedko, E. 235, 761

Meidinger, A. 558

Meinke, R.B. 1990, 1996

Meisner, K. 1736, 1769

Melin, G. 81

Meller, R.E. 2339

Meng, W. 1637, 2144, 2147, 2159, 2598

Meot, F. 444

Merl, R. 2354, 2515, 2518

Merminga, L. 192, 195, 332

Merrill, F. 702

Mertens, V. 1721

Mertins, H.-C. 836

Merz, W. 749

Messina, G. 3285

Meth, M. 1195

Métral, E. 129, 388, 2913, 2916, 3047

Métral, G. 388, 2913, 2916

Meyer, A. 1542

Meyer, B.J. 73

Meyer, F.W. 998

Meyer, T.S. 2491

Meyer Sr., R.E. 2485

Mezentsev, N. 250

Mezi, L. 914, 3285

Mi, C. 2447

Mi, J. 550, 1640, 2147

Michalek, W. 2029

Michelato, P. 1506, 2071, 2114

Michelotti, L. 1557

Michnoff, R. 1706, 2691, 3026

Miglionico, G. 2150

Migliorati, M. 2077, 3285

Mihalcea, D. 2682

Mihara, T. 2198

Mikado, T. 713, 971, 974

Mikhailichenko, A. 167, 1822, 1825, 1828, 1954, 1957, 1960, 1963, 2399, 2781, 2784, 3350

Mikhailov, S.F. 391, 752, 2273, 2276, 2482

Milani, D. 1945

Milardi, C. 366, 2279, 2742, 2945, 3285

Miles, J. 1942

Miller, R.H. 1264, 2760, 2763

Miller, T. 2382, 2892

Mills, G.D. 998

Milner, R. 956, 959, 980

Miltchev, V. 2114

Milton, S.V. 905, 1813

Minagawa, Y. 860, 3077, 3080, 3261

Minehara, E.J. 3443, 3446, 3449

Minervini, J. 1990

Miram, G. 1110, 1113, 1116, 1137, 1140, 1142, 3312

Mishra, C.S. 1, 1649, 1766, 2928, 3434, 3437, 3440

Mistry, N.B. 167, 2399

Mitchell, D. 1213

Mitra, A. 601

Mitrochenko, V.A. 1107, 3303

Mitrochenko, V.V. 1605, 2098, 2878

Mitsuhashi, T. 860, 2503, 2506, 3204, 3207

Miura, T. 2509, 2610

Miyajima, T. 860, 2171

Mizobata, M. 1071

Mizrahi, A. 722, 728

Mizuhara, A. 1142

Mizuhara, M. 1110, 1113, 1116, 1119

Modena, M. 1942

Moffitt, J.R. 2473

Mokhov, N.V. 42, 983, 1503, 1733, 1742, 1745, 1748, 2739, 2936

Möller, W.-D. 467

Molvik, A.W. 132, 312, 536

Monaco, L. 1506, 2071

Moncton, D.E. 959, 980

Monroe, J. 1587, 1652

Monroy, M. 1464, 3377

Montag, C. 51, 135, 1300, 1431, 1694, 1697, 1700, 1706, 2005, 2011, 2691, 2907, 3026, 3186

Montoya, D.I. 1341

Montoya, N. 558

Moog, E.R. 156, 1020

Moore, C. 1652, 2934

Moore, R. 1751, 1754, 2497

Moore, T. 167

Moraes, J.S. 2990

Morcombe, P. 752

Moretti, A. 1183, 1246, 1792, 2023

Morgan, G. 1936

Morgan, J. 641, 1443

Mori, W.B. 731, 1530, 1858, 1864, 1870, 1933, 3174

Mori, Y. 1231, 1234, 1679, 3413, 3452

Moricciani, D. 3285

Morishita, T. 2829

Moritz, G. 589, 2162

Moritz, L. 638

Morley, K. 702

Morris, C. 702

Morris, J. 746, 1542, 1715

Morris, W.A. 1527

Morse, E.C. 3291

Rubin, D.L. 1023, 2056, 2267, 3425

Rudolph, K. 2869, 2872

Rudychev, V. 1619

Ruegg, R. 638, 1584

Ruggiero, A.G. 1637, 2793, 2796

Ruggiero, F. 42, 45, 123, 1727

Ruggiero, R. 1748

Ruggles, S.C. 1168

Ruland, R. 2769

Rumolo, G. 123, 1727, 2234, 2607, 3038, 3041, 3044, 3053

Rusek, A. 1542

Rusnak, B. 989, 1347

Russell, A. 1652

Russell, S. 977

Russo, T. 1545, 3422

Rust, K. 550, 770

Rust, W.W. 635

Ruth, R.D. 1264

Ryan, J. 1542, 2595

Rybarcyk, L.J. 1092, 1566, 3086

Ryne, R.D. 1509, 2954, 3401

Saban, R. 1945

Sabbi, G. 42, 170, 536, 1032, 1521, 1984, 1990

Sabol, D. 2399

Saeki, H. 250

Saewert, G. 1781, 2020

Safranek, J. 235, 890, 3213

Sagan, D. 192, 848, 1023, 2267

Sahuquet, P. 1303

Saigusa, M. 2829

Saino, K. 487

Saito, K. 462

Sajaev, V. 417, 905

Sakai, H.R. 530, 857

Sakai, I. 1512, 1679, 3452

Sakamoto, Y. 860

Sakanaka, S. 860, 1228, 3207, 3365

Sakuda, M. 1807

Sakumi, A. 312

Saleh, N. 1921

Sanchez, B.J. 2515

Sanchez, M. 558

Sandberg, J. 550, 571, 743, 746, 770, 1640, 2144, 2147

Sanderson, D. 138

Sandner, W. 836, 2114

Sanelli, C. 366, 2279, 2742, 3285

Sanfilippo, S. 173

Sannibale, F. 863, 1658, 2527

Santucci, J. 2682

Sapozhnikov, L. 3389

Sarraf, R.H. 238

Sasaki, S. (ANL) 2261

Sasaki, S. (SPring-8) 250, 782

Sato, H. 568, 755, 1165, 1807, 1981

Sato, M. 860

Sato, Y. (IU) 3240

Sato, Y. (KEK) 1679, 2509, 3452

Satogata, T. 51, 54, 272, 278, 405, 1697, 1706, 1712, 1715, 2204, 2207, 2697, 2901, 3026, 3482

Satoh, M. 533, 860, 3368

Sauer, A. 1335, 2820, 2942

Saugnac, H. 1303

Saunders, A. 702

Saunders, J. 2860

Savage, R. 2390

Savalle, A. 2802

Savary, F. 1942

Savatteri, S. 746

Sawamura, M. 3443, 3446, 3449

Sazawa, S. 2829

Scaduto, J. 39, 92, 1631

Scandale, W. 173, 986, 1655

Scanlan, R.M. 170, 1032, 1984

Scarlett, C. 3255

Scarpine, V. 2414, 2494, 3062

Scarvie. T. 869, 2527, 3374

Schächter, L. 722, 728, 1879

Schaerf, C. 3285

Schaetz, T. 112

Schaller, S. 2354

Schamel, H. 3029

Schappert, W. 323, 2494

Schauer, M. 558

Scheer, M. 836

Scheidt, K. 854

Scheitrum, G. 3312, 3315

Schellong, B. 1948

Schempp, A. 598, 1062, 1622, 2817, 2823

Schilcher, T. 3386

Schimizu, J. 250

Schindl, K. 1682

Schirm, K.-M. 1948

Schlabach, P. 1730, 1969, 1972

Schlarb, H. 423, 467, 2074, 2730, 3126, 3129

Schlitt, B. 694, 1062

Schlott, V. 3386

Schlueter, R. 1032, 3458

Schmalzle, J. 1939, 2162

Schmekel, B.S. 375

Schmerge, J.F. 2104, 3216

Schmidt, C.W. 2020

Schmidt, F. 1754, 1757, 2207, 2228, 2231, 3494, 3497

Schmidt, P. 1948

Schmidt, R. 45, 1945

Schmidt-BÅcking, H. 1622

Schmidts, F. 1775

Schmor, P. 6, 439, 1584

Schnase, A. 598, 1216, 1234, 2817, 3428

Schneider, H. 598, 3428

Schneider, W.J. 2863

Schnitter, U. 2201

Schoenlein, R. 186, 2408, 2530

Schrage, D.L. 920, 977, 1341, 1344, 1661, 2083, 2790